RECENT ADVANCES in SYSTEMS

Proceedings of the 19th International Conference on Systems
(part of CSCC '15)

Zakynthos Island, Greece
July 16-20, 2015

RECENT ADVANCES in SYSTEMS

Proceedings of the 19th International Conference on Systems (part of CSCC '15)

Zakynthos Island, Greece
July 16-20, 2015

All papers of the present volume were peer reviewed by no less than two independent reviewers. Acceptance was granted when both reviewers' recommendations were positive.

Series: Recent Advances in Electrical Engineering Series | 52

ISSN: 1790-5117
ISBN: 978-1-61804-321-4

RECENT ADVANCES in SYSTEMS

Proceedings of the 19th International Conference on Systems (part of CSCC '15)

Zakynthos Island, Greece
July 16-20, 2015

Organizing Committee

Editor:
Prof. Valeri Mladenov, Technical University of Sofia, Bulgaria

Associate Editors:
Prof. Dr. Eduardo Mario Dias
Prof. Vladimír Vašek
Prof. Dora Foti
Prof. Dorota Jelonek
Prof. Nikos Bardis
Assistant Prof. Mikhail M. Kucherov
Prof. Rodolfo A. Fiorini
Dr. Evgenia Adamopoulou
Dr. Konstantinos Demestichas

Organizing Committee:
Prof. Kleanthis Psarris, The City University of New York, USA (General Chair)
Prof. Pierre Borne, IEEE France Section Chair, IEEE Fellow, Ec Centr de Lille, France (General Chair)
Prof. Panos M. Pardalos, University of Florida, USA (Co-Chair)
Prof. George Vachtsevanos, Georgia Institute of Technology, Atlanta, Georgia, USA (Co-Chair)
Prof. Tadeusz Kaczorek, IEEE Fellow, Warsaw University of Technology, Poland (Co-Chair)
Prof. Nikos Mastorakis, Technical University of Sofia, Bulgaria (Program Chair)
Prof. Branimir Reljin, University of Belgrade, Belgrade, Serbia (International Liaisons)
Prof. Aida Bulucea, University of Craiova, Craiova, Romania (Publicity Chair)
Prof. Valeri Mladenov, Technical University of Sofia, Bulgaria (Publications Chair)
Prof. Imre Rudas, Obuda University, Budapest, Hungary (Tutorials Chair)
Prof. Vladimir Vasek, Tomas Bata University, Zlin, Czech Republic (Special Sessions Chair)
Prof. Anca Croitoru, Al.I. Cuza University, Iasi, Romania (Workshops Chair)

Steering Committee:
Prof. Yuriy S. Shmaliy, IEEE Fellow, Universidad de Guanajuato, Mexico
Prof. Alaa Khamis, IEEE Robotics and Automation Egypt-Chapter Chair, Egypt
Prof. Ioannis Stathopulos, Technical University of Athens, Greece
Prof. Charalambos Arapatsakos, University of Thrace, Greece
Prof. Fragkiskos Topalis, Technical University of Athens, Greece
Prof. Klimis Ntalianis, Technological Educational Institute of Athens, Greece
Prof. Eduardo Mario Dias, University of Sao Paulo, Brazil
Prof. Miroslav Voznak, VSB-Technical University of Ostrava, Czech Republic
Prof. Abdel-Badeeh M. Salem, Ain Shams University, Cairo, Egypt
Prof. Nikolaos Bardis, M.Inst. of Univ. Educ. (ASEI), Hellenic Army Academy, Athens, Greece
Prof. Antoanela Naaji, Vasile Goldis Western University Arad, Romania
Prof. Elena Zamiatina, Perm State University, Perm Krai, Russia
Prof. Pan Agathoklis, University of Victoria, Canada
Prof. George Tsekouras, M.Inst. of Univ. Educ. (ASEI), Hellenic Naval Academy, Athens, Greece
Prof. Claudio Talarico, Gonzaga University, Spokane, USA

International Scientific Committee:
Prof. Lotfi Zadeh (IEEE Fellow, University of Berkeley, USA)
Prof. Leon Chua (IEEE Fellow, University of Berkeley, USA)
Prof. Michio Sugeno (RIKEN Brain Science Institute (RIKEN BSI), Japan)
Prof. Dimitri Bertsekas (IEEE Fellow, MIT, USA)
Prof. Demetri Terzopoulos (IEEE Fellow, ACM Fellow, UCLA, USA)
Prof. Georgios B. Giannakis (IEEE Fellow, University of Minnesota, USA)

Prof. Abraham Bers (IEEE Fellow, MIT, USA)
Prof. Brian Barsky (IEEE Fellow, University of Berkeley, USA)
Prof. Aggelos Katsaggelos (IEEE Fellow, Northwestern University, USA)
Prof. Josef Sifakis (Turing Award 2007, CNRS/Verimag, France)
Prof. Hisashi Kobayashi (Princeton University, USA)
Prof. Kinshuk (Fellow IEEE, Massey Univ. New Zeland),
Prof. Leonid Kazovsky (Stanford University, USA)
Prof. Narsingh Deo (IEEE Fellow, ACM Fellow, University of Central Florida, USA)
Prof. Kamisetty Rao (Fellow IEEE, Univ. of Texas at Arlington,USA)
Prof. Anastassios Venetsanopoulos (Fellow IEEE, University of Toronto, Canada)
Prof. Steven Collicott (Purdue University, West Lafayette, IN, USA)
Prof. Nikolaos Paragios (Ecole Centrale Paris, France)
Prof. Nikolaos G. Bourbakis (IEEE Fellow, Wright State University, USA)
Prof. Stamatios Kartalopoulos (IEEE Fellow, University of Oklahoma, USA)
Prof. Irwin Sandberg (IEEE Fellow, University of Texas at Austin, USA),
Prof. Michael Sebek (IEEE Fellow, Czech Technical University in Prague, Czech Republic)
Prof. Hashem Akbari (University of California, Berkeley, USA)
Prof. Lei Xu (IEEE Fellow, Chinese University of Hong Kong, Hong Kong)
Prof. Paul E. Dimotakis (California Institute of Technology Pasadena, USA)
Prof. Martin Pelikan (UMSL, USA)
Prof. Patrick Wang (MIT, USA)
Prof. Wasfy B Mikhael (IEEE Fellow, University of Central Florida Orlando,USA)
Prof. Sunil Das (IEEE Fellow, University of Ottawa, Canada)
Prof. Nikolaos D. Katopodes (University of Michigan, USA)
Prof. Bimal K. Bose (Life Fellow of IEEE, University of Tennessee, Knoxville, USA)
Prof. Janusz Kacprzyk (IEEE Fellow, Polish Academy of Sciences, Poland)
Prof. Sidney Burrus (IEEE Fellow, Rice University, USA)
Prof. Biswa N. Datta (IEEE Fellow, Northern Illinois University, USA)
Prof. Mihai Putinar (University of California at Santa Barbara, USA)
Prof. Wlodzislaw Duch (Nicolaus Copernicus University, Poland)
Prof. Michael N. Katehakis (Rutgers, The State University of New Jersey, USA)
Prof. Pan Agathoklis (Univ. of Victoria, Canada)
Dr. Subhas C. Misra (Harvard University, USA)
Prof. Martin van den Toorn (Delft University of Technology, The Netherlands)
Prof. Malcolm J. Crocker (Distinguished University Prof., Auburn University,USA)
Prof. Urszula Ledzewicz, Southern Illinois University , USA.
Prof. Dimitri Kazakos, Dean, (Texas Southern University, USA)
Prof. Ronald Yager (Iona College, USA)
Prof. Athanassios Manikas (Imperial College, London, UK)
Prof. Keith L. Clark (Imperial College, London, UK)
Prof. Argyris Varonides (Univ. of Scranton, USA)
Dr. Michelle Luke (Univ. Berkeley, USA)
Prof. Patrice Brault (Univ. Paris-sud, France)
Prof. Jim Cunningham (Imperial College London, UK)
Prof. Philippe Ben-Abdallah (Ecole Polytechnique de l'Universite de Nantes, France)
Prof. Ichiro Hagiwara, (Tokyo Institute of Technology, Japan)
Prof. Akshai Aggarwal (University of Windsor, Canada)
Prof. Ulrich Albrecht (Auburn University, USA)
Prof. Alexey L Sadovski (IEEE Fellow, Texas A&M University, USA)
Prof. Amedeo Andreotti (University of Naples, Italy)
Prof. Ryszard S. Choras (University of Technology and Life Sciences Bydgoszcz, Poland)
Prof. Remi Leandre (Universite de Bourgogne, Dijon, France)
Prof. Moustapha Diaby (University of Connecticut, USA)
Prof. Brian McCartin (New York University, USA)

Additional Reviewers

Bazil Taha Ahmed	Universidad Autonoma de Madrid, Spain
James Vance	The University of Virginia's College at Wise, VA, USA
Sorinel Oprisan	College of Charleston, CA, USA
M. Javed Khan	Tuskegee University, AL, USA
Jon Burley	Michigan State University, MI, USA
Xiang Bai	Huazhong University of Science and Technology, China
Hessam Ghasemnejad	Kingston University London, UK
Angel F. Tenorio	Universidad Pablo de Olavide, Spain
Yamagishi Hiromitsu	Ehime University, Japan
Imre Rudas	Obuda University, Budapest, Hungary
Takuya Yamano	Kanagawa University, Japan
Abelha Antonio	Universidade do Minho, Portugal
Andrey Dmitriev	Russian Academy of Sciences, Russia
Valeri Mladenov	Technical University of Sofia, Bulgaria
Francesco Zirilli	Sapienza Universita di Roma, Italy
Ole Christian Boe	Norwegian Military Academy, Norway
Masaji Tanaka	Okayama University of Science, Japan
Jose Flores	The University of South Dakota, SD, USA
Kazuhiko Natori	Toho University, Japan
Matthias Buyle	Artesis Hogeschool Antwerpen, Belgium
Frederic Kuznik	National Institute of Applied Sciences, Lyon, France
Minhui Yan	Shanghai Maritime University, China
Eleazar Jimenez Serrano	Kyushu University, Japan
Konstantin Volkov	Kingston University London, UK
Miguel Carriegos	Universidad de Leon, Spain
Zhong-Jie Han	Tianjin University, China
Francesco Rotondo	Polytechnic of Bari University, Italy
George Barreto	Pontificia Universidad Javeriana, Colombia
Moran Wang	Tsinghua University, China
Alejandro Fuentes-Penna	Universidad Autónoma del Estado de Hidalgo, Mexico
Shinji Osada	Gifu University School of Medicine, Japan
Kei Eguchi	Fukuoka Institute of Technology, Japan
Philippe Dondon	Institut polytechnique de Bordeaux, France
Dmitrijs Serdjuks	Riga Technical University, Latvia
Deolinda Rasteiro	Coimbra Institute of Engineering, Portugal
Stavros Ponis	National Technical University of Athens, Greece
Tetsuya Shimamura	Saitama University, Japan
João Bastos	Instituto Superior de Engenharia do Porto, Portugal
Genqi Xu	Tianjin University, China
Santoso Wibowo	CQ University, Australia
Tetsuya Yoshida	Hokkaido University, Japan
José Carlos Metrôlho	Instituto Politecnico de Castelo Branco, Portugal

Table of Contents

ISBN: 978-1-61804-321-4

Plenary Lecture 1

Error Estimation in the Decoupling of Ill-Defined and/or Perturbed Nonlinear Processes

Professor Pierre Borne (IEEE Fellow)
Co-authors Amira Gharbi, Mohamed Benrejeb
Centre de Recherche en Informatique Signal et Automatique de Lille, CRIStAL
Ecole Centrale de Lille
France
E-mail: pierre.borne@ec-lille.fr

Abstract: This lecture deals with the definition of the attractors characterizing the precision of decoupling control laws for a nonlinear process in presence of uncertainties and/or bounded perturbations. This approach is based on the use of aggregation techniques and the definition of a comparison system of the controlled process.

Brief Biography of the Speaker: Pierre BORNE received the Master degree of Physics in 1967 and the Master of Electrical Engineering, the Master of Mechanics and the Master of Applied Mathematics in 1968. The same year he obtained the Diploma of "Ingenieur IDN" (French "Grande Ecole"). He obtained the PhD in Automatic Control of the University of Lille in 1970 and the DSc in physics of the same University in 1976. Dr BORNE is author or co-author of about 200 Publications and book chapters and of about 300 communications in international conferences. He is author of 18 books in Automatic Control, co-author of an english-french, french-english « Systems and Control » dictionary and co-editor of the "Concise Encyclopedia of Modelling and Simulation" published with Pergamon Press. He is Editor of two book series in French and co-editor of a book series in English. He has been invited speaker for 40 plenary lectures or tutorials in International Conferences. He has been supervisor of 76 PhD Thesis and member of the committee for about 300 doctoral thesis . He has participated to the editorial board of 20 International Journals including the IEEE, SMC Transactions, and of the Concise Subject Encyclopedia . Dr BORNE has organized 15 international conferences and symposia, among them the 12th and the 17 th IMACS World Congresses in 1988 and 2005, the IEEE/SMC Conferences of 1993 (Le Touquet – France) and of 2002 (Hammamet - Tunisia) , the CESA IMACS/IEEE-SMC multiconferences of 1996 (Lille – France) , of 1998 (Hammamet – Tunisia) , of 2003 (Lille-France) and of 2006 (Beijing, China) and the 12th IFAC LSS symposium (Lille France, 2010) He was chairman or co-chairman of the IPCs of 34 international conferences (IEEE, IMACS, IFAC) and member of the IPCs of more than 200 international conferences. He was the editor of many volumes and CDROMs of proceedings of conferences. Dr BORNE has participated to the creation and development of two groups of research and two doctoral formations (in Casablanca, Morocco and in Tunis, Tunisia). twenty of his previous PhD students are now full Professors (in France, Morocco, Tunisia, and Poland). In the IEEE/SMC Society Dr BORNE has been AdCom member (1991-1993 ; 1996-1998), Vice President for membership

ISBN: 978-1-61804-321-4

(1992-1993) and Vice President for conferences and meetings (1994-1995, 1998-1999). He has been associate editor of the IEEE Transactions on Systems Man and Cybernetics (1992-2001). Founder of the SMC Technical committee « Mathematical Modelling » he has been president of this committee from 1993 to 1997 and has been president of the « System area » SMC committee from 1997 to 2000. He has been President of the SMC Society in 2000 and 2001, President of the SMC-nomination committee in 2002 and 2003 and President of the SMC-Awards and Fellows committee in 2004 and 2005. He is member of the Advisory Board of the “IEEE Systems Journal” . Dr. Borne received in 1994, 1998 and 2002 Outstanding Awards from the IEEE/SMC Society and has been nominated IEEE Fellow the first of January 1996. He received the Norbert Wiener Award from IEEE/SMC in 1998, the Third Millennium Medal of IEEE in 2000 and the IEEE/SMC Joseph G. Wohl Outstanding Career Award in 2003. He has been vice president of the “IEEE France Section” (2002-2010) and is president of this section since 2011. He has been appointed in 2007 representative of the Division 10 of IEEE for the Region 8 Chapter Coordination sub-committee (2007-2008) He has been member of the IEEE Fellows Committee (2008- 2010) Dr BORNE has been IMACS Vice President (1988-1994). He has been co-chairman of the IMACS Technical Committee on "Robotics and Control Systems" from 1988 to 2005 and in August 1997 he has been nominated Honorary Member of the IMACS Board of Directors. He is since 2008 vice-president of the IFAC technical committee on Large Scale Systems. Dr BORNE is Professor "de Classe Exceptionnelle" at the "Ecole Centrale de Lille" where he has been Head of Research from 1982 to 2005 and Head of the Automatic Control Department from 1982 to 2009. His activities concern automatic control and robust control including implementation of soft computing techniques and applications to large scale and manufacturing systems. He was the principal investigator of many contracts of research with industry and army (for more than three millions €) Dr BORNE is "Commandeur dans l'Ordre des Palmes Acad?miques" since 2007. He obtained in 1994 the french “ Kulman Prize”. Since 1996, he is Fellow of the Russian Academy of Non-Linear Sciences and Permanent Guest Professor of the Tianjin University (China). In July 1997, he has been nominated at the "Tunisian National Order of Merit in Education" by the Republic of Tunisia. In June 1999 he has been nominated « Professor Honoris Causa » of the National Institute of Electronics and Mathematics of Moscow (Russia) and Doctor Honoris Causa of the same Institute in October 1999. In 2006 he has been nominated Doctor Honoris Causa of the University of Waterloo (Canada) and in 2007 Doctor Honoris Causa of the Polytechnic University of Bucharest (Romania). He is “Honorary Member of the Senate” of the AGORA University of Romania since May 2008 He has been Vice President of the SEE (French Society of Electrical and Electronics Engineers) from 2000 to 2006 in charge of the technical committees. He his the director of publication of the SEE electronic Journal e-STA and chair the publication committee of the REE Dr BORNE has been Member of the CNU (French National Council of Universities, in charge of nominations and promotions of French Professors and Associate Professors) 1976-1979, 1992-1999, 2004-2007 He has been Director of the French Group of Research (GDR) of the CNRS in Automatic Control from 2002 to 2005 and of a “plan pluriformations” from 2006 to 2009. Dr BORNE has been member of the Multidisciplinary Assessment Committee of the “Canada Foundation for Innovation” in 2004 and 2009. He has been referee for the nominations of 24 professors in USA and Singapore. He is listed in the "Who is Who in the World" since 1999.

Plenary Lecture 2

Applications of Linear Algebra in Signal Processing, Wireless Communications and Bioinformatics

Professor Erchin Serpedin
Department of Electrical and Computer Engineering
Texas A&M University
USA
E-mail: serpedin@ece.tamu.edu

Abstract: In this talk, we will review some of the most important applications of linear algebra in signal processing, wireless communications and bioinformatics, and then outline some of the major open problems which might benefit by the usage of linear algebra concepts and tools.

Brief Biography of the Speaker: Dr. Erchin Serpedin is currently a professor in the Department of Electrical and Computer Engineering at Texas A&M University in College Station. He is the author of 2 research monographs, 1 textbook, 9 book chapters, 105 journal papers and 175 conference papers. Dr. Serpedin serves currently as associate editor for the Physical Communications Journal (Elsevier) and EURASIP Journal on Advances in Signal Processing, and as Editor-in-Chief of the journal EURASIP Journal on Bioinformatics and Systems Biology edited by Springer. He is an IEEE Fellow and his research interests include signal processing, biomedical engineering, bioinformatics, and machine learning.

ISBN: 978-1-61804-321-4

Plenary Lecture 3

Reliability Life Cycle Management for Engineered Systems

Professor George Vachtsevanos
Professor Emeritus
Georgia Institute of Technology
USA
E-mail: george.vachtsevanos@ece.gatech.edu

Abstract: Engineered systems are becoming more complex and by necessity more unreliable resulting in detrimental events for the system itself and its operator. There is evidence to support the contention that industrial and manufacturing processes, transportation and aerospace systems, among many others, are subjected to severe stresses, external and internal, that contribute to increased cost, operator workload, frequent and catastrophic mishaps that require the development and application of new and innovative technologies to improve system reliability, safety, availability and maintainability. These requirements are not true only for strictly engineered systems but are often discussed in business and finance, biological systems and social networks. We introduce in this talk a systematic and verifiable methodology to improve system reliability, reduce operating costs and optimize system design or maintenance practices. The enabling technologies build upon modeling tools to represent critical system functions, a prognostic strategy to predict the long-term behavior of systems under stress, reliability analysis methods exploiting concepts of probabilistic design and an optimization algorithm to arrive at optimum system design for improved reliability. We demonstrate the efficacy of the approach with examples from the engineering domain.

Brief Biography of the Speaker: Dr. George Vachtsevanos is currently serving as Professor Emeritus at the Georgia Institute of Technology. He served as Professor of Electrical and Computer Engineering at the Georgia Institute of Technology from 1984 until September, 2007. Dr Vachtsevanos directs at Georgia Tech the Intelligent Control Systems laboratory where faculty and students began research in diagnostics in 1985 with a series of projects in collaboration with Boeing Aerospace Company funded by NASA and aimed at the development of fuzzy logic based algorithms for fault diagnosis and control of major space station subsystems. His work in Unmanned Aerial Vehicles dates back to 1994 with major projects funded by the U.S. Army and DARPA. He has served as the Co-PI for DARPA's Software Enabled Control program over the past six years and directed the development and flight testing of novel fault-tolerant control algorithms for Unmanned Aerial Vehicles. He has represented Georgia Tech at DARPA's HURT program where multiple UAVs performed surveillance, reconnaissance and tracking missions in an urban environment. Under AFOSR sponsorship, the Impact/Georgia Team is developing a biologically-inspired micro aerial vehicle. His research work has been supported over the years by ONR, NSWC, the MURI Integrated Diagnostic

ISBN: 978-1-61804-321-4

program at Georgia Tech, the U,S. Army's Advanced Diagnostic program, General Dynamics, General Motors Corporation, the Academic Consortium for Aging Aircraft program, the U.S. Air Force Space Command, Bell Helicopter, Fairchild Controls, among others. He has published over 300 technical papers and is the recipient of the 2002-2003 Georgia Tech School of ECE Distinguished Professor Award and the 2003-2004 Georgia Institute of Technology Outstanding Interdisciplinary Activities Award. He is the lead author of a book on Intelligent Fault Diagnosis and Prognosis for Engineering Systems published by Wiley in 2006.

Plenary Lecture 4

Augmented Reality: The Emerging Trend in Education

Professor Minjuan Wang
San Diego State University
USA
E-mail: mwang@mail.sdsu.edu

Abstract: Augmented Reality (AR) is the layering of virtual information over the real, 3-D world to produce a blended reality. AR has been considered a significant tool in education for many years. It adds new layers of interactivity, context, and information for learners which can deepen and enrich the learning experience. The combination of real and virtual allows the student to engage in learning about a topic from multiple perspectives and data sources at levels that are not always available in traditional classroom settings and interactions.
As the usage of mobile devices in formal settings continues to rise, so does the opportunity to harness the power of augmented reality (AR) to enhance teaching and learning. Many educators have experimented with AR, but has it proven to improve what students grasp and retain? Is AR just another fun way to engage students, with little transformation of learning? This plenary speaking will introduce augmented reality as an emerging trend in education, provide an overview of its current development, explore examples of curriculum integration, and also suggest approaches for success.

Brief Biography of the Speaker: Dr. Minjuan Wang (Professor of San Diego State University; Distinguished Research Professor of Shanghai International Studies University)
Homepage: http://www.tinyurl.com/minjuan
Minjuan is Professor of Learning, Design, and Technology at San Diego State University (California, USA), and distinguished professor of Shanghai International Studies University (Shanghai, China). She was recently selected as the “Oriental Scholar” by the Municipal Educational Committee of Shanghai). In addition, she and her American colleagues obtained a four-year 1.3 million grant to study environment protection (including the Golden monkeys) in Fanjingshan, Guizhou province.
Minjuan’s work has been highly interdisciplinary, covering the field of education, technology, computer science, geography, and communication. In her 14 years at SDSU, she teaches Designing and Developing Learning for the Global Audience, Mobile Learning Development, Technologies for Course Delivery, and Methods of Inquiry. Her research specialties focus on online learning, mobile learning, Cloud Learning, and intelligent learning (as part of the Intelligent Camps initiative launched by British Telecom). Minjuan is the Editor-in-Chief of a newly established journal-- EAI Transactions on Future Intelligent Educational Environments. She also serves on the editorial boards for four indexed journals: Open Education Research,

ISBN: 978-1-61804-321-4

International Journal on E-Learning (IJEL), the Open Education Journal, and Journal of Information Technology Application in Education.
As a winner of several research awards, Minjuan is recognized as one of the high impact authors in blended and mobile learning. She has more than 80 peer-reviewed articles published in indexed journals, such as Educational Technology Research and Development, IEEE Transactions on Education, and British Journal of Educational Technology. She was a keynote and invited speaker to 11 international conferences. In addition, she is also an accomplished creative writer and an amateur flamenco dancer. Her recent Novel--Walking in this Beautiful World—has inspired many young people around the world.

Plenary Lecture 5

Application of Multivariate Empirical Mode Decomposition in EEG Signals for Subject Independent Affective States Classification

Prof. Konstantinos N. Plataniotis
Department of Electrical and Computer Engineering
University of Toronto
CANADA
E-mail: kostas@ece.utoronto.ca

Abstract: Physiological signals, EEG in particular, are inherently noisy and non-linear in nature which are challenging to work with using conventional linear signal processing methods. In this paper, we are adopting a new signal processing method, Multivariate Empirical Mode Decomposition, as a preprocessing method to reconstruct EEG signals according to its instantaneous frequencies. To test its effectiveness, we applied this signal reconstruction technique to analyze EEG signals for a 2-dimensional affect states classification application. To evaluated the proposed EEG signal processing system, a three-class classification experiment were carried out on the "Emobrain" dataset from eNTERFACE'06 with K-nearest neighbors (KNN) and Linear Discriminate Analysis (LDA) as classifiers. A leave-one-subject out cross validation process were used and an averaged correct classification rate of 90.77% were achieved. Another main contribution of this paper was inspired by the growth of non-medical grade EEG headsets and its potential in advanced human-computer interface design. However, to reduce cost and invasiveness, consumer grade EEG headsets have far less number of electrodes. In this paper, we used emotion recognition as a case study, and applied Genetic Algorithm to systematically select the critical channels (or sensor locations) for this application. The results of this study will shed lights on the sensor configuration challenges faced by most consumer-grade EEG headset design projects.

Brief Biography of the Speaker: Konstantinos N. (Kostas) Plataniotis received his B. Eng. degree in Computer Engineering from University of Patras, Greece and his M.S. and Ph.D. degrees in Electrical Engineering from Florida Institute of Technology Melbourne, Florida. He was with the Computer Science Department at Ryerson University, Ontario, Canada from July 1997 to June 1999. Dr. Plataniotis is currently a Professor with The Edward S. Rogers Sr. Department of Electrical and Computer Engineering at the University of Toronto in Toronto, Ontario, Canada, where he directs the Multimedia Laboratory. He is a founding member and the inaugural Director – Research of the Identity, Privacy and Security Institute, IPSI, (www.ipsi.utoronto.ca). Kostas was the Director (January 2010- June 2012) of the Knowledge Media Design Institute, KMDI, (www.kmdi.utoronto.ca) at the University of Toronto.
Dr. Plataniotis was the Guest Editor for the March 2005 IEEE Signal Processing Magazine special issue on "Surveillance Networks and Services", and the Guest Editor for the EURASIP Applied

ISBN: 978-1-61804-321-4

Signal Processing Journal's special issue on "Advanced Signal Processing & Pattern Recognition Methods for Biometrics". He is a member of the IEEE Periodicals Review and Advisory Committee (2011-2013); he has served as a member of the 2008 IEEE Educational Activities Board; he chaired of the IEEE EAB Continuing Professional Education Committee, and he served as the 2008 representative of the Computational Intelligence Society to the IEEE Biometrics Council. Dr. Plataniotis chaired the 2009 Examination Committee for the IEEE Certified Biometrics Professional (CBP) Program (www.ieeebiometricscertification.org) and he served on the Nominations Committee for the IEEE Council on Biometrics. He was a member of the Steering Committee for the IEEE Transaction on Mobile Computing, an Associate Editor for the IEEE Signal Processing Letters as well as the IEEE Transactions on Neural Networks and Adaptive Systems and he has served as the Editor-in-Chief for the IEEE Signal Processing Letters from January 1, 2009 to December 31, 2011. Dr. Plataniotis chaired the IEEE Toronto Signal Processing and Applications Toronto Chapter from 2000 to 2002, he was the 2004-05 Chair of the IEEE Toronto Section and a member of the 2006 as well as 2007 IEEE Admissions & Advancement Committees. He served as the Technical Program Committee Co-Chair for the 2013 IEEE International Conference on Acoustics, Speech and Signal Processing (ICASSP 2013) and he is the Vice President – Membership for the IEEE Signal Processing Society (2014-2016).

Dr. Plataniotis is a Fellow of IEEE, Fellow of the Engineering Institute of Canada, a registered professional engineer in the province of Ontario, and a member of the Technical Chamber of Greece.

The recipient of numerous grants and research contracts as the principal investigator, he speaks internationally and writes extensively in his field and he has been a consultant to a number of companies. He has served as lecturer in 12 short courses to industry and continuing education programs; he is a contributor to seventeen books, the co-author of "Color Image Processing and Applications", Springer Verlag, 2000, (ISBN-3-540-66953-1) and "WLAN Positioning Systems: Principles & applications in Location-based Services", Cambridge University Press, 2012 (ISBN 978-0-521-9185-2), "Multi-linear Subspace Learning: Reduction of multi-dimensional data}, CRC Press, 2013, (ISBN: 978-14398557243). He is the co-editor of "Color Imaging: Methods and Applications", CRC Press, September 2006, (ISBN 084939774X) and the Guest Editor of the IEEE/Wiley Press volume on "Biometrics: Theory, Methods and Applications" published in October 2009 (ISBN: 9780470247822). Dr. Plataniotis has published more than 400 papers in refereed journals and conference proceedings. In 2005 he became the recipient of the IEEE Canada Engineering Educator Award for "contributions to engineering education and inspirational guidance of graduate students". Dr. Plataniotis is the joint recipient of the "2006 IEEE Trans. on Neural Networks Outstanding Paper Award" for the published in 2003 "Face recognition using kernel direct discriminant analysis algorithms", IEEE Trans. on Neural Networks, Vol. 14, No 1, 2003.

Plenary Lecture 6

State of the Art and Recent Progress in Uncertainty Quantification for Electronic Systems (i.e. Variation-Aware or Stochastic Simulation)

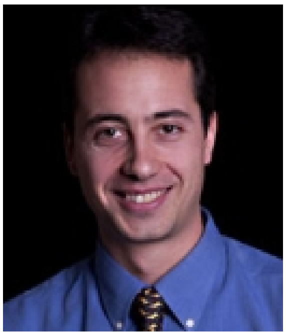

Professor Luca Daniel
Electrical Engin. & Computer Science
Massachusetts Institute of Technology (MIT)
Cambridge, MA, USA
E-mail: luca@mit.edu

Abstract: On-chip and off chip fabrication process variations have become a major concern in today's electronic systems design since they can significantly degrade systems' performance. Existing commercial circuit and MEMS simulators mostly rely on the well known Monte Carlo algorithm in order to predict and quantify such performance degradation. However during the last decade a large variety of more sophisticated and efficient alternative approaches have been proposed to accelerate such critical task. This talk will first review the state of the art of most modern uncertainty quantification techniques including intrusive and sampling-based ones. It will be shown in particular how parameterized model order reduction, and low-rank tensor based representations can be used to accelerate most uncertainty quantification tools and to handle the curse of dimensionality. Examples will be presented including amplifiers, mixers, voltage controlled oscillators with tunable micro-electro-mechanical capacitors and phase locked loops.

Brief Biography of the Speaker: Luca Daniel is an Associate Professor in the Electrical Engineering and Computer Science Department of the Massachusetts Institute of Technology (MIT). Prof. Daniel received the Ph.D. degree in Electrical Engineering from the University of California, Berkeley, in 2003. In 1998, he was with HP Research Labs, Palo Alto. In 2001, he was with Cadence Berkeley Labs.
Dr. Daniel research interests include development of integral equation solvers for very large complex systems, stochastic field solvers for large number of uncertainties, and automatic generation of parameterized stable compact models for linear and nonlinear dynamical systems. Applications of interest include simulation, modeling and optimization for mixed-signal/RF/mm-wave circuits, power electronics, MEMs, nanotechnologies, materials, MRI, and the human cardiovascular system.
Prof. Daniel has received the 1999 IEEE Trans. on Power Electronics best paper award; the 2003 best PhD thesis awards from both the Electrical Engineering and the Applied Math departments at UC Berkeley; the 2003 ACM Outstanding Ph.D. Dissertation Award in Electronic Design Automation; 5 best paper awards in international conferences, 8 additional nominations for best paper award; the 2009 IBM Corporation Faculty Award; and the 2010 IEEE Early Career Award in Electronic Design Automation.

ISBN: 978-1-61804-321-4

ISBN: 978-1-61804-321-4

Application of ultrasound techniques and signal processing tools to milk fouling detection

Marco A. Úbeda, Mohamed A. Hussein and Thomas M. Becker

Abstract— Significant resource investments are needed in order to minimize industrial costs related to cleaning operations. In the case of the dairy industry, accumulation of deposits (fouling or insolubilities) over heat transfer areas in process equipment such as heat exchangers or spray driers poses severe problems. Organic deposit build-up inside heating equipment results in decreased heat transfer efficiency, which potentially compromises microbiological safety and quality of the end product. This requires of intensive, iterative cleaning cycles, which generates additional waste and asks for increased resource investments.

Indeed, the main challenge of cleaning complex heating systems lies on the difficulty related to the assurance of residue absence after each cycle, so cleaning intensity is usually excessive. Hence, accurate monitoring techniques are crucial for proper evaluation of the cleaning success and, therefore, CIP (Cleaning In Place) processes are a target for developing new Process Analytical Technologies (PAT) to enable advanced process control. This study describes an inline ultrasound system for detecting organic deposits behind process walls, based on a non-destructive and non-invasive technique that does not require adaptations of existing heat equipment. The use of signal processing combined with statistical analysis tools allows for evaluation of properties of the residual deposit and thus, for determination of its presence and location and even its quantity. This way, improvement and real-time control of the cleaning processes will be achieved, using the most adequate cleaning products, in optimal proportions and for shorter time lapses, which saves costs, environmental waste and production dead time.

Keywords— Dairy, fouling, signal processing, ultrasound

Marco A. Úbeda is with the RG BioPAT - Bio Process Engineering and Process Analysis department, Technische Universität München, Freising, Bavaria 85354 Germany (phone: +49(0)8161-71-4534; e-mail: marco.ubeda@tum.de).

Mohamed A. Hussein is with the RG BioPAT - Bio Process Engineering and Process Analysis department, Technische Universität München, Freising, Bavaria 85354 Germany (phone: +49 (0)8161-71-3277; e-mail: mohamed.hussein@tum.de).

Thomas M. Becker is with the Lehrstuhl für Brau- und Getränketechnologie, Technische Universität München, Freising, Bavaria 85354 Germany (phone: +49 (0)8161 - 71-3261; e-mail: tb@tum.de).

I. Introduction

OPTIMIZATION in the use of economical and energetic resources has become a priority over the last decades. The dairy industry is undoubtedly affected by this necessity as well. The current data show that Europe can produce over 158,80 million tons of milk per year, from which, 31.50 are destined to drinking milk production and approximately 2.1 are converted into powders [1]. The estimated energetic requirement per kilo of processed milk ranges between 0.5 and 1.2 MJ [2], 30 % of which is used for cleaning operations [3]. Therefore, increasing the efficiency at such process would bring significant time-saving and economic advantages.

Milk is a fluid containing a large number of organic species at variable concentrations [4], which must be heated to extend shelf life and reduce microbiological hazards. Heating above 70 °C induces protein denaturation and agglomeration on heat transfer areas and results in fouling type A (protein fouling), a soft, spongy, white deposit consisting mostly of β-lactoglobulin and salt [5] - [6]. These deposits are composed of nearly 35 % minerals, below 8 % fat and less than 70 % protein [7]. The analysis of the deposits shows that, although whey proteins represent less than 9 % of the milk solids, they can reach up to 50 % of the fouling layer, being the β-lactoglobulin (β-Lg) the dominant protein. When milk is heated above 50 °C, stability of the bonds between its constituents decreases. Above 65 °C the molecule is denatured through hydrogen bond rupture in a second order denaturation reaction. Native proteins are dissociated into chains, which react with other molecules and group together through sulfhydryl groups, forming chaotic structures. Although the process by which proteins adhere to heat transferring walls is not thoroughly understood, it has been shown that as soon as a first layer is fastened, free protein chains in the milk contribute to thicken it. It has been proposed that the presence of calcium could enhance protein deposition as a calcium phosphate precipitate, associating with active ß-Lg molecules [8]. These may in turn, associate with κ-casein present in the casein micelles, dragging them into the deposit. The deposit formation process can be observed particularly during milk spray drying inside the so-called Spray Drying Towers (Fig. 1a). As part of this process, previously evaporated milk is injected through nozzles or atomizers into the towers, where hot air (180-220 °C) in cocurrent or countercurrent flow

ISBN: 978-1-61804-321-4

dehydrates the small milk particles [9]. Milk itself, reaches approximately 80 °C during this drying process, but tower wall temperatures can reach temperatures above 120 °C, influenced by hot air. Exceeding particle moisture results in milk powder adhesion over already hot walls, instead of rebounding [10]. The fouling formation process during milk spray drying is similar to the one observed in heat exchangers during the milk sterilization. It is, however, strongly dependent on particle moisture, which is, in turn, conditioned by process parameters and machinery performance [11]. For particle moistures below 10 %, low fouling can be expected [12]. For moisture contents ranging between 10 % and 30 %, the insolubility generation rate is highly dependent on the air temperature and the process conditions [13]. Intense atomization can lead, for example, to significant deposit accumulation containing higher fat proportions [14]. So far, in the milk spray drying field, little research related to fouling detection has been conducted. However, the soiling process can be predicted indirectly by process parameters such as temperature [15] or absolute and relative humidity [16] gradients between supply and extract air measurements. However, the measurement results of these sensors must be validated empirically to establish appropriate correlations with the real deposit accumulation and removal rate. Visual inspection methods, which are based on camera recordings, have also been carried out by companies like GEA Group AG. However, such methods cannot be automated as they depend on the subjective criterion of an operator.

Mixed with the end-product, fouled matter can cause sensorial and quality loss, as well as sanitary concerns [17], [18]. Furthermore, security concerns arise, as product may ignite, raising the risk of dust explosion [19]. In addition to the mentioned quality issues and security concerns, deposit formation leads to production interruption for cleaning operations, which results in significant resource investments such as cleaning solutions, maintenance costs or prevention against environmental impact. Therefore, an efficient cleaning approach based on reduced timing and optimal use of resources is goal to reach. Food industry is becoming increasingly aware of both, the importance of developing new analytical techniques to study complex food materials, and to monitor properties of foods during processing where strict protocols—issued by FDA—must be maintained to ensure food purity. Ultrasound techniques are ideally suited to both of these applications, despite having a few limitations such as its sensitivity to air gaps formed during the process or its dependency on the specific acoustic properties of sample concentration [20] and temperature [21]. In the present study, ultrasound techniques have been developed, using a newly designed experimental approach, to find ultrasound signal features which are likely to be affected by the presence of milk powder deposits, and which can be later analyzed in more complex heating systems without the need of making any modification to their structure. Our aim is to develop, an inexpensive, non-destructive, non-invasive, hygienic and real time operating technique, able to evaluate the milk protein deposition rate over the internal surfaces of spray drying towers. Hence, cleaning cycles could be adapted to the given insolubility accumulation state and the cleaning success could be validated.

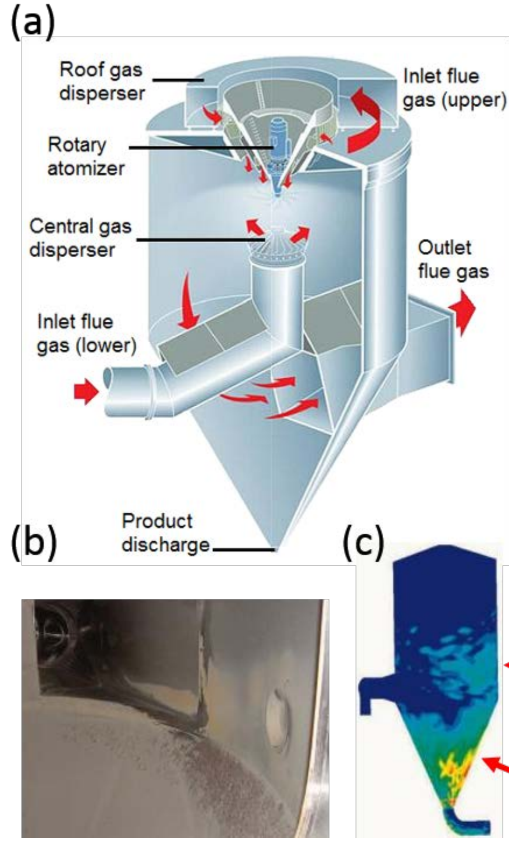

Figure 1. (a) Cross section of a SDT displaying most relevant elements (modified from [22]**). (b) Insolubility accumulation inside a dairy spray drying tower** [19]**. (c) Digital simulation of the drying process. Lighter shades represent internal areas of the tower where deposits are more likely to adhere, according to milk drying process digital simulations (modified from** [19]**). Arrows indicate tower access points for sensor location.**

II. MATERIALS AND METHODS

Despite spray drying machinery (Fig. 1a) is designed to minimize insolubility accumulation, this effect is unavoidable (Fig. 1b). After process runs, deposit thicknesses in the range of 10 mm have been observed. In the case of food industry, avoidance of contact between sensor elements and product is mandatory. Therefore, an even surfaced, non-reactive and non-corroding wall separating the sensor from the product is required. In milk SDT, deposits seem to accumulate in specific locations at varying concentrations and amount (Fig. 1c) depending on the process efficiency and the air flux [19]. Acoustic sensor measurements in specific tower access locations (Fig. 1c) where deposit accumulation is expected can help to estimate fouling intensity in critical areas by extrapolation.

Thorough research led to the conclusion that an application of the Quartz Crystal Microbalance technique could be the most effective solution for adhered deposit mass estimation. The theoretical basis of the QCM developed by Sauerbrey [23], is based on resonant frequency variations in an oscillator due to material adsorption to its surface according to

$$\Delta m = k\Delta f \quad (1)$$

where Δm is the mass adsorbed per unit surface area and $\Delta f = f_0 - f$, where f_0 is the frequency with no mass adsorbed and f is the frequency after mass adsorption. The constant k is a property of the crystal itself, including its exact thickness and surface roughness [24].

In our specific case of study, in order to meet the hygienic restrictions, the surface upon which soiling should take place would be the internal area of a stainless steel Varivent® lid fitting in the tower access locations. Instead of quartz crystal, a handmade sensor containing a lead zirconate titanate piezo element pressed against the external area of the Varivent® lid was designed (Fig. 2). The sensor coupling pressure is applied by compressing 2,50 mm a spring having a known constant of 11,20 N/mm. For a given piezo element radius of 5 mm, the reached pressure is 3,56 bar.

The presence of a wall between the oscillator and the product was known to noticeably influence the measurements. The way to minimize this effect was to substantially reduce the wall thickness to 0,45 ± 0,04 mm. Then, according to the studied moment of inertia in discs,

$$Ic = \int_0^R \frac{2M}{R^2} x^3 dx = \frac{1}{2} MR^2 \quad (2)$$

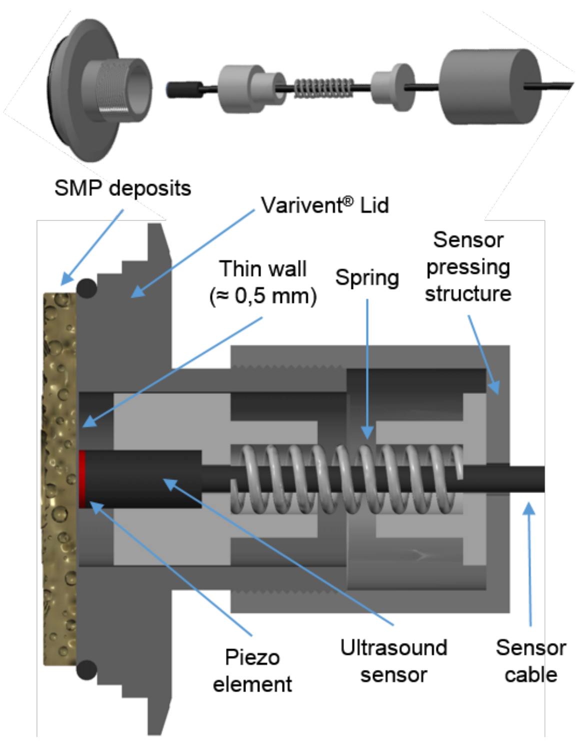

Figure 2. Cross section of the ultrasound sensor construction involving a modified Varivent® lid to allow for acoustic sensing measurements at specific access points in dairy SDT

where M is the mass (disc and deposits), R is the radius and x is the distance between the mass center and the disc perimeter, larger radiuses (30 mm) were expected to allow for freer transverse piezoelectric oscillations at the center of the lid’s wall. In contrast, small radius piezo elements are expected to induce larger disc oscillations, when applied on the disc center. Therefore, 5 mm piezo radiuses were chosen for this application.

Experimentally, 0, 0,5, 1, 2 and 3 g of skimmed milk powder containing 30 % water (Table 1) at room temperature (23 ± 0,30 °C) were applied for acoustic signal variation analysis. The setup used (Fig. 3) consisted of a solid structure holding a

Table 1. Skimmed Milk Powder (SMP) constituents present in samples used in the experiments, resembling insolubility moisture rates detected in dairy drying processes [14].

Components	Content (%)
Protein	14,57
Lactose	19,67
Ash	35,76
Water	30,00

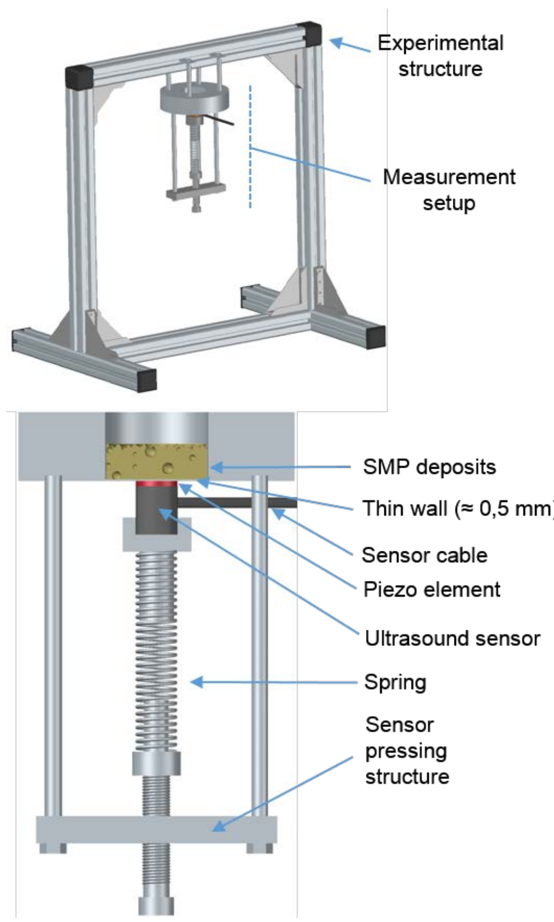

Figure 3. Solid structure assembled for holding the experimental setup (above). Experimental setup used for testing the viability of the ultrasound based sensing technique applied for SMP deposit detection and quantity evaluation (below).

plate with the same wall thickness as the one from the modified Varivent® lid. For an overall measurement surface (disc area) of 7,07 cm², deposit thicknesses between 0 mm (0 g SMP) and 9,72 ± 0,26 mm (3 g SMP) were evaluated. For each selected SMP amount, 150 ultrasound signals were obtained and analyzed, within three process repetitions.

4 MHz was the selected sensor frequency because it showed higher sensitivity to fouling deposit presence over lower frequencies in previous experiments [25]. Several parameters related to the sensor excitation and the signal acquisition were experimentally fixed in order to obtain suitable measurement data for later analysis. The chosen voltage for sensor excitation was 50 V owing to a significant signal output. The signal resolution or the defined sampling period between signal points was set to 20 ns, and a total signal length of 100 µs (5000 signal sampling points) proved to be adequate to cover a wide signal range for later analysis. With the defined signal settings, the microcontroller processor was capable of capturing signals within a period of 6,54 s.

For the acoustic signal processing, several signal features were tested, and those revealing noticeable differences between fouling presence/absence were selected. These features were: the Signal Summation (3), the Temporal Crest Factor (4), and the Temporal Inertia (5) [26].

-Signal Summation (Summ). Local sampling points defining the acoustic signals within a certain signal resolution were expected to suffer amplitude variations depending on the piezo element vibration freedom. The signal summation represents the overall signal sampling point amplitude summation (y axis) over the time domain (x axis).

$$Summ = \sum_{n=1}^{N} |\, x(n)\,| \tag{3}$$

-Temporal Crest Factor (TCF) represents the signal's maxima over the average signal amplitude ratio in the time domain (Equation 8). It is obtained by dividing the signal peak values by the signal average value. Therefore, the difference between signal amplitudes reached as deposits adhere to wall surfaces, and the signal maxima increases progressively.

$$TCF = \frac{\max(|\, x(n)\,|)}{\frac{1}{N}\sum_{n=1}^{N} |\, x(n)\,|} \tag{4}$$

-Temporal Inertia (TI) is the weighted average of the signal amplitude in the time domain. An inertia decrease would be the consequence of a decreased piezo element vibration freedom (i.e. lower acoustic attenuation), leading to a lower variance (Fig. 3C).

$$TI = \sum_{n=1}^{N} n^2 * |\, x(n)\,| \tag{5}$$

III. RESULTS AND DISCUSSION

Acoustic frequency variations due to varying deposit amounts, could not be identified experimentally by sensor measurements and thus, the above described QCM approach could not be applied. Nevertheless, the experimental adaption of this technique for the aimed purpose was successful, as signal processing over raw data (Fig. 4a) in the time domain provided representative results. As deposit amounts over the measurement area increased, the vibration freedom of this stainless steel wall was hindered resulting in higher signal damping. Thus, signal amplitudes decreased linearly as higher quantities of milk powder were in contact with the experimental setup surface.

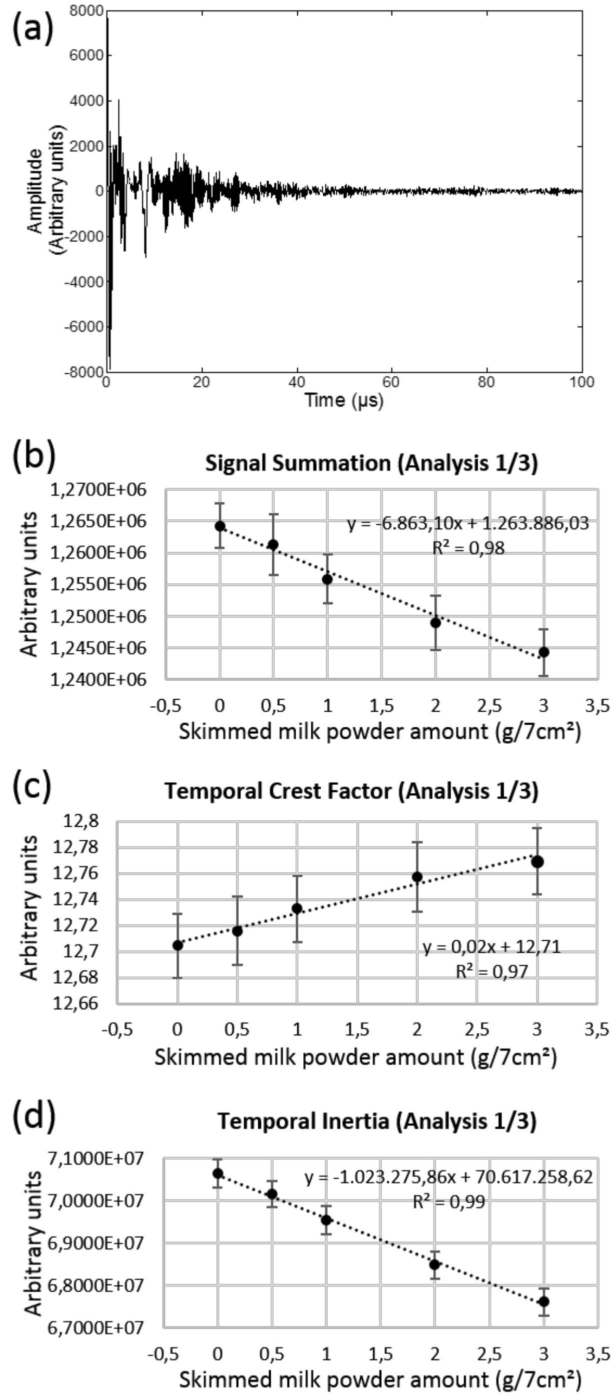

Figure 4. (a) Ultrasound signal in absence of SMP deposits. Signal was obtained by generating vibrations with a 4 MHz piezo element over the thin wall of the measurement setup, in absence of SMP deposits.
(b - d) Acoustic feature values (y axis) calculated from signals obtained experimentally while increasing SMP deposit amounts (x axis) over the measurement area (7,07 cm²) from 0 to 3 grams in five steps. Values represent means ± SD forAnalysis 1/3 (see Table 2)

Table 2. Acoustic feature results of three sequential analysis (1/3 – 3/3: rows) for the 5 different SMP deposit amounts experimentally evaluated (columns) by means of ultrasound sensing. Last column shows the corresponding trend lines applied over average feature values. Values represent means ± SD in arbitrary units.

	Signal Features Average ± SD	Milk powder amounts analyzed (g/7 cm²)					
		0	0,5	1	2	3	Feature trend lines
Analysis 1/3	Summ	1,2643E+06 ±3,5676E+03	1,2613E+06 ±4,7199E+03	1,2559E+06 ±3,8245E+03	1,2490E+06 ±4,2483E+03	1,2443E+06 ±3,6360E+03	y = -6,86E+03x + 1,26E+06 R^2 = 0,98
	TCF	12,7044 ±0,0245	12,7159 ±0,0261	12,7328 ±0,0254	12,7575 ±0,0270	12,7694 ±0,0252	y = 2,24E-02x + 1,27E+01 R^2 = 0,97
	TI	7,0642E+07 ±3,3304E+05	7,0151E+07 ±3,0804E+05	6,9544E+07 ±3,4007E+05	6,8483E+07 ±3,2909E+05	6,7615E+07 ±3,2056E+05	y = -1,02E+06x + 7,06E+07 R^2 = 0,99
Analysis 2/3	Summ	1,2509E+06 ±3,6549E+03	1,2468E+06 ±5,8615E+03	1,2387E+06 ±4,5835E+03	1,2359E+06 ±4,0570E+03	1,2267E+06 ±3,6549E+03	y = -7,70E+03x + 1,25E+06 R^2 = 0,95
	TCF	12,7065 ±0,0394	12,7565 ±0,0394	12,8105 ±0,0302	12,8303 ±0,0272	12,8486 ±0,027	y = 4,43E-02x + 1,27E+01 R^2 = 0,84
	TI	7,0305E+07 ±3,2120E+05	6,8905E+07 ±3,2120E+05	6,8300E+07 ±3,5059E+05	6,8092E+07 ±3,2336E+05	6,6599E+07 ±3,4368E+05	y = -1,06E+06x + 6,98E+07 R^2 = 0,89
Analysis 3/3	Summ	1,2643E+06 ±3,3350E+03	1,2549E+06 ±4,4193E+03	1,2532E+06 ±4,0011E+03	1,2498E+06 ±3,6183E+03	1,2438E+06 ±3,7226E+03	y = -5,89E+03x + 1,26E+06 R^2 = 0,89
	TCF	12,7253 ±0,0227	12,7608 ±0,0309	12,7666 ±0,0284	12,7801 ±0,0261	12,7952 ±0,0267	y = 2,01E-02x + 1,27E+01 R^2 = 0,85
	TI	7,0715E+07 ±3,4194E+05	6,9689E+07 ±3,5070E+05	6,9523E+07 ±3,5226E+05	6,9106E+07 ±3,6206E+05	6,8318E+07 ±3,0917E+05	y = -6,94E+05x + 7,04E+07 R^2 = 0,91

-Signal Summation. The overall signal sampling point amplitude summation over the time domain decreased accordingly owing to the attenuating effect of increasing amounts of SMP in contact with the thin wall (Fig. 4b) (Table 2).

-Temporal Crest Factor. The difference between signal amplitudes reached as deposits entered in contact with wall surfaces, and the signal maxima increased progressively (Fig. 4c) (Table 2). The signal maxima was located within the initial 5 µs of each signal and it is known to represent the so called "ringing" vibrations [27], which reach different intensities depending on the piezo element material as well as various environment conditions (temperature, pressure, and sensor construction). Seemingly, the presence of increasing SMP deposit quantities was able to attenuate the wall vibrations, without affecting the ringing intensity.

-Temporal Inertia. Amplitude variance changes in the signal induced a signal moment of inertia displacement along the x axis (time domain). In the present application, as signal amplitudes decrease for higher deposit amounts while ringing amplitudes remain unalterable, the moment of inertia would suffer a shift towards the signal start (Fig. 4d) (Table 2), resulting in a scalar value decrease.

Despite the same trend could be identified in same acoustic features obtained from different analysis, the acoustic feature values reached for the chosen deposit amounts varied between different analysis, affecting trend line slopes (Table 2). These reproducibility alterations are considered to be influenced principally by factors like the environmental relative humidity. Indeed, due to SMP hygroscopicity, environmental humidity could have influenced the moisture content in samples during experiments, resulting in slight mass increments. This is, as well, a common problem in industrial plants and must be taken into consideration as soon as process monitoring cycles are fully operative.

The presence of a solid steel wall between sensor and product could account for the main reason for sensitivity loss. On the other hand, system sensitivity could be improved after testing different piezoactive element materials and signal resolutions above 50 MHz (period between signal sampling points below 20 ns).

IV. CONCLUSIONS

The objective of the present study is to develop and test a cost-efficient ultrasound sensing strategy capable of accurately monitoring the deposit adhesion rate inside a closed system so the cleaning cycles can be accordingly adapted and validated. In the food industry fouling deposits result in reduced heat transfer efficiency, which can compromise the product's microbiological safety. This requires intensive, iterative cleaning, which generates additional waste and increases resource investments.

Results from previous work [25] confirmed that ultrasound-based techniques are a very sensitive measuring method able to detect fouling presence at accuracy values up to 98%. In a first step, a pulse-echo ultrasound measuring technique was used for generating a wave from which several acoustic signal features were extracted and implemented in statistical classification or decision machines. When signal feature values obtained during a cleaning cycle were sufficiently sensitive to detect changes in media, the decision could be programmed to discern between a clean and a fouled status. However, the soiling intensity could not be evaluated with the implemented measurement approach. Therefore, a new approach had to be planned [28]. The present results indicate that once an acceptable efficiency and accuracy is reached, the proposed methodology for fouling intensity evaluation could contribute to minimize the step duration in cleaning cycles while guaranteeing the same efficiency. This would result in significant improvements by cutting down the associate industrial costs and providing a cost efficient in-line cleaning validation method.

Nevertheless, high deviations were observed in the herein reported measurements obtained from runs repeated in identical experimental conditions, but conducted on different days. Thus, a number of potential sources of variability and outliers have to be considered and identified in order to minimize their unwanted impact. Among them, temperature is known to play the most important role, affecting physical properties of the medium, such as the material expansion and the compressibility or bulk modulus. Other sources of deviation or influencing factors, like air gap distribution, reproducibility limitation in sensor to wall coupling, or seasoning effects in product, need to be further investigated in order to optimize the predictive accuracy of this technique. Furthermore, besides type A milk fouling, type B or mineral fouling deposits are generated over heat transfer areas, and are worth of consideration for a complete evaluation of ultrasound sensitivity to dairy soiling.

The present study intends to shed light on a vanguard application within ultrasound sensing techniques focused on a problem of major concern for the food industry. On the other hand, fouling is a worldwide extended concern associated to industries in countless sectors. Biofouling proliferation detection in nanofiltration, pharmaceutical, or crude oil facilities; sensing of salt ($CaCO_3$ and $CaSO_4$) crystallization and corrosion in thermal desalinization processes; membrane fouling characterization in wastewater treatment; and marine embarkation surface coating performance studies, account for some of the most yearned for applications.

For the time being, outlier detection techniques can palliate acoustic measurement instability. However, due to the broad range of external factors influencing ultrasound sensing, a comprehensive effort in this field would be needed in order to improve the reproducibility and accuracy. In parallel, suitable engineering solutions in terms of hygienicity and acoustic wave propagation knowledge, are required to efficiently adapt sensing equipment to industrial environments.

REFERENCES

[1] European Commission and Eurostat, “Milk and milk product statistics,” *http://epp.eurostat.ec.europa.eu/statistics_explained/index.php/Milk_and_milk_product_statistics*, 2013. [Online]. Available: http://epp.eurostat.ec.europa.eu/statistics_explained/index.php/Milk_and_milk_product_statistics. [Accessed: 30-Apr-2015].

[2] Cowi, “Cleaner Production Assessment in Dairy Processing,” *Production*, 2000. [Online]. Available: http://www.unep.fr/shared/publications/pdf/2480-CpDairy.pdf.

[3] M. H. Eide, J. P. Homleid, and B. Mattsson, “Life cycle assessment (LCA) of cleaning-in-place processes in dairies,” *LWT - Food Sci. Technol.*, vol. 36, pp. 303–314, 2003.

[4] van B. Walstra, P., Geurts, T.J., Noomen, A., Jellema, A., *Heat treatment in Dairy Technology: Principles of Milk Properties and Processes*. New York, NY: Marcel Dekker, 1999.

[5] H. Burton, “Deposits from whole milk in heat treatment plant—a review and discussion,” *J. Dairy Res.*, vol. 35, no. 02, pp. 317–330, Jun. 1968.

[6] H. Visser and T. j. Jeurnik, “General aspects of fouling and cleaning.,” *Bull. IDF*, vol. 328, pp. 5–6, 1997.

[7] A. Sadeghinezhad, E., Kazi, S. N., Dahari, M. ,Safaei, M. R., Sadri, R., Badarudin, “A comprehensive review of milk fouling on heated surfaces,” *Crit. Rev. Food Sci. Nutr.*, 2012.

[8] T. J. M. Jeurnink Walstra P De Kruif C G, “Mechanisms of fouling in dairy processing,” *Netherlands Milk Dairy J.*, vol. 50, no. 1996, pp. 407–426, 1996.

[9] Watson Dairy Consulting, “Milk powder production.” [Online]. Available: http://www.dairyconsultant.co.uk/pdf/milk_powder_production.pdf. [Accessed: 30-Apr-2015].

[10] T. a G. Langrish and T. K. Kockel, “The assessment of a characteristic drying curve for milk powder for use in computational fluid dynamics modelling,” *Chem. Eng. J.*, vol. 84, no. 1, pp. 69–74, 2001.

[11] S. Ohba, T., Takahashi, K., Igarashi, “Mechanism of insoluble material formation in spray-dried whole milk powder,” *Reports Res. Lab.*, vol. 88, pp. 91–108, 1989.

[12] J. Straatsma, G. Van Houwelingen, A. E. Steenbergen, and P. De Jong, “Spray drying of food products: 2. Prediction of insolubility index,” *J. Food Eng.*, vol. 42, no. 2, pp. 73–77, Nov. 1999.

[13] H. T. Walstra, P.; Jenness, R.; Badings, *Dairy chemistry & physics.* New York, NY: Wiley, 1984.

[14] A. J. Baldwin, “Insolubility of milk powder products – A minireview,” *Dairy Sci. Technol.*, vol. 90, no. 2–3, pp. 169–179, 2010.

[15] P. Schuck, A. Dolivet, S. Méjean, and R. Jeantet, “Relative humidity of outlet air: the key parameter to optimize moisture content and water activity of dairy powders,” *Dairy Sci. Technol.*, vol. 88, no. 1, pp. 45–52, 2008.

[16] P. Schuck, S. Méjean, a. Dolivet, and R. Jeantet, “Thermohygrometric sensor: A tool for optimizing the spray drying process,” *Innov. Food Sci. Emerg. Technol.*, vol. 6, no. 1, pp. 45–50, 2005.

[17] P. de Jong, “Impact and control of fouling in milk processing,” *Trends Food Sci. Technol.*, vol. 8, no. 12, pp. 401–405, Dec. 1997.

[18] WHO-FOOD Agriculture Organization of the United Nations, “Code of hygienic practice for milk and milk products,” Rome, 2011.

[19] L. Moser, “Verbesserte Prozessparameter verlängern Reinigungsintervalle in Sprühtürmen - Weniger ist mehr - Konradin Verlag.” [Online]. Available: http://www.prozesstechnik-online.de/chemie/-/article/5829525/25661780/Weniger-ist-mehr/art_co_INSTANCE_0000/maximized/. [Accessed: 26-Apr-2015].

[20] W. B. Hussein, M. a. Hussein, and T. Becker, “Robust spectral estimation for speed of sound with phase shift correction applied online in yeast fermentation processes,” *Eng. Life Sci.*, vol. 12, pp. 603–614, 2012.

ISBN: 978-1-61804-321-4

[21] J. A. Cárcel, J. V. García-Pérez, J. Benedito, and A. Mulet, “Food process innovation through new technologies: Use of ultrasound,” *J. Food Eng.*, vol. 110, no. 2, pp. 200–207, May 2012.

[22] “Changzhou Xiandao Drying Equipment Co., Ltd.,” 2013. [Online]. Available: http://es.made-in-china.com/co_xiandaochina/image_Spray-Dryer-Absorber-1_huoynyuun_MeATPtnBLCio.html. [Accessed: 24-Apr-2015].

[23] G. Sauerbrey, “Verwendung von Schwingquarzen zur Wägung dünner Schichten und zur Mikrowägung,” *Zeitschrift für Phys.*, vol. 155, no. 2, pp. 206–222, 1959.

[24] B. Murray and C. Deshaires, “Monitoring Protein Fouling of Metal Surfaces via a Quartz Crystal Microbalance.,” *J. Colloid Interface Sci.*, vol. 227, no. 1, pp. 32–41, 2000.

[25] J. Hinrichs and T. Becker, “Ultraschallbasiertes Messsystem zur Untersuchung des Foulingverhaltens und zur Validierung des Reinigungserfolgs in Wärmetauschern, Research Project (AiF 16302N).” Freising, pp. 1–22, 2010.

[26] R. Tao, Z. Li, Y. Ji, and E. Bakker, “Music Genre Classification Using Temporal Information and Support Vector Machine,” in *Proc. of the 16th Advanced School for Computing and Imaging Conf.(ASCI),* 2010.

[27] B. S. Hoyle, “Process tomography using ultrasonic sensors,” *Meas. Sci. Technol.*, vol. 7, no. 3, pp. 272–280, 1999.

[28] T. Becker and H. Langowski, “Leistungsverbesserung des CIP (Cleaning in Place)-Prozesses in Sprühtrocknungstürmen basierend auf der Detektion von Foulingbildung mittels Ultraschall, Research Project (AiF 18754N).” Freising, pp. 1–23, 2015.

ISBN: 978-1-61804-321-4

Medical image registration using a non-uniform splines model

Elizabeth Zachariah, A. Vennie Filippas, and Alen Docef

***Abstract*—**Image registration plays an important role in various medical imaging applications, including image-guided radiation therapy. One approach to image registration relies on spline modeling of the deformation vector field (DVF). Uniform splines adequately model smoothly-varying DVFs, but are ill-suited for discontinuous anatomical motion. A method for image registration using non-uniform, non-separable cubic splines is proposed. The method is introduced and evaluated in the context of four-dimensional computed tomography (4D-CT). Its performance is compared to registration using uniform splines. In experiments using a synthetic, but clinically realistic anatomical deformation, the proposed method reduces the modeling error by about 40%. Alternately, while maintaining the accuracy of uniform splines, it reduces the number of free model parameters by a factor of four.

***Keywords*—**CT reconstruction, deformation modeling, image registration, splines

I. INTRODUCTION

A. Image Registration

Image registration is a technique used to establish an exact point-to-point correspondence between two or more pictures. The images may be taken at different times, with different sensors, imaging modalities, or with different viewpoints [1], [2]. Image registration can be also used to map an image of a subject to an image of a different subject or to a reference atlas image [3]. Generally, registration is accomplished by applying a spatial transformation to an image or image set such that it matches a reference image. The spatial transformation is iteratively adjusted to minimize the difference between the transformed image and the reference image through the use of an optimization algorithm [2]. While the registration method proposed in this paper can be used in various imaging applications, it is presented in the context of medical imaging where the images are representations of human anatomy.

Many image registration techniques assume a rigid body, where the distance between any two points in the body is the same, regardless of the way the body is imaged. This has been shown to be a reasonable assumption for imaging the brain of a singular subject with the same or different modalities. For other parts of the body, or even imaging the brain of different subjects, this assumption does not hold, as internal organs change their position and shape during the imaging process and the size of the brain and other organs vary from individual to individual [2], [3]. As such, techniques for non-rigid registration, also known as deformable image registration (DIR), have been developed to address these shortcomings [4].

Deformable image registration is used to map the movement of an anatomy from one moment in time to another during imaging. This mapping is represented by a free-form deformation vector field (DVF), which relates the position of each anatomical element in the deformed image $S'(\boldsymbol{r})$ to the position in the reference image, $S(\boldsymbol{r})$, as follows:

$$S'(\boldsymbol{r}) = S\big(\boldsymbol{r} + \boldsymbol{d}(\boldsymbol{r})\big) \tag{1}$$

Here, $\boldsymbol{r}$ is the 2D spatial variable and $\boldsymbol{d}(\boldsymbol{r})$ is the DVF. In our notation all bold-faced variables are 2D vectors. With this formulation, image registration becomes a problem of DVF estimation.

In this paper we look at image registration for tumor tracking in time-dependent, or four-dimensional, CT studies (4D-CTs) in radiation therapy.

B. 4D-CT

Radiation therapy is the preferred method of eradicating cancerous tumors located in the thorax and abdomen. To accurately target radiation to the tumor, its size, shape and location have to be known for both planning and delivery [5]-[9]. Image-guided radiation therapy (IGRT) techniques, such as conformal radiation therapy and intensity modulated radiation therapy, use CT imaging to optimize coverage of the target volume without affecting surrounding healthy tissue [5], [10]. A critical feature of IGRT is addressing tumor motion. The most prevalent cause for motion in the thorax and abdomen is breathing [5], [11], [12]. 4D-CT has been used for tumor tracking, where the delivery field follows the tumor during the entire breathing cycle, allowing the patient to breathe freely [13].

In the conventional 4D-CT method, a breathing trace is collected as CT projections are acquired [6], [14]-[16]. Based on their temporal locations within a breathing cycle, the projections are partitioned into several bins [9]. Commonly, 10 time bins are used. A 3D-CT image is reconstructed for each time bin using filtered back-projection, resulting in ten CTs covering a typical breathing period.

Image registration can be used to create an accurate and versatile high-resolution DVF for each pair of consecutive reconstructed CT images. A major concern for image registration is the appropriate modeling of DVFs in the presence of discontinuous motion between organs, for

Elizabeth Zachariah (zachariahes@vcu.edu), A. Vennie Filippas (avfilippas@vcu.edu) and Alen Docef (corresponding author, adocef@vcu.edu, 804-827-7032) are with the Department of Electrical and Computer Engineering, Virginia Commonwealth University, Richmond, VA 23284 USA.

example the sliding motion that occurs between the pleural membranes and the lung wall due to contractions of the diaphragm from breathing inhalation and exhalation [17], [18]. Estimating DVFs in image registration poses the significant challenge of modeling both the smooth movements inside the organs, as well as the discontinuous motions of multiple organs moving freely [19], [20].

C. Modeling with Splines

A majority of spline-based spatial modeling techniques in CT image registration employ uniformly distributed splines. The basis functions are identical across the image and they are centered at points on a uniform rectangular grid. (We should point out that in image modeling the splines are bivariate *surfaces* rather than the *curves* more commonly associated with the term *spline*.) The disadvantage of such basis functions is that the spatial resolution is the same across the image. In most practical scenarios, anatomical details are not uniformly similar in space. One such example is the deformation, due to breathing, in the thorax. This is even more so when only part of the anatomy is in motion. As a result, models using uniform splines end up having a large number of parameters. A large number of degrees of freedom drastically diminishes the robustness of the registration algorithm, almost guarantees that the solution will not be globally optimal, and increases computational complexity.

To illustrate the limitations of uniform splines with a simple one-dimensional example, a rectangular signal is modeled with both uniform and non-uniform quadratic B-splines, as shown in Fig. 1. Seven knots are used, depicted by x-marks on the horizontal axis, resulting in four basis functions. The uniform splines blur the discontinuities present at the edges of the rectangular signal. This creates large errors. These errors can be reduced, but only with an increase in the number of knots. The advantage of non-uniform splines for a signal with discontinuities is clear when comparing the relative root mean square (RMS) modeling error for the same number of knots, which is 32% for uniform splines and 8% for non-uniform splines.

Attempts to extend DVF modeling to non-uniform splines have been hampered by the theoretical and computational complexity of multivariate splines. As a result, the only progress in this direction has been made by using separable splines [21]. These splines still use a rectangular grid for the basis functions but the grid lines are non-uniform along each of the x and y axes. This approach works well if motion occurs in a large but spatially limited area of the image, for example when the upper half of the volume exhibits significantly more motion than the lower half. But this method's performance is limited when motion occurs in a region that is not well aligned with the x and y axes.

The aim of this paper is to develop a model that uses truly non-uniform splines, which can be located at arbitrary locations in the image. For simplicity, we chose thin-plate splines. The process by which the spline points are chosen is as follows:

- First, the gradients of DVF_x and DVF_y are estimated, resulting in four gradient images. A single gradient combining the variation in both the x and y directions is computed by summing the squares of these four images. The combined gradient is a local measure of the amount of discontinuity in the DVF.
- If N is the number of desired spline points, N/2 points are placed randomly where the combined gradient of the original DVFs is high. This is achieved by sampling a bivariate distribution equal to the combined gradient. As a result, more points are chosen in highly discontinuous areas.
- Finally, each of the N/2 points is split into 2 separate points a small distance apart in the direction of the gradient motion, i.e. perpendicular to the discontinuity, resulting in N spline points.

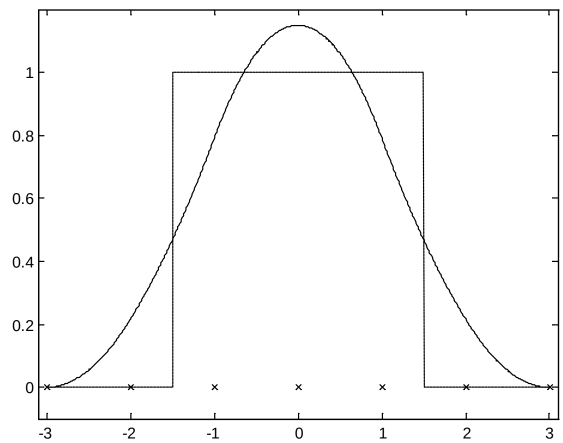

(a)

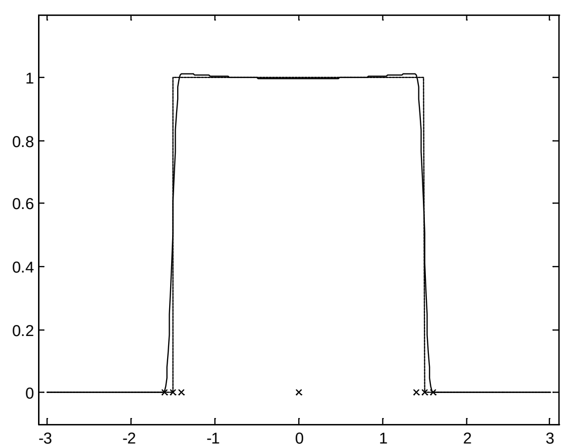

(b)

Fig. 1: Modeling a rectangular signal with (a) uniform splines and (b) non-uniform splines. Both time and amplitude are in arbitrary units. The spline knots are marked by small x-marks.

D. Image Registration with Non-uniform Splines

The image registration process that implements the proposed method is outlined in Fig. 2. The reference image $S(\boldsymbol{r})$ and the deformed image $S^{'}(\boldsymbol{r})$ are the inputs to the algorithm. The output is the optimal set of DVF model parameters, consisting of the amplitudes corresponding to the spline basis functions. Initially, all DVF model parameters are assumed to be zero. An initial DVF is computed using (1) and applied to the reference image. The difference between the computed deformed image and the actual one is then used to drive a gradient-based optimization algorithm. The iterative process is continued until the mismatch converges to a minimum.

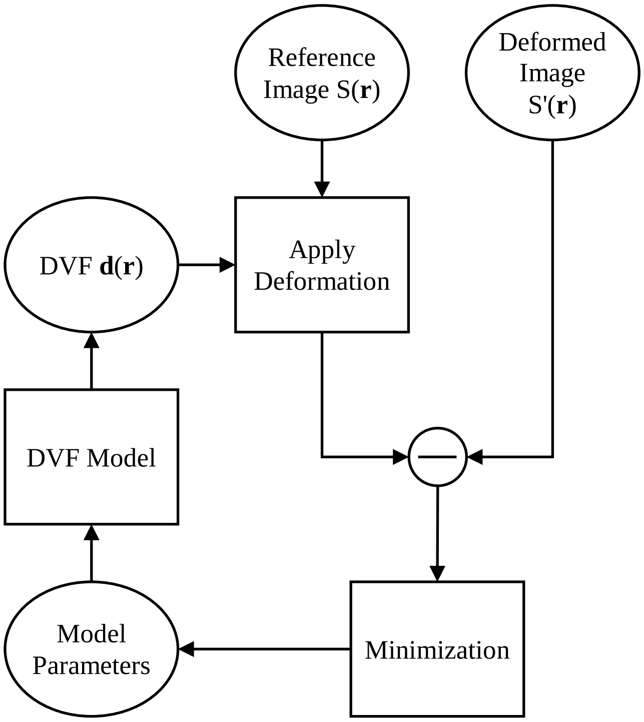

Fig. 2: The image registration process.

II. Experimental setup

Two sets of experiments have been carried out to evaluate the proposed method's registration performance. First, the ability of non-uniform splines to model discontinuous motion is assessed. Second, the suitability of non-uniform spline-based for accurate image registration is investigated.

The CT images in real clinical settings are 3D. In this paper, the feasibility of the proposed registration method is assessed in a simplified setting using 2D CT images.

A. *Image and Displacement Data*

The proposed method is evaluated using a set of synthetic 2D images and DVFs. Three DVFs that represent sliding motion in the lung cavity along different types of boundary are considered: a vertical boundary, a linear diagonal boundary, and a circular boundary. The DVFs are illustrated by quiver plots in Fig. 3.

The *vertical boundary* DVF corresponds to a global displacement to the right by 10% of the image size and a downward motion by 5% for the region to the right of the boundary. The *diagonal boundary* DVF corresponds to a global displacement to the right by 10% of the image size and a downward sliding along the boundary by about 6% for the region to the right of the boundary. The *circular boundary* DVF corresponds to a global displacement to the right by 10% of the image size and a downward rotation along the boundary by 3.6° for the region to the right of the boundary.

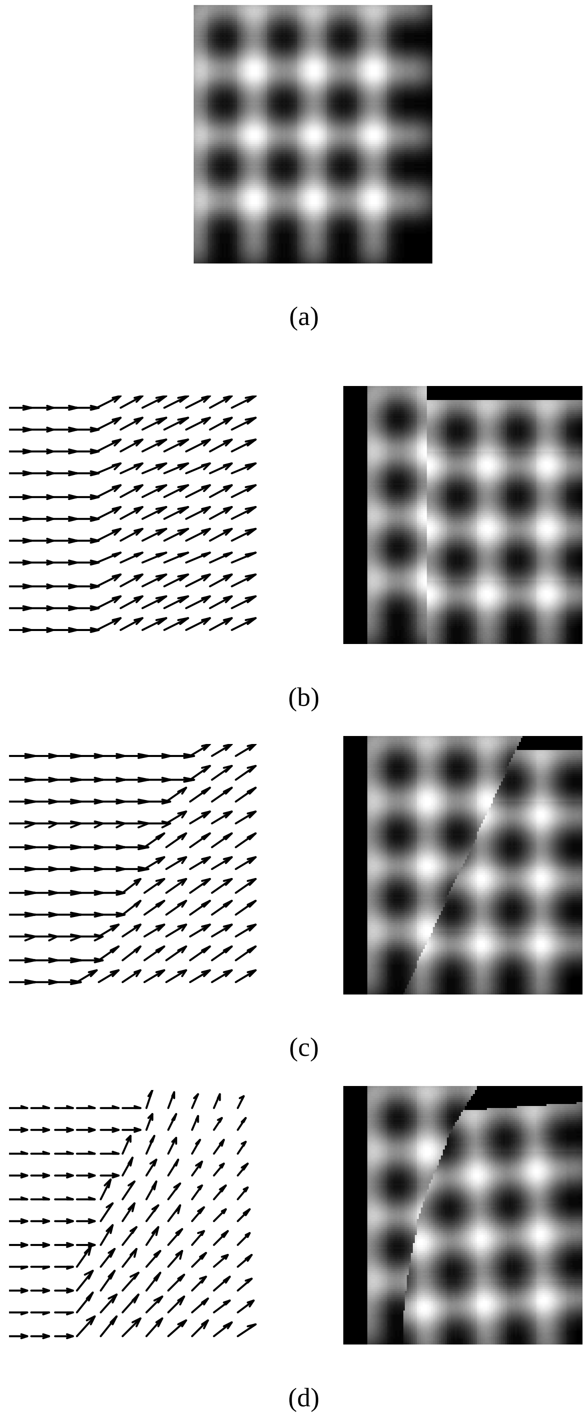

Fig. 3: (a) Original reference image. (b, c, d) Test DVFs with vertical, diagonal, and circular boundaries and their corresponding deformed images.

The test reference image is a 256x256-pixel smooth rectangular grid shown in Fig. 3(a). It is obtained by smoothing a perfect grid of pitch equal to 64 pixels in both directions with a Gaussian lowpass filter with standard deviation equal to 12.8. The three test DVFs are applied to the reference image; the three corresponding deformed images are also shown in Fig. 3.

ISBN: 978-1-61804-321-4

B. Modeling experiments

For the first set of experiments, given the reference image, the deformed image, and the original deformation vector fields, we model a set of estimated deformation vector fields using splines and apply the resulting DVFs to the original deformed image which results in an estimated deformed image.

- Initially the DVFs are reconstructed using a set of 64 spline knots placed on a uniformly distributed grid.
- A combined gradient is computed for the original DVF and 30 spline points are placed randomly in areas where the gradient of the combined gradient is high.
- Each of the 30 knots is split into 2 separate knots placed one pixel apart in the direction of the gradient, resulting in a total of 60 knots.
- One knot is placed at each of the four corners of the image, bringing the total number of knots to 64, same as in the uniformly distributed grid.
- The estimated DVFs, both with uniformly distributed knots and randomly distributed knots, are optimized using the Levenberg-Marquardt iterative optimization method. The nonlinear least squares minimization method terminates when the mismatch in the current iteration is essentially the same (within 10^{-15}) as in the previous iteration.

The accuracy of the method is evaluated by taking the RMS error of the estimated DVFs with the original DVFs.

C. Registration Experiments

In real image registration applications, DVFs are evidently not available a priori; only the reference and deformed images are available. This makes the problem challenging for uniform spline modeling and even more so for non-uniform splines, where an estimate of the gradient of the DVF is also necessary for spline point placement.

To concentrate on assessing the merits of non-uniform splines and avoid the difficulty of actual image registration, in this paper we focus on the challenge of choosing spline point locations from the images themselves when the DVF is actually available. The method we used is a two-step process. First, the DVF is modeled using uniform splines. The estimated DVF is applied to the reference image and the resulting image is subtracted from the original deformed image. The spline points are then randomly chosen in areas where this difference is high. The DVF is then modeled again with non-uniform splines and the modeling performance is compared to the ideal model obtained using the method described in Section II.B.

We are confident that actual image registration, which will be addressed in future work, is achievable with a hierarchical, multi-resolution approach.

III. Results

In the several experiments we carried out, the image registration performance is quantified by the RMS modeling error. It is the RMS value of the difference between the actual DVF and the estimated DVF. Separate modeling errors are computed for the horizontal and vertical components of the DVF (DVF_x and DVF_y). An aggregate error is also computed as the RMS value of the *vector* modeling error. The reported error values are not normalized; they are absolute distances in an image with coordinates extending from -1 to $+1$ in both directions. For instance, a horizontal error of 0.02 corresponds to 1% of the horizontal size of the image.

In a first experiment, we compared the modeling ability of uniform and non-uniform splines for the three test DVFs. The DVFs have been modeled using an 8x8 grid of uniform, separable splines and then using 64 non-uniform splines with points placed randomly using the procedure described previously. The results are summarized in Table I. The aggregate modeling error is reduced by 9%, 36%, and 39%. Not surprisingly, the least impressive improvement is achieved for the simplest, least realistic DVF which best aligns with the uniform rectangular grid.

The breakdown of the aggregate error in the horizontal and vertical directions depends on the nature of the DVF. For the three test DVFs, most of the gain is for the vertical deformation. For example, for the circular boundary DVF, the error is (0.0096, 0.0258) for uniform splines and (0.0070, 0.0154) for non-uniform splines.

To illustrate the modeling error, the estimated circular DVFs have been used to deform the original image and the resulting images are shown in Fig. 4. The uniform splines produced a rough estimation of the original DVF, unable to account for the sharp motion discontinuities. The non-uniform splines produce a visibly superior registered image.

A further optimization of the spline locations was attempted by allowing both spline amplitudes and locations to be free parameters and thus be simultaneously optimized. The amplitudes and locations previously obtained for the circular DVF have been used as the initial guess. The modeling error was reduced insignificantly (by about 10^{-4}); based on this result, no further efforts to optimize the locations have been made.

In a second experiment, we evaluated the effect of the number of free parameters on the modeling accuracy. This accuracy can always be improved by increasing the number of free parameters, but this approach has drawbacks as mentioned earlier. Both uniform and non-uniform splines were used to model the circular boundary DVF with a number of spline points varying from 36 to 144. The results are shown in Table II. We observe that non-uniform splines reduce the modeling error by 40% to 50%. A more illuminating interpretation of the results is that for this example, the accuracy achieved by 144 uniform splines can be achieved by 36 non-uniform splines. The number of free parameters is reduced by a factor of four.

Next, the suitability of the proposed modeling method for image registration is evaluated as described previously. The best trade-off between complexity (as given by the number of free parameters) and accuracy was obtained for 50 splines. The RMS aggregate modeling error is 0.0159, which is slightly better than the error for 64 splines listed in Table I. This somewhat unexpected result indicates that further research into optimal placement of spline points is warranted. The estimated DVF and the image difference-based spline locations are shown in Fig. 6.

IV. CONCLUSION

A novel method for image registration using non-uniform, non-separable cubic splines was proposed. The method has been evaluated in the context of 4D-CT imaging. Experimental results using a synthetic test image and three synthetic DVFs indicate that the proposed method reduces the modeling error by 40% on average. Alternately, it allows the number of free model parameters to be reduced by a factor of four while maintaining the same modeling accuracy.

ACKNOWLEDGMENT

The authors thank Dr. Ou Bai, Dr. Ding-Yu Fei, and Dr. Rosalyn Hobson Hargraves for fruitful discussions and valuable comments.

Table I: Comparison of modeling performance for uniform and non-uniform splines.

	RMS Aggregate Error	
DVF	Uniform Grid	Non-Uniform Grid
Vertical	0.0232	0.0210
Diagonal	0.0278	0.0177
Circular	0.0275	0.0169

Table II: Modeling error for different numbers of control points

	RMS Aggregate Error	
Number of Spline Points	Uniform Grid	Non-Uniform Grid
36	0.0310	0.0185
49	0.0288	0.0171
64	0.0275	0.0169
144	0.0222	0.0112

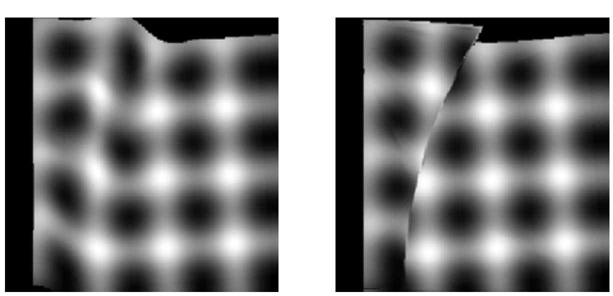

(a) (b)

Fig. 4: Modeled deformation of original image, from DVF model acquired using (a) uniform splines and (b) non-uniform splines.

(a) (b)

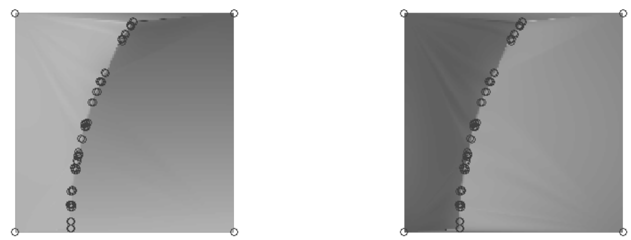

(c) (d)

Fig. 5: (a) Original DVF_x; (b) original DVF_y; (c) and (d) DVF_x and DVF_y modeled using gradient-based non-uniform, non-separable splines. The spline points are marked by small circles.

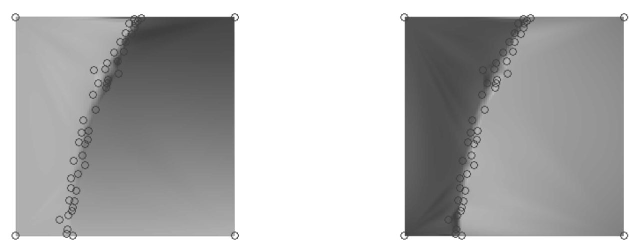

(a) (b)

Fig. 6: (a) DVF_x and (b) DVF_y modeled using image difference-based non-uniform, non-separable splines. The spline points are marked by small circles.

REFERENCES

[1] Lisa Gottesfeld Brown, "A Survey of Image Registration Techniques," *ACM Computing Surveys*, vol. 24, no. 4, pp. 326-376, December 2002.

[2] Derek L. G. Hill, Philipp G. Batchelor, Mark Holden, and David J. Hawkes, "Medical image registration," *Physics in Medicine and Biology*, vol. 46, no. 3, pp. 1-45, June 2000.

[3] Brian F. Hutton, Michael Braun, Lennart Thurfjell, and Dennys Y. H. Lau, "Image registration: an essential tool for nuclear medicine," *European Journal of Nuclear Medicine*, vol. 29, pp. 559-577, 2002.

[4] D. Sarrut, "Deformable registration for image-guided radiation therapy," *Medical Physics*, vol. 16, no. 4, pp. 285-297, 2006.

[5] Lei Xing et al., "Overview of Image-Guided Radiation Therapy," *Medical Dosimetry*, vol. 31, no. 2, pp. 91-112, 2006.

[6] Laura A. Dawson and Michael B. Sharpe, "Image-guided radiotherapy: rationale, benefits, and limitations.," *Lancet Oncology*, no. 7, pp. 848-858, 2006.

[7] L A Dawson and D A Jaffray, "Advances in image-guided radiation therapy," *J Cin Oncol*, vol. 25, pp. 938-946, 2007.

[8] M Baumann, T Holscher, and D Zips, "The future of IGRT - cost benefit analysis," *Acta Oncologica*, vol. 47, no. 7, pp. 1188-1192, 2008.

[9] M. Lecchi, P. Fossati, F. Elisei, R. Orecchia, and G. Lucignani, "Current concepts on imaging in radiotherapy," *European Journal of Nuclear Medicine and Molecular Imaging*, vol. 35, pp. 821-837, 2008.

[10] D. Verellen, M. De Ridder, and G. Storme, "A (short) history of image-guided radiotherapy," *Radiotherapy and Oncology*, vol. 86, pp. 4-13, 2008.

[11] G S Mageras, A Pevsner, and E D Yorke, "Measurement of lung tumor motion using respiration-correlated CT," *Int J Radiat Oncol Biol Phys*, no. 60, pp. 933-941, 2004.

[12] P. Keall, "4-dimensional computed tomography imaging and treatment planning," *Seminars in Radiation Oncology*, vol. 14, pp. 81-90, 2004.

[13] F. Khan et al., "The use of 4DCT to reduce lung dose: a dosimetric analysis," *Medical Dosimetry*, vol. 34, no. 4, pp. 273-278, 2009.

[14] G Chen, J Tang, and S Leng, "Prior image constrained compressed sensing (PICCS): A method to accurately reconstruct dynamic CT images from highly undersampled projection data sets," *Medical Physics*, vol. 35, pp. 660-663, 2008.

[15] P J Keall, G Starkschall, and H Shukla, "Acquiring 4D thoracic CT scans using a multislice helical method," *Phys Med Biol*, no. 49, pp. 2053-2067, 2004.

[16] E. Yorke, K. E. Rosenzweig, R. Wagman, and G. S. Mageras, "Interfractional anatomic variation in patients treated with respiration-gated radiotherapy," *Journal of Applied Clinical Medical Physics*, vol. 6, pp. 19-32, 2005.

[17] Z. Wu, E. Rietzel, V. Boldea, D. Sarrut, and G. Sharp, "Evaluation of deformable registration of patient lung 4DCT with sub-anatomical region segmentations," *Medical Physics*, vol. 35, no. 2, pp. 775-781, 2008.

[18] D. Yang et al., "4D- CT motion estimation using deformable image registration and 5D respiratory motion modeling ," *Medical Physics*, vol. 35, no. 10, pp. 4577-4590, 2008.

[19] L. Risser, F. X. Vialard, H. Y. Baluwal, and J. A. Schnabel, "Piecewise-diffeomorphic image registration: application to the motion estimation between 3D CT lung images with sliding conditions," *Medical Image Analysis*, vol. 17, pp. 182-193, 2013.

[20] D. F. Pace, S. R. Alward, and M. Niethammer, "A Locally Adaptive Regularization Based on Anisotropic Diffusion for Deformable Image Registration of Sliding Organs," *IEEE Transactions in Medical Imaging*, vol. 32, no. 11, pp. 2114 - 2126, July 2013.

[21] Travis J Jacobson and Martin J Murphy, "Optimized knot placement for B-splines in deformable image registration," *Medical Physics*, no. 38, p. 4579, 2011.

Automation for Minimal Processing Combining 3-D Imaging and Ultrasound Imaging as Guidance System

Dominik U. Geier, Mohamed A. Hussein and Thomas M. Becker

Abstract— Minimal processing has recently risen of great value for industrial automation systems. Different resources report cost savings of up to 15 % once a decent automation system is implemented with minimal processing criteria.

In this work the fundamental approach for a robot driven cutting process is tested for the meat processing industry. Therefore, a combination of two vision systems is used contrasting convention. The two vision systems consist of:

- 3-D stereo imaging system for the retrieval of 3-D above surface orientation
- An ultrasound imaging system for under surface guidance

Although the combined guidance system accomplish above- and under-surface guidance, nevertheless a lot of challenges were confronted. Most of the challenges arose due to the nature of the applications. Generally meat processing face similar geometries but with great contrast in dimensions. Other issues addressed include under surface recognition and classification of different tissue segments.

The overall aim is to develop an imaging system, which is able to capture information for guiding the cutting tool above surface and under surface with a minimum energy path which is faster than common practice.

Keywords— Meat Processing, Ultrasound Imaging, Stereo Imaging, Automation, Guidance System

This work was supported by Deutsche Forschungsgemeinschaft DFG (DFG project BE 2245/5-1).

Dominik U. Geier is a member of the Research Group BioPAT - Bio Process Analysis Technology, Technische Universität München, Freising, Bavaria 85354 Germany (phone: +49(0)8161-71-3491; e-mail: dominik.geier@tum.de).

Mohamed A. Hussein is the Leader of the Research Group BioPAT - Bio Process Analysis Technology, Technische Universität München, Freising, Bavaria 85354 Germany (phone: +49 (0)8161-71-3277; e-mail: mohamed.hussein@tum.de).

Thomas M. Becker is the head of the Institute of Brewing and Beverage Technology, Technische Universität München, Freising, Bavaria 85354 Germany (phone: +49 (0)8161 - 71-3261).

I. Introduction

MINIMAL processing has recently risen of great value for different industrial automation systems. In the food processing field, minimal processing is described as "the least possible treatment to achieve a purpose" [1] with the aim of minimizing material and energy input. Once a decent combination automation system with minimal processing criteria is implemented, substantial overall cost savings can be achieved [2,3]. The European Union is a major meat producer, and accounts for over 16 % of global meat production. In Germany, 8.2 million tons of meat have been produced in 2011, a 1.5 % increase over the same period in the prior year. Furthermore, Germany is the European leader in pork production and export [4].

Despite these major economic importance, the meat cutting and especially the fine cutting is still mainly performed by hand due to a lack of automation options. In the manual cutting process, employees divide the pieces of meat, assess the quality and classify the pieces into different quality levels based on that assessment. This is both physically demanding and a monotonous activity. In addition, the ambient temperature is typically less than 12 °C for reasons of hygiene.

These extremely adverse conditions and complexity of meat composition in combination with high expectations of precision, reliability and robustness are determined to fail existing methods for meat fine cutting automation.

In recent years, digital image processing and ultrasonic systems have been increasingly used in various areas of meat processing industry, but not in a combined approach. Especially stereo camera systems provide an improved spatial information than conventional camera systems [5]. Ju et al. used a high resolution stereo camera system to detect the irregular surface anatomy of living pigs and calculated a three-dimensional model of the bodies [6]. The introduction of the B-mode ultrasound (brightness mode) has provided significant advances in examination of living animals and carcasses with ultrasonic waves. By B-mode ultrasound two-dimensional grayscale sectional images of the examined sample are generated in real time using an array transducer. The grayscale value of a pixel is a measure of the amplitude of the ultrasonic echoes at this point and suppresses the so-called echogenicity,

ISBN: 978-1-61804-321-4

i.e. the material's ability to reflect ultrasonic waves [7,8]. B-mode ultrasound systems have been used for reproductive medicine [8–10] as well as for predicting carcass evaluation [7,11,12].

The presented approach combines a stereo imaging based extraction of surface information with an ultrasound based analysis of deeper layers. The stereo camera system results in digital images describing the spatial position and geometry of the carcass, the B-mode ultrasound system delivers section scans describing the internal meat structure.

II. MATERIALS AND METHODS

The stereo camera system consisted of two color cameras with CCD sensors capturing images with a resolution of two megapixels. The two cameras were mounted paraxial at a lightproof measuring box to reduce influences due to fluctuating light conditions. The ham samples were fixed in a special rotating united located inside the measurement box, and with LED light strips homogeneous illumination of the hams was achieved (Fig. 1a). Meanwhile, the vertical fixation of the sample permitted accurate control of rotation about its longitudinal axis, which allows picturing the sample from all necessary views with a rotational step of 9° or less, as described in Fig. 1b.

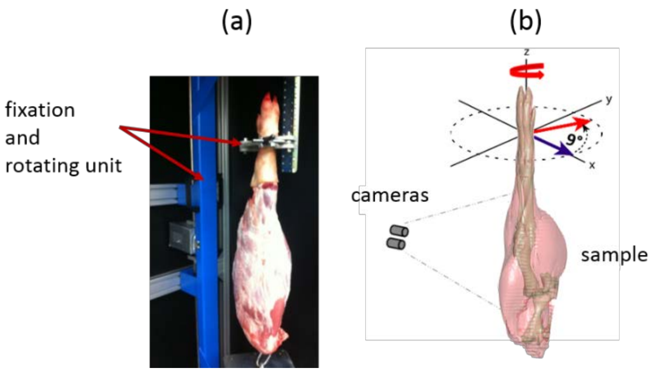

Figure 1. (a) Measurement box with a fixed ham sample in the rotation unit (b) Schematic representation for the rotation technique of the sample around its longitudinal axis by a step of 9°. At each rotational position, images with both cameras are captured and the depth image is calculated

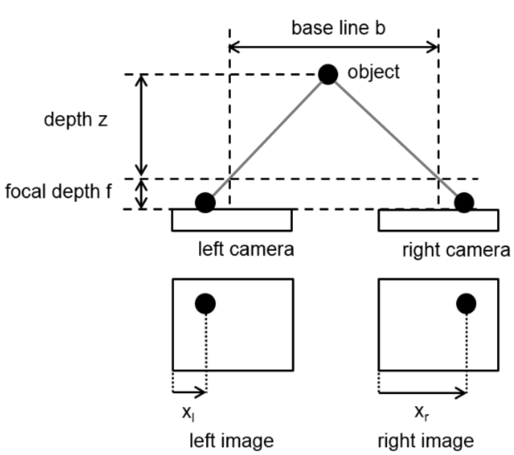

Figure 2. Schematic design of the stereo camera system

The distance of the cameras from each other thereby corresponded to the base line b (Fig. 2). Left and right images were simultaneously captured and with a pixel-based correspondence analysis [13] the disparity d was calculated:

$$d = x_r - x_l \tag{1}$$

where x_r is the image location of an object in the right image and x_l the location of the same object in the left image.
The distance z (depth) of an object point to the camera system was calculated with the relation between focal length f of the cameras, base line b, and disparity d [14] :

$$z = \frac{b*f}{d} = \frac{b*f}{x_r - x_l} \tag{2}$$

From these distance values, a depth image was calculated; where the distance z is represented by different color shades. The reconstruction of missing depth image values was achieved by an anisotropic diffusion filtration based on the Lattice Boltzmann Method. In order to capture the three-dimensional anatomy of the hams; depth images were taken in steps of 9° (Fig. 1b).
For analyzing the inner structure a sonographer (Sonoace X6, ultrasound probe with a center frequency of 2 MHz, Samsung) recording B-mode ultrasound images was used. The ultrasound images were directly digitized with a frame grabber card (2-4 fps) and transferred to a computer for subsequent image processing (Fig. 3).

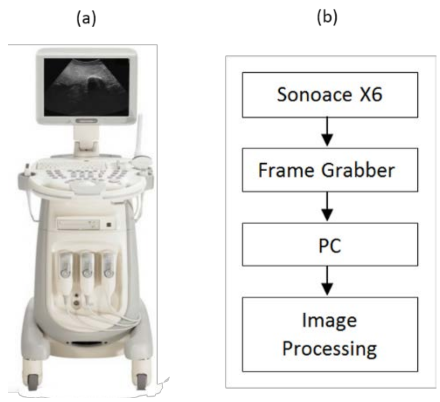

Figure 3. (a) Sonoace X6 machine (b) Ultrasound image grabbing

Because of the large impedance difference between tissue and bones, only a very small part of the ultrasonic waves penetrates into bones. Therefore, the area below a bone in an ultrasound image looks dark, while the bone surface itself causes a strong reflection. This reflection appears in B-mode ultrasound images as a bright stripe of certain thickness [15]. Thus, pixels which are part of a bright stripe possess a high probability to be part of the bone surface. In addition to the strong reflection at the bone surface forming, the so-called acoustic shadow is a characteristic feature for a tissue-bone interfaces and a powerful tool to distinguish bone surfaces from other hyperechoic structures [15,16].
The basic developed algorithm for detecting osseous structures is described in the following paragraph: The ultrasound images were converted to 8-bit grayscale images and cropped. To reduce noise artifacts, which are caused by scattering bodies in the sound field and the main reason for limited quality of ultrasound images [17], the images were processed

ISBN: 978-1-61804-321-4

with an anisotropic filtration [18]. Subsequently, the local maxima were determined for each column of the ultrasound image (see Fig. 5a). Afterwards the characteristics of bones described above were implemented as follows:

- Since osseous structures appear hyperechoic in the ultrasound image, the local maxima were processed with an intensity threshold I. The threshold was 75 % of the maximum intensity I_{max} in each ultrasound image ($I = 0.75 * I_{max}$).
- Subsequently, maxima, which were above the threshold value I were investigated for acoustic shadow formation.

Therefore, the acoustic shadow value (SV) was calculated:

$$SV = (m(a,b) = \frac{\sum_{j=b}^{b+n} I(a,j)}{n+1}$$
(3)

Where m was the particular maximum, a is the column of the ultrasound image, b the row, I is the intensity and n is the number of pixels that were used for acoustic shadow calculation. The shadow value expresses therefore the average brightness value succeeding a local maximum. Thereafter, the relative acoustic shadow value SV_rel was calculated:

$$SV\_rel(a,b) = \frac{I(a,b) - SV(a,b)}{SV(a,b)} \quad (4)$$

Where I (a, b) was the intensity of the maximum m (a, b). Only maxima that had a value of SV_rel > 1.5 were segmented as bone contour. The final step was the image reconstruction from the individual columns and by morphological operations (Closing and Opening) small discontinuities were closed or small structures filtered [19].

A set of 10 different hams was examined with both stereo and ultrasound system. After primal cutting the hams were derinded and stored refrigerated until examination at 4 °C. Then the hams were fixed in the rotation unit and images were captured by steps of 9°. According to equation (1) and equation (2) the disparity and depth were calculated resulting in stereo images. After stereo capturing, the hams were manually scanned with the ultrasound probe aiming for osseous structures. Consequently a set of 256 ultrasound images of 10 different hams was sampled. To check the accuracy of the bone detection algorithm, the bone contours in these ultrasound images were manually segmented by an expert (3-folds, Fig. 5d), and then compared with the results of the automatic segmentation ($I = 0.75 * I_{max}$, n = 60, SV_rel = 1.5). For this, the localization Error (LE) and the length mismatch (Length Agreement, LA) were calculated:

$$LE = \frac{\sum_{i=1}^{k} |Y_i - y_i|}{k}$$
(5)

$$LA = \frac{x}{X} * 100$$
(6)

Where Y is the y-position of a pixel detected as bone with automatic segmentation, y is the y-position with manual segmentation, k is the number of matching data points, X is the overall number of data points detected by automatic segmentation as bone surface, x is the number of data points for manual segmentation.

III. RESULTS AND DISCUSSION

After the depth images were interpolated for gap zones the final depth images were retrieved as seen in Fig. 4a-c. The depth images express color-coded Iso-contours representing the depth of the surface relative to the reference point. The resulted depth images exhibited decent qualitative results. They provided the basis of above-surface cutting tool guidance.

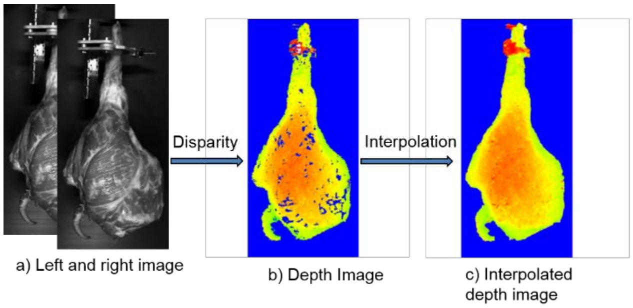

Figure 4. Depth image processing (a-b) and result of the anisotropic filtration

Below surface tool guidance was achieved using ultrasound imaging as expressed earlier. The procedure for the under surface bone detection is seen in Fig. 5a-c. The process handles severe challenges as discussed earlier, such as predicted bone edge discontinuities.

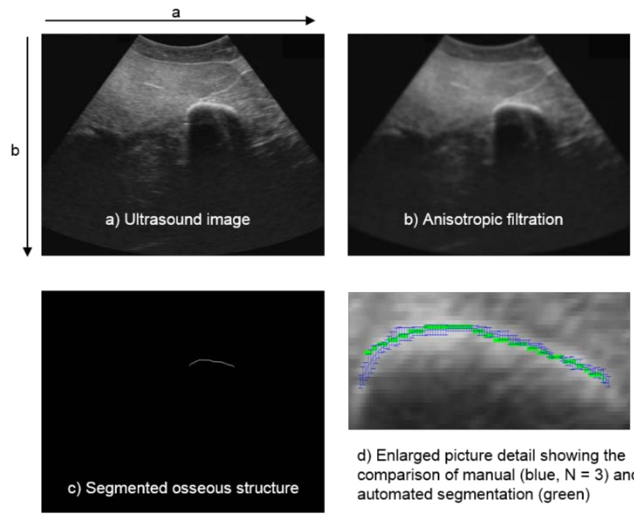

Figure 5. Example steps of the bone detection algorithm

As seen in Fig. 5d the results of the prediction of a shell-shaped bone is shown after the discontinuities were handled, the method possessed an accuracy of 0.30 ± 0.14 mm, the errors of prediction in pixel values are also expressed in Table 1, with a Length Agreement of approximately 85 ± 15 %.

Table 1: Comparison of manual and automatic segmentation (N = 256)

LE [Pixel]	LA [%]
1,00 ± 0,45	84,65 ± 14,23

ISBN: 978-1-61804-321-4

IV. Conclusions And Outlook

The objective of the present study was to develop and evaluate a combined approach for meat process automation. Both systems proved their fundamental qualification in an adverse environment. The described combination of surface structure detection and analysis of the deeper layers provides a novel approach to automated cutting. In addition to the cutting process, contamination analysis could be performed in future, because both superficial and deep tissue anomalies can be detected with such a system. Therefore, food safety of meat could be increased significantly in the context of HACCP (Hazard Analysis of Critical Control Points) concepts by detection of abscesses and foreign bodies such as broken knife blades or bone fragments.

Current research is performed in combining the two systems. Therefore, a 3D-modell describing the spatial position of the sample is devolved. This based on a rotation matrix approach, where the rotation around the y-axis R_y by an angle θ is described as [20]:

$$R_y(\theta) = \begin{bmatrix} x' \\ y' \\ z' \end{bmatrix} = \begin{bmatrix} \cos(\theta) & 0 & \sin(\theta) \\ 0 & 1 & 0 \\ -\sin(\theta) & 0 & \cos(\theta) \end{bmatrix} * \begin{bmatrix} x \\ y \\ z \end{bmatrix} \qquad (7)$$

where x is the x-axis value and z the depth value from the stereo image. Furthermore, a robot arm is equipped with the ultrasound probe. Since the 3D-modell then delivers the spatial position of the sample, a robot guided ultrasound scan can be performed combing surface and inner structure analysis.

V. References

[1] C. Manvell, Minimal processing of food, Food Science and Technology Today 11 (1997) 107–111.

[2] C.A. Moore, Automation in the Food Industry, Springer US, 2012.

[3] Y.H. Hui, Handbook of Food Science, Technology, and Engineering Bd. 3, Taylor & Francis, 2006.

[4] Verband der Fleischwirtschaft e.V., Jahresbericht 2011-2012 (2012).

[5] I.P. Howard, B.J. Rogers, Seeing in Depth, Oxford University Press, 2008.

[6] X. Ju, J. Paul Siebert, N.J. McFarlane, J. Wu, R.D. Tillett, C. Patrick Schofield, A stereo imaging system for the metric 3D recovery of porcine surface anatomy, Sensor Review 24 (2004) 298–307.

[7] V. Pathak, V.P. Singh, Y. Sanjay, Ultrasound as a Modern Tool for Carcass Evaluation and Meat Processing: A Review, International J. of Meat Science 1 (2011) 83–92.

[8] S.J. Moeller, Evolution and use of ultrasonic technology in the swine industry, J. Anim. Sci. 80 (2002) 19–27.

[9] O.J. Ginther, How ultrasound technologies have expanded and revolutionized research in reproduction in large animals, Theriogenology 81 (2014) 112–125.

[10] J. Kauffold, G.C. Althouse, An update on the use of B-mode ultrasonography in female pig reproduction, Theriogenology 67 (2007) 901–911.

[11] M. Theriault, C. Pomar, F.W. Castonguay, Accuracy of real-time ultrasound measurements of total tissue, fat, and muscle depths at different measuring sites in lamb, Journal of Animal Science 87 (2009) 1801–1813.

[12] D.B. Griffin, J.W. Savell, H.A. Recio, R.P. Garrett, H.R. Cross, Predicting carcass composition of beef cattle using ultrasound technology, J. Anim. Sci. 77 (1999) 889–892.

[13] J. Schers, J. Troccaz, V. Daanen, C. Fouard, C. Plaskos, P. Kilian, P6D-1 3D/4D Ultrasound Registration of Bone, in: 2007 IEEE Ultrasonics Symposium Proceedings, pp. 2519–2522.

[14] K. Muhlmann, D. Maier, R. Hesser, R. Manner, Calculating dense disparity maps from color stereo images, an efficient implementation, in: IEEE Workshop on Stereo and Multi-Baseline Vision (SMBV 2001), 9-10 Dec. 2001, pp. 30–36.

[15] A.K. Jain, R.H. Taylor, W.F. Walker, S.Y. Emelianov, Understanding Bone responses in B-mode Ultrasound Images and Automatic Bone Surface extraction using a Bayesian Probabilistic Framework, pp. 131–142.

[16] V. Amin, USOFT: An Ultrasound Image Analysis Software for Beef Quality Research.

[17] R. Vanithamani, G. Umamaheswari, Performance Analysis of Filters for Speckle Reduction in Medical Ultrasound Images, IJCA 12 (2010) 23–27.

[18] P. Perona, J. Malik, Scale-space and edge detection using anisotropic diffusion, IEEE Trans. Pattern Anal. Machine Intell. (IEEE Transactions on Pattern Analysis and Machine Intelligence 12 (1990) 629–639.

[19] R.C. Gonzalez, R.E. Woods, S.L. Eddins, Digital Image processing using MATLAB, Pearson Prentice Hall, Upper Saddle River, N.J, 2004.

[20] B. Siciliano, L. Sciavicco, L. Villani, G. Oriolo, Robotics: Modelling, Planning and Control, Springer, 2009.

Simulation of Impulse Voltage Stresses in Underground Cables

Kaveri Bhuyan
Department of Electric Power Engineering,
Norwegian University of Science and Technology,
Trondheim N-7465, Norway
kaveri.bhuyan@ntnu.no

Saibal Chatterjee, Mudang Taro
Department of Electrical Engineering,
North Eastern Regional Institute of Science and Technology, Arunachal Pradesh, India
saibalda@ieee.org / mtyuce@gmail.com

***Abstract*—**The goal of this work is to study the transient behavior of the cable against the application of standard and non-standard lightning impulse voltage waveforms. A 66 kV cable model has been developed in MATLAB Simulink and standard and non-standard impulse voltages are applied to it. A preliminary comparative study on the obtained voltages indicated that non-standard impulse voltage waveform developed higher voltage stress in the cable. Simulation results helped to investigate which impulses (standard or non-standard) represent the worst possible voltage stresses on the cables. This study provides the basis for further study of effects of non-standard impulse voltage waveforms and make necessary correction in the existing impulse testing standards.

Keywords— Impulse test; Cables; standard and non-standard impulse waves; transients

I. INTRODUCTION

There has been an increasing concern about enhancing the safety and reliability of power equipments. Cables are an integral part of transmission and distribution network. They are exposed to a variety of impulse voltages during their lifetime. The exposure to these impulse voltages deteriorates the cable insulation and leads to breakdown [1]. The severity of insulation degradation depends on steepness of the wave, instant of chopping, time to collapse, frequency of oscillations, overshoot near the peak etc. [2]. Impulse testing is generally done in high voltage laboratory for assessing the insulation strength of equipments [3]. During impulse tests, voltage sequences of standard waveshape are generated in the laboratory and applied to the equipment as per testing standards. The lightning impulse test is done according to IEC 60060-1 (2010) using standard impulse voltage waveform having front time and a time to half-value of 1.2/50 μs and switching impulse test is done using voltage waveform having front time and a time to half-value of 250/2500 μs [3]. During impulse test performed in laboratory, the impulse generator often fails to generate the standard wave shape within tolerance limits due to disagreement in circuit parameters etc. In such case, cables are exposed to non-standard voltages of both unidirectional and bi-directional oscillating waves. Also, several studies have established that naturally occurring transient voltages do not always resemble the standard wave shape [4].

In this work, our aim is to investigate the transient behaviour of a 66 kV underground cable under standard as well as few non-standard impulse voltage waveforms by computational method. The test results will contribute to further study of non-standard impulse voltage that may identify the need for modifying existing test standards or introducing new standards for impulse testing of power equipment.

II. SIMULATED CABLE MODEL DESIGN

A high frequency circuit model of a 66 kV single core cable system is used to simulate transient effects [5]. Fig. 1 [5] shows the structure of the single core 66 kV, 1000 mm^2 aluminum, XLPE single core cable. The cable conductor is stranded aluminium and the cable is concentric with inner and outer semi-conducting layers and the main (XLPE) insulation between the semi-conducting layers. The metallic shielding comprises helical copper strands and the outer covering is polyethylene (PE). Further details about dimensions and material data are given in Table 1 [6].

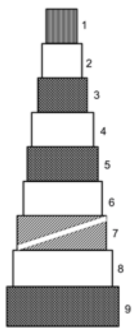

ISBN: 978-1-61804-321-4

Figure 1 Cable structure [5]

1. Conductor 2. Semiconductor tape 3. Inner semiconductor screen 4. XLPE insulation 5. Outer semiconductor screen 6. Water proof screen 7. Copper wire screen 8. Extruded filler 9. Polyethylene (PE) outer sheath

TABLE 1 CABLE DETAILS [6]

Parameters	**Radius (mm)**	**Thickness (mm)**	**Resistivity ρ (Ωm)**
Conductor	19.5		3.46×10^{-8}
Inner semi-conductor		0.8	
XLPE Insulation		14	
Outer semi-conductor		0.4	
PE outer sheath		4	
Wire screen	0.56		1.72×10^{-8}

III. CABLE MODELLING

The transient behavior of cable is sensitive to the accurate mathematical representation of core, main insulation, semiconductors, and the metallic sheath. The basic parameters used to represent the distributed transmission line/cable models are the series impedance matrix (Z) and shunt admittance matrix (Y). Z and Y are expressed in terms of the series resistance (R), series inductance (L), shunt conductance (G), and shunt capacitance (C) per unit length of the cable [5]. These parameters are calculated from cable geometry like location of conductor, thickness of conductive layer, burial depth of the cable system etc. and material properties like resistivity and relative permeability of conductors and surrounding medium, relative permittivity of insulating material etc. They are formulated as below [5]:

$$Z(\omega) = R(\omega) + jL(\omega) \tag{1}$$

$$Y(\omega) = G(\omega) + jC(\omega) \tag{2}$$

These parameters are frequency dependent and so expressed as functions of ω. All elements of equation (1) and (2) are n x n square matrices, where n is the number of parallel conductors of the cable system.

The cable parameters are also determined through experimental analysis by checking the frequency response of the power cable characteristic impedance. The parameters of the cable model are calculated by analyzing the behavior of the short-circuit impedance (Z_{SC}) and open-circuit impedance (Z_{OC}) over a broad range of frequency. The cable characteristic impedance is calculated from short circuit (Z_{SC}) and open circuit impedances (Z_{OC}) according to equation (3) [7]:

$$Z_O = (Z_{OC} Z_{SC})^{1/2} \tag{3}$$

The admittance between core and sheath is modelled as shown in Fig. 2 [6,8]. The parallel combination of resistor and capacitor, R_1C_1 and R_2C_2 represents the inner and outer semi-conductor screens respectively. The capacitor, C represents the main insulation of the cable.

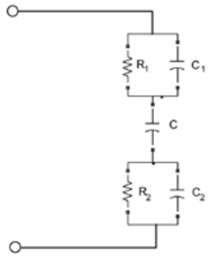

Figure 2 Equivalent circuit for admittance calculation [6,8]

The model parameters are calculated using the following equations (4) to (7) [6, 7]:

$$C_1 = 2\pi\varepsilon_0\varepsilon_r/\ln(r_2/b) \tag{4}$$

$$G_1 = 1/R_1 = 2\pi\sigma/\ln(r_2/b) \tag{5}$$

$$C_2 = 2\pi\varepsilon_0\varepsilon_r/\ln(a/r_1) \tag{6}$$

$$G_2 = 1/R_2 = 2\pi\sigma/\ln(a/r_1) \tag{7}$$

C = 0.24 nF/m (from manufacturer data)

Here,
a = Outer radius of inner semiconductor screen
b = Inner radius of outer semiconductor screen
r_1= Radius of core conductor
r_2= Radius of core conductor and sum of thicknesses of semiconductor screens and main insulation
ε_0 = 8.854 pF/m (Permittivity of free space)
ε_r=100 (Relative permittivity of semiconductor screens)
σ = 0.01 (Conductivity of semiconductor screen)

The admittance of the semiconducting layer plays an important role during transient analysis [9]. Z is calculated using the formula given by Schelkunoff [10].

The per unit length (1 m) circuit of the cable used for simulation studies is shown in Fig. 3. Multiple segment lumped parameter cable model is used in this work for modeling the power cable of lengths 7 m, 14 m, 21 m, 28 m and 35 m.

ISBN: 978-1-61804-321-4

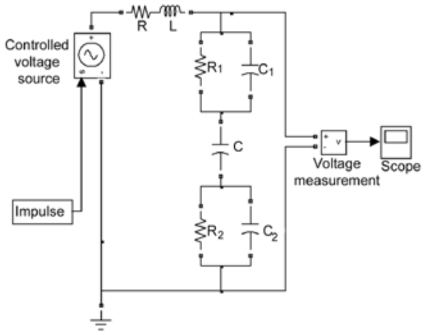

Figure 3 MATLAB-Simulink model for 1 m of cable

The developed cable model consists of the following blocks:

a. The controlled voltage source block converts the Simulink input signal into an equivalent voltage source. The input signal to this block is an impulse voltage (standard and non-standard impulse) generated in MATLAB. The details of the generated signals are desribed in section IV.
b. Series combination of resistor and inductor R and L, representing the core conductor of the cable
c. Parallel combination of resistor and capacitor, R_1C_1 and R_2C_2 representing the semi-conductor screens
d. Single capacitor, C representing the main insulation
e. The voltage measurement block measures the instantaneous voltage between two nodes.
f. Scope displays the output signal. The displayed waveforms can then be used to measure time and voltage values.

Parameter configuration of the cable model in MATLAB is done as below:

Simulation time:

Start time: 0.0

Stop time: 10 µs

Solver options:

Type: Variable step

Solver: ode23t (Mod. stiff/ Trapezoidal)

Max. Step size: auto

Initial step size: auto

Relative tolerance: 10^{-3}

Absolute tolerance: auto

Zero crossing control: use local setting

Solver type Ode23t is an implementation of the trapezoidal rule and can solve problems with a mass matrix that is singular, i.e., differential algebraic equations.

IV. Simulation of Cable Transients

The maximum permissible sheath armour voltage for the 66 kV single core cable is 33 kV and rated lightning withstand voltage is 325 kV_p [6].

A. Input impulse voltage waveforms

Four different types of impulses are applied to the cable model at 325 kV_p namely the standard lightning impulse (1.2/50 µs), chopped impulse (3 µs), chopped impulse (15 µs) and non-standard (oscillating and non-oscillating) impulse voltage waveforms. The non-standard impulse waveforms are used in order to denote some more realistic waveforms than the typical standard waveform. The applied impulse waveforms are generated in MATLAB and are briefly explained below:

A.1 Standard full lightning impulse voltage

As per IEC 60060-1 [3] standard, a full standard lightning voltage rises to its peak value in 1.2 µs and the tail of the wave decay to a level of 50 percent of the peak in 50 µs. The waveform is mathematically modelled by superposition of two exponential functions with different time constants as given in equation (1) [3]. The wave shape of a full lightning impulse used in this work is shown in Fig. 4.

$$V=V_O\,[e^{(-\alpha t)} - e^{(-\beta t)}] \qquad (1)$$

Where $\alpha = 0.0146$, $\beta = 2.467$, and $V_O = 1.04*(325X\ 10^3)$

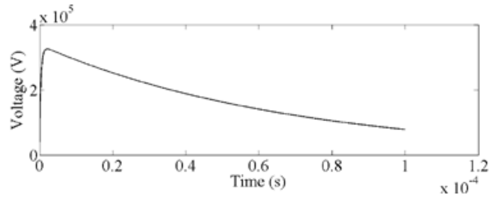

Figure 4 Full standard lightning impulse waveform

A.2 Chopped lightning impulse voltage

Standard lightning waveform can be chopped on the tail, peak or front. It is developed during flashover or puncture. In chopped lightning impulse, the voltage collapse on the tail is rapid compared to rise time and consists of negative overshoot. In this work, impulse waveform chopped on tail is used for analysis. The negative overshoot portion in the chopped impulses is very small and so has been ignored. Impulses with chopping time of 3 µs, and 15 µs on tails are used. The wave shapes of chopped lightning impulses are shown in Fig. 5.

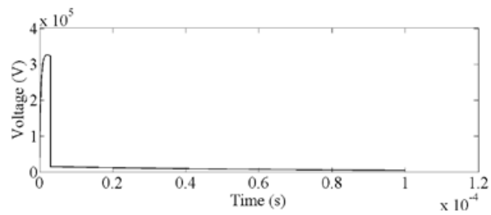

a) Chopped lightning impulse waveform at 3 µs

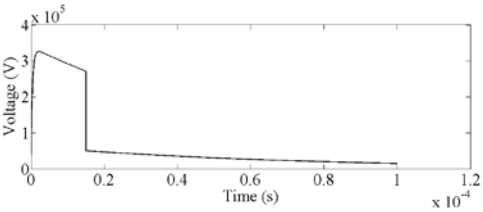

b) Chopped lightning impulse waveform at 15 µs

Figure 5 Chopped lightning impulse waveform at a) 3 µs, and b) 15 µs

A.3 Non-standard non-oscillating single pulse impulse voltage waveform

Impulse waveforms generated in the laboratory have different rise and decay time compared to specified standards. Single pulse waveform is a non-oscillatory non-standard type of impulse. The wavefront time of the impulse is 0.8 µs and the tail of the wave decays to a level of 50 percent of the peak in 2.8 µs. The wave shape of a single pulse impulse waveform is shown in Fig. 6.

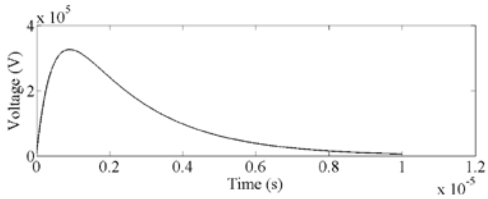

Figure 6 Single pulse impulse waveform

A.4 Non-standard oscillating waveform

Oscillations can occur in the peak or front of impulse waveforms due to resonance or disagreement in circuit parameters of generator. The waveshape of a typical damped oscillating impulse waveform is shown in Fig. 7. It is characterized with damping frequency of 0.5 MHz.

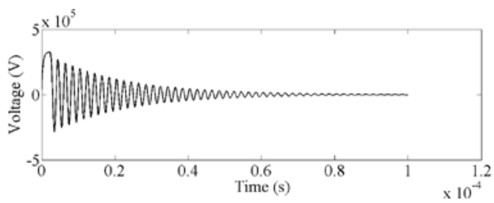

Figure 7 Damped oscillating impulse waveform

B. Output impulse waveforms

The voltage signals observed against the application of standard and non-standard impulse waveforms are shown in Fig. 8.

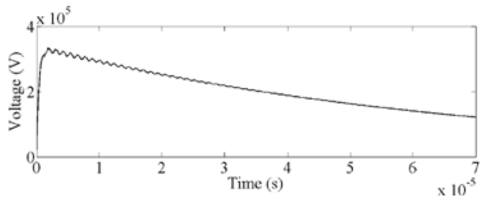

a) Voltage to ground observed in 1 m, 66 kV cable against application of full impulse voltage

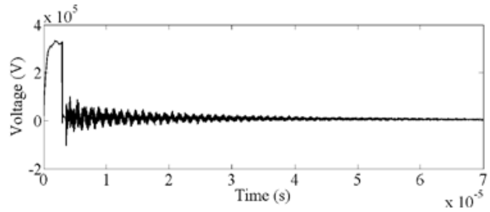

b) Voltage to ground observed in 1 m, 66 kV cable against application of 3 µs chopped impulse voltage

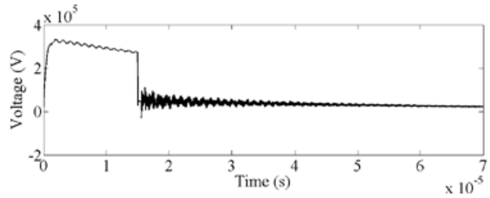

c) Voltage to ground observed in 1 m, 66 kV cable against application of 15 µs chopped impulse voltage

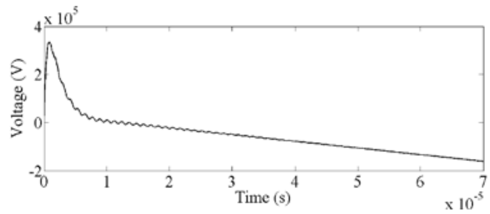

d) Voltage to ground observed in 1 m, 66 kV cable against application of single pulsed impulse voltage

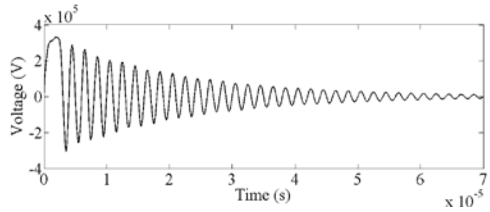

e) Voltage to ground observed in 1 m, 66 kV cable against application of damping impulse voltage

Figure 8 Transient response of cable (1 m) against the application of standard and non-standard impulse waveforms

The voltage to ground is observed at 1 m, 7 m, 14 m, 21 m, 28 m, and 35 m of the cable. The maximum voltage to ground obtained at the different lengths of the cable against the application of different impulse waveforms comprising of standard and non-standard impulses is given in Table 2.

TABLE 2 MAXIMUM VOLTAGE OBTAINED AGAINST THE APPLICATION OF STANDARD AND NON-STANDARD IMPULSE WAVEFORMS

Applied Impulse Waves	Maximum voltage to ground (kV) observed at cable length(s)					
	1 m	7 m	14 m	21 m	28 m	35 m
Full Lightning waveform	334.5	377.5	421	455.6	481.2	488.4
15 µs chopped impulse	334.8	377.9	423	456	481	490
3 µs chopped impulse	334.5	378	420	456	480	488.2
Single pulsed	335	405	475	527	562	574
Damped oscillating	334.5	377.7	420	456	481	490

Fig. 9 shows the percentage increase in voltage with respect to rated lightning withstand voltage of 325 kV_p along the length of cable against the application of standard and non-standard impulse waveforms.

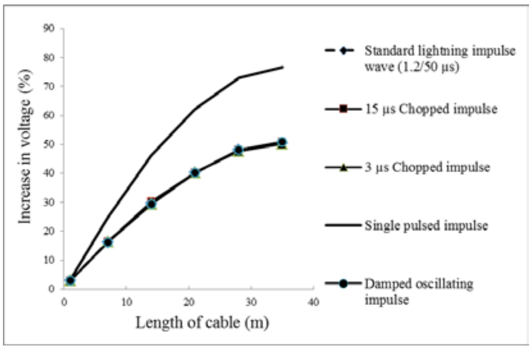

a) Percentage increase in voltage against the length of the cable for different standard and non-standard impulse waves

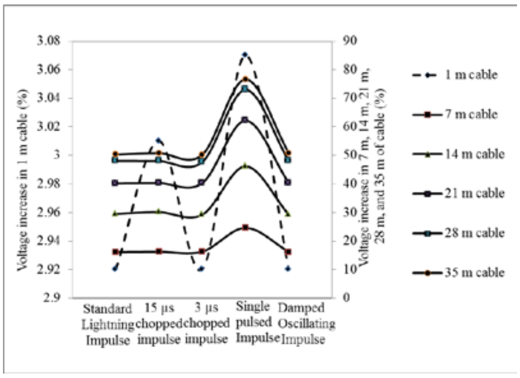

b) Percentage increase in voltage against the application of standard and non-standard impulse waves for various lengths of the cable.

Figure 9 Variation of voltage increase along the cable against the application of different impulse waveforms.

C. Inferences

It is observed from Fig. 8 that for the same applied transient peak voltage, the voltage crest across the cable keeps on increasing with increasing cable length. From Fig. 9, it is clear that maximum voltage profile is obtained for the non-standard single pulsed non-oscillating impulse voltage waveform for all considered lengths of the cable. The general trends of voltage increase except that of the 1 m length is same for all cable lengths. It is thus evident that cable length and impinging voltage shapes strongly influence the overvoltage attenuation in the cable.

V. Conclusion

In this work, MATLAB Simulink is used for modeling and simulation of a 66 kV underground single core cable to study the transient behavior. Four different types of voltage wave shapes impinging the cable have been used for investigation. Transient response is studied against the variation of the input impulse voltage waveforms, and along different lengths of the cable. In comparison to full lightning impulse, the increase in voltage observed for non-standard impulse waveforms is given in Table 3.

Table 3 Comparison of maximum voltage against application of standard and non-standard impulse voltage in cable

Type of non-standard impulse voltage	Percentage increase in voltage in the equipment compared to standard full lightning impulse	Related Standard which shall be affected
Non-standard single pulsed waveform with wavefront time of 0.8 µs and a time to half-value of 2.8 µs	Increase by 17.53 % for 35 m length of the cable	IEC 60230 - ed.1 (1966) IEC 60502-2 ed.3 (2014) IEEE Std. 82 (2002)

However, more number of non-standard impulses representing the actual surges is aimed to be generated in future work to test the cable model establishing the fact that standard testing waveforms do not always develop the worst possible voltage stress to the insulation system of power cables. Cable length plays a relevant role in overvoltage analysis. It is therefore very important to use adequate number of segments in the lumped parameter representation of the cable. Attempts will be made to investigate the applicability and validity of model, detecting and classifying fault transients using different simulation platform and experimental analysis.

References

[1] M. H. Shwehdi, A. S. Farag, C. Belhadj and M. A. Aburaida, "Long and short high voltage cable effects on transient overvoltages," *IEEE International Symposium on Electrical Insulation*, pp. 134-139, June, 1998.

[2] E. Gockenbach, "Impact of new lightning and switching impulse definitions on the test results for insulation systems," *Proceedings of 2005 lntemational Symposium on Electrical Insulating Materials*, Japan, June, 2005.

[3] IEC 60060-1,"High-voltage test techniques part 1: general definitions and test requirements," September, 2010.

[4] Task Force 15.09, "Review of research on non-standard lightning voltage waveson non-standard lightning voltage waves lightning and insulator subcommitte of the T & D Committee," *IEEE Transactions on Power Delivery*, vol. 9, October, 1994.

[5] B. Gustavsen, "A study of overvoltages in high voltage cables with emphasis on sheath overvoltages," *Dr. ing.thesis*, The Norwegian Institute of Technology, Trondheim, Norway, 1993.

[6] B. Gustavsen, "Panel session on data for modeling system transients insulated cables," *IEEE Power Engineering Society Winter Meeting*, vol. 2, pp. 718,723, 2001.

[7] A. F. Moreira, T.A. Lipo, G. Venkataramanan, and S. Bernet, "High-frequency modeling for cable and induction motor overvoltage studies in long cable drives," *IEEE Transactions on Industry Applications,* vol. 38, pp. 1297-1306, October, 2002.

[8] G.C. Stone and S.A. Boggs, "Propagation of Partial Discharge Pulses in Shielded Power Cable", IEEE Proceedings of Conference on Electrical Insulation and Dielectric Phenomena, National Academy of Sciences, Washington, DC, pp. 275-280, October 1982.

[9] A. Ametani, "The history and recent trends of transient analysis in transmission lines," *International Conference on Power Systems Transients (IPST2013) Vancouver, Canada* July, 2013.

[10] S. A. Schelkunoff, "The electromagnetic theory of coaxial transmission line and cylindrical shields," *Bell Systems Technical Journal,* vol. 13, pp. 532-579, 1934.

Fluorometric biomass estimation in *Pichia pastoris* cultures using PLS regression

Vincent J. A. Brunner, Mohamed A. Hussein and Thomas M. Becker

Abstract**—**Real-time monitoring of the key variables biomass, substrate and product is essential for retrieving information about the process state and effectively controlling the bioprocess. However, there is often a lack of reliable analyzers for this key variables due to the inherent complexity of biological systems and the non-linearity of batch and fed-batch bioprocesses. Measurements of single-wavelength fluorescence are promising as a starting point for bioprocess monitoring by providing initial data that are correlated to the central key variables biomass. This data can be used to estimate biomass concentrations in *Pichia pastoris* cultures by data-driven modeling approaches. In this work, the evolution of different biogenic fluorophores involved in the metabolism of *P. pastoris* was determined at four different single wavelength combinations (excitation/emission) in batch cultures. Partial least squares (PLS) regression was used to model the correlation between the fluorescence measurements and biomass. The evolution of cell density was determined by optical density measurements as a reference value for model validation. Results indicate a successful fitting of the PLS regression model for the present case and confirm the relevance of biogenic fluorophores for bioprocess state variables monitoring. The root mean squared error of prediction (RMSEP) between the predicted and measured values for the validation batches was 0.051 g L^{-1} dry cell weight. The information obtained can be used for state estimation and control of the bioprocess.

Keywords**—***Pichia pastoris*, bioprocess monitoring, biomass estimation, partial least squares regression

I. Introduction

THE methylotrophic yeast *P. pastoris* is frequently used in industry and research as a host for expression of heterologous genes with to date over 500 recombinant proteins being expressed in this system [1, 2]. Fed-batch cultivation is generally preferred over continuous cultivation due to the high cell densities and an easier process control. Despite the decades of experience with *P. pastoris* in industry and academia, optimization potential within the production of recombinant proteins in *P. pastoris* can still be found [3, 4]. A common problem in bioprocess monitoring and control is the online determination of the key variables biomass, substrate, and product. The central variable in bioprocess monitoring is the biomass because the measurement of biomass is included in all mathematical models used to describe cell growth [5]. For the measurement of biomass, several techniques have been applied such as optical density measurements, laser cytometry, high performance liquid chromatography (HPLC), nuclear magnetic resonance (NMR), biosensors, or capacity measurements [6].

A promising technique for bioprocess monitoring is fluorescence spectroscopy since many biogenic fluorophores are strongly linked to the progress of biomass development. This interconnection was used in the past to correlate single excitation-emission wavelengths to biomass. The coenzyme nicotinamide adenine dinucleotide (phosphate) NAD(P)H [7] and the amino acid tryptophan [5, 8] were used for this purpose. Another biogenic fluorophore, riboflavin, was later in addition used for estimation of biomass and substrate in a *P. pastoris* bioprocess [9]. The authors used 2D fluorescence spectroscopy to analyze the relevant wavelength pairs (excitation/emission) and showed the sensitivity of the three mentioned biogenic fluorophores with regard to biomass prediction potential.

In this work the single-wavelength fluorescence measurements for the predetermined [9] wavelength combinations for tryptophan, NAD(P)H, and riboflavin where used to predict biomass. The statistical method used for this purpose was partial least squares (PLS) regression.

II. Materials and Methods

A. Strain and culture conditions

A single colony of *P. pastoris* type strain DSMZ 70382 grown on a YPD plate (yeast extract, 10 g L^{-1}; peptone, 20 g L^{-1}; glucose, 20 g L^{-1}; bacteriological agar, 15 g L^{-1}) was used to inoculate a 250 mL shake flask with 100 mL of FM22 medium: $CaSO_4 \cdot 2H_2O$, 0.93 g L^{-1}; K_2SO_4, 18.2 g L^{-1}; $MgSO_4 \cdot 7H_2O$, 14.9 g L^{-1}; KOH, 4.13 g L^{-1}; glycerol, 40 g L^{-1}; and trace element solution, 4.3 mL L^{-1} of the culture medium. The trace element stock solution contained: $CuSO_4 \cdot 5H_2O$, 6 g L^{-1}; KI, 0.8 g L^{-1}; $MnSO_4 \cdot H_2O$, 3 g L^{-1}; $Na_2MoO_4 \cdot 2H_2O$, 0.2 g L^{-1}; H_3BO_3, 0.2 g L^{-1}; $CaSO_4 \cdot 2H_2O$, 0.5 g L^{-1}; $ZnCl_2$, 20 g L^{-1}; $FeSO_4 \cdot H_2O$, 65 g L^{-1}; biotin, 0.2 g L^{-1}; conc. H_2SO_4, 5 mL.

The shake flask culture was used to inoculate 200 µL FM22

This work was supported by the German Federal Ministry of Education and Research (project 031A616D).

Vincent J. A. Brunner is with the RG BioPAT - Bio Process Engineering and Process Analysis department, Technische Universität München, Freising, Bavaria 85354 Germany (phone: +49(0)8161-71-3491; e-mail: vincent.brunner@tum.de).

Mohamed .A. Hussein is with the RG BioPAT - Bio Process Engineering and Process Analysis department, Technische Universität München, Freising, Bavaria 85354 Germany (phone: +49 (0)8161-71-3277; e-mail: mohamed.hussein@tum.de).

Thomas M. Becker is with the Lehrstuhl für Brau- und Getränketechnologie, Technische Universität München, Freising, Bavaria 85354 Germany (phone: +49 (0)8161 - 71-3261; e-mail: tb@tum.de).

ISBN: 978-1-61804-321-4

medium in a black 96 well plate (Greiner Bio-One International GmbH). The plate was incubated with agitation at 30 °C in a Synergy™ H4 Hybrid Multi-Mode Microplate Reader (BioTek Instruments, Inc.) for 60 h. Gas exchange was enabled using the gas-permeable Breathe-Easy® sealing membrane (Sigma-Aldrich Corporation).

B. Biomass determination

Offline biomass concentration was determined as dry cell weight c_X by centrifugation of 5 mL of cell broth in a preweighed centrifuge tube, followed by washing the cells with phosphate buffered saline three times and drying to constant weight at 90 °C in a drying cabinet. Due to the high standard deviation for dry cell weight determinations at small biomass concentrations a correlation between c_X and optical density at 600 nm in transmission mode ($OD_{600/tm}$) was established for concentrations up to c_X = 3 g L^{-1} in threefold determination.

Online biomass concentration was determined by measuring optical density at 600 nm in scattered light mode ($OD_{600/tm}$) in the Synergy™ H4 Hybrid Multi-Mode Microplate Reader (BioTek Instruments, Inc.). Measurement frequency was 15 min. Correlations between $OD_{600/sl}$ and $OD_{600/tm}$ were established for concentrations up to $OD_{600/tm}$ = 8 in fivefold determination.

C. Fluorescence measurements

Fluorescence intensities were measured in the Synergy™ H4 Hybrid Multi-Mode Microplate Reader (BioTek Instruments, Inc.) at the excitation and emission wavelengths listed in Table 1. Measurement frequency was 15 min.

Table 1: Excitation and emission wavelengths for the biogenic fluorophores tryptophan, NAD(P)H, and riboflavin.

Biogenic fluorophor	Excitation wavelength (nm)	Emission wavelength (nm)
Tryptophan	290	350
NAD(P)H	350	450
Riboflavin	370 and 450	530

D. Chemometrics

Data pre-processing and modeling were performed in MATLAB R2015a (The MathWorks, Inc.). The raw batch data consisted of two three dimensional matrices for fluorescence and biomass data gathered online (I x J x K, corresponding to number of batches I, process variables J, and sampling times K). This 3D matrices were unfold lining up the batches into a 2D matrix **X** and the vector **y**. **X** and **y** were mean-centered and used as independent and dependent variables for PLS model calibration, respectively. Data from 15 cultivations were used to calibrate the chemometric model. The model was validated by predicting the biomass of 10 equivalent cultivations. The root mean squared error of prediction (RMSEP) was calculated between measurement and prediction values for evaluating the PLS model (1) with size of test set N, predicted value y_i, and reference value $y_{i/ref}$:

$$\sqrt{\frac{1}{N}\sum_{N}^{i=1}(y_i - y_{i/ref})^2} \tag{1}$$

III. RESULTS AND DISCUSSION

The online biomass $OD_{600/sl}$ was correlated to the offline biomass c_X via (2) and (3) with the correlation factors b_1 = 0.280 g L^{-1} (n = 3; R^2 = 98.21%; data not shown), a_2 = 3.106, and b_2 = 2.204 (n = 5; R^2 = 93.93%; data not shown):

$$c_X = b_1 \cdot OD_{600/tm} \tag{2}$$

$$OD_{600/tm} = a_2 \cdot (OD_{600/sl})^2 + b_2 \cdot OD_{600/sl} \tag{3}$$

As described in the Materials and Methods section, cultivations were conducted for 60 h and fluorescence and optical density (scattered light mode) were measured with a frequency of 15 min. The time course of the normalized mean values for fluorescence and biomass is shown in Fig. 1 for illustration. The lag phase in the 200 µL scale lasts for 7 h followed by exponential growth (maximal growth rate μ_{max} = 0.250 h^{-1}) until 11-12 h. In a subsequent transition phase, which lasts until 36 h, the biomass increases to its maximum ($c_{X/max}$ = 0.459 g L^{-1}). After a short stationary phase until 42 h the biomass declines with a decay rate of µ = -0.015 h^{-1}.

During the time course the biogenic fluorophores tryptophan, NAD(P)H, and riboflavin measured at their characteristic wavelengths (s. Table 1) show a characteristic curve progression. Both NAD(P)H (ex/em 350/450 nm) and riboflavin (ex/em 370/530 nm) fluorescence intensities reach a high value during the lag phase and decline to a minimum shortly before the exponential phase ends (11 h). After 11 h the intensities for these fluorophores increase until the maximum biomass is reached, followed by a plateau phase. The intensity for riboflavin (ex/em 450/530 nm) fluorescence increases during the cultivation with a change of slope at about 11 h. The time course for tryptophan (ex/em 290/350 nm) follows the one for optical density closely, indicating a tight correlation between this amino acid's development and biomass generation.

For creating the PLS model the 25 batches were firstly separated randomly into 15 batches for model calibration and 10 batches for model validation. After data pre-processing by mean-centering and matrix unfolding (s. Material and Methods section) the training set for model calibration consisted of the independent variable matrix **X** (fluorescence intensity for the four fluorophores) and dependent vector **y** (optical density in scattered light mode).

As a first step of PLS model creation the number of PLS components was determined because using all available components may be more than will be needed to adequately fit the data. A quick way to choose the number of components is to plot the percent of variance explained in the independent variables **X** as a function of the number of components, as done in Fig. 2A. The first PLS component explains 48.05% of the variance in **X**. Adding a second PLS component to the model raises the explained variance to 96.96%. Two

ISBN: 978-1-61804-321-4

components were chosen as adequately because addition of the third component only gives a minor increase to 99.23% at the cost of model complexity. Another reason to not use a too large number of components is that this strategy leads to overfitting, i.e. the model fits the data too well and does not generalize well to other data.

The chosen number of components was further confirmed by plotting the estimated mean squared prediction error (4) against the number of components used for model creation, as done in Fig. 2B. This internal validation of the model by a 10-fold cross validation showed that the prediction error does not significantly decrease by using three PLS components, whereas for using only one component it is over double the value as for two components. The mean squared prediction error (MSEP) is defined as follows with size of test set N, predicted value y_i, and reference value $y_{i/ref}$:

$$\frac{1}{N}\sum_{N}^{i=1}(y_i - y_{i/ref})^2 \qquad (4)$$

The next step was to detect outliers and remove them from the training set. For this purpose the fitted response for the PLS regression was plotted against the observed response, as done in Fig. 2C.

Finally, the PLS weights were plotted against the dependent variables contained in **X** in order to describe how strongly each component in the PLS regression model depends on the original variables, and in what direction. Fig. 2D shows the PLS weight for the variables that refer to the fluorescence intensities of tryptophan (ex/em 290/350 nm), NAD(P)H (ex/em 350/450 nm), and riboflavin (ex/em 370/530 and 450/530 nm). As can be seen, the variables tryptophan (ex/em 290/350 nm) and riboflavin (ex/em 450/530 nm) lead to positive PLS weights whereas NAD(P)H (ex/em 350/450 nm) and riboflavin (ex/em 370/530 nm) lead to negative PLS weights for the first component (48.05% explained **X**-variance). This observation could be explained by the initial decrease of fluorescence intensity at the beginning of the cultivation (about 3.5 to 11 h).

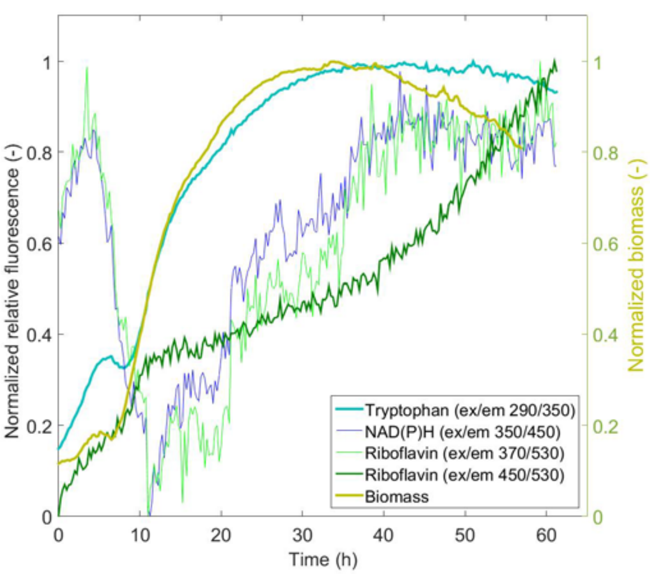

Fig. 1: Time course of normalized fluorescence signals (tryptophan, NAD(P)H, and riboflavin) and biomass. Lines represent mean values for 25 batches.

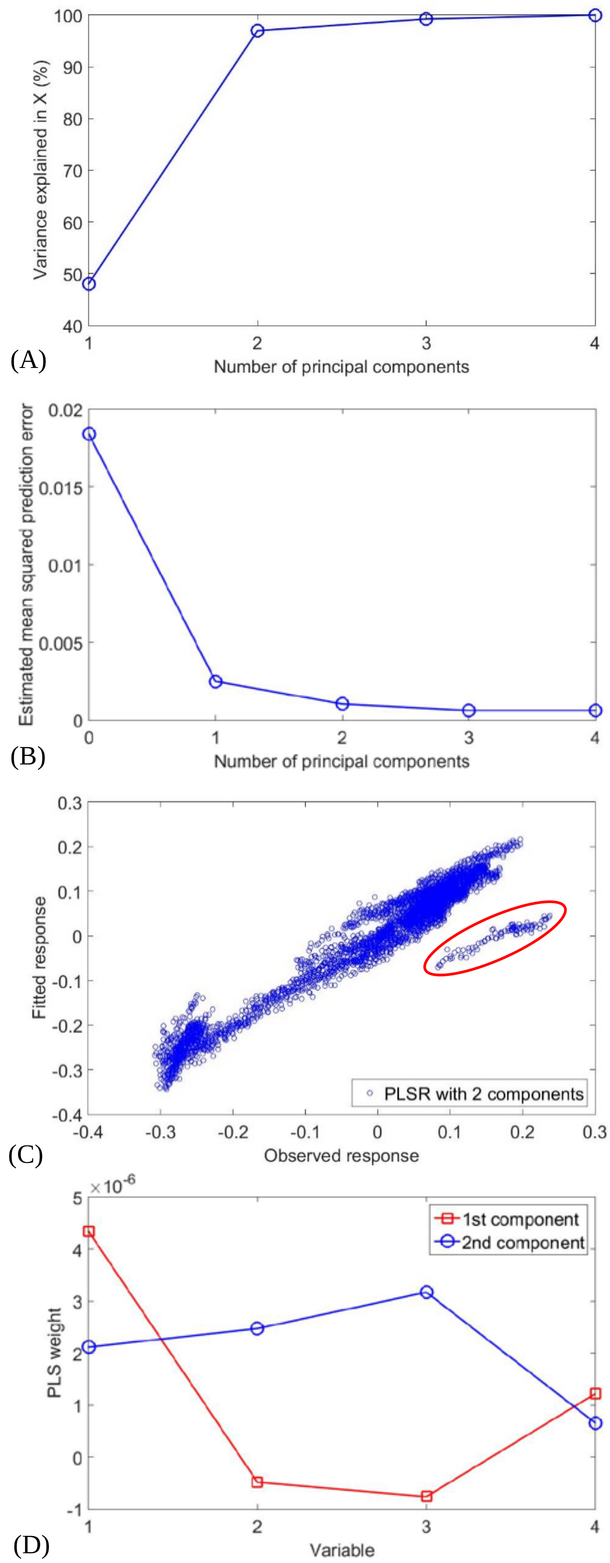

Fig. 2: (A) Variance explained in X and (B) estimated mean squared prediction error for number of principal components. (C) Fitted vs observed response for PLS regression with 2 components and outliers (marked red).

(D) PLS weight for fluorescence variables (1) tryptophan (ex/em 290/350 nm), (2) NAD(P)H (ex/em 350/450 nm) as well as (3) and (4) riboflavin (ex/em 370/530 and 450/530 nm, respectively).

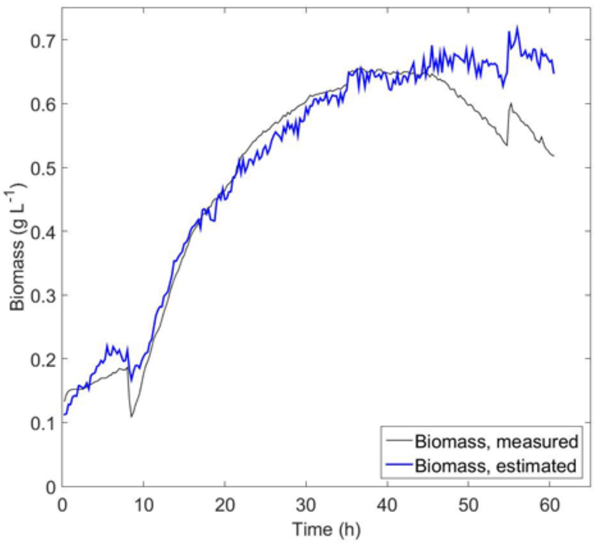

Fig. 3: Time course of measured and predicted biomass for one representative batch.

The final PLS regression model (R^2 = 96.66%) was validated externally by predicting the biomass for 10 validation cultivations. The RMSEP (1) between the predicted and measured values for the validation batches was 0.034 for the optical density measurements in scattered light mode, corresponding to 0.051 g L^{-1} for dry cell weight. Fig. 3 shows the predicted and measured biomass concentration for a representative batch. As can be seen, the estimation fits the measurement well until the beginning of the decline phase at about 42 h cultivation time. In the decline phase the predicted value for biomass falsely increases further. The discrepancy between model estimation and measurements in the stationary and decline phase is most probably due to proteolysis and was described before [9]. However, sudden changes in optical density measurements caused by presumably cell layer formation on the well bottom (55 h) are visible in the predicted curve as well.

IV. CONCLUSIONS

In this work, they key variable biomass was successfully predicted for small-scale *P. pastoris* cultivations based on measurements of fluorescence intensity at four characteristic wavelength combinations (excitation/emission). These wavelength combinations corresponded to the biogenic fluorophores tryptophan, NAD(P)H, and riboflavin, with detection wavelengths identified before by Surribas and coworkers [5, 9]. Contrary to these authors' approaches of taking into account either one single fluorophore (tryptophan) or a whole 2D fluorescence spectrum for modeling, biomass in this work was estimated based on the development of three fluorophores at four single-wavelength combinations.

The results show that biomass can successfully be predicted based on fluorescence measurements of single-wavelength combinations. Based on this finding, the development of an alternative measurement system for expensive 2D fluorescence spectroscopy seems promising. This measurement system would measure only a small set of wavelength combinations and still give enough information for successful biomass prediction.

REFERENCES

[1] Cregg, J.M., et al., Recombinant protein expression in *Pichia pastoris. Molecular biotechnology,* 2000. 16(1): p. 23-52.

[2] Cereghino, G.P.L., et al., Production of recombinant proteins in fermenter cultures of the yeast *Pichia pastoris. Current opinion in biotechnology,* 2002. 13(4): p. 329-332.

[3] Cos, O., et al., Operational strategies, monitoring and control of heterologous protein production in the methylotrophic yeast *Pichia pastoris* under different promoters: a review. *Microbial cell factories,* 2006. 5(1): p. 17.

[4] Potvin, G., A. Ahmad, and Z. Zhang, Bioprocess engineering aspects of heterologous protein production in *Pichia pastoris*: a review. *Biochemical Engineering Journal,* 2012. 64: p. 91-105.

[5] Surribas, A., J.L. Montesinos, and F.F. Valero, Biomass estimation using fluorescence measurements in *Pichia pastoris* bioprocess. *Journal of Chemical Technology and Biotechnology,* 2006. 81(1): p. 23-28.

[6] Zhang, H., Software sensors and their applications in bioprocess, in *Computational Intelligence Techniques for Bioprocess Modelling, Supervision and Control*. 2009, Springer. p. 25-56.

[7] Scheper, T., et al., Measurement of biological parameters during fermentation processes. *Analytica Chimica Acta,* 1984. 163: p. 111-118.

[8] Horvath, J.J., S.A. Glazier, and C.J. Spangler, In situ fluorescence cell mass measurements of *Saccharomyces cerevisiae* using cellular tryptophan. *Biotechnology progress,* 1993. 9(6): p. 666-670.

[9] Surribas, A., et al., State variables monitoring by in situ multi-wavelength fluorescence spectroscopy in heterologous protein production by *Pichia pastoris. Journal of biotechnology,* 2006. 124(2): p. 412-419.

ISBN: 978-1-61804-321-4

Knowledge modeling by ELM in RL for SRHT problem

Jose Manuel Lopez-Guede and Manuel Graña

***Abstract*—Autonomous learning of control algorithms for Linked Multicomponent Robotic Systems (L-MCRS) is an open research issue. Single Robot Hose Transport (SRHT) is a limit case of this kind of systems, when one robot moves the tip of a hose to a desired position, while the other hose extreme is attached to a source position. Reinforcement Learning (RL) algorithms have been applied to learn autonomously the robot control in SRHT, specifically Q-Learning and TRQ-Learning have been applied with success. However storing the state-action value functional information in tabular form produces large and intractable data structures. This paper addresses the problem by learning an Extreme Learning Machine (ELM) from the state-action value Q-table, obtaining a data reduction because the number of ELM parameters is much less than the Q-table's size. Moreover, ELM implements a continuous map which can produce compact representations of the Q-table, and generalizations to increased space resolution and unknown situations. In this paper we evaluate empirically three strategies to formulate ELM learning to provide approximations to the Q-table, namely as classification, multi-variate regression and several independent regression problems adding more results to ones previously published.**

***Index Terms*—Extreme Learning Machine, Linked Multicomponent Robotic Systems, Q-Learning TRQ-Learning, Reinforcement Learning, Hose Control**

I. Introduction

Linked Multi-Component Robotic Systems (L-MCRS) [1] are composed of a collection of autonomous robots linked by a non-rigid uni-dimensional link introducing additional non-linearities and uncertainties when designing the control of the robots to accomplish a given task. The final objective in this field is to design the control of L-MCRS to achieve desired behaviors by autonomous learning.

A paradigmatic task example is the transportation of a hose or wire-like object by the team of robots (or only one robot in its simplest form). In this case, the task is named Single Robot Hose Transport (SRHT) and the system consists of a flexible uni-dimensional object (a hose) that has one end attached to a fixed point (which is set as the middle point of the ground working space), while the other end (the tip) is transported by a mobile robot. The task to be accomplished by the robot is to bring the tip of the hose to an arbitrarily designated destination point by the execution of a sequence of discrete actions of a predefined duration.

We have worked on this paradigmatic task [2], [3], [4], [5] achieving that the learning agent (a robot) learns autonomously how to solve the control task without human intervention by means of Reinforcement Learning (RL) [6] algorithms. These approaches are derived from the Q-Learning [7] and TRQ-Learning [8] algorithms, so the learning final result is the state-action value function encoded in a Q-table. Since the domain of application is complex, the size of the data structures needed to represent the learned Q-tables grows exponentially with several factors, and the computational requirements, both in space and time, grow accordingly, sometimes imposing too great burden on the actual embodiment of the agent, which can have limited resources. For practical applications, such as the hose control, compact functional approximations to the Q-table are desired in order to advance with the actual operation of the system.

This paper proposes to tackle this problem by learning approximations to the maps encoded by those large size Q-tables using Extreme Learning Machines (ELM). The data for training and testing consists in the Q-table entries, so the ELM is desired to predict the actual action that would be selected by the optimal policy according to the given Q-table. ELMs provide quick training with high generalization performance, therefore they are well suited to this problem. This paper explores empirically three approaches to state the approximation problem. The first is a classification problem where the state class is the optimal action selection. The second is a multi-variate regression, where the regressed variables are the values of the actions in this state. The third and last, is a collection of independent regressions, each focused in predicting the value of an specific action.

The content of the paper is as follows. Section II reviews the some methods involved in the present work. Section III introduces the paradigmatic hose control problem to be solved through RL and the related problem of data structures size, discussing the need of compacting the state-action value function acquired by RL. Section IV describes the alternative approaches tested to build approximations to the Q-table by ELM learning. The experimental design carried out to validate the approaches is given in Section V, while section VI discusses the results that have been reached following each approximation strategy. Finally, section VII gives our conclusions and lines for future work.

II. Background

This section reviews some topics needed to understand the problem that we are facing in this paper. Subsection II-A reviews some basic concepts of Reinforcement Learning (RL) as Markov Decision Processes, Q-Learning and TRQ-Learning algorithms, while Subsection II-B recalls basic concepts and references about Extreme Learning Machines (ELMs).

ISBN: 978-1-61804-321-4

Algorithm 1 Q-Learning algorithm

Initialize $Q(s,\, a)$ arbitrarily
Repeat (for each episode):
  Initialize s
  Repeat (for each step of episode):
    Choose a from s using policy derived from Q
    Take action a, observe reward r and new state s'
    $Q(s,\, a) \leftarrow Q(s,\, a) + \alpha \left[r + \gamma \max_{a'} Q\left(s',\, a'\right) - Q\left(s,\, a\right) \right]$
    $s \leftarrow s'$
  until s is terminal

A. Reinforcement Learning

Reinforcement Learning [6] is a class of learning algorithms which assumes that the environment-agent system can be modeled as a discrete time stochastic process formalized as a Markov Decision Process (MDP) [9], [10].

a) Markov Decision Process (MDP) : A Markov Decision Process (MDP) is defined by the tuple $< S,\, A,\, T,\, R >$, where S is the state space, A the action repertoire, specifically A_s are the actions allowed in state $s \in S$, $T:\; S \times A_s \times S \rightarrow \mathbb{R}$ is the probabilistic state transition function, and $R:\; S \times A_s \rightarrow \mathbb{R}$ is the immediate reward function. A policy $\pi:\; S \rightarrow A_s$ is the probabilistic decision of the action $a \in A_s$ to be taken in state $s \in S$. Reinforcement Learning procedures looks for optimal action selection policies maximizing the total reward received by the agent.

b) Q-Learning: Q-Learning [11] is an unsupervised model free Reinforcement Learning algorithm that learns the optimal policy in environments specified by Finite MDP (S and A are finite sets). The learning process is specified in Algorithm 1. The main idea of the algorithm is to fill a look-up table $Q\left(s, a\right)$ of dimensions $|S| \times |A|$, which is initialized arbitrarily, being updated following the rule specified by the following equation:

$$\begin{aligned} Q(s_t,\, a_t) \leftarrow{} & Q(s_t,\, a_t) + \\ & \alpha \left[r_{t+1} + \gamma \cdot \max_a Q\left(s_{t+1},\, a\right) - Q\left(s_t,\, a_t\right) \right]. \end{aligned} \tag{1}$$

It has been proved [12] that, for a discrete FMDP environment, the Q-Learning algorithm converges with probability one to the optimal policy if α decrease complies with the stochastic gradient convergence conditions and if all actions are infinitely sampled in all states.

c) TRQ-Learning: TRQ-Learning [8] is an algorithm derived from Q-Learning which performs an ad-hoc model learning, i.e., besides learning the optimal policy to solve the proposed task, it also learns the response of the environment to the agent's actions. Its update rule is similar to the Q-Learning's rule, but it involves additional data structures $T\left(s,\, a\right)$ and $R\left(s,\, a\right)$ storing the learned transition and the reward functions, respectively, as specified in Algorithm 2. TRQ-Learning is faster than Q-learning, and it is also more successful [8], because the agent learns the environment's response to its actions by means of its transition and reward functions and

Algorithm 2 TRQ-Learning algorithm

Initialize $Q(s,a)$ with arbitrary random values
Initialize $T\left(s,a\right) = \emptyset$, $R\left(s,a\right) = 0$, $\forall s \in S$, $\forall a \in A$
Repeat (for each episode):
  Initialize s
  Repeat (for each step of episode):
    Choose a from s using policy derived from Q
    if $T(s,a) \neq \emptyset$
      $s' \leftarrow T(s,a)$
      $r \leftarrow R(s,a)$
    else
      Take action a, observe reward r and new state s'
      $T(s,a) \leftarrow s'$
      $R(s,a) \leftarrow r$
    $Q(s,a) \leftarrow Q(s,a) + \alpha \left[r + \gamma \underset{a}{max} Q\left(s',a\right) - Q\left(s,a\right) \right]$
    $s \leftarrow s'$
  until s is terminal

B. Extreme Learning Machines

Extreme Learning Machines (ELMs) [13], [14], [15], [16], [17], [18], [19], [20] are classified as Single-Hidden Layer Feedforward Networks (SLFNs). They can be trained without iterative tuning, which confers them several interesting characteristics compared to classical back-propagation algorithm: they are easy to use, they require minimal human intervention, they have a faster learning speed and a higher generalization performance, and they are suitable for several nonlinear activation functions. The ELM approach to SFLN training consists in the following two steps:

1) Generate randomly the hidden layer weights $\mathbf{W}$, computing the hidden layer output $\mathbf{H} = g\left(\mathbf{WX}\right)$ for the given data inputs $\mathbf{X}$, where $g\left(x\right)$ denotes the hidden units activation function, which can be sigmoidal, Gaussian or even the identity.
2) Solve the linear problem $\mathbf{H}\boldsymbol{\beta} = \mathbf{Y}$, where $\mathbf{Y}$ are the outputs of the data sample, and $\boldsymbol{\beta}$ the weights from the hidden layer to the output layer, by the mean least squares approach. Therefore $\hat{\boldsymbol{\beta}} = \mathbf{H}^{\dagger}\mathbf{Y}$, where $\mathbf{H}^{\dagger}$ is the pseudo-inverse.

III. Hose-Robot Control Systems

This section provides a detailed description of the domain in which the L-MCRS has been deployed. Subsection III-A describes the working area and the state spaces that have been used, while subsection III-B gives further insight into the problem related to the representation of the knowledge.

A. Learning Hose-Robot Control Systems

As described in Section I, we have solved the autonomous learning of the L-MCRS applying RL algorithms, which model the problem to solve as a MDP. We have used different state models and different spatial discretization steps in our RL processes, obtaining different Q-tables. Our instance of L-MCRS working space is a square of 2×2 m and to build the state space representation, we have used two spatial

State model	Discretization	$\|S\|$
$X^{(a)} = \{\mathbf{p}_r, \mathbf{p}_g, i\}$	$0,5\,m$	512
	$0,2\,m$	20,000
$X^{(b)} = \{\mathbf{p}_r, \mathbf{p}_g, i, \mathbf{p}_1, \mathbf{p}_2\}$	$0,5\,m$	131,072
$X^{(c)} = \{\mathbf{p}_r, \mathbf{p}_g, i, \mathbf{v}_r\}$	$0,5\,m$	8,192
$X^{(d)} = \{\mathbf{p}_r, \mathbf{p}_g, i, c, \mathbf{v}_r\}$	$0,5\,m$	16,384

Table I
DIFFERENT STATE MODELS USED IN THE MDP SPECIFICATION

State model	Discretization	% goal	Q size
$X^{(a)}$	$0,5\,m$	66	424
	$0,2\,m$	65	15.213
$X^{(b)}$	$0,5\,m$	77	7.575
$X^{(c)}$	$0,5\,m$	79	3.133
$X^{(d)}$	$0,5\,m$	85	4.777

Table II
DIFFERENT STATE MODELS, THEIR MAXIMUM SUCCESS RATIOS AND THE Q-TABLE REQUIRED STORAGE SIZE MEASURED IN KBYTES.

discretization steps per axis: $0,5\,m$ and $0,2\,m$. Table I contains the specification of the state models, spatial discretization steps and size of state space, which is the number of rows in the the learned Q-table.

The agent's perception of states in model $X^{(a)}$ is less complex than in model $X^{(b)}$, i.e., the state models are enumerated in increasing order of sophistication of the perceptual capabilities that the agent needs to perceive an state of such model. The description of the individual components of the state variables in Table I is the following:

- $\mathbf{p}_r$: it describes the position of the robot in a discretized bi-dimensional coordinate system.
- $\mathbf{p}_g$: it describes the position of the goal in a discretized bi-dimensional coordinate system.
- i: set if the line $\overline{\mathbf{p}_r\mathbf{p}_g}$ intersects the linking element of the L-MCRS
- c: set if the box with corners $\mathbf{p}_r$ and $\mathbf{p}_g$ intersects the linking element of the L-MCRS
- $\mathbf{p}_1$, $\mathbf{p}_2$: they describe the position of two points taken in a way that the hose is divided into four segments of the equal length. They are represented in a discretized bi-dimensional coordinate system.
- $\mathbf{v}_r$: it describes a vector of predictions containing one prediction for each available action. Each prediction will be $true$ if there will be a collision between the hose and the robot after doing the corresponding action, otherwise $false$.

Finally, in Table II we recall the best results in the percentage of test episodes ending in goal states (% goal) reported in previous works [4], [21], [22], [8].

B. *Compaction of Q-table representation*

Once the agent has learned autonomously the Q-table encoding the state-action value function to solve the task, it will need to store it for actual robot operation. The Q-table can be very large and the storage and processing capabilities of the agent can be very limited. The size of the Q-table depends mainly on the cardinality of the set S (denoted $|S|$), which in its turn depends on the state model. This model is not unique, and we must reach an balance between model complexity and successful operation. More complex models give better results with large Q-tables. Besides the variables of the system state, the spatial discretization step used in those variables is very important because it has a great impact in $|S|$. We can assume that the learned Q-table is a tabular encoding of the state-action value function. To deal with the problem of large size of the Q-table we have considered to train an artificial neural network [23][24], [25] fitting it to obtain a compact representation of the the knowledge contained the Q-table.

IV. APPROACHES FOR Q-TABLE LEARNING BY ELM

This section describes in detail the different approaches that have been tested to overcome the previously exposed problem of learning the content of Q-table.

A. *Overview*

The approximation of the Q-table by means of an ELM consists in using the Q-table entries as the data for training and testing of the ELM, therefore the obtained ELM is a functional approximation of the Q-table. State values are the map input features and actions or their predicted values are the outputs. Q-tables have as many rows as states reached during the RL training process (n states: $(s_i)_{i\in[1,\,n]}$), and as many columns as actions that can be executed by the agent (m actions: $(a_j)_{j\in[1,\,m]}$), usually $n \ggg m$. In our practical application, n depends on the one state model that has been used (see Table I for a estimation of $n = |S|$ in each case), and the number of actions is $m = 4$ ($A = \{North, South, East, West\}$).

We formulate the task of learning a Q-table either as a classification problem (introduced in subsection IV-B), or as a multi-variate regression problem (introduced in subsection IV-C) or as four independent regression problems (introduced in subsection IV-D).

B. *Q-table approximation by classification*

The task of learning a Q-table consists in given a particular state of the system, the ELM must learn the maximum value action in that state according to the information contained in the Q-table. Thus we have a multi-label classification problem, where the set S of states is partitioned in four classes and each class is a subsets of S containing all the states whose best action is the same. We have only four classes corresponding to the four available actions.

C. *Q-table approximation by multi-variate regression*

The task of learning a Q-table consists in given a particular state of the system, the ELM must obtain the value of each available action for that state. Thus the ELM has to learn a four real valued function because there are four available actions.

D. *Q-table approximation by four independent regressions*

The task of learning a Q-table consists in given a state of the system, a collection of four independent ELMs must obtain the value of each available action for that state solving four independent regression problems.

V. Experimental design

Regarding the training process of ELMs, we have adopted a common parametrization for all the approaches, as explained following.

A. Parameters related to the state model and discretization step

We have used the four different state models that are in Table I. For the first state model, two different discretization steps have been used ($0,5\,m$ and $0,2\,m$), while with the remaining state models only a discretization step of $0,5\,m$ has been used.

B. Extraction of the train/test datasets from the Q-table

For each combination of state model and discretization step, we started from the original Q-table as generated by the learning process carried out with Q-Learning or TRQ-Learning algorithms. Then we perform random selection of the 75% of the table entries as the train set and the remaining 25% as the test set. We also have considered normalizing the input attributes of the train and the test sets into the range $[-1,\, 1]$. So, we have two versions of each training and testing dataset: raw unnormalized and normalized datasets.

Besides, for each one of these two versions we have generated several subversions by the addition of noise to each input attribute based on uniformly distributed pseudo-random numbers in the range $r \in [-1,\, 1]$ and weighted by a parameter $noisew \in [0,\, 100]$, as indicated in the Eq. (2):

$$attribute \leftarrow attribute \cdot \{1 + [noisew \cdot (2r - 1)]\} \quad (2)$$

This modification rule is intended for generating additive or subtractive noise of magnitude $noisew$ percent of the value of each input attribute. We have used the following values: $noisew \in \{0,\, 1,\, 5,\, 10,\, 20\}$. This combination of parameters means that we have 10 different training and testing datasets for each combination of state model and discretization step.

C. ELM related parameters

They are typical ELM networks with the following configurations:

- Activation function in the hidden nodes: sigmoidal, sine, hardlim, triangular basis function and radial basis function.
- Hidden nodes: We have used logarithmically equally spaced integer values between 1 and 1000, giving 43 different values.
- Trials: For the resulting combinations, we have performed 10 trials and we have measured individual and mean values.

D. ELM training parameters for the four independent regressions

In the subsection IV-D we formulated the Q-table learning task as four independent regression tasks. In this case, we have taken into consideration only the Q-tables generated with the state model which give higher goal percentage in the original Hose-Robot system, i.e., we have tried to approximate the Q-table of the state model $X^{(a)} = \{\mathbf{p}_r,\, \mathbf{p}_g,\, i\}$ for $discretization\, step = 0,2\,m$ and Q-table of the state model $X^{(d)} = \{\mathbf{p}_r,\, \mathbf{p}_g,\, i,\, c,\, \mathbf{v}_r\}$ for $discretization\, step = 0,5\,m$. We have not normalized the train nor the test data, and we have not built noise perturbed dataset. Regarding the ELM structure, we have used the sin activation function, and logarithmically equally spaced integer values between 1 and 1000 as number of hidden nodes when testing diverse architectures.

Algorithm 3 Validation procedure for ELM classification and multi-variate regression approximations of Q tables.

```
For each formulation of the task
  For each state model
    For each discretization step
      For each possibility regarding to the normalization
        For each noise percentage
          Load training and testing datasets with:
              - inputs according to the state model
              - outputs according to the task
              - discretization step
              - normalization according to
              - noise percent
          For each number of hidden nodes
            For each activation function
              For each initialization
                Create an ELM suited to the task with:
                    - inputs according to the state model
                    - outputs according to the task
                    - the corresponging hidden nodes
                    - the corresp. activation function
                Train the ELM using the training dataset
                Test the ELM using the testing dataset
              Obtain train/test mean values
```

E. Validation procedure for approximation tasks

Algorithm 3 summarize the experimental design that we have carried out to validate the classification and multi-variate regression ELM approaches.

VI. Experimental results

In this section the results achieved with the experimental design proposed in subsection V-D are discussed. The experiments have been carried out with the public software available at the ELM web page[1], customizing it where needed.

A. Results of the Q table approximation by classification

The accuracy results of this approximation are given in Tables IV and V, for different state models.

However, there is a great advantage in using ELMs because the space saving is significant. In Table II we can see the space requirements to store the original Q-table for each combination of state model and discretization step, while Table III contains

[1] http://www.ntu.edu.sg/home/egbhuang/ELM_Codes.htm

	$Matrix$	$Size$	KB
$X^{(d)}$ ={$\mathbf{p}_r$, $\mathbf{p}_g$, i, c, $\mathbf{v}_r$} $0,5\,m$	Bias Hidden	282 x 1	2
	Input Weight	282 x 10	22
	Output Weight	282 x 4	9
	TOTAL		39

Table III
SPACE REQUIREMENTS OF THE BEST ELM LEARNING THE Q-TABLE AS A CLASSIFICATION PROBLEM $\left(X^{(d)}\right)$.

			$Classif.$	$Multivariate\,regress.$		
$Step$	$Norm$	$Noise$	$Acc.$	$Acc.$	$\overline{x}$	σ
0.5	No	0	0,61	40,58	-3,21	55,00
“	“	1	0,57	40,65	“	“
“	“	5	0,60	41,11	“	“
“	“	10	0,60	41,70	“	“
“	“	20	0,57	43,32	“	“
“	Yes	0	0,60	42,02	“	“
“	“	1	0,60	43,22	“	“
“	“	5	0,53	42,89	“	“
“	“	10	0,59	40,85	“	“
“	“	20	0,53	44,55	“	“
0.2	No	0	0,72	244,19	-158,54	367,75
“	“	1	0,71	247,00	“	“
“	“	5	0,70	253,26	“	“
“	“	10	0,70	268,52	“	“
“	“	20	0,70	286,48	“	“
“	Yes	0	0,71	246,34	“	“
“	“	1	0,72	241,88	“	“
“	“	5	0,70	249,90	“	“
“	“	10	0,71	268,28	“	“
“	v	20	0,70	289,80	“	“

Table IV
ACCURACY RESULTS FOR CLASSIFICATION AND MULTI-VARIATE REGRESSION LEARNING OF THE Q-TABLES OBTAINED WITH THE MODEL STATE $X^{(a)}$, MERGING THE RESULTS OBTAINED WITH ALL COMBINATIONS OF HIDDEN NODES AND ACTIVATION FUNCTIONS

			$Classif.$	$Multivariate\,regress.$		
$State$	$Norm$	$Noise$	$Acc.$	$Acc.$	$\overline{x}$	σ
$X^{(3)}$	No	0	0,65	44,01	23,96	58,56
“	“	1	0,66	43,99	“	“
“	“	5	0,65	45,74	“	“
“	“	10	0,64	45,77	“	“
“	“	20	0,65	47,74	“	“
“	Yes	0	0,64	44,24	“	“
“	“	1	0,66	45,67	“	“
“	“	5	0,66	45,71	“	“
“	“	10	0,64	46,31	“	“
“	“	20	0,61	47,33	“	“
$X^{(4)}$	No	0	0,67	0,41	0,20	0,56
“	“	1	0,67	0,40	“	“
“	“	5	0,70	0,41	“	“
“	“	10	0,68	0,41	“	“
“	“	20	0,65	0,41	“	“
“	Yes	0	0,66	0,42	“	“
“	“	1	0,68	0,41	“	“
“	“	5	0,66	0,42	“	“
“	“	10	0,65	0,41	“	“
“	“	20	0,66	0,44	“	“
$X^{(5)}$	No	0	0,69	0,43	0,20	0,57
“	“	1	0,69	0,43	“	“
“	“	5	0,65	0,41	“	“
“	“	10	0,69	0,42	“	“
“	“	20	0,68	0,43	“	“
“	Yes	0	0,66	0,45	“	“
“	“	1	0,68	0,44	“	“
“	“	5	0,66	0,45	“	“
“	“	10	0,66	0,44	“	“
“	“	20	0,65	0,45	“	“

Table V
ACCURACY RESULTS FOR CLASSIFICATION AND MULTI-VARIATE REGRESSION LEARNING OF THE Q-TABLES OBTAINED WITH THE MODEL STATE $X^{(b)}$, $X^{(c)}$, $X^{(d)}$ AND THE DISCRETIZATION STEP OF $0,50\,m$, MERGING THE RESULTS OBTAINED WITH ALL COMBINATIONS OF HIDDEN NODES AND ACTIVATION FUNCTIONS

the space requirements to store the ELM that has been tested more in detail. For the case of $X^{(d)}$ ={$\mathbf{p}_r$, $\mathbf{p}_g$, i, c, $\mathbf{v}_r$} and $discretization\,step\,=\,0,5\,m$, the space saving is $99,18\%$, i.e., only the $0,82\%$ of the original space is needed.

After performing all the experiments that are specified in the subsection V-E, we reach the following general conclusions regarding the approximation of the Q-table modeled as a classification task:

- We do not observe significant differences between normalizing or not the training and test datasets. This is probably because in this particular domain we have only two types of individual variables composing the state models: binary and discretized. The binary variables are normalized by their nature, and the discretized variables are defined in the range $[-1,\,1]$ by the nature of the RL problem. Therefore, the train/test raw data are quite normalized.
- There is no difference between adding or not different ratios of noise to the train and test datasets, maybe because in our domain the discretization that was done to solve the RL problem is very rough, and noise is added to the variables of the model state.
- The accuracy value provided by the $discretization\,step\,=\,0,2\,m$ is clearly better than the obtained using the $discretization\,step\,=\,0,5\,m$. This is a reasonable consequence of having a higher variety of values to let the ELMs to learn differences between different states.
- Increasing the number of neurons does not help to improve the accuracy of the ELMs. We have not included more tables nor graphics, but the best results are obtained with intermediate number of hidden nodes inside the range $[1,\,1000]$, in which we have trained the ELMs.
- The results show that state model and discretization step are the most relevant elements, obtaining similar accuracy values to all datasets sharing these characteristics. Except extreme values of number of hidden nodes, the remaining variables of the training process have a relative effect in the ELMs learning.
- In general, the results are not good, maybe because the number (very few) and the nature (binary and discretized with very little variability) of the individual components of the state model do not allow the ELMs to learn the content of the Q-tables.

B. Results of the Q table approximation by multi-variate regression

Regression's mean squared error results are given in Tables IV and V. To contextualize that value we have calculated the mean $\bar{x}$ and the standard deviation σ of the values of the Q-table that was learned in each case, which is the same for

ISBN: 978-1-61804-321-4

each combination of state model and discretization step. We focus on two specific ELMs, corresponding to those whose accuracy has been the best learning the most successful Q-tables. To provide further insight into the learning process, a new learning performance measure is defined by means of the function $Match\,(s)$ and given in Eq. (3): the output of the ELM can be considered $accurate$ if given a state $s \in S$, the optimal action according to the ELM for this state is the same as in the original Q-table.

$$Match\,(s) = \begin{cases} 1 & i_1 = i_2 \wedge ELM\,(s,\, i_1) = max\,(ELM\,(s)) \\ & \wedge\, Q_r\,(s,\, i_2) = max\,(Q_r\,(s)) \\ 0 & else \end{cases} \tag{3}$$

where:

- $ELM\,(s)$ is the output vector of the ELM (with all values) when the state $s \in S$ is at the input layer,
- $ELM\,(s,\, i)$ is the value of the $i-th$ position ($i-th$ action) of the ELM output vector when the state $s \in S$ is at the input layer,
- $Q_r\,(s)$ is the vector of the original Q-table with all values for the state $s \in S$,
- $Q_r\,(s,\, i)$ is the value of the $i-th$ position ($i-th$ action) of the original Q-table for the state $s \in S$.

We define the success rate of an ELM with a testing dataset in Eq. (4):

$$success = \frac{\sum_{j=1}^{t} Match\,(s_j)}{t} * 100 \tag{4}$$

where t is the number of states of the testing dataset. Taking into account the definition of Eq. (4), to the case of $X^{(5)} = \{\mathbf{p}_r,\, \mathbf{p}_g,\, i,\, c,\, \mathbf{v}_r\}$ and $discretization\,step = 0,5\,m$, the success rate is $57,10\%$.

We reach the following conclusions on the Q-table approximation as a multi-variate regression task:

- The multi-variate regression task is more difficult that the four-classes classification one because with the same inputs, the ELM has to learn four values instead only one. So, we can expect to get worse accuracy ratios.
- There is no difference between normalizing or not the training and testing datasets, as in classification task case. This is coherent because the training and testing datasets are the same in both tasks.
- There is no difference between adding or not different ratios of noise to the training and testing datasets. Again, this is reasonable because it is an effect derived from the training and testing datasets which we have used, and we have stated that they are the same in both tasks.
- The absolute value of the accuracy (mean squared error) for each ELM must be contextualized within the values contained into the Q-table. It depends strongly on the reward function range, i.e., an ELM with a smaller error learning a Q table derived using a narrow reward function may have done a worse learning than another ELM with a higher error learning a Q-table derived using a wide reward function. So, there are cases in which the accuracy value provided by the $discretization\,step = 0,2\,m$ is worse than the obtained using the $discretization\,step = 0,5\,m$.
- As in the classification task, increasing the number of neurons does not help to improve the accuracy of the ELMs. Again the better results are obtained with intermediate number of hidden nodes inside the range $[1,\, 1000]$, in which we have trained the ELMs.
- The results show that state model and discretization step are the most relevant elements, obtaining similar accuracy rates with all datasets sharing these characteristics. Except extreme values of number of hidden nodes, the remaining variables of the training process have a relative effect in the ELMs learning.
- Again, the results are not goods probably due to the same reason that in case of classification task: the number (very few) and the nature (binary and discretized with very few values) of the individual components of the state model do not allow the ELMs to learn the content of the Q-tables, besides the higher complexity of the regression task.

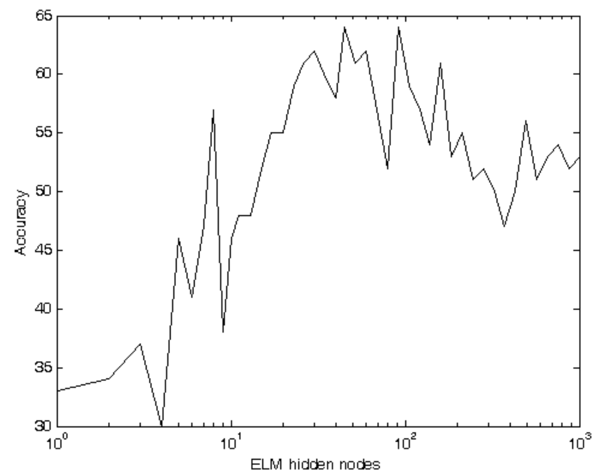

Figure 1. Accuracy varying the number of hidden nodes in the four regression tasks

C. Results of the Q table approximation by four independent regressions

As we stated in subsection V-D, in this case we have simplified the experimentation taking in consideration only the Q-table which is generated with the state model which give higher goal percentage for each of the available discretization steps. I.e., we have tried to learn the Q-table of the state model $X^{(5)} = \{\mathbf{p}_r,\, \mathbf{p}_g,\, i,\, c,\, \mathbf{v}_r\}$, without normalizing nor adding noise to the training/testing datasets, and using the sin activation function, trying hidden layers of increasing number of hidden nodes following a logarithmic progression of integer values between 1 and 1000. Fig. 1 shows the accuracy of the ELMs varying the number of the hidden nodes in that range.

For these regression tasks, accuracy alone has the limited value to evaluate learning results, therefore we compute success as defined by the Eq. (4), reaching a success rate of 65% with 45 hidden nodes.

ISBN: 978-1-61804-321-4

VII. Conclusions and future work

In this paper we have addressed one practical problem when Linked Multi-Component Robotic Systems (L-MCRS) learn autonomously complex behaviors through Reinforcement Learning: the intractable size of the data structures needed to contain the learned Q-tables. We have given a short background on Markov Decision Processes, Reinforcement Learning (more specifically on Q-Learning and TRQ-Learning algorithms) and Extreme Learning Machines. We have explained the specific problem of autonomous learning in L-MCRS with RL algorithms: the intractable size of the data structures which contains the knowledge. To deal with this problem, we have proposed to compute their approximation using ELMs. Due to the flexibility of the ELMs, we have formalized the task of Q-table approximation in three ways. The first of them is a classification task, where the ELM has to classify states into different classes, each of one corresponding to a different better available action. The second is a multivariate regression task, where the ELM has to predict an estimate of the value of each available action for all states. Finally, the third was through four simple regression tasks, where each ELM has to predict an estimate of the value of the corresponding available action for each state. The best results were obtained using the classification task approach, where classification accuracy reached the 72%, and the space savings to store the Q-table knowledge have reached more than the 99%.

Future work will consist in testing the embedding of the obtained ELMs into the real Robot-Hose system to predict the optimal policy in real-world implementations of the L-MCRS. Preliminary experiments are encouraging, showing acceptable loss of task completion success relative to the original Q-table. To improve ELM embedding results we have to explore the possibility of using training and testing datasets with not so rough discretization and with more variables in the state model, because these two elements have proven to be the most relevant ones.

Acknowledgements

The research was supported by the Computational Intelligence Group, funded by the Basque Government with grant IT874-13.

References

[1] R. Duro, M. Graña, and J. de Lope, "On the potential contributions of hybrid intelligent approaches to multicomponen robotic system development," *Information Sciences*, vol. 180, no. 14, pp. 2635–2648, 2010.

[2] J. M. Lopez-Guede, M. Graña, and E. Zulueta, "On Distributed Cooperative Control for the Manipulation of a Hose by a Multirobot System," in *Hybrid Artificial Intelligence Systems*, ser. Lecture Notes in Artificial Intelligence, Corchado, E and Abraham, A and Pedrycz, W, Ed., vol. 5271, 2008, pp. 673–679, 3rd International Workshop on Hybrid Artificial Intelligence Systems, Univ Burgos, Burgos, Spain, Sep 24-26, 2008.

[3] Z. Echegoyen, I. Villaverde, R. Moreno, M. Graña, and A. d'Anjou, "Linked multi-component mobile robots: modeling, simulation and control," *Robotics and Autonomous Systems*, vol. 58(12, SI), pp. 1292–1305, 2010.

[4] B. Fernandez-Gauna, J. Lopez-Guede, E. Zulueta, and M. Graña, "Learning hose transport control with q-learning," *Neural Network World*, vol. 20, no. 7, pp. 913–923, 2010.

[5] B. Fernandez-Gauna, J. M. Lopez-Guede, E. Zulueta, Z. Echegoyen, and M. Graña, "Basic results and experiments on robotic multi-agent system for hose deployment and transportation," *International Journal of Artificial Intelligence*, vol. 6, no. S11, pp. 183–202, March 2011.

[6] R. Sutton and A. Barto, *Reinforcement Learning: An Introduction*. MIT Press, 1998.

[7] C. Watkins and P. Dayan, "Q-Learning," *Machine Learning*, vol. 8, no. 3-4, pp. 279–292, MAY 1992.

[8] J. M. Lopez-Guede, B. Fernandez-Gauna, M. Graña, and E. Zulueta, "Improving the control of single robot hose transport," *Cybernetics and Systems*, vol. 43:4, pp. 261–275, May 2012.

[9] R. Bellman, "A markovian decision process," *Indiana Univ. Math. J.*, vol. 6, pp. 679–684, 1957.

[10] H. Tijms, *Discrete-Time Markov Decision Processes*. John Wiley & Sons, Ltd, 2004, pp. 233–277.

[11] C. Watkins, "Learning from Delayed Rewards," Ph.D. dissertation, University of Cambridge,England, 1989.

[12] C. Watkins and P. Dayan, "Technical note: Q-learning," *Machine Learning*, vol. 8, pp. 279–292, 1992.

[13] D. H. W. G.-B. Huang and Y. Lan, "Extreme learning machines: a survey," *International Journal of Machine Leaning and Cybernetics*, vol. 2, no. 2, pp. 107–122, 2011.

[14] G.-B. Huang, Q.-Y. Zhu, and C.-K. Siew, "Extreme learning machine: Theory and applications," *Neurocomputing*, vol. 70, no. 1–3, pp. 489 – 501, 2006.

[15] G.-B. Huang, L. Chen, and C.-K. Siew, "Universal approximation using incremental constructive feedforward networks with random hidden nodes," *IEEE Trans. Neural Networks*, vol. 17, no. 4, pp. 879–892, 2006.

[16] G.-B. Huang and L. Chen, "Convex incremental extreme learning machine," *Neurocomputing*, vol. 70, no. 16–18, pp. 3056 – 3062, 2007.

[17] G.-B. Huang, M.-B. Li, L. Chen, and C.-K. Siew, "Incremental extreme learning machine with fully complex hidden nodes," *Neurocomputing*, vol. 71, no. 4–6, pp. 576 – 583, 2008.

[18] G.-B. Huang and L. Chen, "Enhanced random search based incremental extreme learning machine," *Neurocomputing*, vol. 71, no. 16–18, pp. 3460 – 3468, 2008.

[19] L. Chen, G.-B. Huang, and H. K. Pung, "Systemical convergence rate analysis of convex incremental feedforward neural networks," *Neurocomputing*, vol. 72, no. 10–12, pp. 2627 – 2635, 2009.

[20] G.-B. Huang, D. Wang, and Y. Lan, "Extreme learning machines: a survey," *International Journal of Machine Learning and Cybernetics*, vol. 2, no. 2, pp. 107–122, 2011.

[21] J. M. Lopez-Guede, B. Fernandez-Gauna, M. Graña, and E. Zulueta, "Empirical study of q-learning based elemental hose transport control," in *Hybrid Artificial Intelligent Systems*, ser. Lecture Notes in Computer Science, E. Corchado, M. Kurzynski, and M. Wozniak, Eds. Springer Berlin / Heidelberg, 2011, vol. 6679, pp. 455–462.

[22] J. Lopez-Guede, B. Fernandez-Gauna, M. Graña, and E. Zulueta, "Further results learning hose transport control with q-learning," *Journal of Physical Agents*, 2012 (in press).

[23] B. Widrow and M. Lehr, "30 years of adaptive neural networks: perceptron, madaline, and backpropagation," *Proceedings of the IEEE*, vol. 78, no. 9, pp. 1415 –1442, sep 1990.

[24] J. M. Lopez-Guede, M. Graña, E. Zulueta, and O. Barambones, "Economical Implementation of Control Loops for Multi-robot Systems," in *ADVANCES IN NEURO-INFORMATION PROCESSING, PT I*, ser. Lecture Notes in Computer Science, Koppen, M and Kasabov, N and Coghill, G, Ed., vol. 5506, 2009, pp. 1053–1059, 15th International Conference on Neuro-Information Processing, Auckland, NEW ZEALAND, NOV 25-28, 2008.

[25] J. M. Lopez-Guede, B. Fernandez-Gauna, M. Graña, and E. Zulueta, *Robot Learning*. SCIYO, 2010, ch. Multi-Robot Systems Control Implementation, pp. 137–150.

J ose Manuel Lopez-Guede received the M.Sc. degree in 1999 and the Ph.D. degree in 2012, both in Computer Engineering from the University of the Basque Country (UPV/EHU), Spain. From 2000 to 2004 he worked at an Industrial Informatics company. Since 2004 he is working at the University of the Basque Country (UPV/EHU), Spain. His current position is Aggregate. Prof. (roughly equivalent to Assoc. Prof.) in Systems Engineering and Automatic Control Department of the University College of Engineering of Vitoria-Gasteiz, Spain. His research interests are computational intelligence, robotics and reinforcement learning.

Manuel Graña Romay received the M.Sc. and Ph.D. degrees from Universidad del Pais Vasco (UPV/EHU), Donostia, Spain, in 1982 and 1989, respectively, both in Computer Science. His current position is a Full Professor (Catedrático de Universidad) in the Computer Science and Artificial Intelligence Department of the Universidad del Pais Vasco (UPV/EHU). He is the Head of the Computational Intelligence Group (Grupo de Inteligencia Computational). His current research interests are in applications of computational intelligence to linked multicomponent robotic systems, medical image in the neurosciences, multimodal human computer interaction, remote sensing image processing, content based image retrieval, lattice computing,

Application of an ultrasound-based measuring system for density measurement of wheat dough in continuous process

X. Chen, M. A. Hussein, T. Becker

***Abstract*—**So far majority of studies in the baking industry only focus on off-line analysis of dough properties and classification of flour quality. Application of ultrasonic technology in the baking industry attracts increasing attention, because it can be used not only for investigating complex food, but also for monitoring food properties during a continuous production process. This paper presents a method using ultrasound-based measuring system for determining dough density in a continuous process. The system was in pulse-echo mode using an in-house manufactured ultrasound sensor with a central frequency of 500 kHz. In order to estimate the dough density, a feedforward back-propagation network based on Levenberg-Marquardt (LM) algorithm was implemented to perform the modeling task. The estimated density was then parallelly validated by the reference method. The results have shown that the developed NN-DT model is capable of predicting the dough density for a set of input parameters including ultrasound features and dough thickness. The accuracy of the proposed method can achieve, in the form of mean absolute percentage error, 0.81%. This paper demonstrates that the currently developed system has a large potential to be implemented in the in-line measurement of baking industry.

***Keywords*—** Ultrasound, density, dough, neural network.

I. Introduction

Determination of dough density plays an important role for evaluating the final quality of the baked goods.

Production of an aerated dough normally undergoes mixing and proving stages. In both stages, the gas retention ability affects the dough density. At the mixing stage, air bubbles are incorporated into the dough and the gas cells are thus generated; during the proving stage, yeasts metabolize the sugar in dough and produce carbon dioxide which in turn diffuses into the gas cells, increasing the dough volume and thus reducing its density. Therefore, measurement of dough density is a key measurement for studying the gas retention ability of dough [1].

This work was supported by the Arbeitsgemeinschaft industrieller Forschungsvereinigungen under grant AiF17480N.

Xue Chen is with the chair of Brewing and Beverage Technology, Technische Universität München, Weihenstephaner Steig 20, 85354 Freising, Germany. (e-mail: xue.chen@tum.de).

Mohamed A. Hussein is with the chair of Brewing and Beverage Technology, Technische Universität München, Germany (phone: +49 (0)8161-71-3277; e-mail: mohamed.hussein@tum.de).

Thomas Becker is with the chair of Brewing and Beverage Technology, Technische Universität München, Germany (e-mail: tb@tum.de).

Moreover, the density measurement is required for determination of gas void fraction. It is commonly used to evaluate the development of the aerated structure in a dough during proving stage [2]. The gas-free dough density and the density after proving are both measured in order to estimate the void fraction [2].

A number of studies have proposed different methods to investigate dough density measurement. This includes the specific gravity determination method [3], the graduated cylinder method, the free expansion method [4], and the digital imaging method [4]. Although these methods are easy to apply because of their relatively simple principles, development of much preciser measurement is still required. Additionally, these methods are off-line meaning the samples must be sent to the laboratory for analysis. The subsequent time delay can cause the dough structure change and increase the measuring uncertainty. So bread production in a continuous process becomes increasingly popular, and it requires new analytical techniques to analyze in-line complex food materials and monitor the food processing state.

The ultrasonic technique, widely applied in medicine and chemical engineering processes, can meet these requirements. It offers several advantages over other already existing techniques. On one hand, ultrasonic measurements can be carried out without direct contact with measured subjects, thus can avoid hygienic issues during measurement. On the other hand, the measurements can be performed fast, continuously, and automatically. Therefore, the ultrasonic technique is very suitable for food industries. In the research field of ultrasonic detection for dough, the major of studies focused on the off-line measurement of rheological properties [5-7], bubble size change [8]. One publication proposed an off-line measuring method to estimate density of the water-flour dough [9]. Application of ultrasonic technology to determine dough density in continuous process still remains underdeveloped.

The objective of this paper is to establish an in-line ultrasound-based measuring system for dough density estimation. To achieve this, an ultrasound-based measuring system was first developed and then adapted to the prototype conveyer device. It was hypothesized that, a model using back propagation neural network algorithm can be established to estimate the dough density.

II. Material and Methods

A. Sample preparation

Wheat flour type 550 (Rosenmühle, Ergolding, Germany), fine salt, distilled water, butter (Meisterbacken, Germany), dried yeast were used for preparation of dough samples. In order to train model, different values of dough thickness are required. Therefore, the content of water/yeast/salt/butter, the mixing time and the mixing speed were varied. The variations are listed in Table 1. All samples were produced using a spiral dough mixer (XTS Mod. 20, Germany) at temperature of 24 ± 1 °C.

Tab. 1: Formula of dough sample in experiments.

Recipe					Mixing operation	
Flour [g]	Water [g]	Yeast [g]	Salt [g]	Butter [g]	Time [min]	Speed [rpm]
1000	625	10	20	15	10	60
1000	625	10	20	15	6	150
1000	625	10	20	30	6	60
1000	500	20	20	15	6	60
1000	625	20	20	30	6	60
1000	625	10	20	30	6	60
1000	500	20	20	15	6	60
1000	625	20	20	30	6	60
1000	625	10	20	30	6	60
1000	500	20	20	15	6	60
1000	625	20	20	30	6	60

Once a dough sample was produced, five pieces of the sample were taken and weighted. After molded by hand, the piece was placed onto the conveyer and the thickness was measured. For each piece sample 15 ultrasound signals were measured.

B. Dough density determination

For all experiments, reference density measurements of dough density were conducted, so as to control the measurement accuracy of the ultrasonic method. They are based on the Archimedes principle. The weights of a sample in the air and of a sample immersed in silicone oil were both measured. All experiments were conducted at temperature of 25 ± 1 °C. The reference density can be calculated using (1):

$$\rho_{dough} = \frac{m_{air}\rho_{oil}}{m_{air} - m_{oil}} \tag{1}$$

Where ρ_{dough} and ρ_{oil} refer to density of dough and oil, respectively. m_{air} and m_{oil} denote weight of dough placed in air and in oil, respectively.

C. Ultrasonic measurement

The ultrasonic measurements were carried out using an experimental setup consisting of an ultrasonic measuring system and a dough conveyer prototype, as shown in Fig. 1. Considering different applications in bakery, two types of gear motors (MFA, 950D; MODELCRAFT, RB350600-0A101R) were mounted on the conveyer prototype, so as to conduct experiments at two speed levels (slow-speed level with 0.019m/s and a high-speed one with 1.5 m/s).

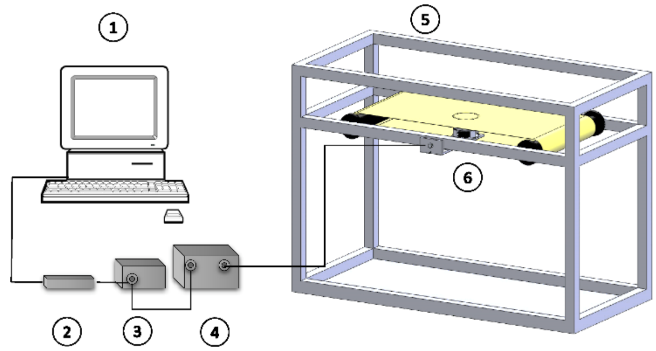

Fig. 1: Experimental setup: 1: computer 2: ADC-converter, 3: power supply device, 4: microcontroller, 5: conveyer prototype, 6: ultrasound measuring device.

The ultrasonic measuring system was composed of an in-house produced ultrasound sensor with a center frequency of 500 kHz, a transducer holder structure, an in-house developed ultrasound generation system, an analog-digital (A/D) converter (Transio A52, MOXA®) and a personal computer. This holder structure was designed to fix ultrasound sensor stably under conveyer and to ensure an optimal contact between ultrasound sensor and conveyer belt. A Plexiglas (Polymethyl Methacrylate, PMMA) with a height of 25 mm was used as buffer layer.

An in-house developed software “VirtualExpert“ was used to control the ultrasound measuring device. By using this software, sampling time, applied voltage, pulse repetition time and pulse interval can be set for obtaining an ideal data acquisition. A sample signal is presented in Fig. 3.

Once aforementioned parameters were confirmed, calibration measurements were conducted. Ultrasound signals were measured without placing dough onto the conveyer belt.

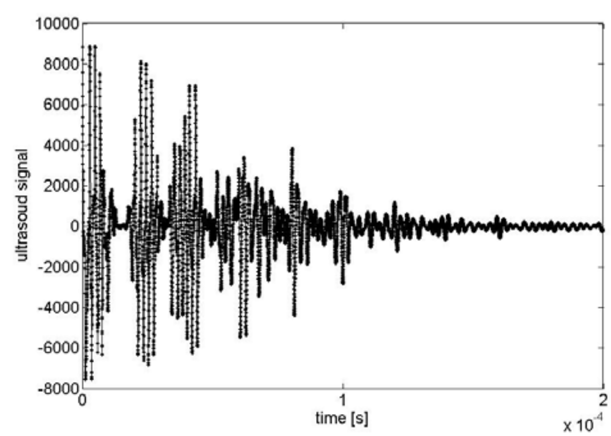

Fig. 3: Ultrasound signal using the development experimental setup.

After calibration measurement, ultrasound signals were measured for dough samples. Before putting the dough onto

ISBN: 978-1-61804-321-4

the belt, distilled water was used as the coupling material to ensure a good signal. Each ultrasound experiment was repeated 5 times.

D. Data analysis method

The entire data analysis process was performed in MATLAB® R2010a using the algorithm, which allows to extracting the ultrasound features from the measured ultrasound signals. In addition, the initiation of the data matrix for nonlinear regression can be easily realized by using the MATLAB neural network Toolbox™ as well. The input dataset of the data analysis process includes the ultrasound signal, the reference data and the additional data such as data of dough thickness (DT), mixing speed (MS), and mixing time (MT). The schematic algorithm for data analysis is illustrated in Fig. 4. And the main procedures of the data analysis process are explained as follow:

1) As the first step, the signal pre-processing should be performed to remove the digital component offset from the inputted ultrasound data, so that the mean power value of the signal can be kept at zero. This step is necessary for the further estimation of the spectral quantities in frequency domain.

2) In the second step, the relevant signal echo in the pre-processed data needs to be recognized through comparing the ultrasound signals, which were measured with and without dough sample on the conveyer belt. This step is required, since the signal echo contains the necessary information about dough property which will be used for the estimation of the dough density in the next steps.

3) In the third step, the ultrasound features, including temporal crest-factor (X_{tcf}), temporal power (X_{tp}), zero-crossing rate (X_{zcr}), and spectral crest-factor (X_{scf}) were extracted from the signal echo (S_t). The descriptions of aforementioned ultrasound features are clarified as follow:

Temporal crest-factor is related to a time-domain signal. It is defined as the ratio of the maximum amplitude value of the signal to its root mean squared value over a certain time period [10], as written in (2):

$$X_{tcf} = \frac{\max|S_t|}{\frac{1}{L}\sqrt{\sum_{n=0}^{N} S_t^2}} \tag{2}$$

where S_t is the discrete values of the selected signal echo. L refers to the signal length.

Temporal power estimates the energy of a signal echo, which is the sum of the squared amplitude value within the selected time frame [11]. It is calculated as (3):

$$X_{tp} = \frac{1}{L}\sum_{t=1}^{N} S_t^2 \tag{3}$$

Zero-crossing rate is defined as the rate of sign-changes along the selected signal echo [10], as written in (4):

$$X_{zcr} = \frac{1}{L}\sum_{t=1}^{N}\{s_t s_{t-1} < 0\} \tag{4}$$

where, s_t denotes to the signal values with length L.

Spectral crest factor is used to characterize its spectral shape, which is defined as the ratio of the maximum spectrum power of the mean spectrum power [12]:

$$X_{scf} = \frac{\max\{M(t_n)\}}{\frac{1}{L}\sqrt{\sum_{n=0}^{N} M(t_n)}} \tag{5}$$

where $M(t_n)$ refers to power intensity of the entire power spectrum.

4) In the fourth step, each of those additional data (sample thickness, mixing speed, and mixing time) is selected for generating the initial data based on the referenced data as well as the ultrasound features obtained in the third step. Therefore, three different data matrixes were generated: matrix M-DT, M-MT and M-MS. Each matrix was divided into training set and validation set. Here, 60% data were used as training set for calibrating models, while 40% data were used as validation set for model validation.

5) The main purpose the fifth step is to find the most accurate model for density estimation. The generated data matrixes were imported into neural network toolbox™ shipped with the Matlab software, where the so-called feedforward back-propagation network was used for the modeling process. So, three models including NN-DT, NN-MT, and NN-MS were established based on the training dataset M-DT, M-MT and M-MS, respectively. Each model was trained based on Levenberg-Marquard (LM) algorithm, which is an efficient iterative training algorithm and can provide a rapid convergence [13]. The value of the coefficient of determination (R-squared) was used as an indicator to evaluate the training performance. If the value of the R-squared was greater than 0.8, the exit criterion was fulfilled and the training process will be terminated immediately. Otherwise, the training process will be performed until the exit criterion is fulfilled. After the three models were established, they should be validated by using the validation set, and the mean absolute percentage error of each model can be obtained according to the results of the reference measurement. The model with the smallest mean absolute percentage error was selected as the most accurate model.

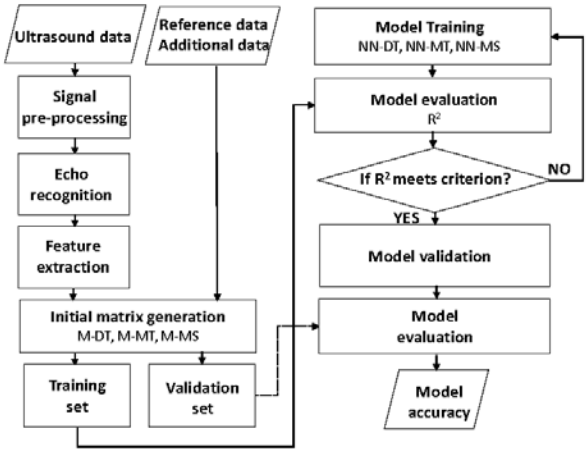

.

Fig. 4: Schematic algorithm of data processing.

III. Result

The analyzed dough density was in the range of 1060-1150 kg/m^3. The model accuracy can be quantitatively reflected by the value of mean absolute percentage error and the coefficient of determination, which are given in Table 2. The value of coefficient of determination (R-squared) indicates the statistic evaluation of correlation between training data set and density data set. Model NN-DT and NN-MT can provide R-squared with 0.91 and 0.92, respectively, while model NN-MI can achieve 0.87.

However, the value of mean absolute percentage error of NN-DT is lower than the value of NN-MT. It is demonstrated that, the model NN-DT can estimate density more accurately than NN-MT.

Tab. 2: Results of the density estimation using model NN-DT, NN-MI and NN-MT. Mean absolute percentage error and R-squared are used to evaluate the model performance.

	mean absolute percentage error [%]	R-squared
NN-DT	0.81	0.91
NN-MI	1.53	0.87
NN-MT	2.00	0.92

The quality of model NN-DT is presented by parity plot in the Fig. 5. The estimated values using model NN-DT are plotted against those of reference measurement. The y = x line is plotted as the reference. It is observed that, the results scatter randomly around the y = x line. This demonstrates that, the estimated results show a good agreement with the reference results.

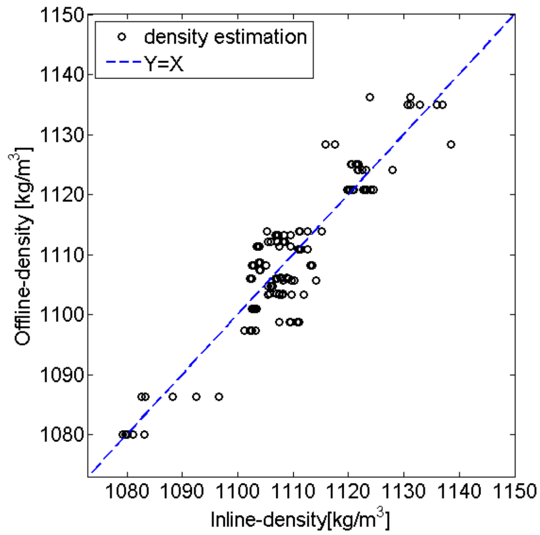

Fig. 5: Parity-plot for presenting results of the off-line density and in-line estimation using the most accurate NN-DT model.

IV. Conclusion

In this paper an ultrasonic method for estimating dough density in a continuous process is presented. An ultrasound sensing system was developed for investigating this method at laboratory scale. In order to estimate dough density, five parameters including zero-crossing rate, temporal crest factor, temporal power, spectral crest factor, and dough thickness were used for building up a model. The accuracy in form of relative standard deviation shows that the proposed method is able to estimate density accurately. Moreover, the presented measuring system can also be investigated and combined with other technology applied for processing monitoring. As the initial investigation, the selected features with the used parameters were attempted to establish the models. For further investigations it is suggested that other methods, e.g. principle component analysis, should be used to select efficient features to improve estimation accuracy.

References

[1] G.M. Campbell, P.J. Martin, “Bread aeration and dough rheology: an introduction,” in: *Breadmaking: improving quality*, UK, Woodhead Publishing, 2012, pp. 299-329.

[2] G.M. Campbell, C.D. Rielly, and P.A. SADD, "Measurement and interpretation of dough densities," *Cereal Chem.*, 2003, vol. 70(5), pp. 517-521.

[3] J.C. Backer and M.D. MIZE, "Mixing doughs in vacuum and in the presence of various gases," *Cereal Chem.*, 1937, vol. 14, pp. 721-734.

[4] H.M. Elmehdi, J.H. Page, and M.G. Scanlon, "Evaluating Dough Density Changes During Fermentation by Different Techniques," *Cereal Chem.*, 2007, vol. 84(3), pp. 250-252.

[5] H.O. Lee, H. Luan, and D.G. Daut, "Use of an ultrasonic technique to evaluate the rheological properties of cheese and dough," *Journal of Food Engineering*, 1992, vol. 16(1–2), pp. 127-150.

[6] S A. kaf, et al., "A new acoustic technique to monitor bread dough during the fermentation phase," *Journal of Food Engineering*, 2009, vol. 93(3), pp. 365-378.

[7] H.M. Elmehdi, J.H. Page, and M.G. Scanlon, "Using ultrasound to investigate the cellular structure of bread crumb," *Journal of Cereal Science*, 2003, vol. 38(1), pp. 33-42.
[8] A. Strybulevych, et al., "Use of an ultrasonic reflectance technique to examine bubble size changes in dough," in *International Symposium on Ultrasound in the Control of Industrial Processes* (UCIP 2012), 2012.
[9] H. Elfawakhry, M.A. Hussein, and T. Becker, "Possibility of Using Acoustic Techniques for Dough Processing Evaluation," in *Procedia Food Science*, 2011, 1(0), pp. 2023-2032.
[10] O. Kramer, and T. Hein, "stochastic featue selection in SVM based instrument recogonition," in *KI 2009: Advances in Artificial Intelligence*, 2009, Paderborn, Germany.
[11] S.D. Stearns, *Digital signal processing with examples in MATLAB*, CRC Press LLC, New York, 1996.
[12] D. Mitrović, M. Zeppelzauer, and C. Breiteneder, "Features for Content-Based Audio Retrieval," *Advances in Computers*, 2010, vol.78, pp. 71-150.
[13] P. Rausch, A.F. Sheta, and A. Ayesh, "Business Intelligence and Performance Management: Theory, System and industrial Appications," *pringer Science & Business Media*, 2013.

Xue Chen, received the M.Sc. degree at the Technische Universität München (TUM) in 2014. Currently, she is working as a PhD candidate at the Technische Universität München in the chair of Brewing and Beverage Technology, Bio-Process Analysis Technology department. Her research interests are in the field of application of the ultrasound-based measurement system in analysis and monitoring of food processing.

Mohamed A. Hussein is group leader of Bio-Process Analysis Technology department at TUM, working in the entity since June 2009. He is an expert in Bioprocess Analysis, Multi-scale Modelling, Imaging, Ultrasound, Micro-Sensing, and Control.

Thomas Becker, received his Ph.D. in 1995. From 1996 to 2004 he worked as Deputy Head of Department and assistant lecturer at the Institute of Fluid Mechanics and Process Automation of Technische Universität München. His habilitation took place in 2002. In 2009, he became the professor of Brewing and Beverage Technology Department at Technische Universität München.

Syntactic Pattern Recognition of Power System Signals

C. Pavlatos, V. Vita, and L. Ekonomou

***Abstract*—**This paper presents an application of the syntactic methods to the recognition of power system signals and to the measurement of its parameters. The subproblems of primitive pattern selection, linguistic representation, and pattern grammar formulation are faced. Attribute grammars are used as the model for the pattern grammar because of their descriptive power, which is due to their ability to handle syntactic as well as semantic information. A software implementation has been developed in order the functionality of the proposed system to be tested using waveforms and data provided by the Independent Power Transmission Operator (IPTO) in Greece. The proposed methodology will be applied to the implementation of a protective relay that would efficiently prevent safety problems and economic losses caused by faults presented in power systems.

***Keywords*—** Attribute Grammars, Power Signals, Syntactic Pattern Recognition.

I. Introduction

POWER systems are large and complex systems where faults frequently occur that may cause personnel and equipment safety problems, and result in substantial economic losses. An efficient protective relay would efficiently prevent these problems and losses. Microprocessor-based digital protective relays bring unquestionable improvements of the protection relays since: i) criteria signals are estimated in a shorter time, ii) input signals are filtered-out more precisely, iii) sophisticated corrections are applicable, iv) the hardware is standardized and may communicate with other protection and control systems, and v) relays are capable of self-monitoring. However, digital relays did not make a major breakthrough in power system protection as far as security, dependability and speed of operation are considered. The key reason behind this is that the principles used by digital relays blindly reproduce the criteria known for decades. In addition, problems result mainly from the trade-off between the security demand (no false trippings), and the speed of operation and the dependability (no missing operations) requirements. The more secure is the relay (both the algorithm and its particular settings), the more it tends to misoperate or operate slowly, while the faster is the relay, the more it tends to operate falsely. There are basically two ways to mitigate the problem of limited recognition power of the classical relaying principles. One of them is to improve the recognition process itself, while the second way is to increase the performance of the implementation. Previous approaches [1] in facing the problem of improving protective relays in power systems were mainly software implementations based on artificial neural networks.

In this paper, for the first time in the literature the recognition of power system signals based on Syntactic Pattern Recognition techniques is presented. The underlying model of implementing a system for the aforementioned application can be that of an Attribute Grammar parser. In [1] the Artificial Intelligence (AI) approaches to power system protection are reviewed and the application of artificial neural networks and fuzzy logic techniques is presented. A number of novel applications and concepts have been presented including fuzzy logic approach to differential transformer protection and artificial neural networks application to the transformer protection, CT (current transformer) and CVT (capacitor voltage transformer) transients correction, and fault-type classification. However, the implementations presented are software approaches and do not achieve the maximum possible speed-up.

In [2] a real-time system implemented on an FPGA board is presented that tracks time – varying waveforms distortions in power systems based mainly on a proposed amplitude tracking algorithm derived from amplitude demodulation. However, the frequency of the fundamental signal is assumed constant but in power systems, the fundamental frequency of the current and voltage is not always exactly the nominal value.

Although the syntactic method seems suitable to the problem of protection relays and parameter measurement, not much progress has been made to date. The proposed methodology presents the application of the syntactic pattern recognition method to recognition of power systems waveforms and to the measurement of power system parameters.

In syntactic pattern recognition, the task of recognition is

C. Pavlatos is with the Department of Computer Science, Hellenic Air Force Academy, Dekelia Air Base Tatoi, 14451, Greece (e-mail: pavlatos@cslab.ece.ntua.gr).

V. Vita is with Department of Electrical and Electronic Engineering, School of Mathematics, Computer Science and Engineering, City University London, Northampton Square, London EC1V 0HB, United Kingdom (e-mail: vasiliki.vita.1@city.ac.uk).

L. Ekonomou is with Department of Electrical and Electronic Engineering, School of Mathematics, Computer Science and Engineering, City University London, Northampton Square, London EC1V 0HB, United Kingdom. (corresponding author, phone: +44 (0) 207040 8111; e-mail: lambros.ekonomou.1@city.ac.uk).

ISBN: 978-1-61804-321-4

essentially reduced to that of parsing a linguistic representation of the patterns to be recognized with a parser that utilizes a certain grammar, called pattern grammar. The pattern grammar describes the patterns to be recognized in a formal way, and the formulation of the pattern grammar is always the crucial sub problem in any pattern recognition application that is to be tackled by the syntactic approach. The proposed project aims to give solutions to the sub problems of primitive pattern selection, linguistic representation, and pattern grammar formulation for the waveforms received by a protection relay. In the case of power systems waveforms where added morphologies can be found due to noise, and where measurements of the various parameters have to be performed, powerful grammars capable of describing syntax as well as semantics are needed as a model for the formulation of a pattern grammar. The contribution of this paper is summarized at the following:

I. Define the linguistic representation of waveforms received by a protection relay.

II. Define an attribute grammar capable of modelling the power system signals using the linguistic representation of objective I.

The above items are novel and have not been addressed in the literature before. Our future plans is to design a hardware parser for power system signals that will be based on a proposed extension of Earley's [3] parallel parsing algorithm using the architecture proposed in [14], which given an input string, generates the parse trees in the form of an And-Or parse tree. This And-Or parse tree will be then traversed using a proposed tree traversal technique in order to execute the corresponding actions in the correct order, so as to compute the necessary attributes and define the relay's action. The proposed system will be described in Verilog hardware description language (HDL), simulated for validation, synthesized and tested on an XILINX [5] FPGA board.

II. Theoretical Background

A significant part of computer science is language theory, which copes with both theoretical and practical issues. Grammars can be found in many applications and especially Context-Free Grammars (CFG) [6] are well known for their necessity in the field of compilers and interpreters. CFGs combine expressive power and simplicity; consequently they are powerful enough to describe the syntax of programming languages (almost all programming languages are defined via CFGs) and simple enough to allow the construction of efficient parsing algorithms. Furthermore, general context-free methods and their augmentation are exploited today in various application domains.

Two well-known parsing algorithms for general CFGs are the Earley's algorithm [3] and the Cocke-Younger-Kassami (CYK) algorithm [7]. Both of them are basically dynamic programming procedures and have a time complexity $O(n^3|G|)$, where n is the length of the input string and $|G|$ is the size of the grammar. In order to increase the expression capability and usability of CFG, they may be augmented with either attributes or probabilities, forming Attribute Grammars (AG) [8] and Stochastic Context-Free Grammars (SCFG) [9] respectively. A CFG can be defined as a quadruple G = (N, T, P, S), where N is the set of non-terminal symbols, T is the set of terminal symbols, P is the set of grammar rules and S is the start symbol of the grammar. $V = N \cup T$ is defined as the vocabulary of the grammar. Grammar rules are written in the form $B \rightarrow \gamma$, where $B \in N$ and $\gamma \in V^*$.

After the introduction of Earley's and CYK algorithms, several modifications and improvements via parallelization have been proposed for these algorithms. Chiang & Fu [10] and Cheng & Fu [11] have presented designs using VLSI (very large scale integration) arrays for the hardware implementation of the aforementioned parsing algorithms, although they do not propose an efficient implementation for the operator they use. These approaches are not implemented in reconfigurable hardware and the scale of the hardware is input string length dependent. The hardware oriented approach was reinvigorated by presenting implementations in reconfigurable FPGA boards of the CYK algorithm [12, 13]. In order to relax the hardware complexity, most of the proposed architectures implement the CYK algorithm, whose basic operations are much simpler than those of Earley's. The first FPGA implementation of Earley's algorithm was given in [14]. The approach proposed in [15] uses a combinatorial circuit for the fundamental operator of Earley's algorithm.

A CFG may be extended by associating attributes to each symbol $X \in V$. Each attribute represents a specific context-sensitive property of the corresponding symbol. The augmented CFG is called Attribute Grammar (AG) and is also defined as a quadruple AG = (G, A, SR, d), where G is a CFG, $A = \cup A(X)$ where A(X) is a finite set of attributes. The notation X.z is used to indicate that attribute z is an element of A(X). A(X) is partitioned into two disjoint sets; the set of synthesized attributes AS(X) and the set of inherited attributes AI(X). Synthesized attributes X.s are those whose values are defined in terms of attributes at descendant nodes of node X of the corresponding decorated parse tree. Inherited attributes X.i are those whose values are defined in terms of attributes at the parent and (possibly) the left sibling nodes of node X of the corresponding decorated parse tree. Finally d is a function that gives for each attribute a its domain d(a). The primary field of AG usage is in computer languages but they are also convenient in fields such as Artificial Intelligence, Pattern Recognition, or even Biomedicine. An efficient Attribute Grammar evaluator was presented in [4].

Our future goal is to design a hardware parser for power system signals on an XILINX FPGA board that will be based on a proposed extension of Earley's [3] parallel parsing algorithm, using the architecture propose on [4].

III. THE SYNTACTIC APPROACH IN POWER SYSTEMS SIGNALS

A. *Primitive Pattern Selection*

Various segments have mainly been proposed in the past as primitive such as lines and triangles. The first are low level while the second are difficult to extract. In regards to the linguistic representation of power system signals we have chosen the peak as primitive pattern. Peaks have also been used during recognition of a considerable number of signals such as ECG (ElectroCardioGram)[16]. This choice seems to be a natural one because power system signal are mainly sinusoidal. The peak pattern is shown in Fig. 1. This pattern is that part of a signal which is demarcated by three characteristic points. The first point is called left peak boundary, the second peak extremum, and the third right peak boundary. The sample points between the left peak boundary and the peak extremum form the left arm of the peak. The sample points between the peak extremum and the right peak boundary form the right arm of the peak. In what follows peaks will be symbolized as Π_1, Π_2 . . . where Π_i is the name of peak i. A peak can be other positive or negative.

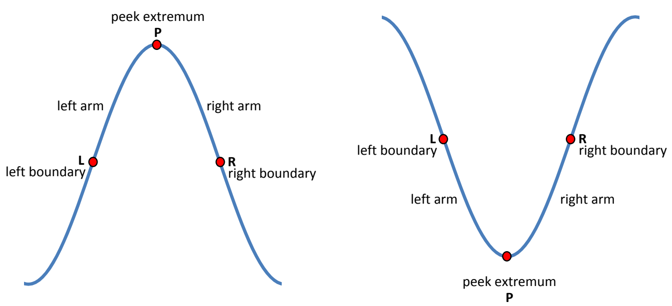

Fig. 1 positive and negative peak patterns

Each sample point of a power system signal is presented as a couple (x_i, y_i), where y_i is the amplitude in volts or amperes of the sample point i and x_i is the corresponding time. A set of attributes is assigned to each primitive pattern. The values of these attributes are calculated during the primitive extraction phase and they are utilized during the recognition process. They contribute both to the recognition of the patterns and to the measurement of their parameters. That is, they are used in a quantitative way for qualitative and quantitative purposes. A set of seven attributes is assigned to each peak Π_i. This set is symbolized as $\{x_{li}, y_{li}, x_{mi}, y_{mi}, x_{ri}, y_{li}, e_i\}$, where:

x_{li}, y_{li} is the left boundary of the peak Π_i.

x_{mi}, y_{mi} is the peak extremum of the peak Π_i.

x_{ri}, y_{li} is the right boundary of the peak Π_i

e_i is the energy of the peak Πi defined as:

$$\boldsymbol{e_i} = \sum_{\boldsymbol{i=p}}^{\boldsymbol{q}} (\boldsymbol{y_i} - \boldsymbol{y_{i-1}})^2 \quad (1)$$

$where: \ \boldsymbol{p} = x_{li} + 1 \ and \ \boldsymbol{q} = x_{ri}$

For example, the normal e i.e. e_{normal} for a sinusoidal, when frequency is equal to 50Hz and amplitude is 230V, is 64,428.36 V^2.

B. *Linguistic Representation Final Stage*

The alphabet of terminal symbols T = {p, n} has been adopted for encoding the power system waveforms, where p denotes positive peak and n a negative peak. Thus, a power system waveform is linguistically represented as a string of symbols from the set T such as *pnpnpn* or *npnpnp*. Each symbol is associated with the values of the corresponding attributes.

C. *Pattern Grammar AG_{PS}*

In syntactic pattern recognition, the task of recognition is essentially reduced to that of parsing a linguistic representation of the patterns to be recognized with a parser that utilizes a certain grammar, called pattern grammar. The pattern grammar describes the patterns to be recognized in a formal way, and the formulation of the pattern grammar is always the crucial sub problem in any pattern recognition application that is to be tackled by the syntactic approach. The proposed methodology aims to give solutions to the sub problems of primitive pattern selection, linguistic representation, and pattern grammar formulation for the waveforms received by a protection relay.

Table 1. Syntactic and semantic Rules of AG_{PS}

#	Syntactic Rules	Semantic Rules
1	S → WAVE	S.fr = (WAVE.c/2) * (1/ (WAVE.f - WAVE.s)) S.noise =1 - (e_{normal} * WAVE.c)/ (WAVE.e)
2	WAVE → FP	WAVE.c = FP.c WAVE.s = FP.s WAVE.f = FP.f WAVE.e = FP.e
3	WAVE → FN	WAVE.c = FN.c WAVE.s = FN.s WAVE.f = FN.f WAVE.e = FN.e
4	FP → FP_1 FP_2	FP.c = FP_1.c + FP_2.c FP.s = FP_1.s FP.f = FP_2.f FP.e = FP_1.e + FP_2.e
5	FN → FN_1 FN_2	FN.c = FN_1.c + FN_2.c FN.s = FN_1.s FN.f = FN_2.f FN.e = FN_1.e + FN_2.e
6	FP → p	FP.c = 1; FP.s = p.xl; FP.f = p.xr; FP.e = p.e;
7	FP → p n	FP.c = 2; P.s = p.xl; P.f = n.xr; FP.e = p.e + n.e;
8	FN → n	FN.c = 1; FN.s = n.xl; FN.f = n.xr; FN.e = n.e;
9	FN → n p	FN.c = 2; FN.s = n.xl; FN.f = p.xr; FN.e = n.e + p.e;

In the case of power systems waveforms, where added morphologies can be found due to noise, and where measurements of the various parameters have to be performed, powerful grammars capable of describing syntax as well as

ISBN: 978-1-61804-321-4

semantics are needed as a model for the formulation of a pattern grammar. Due to their power in describing structural and statistical features and their ability to handle syntactic and semantic information Attribute Grammars has been selected. Attribute Grammar AGPS presented in Table.1 is proposed for the recognition of power systems waveforms.

AG_{PS} is consisted of the non-terminal symbols belonging in set N = {S, WAVE, FP, FN} where S is the start symbol; the terminal symbols belonging in set T = {n, p} where n denotes positive peak and n denotes negative peak; vocabulary of the grammar is equal to V = N ∪ T. The syntactic rules of the grammar are shown in the second column of Table.1, while the semantic rules in the third column of the same table.

Non terminal symbols p, n have the attributes presented in section “Primitive Pattern Selection”, while the terminal symbols have the attributes c, s, f and: c attribute is used as a counter in order to store the number of peaks recognized till that point; s attribute is used to store the start point of the recognized substring; f attribute is used to store the last point of the recognized substring; and e attribute is used to store the sum of the energy e of peaks recognized till that point. In addition, start symbol S has two additional attributes called fr and noise so as to calculate the frequency of the recognized waveform and the ratio of the normal energy e (e_{normal}) the waveform should have over the actual energy e the waveform has. It should be noted that all attributes are synthesized.

IV. Results

A software implementation has been developed in order the functionality of the proposed system to be tested using various waveforms and data provided by the Independent Power Transmission Operator (IPTO) [17] in Greece. In this subsection, as a demonstration, an example of the recognition of five peaks will be presented.

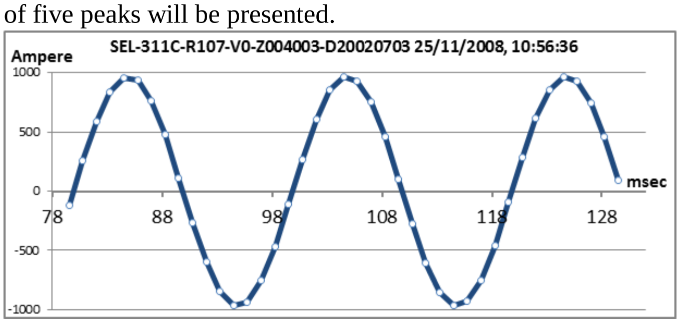

Fig .2 Examined peaks of IA waveform provided by IPT0

The five peaks are part of a current waveform IA measured by IPTO in November of 2008 and presented in Fig. 2. The sampling frequency is 800 Hz; consequently, there is one sample every 0.00125 sec. In this example 41 samples are presented. After the pattern extraction, the input string to be recognized is *pnpnp*, while the values of peaks’ attributes are shown in Table.2.

Table 2. Values of peaks’ attributes of input string “*pnpnp*”.

Peak #	Attribute Values
1	x_{l1} = -79.5 msec, y_{l1} = -124 A x_{m1} = 84.5msec, y_{m1} = 956 A x_{r1114} = 89.5 msec, y_{l1} = 114 A e_1 = 510,036 A^2
2	x_{l2} = 90.75 msec, y_{l2} = -265 A x_{m2} = 94.5 msec, y_{m2} = -961 A x_{r2} =, 99.5 msec, y_{l2} = -110 A e_2 =515,018 A^2
3	x_{l3} = 100.75 msec, y_{l3} = 268 A x_{m3} = 104.5 msec, y_{m3} = 961 A x_{r3} = 109.5 msec, y_{l3} = 101 A e_3 =516,122 A^2
4	x_{l4} = 110.75 msec, y_{l4} = -277 A x_{m4} = 114.5 msec, y_{m4} = -965 A x_{r4} =, 119.5 msec, y_{l4} = -96 A e_4 =521,524 A^2
5	x_{l5} = 120.75 msec, y_{l5} = 282 A x_{m5} = 124.5 msec, y_{m5} = 962 A x_{r5} = 129.5 msec, y_{l5} = 92 A e_5 =519,898 A^2

For this waveform e_{normal} is equal to 460,509 A^2. After the recognition process and the attribute evaluation, the frequency of the waveform i.e. the value of S.fr attribute was found really close to the frequency that IPTO has measured and was equal to 50,16Hz and noise was found 12,67%.

V. Future Work

Our future plans in designing a hardware parser for power system signals that will be based on the architecture proposed in [4]. This system will be described in Verilog hardware description language (HDL), simulated for validation, synthesized and tested on an XILINX [5] FPGA board. The produced system will be applied to the implementation of an efficient protective relay that would efficiently prevent safety problems and economic losses caused by faults presented in power systems.

VI. Conclusions

This paper presents a methodology of recognizing power systems signal and measure its parameters using syntactic pattern recognition techniques. A software implementation has been developed in order the functionality of the proposed system to be tested using waveforms and data provided by the Independent Power Transmission Operator (IPTO) in Greece. The proposed methodology may be applied to the implementation of an efficient protective relay that would efficiently prevent safety problems and economic losses caused by faults presented in power systems.

References

[1] Saha MM, Rosolowski E, Izykowski J, Artificial Intelligent Application to Power System Protection, Proceedings of the Eleventh National Power Systems Conference (NPSC`2000), Bangalore, New Delhi, Allied Publishers 2000, 2:595-600, 2000.

[2] Jinglin Xu ,Uwe Meyer-Baese, Real Time Digital Signal Processing in Power Systems using FPGAs: An Analysis of Time-Varying Waveform

Distortions and Power Disturbances, April 3, 2011, ISBN-13: 978-3844321722.

[3] Earley J, An efficient context-free parsing algorithm, Communications of the ACM, 13(2) 94-102, 1970. doi:http://doi.acm.org/10.1145/362007.362035.

[4] Dimopoulos AC, Pavlatos C, Papakonstantinou G, A platform for the automatic generation of attribute evaluation hardware systems, Computer Languages, Systems & Structures, 36(2):203-222, 2010.

[5] Xilinx Inc., www.xilinx.com.

[6] Aho V, Ullman JD, The Theory of Parsing, Translation, and Compiling, Vol. I: Parsing of Series in Automatic Computation, Prentice Hall, Englewood Cliffs, New Jersey, 1972.

[7] Younger DH, Recognition and parsing of context-free languages in n 3, Information and Control, 10:189-208, 1967.

[8] Graham SL, Harrison MA, Ruzzo WL, An improved context-free recognizer, ACM Trans. Program. Lang. Syst., 2(3):415-462, 1980.

[9] Stolcke A, An efficient probabilistic context-free parsing algorithm that computes prefix probabilities, Computational Linguistics, 21(2):165-201, 1995.

[10] Chiang Y, Fu K, Parallel parsing algorithms and VLSI implementations for syntactic pattern recognition, IEEE Transactions on Pattern Analysis and Machine Intelligence, 6:302-314, 1984.

[11] Cheng HD, Fu K, Algorithm partition and parallel recognition of general contextfree languages using fixed-size VLSI architecture, Pattern Recognition, 19(5):361-372, 1986.

[12] Ciressan A, Sanchez E, Rajman M, Chappelier JC, An fpga-based coprocessor for the parsing of context-free grammars, Proceedings of the 2000 IEEE Symposium on Field-Programmable Custom Computing Machines (FCCM '00), IEEE Computer Society, Washington, DC, USA, pp. 236-245, 2000.

[13] Bordim J, Ito Y, Nakano K, Accelerating the CKY parsing using FPGAs, IEICE Transactions Information & Systems, E-86D(5):803-810, 2003.

[14] Pavlatos C, Panagopoulos I, Papakonstantinou G, A programmable pipelined coprocessor for parsing applications, in: Workshop on Application Specific Processors (WASP) CODES, Stockholm, 2004.

[15] Pavlatos C, Dimopoulos AC, Koulouris A, Andronikos T, Panagopoulos I, Papakonstantinou G, Efficient reconfigurable embedded parsers, Comput. Lang. Syst. Struct., 35(2):196-215, 2009.

[16] Trahanias P, Skordalakis E., Syntactic pattern recognition of the ECG. IEEE Transantions on Pattern Analysis and Machine Intelligence (PAMI), vol. 12, no. 7, July.

[17] http://www.admie.gr/nc/en/home/

Spectral Imaging as a Tool for Baking Industry

Ronny Takacs, Mohamed A. Hussein and Thomas Becker

***Abstract*—** Spectral Imaging has recently proven of great potential for monitoring useful information outside the optical range. Such sensors emit/receive waves in ranges from 370nm to 700nm and 7500nm to 14000nm reflecting chemical bonds and radiation patterns, respectively. Such information proved of great value for baking industry; two main approaches addressed in this work.

- A reliable inline spectral-based insight of the protein properties reflected by means of chemical bonds, in contrast to offline, which is subject to experimental failures such as the gluten-index measurement. This approach can be used in the milling and pre-mixing step
- In the second approach during the baking process, thermo-imaging applied by means of infrared pattern capturing, which reflects the different development of heat fronts and phase change fronts in the baked goods.

Both approaches intensify the monitoring of baking processes, which is a new trend in baking industry in contrast to conventional methods based upon human expertise. The system is aiming for Industrial scale baking, were failures are common and losses are in millions of euros.

***Keywords*—** Spectral Imaging, Gluten, Image Processing, Thermal Imaging, Baking Industry

The spectral measurement of gluten properties is a future project, which comes out of a master thesis at the Research Group BioPAT - Bio Process Analysis Technology, Technische Universität München.

The thermal imaging approach is a part of AiF project 17735 N which is supported by Forschungskreis der Ernährungsindustrie, German Ministry of Economics and Technology and AIF (AiF project 17735 N). It includes baking tests and the analysis of thermal imaging with image processing tools.

Ronny Takacs is a member of the Research Group BioPAT - Bio Process Analysis Technology, Technische Universität München, Freising, Bavaria 85354 Germany (phone: +49(0)8161-71-2627; e-mail: r.takacs@tum.de)

Mohamed A. Hussein is the Leader of the Research Group BioPAT - Bio Process Analysis Technology, Technische Universität München, Freising, Bavaria 85354 Germany (phone: +49 (0)8161-71-3277; e-mail: mohamed.hussein@tum.de).

Thomas M. Becker is the head of the Institute of Brewing and Beverage Technology, Technische Universität München, Freising, Bavaria 85354 Germany (phone: +49 (0)8161 - 71-3261).

I. INTRODUCTION

WHITE bread is made of Water, Flour, Salt and Yeast. The production can be divided into four main tasks: the dosing of the ingredients, mixing and fermenting of the dough and baking of the bread. Each of them has his own influence on the end-product quality. Figure 1 shows an overview of the baking production, from the raw materials up to the end-product.

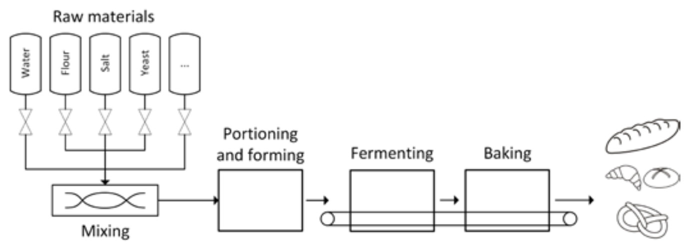

Fig. 1: Process Overview of the main process in the production of bakery products

Flour is in addition to water the main constituent of dough, its structure built upon the gluten network. The importance of measuring gluten content and functionality is the direct impact on the rheological properties of the dough [1–3]. These compels mills to produce a constant flour quality trying to satisfy the bakeries need. This shows the great relevance for measuring the gluten parameter continuously in mills and bakeries. The determination of gluten content and quality currently carried out mainly in the laboratory. The most reliable and technically used methods are: hand washing by AACC 38-10, Glutomatic system (Perten Instruments; ICC No. 106/2, AACC 38-12A.), Measured by the farinograph (loudly AACC 38-20, ICC 115/1), measuring per Extensograph (loudly: AACC 54-10, ICC 114/1) and the determination of gluten functionality by baking trials using suitable standard procedures (ICC 131, AACC 10-09, AACC 10-10B, AACC 10-11, AACC 10-13). Other established laboratory methods serve only the qualitative and quantitative determination of proteins, for example: As molecular biological analyzes such as PCR [16], HPLC [10], MALDI-TOF-MS [10], ELISA [6] and near-infrared spectroscopy [1, 7, 11]. The proposed spectral Tool to predict the gluten parameters works with the spectral properties of gluten and starch. Gluten possess a fluorescence response, as gluten containing aromatic amino acids such as tyrosine and phenylalanine [12]. This caused by delocalized electrons (π-electron system). A further effect, which is due to the composition of the gluten proteins, is the absorption of light in UV-, visible- and near-infrared-light region. Starch possess as absorption in UV-region about 300 nm [4]. To predict the gluten properties, a spectral setup is necessary. The most of optical analyses work with broadband light sources, expensive light filter and there are only able to scan pointwise. The clear disadvantage of these systems are the expensive components and the less reliable of the results. The novel approach uses light emitter diodes (LED), laser diodes (LD) and cameras. Which leads to a cost efficient and statistical more reliable measurement. In the last years, light emitter diode and laser diodes developed a lot and now there are available for low costs and in many wavelengths. Thus, a LED / LD / camera system is hypothesized to replace the expensive spectral units.

Thermal Imaging or temperature measurements is an important process in food processing. These new approaches to measure the temperature of the surface is non-invasive, non-destructive and hygienic approach. The mapping of the temperature profile leads to novel image processing technics. All objects above 0 K emits infrared radiation dependents on the material and temperature of the object [14, 15]. These radiations can be captured using radiation-sensitive sensor and transferred to an electrical signal, these signals converted into an image with spatial coordinates. Existing food assessments applications use such thermo-imaging systems in detection of fungal infection of stored wheat as in Chelladurai et al. [13]. Baranowski et al. [9] developed a method to detect bruises in apples with thermal hyperspectral data. Miah et al. [5] used thermal imaging to analyze the heat integration in food industry. The approach to quantify the energy efficiency of bakery plants leads also to a novel approach of high interest for bakery industry. Spectral measurements in the range of 7000 nm up to 14000 nm during the baking process opens a new field for assessing the production of baked goods. Thermal imaging is able to determine heat fronts and phase change fronts propagating during baking, opening new insights into thermal transport whilst processing. The mid infrared range opens up the possibility to observe the temperature distribution on the bread surface and additionally other physical parameters like size and volume change of the dough/bread (so called oven spring [2, 3, 8]).

II. Material and Methods

A. Gluten properties

a) Sample preparation

For the measurements, the samples were prepared with pure starch (Mühle Schlingemann e. K., Germany) and 80% pure wheat gluten (LORYMA GmbH, Germany) with several gluten concentrations. Afterwards the samples were homogenized with a Tubular shaker Type T2C for 30 minutes. For the measurement of the gluten quality commercial flours type 405 were used. The gluten content and quality were analyzed with Glutomatic 2000 (Perten Instruments, Sweden). Furthermore, dough samples were prepared with the commercial flours (double-Z-kneader, kneader time 5 min. 63 rpm, standard recipe: 100 parts flour, 55 parts water).

b) Imaging System

The imaging system consist of a light shielded box with UV-A-LEDs (wavelength peak 375 nm, 700 mA, 3.2 V, view angle 120°), green LEDs (wavelength peak 568 nm, 20 mA, 3.0 V, view angle 25°), iCube Camera (NS1500CU, Basler AG, Germany) and a processing unit. The Light source and Camera are changeable in distance to the sample and in angle to the sample (cf. Figure 1). To measure the gluten quality supplementary two light filters were used (central wavelength: 540 and 560 nm, bandwidth: 10 nm, diameter: 25 mm, Edmund Optics GmbH, Karlsruhe, Germany). For statistically reliable measurements, each flour sample was divided in to 15 single samples and measured 15 times. To acquire the images MALTAB R2013 and Image Acquisition Toolbox (MathWork Inc.) were used.

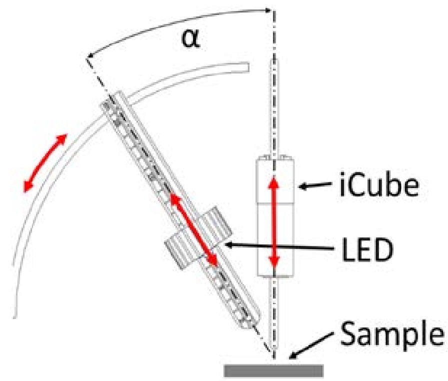

Fig. 2: Representation of the settings for lighting and camera.

c) Image Processing and data handling

Image features for all three-color layers (RGB) and gray matrix were captured. Images features, for example color features were extracted like color mean, color modus and color moment, textural features like homogeneity, entropy, energy and cosine similarity (cf. equation 1-6).

Color mean $$\frac{1}{n}\sum_{i,j=1}^{n} I(i,j) \tag{1}$$

Color moment $$\sqrt{\frac{\sum_{i=0}^{255}\left(NoE(i) * \left(h(i)-\bar{h}\right)^{n}\right)}{\sum_{i=0}^{255} NoE(i)}} \tag{2}$$

Homogeneity $$\sum_{i,j=0}^{N-1} \frac{P_{i,j}}{1+(i-j)^2} \tag{3}$$

Entropy $$\sum_{i,j=1}^{N-1} P_{i,j}(-\ln P_{i,j}) \tag{4}$$

Energy $$\sum_{i,j=0}^{N-1} P_{i,j}^2 \tag{5}$$

Cosine similarity $$\frac{\bar{G}\cdot\overline{I_{RGB}(x,y)}}{\left|\left|\bar{G}\right|\right| * \left|\left|\overline{I_{RGB}(x,y)}\right|\right|} \tag{6}$$

P … Gray-level co-occurrence matrix
i, j … Index gray-level co-occurrence matrix
I … Image matrix
x, y … Index image matrix
NoE … Number of elements
G … RGB Vector presents Gluten
h … Color histogram vector
μ … GLCM Mean
σ^2 … Variance
n … Power

The finally used independent three features were identified iteratively. The measurement data were split into two sets, one training set (60 % of data) and a test set (40 % of data). The prediction of the gluten content and quality was modelled by means of linear regression. Equation 7 shows the training of the model to calculate the transformation matrix [M]. [X] are the calculated features and [Y] are the laboratory observed values for gluten amount and quality. Equation 8 shows the application of the regression model, to predict the gluten parameter with the input [X] (measured image features).

$$[M] = ([X]^T[X]^{-1})[X]^T[Y] \tag{7}$$

$$[Y] = [M]^T[X]^T \tag{8}$$

To assess the goodness of fit, the mean square error (MSE) (as in equation 9) between real and predicted values were calculated.

$$MSE = \frac{1}{n}\sum_{i=1}^{n}(x_{real} - x_{observed})^2 \tag{9}$$

B. *Thermal imaging of bread baking*

a) Sample preparation

The samples were prepared following a standard recipe and procedure (ICC 131) shown in table 1 and 2. To prepare the dough a flour type 405 was used.

Tab. 1: Standard recipe of the Bread samples (following ICC 131)

Ingredient	Quantity	Parts
Flour	493.46 g	100.0
Water	288.67 g	58.5
Salt	8.88 g	1.8
Dried Yeast	6.41 %	1.3

Tab. 2: Standard processing parameters

Processing step	Time	Parameter
Premixing	60 s	
Mixing	300 s	
Proofing	60 min	30°C, 90 % Humidity
Backing	40 min	240°C

For fermenting, a proving chamber CP1 / SunRiser-AT (KOMA Koeltechnische Industrie, Netherlands) and for baking, a MATADOR 12.8.4 (Werner & Pfleiderer, Germany) oven were used.

b) Imaging System

The Imaging system consist of a FLIR A655sc thermal camera with 45° Lens (Wavelength: 7500 nm – 1400 nm, resolution: 640 x 480 pixel, FLIR Systems Trading Belgium BVBA, Belgium) and a processing unit. The camera is mounted on the left hand side of the MATADOR oven and monitors the inner baking chamber, as seen in Figure 2. The camera in the baking chamber is marked yellow.

Fig. 3: Left hand side the attached FLIR A655sc thermal camera, right hand side the baking chamber of the MATADOR 12.8.4 oven and the camera position is pointed

c) Image Processing and data handling

The imaging system has two objectives: the first is the observation of the heat distribution on the bread surface and the second is the prediction of the oven spring during the baking time. The surface heat is observed directly with the camera. This temperature information is captured using a template to process only the bread surface. The template was created using Sobel edge detection, edge dilation, areas size filtering, template erode and stored as a binary template.

The head distribution mainly were analyze by contour plot and root means squared Euclidean distance error (RMSEDE) (cf. equation 10).

$$RMSEDE = \sqrt{\frac{\sum_{i,j}\left(P(i,j) - P_{Ref}(i,j)\right)^2}{\sum_{i,j}\left(P_{Ref}(i,j)\right)^2}} \tag{10}$$

The oven spring was compared manually and automatically. The manual measurement was done with ImgPro V 0.6. The automatically detection proceed with binary template and adaptation of the smallest bounding box. The rectangle dimension are equal to the bread width and height.

III. RESULTS AND DISCUSSION

A. *Gluten properties*

The pre-mentioned measurements and analysis were applied to predict the gluten content and quality. The samples measured with reference analysis and with the developed measurement system were compared. The model was trained and tested with 60 % : 40 % ratio of the data. Furthermore, the model goodness of fit was evaluated to predict the most useful images features. Equation 11 shows the final linear model.

$$Y = \sum_{i,j} M_{i,j}X_iX_j \tag{11}$$

Finally, the model shows the following goodness of fit in the training step (total images: 2310).

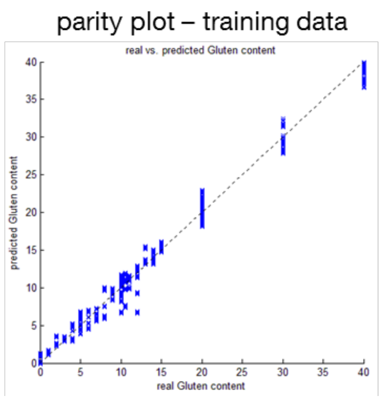

Fig. 4: Parity plot of the training data of gluten content showing MSE of 1.31 %

The resulted MSR is 1.31 % and the slope (R^2) is 1.011. The testing with 1485 images shows a MSE of 1.34 % and a slope (R^2) of 0.984. Figure 4 shows the parity plot for evaluating the linear regression model.

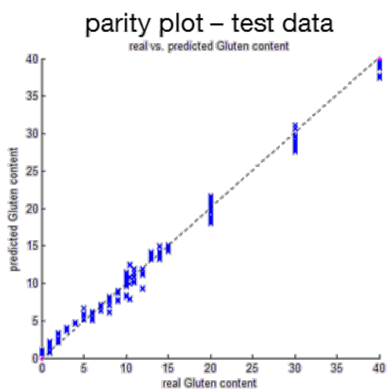

Fig. 5: Parity plot of the testing data of gluten content showing MSE of 1.34 %

The spectral evaluation of gluten quality was also done. The measurement of the gluten quality is a combination of the UV-A and VIS (540 nm and 560 nm) measurement. Figure 5 shows the parity plot of the model testing. The method was able to predict the gluten quality with an MSE of 2.7 % and a slope (R^2) of 0.98.

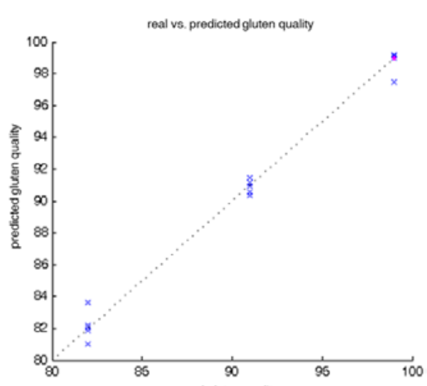

Fig. 6: Parity plot of the testing data of gluten quality showing MSE of 2.7 %

The novel approach shows a new method to measure the gluten content and quality without expensive spectral systems. Additionally the measurement system is reduced to the minimum number of measurement components.

B. Thermal imaging of bread baking

The baking process was measured with the thermal imaging, figure 6 shows an example for the recorded data.

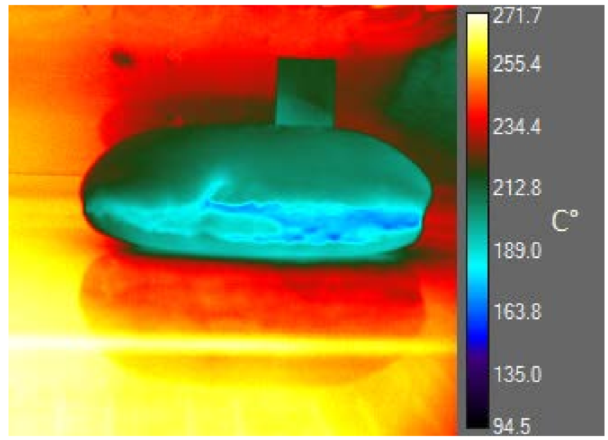

Fig. 7: An example thermal image captured with Infrared camera FLIR, showing the thermal iso-contours of bread inside the MATADOR oven

An automatic template matching was implemented and the bounding box was determined. Figure 7 shows an example for the determined template (white area) and bounding box (red rectangle).

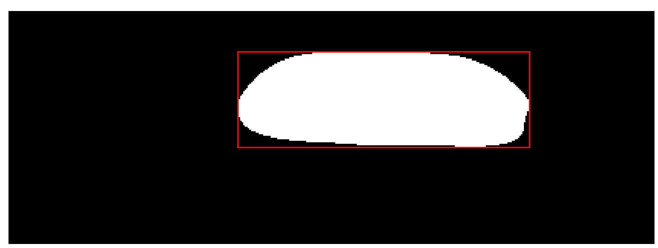

Fig. 8: Example for determined template and bounding box to the height and width of the breads. White is bread template, red is the bounding box

The automatic detection was compared with manually detected bread dimensions. The maximum deviation was 1.28 mm (2 pixel) in the height and 1.92 mm (3 pixel) in the width. These results show that thermal imaging can be used to determine the spatial resolution of the baking process.

The heat distribution during the baking time was also determined with template matching and RMSEDE. For the single temperature data, the error was calculate related to the first temperature data (0 s) and plotted over the whole baking time (cf. figure 8).

ISBN: 978-1-61804-321-4

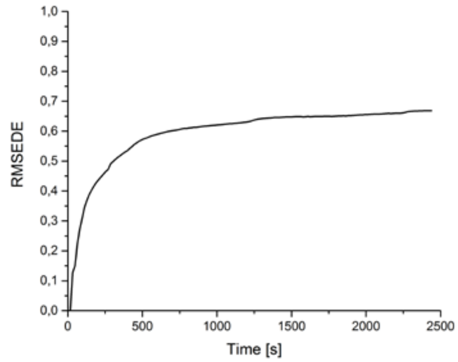

Fig. 9: RMSDED for one bread trial during baking time, expressing the evolution of the temperature distribution eventually reaching a steady-state temperature profile

The results shows the increasing of the RMSEDE with time and adjust to a steady-state profile. Figure 8 shows a contour plot for the RMSEDE over baking time. The contour plot shows heat fronts of the bread during baking time. The time steps 60 s, 600 s, 1200 s and 1800 s are shown in Figure 9.

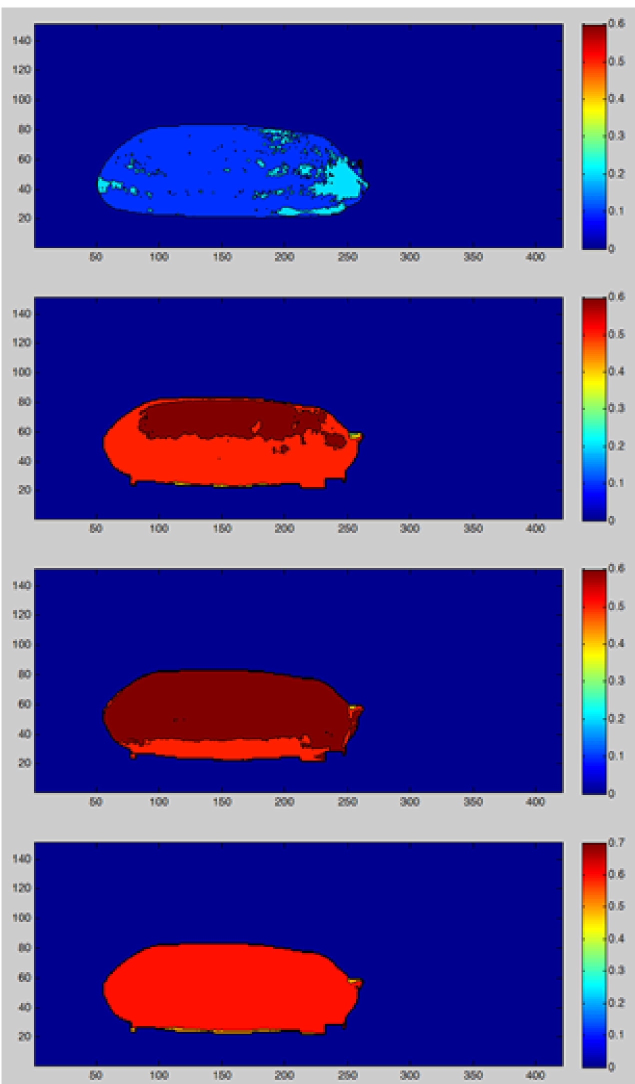

Fig. 10: Heat fronts of the bread during baking time at time-steps 60 s, 600 s, 1200 s and 1800 s

The contour plot shows the heat fronts of the bread during the baking process. At the beginning the RMSEDE of the first captured temperature data is less and inhomogeneous. With time propagation, the temperature on the bread surface rises and leads to a homogeneous temperature distribution on the bread surface.

The combination of determining the baking spring and temperature distribution can be used for a more economically efficient baking process. For example, it is possible to drive single heater elements for an optimal baking process and to save a lot of energy. In addition, the evaluation of the bread volume-growth helps to modify the baking process to reduce failure sources.

IV. Conclusion

The objective of this work is to show two novel process-monitoring approaches for the baking industry. To implement cheap and more accurate measurement systems. With the measurement of the gluten parameters, it is possible to develop a cheap online measurement system with higher statistical reliability. The pre measurements shows the ability to measure the content with an error of 1.34 % for the gluten content and 2.7 % for the gluten quality. In the second approach, the thermal measurement is a new technic used for bakeries. The results presented in this work shows the high potential of the thermal imaging for baking industries. With the thermal camera, it is possible to determine the baking spring and the heat distribution. The method has great potential for large-scale baking facilities. It may be possible to identify the optimal baking time and control single heating zones in order to save costs.

V. References

[1] Başlar, M. and Ertugay, M. F. 2011. Determination of protein and gluten quality-related parameters of wheat flour using near-infrared reflectance spectroscopy (NIRS). *Turkish Journal of Agriculture and Forestry* 35, 2, 139–144.

[2] Cauvain, S. P. 2012. *Breadmaking*. *Improving quality*. Woodhead Publishing series in food science, technology and nutrition no. 229. Woodhead Pub, Philadelphia, Pa.

[3] Edelstein, S. 2014. *Food science*. *An ecological approach*. Jones & Bartlett Learning, Burlington, MA.

[4] Gunasekaran, S. and Devi, M. K. 2007. UV-Vis Spectroscopic Investigation on Hydrolysis of Starch and Starch-Drug Interaction. *Asian Journal of Chemistry* 19, 5, 3363.

[5] J.H. Miah, A. Griffiths, R. McNeill, I. Poonaji, R. Martin, A. Yang, and S. Morse. 2014. Heat integration in processes with diverse production lines: A comprehensive framework and an application in food industry. *Applied Energy* 132, 0, 452–464.

[6] Mena, M., Manuel, L., Hernando, A., Méndez, E., and Albar, J. P. 2012. Comprehensive analysis of gluten in processed foods using a new extraction method and a competitive ELISA based on the R5 antibody. *Talanta* 91, 33–40.

[7] Mutlu, A. C., Boyaci, I. H., Genis, H. E., Ozturk, R., Basaran-Akgul, N., Sanal, T., and Evlice, A. K. 2011. Prediction of wheat quality parameters using near-infrared spectroscopy and artificial neural networks. *Eur Food Res Technol* 233, 2, 267–274.
[8] Penfield, M. P. and Campbell, A. M. 1990. *Experimental food science*. Food science and technology. Academic Press, San Diego.
[9] Piotr Baranowski, Wojciech Mazurek, Joanna Wozniak, and Urszula Majewska. 2012. Detection of early bruises in apples using hyperspectral data and thermal imaging. *Journal of Food Engineering* 110, 3, 345–355.
[10] Qian, Y., Preston, K., Krokhin, O., Mellish, J., and Ens, W. 2008. Characterization of wheat gluten proteins by hplc and MALDI TOF mass spectrometry. *Journal of the American Society for Mass Spectrometry* 19, 10, 1542–1550.
[11] Taeko Ogawa and Michio Nomura. 2012. *Using NIRS to Investigate Social Relationship in Empathic Process*. INTECH Open Access Publisher.
[12] Teale, F. W. J. 1960. The ultraviolet fluorescence of proteins in neutral solution. *Biochem J* 76, 2, 381–388.
[13] V. Chelladurai, D.S. Jayas, and N.D.G. White. 2010. Thermal imaging for detecting fungal infection in stored wheat. *Journal of Stored Products Research* 46, 3, 174–179.
[14] Vadivambal, R. and Jayas, D. 2011. Applications of Thermal Imaging in Agriculture and Food Industry—A Review. *Food and Bioprocess Technology* 4, 2, 186–199.
[15] Vollmer, M. and Möllmann, K.-P. 2010. *Infrared thermal imaging*. *Fundamentals, research and applications*. Wiley-VCH, Weinheim.
[16] Zeltner, D., Glomb, M., and Maede, D. 2009. Real-time PCR systems for the detection of the gluten-containing cereals wheat, spelt, kamut, rye, barley and oat. *European Food Research and Technology* 228, 3, 321–330.

ISBN: 978-1-61804-321-4

Battery Energy Storage Benefit Assessment in Small Islands

G. Abbatantuono, S. Lamonaca, M. La Scala and R. Sbrizzai

***Abstract* —** Energy storage systems represent a fundamental element for the full realization of the Smart Grid paradigm. They allow the grid operator to manage energy flows in a more efficient way performing peak shaving and load shedding operations, improving network stability and eliminating every possible lack of energy supply toward final users. In this paper, the installation of a Battery Energy Storage System (BESS) on a small isolated electric grid has been discussed and both technical and financial issues have been analyzed. The feasibility study and test results show how this kind of technical solution would improve the overall safety and power quality levels of the network, also providing good economical benefit to many different stakeholders.

Keywords — electric energy storage applications, isolated systems, microgrids feasibility study

I. INTRODUCTION

THE energy storage systems are experiencing a substantial growth in performances together with a significant price reduction. In this way, their use in electrical grids is becoming very attractive, especially if compared with other technologies capable of providing security and ancillary services (electric energy time-shift, load following, area regulation, electric supply reserve capacity, voltage support, power quality, demand charge management, time-of-use energy cost management, etc.) [1], [2].

The aim of storage devices is to store energy and provide it during specified time periods, according to the objectives set by operating, functional and economic conditions. So, the energy storage allows to produce and distribute electricity to many users in a safe way, maximize the grid efficiency and possibly reduce the size of generators and also of infrastructure investments. In addition, it can usefully attend to frequency and voltage regulation by quickly making power available for this purpose, improving the overall reliability of the grid.

Gaetano Abbatantuono was with Department of Electrical and Information Engineering, Politecnico of Bari, via Orabona, 4 - 70125 Bari, Italy (e-mail: gaetano.abbatantuono@poliba.it).

Silvia Lamonaca was with Department of Electrical and Information Engineering, Politecnico of Bari, via Orabona, 4 - 70125 Bari, Italy (e-mail: silvia.lamonaca@poliba.it).

Massimo La Scala., was with Department of Electrical and Information Engineering, Politecnico of Bari, via Orabona, 4 - 70125 Bari, Italy (e-mail: massimo.lascala@poliba.it).

Roberto Sbrizzai was with Department of Electrical and Information Engineering, Politecnico of Bari, via Orabona, 4 - 70125 Bari, Italy (e-mail: roberto.sbrizzai@poliba.it).

The energy storage can also find very useful applications in a modern microgrid, operating in both grid-connected or island mode, aimed at improving its characteristics of efficiency, dynamism, flexibility, reliability and security.

Energy storage systems become basic to solve particular issues related to the quality of service of a microgrid when the connection to the national distribution system is hampered by complex geographical conditions.

Typical examples are represented by islands, especially the smaller ones, characterized by some common features:

- very different energy consumption and demand for mobility between winter and summer periods, caused by considerable seasonal demographic variation;
- significant annual increases in energy demand and limited fresh water resources due to tourism development;
- high cost of fuel due to supply difficulties;
- tourist-environmental priorities.

In order to meet the growing energy needs while keeping acceptable costs, investments on traditional power sources (normally diesel generators) might be economically and environmentally inappropriate if the plant is sized for the maximum expected load. An energy storage system instead has high financial attractiveness due to possible curtailment of capital investment and payback time and could avoid generators revamping, also deferring the upgrade of the transmission/distribution system.

At the same time, an energy storage system can optimize the microgrid management. Most of the smaller islands, in fact, might become energetically autonomous by means of microgrids equipped with renewable energy sources, smart systems and storage systems. In this way they might reduce the high noise and environmental pollution arising from small power stations, operate the power plants at yield outputs even in partial load conditions and improve the power quality (outages, network instability, etc.) often conditioned by the inadequacy of the existing facilities [3], [4].

For this purposes, an useful energy storage system is represented by electrochemical batteries. They are basically used to store energy in times of abundant production and to supply it during low generation periods, peak demand hours or, in general, when load demand exceeds produced energy.

The batteries are a good solution for microgrid with renewable sources and/or cogeneration units: the grid would charge them in case of overproduction or low demand, and use the stored energy when needed, or when technical problems

ISBN: 978-1-61804-321-4

occur on one or more subsystems. Compared to other storage systems, a relatively significant amount of energy can easily and efficiently be stored and discharged in the batteries throughout the year. Applications based on the battery capacities defer or reduce the need for generation or T&D equipments and involve various technical benefits related to quality of electrical services.

In this paper a feasibility study on a microgrid located at the same latitude of the Aeolian Islands (Italy) has been developed. The microgrid, operating in islanded mode, is a small scale distribution system constituted by a set of diesel and wind generators, loads and a Battery Energy Storage System (BESS) suitably dimensioned (Fig. 1).

By means of properly controlled converters, the batteries allow to balance power generation and load, take part in the voltage and frequency control in the presence of rapid power variations due to generation and/or loads and maintain necessary voltage levels with the required stability. Besides they allow to increase the reliability of microgrid by offsetting the unavailability of generator due to faults.

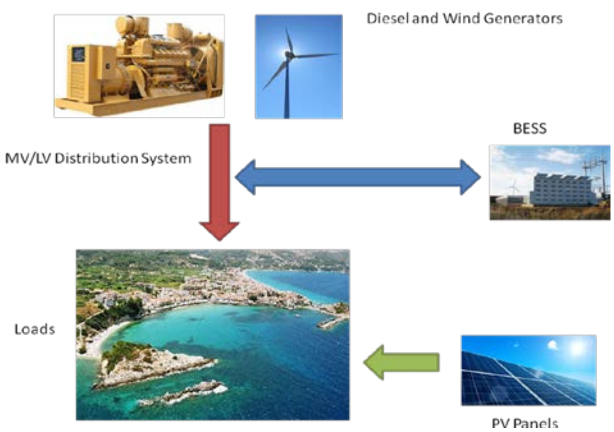

Fig. 1 – Schematization of the microgrid

II. FEASIBILITY STUDY

A feasibility study is classically based on cost-benefit analysis aimed to evaluate the validity of the investment from the point of view of different stakeholders. The convenience of an investment, in fact, may differ from one subject to another in case of diverging economic interests. Determining feasibility depends by different factors, from economic aspects up to more global elements as the improvement of system performance obtained by final user or the environmental sustainability.

This study was based on the concepts of the Standard Practice Manual for Economic Analysis of Demand-Side Management Programs (DSM Programs) [5], suitably adapted to the analysis in question. The methodology allows the evaluation of the suitability of an investment to improve the energy efficiency of a BESS, according to different prospects. A DSM program involves changes in the provision of electrical services [6], and basically three types of stakeholders:

- the utility, power company that provides the services;
- the end-user, beneficiary of the services;
- the society, utility customers as a group and/or to society as a whole, leading to global interests.

Each of these three subjects detects particular values of the services that represent a balance between benefits and negative impacts provided by them.

In particular, as mentioned, an energy storage system may have many applications that are analyzable and classifiable under different benefits. Each application can take on different connotations depending on the point of view of the subject to which it is addressed the advantages.

The study has been developed by considering applications and benefits related to two different approaches:

- producer/distributor approach, which assesses costs and benefits of the utilities that supply and distribute energy through the island;
- society approach, which evaluates global costs and benefits among stakeholders.

The adopted applications and benefits that are best suited for a BESS to be built on an island are shown in Table I. Costs and benefits have been quantified in steady-state conditions.

TABLE I
APPLICATIONS AND BENEFITS ADOPTED FOR FEASIBILITY STUDY

approach	application	benefit (avoided cost)
producer / distributor	Renewables Energy Time-shift	fossil fuels
	Voltage Support	centralized control of reactive
	Distribution Upgrade Deferral	T&D upgrade
	Electric Service Reliability	power outages
Society	Environmental prospect	CO_2 emissions
	User's prospect	energy not supplied
	Utility's prospect	all benefits of the above approach

A. Producer/distributor approach

The first important issue is the evaluation of the economic interest in the investment from the Company that operates the energy infrastructure of the island.

The following applications have been considered [1], [2], [3]:

- Renewables Energy Time-shift;
- Voltage Support;
- Distribution Upgrade Deferral;
- Electric Service Reliability.

The *Renewables Energy Time-shift* is the ability to charge the storage system during off-peak times (e.g., at night, on weekends and during holidays) when RES generators produce electric energy but demand is low, and supply is adequate to deliver energy during peak times, when demand is high and supply is tight. The electrical energy at off-peak times has a low financial value while it has higher price in peak periods.

In case of microgrid in islanded mode, the energy is charged by RES at low-demand time and is discharged at high demand-time avoiding the energy production using more expensive sources (e.g. from fossil fuel). It can also help to avoid congestion of the transmission and distribution systems, delay the increase in supply capacity, strenghten reliability and improve power quality of microgrid.

The benefit is represented by the avoided cost of generation from no-RES as a function of the amount of shifted energy.

The *Voltage Support* is the ability to inject/absorb reactive power in order to maintain the right voltage level on the network.

This task is traditionally provided by large generation through centralized control of reactive energy to the grid when region-wide voltage emergencies occur. It can alternatively and easily obtained by means of distributed energy storages placed close to load centers [2]. It may be extremely attractive because reactive power cannot be transmitted efficaciously over long distances. So, the benefit is the disposal of centralized control of reactive power and its related cost.

The *Distribution Upgrade Deferral* is the exploitation of energy storage to meet peak load demand that occurs on limited and specific time/period of year avoiding/deferring utility investments in transmission and/or distribution system upgrades [7].

Energy storage, in fact, represents an electric supply reserve capacity and allows the overcoming of momentary overloads avoiding incremental production capacity and major infrastructure investments.

The benefit is the financial value associated with deferring a utility T&D upgrade.

The *Electric Service Reliability* is related to the capacity of supplying energy, even in the event of a partial/complete power outage for few/extended duration.

An energy storage provides backup energy for electric service reliability so that distributors can provide energy to users in case of unavailability of generation, thus avoiding more expansive standard/conventional alternatives as on-site backup generation and relative costs of purchase, installation and management.

The benefit comes from the specific value of avoided not provided energy because of power outage.

B. *Society approach*

The second issue considers the impact of investment from the point of view of Society at large, that pursues the overall interests among stakeholders, as improved environmental quality and economy or improved utilization of grid assets.

This assessment takes into account:

- Environmental prospect;
- Users' prospect;
- Utility's prospect.

The *Environmental prospect* concerns with the exploiting of the storage system to improve environmental quality reducing emissions of greenhouse gases caused by natural gas and petroleum-based fuels. With the increase in the use of RES, in fact, a system storage can be used to provide electric supply when and where needed, through appropriate energy management, and to improve prospects for environment restraining CO_2 and NO_X emissions.

In particular, in this study the benefit is represented by the avoided CO_2 on-peak emissions from diesel generation.

The *User's prospect* concerns with the ability to ensure the continuity of supply provided by the storage system in case of black-out. The seasonal energy demand of small islands is one of the critical factors in the process of production and dispatch of electricity because the power stations might be not adequate. This would create inefficiencies to the private and public users due to inadequacy of the transfer structures and risks of black-out.

The storage system is able to supply continuously energy to users who do not suffer inefficiencies in the event of lack of generation. Therefore, the benefit is the avoided costs of inefficiency due to energy not supplied.

The *Utility's prospect* concerns with assessment all costs including Operation & Maintenance (O&M) costs, and benefits for utility, needed to install and manage BESS.

III. TEST CASES

The test case has been developed considering a small isolated distribution system (Fig. 2) mainly supplied by four 600 kVA diesel generators, whose power output is injected in a small 10 kV primary distribution system. MV/LV transformers permit to feed five secondary distribution systems that supply electricity to 845 three-phase and single-phase loads. The overall LV system is composed by 421 nodes and 417 lines, for a total extension of about 15.7 km. The average load is about 2 MW. The system model includes the representation of 19 PV generators, installed at low voltage level, with a total capacity of about 97.3 kW. All PV generators have small peak capacity, ranging in the interval 2-20 kW.

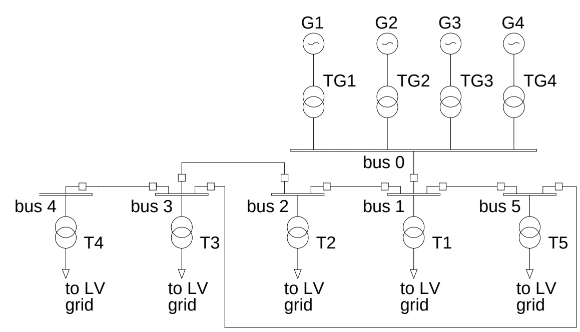

Fig. 2 – Microgrid test case

Two wind turbines with a maximum capacity of 120 kW have also been considered as additional RES. Finally, a Na/NiCl type 100 kW BESS (Battery Energy Storage System) has been placed: this particular technology uses high temperature (240÷320 °C) batteries, characterized by high energy efficiency, temperature-independent performances, a remarkable number of charge/discharge cycles and low risks.

The BESS has been sized in order to avoid load shedding and preserve the overall efficiency of the isolated microgrid. This was made possible also modifying the droop percentage of the controllers of diesel generators model and fixing them equal to 6%, instead of the standard value of 2.8% In this way, the overall system dynamic was improved and able to preserve grid operations for enough time to restore primary electric parameters and bring them back to acceptable values, or at least close to them. Simulations have analyzed the behavior of the microgrid following the failure of a diesel generator. This event can lead the whole system out of service, because of the absence of resources that can provide primary regulation, compensate the sudden lack of power and bring back main electric parameters toward stable conditions. The following figures show the performances of active power and electric frequency with and without the presence of energy storage. Figure 3 represents the power output of the four diesel generators. The failure occurs for t = 20 s. When the active power supplied by the blue generator drops to zero, the others automatically increase their outputs but these conditions can't be kept for more than few seconds, because of technical constraints of the machines.

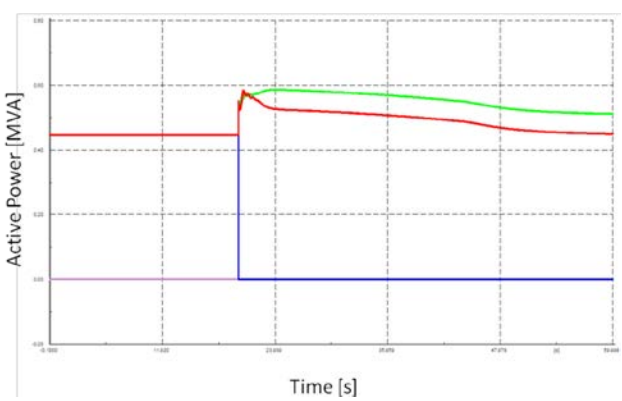

Fig. 3 – Active power levels during generator failure without BESS

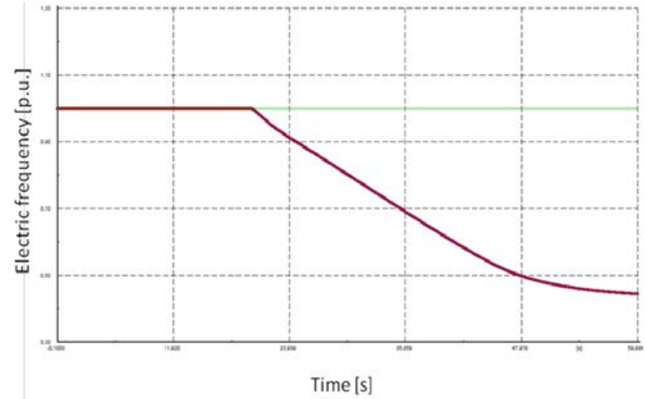

Fig. 4 – Electric frequency during generator failure without BESS

Figure 4 shows the consequent fall of electric frequency levels, which leads to an irreversible collapse of the grid and at least to a long outage of some low voltage subsystems, until the faulted generator is repaired.

The application of battery system can manage the event without compromising the global reliability of the grid and possibly avoiding the disconnections of LV lines, as reported in figures 5- 6. It can be seen how the increase of active power outputs from sane generators is kept on bearable levels, thanks to the extra power supplied from BESS. The electric frequency too, after the decrease in coincidence with the fault instant, recovers its standard level of 50 Hz after few seconds. Never breaking the lower limit of 47,5 Hz suggested by Italian TransCo. regulations [8].

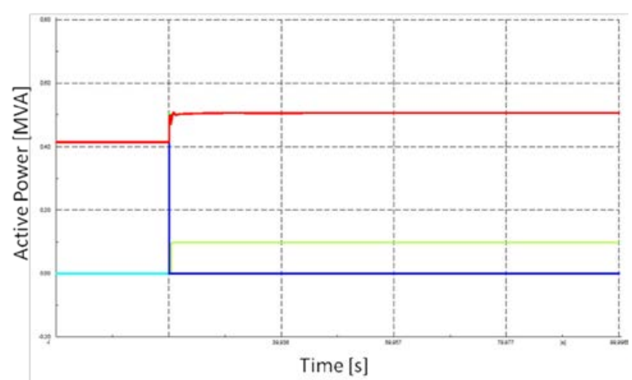

Fig. 5 – Active power levels during generator failure with BESS

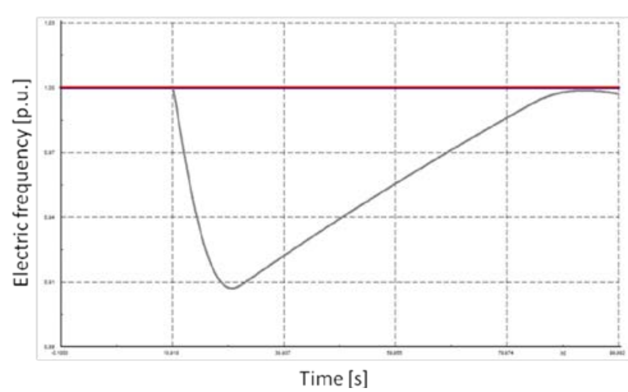

Fig. 6 – Electric frequency during generator failure with BESS

A financial analysis was then carried out based on general outlines given in [9]. In particular, in order to allow a fair comparison and obtain reliable results, the three previously described approaches were analyzed adopting the Discounted Cash Flow analysis.

The following indices have been adopted:

- Net Present Value (NPV): expected return foregone by bypassing other potential investment activities for a given capital

$$NPV(k€) = \sum_{j=0}^{n} \frac{r_j - c_j}{(1+i)^j} \quad (1)$$

- Discounted Pay-Back Period (DPBP): minimum operating time necessary for recovering the total investment

$$DPBP(years) = \min m \in [0, n] \ni' \sum_{j=0}^{m} \frac{r_j - c_j}{(1+i)^j} \geq 0 \quad (2)$$

where n is the investment time horizon, and, for each year j, r_j, is the sum of investment and operating costs, c_j is the sum of the expected revenues and i is the discount rate.

The Table II shows the input technical and economical data adopted for BESS.

TABLE II
TECHNICAL AND ECONOMICAL BESS DATA

Cost of BESS [€/kW]	2.000,00
Cost of Operation & Maintenance [€/kW]	50,00
Power size [kW]	100
Number of charge/discharge cycles	4.500
Investment time horizon (years)	12
Discount rate (%)	10,0

The following assumptions were made for each application in order to estimate economic benefits as described in the previous section.

A. Producer/distributor approach

Renewables Energy Time-shift

This application is implemented using the exceeding energy produced by renewable energy plants. The amount of energy charged on BESS at low load and provided at full load is equal to 131.400 kWh/year corresponding to an operation period of 1460 h/year. The economic benefit, corresponding to the avoided cost of production of equivalent energy from Diesel plant, is equal to 18,400 €.

Electric Supply Reserve Capacity

Generation capacity that is online but unloaded and that can respond within 10 min to compensate for generation or transmission outages. ‘Frequency responsive’ spinning reserve responds within 10 s to maintain system frequency. Spinning reserves are the first to be used when a shortfall occurs [1], [3]. The economic benefit is the avoided cost of energy production by diesel generators. It has been assumed a value equal to 1.100 €/kW that represents a typical cost production for a diesel plant of 100 kW.

Voltage Support

The technical benefit is the elimination of the centralized control of the reactive power. The economic value of benefit was assumed to be equal to 370 €/kW corresponding to the low value stated in [1].

Distribution Upgrade Deferral

The annual benefit related to this application is given by the financial value associated with the delay of one year the upgrade of electricity infrastructure. The economic value of benefit was assumed to be equal to 445 €/kW corresponding to the "T&D Upgrade Deferral 50th percentile" value stated in [1].

Electric Service Reliability

The unavailability of generation was estimated by means of a reliability analysis. Since the failure rates and the Mean Time To Repair (MTTR) of diesel generators [10], the following probability has been calculated:

- Rates of failure of diesel generators: 1.14653
- Unavailability: 28.375 h/year
- Probability of failure: 0.00324

So, an energy loss of 1.320 kWh/year of non-operation of the system was quantified related to the previous probability and considering different events, to estimate the energy amount that can be included in this prevision.

The production cost by diesel generator may be assumed equal to the proceeds from the sale of energy. Consequently the economic benefit was assumed equal to 0,30 €/kWh only corresponding to the adjustment that Italian Authority for Electricity, Gas and Water System distributes to companies operating on smaller islands for dispatching service [11].

Test results led to the following financial performance:

- NPV [k€] = 44,00
- DPBP [years] = 6.5

B. Society approach

Environmental prospect

It was assumed an emission factor of 667.10 gCO_2/kWh [12] and, consequently, the avoided emissions of CO_2 are equal to 97.66 tons/year. The economic factors was assumed equal € 33.6 €/ton of CO_2 [13].

User's prospect

In case of lack of supply from power generation systems, the BESS, is able to supply energy. The users would a failure cost (therefore a revenue item in the analysis) related to various disruptions that would otherwise suffer. The users would avoid cost (therefore a revenue item in the analysis) related to avoided inefficiency. By means of reliability analysis an annual energy lost has been estimated equal to 1.320 kWh/year. The cost of energy not supplied is fixed to 10.8 €/kWh [14].

Utility's prospect

In this application, costs and benefits, including the O&M costs, supported by utilities have been considered.

Test results led to the following financial performance of :

- NPV [k€] = 164,00
- DPBP [years] = 3.3

Results of the analysis are given in Table III, whereas Figure 7 gives a graphical benchmark of the financial performance comparing the two approaches.

TABLE III
FINANCIAL PERFORMANCE INDICES FOR DIFFERENT APPROACHES

approach	financial performance	
	NVP [k€]	DPBP [years]
producer/distributor	44,00	6.5
Society	164,00	3.3

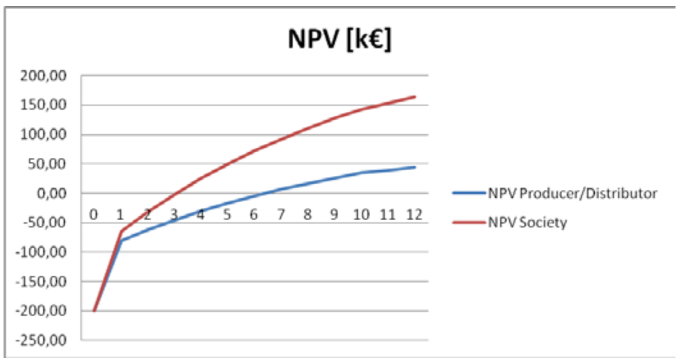

Fig. 7 - FVNP indices vs time for different approaches

Thanks to all the previously mentioned advantages, the society approach provides the best result showing a considerably shorter DPBP. This is a very important item, because it also regards the best conditions for environmental preservation, which is probably the most important outcome for areas where tourism plays a fundamental economic role.

IV. CONCLUSIONS

In this paper, the possible achievements, in terms of technical and financial performances, that can be obtained by adopting Battery Energy Storage System (BESS) on a small isolated electric grid have been investigated.

The feasibility study shows the BESS opportunities involving numerous stakeholders and interests, while test results highlight the technical advantages provided to the grid by the installation of electric storage systems, in terms of continuity of service and primary regulation.

ACKNOWLEDGMENT

The present study was developed within the framework of the project PON RES NOVAE (Reti, Edifici, Strade, NuoviObiettivi Virtuosi per l'Ambiente e l'Energia), supported by the Italian Ministry for Education, University and Research, under the research and competitiveness program to promote "Smart Cities Communities and Social Innovation".

REFERENCES

[1] J. Eyer, G. Corey, "Energy Storage for the Electricity Grid: Benefits and Market Potential Assessment Guide. A Study for the DOE Energy Storage Systems Program", Sandia National Laboratories Report, Feb. 2010.

[2] *L'accumulo di energia elettrica*, Ricerca sul Sistema Energetico - RSE S.p.A., 2011

[3] R. Giglioli, D. Poli, "Valutazione dell'impatto dell'utilizzo delle batterie al litio nelle applicazioni stazionarie", Report Ricerca Sistema Elettrico, Sept. 2010.

[4] D. Mears, H. Gotschall, H. EPRI-DOE Handbook of Energy Storage for Transmission and Distribution Applications. Electric Power Research Institute Report #1001834. December 2003

[5] California Standard Practice Manual. Economic Analysis of Demand-Side Programs and Projects, Oct. 2001.

[6] A. Capozza, A. Porrino, W. Grattieri, "Disamina delle metodologie per le valutazioni tecnico-economiche di Gestione della Domanda (Demand-Side Management) nell'industria elettrica", Rapporto Ricerca di Sistema, CESI SFR-A0/021337

[7] Eyer, James M. Electric Utility Transmission and Distribution Upgrade Deferral Benefits from Modular Electricity Storage: A Study for the DOE Energy Storage Systems Program, Sandia National Laboratories. Sandia National Laboratories Report #SAND2009-4070. June 2009.

[8] Allegato A-70 di "Regolazione Tecnica dei Requisiti di Sistema della Generazione Distribuita" – Terna S.p.A, 2012.

[9] European Commission - Directorate General Regional Policy, "Guide to Cost-Benefit Analysis of Investment Projects", Final Report, 2008

[10] IEEE-Gold book "IEEE Recommended Practice for the Design of Reliable Industrial and Commercial Power Systems", IEEE Std 493™-2007

[11] "L'isola diventa rinnovabile" A. Codegoni. QualEnergia, febbraio/marzo 2013

[12] "Fattori di emissione di CO_2 nel settore elettrico e analisi della decomposizione delle emissioni". Rapporto ISPRA– Istituto Superiore per la Protezione e la Ricerca Ambientale. Rapporto 172/2012

[13] Report Ricerca sul Sistema Energetico – RSE SpA "Energia elettrica, anatomia dei costi". 2014

[14] "The use of customer outage cost surveys in policy decision-making: the Italian experience in regulating quality of electricity supply" A. Bertazzi, E. Fumagalli, L. Lo Schiavo. CIRED 18th International Conference on Electricity Distribution. Turin, 6-9 June 2005.

G. Abbatantuono was born in Bitonto (BA), Italy, in 1980. He received the degree in Electrical Engineering from Politecnico di Bari (Italy) in 2008; is actually attending the Ph. D. course in Electrical and Information Engineering at Politecnico di Bari. His research activities focus on active grids, energy hubs and Power Systems optimization.

S. Lamonaca was born in Canosa di Puglia (BA), Italy, in 1975. She received the degree in Management Engineering from Politecnico di Bari (Italy) in 2006 and her Ph.D in Engineering at Politecnico di Bari in 2010. Her researches focus on electricity markets and advanced demand response techniques.

M. La Scala was born in Bari, Italy, in 1959. He received the degree in Electrical Engineering from University of Bari (Italy) in 1984. In 1989, he received his Ph.D. in Electrical Engineering from the University of Bari. He is currently Professor of Electrical Energy Systems at the Politecnico di Bari (Italy). His research activity deals with Power System Analysis and Control, reregulated Markets. He is IEEE Fellow and Regional President of the A.E.I.T. – Puglia.

R. Sbrizzai was born in Bari, Italy, in 1962. He received the degree in Electrical Engineering from University of Bari (Italy) in 1986. In 1992, he received his Ph.D. in Electrical Engineering from the University of Bari. He is

currently Associate Professor of Electrical Energy Systems at the Politecnico di Bari (Italy). His research activity deals with Power System Analysis and Control, reregulated Markets.

ISBN: 978-1-61804-321-4

Synchronization Phenomena in Coupled Hindmarsh – Rose Neuron Models

Christos K. Volos, D. A. Prousalis, Ioannis M. Kyprianidis, Ioannis N. Stouboulos, H. E. Nistazakis, and G. S. Tombras

***Abstract*—**In this work the coupling between two identical coupled Hindmarsh–Rose neuron models is investigated analytically and numerically. As coupling scheme, the unidirectional one is chosen, which is designed by using Nonlinear Open Loop Controllers to target two of the more interesting types of synchronization the complete synchronization and antisynchronization. The stability of the proposed method is ensured by using the Lyapunov function stability theory. Simulation results verified that the proposed coupling scheme drives the system either to complete synchronization or antisynchronization depending on the choice of the signs of the error function's parameters.

***Keywords*—**Chaos, Hindmarsh–Rose neuron model, synchronization, antisynchronization, unidirectional coupling, nonlinear open loop controller.

I. Introduction

Neurons are the core component of the nervous system. Organized internally similar to other cells, they are specialized for intercellular communication by way of their membrane potential. Biological experiments and numerical analysis of models for the oscillations of isolated neurons, have led the researchers to construct low dimensional analog electronic neurons which properties are designed to emulate the membrane voltage characteristics of the individual neurons. So, in the case of modeling a biological neuron, physical analogues are used in place of abstractions such as "weight" and "transfer function". The input to a neuron is often described by an ion current through the cell membrane that occurs when neurotransmitters cause an activation of ion channels in the cell. We describe this by a physical time-dependent current $I(t)$. The cell itself is bound by an insulating cell membrane with a concentration of charged ions on either side that determines a capacitance C_m.

Christos K. Volos, D. Prousalis, Ioannis M. Kyprianidis and Ioannis N. Stouboulos are with the Physics Department of the Aristotle University of Thessaloniki, GR-54124, Thessaloniki, Greece (corresponding author to provide phone: +30-2310998284; fax: +30-2310998284; e-mail: volos@ physics.auth.gr).

H. E. Nistazakis and G. S. Tombras are with the Department of Electronics, Computers, Telecommunications and Control, Faculty of Physics, National and Kapodistrian University of Athens, GR-15784, Athens, Greece.

Finally, a neuron responds to such a signal with a change in voltage, or an electrical potential energy difference between the cell and its surroundings, which is observed sometimes as a voltage spike called an action potential. This quantity, then, is the quantity of interest and is given by V_m.

Until now, many models of biological neurons have been reported in literature [1,2]. Next, the most important of them are presented.

1. *Hodgkin-Huxley model*: It is the most successful and widely-used model of neuron, which has been based on the Markov kinetic model developed from Hodgkin and Huxley's 1952 work based on data from the squid giant axon [3]. This model tries to replicate the electrophysiological process of biological neurons. In more details, the semi-permeable cell membrane separates the interior of the cell from the extracellular liquid and acts as a capacitor. If an input current $I(t)$ is injected into the cell, it may add further charge on the capacitor, or leak through the channels in the cell membrane. Because of active ion transport through the cell membrane, the ion concentration inside the cell is different from that in the extra-cellular liquid. The "Nernst" potential generated by the difference in ion concentration is represented by a battery. The conservation of electric charge on a piece of membrane implies that the applied current $I(t)$ may be split in a capacitive current I_C which charges the capacitor C and further components I_k which pass through the ion channels. Thus

$$I(t) = I_C(t) + \sum_{\mathrm{k}} I_k(t) \tag{1}$$

where the sum runs over all ion channels. In the standard Hodgkin-Huxley model there are only three types of channel: a sodium channel with index Na, a potassium channel with index K and an unspecific leakage channel with resistance R.

From the definition of capacity $C = Q/u$, where Q is a charge and u the voltage across the capacitor, we find the charging current $I_C = C\,\mathrm{d}u/\mathrm{d}t$. Hence from (1):

$$C\frac{\mathrm{d}u}{\mathrm{d}t} = I(t) - \sum_{\mathrm{k}} I_k(t) \tag{2}$$

In biological terms, u is the voltage across the membrane and $\sum_{\mathrm{k}} I_k(t)$ is the sum of the ionic currents which pass through the cell membrane.

As mentioned above, the Hodgkin-Huxley model describes three types of channel. All channels may be characterized by their resistance or, equivalently, by their conductance. The leakage channel is described by a voltage-independent conductance $g_L = 1/R$; the conductance of the other ion channels is voltage and time dependent. If all channels are open, they transmit currents with a maximum conductance g_{Na} or g_K, respectively. Normally, however, some of the channels are blocked. The probability that a channel is open is described by additional variables m, n and h. The combined action of m and h controls the Na^+ channels. The K^+ gates are controlled by n. Specifically, Hodgkin and Huxley formulated the three current components as:

$$\sum_k I_k = g_{\mathrm{Na}} m^3 h(u - E_{\mathrm{Na}}) + g_{\mathrm{K}} n^4 (u - E_{\mathrm{K}}) + g_{\mathrm{L}} (u - E_{\mathrm{L}}) \qquad (3)$$

where the parameters E_{Na}, E_K, and E_L are the reversal potentials.

The three variables m, n, and h are called gating variables. They evolve according to the differential equations

$$\begin{cases} \dfrac{\mathrm{d}m}{\mathrm{d}t} = \alpha_m(u)(1-m) - \beta_m(u)m \\ \dfrac{\mathrm{d}n}{\mathrm{d}t} = \alpha_n(u)(1-n) - \beta_n(u)n \\ \dfrac{\mathrm{d}h}{\mathrm{d}t} = \alpha_h(u)(1-h) - \beta_h(u)h \end{cases} \qquad (4)$$

where α and β are empirical functions of u that have been adjusted by Hodgkin and Huxley to fit the data of the giant axon of the squid.

2. *FitzHugh-Nagumo model*: Sweeping simplifications to Hodgkin-Huxley were introduced by FitzHugh and Nagumo [4,5]. Seeking to describe “regenerative self-excitation” by a nonlinear positive-feedback membrane voltage and recovery by a linear negative-feedback gate voltage, they developed the model described by

$$\begin{cases} \dfrac{\mathrm{d}x}{\mathrm{d}t} = \gamma\left(x - \dfrac{1}{3}x^3 + y + z\right) \\ \dfrac{\mathrm{d}y}{\mathrm{d}t} = -\dfrac{1}{\gamma}\left(x - \alpha + \beta y\right) \end{cases} \qquad (5)$$

where variable x describes the potential difference across the neural membrane and y can be considered as a combination of the different ion channel conductivities, present in the Hodgkin-Huxley model. The control parameter z of the FitzHugh system describes the intensity of the stimulating current.

3. *Hindmarsh-Rose model (HR)*: The Hindmarsh-Rose (HR) model is based on the global behavior of the neuron and its underlying operation is removed from the actual biological process. For this reason, it is one of the most interesting neuron models which is used for studying the neuronal activity and more specifically the spiking-bursting behavior of the membrane potential observed in experiments made with a single neuron. This phenomenological neuron model, which has been proposed by Hindmarsh and Rose [6], may be seen either as a generalization of the Fitzhugh equations or as a simplification of the physiologically realistic model proposed by Hodgkin and Huxley. It has been proven to be a single-compartment model providing a good compromise between two seemingly mutually exclusive requirements: The model for a single neuron must be both computationally simple, and capable of mimicking almost all the behaviors exhibited by real biological neurons, in particular the rich firing patterns [7].

So, the three-variable HR model of action potential was proposed as a mathematical representation of the firing behavior of neurons, and it was originally introduced to give a bursting type with long InterSpike Intervals (ISIs) of real neurons. It can be used to simulate spiking/bursting and chaos phenomena in real neurons. The equations of the HR model are given as follows:

$$\begin{cases} \dfrac{\mathrm{d}X}{\mathrm{d}\tau} = Y - X^3 + a \cdot X^2 - Z + I \\ \dfrac{\mathrm{d}Y}{\mathrm{d}\tau} = 1 - d \cdot X^2 - Y \\ \dfrac{\mathrm{d}Z}{\mathrm{d}\tau} = r \cdot \left(s \cdot (X + \chi) - Z\right) \end{cases} \qquad (6)$$

where, X represents the membrane action potential, Y is a recovery variable and Z is a slow adaptation current; I mimics the membrane input current for the biological neurons; a, b allows one to switch between bursting and spiking behaviors and to control the spiking frequency; r controls the speed of variation of the slow variable Z in Eq.(6), (i.e., the efficiency of the slow channels in exchanging ions) and in the presence of spiking behaviors, it governs the spiking frequency, whereas in the case of bursting, it affects the number of spikes per burst; s governs adaptation: a unitary value of s determines spiking behavior without accommodation and sub-threshold adaptation, whereas values around $s = 4$ give strong accommodation and sub-threshold overshoot, or even oscillations; χ sets the resting potential of the system.

In any study of neuronal dynamics, there are two crucial issues, which are: (i) what model describes better the spiking dynamics of each neuron and (ii) how the neurons are connected. In this work, the Hindmarsh-Rose neuron model is used because it exhibits all the computational properties of biological spiking neurons. Also, for studying the unidirectional coupling scheme of two identical Hindmarsh-Rose neuron models, a recently new proposed method by using Nonlinear Open Loop Controllers (NOLCs) is applied. The simulation results from coupling system’s numerical integration verify the appearance of the complete synchronization and antisynchronization phenomenon.

The paper is organized as follows. In Section 2 the cases of synchronization and antisynchronization between unidirectionally coupled nonlinear systems by using the nonlinear open loop controllers, are presented. Section 3 presents the simulation results which confirm the feasibility of the proposed coupling schemes. Finally, the conclusive remarks are drawn in the last Section.

ISBN: 978-1-61804-321-4

II. The Coupling Scheme

In the last three decades the phenomenon of synchronization between coupled chaotic systems has attracted the interest of the scientific community because it is a rich and multi-disciplinary phenomenon with broad range applications, such as in a variety of complex physical, chemical, and biological systems [8-14], as well as in secure communications [15], cryptography [16,17] and broadband communication systems [18]. In more detail, synchronization of chaos is a process, where two or more chaotic systems adjust a given property of their dynamics motion to a common behavior, such as identical trajectories or phase locking, due to coupling or forcing. Because of the exponential divergence of the nearby trajectories of a chaotic system, having two chaotic systems being synchronized, might be a surprise. However, today the synchronization of coupled chaotic oscillators is a phenomenon well established experimentally and reasonably well understood theoretically.

The history of chaotic synchronization's theory began with the study of the interaction between coupled chaotic systems in the 1980's and early 1990's by Fujisaka and Yamada [19], Pikovsky [20], Pecora and Carroll [21]. Since then, a wide range of research activity based on synchronization of nonlinear systems has risen and a variety of synchronization's types depending on the nature of the interacting systems and of the coupling schemes has been presented.

In particular, the phenomenon of complete synchronization is the most studied type of synchronization. In this case, two coupled chaotic systems are leaded to a perfect coincidence of their chaotic trajectories i.e.,

$$x_1(t) = y_1(t) \text{ as } t \to \infty \tag{7}$$

Another interesting phenomenon is the antisynchronization, in which two coupled systems x_1 and y_1, can be synchronized in amplitude, but with opposite sign, for initial conditions chosen from large regions in the phase space, that is

$$x_1(t) = -y_1(t) \text{ as } t \to \infty \tag{8}$$

The coupling scheme between two identical Hindmarsh-Rose neuron models can be either unidirectional, in which the dynamics only of the first coupled neuron model affects the second one, or bidirectional, in which the dynamics of both coupled neuron models affects each other.

As it is mentioned, in this work, the unidirectional coupling scheme, described by the following system of differential equations:

$$\begin{cases} \dot{x} = f(x) \\ \dot{y} = f(y) + U_Y \end{cases} \tag{9}$$

has been chosen.

In this system, $(f(x), f(\mathrm{y})) \in R^n$ are the flows of the master and slave system respectively, while $U_Y = [U_{Y1}, U_{Y2}, U_{Y3}, U_{Y4}]^T$ are the Nonlinear Open Loop Controllers [22]. The error function is defined by $\boldsymbol{e} = \gamma\boldsymbol{y} - \delta\boldsymbol{x}$, with $\boldsymbol{e} = [e_1, e_2, e_3, e_4]^T$, $\boldsymbol{x} = [x_1, x_2, x_3, x_4]^T$ and $\boldsymbol{y} = [y_1, y_2, y_3, y_4]^T$.

By changing the variables of system (6) according to the following equations: $x_1 \to X$, $x_2 \to 1 + Y$, $x_3 \to 1 + Z + I$, $d \to -a + b$, $c \to -s\chi - 1 - I$, the number of parameters can be reduced and the system (6) is written as:

$$\begin{cases} \dfrac{\mathrm{d}x_1}{\mathrm{d}\tau} = x_2 - x_1^3 + a x_1^2 - x_3 \\ \dfrac{\mathrm{d}x_2}{\mathrm{d}\tau} = (a+b)\,x_1^2 - x_2 \\ \dfrac{\mathrm{d}x_3}{\mathrm{d}\tau} = r\cdot(s\cdot x_1 + c - x_3) \end{cases} \tag{10}$$

In Fig.1 the chaotic attractors of the Hindmarsh-Rose neuron system (10), for $a = 3$, $b = -8.2$, $c = 2.15014$, $r = 0.008$ and $s = 4$, is shown.

In the case of unidirectional coupling (see Eq.(9)) of two coupled Hindmarsh-Rose neuron models of system (10), the error dynamics are written as:

$$\begin{cases} \dfrac{\mathrm{d}e_1}{\mathrm{d}\tau} = a\left(\gamma y_1^2 - \delta x_1^2\right) - \left(\gamma y_1^3 - \delta x_1^3\right) + e_2 - e_3 + \gamma U_{Y1} \\ \dfrac{\mathrm{d}e_2}{\mathrm{d}\tau} = (a+b)\left(\gamma y_1^2 - \delta x_1^2\right) - e_2 + \gamma U_{Y2} \\ \dfrac{\mathrm{d}e_3}{\mathrm{d}\tau} = r\cdot\left[s e_1 + c(\gamma - \delta) - e_3\right] + \gamma U_{Y3} \end{cases} \tag{11}$$

For stable synchronization $\boldsymbol{e} \to 0$ with $t \to \infty$. By substituting the conditions in Eqs.(10) and taking the time derivative of Lyapunov function

$$\begin{aligned} \dot{V} &= e_1\frac{\mathrm{d}e_1}{\mathrm{d}\tau} + e_2\frac{\mathrm{d}e_2}{\mathrm{d}\tau} + e_3\frac{\mathrm{d}e_3}{\mathrm{d}\tau} = e_1[a(\gamma y_1^2 - \delta x_1^2) - (\gamma y_1^3 - \delta x_1^3) + \\ &+ e_2 - e_3 + \gamma U_{Y1}] + e_2[(a+b)(\gamma y_1^2 - \delta x_1^2) - e_2 + \gamma U_{Y1}] + \\ &+ e_3\left[r\cdot\left[s e_1 + c(\gamma-\delta) - e_3\right] + \gamma U_{Y3}\right] \end{aligned} \tag{12}$$

the following NOLCs functions can be considered:

$$\begin{cases} U_{Y1} = \dfrac{1}{\gamma}\left[-e_2 - a\left(\gamma y_1^2 - \delta x_1^2\right) + \left(\gamma y_1^3 - \delta x_1^3\right) + e_3 - e_1\right] \\ U_{Y2} = \dfrac{1}{\gamma}\left[-(a+b)\left(\gamma y_1^2 - \delta x_1^2\right)\right] \\ U_{Y3} = \dfrac{1}{\gamma}\left[-r\cdot\left[s e_1 + c(\gamma - \delta)\right]\right] \end{cases} \tag{13}$$

such that:

$$\dot{V} = e_1\frac{\mathrm{d}e_1}{\mathrm{d}\tau} + e_2\frac{\mathrm{d}e_2}{\mathrm{d}\tau} + e_3\frac{\mathrm{d}e_3}{\mathrm{d}\tau} < 0 \tag{14}$$

Equation (14) ensures the asymptotic global stability of synchronization.

III. Simulation Results

According to the specific method of coupling, by using the appropriate NOLCs functions U_X, U_Y and error function's parameters γ, δ, a unidirectional coupling scheme can be implemented. Also, the signs of γ, δ play a crucial role to the type of synchronization (complete synchronization or antisynchronization), which is observed. On the other hand the ratio of γ over δ determines the amplification or attenuation of one oscillator relative to the other one.

ISBN: 978-1-61804-321-4

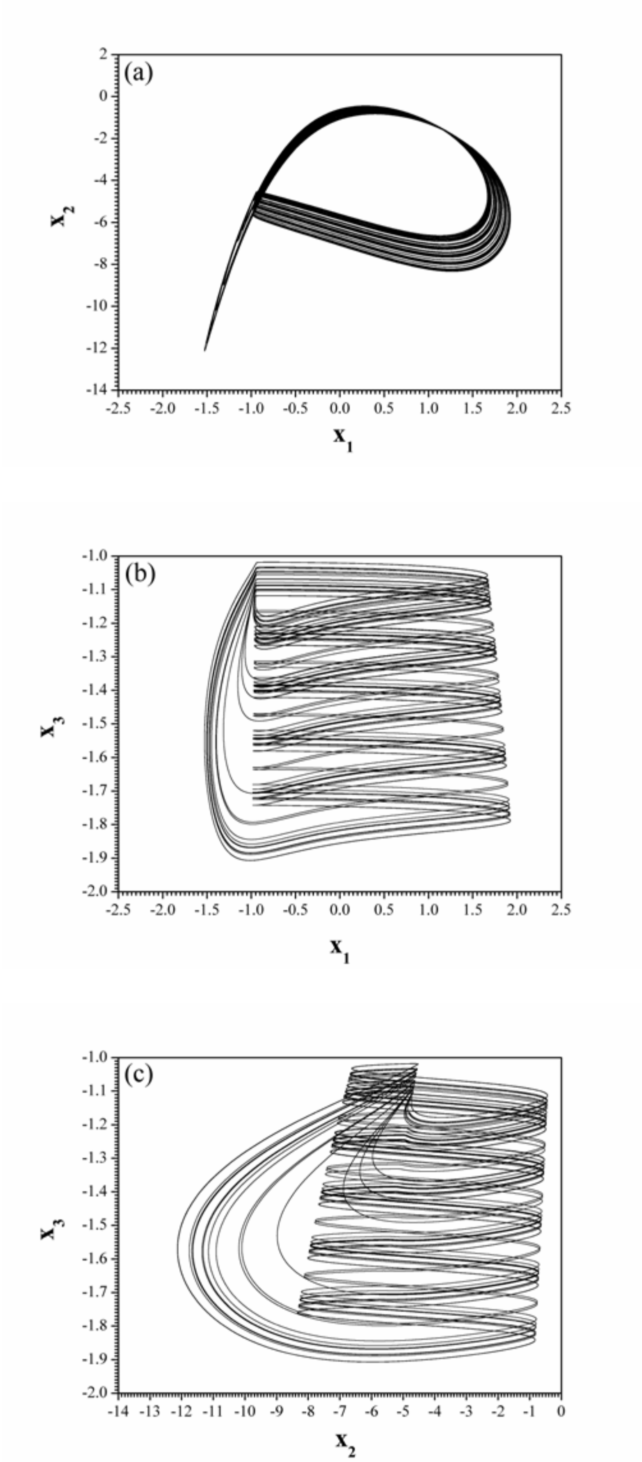

Fig. 1 The chaotic attractors of Hindmarsh-Rose neuron model, for a = 3, b = –8.2, c = 2.15014, r = 0.008 and s = 4, in (a) x_1-x_2 plane, (b) x_1-x_3 plane and (c) x_2-x_3 plane.

So, in this section, the results of the simulation process in the unidirectional coupling scheme and for the two types of synchronization (complete synchronization or antisynchronization), are presented. For this reason, the coupling system is solved numerically by using the forth order Runge-Kutta algorithm.

Firstly, the case of unidirectional coupling of two identical coupled Hindmarsh-Rose neuronal models of system (10), for $a = 3$, $b = –8.2$, $c = 2.15014$, $r = 0.008$ and $s = 4$ and for initial conditions, $(x_1, x_2, x_3, y_1, y_2, y_3)$ = 0.55, 0.49, 0.08, 0.50, 0.40, 0.05), is studied. By choosing the error's parameters $\gamma = 3$ and $\delta = 2$ the coupled system's chaotic attractors are asymmetric as can be verified by the phase portraits of Fig.2 as well as from Fig.3, in which the time-series of the signal y_1 in regard to the signal x_1, are depicted. As it is shown, the amplitude of the spikes of the first system have been amplified in regard to the spikes of the second system due to the fact that $\gamma > \delta$. Furthermore, in Fig.4 the plot of $(3y_1)$ versus $(2x_1)$, which are the two terms of the error function, confirms that the coupled system is in complete synchronization state. The error plots $e_i = \gamma y_i - \delta x_i$ with i = 1, 2, 3, in Fig.5, shows the exponential convergence to zero that verifies the chaotic synchronization state. From this figure, the slower convergence of the signal e_3 to zero in regard to the other two error's signals is shown, due to the fact that the variable z is varied slowly.

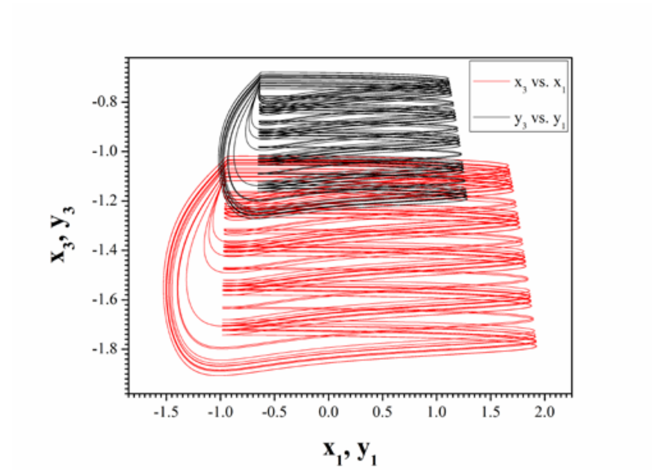

Fig. 2 The phase portrait of x_3 vs. x_1 (red color) and y_3 and y_1 (black color), for $\gamma = 3$ and $\delta = 2$.

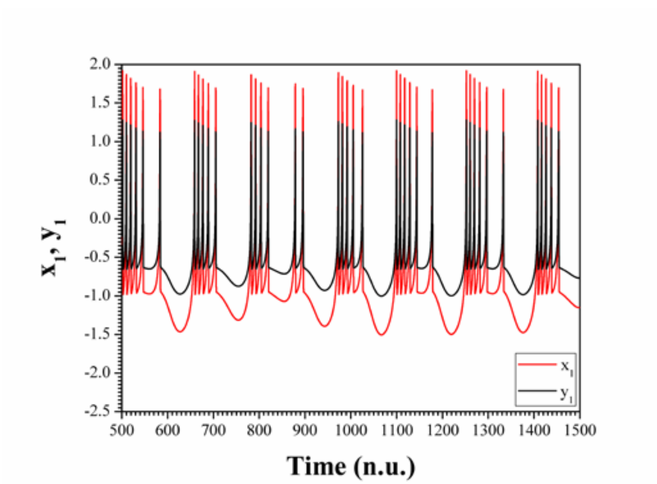

Fig. 3 The time-series of x_1 (red color), y_1 (black color), for $\gamma = 3$ and $\delta = 2$.

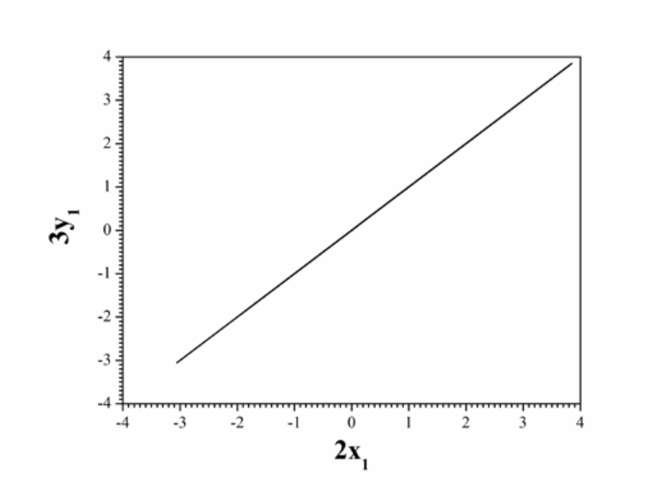

Fig. 4 The phase portrait of $3y_1$ versus $2x_1$ (complete synchronization has been achieved).

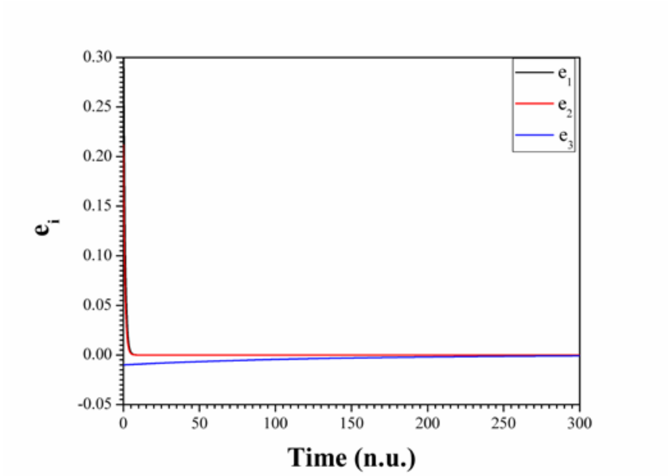

Fig. 5 The plot of errors e_i ($= \gamma y_i - \delta x_i$), for $\gamma = 3$ and $\delta = 2$.

As a second case of study in the unidirectional coupling scheme, the following values of the error's parameters $\gamma = 3$ and $\delta = -2$ have been chosen. For the opposite value of δ, in regard to the previous case, the coupling system tends to the antisynchronization state, as it can be concluded from Figs.6 & 7. Also, the signals of the second coupled system (i.e. signal y_1 in Fig.8) have been inverted in regard to the signals of the previous case.

V. Conclusion

In this work the case of unidirectionally coupling scheme of two identical Hindmarsh-Rose neuron models was studied. As a coupling method a recently new proposed scheme based on the nonlinear open loop controller was used. According to the simulation results from system's numerical integration the appearance of complete synchronization and antisynchronization, depending on the signs of the parameters of the error functions, was investigated. So, by choosing an appropriate sign for the error functions one could drive the coupling system either in complete synchronization or antisynchronization behavior. As a next step in this research direction the application of the proposed method in non-identical coupled Hindmarsh-Rose neuronal models in order to satisfy the goal of control of such systems, which are in totally different dynamical behaviors, is planned.

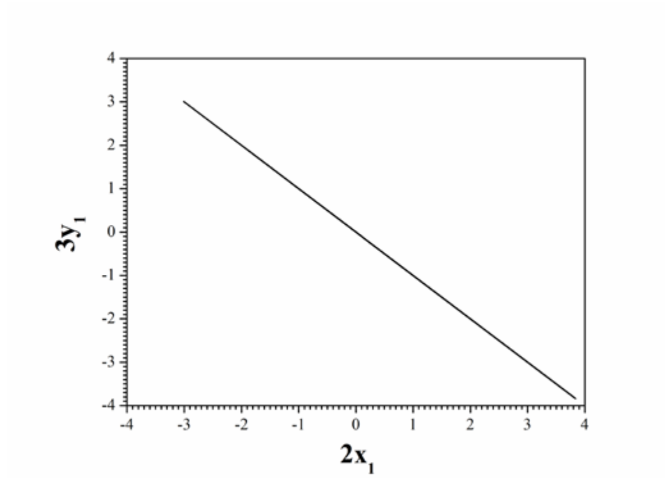

Fig. 6 The phase portrait of $3y_1$ versus $2x_1$ (antisynchronization has been achieved).

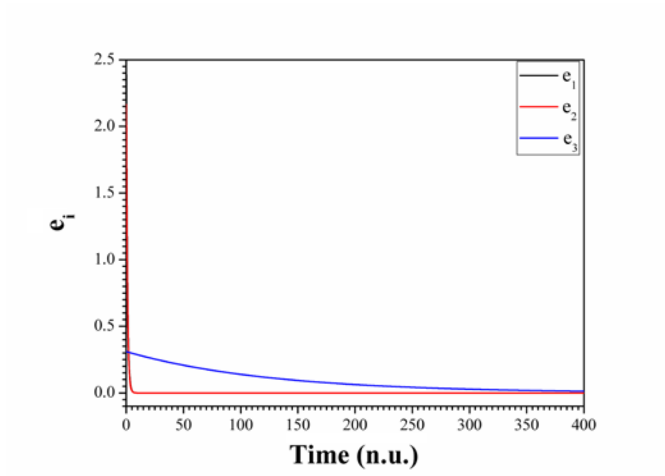

Fig. 7 The plot of errors e_i ($= \gamma y_i - \delta x_i$), for $\gamma = 3$ and $\delta = -2$.

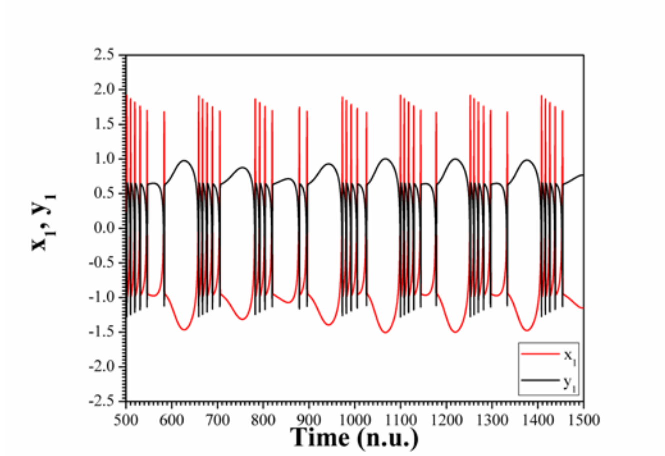

Fig. 8 The time-series of x_1 (red color), y_1 (black color), for $\gamma = 3$ and $\delta = -2$.

ISBN: 978-1-61804-321-4

REFERENCES

[1] W. Gerstner and W. M. Kistler, "Spiking neuron models: Single neurons, populations, plasticity," *Cambridge University Press*, 2002.

[2] E. M. Izhikevich, "Which model to use for cortical spiking neurons?," IEEE Transactions on Neural Networks, vol. 15(5), pp. 1063-1070, 2004.

[3] A. L. Hodgkin and A. F. Huxley, "A quantitative description of membrane current and its application to conduction and excitation in nerve," *Journal of Physiology-London*, vol. 117, pp. 500-544, 1952.

[4] R. FitzHugh, "Impulses and physiological states in theoretical models of nerve membrane," *Biophysical Journal*, vol. 1, pp. 445-466, 1961.

[5] I. M. Kyprianids and A. T. Makri, "Complex dynamics of FitzHugh-Nagumo type neurons coupled with gap junction under external voltage stimulation," Journal of Engineering Science and Technology Review, vol. 6(4), pp. 104-114 2013.

[6] J. L. Hindmarsh and R. M. Rose, "A model of neuronal bursting using three coupled first order differential equations," *Proc. of Royal Society London, Series B*, vol. 221, pp. 87-102, 1984.

[7] A. V. M. Herz, T. Gollisch, C. K. Machens, and D. Jaeger, "Modeling single-neuron dynamics and computations: A balance of detail and abstraction," *Science*, vol. 314, pp. 80-85, 2006.

[8] A. S. Pikovsky, M. Rosenblum, and J. Kurths, "Synchronization: A universal concept in nonlinear sciences," *Cambridge University Press*, Cambridge, 2003.

[9] E. Mosekilde, Y. Maistrenko, and D. Postnov, "Chaotic synchronization: applications to living systems," *World Scientific*, Singapore, 2002.

[10] I. Szatmári and L. O. Chua, "Awakening dynamics via passive coupling and synchronization mechanism in oscillatory cellular neural/nonlinear networks," *Int. J. Circ. Theor. Appl.*, vol. 36, pp. 525-553, 2008.

[11] N. H. Holstein-Rathlou, K. P. Yip, O. V. Sosnovtseva, and E. Mosekilde, "Synchronization phenomena in nephron-nephron interaction," *Chaos*, vol. 11, pp. 417-426, 2001.

[12] X. Liu and T. Chen, "Synchronization of identical neural networks and other systems with an adaptive coupling strength," *Int. J. Circ. Theor. Appl.*, vol. 38, pp. 631-648, 2010.

[13] E. Tognoli and J. A. S. Kelso, "Brain coordination dynamics: True and false faces of phase synchrony and metastability," *Prog. Neurobiol.*, vol. 87, pp. 31-40, 2009.

[14] J. Wang, Y. Q. Che, S. S. Zhou, and B. Deng, "Unidirectional synchronization of Hodgkin-Huxley neurons exposed to ELF electric field," *Chaos Solitons Fract.*, vol. 39, pp. 1335-1345, 2009.

[15] S. Jafari, M. Haeri, and M. S. Tavazoei, "Experimental study of a chaos-based communication system in the presence of unknown transmission delay," *Int. J. Circ. Theor. Appl.*, vol. 38, pp. 1013-1025, 2010.

[16] Ch K. Volos, I. M. Kyprianidis, and I. N. Stouboulos, "Experimental demonstration of a chaotic cryptographic scheme," *WSEAS Trans. Circ. Syst.*, vol. 5, pp. 1654-1661, 2006.

[17] G. Grassi and S. Mascolo, "Synchronization of high-order oscillators by observer design with application to hyperchaos-based cryptography," *Int. J. Circ. Theor. Appl.*, vol. 27, pp. 543-553, 1999.

[18] A. S. Dimitriev, A. V. Kletsovi, A. M. Laktushkin, A. I. Panas, and S. O. Starkov, "Ultrawideband wireless communications based on dynamic chaos," *J. Commun. Technol. Electron.*, vol. 51, pp. 1126-1140, 2006.

[19] H. Fujisaka and T. Yamada, "Stability theory of synchronized motion in coupled-oscillator systems," *Prog. Theory Phys.*, vol. 69, pp. 32-47, 1983.

[20] A. S. Pikovsky, "On the interaction of strange attractors," *Z. Phys. B - Condensed Matter*, vol. 55, pp. 149-154, 1984.

[21] L. M. Pecora and T. L. Carroll, "Synchronization in chaotic systems," *Phys. Rev. Lett.*, vol. 64, pp. 821-824, 1990.

[22] E. Padmanaban, C. Hens, and K. Dana, "Engineering synchronization of chaotic oscillator using controller based coupling design," *Chaos*, vol. 21 pp. 013110, 2011.

On path planning for obstacle avoidance: comparison between two finite element approaches

Stratis Kanarachos, Andreas Kanarachos

***Abstract*—** When an obstacle suddenly appears in the trajectory of a vehicle a path has to be designed in real time to avoid the collision. A vast number of path planning methods for ground vehicles have been proposed until now. A comparative evaluation of the different methods is necessary to illustrate their advantages and disadvantages and ease their selection. In this paper, two different finite element formulations for collision avoidance are presented and compared for case study. Conclusions regarding the performance of the methods are drawn.

Keywords- collision avoidance, path planning, finite elements, dynamics optimization.

I. Introduction

THE main cause of road fatalities is human errors in decision making and handling of the vehicle while driving. Further research and development in Advanced Driver Assistance Systems like Lane Keeping and Collision Avoidance Systems has the potential to bring the total number of road fatalities close to zero [1]. A core module for both systems is the path planner. A path has to be designed in real time to avoid the collision and remain within the road boundaries. The path has to be designed in such a way to satisfy vehicle's maneuverability requirements. Although many approaches have been proposed until now there is still lack of a flexible methodology which can satisfy all the above requirements.

Gray et al investigated the performance of a point mass path planner and concluded that the trajectory generated, although real-time capable, was not always feasible [2]. The lower level tracking controller could not follow the planned path and obstacle collisions were observed in conditions where the obstacle could have been avoided. Thus, they proposed a path planner based on motion primitives that respect a priori the vehicle dynamics constraints. The main drawback is that motion primitives aren't suitable for complex driving scenarios where arbitrary boundary conditions may hold.

Stratis Kanarachos is with the Faculty of Engineering & Computing at Coventry University,CV12JH UK (corresponding author to provide phone: +442477657720; fax: +442477657720; e-mail: stratis.kanarachos@ Coventry.ac.uk).

Andreas Kanarachos is with the Mechanical Engineering Department, Frederick University, Lefkosia, 1036 Cyprus (e-mail: eng.ka@frederick.ac.cy).

The main reason for which a planned path becomes intractable is because it violates the maneuverability limits of the vehicle. This happens mainly for two reasons (a) the commanded -by the control law- tire forces are too large with respect to the available tire-road friction and/or actuator dynamics and (b) the dynamics of the planned path and the actual vehicle states when path tracking starts have a large discrepancy.

Collision avoidance paths are essentially time optimal two point boundary value problems and thus -from Guidance point of view- should satisfy Pontryagin's Maximum Principle (PMP) [3]. In order to apply the PMP a tire-road friction estimator like the one in [4] is necessary.

Reference [5] has developed, based on PMP, a flexible methodology that could plan obstacle avoidance paths for any vehicle model, however nonlinear it is. The main disadvantage of the method was the computational cost and thus the hardness to meet the real time requirements. In an effort to reduce the computational effort a neural network methodology has been proposed [6]. The neural network was able to plan collision avoidance paths and was real time capable. However, it performed well only in cases for which it has been trained. It was lacking the flexibility to address complex driving scenarios, as one may experience in real life.

In this context, a finite element path planning method which can cope with complex scenarios and arbitrary boundary conditions has been developed and proposed in [7]. The method decomposes the path in finite standardized segments which are then glued to each other in the same sense as in the direct finite element method. The method can handle complex scenarios and is real time capable.

In this paper, two different formulations of the finite element path planning method are presented and compared. The main driver for it is to evaluate the advantages and disadvantages of each method and thus ease the selection. This work is – to our knowledge- performed for the first time. The rest of the paper is organized as follows: In Sections 2 and 3 the vehicle model used and the finite element formulation which recasts the dynamic optimization problem into a nonlinear algebraic one are discussed respectively. In Section 4 the two finite element formulations are evaluated and compared for different driving scenarios. In Section 5 conclusions and future research directions are drawn.

II. MATHEMATICAL MODEL

A. Vehicle model and model based constraints

Since a very detailed vehicle model can be difficult to obtain and use, the method described in this paper makes use of a model that approximates vehicle motion. Furthermore, it is assumed that the vehicle is equipped with an Electronic Stability Control (ESC) system, such as the one described in [8]. Furthermore, we assume that the ESC system utilizes the same limit $r_{\max 0}$ as the path tracking system. This effectively means that any commanded yaw rate $r_{des} > r_{\max 0}$ will cause ESC's system activation and thus bring the vehicle from a path tracking to a stability mode.

The two track vehicle model (TTVM), shown in Figure 1, is employed to derive the equations of motion described by forward velocity u_f, lateral velocity v and yaw rate r [9].

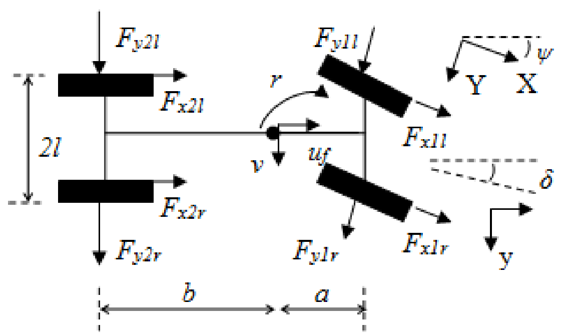

Fig. 1 Top view of TTVM

For simplification reasons shock absorbers and suspension springs are neglected. Also neglected are roll angle, steer angle and roll axis inclination which are assumed small enough. Effects of additional steer angles due to suspension kinematics and steer compliance are ignored [9]. The equations of motion, Eq. (1)-(3), are:

$$m \cdot (\dot{u}_f - r \cdot v) = \sum F_x = F_{x1} - F_{y1} \cdot \delta + F_{x2} \tag{1}$$

$$m \cdot (\dot{v} + r \cdot u_f) = \sum F_y = F_{x1} \cdot \delta + F_{y1} + F_{y2} \tag{2}$$

$$I_z \dot{r} = \sum M = a \cdot F_{y1} - b \cdot F_{y2} \tag{3}$$

Vehicle velocities and in the global coordinate system O(X,Y) are a function of local velocities and (expressed in the vehicle coordinate system o(x,y) and angle (shown in Figure 1). The vehicle's trajectory (*X*, *Y*), expressed in the global coordinate system, is:

$$X = \int_0^T \dot{X} \cdot \cos\psi \cdot dt \tag{4}$$

$$Y = \int_0^T \dot{Y} \cdot \sin\psi \cdot dt \tag{5}$$

where *T* is the maneuvering time.

Vehicle's yaw rate *r* is limited either because of the available tire-road friction or because of stability reasons. In the first case, the yaw rate limit $r_{\max 0}$ results from Equation (2):

$$a_y = \dot{v} + u_f \cdot r \approx u_f \cdot r \le a_{y\max} = \mu \cdot m \cdot g \Rightarrow$$

$$r_{\max 0} = \frac{c_0 \cdot \mu \cdot m \cdot g}{u_f} \tag{6}$$

where g is the gravitational acceleration and $c_0 \in [0.85, 0.95]$ a coefficient compensating the influence of vehicle slip angle β which is omitted in calculations [10]. In Table 1 the vehicle parameters used in the study are listed.

Table 1 Vehicle parameters.

Name	Parameter	Value
Vehicle mass	m [kg]	1737
Distance from ground to CG	h [m]	0.58
Moment of inertia - to z axis	I_z [kgm^2]	2877
Half length of the wheel axle	l [m]	0.765
Distance of front axle from cog	a [m]	1.3

B. Tire model and yaw rate limit

Tire forces are mathematically described using the well-known Magic Formula model. For pure side slip α_s the tire's lateral force F_{y0} is:

$$F_{y0}(\alpha_S) = D \cdot \sin\left(C \cdot \arctan\left(B \cdot \alpha_S - E \cdot \left(B \cdot \alpha_S - \arctan(B \cdot \alpha_S)\right)\right)\right) \tag{7}$$

where $\alpha_S = \tan(\alpha)$ is the slip angle, $D = \mu \cdot F_z$ the peak value, C the shape factor, $B = \frac{C_{F\alpha}}{C \cdot D}$ the stiffness factor and E the curvature factor. A graphical illustration of lateral force F_y versus slip angle α for four different normal loads is shown in Figure 2. We denote with $\alpha_{\max}(\mu, F_z)$ the tire slip angle for which the lateral force is maximized $F_{y_{\max}}$. In Table 2 the tire parameters used in the study are listed.

Tire slip angles α_1 and α_2 on front and rear wheels are considered small ($\sin\alpha_i \approx \alpha_i$) and expressed as:

$$\alpha_1 = \delta - \frac{1}{u_f} \cdot (v + a \cdot r) \tag{8}$$

$$\alpha_2 = -\frac{1}{u_f} \cdot (v - b \cdot r) \tag{9}$$

where δ is the steer angle. We assume equal slip angles at both left and right wheels ($\alpha_{1r} = \alpha_{1l} = \alpha_1$ and $\alpha_{2r} = \alpha_{2l} = \alpha_2$) which is a valid assumption when $l \cdot |r| << u_f$.

Table 2 Tire parameters.

Name	Parameter	Value
Shape factor	C	1.3
Tire-road friction coefficient	M	0.5
Curvature factor	E	-3
Stifness coefficient	$C_{F\alpha} = c_1 \cdot \sin\left(2 \cdot \arctan\left(\frac{F_z}{c_2}\right)\right)$	
Maximum cornering stiffness [N/rad]	c_1	60000
Load at max. cornering stiffness [N]	c_2	4000

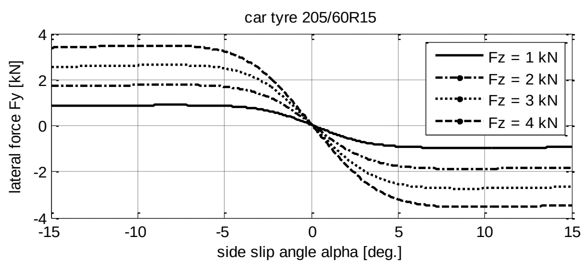

Fig. 2 Lateral force versus tire slip angle for different normal loads

From Equation (8) and (9) and assuming -for simplification reasons - that velocity v is negligible we get respectively:

$$\delta_{\max} = \alpha_{\max} + \frac{1}{u_f} \cdot a \cdot r \tag{10}$$

$$\alpha_{\max} = -\frac{1}{u_f} \cdot \left(v - b \cdot r_{\max_2}\right) \Rightarrow r_{\max 1} = \frac{\alpha_{\max} \cdot u_f}{b} \tag{11}$$

The minimum of yaw rate limits $r_{\max 0}$, and $r_{\max 2}$ is denoted as $r_{\max} = \min(r_{\max 1}, r_{\max 0})$. By implementing a constraint on the maximum yaw rate and maximum tire slip angle we indirectly define a maximum value for the vehicle slip angle.

III. THE FINITE ELEMENT FORMULATION

in this study, two finite element formulations – a third and a second order - are compared. Due to the fact that the first one has been discussed in detail in [7], only the second is presented, in this paper.

A. Second order Finite Element Formulation

A schematic of the approach is shown in Figure 6. The total path is decomposed in N finite elements/segments. Each finite element is denoted with a number $n=1…N$, and has two nodes: the start node $\mathbf{n}_a$ and end node $\mathbf{n}_b$. The EP is constructed by joining end node $\mathbf{n}_b$ and start node $(\mathbf{n+1})_a$ of two consecutive finite elements $\mathbf{n}$ and $\mathbf{n+1}$, for $n=1:..:N-1$.

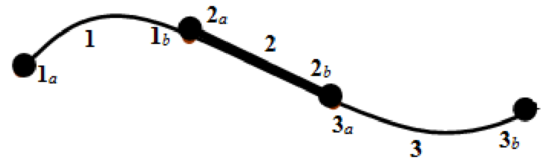

Fig. 3 Collision avoidance path decomposed in 3 finite elements

Each finite element is parameterized using two variables: time span $t_{n\,span}$ and the highest order constrained state variable. Time span $t_{n\,span}$ may be uniformly chosen by decomposing the total maneuvering time in n segments or by considering other parameters such as change of tire-road friction coefficient μ and road curvature. In this formulation, angular acceleration is the highest order constrained state variable and assumed constant in each segment for $t_n \in [0, t_{nspan}]$. In this context, angular velocity r_n and position θ_n are:

$$\dot{r}_n = a_{2n} \tag{12}$$

$$r_n = \int_0^{t_{n,span}} \dot{r}_n \cdot dt = a_{2n} \cdot t + a_{1n} \tag{13}$$

$$\theta_n = \int_0^{t_{n,span}} r_n \cdot dt = 0.5 \cdot a_{2n} \cdot t^2 + a_{1n} \cdot t + a_{0n} \tag{14}$$

where $t_n \in [0, t_{nspan}]$.

The states $y_n = \begin{bmatrix} \dot{r}_{n,a} & r_{n,a} & \theta_{n,a} & \dot{r}_{n,b} & r_{n,b} & \theta_{n,b} \end{bmatrix}^T$ at the boundaries of the finite element are expressed in matrix form as:

$$\mathbf{y_n} = \mathbf{A_n} \cdot \mathbf{x_n} \tag{15}$$

$$\mathbf{y_n} = \begin{bmatrix} r_{n,a} & \theta_{n,a} & r_{n,b} & \theta_{n,b} \end{bmatrix}^T \tag{16}$$

$$\mathbf{x_n} = \begin{bmatrix} a_{2n} & a_{1n} & a_{0n} \end{bmatrix}^T \tag{17}$$

$$\mathbf{A}_n = \begin{bmatrix} 0 & 1 & 0 \\ 0 & 0 & 1 \\ t_{nspan} & 1 & 0 \\ 0.5 \cdot t_{nspan}^2 & t_{nspan} & 1 \end{bmatrix} \tag{18}$$

The finite element matrix $\boldsymbol{A_n}$ constitutes the basis for joining

ISBN: 978-1-61804-321-4

subsequent elements and deriving the system's solution. For a detailed description the reader is referred to [7].

B. Solution methodology

The path is decomposed in $N=3$ uniform finite elements with the same time span $t_{n\,span}$. The EP is computed by solving the following linear system of equations:

$$\mathbf{y}_{bc} = \mathbf{A} \cdot \mathbf{x}_u \quad (19)$$

$$\mathbf{y}_{bc} = \left[r_{1,ades} \quad \theta_{1,ades} \quad \ldots \quad r_{n,bdes} \quad \theta_{n,bdes}\right]$$

$$\mathbf{x}_u = \left[a_{21} \quad a_{11} \quad a_{01} \quad \ldots \quad a_{2n} \quad a_{1n} \quad a_{0n}\right]$$

$$\sum_{i=1}^{N} t_{nspan} = T$$

where $\mathbf{y}_{bc}$ is the vector of boundary conditions, $\mathbf{x}_u$ is the vector of unknown coefficients and **A** the system's matrix.

Vectors $\mathbf{x}_u$ and $\mathbf{y}_{bc}$ as well as system matrix **A** are formed by joining subsequent elements. In particular, we use the desired conditions at beginning ($t=0$) and end ($t=T$) of the EP:

- $r(t=0) = r_{1,ades}$ and $\theta(t=0) = \theta_{1,ades}$
- $r(t=T) = r_{N,bdes}$ and $\theta(t=T) = \theta_{N,bdes}$

To assemble system matrix **A** we use the continuity equations between subsequent elements

$$r_{n,b} = r_{n+1,a}\,,\ \theta_{n,b} = \theta_{n+1,a} \quad (20)$$

and the desired lateral displacement Y_{des} at the end ($t=T$) of the EP:

$$\sum \delta Y_n = Y_{des} \quad (21)$$

where δY_n is the lateral displacement of a finite element:

$$\delta Y_n = \int_0^{t_n S_{pan}} u_f \cdot \sin(\theta_n) \cdot dt \approx u_f \cdot \int_0^{t_n S_{pan}} \theta_n \cdot dt = \left(\frac{1}{6} \cdot \alpha_{2n} \cdot t_n^3 + \frac{1}{2} \cdot \alpha_{1n} \cdot t_n^2 + \alpha_{0n} \cdot t_n \right) \cdot u_f \quad (22)$$

In Equation (22) the incremental lateral displacement δY_n is linearized by assuming $\sin(\theta_n) \approx \theta_n$. The proposition is valid only for small angles $\theta_n \leq 5^o$. For larger angular displacement θ_n the path has to be decomposed into a greater number of finite elements.

It is obvious that different path decomposition would lead to a different system matrix **A** and subsequently a different solution. Actually, there are infinite EPs that satisfy the boundary conditions and that can be computed using the FE method. This is exactly the reason why we are interested in comparing the two different formulations.

IV. NUMERICAL RESULTS

The finite element formulations have been tested for an extensive number of driving scenarios in Matlab simulation environment. The numerical examples are based on the vehicle data listed in Table 1 and tire parameters listed in Table 2. One driving scenario which highlights their features are presented and discussed.

A. Case study: Collision avoidance in a straight line segment: Lane change maneuver with Time To Collision TTC=1.5 s

In this scenario it is assumed that the vehicle moves in a straight line road segment with a speed $u_f = 30\, m/s$. The road surface is dry $\mu = 1$ and an obstacle at distance $d = 45\, m$ suddenly appears in its direction of travel. To avoid the collision the vehicle has to displace laterally by $Y_{des} = 3\, m$.

We solve the problem by decomposing the path in uniform road segments and apply the solution methodology described in the previous section and in [7]. The numerical results using the second order finite element methods are shown in Figs 4-6, while those with the 3rd order method in Figs 7-10.

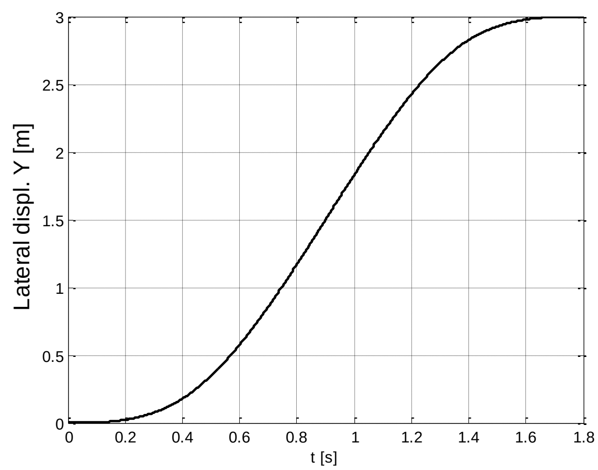

Fig. 4 Lateral displacement using the 2nd order FE method

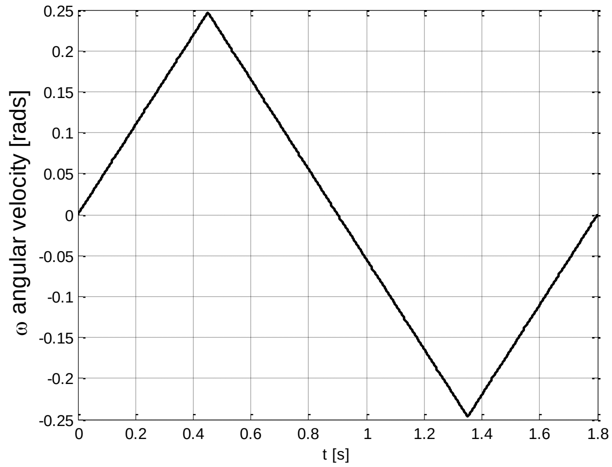

Fig. 5 Angular velocity using the 2nd order FE method

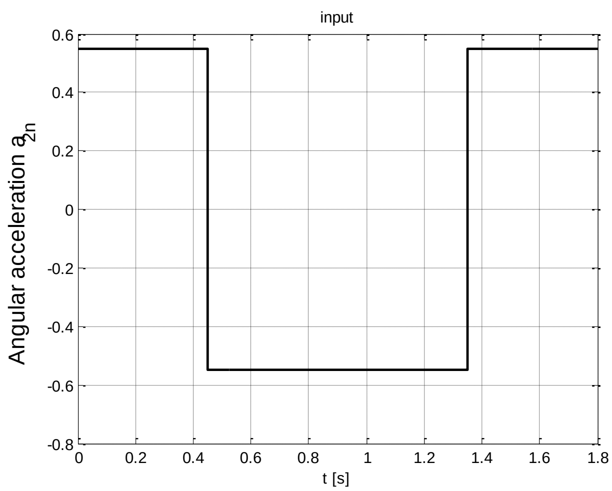

Fig. 6 Angular acceleration using the 2nd order FE method

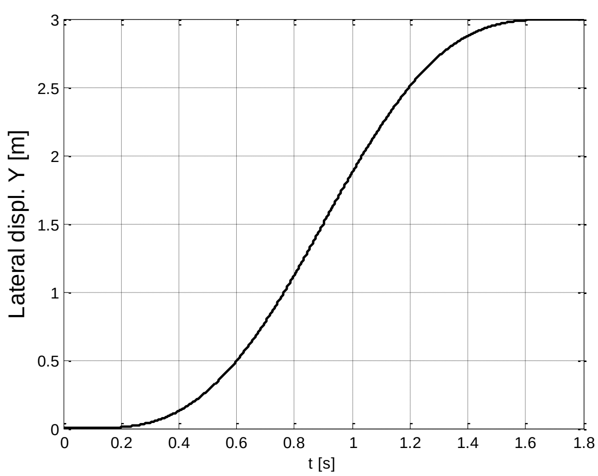

Fig. 7 Lateral displacement using the 3rd order FE method

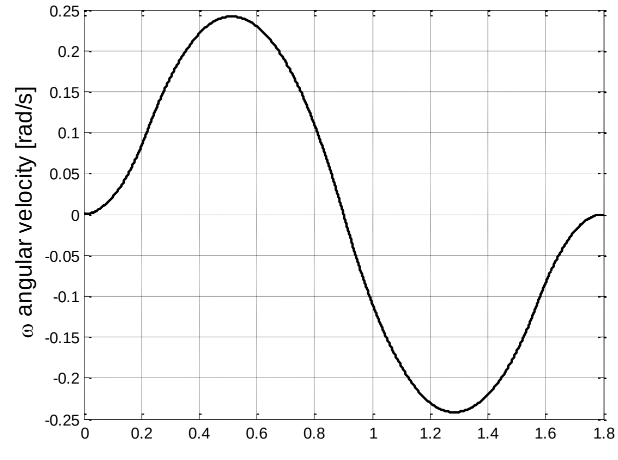

Fig. 8 Angular velocity using the 3rd order FE method

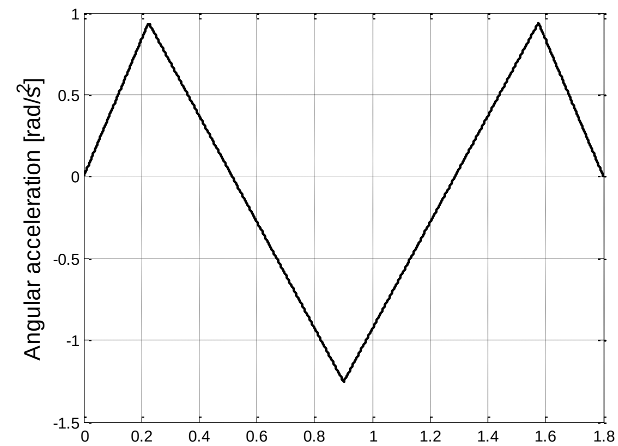

Fig. 9 Angular acceleration using the 3rd order FE method

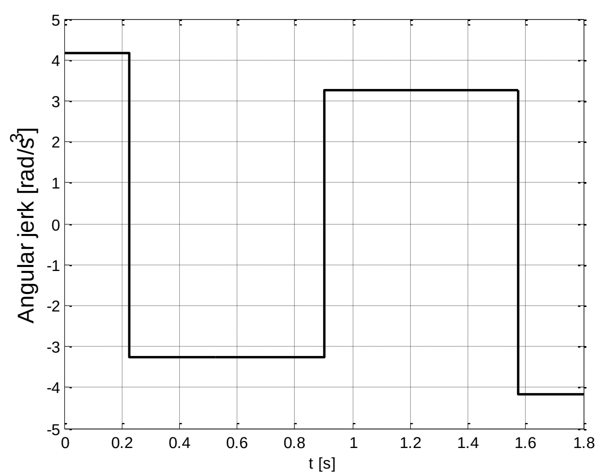

Fig. 10 Angular jerk using the 3rd order FE method

ISBN: 978-1-61804-321-4

B. Discussion of numerical results

The main outcomes from the numerical results summarized in Table 3:

Table 3 Path dynamics

	2^{nd} order FE method	3^{rd} order FE method
Max r *[rad/s]*	0.25	0.25
Max dr/dt [rad/s^2]	0.55	1.25
Max d^2r/dt [rad/s^3]	∞	4.1
Computational cost [s]	0.000071	0.000091

Both methods succeed in designing a path that reaches smoothly the lateral displacement target of Y=3 m withing 1.8 s. Furthermore, it can be easily observed that the maximum yaw rate r_{max}=0.25 rad/s of both paths is below the maximum admissible limit r_{limit}=0.28 rad/s, as defined in Section. It is highlighted that the FE solution using the 2^{nd} order method with uniform time mesh calculated a path with r_{max}=0.4 rad/s, while with the 3^{rd} order method a path with r_{max}=0.33 rad/s. In both cases, the treatment of the problem as an inverse PMP problem improved the path dynamics considerably.

The differences between the two methods lie in the maximum angular acceleration and maximum angular jerk. With the 2^{nd} order method max(dr/dt)= 0.55 rad/s^2 and angular jerk is infinite. Contrary with the 3^{rd} order method the maximum angular acceleration is max(dr/dt)= 1.25 rad/s^2 (larger than the 2^{nd} order), while the maximum angular jerk max d^2r/dt=4.1 rad/s^3. The computational cost is about 25% higher for the 3^{rd} order method. However, the computational cost of the FE method is negligible.

V. Conclusion

When an obstacle suddenly appears in the trajectory of a vehicle a path has to be designed in real time to avoid the collision. A vast number of path planning methods for ground vehicles have been proposed until now. A comparative evaluation of the different methods is necessary to illustrate their advantages and disadvantages and ease their selection. In this paper, two different finite element formulations for collision avoidance are presented and compared for a case study.

A finite element (FE) method has been developed based on a reformulation of Pontryagin's Maximum Principle to plan collision avoidance-time optimal paths. Two different formulations, which differ in the order of approximation, have been presented and evaluated in this study for a typical collision avoidance scenario.

From the numerical results it becomes clear that both methods a) improve the path dynamics compared to the solution obtained with a uniform time mesh and b) satisfy the maneuverability requirements of the vehicle with respect to the maximum admissible yaw rate However, the methods differ in the achievable maximum acceleration and maximum jerk. In the 2^{nd} order method the maximum acceleration is smaller (44%) compared to the one obtained with the 3^{rd} order method. However, the angular jerk is infinite which is negative in terms of comfort. Furthermore, if an active steering system is used to guide the vehicle it is a wrong assumption since the steering dynamics isn't negligible. In case a differential braking system is used then it is an acceptable solution.

In the future the design of collision avoidance paths should become standard and available through the communication protocols between vehicles. The development of a simple but powerful method like the one presented in this paper is considered to be a contribution in this direction.

References

[1] Sotelo Miguel, Advanced Techniques for Vision-based Pedestrian Recognition, *Proceeding VIS'08 Proceedings of the 1st WSEAS international conference on Visualization, imaging and simulation* , 2008.

[2] Gray, A., Yiqi Gao, Lin, T., Hedrick, J.K., Tseng, H.E., Borrelli, F. (2012) 'Predictive control for agile semi-autonomous ground vehicles using motion primitives', *Proceedings of the American Control Conference* 2012, pp. 4239-4244, 27-29 June 2012.

[3] Kanarachos, S., Koulocheris, D., Spentzas, C., Optimal open loop control of dynamic systems using a "min-max" Hamiltonian method, *Forschung im Ingenieurwesen/Engineering Research*, 69 (1), 2004, pp. 1-10.

[4] Valentin Ivanov, Barys Shyrokau, Klaus Augsburg, Vladimir Algin, Fuzzy evaluation of tyre–surface interaction parameters, *Journal of Terramechanics,* Volume 47, Issue 2, April 2010, pp. 113-130.

[5] Kanarachos, S.A., A new method for computing optimal obstacle avoidance steering manoeuvres of vehicles, *International Journal of Vehicle Autonomous Systems,* 7 (1-2), 2009 pp. 73-95.

[6] Kanarachos, S. Design of an intelligent feed forward controller system for vehicle obstacle avoidance using neural networks, *International Journal of Vehicle Systems Modelling and Testing*, 8 (1), 2013, pp. 55-87.

[7] Kanarachos, S., Alirezaei M., An adaptive finite element method for computing emergency maneuvers of ground vehicles in complex driving scenario- Accepted for publication, *International Journal of Vehicle Systems Modelling and Testing*, to be published.

[8] Kanarachos, S., Alirezaei, M., Jansen, S., Maurice, J.-P., Control allocation for regenerative braking of electric vehicles with an electric motor at the front axle using the state-dependent Riccati equation control technique, Proceedings of the Institution of Mechanical Engineers, Part D: Journal of Automobile Engineering, 228 (2), (2014) pp. 129-143.

[9] Pacejka, B., *Tire and Vehicle Dynamics*, Chapter 1, Society of Automotive Engineers, Warrendale. 2005.

[10] R. Rajamani, Vehicle Dynamics and Control - Chapter 8: Electronic Stability Control, Springer, New York, 2012

Method of Monte-Carlo for Generation of Possibility Levels of the Transport Movement on the Routes in Fuzzy Vehicle Routing Problem

Gia Sirbiladze

***Abstract*—**The difficulty of movement between different customers in Fuzzy Vehicle Routing Problems cause the uncertainty of time of movement. In this work the uncertainty is presented by a possibility distribution on the set of customers of a closed route. Based on the possibility distribution a new multiple criteria fuzzy optimization approach for the solution of the optimal vehicle routing problem is considered. The min-max bi-criteria Vehicle Routing Problem is considered in fuzzy environment. A new subjective criterion – maximization of expectation of reliability of movement on closed routes is constructed. This problem is reduced on the Min-max bi-criteria fuzzy partitioning problem. For the generation of an unknown possibility distribution on the set of customers of a closed route a Monte-Carlo simulation algorithm is constructed. A numerical example is presented.

***Keywords*—**Vehicle routing problem, multiple-criteria optimization, possibility theory, fuzzy partitioning problem, Monte-Carlo simulation.

I. Introduction

The timely distribution of goods to different customers is much complicated in extreme and difficult situations, such as: roads with overloaded traffic, public demonstrations and strikes, slippery, snowy roads or roads with less visibility, damaged roads because of natural disasters, earthquakes, and other causes, etc. In such case it is important to assess the reliability and possibility levels of movement on routes. Of course, this changes the movement time as well. It becomes uncertain. Using the software for route planning in stationary environment has less sense in such cases for distribution companies. They should use the intelligent support system for optimal route planning in complex and extreme situations, which would enable experts to introduce corrections to the route planning problem based on experts' evaluations. First of all they will consider the criterion of reliability of route together with other objective information. In such technologies experts become involved in data gathering process, and create the possibility levels of movement (travel) between customers based on embedded knowledge engineering methods and algorithms.

Let's denote these possibility levels by $\|\pi_{ij}\|$, where π_{ij} is a possibility (conditional) level of moving from i-th customer to j-th customer. Thus expert knowledge engineering serves the optimal route planning in extreme situations. In this paper we developed a Monte-Carlo simulation method to evaluate this possibility levels using results of our research [9] (see Section V).

Possibility theory was proposed by L.A. Zadeh in 1978 [12] and developed by D. Dubois and H. Prade in 1988 [1]. Since the 1980s, the possibility theory has become more and more important in the decision and optimization field and several methods have been developed to solve possibilistic programming problems ([8] and others)]. Our aim is to create possibilistic environment of knowledge engineering for optimal vehicle routing problem when movement on roads is difficult. Based on this and other objective information the possibilistic criterion is developed – called the reliability of moving on closed routes.

The systems approach and analysis play determining role in the vehicle routing problem (VRP) ([6-8] and others). The classical VRP is developed by many well-known authors ([7] and others). Here we present a new vision of the fuzzy vehicle routing problem (FVRP), which is different from the approaches given in other researches. This new problem is connected with difficulties of optimal routing of vehicles in different extreme situations.

II. The Main Problem of VRP

We consider the following problem of optimal routing of vehicles as a Main problem. Let the set of geographical points (called customers later on) $I = \{1, 2, \dots, n+1\}$ be given, where $n+1$-th node is depot. Other customers are supplied from depot by vehicles with uniform goods. The demand of goods from customers is known, as well as maximum load and mileage of the vehicles.The problem is the following (first criterion): *It is necessary to deliver the demanded goods to*

G. Sirbiladze is a Professor with the Department of Computer Sciences, Iv.Javakhishvili Tbilisi State University, 13, University street, 0186 Tbilisi, GEORGIA e-mail: gia.sirbiladze@tsu.ge.

customers by vehicles in such way that total distance traveled by vehicles is minimal. It is meant that the demand of goods by each customer is much less than maximum load of vehicles.

Suppose, that $C = \| c_{ij} \|$, $i, j \in I$ is a matrix of positive real numbers and represents the distances between customers; Q and D are real numbers – the constraints of load and mileage of vehicles. P_i, $i = 1, 2, \dots, n$ are also real numbers and represent the demand for goods by i-th customer $1 \le P_i < Q$, $i = 1, 2, \dots, n$.

We have to find such closed set of routes $\{ M_k \}$, $k = 1, 2, \dots, m$, t, $M_k = \left\{ n+1, i_1^k, \dots, i_{\ell_k}^k, n+1 \right\}$, $i_j^k \in \{ 1, 2, \dots, n \}$, $j = 1, \dots, \ell_k$, $1 \le \ell_k \le n$ (m and ℓ_k are not fixed in advance), that satisfy the constraints

$$\bigcup_{k=1}^{m} M_k = I; \quad M_k \bigcap M_q = \{ n+1 \},$$

$$k, q \in \{ 1, 2, \dots, m \}, \quad k \ne q; \qquad \sum_{j=1}^{\ell_k} P_{i_j^k} \le Q; \tag{1}$$

$$c_k = c_{n+1,\, i_1^k} + c_{i_{\ell_k}^k,\, n+1} + \sum_{j=1}^{\ell_k - 1} c_{i_j^k,\, i_{j+1}^k} \le D, \quad k = 1, 2, \dots, m;$$

and that have minimal total distance (objective function, first criterion)

$$\sum_{k=1}^{m} c_k = \sum_{k=1}^{m} \left(c_{n+1,\, i_1^k} + c_{i_{\ell_k}^k,\, n+1} + \sum_{j=1}^{\ell_k - 1} c_{i_j^k,\, i_{j+1}^k} \right). \tag{2}$$

Presented problem corresponds to some mathematical model of above presented problems, connected with distribution of uniform goods in small-sized portions between different customers. It is a complex combinatorial optimization problem and is known as NP-hard [6-8].

III. Formation of the Subjective Input Data in the Vehicle Routing Problems

For the vehicle routing problem represented in this paper, when discussing extreme situations on roads, exact or stochastic models may not work because some input parameters are unknown due to their vague nature. These parameters include transport movement time, representing a total value of point-to-point movement. It is clear that in such circumstances point-to-point traffic delays and probability distribution of the latter often become unknown. Evaluation task of the route reliability is required that involves minimization of the route travel time to some extent. The route turns to be reliable if the difference between the expected travel time and the planned one is minimal. Simply, delay time is the lowest. Therefore, it is planned to construct the second, subjective criterion – to maximize reliability of movement removing on the routes.

We use fuzzy modeling using representation and formation methods and schemes of the expert knowledge. There are a number of publications about fuzzy methods of the vehicle routing tasks. However, all of them have a common approach. They use only one pole of the expert knowledge as a representation of incomplete information – imprecision of the expert information. It represents parameters in fuzzy values, mainly fuzzy-triangular numbers [11] and development methods in transport routing problems called Fuzzy Vehicle Routing Problem (FVRP) [8]. Our approach is different from all and means to use also the other pole of representation of the expert information- uncertainty of the information. It is giving us more convincing aggregation tool, both to evaluate parameters and construct subjective criterion. As the fuzzy uncertaintry, there will be used possibilistic uncertainty and possibility theory in aggregations.

A little about using possibility theory [8] in formation of the transport routing schemes: if the transport is in point i-area of an allowable route, let use set of point of the nearest movement areas denote by $X^{(i)}$. Conditional probability distribution of shifting $\{ P_{ij} \}_{j \in X^{(i)}}$ is unknown as well as time spent on moving. In extreme situations, it is impossible even to evaluate these distributions due to lack of appropriate stochastic data. I.e. stochastic approaches cannot be applied. In our case, we use expert knowledge and create methods that will form the following input parameters:

A. What will be an approximate time delay of transport to move from i to j ($j \in X^{(i)}$) point? Let us denote the value by $\tilde{\tau}_{ij}$. It is represented with fuzzy triangular number $\tilde{\tau}_{ij} = \tilde{t}_{ij} - t_{ij}$, where $\tilde{t}_{ij}$ is the approximate time spent on moving , and t_{ij} planned time for moving (this is the first pole of the expert information – information inaccuracy);

B. What is a possibility of transport to move from one point i to another j in planned timeframe? Let us denote this value by π_{ij}, $0 \le \pi_{ij} \le 1$; $\{ \pi_{ij} \}_{j \in X^{(i)}}$ be conditional possibility distribution on set $X^{(i)}$, which is the other pole of expert information – information uncertainty.

According to the possibility theory, possibility of any event is maximal among its supportive elementary events {9,11,12]:

$$Pos\,(A) = \max_{j \in A} \pi_{ij}, \quad \forall \; A \subseteq X^{(i)},$$

and there is even if one clause $j_0 \in X^{(i)}$, that $\pi_{ij_0} = 1$. So moving with the highest possibility guaranteed.

In the Section V we will represent efficient Monte-Carlo interactive algorithm of formation of $\{ \pi_{ij} \}_{j \in X^{(i)}}$ parameters, based on the knowledge engineering approach. Mentioned algorithms in turn will be the foundation for construction of new, subjective criterion presented in Section IV.

The difficulty of movement between different customers and other problems cause the uncertainty of time of movement. Suppose, that the expert evaluation of time for moving from i-th customer to j-th customer is represented by nonnegative normalized fuzzy-triangular numbers $\tilde{t}_{ij} = \left(t_{ij}^{(1)}, t_{ij}^{(2)}, t_{ij}^{(3)}\right)$, the membership function of which is defined by formula

$$\mu_{\tilde{t}_{ij}}(t) = \begin{cases} 0, & t \le t_{ij}^{(1)}; \\ \dfrac{t - t_{ij}^{(1)}}{t_{ij}^{(2)} - t_{ij}^{(1)}}, & t_{ij}^{(1)} < t \le t_{ij}^{(2)}; \\ \dfrac{t_{ij}^{(3)} - t}{t_{ij}^{(3)} - t_{ij}^{(2)}}, & t_{ij}^{(2)} < t \le t_{ij}^{(3)}; \\ 0, & t > t_{ij}^{(3)}. \end{cases} \tag{3}$$

Then the movement time on closed route M_k will also be fuzzy-triangular number:

$$\tilde{t}_k = \sum_{j=1}^{\ell_k - 1} \tilde{t}_{i_j^k, i_{j+1}^k} + \tilde{t}_{n+1, i_1^k} + \tilde{t}_{i_{\ell_k}^k, n+1} \tag{4}$$

In usual conditions c_k and $\tilde{t}_k$ are identical, but in our case $\tilde{t}_k$ shouldn't depend much on c_k. In extreme situations the reliability of moving on route M_k is determined by smallness of $\tilde{t}_k$. So we introduce the following parameter normalized in [0,1] as a measure of reliability of route M_k:

$$\tilde{\delta}_k = \frac{1}{1 + \left(\tilde{t}_k\right)^{\gamma_1}}. \tag{5}$$

Also we introduce the objective weight of moving from *i*-th to *j*-th customer on route M_k:

$$w_{ij}^{(k)} = \frac{(1/c_{ij})^{\gamma_2}}{\sum_{\mu,\nu} (1/c_{\mu\nu})^{\gamma_2}}, \quad i, j, \mu, \nu \in M_k. \tag{6}$$

γ_1 and γ_2 are positive numbers, selected using the principle of closeness to experimental data. We have to consider $w_{ij}^{(k)}$ weights and π_{ij} possibilities, when constructing the weighted possibility level of movement on route M_k:

$$\pi_k^0 = \sum_{j=1}^{\ell_k - 1} w_{i_j^k, i_{j+1}^k}^{(k)} \cdot \pi_{i_j^k, i_{j+1}^k} + w_{n+1, i_1^k}^{(k)} \cdot \pi_{n+1, i_1^k} + w_{i_{\ell_k}^k, n+1}^{(k)} \cdot \pi_{i_{\ell_k}^k, n+1}. \tag{7}$$

IV. Formation of Subjective Criteria and Construction of Bi-Criteria Optimization Problem

Suppose $\overline{M} = \{M_k\}_{k=1}^m$ is a set of some closed routes, satisfying the (1)-(2) constraints of the Main Problem. To construct the reliability measure of routes $\{M_k\}_{k=1}^m$ we use Choquet integral ([4,5] and others), which condenses the reliabilities $\tilde{\delta}_k$ of routes M_k, $k = 1,2,\ldots,m$ and their possibility distribution

$$\pi_k = \frac{\pi_k^0}{\max\limits_{k=1,m} \pi_k^0}, \tag{8}$$

on the set $\overline{M} = \{M_k\}_{k=1}^m$. In fuzzy statistics the Choquet integral defined on finite set is known as Monotone Expectation (ME) [3-5]. Here we introduce the notion of Monotone Expectation of reliability of the set $\overline{M}$ of closed routes with respect to possibility measure:

$$\begin{aligned} ME\left(\tilde{\delta}_1, \tilde{\delta}_2, \ldots, \tilde{\delta}_m\right) &\overset{\Delta}{=} \int_0^1 Pos\left(\left\{M_j \in \overline{M} / \tilde{\delta}_j \ge \alpha\right\}\right) d\alpha = \\ &= \sum_{i=1}^m \left[Pos\left(\left\{M_{j(1)}, \ldots, M_{j(i)}\right\}\right) - Pos\left(\left\{M_{j(1)}, \ldots, M_{j(i-1)}\right\}\right)\right] \cdot \tilde{\delta}_{j(i)} = \\ &= \sum_{i=1}^m \left[\max_{j=1,i} \pi_{j(i)} - \max_{j=1,i-1} \pi_{j(i-1)}\right] \cdot \tilde{\delta}_{j(i)}, \end{aligned} \tag{9}$$

where $\pi_{j(0)} = 0$; $Pos\left(\left\{M_{j(0)}\right\}\right) \equiv 0$; $\tilde{\delta}_{j(1)} \ge \tilde{\delta}_{j(2)} \ge \cdots \ge \tilde{\delta}_{j(m)}$ – is the permutation of $\left\{\tilde{\delta}_1, \tilde{\delta}_2, \ldots, \tilde{\delta}_m\right\}$ which decreasingly orders the reliability levels. Let's denote: $P^{(i)} \equiv \max\limits_{\nu=1,i} \pi_{j(\nu)} - \max\limits_{\nu=1,i-1} \pi_{j(i-1)}$.

It can be easily checked that $\left\{P^{(i)}\right\}_{i=1}^m$ values have properties of probability distribution on $\overline{M}$. In this case (9) can be written as:

$$ME\left\{\tilde{\delta}_1, \tilde{\delta}_2, \ldots, \tilde{\delta}_m\right\} = \sum_{i=1}^m P^{(i)} \cdot \tilde{\delta}_{j(i)}, \tag{10}$$

This is a second criterion– *maximization of monotone expectation of reliability of movement on the closed routes* $\{M_k\}_{k=1}^m$..

The objective of our research is planned to be implemented to two-phase scheme of solving bi-criteria problem.

Phase I: Allowed closed routes (which satisfy (1)-(2) constraints) should also satisfy additional criteria: 1) The time of movement on closed route M_k must not exceed some maximum limit $\tilde{t}_k \le \tilde{t}_{\max}$, and 2) The possibility level of movement on route M_k must exceed some minimum level: $\pi_k \ge \pi_{\min}$ ($\pi_{\min}$ and $\tilde{t}_{\max}$ are predefined by expert group based on their needs).

Among all allowable closed routes (in case of large dimension of problem, when the number of allowable routes is in order of $10^4 - 10^6$) during the first phase the sample of so-called "rational" routes are selected

$$\overline{M} = \{M_1, M_2, \ldots, M_q\},$$

which satisfy above criteria(the number of such promising routes should be in order of 10^3 –due to limitations of second phase solutions). We plan to make this selection using the specially created algorithm of preferences. Note that this phase

ISBN: 978-1-61804-321-4

will be necessary only in cases when problem's dimension is large.

Phase II: For the rational routes $\overline{M} = \{M_1, M_2, \ldots, M_q\}$ selected during 1st phase, new bi-criteria problem will be solved. The two criteria are minimization of total traveled distance and maximization of reliability of routes. The problem will be stated as a fuzzy-partitioning problem (FPP) [3,4,10].

Our further discussion concerns to a fuzzy partitioning problem(FPP). Some questions of FPP with possibility-probability uncertainty have already been investigated by the authors of this work ([2,8] and others). Now we consider a new variant of a presentation of the optimal FPP for the solution of the FVRP presented here.

Let $A = \| a_{ij} \|_{n\times q}$ be an incidence matrix, and $a_{ij} = 1$ if route M_j goes through customer i and $a_{ij} = 0$ otherwise. All subset of routes $M' = \{M_{j_1}, M_{j_2}, \ldots, M_{j_p}\} \subseteq \overline{M}$ is presented by means of its characteristic vector which has a component $x_j = 1$ if the route M_j is contained in the subset M' and $x_j = 0$ otherwise. As determined in previous section, each route M_j has the level of possibility of movement on it - π_j, level of reliability $\tilde{\delta}_j$ and, of course, the total distance of route C_k. Then we create the distance vector $\overline{C} = \{c_1, c_2, \ldots, c_q\}$ of route $\overline{M}$; $\tilde{\delta} = \{\tilde{\delta}_1, \tilde{\delta}_2, \ldots, \tilde{\delta}_q\}$ – is the vector of reliabilities; $\pi = \{\pi_1, \pi_2, \ldots, \pi_q\}$ – the vector of possibilities (possibility distribution on $\overline{M}$); Also $\overline{x} = \{x_1, x_2, \ldots, x_q\} \in \{0,1\}^q$ – Boolean vector. Then criteria (2) in partitioning problem sounds this way: the set of routes M' is called the partitioning of sets of customers I (otherwise we can say that for any customer from I there exist only one route from M' that travels through that customer, except the depot, which is the starting and ending point of all routes), if

$$\bigcup_{\nu=1}^{p} M_{j_\nu} = I\,,\ M_{j_\nu} \cap M_{j_\mu} = \{n+1\},\ j_\nu,\ j_\mu \in \{j_1, j_2, \ldots, j_p\}. \quad (11)$$

The partitioning condition is similar to the following system of linear equations:

$$A\overline{x} = \overline{e}\,, \quad (12)$$

where $\overline{e} = (1,1,\ldots,1)$ is a vector consisting from 1s. Note that because of 1st phase, the partitioning routes satisfy the following conditions: if $M_k \in M'$, then

$$\sum_{j=1}^{\ell_k} P_{i_j k} \le Q\,,\ \ c_k \le D\,,\ \ \pi_k \ge \pi_{\min}\,,\ \ \tilde{\delta}_k \ge 1\Big/\left(1 + \left(\tilde{t}_{\max}\right)^{\gamma_2}\right). \quad (13)$$

Because of (1)-(2) for each partitioning M' we construct the objective function for the total distance of route:

$$\sum_{i=1}^{q} c_i x_i\ ,\ A\overline{x} = \overline{e} \quad (14)$$

and based on (10) – the objective function of their reliability:

$$\sum_{i=1}^{q} P^{(i)} \cdot \tilde{\tilde{\delta}}_{j(i)} x_{j(i)}\ . \quad (15)$$

So, we consider the Min-max bi-criteria fuzzy-partitioning problem:

$$f_1 \equiv \sum_{i=1}^{q} c_i x_i \Rightarrow \min \quad (16)$$

minimization of the distances of routes in partitioning and

$$f_2 \equiv \sum_{i=1}^{q} P^{(i)} \cdot \tilde{\tilde{\delta}}_{j(i)} x_{j(i)} \Rightarrow \max \quad (17)$$

maximization of monotone expectation of reliability of routes in partitioningwith linear constraints

$$A\overline{x} = \overline{e}\,,\quad x_i \in \{0,1\}. \quad (18)$$

For solving the bi-criteria problem (16)-(18), two approaches will be considered in our future investigations:

1). The method of compromise will be created for bi-criteria problems (16)–(18) based on the idea of ordering of criteria.

2). Scaling of the bi-criteria problem (16)–(18) and reducing the problem to classical partitioning problem $f = \lambda f_1 + (1-\lambda)(1 - f_2)$, $(0 < \lambda < 1)$ with one criterion. The exact solution of classic partitioning problem will be realized by D.Knuth Algorithm of Dancing Links-X (DLX) [2].

V. Method of Generation of Possibility Levels of Timely Transport Movement between the Points on Roads

The possibility theory is based on the idea of a fuzzy set [21-24]. A degree of membership of an element in a set, as well as a degree of possibility of the same element can be any number of the unit interval $[0,1]$, and not only one of the two values $\{0,1\}$ ([1,9-12] and others).

The formalization of this definition has turned out very helpful in developing the principles of applied intelligent systems which model the knowledge of experts in various spheres of man's activity. The theory of fuzzy sets and the related possibility theory are an indispensable tool for the solution of these problems.

Our aim is to create the method of definition or generation of degrees of possibilities of timely transport movement between the nearby points on roads in extreme conditions when the traffic is complicated by extreme processes or phenomena and also when the absence of past statistical data makes it impossible to obtain probability distributions of transport movement from one point to another point. In such situations, stochastic analysis (and the more so an exact method) cannot be used for determining the optimal routes for transport movement. In that case, the possibility theory is applied when data on transport movement can be provided only by an expert. As different from stochastic or exact analysis, one of the advantages of the possibility theory consists in that it allows us to simultaneously model the imprecision of expert's incomplete information (in the form of a fuzzy set) and to quantitatively characterize the uncertainty of the same incomplete information (in the form of a pair of numbers: "possibility" and "necessity" [5]).

Our methodology is based on the use of the concept of level sets [11] induced by the possibility distribution [1] on the set of points lying in the neighborhood of a given point. We will construct the process of subjective (expert) definition of level sets, which, in its turn, will provide the generation of possibility degrees for timely transport movement from a given point to a nearby point. Finally, we obtain the matrix of possibilities of transport movement between the neighboring points.

A. Level Sets and the Matrix of Possibilities

Let $X^{(x_o)} = \{x_1, x_2, ..., x_{n_o}\}$ be the set of neighboring points for some point x_o, $x_o \in I$.

Denote by $\pi^{(x_o)}(x_i) = \pi(x_i) \equiv \pi_i$ the conditional possibility degrees of timely transport movement from the point x_o to the point x_i $(i = 1,2,...,n_o)$. Assume without loss of generality that the elements (points) of the set $X^{(x_o)}$ are indexed so that $\pi(x_i) \geq \pi(x_j)$ if $i > j$ and $\pi(x_{n_o}) = 1$ (i.e. the movement from x_o in $X^{(x_o)}$ occurs with a maximal possibility degree equal to 1).

We obtain the distribution of possibilities on the set of points - $X^{(x_o)}$. To this distribution we may put into correspondence a fuzzy subset of the set $X^{(x_o)}$ that contains all elements (points), where the degree of possibilities of timely transport movement is equal at least to α $(0 < \alpha \leq 1)$: $X_\alpha = \{x / x \in X^{(x_0)}, \pi(x) \geq \alpha\}$. Note that $X_{\alpha_2} \supseteq X_{\alpha_1}$ if $\alpha_1 > \alpha_2$.

Before we describe the procedure of determining the degrees of possibilities $0 \leq \pi_1 \leq \pi_2 \leq ... \leq \pi_{n_0} = 1$, we will discuss a Monte-Carlo simulation experiment, in which the notion of a level set X_α is used. Then we can easily write the level sets

for $0 < \alpha \leq \pi_1$, $X_\alpha = \{x_1, x_2, ..., x_{n_o}\} \equiv X_1$,

for $\pi_1 < \alpha \leq \pi_2$, $X_\alpha = \{x_2, ..., x_{n_o}\} \equiv X_2$,

for $\pi_2 < \alpha \leq \pi_3$, $X_\alpha = \{x_3, ..., x_{n_o}\} \equiv X_3$,

....

for $\pi_{n_o-2} < \alpha \leq \pi_{n_o-1}$, $X_\alpha = \{x_{n_o-1}, ..., x_{n_o}\} \equiv X_{n_o-1}$,

for $\pi_{n_o-1} < \alpha \leq \pi_{n_o} = 1$, $X_\alpha = \{x_{n_o}\} \equiv X_{n_o}$.

In the experiment, the values for α are chosen in a random manner (with uniform distribution on $(0,1)$). Then the probability that one of the points of the set X_j will be chosen as a point to which transport will move from the initial point x_o is equal to $P(X_j) = \pi_i - \pi_{i-1}$, $j = 1,2,...,n_o$; $(\pi_o \equiv 0)$.

Moreover note that the choice of some point x_i from the set X_j is directly proportional to the inverse value of the distance between the points x_o and x_i (we denote this distance by e_i). Then to define this probability we use the definition of geometrical probability

$$P(x_i / X_j) \equiv P\{point\, x_i \text{ is chosen for the movment} / X_j\} = \\ = \begin{cases} 0, & x_i \notin X_j \\ \dfrac{\frac{1}{e_i}}{\sum\limits_{x_k \in X_j} \frac{1}{e_k}}, & x_i \in X_j \end{cases} \tag{19}$$

As a result we obtain the embedded consonant structure of focal elements as a basis of the Body of Evidence: $X = X_1 \supset X_2 \supset ... \supset X_{n_o-1} \supset X_{n_o}$ with the Basic Probability Assignment [1]:

$$m(X_j) = \pi_j - \pi_{j-1}, \quad j = 1,..,n_o;\ \pi_o = 0. \tag{20}$$

Using the structure of focal elements in the role of a complete system of events and applying the formula of a complete probability, we define the probability that the point $x_i : x_i \in X^{(x_o)}$ will be chosen as the point to which transport will move from the point x_o.

$$P(x_i) \equiv P(\text{point } x_i \text{ is chosen for the movement}) = \sum_{j=1}^{n_o} P(x_i / X_j) \cdot m(X_j). \tag{21}$$

It is a priori assumed that when the transport movement transfer takes place in extreme conditions, the probabilities of movement transfer (21) from one point to another become fuzzy values, which can be estimated only by means of an expert's knowledge of a possibility of timely transfer of transport movement to the nearest points.

Using formulas (20) and (21), we can calculate the probabilities $P(x_i)$ of such timely transfer:

$$P(x_1) = \frac{e_1^{-1}}{\sum\limits_{x_j \in X_1} e_j^{-1}} \cdot \pi_1;$$

$$P(x_2) = \frac{e_2^{-1}}{\sum\limits_{x_j \in X_1} e_j^{-1}} \cdot \pi_1 + \frac{e_2^{-1}}{\sum\limits_{x_j \in X_2} e_j^{-1}} \cdot (\pi_2 - \pi_1);$$

$$P(x_3) = \frac{e_3^{-1}}{\sum\limits_{x_j \in X_1} e_j^{-1}} \cdot \pi_1 + \frac{e_3^{-1}}{\sum\limits_{x_j \in X_2} e_j^{-1}} \cdot (\pi_2 - \pi_1) + \frac{e_3^{-1}}{\sum\limits_{x_j \in X_3} e_j^{-1}} \cdot (\pi_3 - \pi_2);$$

....

$$P(x_{n_o-1})=\frac{e_{n_o-1}^{-1}}{\sum\limits_{x_j\in X_1}e_j^{-1}}\cdot\pi_1+\frac{e_{n_o-1}^{-1}}{\sum\limits_{x_j\in X_2}e_j^{-1}}\cdot(\pi_2-\pi_1)+\ldots+ +\frac{e_{n_o-1}^{-1}}{\sum\limits_{x_j\in X_{n_o-1}}e_j^{-1}}\cdot(\pi_{n_o-1}-\pi_{n_o-2});$$

$$P(x_{n_o})=\frac{e_{n_o}^{-1}}{\sum\limits_{x_j\in X_1}e_j^{-1}}\cdot\pi_1+\frac{e_{n_o}^{-1}}{\sum\limits_{x_j\in X_2}e_j^{-1}}\cdot(\pi_2-\pi_1)+\ldots+ +\frac{e_{n_o}^{-1}}{\sum\limits_{x_j\in X_{n_o-1}}e_j^{-1}}\cdot(\pi_{n_o-1}-\pi_{n_o-2})+\frac{e_{n_o}^{-1}}{\sum\limits_{x_j\in X_{n_o}}e_j^{-1}}\cdot(\pi_{n_o}-\pi_{n_o-1}). \quad (22)$$

It can be easily verified that (22) is a probabilistic distribution on the set $X^{(x_o)}$. Therefore

$$P(x_1)+P(x_2)+P(x_3)+\ldots+P(x_{n_o-1})+P(x_{n_o})=\frac{1}{\sum\limits_{x_j\in X_1}e_j^{-1}}\cdot(e_1^{-1}+e_2^{-1}+..+e_{n_o}^{-1})\cdot\pi_1+$$

$$+\frac{1}{\sum\limits_{x_j\in X_2}e_j^{-1}}\cdot(e_2^{-1}+e_3^{-1}+..+e_{n_o}^{-1})\cdot(\pi_2-\pi_1)+\frac{1}{\sum\limits_{x_j\in X_3}e_j^{-1}}\cdot(e_3^{-1}+..+e_{n_o}^{-1})\cdot(\pi_3-\pi_2)+$$

$$+..+\frac{1}{\sum\limits_{x_j\in X_{n_o-1}}e_j^{-1}}\cdot(e_{n_o-1}^{-1}+e_{n_o}^{-1})\cdot(\pi_{n_o-1}-\pi_{n_o-2})+\frac{1}{\sum\limits_{x_j\in X_{n_o}}e_j^{-1}}\cdot e_{n_o}^{-1}\cdot(\pi_{n_o}-\pi_{n_o-1})=$$

$$=\pi_1+(\pi_2-\pi_1)+(\pi_3-\pi_2)+\ldots+(\pi_{n_o-1}-\pi_{n_o-2})+(\pi_{n_o}-\pi_{n_o-1})=\pi_{n_o}=1.$$

The probabilistic distribution (22) can also be rewritten in a simple recurrent form

$$P(x_1)=\frac{e_1^{-1}}{\sum\limits_{x_j\in X_1}e_j^{-1}}\cdot\pi_1;$$

$$P(x_2)=\frac{e_2^{-1}}{e_1^{-1}}\cdot P(x_1)+\frac{e_2^{-1}}{\sum\limits_{x_j\in X_2}e_j^{-1}}\cdot(\pi_2-\pi_1);$$

$$P(x_3)=\frac{e_3^{-1}}{e_2^{-1}}\cdot P(x_2)+\frac{e_3^{-1}}{\sum\limits_{x_j\in X_3}e_j^{-1}}\cdot(\pi_3-\pi_2);$$

....

$$P(x_{n_o-1})=\frac{e_{n_o-1}^{-1}}{e_{n_o-2}^{-1}}\cdot P(x_{n_o-2})+\frac{e_{n_o-1}^{-1}}{\sum\limits_{x_j\in X_{n_o-1}}e_j^{-1}}\cdot(\pi_{n_o-1}-\pi_{n_o-2});$$

$$P(x_{n_o})=\frac{e_{n_o}^{-1}}{e_{n_o-1}^{-1}}\cdot P(x_{n_o-1})+\frac{e_{n_o}^{-1}}{\sum\limits_{x_j\in X_{n_o}}e_j^{-1}}\cdot(\pi_{n_o}-\pi_{n_o-1}). \quad (23)$$

B. *Determination of Possibility Degrees of Timely Transport Movement Transfer to the Nearest Points*

The real problem, in the solution of which we are interested, occurs when the possibility degrees are not given by experts and the problem exists only in terms of an expert who evaluates $\pi_1\le\pi_2\le\ldots\le\pi_{n_o}=1$.

The problem consists in trying to determine the possibility degrees as a result of generating possibility degrees in a random experiment. Using the results of the preceding section, we can construct a consistent method of generation of possibility degrees.

Let us express the possibility degrees π_i via probabilities $P(X_j)$. From system (23), after algebraic transformations, we obtain

$$\pi_1=\frac{\sum\limits_{x_j\in X_1}e_j^{-1}}{e_1^{-1}}\cdot P(x_1);$$

$$\pi_2=\frac{\sum\limits_{x_j\in X_2}e_j^{-1}}{e_2^{-1}}\cdot P(x_2)+P(x_1);$$

$$\pi_3=\frac{\sum\limits_{x_j\in X_3}e_j^{-1}}{e_3^{-1}}\cdot P(x_3)+P(x_2)+P(x_1); \quad (24)$$

....

$$\pi_{n_o-1}=\frac{\sum\limits_{x_j\in X_{n_o-1}}e_j^{-1}}{e_{n_o-1}^{-1}}\cdot P(x_{n_o-1})+\sum_{j=1}^{n_o-2}P(x_j);$$

$$\pi_{n_o}=P(x_{n_o})+\sum_{j=1}^{n_o-1}P(x_j)=1.$$

Recall that if $i>j$, then $\pi_i\ge\pi_j$. From system (24) we see that if we know the probabilities with which in the experiment described here the points are chosen from $X^{(x_o)}$, then this information can be used for determining the possibility degrees. Therefore if we know how to derive estimates for the probabilities contained in the right-hand parts of the equations of system (24), then we can use these estimates for calculating the degrees of transport movement transfer.

We think that the generation algorithm described below and based on the systematic sampling of level sets is suitable for evaluating the probabilities in (24).

With each point x_i we connect the value T_i, initially equal to zero, which will be equal to the number of occurrences of x_i in the role of the sampling of a point from X_i.

Algorithm 1:

0) Fix the initial point x_o and the set $X^{(x_o)}$.
1) Determine the size of the sampling M (e.g. $M=25$, $M=50$, $M=100$) needed for successful work.
2) Divide the unit interval into M parts of equal length. For example, if $M=50$, we obtain $\{1, 0.98, 0.96, ..., 0.02\}$. Denote this set by S.
3) Choose randomly without replacement an element α from S.

ISBN: 978-1-61804-321-4

4) Ask the expert who determines the possibility degrees of timely point-to-point transport movement transfer to enumerate all the elements (points) from $X^{(x_o)}$, which in his opinion belong to the points of transfer from the initial point x_o corresponding to the chosen value of the level α.
5) If k is the number of elements (points) included in the level set, which is constructed in step 4, then for each occurrence of a new point x_i, for this level we must add $\frac{e_i^{-1}}{\sum_{x_s \in X_k} e_s^{-1}}$ to T_i; $T_i = T_i + \frac{e_i^{-1}}{\sum_{x_S \in X_k} e_S^{-1}}$.
6) Repeat steps 3 – 5 until all $\alpha \in S$ are used.
7) Calculate $P(X_i)$; $P(X_i) = \frac{T_i}{M}$.
8) Arrange the obtained probability estimates in the increasing order and substitute them into (24). Calculate the degrees of possibilities of the set of neighboring points $X^{(x_o)}$.
9) Repeat steps 1 - 8 for each point $x \in I$ and determine all degrees of possibilities in the graph. Form the matrix of transport movement transfer possibilities for all points (customers).

C. Numerical Example

Let $X^{(x_o)} = \{a,\ b,\ c,\ d,\ e,\ f\}$. Suppose that the distances from the initial point x_o to the points of $X^{(x_o)}$ are as follows:

$$e_a = 1{,}5\,km,\ e_b = 2{,}0\,km,\ e_c = 3{,}0\,km,\ e_d = 1{,}5\,km,$$
$$e_e = 3{,}5\,km,\ e_f = 1{,}8\,km.$$

On the basis of experts' knowledge it is assumed that

$$0 < \pi(f) \le \pi(c) \le \pi(a) \le \pi(e) \le \pi(b) \le \pi(d) = 1.$$

Assume that the sampling size is $M = 25$.

Then $S = \{1,\ 0.96,\ 0.92,\ ....,\ 0.8,\ 0.4\}$.

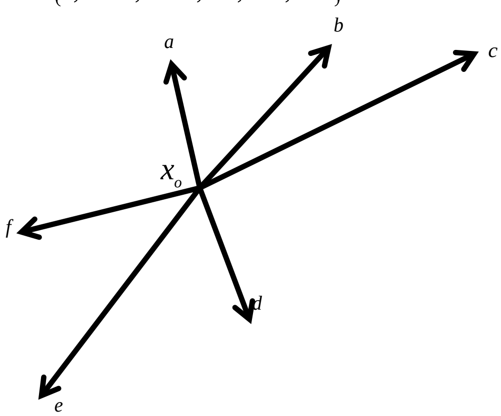

Fig.1. Points in the neighborhood of x_o.

Suppose that, choosing the values of the level α in a random manner, we obtain from the expert the following level sets of nearest points (they can be obtained in the interactive mode):

$X_{0.92} = \{d\}$ $X_{0.04} = \{f, c, a, e, b, d\}$ $X_{0.56} = \{e, b, d\}$
$X_{0.60} = \{e, b, d\}$ $X_{0.68} = \{e, b, d\}$ $X_{1.00} = \{d\}$
$X_{0.36} = \{c, a, e, b, d\}$ $X_{0.24} = \{c, a, e, b, d\}$ $X_{0.28} = \{e, a, c, b, d\}$
$X_{0.32} = \{c, a, e, b, d\}$ $X_{0.76} = \{b, d\}$ $X_{0.16} = \{c, a, e, b, d\}$
$X_{0.72} = \{b, d\}$ $X_{0.52} = \{e, b, d\}$ $X_{0.20} = \{c, a, e, b, d\}$
$X_{0.44} = \{a, e, b, d\}$ $X_{0.40} = \{c, a, e, b, d\}$ $X_{0.48} = \{a, e, b, d\}$
$X_{0.88} = \{b, d\}$ $X_{0.12} = \{c, a, e, b, d\}$ $X_{0.96} = \{d\}$.
$X_{0.08} = \{f, c, a, e, b, d\}$ $X_{0.80} = \{b, d\}$ $X_{0.84} = \{b, d\}$
$X_{0.64} = \{e, b, d\}$

Using the obtained answers of the process of intellectual simulation of the expert's knowledge, we can calculate T for each point.

First we compile the table of the values of $P_{i/k} \equiv P(x_i / X_k) = \frac{e_i^{-1}}{\sum_{x_s \in X_k} e_s^{-1}}$, which depend on two indexes i and k:

TABLE I
THE VALUES OF THE SET $P_{i/k}$

i	k	X_1: $\{f, c, a, e, b, d\}$	X_2: $\{c, a, e, b, d\}$	X_3: $\{a, e, b, d\}$	X_4: $\{e, b, d\}$	X_5: $\{b, d\}$	X_6: $\{d\}$
1	f	0.184					
2	c	0.111	0.135				
3	a	0.222	0.271	0.314			
4	e	0.095	0.116	0.134	0.195		
5	b	0.167	0.206	0.238	0.347	0.431	
6	d	0.221	0.272	0.314	0.458	0.569	1

Then

$$T_a = 2 \cdot 0.222 + 8 \cdot 0.271 + 2 \cdot 0.314 =$$
$$= 3.24 \Rightarrow P(a) = \frac{T_a}{25} = 0.1296$$
$$T_b = 2 \cdot 0.167 + 8 \cdot 0.206 + 2 \cdot 0.238 + 5 \cdot 0.347 + 5 \cdot 0.431 =$$
$$= 6.348 \Rightarrow P(b) = 0.2539$$
$$T_c = 2 \cdot 0.111 + 8 \cdot 0.135 = 1.302 \Rightarrow P(c) = 0.0521$$
$$T_d = 2 \cdot 0.221 + 8 \cdot 0.272 + 2 \cdot 0.314 + 5 \cdot 0.458 + 5 \cdot 0.569 +$$
$$+ 3 \cdot 1 = 11.381 \Rightarrow P(d) = 0.4552$$
$$T_e = 2 \cdot 0.095 + 8 \cdot 0.116 + 2 \cdot 0.134 + 5 \cdot 0.195 =$$
$$= 2.361 \Rightarrow P(e) = 0.0945$$
$$T_f = 2 \cdot 0.184 = 0.368 \Rightarrow P(f) = 0.0147.$$

Substituting the obtained probabilities values into (24), we calculate the degrees of possibilities of a timely transport movement transfer from the point x_o to the points a, b, c, d, e, f:

Let us compile the table of the values of

$\frac{1}{P_{i/i}} = \frac{\sum_{x_s \in X_i} e_s^{-1}}{e_i^{-1}}$ needed for calculation of degrees of possibilities in (24):

TABLE II

THE VALUES OF THE SET $1/P_{i/i}$

$1/P_{1/1}$	$1/P_{2/2}$	$1/P_{3/3}$	$1/P_{4/4}$	$1/P_{5/5}$	$1/P_{6/6}$
5.434	7.407	3.185	5.128	2.320	1

Then we obtain

$$\pi_f = 5.434 \cdot 0.0147 = 0.0798$$
$$\pi_c = 7.407 \cdot 0.0521 + 0.0147 = 0.4006$$
$$\pi_a = 3.185 \cdot 0.1296 + 0.0147 + 0.0521 = 0.4796$$
$$\pi_e = 5.128 \cdot 0.0945 + 0.0147 + 0.0521 + 0.1296 = 0.6810$$
$$\pi_b = 2.320 \cdot 0.2539 + 0.0147 + 0.0521 + 0.1296 + 0.0945 = = 0.8799$$
$$\pi_c = 1 \cdot 0.4552 + 0.0147 + 0.0521 + 0.1296 + 0.0945 + + 0.2539 = 1 .$$

At the end of the example we give the combined probability and possibility data for the points a, b, c, d, e, f .

TABLE III

TRANSPORT MOVEMENT TRANSFER PROBABILITIES AND POSSIBILITIES

i		$P(\cdot)$	$\pi(\cdot)$
1	f	0.0147	0.0798
2	c	0.0521	0.4006
3	a	0.1296	0.4796
4	e	0.0945	0.6810
5	b	0.2539	0.8799
6	d	0.4552	1

And the diagram of the neighboring points of x_o if the ranging of the choice of point was like this: $f \prec c \prec a \prec e \prec b \prec d$.

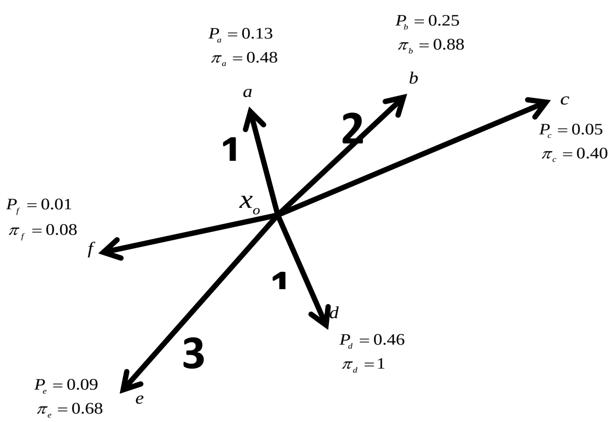

Fig.2. .Diagram of the neighboring points of x_o .

VI. CONCLUSION

A new multiple criteria optimization approach for the solution of the vehicle routing problem is considered. This problem is reduced on the Min-max bi-criteria fuzzy partitioning problem. It should be said that the Monte-Carlo simulation interactive algorithm proposed here does not pretend in any way to the optimality of a solution of the considered problem and is not regarded as a unique possibilistic procedure. But it seems to us that for some experts the method proposed here is more acceptable from the emotional standpoint than the procedure of direct assignment of possibility degrees of timely transport movement transfer to the neighboring points in extreme traffic conditions. This allows such experts to reveal their intellectual activity in the interactive regime of generation of level sets of neighboring points.

ACKNOWLEDGMENT

This work was supported in parts by the International Scientific and Technology Center in Ukraine (STCU), grant No. #5891 and Shota Rustaveli National Scientific Fund (SRNSF) (Georgia) grant No. MTCU/23/4-102/13.

REFERENCES

[1] D.Dubois and H.Prade (1988), “Possibility Theory”. New York: Plenum Press.

[2] D. E. Knuth (2000), “Dancing Links”. Millennial Perspectives in Computer Science, Palgrave, Houndmills, Basingstoke, Hampshire, 187-214.

[3] G. Sirbiladze, B. Ghvaberidze, T. Latsabidze and B. Matsaberidze (2009), “Using a Minimal Fuzzy Covering in Decision-making Problems”, *Information Sciences*, 179, 2022-2027.

[4] G.Sirbiladze, A.Sikharulidze, B. Ghvaberidze and B. Matsaberidze (2011), “Fuzzy-probabilistic Aggregations in the Discrete Covering Problem”. *International Journal of General Systems*, 40(2): 169 -196.

[5] G. Sirbiladze and A. Sikharulidze (2003), “Weighted Fuzzy Averages in Fuzzy Environment, Parts I, II”. *International Journal of Uncertainty, Fuzziness and Knowledge-Based Systems*, 2(2): 139-157, 159-172.

[6] R.E.Steuer (1989), “Multiple Criteria Optimization: Theory: Computation and Application”, J. Wiley.

[7] P. Toth and D. Vigo (2002), “The Vehicle Routing Problem”. Society for Industrial & Applied Mathematics, SIAM, Philadelphia.

[8] J. L. Verdegay (1982), “Fuzzy mathematical programming”, In: M. M. Gupta, E. Sanchez, eds., Fuzzy Information and Decision Processes, Amsterdam.

[9] R. R. Yager (ed.)(1982), “Fuzzy Set and Possibility Theory: Recent Developments”. Pergamon Press, New York.

[10] N. Yaodong (2008), “Fuzzy minimum weight edge covering problem”. *Applied Mathematical Modeling*, 32(7): 1327-1337.

[11] L. A. Zadeh (1965), “Fuzzy Sets”, *Information and Control*, 8, 338-353.

[12] L. A. Zadeh (1978), “Fuzzy Sets as a Basis for the Theory of Possibility.” *Fuzzy Sets and Systems*, 1, 3-38.

New Two-Stage Approach for Bi-criteria Vehicle Routing Problem in Extreme Environment

Bezhan Ghvaberidze, Gia Sirbiladze, Bidzina Matsaberidze and Zurab Modebadze

***Abstract*—**A fuzzy Vehicle Routing Problem is considered in the possibilistic environment. A new criterion – maximization of expectation of reliability for movement on closed routes is constructed. The objective of the research is to implement a two-stage scheme for solution of this problem. Based on the algorithm of preferences on the first stage the sample of so-called rational routes will be selected. On the second stage for the selected rational routes new bi-criteria problem will be solved - minimization of total traveled distance and maximization of reliability of routes. The problem will be stated as a fuzzy-partitioning problem. Two possible solutions of this scheme are considered.

***Keywords*—**Vehicle routing problem, fuzzy partitioning problem, multiple-criteria optimization, possibility theory.

I. Introduction

ROUTE planning problems are among the activities that have the highest impact in logistical planning, transport and distribution because of their effects on efficiency in resource management, service levels, and client satisfaction.

Route distribution planning problems, also known as Vehicle Routing Problems (VRP), have been thoroughly studied in a variety of areas, such as Operations Research, Artificial Intelligence, etc. The standard VRP was originally introduced by Dantzig and Ramser (1959), and is NP–hard, which is a complex combinatorial optimization problem [3]. Several variants of the basic problem have been put forward and strong formulations have been proposed ([24] and others). Most of these problems can be modeled as linear programming problems. The most common solution techniques are exact methods that guarantee finding an optimal solution if it exists. These approaches have also been applied together with numerous heuristics solution techniques developed with enough flexibility in optimization systems and can be adapted to various practical contexts.

B. Ghvaberidze is an Associate Professor with the Department of Computer Sciences, Iv.Javakhishvili Tbilisi State University, 13, University street, 0186 Tbilisi, GEORGIA (e-mail: bezhan.ghvaberidze@tsu.ge).

G. Sirbiladze is a Professor with the Department of Computer Sciences, Iv.Javakhishvili Tbilisi State University, 13, University street, 0186 Tbilisi, GEORGIA (e-mail: gia.sirbiladze@tsu.ge).

B. Matsaberidze is an Assistant Professor with the Department of Computer Sciences, Iv.Javakhishvili Tbilisi State University, 13, University street, 0186 Tbilisi, GEORGIA (e-mail: bidzina.matsaberidze@tsu.ge).

Z. Modebadze is an Assistant Professor with the Department of Computer Sciences, Iv.Javakhishvili Tbilisi State University, 13, University street, 0186 Tbilisi, GEORGIA (e-mail: zurab.modebadze@tsu.ge).

Given that the complex, flexible, and dynamic nature of real logistical planning produces a high degree of uncertainty related to the decision making process, is not always possible to have all of the necessary information available at the onset of the problem. Consequently, the most common scenario provides incomplete or imprecise information of the parameters and variables. The use of fuzzy sets in these situations is very appropriate to build computing systems for resolving and optimizing purposes. The modeling of these problems is complicated at various levels: not only are they difficult to define accurately and need to manage uncertainty, but there is also imprecision in the available information and stated preferences.

A frequent occurrence in real decision-making problems, such as those found in VRP, is the lack of precision and uncertainty in the information available in them. This characteristic complicates the process concerning the definition of their objectives and parameters. Although this type of uncertainty found in the nature of the data and their settings has traditionally been handled by means of probability theory, in most of the cases they cannot be considered random phenomena and, therefore, probability theory cannot be applied successfully, rather we have to apply corresponding fuzzy versions, which are called Fuzzy VRP.

Although there are different stochastic approaches to modeling and solving the VRP in the literature, this is not the case with the proposed approaches from fuzzy set theory [29]. Furthermore, the literature offers very little in terms of modeling VRP proposals, both from the standpoint of the solutions modeled as Fuzzy Mathematical Programming [25], and Fuzzy VRP (FVRP). Specifically, if we look at the FVRP models in the literature, the majority only assume vagueness for some of the following elements that are described in the model: a) Fuzzy demands (to be collected): customer demand is a imprecise variable and 2) Fuzzy times: service time and travel time can be imprecise variables.

The first problem deals with the demand vector of each client's ordered goods. Planning the ordered quantity by the clients is difficult to establish with sufficient notice and precise form, therefore we do not have access to a specific quantity. In other words, the information about vehicle demand at some nodes is often not precise enough. Thus, there is often imprecision regarding the amount of demand at some nodes. This FVRP with fuzzy customer demand was first instructed by Teodorović and Kikuchi [23]. In this paper, they treated the travel time and the transportation costs between

ISBN: 978-1-61804-321-4

two nodes in a network as fuzzy numbers. They modified the Clarke and Wright algorithm where travel times in a network are treated as fuzzy numbers. Later, Teodorović and Pavković [22] solved a VRP when demand at the nodes is imprecise and is represented by a triangular fuzzy number.

The model is based on the heuristic "sweeping" algorithm, which uses fuzzy approximate reasoning procedures to decide whether to include a node in the route. In first uses the approximate reasoning algorithm to calculate the preference index. Once the membership function of the preference index has been determined, defuzzification must take place. In recent years, these same authors have proposed solutions to this problem [10], [11], where actual demand value is known only after the visit to the node. Their solution combines Bee and Ant systems with rules based on fuzzy logic. The paper [9] has recently appeared which considers the VRP with imprecise demand at node. It uses the approximate reasoning algorithm to determine the preference strength to send the vehicle to next node, and the improved sweeping algorithm with vehicle-coordinated strategy to determine a set of vehicle routes that minimizes costs.

The second problem, (fuzzy times in both service and travel) is characterized by other pieces of information that are increasingly imprecise, these are concerning the daily circumstances found in routing networks and traffic. In these cases service time, time windows and travel time are expressed as fuzzy numbers.

In [21] the travel time based on the fuzzy mathematical model of the VRP takes the time window as a fuzzy variable. Information entropy and the path chosen by the use of random disturbance control strategy to the Ant algorithm is used to the vehicle routing problem with fuzzy travel time.

Reference [5] focuses on modeling and solution of the dynamic VRP with time-dependent and fuzzy travel time. A model of this problem is set up based on fuzzy service times of the customer, its demand and its time windows, which is regarded and ordering as a triangular fuzzy number. A hybrid genetic algorithm, which is seasoned with the model and combined with the ant colony algorithm, is presented.

In [6] the authors present a model of the real world vehicle routing and dispatching problem. The time-dependent and fuzzy travel speeds are introduced into the model. A dispatching period is divided into some time slices and each time slice is designs a triangular fuzzy speed. The method of comparing two triangular fuzzy numbers is applied to check whether customers' time windows are satisfied. A hybrid intelligent approach combining a genetic algorithm and an ant colony algorithm is proposed for solving the dispatching model.

In [8] the author considers the VRP with time window, assuming that the travel times cannot be precisely known, but can be regarded as fuzzy variables. Since the travel times are fuzzy variables, every customer will be visited at a fuzzy time. Credibility is introduced as a measure of confidence in the constraints, so that, it ensures that all customers are visited within their time windows with a confidence level, then following Chance Constraint Programming and also a hybrid intelligent algorithm by integrating fuzzy simulation and GA to solve the VRP.

All of the above VRP can be formalized as problems of combinatorial optimization. These problems in their most general form have integer LP formulations, based on the proposal given by Bodin et al. [2].

In general, fuzzy optimization approaches presented above, can be divided into four different types of problems. Two of these problems include an imprecision in the objective function(s), such as the case with fuzzy goals and the case with fuzzy costs. The remaining two problems consider fuzzy comparison in the constraints and in the coefficients of the technological matrix. In addition The fifth problem, the general fuzzy problem, could be studied in which all of the parameters will be subject to fuzzy considerations. In practice, the search for optimal solutions to FVRP can be done with the following approaches. The simplest approach applies procedures for the fuzzification and defuzzification of variables. It transforms the imprecise information in fuzzy parameters and uses procedures that integrate fuzzy arithmetic to obtain fuzzy solutions. The fuzzy solution is then transformed into a crisp one using some known formulations. This approach may also be used for the introduction of sophisticated fuzzy rules in the decision-making processes to improve their quality. Linguistic variables could be used to facilitate the incorporation of "intelligent" procedures as automatic reasoning, adaptive control or automatic learning.

It should be noted that the criteria and constraints in approaches presented here use only fuzzy set theory, as an instrument to describe imprecision of expert data and there is no research which would consider monotone measures of reliability and possibility of information uncertainty [4],[13],[20],[26] which is the second pole of expert information. To be more specific, the weak side of these studies is that their authors introduce fuzzy imprecision, connected with expert judgment but don't use such well-known instruments for aggregation of fuzzy data as: Choquet Integral, Sugeno Integral, Dempster's extremal expectations, OWA type operators ([4],[13],[20],[26],[27]) and others. The reason is understandable - such aggregations require the use of monotone measures of the second pole of expert information – uncertainty. Obviously, the use of such aggregation instruments in FVRP models would make them more reliable, because the expert judgment on the difficulty of movement on the routes in extreme situations would be also considered. This judgment can be represented by the levels of possibility of movement.

The timely distribution of goods to different customers is much complicated in extreme and difficult situations, such as: roads with overloaded traffic, public demonstrations and strikes, slippery, snowy roads or roads with less visibility, damaged roads because of natural disasters, earthquakes, and other causes, etc. In such case, it is important to assess the reliability and possibility levels of movement on routes. Of course, this changes the movement time as well. It becomes uncertain. Using the software for route planning in stationary environment has less sense in such cases for distribution companies. They should use the intelligent support system for optimal route planning in complex and extreme situations, which would enable experts to introduce corrections to the route planning problem based on experts' evaluations. First of all they will consider the criterion of reliability of route together with other objective information. In such technologies experts become involved in data gathering process, and create the possibility levels of movement (travel) between customers based on embedded knowledge engineering methods and algorithms.

Let us denote these possibility levels by $\| \pi_{ij} \|$, where π_{ij} is a possibility (conditional) level [4] of moving from i-th customer to j-th customer. Thus, expert knowledge engineering serves the optimal route planning in extreme situations. We plan to develop a control system based on fuzzy statistics to evaluate this possibility levels using results of our research [12],[13].

Possibility theory was proposed by L.A. Zadeh in 1978 [29] and developed by D. Dubois and H. Prade in 1988 [4]. Since the 1980s, the possibility theory has become more and more important in the decision and optimization field and several methods have been developed to solve possibilistic programming problems ([1],[8],[12]-[18],[25],[28] and others). Our aim is to create possibilistic environment of knowledge engineering for optimal vehicle routing problem when movement on roads is difficult. Based on this and other objective information the possibilistic criterion is developed – called the reliability of moving on closed routes.

The systems approach and analysis play determining role in the vehicle routing problem (VRP) ([24] and others). Here we present a new vision of the fuzzy vehicle routing problem (FVRP), which is different from the approaches given in other researches. This new problem is connected with difficulties of optimal routing of vehicles in different extreme situations.

II. Construction of bi-criteria optimization problem

We consider the following problem of optimal routing of vehicles as a Main problem in extreme situations. Let the set of geographical points (called customers later on) $I = \{1, 2, \dots, n+1\}$ be given, where $n+1$-th node is depot. Other customers are supplied from depot by vehicles with uniform goods. The demand of goods from customers is known, as well as maximum load and mileage of the vehicles. The problem is the following (first criterion): *It is necessary to deliver the demanded goods to customers by vehicles in such way that total distance traveled by vehicles is minimal.* It is meant that the demand of goods by each customer is much less than maximum load of vehicles.

Suppose, that $C = \| c_{ij} \|$, $i, j \in I$ is a matrix of positive real numbers and represents the distances between customers; Q and D are real numbers – the constraints of load and mileage of vehicles. P_i, $i = 1, 2, \dots, n$ are also real numbers and represent the demand for goods by i-th customer $1 \le P_i < Q$, $i = 1, 2, \dots, n$.

We have to find such closed set of routes $\{ M_k \}$, $k = 1, 2, \dots, m_j$, $M_k = \{ n+1, i_1^k, \dots, i_{\ell_k}^k, n+1 \}$, $i_j^k \in \{1, 2, \dots, n\}$, $j = 1, \dots, \ell_k$, $1 \le \ell_k \le n$ (m and ℓ_k are not fixed in advance), that satisfy the constraints

$$\bigcup_{k=1}^{m} M_k = I\,; \quad M_k \cap M_q = \{ n+1 \},$$

$$k, q \in \{1, 2, \dots, m\}, \quad k \ne q\,; \quad \sum_{j=1}^{\ell_k} P_{i_j^k} \le Q\,; \tag{1}$$

$$c_k = c_{n+1,\, i_1^k} + c_{i_{\ell_k}^k,\, n+1} + \sum_{j=1}^{\ell_k - 1} c_{i_j^k,\, i_{j+1}^k} \le D\,, \quad k = 1, 2, \dots, m\,;$$

and that have minimal total distance (objective function, first criterion)

$$\sum_{k=1}^{m} c_k = \sum_{k=1}^{m} \left(c_{n+1,\, i_1^k} + c_{i_{\ell_k}^k,\, n+1} + \sum_{j=1}^{\ell_k - 1} c_{i_j^k,\, i_{j+1}^k} \right). \tag{2}$$

Presented problem corresponds to some mathematical model of above presented problems, connected with distribution of uniform goods in small-sized portions between different customers. It is a complex combinatorial optimization problem and is known as NP-hard [19].

The difficulty of movement between different customers and other problems cause the uncertainty of time of movement. Suppose, that the expert evaluation of time for moving from i-th customer to j-th customer is represented by nonnegative normalized fuzzy-triangular numbers $\tilde{t}_{ij} = \left(t_{ij}^{(1)}, t_{ij}^{(2)}, t_{ij}^{(3)} \right)$ ([4], etc.), the membership function of which is defined by formula (3).

$$\mu_{\tilde{t}_{ij}}(t) = \begin{cases} 0, & t \le t_{ij}^{(1)}; \\ \dfrac{t - t_{ij}^{(1)}}{t_{ij}^{(2)} - t_{ij}^{(1)}}, & t_{ij}^{(1)} < t \le t_{ij}^{(2)}; \\ \dfrac{t_{ij}^{(3)} - t}{t_{ij}^{(3)} - t_{ij}^{(2)}}, & t_{ij}^{(2)} < t \le t_{ij}^{(3)}; \\ 0, & t > t_{ij}^{(3)}. \end{cases} \tag{3}$$

Then the movement time on closed route M_k will also be fuzzy-triangular number:

$$\tilde{t}_k = \sum_{j=1}^{\ell_k - 1} \tilde{t}_{i_j^k,\, i_{j+1}^k} + \tilde{t}_{n+1,\, i_1^k} + \tilde{t}_{i_{\ell_k}^k,\, n+1}\,. \tag{4}$$

In usual conditions c_k and $\tilde{t}_k$ are identical, but in our case $\tilde{t}_k$ shouldn't depend much on c_k. In extreme situations the reliability of moving on route M_k is determined by smallness of $\tilde{t}_k$. So we introduce the following parameter normalized in [0,1] as a measure of reliability of route M_k:

ISBN: 978-1-61804-321-4

$$\tilde{\delta}_k = \frac{1}{1+\left(\tilde{t}_k\right)^{\gamma_1}}. \tag{5}$$

In addition, we introduce the objective weight of moving from *i*-th to *j*-th customer on route M_k :

$$w_{ij}^{(k)} = \frac{(1/c_{ij})^{\gamma_2}}{\sum_{\mu,\nu}(1/c_{\mu\nu})^{\gamma_2}}, \quad i,j,\mu,\nu \in M_k. \tag{6}$$

γ_1 and γ_2 are positive numbers, selected using the principle of closeness to experimental data. We have to consider $w_{ij}^{(k)}$ weights and π_{ij}^0 possibilities, when constructing the weighted possibility level of movement on route M_k :

$$\pi_k^0 = \sum_{j=1}^{\ell_k - 1} w_{i_j^k, i_{j+1}^k}^{(k)} \cdot \pi_{i_j^k, i_{j+1}^k} + w_{n+1, i_1^k}^{(k)} \cdot \pi_{n+1, i_1^k} + w_{i_{\ell_k}^k, n+1}^{(k)} \cdot \pi_{i_{\ell_k}^k, n+1}, \tag{7}$$

Suppose $\overline{M} = \{M_k\}_{k=1}^m$ is a set of some closed routes, satisfying the (1)-(2) constraints of the Main Problem. To construct the reliability measure of routes $\{M_k\}_{k=1}^m$ we use Choquet integral ([4], [13] and others), which condenses the reliabilities $\tilde{\delta}_k$ of routes M_k, $k = 1,2,\ldots,m$ and their possibility distribution $\pi_k = \dfrac{\pi_k^0}{\max\limits_{k=1,m} \pi_k^0}$ on the set $\overline{M} = \{M_k\}_{k=1}^m$. As known, this later creates possibility uncertainty with possibility measure: $Pos : 2^{\overline{M}} \to [0,1]$

$$Pos\left(\left\{M_{j_1}, M_{j_2}, \ldots, M_{j_p}\right\}\right) = \max_{j=1,p} \pi(M_{j_\nu}) = \max_{j=1,p} \pi_{j_\nu}, \tag{8}$$

if $\left\{M_{j_1}, M_{j_2}, \ldots, M_{j_p}\right\} \subseteq \overline{M}$.

In fuzzy statistics the Choquet integral defined on finite set is known as Monotone Expectation (ME) [18]. Here we introduce the notion of Monotone Expectation of reliability of the set $\overline{\mathrm{M}}$ of closed routes with respect to possibility measure:

$$\begin{aligned} ME\left(\tilde{\delta}_1, \tilde{\delta}_2, \ldots, \tilde{\delta}_m\right) &\overset{\Delta}{=} \int_0^1 Pos\left(\left\{M_j \in \overline{M} / \tilde{\delta}_j \geq \alpha\right\}\right) d\alpha = \\ &= \sum_{i=1}^m \Big[Pos\left(\left\{M_{j(1)}, M_{j(2)}, \ldots, M_{j(i)}\right\}\right) - \\ &\qquad - Pos\left(\left\{M_{j(1)}, M_{j(2)}, \ldots, M_{j(i-1)}\right\}\right) \Big] \cdot \tilde{\delta}_{j(i)} = \\ &= \sum_{i=1}^m \left[\max_{j=1,i} \pi_{j(i)} - \max_{j=1,i-1} \pi_{j(i-1)} \right] \cdot \tilde{\delta}_{j(i)}, \end{aligned} \tag{9}$$

where $\pi_{j(0)} = 0$; $Pos\left(\left\{M_{j(0)}\right\}\right) \equiv 0$; $\tilde{\delta}_{j(1)} \geq \tilde{\delta}_{j(2)} \geq \cdots \geq \tilde{\delta}_{j(m)}$, – is the permutation of $\left\{\tilde{\delta}_1, \tilde{\delta}_2, \ldots, \tilde{\delta}_m\right\}$ which decreasingly orders the reliability levels. Let's denote: $P^{(i)} \equiv \max\limits_{\nu=1,i} \pi_{j(\nu)} - \max\limits_{\nu=1,i-1} \pi_{j(i-1)}$. It can be easily checked that $\left\{P^{(i)}\right\}_{i=1}^m$ values have properties of probability distribution on $\overline{M}$. In this case (9) can be written as:

$$ME\left\{\tilde{\delta}_1, \tilde{\delta}_2, \ldots, \tilde{\delta}_m\right\} = \sum_{i=1}^m P^{(i)} \cdot \tilde{\delta}_{j(i)}, \tag{10}$$

This is a second criterion – *maximization of monotone expectation of reliability of movement on the closed routes* $\{M_k\}_{k=1}^m$. As in previous case (formula (7)) we plan to engineer new aggregation instruments in possibility theory.

The objective of our research is planned to be implemented to a two-phase scheme of solving bi-criteria problem.

Phase I: Allowed closed routes (which satisfy (1)-(2) constraints) should also satisfy additional criteria: 1) The time of movement on closed route M_k must not exceed some maximum limit $\tilde{t}_k \leq \tilde{t}_{\max}$, and 2) The possibility level of movement on route M_k must exceed some minimum level: $\pi_k \geq \pi_{\min}$ ($\pi_{\min}$ and $\tilde{t}_{\max}$ are predefined by expert group based on their needs).

Among all allowable closed routes (in case of large dimension of problem, when the number of allowable routes is in order of $10^4 - 10^6$) during the first phase the sample of so-called "promising" routes are selected (see Appendix A)

$$\overline{M} = \left\{M_1, M_2, \ldots, M_q\right\},$$

which satisfy above criteria (the number of such promising routes should be in order of 10^3 –due to limitations of second phase solutions). Note that this phase will be necessary only in cases when problem's dimension is large.

Phase II: For the promising routes $\overline{M} = \left\{M_1, M_2, \ldots, M_q\right\}$ selected during 1st phase, new bi-criteria problem will be solved. The two criteria are minimization of total traveled distance and maximization of reliability of routes. The problem will be stated as a fuzzy-partitioning problem (FPP). Our further discussion concerns to a fuzzy partitioning problem. Some questions of FPP with possibility-probability uncertainty have already been investigated by the authors of this work ([12],[16] and others). Now we consider a new variant of a presentation of the optimal FPP for the solution of the FVRP presented here.

Let $A = \| a_{ij} \|_{n \times q}$ be an incidence matrix, and $a_{ij} = 1$ if route M_j goes through customer i and $a_{ij} = 0$ otherwise.

All subset of routes $M' = \left\{M_{j_1}, M_{j_2}, \ldots, M_{j_p}\right\} \subseteq \overline{M}$ is presented by means of its characteristic vector, which has a component $x_j = 1$ if the route M_j is contained in the subset M' and $x_j = 0$ otherwise. As determined in previous section, each route M_j has the level of possibility of movement on it - π_j, level of reliability $\tilde{\delta}_j$ and, of course, the total distance of route C_k. Then we create the distance vector $\overline{C} = \{c_1, c_2, \dots, c_q\}$ of route $\overline{M}$; $\tilde{\delta} = \{\tilde{\delta}_1, \tilde{\delta}_2, \dots, \tilde{\delta}_q\}$ – is the vector of reliabilities; $\overline{\pi} = \{\pi_1, \pi_2, \dots, \pi_q\}$ – the vector of possibilities (possibility distribution on $\overline{M}$); Also $\overline{x} = \{x_1, x_2, \dots, x_q\} \in \{0, 1\}^q$ – Boolean vector. Then criteria (2) in partitioning problem sounds this way: the set of routes M' is called the partitioning of sets of customers I (otherwise we can say that for any customer from I there exist only one route from M' that travels through that customer, except the depot, which is the starting and ending point of all routes), if

$$\bigcup_{\nu=1}^{p} M_{j_\nu} = I, \; M_{j_\nu} \cap M_{j_\mu} = \{n+1\}, \; j_\nu, \; j_\mu \in \{j_1, \dots, j_p\}. \quad (11)$$

The partitioning condition is similar to the following system of linear equations:

$$A\overline{x} = \overline{e}, \quad (12)$$

where $\overline{e} = (1,1,...,1)$ is a vector consisting from 1s. Note that because of 1st phase, the partitioning routes satisfy the following conditions: if $M_k \in M'$, then

$$\sum_{j=1}^{\ell_k} P_{i_j k} \le Q, \; c_k \le D, \; \pi_k \ge \pi_{\min}, \; \tilde{\delta}_k \ge 1 \big/ \left(1 + (\tilde{t}_{\max})^{\gamma_2}\right). \quad (13)$$

Because of (1)-(2), for each partitioning M′ we construct the objective function for the total distance of route:

$$\sum_{i=1}^{q} c_i x_i, \quad A\overline{x} = \overline{e} \quad (14)$$

and based on (10) – the objective function of their reliability:

$$\sum_{i=1}^{q} P^{(i)} \cdot \tilde{\delta}_{j(i)} x_{j(i)}; \quad (15)$$

Therefore, we consider the Min-max bi-criteria fuzzy-partitioning problem:

$$f_1 \equiv \sum_{i=1}^{q} c_i x_i \Rightarrow \min \quad (16)$$

minimization of the distances of routes in partitioning and

$$f_2 \equiv \sum_{i=1}^{q} P^{(i)} \cdot \tilde{\delta}_{j(i)} x_{j(i)} \Rightarrow \max \quad (17)$$

maximization of monotone expectation of reliability of routes in partitioning with linear constraints

$$A\overline{x} = \overline{e}, \quad x_i \in \{0, 1\}. \quad (18)$$

Note that the monotone expectation of reliability of routes in partitioning is triangular fuzzy number (TFN) and maximization of (17) criterion must be understood as fuzzy-maximization.

For solving the bi-criteria problems (16)-(18), two approaches will be considered in our future investigations:

1). The method of compromise will be created for bi-criteria problems (16)–(18) based on the idea of ordering of criteria.

2). Scaling of (16)–(18) bi-criteria problems and reducing the problem to classical partitioning problem $f = \lambda f_1 + (1-\lambda) f_2$, $(0 < \lambda < 1)$ with one criterion. The exact solution of the classic partitioning problem will be realized by D.Knuth Algorithm of Dancing Links-X (DLX) [7].

III. Constructing rational routes for vehicles between the points of consumption

Today NP-hard problems are usually solved using approximate algorithms (including heuristic ones), which are based on various reasonable considerations and allows you to find "good" solution in acceptable time.

Following this trend, we propose the two-step approach to solving the VRP.

At the first stage admissible (rational) routes are constructed. In the second stage - from the constructed rational routes optimal (in the sense of problem statement) ones are chosen. This is done by solving the minimum partitioning problem (MPP).

In practice, building all admissible routes in the first stage of the algorithm is impossible because of their large number in real problems. Therefore we are considering only a limited number of promising routes based on heuristic arguments.

In the algorithms described below, construction of rational routes is performed by the analysis of individual consumer demand values, their geographical location and defined limits on the maximum route length and load capacity of the vehicles.

A. Problem Formulation

Let's consider the matrix of positive real numbers $C = \{c_{i,j}\}, i, j \in I$, $I = \{1, 2, \dots, n+1\}$; and let D, Q and p_i, $i = 1, 2, \dots, n$ be the predefined positive integers. It is assumed, that $1 \le p_i < Q$, $i = 1, 2, \dots, n$.

The task is to find a set of closed routes $\{M_k\}$, $k = 1, 2, \dots, m$, where $M_k = \{n+1, i_1^k, \dots, i_{l_k}^k, n+1\}$, $i_j^k \in \{1, 2, \dots, n\}$, $j = 1, \dots l_k, 1 \le l_k \le n$ (M and l_k are not fixed in advance), satisfying following conditions:

$$\bigcup_{k=1}^{m} M_k = I; \; M_k \cap M_q \supseteq \{n+1\}, k, q \in \{1, \dots m\}, k \ne q$$

$$\sum_{j=1}^{l_k} p_{i_j^k} \le Q;$$

At the first stage the so called “individual route” is built for each point i, which in addition to i includes following points: points near the point i, points near the depot (the base), points on the shortest route from the base to the point i, and the restrictions on the maximum load capacity and range of the vehicle are satisfied.

B. The Algorithm

The notation:

C - the matrix of distances between points, having size $(n+1)\times(n+1)$:

$$c_{ij} = \begin{cases} \text{the distance between the points } i \text{ and } j, \\ \quad \text{if the points are neighbors} \\ \infty, \text{if the points are not neighbors} \end{cases}$$

Z - the matrix having size $(n+1)\times(n+1)\times n$ for holding shortest routes between the points;

n_1 - maximum number of rational routes (in practice $n_1 = 5n$ is recommended);

L - the vector having dimension n_1 for holding the lengths of the routes;

P - the vector having dimension n for holding the demands of the points;

Z_0 - the matrix having size $(n+1)\times n_1$ for holding rational routes;

R - the helper vector having size n. If $R_i = 1$, it is prohibited to include the i-th point in the generated route;

Y - the helper vector having size n. Used to generate the next route;

Q - the maximum load capacity of the vehicle;

D - the maximum distance range of the vehicle;

Without loss of generality let’s assume that the points are numbered in increasing consumption needs.

Step 1. Set

$$Z_0(\alpha,\beta) = 0, \alpha = 1,\dots,n, \beta = 1,\dots,n_1; L(\alpha) = 0, \alpha = 1,\dots,n_1,$$
$$R(\alpha) = 0, \ \alpha = 1,\dots,n;$$

Step 2. Using Floyd’s algorithm, transform C in the matrix of shortest routes (at the same time computing Z). Set $i = 1; k = 0;$

Step 3. Set $L(k+1) = C(n+1,i); Y(\alpha) = 0, \alpha = 1,\dots,n; i_1 = i;$

$$k_p = i_1; B_1 = Q;$$

Step 4. Set: $Y(i_1) = 1, B_1 = B_1 - P(i_1); R(i_1) = 1;$

Step 5. If $P(\alpha) > B_1$, for all $\alpha \in \{1,2,\dots,n\}$, $R(\alpha) = 0$, then go to the step 8, else find index k_1, satisfying $P(k_1) \le B_1$ and $P(k_1+1) > B_1$ and set $R(j) = 1, \ j = k_1+1,\dots,n$;

Step 6. If for all $j = 1,\dots,n$ we have $R(j) = 1$, then go to the step 8; else build the subset of points $M \subset \{1,\dots,k_1\}$, satisfying condition $j \in M$ if and only if $R(j) = 0$ and j is on the shortest route from the point k_p to the point *n+1* (depot).

If $M = \varnothing$, then for all points α, satisfying $R(\alpha) = 0$, find the nearest point to the k_p. Let’s consider it’s number to be *j*. Set $i_1 = j$;

If $M \ne \varnothing$, then for the points of *M* select the nearest point *j* to the k_p and set $i_1 = j$;

Step 7. If $L(k+1) + C(k_p,i_1) + C(i_1,n+1) \le D$, then set $L(k+1) = L(k+1) + C(k_p,i_1); \ k_p = i_1$ and go to the step 4, else build the set $N = \{n+1,\alpha_{j_1},\dots,\alpha_{j_s},i_1,n+1\}$, where α_{j_β} are the indexes for which $Y(\gamma) = 1, \gamma = 1,\dots,n$ (e.g., if Y={0,0,1,1,0,1,0}, then $N = \{9,3,4,6,i_1,9\}$); Build the matrix by deleting the columns and the rows from the matric *C*, not included in N and solve the traveler salesman problem to get the matrix, that is to find the sequence $\pi(n+1),\pi(\alpha_{j_1}),\dots,\pi(\alpha_{j_s}),\pi(i_1),\pi(n+1)$, for which

$$C\big(\pi(n+1),\pi(\alpha_{j_1})\big) + \sum_{t=1}^{s-1} C\big(\pi(\alpha_{j_t}),\pi(\alpha_{j_{t+1}})\big) + C\big(\pi(\alpha_{j_s}),\pi(i_1)\big) + $$
$$+ C\big(\pi(i_1),\pi(n+1)\big)$$

is minimal.

Consider $D_{\min}$ is the minimum, if $D_{\min} \le D$, then find the point *j* following the point *n+1* on the route of the salesman (it’s clear, that $j = \pi(\alpha_{j_1})$, and after setting $i_1 = j; \ L(k+1) = D_{\min} - C(i_1,n+1); k_p = i_1$, go to the step 4.

Step 8. Similarly to the method described above for the set $N = \{n+1,\alpha_{j_1},\dots,\alpha_{j_s},n+1\}$ build the matrix and solve the traveler salesman problem. Consider $D_{\min}$ is the length of the route of salesman. Set $L(k+1) = D_{\min}$;

Step 9. If for some $\beta \in \{1,2,\dots,k\}$ and for all $\alpha = 1,2,\dots,n$ we have $Y(\alpha) = Z_0(\alpha,\beta)$ (*Y* coincides with at least one of the previously constructed routes), then go to the step 10, else set $k = k+1; Y(\alpha) = Z_0(\alpha,\beta)$, $\alpha = 1,2,\dots,n$;

Step 10. Set $R(\alpha) = 0, \alpha = 1,\dots,n; i = i+1$, if $i \le n$, then go to the step 3, else stop (finish).

C. Algorithms for expanding found rational routes of vehicles between the points of consumption

Algorithm 1[1]

Step 1. Set $j = k+1; l_p = 1;$

Step 2. Set $R_1(\alpha) = Z_0(\alpha,l_p), \alpha = 1,\dots,n;$

[1] The notation of the basic algorithm is used.

ISBN: 978-1-61804-321-4

Step 3. Find the index i_1 satisfying $i_1 = \min\{\alpha | R_1(\alpha) = 0, \alpha = 1,\dots,n\}$. For building the route Y perform steps 3-8 **of basic algorithm** when $i = i_1$; $k = j-1$; $R(\alpha) = R_1(\alpha), \alpha = 1,\dots,n$;

Step 4. If for some $\beta \in \{1,\dots, j-1\}$ and for all $\alpha = 1,\dots,n$ we have $Y(\alpha) = Z_0(\alpha,\beta)$, then go to the step 6; Else set $Z_0(\alpha, j) = Y(\alpha), \alpha = 1,\dots,n;$

Step 5. Set $j = j+1$; if $j > n_1$, then stop (finish);

Step 6. Construct the new vector R_1: for all $\alpha = 1,\dots,n$ set

$$R_1(\alpha) = \begin{cases} 0, if\ R_1(\alpha) = 0\ u\ Y(\alpha) = 0 \\ 1,\ for\ other\ cases \end{cases};$$

Step 7. If there exists the index α, satisfying $R_1(\alpha) = 0$, then go to the step 3; else set $l_p = l_p + 1$;

Step 8. If $l_p \le k$ then go to the step 2, else stop (finish).

Algorithm 2

Step 1. Set $j = 1; l_p = 0$;

Step 2. Set $Y(\alpha) = 0, \alpha = 1,\dots,n; Y(j) = 1;$

Step 3. If for some $\beta \in \{1,\dots,k+l_p\}$ and for all $\alpha = 1,\dots,n$ we have $Y(\alpha) = Z_0(\alpha,\beta)$, then go to the step 5;

Else set $l_p = l_p + 1;$ $Z_0(\alpha, k+l_p) = Y(\alpha), \alpha = 1,\dots,n;$ $L(k+l_p) = 2C(j, n+1)$;

Step 4. If $k + l_p = n_1$, then stop (finish);

Step 5. Set $j = j+1$; if $j \le n$, then go to the step 2;

Step 6. Set $j = k + l_p + 1; l_p = 1; i_2 = 1;$ $R_1(\alpha) = 0, \alpha = 1,\dots,n;$

Step 7. Construct the new vector R_1: for all $\alpha = 1,\dots,n$ set

$$R_1(\alpha) = \begin{cases} 0, if\ R_1(\alpha) = 0\ u\ Z_0(\alpha, l_p) = 0 \\ 1,\ for\ other\ cases \end{cases};$$

Step 8. If there exists the index j_1 satisfying $j_1 = \min\{\alpha | R_1(\alpha) = 0, \alpha = i_2,\dots,n\}$, then perform the steps 3-8 of **basic algorithm** when $i = j_1; k = j-1;$ $R(\alpha) = R_1(\alpha), \alpha = 1,\dots,n$;

Else go to the step 11;

Step 9. If for some $\beta \in \{1,\dots, j-1\}$ and for all $\alpha = 1,\dots,n$ we have $Y(\alpha) = Z_0(\alpha,\beta)$, then set $i_2 = j_1 + 1$ and go to the step 5;

Else set $Z_0(\alpha, j) = Y(\alpha), \alpha = 1,\dots,n;$

Step 10. Set $j = j+1;$ $i_2 = j_1 + 1$. If $j > n_1$, then stop (finish). Else go to the step 8;

Step 11. If $R_1(\alpha) = 1, \alpha = 1,\dots,n$, then set $R_1(\alpha) = 0,$ $\alpha = 1,\dots,n;$

Step 12. Set $l_p = l_p + 1$. If $l_p \ge k$, then set $i_2 = 1$ and go to the step 7.

Else stop (finish).

IV. Conclusion

A new multiple criteria fuzzy optimization approach for the solution of the optimal vehicle routing problem is considered. This problem is reduced on the Min-max bi-criteria fuzzy partitioning problem. Consequently, Fuzzy Expectation Programming Problems is constructed. Two-phase scheme is used for the numerical solution of the FVRP. The algorithms for the construction of rational routes are presented. Numerical experiments and results will be presented in our future works.

Acknowledgment

This work was supported in parts by the International Scientific and Technology Center in Ukraine (STCU), grant No. #5891 and Shota Rustaveli National Science Foundation (SRNSF) (Georgia) grant No. MTCU/23/4-102/13.

References

[1] R. E. Bellman and L. A. Zadeh (1970), “Decision making in a fuzzy environment”, *Management Science*, 17(B)(4), 141-164.

[2] B. Bodin et al. (1983), “Routing and scheduling of vehicles and crews: The state of the art”. *Computers and Operations Research* 10, 63-211, MathSciNet.

[3] G.B. Dantzig and R.H. Ramser (1959), “The truck dispatching problem”. *Management Science*, 6:80-91.

[4] D. Dubois and H. Prade (1988), “*Possibility theory: An approach to computerized processing of uncertainty*”. Kluwer.

[5] L. Hong and M. Xu (2008), “A model of MDVRPTW with fuzzy travel time and time-dependent and its solution”. *In proceedings, IEEE Fifth International Conference on Fuzzy Systems and Knowledge Discovery*.

[6] L. Hong and M. Xu (2008), “Real Vehicle Routing and Dispatching with Dynamic Fuzzy Travel Times”. *In proceedings, IEEE Second International Conference on Genetic and Evolutionary Computing.*

[7] D. E. Knuth (2000), “*Dancing Links*”. Millennial Perspectives in Computer Science, Palgrave, Houndmills, Basingstoke, Hampshire, 187-214.

[8] B. Liu (2002), “*Theory and practice of uncertain programming*”. Physica-Verlag.

[9] C.S. Liu and M.Y. Lai (2009), “The vehicle routing problem with uncertain demand at nodes”. *Transportation Research Part E: Logistics and Transportation Review*, 5(4), 517-524.

[10] P. Lucić and D. Teodorović (2003), “Vehicle routing problem with uncertain demand at nodes: The Bee System and fuzzy logic Approach”. *In Fuzzy Sets Based Heuristics for Optimization*, Springer-Verlag, 67-82.

[11] P. Lucić and D. Teodorović (2007), “The fuzzy ant system for the vehicle routing problem when demand at nodes is uncertain”. *Journal on Artificial Intelligence Tools (IJAIT)*, 16(5), 751-770.

[12] G. Sirbiladze, B. Ghvaberidze, T. Latsabidze and B. Matsaberidze (2009), “Using a Minimal Fuzzy Covering in Decision-making Problems”. *Information Sciences*, 179, 2022-2027.

[13] G. Sirbiladze (2013), “Extremal Fuzzy Dynamic Systems: Theory and Applications”. *IFSR International Series on Systems Science and Engineering*, Vol. 28, 1st Edition. Springer, 396p.

[14] G. Sirbiladze (2006), “Modeling of Extremal Fuzzy Dynamic Systems. Part V: Optimization of Continuous Controllablale Extremal Fuzzy Processes and the Choice of Decisions”. *International Journal of General Systems*. 35, 5, 529-554.

[15] G. Sirbiladze (2010), “Fuzzy Dynamic Programming Problem for Extremal Fuzzy Dynamic Systems”. In *Fuzzy Optimization: Recent*

Developments and Applications, W. A. Lodwick and J. Kacprzyk (Eds.*)*, *Studies in Fuzziness and Soft Computing*, Vol. 254, 231-270.

[16] G. Sirbiladze, A. Sikharulidze, B. Ghvaberidze and B. Matsaberidze (2011), “Fuzzy-probabilistic Aggregations in the Discrete Covering Problem”. *International Journal of General Systems*, 40: 2, 169 -196.

[17] G. Sirbiladze (2010), “Fuzzy Identification Problems for continuous Extremal Fuzzy Dynamic System”. *Fuzzy optimization and decision making*, 9, 233-274.

[18] G. Sirbiladze and A. Sikharulidze (2003), “Weighted Fuzzy Averages in Fuzzy Environment, Parts I, II”. *International Journal of Uncertainty, Fuzziness and Knowledge-Based Systems*, 2 (2), 139-157, 159-172.

[19] R. E. Steuer (1989), “*Multiple Criteria Optimization: Theory: Computation and Application*”. New York. John Wiley.

[20] M. Sugeno (1974), “Theory of fuzzy integrals and its applications”, Thesis (PhD). Tokio Institute of Technology.

[21] L. Tang, W. Cheng, Z. Xhang and B. Zhong (2007), “Ant colony algorithm based on information entropy theory to fuzzy vehicle routing problem”. *Proceedings ISKE, Series: Advances in Intelligent Systems Research*.

[22] D. Teodorović and P. Lucić (2007), “The Fuzzy Ant System for the vehicle routing problem when demand at nodes is uncertain”. *International Journal on Artificial Intelligence Tools*, 16(5):751-770.

[23] D. Teodorović and S. Kikuchi (1991), “Application of fuzzy set theory to the saving based vehicle routing algorithm”. *Civil Engineering Systems* 8, 87-93.

[24] P. Toth and D. Vigo, eds (2002), “The Vehicle Routing Problem”. *Society for Industrial & Applied Mathematics*, SIAM, Philadelphia.

[25] J. L. Verdegay (1982), “Fuzzy mathematical programming”, In: M. M. Gupta, E. Sanchez, eds., Fuzzy Information and Decision Processes.

[26] Z. Wang and G.J. Klir (2009), “*Generalized Measure Theory*”. IFSR International Series of Systems Science and Engineering 25, 1st Edition. Springer; 384 p.

[27] R.R. Yager (1988), “On Ordered Weighted Averaging aggregation operators in multicriteria decision making”. *IEEE Trans. On Systems, Man and Cybernetics*, 18 (1): 183-190.

[28] N. Yaodong (2008), “Fuzzy minimum weight edge covering problem”. *Applied Mathematical Modeling*, 32(7): 1327-1337.

[29] L.A. Zadeh (1978), “Fuzzy sets as a basis for a theory of possibility”. *Fuzzy Sets and Systems*, 1(1): 3-28.

TOPSIS based Hesitant Fuzzy MADM for Optimal Investment Decisions

Irina Khutsishvili, Gia Sirbiladze and Bezhan Ghvaberidze

***Abstract*—**The work proposes a novel two-stage multi-attribute decision making (MADM) approach for optimal selection of the investment projects. The methodology firstly makes ranking of projects based on TOPSIS (Technique for Order Preference by Similarity to Ideal Solution) method presented under hesitant fuzzy environment. The case when the information on the attributes weights is completely unknown is considered. The attributes weights identification based on De Luca-Termini information entropy is offered in context of hesitant fuzzy sets. The ranking of alternatives is made in accordance with the proximity of their distance to the positive and negative ideal solutions. Secondly, the methodology allows making the most profitable investments in several projects simultaneously. Using the method developed by authors for a possibilistic bicriteria optimization problem, the decision on an optimal distribution of the allocated investment amount among the selected projects is provided. An investment example is presented to illustrate the application of the proposed approach.

***Keywords*—**Multi-attribute decision making, hesitant fuzzy set, information entropy, TOPSIS method, ranking of investment projects, mathematical programming problem.

I. Introduction

A multi-attribute decision-making (MADM) problem deals with a selection of one alternative (decision) or several ranked alternatives involving multiple attributes. From this perspective, the investment decision-making is a MADM problem.

Investment decision making is based on the various special methods. The further development in the field has received the probabilistic approach to the assessment of investment decisions [1],[2]. Along with that, many other methods were developed based on possibility analysis [3] and fuzzy-set approach [4]-[10].

When there not enough objective data, or they aren't present to make the investment decision, experienced experts (decision makers - DMs) are commissioned to solve the problem. In this case, knowledge and intellectual activities of the experts produce expert evaluations on the attributes. Thus, the analysis of investment projects involves experts' evaluations that may become dominant in decision making process.

Because of the inherent uncertainty of expert preferences, as well as due to the fact that objects can be fuzzy and uncertain, evaluations of attributes involved in the decision making problems most often are expressed in fuzzy numbers, triangular fuzzy numbers, confidence intervals, linguistic variables, intuitionistic fuzzy values, hesitant fuzzy elements, interval-valued hesitant fuzzy elements and so on. In this connection, many well-known MADM methods have been extended to take into account fuzzy types of attributes values [11],[12].

Nowadays there exists a large amount of literature for the theory of hesitant fuzzy sets (HFS) and their application in MADM. Different from other studies, in this paper the novel approach based on hesitant fuzzy TOPSIS decision making model with entropy weights is developed. The case when the information on the attributes weights is completely unknown is considered. The attributes weights are obtained by applying De Luca-Termini non-probabilistic entropy concept [13], which is offered in context of hesitant fuzzy sets. After that, a fuzzy hesitant TOPSIS method is employed to ranking the alternatives. The developed method is applied to evaluation of investment projects with the aim of their ranking and identification of high-quality projects for investment. The method is described in Section III.

In practice, the capital is frequently invested in several projects simultaneously, each of them requiring a different credit amount. At the same time, the total investment amount is predetermined and fixed. In such cases, it becomes necessary to decide which of the projects and to what extent should share the initial investment amount. On the basis of the fuzzy hesitant TOPSIS method the projects' group ranking maximum criteria is constructed. Taking into account the levels of ranking of projects' group and also considering initial investment amount the possibilistic bicriteria optimization problem [14]-[17] is applied for the most advantageous investment in several projects simultaneously. Thus, those projects are selected, which possess a maximum of projects' group ranking and of gaining a maximum profit for the investment fund. The method is discussed in Section IV.

The research of the authors resulted in a new methodology and, consequently, software package development. The software package, which is based on the combined approach, was used in investment tender and supported the decision making. In Section V the authors provide an example clearly illustrating the work of the proposed methodology.

II. Preliminaries

Hesitant fuzzy set (HFS) was introduced by Torra and Narukawa in [18] and Torra in [19] as a generalization of a fuzzy set. In HFS the degree of membership of an element to a reference set is presented by several possible fuzzy values.

I. Khutsishvili, Associate Professor, G. Sirbiladze, Professor, and B. Ghvaberidze, Associate Professor, are with the Department of Computer Sciences, Iv.Javakhishvili Tbilisi State University, 13, University street, 0186 Tbilisi, Georgia (e-mail: irina.khutsishvili@tsu.ge, gia.sirbiladze@tsu.ge, b.ghvaberidze@tsu.ge, respectively).

This allows describing situations when DMs have hesitancy in providing their preferences over alternatives. The HFS is defined as follows:

Definition 1. [18,19]. Let $X=\{x_1,x_2,...,x_n\}$ be a reference set, a hesitant fuzzy set E on X is defined in terms of a function $h_E(x)$ when applied to X returns a subset of $[0,1]$:

$$E=\{<x,h_E(x)>|\,x\in X\},\qquad(1)$$

where $h_E(x)$ is a set of some different values in [0,1], representing the possible membership degrees of the element $x\in X$ to E; $h_E(x)$ is called a hesitant fuzzy element (HFE).

Definition 2: [20]. Let M and N be two HFSs on $X=\{x_1,x_2,...,x_n\}$, then the distance measure between M and N is defined as $d(M,N)$, which satisfies the following properties:

1). $0\le d(M,N)\le 1$;
2). $d(M,N)=0$ if and only if $M=N$;
3). $d(M,N)=d(N,M)$.

It is clear that the number of values (length) for different HFEs may be different. Let $l(h_E(x))$ be the length of $h_E(x)$. After arranging the elements of $h_E(x)$ in a decreasing order, let $h_E^{\sigma(j)}(x)$ be the jth largest value in $h_E(x)$. To calculate the distance between M and N when $l(h_M(x_i))\ne l(h_N(x_i))$, it is necessary extend the shorter one by adding any value in it, until both will have the same length. The choice of this value depends on the DMs' risk preferences. Optimists DMs' may add the maximum value from HFE, while pessimists may add the minimal value.

In this work the hesitant weighted Hamming distance is used that is defined by following formula

$$d_{hwh}(M,N)=\sum_{i=1}^{n}w_i\left[\frac{1}{l_{x_i}}\sum_{j=1}^{l_{x_i}}\left|h_M^{\sigma(j)}(x_i)-h_N^{\sigma(j)}(x_i)\right|\right],\qquad(2)$$

where $h_M^{\sigma(j)}(x_i)$ and $h_N^{\sigma(j)}(x_i)$ are the jth largest values in $h_M(x_i)$ and $h_N(x_i)$ respectively;
$l_{x_i}=\max\{l(h_M(x_i)),l(h_N(x_i))\}$ for each $x_i\in X$;
w_i $(i=1,2,...,n)$ is the weight of the element $x_i\in X$ such that $w_i\in[0,1]$ and $\sum_{i=1}^{n}w_i=1$.

Definition 3: [21] For a HFE $h_E(x)$, the score function $s(h_E(x))$ is defined as follows:

$$s(h_E(x))=\sum_{j=1}^{l(h_E(x))}h_E^{\sigma(j)}(x)\Big/l(h_E(x)),\qquad(3)$$

where $s(h_E(x))\in[0,1]$.

Let h_1 and h_2 are two HFEs. Based on score function it is possible to make ranking of HFEs according to the following rules: $h_1>h_2$, if $s(h_1)>s(h_2)$; $h_1<h_2$, if $s(h_1)<s(h_2)$ and $h_1=h_2$, if $s(h_1)=s(h_2)$.

III. Formulation of Investment MADM Problem in Hesitant Fuzzy Environment

Consider a MADM problem for investment decision making.

Assume that there are m investment projects – decision making alternatives $A=\{A_1,A_2,\dots,A_m\}$, and the group of DMs evaluates them with respect to an n attributes $X=\{x_1,x_2,\dots,x_n\}$. DMs give the evaluations over attributes in form of hesitant fuzzy numbers. Therefore, their joint assessments concerning each alternative represent HFSs.

A HFS A_i of the ith alternative on X is given by

$$A_i=\left\{\left\langle x_j,h_{A_i}(x_j)\right\rangle|\,x_j\in X\right\},$$

where $h_{A_i}(x_j)=\{\gamma\,|\,\gamma\in h_{A_i}(x_j),0\le\gamma\le 1\}$, $i=1,2,\dots,m$; $j=1,2,\dots,n$. $h_{A_i}(x_j)$ indicates the possible membership degrees of the ith alternative A_i under the jth attribute x_j, and it can be expressed as a HFE h_{ij}.

Considering that the attributes have different importance degrees, the weight vector of all attributes, given by the DMs, is defined by $w=(w_1,w_2,\dots,w_n)^T$, where $0\le w_j\le 1$, $\sum_{j=1}^{n}w_j=1$, and w_j is the importance degree of jth attribute.

Then a hesitant MADM problem can be expressed in matrix format as follows

$$H=\begin{array}{c}\\A_1\\A_2\\\vdots\\A_m\end{array}\!\!\begin{array}{c}\begin{array}{cccc}x_1&x_2&\cdots&x_n\end{array}\\\begin{bmatrix}h_{11}&h_{12}&\cdots&h_{1n}\\h_{21}&h_{22}&\cdots&h_{2n}\\\vdots&\vdots&\vdots&\vdots\\h_{m1}&h_{m2}&\cdots&h_{mn}\end{bmatrix}\end{array},$$

$$w=(w_1,w_2,\dots,w_n)^T,$$

where H is the hesitant decision matrix, each element of which represents a HFE h_{ij}.

A. Determination of the attributes weights using De Luca-Termini entropy

Complexity and uncertainty of investment decision making problems leads to the fact that the information about attributes weights is usually incomplete or completely unknown. Here the case when the attributes weights are unknown is considered.

ISBN: 978-1-61804-321-4

De Luca and Termini [13] defined a non-probabilistic entropy formula of a fuzzy set based on Shannon's function on a finite universal set X as:

$$E_{LT} = -k\sum_{i=1}^{n}\left[\mu_A(x_i)\ln\mu_A(x_i) + (1-\mu_A(x_i))\ln(1-\mu_A(x_i))\right],$$
$$k > 0,$$

where $\mu_A : X \to [0,1]$; k is a positive constant.

The attributes weights definition method based on the De Luca-Termini entropy can be described as follows:

Step1: Calculate the score matrix $S = (s_{ij})_{m\times n}$ of hesitant decision matrix H, where $s_{ij} = s(h_{ij})$ is the score value of h_{ij} (see (3)).

Step2: Calculate the normalized score matrix $S' = (s'_{ij})_{m\times n}$, where

$$s'_{ij} = s_{ij} \Big/ \sum_{i=1}^{m} s_{ij} . \tag{4}$$

Step3: Determine the attributes weights

By using De Luca-Termini normalized entropy in context of hesitant fuzzy sets

$$E_j = -\frac{1}{m\ln 2}\sum_{i=1}^{m}\left(s'_{ij}\ln s'_{ij} + (1-s'_{ij})\ln(1-s'_{ij})\right), \tag{5}$$
$$j = 1, 2, \dots, n,$$

the definition of the attributes weights is expressed by the formula

$$w_j = \frac{1-E_j}{\sum_{j=1}^{n}(1-E_j)}, \quad j = 1, 2, \dots, n . \tag{6}$$

where the value of w_j represents the relative intensity of x_j attribute importance.

B. Hesitant fuzzy MADM approach based on TOPSIS method

The idea of TOPSIS method as applied to the problem of MADM is to choose an alternative with the nearest distance from the so-called positive ideal solution (PIS) and the farthest distance from the negative ideal solution (NIS).

This Section presents a MADM approach based on the hesitant fuzzy TOPSIS with entropy weights model (proposed in Section III - Subsection A). Different from existing extensions of TOPSIS under hesitant fuzzy environment, here the attributes of both types are considered: as attributes of benefit type, as well as attributes of cost type.

The algorithm of practical solving an investment MADM problem can be formulated as follows:

Step1: Based on the DMs hesitant evaluations construct the aggregate hesitant decision matrix $H = (h_{ij})_{m\times n}$.

Step2: Determine the attributes weights $w = (w_1, w_2, \dots, w_n)^T$ based on the method in Section III (Subsection *A*).

Step3: Determine the corresponding hesitant fuzzy PIS A^+ and the hesitant fuzzy NIS A^- by formulas:

$$A^+ = \left\{\max_i\left\langle h_{ij}^{\sigma(\lambda)}\right\rangle \mid j \in J';\ \min_i\left\langle h_{ij}^{\sigma(\lambda)}\right\rangle \mid j \in J''\right\}, \tag{7}$$

$$A^- = \left\{\min_i\left\langle h_{ij}^{\sigma(\lambda)}\right\rangle \mid j \in J';\ \max_i\left\langle h_{ij}^{\sigma(\lambda)}\right\rangle \mid j \in J''\right\}, \tag{8}$$

where J' is associated with a benefit attributes, and J'' - with a cost attributes.

Step4: Using (2) calculate the separation measures d_i^+ and d_i^- of each alternative A_i from the hesitant fuzzy PIS A^+ and the hesitant fuzzy NIS A^-, respectively:

$$d_i^+ = \sum_{j=1}^{n} d(h_{ij}, h_j^+)\, w_j = \sum_{j=1}^{n} w_j\left[\frac{1}{l}\sum_{j=1}^{l}\left|h_{ij}^{\sigma(j)} - (h_j^{\sigma(j)})^+\right|\right], \tag{9}$$

$$d_i^- = \sum_{j=1}^{n} d(h_{ij}, h_j^-)\, w_j = \sum_{j=1}^{n} w_j\left[\frac{1}{l}\sum_{j=1}^{l}\left|h_{ij}^{\sigma(j)} - (h_j^{\sigma(j)})^-\right|\right], \tag{10}$$

$$i = 1, 2, \dots, m .$$

Step 5: Calculate the relative closeness coefficient δ_i of each alternative A_i to the hesitant fuzzy PIS A^+:

$$\delta_i = \frac{d_i^-}{d_i^+ + d_i^-} . \tag{11}$$

Step 6: Perform the ranking of the alternatives A_i, $i = 1, 2, \dots, m$ according to the relative closeness coefficients δ_i, $i = 1, 2, \dots, m$ by the rule: for two alternatives A_α and A_β we say that A_α is more preferred than A_β, i.e. $A_\alpha \succcurlyeq A_\beta$, if $\delta_\alpha \geq \delta_\beta$, where $\succcurlyeq$ is a preference relation on A.

IV. Problem of the Investment's Optimal Distribution

Assume that after evaluation the projects with hesitant fuzzy TOPSIS method, there are n ranking projects, and for each alternative (project) A_j the ranking level δ_j of its choice is calculated.

We consider the issue of possible financing of the projects in ℓ years.

Let's assume there are additional conditions for financing the projects. In particular, it is known that

for financing of jth project $j \in \{1, 2, \dots, n\}$ within ith year $i \in \{1, 2, \dots, \ell\}$, a_{ij} monetary units are required;

the profit received from implementation of jth project constitutes c_j monetary units;

b_i monetary amount is allocated to finance projects within

i th year.

In practice, the amount of funding, as a rule, is insufficient to satisfy all projects. Therefore, it is supposed that for at least one $i \in \{1, 2, \ldots, \ell\}$ the inequality $\sum_{j=1}^{n} a_{ij} > b_i$ is true.

Considering the listed constraints, we have to find an answer to the question as to which of the chosen projects should be financed to get a maximum investment profit at a minimum risk.

We offer the following solution of the problem.

If we introduce a Boolean variables x_j, $j \in \{1, 2, \ldots, n\}$ by the rule

$$x_j = \begin{cases} 1, & \text{if the j-th project is selected for finance} \\ 0, & \text{otherwise}, \end{cases}$$

we obtain the following bicriteria Boolean linear programming problem:

$$\begin{cases} \max \sum_{j=1}^{n} \delta_j x_j, & (i) \\ \max \sum_{j=1}^{n} c_j x_j, & (ii) \\ \sum_{j=1}^{n} a_{ij} x_j \le b_i, \ i = 1, \ldots, \ell, & (iii) \\ x_j = 0 \vee 1, \end{cases} \tag{12}$$

where the criterion (i) represents the decision on the selection of the projects' group with the maximum level of ranking, the criterion (ii) represents the decision on selection of the group of projects giving the maximum profit, while the conditions (iii) corresponds to the financial constraints.

Thus, the objective functions will be:

1) $f_1 = \max \sum_{j=1}^{n} \delta_j x_j$ – selection the projects' group with the maximum ranking level;

2) $f_2 = \max \sum_{j=1}^{n} c_j x_j$ – selection the projects' group ensuring a maximum profit.

To solve this problem we apply the method developed by the authors for possibilistic bicriteria optimization problems [16], [17].

In other words X is the set of all Boolean vectors satisfying the conditions of the bicriteria optimization problem. Then by considering the scalar optimization problem

$$\lambda f_1 + (1-\lambda) f_2 \to \max, (x_1, x_2, \ldots, x_n) \in X, \ \lambda \in (0,1), \tag{13}$$

with conditions (iii), where λ is a weighted parameter, we can find, in the general case, some Pareto optima [14]-[17].

Thus, the bicriteria optimization problem can be solved by linear convolution of criteria.

V. An Example of the Application of Fuzzy Decision Making Approach

We have developed a software package supporting decision making for optimal credit granting. The decision making block consists of two main soft computing modules: the first provides the software platform for the application of the hesitant fuzzy TOPSIS method, and the second is used to solve a bicriteria optimization problem.

The software was tested on concrete data. The required information was provided by the group of 4 experts – expert commission – from the Bank of Georgia and filtered according to our demands after consultations with the managers of the Bank's crediting department.

A. Comparison and Ranking the Projects Using the TOPSIS method

Suppose that in the competition for investment five construction companies are involved. The group of DMs evaluates the investment projects taking into account the four attributes, by which the experts will score each candidate seeking an investment:

x_1 - business profitability;

x_2 - pledge guaranteeing repayment of the credit;

x_3 - location of construction object;

x_4 - workmanship.

All attributes are of a benefit type. DMs give evaluations in form of hesitant values. If the evaluation values of any attribute given by DMs are coincident, then such values are included in HFE only once. Assume the hesitant fuzzy decision matrix H looks like Table I:

TABLE I

THE HESITANT FUZZY DECISION MATRIX H

	x_1	x_2	x_3	x_4
A_1	(0.4,0.3,0.1)	(0.9,0.8,0.7,0.1)	(0.9,0.6,0.5,0.3)	(0.5,0.4,0.3)
A_2	(0.5,0.4)	(0.9,0.7,0.6,0.3)	(0.7,0.4,0.3)	(0.6,0.5)
A_3	(0.3,0.2,0.1)	(0.9,0.6)	(0.8,0.7)	(0.7,0.4,0.1)
A_4	(0.2,0.1)	(0.8,0.7,0.5,0.3)	(0.9,0.8,0.6)	(0.8,0.5,0.4)
A_5	(0.7,0.5,0.3)	(0.7,0.4,0.2)	(0.9,0.7,0.6,0.4)	(0.9,0.7,0.6,0.2)

We assume that the DMs are pessimistic, and the hesitant fuzzy data in HFEs are changed by adding the minimal values. According to the method of determining the attributes weights given in Section III (Subsection A), we first calculate the score matrix S of hesitant decision matrix H based on (3):

$$S = \begin{bmatrix} 0.267 & 0.625 & 0.575 & 0.4 \\ 0.45 & 0.625 & 0.467 & 0.55 \\ 0.2 & 0.75 & 0.75 & 0.4 \\ 0.15 & 0.575 & 0.575 & 0.567 \\ 0.5 & 0.433 & 0.65 & 0.5 \end{bmatrix}$$

Secondly, we obtain the normalized score matrix S' using (4):

$$S' = \begin{bmatrix} 0.1702 & 0.2078 & 0.1906 & 0.1589 \\ 0.2872 & 0.2078 & 0.1547 & 0.2185 \\ 0.1277 & 0.2493 & 0.2486 & 0.1589 \\ 0.0957 & 0.1911 & 0.1906 & 0.2252 \\ 0.3191 & 0.144 & 0.2155 & 0.2384 \end{bmatrix}$$

Then the weighting vector of attributes is determined using (5) and (6):

$$w = (0.2695, 0.2437, 0.2428, 0.244)^T$$

Following the hesitant fuzzy TOPSIS method, we determine the hesitant fuzzy PIS A^+ and the hesitant fuzzy NIS A^- by (7) and (8), respectively:

$$A^+ = \{(0.7,0.5,0.4,0.4), (0.9,0.8,0.7,0.6), (0.9,0.8,0.7,0.7), (0.9,0.7,0.6,0.5)\};$$

$$A^- = \{(0.2,0.1,0.1,0.1), (0.7,0.4,0.2,0.1), (0.7,0.4,0.3,0.3), (0.5,0.4,0.1,0.1)\}.$$

Here, we take into account that all attributes are of a benefit type.

Then we calculate the distances d_i^+ and d_i^- of each alternative A_i from the hesitant fuzzy PIS A^+ and the hesitant fuzzy NIS A^- by formulas (9) and (10), respectively:

$$d_1^+ = 0.22639,\ d_2^+ = 0.44643,\ d_3^+ = 0.19673,$$

$$d_4^+ = 0.19253,\quad d_5^+ = 0.22763;$$

$$d_1^- = 0.15479,\ d_2^- = 0.20887,\ d_3^- = 0.17772,$$

$$d_4^- = 0.18868,\quad d_5^- = 0.22761.$$

Using (11) to calculate the relative closeness coefficient δ_i of each alternative A_i to the hesitant fuzzy PIS A^+ we obtain:

$$\delta_1 = 0.40608,\quad \delta_2 = 0.31874,\quad \delta_3 = 0.47462, \qquad (14)$$

$$\delta_4 = 0.49495,\quad \delta_5 = 0.49998.$$

Finally, we perform the ranking of the alternatives A_i, $i = 1, 2, \dots, 5$ according to the relative closeness coefficients δ_i and obtain:

$$A_5 \succ A_4 \succ A_3 \succ A_1 \succ A_2 .$$

This means that when investing the capital only in one project, DMs prefer to the investment project A_5, i.e. the project A_5 receive investment.

Frequently, the investment amount has to be distributed among several projects. We can do this in the second stage of the proposed approach.

B. Problem of the Optimal Distribution of Investment

Using the formulas (12)-(13) we will deal with the possibilistic bicriteria optimization problem allowing for the most profitable investments into a number of projects.

Bank considers an investment that totals to \$ 120 million over three years ($i = 1, 2, 3$), \$ 40 million a year ($b_i = 40$).

The values a_{ij} of investments, that are required for j th project in i th year, as well as the c_j magnitudes of profits from the realization of j th project during three years are shown in the following table (see Table II):

TABLE II

THE VALUES OF a_{ij} AND c_j

	Years	Projects				
		A_1	A_2	A_3	A_4	A_5
a_{ij}	1	10	6	14	12	8
	2	4	14	20	16	10
	3	10	10	20	14	9
c_j		25	20	35	30	18

We use obtained distribution of projects ranking levels (14), the information given in Table II, and solve problem (12)-(13) taking for value $\lambda = 0.5$. Such choice of λ means that DMPs lonely are inclined both to the subjective criterion f_1 and to the objective criterion f_2.

As a result, we obtain the following set of Boolean variables

$$\{\ 1,\ 1,\ 0,\ 1, 0\ \}.$$

This means that the projects' group (A_1, A_2, A_4) receive a credit.

At the same time, investment over the years amounted as \$ 38 million in the first year, \$ 40 million in the second year and in the third year will bring the bank a total profit of \$ 80 million in three years.

VI. CONCLUSION

In this paper the novel approach for solving MADM problem based on hesitant fuzzy TOPSIS method with entropy weights is developed.

The new aspects in the TOPSIS approach have been used: a). we proposed a new attributes weighting method based on De Luca-Termini information entropy to express the relative intensities of attribute importance and determine the attributes weights; b). there are many methods of the applicability of the TOPSIS approach under hesitant environment. The novelty in our work is that we proposed the formulas to calculate PIS and

ISBN: 978-1-61804-321-4

NIS, which take into account as the attributes of a benefits type, as well as the attributes of a cost type.

The developed approach was applied in the problem of investment decision making with the aim of optimal distribution of investments among several of projects.

Based on proposed two-stage methodology we have developed software package which is used in real investment decision making problem. The application and testing of the software was carried out based on the data provided by the "Bank of Georgia". The results are illustrated in the example.

REFERENCES

[1] J. M. Merigó, "Probabilistic Decision Making with the OWA Operator and its Application in Investment Management", *In Proceedings of the Conference European Society for Fuzzy Logic and Technology – EUSFLAT*, Lisbon, Portugal, 2009, 1364-1369.

[2] J. M, Merigó, "Fuzzy Multi-Person Decision Making with Fuzzy Probabilistic Aggregation Operators", *Int. Journal of Fuzzy Systems*, 13, 2011, pp. 163-174.

[3] D. Dubois and H. Prade, *Possibility Theory: An Approach to Computerized Processing of Uncertainty*. New-York: Plenum Press, 1988.

[4] R. E. Bellman and L. A. Zadeh, "Decision-Making in a Fuzzy Environment", *Management Science*, 17(4), 1970, B-141-B-164.

[5] D. Ruan, J. Kacprzyk and M. Fedrizzi, *Soft Computing for Risk Evaluation and Management: Applications in Technology, Environmenf and Finance. Studies in Fuzziness and Soft Computing*. Heidelberg, New York: Physica-Verlag, 2001.

[6] R. R. Yager, "On Ordered Weighted Averaging aggregation operators in multicriteria decision making", *IEEE Trans. On Systems, Man and Cybernetics* B, 18, 1988, pp. 183-190.

[7] R. R. Yager, J. Kacprzyk and G. Beliakov, *Recent Development in the ordered Weighted Averaging Operations: Theory and Practice. Studies in Fuzziness and Soft Computing* 265. Berlin: Springer-Verlag, 2011.

[8] I. Khutsishvili and G. Sirbiladze, "Decision Support's Precising Technology in the Investment Project Risk Management", *In Proceedings of the 11th WSEAS International Conference on Automatic Control, Modelling and Simulation (ACMOS '09)*, Istanbul, Turkey, 2009, pp. 303-311.

[9] G. Sirbiladze, I. Khutsisvili and P. Dvalishvili, "Decision Precising Fuzzy Technology to Evaluate the Credit Risks of Investment Projects", *In Proceedings of IEEE 10-th International Conference on Intelligent Systems Desigh and Applications (ISDA 2010), Cairo, Egypt*, 2010, pp. 103-108.

[10] Sirbiladze G., Khutsishvili I. and Ghvaberidze B., "Multistage decision-making fuzzy methodology for optimal investments based on experts' evaluations", *European Journal of Operational Research*, vol. 232, issue 1, 2014, pp. 169–177.

[11] Xu Z. and Zhang X., "Hesitant fuzzy multi-attribute decision making based on TOPSIS with incomplete weight information", *Knowledge-Based Systems* 52, 2013, pp. 53–64.

[12] Tian J., Yu D., Yu B. & Ma S., "A fuzzy TOPSIS model via chi-square test for information source selection", *Knowledge-Based Systems* 37, 2013, pp. 515–527.

[13] De Luca A. & Termini S., A Definition of a Nonprobabilistic Entropy in the Setting of Fuzzy Sets Theory, *Information and Control* 20, 1972, pp. 301-312.

[14] M. Ehrgott, *Multicriteria optimization*, 2nd Edition. Berlin Heidelberg: Springer, 2005.

[15] A.Taha Hamdy, *Operations Research: An Introduction*, 9th Edition. Upper Saddle River, N.J.: Pearson/Prentice Hall, 2011.

[16] Sirbiladze, G., Ghvaberidze, B., Latsabidze, T., and Matsaberidze, B., "Using a minimal fuzzy covering in decision-making problems", *Information Sciences*, 179 (12), 2009, pp. 2022-2027.

[17] G. Sirbiladze, A. Sikharulidze, B. Ghvaberidze and B. Matsaberidze, "Fuzzy-probabilistic Aggregations in the Discrete Covering Problem", *International Journal of General Systems*, 40(2), 2011, pp. 169 -196.

[18] Torra V. and Narukawa Y., "On hesitant fuzzy sets and decision", *in: The 18th IEEE International Conference on Fuzzy Systems*, Jeju Island, Korea, 2009, pp. 1378–1382.

[19] Torra V., "Hesitant fuzzy sets", *International Journal of Intelligent Systems* 25, 2010, pp. 529–539.

[20] Xu Z. and Xia M., "Distance and similarity measures for hesitant fuzzy sets", *Information Sciences* 181, 2011, pp. 2128–2138.

[21] Xia M. and Xu Z., "Hesitant fuzzy information aggregation in decision making", *International Journal of Approximate Reasoning*, vol. 52, no. 3, 2011, pp. 395–407.

Possibilistic OWA-type Aggregations in the Business Start up Decision Making

Otar Badagadze and Gia Sirbiladze

Abstract— This work proposes a fuzzy methodology to support the Business Start up decisions. The methodology makes ranking of possible alternatives using the new aggregation OWA-type operator – AsPOWA, presented in the environment of possibility uncertainty. For numerical evaluation of the weighting vector associated with the AsPOWA operator the mathematical programming problem is constructed. The article provides an example of the investment decision-making that explains the work of the proposed methodology.

Keywords—Expert evaluations, investment fuzzy decision making, OWA operator, possibility uncertainty.

I. Introduction

IN the environment of market economy and competition, investments are exposed to the risk of loss, especially in the sphere of crediting. Hence the issue of increasing the effectiveness of credit policies and lowering credit risks becomes very important ([6], [7], [11], [12] and others).

When there is little or no objective data to make an investment decision, experienced experts and decision making are persons commissioned to solve the problem. In that case, the knowledge and intellectual activity of experts yield expert data. Thus, the analysis of investment projects involves experts' evaluations that may become dominant in the decision making process. Experts' qualitative (verbal) evaluations can be correctly processed by applying possibility analysis [1], [2] and the fuzzy-set approach [1] - [7].

Very useful approach for decision making under uncertainty is the use of the ordered weighted averaging (OWA) operator, which was introduced by R.R. Yager in [15]. The OWA operator has been studied and applied in a wide range of problems ([3-5, [15], [16] and others) including the problem of investment decisions ([5] and others).

In [3]-[5] the probabilistic generalization of the OWA operator - POWA is presented. Along with probabilistic generalization we propose the possibilistic generalization of the OWA operator - AsPOWA. For a numerical evaluation of the weighting vector associated with the AsPOWA operator a mathematical programming problem is constructed.

In this paper the AsPOWA operator is used in the problem of Business Start- up decision making and to make their ranking. The description of this approach is given in Section II.

O. Badagadze, PhD Student, G. Sirbiladze, Professor are with the Department of Computer Sciences, Iv.Javakhishvili Tbilisi State University, 13, University street, 0186 Tbilisi, Georgia (e-mail: otba@myself.com, gia.sirbiladze@tsu.ge).

The research of the authors resulted in a new methodology and, consequently, software package development. In Section III the authors provide an example clearly illustrating the work of the proposed methodology.

II. Possibilistic Aggregations in the OWA Operator

It is well recognized that intelligent decision making systems (IDMS) and technologies ([4], [8-14] and others) have been playing an important role in improving almost every aspect of human society. In this type of problem the decision making person (DMP) has a collection $D=\{d_1,d_2,...,d_n\}$ of possible uncertain alternatives from which he/she must select one or more decisions by some expert's preference relation values. Associated with this problem as a result is a variable of characteristics, activities, symptoms and so on, acts on the decision procedure. This variable normally calls the state of nature, which affects the payoff, utilities, valuations and others to the DMP's preferences or subjective activities. This variable is assumed to take its values (states of nature) in the some set $S=\{s_1,s_2,...,s_m\}$. As a result the DMP knows that if he/she selects d_i and the state of nature assumes the value s_j then his/her payoff (valuation, utility and so on) is a_{ij}. The objective of the decision is to select the "best" alternative, get the biggest payoff. But in IDMS the selection procedure becomes more difficult. In this case each alternative can be seen as corresponding to a row vector of possible payoffs. To make a choice the DMP must compare these vectors, a problem which generally doesn't lead to a compelling solution.

Assume d_i and d_k are two alternatives such that for all $j, j=1,2,....,m$ $a_{ij} \geq a_{kj}$. In this case there is reason to select d_i. In this situation we shall say d_i dominates d_k ($d_i \succeq d_k$). Furthermore, if there exists one alternative (optimal decision) that dominates all the alternatives then it will be optimal solution. Facing the general difficulty of comparing vector payoffs we must provide some means of comparing these vectors. Our focus in this work is on the construction of aggregation operator F that can take a collection of m values and convert them into a single value, $F:R^m \Rightarrow R^1$. In [15] Yager introduced a class of mean aggregation operators called Ordered Weighed Averaging (OWA) operator.

Definition 1 [15]: An OWA operator of dimension m is mapping $OWA:R^m \Rightarrow R^1$ that has an associated weighting

ISBN: 978-1-61804-321-4

vector W of dimension m with $w_j \in [0;1]$ and $\sum_{j=1}^{m} w_j = 1$, such that

$$OWA(a_1,....,a_m) = \sum_{j=1}^{m} w_j b_j \ , \qquad (1)$$

where b_j is the jth largest of the $\{a_i\}, i = 1,2,..., m$.

In the role of uncertainty measure a possibility distribution is taken. So, we consider possibilistic aggregations based on the OWA operator. Therefore, we introduce the definition of a possibility measure [1]:

Definition 2: A possibility measure - Pos on 2^S can be uniquely determined by its possibility distribution function $\pi : S \to [0,1]$ via the formula:

$$\begin{aligned} &\forall A \in 2^S \\ &Pos(A) = \max_{s \in A} \pi(s). \end{aligned} \qquad (2)$$

Let S_m be the set of all permutations of the set $\{1,2,..,m\}$, Let $\{P_\sigma\}_{\sigma \in S_m}$ be the associated probabilities class [5] of a possibility measure - Pos. Then, we have the following connections between $\{\pi_i\}$ and $\{P_\sigma\}_{\sigma \in S_m}$:

$$\begin{aligned} &\forall \sigma \in S_m , \\ &P_\sigma\left(s_{\sigma(i)}\right) = \max_{\nu=1,i} \pi(s_{\sigma(\nu)}) - \max_{\nu=1,i-1} \pi(s_{\sigma(\nu)}) , \end{aligned} \qquad (3)$$

for each $\sigma = (\sigma(1), \sigma(2),..., \sigma(m)) \in S_m$, which are called the associated probabilities [12-14].

Definition 3: An associated probabilistic OWA operator - AsPOWA of dimension m is mapping $AsPOWA : R^m \Rightarrow R^1$, that has an associated objective weighted vector W of dimension m such that $w_j \in [0,1]$ and $\sum_{i=1}^{m} w_j = 1$, some possibility measure $Pos : 2^S \Rightarrow [0,1]$ with associated probability class $\{\mathrm{P}_\sigma\}_{\sigma \in S_m}$, according to the following formula:

$$\begin{aligned} &AsPOWA(a_1, a_2, ..., a_m) = \beta \sum_{j=1}^{m} w_j b_j + (1-\beta) \cdot \\ &M\left(\sum_{i=1}^{m} a_i \mathrm{P}_\sigma(s_i) \Big/ \sigma \in S_m \right) = \beta \sum_{j=1}^{m} w_j b_j + \\ &+ (1-\beta) \cdot M\left(E_{P_{\sigma_1}}(a), E_{P_{\sigma_2}}(a), ..., E_{P_{\sigma_k}}(a)\right) \end{aligned} ,$$

where b_j is the jth largest of the $\{a_i\}, i = 1,...,m.$; $E_{P_{\sigma_i}}(a)$ is a Mathematical Expectation of a with respect to associated probability P_{σ_i}, $k = m!$.

We will consider an AsPOWA operator for a mean function M : AsPOWAmean if M = *Mean* in the decision making procedure.

$$\begin{aligned} &AsPOWAmean(a_1, a_2, ..., a_m) = \beta \sum_{j=1}^{m} w_j b_j + \\ &+ (1-\beta) \cdot (\sum_{i=1}^{k} E_{P_{\sigma_i}}(a)) / k. \end{aligned} \qquad (4)$$

We obtain the components of vector W by solving following mathematical programming problem:

$$\begin{cases} \max \ H(W) = -\sum_{i=1}^{m} w_i \ln w_i \\ \sum_{i=1}^{m} w_i = 1; & (i) \\ 0 \le w_i \le 1, \quad i = 1, \dots, m; & (ii) \\ \sum_{j=1}^{m} \dfrac{m-j}{m-1} w_j = \dfrac{\hat{\alpha}}{\beta} - \dfrac{1-\beta}{\beta} M\left\{ \sum_{j=1}^{m} P_{\sigma(j)} \cdot \dfrac{m-\sigma(j)}{m-1} \right\} & (iii) \end{cases} \qquad (5)$$

where $\hat{\alpha} = Orness\,(W)$ is an expert parameter, which measure decision –making person’s preferences on the decision risks [15]. The method of generation of the parameter *Orness* is described in [16].

We perform the ranking of pair decisions: $d_i \succcurlyeq d_j$ if

$$AsPOWAmean\,(d_i) \ \geq \ AsPOWAmean\,(d_j),$$

where $\succcurlyeq$ is the total ranking relation on *D.*

III. An example: Business start-up decision making in OB-IDSS system

A. Business start-up decision making problem formation

G-FOOD Ltd. Operates the Georgian restaurant “TIFLISO” located in picturesque and historic place, on SHARDIN Str. There are various Café-Bar and Restaurants deployed. The restaurant has two floors with 350 m^2 whole space, adjusting the restaurant building there is 40 m^2 space, which belongs to “TIFLISO” restaurant also but the space is not occupied yet.

Ltd G-FOOD plans to give some function to this space to use for business. There are the following alternatives:

d_1 – *Wine Shop*
d_2 – *Fast-food Café*
d_3 – *Ice-cream and Confectionery*
d_4 – *Hookah bar*
d_5 – *Grill-Café*

To choose one from these alternatives is not an easy job as they are dependent on various factors which are aroused from the company’s interests.

These factors are the following:

s_1 – *Investment amount*

s_2 – *Project implementation time*

s_3 – *Revenue needed for 0-Profit*

s_4– *The Relativity (Ratio) of Revenue needed for 0-profit and approximate industrial revenue*

s_5 – *The competitive persons point of view*

The project was created for G-FOOD Ltd. around the above mentioned problem. That will support decision making process and fix the alternatives selection problem.

B. Problem solving Scheme

Problem Solving Scheme is following:

1. Enquire the relevant information on the factors and alternatives from such sources as business-plan and survey of competitive persons. Based on this information the method will be formed for optimal decision making.
2. Erect the project implementation matrix of data, the elements of that matrix are real numbers or intervals.
3. Formation of appraisal decision making matrix by experts based on the project implementation matrix of data.
4. Generation of decision making operators which scale alternative's data into decision levels.
5. Decision making by ranking the alternatives from high to low by their levels. The decision will be the alternative with highest level.

C. Description of the factors influencing on the alternatives

Alternative d_1 – *Wine-Shop*

Factor s_1 – *Investment amount: 38 200 Gel.* Based on the business-plan.

Factor s_2 – *Project implementation time: 35 Days.* Provided by the construction company.

Factor s_3 – *Revenue needed for 0-Profit: 6785.7 Gel.* Provided by the economics calculations of BEP (Break Even Point) based on the data from business-plan.

Factor s_4 – *The Relativity (Ratio) of Revenue needed for 0-profit and approximate industrial revenue*: $\frac{R_0}{R_{ind}} = \frac{6\,785.7}{14\,000}$ $\approx 0.485 \rightarrow 48.5\%$. Information is collected from the like hood existing projects financial documents.

Factor s_5 – *The competitive persons' point of view: 4 points.* This information is provided by the following method: 12 Competitive independent experts were surveyed, who were giving points from 1 to 10 for the concrete alternative, based on if the alternative is good idea or not and then the average of the data is calculated.

The same scheme is used for the description of other alternatives $(d_2; d_3; d_4; d_5)$ by factors and is presented through the following *matrix of data*:

TABLE I

THE MATRIX OF DATA

	s_1	s_2	s_3	s_4	s_5
d_1 – *Wine-Shop*	38 200	35	6785.7	48.5%	4
d_2 – *Fast-Food Cafe*	56 000	50	17 885	44.7%	4.4
d_3 – *Ice-cream & Confectionery*	41 200	45	8750	35%	5.3
d_4 – *Hookah Bar*	52 500	60	8625	23%	7.5
d_5 – *Grill-Cafe*	66 500	60	10885	24%	6.1

D. Results of the realization and decision making

The four persons who ordered the project (Decision making persons - DMPs) are making the appraisal of the data from the above provided matrix of data. The appraisal is done under 1-10 grades system, then the data are normalized in [0;1] interval. The relative matrix is following:

TABLE II

APPRAISAL MATRIX BY DMP1

	s_1	s_2	s_3	s_4	s_5
d_1 – *Wine-Shop*	0.4	0.9	0.5	0.9	0.5
d_2 – *Fast-Food Cafe*	0.6	0.8	0.7	0.6	0.5
d_3 – *Ice-cream & Confectionery*	0.3	1	0.9	0.9	0.7
d_4 – *Hookah Bar*	0.8	1	0.6	0.9	0.7
d_5 – *Grill-Cafe*	0.3	0.7	0.9	0.7	0.6

Such kinds of matrixes are erected for other 3 decision makers (DMP2; DMP3; DMP4).

The experts have generated the factor weights based on the consensus:

$$w_1 = 0.25; \quad w_2 = 0.15; \quad w_3 = 0.25; \quad w_4 = 0.2; \quad w_5 = 0.15.$$

There were measured the possibility distribution of factor influence on the decisions. Possibility levels are:

$$\pi_1 = 0.85; \quad \pi_2 = 0.57; \quad \pi_3 = 1; \quad \pi_4 = 0.85; \quad \pi_5 = 0.57.$$

Using the AsPOWA operator we developed the Software – *OWA Based Intelligent Decision Support System* (OB-IDSS) for processing and synthesizing expert information and applied it to the problem of Business Start- up decision making. The OB-IDSS provides the etalon appraisal matrix by the Expertons Method ([7-9], [12]):

TABLE III

ETALON APPRAISAL MATRIX

Wine-Shop	0.75	0.95	0.75	0.55	0.42
Fast-food Cafe	0.70	0.82	0.52	0.62	0.52
Ice Cream& Confectionery	0.70	0.90	0.82	0.77	0.62
Hookah Bar	0.80	0.75	0.85	0.92	0.77
Grill-Cafe	0.42	0.70	0.80	0.82	0.67

The OB-IDSS generated Table of ranking of possible alternatives by the aggregation operators – MIN, MAX,

ISBN: 978-1-61804-321-4

AVERAGE, OWA, GOWA, IGOWA and AsPOWA.

TABLE IV

TABLE OF RANKING OF POSSIBLE DECISIONS BY SOME AGGREGATIOM OPERATOTS

Aggregation operator	Quantifier	Ranking of Alternatives
Min		Hookah Bar ≻ Ice-cream & Confectionery ≻ Fast-Food Café ≻ Wine-Shop ≻ Grill-Café
Max		Wine-Shop ≻ Hookah Bar ≻ Ice-cream& Confectionery ≻ Fast-Food Café ≻ Grill-Café
Average		Hookah Bar ≻ Ice-cream&Confectionery ≻ Wine-Shop ≻ Grill-Café ≻ Fast-Food Cafe
OWA		Hookah Bar ≻ Ice-cream&Confectionery ≻ Wine-Shop ≻ Grill-Café ≻ Fast-Food Cafe
IOWA		Hookah Bar ≻ Ice-cream&Confectionery ≻ Grill-Café ≻ Wine-Shop ≻ Fast-Food Cafe
GOWA	1.2	Hookah Bar ≻ Ice-cream&Confectionery ≻ Wine-Shop ≻ Grill-Café ≻ Fast-Food Café
IGOWA		Hookah Bar ≻ Ice-cream&Confectionery ≻ Grill-Café ≻ Wine-Shop ≻ Fast-Food Café
AsPOWA Min	0.3	Hookah Bar ≻ Ice-cream&Confectionery ≻ Wine-Shop ≻ Fast-Food Café ≻ Grill-Café
AsPOWA Max	0.3	Hookah Bar ≻ Ice-cream&Confectionery ≻ Wine-Shop ≻ Grill-Café ≻ Fast-Food Café
AsPOWA Mean	0.3	HookahBar ≻ Grill-Café ≻ Ice-cream& Confectionery ≻ Fast-Food Café ≻ Wine-Shop
AsPOWA Min	0.7	Hookah Bar ≻ Icecream&Confectionery ≻ Wine Shop ≻ Grill-Café ≻ Fast-Food Cafe
AsPOWA Max	0.7	Hookah Bar ≻ Ice-cream&Confectionery ≻ Wine-Shop ≻ Grill-Café ≻ Fast-Food Café

The quantifier parameter is an input value of the aggregation OWA-type operators [15], [16].

It is obvious that the results provided by various aggregations gives advantage to alternative d_4 – *Hookah bar* (14 operators from 15 supports d_4 – *Hookah bar*).

IV. Conclusion

In this work our focus is directed on the construction of a new generalization of the aggregation OWA operator – AsPOWA in the possibilistic uncertainty environment. The mathematical programming problem for the estimation of weights of the AsPOWA operator is constructed. This approach is based on the expert psychometrical parameter-*Orness* [19]. Using the AsPOWA operator we developed the Software for processing and synthesizing expert information and applied it to the problem of Business Start- up decision making.

References

[1] D. Dubois and H. Prade, *Possibility Theory: An Approach to Computerized Processing of Uncertainty*. New-York: Plenum Press, 1988.

[2] G. J. Klir and M. J. Wierman, *Uncertainty-Based Information. Elements of Generalized Information Theory. Second edition. Studies in Fuzziness and Soft Computing*, Physica-Verlag, Heidelberg, 1999.

[3] J. M. Merigó, "Probabilities in the OWA operator", *Expert Systems with Applications*, 39, 2012, 11456-11467.

[4] J. M, Merigó, "Fuzzy Multi-Person Decision Making with Fuzzy Probabilistic Aggregation Operators", *Int. Journal of Fuzzy Systems*, 13, 2011,163-174.

[5] J. M. Merigó, "Probabilistic Decision Making with the OWA Operator and its Application in Investment Management", *In Proceedings of the Conference European Society for Fuzzy Logic and Technology – EUSFLAT*, Lisbon, Portugal, 2009, 1364-1369.

[6] D. Ruan, J. Kacprzyk and M. Fedrizzi, *Soft Computing for Risk Evaluation and Management: Applications in Technology, Environmenf and Finance. Studies in Fuzziness and Soft Computing.* Heidelberg, New York: Physica-Verlag, 2001.

[7] G. Sirbiladze, A. Sikharulidze and G. Korakhashvili, "Decision-making Aiding Fuzzy Informational Systems in Investments. Part I – Discrimination Analysis in Investment Projects", *Proceedings of Iv.Javakhishvili Tbilisi State University. Applied Mathematics and Computer Sciences*, 353 (22-23), 2003, 77-94.

[8] G. Sirbiladze and T. Gachechiladze, "Restored fuzzy measures in expert decision-making ", *Information Sciences*, 169 (1/2), 2005, 71-95.

[9] G. Sirbiladze and A. Sikharulidze, "Weighted Fuzzy Averages in Fuzzy Environment, Parts I, II", *International Journal of Uncertainty, Fuzziness and Knowledge-Based Systems*, 11(2), 2003, 139-157, 159-172.

[10] Sirbiladze, G., Ghvaberidze, B., Latsabidze, T., and Matsaberidze, B., Using a minimal fuzzy covering in decision-making problems. Information Sciences, 179 (12), 2009, 2022-2027.

[11] G. Sirbiladze, I. Khutsisvili and P. Dvalishvili, "Decision Precising Fuzzy Technology to Evaluate the Credit Risks of Investment Projects", *IEEE 10-th International Conference on Intelligent Systems Desigh and Applications (ISDA 2010), Cairo, Egypt*, 2010, 103-108.

[12] G.Sirbiladze, I. Khutsishvili and B. Ghvaberidze, "Multistage decision-making fuzzy methodology for optimal investments based on experts' evaluations", European Journal of Operational Research, 232(1), 2014, 169–177.

[13] G. Sirbiladze, A. Sikharulidze, B. Ghvaberidze and B. Matsaberidze, "Fuzzy-probabilistic Aggregations in the Discrete Covering Problem", *International Journal of General Systems*, 40: 2, 2011, 169 -196.

[14] G. Sirbiladze, Extremal Fuzzy Dynamic Systems: Theory and Applications, IFSR International Series on Systems Science and Engineering, Vol. 28, 1st Edition. 2013, Springer, 396p.

[15] R. R. Yager, "On Ordered Weighted Averaging aggregation operators in multicriteria decision making", *IEEE Trans. On Systems, Man and Cybernetics* B, 18, 1988, 183-190.

[16] R. R. Yager, J. Kacprzyk and G. Beliakov, Recent Development in the ordered Weighted Averaging Operations: Theory and Practice. Studies in Fuzziness and Soft Computing, 265, 2011, Berlin: Springer-Verlag.

External fuzzy logic control of simulated technological processes

K.Hyniova

Abstract—The paper deals with a variable multifunctional simulation tool that enables to design and assemble animated models of various technological processes controlled by externally connected fuzzy logic unit. It enables to verify the correctness of fuzzy controller settings in the future control of real technological processes in practice. This work represents an effective, innovative, and creative concept important to understanding fuzzy logic control approach to model technological processes as an insight to behavior of real industrial processes and their control which is based on fuzzy logic. On the base of this animated simulation, real technological processes control can be realized successfully according to producer demands afterwards. Models of technological processes assembled by this simulation tool can be then externally controlled by various control strategies (traditional PID controllers, PLC controllers, fuzzy logic controllers etc.) via the proper controller connected to the computer. In the paper, two-conveyor-belt system for product packing is shown. The goal consists in control of synchronization of products and boxes placed on individual conveyor belts. The main concern here is to improve dynamic performance and control efficiency with the help of assembling the animated model of the controlled technological process and its external control by fuzzy logic unit.

Keywords —control, conveyor, fuzzy logic, process, controller, simulation

I. Introduction

It is desirable nowadays for researchers in engineering to try as much as possible to use some of their more understandable and/or practical work as a material to give an insight to behavior of real industry processes to industry technologists. In industry, there are still mostly used PID control, sliding mode control for multi degree of freedom analytical structural systems, PLC control and fuzzy logic control and their modifications like neuro-fuzzy technique etc.

The main goal of my research was to create a variable multifunctional simulation system that enables to design and assemble animated models of complicated technological processes with the help of personal computers and their external control by a fuzzy logic control unit The main concern in the paper is to improve dynamic performance of conveyors synchronization and control efficiency with the help of assembling an animated model of the controlled technological process and its external control by fuzzy logic unit. The simulation technique that will be discussed in the paper can take many forms and offers interesting ways for the technologists to explore and navigate them through the possibilities [1].

The presented paper reports how the work, I carried out in the areas of control of technological processes, has been used as a simulation tool to gain optimal settings of technological processes fuzzy controllers to reach the best process behavior in practice. In case of control of technological processes, the research work is concerned on the development of advanced solutions in fuzzy control strategy. These solutions are simulation-based and implement an active approach whereby control schemes react to random disturbances.

II. Simulation Tool

At the Czech technical University CTU in Prague, I developed a variable multifunctional simulation tool that enables to design and assemble animated models of technological processes with the help of personal computers. Such models of technological processes can be externally controlled by traditional PID controllers, PLCs and fuzzy logic. controllers.

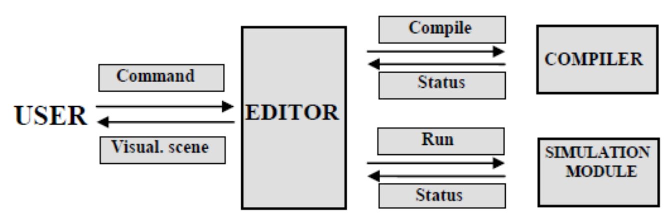

Fig. 1 communication between modules

I concentrated my attention on creating a universal, modular and user friendly system that would be easily extendable according to the user demands. To satisfy all these requirements, I created a system with a built-in editor, compiler, and simulation modules that would allow assembling wide class of technological scenes. The block diagram illustrating communication between the individual modules is shown in Fig.1.

Research supported by Project MSMT INGO II LG14005.
Assoc.Prof. K.Hyniova is with the Departmnt of Digital Design, Faculty of Information Technology, Czech Technical University in Prague, Thakurova 9, 160 00 Prague, Czech Republic, (phone: (+420) 722575989; e-mail: hyniova@fit.cvut.cz).

To ensure correct understanding behavior of the simulated technological processes, I created a concept of real-time animation. The only part with the help of which standard users can build up the simulated technological scene is the editor module. It contains a library of various objects which is comfortably extendable according to the user demands. The objects can be sorted into six categories:

- input objects (generators of analog and binary signals ...)
- drives
- actuators (conveyor belts, robots, start and destination points of transported subjects, ...)
- sensors (position sensors, tachogenerators, counters, etc.)
- output objects (scales, displays...)
- connections / linkages (cables, wires, pipelines)

The editor is equipped with a built-in checker for testing if all objects of the created scene are correctly located and do not cover each other. After the compilation command has been received, the compiler executes syntactic tests of the built scene and creates connections between the individual objects. If the compilation process is successful the compiler gives control back to the editor module that runs the simulation phase and announces a message about successful compilation.

In case of abortive compilation, the editor takes over the error code and announces an error message. The simulation module is represented by a simulation cycle that ensures testing of all scene objects every 50 ms. The simulation process can be externally interrupted by the user (by pushing a key) or internally by an error whose code is immediately announced in an error message.

The simulation module is a useful tool to check the knowledge of hardware structure and connections in the controlled process. It leads not only to understanding which components are suitable or necessary for the design but also gives a real imagination of all parameter levels in the process (supply voltages, actuator revolves, etc.). The simulation by itself gives immediately information to the user whether the created configuration of the simulated scene is correct or not.

III. Simulated Technological Process

To illustrate a built up scene and its connection to external control executed by fuzzy logic controller, I will show an illustrative example- externally controlled two conveyor belt process by the modular PLC C200H with fuzzy logic unit FZ001 OMRON .

The unit is used to control two conveyor belts for products packaging (Fig.2). The products are carried on the conveyor belt A at random intervals, but at a fixed speed. The boxes are carried at regular intervals on conveyor belt B, which runs in parallel to conveyor A at speed controlled by fuzzy logic unit. The fuzzy logic unit adjusts the speed of conveyor B so that the boxes arrive to the same point at the same time as the products. Actually, the goal is to synchronize occurrence of boxes and products at a place where the product will be packed in the box. The required information for conveyor B control is the offset E between the product and the box and the rate DE that the offset is changing.

The components of the simulated process and their function are given in the part list (Table I).

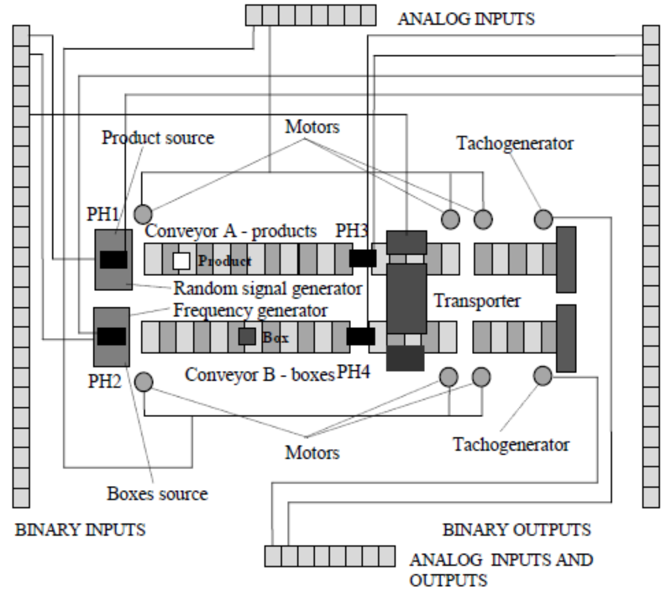

Fig. 2 simulated technological process - two conveyor belt system

Table I component list

Component	Component function
Motor A (B)	Drives conveyor belt A (B)
Tachogenerator A (B)	Tachogen. for conveyor belt A (B)
Photoelectric sensors (4)	Sense passing products and boxes
Input unit	Receives photoelectric sensor inputs
Output unit	Otputs to motors and conveyors
Analog input unit	Converts analog speed data to digital form
Analog output unit	Converts the digital output from fuzzy logic processing to analog data and outputs it

IV. Process Control

To control the technological process described above I chose the modular PLC C200H with fuzzy logic unit FZ001 OMRON [1], [2], [3], [4], [5]. It controls the process via interface boards AX 5212 (8 output analog voltage/current channels) and AX 5411 (16 input and 2 output analog channels, 24 input and output binary channels) manufactured

ISBN: 978-1-61804-321-4

by AXIOM. External control of the simulated process is then executed by PLC C200H OMRON with fuzzy logic unit FZ001 of the following configuration:

- binary inputs (sensors PH1, PH2, PH3 and PH4)
- analog inputs (conveyor A speed, Conveyor B speed)
- binary outputs (random frequency generator generating products and adjustable frequency generator generating boxes)
- analog outputs (conveyor A speed, conveyor B speed)
- configuration [4] :

C200H-CPU31	C200H-FZ001
C200H-OD212	C200H-ID21
C200H-PRO15-E	C200H-DA001
C200H-AD002	C200H-BC081
C200H-LK20	

The way how to set the fuzzy controller I will show in the next paragraph. Fuzzy logic controller provides an effective tool of capturing the inexact nature of the described industrial process. Basically, fuzzy logic controller converts linguistic control rules based on expert knowledge and experience into automatic control [1]. As the process behaves randomly conventional precise mathematical control is impossible.

V. FUZZY CONTROLLER

The basic configuration of fuzzy logic controller is shown in Fig.3. It consists of four basic components: a fuzzification interface, knowledge base, decision making logics that is also called inference machine and defuzzification interface.

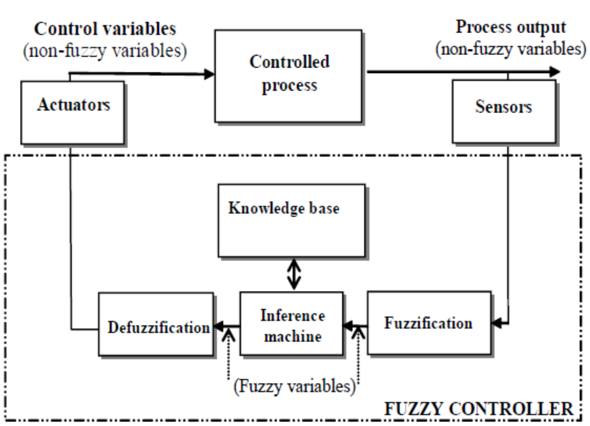

Fig.3 basic configuration of fuzzy logic controller

The fuzzification converts crisp output data of the controlled process into suitable linguistic variables [6].

To adjust the conveyor B speed VB to move the boxes to the same point where products occur at the same time, the information about offsets E between the products and the boxes and the rate DE that the offset is changing is necessary.

♦ The input data for product/box offset are taken from the relative product/box offset position E:

$$E=POS(Product) - POS(Box) \quad (1)$$

♦ The input data for the rate of change of the offset DE is the difference between the most recent value of E (i.e. E(n)) and the previous value of E (i.e. E(n-1)):

$$DE=E(n)-E(n-1) \quad (2)$$

The condition/conclusion membership functions that assign numerical values to how well a specific value of a fuzzy variable (E, DE /VB) satisfies the condition/conclusion part of the rule are shown in Fig.3.

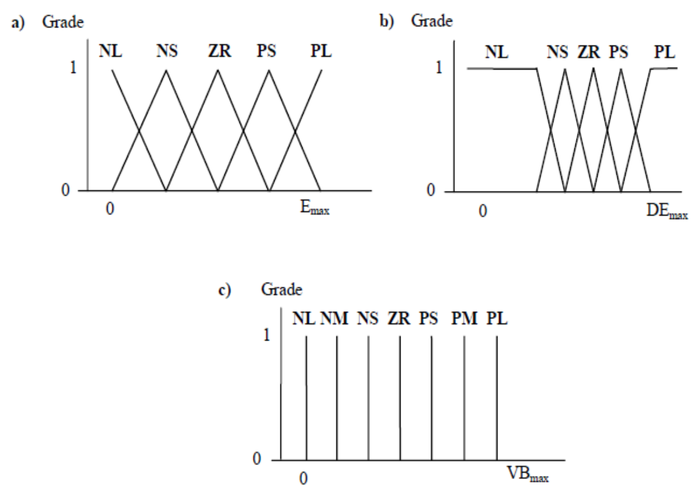

Fig. 4. condition membership functions for:
a) product/box offset E
b) offset rate of change DE
c) conclusion membership function (conveyor B speed VB adjustment)

In Fig. 4:

NL… Negative Large	PS … Positive Small
NM… Negative Medium	PM … Positive Medium
NS … Negative Small	PL … positive Large
ZR … Zero	

I created the rules by organizing my know-how about the simulated process in everyday expressions. These IF-THEN statements that show how much the conveyor B speed has to be adjusted depending on E and DE are presented in Table II.

ISBN: 978-1-61804-321-4

The linguistic rules given in Table II need to be converted to a simplified form (Table III) than can be entered into the fuzzy logic unit.

Table II expressing rules

E / DE	Box is ahead a lot	Box is ahead	About even	Product is ahead	Product is ahead a lot
Box is much faster	Slow box a lot	Slow box	Slow box a little	Speed the box up a little	Speed the box up
Box is faster	Slow box a lot	Slow box	Slow box a little	Speed the box up a little	Speed the box up
About even	Slow box a lot	Slow box a little	Do not change	Speed the box up a little	Speed the box up a lot
Box is slower	Slow box	Slow box a little	Speed the box up a little	Speed the box up	Speed the box up a lot
Box is much slower	Slow box	Slow box a little	Speed the box up a little	Speed the box up	Speed the box up a lot

Table III converting to labels

DE / E	NL	NS	ZR	PS	PL
NL	*NL*	*NM*	*NS*	*PS*	*PM*
NS	*NL*	*NM*	*NS*	*PS*	*PM*
ZR	*NL*	*NS*	*ZR*	*PS*	*PL*
PS	*NM*	*NS*	*PS*	*PM*	*PL*
PL	*NM*	*NS*	*PM*	*PM*	*PL*

The final result of the fuzzy logic processing for the fuzzy logic outputs is calculated by center of gravity method.

The crisp value of the controller output defuzzification is calculated according to the following center of gravity formula:

$$x_T = \frac{\int_{-FFF}^{+FFF} \mu^*(x)\,x\,dx}{\int_{-FFF}^{+FFF} \mu^*(x)\,dx}, \qquad (3)$$

where $\mu^*(x)$ is the area line determined by the output value membership function.

Center of gravity method computes the center of gravity of singletons (Fig.4c) that have been defined by firing of any of the rules. These singletons are weighted by the given rule weight. It can be immediately verified on the computer screen that the simple knowledge base shown above gives surprisingly good results.

VI. Conclusion

A simple example of simulated externally controlled technological process has been presented. A series of such illustrative examples is used in the university courses ”Processes Control at the Dept. of Digital Design at the Czech Technical University in Prague to make control strategies and techniques more understandable and creative.

The simulation tool has been tested in industry, namely in a soap manufacture. On the base of the simulation, they reached satisfactory results in fuzzy logic control of synchronized conveyor belts in practice. They set the same fuzzy controller parameters like during the simulation and gained very satisfactory synchronization of products and boxes carried on the conveyer belts.

References

[1] K.Hyniova, A. Stribrsky, “*Instrumentation of processes*,” FEE CTU. Prague, pp. 160-189,2014, 1964

[2] *OMRON C200H – operation manual, OMRON* 1992.

[3] *OMRON C200H –FZ001Fuzzy logic unit-Operation manual, OMRON,* 1992.

[4] *OMRON Programming tool for OMRON PLC, OMRON,* 1996.

[5] *OMRON Fuzzy Support Software-Operation manual, OMRON,* 1992.

[6] L. A. Zadeh, “Outline of a New Approach to The Analysis of complex Systems and Decision Processes,” *Trans .Syst,. Man, Cyber. Vol-SMC-3,no.1, pp.28-44, 1973.*

K. Hyniova (born in 1963)
Ing. in technical cybernetics at the Faculty of Electrical Engineering at the Czech Technical university (CTU) in Prague, Czech Republic, (1987), PhD in technical cybernetics at the Faculty of Electrical Engineering, CTU in Prague, Czech Republic, (1991), Assoc. Prof. in control engineering and measurement, at Faculty of Electrical Engineering, at the CTU in Prague, CZ, (2000).

She has worked at the Department of Control Engineering, Faculty of Electrical Engineering, CTU in Prague, CZ first as an assistant professor, later as an Associated Professor. Currently she is working as an Associated Professor at the Department of Digital Design, Faculty if Information technology, CTU in Prague, CZ. She published 5 books and over 70 papers (Hyniova, K.: Instrumentation of processes, Prague, Czech Republic, CTU Publishing, 1999; Hyniova, K.: Control Systems, Prague, Czech Republic, CTU Publishing, 2012; Hyniova, K.: An Innovative Active Suspension System for Autonomous Vehicles: A Safe and Comfortable Ride and Good Handling, In *ERCIM NEWS*, No. 94, ERCIM EEIG, France, pp.28-29, 2013)). She is interested in intelligent vehicles control systems, vehicle dynamics and in consistency in networks of relations.

She is a member of Technical Committee 4.2 on Mechatronic Systems, IFAC.

Home office as a benefit in relation to job satisfaction

V. Zubr, M. Sokolová

Abstract**—**Job satisfaction plays an important role in the development and position of each company in the market. To ensure employees' satisfaction, companies offer them a variety of benefits. A satisfied employee is then more loyal, committed, motivated and shows higher performance levels. Home office in the Czech Republic represents quite a rarely used benefit but it would be welcomed by almost three-quarters of employees. The aim of the survey was to determine employees' satisfaction with their benefits and to map the degree of providing choice of benefits in the Czech Republic. Also, the aim was to determine the extent of use of home office and the interest in this benefit. The survey was conducted by a questionnaire survey, the questionnaires were distributed during the period from March to May 2013. There was 1,776 valid questionnaires successfully processed, the survey was attended by 762 men and 1,014 women aged 17 - 74 years. The results suggest the dissatisfaction of employees with the benefits provided, the differences in the provided benefits as well as their equitable distribution.

Keywords**—**job satisfaction, employee, benefits, home office

I. INTRODUCTION

EMPLOYEES' satisfaction - a key factor that affects not only the employees themselves, but also the success and operation of each enterprise (company) and which is regularly monitored by each company or employer. Why is employees' satisfaction so important and what does the term of "employees' satisfaction" actually mean?

According to the business vocabulary "employees' satisfaction" is defined as "a satisfaction (or lack thereof) that emerges from the interplay of positive and negative feelings of an employee in relation to their employment" [1]

Employees who are satisfied with their work, are more involved, loyal, productive, absent less often at work and prefer to stay working in the organisation. Conversely, if the employees are not satisfied, it leads to their higher turnover in the company and at the same time it increases their absence. [2]

Employees' satisfaction doesn't only affect only the company but also the employees themselves. It has been proven that level of job satisfaction is among the most important factors that affect the health of employees. [3]

Employees contribute significantly to a company's success in the market, and if they are not satisfied, they can harm the company in some way, even if unintentionally. These facts show that for proper functioning of an organisation the support of employee's satisfaction is needed. This is often accomplished through various employee supports and benefits and the private employees' satisfaction is monitored and detected by personal interviews or questionnaires. [4]

II. THEORY

Employees' benefits are an indisputable role in building employees' satisfaction. Most often, these benefits are for example, the balance between personal and professional life, pension plan, defined benefit plans, flexible working hours and the possibility of working at home. The survey report of the Companies for Human Resources Management from 2013 shows that in relation to job satisfaction, employees indicated the following five factors as very important:

- total compensation (payment),
- work safety,
- opportunities to use the knowledge and skills,
- relationship with direct supervisor
- overall benefits.

Historically, benefits have been a significant factor in regards to contributors towards job satisfaction for employees. From 2002 to 2010, the benefits aspect ranked amongst the top two contributors of job satisfaction. In 2013, approximately three-fifths (62%) of employees indicated that they were satisfied with their benefits. From the specific health benefits, 62% of the respondents indicated the option of health care as important, 4% fewer employees consider the option of paid time off as an important benefit. Especially women appreciate the benefit in the form of flexibility of personal and professional life. [5]

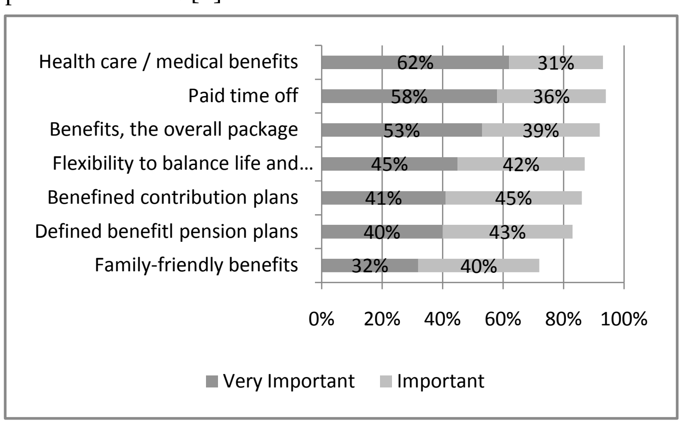

Fig. 1: Importance level of benefits aspects

This benefit is directly related to the ability to work from home, which is quite often offered by different companies. The following chart describes the results of the survey on the positives and negatives of work from any place other than the workplace. [6]

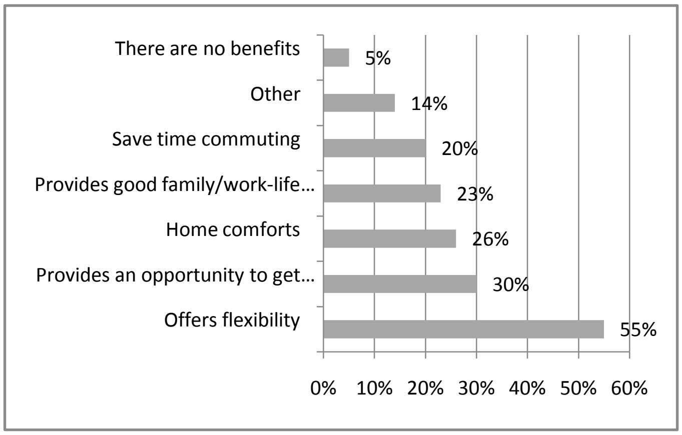

Fig. 2: Perceived benefits of working away from any place other than the workplace

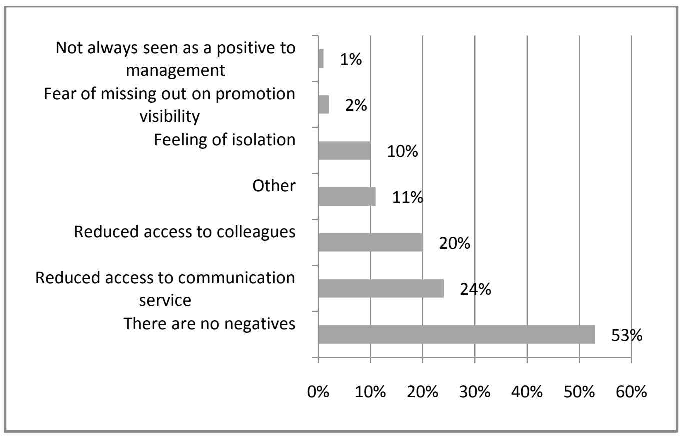

Fig. 3: Perceived negatives of working away from any place other than the workplace

In the case that employees are able to work from any place other than their own workplace, 82% of them choose to work from home. According to a survey from May 2013, 22% of employees work from any place other than workplace for more than 4 days a week. [6]

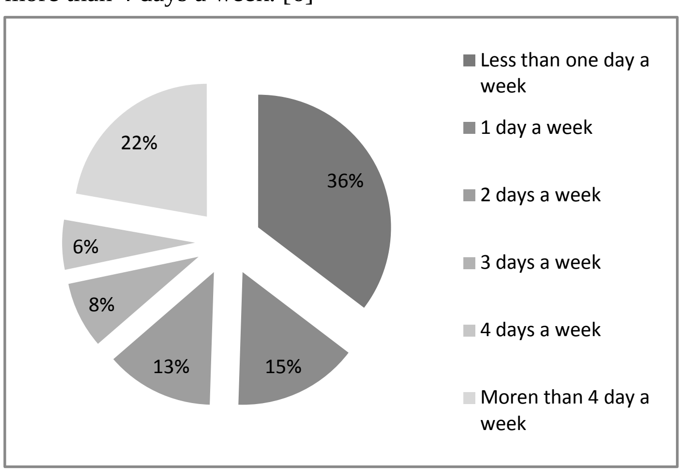

Fig. 4: Frequency of working away from workplace via the internet

According to the work from home survey in the it has been discovered pharmaceutical sector that there is an increase in flexible working with 45% of companies allowing staff to work from home on two or more days and only a quarter of companies allowing no time at all to work from home.

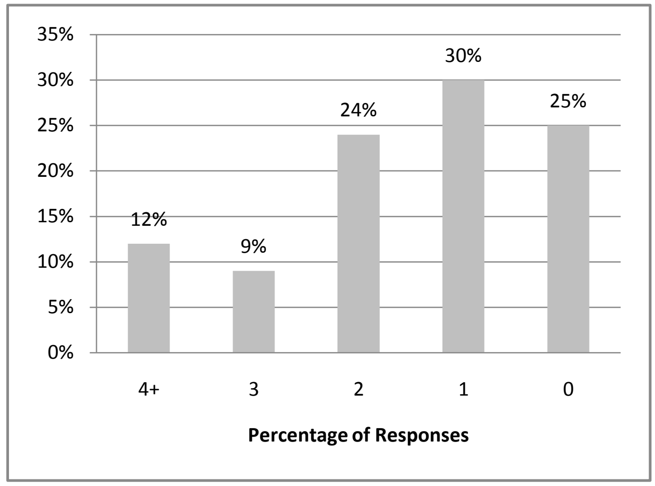

Fig. 5: Days per week worked from home [7]

Assessment of home office as a work benefit in relation to employees' satisfaction is the subject of the survey.

III. Methodology

The questionnaire survey was conducted with 1,776 valid questionnaires. The questionnaire survey was implemented from March to May 2013, the questionnaires were distributed among the respondents by trained interviewers from students of the Faculty of Informatics and Management of Hradec Králové from combined form of study. The respondents were mainly from the north-eastern regions of the Czech Republic (regions of Hradec Králové, Pardubice and part of the respondents were from the Vysočina region). The respondents consisted of 762 men and 1,014 women aged 17-74 years. The average age of the respondents was 36.3 years (SD = 10.80). The distribution of the respondents by occupation is described in Table 1.

Human work activities	**Total**
Without specification	41
Accommodation and food service activities	87
Administrative and support service activities	47
Agriculture, forestry and fishing	29
Arts, entertainment and recreation	17
Construction	79
Education	214
Electricity, gas, steam and air-conditioning supply	44
Financial and insurance activities	80
Human health services	62
IT and other information services	100
Legal, accounting, management, architecture, engineering, technical testing and analysis activities	44

Manufacture of basic metals and fabricated metal products, except machinery and equipment	25
Manufacture of computer, electronic and optical products	17
Manufacture of electrical equipment	25
Manufacture of food products, beverages and tobacco products	23
Manufacture of chemicals and chemical products	30
Manufacture of machinery and equipment n.s.e.	41
Manufacture of pharmaceuticals, medicinal chemical and botanical products	2
Manufacture of rubber and plastics products, and other non-metallic mineral products	20
Manufacture of textiles, apparel, leather and related products	22
Manufacture of transport equipment	30
Manufacture of wood and paper products, and printing	20
Other manufacturing, and repair and installation of machinery and equipment	26
Other professional, scientific and technical activities	13
Other services	51
Public administration and defence, compulsory social security	134
Publishing, audio-visual and broadcasting activities	5
Real estate activities	8
Residential care and social work activities	23
Scientific research and development	5
Telecommunications	21
Transportation and storage	111
Water supply, sewerage, waste management and remediation	11
Wholesale and retail trade, repair of motor vehicles and motorcycles	269
Total	**1776**

Tab. 1: Spectrum of human work activities sorted by SNA/ISIC aggregation

IV. Results

The questionnaire survey was completed by a total of 746 respondents employed in an organisation with a Czech owner, 375 respondents employed in a foreign organisation, 238 respondents employed in an international company and 417 respondents working for the state, contributory or budgetary organisation.

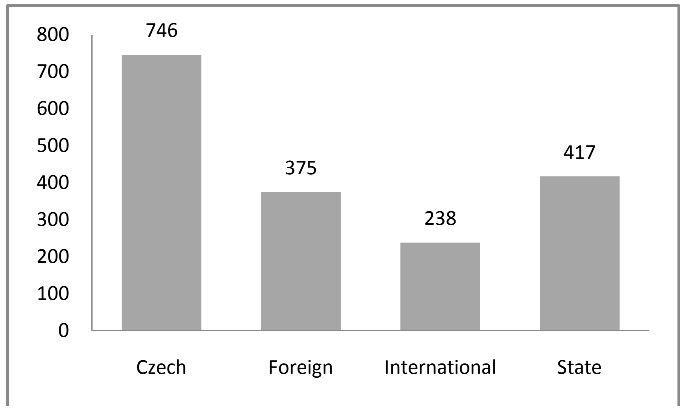

Fig. 6: Type of organisation

Of all respondents, the majority (637) were employed in companies with fewer than 50 employees, 535 respondents were employed in companies with up to 250 employees. The least number of respondents (161) works in companies with up to 500 employees and 443 respondents work in companies with more than 500 employees. The distribution of the respondents by size of organisation can be seen from the chart.

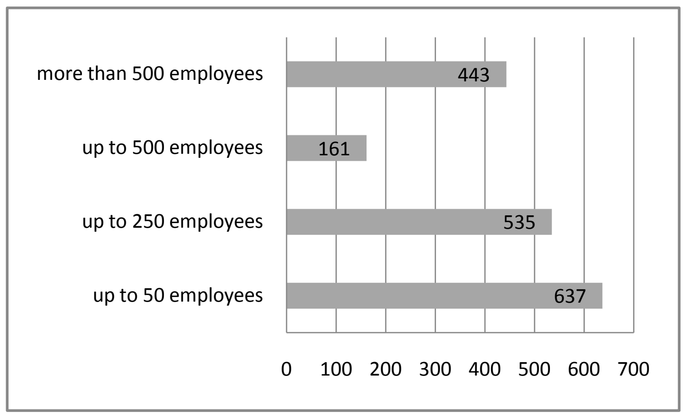

Fig 7: Company size

The following chart shows the percentage distribution of the responses to the question of whether the employees are confident of fair financial rewards for their work. As it is clear from the survey, more than half of the respondents somewhat agree or agree with their financial rewards. Less than half of the respondents expressed disagreement to this claim.

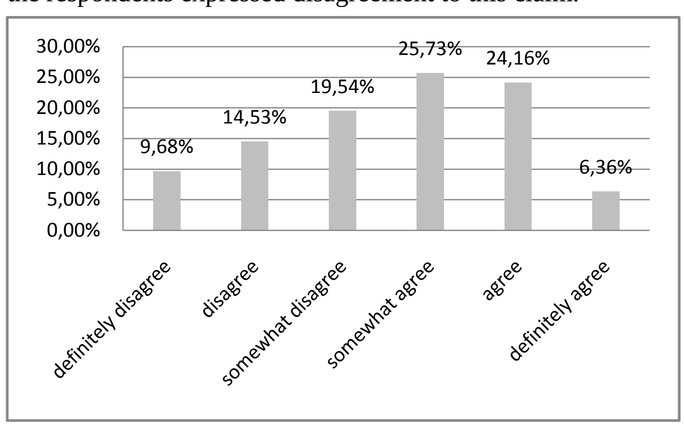

Fig. 9: Equitable financial rewards of work

When comparing the benefits offered in the company with benefits in other companies, nearly 55% of respondents answered somehow disapprovingly to the question: "The benefits that we have in our company are comparable with benefits in other companies." The overall distribution of the percentage representation of individual responses can be seen from the chart.

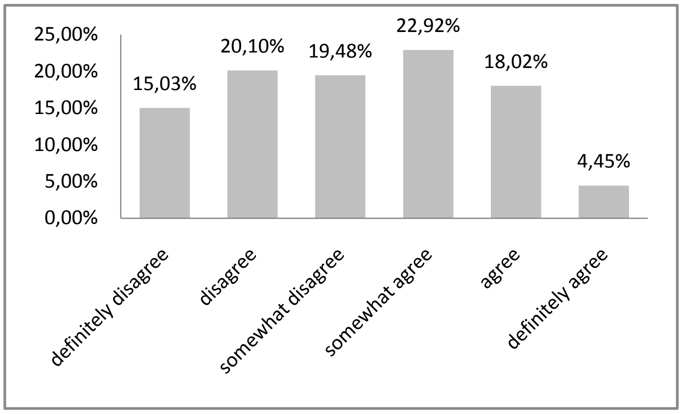

Fig. 10: Comparable benefits

The benefits which the given company provides, may or may not lead to employees' satisfaction. As shown in the chart below, more than 53% of employees in some way agree with the statement: "I am not satisfied with the benefits which I receive."

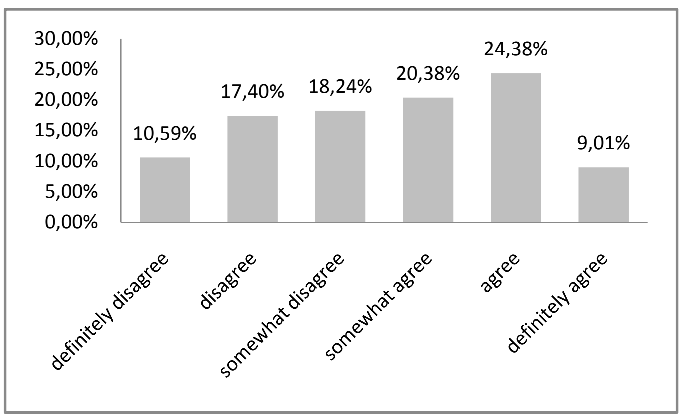

Fig. 11: Dissatisfaction with benefits

Almost 61% of the respondents replied with disagreement to the question: "There are benefits that we do not have, even though we should definitely have them".

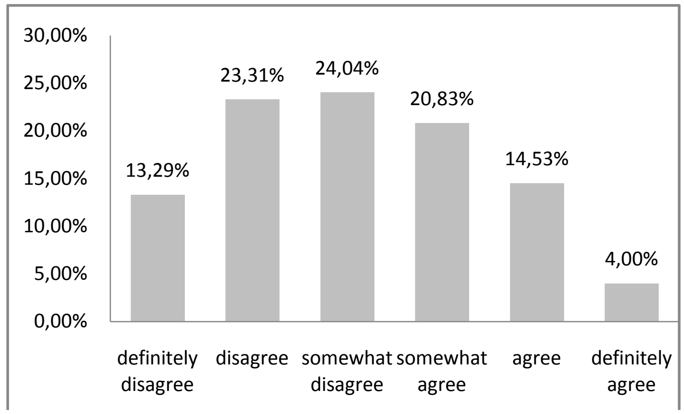

Fig. 12: Lacking benefits that employees want

More than half of the respondents agree with the statement that the benefits, which the companies provide, are distributed fairly.

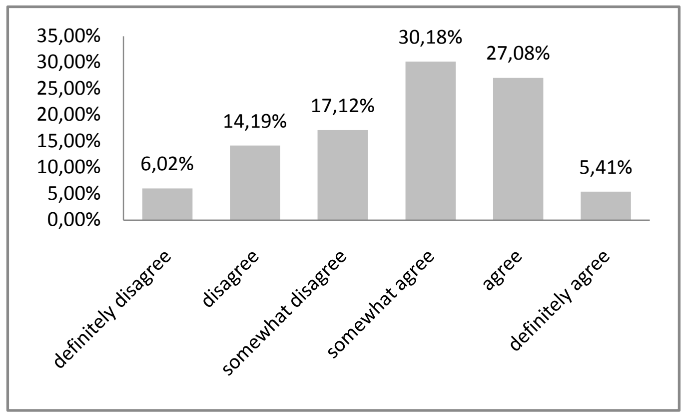

Fig. 13: Fair distribution of benefits

V. Discussion

One of the points that affects employees' satisfaction is their financial reward. As is clear from the survey, more than half of the respondents are satisfied with their financial rewards. The effect of financial remuneration and benefits on job satisfaction and work motivation is illustrated in the following figure:

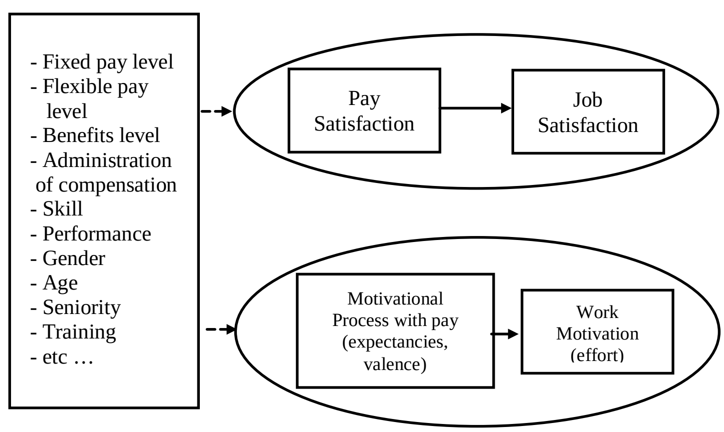

Fig: 14: The role of financial rewards [8]

The survey also shows that the benefits usually differ in different companies. According to the study of employees' benefits of the ING Insurance Company and the Confederation of Industry and Transportation of the Czech Republic, up to 99% of companies provide benefits to their employees. On average, they offer 10 benefits, larger companies offer more benefits. [9]

Due to the variability of the respondents, the diversity of benefits is also reflected in our survey.

Some respondents also expressed the view in our survey that they would like to have benefits that are not yet established in the company. Overall, the provision of benefits in such form as now, according to the survey, does not satisfy more than 53% of respondents. This can be attributed to the low attractiveness of the provided benefits. According to the study of employees' benefits of the ING Insurance Company and the Confederation of Industry and Transportation of the Czech Republic, the most common benefits provided in the Czech Republic include a mobile phone (87%), the possibility of training (58%), drinks and food vouchers (82%). Lower interest was recorded in the survey for contributions to additional pension insurance and additional pension savings. Benefits such as medical examinations or sick days become more common among employee benefits, life insurance is provided to its employees by 53% of companies. [9]

The most common employee benefits provided in the Czech Republic miss the opportunity to work from home which is quite often used in the world. According to "The survey results no. 7 AMSP of the Czech Republic: Opinions of entrepreneurs regarding employment policy and labour law", only 30% of the surveyed business owners offer its employees the opportunity to work from home. As the main disadvantage of working from home, 44% of business owners see the fact that it is not possible to control the employees during work. The advantage of working from home is seen by most respondents in cost savings in the company. [10]

Other possible reasons for the low use of working from home may be greater administrative burdens in the implementation of home office and the calculation of labour-law rights of employees working from home and more difficulties for the protection of trade secrets and confidential information. [11]

According to research by KPMG Czech Republic from 2013, three quarters of Czechs would like to work from home, while working from home is the most attractive for respondents aged 18 to 29 years (88%), it is the least popular for people over 45 years old (67%). [12]

Home office provides time flexibility to these people, time and cost savings, while the employers allowing home office obtain benefits such as employees' satisfaction, their motivation and greater productivity. [11]

Handling benefits from the overall survey appears to be equal for all employees, of which the absolute majority is in agreement with their equitable distribution.

VI. Conclusion

This paper highlights the issue of employees' satisfaction and providing employee benefits. It turns out that employees are often not satisfied with the benefits that their employer provides, while in most cases, they are interested in the possibility of working from home. In the case of overcoming the possible negatives in terms of the employer, the introduction of home office would bring highly prized benefits in a number of areas - employees satisfied with employment, being more productive and creative.

Acknowledgment

The paper was written with the support of the specific project grant "Determinants affecting job satisfaction" granted by the University of Hradec Králové, Czech Republic.

References

[1] BusinessDictionary.com. (2015) Job Satisfaction [Online]. Available: http://www.businessdictionary.com/definition/job-satisfaction.html

[2] P. Lotich (2014, October). How to Improve Job Satisfaction and Job Performance [Online]. Available: http://thethrivingsmallbusiness.com/job-satisfaction-and-job-performance/

[3] E. B. Faragher. The relationship between job satisfaction and health: a meta-analysis. Occupational and Environmental Medicine [online]. vol. 62, issue 2, 2005, pp. 105-112. DOI: 10.1136/oem.2002.006734. Available: http://oem.bmj.com/content/62/2/105.full.pdf+html

[4] survio.com (2015). Employee Satisfaction [Online]. Available: http://www.survio.com/en/employee-satisfaction-surveys

[5] Ch. Lee, A. Alonso, E. Esen, J. Coombs and Y. Dong. Society for Human Resource Management (2014). Employee Job Satisfaction and Engagement. [Online]. ISBN 978-1-586-44371-9. Available: http://www.shrm.org/Research/SurveyFindings/Documents/14-0028%20JobSatEngage_Report_FULL_FNL.pdf

[6] H. Polites (2013, October) Teleworking trend picks up pace: ACMA. [Online]. Available: http://www.businessspectator.com.au/news/2013/10/16/technology/teleworking-trend-picks-pace-acma

[7] Blue Pelican (2012). 10 ways to justify working from home. [Online]. Available: http://www.bluepelican.com/news/10-ways-justify-working-home

[8] J. Igalens, P. Roussel (1999 A study of the relationships between compensation package, work motivation. Journal of Organizational Behavior. vol. 20, pp. 1003-1025. [Online]. Available: http://www.managementcheck.de/Downloads/Research%20Studies/BenefitsMotivation%20-%20JoOB%20-%201999.pdf

[9] HR News (2013, August). Study: Most common benefits in the Czech Republic are cellphone and education. [Online]. Available: http://www.hrnews.cz/portal/template/EcNewsArticleDetail/id/1915309

[10] AMSP ČR (2010, August). Opinions of entrepreneurs to employment policy and labor law. [Online]. Available: http://www.amsp.cz/uploads/Pruzkum_c7.pdf

[11] P. Sochorová, V. Plešková, M. Mínárová, Z. Lara (2013). HOME OFFICE or work from home. [Online]. Available: http://www.aperio.cz/zdrava-firma-2014/doc/19_PMF_Home_office_aneb_prace_z_domova.pdf

[12] KPMG (2013, April). Popular home-office: work from home want three quarters of Czechs. [Online]. Available: http://www.kpmg.com/cz/cs/issuesandinsights/articlespublications/press-releases/stranky/popularni-home-office.aspx

Towards near-nadir estimation of wind over water surface

Alexey Nekrasov

***Abstract*—**The possibility of recovering near-surface wind over water from near-nadir backscatter measurements is discussed. Anisotropic water surface approach is considered. A particular case to obtain backscatter data for combinations of various numbers of azimuth and incidence angles limited due to peculiarity of measuring geometry that is similar to the Airborne Precipitation Radar-2 geometry is analyzed. An algorithm for measuring the water surface slope variance and estimating the wind speed and direction over water is presented.

***Keywords*—**Airborne Precipitation Radar, near-nadir water-surface backscatter, sea wind retrieval.

I. Introduction

BACKSCATTER of radio waves from sea surface varies considerably according to the incidence angle [1]. Near nadir, there is a region of quasi-specular return with a maximum of normalized radar cross section (NRCS) that decreases when increasing angle of incidence. Between incidence angles of about 20° and 70°, NRCS falls smoothly in a so-called "plateau" region. For these incidence angles, microwave radar backscatter is predominantly due to presence of capillar-gravity wavelets, which are superimposed on large gravity waves on the sea surface. Small-scale sea waves approximately one half the radar wavelength are in Bragg resonance with an incident electromagnetic wave. At incidence angles greater than about 70°, there is a "shadow" region in which the NRCS falls dramatically, due to the shadowing effect of waves closer to the radar blocking waves further away.

The wind blowing over water modifies surface backscatter properties. They depend on wind speed and direction. Wind speed U can be determined by a scatterometer because a stronger wind will produce a smaller NRCS at a small (near nadir) incidence angle θ, and a larger NRCS at a medium incidence angle. Wind direction can also be inferred, especially at medium incidence angles, because NRCS $\sigma^\circ(U,\theta,\alpha)$ varies as a function of azimuth illumination angle α relative to up-wind direction [2].

This work was supported in part by the German Academic Exchange Service (DAAD)

A. Nekrasov was with the Institute of High Frequency Technology, Hamburg University of Technology, Hamburg, 21073, Germany. He is now with the Taganrog Institute of Technology, Southern Federal University, Taganrog 347922, Russia (e-mail: alexei-nekrassov@mail.ru).

To retrieve the wind speed from altimeter (nadir-looking scatterometer) NRCS measurements, a relationship between NRCS and near-surface wind (altimeter wind retrieval algorithm) is used. A number of altimeter wind retrieval algorithms of various forms have been developed during last several decades. For instance, some of such Ku-band algorithms are [3]

$$\sigma^\circ(U,0^\circ)[dB] = 10\left(G_1 + G_2 \log_{10} U_{19.5}\right), \tag{1}$$

where G_1 and G_2 are the known parameters, $G_1 = 1.502$, $G_2 = -0.468$, $U_{19.5}$ is the wind speed at 19.5 m above the water surface, and [4]

$$U_{10} = U_m + 1.4 U_m^{0.096} \exp(-0.32 U_m^{1.096}), \tag{2}$$

where U_{10} is the wind speed at 10 m above the water surface, U_m is the first-guess estimation of the wind speed presented as a two segment function based on a linear dependence and a power law relation for low and high backscatter values respectively,

$$U_m = \begin{cases} 46.5 - 3.6\sigma^\circ(0^\circ)[dB], \\ \qquad \text{for } \sigma^\circ(0^\circ) \le 10.917\, dB; \\ 1690\exp(-0.5\sigma^\circ(0^\circ)[dB]), \\ \qquad \text{for } \sigma^\circ(0^\circ) > 10.917\, dB. \end{cases} \tag{3}$$

Remote sensing of sea surface wind by means of a radar altimeter is based on specular returns from water surface. Typical accuracy of wind speed measurement by nadir-looking scatterometer (altimeter) is about ±2 m/s at moderate winds (3–12 m/s) [5]. Unfortunately, for some special cases of measurement geometry, specific radar instrument configuration or its installation on board of an aircraft, the near-nadir NRCSs only can be available during the measurement. Such a case takes place for example when a measuring geometry of the Airborne Precipitation Radar-2 (APR-2) is used. In this connection, a principle of recovering the sea surface wind along with surface slope variance from near-nadir NRCS data is discussed in this paper.

II. Water-Surface Wind Retrieval

APR-2 is an airborne, dual-frequency (Ku- and Ka-band), dual-polarization Doppler rain profiling radar. Its antenna scans in the $\pm 25°$ cross-track elevation range allowing the radar to measure atmospheric precipitation and water surface NRCS. Each cross-track scan is sampled at 23 positions (since 2003, the 24th position is used for noise floor measurements) [6], [7]. Since during the Wakasa Bay Experiment in 2003, the radar was configured to operate at a forward-looking angle of 3° and aircraft pitch angle was about + 1° we may assume that the incidence angle θ_0 in that case was no more than 4°.

Let an aircraft equipped with APR-2 or radar with the observation geometry similar to APR-2 (Fig. 1) perform a horizontal rectilinear flight with speed V at some altitude H above mean sea surface.

Let the radar operate in a scatterometer mode, its antenna have beamwidths $\theta_{a.v}$ and $\theta_{a.h}$ in the vertical and horizontal planes, respectively, scan periodically over cross-track elevation range of $\pm\,\theta_s$, and provide NRCS measuring from a current selected cell as shown in Fig. 1. Then, measured NRCS will correspond to the current near-surface wind speed U, incidence angle θ, and azimuth illumination angle α relative to the up-wind direction.

In accordance with the measuring geometry of Fig. 1 the current incidence angle and horizontal angle φ of the selected sell relative to the aircraft course ψ are as follows

$$\theta = \arccos(\cos\theta_0 \cos\theta_s)\,, \tag{4}$$

$$\varphi = \arctan\left(\frac{\tan\theta_s}{\sin\theta_0}\right) \quad \text{for} \quad \theta_0 > 0^\circ\,, \tag{5}$$

where θ_0 is the incidence angle for the selected cell when scanning beam direction in the vertical plane coincides with the aircraft course,

$$\theta_0 = \theta_m + \theta_{fl}\,, \tag{6}$$

where θ_m is the antenna mounting angle, and θ_{fl} is the aircraft pitch angle.

If near-nadir NRCSs are available for incidence angles of up to 15° – 20° during measurement, water surface is considered as anisotropic and expressed by Gaussian statistics. Then, the incidence and azimuth angle dependence for the quasi-specular scattering is expressed as following [8]

$$\sigma^\circ(\theta,\alpha) = \frac{\left|R(0^\circ)\right|^2}{2S_uS_c}\cdot\frac{1}{\cos^4\theta}\exp\left(-\frac{\tan^2\theta}{2S^2(\alpha)}\right), \tag{7}$$

where $\sigma^\circ(\theta,\alpha)$ is the NRCS depending on the incidence angle and the azimuth angle α relative to the up-wind direction, S_u and S_c are the up-wind and cross-wind standard deviations of slopes, and $S^2(\alpha)$ is the water surface slope variance in the azimuthal direction α (with respect to the up-wind direction) [8],

$$S^2(\alpha) = \frac{S_u^2S_c^2}{S_u^2\sin^2\alpha + S_c^2\cos^2\alpha}\,. \tag{8}$$

Hence, for nadir incidence angle, equation (7) is simplified to

$$\sigma^\circ(0^\circ) = \frac{\left|R(0^\circ)\right|^2}{2S_uS_c}\,. \tag{9}$$

As three parameters are unknown in (7) and azimuth water surface slope variance is represented in the elliptical form of (8), at least five NRCSs from essentially different azimuth angles are required to calculate them. A star-beam location is the most preferable for such azimuth NRCSs in this case.

If a number of NRCSs available from essentially different azimuth directions is $N \geq 5$, then using (7), the following system of N equations can be written down

$$\begin{cases} \sigma_1^\circ(\theta_1,\alpha) = \dfrac{\left|R(0^\circ)\right|^2}{2S_uS_c}\cdot\dfrac{1}{\cos^4\theta_1}\exp\left(-\dfrac{\tan^2\theta_1}{2S^2(\alpha)}\right), \\ \sigma_2^\circ(\theta_2,\alpha+\Delta\varphi_{1,2}) = \dfrac{\left|R(0^\circ)\right|^2}{2S_uS_c}\cdot\dfrac{1}{\cos^4\theta_2}\times \\ \qquad \exp\left(-\dfrac{\tan^2\theta_2}{2S^2(\alpha+\Delta\varphi_{1,2})}\right), \\ \cdots\cdots\cdots\cdots\cdots\cdots\cdots\cdots\cdots \\ \sigma_N^\circ(\theta_N,\alpha+\Delta\varphi_{1,N}) = \dfrac{\left|R(0^\circ)\right|^2}{2S_uS_c}\cdot\dfrac{1}{\cos^4\theta_N}\times \\ \qquad \exp\left(-\dfrac{\tan^2\theta_N}{2S^2(\alpha+\Delta\varphi_{1,N})}\right), \end{cases} \tag{10}$$

where $\sigma^\circ(\theta_1,\alpha)$, $\sigma^\circ(\theta_2,\alpha+\Delta\varphi_{1,2})$, …, $\sigma^\circ(\theta_N,\alpha+\Delta\varphi_{1,N})$ are NRCSs corresponding to appropriate incidence angle θ_1, …, θ_N and appropriate azimuthal direction, $\Delta\varphi_{1,2}$, …, $\Delta\varphi_{1,N}$ are the azimuth angles between the azimuth NRCS 1 and the appropriate azimuth NRCS 2, …, N (angles between azimuth of $\sigma^\circ(\theta_1,\alpha)$ and appropriate azimuth of $\sigma^\circ(\theta_2,\alpha+\Delta\varphi_{1,2})$, …, $\sigma^\circ(\theta_N,\alpha+\Delta\varphi_{1,N})$).

Solving the system of equations (10) approximately using searching procedure within the ranges of discrete values of possible solutions, the up-wind direction as well as the up-wind and cross-wind standard deviations of slopes can be calculated. Then, an appropriate nadir NRCS value can be found from (9) and used in an appropriate altimeter wind

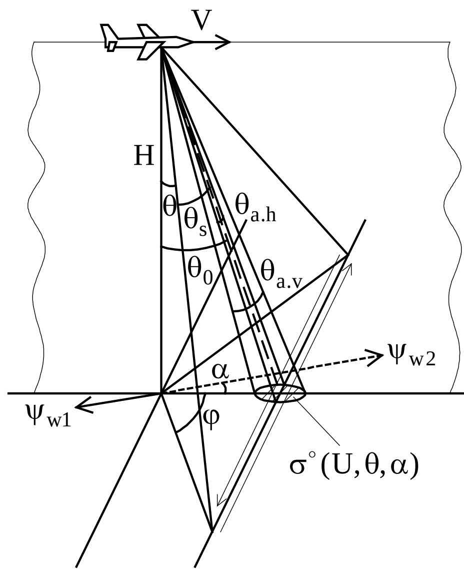

Fig. 1 Airborne precipitation radar measuring geometry

retrieval algorithm to recover the near-surface wind speed over water. Also, as the azimuth water surface slope variance has been assumed to be elliptical as given by (8), the wind direction ψ_w can be obtained but with an ambiguity of 180°

$$\psi_{w1,2} = \begin{cases} \alpha \pm 180^{\circ}, \\ \alpha. \end{cases} \quad (11)$$

In common case, the incidence angles θ_1, …, θ_N can be the same or different. To provide more precise estimation of the wind direction, the incidence angles should be as far from nadir as possible but within the range of validity of backscatter model (7).

Thus, a nadir wind speed retrieval algorithm can be adapted for recover of the wind speed over sea from the near-nadir NRSC measurement taking into account anisotropic properties of the water surface. Furthermore, if during the measurement the NRCSs are available for incidence angles up to 15°–20°, the wind direction corresponding to the up-wind (maximum) standard deviations of the water surface slopes also can be estimated.

The wind measurement using the measuring geometry of Fig. 1 is started when a stable rectilinear flight at the given altitude and speed of flight has been established. The measurement is finished when a required number of NRCS samples for each given incidence angle is obtained. To obtain a greater number of NRCS samples for each incidence angle several consecutive beam sweeps may be used.

III. Conclusion

The study has shown that the airborne radar instrument that has a measuring geometry similar to the APR-2 measuring geometry and operating in the scatterometer mode can be applied for remote measurement of the sea surface wind speed and direction at near-nadir incidence angles based on the measuring algorithm developed in case of precipitation absence. Otherwise, wind measuring algorithm should take into account precipitation. As the azimuth water surface slope variance has been assumed to be elliptical, the wind direction can be estimated, unfortunately, only with an ambiguity of 180°. It means that in principle the APR-2 also can be applied for the wind retrieval over the water surface at a rectilinear flight in addition to its typical meteorological application.

The principle considered and algorithm proposed in this paper can be used for enhancement of APR-2 or similar radars, as well as for designing new radar systems for operational measurement of the sea roughness characteristics and for estimation of wind speed and direction over water at near-nadir NRCS measurement.

Acknowledgment

I would like to express my sincere thanks to the German Academic Exchange Service (DAAD) for research fellowship partially supported this research and the Hamburg University of Technology for the research opportunity provided.

References

[1] P. H. Hildebrand, "Estimation of sea-surface wind using backscatter cross-section measurements from airborne research weather radar," *IEEE Trans. Geosc. Remote Sens.*, 1994, vol. 32, no. 1, pp. 110–117, Jan. 1994.

[2] M. W. Spencer and J. E. Graf, "The NASA scatterometer (NSCAT) mission," *Backscatter*, vol. 8, no. 4, pp. 18–24, Nov. 1997.

[3] D. B. Chelton and P. J. McCabe, "A review of satellite altimeter measurement of sea surface wind speed: With a proposed new algorithm," *J. Geophys. Res.*, vol. 90, no. C3, pp. 4707–4720, May 1985.

[4] S. Abdalla, "Ku-band radar altimeter surface wind speed algorithm", in *Proc. Envisat Symposium 2007*, Montreux, Switzerland, 23–27 Apr. 2007, 6 p.

[5] G. J. Komen, L. Cavaleri, M. Donelan, K. Hasselmann, S. Hasselmann, and P.A.E.M. Janssen, *Dynamics and Modelling of Ocean Waves*, Cambridge, UK: Cambridge University Press, 532 p., 1994.

[6] S. Tanelli, J. P. Meagher, S. L. Durden, and E. Im, "Processing of high resolution, multiparametric radar data for the Airborne Dual-Frequency Precipitation Radar APR-2," in *Proc. SPIE*, Dec. 2004, vol. 5654, pp. 25–32.

[7] S. Tanelli, S. L. Durden, and E. Im, "Simultaneous measurements of Ku- and Ka-band sea surface cross sections by an airborne radar," *IEEE Geosci. Remote Sens. Lett.*, vol. 3, no. 3, pp. 359–363, Jul. 2006.

[8] M. A. Donelan and W. J. Pierson, "Radar scattering and equilibrium ranges in wind-generated waves with application to scatterometry," *J. Geophys. Res.*, vol. 92, no. C5, pp. 4871–5029, May 1987.

Alexey Nekrasov received the diploma in radio engineering, the Ph.D. degree (Candidate of Technical Science) and the academic title of Associate Professor from Taganrog State University of Radio Engineering (TSURE), Taganrog, Russia, in 1991, 1998, and 2000, respectively.

From 1991 to 1999, he was an Assistant Professor of the Department of Radio Receiver Equipment and Television at the TSURE. In 1994-2007, he also has worked as a Researcher in the Sea and Land Remote Sensing Group. From

1999 to 2007, he was an Associate Professor at the Department of Radio-Electronic Facilities of Protection and Service, and since 2007, he has been an Associate Professor at the Department of Security of Information Technologies, and a Senior Scientist of the Research Department at Taganrog Institute of Technology of the Southern Federal University (TIT SFedU, former TSURE).

His research interests include sea and land remote sensing from aircraft and satellite, oceanography, sea winds, scattering from rough surfaces, radar system design, and information security.

Computer-based simultaneous measurements of electrocardiographic and photoplethysmographic signals on a smart chair

Damjan Zazula, Boris Cigale, Jernej Škrabec, Jernej Kranjec

***Abstract*—**The paper reveals a computer hardware and software solution to simultaneously measure electrocardiographic (ECG) and photoplethysmographic (PPG) signals on a smart chair. A special sensory embodiment was constructed to be placed under the chair armrests. When a person is seated and touches the sensors by both hands, the signals are acquired and medically relevant features are extracted automatically. We conducted several experiments at rest and after exercise to detect R waves in ECGs and heartbeats in PPGs at the same time. Pulse transit times (PTT) were determined upon this basis for the left and right arm in 11 healthy males. Referential observations of systolic and diastolic blood pressure were obtained by the Critikon Dinamap Pro 300 sphygmomanometer. These were combined with the PTT estimates in an analytical model that depends on vascular parameters, such as blood vessel compliance and volumes that were computed in all subjects. In PTTs, only 0.3±0.3% absolute differences between the left and right arm were found at rest and 0.2±0.2% after exercise. Overall mean of the compliance versus blood volume equals 2.3±1.6%/mmHg for the left arm and 3.1±2.6 %/mmHg for the right. Overall mean of blood volume ratios yields 1.7±0.2 for the left arm and 1.8±0.2 for the right.

***Keywords*—**Smart chair, Photoplethysmography, Electrocardiography, Pulse transit time.

I. Introduction

ELDERLY or impaired persons need attention of caregivers if they want to stay at home and live independently. This help is both limited in time and running short the national budgets, which calls for more stable solutions. Today's technology is mature enough to be involved in monitoring elderly in their homes. Caregivers and budgets become less burdened this way. Nevertheless, technological help must not carry the burden over to monitored persons. For the elderly or impaired subjects, even simplest tasks, such as pressing a button, may not be feasible. Also persons without physiological or mental problems often feel discomfort if they are expected to take care about a measuring device, measuring procedure, and data forwarding or interpretation. For example, if they are instructed to regularly measure their blood pressure, it means taking and switching on a device, mounting a pressure cuff, activating and monitoring the measurement, reading out the results and forwarding it to a caregiver. This is very hard for elderly, if not impossible, and very error-prone.

It is then obvious that any home measurement must run automatically, without a need of any personal awareness or interaction. This, of course, implies unobtrusiveness. Sensors, or sensing devices, must reside in dwelling environments in such a way that daily activity of people living there, and also all abnormal situations, are being measured all the time.

We have developed a system of unobtrusive sensors and devices for observing functional health parameters in home environments. The system includes measuring of biopotentials from human body parts, in particular palms and fingers, mechanical and acoustic vibrations due to the activity of internal organs, such as the heart and lungs, mechanical movements of the body and body parts, changes of pulsative pressure in blood vessels, blood oxygenation, the temperature of body parts, and face colour and emotions [1].

A typical example of unobtrusive sensing of human vital functions is our smart chair [2]. It detects the siting subject's heartbeat, computes heart rate, estimates the level of oxygen in the blood and blood pressure, acquires nonstandard electrocardiographic (ECG) leads and the temperature of fingers, follows respiration by the breathing curve, and detects movement and the subject's posture and position.

In this paper, we reveal a sensory device which combines measuring photoplethysmographic (PPG) [4], [12] and ECG signals in parallel. In Section II, the construction of the device and signal-processing methods are described. Section III explains the experiments and results, while Section IV discusses the results and concludes the paper.

II. Sensors and Signal Processing

A few different embodiments of smart chairs have been developed worldwide. They differ from each other mainly in sets of sensors and the positions of their installation. In the following, we are revealing a construction of sensory unit that

Authors acknowledge a financial support of the Slovenian Ministry of Education, Science, and Sport within the Programme Funding Scheme P2-0041.

D. Zazula is with the System Software Laboratory, Faculty of EE and CS, University of Maribor, Smetanova 17, 2000 Maribor, Slovenia (corresponding author: +386 2 220 74 80, +386 2 220 72 72, damjan.zazula@um.si).

B. Cigale is with the System Software Laboratory, Faculty of EE and CS, University of Maribor, Smetanova 17, 2000 Maribor, Slovenia (boris.cigale@um.si).

J. Škrabec is with LOGICDATA Electronic & Software Entwicklungs GmbH, Maribor, Slovenia (jernej.skrabec@gmail.com).

J. Kranjec is with the System Software Laboratory, Faculty of EE and CS, University of Maribor, Smetanova 17, 2000 Maribor, Slovenia (jernej.kranjec@gmail.com).

can be placed under the chair armrests to acquire ECG, PPG, and temperature data.

The unit's sensors are mounted on a printed-circuit board as depicted in Fig. 1. Centrally, three light-to-voltage optical sensors (TSL250R-LF, ams AG) receive the light of wavelengths between 400 and 1000 nm. The output voltage is amplified and follows the irradiation of the input photodiode. Two light-emitting diodes (LED) are in a lateral position; one emits infrared light with the wavelength of 940 nm, the other emits red light with the wavelength of 660 nm. In between LEDs and optical sensors, there are two light barriers to prevent direct illumination from LEDs to the sensors. The barriers are just of the height that ensures light reflection from a finger when placed along with the three optical sensors.

The two light barriers have to stop both red and infrared light. In the development phase, different polymeric materials of different colours were examined. While the red light was eliminated by all dark coloured materials, infrared passed all of those enough to influence sensors directly. Only after the barriers were tinged by black nail varnish, a direct illumination with infrared light was suppressed.

Sensory unit takes care of PPG and temperature measurements when a finger is placed alongside the three optical sensors. We combined it with a dry ECG electrode in order to obtain both the ECG and PPG signals acquired at the same time. The electrode is U-shaped and the sensory unit fits within its inner dimensions and is incorporated as the electrode holder. Its size respects the diameter of human index finger. The electrode's metallic surface gets in contact with the skin when a person slides his or her finger inside the electrode. Its shape guarantees a stable and good contact between the subject's skin and the electrode conductive surface, which improves the quality of ECG measurements, while at the same time minimizes the influence of ambient illumination on PPG sensing (Fig. 2).

A common human posture when sitting in a chair is with hands leaned on the armrests. If the armrests have rounded and rather thin endings, sitting persons usually grasp it and bend their fingers under it. We took advantage of this fact and fixed the U-shaped electrodes under the armrests. When both the left and right hand touch the two electrodes, the acquired ECG signal corresponds approximately to the standard lead I.

Due to dry contacts with the electrodes, recorded ECGs are of inferior quality. Most disturbing is the induction of mains frequency (50 Hz in Europe). Therefore we paid special attention to the construction of the input filtering units that condition the recorded signals.

The input signals acquired by our U-shaped dry electrodes enter first an instrumentation amplifier (AD623, Analog Devices) with rather low amplification not to saturate it when high mains-frequency disturbances appear. The amplified signals are further led through two different paths. One connects directly to the A/D converter input (channel 1) of a microcontroller (dsPIC30F6015, Microchip), whereas the second one begins with an active high-pass filter at 0.5 Hz cut-off frequency to suppress low-frequency signal swings. Next stage in this path is a notch filter to suppress mains interference and is implemented as a switched-capacitor (SC) filter (LTC1060, LinearTechnology).

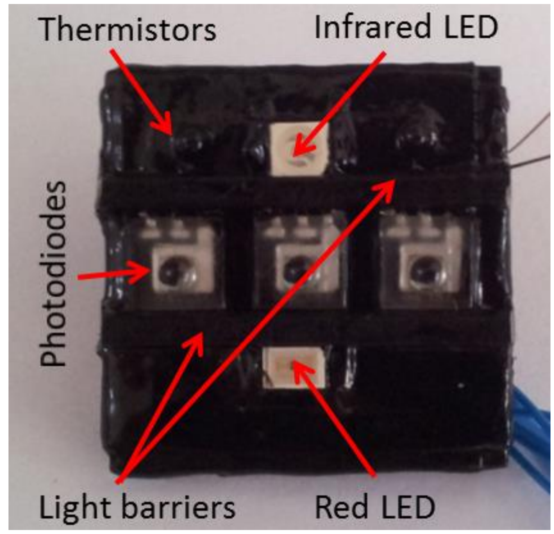

Fig. 1. Layout of sensory unit: components for photoplethysmographic and temperature measurements.

Fig. 2. A detail: dry U-shaped ECG electrode having incorporated components for photoplethysmographic and temperature measurements.

SC filters have a very deep attenuation and narrow stop-bands around its central frequency and the harmonics. An important characteristic of SC filters refers to the central frequency which is adaptable and externally controlled by a multiple of the central frequency. A common solution utilises phase-locked loop (PLL) that is driven by the voltage coming from the device's power transformer. Thus, the PLL synchronises to the mains frequency and, via an additional multiplier, controls SC notch filter [3]. As the power lines may be very corrupted by different noises and disturbances, PLL often loses synchronisation and the quality of SC notch degrades.

When ECG is acquired by dry electrodes, mains frequency corruption can be very strong and needs very sharp and adaptable suppression. This cannot be achieved by the abovementioned PLL approach satisfactory, which encouraged us to look for an innovative solution.

The amplified ECG signal, $u(n)$, is directly connected via the first signal paths to the A/D input, channel 1. This signal contains the mains disturbances at every moment with their instantaneous frequencies. After being sampled by the A/D, the signal is processed by an algorithm that precisely defines the frequency of a sinusoid found in the range ±0.5 Hz around the mains frequency (in our case 50 Hz).

This algorithm is based on two sinusoidal referential signals $r_1(n)$ and $r_2(n)$ whose frequencies are f_{r1}=49.5 Hz and f_{r2}=50.5 Hz, respectively. The length of references is $N_r = \frac{f_{s2}}{10}$ and f_{s2} is the applied sampling frequency (in our case 5 kHz). Two correlations are computed between the input ECG and the two references as follows:

$$x_1(m) = \sum_{n=0}^{N_r-1} u(n+m) r_1(n); \quad m = 0,\ldots, N-1$$
$$x_2(m) = \sum_{n=0}^{N_r-1} u(n+m) r_2(n); \quad m = 0,\ldots, N-1 \tag{1}$$

Zero-crossings are searched in the two correlation sequences $x_1(m)$ and $x_2(m)$. Distances between consecutive zero-crossings are averaged and the average represents the wavelength of disturbing mains frequency.

Now, when this frequency is precisely defined, a clock signal with 100-times higher frequency is generated on a digital output of the microcontroller. The clock signal is used to drive SC filtering and centre its notch frequency exactly at instantaneous mains frequency.

Thus, SC filter suppresses the mains frequency disturbances adaptively with a very high attenuation. ECG signals are finally low-pass filtered with cut-off frequency at 75 Hz and digitised by A/D converter (channel 2) that is built in the microcontroller. The ECG filtering stages are schematically depicted in Fig. 3.

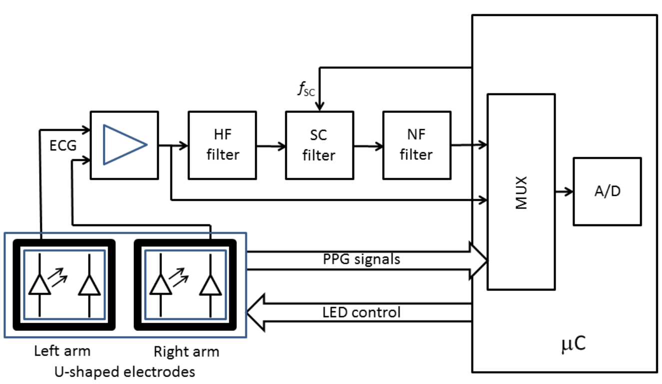

Fig. 3. Novel design of the input stage for ECG filtering: suppression of the mains frequency is introduced by SC filter that is controlled by a software algorithm.

The microcontroller used to digitise ECG also controls the PPG signal acquisition. It alternatively switches on and off red and infrared LEDs in two subsequent thirds of each duty cycle, while last third of the cycle elapses with both LEDs switched off (only environmental light illuminates optical sensors during this interval).

Outputs of 6 optical sensors (3 on the left-hand side and 3 on the right-hand side) are linked with 6 input channels of the microcontroller's A/D converter. Six PPG signals are digitised this way.

All ECG and PPG measurements are synchronized up to one sampling interval difference by the fact that they are all sampled from multiplexed inputs of the same A/D converter in every sampling interval. Acquired signals are wirelessly transmitted to a host computer. Analysis algorithms extract relevant features and can estimate parameters of functional health. These are rendered by user interface that is adapted to run on different mobile devices.

A. Detection of heartbeats

We have developed a robust approach to the heartbeat detection from the PPG signals and published it in [5]. The same idea was used with the chair PPG sensors.

The heartbeat detections can be robust due to the observation of the same phenomenon by 3 sensors in parallel for each hand and with two different light sources. To avoid high-frequency disturbances, we applied low-pass digital filtering to every signal and averaged the six acquired in each hand to a single recording. Denote obtained PPG signal by $\mathbf{s} = [s(0), \ldots, s(N\text{-}1)]$. The PPG values decrease fast to the PPG foot at every systole and increase slower to the PPG peak during diastolic intervals. Fast systolic changes can be detected by differentiating the signals:

$$d(n-1) = s(n) - s(n-1); \; n = 1,\ldots, N-1 \tag{2}$$

Differences in $d(n)$ from Eq. (2) introduce high-frequency components due to the differentiation. There is also a contribution of the frequencies caused by regular heartbeats. These depend on heart rate, which is physiologically limited to a range between 40 and 210 beats per minute, i.e. 0.67 and 3.5 Hz. Heartbeat detection is then looking for these frequencies, and to do it most efficiently all other frequencies should be suppressed. We completed the job by constructing an adequate band-pass filter based on wavelets. A suitable range of scales α was applied, so that a set of wavelets, $\psi_\alpha(n)$, was built. A sum of the wavelets over the selected scales produced desired filtering band-pass characteristic:

$$\psi(n) = \sum_{\alpha \in S} \psi_\alpha(n); \; n = 0,\ldots, N_\alpha \tag{3}$$

where ψ_α designates the chosen mother wavelet at scale α, ψ the constructed band-pass filter, S a set of preselected scales, and N_α the length of the wavelet at highest scale chosen.

The filter from Eq. (3), when applied to the PPG gradient $\mathbf{d}$, maximizes the response at different frequencies dependent on heart rates. Optimum heartbeat detections, therefore, reside on the following signal:

$$p(n)=\sum_{k=0}^{N-1} d(k)\psi(n-k);\ n=0,...,N-1 \quad (4)$$

Local minima in $p(n)$ represent heartbeats as detected in the PPG signal.

B. Blood pressure and pulse transit times

Following the example from [9], we computed pulse transit times (PTT) as a time interval between an ECG R-wave peak and the nearest subsequent heartbeat location in the analysed PPG. PTTs are inversely proportional to the instantaneous blood pressure [6], [7], [7]. However, there are several properties of the individual physiology that influence the relationship between blood pressure and PTT. Referring to [10], PTTs change with transmural blood pressure, i.e. the pressure that appears as a difference of inner distending blood pressure and outer contact pressure across the vessel walls. If there is no contact pressure [13], transmural pressure is positive and equals intra-arterial pressure. PTT decreases with the increasing transmural pressure.

The functional relationship of PTT versus transmural pressure depends mainly on four individual physiology parameters. It depends on maximum blood vessels compliance, maximum arterial volume, the arterial volume at zero transmural pressure, and the distance between aortic valve and the place of PPG measurements. Our smart chair experiments consider index fingers placed into the photoplethysmograph (connected to U-shaped ECG electrodes). It is assumed that paths from the aortic valve to the left or right index finger are of the same length. PTTs computed for the left and right arm can then be expected the same if the same physiological properties may be attributed to both arms, which we empirically verified.

Due to the fact that we didn't calibrate individual vascular parameters prior to our smart-chair experiments, we were not in the position to estimate blood pressure from the measured PTTs directly. However, if two PTTs are available from the same PPG measuring position at different blood pressures, a ratio of the estimated PTTs equals the ratio of corresponding blood pressures if maximal values of compliance and arterial volumes remain unchanged. We verified this too and show the results in the next section.

Referring to [10], PTT can analytically be established by the following relationship:

$$PTT = L\sqrt{\frac{\rho C_m e^{-\frac{C_m}{V_m-V_0}P_t}}{V_m-(V_m-V_0)e^{-\frac{C_m}{V_m-V_0}P_t}}} \quad (5)$$

where L, ρ, C_m, V_m, V_0, and P_t stand for the distance from the aortic valve to the PPG measuring location, blood density, maximum vessel compliance, maximum arterial volume, arterial volume at zero transmural pressure, and transmural pressure, respectively.

When two measurements are available at two different blood pressures, P_{t1} and P_{t2}, the following ratio can be derived from Eq. (5):

$$\left(\frac{PTT_1}{PTT_2}\right)^2=\frac{-\frac{V_m}{V_m-V_0}e^{\frac{C_m}{V_m-V_0}P_{t2}}+1}{-\frac{V_m}{V_m-V_0}e^{\frac{C_m}{V_m-V_0}P_{t1}}+1} \quad (6)$$

if PTT_1 and PTT_2 are measured at pressures P_{t1} and P_{t2}, respectively.

III. Experiments and Results

Experimental trials were performed in two-phase measurement sessions where subjects relaxed on our smart chair by grasping properly the U-shaped sensors under the both armrests by fingers. In the first phase, referential blood pressure was verified before a 3-minute smart-chair signal acquisition at rest by a sphygmomanometer (Critikon Dinamap Pro 300). In the second phase, subjects were asked to keep squatting for one minute and, immediately after that, referential blood pressure was verified again. A second 3-minute interval of measurements followed with subjects relaxing on the chair.

Their ECGs were recorded between the two hands as lead I and, in parallel, also the PPG signals (Fig. 4).

All the PPG and ECG signals were synchronized by the microcontroller firmware and resampled to a common sampling frequency of 200 Hz.

The R-wave peaks were detected in the ECGs by well-known Pan-Tompkins algorithm [11]. All R-wave detections were checked and, if necessary, corrected manually. Heartbeats were also detected from the PPG signals by our own algorithm based on continuous wavelet transform [5] as described in Subsection II.A. Low-pass filtering was applied to the signals with cut-off frequency at 10 Hz prior to the differentiation. After that, band-pass filtering was based on a combination of Morlet wavelets at scales 60, 72, 84, 96, 108, 120, 132, 144, 156, and 168.

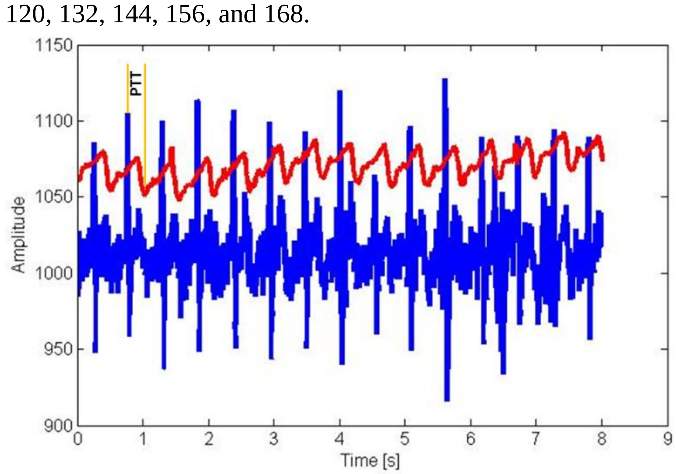

Fig. 4. A combination of ECG (blue) and PPG measurements (red) that enable an estimation of blood pressure based on PTTs. The principle of PTT estimation is marked as a distance between the ECG R peak and a subsequent PPG foot.

Eleven healthy male subjects participated in experiments. Their mean age is 28.9±6.6 years, their height 180.6±5.1 cm, and their weight 90.2±16.9 kg. All gave their informed consent prior to experimental trials. Referential systolic and diastolic blood pressures were estimated in every participant before every trial.

After detecting ECG R waves and PPG-based heartbeats, we computed corresponding PTTs for the left and right arm at rest and after exercise. We measured time distances from the referential R peaks to the PPG foots as detected by our heartbeat search. PTT values were averaged from 10 consecutive heartbeats at the beginning of every trial.

Table I summarises referential blood pressures and estimated PTTs for all 11 participants on their left and right arms at rest and after exercise.

TABLE I. SYSTOLIC AND DIASTOLIC BLOOD PRESSURES MEASURED BEFORE EVERY TRIAL AND MEAN PTTS ESTIMATED AT THE BEGINNING OF EVERY TRIAL ON THE LEFT AND RIGHT ARMS

Sub-ject	At rest		After exercise	
	Systolic/ diastolic BP [mmHg]	*Mean PTTs* [ms] left, right	*Systolic/ diastolic BP* [mmHg]	*Mean PTTs* [ms] left, right
1	129/70	236.5, 237.0	137/85	196.0, 194.5
2	153/87	197.5, 232.5	143/67	161.0, 172.0
3	121/73	223.5, 217.0	119/67	269.0, 275.0
4	110/69	250.0, 259.5	120/74	233.0, 233.5
5	129/79	285.0, 244.5	163/79	168.0, 181.5
6	126/78	244.0, 246.5	134/84	213.5, 212.5
7	135/72	268.5, 264.5	212/78	201.5, 199.0
8	161/94	190.0, 189.5	240/108	135.5, 120.5
9	134/65	259.5, 230.5	153/72	172.5, 171.0
10	140/84	191.5, 220.0	149/77	174.5, 146.5
11	121/65	270.0, 279.0	150/72	225.0, 217.0

It is evident from Eq. (5) that PTT decreases when intra-arterial pressure increases. Comparing referential blood pressures at rest and after exercise in Table I and considering the expected physiological reaction of increased systolic blood pressure after exercise, we realise that persons 2 and 3 show the opposite reactions. Typically, a more significant increase is expected in pulse pressure, which is a difference of systolic and diastolic pressure. Pulse pressure in 11 participants averaged to 56.6±9.1 mmHg at rest and 77.9±30.5 mmHg after exercise. Actually, it increased after exercise in all tested persons, except in Subject 1.

If we now observe PTTs, these comply with expected shortening at higher pressures and lengthening at lower pressures in both arms, except for Subject 2 whose PTTs shorten with decreased systolic and diastolic pressures, although pulse pressure in this person increases at the same time.

PTTs related to the left and right arm differ slightly; mean absolute difference equals 13±13 ms at rest (0.3±0.3 % referring to the overall mean PTT) and 8±8.4 ms after exercise (0.2±0.2 %).

We analysed Eq. (666) next. By definition, expression $\frac{V_m}{V_m - V_0}$ can never be lest than 1. If we consider P_{t1} blood pressure at rest and P_{t2} after exercise in the same person, and pulse transit times PTT_1 and PTT_2 analogously, then intervals for $\frac{C_m}{V_m - V_0}$ and $\frac{V_m}{V_m - V_0}$ can be determined that guatantee Eq. (6) solved under the condition $\frac{V_m}{V_m - V_0} > 1$.

Numerical solution of Eq. (666) yielded acceptable intervals of ratios $\frac{C_m}{V_m - V_0}$ and $\frac{V_m}{V_m - V_0}$ that verify the condition $\frac{V_m}{V_m - V_0} > 1$. Fig. 5 depicts ratios $\frac{C_m}{V_m - V_0}$ for the left arm and Fig. 6 for the right. Circles stand for mean values, whereas bars bound the acceptable intervals.

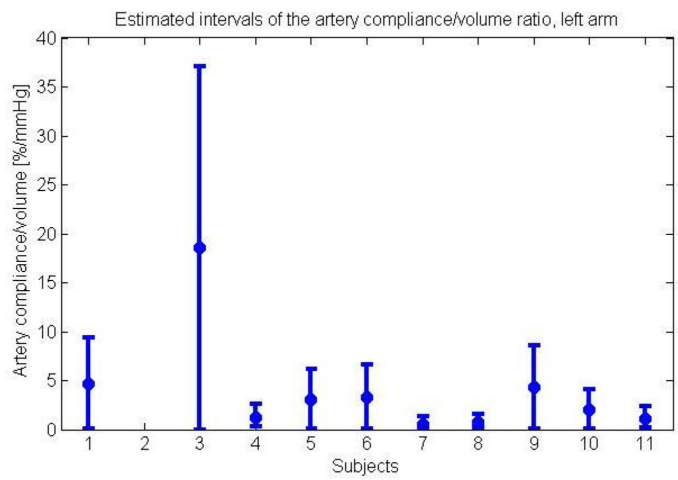

Fig. 5. Estimated ratios $\frac{C_m}{V_m - V_0}$ that verify Eq. (666) for the left arm: circles denote mean values, bars the spans of the intervals.

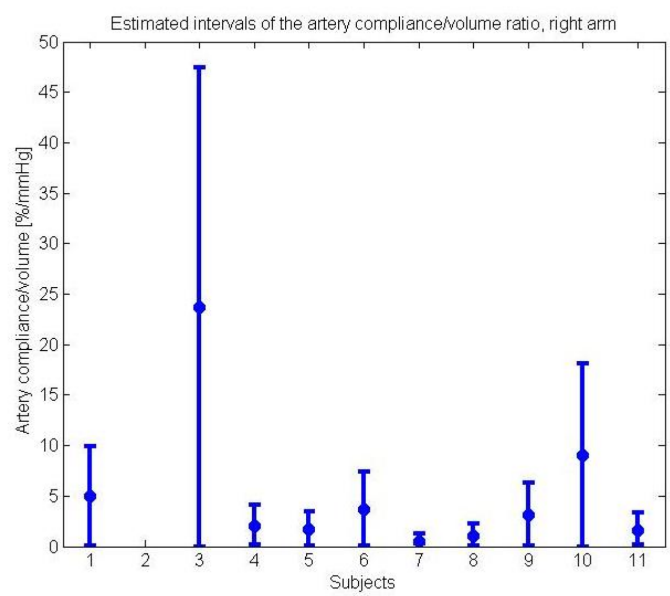

Fig. 6. Estimated ratios $\frac{C_m}{V_m - V_0}$ that verify Eq. (666) for the right arm: circles denote mean values, bars the spans of the intervals.

ISBN: 978-1-61804-321-4

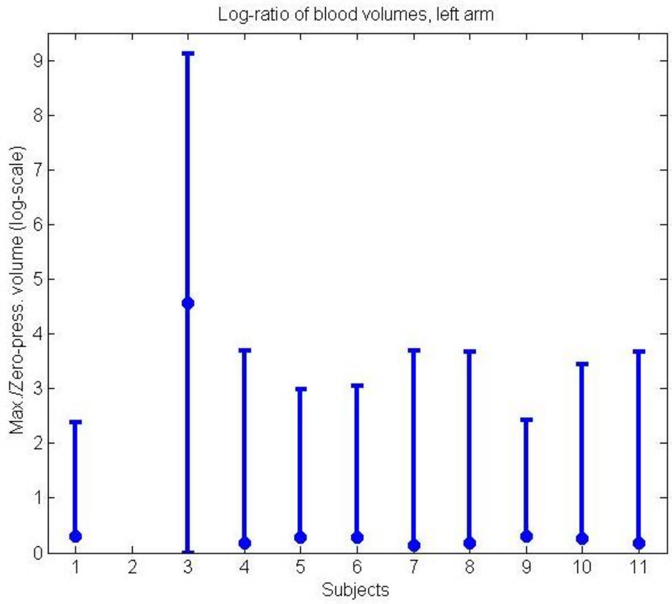

Fig. 7. Estimated ratios $\frac{V_m}{V_m - V_0}$ that verify Eq. (666) for the left arm: circles denote the values that correspond to the mean $\frac{C_m}{V_m - V_0}$, bars the spans of the intervals (log-scale used for best visualisation).

Similarly, Fig. 7 depicts ratios $\frac{\mathrm{V_m}}{\mathrm{V_m} - \mathrm{V_0}}$ for the left arm and Fig. 8 for the right. Circles denote the values that correspond to the means of $\frac{\mathrm{C_m}}{\mathrm{V_m} - \mathrm{V_0}}$, whereas bars bound the acceptable intervals. Volume ratios are depicted in the logarithmic scale for best visualisation purpose.

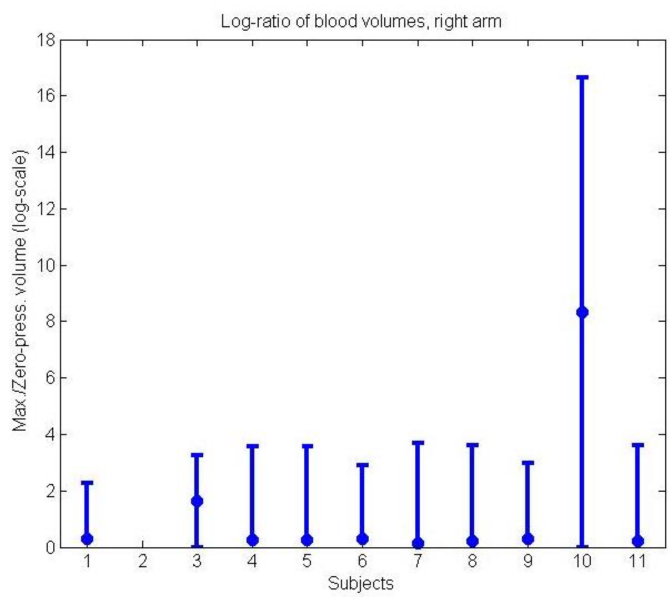

Fig. 8. Estimated ratios $\frac{V_m}{V_m - V_0}$ that verify Eq. (666) for the right arm: circles denote the values that correspond to the mean $\frac{C_m}{V_m - V_0}$, bars the spans of the intervals (log-scale used for best visualisation).

Overall mean of the compliance versus blood volume equals 2.3±1.6 %/mmHg for the left arm and 3.1±2.6 %/mmHg for the right arm (Subject 3 excluded). Overall mean of blood volume ratios yields 1.7±0.2 for the left arm and 1.8±0.2 for the right (Subject 3 excluded for the left arm, Subjects 3 and 10 for the right).

IV. Discussion and conclusions

Smart chair that we developed introduces two innovative embodiments: combined sensory unit with a U-shaped ECG electrode and a photoplethysmograph, and an adaptive SC notch filter controlled by a software algorithm to increase its efficiency of mains frequency suppression. This improves ECG and PPG measurements, which mitigates unobtrusive signal acquisition in persons siting on the chair.

By detecting ECG R waves and PPG-based heartbeats we were able to compute PTTs. A comparison of the PTTs related to the left and right arms confirms that the two physiological paths are very similar as far as the length, blood volumes, and blood vessel compliance are concerned. Only 0.3±0.3 % absolute differences at rest were established and 0.2±0.2 % after exercise.

In all experimental trials referential systolic and diastolic pressures were also measured by medically approved sphygmomanometric device. As Eq. (6) links a ratio of PTTs with blood volumes, vessel compliances, and pressures, we applied it to assess vascular parameters based on the measured PTTs and referential blood pressure. At least two different measurements are needed to solve Eq. (6). The equation builds on vascular parameters, i.e. maximum compliance, C_m, maximum arterial volume, V_m, and arterial volume at zero transmural pressure, V_0. In a passive system, these can be considered constant regardless the blood pressure. Human vascular system, however, depends on various factors, such as autonomic nervous system. We tried to observe its influence by solving Eq. (6) with blood pressures obtained in test persons at rest and after exercise.

Fig. 5 and Fig. 7 relate to PTTs measured on left arms and unveil Subject 3 that deviates from the general picture; his compliance and blood volume ratios are very different to the others and also dissent from expected values that are between 0.5 and 4 %/mmHg [10]. The anomaly may be attributed to the fact that a minor decrease of systolic and diastolic blood pressure appeared with exercise, while the corresponding PTTs demonstrate a disproportionate increase. As the same deviation arises on the right arm too, its probable origin lies in wrong referential measurements of blood pressure, otherwise PTTs on the left and right arms would not coincide that significantly. In spite of an automated, professional measuring device deployed, errors cannot be excluded.

Another discrepancy turns up in Subject's 10 right arm; although the exercise induces only an insignificant increase of blood pressure, the corresponding PTT decreases disproportionally and cannot be seen with the left arm at the same time. In this case incorrect referential blood pressure is less probable. Also the correctness of ECG and PPG heartbeat detections were double-checked and no mistake was found. Therefore, this question remains open and needs proper physiological explanation.

Additional research is planned with more participants for better statistical assessment. Deeper insights will be induced into the vascular parameters and also more attention paid to possible stress and muscle tonus of participants throughout the experiments.

REFERENCES

[1] The Biomedical Engineering Competence Centre, “Connected Home Devices in Support of Independent and Healthy Living,” http://storm.uni-mb.si/kcbme/index-en.php.

[2] D. Zazula, J. Kranjec, P. Kranjec, B. Cigale, “Assessing blood pressure unobtrusively by smart chair,” 38th International Convention MIPRO 2015, Opatija, Croatia, 2015, pp. 404-409.

[3] S. K. Yoo, N. H. Kim, J. S. Song, T. H. Lee, K. M. Kim, “Simple self-tuned notch filter in a bio-potential amplifier,” *Medical and Biological Engineering and Computing*, vol. 35, iss. 2, pp. 151-154, 1997.

[4] B. D. Zislin and A. V. Chistyakov, “The History of Oximetry,” *Biomedical Engineering*, vol. 40, no. 1, pp. 53-56, 2006.

[5] C. Pirš, B. Cigale and D. Zazula, “A Feasibility Study of Heartbeat Detections from Photoplethysmograms With Fingers Compressed,” *Proc. of the 5th WSEAS International Conference on Sensors and Signals*, Sliema, Malta, 2012, pp. 47-52.

[6] J. Spigulis, R. Erts and U. Rubins, “Micro-circulation of skin blood: optical monitoring by advanced photoplethysmography techniques,” *Proc. of the SPIE*, vol. 5119, Bioeng. and Bioinspir-ed Syst., Maspalomas, Canary Islands, Spain, 2003, pp. 219-225.

[7] Y. Choi, Q. Zhang and S. Ko, “Noninvasive cuffless blood pressure estimation using pulse transit time and Hilbert–Huang transform,” *Computers and Electrical Engineering*, vol. 39, pp.103-111, 2003.

[8] D. B. McCombine, A. T. Reisner and H. H. Asada, “Motion Based Adaptive Calibration of Pulse Transit Time Measurements to Arterial Blood Pressure for an Autonomous, Wearable Blood Pressure Monitor,” *Proc. of the 30th Annual International IEEE EMBS Conference*, Vancouver, 2008, pp. 989-992.

[9] A. Arza, J. Lazaro, E. Gil, P. Laguna, J. Aguilo and R. Bailon, “Pulse Transit Time and Pulse Width as Potential Measure for Estimating Beat-to-Beat Systolic and Diastolic Blood Pressure,” *Computing in Cardiology*, vol. 40, pp. 887-890, 2013.

[10] X.-F. Teng and T. Zhang, “Theoretical Study on the Effect of Sensor Contact Force on Pulse Transit Time,” *IEEE Trans. Biomed. Eng*., vol. 54, no. 8, pp. 1490-1498, 2007.

[11] J. Pan and W. J. Tompkins, “A real-time QRS detection algorithm,” *IEEE Trans. on Biomed. Eng*., vol. 3, pp. 230-236, 1985.

[12] S. Rhee, “Design and Analysis of Artifact-Resistive Finger Photoplethysmographic Sensors for Vital Sign Monitoring,” PhD Thesis, Massachusetts Institute of Technology, Boston, 2000.

[13] D. Zazula, C. Pirš, K. Benkič, D. Đonlagić, B. Cigale, “Short-Term Photoplethysmography Embedded in Household Appliances,” *6th European Conference of the International Federation for Medical and Biological Engineering*, MBEC 2014, Dubrovnik, Croatia. IFMBE proceedings, vol. 45, pp. 922-925, Sept. 2014.

ISBN: 978-1-61804-321-4

Lean user interface: Design & Optimalisation

H. Mohelska, J. Ansorge

***Abstract*—**Although we can encounter the elements of user interface optimisation more and more, there is still a large proportion of applications without optimisation. The situation is made even worse because most applications without an optimised user interface are business applications. An employee spends more of their time working with these applications, often most of their work time as well. For this reason, application interface optimisation is important but a chapter often neglected in application design. This paper will marginally focus on expanding the eight golden rules for user interface design.

***Keywords*—** lean, user interface, optimalisation, design

I. Introduction

THE concept of downsizing and optimisation has been connected mainly with production since the early 20th century. Continuous improvement of existing processes has resulted in an ever-decreasing amount of savings that result from continuous improvement. That is why management also focus more and more on savings in other areas of an enterprise and beyond. For example, in internal and external logistics, when the maximum utilisation of especially carriers and warehouses is optimised. Also increasingly frequent is the optimisation with suppliers, when with well-set contract terms, a company can claim a lower price for a product, after proven savings with their supplier. One of the recent hitherto neglected area is the optimisation of office workers.

Although there are methods for downsizing administrative processes, the issue is not very dedicated to the optimisation of user interface, when the speed of work in it directly affects the performance of an employee, who works within the system.

This paper will focus primarily on optimising the user interface, when the user interface is one of the most important elements of an application. Its simplicity, arrangement and friendliness affects the number of users and therefore its marketability. Particular emphasis will be placed on optimising the design of the user interface in terms of ergonomics and the time required for the completion of a form..

II. Eight golden rules for designing a user interface

When designing a user interface, eight golden rules must be respected [4-8] .

A. Consistency of user interfaces

User interface should be as simple as possible and yet interaction with the user shouldn't be lacking. All interface should be similar and not constantly changing, including a single style and colours. Font size should be the same everywhere. Equally important is a similar organisation of elements, as it is in a system or application, with which the user is already familiar and able to work with (such as the operating system.)

B. The diversity of users

Each user is unique. The user should match their needs and should be pleasing its end-users. To support a pleasing interface and easily readable content, it should be possible to change colour schemes and font size, which encompasses a wide age range of end users.

C. Feedback

The user should be informed about current system activities, preferably via an optional status bar. Feedback can be subdivided into feedback with or without the user's intervention, where the user has to confirm the information or action.

D. Navigation

Quality navigation allows users easy orientation in longer forms where it is needed to fill in more information. The user in this case should always know which part they are in, what parts are already fully completed and what parts still need to be modified.

E. Prevent error

The user interface should indicate a possible error during form filling and inform the user so that they do not have to return to the incorrect entry at a later time. The basic method for eliminating errors is the appropriate setting of data type, their shape, length and format.

F. Undo, cancel and delete

The user should have the option to go back to the previous screen, cancel the whole activity or delete all data from the form in one go. These options give them the assurance that the data written down can be edited or deleted, and therefore the user can be in peace during filling out their forms, which eliminates the stress resulting from potential irreversible inaccurate filling.

G. Internal organisation

The system should be predictable. The user must be the one who controls the system and not vice versa. The unpredictability of the system increases the probability of a user's confusion.

H. Load of the user

The user should not be overburdened with unnecessary information, which they don't really need to know. Clearly arranged objects should be part of the total units, and the entire unit should fit on the screen with the normal resolution without the need for scrolling.

III. Arrangement of the form objects

Suitable sequence and division of objects into units (bookmarks) is usually commonplace, but still many user interfaces do not contain the objects to save time when entering information. The tools that can save time on data entry include:

A. Text auto-complete in a text field

Use of existing databases to facilitate the entry of input data as much as possible. Input data include names, street names, addresses, etc. For example, entering a postcode can limit the selection of streets to a specific city/town.

B. Automatic arrangement according to frequency of use by the user

User interface teaching itself, according to frequency of use, the items could automatically move within one bookmark (unit) with a single focus. Similarly, the bookmarks (units) where the display order would be changed, would automatically organise. The user would have to be informed of this change and would have to approve it. After some time the user interface would fully adapt to the user and not vice versa. There could then be the option of setting the order of objects and bookmarks manually.

C. Distances between controls of a form

Minimising the gaps between individual form elements can shorten the time required for passage with a cursor as well as letting the user know visually that the elements are linked together. For example, a description of form elements doesn't need to be stated outside of the element, but right inside. When editing it then disappears or appears as part of the context help when filling. This can save space on the form and streamline the form by removing unnecessary descriptions that can distract the user. There is always a need to ensure that excessive thickening of the form elements does not affect its clarity.

D. Minimising the text fields

Although text fields are the most common, their evaluation is usually the most difficult. The reason is the different length of the text string, use of synonyms and different expressions of our own. Therefore, it is necessary to think about replacing a text string by a switch or a list of possible options. In the case that a user cannot find the appropriate answer in the list of answers offered, they should have the option to fill it in, however, such filled answers, should be checked if it is not a duplicate entry, before the actual inclusion in the list.

E. Colour indication of an error

The user is usually informed of an error during filling when they try to send the form. Therefore they lose the time in finding errors. Modern applications highlight or even visually identify a specific error and element. If a user has already been alerted in the course of filling, they should have the chance to return to correct it, without undue contemplation and searching for the errors. A warning regarding an error would mean a colour tint of the element or description. A warning for less minor error in yellow, a critical error in red and correctly filled element should be in green.

F. Suggested correction in case of incorrectly entered information

Similar to automatic correction and prediction when typing on a smart mobile device could also be used when filling in forms. The system can learn from the already evaluated and stored data of the same form, thereby facilitate, make the inputs, checks and automatic data correction more precise.

G. Hiding items on the basis of already collected information

Items that the system evaluates as unnecessary, can be hidden automatically, the form becomes clearer and the user will not have to unnecessarily deal with filling it. For example, birth surname could be omitted, or automatically completed, if the user enters or the system finds out from the entered data that it is a male.

IV. Duration of unnecessary operations in the user interface

Filling out forms can be described as the most time demanding. Saving time in this case can be achieved primarily by using the automatic prediction. As a model form an order form of any e-commerce may be used, where the user fills out the contact information. In the event that this would be a company, purely theoretically, during linking trade pages with business and a trade index, it would be enough just to enter the identification number of the organisation and the rest of the information would be loaded automatically, that's why an individual not engaged in business will be selected, which is protected by the Privacy Policy.

- Name and surname - can be predicted according to the first characters entered and the frequency of names
- Company name - can be automated based on the information loading of the central registry with the help of identification number of the entrepreneur
- Street - can be predicted on the basis of the streets in the given city/town
- City/town - can be accurately determined based on postcode (ZIP code)
- ZIP code - cannot be automated, but it can serve to automatically fill the city/town
- Phone and contact email cannot be automated

AutoComplete strings of text, which can count on the likelihood of finding the correct title after entering the first 3-4 characters can reduce the time required to a fraction of its original value, when the specific size of time savings will depend on the length of the entered text string.

Colour error indication allows the user to solve the error at the time of its occurrence, and not when sending the form when they have to then go back with the cursor as well as their thoughts, therefore saving time with searching for errors.

Colour error indication can be supplemented with automatic suggestion for corrections in the case of incorrectly entered information. The system could draw on existing dictionaries and previously entered information and then it would suggest the proper correction. Of course it is important that the replacement of an error with a proposed solution is approved by the user.

Automatic arrangement according to use frequency by the user, the distance between the controls of the form, minimising text fields and hiding items on the basis of already collected information then means purely savings on cursor movements. It is always necessary to handle as many tasks of the form by keyboard. Grasping pointing device, locating the cursor on the screen and the cursor movement itself is a set of activities that are not recommended in terms of ergonomics and optimisation because they distract users from filling data.

A. Ergonomics and possible risks resulting from optimisation

Removing unnecessary tasks when entering input data in the user interface, increases the proportion of performed monotonous work without any diversification. This may result in risks associated with working on the computer.

The most major risks include the increased likelihood of RSI occurrence – Repetitive strain Injuries [9-10], i.e. occupational diseases associated with excessive stress while operating a PC. For this reason, employees constantly working on computer should comply with safety breaks or alternate manual and intellectual work. Although employees create perfect ergonomic conditions for the elimination of objective diseases (inflammation etc.), there is always the risk of subjective disease (psychological stress, fatigue, inability to concentrate) for which the employer is responsible.

An ideal system alone can measure the performance of employees in different parts of their working hours, and according to decreasing speed and increasing errors it can detect exhaustion of employees and recommend a break.

V. Conclusion

Today, the optimisation of user interface is at a high level, but adding tools described above to the user interfaces, allow employees to accelerate their work many times over. This is essentially a manual entry of data into a computer, which cannot be managed by a machine. It is always necessary to look at the risks arising from excessive optimisation and especially at the individuality of each employee. Appropriate designing of the user interface, which will intuitively control the entire process through keyboard is only a part of the success. Another often neglected phase of implementation of the application is thorough user training, including personalisation options. By appropriate training, employees will use the system according to the original intent of the creator.

VI. Acknowledgment

The paper was written with the support of the specific project grant "Determinanty Ovlivňující Pracovní Spokojenost" granted by the University of Hradec Králové, Czech Republic.

References

[1] T. L. Jackson; K. R Jones; N. Bodek, *Implementing a lean management system*. Portland: Productivity Press, 1996.

[2] J. K. Liker, *The toyota way*. Esensi, 2005.

[3] B. J. Hicks, *Lean information management: Understanding and eliminating waste*, International journal of information management 27.4, 2007, p.233-249.

[4] D. Norman, *The Design of Everyday Things*. MIT Press, 1998. ISBN 0-262-64037-6

[5] ISO 9241-210, *Ergonomics of human-system interaction – Part 210: Human-centered design for interactive systems*. Geneve: ISO, 2011.

[6] A. Cooper.,A. Reinmann, D. Cronin, *About Face 3: The essentials of interaction design*, Indianapolis: Wiley Publishing, 2007. ISBN 978-0-470-08411-3

[7] D. Benyon, P. Turner, S. Turner, *Designing Interactive Systems: People, Activities, Contexts, Technologies,* Maidenhead: Pearson Education, 2005. ISBN 978-0321116291

[8] B. Shneiderman, C. Plaisant, *Designing the User Interface: Strategies for Effective Human-Computer Interaction*, 4th Edition. Pearson Addison Wesley, 2004. ISBN 0-321-19786-0

[9] F. E. Pascarelli, D. Quilter, *Repetitive strain injury: A computer user's guide*, J. Wiley, 1994.

[10] K. Keller, J. Corbett, D. Nicholsy *Repetitive strain injury in computer keyboard users: pathomechanics and treatment principles in individual and group intervention*. Journal of Hand Therapy, 1998, p. 9-26.

Further analysis on network-induced time-varying delay modeling methods used in GPC design

Constantin Florin Caruntu, *Member, IEEE*

***Abstract*—The networked control systems (NCSs) have nowadays applications ranging from factory and home automation, to automotive and avionic control systems and to military and spatial applications. Their widely inclusion in the industry was mainly due to the inherent advantages, e.g. lower costs, simpler installation and maintenance, higher reliability and greater flexibility. Still, although the subject was extensively studied during the last decades, there are some disadvantages that need more attention from the academia and their effect on the performances of the control system needs to be more carefully studied. The main disadvantage is considered to be the network-induced time-varying delay which can degrade the control systems performances and can even lead to the instability of the networked control system. This paper studies and analyses the effect of different modeling methods for the network-induced time-varying delays on the networked control systems performances. The modeling methods are used in the design phase of a generalized predictive control (GPC) strategy and the performance evaluation is performed on a typical networked application, i.e. DC motor controlled through an Ethernet network.**

***Index Terms*—Networked Control Systems, Time-Varying Delay, Delay Modeling, Predictive Control.**

I. Introduction

The networked control systems (NCSs) are feedback control systems in which the data exchange between the controllers, sensors and actuators is performed over a real-time communication network. These NCSs are now widely used in different industries, ranging from automated manufacturing plants to automotive and aero-spatial applications due to their many attractive advantages which include: lower costs, simpler installation and maintenance, increased system agility, higher reliability and greater flexibility, but the use of communication networks makes it necessary to deal with the effects of the network-induced delays in the control loop. These delays may be unknown and time-varying and may deteriorate the performances of the control systems designed without considering them and may even destabilize the closed-loop control system.

Various research has been done on compensating the time-varying delays induced in NCSs using generalized predictive control strategies for different control applications: active suspension system [1], electro-hydraulic actuated wet clutch [2], cylindrical laboratory tank [3], DC servo motor [4], engine control unit and battery management control unit [5], wireless coal mine control [6].

In this paper, a networked controller based on a generalized predictive control (GPC) strategy is designed to decrease the influence of the time-varying delay induced in a NCS on the control system performance. It is assumed that the delays in the communication network are time-varying, but bounded, and two methods of considering the delays by the predictive control algorithm are illustrated: an average delay method, an identification method, which uses an estimated model that includes the delays in the plant model, and an adaptation method, which adapts the control algorithm to the time-varying delays in the communication network. The strategy is then tested in simulation on a a typical networked application, i.e. DC motor controlled through an Ethernet network, and the results are analyzed and the performances evaluated.

This paper is organized as follows. Section II describes the generalized predictive control strategy and Section III illustrates the two modeling methods for the network-induced time-varying delays (average method and identification method) to be used by the predictive control strategy. In Section IV firstly the networked DC motor control application is introduced and afterwards the modeling of the DC motor is briefly described followed by the simulation results analysis and the performance evaluation. Finally, the paper ends with a concluding chapter in Section V.

II. GPC strategy

The predictive control techniques were mainly introduced to deal with plants that have complex dynamics (unstable inverse systems, processes with time-varying delay, etc.) and plant model mismatch. They are of a particular interest from the point of view of both broad applicability and implementation simplicity, being applied on large scale in industry processes, having good performances and being robust at the same time.

Consider the plant described by the CARIMA (Controlled AutoRegressive Integrated Moving Average) model [7]

$$A\left(z^{-1}\right)y\left(k\right)=z^{-d}B\left(z^{-1}\right)u\left(k-1\right)+\frac{e\left(k\right)C\left(z^{-1}\right)}{D\left(z^{-1}\right)},\quad(1)$$

where u is the control input of the process, y is the measured controllable output of the process, d is the delay introduced by the communication network and $e(k)$ is white noise with zero mean value.

$A\left(z^{-1}\right)$ and $B\left(z^{-1}\right)$ are the system polynomials

$$\begin{aligned}A\left(z^{-1}\right)&=1+a_1z^{-1}+...+a_{n_A}z^{-n_A},\\B\left(z^{-1}\right)&=b_0+b_1z^{-1}+...+b_{n_B}z^{-n_B},\end{aligned}\quad(2)$$

where n_A and n_B represent the polynomials degrees and $C\left(z^{-1}\right)$ and $D\left(z^{-1}\right)$ are the disturbances polynomials

$$\begin{aligned}C\left(z^{-1}\right)&=1,\\D\left(z^{-1}\right)&=\Delta=1-z^{-1}.\end{aligned}\quad(3)$$

C. F. Caruntu is with the Department of Automatic Control and Applied Informatics, Gheorghe Asachi Technical University of Iasi, Romania, e-mail: caruntuc@ac.tuiasi.ro.

ISBN: 978-1-61804-321-4

A. Prediction model

The prediction model is given by

$$\hat{y}\left(k+j|k\right)=G_{j-d}\left(z^{-1}\right)z^{-d-1}\Delta u\left(k+j\right)+ \\ +\hat{y}_0\left(k+j|k\right) \tag{4}$$

where

$$\hat{y}_0\left(k+j|k\right)=\frac{H_{j-d}\left(z^{-1}\right)}{C\left(z^{-1}\right)}\Delta u\left(k-1\right)+ \\ +\frac{F_{j-d}\left(z^{-1}\right)}{C\left(z^{-1}\right)}y\left(k\right) \tag{5}$$

represents the free response, with $j=\overline{hi,hp}$, where hi is the minimum prediction horizon and hp is the prediction horizon. $u(k+j),\ j=\overline{1,hc}$ is the future control, computed at time k and $\hat{y}\left(k+j|k\right)$ are the predicted values of the output, hc being the control horizon.

The polynomials $F_{j-d}\left(z^{-1}\right)$, $G_{j-d}\left(z^{-1}\right)$ and $H_{j-d}\left(z^{-1}\right)$ can be determined using the two Diophantine equations given in [2].

Considering as inputs $\Delta u(k)$ and collecting the j-step ahead predictors in a matrix notation, the prediction model can be written as

$$\hat{\mathbf{y}}=\mathbf{G}\mathbf{u}_d+\hat{\mathbf{y}}_0 \tag{6}$$

where

$$\hat{\mathbf{y}}=[\hat{y}(k+hi\,|k),\hat{y}(k+hi+1\,|k),\ldots,\hat{y}(k+hp\,|k)]^T, \tag{7}$$

$$\mathbf{G}=\begin{bmatrix} g_{hi-d-1} & \cdots & g_0 & 0 & \cdots & 0 \\ g_{hi-d} & \cdots & g_1 & g_0 & \cdots & 0 \\ \cdots & \cdots & \cdots & \cdots & \cdots & \cdots \\ g_{hc-1} & \cdots & \cdots & \cdots & \cdots & g_0 \\ g_{hp-d-1} & \cdots & \cdots & \cdots & \cdots & g_{hp-hc-1} \end{bmatrix}, \tag{8}$$

$$\mathbf{u}_d=[\Delta u(k),\ldots,\Delta u(k+hc-1)]^T, \tag{9}$$

$$\hat{\mathbf{y}}_0=[\hat{y}_0(k+hi\,|k),\hat{y}_0(k+hi+1\,|k),\ldots,\hat{y}_0(k+hp\,|k)]^T, \tag{10}$$

where $g_i,\ i=\overline{0,hp-d-1}$ are the coefficients of the $G_{j-d}\left(z^{-1}\right)$ polynomial.

B. Control algorithm

The objective function is based on the minimization of the tracking error and on the minimization of the controller output, the control weighting factor λ being introduced in order to make a trade-off between these two contradicting objectives

$$J=\left(\mathbf{G}\mathbf{u}_d+\hat{\mathbf{y}}_0-\mathbf{y^r}\right)^{\mathrm{T}}\left(\mathbf{G}\mathbf{u}_d+\hat{\mathbf{y}}_0-\mathbf{y^r}\right)+\lambda\mathbf{u}_d{}^{\mathrm{T}}\mathbf{u}_d, \tag{11}$$

subject to $\Delta u(k+i)=0$ for $i\in[hc,hp-d-1]$, where $\mathbf{y^r}$ is the reference trajectory vector with the components $y^r(k+j\,|k),\ j=\overline{hi,hp}$. Minimizing the objective function ($\partial J/\partial u_d=0$), the optimal control sequence yields as

$$\mathbf{u}_d^*=\left(\mathbf{G}^{\mathrm{T}}\mathbf{G}+\lambda\mathbf{I}_{hc}\right)^{-1}\mathbf{G}^{\mathrm{T}}\left[\mathbf{y^r}-\hat{\mathbf{y}}_0\right]. \tag{12}$$

Using the receding horizon principle and considering that $\gamma_j, j=\overline{hi,hp}$ are the elements of the first row of the matrix $\left(\mathbf{G}^{\mathrm{T}}\mathbf{G}+\lambda\mathbf{I}_{hc}\right)^{-1}\mathbf{G}^{\mathrm{T}}$, the following control algorithm results:

$$\Delta u\left(k\right)=\sum_{j=hi}^{hp}\gamma_j\left[y^r\left(k+j\left|k\right.\right)-\hat{y}_0\left(k+j\left|k\right.\right)\right]. \tag{13}$$

With $\hat{y}_0\left(k+j|k\right)$ from (5), the control algorithm can be rewritten as

$$\begin{aligned} &C(z^{-1})\Delta u(k)= \\ &-\sum_{j=hi}^{hp}\gamma_j H_{j-d}(z^{-1})\Delta u(k-1)- \\ &-\sum_{j=hi}^{hp}\gamma_j F_{j-d}(z^{-1})y(k)+\sum_{j=hi}^{hp}\gamma_j C(z^{-1})y^r(k+j). \end{aligned} \tag{14}$$

The algorithm can be easily implemented using the classical RST form:

$$R(z^{-1})\Delta u(k)=T(z^{-1})y^r(k+hp)-S(z^{-1})y(k), \tag{15}$$

where the R, S and T polynomials are given by

$$\begin{aligned} R(z^{-1})&=C(z^{-1})+\sum_{j=hi}^{hp}\gamma_j z^{-1}H_{j-d}(z^{-1}), \\ S(z^{-1})&=\sum_{j=hi}^{hp}\gamma_j F_{j-d}(z^{-1}), \\ T(z^{-1})&=C(z^{-1})\sum_{j=hi}^{hp}\gamma_j z^{-hp+j}. \end{aligned} \tag{16}$$

III. NETWORKED CONTROL SYSTEMS

Consider the standard NCS illustrated in Fig. 1, which is composed of five parts: a communication network, where it is assumed that delay occurs completely randomly, a physical plant, one sensor node (S), one controller node and one actuator node (A).

A. Time-varying delays

When sensors, actuators and controllers exchange data across the network, various delays with variable length occur due to sharing the common network medium. These delays are called network-induced delays and can vary widely according to the transmission time of messages and the overhead of the network. Usually, these network delays are randomly time-varying and can be smaller and larger than a sampling period. In Fig. 1 they are represented as τ^{ca} for the delay in the forward channel (controller-to-actuator delay) and as τ^{sc} for the delay in the feedback channel (sensor-to-controller delay). In the same figure, $u(t)$ and $y(t)$ represent the control signal and the output of the system, respectively.

The time delay generated in the communication line makes the feedback signal delayed relative to the control input, so, from the controller point of view, Fig. 1 and Fig. 2 are equivalent if at least one of the following holds:

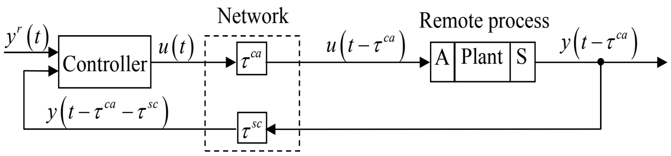

Fig. 1. Control system with network-induced time delay.

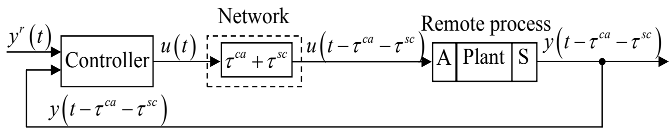

Fig. 2. Control system with grouped network-induced time delay.

- the time-varying delays are smaller than the sampling period [8]: $\tau_{\max} \leq T_s$, where $\tau_{\max} = \tau^{ca}_{\max} + \tau^{sc}_{\max}$, $\tau_{\max} \in \mathbb{R}_{>0}$ is the maximum delay that can be introduced by the communication network in both the forward and feedback channels, T_s is the sampling period of the system, $\tau^{ca}_{\max} \in \mathbb{R}_{>0}$ and $\tau^{sc}_{\max} \in \mathbb{R}_{>0}$ are the maximum delays that can be introduced in the forward and feedback channels, respectively;
- a buffer is introduced before the controller and another one before the actuator [9] with length $\lceil \tau^{sc}_{\max}/T_s \rceil$ and $\lceil \tau^{ca}_{\max}/Ts \rceil$, respectively; by using this method, the time-varying delay may be kept constant at the expense of making it larger;
- a low-pass filter is implemented in the controller or before the controller, similar to the one in [10], with cutoff frequency $f_t = \omega_t/2\pi$; the filter is introduced to reduce the influence of the fast time-varying delays on the signal that is transmitted from the sensor to the controller as the plant filters the effects of the fast time-varying delays on the control signal that is transmitted from the controller through the network; ω_t is the angular cutoff frequency of the plant;
- the delays do not increase as fast as the time [11]: $\dot{\tau}(t) < 1, \forall t \in \mathbb{R}_+$.

B. Delay modeling

Consider that the delay introduced by the communication network d_c is time-varying, but bounded

$$d_m \leq d_c \leq d_M, \tag{17}$$

where

$$d_m = \frac{\tau^{ca}_{\min} + \tau^{sc}_{\min}}{T_s} \tag{18}$$

is the minimum delay, with $\tau^{ca}_{\min}$ and $\tau^{sc}_{\min}$ the minimum delays that can appear in the forward and feedback channel, respectively, and

$$d_M = \frac{\tau^{ca}_{\max} + \tau^{sc}_{\max}}{T_s} \tag{19}$$

is the maximum delay.

In this paper, two methods of considering the communication delay by the predictive algorithm [12] are discussed, which are presented in the sequel.

1) Average method: The delay considered by the prediction model (4) is calculated using

$$d = \frac{d_m + d_M}{2}. \tag{20}$$

2) Identification method: The delay in (4) is considered equal to the minimum delay that can appear in the communication network

$$d = d_m \tag{21}$$

and instead of the polynomial B, another polynomial $\tilde{B}$, identified in order to model the system including the delays between d_m and d_M is introduced

$$\tilde{B}\left(z^{-1}\right) = \tilde{b}_0 + \tilde{b}_1 z^{-1} + ... + \tilde{b}_{n_{\tilde{B}}} z^{-n_{\tilde{B}}}, \tag{22}$$

with

$$\begin{aligned} &n_{\tilde{B}} = n_B + d_M - d_m, \\ &\tilde{b}_0 = \tilde{b}_1 = ... = \tilde{b}_{n_{\tilde{B}}} = \frac{b_0 + b_1 + ... + b_{n_B}}{n_{\tilde{B}} + 1}, \\ &B(1) = \tilde{B}(1). \end{aligned} \tag{23}$$

IV. Illustrative Example

DC motors are extensively used in industry for applications such as robot arm drives, machine tools, steel rolling mills, electric trains, positioning systems in the automotive industry and even aircraft control [13], requiring speed controllers to perform the desired tasks. In this paper, the remote DC motor speed control application is used to study and analyze the effect of considering different modeling methods for the network-induced time-varying delays on the performances of the networked control system. The goal of the control algorithm is to achieve zero steady-state error and smooth, fast response of the DC motor to step inputs, which are popular desired DC motor performance characteristics for many industrial applications.

A. Networked control architecture

The complete networked DC motor control architecture, which is graphically depicted in Fig. 3, consist of the following actions:

- The sensor measures the output of the physical plant (DC motor), converts the signal with the A/D converter, and sends the samples y to the controller through Ethernet;
- The DC motor controller receives the delayed sampled measurements from the sensors y^c and the desired reference trajectory y^r and computes the required control signal, while handling the physical/control constraints and the delays induced by Ethernet;
- The control signal computed by the controller, i.e., u, is sent to the remote process through Ethernet;
- The actuator, which is a power conversion unit with a D/A converter, receives the delayed control signal u^a and acts the DC motor.

In Fig. 3 the dashed lines represent the direction of the messages sent to and from the controller.

ISBN: 978-1-61804-321-4

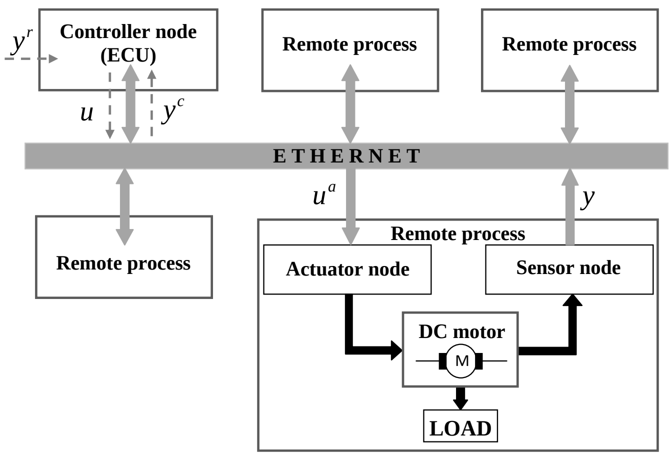

Fig. 3. DC motor networked control system.

Note that the sensors send the monitored signals y to the controller and the value that reaches the controller, y^c, can be related to y as

$$y_k^c = y(kT_s - \tau^{sc}). \tag{24}$$

Also, the control value that reaches the DC motor u^a can mathematically be expressed as

$$u_k^a = u(kT_s - \tau^{ca}). \tag{25}$$

The time delays τ^{sc} and τ^{ca} are composed of at least the following parts: waiting time delay (the time the node has to wait for the network to be free), frame time delay (the time needed to encapsulate a message with the available data to be sent over the communication network) and propagation delay (the time needed for the message to be sent through the communication network from the transmitter to the receiver). These three delay parts are fundamental delays that occur on a local area network, i.e., Ethernet.

B. DC motor modeling

The loop equation for the electrical circuit of the DC motor [13] is given by

$$e_a = L\frac{di_a}{dt} + Ri_a + K_b\omega \tag{26}$$

and the mechanical torque balance based on Newton's law is

$$J\frac{d\omega}{dt} + B\omega + T_l = Ki_a, \tag{27}$$

where e_a is the armature input voltage, L is the armature inductance, i_a is the armature current, R is the armature resistance, J is the system moment of inertia, B is the system damping coefficient, K and K_b are the torque constant and the back emf constant, respectively, T_l is the load torque and ω is the angular velocity of the rotor. Note that the DC motor has a driven load, that can be a robot arm or an unmanned electric vehicle.

Using $u = e_a$ as the control signal for the DC motor and considering the angular velocity of the rotor as the output of the system $y = \omega$ the electro-mechanical dynamics of the

TABLE I
SIMULATION DC MOTOR PARAMETER VALUES

Symbol	Value	Description
J	$42.6 \cdot 10^{-6}$ kg-m^2	Inertia
L	$170 \cdot 10^{-3}$ H	Inductance
R	4.67 Ω	Terminal resistance
B	$47.3{\cdot}10^{-6}$ N-m-s/rad	Damping coefficient
K	$14.7 \cdot 10^{-3}$ N-m/A	Torque constant
K_b	$14.7 \cdot 10^{-3}$ V-s/rad	Back-EMF constant
T_l	0 N-m	Load torque

DC motor can be described by the following transfer function representation

$$\Omega(s) = G(s)E_a(s), \tag{28}$$

with

$$G(s) = \frac{K}{JLs^2 + (JR + BL)s + BR + KKb}, \tag{29}$$

where $\Omega(s)$ is the Laplace transform of $\omega(t)$, $E_a(s)$ is the Laplace transform of $e_a(t)$ and is considered that $T_l = 0$ for simplicity.

C. Simulation results

In this subsection the presented predictive controller is tested on the DC motor model, subject to uncertain time-varying input and output delay. The network-based DC motor control system was simulated using Matlab, where the sampling period of the system was chosen as $T_s = 0.02$s and the values of the parameters are given in Table I.

The resulting transfer function model of the DC motor yielded as follows

$$G(s) = \frac{2029.826}{s^2 + 25.5809s + 60.3398}. \tag{30}$$

In order to apply the predictive control strategy, a CARIMA model (1) for the DC motor was developed, using as input the armature input voltage e_a and as output the angular velocity of the rotor ω, which is given by the following system polynomials

$$\begin{aligned} A\left(z^{-1}\right) &= 1 - 1.5463z^{-1} + 0.5446z^{-2}, \\ B\left(z^{-1}\right) &= 0.3379 + 0.2793z^{-1}. \end{aligned} \tag{31}$$

For the disturbances model, the polynomial C is considered to equal one and $D\left(z^{-1}\right) = 1 - z^{-1}$ to obtaining a zero steady-state error.

The upper bound of the delays that are induced by Ethernet was chosen as $\tau_{max}^{ca} = \tau_{max}^{sc} = 3T_s = 0.06$s and it was considered that the delays are time-varying and uniformly distributed in the interval $[0, \tau_{max}^{ca}]$ for the delays in the forward channel and in the interval $[0, \tau_{max}^{ca}]$ for the delays in the feedback channel, respectively. The sum of the network-induced time-varying delays as illustrated in Fig. 2 is represented in Fig. 4.

It was considered that $d_m = 0$ and $d_M = 6$ from (17) and the polynomial $\tilde{B}$ was identified using (22), which yielded

ISBN: 978-1-61804-321-4

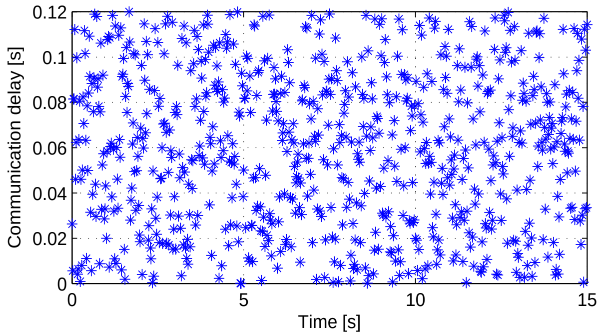

Fig. 4. Delays introduced by the communication network.

$$\tilde{B}\left(z^{-1}\right) = 0.0771 + 0.0771z^{-1} + \ldots + 0.0771z^{-6} + 0.0771z^{-7}. \tag{32}$$

The predictive control strategy was designed using the following parameters: $hc = na + nd = 3$, $hi = d + 1$, $hp = hc + d$, with d from (21).

In what follows the performance of the resulting networked closed-loop control system is analyzed using the trajectories plotted in Fig. 6, Fig. 7 and Fig. 9. In these figures five signals are represented:

- the reference value for the rotor angular velocity,
- the output of the system when there are no delays introduced by the communication network (which is used for comparison reasons),
- the output of the networked control system when using the average delay modeling method presented in subsection III-B1,
- the output of the networked control system when using the identification method presented in subsection III-B2 and
- the output of the control system when using a method which considers that the delays introduced by the communication network can be measured (measured delay method) and taken into account at each sampling period by a switching GPC controller; the measured delay is obtained in Matlab as $\lceil(\tau^{ca} + \tau^{sc})/T_s\rceil$ and is illustrated in Fig. 5.

Fig. 6 shows the closed-loop response of the networked control system subject to tracking a 200rad/s reference signal, where one can see that the rotor angular velocity reference is reached in a short time and with an overshoot less than 2.5% as illustrated in Fig 7.

Moreover, from $t = 9$s to $t = 10$s a load torque is applied to the system as illustrated in Fig. 8 in order to observe how each control structure rejects the disturbance caused by it. The responses are represented in Fig. 9 where it can be seen that the disturbance is rejected very quickly without oscillations.

The armature voltage is represented in Fig. 10, where it can be seen that the control signal for the measured delay method is very fluctuating due to the fact that the predictive control strategy is changed every sampling period in accordance with the measured delay. This leads also to steady-state errors for

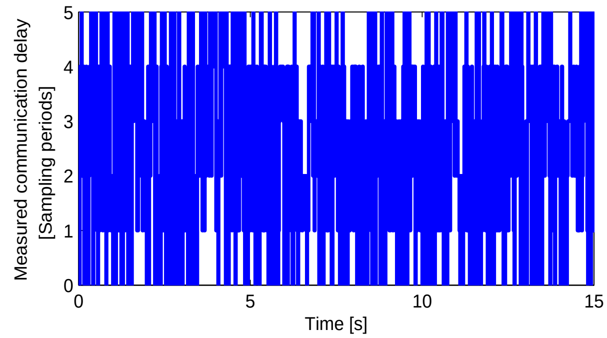

Fig. 5. Measured delays.

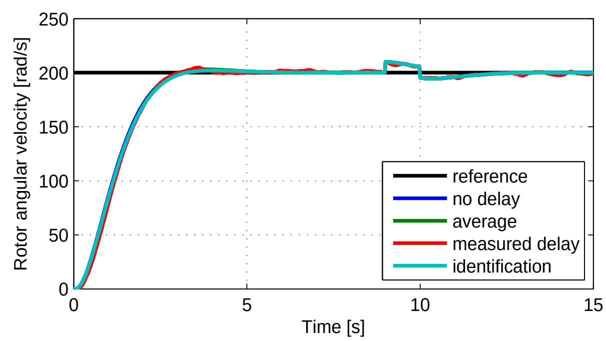

Fig. 6. Rotor angular velocity.

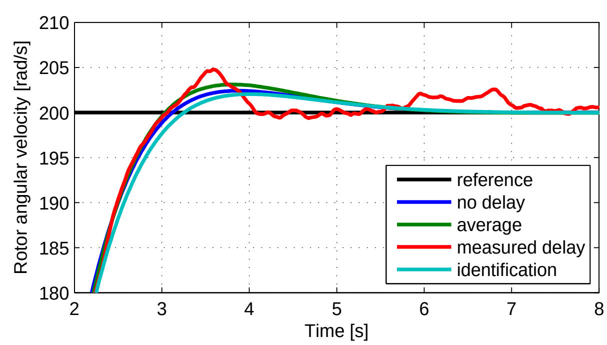

Fig. 7. Rotor angular velocity - detail 1.

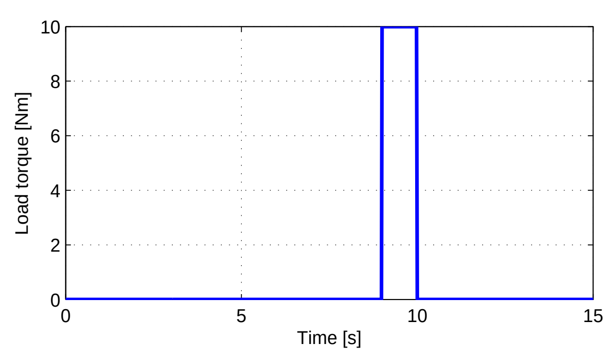

Fig. 8. Load torque.

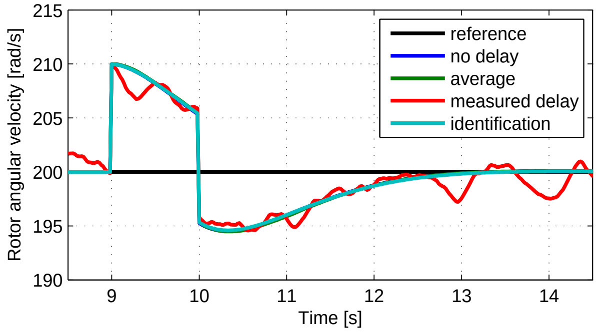

Fig. 9. Rotor angular velocity - detail 2.

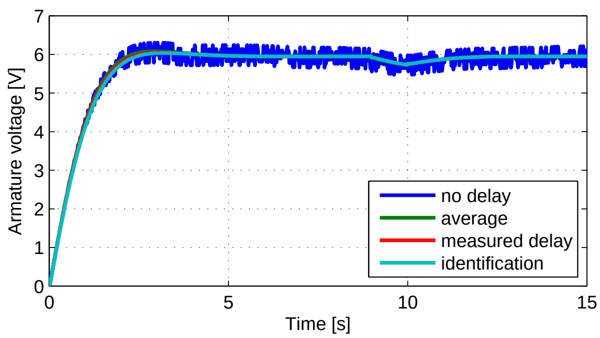

Fig. 10. Armature voltage (control signal).

the rotor angular velocity which can be observed in Figs. 6, 7 and 9.

D. Performance evaluation

A characteristic index that is usually used to evaluate the control system design and performances is considered in this paper:

- The *ITAE* index corresponds to the integral of the error absolute value weighted by time

$$ITAE = \int_0^\infty t|e(t)|dt. \tag{33}$$

  It gives less importance to initial errors, whereas the present errors are much more considered.

A control system is considered to be the best when it has the smallest values for the characteristic index and it can be seen in Table II that the smallest value is the one obtained by the control system with no delays introduced by the communication network followed by the identification method.

TABLE II
RESPONSE CHARACTERISTICS

Method	**No delay**	**Average**	**Measured**	**Identification**
ITAE	379.37	394.84	431.14	**386.16**

V. Conclusion

In order to overcome the influences of time-varying delays on the NCS performance, a predictive control strategy was designed in this paper. It is based on two modeling methods for the network-induced time-varying delays (average and identification) and it was applied to control a DC motor through an Ethernet communication network. Moreover, comparisons were performed with a method which considers that the network-induced delays can be measured and taken into account at each sampling period by a switching GPC controller. The obtained results are analyzed and the performances evaluated suggesting that the designed methods are able to compensate the effects of the delays.

References

[1] Y. Shoukry, M. Al-Shafie, and S. Hammad, "Networked embedded generalized predictive controller for an active suspension system," in *American Control Conference*, Baltimore, USA, 2010, pp. 4570–4575.

[2] C. F. Caruntu and C. Lazar, "Networked predictive control for time-varying delay compensation with an application to automotive mechatronic systems," *Journal of Control Engineering and Applied Informatics*, vol. 13, 2011.

[3] E. Miklovicova and M. Mrosko, "Model predictive control for networked control systems with random data dropouts," *International Journal of Communications*, vol. 6, pp. 10–17, 2012.

[4] X. Yin, S. Zhao, Q. Cui, and H. Zhang, "Predictive control applied to networked control systems in Frontiers of model predictive control," ser. Control Engineering. InTechOpen, 2012.

[5] Y. Zhang, V. Sircoulomb, and N. Langlois, "H∞ predictive control design for discrete-time networked control systems," in *11th IFAC International Workshop on Adaptation and Learning in Control and Signal Processing*, Caen, France, 2013, pp. 57–61.

[6] X. Zhao, M. Zhang, C. Hu, and Q. Zhang, "The research of time delay of wireless network control system in coal mine," *Sensors and Transducers*, vol. 168, pp. 16–22, 2014.

[7] E. F. Camacho and C. Bordons, *Model Predictive Control*. Springer Verlag, 2004.

[8] C. Huang, Y. Bai, and X. Liu, "H-Infinity state feedback control for a class of networked cascade control systems with uncertain delay," *IEEE Transactions on Industrial Informatics*, vol. 6, pp. 62–72, 2010.

[9] J. P. Richard, "Time delay systems: an overview of some recent advances and open problems," *Automatica*, vol. 99, pp. 1667–1694, 2003.

[10] J. Mu, G. P. Liu, and D. Rees, "Design of robust networked predictive control systems," in *American Control Conference*, Portland, USA, 2005.

[11] E. Witrant, D. Georges, C. Canudas-de-Wit, and M. Alamir, "On the use of state predictors in networked control systems," in *Applications of Time Delay Systems*, ser. Lecture Notes in Control and Information Sciences, vol. 352. Springer Verlag, 2007, pp. 17–35.

[12] C. F. Caruntu, A. E. Balau, and C. Lazar, "Networked predictive control strategy for an electro-hydraulic actuated wet clutch," in *6th IFAC Symposium Advances in Automotive Control*, Munchen, Germany, 2010, pp. 419–424.

[13] M. Y. Chow and Y. Tipsuwan, "Gain adaptation of networked DC motor controllers based on QoS variations," *IEEE Transactions on Industrial Electronics*, vol. 50, pp. 936–943, 2003.

Constantin Florin Caruntu was born in 1985. He received his Ph.D. degree in Systems Engineering from the Gheorghe Asachi Technical University of Iasi, Romania, November 2011. He is currently an assistant professor in the Automatic Control and Applied Informatics Department at the same university, Faculty of Automatic Control and Computer Engineering. His current research interests include the modeling and control of automotive networked systems.

Virtual enterprise management

Constantin Girdu, Luminita Popa, Badea Lepadatescu, and Adela-Eliza Dumitrascu

***Abstract*—**In this paper is developed a theoretically and methodologically framework that can provide the basis for developing information systems and management software products for industrial virtual enterprises. Virtual Enterprise Management is organizing, allocating and coordinating resources and corresponding activities and managing inter-interdependencies, in order to achieve its objectives while respecting its restrictions of time, cost and quality requirements. In the context of network economy (net economy), the society based on information and knowledge products and collaborative work processes are changing their nature by turning through virtualization.

***Keywords*—** collaborative system, reference model, virtual communities, virtual enterprise.

I. Introduction

VIRTUAL enterprise is an alliance of companies that share re- sources and knowledge (know-how) to achieve a common goal. Businesses operate as nodes in a network of sup- pliers, customers/consumers, distributors, service, based on critical technical support provided by information and communication technologies (ICT).

Virtual Collaborative Engineering (Integrated) is a methodology that tends to bring to upstream knowledge of the professions which are involved in downstream design (the manufacturing preparation, production and marketing). It involves effective participation of specialists from different professions starting with the earliest stages of conception.

The highly dispersed and globalized nature of product development today has changed the way that product development teams come together on a design. Virtual meetings, emailed design data and lightweight design visualization have replaced white board sessions as product development departments become complex design chains dispersed across time zones, legal and regulatory boundaries.

This work was supported in part by the Transilvania University of Brasov, the structural founds project PRO-DD (POS-CCE, O.2.2.1., ID 123, SMIS 2637, ctr. No 11/2009).

C. Girdu is with the ISJ Gorj, Str. Victoriei, nr.132-134, (e-mail: girdu2003@yahoo.com).

B. Lepadatescu is now with the Department of Manufacturing Engineering, Transilvania University of Brasov, 29 Eroilor Street, Brasov, Romania (corresponding author to provide e-mail: lepadatescu@unitbv.ro).

L. Popa is with the Faculty of Electrical Engineering and Computer Science, Transilvania University of Brasov, 29 Eroilor Street, Brasov, Romania (e-mail: mluminita2011@yahoo.com).

A.-E. Dumitrascu is with the Department of Manufacturing Engineering, Transilvania University of Brasov, 29 Eroilor Street, Brasov, Romania (e-mail: dumitrascu_a@unitbv.ro).

II. Virtual Enterprise Features

Virtual enterprise objective is to respond quickly to varying conditions of doing business environment and deal quickly with the emergence of new business opportunities.

Now there is a tendency for virtual enterprises to rely on stable business networks, also called *virtual communities*.

Virtual community members are involved in temporary relations of cooperation oriented project. Interactions that occur in the network business between community members are multilateral and complex. We need to identify core competencies of each potential contributor to the development of a common concept describing business development and defining the decentralized organizational structures and innovative management.

The distinctive features of Virtual Enterprise as, limited life time, partners focus on core competencies and operations distribution between independent (but interdependent) organizations, contribute to the difficulty and complexity of its management.

To meet these challenges is necessary to use new concepts and technologies in ICT support and new strategies and practices of doing business. In this regard, one of the research directions is the investigation and development of enterprise architecture models.

Their purpose is to provide all decision makers interested in to create a Virtual Enterprise, a common and efficient representation, which will facilitate company engineering.

Information provided by such a model allows the development of a standardized practice design called method- ology and define the characteristics and functions that must be provided by hardware and software that manage function of the organization.

One of the determining factors in ensuring Virtual Enterprise agility, ie the ability to dial and to respond quickly to environmental changes is its readiness.

One means of ensuring a high degree of Virtual Enterprise readiness which decisively influences its competitive potential is reference model adaptation.

A reference model is a model that incorporates features and common vision shared by members of a group of entities, as Virtual Enterprise is. Its purpose is to facilitate and make more efficient the process of developing a business model by formalizing and capitalization prior knowledge and the development of libraries and other tools to facilitate its reuse.

Another basic requirement for the design and implementation of Virtual Enterprise is to identify and use

ISBN: 978-1-61804-321-4

basic skills of each partner. These can be assembled in different ways to form various products and services. Using the way of attracting and selecting multiple sources for basic skills, the variety of products and services becomes even greater. A Virtual Enterprise model must reflect the structural and dynamic aspects which are relating to the activities, processes, flows and information sources, objectives and constraints operating within. The model processes and representation methods are capable of reflecting the processes dynamism, flexibility and interoperability requirements within Virtual Enterprise.

A business process is a specific task for achieving a business goal. In the Virtual Enterprise business process to be executed is a distributed business process.

It breaks down the components that are assigned for execution by the Virtual Enterprise members.

Achieving the overall objective of Virtual Enterprise involves management, orchestration and coordination of the various processes that occur at Virtual Enterprise members. The success key for Virtual Enterprise is execution and coordination of distributed business process on its various levels of decomposition and on all Virtual Enterprise member organizations.

III. The Collaborative Systems

A collaborative system is defined by a large number of users or agents which are engaged in a shared activity, usually located in distant locations. As part of the distributed applications, the collaborative systems represent a separate category, because the agents within the system are working together in order to achieve a common goal and having a great need to interact each other. Table 1 shows the components of a collaborative system.

Table 1. The components of a collaborative system

Material Component	Human Component	Energy Component	Information Component
Activity	People	Energy Resource	Procedures
Place			Flows
Material Resources			

Collaborative systems from consciousness society are ordered after collaborative systems from the knowledge and information society, being systems that include a uniform set of procedures which are governing relations between components. In the conscious- ness society, the human component plays a significant role over the conduct of any collaborative system. A collaborative system is one that works with people and other systems to get jobs done faster. Each person and each software program has various strengths and weaknesses. Working alone they can only accomplish so much. Working together, strength combines with strength to increase the likelihood of success [3]. The collaborative systems are an important subject of knowledge-based society and an important part of the human activities is involved in this field.

The collaborative systems in production are designed to increase production capacity and product quality in different units producing goods and services;

Collaboration Engineering is an approach to the de- sign of re-usable collaboration processes and technologies meant to engender predictable and success among practitioners of recurring mission-critical collaborative tasks [7]. Collaborative/ integrated engineering is defined as a methodology that allows integrated and simultaneous conception of products and production processes and associated maintenance. This ensures consideration, since the origin of all phases of product life cycle, starting with conception and ending with disposal, integrating quality problems, deadlines, demanding user costs, etc.

IV. Information and Communication Technologies

Improved information and communication technologies (such as linked CAD tools, shared databases of engineer- ing information, e-mail, and voice mail) can serve to break down common barriers to communication and to increase the capacity of an organization to transfer information [1,2].

Whitney [4] points to many examples where innovative CAD tools are being successfully used to facilitate concurrent engineering in complex development projects. Though this approach may increase information transfer, it might not be sufficient for coordinating team activities since the transfer of the most essential and difficult information is not assured. The web-based Product Lifecycle Data Management System is shown in Figure 1.

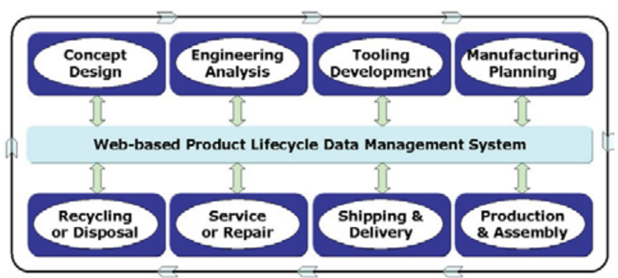

Figure 1. The web-based Product Lifecycle Data Management System.

V. Computer-Aided Product Development

Large figures and tables may span both columns. Place figure captions below the figures; place table titles above the tables. If your

The virtual product comprises a digital assembly of its part models. The parts are modelled in 3D using computer- aided design (CAD) programs and saved in standard for- mats (ex. IGES and STEP) for exchange between different programs (Figure 2).

Computer-aided engineering (CAE) programs enable simulating the product mechanism and optimizing the shape of

ISBN: 978-1-61804-321-4

each part under static/dynamic loads by simulating the internal stresses. The part models can be sent to a rapid prototyping (RP) system for automatic fabrication of a physical replica for form fit and function testing. The tooling models (molds, dies, jigs and fixtures) can be quickly developed by modifying the corresponding part models. Computer-aided manufacturing (CAM) programs enable planning, simulation and optimization of process parameters. Finally, computer-aided inspection systems enable automatic comparison of virtual and real parts for quality assurance.

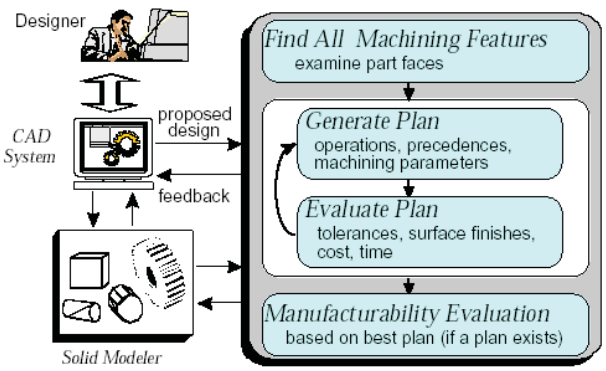

Figure 2. Computer aided design and manufacturing.

The 3D model is the connecting link in various CAX programs (X=design, engineering, manufacture and inspection). The programs generate a huge amount of data, which includes the solid models of different iterations and previous versions of products, as well as tooling, materials, process plans and results of analysis. This necessitates a systematic approach to data storage, verification and retrieval, which is achieved by a product data management (PDM) system.

The Collaboration Engineering way working describes the steps that need to be taken to design collaboration processes. In other words, the way of working defines the de- sign activities in the Collaboration Engineering approach. Overview of Collaboration Engineering Way of Working is shown in Figure 3.

There are a number of phases that can be distinguished when we are designing a collaboration process for a mission critical collaborative task that will deliver organizational value.

It is expected that these modeling tools, a.k.a. CACE (Computer Assisted Collaboration Engineering), can greatly increase design efficiency and effectiveness. Together these and other research challenges constitute an exciting agenda for the coming years. The practical value of Collaboration Engineering has been demonstrated convincingly. The Collaboration Engineering research community has only recently begun to take up the academic challenge yet the results so far are promising and stimulating.

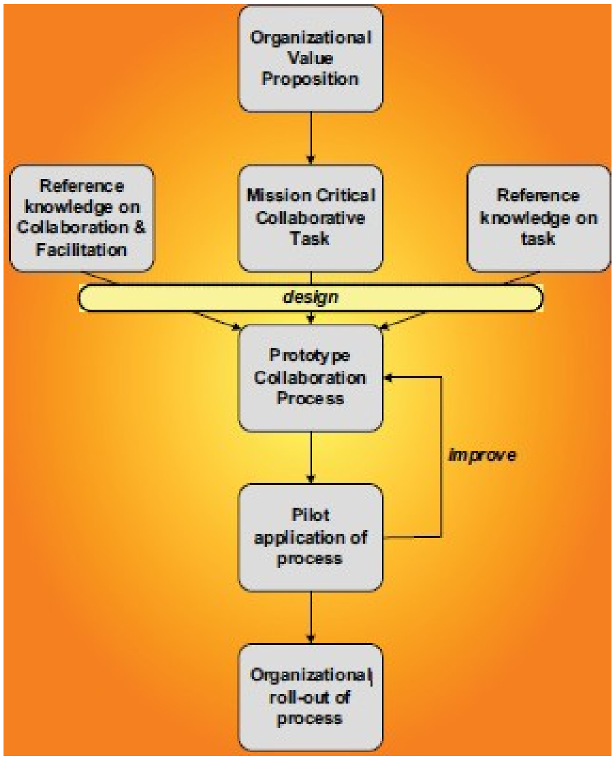

Figure 3. Overview of collaboration engineering way of working.

VI. Computer-Assisted Collaborative Systems

Computer-assisted collaborative systems present an immediate application and major advantages as follows:

- creative activity in research, design and development of new products and applications in collaboration with other authors areas such as: CAD/CAM (Computer Aided Design/Computer Aided Manufacturing); concurrent engineering; CASE system.
- administrative and economic processes such as: marketing, sales, purchasing and financial (management of orders and invoices, etc.); activities; transactions processing; workflow management; staffing; office activities.

To use and develop computer-assisted collaborative systems we should consider the following key elements: group awareness; space, collections and types of shared in- formation; methods and types of communication; knowledge of developing environmental facilities; multi-user interfaces; coordination within the group; support the hetero geneous and open environment that integrates single user applications.

A. Specific functional requirements for systems and collaborative engineering development platforms

To be functional in a given organizational and economic framework, systems and collaborative development plat- forms must meet the following general requirements:

- Possibility of integration with external sources ñ the information origin for cooperating community is “group- ware” external environment (examples: tools for PCs, various collections of information from relational databases, etc.);

ISBN: 978-1-61804-321-4

- Platform independence – “group-ware” applications often begin as departments implementations, further results can be extended on a much wider area; platform in- dependence is a basic element to ensure extensive use and investment protection;
- Mobility – “group-ware” infrastructure must be able to support many geographically dispersed locations, including a heterogeneous range of equipment;
- Common coexistence of multiple drive applications ñ economic relations are linking economic partners as key ac- tors in business processes automation, requiring the ability to easily extend the application page by successive additions.

B. Collaborative product development (CPD)

The challenge of keeping an engineering team working efficiently without getting in each other’s way can be difficult to manage. Product development projects now involve people from multiple departments trying to collapse product introduction lead times. As if this was not complex enough, many companies are distributing these resources around the globe and forming virtual teams of people from different companies. Global design, a commonly cited alternative to the term of collaborative product design, has cost benefits that are very attractive to today’s manufacturing, but adds new communication, control, and collaboration challenges and intensifies existing problem areas such as protecting intellectual property.

The essence of collaborative product design revolves around the need to involve the entire product development team ñ including the company’s personnel, customers and suppliers - during the development phase when a product’s most distinctive characteristics are defined. More participation by team members early in the process sharply reduces the need for changes later especially during tooling and manufacturing, eliminating delays and potential cost increases.

Product design and development are in the midst of a revolution thanks to collaboration technologies. The tools used for product design, the process of gathering input and revising designs, and the roles of those in the extended enterprise are all changing. A new generation of online collaboration tools integrated with traditional CAD is trans- forming the product development phase. Everyone in the product development process participates, sharing and building on one another’s insights and ideas.

New technologies allow people from different companies with incompatible computing systems to meet virtually on Web environments. Instead of simply sending data from PC to PC, Web tools let people talk via their computers while looking at shared documents, carry on e-mail chats, and use electronic white boards where two or more people can draw pictures or charts, in real-time, as others watch and respond.

The benefits of such collaboration are all encompassing. Using the collaborative platform to optimize communications, schedule and to resource usage, manufacturers can significantly reduce the cycle time to bring new products to market. They can implement solutions like DiFac for design and production tasks in order to reduce costs. By exploring design alternatives together, team members can leapfrog to truly innovative solutions. CPD is in demand because of its potential to cut product development cycle times. Design collaboration entails all the issues associated with discrete manufactured products, as well as those that are engineered or configured to order. These products can have a long procurement cycle, a seasonal cycle, or a short production cycle, but the key similarity is that they all start with specification documents, e.g., line drawing, schematic diagram and engineering drawing. This type of collaboration requires the specification documents to be shareable and modifiable by both parties, with appropriate audit trails, particularly with respect to the effective bill of materials and process plan referencing the documents.

In this space, computer-aided design vendors such as CATIA can leverage their design products. Traditionally, in this first phase, one party sends the document to an- other for review and costing via e-mail or regular mail and then collaborates on the document via telephone, e-mail, or regular mail, creating significant delays and cost over- head. The next step in the product design cycle may be to send color/material samples for approval/pricing, as in textiles which are the industrial sector of PPS. Collaboration tools that support this phase must manage the activities associated with it.

C. Product development teams

Collaborative work can be successful if all members show goodwill and responsibility. Collaboration is necessary to deal with such large projects. The collaborative and essentially social character of work needs to be appreciated in undertaking interactive systems design. A collaborative system creates an environment where people can work better together, can share information without the constraints of time and space, being characterized by three fundamental aspects: joint activities, sharing environment and way of interaction. The solution lies in connecting the team members through a digital communications network and providing them appropriate software programs to create, to analyses and to modify a virtual model of the product. The model and results are stored in digital form in a central or distributed server and accessible to all team members over a local area network or Internet. This approach to product development is referred to as Collaborative Product Lifecycle Engineering [6].

Product development teams are no longer constrained within the same four walls of the department. They are spread across different facilities, states, and increasingly across the globe. This has brought new challenges to product development, as designers must find new ways to share designs with collaborators who may never be in the same room. Companies are finding some measure of relief through a number of collaboration technologies that can help bring dispersed teams together. One solution that may often be overlooked but has a lot to bring to the collaboration table is video-conferencing [5].

VII. Conclusion

The traditional work teams are transforming in virtual teams and are operating within workgroups from/at long distance of the main organizations headquarters. Collaborative Engineering is a virtual methodology that tends to bring to upstream knowledge professions involved in downstream design as preparation of manufacture, production and marketing. It involves effective participation of different professions specialists in the earliest stages of conception. Collaboration Engineering is a design approach for recurring collaboration processes that can be transferred to groups that can be self-sustaining in these processes using collaboration techniques & technology. The above sections have presented the different "ways" of the Collaboration Engineering approach.

The collaborative conception or co-design of products and associated processes takes place in space, through meetings of experts of different professions and in time, by organizing parallel activities. In this way now arises the new products development issue. The integrated approach is ensuring short terms for products conception and launch, increasing quality and reducing production costs. The timely relevant and easily accessible obtained information is a key element in the operation of modern companies. In the company systemic approach, information system is linking the components of management and other systems at the micro level.

References

[1] O. Hauptman, T.J. Allen, *The Influence of Communication Technologies on Organizational Structure: A Conceptual Model for Future Research*, Working Paper, MIT Sloan School of Management. 1987.

[2] M.J. Jakiela, W.J. Orlikowski, *Back to drawing board? Computer-mediated communication tools for engineers*, Working Paper, MIT International Center for Research on the Management of Technology. 1990.

[3] C. Ciurea, "A Metrics Approach for Collaborative Systems," Economic Informatics Department, Academy of Economic Studies, Bucharest, Romania, *Informatica Economic*„ vol. 13, no. 2/2009 41, http://www. collaborative-systems.org/

[4] D.E. Whitney, "Electro-Mechanical Design in Europe," *University Research and Industrial Practice*, ESNIB. vol. 93-01, pp 1-52.

[5] www.aberden.com

[6] B. Ravi, *Collaborative Product Lifecycle Engineering*, Mechanical Engineering Department, Indian Institute of Technology Powai, Mumbai-400076, bravi@me.iitb.ac.in

[7] Gert-Jan de Vreede, R.O. Briggs, "Collaboration Engineering: Designing Repeatable Processes for High-Value Collaborative Tasks," in *Proceedings of the 38th Hawaii International Conference on System Sciences*, 2005.

[8] L.M. Camarinha-Matos, H. Afsarmanesh, "Creation of Virtual Organizations in a Breeding Environment," In Proc. of INCOM'06, St. Etienne, France, 17-19 mai 2006.

[9] L.M. Camarinha-Matos, H. Afsarmanesh, "Elements of a base VE infrastructure," *Journal Computers in Industry*, Vol. 51, nr. 2, June 2003, pp. 139-163.

[10] IFIP-IFAC Task Force, *Architectures for Enterprise Integration*, final report, 2002, http://www.cit.gu.edu.au/~bernus/ taskforce/finalreport/TFFinalReport.html

[11] M. Tolle, *Management and Engineering of Virtual Enterprises*, Ph.D. dissertation, Department of Manufacturing Engineering and Management, IPL - Department of Manufacturing Engineering and Management, Technical University of Denmark, 2004.

[12] I. Karvonen, P. Bernus, Y. Fukuda, M. Hannus, I. Hartel, J. Vesterager: *Global Engineering and Manufacturing in Enterprise Networks*, 2002

[13] A.J. Berre, A. Hahn, D. Akehurst, J. Bezivin, A. Tsalgatidou, F. Vermaut, L. Kutvonen, F. Linington, "State-of-the art for Interoperability architecture approaches," *Interoperability Research for Networked Enterprises Applications and Software*, Deliverable D9.1, November 19, 2004, http://interop-noe.org/deliv/ D91/attachment–_download/D9.1..pdf

[14] A.P. Klen, R.J. Rabelo, A.C. Ferreira, L.M. Spinosa, "Managing Distributed Business Processes in the Virtual Enterprise," *Journal of Intelligent Manufacturing*, Vol. 12, n. 2, 2001, pp. 185-197.

[15] L.M. Camarinha-Matos, "Virtual organizations in manufacturing: Trends and challenges," *12th Int. Conf. On Flexible Automation and Intelligent Manufacturing*, ISBN 3-486-27036-2, pp. 1036-1054, Dresden, Germany, 15-17 Jul 2002.

[16] T. Dufresne, J. Martin, "Process Modeling for e-Business", *Information Systems Department*, George Mason University, L. Kerschberg (ed), 2003.

Cascaded Wavelength Converter Using Dual Pumping Power Based on Commercial SOA With Remarkable BER and Conversion Efficiency

Mohamed I. Shehata, Osama A. Omer, Abdel-magid M. Ali

***Abstract*—**The aim of this work is to demonstrate the efficiency of a cascaded wavelength conversion by four-wave mixing in a commercial traveling wave semiconductor optical amplifier. A system of two wavelength converters spanning 100 km of single-mode fiber is suggested. The proposed scheme differs from the previous conventional systems as utilizing cascaded two commercial TW-SOA for each wavelength converter stage rather than using only one SOA in addition to Erbium-doped fiber amplifier (EDFA). This scheme overcomes the main problem appeared in the conventional schemes that suffer from the amplified spontaneous emission which considered as a noise that degrades optical signal to noise ratio of the converted signal. Based on the simulation results, bit-error-rate performance of $1.06{\times}10^{-13}$ at 40 Gb/s is achieved for two conversions up to 32 nm as a conversion range. A power penalty of 2.1 dB and a remarkable conversion efficiency of 97.03% are measured for overall system.

***Keywords*—**Four-wave mixing (FWM), Traveling wave semiconductor optical amplifier (TW-SOA), Bit-error rate (BER), Conversion efficiency, Optical signal to noise ratio (OSNR).

I. INTRODUCTION

NOWDAYS, All-optical wavelength conversion refers to the operation that consists of the transfer of the information carried from one wavelength channel to another wavelength channel in the optical domain. It is a key requirement for all optical networks because it is used to extend the degree of freedom to the wavelength domain. Moreover, All-optical wavelength conversion is also indispensable in future optical packet switching (OPS) networks to optimize the network performance metrics, such as packet loss rate and packet delay [1]. Also, it is very useful in the implementation of switches in wavelength division multiplexing (WDM) networks.

Mohamed I. Shehata is with Department of Electronics and Communication, Faculty of Engineering Arab Academy for Science, Technology and Maritime Transport, South Valley, Aswan, Egypt. Email: m.ismail34@yahoo.com.

Osama A. Omer is with Department of Electronics and Communication, Faculty of Engineering, Aswan University, Aswan, Egypt. Email: omer.osama@gmail.com.

Abdel-magid M. Ali is with [3] Department of Electrical, Faculty of Engineering, Aswan University, Aswan, Egypt. Email: abdel.magidali56@gmail.com.

In addition, it is crucial to lower the access blocking probability and therefore to increase the utilization efficiency of the network resources in wavelength routed optical networks. While a significant part of network design, routing and wavelength assignment depends on the availability and performance of wavelength converters.

Semiconductor Optical Amplifiers (SOAs) are considered to be the key components in all optical signal processing functions required for WDM-DWDM networks. Some of these functions that utilize SOA nonlinearities are: 1) wavelength converters [2], 2) optical logic-gates [3], 3) bit-comparators [4], 4) all-optical-switching[1], 5) 3R regenerators[5] and 6) routing [6].

Nonlinearities in SOAs are principally caused by carrier density changes induced by the amplifier input signals. The four main types of nonlinearity are: Cross gain modulation (XGM), Cross phase modulation (XPM), Self-phase modulation (SPM) and Four-wave mixing (FWM) [7].

In order to demonstrate a wavelength converter with a remarkable performance, it is required to have wide conversion range, high conversion efficiency, high optical-signal-to noise ratio and low input power [8]. It is also preferable to achieve these specifications with a simple designs, configurations and setups.

Literates indicates that multicasting based on XPM [9,10], looping utilizes SPM[11] and cascadability with FWM[12,13] are the preferable techniques that provide a remarkable wavelength converter performance over the O-S-C-L bands with nonlinearities in SOAs. Among all optical bands required to be covered by these techniques, C band still the most desirable band required to be covered in all SOA wavelength converter researches[14-16]. For all-optical multicasting with such large window hopping, the broadband wavelength conversion plays an important role in expanding the hopping range [17]. In particular, for SOAs XPM can provide large hop wavelength conversion, because of its effectiveness in a wide wavelength range[18]. Using a single SOA with a 1.3 µm gain band, broadband wavelength conversions to a much longer wavelength (1.55 µm) have been already demonstrated [19]. Although, multicasting has the previous advantages but it suffers from difficulty in converting into a much shorter wavelength, since the optical signal-to-noise ratio (OSNR) of the converted (probe) signal is drastically degraded [18].

Looping technique that utilizes SPM provide an acceptable SOA based wavelength conversion performance [20]. Single loop wavelength converter architecture provides significant merits like simple implementation and not requiring a high-speed short pulse laser or a clock recovery unit [11]. Unfortunately, this type of a simple wavelength converter has also been shown to be capable of a very limited number of repeated cascades, significantly restricting its use in a high-speed fiber transmission line [21]. These are partly compensated using the bi-directional data injection scheme and improves further on the performance but with the cost of adding large complexity to the looping technique[18,22].

Cascading with FWM is another attractive technique that is used in achieving acceptable performance for all optical SOA based wavelength converter [12]. Cascading shows a little simpler designs than looping for the same wavelength range required to be covered [11,23]. In addition cascadability can cover effectively the shorter wavelength range than multicasting in a cost of increasing cascading stages [18,24]. On the other hand FWM has the following merits over XPM & SPM as 1) utilizing ultra-fast intra-band nonlinearities in semiconductor optical amplifiers (SOA's), 2) independent of the bit rate, 3) modulation format transparency, 4) minimum degradation in system performance for a single SOA wavelength converter, and 5) None pulse broadening shape [13,25]. However this technique suffers from low conversion efficiency, polarization sensitivity and the frequency shift dependent conversion efficiency [25]. In a conclusion, cascadadiability with FWM can be an effective choice in designing and testing high performance all optical SOA based wavelength converter as will be shown in this work.

L. Krzczanowicz and M. J. Connelly [26] utilize the merits of DQPSK in designing a 40 Gb/s wavelength converter using bulk SOA-FWM over 1534.6 to 1536.6 nm. A parametric experimental study leads to the choice of bulk SOA gain with 21 dB, 10 dB saturation output power and 250 mA injection current to achieve an acceptable Q-factor operation.

An optimization process is then carried and results in improving the Q-factor to 10.25 dB. Two-fold cascade of SOA-based wavelength converters with 10 Gb/s DPSK signals are demonstrated in [27].The wavelength is converted from λ_1=1550 nm to λ_2=1560nm at the first stage, and back to 1550 nm at the second stage. An error free wavelength conversion operation is obtained at about -31dBm of received optical power. The second-stage of the converter showed a negligible increase in power penalty.

In this work, a remarkable C-band SOA wavelength converter based on cascading with FWM technique is evaluated. A commercial Traveling-Wave Semiconductor Optical amplifier (TW-SOA) is used in simulations and optimizations. Optimization parametric process is carried targeting unique BER, remarkable conversion efficiency, acceptable converter complexity and acceptable injection current level. A comparison with related literates that utilize the same technique and converter design is carried to prove the merits of this work.

This work is organized as follows: Section II provides a review on physics of FWM and the general SOA-based wavelength converter architecture using cascading with FWM. A detailed description for the simulation setup and its components/parameters is presented in section III. Results of the designed cascaded wavelength converter using commercial TW-SOA based on FWM nonlinearity technique and a comparison between our work and other related literatures are discussed in section IV. Finally, a conclusion of this work is stated in section V.

II. THE TWO STAGES SOA-BASED WAVELENGTH CONVERTER

Figure 1 is a schematic diagram that shows four-wave mixing in the frequency domain. It can be seen that the light before launching, sandwiching the two pumping waves in the frequency domain, is called the probe light (or signal light). The idler frequency f_{idler} may then be determined by:

$$f_{\mathrm{idler}} = 2\, f_{\mathrm{p}} - f_{\mathrm{probe}} \qquad (1)$$

Where: f_{p} is the frequency of the degenerated pumping wave[28][29]. This condition is called the frequency phase - matching condition and will be a key concept for the first and second wavelength conversion stages as shown in Fig.2.

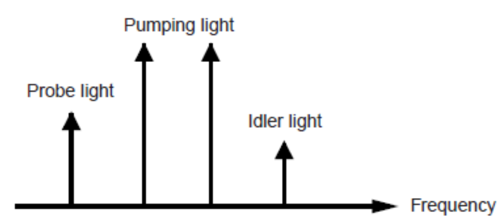

Fig.1. Schematic of Four-Wave Mixing in The Frequency Domain For Two Channel Pump Wave

Figure 2 illustrates a general block diagram for the proposed two stages SOA-based wavelength converter that utilize FWM.

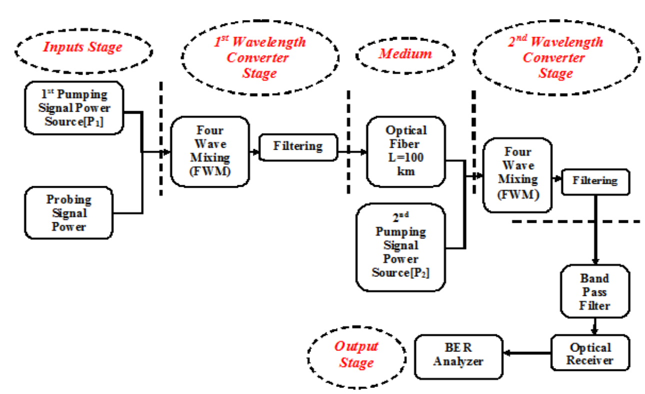

Fig.2. General Block Diagram For The Two Cascaded Stages SOA-Based Wavelength Converter

ISBN: 978-1-61804-321-4

Probing and 1st Pumping signals are combined together at input stage. Then, two input signals (P_o & P_1) undergo processing in FWM module at the first conversion stage , producing two converted signals at two wavelength channels carrying the same data (information) contents at the probe signal wavelength.

The selection of the preferable 1st converted signal is processed through filtering. Afterwards, the 1st converted signal passes through an optical fiber of length of 100 km and then combined again with the 2nd Pumping signal (P_2). Repeating the same steps processed at first wavelength conversion stage in order to achieve the second wavelength conversion process.

Finally, at output stage, the 2nd converted wavelength will be carried at the same data of the probing signal extending the conversion range.

III. SIMULATION SETUP DESIGN AND ITS COMPNENTS/PARAMETERS

Figure 3 shows the proposed setup which is used to realize two stages cascaded wavelength converter operations. Table I represents the overall components/parameters and there corresponding values which are used to simulate and evaluate the proposed wavelength converter and extracted from related literatures [4,30].

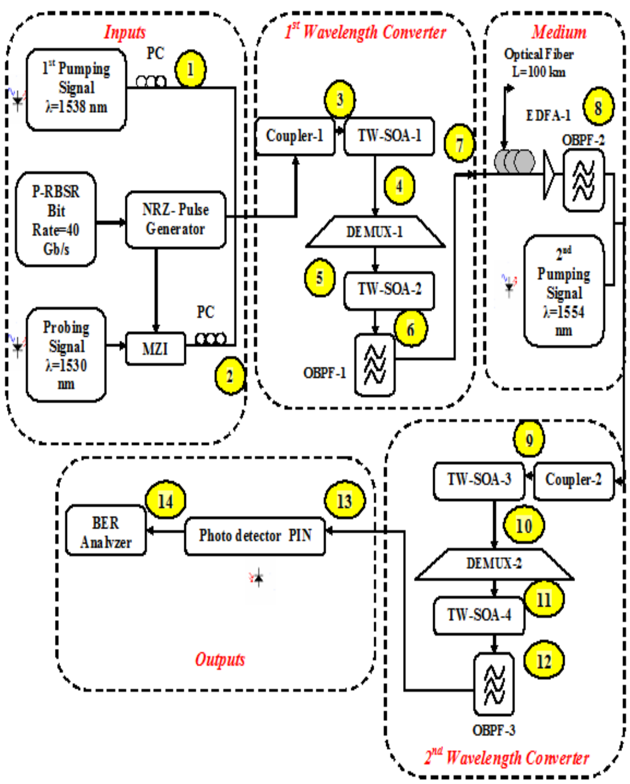

Fig.3. Proposed Setup for Cascaded Wavelength Conversion Spanning 100 km Transmission in a Single-Mode Fiber. PC: Polarization Controller, EDFA: Erbium-Doped Fiber Amplifier, OBPF: Optical Band-Pass Filter , MZI: MOD: LiNbO3 Mach–Zehnder Modulator, TW-SOA: Traveling Wave Semiconductor Optical Amplifier, P-RBSR: Pseudo-Random Bit Signal Generator, NRZ: Non-Return to Zero, DEMUX: Demultiplxer.

Table I
Components , Parameters and Values

Components	Parameters	Value Range	Unit
Inputs			
CW Laser Source (Probing Signal)	Center Frequency	1530	[nm]
		195.943	[THz]
CW Laser Source (1st Pumping Signal)		1538	
		194.924	
CW Laser Source (2nd Pumping Signal)		1554	
		192.917	
Pseudo-Random Bit Sequence Generator	Bit-Rate	40	Gbits/s
NRZ Pulse Generator	Rectangle Shape	Gaussian	N/A
LiNob3 MZM	Splitting Ratio	1.3	N/A
	Bias Voltage 1	+3	V
	Bias Voltage 2	-3	
1st & 2nd Wavelength Converters			
Polarization Controller	Phase	[90,-90[	deg.
Pump Coupler Co-Propagating 3-dB coupler-1 3-dB coupler-2	Signal Attenuation	0	dB
	Pump Attenuation	0	
Traveling Wave Semiconductor Optical Amplifier (TW-SOA-1) (TW-SOA-2) (TW-SOA-3) (TW-SOA-4)	Length	0.0005	m
	Width	3×10^{-6}	
	Height	8×10^{-8}	
	Optical Confinement Factor	0.15	N/A
	Differential Gain	2.78×10^{-20}	m^2
	Carrier density at transparency	1.4×10^{24}	m^3
	Line width enhancement factor	5	N/A
	Recombination Coefficient (A)	143000000	s^{-1}
	Recombination Coefficient (B)	1.0×10^{-16}	$m^3 s^{-1}$
	Recombination Coefficient (C)	3.0×10^{-41}	$m^6 s^{-1}$
	Initial carrier density	3.0×10^{24}	m^{-3}
	Injection Current	250	mA
WDM-DEMUX-1	No. of output	2	N/A
	Bandwidth	10	GHz
	Channel Frequency	193.915	THz
		194.924	
WDM-DEMUX-2	No. of output	2	N/A
	Bandwidth	10	GHz
	Channel Frequency	191.929	THz
		192.917	
EDFA-1	Gain Control	25	dB
	Noise Figure	10	dB
OBPF - 1 OBPF - 2	Center Frequency	193.915	THz
	Bandwidth	1	nm
Medium			
Optical Fiber	Length	100	Km
Outputs			
OBPF - 3	Center Frequency	191.929	THz
	Bandwidth	1	nm
Optical Receiver	Photo-detector	PIN	N/A
	Cut-off Frequency	5	GHz
	Center Frequency	192.917	THz

The probing signal source (P_0) and pumping signal sources (P_1 & P_2) are emitted utilizing continuous wave lasers. The probing signal (P_0) is simultaneously modulated by a 2^{10}-1 bit sequence using $LiNob_3$-Mach-Zehnder modulator with NRZ data format at 40 Gb/s.

After modulation, 1st pumping signal (P_1) is combined with probing signal (P_0) at (*Point (3)*) through 3-dB coupler-1 and mechanical polarization controllers which are used to independently align the pumping and probing signals to the TE polarization of the SOA.

Subsequently, the combining signal exposes to the FWM-1 medium which consists of 0.5-mm long commercial traveling wave semiconductor optical amplifier (TW-SOA-1) operating at 250-mA bias current. At the output of the TW-SOA-1 (*Point (4)*), the 1st converted signal is isolated using WDM-DEMUX-1 at (*Point (5)*).

At (*Point (6)*) , we obtain the 1st converted signal from the FWM-1. After demultiplexing 1st converted signal is amplified through TW-SOA-2 and filtered through OBPF-1.

In this experiment, dual sources provide the pumping waves for the two converters spanning 100-km transmission link between them, then in order to compensate the propagation losses in the 100 km length of dispersive single-mode fiber (SMF) at (*Point (8)*), EDFA-1 - OBPF-2 pair will be employed. Afterwards, 2nd pumping signal (P_2) and 1st converted signal are coupled again at (*Point (9)*) through 3-dB coupler-2, then injected to FWM-2 module consisting of TW-SOA-3, DEMUX-2 and TW-SOA-4.

It is observed that the second wavelength conversion will be achieved by generating another converted signals depending on the nonlinearity mechanism of passing through TW-SOA-3 at (*Point (10)*), then 2nd converted signal is separated by DEMUX-2 at (*Point (11)*) and amplified through TW-SOA-4 at (*Point (12)*). Finally, 2nd converted signal will be taken after OBPF-3 at (*Point (13)*).

In the receiver, 2nd converted signal is detected using photo-detector PIN at (*Point (14)*) and this receiver output is then introduced by a probe at the bit-error rate (BER) analyzer input in order to facilitate both Q-factor and BER measurements.

IV. RESULTS AND DISCUSSION

The first stage in this paper is bit-error rate (BER) and conversion efficiency optimization process and this will be done in section (IV-A). This optimization process maintains the injection current (I) at specific value extracted from famous literatures [11,13,31,33]. Noticing that the value of probing signal power (P_0) ranged from -3 to -1 dBm (from 0.502 to 0.7943 mW), while values of the pumping signals power (P_1 & P_2)) varied from 0 to 6 dBm (from 1 to 3.981 mW) [11,13 ,31,33].

Searching through trials on the optimum value of 1st pumping signal (P_1), 2nd pumping signal (P_2) and probing signal (P_0) that can provide both minimum BER in the range of 10^{-13} and highest conversion efficiency.

After extracting the optimum values of P_0, P_1 and P_2 that achieve 10^{-13} of BER and maximum conversion efficiency as will be shown from Figs. 4-7, these values will be applied to the simulation setup mentioned in section III and a full system trace that give a remarkable wavelength converter covering all C-band using commercial traveling wave semiconductor optical amplifier (TW-SOA) will be presented in section (IV-B).

A. Optimization Process Based on Bit-Error Rate (BER) & Conversion Efficiency

The FWM conversion efficiency is defined as the converted signal power at the TW-SOA output divided by signal power at TW-SOA input.

Firstly, the effect of the pumping signals (P_1 & P_2) are investigated while maintaining the injection current (I) at 250 mA and the probing signal (P_0) of -2 dBm which is chosen from our trials that achieve best values of BER in addition to conversion efficiency.

The results obtained in Figs. 4-5, showing that with increasing of pumping signals powers (P_1 & P_2) the conversion efficiency decreases, while the converted signal power keeps increasing and wavelength conversion process occurred successfully with the required BER and conversion efficiency.

It was noticed that when the 1st and 2nd pumping signals power is higher than 5 dBm (3.162 mW), the converted signal power decreased due to the gain saturation effect of the TW-SOA, leading to have bad BER for our proposed wavelength converter .

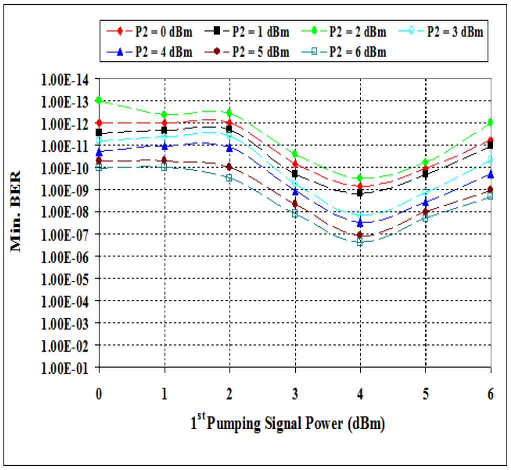

Fig. 4 Variation of Pumping Signals (P_1 & P_2) Versus BER at P_0 =- 2 dBm and I=250 mA

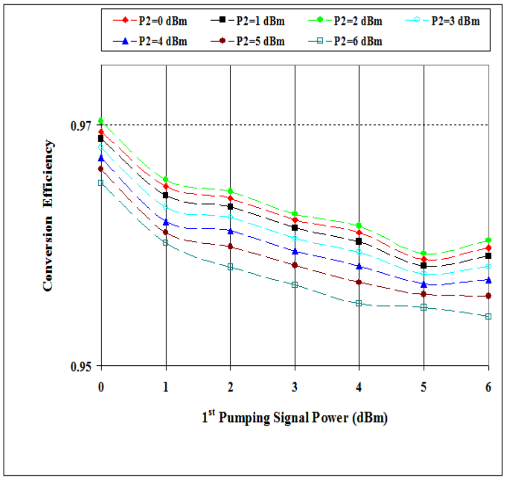

Fig. 5 Variation of Pumping Signals (P1 & P2) Versus Conversion Efficiency at P_0 =- 2 dBm and I=250 mA

Again, the procedure of calculating minimum BER and maximum conversion efficiency is repeated to study the effect of the probing signal (P_0), in the range of $-3 \le P_0 \le -1$. Keeping the other affecting parameters constant, the obtained results are displayed in Figs. 6-7.

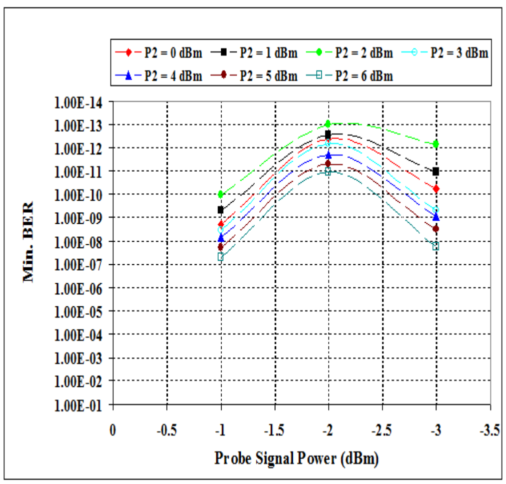

Fig. 6 Variation of Probing Signal (P_0) Versus BER at P_1=0 dBm and I=250 mA

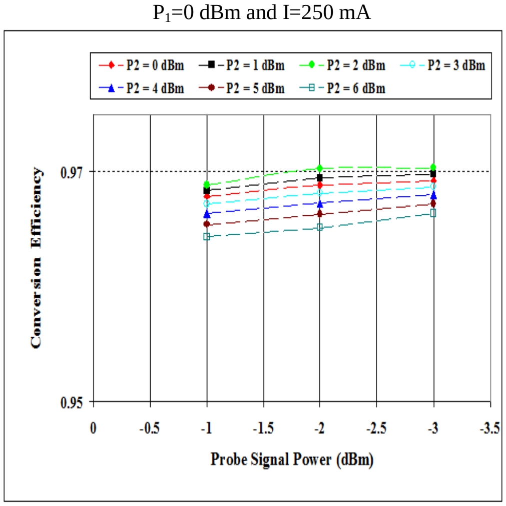

Fig. 7 Variation of Probing Signal (P_0) Versus Conversion Efficiency at P_1=0 dBm and I=250 mA

It is clear from Fig. 7, that the probing signal (P_0) has a negligible effect on the value of the maximum conversion efficiency. Finally from Figs. 4-7, our proposed two stages cascaded wavelength converter with a unique BER of 1.06×10^{-13} and a remarkable conversion efficiency near by 97.03% with an acceptable converter complexity are realized by hiring an optimized values of probing signal power (P_0) of -2 dBm, pumping signals power (P_1 & P_2) of 0 and 2 dBm respectively, in addition to the most famous value of the injection current (I) of 250 mA. A comparison with related literates that utilize the same technique and converter design is carried at Table II to prove the merits of this work. From this table, it can be shown that the proposed scheme outperforms works in [11,27,31,32,33], in sense of spanning distance, bit-rate and BER. In other hand, it gives better power penalty compared to [11,31,32] and a comparable value as [27]. In addition, it gives comparable results in sense of conversion efficiency compared to [11]. Finally, the proposed scheme gives better results in sense of up-conversion range compared to [11,27,31,32].

Table II
A Comparison Between Proposed Work and Related Works

Author Year	**Dist. (Km)**	**Bit Rate Gb/s**	**BER**	**Up Conv. Range (nm)**	**Conv. Efficiency (%)**	**Power Penalty (dB)**
David F. Geraghty 1997[32]	40	10	$<10^{-9}$	9	NA	2.2
Dar-Zu Hsu 2004[31]	NA	10	$<10^{-10}$	25	NA	2.5
D.Apostol-opoulos 2009[11]	80	10	10^{-4}	NA	Free-error 100%	4
Tomofumi Kise 2011[27]	20	10	10^{-12}	10	NA	2
A. K. Jaiswal 2013[33]	NA	10	$<10^{-9}$	35	NA	< 1
Proposed Work	**100**	**40**	$\mathbf{10^{-13}}$	**32**	**97.03**	**2.1**

B. *System Trace*

As described in details in section 3, a complete system trace for the proposed wavelength converter depending on the optimized values that estimated in section (IV-A) is introduced in this section. As indicated, (*Point (1)*) represents the 1st pumping signal (P1) at λ=1538 nm with a power of 0 dBm as shown in Fig. 8.

While (*Point (2)*) provides the probing signal (P_0) at λ=1530 nm with a power of -2 dBm as seen in Fig. 9 but after modulation using $LiNob_3$-Mach-Zehnder modulator with NRZ data format at 40 Gb/s.

ISBN: 978-1-61804-321-4

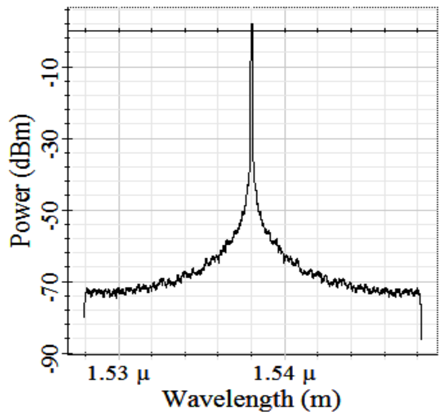

Fig.8 1st Pumping Signal at λ=1538 nm

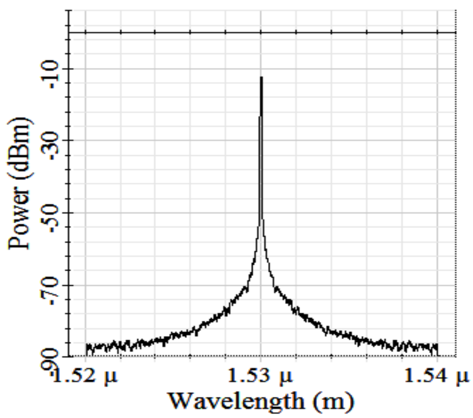

Fig.9 Probing Signal at λ=1530 nm

Then, the 1st pumping signal (P1) and the probing signal (P_0) are merging together using 3-dB-coupler-1 at (*Point (3)*) as declared in Fig.10 and in order to transfer our data from the probing signal (P_0) located at wavelength 1530 nm to other converted signals at new wavelengths at (*Point (4)*), the merging signal must be introduced to TW-SOA-1 and the output is presented at Fig.11.

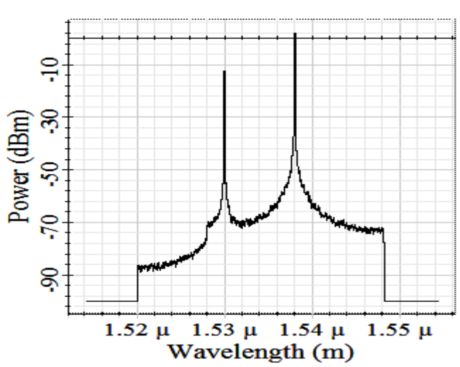

Fig.10 1st Pumping and Probing Signals Combined Together Using a 3-dB Coupler-1

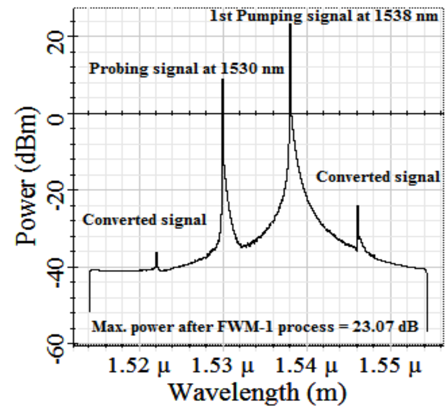

Fig.11 Converted Signals After Exposing Two Signals (Combining Signal) to TW-SOA-1

Output result from passing the combining signal through TW-SOA-1 which is located at (*Point (4)*) showing two converted signals appear at wavelengths 1522 and 1546 nm respectively with maximum power of 23.07 dB. As up-conversion process is needed for achieving our proposed wavelength converter , so WDM-DEMUX-1 with bandwidth of 10 GHz will be used to filter the first converted signal at (*Point (5)*) which located at λ=1546 nm.

At (*Point (6)*), 1st converted signal from the FWM-1 will be separated at λ=1546 nm after demultiplexing with maximum power equals 23 dB as appeared in Fig.12, which is comparable as obtained at (*Point (4)*) and that's executed by amplifying the signal at (*Point (5)*) using TW-SOA-2 with the same properties as TW-SOA-1.

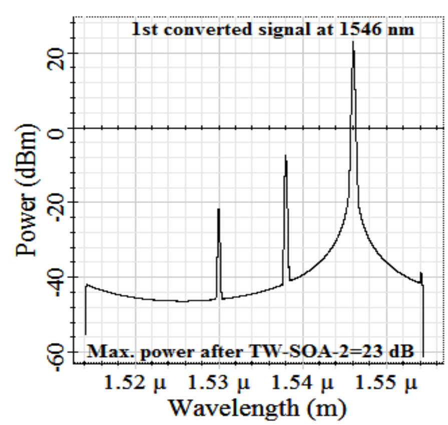

Fig.12 1st Converted Signal After Applying DEMUX-1 & TW-SOA-2

Then at Fig.13, the 1st converted signal at (*Point (7)*) will be isolated from its neighbors signals by passing through OBPF-1 which specified by 1nm bandwidth and center frequency of 193.915 THz with maximum power of 22.9 dB.

ISBN: 978-1-61804-321-4

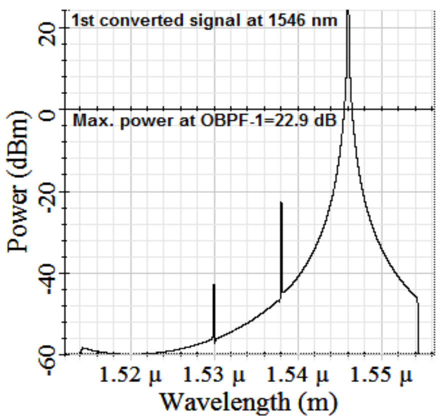

Fig.13 1st Converted Signal After Exposing to OBPF-1

Resulting from our first wavelength converter, the signal is up shifted in wavelength from λ=1530 nm as shown in Fig.9 to λ=1546 nm which introduced at Fig.13, so the first conversion range achieves 16 nm at (*Point (7)*) which is presented in Fig.3 at section III.

Afterwards, the 1st converted signal propagates a distance of hundred kilometers through a dispersive single-mode fiber (SMF), leading to great propagation losses. These losses will be compensated using EDFA-1 with a gain of 25 dB, which was used to amplify the signal. Following the amplification, an optical band pass filter (OBPF-2) is used to reduce the amplified spontaneous emission (ASE) in order to provide improved OSNR of the 1st converted signal at (*Point (8)*). Maximum power of 1st converted signal after spanning 100 km and exposing to EDFA-1-OBPF-2 pair estimated of 21.8 dB and that's will be extracted from Fig.14.

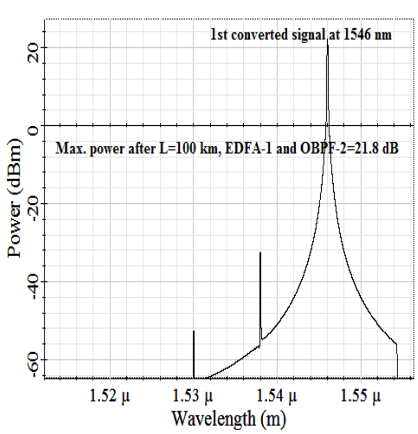

Fig.14 1st Converted Signal After Spanning 100 Km, Then Exposing to EDFA-1 and OBPF-2

Subsequently, 2nd pumping signal (P_2) at λ=1554 nm with a power of 2 dBm, shown in Fig. 15. 1st converted and 2nd pumping signals are combined again at (*Point (9)*) through 3-dB coupler-2.

Then repeated the same steps as performed previously in order to achieve 2nd wavelength converter through injected coupled signal to FWM-2 module consisting of TW-SOA-3, DEMUX-2 and TW-SOA-4 during (*Points(9-12)*) in section III.

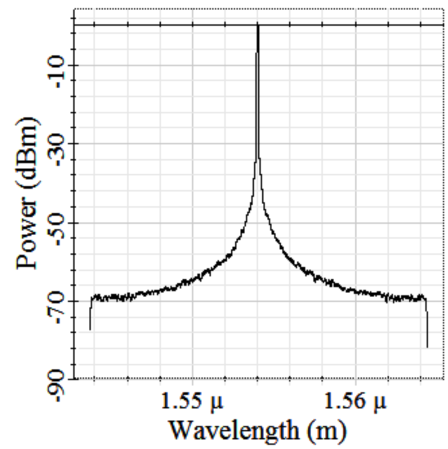

Fig.15 2nd Pumping Signal at λ=1554 nm

So 2nd wavelength conversion process displayed as seems at Figs. 16-17 with maximum power degraded from 21.2 to 20.96 dB.

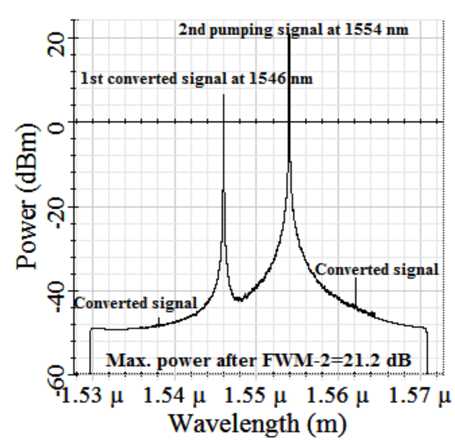

Fig.16 2nd Pumping and 1st Converted Signals Coupled using 3-dB-Coupler-2 and Introduced to TW-SOA-3

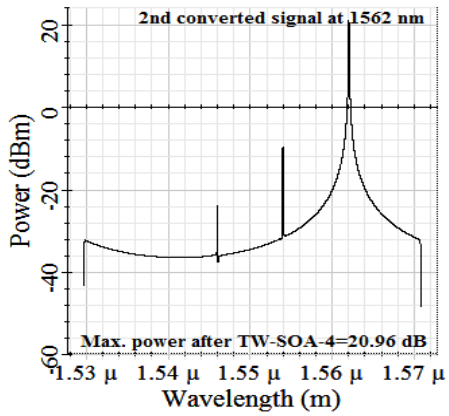

Fig.17 2nd Converted Signal After Applying DEMUX-2 & TW-SOA-4

The 2nd converted signal was isolated at (*Point (13)*) by passing through OBPF-3 which described by 1nm bandwidth and center frequency of 191.929 THz with maximum power equals 20.9 dB as shown in Fig.18.

Then the output of 2nd wavelength converter stage introduced to the receiving stage to support the calculation of both Q-factor and BER measurements at (*Point (14)*).

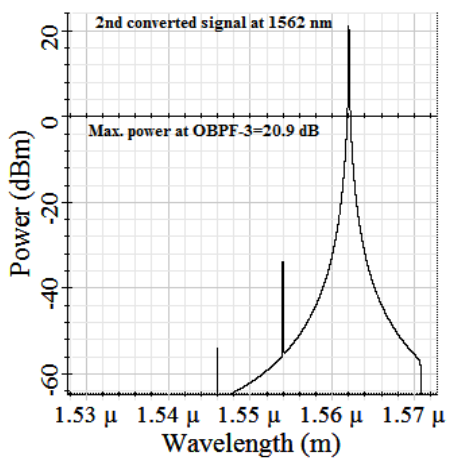

Fig.18 2nd Converted Signal After Exposing to OBPF-3

Finally, in the second wavelength converter, the signal is up shifted again approximately by an equal amount that obtained in the first wavelength converter as it is ranging from λ=1546 to λ=1562 nm.

Therefore as a result we can transfer our data from λ=1530 nm to λ=1562 nm at approximately 32 nm as a conversion range using only two cascaded stages which cover approximately all C-band ranging from (1530 nm to 1565nm) [34].

V. Conclusion

This work has the advantages of getting a remarkable C-band [34] wavelength converter using a commercial semiconductor optical amplifier and also providing a closed look about the specification that required to get a unique BER of 10^{-13} and a remarkable conversion efficiency with a small power penalty.

A complete trace for the proposed two stages wavelength converters is presented. After making a comparison between the results of our main work and related literatures as shown in Table II, it is clear that this work gives merits for the network designers to utilize commercial components in all optical signal processing.

References

[1] Rafael C. Figueiredo, Napole˜ao S. Ribeiro, Antonio Marcelo Oliveira Ribeiro, Cristiano M. Gallep, and Evandro Conforti, "Hundred-Picoseconds Electro-Optical Switching With Semiconductor Optical Amplifiers Using Multi-Impulse Step Injection Current," *J.Lightw. Technol.*, vol. 33, no. 1, Jan.1, 2015.

[2] A. Anthur, R. Watts, J. O'Carroll, D. Venkitesh and L. P. Barry, "Dual correlated pumping scheme for phase noise preservation in all-optical wavelength conversion," *Opt. Expr*., vol. 21, no. 13, pp. 15568-15579 , (2013).

[3] A. Kotb et al., "NAND gate with quantum dot-semiconductor optical amplifiers-based Mach-Zehnder interferometer," *Opt. Elect. Lett*., vol. 9, no. 2, Mar., 2013.

[4] R. Mehra et al., "Ultra-fast all-optical 4-bit digital encoders using differential phase modulation in semiconductor optical amplifier-Mach-Zehnder interferometer configuration," *Opt. Eng*. 52(3), 035202 (March 2013).

[5] Wenham Wu, Yu Yu, Bingrong Zou, Weili Yang and Xinliang Zhang, "Single SOA based simultaneous amplitude regeneration for WDM-PDM RZ-PSK signals," *Opt. Expr*., vol. 21, no. 6, pp. 6718-6723, Mar., 2013.

[6] K.E. Stubkjaer, "Semiconductor optical amplifier based all optical gates for high speed optical processing," *IEEE J. of Select Topics in Quant. Electron*.6, no.6, pp. 1428-1435, (2000).

[7] G.P. Agrawal, "Fiber Optic Communication Systems," 4th Edition, John Wiley & Sons Inc., 2011.

[8] Connelly M., "Semiconductor Optical Amplifiers," Jun. 13, 2009.

[9] Motoharu Matsuura, Naoto Kishi and Tetsuya Miki, "Ultrawideband Wavelength Conversion Using Cascaded SOA-Based Wavelength Converters," *J.Lightw. Technol*., vol. 25, no. 1, Jan, 2007.

[10] Zhan-Qiang Hui and Jian-Guo Zhang, "Wavelength conversion, time demultiplexing and multicasting based on cross-phase modulation and four-wave mixing in dispersion-flattened highly nonlinear photonic crystal fiber," *J. of opt*., vol. 14, no. 5, Apr., 2012.

[11] D. Apostolopoulos, D. Klonidis, P. Zakynthinos, K. Vyrsokinos, N. Pleros, I. Tomboys, and H. Avramopoulos, "Calculability Performance Evaluation of a New NRZ SOA-MZI Wavelength Converter," *IEEE Photon. Technol. Lett*, vol. 21, no. 18, Sept. 15, 2009.

[12] Robert Elschner, Alexander Bunge, Alexandre Gual Coca, Carsten Schmidt-Langhorst, Reinhold Ludwig, Colja Schubert, and Klaus Petermann, "Impact of Pump-Phase Modulation on FWM-Based Wavelength Conversion of D(Q)PSK Signals," *IEEE J. of Select Topics in Quant. Electron*.14, no.3, (2008).

[13] Zhihong Li, Yi Dong, Jinyu Mo and Yixin Wang, "Cascaded all-optical wavelength conversion for RZ-DPSK signal based on four-wave mixing

in semiconductor optical amplifier," *IEEE Photon. Technol. Lett*., vol. 16, no. 7, July, 2004.

[14] G. Contestabile, Y. Yoshida, A. Marti, and K. Kitayama, "Ultra-broad band, low power, highly efficient coherent wavelength conversion in quantum dot SOA," *Opt. Expr*., vol. 20, no. 25, Nov 2012.

[15] B. Filion, S. Amiralizadeh, A. T. Nguyen, L. A. Rusch, and S. LaRochelle, "Wideband Wavelength Conversion of 16 Gbaud 16-QAM Signals in a Semiconductor Optical Amplifier," in Optical Fiber Communication Conference/National Fiber Optic Engineers Conference 2013, OSA Technical Digest (online) (Optical Society of America, 2013), paper OTh1C.5.

[16] Amy C. Foster, Mark A. Foster, Michal Lipson, Alexander L. Gaeta and Keren Bergman, " Continuous Wavelength Conversion of 40-Gb/s Data Over 100 nm Using a Dispersion-Engineered Silicon Waveguide," *IEEE Photon. Technol. Lett.*, vol. 5, no. 2, Jan. 15, 2011.

[17] Katsunari Okamoto, Satoru Yamano and S. J. Ben Yoo, Senior Member, "Advanced Optical-Label Routing System Supporting Multicast, Optical TTL, and Multimedia Applications," *J.Lightw. Technol* ,vol.23, no.10, Oct, 2005.

[18] M.Matsuura, N. Kishi, and T. Miki, "All-optical wavelength conversion with large wavelength hopping by utilizing multistage cascaded SOA-based wavelength converters," *IEEE Photon. Technol. Lett.*, vol. 18, no. 8, pp. 926–928, Apr.15, 2006.

[19] J. P. Turkiewicz, G. D. Khoe, and H. de Waadt, "All-optical 1310 to 1550 nm wavelength conversion by utilizing nonlinear polarization rotation in semiconductor optical amplifier," *Electron. Lett*., vol. 41, no. 1, pp. 29–30, Jan. 2005.

[20] Z. Zhu, M. Funabashi, Z. Pan, B. Xiang, L. Paraschis, and S. J. B. Yoo, "Jitter and amplitude noise accumulations in cascaded all-optical regenerators," *J. Lightw. Technol.*, vol. 26, no. 12, pp. 1640–1652, Jun.15, 2008.

[21] O. Zouraraki, K. Yiannopoulos, P. Zakynthinos, D. Petrantonakis, E. Varvarigos, A. Poustie, G. Maxwell, and H. Avramopoulos, "Implementation of an all-optical time-slot-interchanger architecture," *IEEE Photon. Technol. Lett*., vol. 19, no. 17, pp. 1307–1309, Sep., 2007.

[22] M. Hattori, K. Nishimura, R. Inohara, and M. Usami, "Bidirectional data injection operation of hybrid-integrated SOA-MZI all-optical wavelength converter," *J. Lightw. Technol.*, vol. 25, no. 2, pp. 512–519, Feb., 2007.

[23] M. Funabashi et al, "Cascadability of optical 3R regeneration for NRZ format investigated in recirculation loop transmission over field fibers," *IEEE Photon. Technol. Lett*., vol. 18, pp. 2081-2083, 2006.

[24] Motoharu Matsuura, Naoto Kishi and Tetsuya Miki, "All-Optical Regenerative Multicasting From 1.55- to 1.3-μm Wavelength Window Using Dual-Stage Cascaded SOA-Based Wavelength Converter," *IEEE Photon. Technol. Lett.*, vol. 18, no. 24, Dec.15, 2006.

[25] G. Contestabile, A. Maruta and K. Kitayama, "Four Wave Mixing in Quantum Dot Semiconductor Optical Amplifiers," *IEEE J. Quantum Electron*., 2013.

[26] Lukasz Krzczanowicz and Michael J. Connelly, "40 Gb/s NRZ-DQPSK Data All-Optical Wavelength Conversion Using Four-Wave Mixing in a Bulk SOA," *IEEE Photon. Technol. Lett.*, vol. 25, no. 24, Dec.15, 2013.

[27] Tomofumi Kise, Kimchau N. Nguyen, John M. Garcia, Henrik N. Poulsen, and Daniel J. Blumenthal, "Demonstration of Cascadability and Phase Regeneration of SOA-Based All-Optical DPSK Wavelength Converters," *J. of Opt. Soc. Am.*, (2011).

[28] G. P. Agrawal, "Nonlinear Fiber Optics," Second Edition, Academic Press, San Diego, USA, (1995) Chap. 10.

[29] Yamamoto and Nikkan Kogyo Shimbun, "Optical Fiber Communications Technology," Chap. 11. (in Japanese), 1995.

[30] M.-H.Lee, J.-M.Kang. and S.-K.Han, "All optical signal regeneration in cascaded Mach-Zehnder interferometer wavelength converter," *IEE Proc. J. Optoelectron.*, vol.148, no. 4, Aug., 2001.

[31] Dar-Zu Hsu, San-Liang Lee, Pei-Miin Gong, Yu-Min Lin, Steven S. W. Lee and Maria C. Yuang, "High-Efficiency Wide-Band SOA-Based Wavelength Converters by Using Dual-Pumped Four-Wave Mixing and an Assist Beam," *IEEE Photon. Technol. Lett*., vol. 16, no. 8, Aug., 2004.

[32] Robert B. Lee, David F. Geraghty, Marc Verdiell, Atul Mathur and Kerry J. Vahala, "Cascaded Wavelength Conversion by Four-Wave Mixing in a Strained Semiconductor Optical Amplifier at 10 Gb/s," *IEEE Photon. Technol. Lett*., vol. 9, no. 6, June, 1997.

[33] A. K. Jaiswal and Shreyashree Verma, " Performance on SOA Based Wavelength Conversion at 10 GB/s by dual pump four wave mixing over a 50 nm," International Journal of Advanced Research in Computer and Communication Engineering, vol. 2, Issue 5, May 2013.

[34] Malcolm Johnson, "Optical fibers, cables and systems," ITU-T Manual, 2009.

High speed briquetting of metal chips using rocket engine

Todor Penchev, Stanislav Gyoshev, Dimitar Karastoianov

Abstract—Preparation of briquettes of metal chips with good density and quality is of great importance for the efficiency of this process. In this paper is investigated the possible to produce brackets from chips of two types of metal. Chips of different shapes and sizes are compared, some of which are free of water and oil (cleaned chips), while the rest are left without cleaning (soiled chips). For briquetting with controlled impact a rocket engine is used. For 3D reconstruction of the internal structure a X-ray tomography is used.

Keywords— briquetting, chips briquetting, impact briquetting, rocket engine.

I. INTRODUCTION

FOR briquetting of metal chips are used mechanical and hydraulic presses with nominal force of several hundred to several thousands of kN. To obtain briquettes with good density the ratio H/D for different materials vary within wide limits (H / D = 0,8-0,25), where H is the height, and D is the diameter of the briquette. The greater is the density of the briquettes, the smaller are the losses in the transport and melting. Basic data used to evaluate the effect of briquetting operation are specific density of the briquette (ρ), g/sm^3, and specific contact pressure for briquetting (p), MPa.

At briquetting with hydraulic presses it is achieved 60% - 75% briquette's density in comparison with solid material density. The specific pressure reaches values p = 200-400 MPa, in briquetting of steel chips [1, 2].

Due to the large size of briquetting presses, large power consumption, and relatively low productivity, methods are searching to improve the efficiency of this process. One such method is high velocity impact briquetting [3, 4].

In [5] are presented the results of use of high velocity explosive presses for briquetting of metal chips. The obtained briquette's density is (g/sm^3): aluminum alloy - 2.2 to 2.4 (2.7 to 2.75); carbon steel - 5.0 to 5.5 (7.85); alloyed steel - 5.0 to 5.5 (7.48 to 8.0). In parenthesis is given the density of the respective solid metal. As a major drawback of this briquetting method is the impossibility of process control.

In [6] is described construction of die forging hammer propelled by industrial rocket engine – fig. 1a.

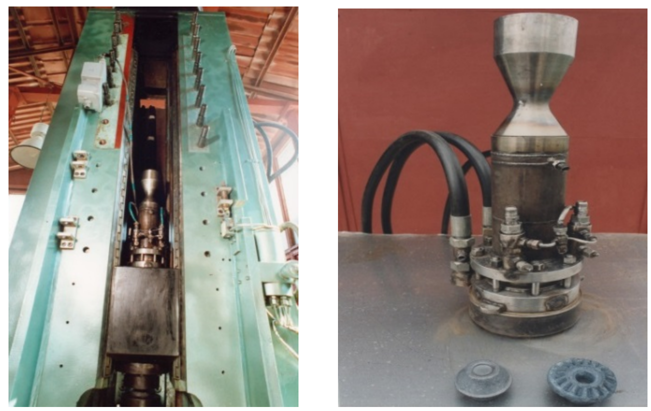

a) b)

Fig. 1 a) Front view of rocket engine propelled hammer.
b) Rocket engine and die forged conical gear

Whit this machine is possible to work with controlled impact and with impact velocities from 4,5 m/s up to 20 m/s. Laboratory set-up for controlled impact, and the results of experimental study of metal chips briquetting by controlled impact with impact speed of 7 m/s are presented in [7]. Fig.1(b) shows industrial rocket engine used at this hammer and die forged conical gear (low carbon alloyed steel). As can be seen, the hammer design is very simple and as a result, it is more reliable in operation compared to other similar machines.

Before briquetting chips are cleaned from residues of water and oil, which raises the cost of the production process. In this paper the possibility of briquetting of uncleaned chips is studied.

It is shown in [7] that it is possible to obtain briquettes from aluminum alloy chips with density close to density of the solid alloy. The potentiality to produce parts using such briquettes is also investigated.

II. LABORATORY SET-UP

The laboratory set-up is shown in Fig.2. The falling part 13 is accelerated by cold rocket engine 12, working with compressed air. The trust R of the engine is R = 226 N. Maximum height of fall and impact speed with 9.12 kg falling part mass are 1.1m and 7 m/s respectively. Largest

This work was supported by the project AComIn - Advanced Computing for Innovation, Grant 316087, funded by the FP7 Capacity Program (Research Potential of Convergence Regions initials).

D. N. Karastoyanov is with the Institute of Information and Communication Technologies (IICT) - BAS, Sofia, Bulgaria (phone: +359-2-979-27-23; Sofia, Bulgaria, (e-mail: dkarast@iinf.bas.bg).

T. N. Penchev with the Institute of Information and Communication Technologies (IICT) - BAS, Sofia, Bulgaria (e-mail: tzpenchevi@abv.bg).

S. D. Gyoshev is with the Institute of Information and Communication Technologies (IICT) - BAS, Sofia, Bulgaria (e-mail: stanislavgyoshev@mail.bg).

impact energy is 223 J. In Fig.2 are presented controlled impact schemes of the device. Specific scheme of work is set by the control unit 16 and is performed by sensors 4, 5, 10, 11, 15.

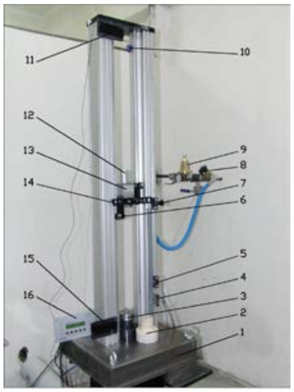

a)

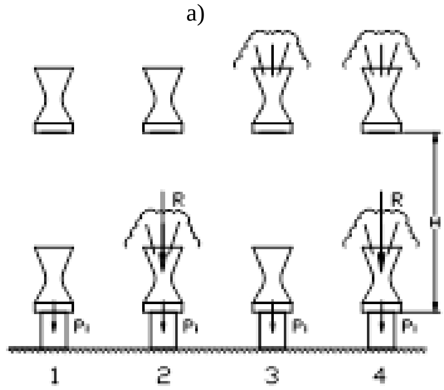

b)

Fig. 2a. A laboratory set up for studying of collision processes: 1 – base plate with a mass of 235 kg; 2 – lower fixed body for elastic impact; 3 – lower fixed tool for plastic impact; 4 – induction speed sensors; 5 – air on/off induction sensor; 6 – guides for the falling part; 7 – trigger mechanism; 8 electro-magnetic valve; 9 – air pressure control valve; 10 - air ‘On’ sensor; 11 – receiver of the light sensor for speed; 12 – cold rocket engine; 13 – 6,17 kg mass falling part; 14 – plate for activation of sensors 4, 5 and 11; 15 – light speed sensor emitter; 16 – electronic control board; Fig. 2b. Impact schemes of the device from Fig.2a: 1- free fall (max.V_i =4.5 m/s); 2 – free fall with additional force R at the time of impact (controlled impact with max.V_i =4.5 m/s); 3 – fall with acceleration by a rocket engine, without additional force in the time of impact (max.V_i = 8.5 m/s); 4 - fall with acceleration by rocket engine + additional force R in the time of impact (controlled impact with max.V_i = 8.5 m/s)

III. METHODS

In Fig.3 are shown the aluminum alloy chips used in the experiments. To account for the influence of the size and type of chips used in the present work (type A) are compared with those of work [7] (type B). In order to investigate the influence of the residual water and oil on the density of the briquettes produced by the impact briquetting part of the type A chips were cleaned (type A_C) while others had been left uncleaned (type A_{UC}).

Diameter of the produced briquettes is 20 mm, as it is the hole of the die for briquetting. Diameter of the punch is 19.6 mm. The gap between the die and the punch is left out to ensure exit of the air that remains between the chips in the filling into the die.

Briquetting is carried out using controlled impact (regime 4 in Fig.2) and with maximum impact energy of 223 J. In order to investigate their density and structure the obtained briquettes are measured, weighed on an analytical balances and pictured on 3D X-ray tomography (Nikon XTH 225 Compact Industrial CT Scanner) – fig. 5.

a)

b)

Fig.3. a- chips used in present paper (type A); b – chips used in [7] (type B).

In Fig.4a are shown used cast iron chips. Their average sizes are: length 25 mm, width 15 mm, thickness 1 mm. Diameter of the produced briquettes is 20 mm, as it is the hole of the die for briquetting. Diameter of the punch is 19.6 mm. The gap between the die and the punch is left out to ensure exit of the air that remains between the chips in the filling into the die.

Impact process is recorded with a high-speed camera Nac Memrecam HX6 - fig. 6. The video is processed with the software Vicsasso 2009 which defines impact speed (V_i) and acceleration (a_i).

ISBN: 978-1-61804-321-4

a)

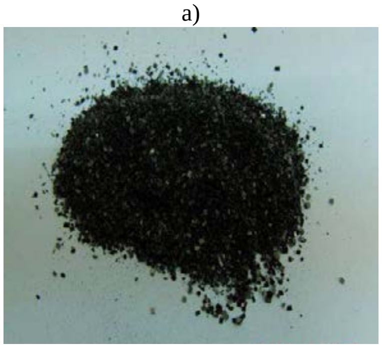

b)

Fig.4. a- chips used in present paper (type A); b – chips used in [8] (type B)

Fig. 5. 3D X-ray Nikon XTH 225 Tomograph

Fig. 6. High speed Camera Nac Memrecam HX6

The impact force P_i and impact energy E_i are calculated by formulas

$$P_i = a_i m \text{, N,} \tag{1}$$

$$E_i = \frac{mV_i^2}{2}\text{, J,} \tag{2}$$

where *m* is the mass of the falling part, in kg.

The specific impact energy for briquetting is calculated by the formula

$$E_s = \frac{E_i}{\Theta}\text{, J/sm}^3\text{,} \tag{3}$$

where Θ, sm^3, is the briquette volume. The use of this indicator makes it possible to compare the results obtained under different conditions of briquetting.

IV. RESULTS

- Briquetting

In Fig.7 are shown the diagrams for velocity and acceleration by one of the experiments. It can be seen that acceleration is very high - 1610 m/s^2 (164 *g*, were *g* is the acceleration of gravity). Due to the action of the thrust of the rocket engine during the impact, the rebound is small – 28 mm (the coefficient of restitution *e* = 0.158).

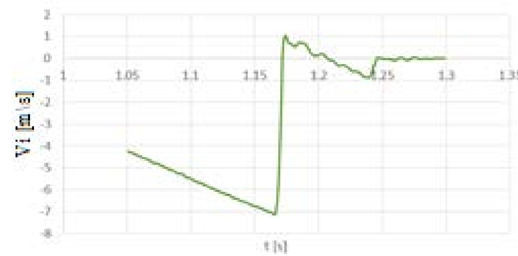

a)

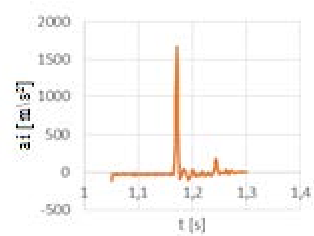

b)

Fig.7. Diagrams for: a – velocity; b –acceleration in controlled impact briquetting

Briquettes shown in Figure 8 are further processed by removing the protrusions, weighting and scanning.

Fig.8. A1-A4 - briquettes from cleaned chips (type A_C); AM1-AM4 – briquettes from uncleaned chips (type A_{UC})

In Fig.9 is shown the scanned picture of an Al-alloy briquette. It is seen from Fig.9a that the highest density is in the middle area which covers about 0.5 D_{briq}. From the vertical sections (Fig.9b, Fig.9c) it can be seen that the density is the lowest in the peripheral areas of the briquette. Because of the little impact time the air cannot be forced out of the briquette and remains in these areas. When using a large thrust R of the engine and it acts for a longer time, this air can be removed to obtain a briquette having a density of solid alloy. Such a briquette may be used to prepare parts by machining or by plastic deformation. This subject will be discussed below.

In Fig.9b, Fig.9c in the middle of the briquette heights there is a line which shows the material stratification. This defect in our opinion, is caused by the distribution of tensile plastic waves and has no bearing on the quality of briquettes. In the manufacturing of parts from such briquettes it can be removed by subsequent plastic deformation.

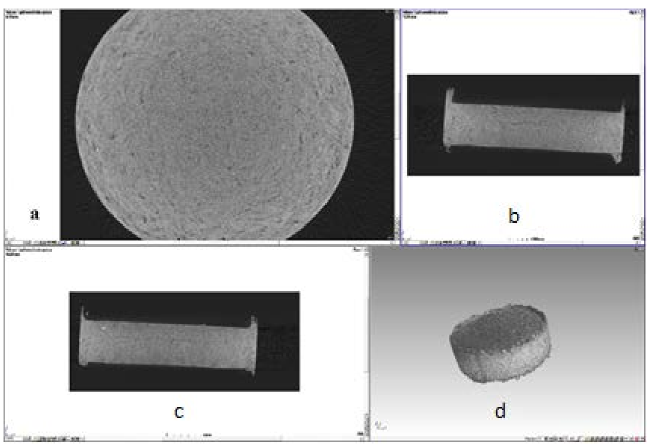

Fig.9. Photos of X-ray tomography briquette of Al - alloy: a - cross-section in the middle of the briquette height; b, c - orthogonal vertical sections through the center of the briquette; d - 3-D image

Four of the briquettes (two A_C and two A_{UC}) were deformed by reverse extrusion – Fig.10. In this case for deformation is used Hydraulic press with maximum force 400 kN. Wall thickness of the specimen is 2 mm. It can be seen that the bottom aria, which is deformed by pressure, is realized very large deformation without defects. On the walls of the specimen are noted transverse defects, which are obtained by the action of the tensile stresses. From these results it can be concluded that the schemes of deformation with predominantly compressive stresses can obtain parts without defects, while the schemes of deformation with predominantly tensile stresses are obtained parts with poor quality. It is necessary to be carried further and more extensive research in this field.

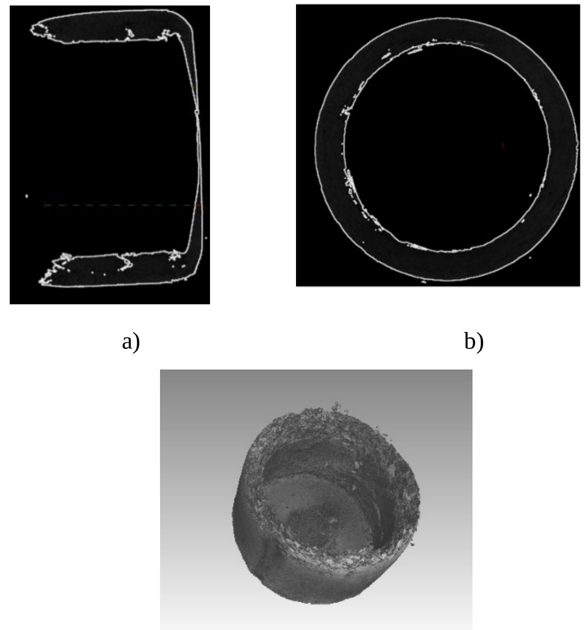

a) b)

c)

Fig.10. Photos of X-ray tomography of deformed by reverse extrusion briquette: a - cross-section in the middle of the briquette height; a - vertical section through the center of the briquette; b - cross-section in the middle of the specimen height; c - 3-D image

The X-Ray tomography images of one of the briquettes shown on Fig.11 defined low density (average density is about 2 gr/sm^3) and poor quality of the briquettes. It can be seen that the orientation of the chips is different for the separated areas of the briquette. In the volume of the briquette the chips are horizontally arranged and are wavy bended. This arrangement and deformation of the chips is a clear illustration on the operation of vertical and horizontal plastic waves in the impact briquetting process.

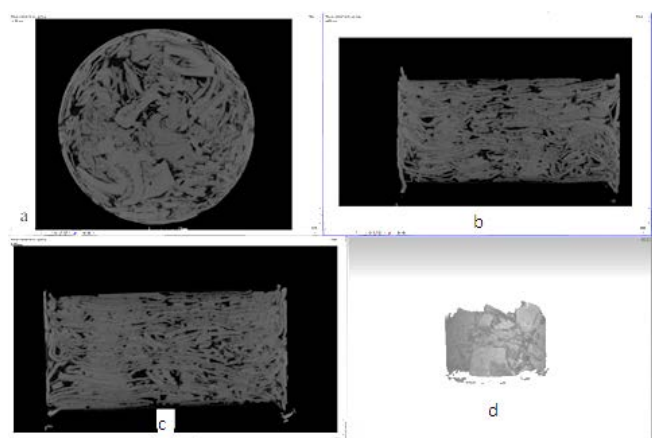

Fig.11. X-ray tomography images of gray cast iron briquette obtained in present paper: a - cross-section in the middle of the briquette height; b, c - orthogonal vertical sections through the center of the briquette; d - 3-D image

ISBN: 978-1-61804-321-4

V. CONCLUSION

The studies reveal that it is possible to obtain high-quality briquettes from aluminum alloys chips by controlled impact, regardless of the type and size of the chips. The advantages of this method are as follows:

• Allows to obtain briquettes with a high density using chips which are not cleaned from residues of water and oil. Dropping out of the cleaning operations will reduce production costs for briquetting. This technology can be used only in cases where the briquettes will be used for melting.

• The density of the obtained in this work and in [7] briquettes is 93% - 96% of the density of the respective solid materials. Applied specific impact energy is $E_s = 150$ J/sm^3 and the thrust of a rocket engine, which provides additional pressure during briquetting is R = 224 N. Using industrial hammer propelled by a rocket engine described in [6], can be achieved much larger values of E_s and R, which makes it possible to produce briquettes from aluminum alloys chips with a density very close to the density of solid metal.

• Greater density of the briquettes from Al - alloys allows obtaining a workpieces by subsequent plastic deformation when using processes with predominant compressive stresses (upsetting, die forging, extrusion). In this case, for obtaining of briquettes should be used free of water and oil chips. These options require further research for each separate workpiece type.

The conducted study of briquetting of cast iron chips with controlled impact showed that the shape and size of the chips is essential for producing of high quality briquettes. Can be drawn the following important conclusions

• It has been found that at impact briquetting of the chips with rectangular shape their location on the peripheral wall of the briquette is such that prevents the exit of the air out of it. As a result, are prepared briquettes with a low density and poor quality.

• Comparison with briquettes produced by impact of chips with small size indicates that by using of small size chips are produced briquettes with good density and quality. This means that large chips must first be ground to obtain chips with smaller dimensions.

ACKNOWLEDGMENTS

This research was performed with the support by the project AComIn "Advanced Computing for Innovation", grant 316087, funded by the FP7 Capacity Programme (Research Potential of Convergence Regions).

REFERENCES

[1] Stepanskii L.V., Metal waste briquetting, Mashgis, 1975, (in Russian).

[2] http://www.johnhartinternational.com/briquetting/

[3] Poljakov A.P., Zalazinskaja E.A., Impact extrusion of powder material billets, Zvetnaja metallurgia, 2003, 1, 30-35, (in Russian).

[4] Wang J., Yn H., Qu X., Analysis of density and mechanical properties of high velocity compacted iron powder, Acta Metallurgica Sinica (English Letters), v.22, 6, 2009, 447 – 453.

[5] Stepanov W.G., Shavrov I.A., High energy impulse methods for metal working processes, Mashinostroenie, 1975, (in Russian).

[6] T.Penchev, S. Gyoshev , D.Karastojanov, Study of parameters of controlled impact by impact deformation of elastic and elastic-plastic materials, Proceedings of Recent Advances in Mechanical Engineering Conference, 21-23.11.2014, Florence, 113-118.

[7] Penchev T., D. Karastoyanov., Experimental Study of Upsetting and Die Forging with Controlled Impact., International Conference on Manufacturing Science and Engineering (ICMSE 2014), 17-18 April 2014, Lisbon, Portugal, published in: International Science Index Vol: 08 No:04 Part IV, eISSN 1307-6892, pp 529-533,

[8] T.Penchev, I.Altaparmakov, Experimental Investigations on “Controlled Impact” Effect, International Conference METAL 2013, Brno, 15-17.05, 2013.

Todor N. Penchev is a member of the Bulgarian Scientists Association. He was born in Sofia, Bulgaria in 1941. He has a master degree in Mechanical engineering. He graduated Technical University Sofia in 1967. The author received a doctoral degree in 1979, Industrial Technology from the Technical University Sofia. Dr.Penchev is an assoc. professor in Institute of Information and Communication Technologies (BAS). Dr. Penchev is an assoc. professor under AcomIn project at the IICT – BAS. He is conducting research on design, dynamics and mechanics of mechatronic systems and industrial processes. His professional interests refer to forging systems, industrial engineering and technology.

Stanislav D. Gyoshev was born in Sofia, Bulgaria in 1988. He has a master degree in Mechanical engineering. He graduated Technical University Sofia in 2013. S. Gyoshev is a PhD student in Institute of Information and Communication Technologies (BAS). He is conducting research on design, dynamics and mechanics of mechatronic systems and industrial processes. His professional interests refer to forging systems, industrial engineering, technology and robotics.

Dimitar N. Karastoyanov is a member of the Bulgarian Scientists Association. He was born in Stara Zagora, Bulgaria in 1952. He has a master degree in Electrical engineering. He graduated Technical University Sofia in 1977. The author received a doctoral degree in 1982, Robotics from the Institute of engineering cybernetics and robotics (BAS). Dr. Karastoyanov is a professor in Institute of Information and Communication Technologies (BAS). Prof. Dr. Karastoyanov is a key professor under AcomIn project at the IICT – BAS. He is conducting research on design, dynamics and intelligent control of robots and mechatronic systems. His professional interests refer to real time systems, adaptive control, industrial engineering and robotics.

Technology for production of high-temperature materials and alloys including nano elements

Dimitar Karastoyanov Desislava Ivanova Nikolay Stoimenov

Abstract**—**This work discusses methods and means of obtaining materials and alloys with improved technological properties, such as hardness and wear resistance by heat treatment and addition of micro- and nano-particles in the heating mixtures. Some examples of high temperature processing are presented and some types of micro and nanoparticles are described. A process for the preparation of materials and alloys at high temperatures - up to 2300 ^{0}C, with the addition of micro and nano particles, is proposed. Presented are means of control and process optimization.

Keywords—Tammann furnace, nano elements, hardness, wear resistance

I. INTRODUCTION

HIGH temperatures obtaining or heat treatment of metals and alloys described in different types of kilns, with different technologies and at different temperatures. The general objectives are the homogenization of the output, a good separation of the metal from the slag in the casting and the improvement of its properties - hardness and abrasion resistance [1].

Some examples here are utilization of poor ore raw materials and also available waste materials through their thermal processing in a Tammann furnace - Fig. 1.

Fig.1.Common type of a Tammann furnace

For carbothermal obtaining of multi component alloys in a Tammann furnace are taken an agglomerate and a catalyst as a reducing agent. Agglomerate and the calculated reducing agent are mixed and disintegrated to a particle size below 1 mm, and then loaded into separate graphite crucibles. A loaded with the batch melting pot in a working furnace is shown in Fig. 2.

An electro alumothermal obtaining of an alloy out of sinter concentrate and catalyst in Tammann furnaceis is achieved through an alumothermal balance calculation for the expected amount of alloy, slag and gas phase. For the calculation are used the same ratios of the switching elements in the alloy, the slag and the gas phase, as in the previous (carbothermal) process.

Fig. 2. Melting pot in a Tammann furnace

Agglomerate and the calculated reducing agent are mixed and disintegrated to a particle size below 1 mm, and then a graphite crucible is charged. A Tammann furnace is used, whose general appearance, the loaded melting pot and thermocouple, as well as the work with it, are shown above. A good separation of metal and slag is achieved during the casting process.

An electrosilicoalumothermal way to obtain ferro-alloys out of agglomerate, concentrate and catalyst in a Tammann furnace is made through a silikoalumothermal balance calculation for the expected amount of alloy, slag and gas phase. For the calculation are used the same ratios of the switching elements in the alloy, the slag and the gas phase as in the previous cases. Subsequent to the calculation is available a blend for the preparation of multi-component alloy in a Tammann furnace. The blend consists of agglomerate, catalyst (broken into small pieces) and a reducing agent - in the form of aluminum flakes. [2] The agglomerate and the calculated reducing agent are mixed and disintegrated to a particle size below 1 mm, and then loaded into graphite crucible. A good separation of metal and slag during the casting process is achieved.

The main components of the innovative technology in this paper are:

- High temperature processed materials and alloys.

- Materials and alloys containing micro- and nano-elements.

This work was supported by the project AComIn - Advanced Computing for Innovation, Grant 316087, funded by the FP7 Capacity Program (Research Potential of Convergence Regions initials).

D. N. Karastoyanov is with the Institute of Information and Communication Technologies (IICT) - BAS, Sofia, Bulgaria (phone: +359-2-979-27-23; Sofia, Bulgaria, (e-mail: dkarast@iinf.bas.bg).

D. I. Ivanova is with the Institute of Information and Communication Technologies (IICT) - BAS, Sofia, Bulgaria (e-mail: divanovaacomin@gmail.com).

N. I. Stoimenov is with the Institute of Information and Communication Technologies (IICT) - BAS, Sofia, Bulgaria (e-mail: nikistoimenow@gmail.com).

ISBN: 978-1-61804-321-4

II. APPLICATION OF MICRO AND NANO PARTICLES

There are various technologies and various types of particles with respect to micro- and nano-particles for use in a variety of metals and alloys.

The most types of nano technology are usually low-temperature, in some cases also no current (electroless) ones. One example of the last type is the chemical nickel-plating of the working surfaces of various working instruments or internal surfaces of equipment and instruments. In this case different types of micro- and nano-elements are applied to improve the hardness and wear resistance of the tread, in cases of small thicknesses because of economic considerations. In the process are used SiC, Al_2O_3, nano diamonds et al., which are fixed in a crystal lattice of nickel.

Essentially, the technologies represent a metal matrix formed by galvanic or chemical (reduction) process, and broken (more or less uniformly) therein micro- or nano- particles - second phase. Generally, the combination of the properties of the metal matrix (coating) and the type of particles (dispersoids) enhance certain properties, such as hardness, wear resistance, low coefficient of friction, corrosion resistance and so on. As a rule, the second phase is a non-metal such as graphite [3] -[8]. molybdenum sulfide, silicon carbide, corundum, polymer powders, diamonds and more.

Different micropowders of refractory oxides, carbides, silicides, borides, nitrides, diamond and etc. can serve as a dispersoid in the micro area.

Oxides are different types of aluminum, titanium dioxide, zirconiadioxide and others.

Carbides are based on aluminum, silicon, boron, titanium and others.

Diamond powder and various polymer powders (Teflon etc.) are used.

Nanoparticles are produced naturally (volcanic eruption or wildfire), but also as a resut of human activity (waste gases from industry and automobiles). Synthetic nanoparticles are prepared and have novel properties and functions such as physical constant, electrical conductivity, chemical reactivity, and so on. They can be classified in various ways, for example:

- Nanoparticles comprising hydrogen,
- Metallic and nonmetallic oxides (SiO_2, TiO_2, Al_2O_3, Fe_2O_3),
- Semiconductors (CdTe, CdSe, Si),
- Metals (gold, silver, iron)
- Metal sulphides (MoS_2, SnS_2),
- Polymers or block polymers.

The nanoscale particles have special chemical and physical properties that distinguish them from those of larger particles and rigid bodies. Some of them are:

- with greater reactivity, due to the high specific surface
- with reduced impact of mass forces (weight) and increased influence of surface forces
- with increasing importance of the thermodynamic effects (molecular Brownian motion)
- are able to form stable suspensions or form aggregates,
- with special optical properties.

Some examples of the dispersoid of the nano-sphere are:

- Oxide - Titanium dioxide, TiO_2 [9]
- Carbides - Silicon carbide SiC [10]
- Nano diamond - Company NanoAmor, USA [11] offers nano diamond: spherical, flaked: 52-65% purity, size 4-25 nm, density 0.16 g / cm3.
- PTFE nano-powders - To offer is the promising material specification of a Chinese company [12] - CAS 9002-84-0.

III. APPLICATION OF HIGH-TEMPERATURE TREATMENT

High temperature processed materials and alloys are used in:

1. Sintering of articles from composite hard alloy: tungsten carbide-cobalt, titano- tungsten carbide-cobalt, hard alloys doped with nickel, niobium-tantalum. The so produced parts are used as chip extraction tools, hammer-press tools, and deformation matrices for wire drawing, die tools in electrical industry, as well as wear parts.

2. Sintering of electric-bodies: copper-tungsten for high voltage adapters, low voltage contact buds, nickel-silver, silver-cadmium oxide, silver -tungsten, etc. It is possible sintering the contacts out of pure tungsten.

3. High-temperature furnace - possible by impregnating receipt of diamond segments for large blades for cutting stone (granite, marble, limestone, gabbro) and diamond profile tools. By impregnating are also produced tools of tungsten - copper for electro cutting of big cutting.

4. Production of ultra-hard materials (methallylene) by synthesis in high-temperature furnace. These are chemical compounds such as borides and nitrides that possess high electrical conductivity similar to that of metals.

They are used as modifiers for ferrous and nonferrous metals in electrical engineering and electronics for various products. Methallylene can be prepared in a high temperature furnace to a particle size of from 3 to 100 nanometers (i.e. nanopowders) and fine-grain powder (up to 500 nm).

5. The refractory metals tungsten and molybdenum are used for different products used in high-temperature technique, atomic radiation protection, aerospace equipment, etc. In the Tammann furnace it is possible to carry out the activation process of sintering articles of tungsten, molybdenum and others. Refractory metals melt in this case at temperatures with 700 ° C to 1000 ° C

ISBN: 978-1-61804-321-4

lower than those at which the products should be usually prepared.

6. The high-temperature furnace ensures the most appropriate conditions for graphitization of the fibers with the output of a glass-graphite when heated to 2200 ° C on pretreated fiber. Their production of graphite fibers and fabrics can be used for reinforcing the composite of vehicles, aircraft and machinery

IV. PRODUCTION OF HIGH-TEMPERATURE SYSTEMS

The German company RUHSTRAT, [13] produces industrial Tammann furnaces heated up to 3000 ° C - Fig. 3. The type of design is NERNST-TAMMANN, standard IEC 519 I EN 60519, EN 746, ISO I EN 12100.The type of the used furnace is HTRK, radial, gas-impermeable measuring-purifying section with press quartz screen for the cleaning of powder particles. Graphite heating pipes with an inner diameter of 120 mm and length of heating time 276 mm. The power supply is 60 kW and 89 kVA.

Fig. 3. Tammann furnace

The following modern research instruments can be used for research and analysis of the materials and processes[14]:

To study and optimize the thermal processes we use an infrared thermal camera FLIR P640 (Fig. 4) with a field of 24 ° / 16 °, a minimum range of measurement temperature from -40 ° C to + 500 ° C (optional up to 2000 ° C), a temperature sensitivity 0.06 ° C at 30 ° C (optional 0.006 ° C), detector matrix 640/480 pixels, integrated color digital camera, image settings, metering mode, various lenses, 1 GB of memory and management software.

Fig. 4. Thermal camera

In our case, we can accurately measure and monitor high material temperatures in Tammann furnace, and the length and uniformity of process cooling of materials and alloys.

To examine the particle size and the size distribution in the material [15] we use a laser particle size nano analyzer ANALYSETTE 22 Nano Tec plus-fig. 5. It contains a module for measuring, dispersion modules for "wet" measurement with an range of 0.01-2000 microns and for "dry" measurement with an range of 0.1-2000 microns, 3 semiconductor lasers with 10,000 hours life, protection class EN 60825.

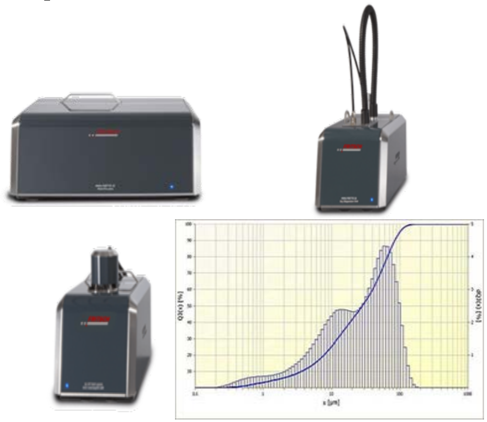

Fig. 5. Nano-granulomer

In our case, we can use it for precise measurement and dosing concentration, size and size distribution of micro and nano particles in a mixture of materials or alloys for high temperature processing.

The industrial computerized tomography STDS-600-200 / XTH 225 (fig. 6) is used to noninvasive scaning of the internal structure of the objects. It has up to 225 kV, 225 W X-ray with integrated anti-radiation protection, with spot of X-rays below 3 μm, with a 5 axes manipulator for adjustment the position of the object, weight and size of the object 15 kg / 200x300x600 mm, a special software for 3D reconstruction.

Fig. 6. 3D tomography

In our case, we examine the internal 3D structure of the data obtained through the heat treatment of materials, and alloys containing micro- and nano-elements.

ISBN: 978-1-61804-321-4

V. INNOVATIVE HIGH TEMPERATURE PRODUCTION OF MATERIALS AND ALLOYS WITH NANO ELEMENTS

For the realization of the innovative technology is used a heating furnace based on Tammann technology (Fig. 7). The micro and nano-elements, used for the modification, are based on diamond powders, SiC, Al2O3. Based on the processes to be carried out in a furnace, the maximum temperature at which it will work is 2200-2300 ° C, the minimum - 1400 ° C. The work graphite tubes are with a clearance of 125-130 mm and a thickness up to 10 mm. Their length is 1400 mm. The reflecting graphite tube is with a diameter of the lumen up to 140 mm and a length of 1500 mm. The isolation consists of a graphite powder (Fig. 8). The power supply of the high-temperature Tammann furnace is based on IGBT technology with an input voltage of 0-18 V, a single phase with adjustable output currents from 0 to 6.5 A, an adjustable high-frequency transformer, a water-cooling system and with high protections against incoming and outgoing low voltage, strong output current and voltage, overheating, as well as a good interface and a digital control.

It is equipped also with an electrical switch gear including an industrial terminal, a PID regulator, a stationary radiation (infrared) pyrometer with interface, a wiring to valves, chokes, flow meters, indicator lights, a keyboard as well as a terminal and programmable PLC controller. Programmable controller manages the test devices mounted on the electrical switchboard and the current-carrying heads, based on data from the measuring devices and provides signals to the control the power supply according to a given program.

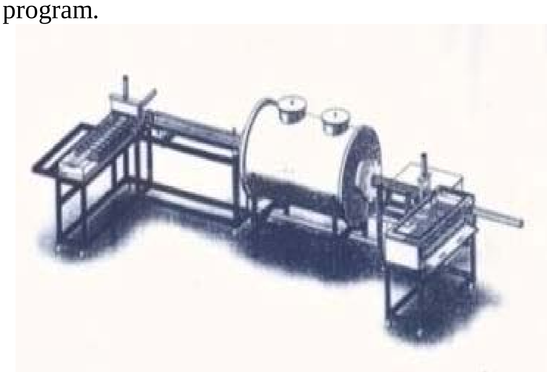

Fig. 7. Overview of the system for high temperature treatment

1.Construction of the heating part.

The main part of the system is a graphite tube with thick walls, connected to a powerful transformer. The current flowing through the tube is heating it. The tube middle part is with reduced thickness in order to realize a higher temperature in its. In the operational tube is passed a protective gas, most commonly dissociated into hydrogen and nitrogen ammonia. In the workspace, in the opposite direction of the incoming shielding gas are moving graphite boats, which fits the heated production.

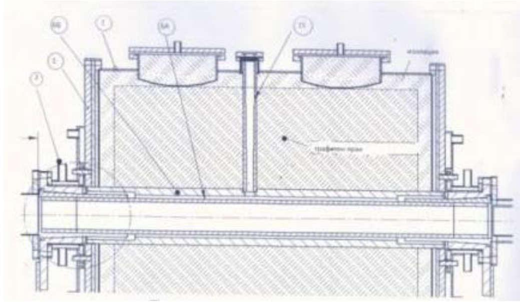

Fig. 8. Location of the graphite tube and graphite isolation

In the reception of the boats is fitted a protective valve to isolate the working gas from the air in order tto prevent a possible explosion. A security valve is mounted also in the outlet pipe, in which the boats are cooled. The whole structure of the work and screen tube is placed in a steel housing, insulation of which is done with graphite meal. For the realization of maximum performance of the furnace are mounted devices for automatic feeding of the working boats and devices for receiving the finished products. The control of the heating and the duration of the flow of a certain product are carried out with modern equipment by computer modeling of the process and a carried out on-screen movement of the working boats. The dissociated ammonia is obtained from liquefied ammonia. The decomposition of the ammonia is carried out catalytically by heating in the presence of iron filings as an catalyst. The temperature of heating is 740-760 ° C. The drying of the gas before blowing it into the furnace is carried out in a container with silica gel or zeolite. For this purpose, two containers are needed: a working one and another one for the drying of the already used zeolite.

2.The following high-temperature processes are planned to be implemented:

- Preparation of powders of carbides of tungsten, titanium, niobium tantal. The required temperature is 1800-2000 ° C;
- Preparation of powders of borides of titanium and chromium. The required temperature is 1450-1550 ° C;
- Preparation of powders for welding of the type "relit" (a mixture of tungsten carbide and tungsten policarbide). The required temperature is 1800-1900 ° C;
- Sintering of composite materials by type hard alloys. Required temperature 1420-1530 ° C;
- Sintering of articles from superhard wear-resistant carbide ceramics (boron carbide and titanium carbide). The required temperature is 1700-1900 ° C;

ISBN: 978-1-61804-321-4

- Active sintering of the products of tungsten and molybdenum. Required temperature -1600-1700 ° C.

3. Other technical parameters:

- Input /output drivers with the possibility of wired and wireless connection,
- Programmable regulator for high temperatures 2300 ^{0} C,
- Information system with 2 terminals.
- A system for the registration, archiving and protection
- Communication drivers and database
- Specialized programmable controller.

4. Selection of the type of power suply:

For the supplying the furnaces are used as well a range of various other connections of the transformer and the control by reactor with variable saturation of the core. In this case electricity is distributed equally between the two phases and the third one and it is achieved a 50% asymmetry - Fig. 9.

The asymmetric loading of the phases is avoided substantially completely by using a thyristor or an IGBT technology implementation. The second one also reduces significantly the inductive loads due to the use of a high-frequency transformer, which is operating at about 20 kHZ. Recently, this has led to a significant reduction in their price and they became cheaper than the thyristor performance. Fig. 10. shows a diagram of such a rectifier.

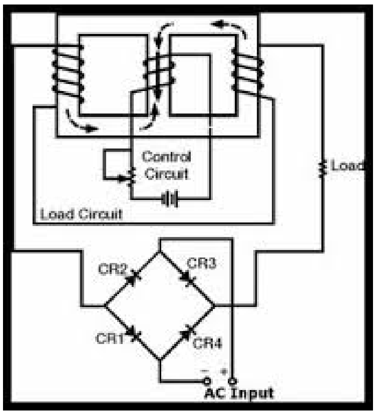

Fig. 9. Sample scheme

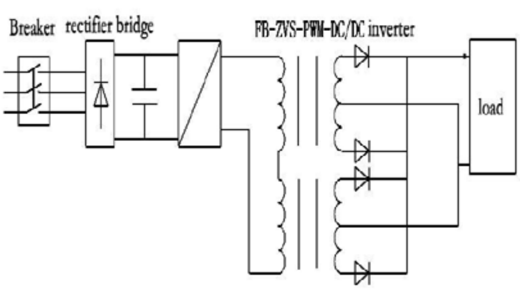

Fig. 10. Scheme of rectifier/converter

CONCLUSION

The high temperature producing of materials and alloys including nano elements increases their hardness and resistance and is usefully for special instruments and tempered materials.

ACKNOWLEDGEMENTS

This work was supported by the project AComIn - Advanced Computing for Innovation, Grant 316087, funded by the FP7 Capacity Program (Research Potential of Convergence Regions initials).

REFERENCES

[1] Petrov P., Industrial produsing of Silicon Mangan Vanadium Fero Alloy., Disertation, Sofia, Bulgaria, 2012
[2] 14. Stanislav Gyoshev., Study of parameters of controlled impact by impact deformation of elastic materials., International Conference RAM 2014, November 5-7, 2014, Sofia, Bulgaria, ISSN 1314-4634, pp 46-50
[3] US. Pat. 2942990
[4] DAS 1621106
[5] Bnt. Pat 1219813
[6] Us Pat 3617363
[7] DOS 2001869
[8] US Pat. 3562000
[9] Krug, F. UWSF 4,223 (2005)
[10] Samulat, G. Vom Wohl und Wehe ser Zwergeuwelt
[11] NanoAmor, Houston TX77084 USA
[12] Shanghai SMEC Trading Co
[13] Tamman Furnace – RUHSTRAT GMBH, Manual and Application, Berlin, 2012
[14] www.iict.bas.bg/AComIn
[15] Nikolay Stoimenov., Motion simulation of spherical grinding media in laboratory mill with EDEM software. International Conference RAM 2014, November 5-7, 2014, Sofia, Bulgaria, ISSN 1314-4634, pp 59-63

Dimitar N. Karastoyanov is a member of the Bulgarian Scientists Association. He was born in Stara Zagora, Bulgaria in 1952. He has a master degree in Electrical engineering. He graduated Technical University Sofia in 1977. The author received a doctoral degree in 1982, Robotics from the Institute of engineering cybernetics and robotics (BAS). Dr. Karastoyanov is a professor in Institute of Information and Communication Technologies (BAS). Prof. Dr. Karastoyanov is a key professor under AcomIn project at the IICT – BAS. He is conducting research on design, dynamics and intelligent control of robots and mechatronic systems. His professional interests refer to real time systems, adaptive control, industrial engineering and robotics.

Desislava Ivanova is a member of the Bulgarian Scientists Association. She was born in Rousse, Bulgaria in 1983. She has a master degree in Economics. She graduated Fern University -Germany in 2013. The author is PhD student in Automation and Cybernetics at the Institute of Information and Communication Technologies (BAS).

Nikolay Stoimenov is a member of the Bulgarian Scientists Association. He was born in Sofia, Bulgaria in 1988. He has a master degree in Automation of Discrete Production. He graduated Technical University Sofia in 2013. The author is PhD student in Automation and Cybernetics at the Institute of Information and Communication Technologies (BAS).

System approach to strategic management of intellectual capital in the knowledge based society

Marcela Sokolová, Václav Zubr

Abstract— The paper deals with the issue of a systemic approach to strategic management in the period of the transformation of information-based to knowledge-based society, where one of the strategic factors in the process is the use and development of intellectual capital. Described in the first part is the main contexts of the given issue, and then there is a design of a general model of the systemic approach to the development of a knowledge-based society.

Keywords— intellectual capital, systemic approach, strategic concept, knowledge-based society.

I. Introduction

MOST organisations face problems that were difficult to imagine just a few decades ago.

In general we can say that business success in market economy conditions is mainly dependent on the timely recognition of market opportunities and solutions of potential threats that comes with time.

The old, relatively clear and quite predictable, hierarchically organised corporate world is quickly extinguishing. With probability bordering almost certainty, in the next few years, the fact that the current global social changes will continue perhaps at an even faster pace than ever before will be important for management. Proceedings under rules that constantly undergo more or less irrational changes becomes irrational itself. For the new world, whether we call it information, post-industrial, post-capitalist or knowledge-based society, organisations need new knowledge and skills. In the knowledge-based society in which we enter, there is a shift from the traditional domination of manufacturers to a permanent preponderance of customers and consumers. In the context of the emerging knowledge-based society, the emphasis is on knowledge, i.e. the use of information, where intellectual capital is the principal means of establishing value. Other forms of capital such as money, land and technology are and will be very dependent on knowledge.

In addition to knowledge, a very frequent attribute of today's society is systemic. The systemic approach along with systemic thinking are increasingly applied in solving various issues, which caused the emergence of new disciplines such as operation research, system analysis and system engineering. System engineering is traditionally associated with the design, creation and introduction of hard systems, since it has its roots in electronics and communications, and it is widely mentioned in connection with information and communication technologies. Its place is also overwhelmingly in soft systems. In most problems that it addresses, it is interdisciplinary, it is essentially a process of integration of methods and knowledge in order to effectively achieve the objective.

In this context, system engineering has its place and application in the management of organisations, it is practically one of the possible approaches of modern management. An organisation is essentially a system whose purpose is to efficiently achieve the set objective.

If organisations want to be competitive in the long run, they must adhere to societal development - create strategic concepts that will systematically exploit opportunities and deal with potential threats; organisations must be an optimised operating system that efficiently utilises the internal resources of the organisation, where the main priorities include the use and development of knowledge (system conditions for the development of intellectual capital of an organisation), creating a pro-innovation environment, introduction of modern ICT technologies etc.

II. INFORMATION-BASED OR KNOWLEDGE-BASED SOCIETY?

The first mention of information-based society can be found in the works of Daniel Bell [3] [4], he states the idea that post-industrial society can be called information society, although the growing importance of information had already been discovered in ancient times.

The concept of an information-based society is a very busy term describing the general situation of contemporary humanity, it can essentially be considered as a generalising term without a generally accepted definition.

The concept of an information-based society is based on the dominant role of sectors of the economy, which are based primarily on work with information and use advanced technology. Such sectors not only include research, development and education, but also the area of communications transmitting information between people, everything related to information processing as well as creative activities forming information in the broad sense (e.g. artistic disciplines and media activities).

The theories of an information-based society are linked to the development of information and communication technologies that alter the composition of industry and therefore influence the economy, reduce or completely eliminate distances and relativize human cognition, knowledge and culture.

Webster [33] in his conception of information-based society goes back to the importance of the theoretical knowledge of Bella and points to the emergence of a "new" society called knowledge society, which is a term that refers to the nature of contemporary Western society dependant on knowledge. We will deal with this concept later.

Now we come to the fundamental question of whether it is relevant to indicate current society as knowledge or still as the information society?

First, it is important to define the concept of a knowledge-based society. Traditional economics (in a neoclassical microeconomic theory) focuses on the product, contrary to the environment of knowledge economy emphasises the importance of knowledge, provided the use of technological and information resources for economic development. At the forefront is getting know-how, which becomes the most important resource.

The emphasis in a knowledge economy is given to the area of human resources and training system, innovation or research and development, which is also confirmed by Kislingerová [23,9], who says that "the possibility of using a certain level of knowledge and skills in economics and dynamically develop them, is conditioned by the quality of the education system within the country."

Bureš notes [9,15] that "knowledge-based economy lies in the creation of value added by making use of knowledge, also thanks to manual production, and it stresses the importance of training and the utilisation of scientific knowledge in terms of the overall competitiveness of the country."

Knowledge is the source of economic growth not only of individuals and organisations but also individual national economies and transnational groupings. In this context the attention is devoted to the knowledge on several levels. These levels are:

1) transnational level,
2) national level,
3) organisational level,
4) level of knowledge management.

The foregoing suggests that a knowledge economy requires demands on all these levels, where these levels must be systemically interconnected to achieve optimum effect.

The good news is that information and communication technologies enable seamless and universal access to information and at the same time the overall character of society substantially change - more and more households have access to the Internet, work on automating agendas of public administration, the average citizen in developed parts of the world has one or more mobile phones, the number of people partly or fully working from home increases etc.

These aspects are certainly positive, but there are also many problems and obstacles that are in conflict with the concept of a knowledge-based society. Firstly, we can see territorial differences, where the developing parts of the world lack even the aforementioned "normal" things of developed countries. On the other hand, even in developed countries there is very low proportion of university-educated people, absence of lifelong learning, low ability of orientation in the available information sources and their subsequent interpretation and creational knowledge of them, which is one of the basic requirements of a knowledge-based society.

Various economic theories perceive the development of a knowledge-based economy differently [7][17][24][35]. A comparable situation is also in the area of efforts to develop a knowledge-based economy in practice, i.e. in the area of pursuing that effort. Currently, there are several approaches that can be used to monitor the state of the knowledge-based economy in each country.

We could say that society is located on the border between the information and knowledge-based societies.

III. SYSTEM APPROACH TO THE DEVELOPMENT OF A STRATEGIC CONCEPT UNDER THE CONDITIONS OF A KNOWLEDGE-BASED SOCIETY

To work with complex and large objects, such as an organisation, it is necessary to have a system approach.

The system approach is based on the assumption that the phenomena that occur in solving problems are understood comprehensively, with all connections in their dynamic development. The system is defined as a purposefully ordered set of elements and relationships between them, with dynamic behaviour, which together determine the characteristics of the total.

Within the decomposition of the system, we can divide system into sub-systems. These sub-systems represent a sub-set of system elements and relationships that are excluded from the system and can be understood separately as a new system or as an element of the original system. System decomposition into simpler elements increases the resolution level, allowing detailed examination of the system.

System (S) can be defined as a finite set of elements (E) and a plurality of links between them (L) with dynamic, purposeful behaviour

$$S = \{E, L\},$$

where the behaviour of the system represents a way of reaction of the system towards the stimulus from the environment, i.e. the realisation of objectives. The behaviour is defined by relationships between the inputs and outputs of the system:

$$Y(t) = T\,(X(t), Q(t))$$

wherein: $Y(t)$ is a vector of response to the stimulus vector $X(t)$,
$Q(t)$ is a vector of state variables determining the state of the system, T is the operator of transformation.

Organisation can be seen as an open system, which is schematically shown in the following figure.

The system approach to management is therefore based on the assumption that an organisation is an open system that transforms inputs - orders set by internal processes to outputs - products or services. These processes use four basic internal resources - human, physical, financial and information resources. Organisations can change, expand and modernise these resources in the interaction with the environment (i.e. the principle of equifinality does not apply). Due to the openness, the system is sensitive to changes within the system as well as the action of external risks.

System approach is very important for strategic management and strategy creation, since it structures themes of strategic management in a clear and logical manner and observes the principle of integrity, the existence of links between parts and emphasises the connection of the concept with the dynamic development of the environment. [12,85] System view of management in organisations brings wider opportunities in understanding the patterns of phenomena and processes and examining the patterns in their entirety.

IV. INTELLECTUAL CAPITAL IN A KNOWLEDGE-BASED SOCIETY

The characteristics of a knowledge-based society stated that the means bringing value added in a knowledge-based society is intellectual capital.

Armstrong [1] states that in the process of globalisation there is an increasing importance of creative human potential and the development of "human capital" (as one of the components of intellectual capital). Holátová [19] notes that there is a paradigm starting of a new "post-industrial" world, where apparently the basis of the economy will not be land, money or resources, but intellectual capital. Gibson [16] also says that the world is entering a "new economy" - the knowledge-based economy - associated with the use of human and intellectual capital, which emphasises the ability to put knowledge, understanding and skills into new connections, as driving forces of changes, innovations and competitiveness.

Nowadays, when most scientists emphasise the role of knowledge, they also increasingly refer to intangible assets (IA – something intangible valuable such as reputation) or intellectual capital (IC - the value of all knowledge and ideas of people in an organisation, company etc.), which play a crucial role in achieving a competitive advantage [10][30] and successful completion of important processes, such as trade [28]. In the past the role of intangible assets was not significantly emphasised enough (e.g. characteristics, talent). Non-recognition of IC and IA in the financial statements can have a negative impact if they are the important values of financial information, the allocation of resources in the capital market, the growth of intangible investments and the market value of the company [34]. The result is that managers more and more sensitively perceive the role played by intellectual capital in the context of making a profit [32], and the demand for capturing, assessing and reporting on the value and performance of IC is growing [27]. The components of intellectual capital can improve the competitive advantage of organisations, and thereby create value for shareholders.

Several authors have proposed models that are focused on the development and impact of intangible assets to increase the values of the company [2][8][20][21][31] or to calculate the success and growth of the company's intellectual capital [13][25]. In fact, the index can improve the ability of managers to assess the level of corporate IC and understand the priorities and relationships that exist between the selected indicators [5]. On the other hand, these indices have several drawbacks that prevent them from being universally applied. In addition, none of these indexes were able to assess the inter-dependence that exists between IC elements and assess their contribution to the total value of IC.

A. INTELLECTUAL CAPITAL COMPONENTS

Intellectual capital is often regarded as the sum of the following three categories [18][31][29]:

a) Human capital (HC) refers to people in the organisation and describes their tacit knowledge; e.g. competence, creativity, education, commitment and loyalty of employees, formal relationships, work-related knowledge, etc.
b) Structural capital (SC) indicates the specific knowledge, which are part of the organisation; e.g. corporate culture, information systems, international co-operation, the use of technology, organisational structure, research and development, technology, product quality, strategies, etc.
c) Customer (relational) capital (RC) represents the relationships between an organisation and its external partners; e.g. advertising, partnerships, brand image, competition, relationships with customers, distribution channels, network systems, supplier relations.

From the perspective arising from these sources, these components of IC have advantage potential in the market and may therefore enhance the created value, assuming that the organisation is able to use them appropriately [6]. IC components can be really crucial when trying to meet and exceed the expectations of direct and indirect participants, such as employees, clients, pressure groups and communities [6]. A good relationships with owners help the company develop valuable intangible assets (resources and skills) and therefore they may be a source of advantage in the market [11]. At the same time, obtaining legitimacy (defined as the perception of the entity acts as a desirable and correct) can lead the organisation to easier access to resources, reputation and advantages over the competition [14].

V. SUMMARY OF THE RESULTS

On the basis of the theoretical data and analyses carried out, whether original or processed from the ones published, we can state that society is located on the border between the

ISBN: 978-1-61804-321-4

information and knowledge societies. The mean factor in a knowledge-based society is the intellectual capital that still needs to be developed, for which it is necessary to have a functioning system of lifelong learning. Based on the use of intellectual capital potential it is possible to meet another prerequisite for a knowledge-based society, which is the potential for innovation. The condition persistent from an information-based society is of course the use and development of information and communication technologies.

Some conditions of a knowledge-based society are met, others aren't or only partially. Considerable differences are for example in terms of territorial; developed countries are doing much better. The Czech Republic has certainly poised in the right direction, in certain respects it stands well, elsewhere it is worse and it lags significantly behind the developed economies. Differences also exist in the various organisations that are part of the economy, in the use of knowledge and intellectual capital.

An important element of any system is human capital - a human who can fundamentally affect the functioning of the system. An important role is played by their knowledge, abilities and skills, as well as their attitude to a given problem in a particular situation. To simplify, we could say that motivation plays an important role, which affects the willingness to use existing knowledge, skills and abilities, and to distribute and develop them. Can there be a connection? If people were more satisfied with work, would they be willing to learn more and would they be even more innovative? There is probably no clear answer, it is basically a kind of closed circle, which can operate effectively only providing the fulfilment of certain conditions are met.

As part of the investigation carried out in the Czech Republic, a relatively small degree of satisfaction with the work was discovered, which is not good from the perspective of motivation (according to for example Herzberg), [15].

VI. DRAFT MODEL OF A SYSTEM APPROACH TO THE DEVELOPMENT OF A KNOWLEDGE-BASED SOCIETY

The system approach is based on the assumption that the phenomena that occurs when solving problems, must be comprehensively understood, with all connections in their dynamic development. Within the decomposition of the system, the system can be divided into sub-systems. These sub-systems therefore represent a sub-set of system elements and relationships that are excluded from the system and can be understood separately as a new system or as an element of the original system. System decomposition into simpler elements increase the resolution level, allowing a detailed examination of the system.

If we want to solve the issue of the transition to a knowledge-based society, it is then necessary to carry out the implementation of the system approach. The society itself is a very complex system, which consists of many components and connections. The individual elements are themselves systems that within the system decomposition are the sub-systems of the master system. The hierarchical decomposition of the "system" of society is suggested in the following diagram.

The model proposes four basic levels of decomposition of society, where below the last level is a human. A particular person may not be part of any organisational level or vice versa they may be part of several at the same time.

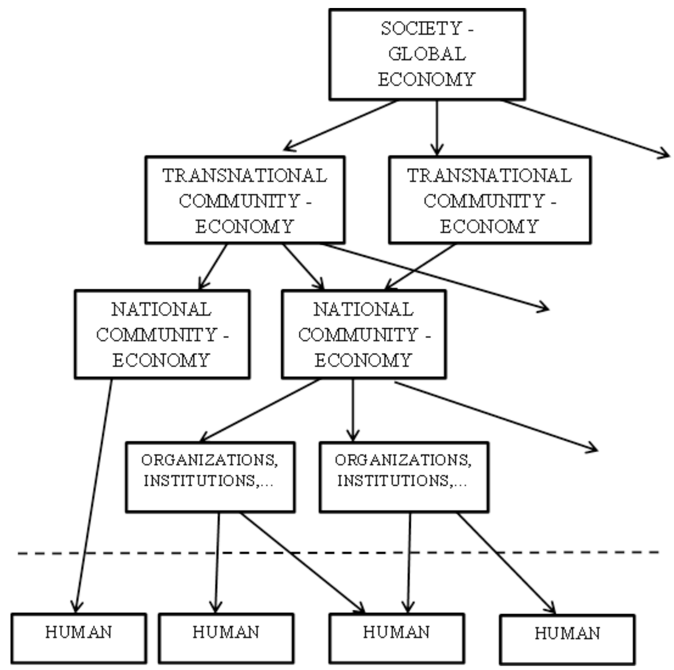

Fig. 1 The hierarchical decomposition of the system - society

The next diagram shows the position of a human - worker across the society's system, where it is seen that they are a certain elementary element of several hierarchical systems. If we embraced the hypothesis that even a human is "a system", which in its essence is, then we can talk about the five-level model.

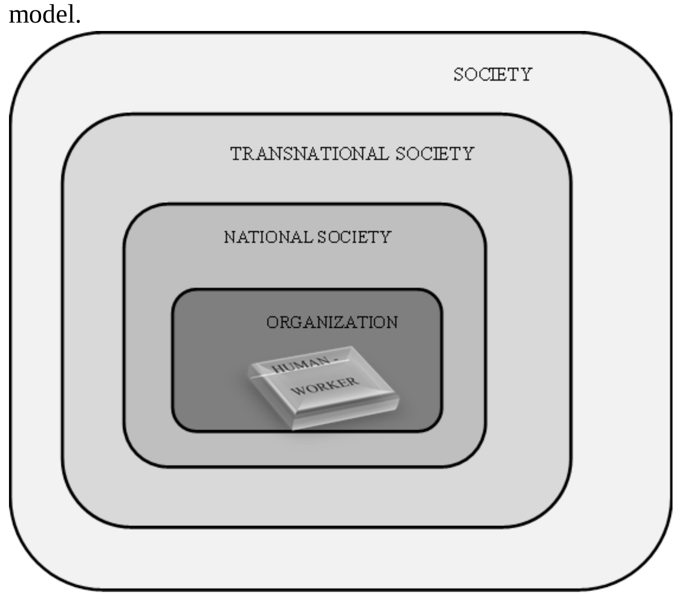

Fig. 2 Human - worker as an elementary element of hierarchical decomposition of the system

This is a starting model from which it is necessary to start when processing the transformation of society into a knowledge-based society. If the entire system is supposed to meet the parameters of the knowledge-based economy, then it must be supported in this direction and all sub-systems across all levels must be optimally adjusted. This is a very complex problem, where it is not easy to set the parameters of the system and its sub-systems, because the conditions inside and outside of individual systems change dynamically. It is possible to set some strategic directions, to which certain recommendations and supports can be linked.

VII. STRATEGIC CONCEPTS OF THE TRANSFORMATION OF INFORMATION-BASED SOCIETY TO KNOWLEDGE-BASED – MODEL EXAMPLE: THE CZECH REPUBLIC

The following section identifies the main strategic directions of the development of society, which will respect the system approach and will be divided according to the different levels, which were mentioned in the previous chapter.

A. *KNOWLEDGE-BASED SOCIETY*

Within this level, the directions are given to us by the characteristic of the knowledge-based society/economy (based on [22]):

- teaching and learning is becoming the focus of people as well as organisations
- economy consists of networks of innovative organisations using new technologies
- the intensity of the use of information and communication technologies (ICT) increases
- scientific co-operation is significant,
- is characterised by increased codification of knowledge,
- growing proportion of Gross Domestic Product (GDP) devoted to knowledge assets,
- boundaries are not rigidly defined (knowledge exceed corporate, industry and often also the state borders)
- technologies allow to create virtual organisations and provide new opportunities for inter-connection, co-operation and forming of partnership.
- products to customers are in a personalised form (according to customer requirements), transactions are executed in real time, there is more dynamic pricing.

B. TRANSNATIONAL AND NATIONAL LEVEL

Transnational and national level can be solved in this context simultaneously. Transnational level is understood as a purposeful connection of national economies (e.g. EU, NATO, etc.). Individual economies should establish their own priority directions, which will be based on the analysis of the current state of the economy. These must be directed with regional support. It is necessary to create an effective support system, which will be addressed systematically across all levels of the economy - from transnational to organisational (or human's).

Czech economy as a whole needs to build and develop new competitiveness factors so as to succeed in the global marketplace and reach the societal trends.

- ***Lifelong learning***

The key pillar of success for the Czech Republic is in particular the ability of our citizens to compete in the rapidly changing global labour market. At present, our workforce is recognised primarily for its qualification, skills, precision and flexibility for responding to unexpected situations.

The lifelong learning system must follow the functioning education system (from pre-school to university education).

Lifelong learning is beneficial not only for the people themselves but also for employers and the state. (Ministry of Education)

- ***State innovation policy***

Innovation is the driving force of economies. Even the state may become a significant contributor to the creation of innovative climate by their pro-innovation policy.

Certainly it is necessary to continue in the support of innovative activities and secure the connection of academic spheres more intensively (research, education and innovation activities) with practice, i.e. business sphere, and therefore create a network of innovative organisations.

- Encouraging the development and use of information and communication technologies (ICT) by educated knowledgeable workers.

C. ORGANISATIONAL LEVEL

A knowledge-based economy cannot exist without knowledge organisations.

The interest of each organisation must also focus on their abilities, culture, management style and conduct internal changes that are in line with the external environment, if it wants to be competitive in the long run.

The important directions for further development include:

- ***Employees' education and development***

It can be stated that human capital is a strategic resource for any organisation with which the prosperity and competitiveness of the company rises and falls. One possible modern approach is the implementation of the concept of a learning organisation.

- ***Innovation***

Innovation activities and the innovative behaviour of firms can be effectively influenced mainly by changing the following factors:

ISBN: 978-1-61804-321-4

- the existence and application of innovative business strategies,
- co-operation with suppliers and customers,
- monitoring and evaluation of customers' satisfaction,
- monitoring competitor's activities (domestic and foreign)
- greater involvement of employees in the innovation process,
- collecting and evaluating ideas from employees.

Therefore it is often necessary, in accordance with the change of the innovation strategy, to also change the corporate culture. Although it is a time consuming process, it has long-term positive effects.

We cannot therefore ignore also various local and cultural practices.

One of the new approaches is the use of open innovations.

- ***Knowledge management***

Knowledge is the phenomenon of each organisation and it is necessary to work with them efficiently. Existing knowledge should be effectively used, recorded, stored and distributed. It is also important to focus on the creation of new knowledge.

- ***Modern information and communication technologies***

Modern ICT technologies are irreplaceable in many areas in today's society. At random, we can mention - they are able to handle routine activities - replace human labour, store data, information and knowledge and are able to work with them efficiently, enable streamline work and communication (virtual teams, remote accesses, etc.), support the decision-making processes, etc.

ICT technologies are involved in all areas of human activity and play an irreplaceable role in all areas, which have been mentioned above (they complement, support and streamline them).

- ***BUSINESS STRATEGY***

The last point of the presented "recommendations" is the existence of corporate strategy. All of the above points (and more) must be among the key strategic areas of the organisation and must be incorporated into the corporate (business) strategy (see diagram below).

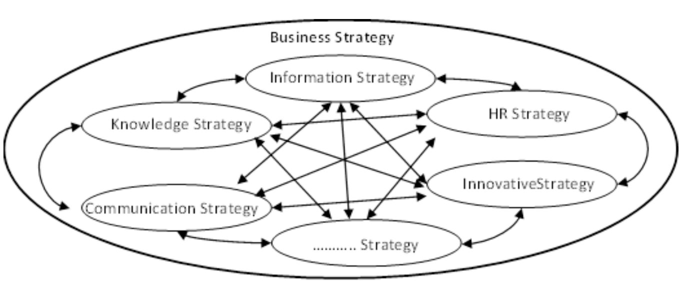

Fig. 3 Consistency of sub-strategies of an organisation to a business (entrepreneur's) strategy

VIII. CONCLUSION AND DISCUSSION

Probably one of the strategic management concepts mentioned in the introduction text is not universal instruction on how to strategically manage an organisation, nor any of the strategies is a universal strategy, which can easily be copied. Each organisation must find their unique strategy and so must look for its unique concept of how to perceive the strategy. Strategic concept is actually a mental understanding of the strategy and its implementation. On the other hand, it is clear that in a knowledge-based society, one of the main strategic directions must include - intellectual capital development, support and motivation of employees to education, pro-innovation climate, support for the introduction of modern ICT technologies, etc. The ideal situation is when these targets are systematically promoted at national level. Organisations must then effectively use this support to their advantage.

A unique place in the whole system belongs to - human, employee, worker, human capital - or whatever we call them. Today, in the context of the knowledge-based society, the most common term is knowledge worker.

ACKNOWLEDGMENT

The paper was written with the support of the specific project grant "Determinants affecting job satisfaction" granted by the University of Hradec Králové, Czech Republic.

REFERENCES

[1] Armstrong, M. (2007). „Řízení lidských zdrojů“, Praha : Grada Publishing, ISBN 80-247-1407-8.

[2] Barsky, N.P., Marchant, G. (2000). „The most valuable resource – measuring and managing intellectual capital“, Strategic Finance, Vol. 81 No. 8, pp. 58-62.

[3] Bell D. (1974). „The Coming of Post-Industrial Society: A Venture in Social Forecasting“, London: Heinemann.

[4] Bell D. (1980). „The Social Framework of the Information Society in T. Forester (ed.): The Microelectronics Revolution“. Oxford: Blackwell.

[5] Bontis, N. (2001). „Assessing knowledge assets: a review of the models used to measure intellectual capital“, International Journal of Technology Management, Vol. 3 No. 19, pp. 41-60.

[6] Branco, M.C., Rodrigues, L.L. (2006). „Corporate social responsibility and resources-based perspectives“, Journal of Business Ethecs, Vol. 69 No. 2, pp. 111-132.

[7] Brinkley, I. (2006). „Defining the knowledge economy“, Knowledge economy programme report, The Work Foundation, London, [online], [cit. 2014-06-04]. Dostupný z WWW: <http://www.theworkfoundation.com/assets/docs/publications/65_defining%20knowledge%20economy.pdf>.

[8] Brooking, A. (1996). „Intellectual Capital: Core Assets for the Third Millennium Enterprise“, Thomson Business Press, London.

[9] Bureš, V. (2007). „Znalostní management a proces jeho zavádění“, 1. vyd. Praha: Grada Publishing, ISBN 978-80-247-1978-8.

[10] Coleman, S., Robb, A. (2010) „Capital structure theory and new technology firms: is there a match?“, Management Research Review, Vol. 35 No. 2, pp. 106-120.

[11] Cricelli, L., Greco, M. (2013) „Relational capital and performances in interuniversity research consortia“, International Journal of Engineering Business Management, Vol. 5 No. 4, pp. 1-7.

[12] Doucek, P. (2010). “Informační management”. Professional Publishing, ISBN 978-80-7431-010-2.

[13] Edvinsson, L., Malone, M.S. (1997) „Intellectual Capital: The Proven Way to Establish Your Company's Real Value by Measuring Its Hidden Values“, Piatkus, London.

[14] Fernandez-Alles, M., Valle-Cabrera, R. (2006). „Reconciling institutional theory with organizational theories: how neoinstitutionalism resolves five paradoxes“, Journal of Organizational Change Management, Vol. 19 No. 4, pp. 503-517.
[15] Franěk, M., Mohelská, H., Zubr, V., Bachmann, P., Sokolová, M. (2014). „Organizational and sociodemographic determinants of job satisfaction in the Czech Republic“, SAGE Open 2014 4: DOI: 10.1177/2158244014552426.
[16] Gibson, R. (2000). „Nový obraz budoucnosti: přední osobnosti světového managementu a sociálního myšlení o budoucnosti podnikání, konkurence, řízení a trhu“, Praha: Management Press.
[17] Gordon, R. J. (1999). „Has the “New Economy” Rendered the Productivity Slowdown Obsolete?“, Meeting of economic advisers at the Federal Reserve Bank of Chicago, [online], [cit. 2014-07-05]. Dostupný z WWW: <http://research.stlouisfed.org/conferences/workshop/gordon.pdf>.
[18] Hall, R. (1992). „The strategic analysis of intangible resources“, Strategic Management Journal, Vol. 13 No. 2, pp. 135-144.
[19] Holátová, D., Krninská, R. (2012). „Lidské zdroje v rozvoji venkova“, Praha: Alfa nakladatelství.
[20] Jacobsen, K., Hofman-Bang, P., Nordby, R. Jr. (2005). „IC rating“, Journal of Intellectual Capital, Vol. 6 No. 4, pp. 570-587.
[21] Kaplan, R.S., Norton, D.P. (1996). „Using the balanced scorecard as a strategic management systém“, Harward Business Review, Vol. 74 No. 1, pp. 75-85.
[22] Kelemen, J., Berka, P., Bureš, V., Horáková, J., Hvorecký, J., Mikulecký, P. (2007). „Pozvanie do znalostnej spoločnosti“, Iura Edition – Wolters Kluwer, Bratislava, 265 str., ISBN 978-80-8078-149-1.
[23] Kislingerová, E. (2008). „Inovace nástrojů ekonomiky a managementu organizací“, Praha: C. H. Beck, ISBN 978–80–7179–882–8.
[24] Klaus, V. (2005). „Stále dokonalejší technologie a nebezpečné sny a utopie naší doby“, Projev na Konferenci společnosti Microsoft, Praha, [online], [cit. 2014-05-04]. Dostupný z WWW: <http://www.klaus.cz>.
[25] Lev, B., Feng, G. (2001). „Intangible assets: measurement, drivers, usefulness“, Advances in the Measurement of Intangible (Intellectual) Capital Conference, New York University, New York, NY.
[26] Luthy, D.H. (1998). „Intellectual capital and its measurement“, Proceedings of the Asian Pacific Interdisciplinary Research in Accounting Cinference (APIRA), Utah State University, Logan, [online], [cit. 2013-05-04]. Dostupný z WWW: <http://scholar.google.cz/scholar_url?hl=cs&q=http://www.apira2013.org/past/apira1998/archives/pdfs/25.pdf&sa=X&scisig=AAGBfm1Umu08wB5L5P7IOiFV0EYJg5SW5g&oi=scholarr&ei=vDyHVKziKIbsO4aSgIgD&sqi=2&ved=0CB4QgAMoADAA>.
[27] Marr, B. (2007). „What is intellectual capital?“, Strategies for Information Technology and Intellectual Capital, Challenges and Opportunities, Idea Group, London, pp. 1-9.
[28] Riviezzo, A. (2013). „Acquisitions in knowledge-intensive industries: exploring the distinctive characteristics of the effective acquirer“, Management Research Review, Vo. 36 No. 2, pp. 183-212.
[29] Roos, J., Roos, G., Dragonetti, N.C., Edvinsson, L. (1997). „Intellectual Capital, Navigating The New Business Landscape“, Macmillan Press, London.
[30] Selcuk, P. (2010). „Use of analytic network process in selecting knowledge management strategies“, Management Research Review, Vol. 33 No. 5, pp. 452-471.
[31] Sveiby, K.E. (1997). „The intangible asset monitor“, Journal of Human Resource Costing and Accounting, Vol. 2 No. 1, pp. 73-97.
[32] Tayles, M., Pike, R.H., Sofian, S. (2007). „Intellectual capital, management accounting practices and corporate performance: perceptions of managers“, Accounting, Auditing and Accountability Journal, Vol. 20 No. 4, pp. 522-548.
[33] Webster, F. (2006). „Theories of the Information Society“. 3. přepracované vyd. London: Routledge.
[34] Zéghal, D., Maaloul, A. (2011). „The accounting treatment of intangibles: a critical review of the literature“, Accounting Forum, Vol. 35 No. 4, pp. 262-274.
[35] Zlatuška, J. (2000). „Informační technologie mění ekonomiku“, Virtuální Inovační Park, ISSN 1212-1347, [online], [cit. 2013-05-04]. Dostupný z WWW: <http://www.park.cz>.

Software Tool Application for Dynamic Response Analysis of a Microgrid

Alessia CAGNANO, Enrico DE TUGLIE, Maria DICORATO, Giuseppe FORTE, Michele TROVATO

***Abstract*—** Microgrid (MG) robustness and flexibility are some of the issues to improve for complying with grid connection rules. To this purpose, an ex-ante short-term programming tool and optimizing procedure, that updates set-points in a time step of 15 minutes, should be developed to define the production of programmable power generation plants and forecast the production of non-programmable power plants. During the updating time steps, it should be considered that some dynamic events can suddenly modify operation with respect to established set-points. Dynamic tests need to be conducted for evaluating MG behavior, over a 15-minutes time-horizon, in case of wind, solar radiation or load variations. In this paper, the MG dynamic response to unpredictable variations of source availability and load is evaluated in order to ensure the compliance with technical and economical requirements.

***Keywords*—** Dynamic analysis software tool, Microgrid, Renewable Energy Sources, Energy Storage System, dynamic modeling.

I. Introduction

THE concept of Microgrid (MG) refers to small-scale low-voltage supply networks designed to supply electrical and heat loads for a limited region [10]. The MG can operate both in connected or islanded mode, and includes distributed generators, usually Renewable Energy Sources (RES), small and medium size power plants or Combined Heat and Power (CHP) systems, Energy Storage System (ESS), and load.

This innovative network configuration brings technical, environmental, and economical benefits, contributing to reduce global pollution, to increase involvement of end-users in system operation and to optimize power withdrawal from each load according to market price signals and/or to production costs of power sources available at a given time in the MG. In addition, the coordinated operation of energy storage devices and generation technologies has to be deeply evaluated both in the grid-connected and in islanding mode. However, to achieve a stable and secure operation, a number of technical and regulatory issues have to be solved.

MG components should be equipped with control devices to achieve flexibility, to improve robustness and to interact with the power distribution utility as a single controlled unit complying with connection rules while meeting local energy needs [10]. The control of programmable power generation plants and the production forecast of non-programmable power plants require an ex-ante short-term programming, optimizing generation and storage technologies of the MG, performed the day before operation (Day Ahead Operation Plan). The optimization routine provides set-point update in specific time intervals (e.g. 15 minutes). During updating time steps, some dynamic events can suddenly modify operation with respect to set points established by the optimization procedure. Therefore, suitable operating conditions should be selected.

Various studies have been conducted to investigate stability or connection issues, considering non-programmable and programmable production systems separately [1-4]. As well, ESS management techniques have been developed testing results in isolated systems as [5-8].

In this paper, MG response to short-term dynamic phenomena, such as wind, solar radiation or load variations, is addressed. In particular, voltage magnitudes, state of charge, active and reactive power levels are detected in order to comply with utility connection requirements. Dynamic simulations are carried out on a test-bed MG over a time horizon of 15 minutes, according to time step of ex-ante optimization routine. Simulation results allow to elaborate management strategies to be applied during real-time operation.

II. The experimental microgrid

An outline of the experimental MG analyzed in simulations is reported in Fig. 1. The MG includes distributed sources, like wind turbine (WIND) with Doubly Fed Induction Generator (DFIG), Proton Exchange Membrane Fuel Cell generator (FC), Photovoltaic Generator (PV), Gas Microturbine (GAST). Moreover, two ESS technologies are considered: Lead-Acid batteries (DC-BATT) and Flywheel with direct current generator (DC-FW). Each component is connected to an AC common bus where programmable load banks are connected. The MG is linked to the main grid, modeled as an infinite power bus, by a synchronous machine with an infinite inertia. Rated power values of each element are listed in Table I. Table II summarizes parameters of lines connecting MG buses.

Authors are with Dipartimento di Ingegneria Elettrica e dell'Informazione, Politecnico di Bari, 70125 Bari, Italia (corresponding author Maria Dicorato +39 080 5963516; fax + 39 0805963410; e-mail: maria.dicorato@poliba.it).

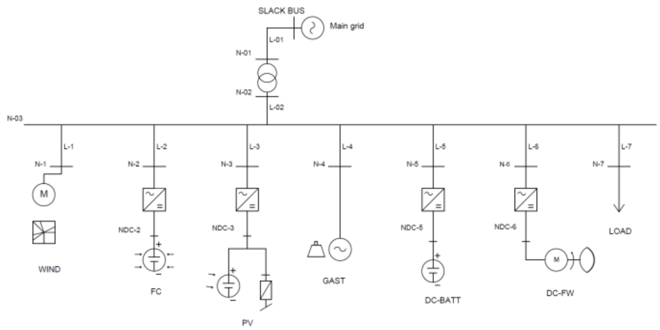

Fig. 1. The experimental MG layout

The MG is a low-voltage three-phase distribution network (with nominal voltage of 400 V), connected to the external grid through a smart static switch and a by-pass inverter. It is a combination of distributed generation units, loads and storage devices. In particular, it consists of two electrical loads that will simulate commercial, industrial and residential users, with a total maximum capacity of 250 kW, mini-wind generators, exploiting horizontal and vertical axis, with total installed capacity of 62 kW, a photovoltaic system with three different technologies and a total installed capacity of 50 kW roughly, two storage devices a set of Sodium-Nickel batteries (SoNick) (100 kW peak / 1 h) and a flywheel (5 kW / 20 min), a Combined Heat and Power (CHP) generator fed by natural gas is present, able to supply electric and heat load, with a maximum capacity of 100 kWe, a 30kW micro-turbine and a two electrical vehicles able to perform vehicle-to-grid (V2G).

TABLE I. RATED POWER OF MG ELEMENTS

Element	Rated Power or Capacity
WIND	110 kW
FC	100 kW
PV	105 kW
GAST	150 kW
DC-BATT	6.5 Ah
DC-FW	20 kW
LOAD	240 kW

TABLE II. PARAMETERS OF MG LINES

Line	S [mm^2]	Parameters [Ω/km]	Length [km]
L-1	35	R = 0.554 X = 0.074	0.2
L-2	70	R = 0.272 X = 0.072	0.1
L-3	50	R= 0.386 X = 0.073	0.4
L-4	150	R = 0.129 X = 0.070	0.1
L-5	25	R = 0.780 X = 0.076	0.1
L-6	6	R = 3.300 X = 0.085	0.02
L-7	2x120	R = 0.077 X = 0.035	0.02
L-02	2x185	R = 0.038 X = 0.035	0.02
L-01	70	R = 0.308 X = 0.186	1

Dynamic models of each component are accounted. Wind turbine with DFIG, modeled as in [1][11], has a control scheme including: the Maximum Point Tracking (MPT) section, in order to provide the maximum active power reference at every wind speed value; the pitch control block, that provides the best blade angulation according to the wind speed and the active power reference; the active and reactive (PQ) power control block, realized by PI control of d-q current components, that enables to follow the given input of active and reactive power references, as Fig. 2 shows [2][12][14][15].

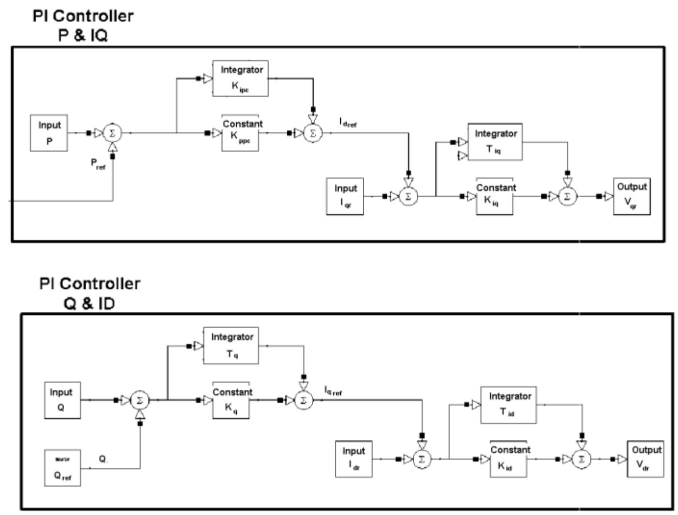

Fig. 2. Wind turbine PQ control scheme

The basic equations describing the PV system relate open circuit voltage $V_{oc(T)}$ and short circuit current $I_{sc(T)}$ to temperature variations [3][9][13], as reported in (1) (2):

$$V_{oc(T)} = V_{oc(T_r)} \cdot (1 - \beta_{V_{oc}} \cdot (T - T_r)) \tag{1}$$

$$I_{sc(T)} = I_{sc(T_r)} \cdot (1 + \alpha_{I_{SC}} \cdot (T - T_r)) \tag{2}$$

Values at reference temperature depend on actual solar radiation G , as follows, being G_r = 1000 W/m^2.

$$I_{sc(T_r)} = I_{sc(T_r)} \cdot \frac{G}{G_r} \tag{3}$$

Battery is modeled as a DC-voltage controlled source. DC-voltage value is calculated differently during charging and discharging mode, as reported in (4) and (5) respectively. It depends on battery constant voltage E_0, the internal resistance R, the polarization constant K, the actual state of charge $\tilde{q}$, and an exponential function that describes battery time behavior along the exponential zone [5][6][9].

$$V_{batt} = E_0 - Ri - K\left(\frac{\tilde{q}}{\tilde{q} - it}\right)\left(it - i^*\right) + \exp_c(t) \tag{4}$$

$$V_{batt} = E_0 - Ri - K\left(\frac{\tilde{q}}{it - 0.1\tilde{q}}\right)\left(it - i^*\right) - \exp_d(t) \tag{5}$$

Fuel Cell has a voltage controlled value obtained by summing together Nernst voltage E_n, the voltage drop associated to the electrodes (activation over potential V_{act}), the voltage drop V_{conc} resulting from the concentration or mass transportation of oxygen and hydrogen, and ohmic voltage drop V_{ohm}, a measure of the losses associated with the conduction of protons through the solid electrolyte and internal electronic resistances [7][9], as follows:

$$V_{fc} = E_n - V_{act} - V_{conc} - V_{ohm} \quad (5)$$

Flywheel model includes equations of a DC-machine [11], considering the total inertia of the machine together with the flywheel [8].

DC-voltage of Battery, PV, Fuel cell, and Flywheel is converted in AC-voltage by separate PWM converters. Fast dynamics of control systems are neglected, therefore converters are modelled through algebraic equations (7-10), linking DC-voltage to AC-voltage components in the d-q frame, and accounting for active power balance with source production.

$$V_{d(AC)} = M_d \cdot V_{DC} \quad (7)$$

$$V_{q(AC)} = M_q \cdot V_{DC} \quad (8)$$

$$P = V_{d(AC)} \cdot I_{d(AC)} + V_{q(AC)} \cdot I_{q(AC)} \quad (9)$$

$$Q = V_{q(AC)} \cdot I_{d(AC)} - V_{d(AC)} \cdot I_{q(AC)} \quad (10)$$

Gas turbine is modeled as classical synchronous machine [11], whose control scheme reported in Fig. 3 [4] for purpose of brevity.

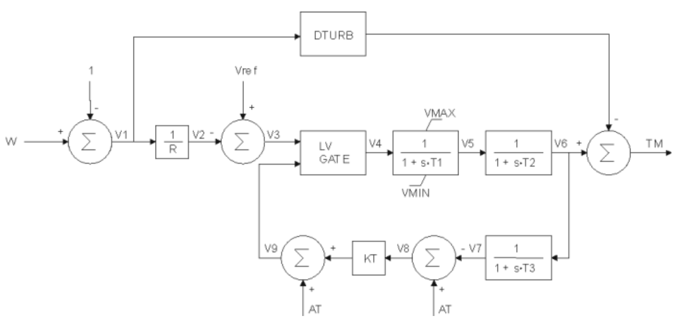

Fig. 3 Gas turbine control scheme

III. MICROGRID DYNAMIC ANALYSIS

The effects on MG dynamic due to unpredictable sources and load variations are analyzed. Simulations are carried out over 15 minutes, exploiting transient stability analysis techniques, by means of NEPLAN® software. The following phenomena are simulated separately in three different cases:

- Case 1: Slow increase of wind speed;
- Case 2: Load variations;
- Case 3: Solar radiation step.

In all the tests injected power is represented by positive value, whereas drained power is negative. Voltage measurements refer to AC-buses (N-1 – N-7).

The presence of a slow increase of wind speed, considered in Case 1, is drawn in Fig. 4.a, reaching turbine rated speed at roughly 650 s. When wind speed exceeds rated speed, active power of WIND keeps constant at rated value, as Fig. 4.b reveals.

It can be observed that bus voltage magnitude at each node of the MG is greatly affected by wind variations, as reported in Fig. 5. Voltage grows up along with wind power, though complying with connection requirements (voltage magnitude must be included in a range of ±10% of the rated value).

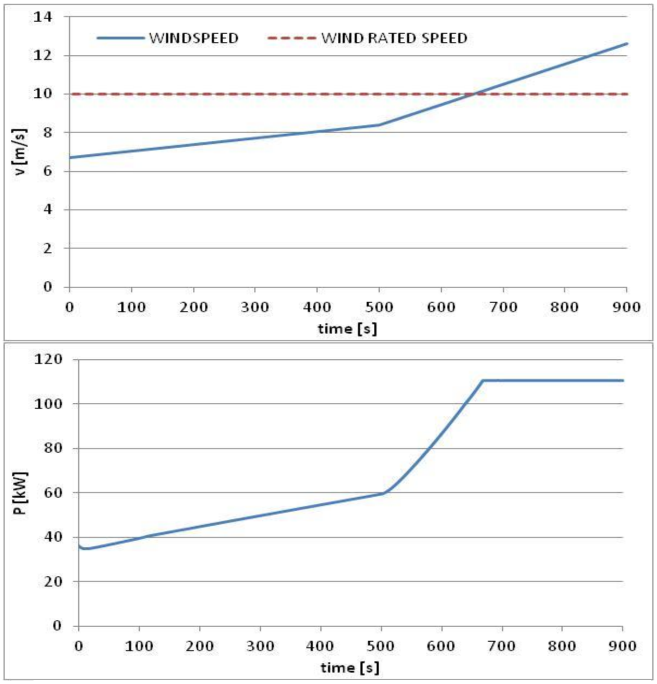

Fig. 4 Case 1. (a) Wind Speed (b) active power of WIND

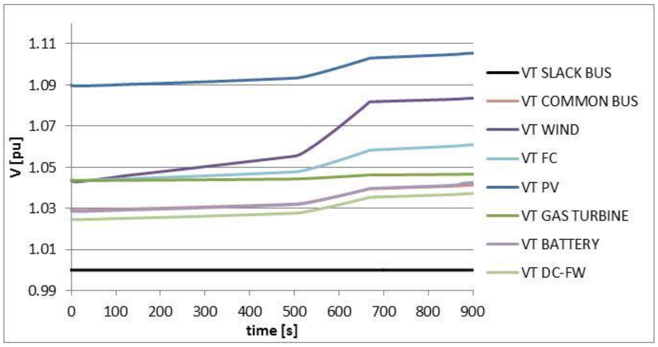

Fig. 5 Case 1. Bus Voltage

Effects on the ESS can be addressed as well, in order to verify the State of Charge of battery. In Fig. 6.a, it can be observed that, while the power injected in the MG slowly increases, because of the growing wind power, DC-BATT stores energy, until the maximum level of state of charge (SOC), i.e. 110%. Once this point is reached, at 870 s, the battery stops accumulating energy and charge power becomes equal to zero, as shown in Fig. 6.b.

An analogous behavior of wind turbine control system is observed by simulating a slow wind decrease below the cut in

ISBN: 978-1-61804-321-4

speed. Wind power reduction implies bus voltage decrease at each node, causing has a sudden reduction of battery SOC.

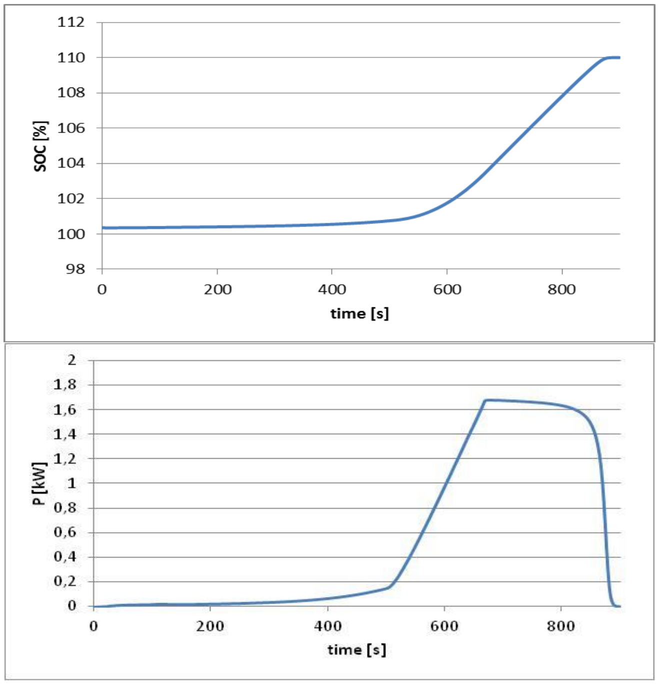

Fig. 6. Case 1. Battery: (a) SOC (b) charge power

In Case 2 deals with multiple step load variations of different magnitude and duration are simulated, as reported in Fig. 7. Variations are included in a range between +180% and -90% of initial value (80 kW). Despite the stressful load condition, voltage magnitude is included in ±10% range of nominal value, at all the buses, except for PV system (VT PV), as Fig. 8 reveals.

As MG is operating in connected mode, load withdrawal is mainly balanced by grid drained active power (Fig. 9), and battery. In particular, battery management is closely related to load variations. In Fig. 10, it can be observed that battery charge power becomes equal to zero when load active power is higher than the initial value (see Fig. 7), whereas, when the load is lower, battery drains power from the MG in order to store more energy. Battery power experiences spikes in correspondence of load step variations, due to fast response of algebraic converter models, and the recovery of final values is related to its dynamic model, see eq. (4-5).

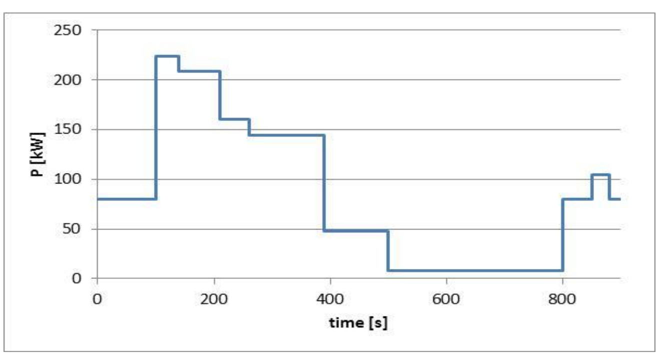

Fig. 7. Case 2. Load active power

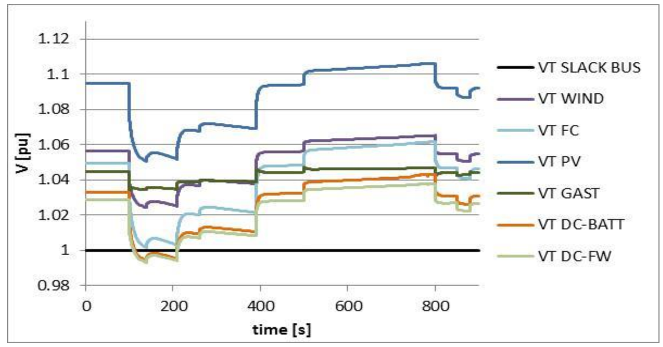

Fig. 8. Case 2. Bus Voltage

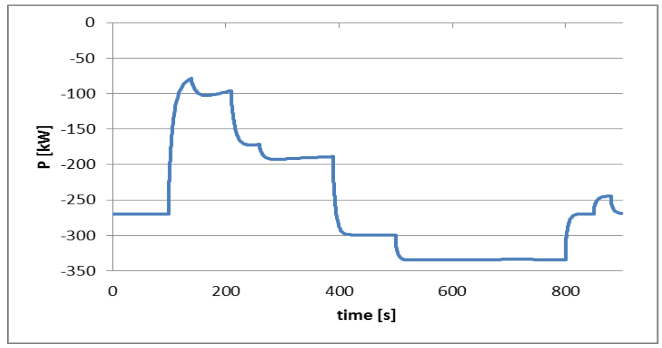

Fig. 9. Case 2. Grid active power

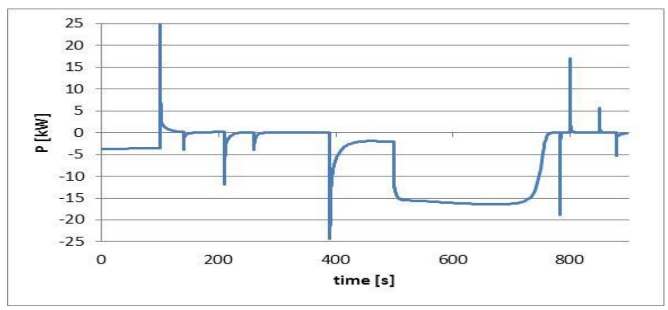

Fig. 10 Case 2. Battery charge power

In the case of solar variation step (Case 3), an analogous attitude of the battery could be verified. In fact, it provides to withdraw exceeding power injected by the PV system.

In particular, simulating an increase of solar radiation by 30 W/m^2, PV injected power gains 3 kW (Fig. 11.a). This extra power is partly absorbed by the main grid (Fig. 11.b) and the remaining part by the battery (Fig. 11.c).

It can be observed that battery is able to promptly follow MG variations, therefore it could be straightforwardly involved into management strategies of the MG.

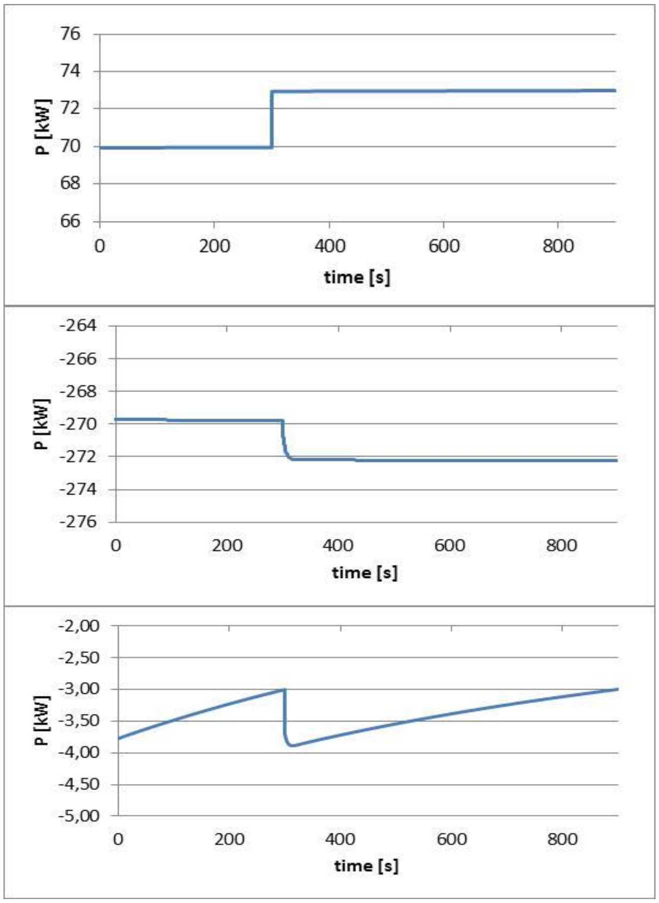

Fig. 11. Case 3: (a) PV generation (b) Grid active power (c) Battery charge power

IV. Conclusion

In this work, analysis of dynamic phenomena, due to non-programmable sources and load, have been conducted. Simulations carried out on the experimental MG have revealed that:

- monitoring bus voltage is fundamental to verify sources operational limits as well as to comply with limits imposed by connection rules;
- ESS, like the battery, is useful to efficiently balance active power injection or withdrawal.

These considerations have put in evidence that, in order to choose the suitable operating conditions, during MG real-time operation, an appropriate voltage control system and basic strategies of MG operation management need to be developed.

Furthermore, future purposes are addressed to realize MG control and management in isolated operation condition, balancing load withdrawal only with energy stored by ESS.

References

[1] J. C. Muñoz, C. A. Cañizares, "Comparative stability analysis of DFIG-based wind farms and conventional synchronous generators" in Proc. 2011 IEEE/PES PSCE Conference, pp. 1-7.

[2] M. Lockwood, "Detailed simulation of doubly-fed induction machines based wind generators" in Proc. 2003 CIRED 17th International Conference on Electricity Distribution, Paper n.71.

[3] P. Giroux, G. Sybille, S. Chandrachood, *Grid-Connected PV Array*, The Mathworks, 2010. [Online]. Available: http://www.mathworks.com/matlabcentral/fileexchange/34752-grid-connected-pv-array.

[4] A. K. Saha, S. Chowdhury, S. P. Chowdhury, P. A. Crossley, "Modeling and simulation of microturbine in islanded and grid-connected mode as distributed energy resource", in Proc. 2008 IEEE Power and Energy Society General Meeting - Conversion and Delivery of Electrical Energy in the 21st Century, pp. 1-7.

[5] Z. Zhang, W. J. Lee, M. Liu, "PEM fuel cell and battery hybrid power supply system design based on fuel flow rate control" in Proc. 2011 IEEE 4th International DRPT Conference, pp 284-291.

[6] J. Jia, Y. Wang, D. Lian, "Matlab / simulink based-study on PEM fuel cell and battery hybrid system" in Proc. 2008 IEEE 10th ICARCV Conference, pp 2108-2113.

[7] D. M. Ali, "A Simplified Dynamic Simulation Model (prototype) for a Stand-Alone Polymer Electrolyte Membrane (PEM) Fuel Cell Stack", in Proc. 2008 IEEE Power System Conference, 2008. MEPCON 2008. 12th International Middle-East, pp. 480-485.

[8] J. Zhang, Z. Chen, L. Cai, Y. Zhao, "Flywheel energy storage system design for distribution network" in Proc. 2000 IEEE Power Engineering Society Winter Meeting, pp. 2619-2623 vol.4.

[9] F. A. Farret, M. Godoy Simões, *Integration of Alternative Sources of Energy*, John Wiley & Sons, 2006.

[10] S. P. Chowdhury, P. Crossley, *Microgrids and Active Distribution Networks*, The Institution of Engineering and Technology, 2009.

[11] P. Kundur, *Power System Stability and Control*, McGraw-Hill Education, 1994.

[12] Technical Application Papers No.13 - Wind power plants, ABB SACE, 2011. [Online]. Available: http://www05.abb.com/global/scot/scot209.nsf/veritydisplay/92faf0c1913f5651c1257937002f88e8/$file/1SDC007112G0201.pdf.

[13] Technical Application Papers No.10 - Photovoltaic plants, ABB SACE, 2011. [Online]. Available: http://www05.abb.com/global/scot/scot209.nsf/veritydisplay/27f1bc42dc092715c1257ac500392aff/$file/1SDC007109G0202.pdf.

[14] S. Heier, *Grid Integration of Wind Energy Conversion Systems*, John Wiley & Sons Ltd, 1998.

[15] T. Ackermann, *Wind Power in Power Systems*, John Wiley & Sons Ltd, 2005.

Alessia Cagnano received her B.Sc. and M.Sc. degrees in Electrical Engineering from the Polytechnic University of Bari (Italy) in 2005 and 2007, respectively. She received her Ph.D. in Electrical Engineering at the Polytechnic University of Bari. Her research interests are in power system analysis and control.

Enrico De Tuglie received the M.Sc. and Ph.D. degrees in electrical engineering from the Polytechnic University of Bari. He was visiting scientist at the Pacific Northwest National Laboratory (PNNL) operated by Battelle under the Department Of Energy (USA). Since December 2003 he has been Associate Professor at the Polytechnic University of Bari. His research interests include power system analysis and control and reregulated markets.

Maria Dicorato (M '01) received her M.Sc. and Ph.D. degrees in Electrical Engineering from the Politecnico di Bari (Italy) in 1997 and 2001 respectively. Currently she is Assistant Professor at the Electrical and Electronic Engineering Department of the Politecnico di Bari. Her research interests deal with dynamic security assessment, energy planning, energy market modeling. Dr. Dicorato is a member of IEEE-PES and AEIT.

Giuseppe Forte (S '08, M '11) received B.Sc. and M.Sc. degree in Electrical Engineering from the Politecnico di Bari (Italy) in 2004 and 2006 respectively. In 2010 he gained Ph.D. in Electrical Engineering at Politecnico di Bari (Italy). He is currently a post-doc research assistant at Politecnico di Bari. His research interests are renewable energy integration and control. Dr. Forte is a member of IEEE-PES and AEIT.

Michele Trovato (M '93) received the Electrical Engineering degree in 1979 from the University of Bari, Bari, Italy. In 1980, he joined the Electrical Engineering Institute, University of Bari, where he became an Associate Professor of transmission and distribution systems.

Currently, he is a Full Professor of electrical energy systems at the Electrical and Electronic Engineering Department, Politecnico di Bari. His areas of interest are power system analysis and control. Prof. Trovato is Member of IEEE-PES and AEIT.

ISBN: 978-1-61804-321-4

Mathematical modeling and simulation of an automatic electric heating system

M. I. Neacă, A. M. Neacă

***Abstract*—**Mathematical modeling and simulation in order to simulate different equipment is a strictly actual subject. This is due to the many possibilities of validating different functioning regimes of the plants. Some of these regimes might be destructive and cost consuming. The problem becomes very difficult to resolve when is wanted to simulate transient regimes that can occur at a certain time in a real physical system, characterized by large time constants. In this case the state parameters are very important and changing their values can be made in a long time. This paper presents a practical way of solving this problem in a difficult case, when the mathematical model is composed of a large number of equations and the transition must ensure the conservation of many state parameters. The paper refers to an electric oven for thermal treatments. The temperature of the pieces inserted into the oven to follow the temperature set through the imposed technological cycle. This prescription can be done using a ventilation or exhaust system and an automation system.

***Keywords*—**automated control, electric heating, system modeling, thermal treatment.

I. Introduction

Mathematical modeling and especially simulation have been favored by the development of some specific software packages. These allow highlighting some fine phenomena, many times described by transcendental equations. These equations deal with much nonlinearity which was hard to model in the past.

The problem of modeling and simulation of the dynamic regimes of the electrical ovens and of the electro-thermal plants in general, proves to be extremely complex. Such a simulation must take into consideration many parameters which can modify depending on the plant temperature. Such evolutions (with different degrees of nonlinearity), can appear close to the heat sources, but also in the areas using heat.

The ovens with resistors occupy an important place in the industrial electro-thermal plants. This approach is favored by the fact that such an oven can be designed and created not only for different capacities, but also for a wide range of temperatures. As a result of this last aspect, the ovens with resistors can be utilized to melt some materials but also for thermal and thermochemical treatments.

M. I. Neacă is with the Department of Electrical, Energetic and Aerospace Engineering, Faculty of Electrical Engineering, University of Craiova, Craiova, Romania (e-mail: ineaca@elth.ucv.ro).

A. M. Neacă was with the Department of Electrical, Energetic and Aerospace Engineering, Faculty of Electrical Engineering, University of Craiova. She is now with HELLA Craiova (e-mail: neaca_andreea@yahoo.com).

II. The MATLAB-SIMULINK modell

When simulating an electrical oven for thermal treatments, we must take into consideration the phenomena such as auto-heating of the electrical resistors, of the walls of the oven, of the parts and of the air from inside the oven. The modeling of the dynamic regime of heating the electrical oven, allowed us to emphasize some conclusions extremely useful in the design activity.

At a superficial approach, the phenomena form inside the oven seems very simple: the resistors supplied from an electrical energy source are getting worm, sending the heat by radiation and convection [1]. The thermal flux reaches the parts to be heated and the walls, which get hot gradually. A part from the energy passes through the walls, to exterior, and is called the lost thermal flux.

In fact, the problems are much more complex. The heating of the electrical resistors is realized with a relatively small time constant, based on a part of the absorbed electrical energy. During this period, the energy emitted as a thermal flux (radiation + convection) depends on the momentary temperature of the resistors, pieces, walls and air, and on the outfit of self-heating from that moment.

On the other side, the temperature of the stratified wall depends on its construction, and grows up based on the thermal flux received from the resistors with a time constant much bigger. The growth of temperature of the different layers from which are made the walls, including the exterior carcass, leads to a continuum modification of the thermal flux lost in the ambient medium. During the heating period of the oven, the part from inside of it gets hot with a proper time constant. Finally, the air from inside the oven takes the heat from the walls but also from the resistors through convection. The value of the thermal flux overtaken by the air and its sense is permanently changing during the heating transient regime of the oven [2].

From all the electrical ovens, the ovens with resistors permit the highest flexibility. To obtain the best results it is necessary that these ovens to be supplied through power electronically plants that can precisely control the electrical energy transformed into heat, in each moment of time.

For the simulation to be complete, the command, automatic control and power supply subsystem must be modeled. These models must be coupled with the model of the oven itself, in order to simulate the functional regimes.

The main purpose of automation of the electric ovens with resistors is automatic adjustment of the temperature. This leads to a reduction of the specific consumption of electricity on electro-thermal process and technological process.

For a better work precision and for the automatic temperature adjustment are basically used all the usual control methods: continuous, semi-continuous and discontinuous. Continuous adjustment methods (algorithms PID and predictive) are, compared with the semi-continuous and discontinuous ones, more complex and more expensive, but it provides a better accuracy of the set temperature.

The paper highlights some aspects resulted from the over 4 years research work done by the authors.

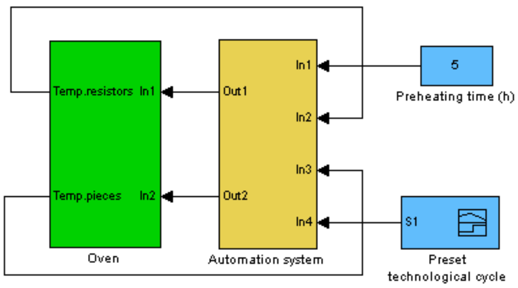

Fig.1. The oven together with the control system

Fig.1 shows a block diagram of the simulated assembly of the plant. The block that simulates the oven receives as inputs the outputs of the control block. These inputs are the commands related to the control of the electrical energy transformed into heat through the heating resistors and through the exhausting and ventilation system.

The ventilation system can't be neglected because it is vital in the conditions of an imposed technological cycle. The technological cycle must be followed by the parts inside the oven in order to accomplish thermal treatment. The proposed simulation system allows us to set the preheating time for the oven. The preheating time is necessary in order to ensure the heating speed for the parts. It is also an integrated part of the calculus of such an electro-thermal plant. The fourth block sets the imposed technological cycle.

In Figure 2 it is presented the automatic control system in one of the tested variants, e.g. the automatic control with PID regulators for heating and ventilation. For this control system have been tested some variants: with on-off regulators, with P, PI, PID regulators (with or without predictive circuit), with auto-adaptive regulators. Part of the results was presented in [3], [4] and [5].

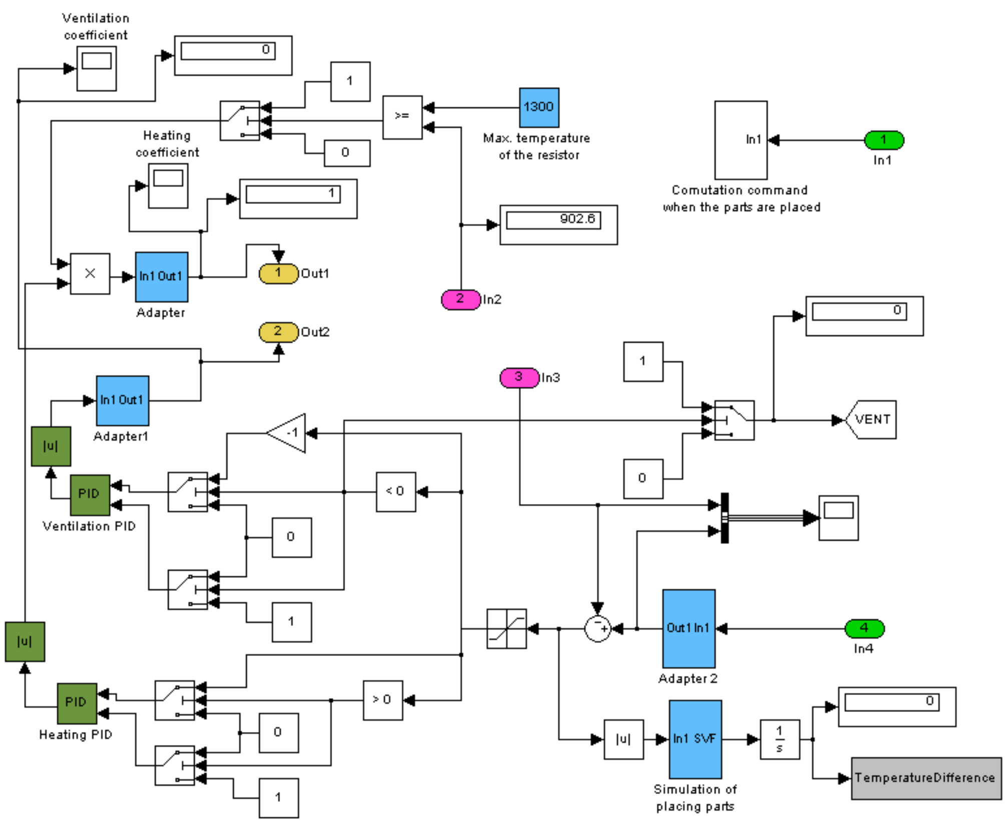

Fig.2. The automatic command system

ISBN: 978-1-61804-321-4

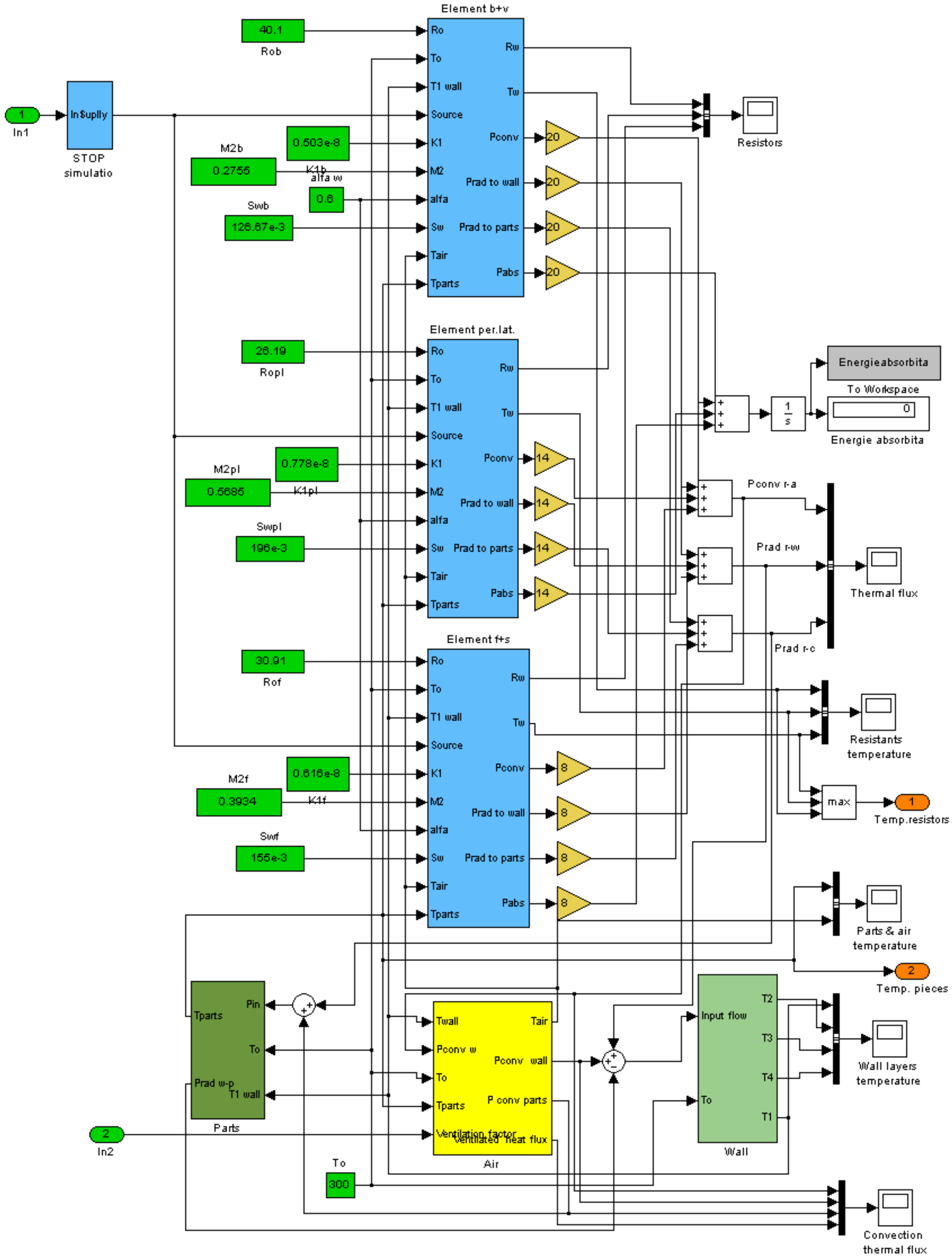

Fig.3. The Simulink model of the oven

From Fig.3 it can be easily seen the complexity of the model of such an industrial plant. We need to tell that the mathematical model of the oven (without automatic control) involves 67 equations for the heating process (ANNEX) and 65 equations for ventilation. The projecting calculus done previously for the oven described in [6], have led to the conclusion that the oven is equipped with three types of resistors. Each type is modeled through a similar block, but for each of them the inputs are different. These input values depend on the physical dimensions of the resistors. The outputs of these three blocks are then multiplied with the corresponding number of the similar resistors. A simulation

ISBN: 978-1-61804-321-4

block for a heating resistor was presented in [7]. We highlight the fact that the Simulink model of this block contains some elements that model dynamically the variation coefficient of the resistance and of the caloric capacity with the temperature. They also depend on the changes that appear when inserting the parts into the oven.

This kind of elements with specific parameters is also present into the block that simulates the parts. It is a block that models the specific heat temperature dependency and that commute parameters from the status of the oven with parts inside, and the preheating period (without parts inside) [8].

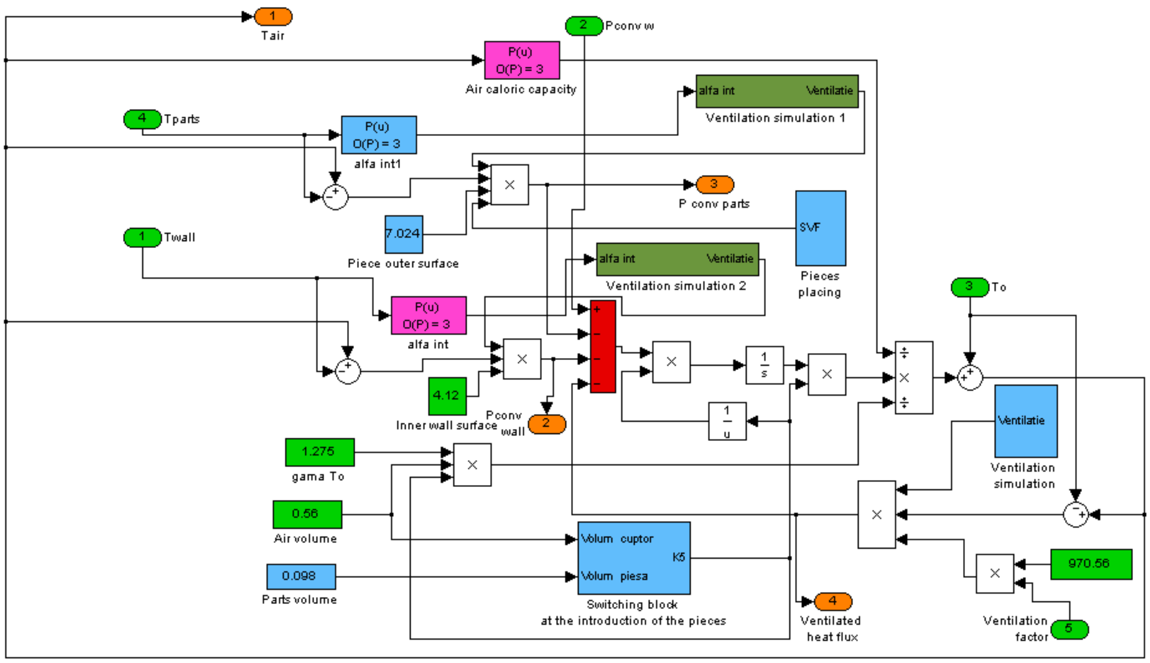

Fig.4. The Simulink model of the air from inside the oven

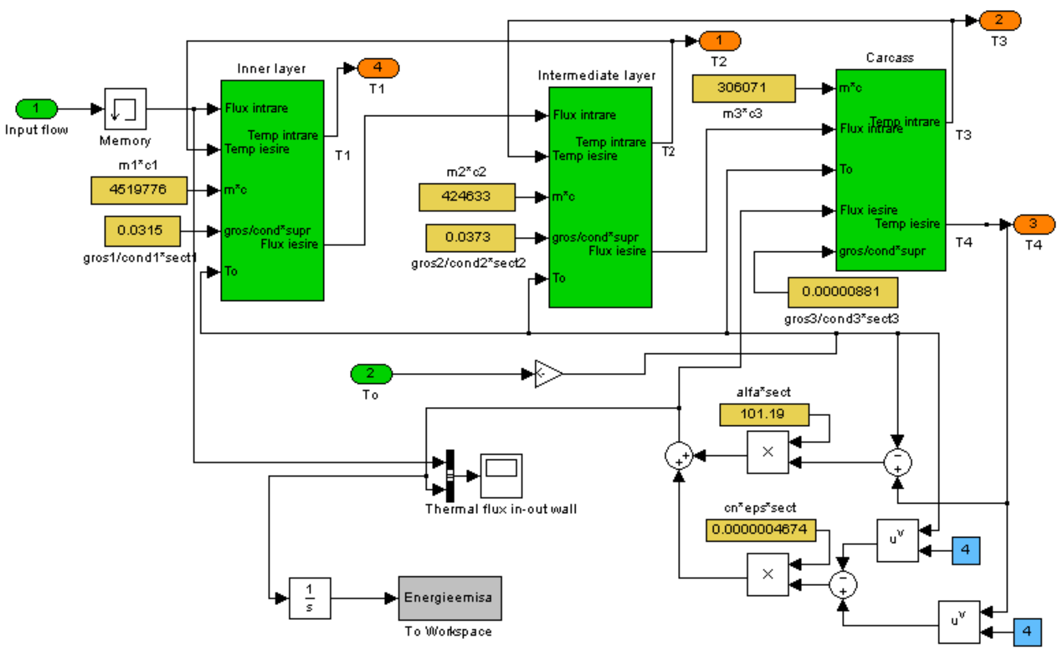

Fig.5. The wall of the oven

In Fig.4 is presented the simulation block of the air from inside the oven. It can be seen the three blocks that model the temperature nonlinear dependencies. This block makes the corrections imposed when inserting the parts into the oven. It contains also the three blocks that ensure the dynamic changes of the functional parameters when starting the ventilation (we consider that during the ventilation the airflow inside the oven becomes turbulent, and during the heating it is laminar). In [9] there are presented details regarding the functionality of these blocks.

The block that simulates the wall of the oven is presented in Fig.5 and a detailed analysis of it is presented in [10].

We can observe that each layer has as output variables the thermal flux transferred by the next layer and the temperature at the inner face of the layer. In this way, by connecting successively the models that simulate the layers of the wall, we can make the calculus of the temperatures $T_1 \div T_4$ and the thermal fluxes through the exterior.

This approach allows us to easily adapt when we want to insert an intermediate layer. Practically, all we need to do is to insert a block of “intermediate layer” with specific constructive parameters.

III. THE RESULTS OF THE SIMULATION

The model made in Matlab-Simulink is able to offer many parameters, from which we can enumerate: instantaneous value and the temperature of the heating resistors, the temperatures of the layers of the wall, the temperature of the parts and the temperature of the air from inside the oven, convection and radiation thermal flows from inside and outside the oven, the produced, stored and lost thermal energy, etc.

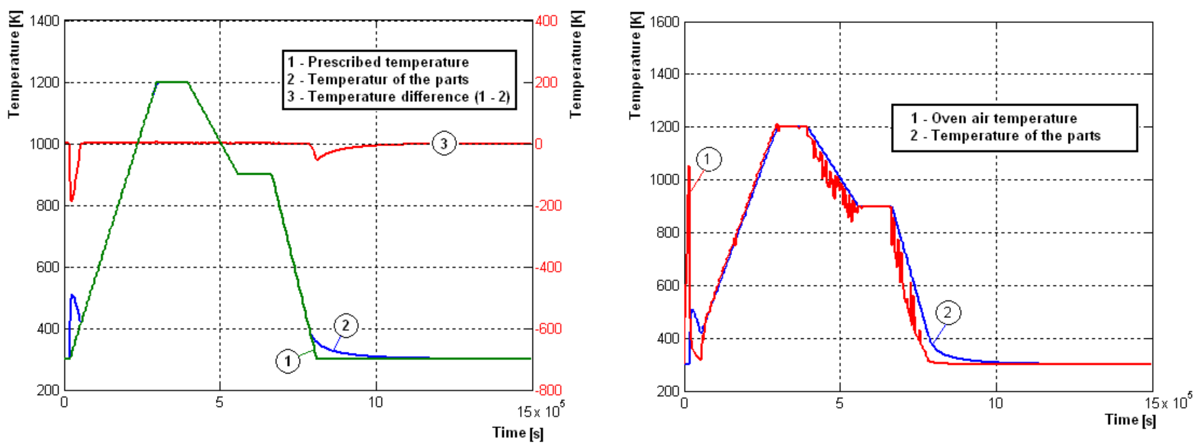

Fig.6. The simulation with imposed technological cycle

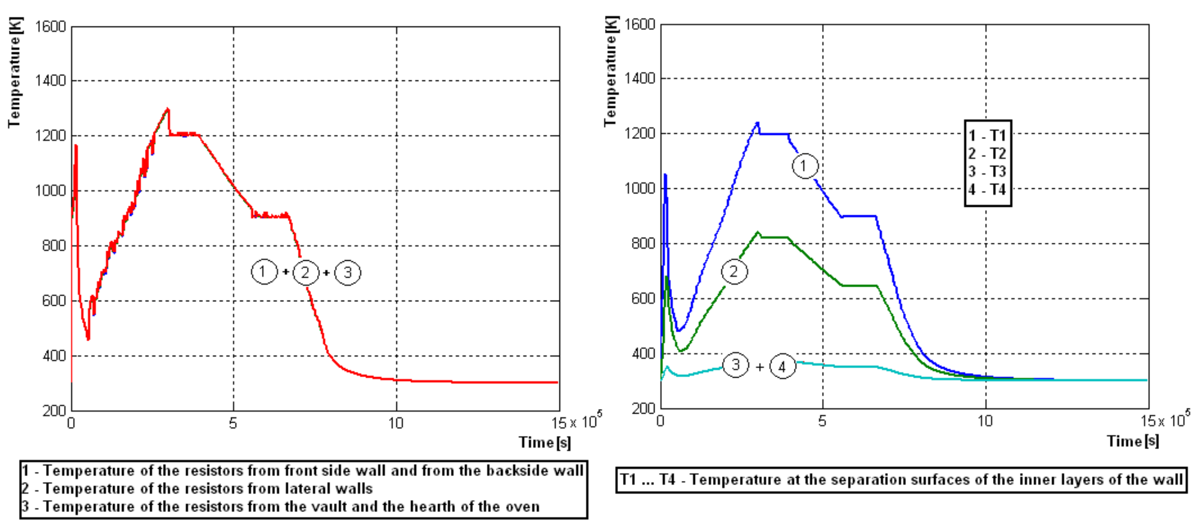

Fig.7. The evolution of the temperatures of the resistors and the temperatures from inside the wall

The simulation started by defining a technological cycle for thermal treatment. In Fig.6 is presented such a technological cycle chosen for simulation and the obtained results. The differences, seen in the left figure, between the curve of the imposed temperature (1) and the curve of the parts temperature (2) are only at small temperature, where there are no structural transformations. The differenced from the beginning are determined by the preheating period of the oven, and those from the end of the cycle are determined by the difficulty to ventilate at small temperatures, when the temperature of the exterior air is almost equal with the temperature of the parts. Curve (1) from the right figure shows the evolution of the air temperature from inside the oven.

Fig.7 also shows information regarding the temperature. It is presented the evolution in time of the temperature of the heating resistors and of the surfaces of the layers of the wall.

In the right figure:

T_1 = the temperature of the inner side of the refractory layer

T_2 = the temperature between the refractory - insulated layer

T_3 = the temperature between the insulated layer - metallic carcass

T_4 = the temperature of the exterior side of the metallic carcass

An interesting diagram is presented in Fig.8. There are presented the convection thermal flows that appear inside the oven. The right figure shows a detail of the evolution highlighted into the left figure.

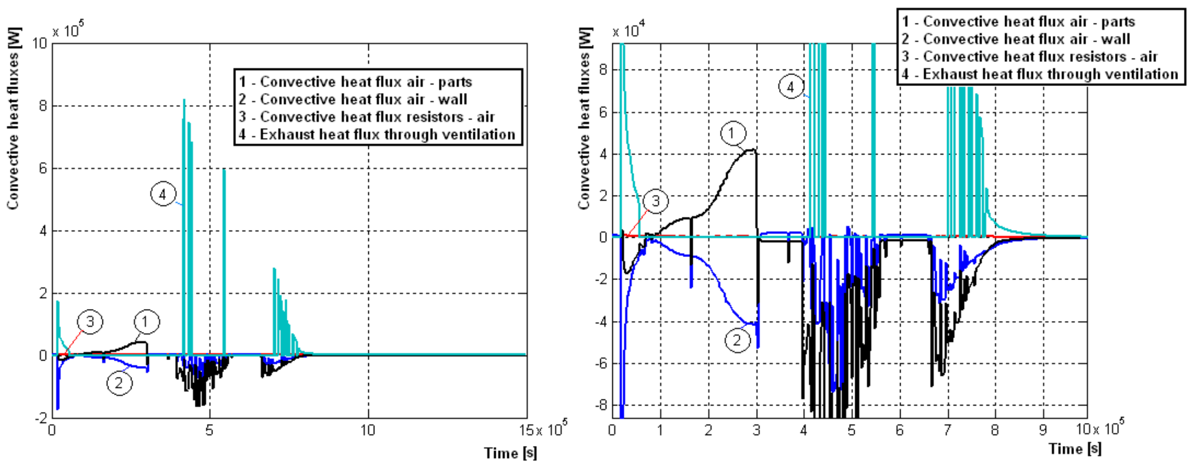

Fig.8. Convection flows

IV. Conclusion

Modeling and simulation of a physical system of high complexity, that implies various nonlinearities and interdependencies, is also a challenge. In this case, the realization of such a model provided to be very useful because our simulations highlighted some aspects that have led to the prevention and the elimination of fault situations. An example is the fact that the simulations have clearly shown the necessity to monitor the temperature of the heating resistors, not only to monitor the temperature of the parts. This is due in order to prevent overheating and damage of the resistors (that appears mostly during the preheating period). There have been also highlighted some aspects related to the dimensioning of the ventilation system.

The proposed modeling and simulation system was successfully applied for an oven with smaller dimensions. The automatic command electronic system was physically realized around an acquisition board with a microcontroller. The process was lead through real-time bidirectional communication between the acquisition board and a PC that as implemented a technological cycle necessary for the thermal treatment of the parts. The computer runs in Matlab and the obtained experimental results have shown a good accuracy in the accomplishment of the technological thermal treatment.

Using this system it is relatively simple to test the functionality of the oven for different types of applied command processes (with different regulators for heating and ventilation, with or without protection systems, with or without auto adaptive systems, etc.)

References

[1] F. P. Incropera, D. P. DeWitt, *Fundamentals of Heat and Mass Transfer*, WILEY, ISBN: 978-0-470-05554-0

[2] M. C. Potter, C. W. Somerton, *Thermodynamics for Engineers*, Mc.GRAW-HILL, 1993

[3] A. M. NEACĂ, M. I. NEACĂ, *Methods of Automatic Control applied to a Resistive Furnace for Thermal Treatments*, Analele Universității din Craiova, seria Inginerie Electrică, no.37, 2013, ISSN 1842-4805

[4] A. M. NEACĂ, M. I. NEACĂ, *Improving the performance of a control system for a heat treatment oven using a predictive controller*, Proceedings of the 11th WSEAS International Conference on Heat Transfer, Thermal Engineering and Environment (HTE '13), Vouliagmeni, Athens, Greece, May 14-16, 2013, ISSN: 2227-4596, ISBN: 978-1-61804-183-8.

[5] A. M. NEACĂ, M. I. NEACĂ, *Real-Time Automated Control of a Resistive Furnace*, http://ieeexplore.ieee.org/xpl/articleDetails.jsp?tp=&arnumber=6972603&searchWithin%3DNeaca%26refinements%3D4269102461%2C4269102460%2C4262047182%26queryText%3DICATE+2014.

[6] M. I. NEACĂ, A. M. NEACĂ, *Modeling and simulation of the transient heating regime in an electrical oven*, http://ieeexplore.ieee.org/xpl/articleDetails.jsp?arnumber=5520672&searchWithin%3DNeaca%26sortType%3Dasc_p_Sequence%26filter%3DAND%28p_IS_Number%3A5520659%29

[7] M. I. NEACĂ, A. M. NEACĂ, *The Modeling of the Heating Resistors in Transient Regime*, http://www.davidpublishing.com/journals_info.asp? jId=474

[8] A. M. NEACĂ, M. I. NEACĂ, E. BUNCIU, *Thermal treatment in electrical resistive ovens - modeling and simulation of the air temperature and the parts to be treated*, http://ieeexplore.ieee.org/xpl/articleDetails.jsp?arnumber=6231891&refinements%3D4270607169%2

6sortType%3Dasc_p_Sequence%26filter%3DAND%28p_IS_Number%3A6231751%29
[9] M. I. NEACĂ, A. M. NEACĂ, *Preserving the value of the status variables when changing the mathematical models during the simulation of complex dynamical regimes*, http://www.wseas.org/main/books/2013/ Vouliagmeni/FLUHE.pdf
[10] A. M. NEACĂ, E. STOENESCU, M. I. NEACĂ, *The simulink model of a multilayer wall for the study of the thermal transfer in transient regime*, Analele Universităţii din Craiova, seria Inginerie Electrică, no.34, 2010, ISSN 1842-4805

ANNEX

MATHEMATICAL MODEL FOR THE OVEN (HEATING PERIOD)

A Heating elements

A1 The vault and hearth (20 identical elements)

$$i_{bv}(t)=\frac{u(t)}{R_{bv}(T)} \tag{1}$$

$$R_{bv}(T)=R_{0-bv}\cdot C_R(\Delta T_{rezistor-bv}) \tag{2}$$

$$C_R(\Delta T_{rezistor-bv})=a_1\cdot(\Delta T_{rezistor-bv})^3+a_2\cdot(\Delta T_{rezistor-bv})^2+ +a_3\cdot(\Delta T_{rezistor-bv})+a_4 \tag{3}$$

$$p_{el-bv}=u(t)\cdot i_{bv}(t)=\dot{Q}_{stocat-bv}+\dot{Q}_{rad-bv}+\dot{Q}_{conv-bv} \tag{4}$$

$$\dot{Q}_{stocat-bv}=\frac{d}{dt}(Q_{stocat-bv})= =\frac{d}{dt}(m_{bv}\cdot C_C(T_{rezistor-bv})\cdot\Delta T_{rezistor-bv}) \tag{5}$$

$$C_C(T_{rezistor-bv})=b_1\cdot(T_{rezistor-bv})^3+b_2\cdot(T_{rezistor-bv})^2+ +b_3\cdot(T_{rezistor-bv})+b_4 \tag{6}$$

$$\Delta T_{rezistor-bv}=T_{rezistor-bv}-T_0 \tag{7}$$

$$\dot{Q}_{rad-bv}=\dot{Q}_{rad-bv(rez-perete)}+\dot{Q}_{rad-bv(rez-piesa)} \tag{8}$$

$$\dot{Q}_{rad-bv(rez-piesa)}=K_7\cdot\varepsilon\cdot c_n\cdot S_{rezistor-bv}\cdot\left(T^4_{rezistor-bv}-T^4_{piesa}\right)= =K_7\cdot K_{1-bv}\cdot\left(T^4_{rezistor-bv}-T^4_{piesa}\right) \tag{9}$$

$$\dot{Q}_{rad-bv(rez-perete)}=(1-K_7)\cdot\varepsilon\cdot c_n\cdot S_{rezistor-bv}\cdot\left(T^4_{rezistor-bv}-T_1^4\right) =(1-K_7)\cdot K_{1-bv}\cdot\left(T^4_{rezistor-bv}-T_1^4\right) \tag{10}$$

$$\dot{Q}_{conv-bv}=\alpha\cdot S_{rezistor-bv}\cdot(T_{rezistor-bv}-T_{aer}) \tag{11}$$

A2 Lateral walls (14 identical elements)

The 11 equations are similar to those of the A1 (12 – 22)

A3 Front and rear (8 identical elements)

The 11 equations are similar to those of the A1 (23 – 33)

B. Heat transfer in the resistance area

$$\dot{Q}_{conv.\ tot}=\sum_i n_i\cdot\dot{Q}_{conv.\ i}=20\cdot\dot{Q}_{conv-bv}+14\cdot\dot{Q}_{conv-pl}+ +8\cdot\dot{Q}_{conv-fs} \tag{34}$$

$$\dot{Q}_{rad.\ tot(rez-perete)}=\sum_i n_i\cdot\dot{Q}_{rad.\ i(rez-perete)}=20\cdot\dot{Q}_{rad-bv(rez-perete)} +14\cdot\dot{Q}_{rad-pl(rez-perete)}+8\cdot\dot{Q}_{rad-fs(rez-perete)} \tag{35}$$

$$\dot{Q}_{rad.\ tot(rez-piesa)}=\sum_i n_i\cdot\dot{Q}_{rad.\ i(rez-piesa)}=20\cdot\dot{Q}_{rad-bv(rez-piesa)} +14\cdot\dot{Q}_{rad-pl(rez-piesa)}+8\cdot\dot{Q}_{rad-fs(rez-piesa)} \tag{36}$$

$$T_{\max rezistor}=\max(T_{rezistor-bv},T_{rezistor-pl},T_{rezistor-fs}) \tag{37}$$

C. The air in the oven

$$\dot{Q}_{conv.\ tot}=\dot{Q}_{conv_{aer-perete}}+\dot{Q}_{stocat_{aer}}+\dot{Q}_{conv_{aer-piesa}} \tag{38}$$

$$\dot{Q}_{conv_{aer-piesa}}=\alpha_{piesa}(T_{piesa})\cdot S_{piesa_{conv}}\cdot(T_{aer}-T_{piesa}) \tag{39}$$

$$\alpha_{piesa}(T_{piesa})=e_1\cdot(T_{piesa})^3+e_2\cdot(T_{piesa})^2+e_3\cdot(T_{piesa})+e_4 \tag{40}$$

$$\dot{Q}_{stocat_{aer}}=\frac{d}{dt}\left(Q_{stocat_{aer}}\right)=\frac{d}{dt}\left(m_{aer}\cdot C_{aer}(T_{aer})\cdot(T_{aer}-T_0)\right) \tag{41}$$

$$C_{aer}(T_{aer})=c_1\cdot(T_{aer})^3+c_2\cdot(T_{aer})^2+c_3\cdot(T_{aer})+c_4 \tag{42}$$

$$m_{aer}=V_{aer}\cdot\gamma_{aer}=(V_{cuptor}-V_{piesa})\cdot\gamma_{aer} \tag{43}$$

$$\dot{Q}_{conv_{aer-perete}}=\alpha_{perete}(T_1)\cdot S_{perete-\text{int}}\cdot(T_{aer}-T_1) \tag{44}$$

$$\alpha_{perete}(T_1)=d_1\cdot(T_1)^3+d_2\cdot(T_1)^2+d_3\cdot(T_1)+d_4 \tag{45}$$

D. The pieces

$$\dot{Q}_{in_{piesa}}=\dot{Q}_{rad.tot(rez-piesa)}+\dot{Q}_{conv_{aer-piesa}}+\dot{Q}_{rad_{perete-piesa}} \tag{46}$$

$$\dot{Q}_{in_{piesa}}=\dot{Q}_{stocat_{piesa}}=\frac{d}{dt}\left(Q_{stocat_{piesa}}\right)= =\frac{d}{dt}\left(m_{piesa}\cdot C_{piesa}(T_{piesa})\cdot(T_{piesa}-T_0)\right) \tag{47}$$

$$C_{piesa}(T_{piesa})=\sum_{i=1}^{10} f_i\cdot(T_{piesa})^{10-i} \tag{48}$$

$$\dot{Q}_{rad_{perete-piesa}} = \varepsilon_{perete} \cdot c_n \cdot S_{piesa_{rad}} \cdot \left(T_1^4 - T_{piesa}^4\right) \qquad (49)$$

E. Wall multilayer considered as a whole

$$\dot{Q}_{in\ perete} = \dot{Q}_{rad.tot(rez-perete)} + \dot{Q}_{conv_{aer-perete}} - \dot{Q}_{conv_{perete-piesa}} \qquad (50)$$

$$\dot{Q}_{in\ perete} = \dot{Q}_{stocat_{perete}} + \dot{Q}_{conv._{perete-ext}} + \dot{Q}_{rad_{perete-ext}} \qquad (51)$$

$$\dot{Q}_{rad._{perete-ext}} = \varepsilon \cdot c_n \cdot S_{p.ext} \cdot (T_4^4 - T_0^4) = K_{2-ext} \cdot (T_4^4 - T_0^4) \qquad (52)$$

$$\dot{Q}_{conv_{perete-ext}} = \alpha_{ext} \cdot S_{p.ext} \cdot (T_4 - T_0) = K_{3-ext} \cdot (T_4 - T_0) \qquad (53)$$

E.1. The outer metal housing

$$Q_{stocat.3} = m_3 \cdot c_3 \cdot [(T_4 + T_3)/2 - T_0] = K_4 \cdot [(T_4 + T_3)/2 - T_0] \qquad (54)$$

$$\dot{Q}_{OUT.C} = \dot{Q}_{rad_{perete-ext}} + \dot{Q}_{conv._{perete-ext}} \qquad (55)$$

$$\dot{Q}_{IN.C} = \dot{Q}_{OUT.C} + \frac{d}{dt}(Q_{stocat.3}) \qquad (56)$$

$$T_3 = \frac{T_3 + T_4}{2} + \frac{T_3 - T_4}{2} \quad \text{auxiliary equation} \qquad (57)$$

$$T_4 = \frac{T_3 + T_4}{2} - \frac{T_3 - T_4}{2} \quad \text{auxiliary equation} \qquad (58)$$

$$T_3 - T_4 = R_{termic-3} \cdot \dot{Q}_{OUT.C} \quad \text{auxiliary equation} \qquad (59)$$

E.2. The thermal insulating layer

$$Q_{stocat.2} = m_2 \cdot c_2 \cdot [(T_3 + T_2)/2 - T_0] = K_5 \cdot [(T_3 + T_2)/2 - T_0] \qquad (60)$$

$$\dot{Q}_{out.2} = \dot{Q}_{IN.C} = \frac{\lambda_{TIZ} \cdot S_{TIZ}}{g_{TIZ}} \cdot (T_2 - T_3) = \frac{(T_2 - T_3)}{R_{termic-2}} \qquad (61)$$

$$\dot{Q}_{in.2} = \dot{Q}_{out.2} + \frac{d}{dt}(Q_{stocat.2}) \qquad (62)$$

$$T_2 = 2 \cdot \frac{T_3 + T_2}{2} - T_3 \quad \text{auxiliary equation} \qquad (63)$$

E.3. The refractory layer

$$Q_{stocat.1} = m_1 \cdot c_1 \cdot [(T_1 + T_2)/2 - T_0] = K_6 \cdot [(T_1 + T_2)/2 - T_0] \qquad (64)$$

$$\dot{Q}_{out.1} = \dot{Q}_{in.\ 2} = \frac{\lambda_R \cdot S_R}{g_R} \cdot (T_1 - T_2) = \frac{(T_1 - T_2)}{R_{termic-1}} \qquad (65)$$

$$\dot{Q}_{in.p} = \dot{Q}_{out.1} + \dot{Q}_{stocat.1} = \dot{Q}_{out.1} + \frac{d}{dt}(Q_{stocat.1}) \qquad (66)$$

$$T_1 = 2 \cdot \frac{T_2 + T_1}{2} - T_2 \quad \text{auxiliary equation} \qquad (67)$$

ISBN: 978-1-61804-321-4

Error estimation in the decoupling of ill-defined and/or perturbed nonlinear processes

Amira Gharbi[*,**], Mohamed Benrejeb[*] and Pierre Borne[**]

[*]Laboratoire de Recherche en Automatique, LARA
Ecole Nationale d'Ingénieurs de Tunis BP 37 Le Belvédère 1002 Tunis, Tunisie.
[**]Centre de Recherche en Informatique Signal et Automatique de Lille, CRIStAL.
Ecole Centrale de Lille. Cité scientifique BP 48-59651 Villeneuve d'Ascq Cedex, France
Email: merkarim@gmail.com, mohamed.benrejeb@enit.rnu.tn, pierre.borne@ec-lille.fr

Abstract— This paper deals with the definition of the attractors characterizing the precision of decoupling control laws for a nonlinear process in presence of uncertainties and/or bounded perturbations. This approach is based on the use of aggregation techniques and the definition of a comparison system of the controlled process.

Keywords— Attractor, aggregation technique, comparison system, nonlinear system.

I. Introduction

A classical way to control nonlinear systems is to compute a linear controller using the first-order approximation of the system dynamics around the origin $x = 0$, which gives a local linear approximation of the system. A non-approximating method consists to define a nonlinear feedback control law which realizes an input-output decoupling by linearization [1]-[5]. For an ill-defined model or a perturbed process the determination of a suitable control appears more difficult and is usually achieved by a precise and non-perturbed model. In such a case it appears very important to estimate by overvaluation the error induced by this simplification.

In this paper, the proposed approach consist to determine an attractor, which localizes the induced error, and is achieved by using aggregation techniques and the Borne-Gentina stability criteria, with the use of vector norms and of comparison systems [6]-[11].

The aim of this work is to present an approach to the study of stability of nonlinear systems and the estimation, by overvaluation, of the attractor. In section 2, we propose a decoupling linearization method. In section 3 we propose an attractor determination method in presence of disturbances and/or uncertainties by the use of the aggregation technique for stability study. The determination of the attractor for a third order nonlinear complex system is proposed, in section 4, to illustrate the efficiency of this approach.

II. Decoupling linearization-Basic Idea

Let us consider a smooth nonlinear control affine system whose evolution is described by the equations:

$$\begin{aligned} \dot{x} &= f(x) + G(x)u \\ y &= h(x) \end{aligned} \tag{1}$$

where $x \in \mathbb{R}^n$ is the state vector, $y \in \mathbb{R}^m$ the output vector and $u \in \mathbb{R}^m$ the control vector.

The method consists of deriving each component y_i of the output vector to display the control vector.

With the notation $y_i^* = y_i^{(d_i+1)} \quad \forall i = 1,\ 2,\ \cdots,\ m$, it comes [12]:

$$y^* = f^*(x) + G^*(x)u \tag{2}$$

If G^* is invertible in the domain of evolution of the state vector we can define the control law:

$$u = G^{*^{-1}}(x)(v - f^*(x)) \tag{3}$$

which leads to the relations:

$$y_i^{(d_i+1)} = v_i,\ \forall i = 1,\ 2,\ \cdots,\ m \tag{4}$$

This representation is valid only if the instable variables of the initial system are observable.

ISBN: 978-1-61804-321-4

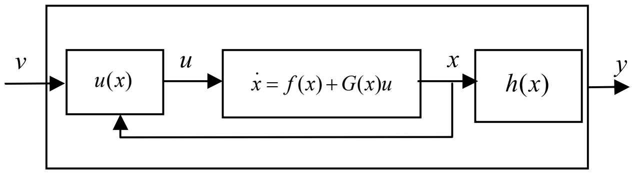

Fig. 1 Representation of the decoupled system

III. ATTRACTOR DETERMINATION IN PRESENCE OF DISTURBANCES AND/OR UNCERTAINTIES

Let us consider the system (1) submitted to the bounded errors δf and δG such that $|\delta G| \leq \Delta G$ and $|\delta f| \leq \Delta f$.
it comes

$$\begin{aligned} \dot{x} &= f(x) + \delta f + (G(x) + \delta G)u \\ &= f(x) + G(x)u + \delta f + \delta G u \end{aligned} \tag{5}$$

Hence using the previously defined control law we obtain a description of the form

$$\frac{dx}{dt} = A(x)x + B(x,.) \tag{6}$$

We can now study the stability of the controlled system by determination of the attractor, possibly reduced to the origin $x = 0$, by using aggregation techniques and definition of a comparison system such that the instantaneous matrix of the non-perturbed system be the opposite of an M-matrix.

For the vector norm $p(x) = \left[|x_1|, |x_2| \ldots, |x_n| \right]^T$, we obtain by overvaluation the linear comparison system:

$$z \in \mathbb{R}^n \,/\, \dot{z}(t) = Mz(t) + N \tag{7}$$

Notation $M(.) = \{m_{i,j}(.)\}$ such that:

$$\begin{cases} m_{i,i}(.) = a_{i,i}(.) & \forall i = 1,2,\ldots n \\ m_{i,j}(.) = \left| a_{i,j}(.) \right| & \forall i \neq j \end{cases} \tag{8}$$

and the vector $N(.)$ defined by

$$N(.) = |B(.)| \tag{9}$$

we can define the constant matrices M and N by

$$\begin{aligned} M &= \{m_{i,j}\}; \quad m_{i,j} = \max\{m_{i,j}(.)\} \\ N &= \{n_i\}; \qquad n_i = \max\{n_i(.)\} \end{aligned} \tag{10}$$

If M is the opposite of an M-matrix, it exists an attractor D asymptotically stable such that

$$D = \left\{ x \in R^n ; p(x) \leq -M^{-1}N \right\} \tag{11}$$

with

$$z(t) \geq p(x(t)) \tag{12}$$

$\forall t \in \tau_0 = [t_0 ; +\infty]$; we have:

$$\lim_{t\to\infty} z(t) = z(+\infty) = -M^{-1}N \text{ then } \lim_{t\to+\infty} p(x) \leq -M^{-1}N \tag{13}$$

IV. APPLICATION TO A THIRD ORDER NONLINEAR SYSTEM

Let us consider the nonlinear system

$$(S): \begin{cases} \dot{x}_1 = -2x_1 \cos x_2 + x_3 + (1 + e^{-x_1^2})u_1 + u_2 \\ \dot{x}_2 = -3x_2 + \sin x_3 + 3u_1 \\ \dot{x}_3 = x_1 - x_2^2 x_3 - 0.4x_3 - 0.1\mathrm{sat}x_3 \end{cases} \tag{14}$$

$$\mathrm{sat\,v} = \mathrm{v} \text{ if } |\mathrm{v}| \leq 1, \mathrm{sat\,v} = \mathrm{sig\,v} \text{ if } |\mathrm{v}| \succ 1 \tag{15}$$

with the outputs

$$\begin{cases} y_1 = x_1 \\ y_2 = x_2 \end{cases} \tag{16}$$

It comes the following notations:

$$f(x) = \begin{bmatrix} -2x_1 \cos x_2 + x_3 \\ -3x_2 + \sin x_3 \\ x_1 - x_2^2 x_3 - 0.4x_3 - 0.1\mathrm{sat}x_3 \end{bmatrix}; G(x) = \begin{bmatrix} 1 + e^{-x_1^2} & 1 \\ 3 & 0 \\ 0 & 0 \end{bmatrix} \tag{17}$$

and

$$h(x) = \begin{bmatrix} x_1 \\ x_2 \end{bmatrix} \tag{18}$$

To verify if the system admits an input-output linearization, we must determine the relative degree. We obtain by derivation of the outputs:

$$\begin{cases} \dot{y}_1 = \dot{x}_1 = -2x_1 \cos x_2 + x_3 + (1 + e^{-x_1^2})u_1 + u_2 \\ \dot{y}_2 = \dot{x}_2 = -3x_2 + \sin x_3 + 3u_1 \end{cases} \tag{19}$$

as $h_{i_x}^T G \neq 0$, we have

$$h^*(x) = f(x) = \begin{bmatrix} -2x_1 \cos x_2 + x_3 \\ -3x_2 + \sin x_3 \end{bmatrix}, G^* = \begin{bmatrix} 1 + e^{-x_1^2} & 1 \\ 3 & 0 \end{bmatrix} \tag{20}$$

G^* being invertible, we can impose the input u defined by (3)

$$\begin{bmatrix} u_1 \\ u_2 \end{bmatrix} = \begin{bmatrix} \dfrac{3x_2 - \sin x_3 + v_2}{3} \\ 2x_1 \cos x_2 - x_3 + v_1 - \dfrac{1}{3}(1 + e^{-x_1^2})(3x_2 - \sin x_3 + v_2) \end{bmatrix} \tag{21}$$

$$\begin{cases} \dot{y}_1 = \dot{x}_1 = -2x_1 \cos x_2 + x_3 + (1 + e^{-x_1^2})\left(\dfrac{3x_2 - \sin x_3 + v_2}{3}\right) \\ \quad + \left(2x_1 \cos x_2 - x_3 + v_1 - \dfrac{1}{3}(1 + e^{-x_1^2})(3x_2 - \sin x_3 + v_2)\right) \\ \dot{y}_2 = \dot{x}_2 = -3x_2 + \sin x_3 + 3\left(\dfrac{3x_2 - \sin x_3 + v_2}{3}\right) \end{cases} \tag{22}$$

it comes

$$\begin{cases} \dot{y}_1 = v_1 \\ \dot{y}_2 = v_2 \end{cases} \quad (23)$$

Let us choose

$$v_1 = \frac{1}{\tau_1}(y_1^c - y_1)$$
$$v_2 = \frac{1}{\tau_2}(y_2^c - y_2) \quad (24)$$

For constant inputs $y_j^c \quad \forall j = 1,2$ it comes:

$$\dot{v}_1 = -\frac{\dot{y}_1}{\tau_1} = -\frac{\dot{x}_1}{\tau_1} = -\frac{1}{\tau_1}v_1$$
$$\dot{v}_2 = -\frac{\dot{y}_2}{\tau_2} = -\frac{\dot{x}_2}{\tau_2} = -\frac{1}{\tau_2}v_2 \quad (25)$$

If we now take into account, the presence of uncertainties on f and G, it comes

$$\begin{aligned} \dot{x}_1 &= v_1 + \delta f_1 + G_{11}u_1 + \delta G_{12}u_2 \\ \dot{x}_2 &= v_2 + \delta f_2 + G_{21}u_2 + \delta G_{22}u_2 \\ \dot{x}_3 &= \delta f_3 + x_1 - x_2^2 x_3 - 0.4x_3 - 0.1\text{sat}x_3 \end{aligned} \quad (26)$$

with: $$|\delta G| \le \begin{bmatrix} 0.01 & 0.01 \\ 0.03 & 0.01 \\ 0 & 0 \end{bmatrix} \text{ and } |\delta f| \le \begin{bmatrix} 0.01 \\ 0.02 \\ 0.02 \end{bmatrix} \quad (27)$$

$$\begin{cases} \dot{x}_1 = -\dfrac{x_1}{\tau_1} + \delta f_1 + \delta G_{11}u_1 + \delta G_{12}u_2 \\ \dot{x}_2 = -\dfrac{x_2}{\tau_2} + \delta f_2 + \delta G_{21}u_1 + \delta G_{22}u_2 \\ \dot{x}_3 = \delta f_3 + x_1 - x_2^2 x_3 - 0.4x_3 - 0.1\text{sat}x_3 \end{cases} \quad (28)$$

for the vector norm $p(x) = \left[|x_1|,|x_2|,|x_3|\right]^T$, it comes the overvaluation:

$$\begin{aligned} \frac{d|x_1|}{dt} &\le -\frac{|x_1|}{\tau_1} + Max|\delta f_1| + Max|\delta G_{11}u_1| + Max|\delta G_{12}u_2| \\ \frac{d|x_2|}{dt} &\le -\frac{|x_2|}{\tau_2} + Max|\delta f_2| + Max|\delta G_{21}u_2| + Max|\delta G_{22}u_2| \\ \frac{d|x_3|}{dt} &\le Max|\delta f_3| + |x_1| - x_2^2|x_3| - 0.4|x_3| - 0.1|\text{sat}x_3| \end{aligned} \quad (29)$$

$$\frac{d|x_1|}{dt} \le -\frac{|x_1|}{\tau_1} + Max|\delta f_1| + Max\left|0.01\left(\frac{3x_2 - \sin x_3 + v_2}{3}\right)\right|$$
$$+Max\left|0.01\left(2x_1\cos x_2 - x_3 + v_1 - \frac{1}{3}(1+e^{-x_1^2})(3x_2 - \sin x_3 + v_2)\right)\right|$$

$$\frac{d|x_2|}{dt} \le -\frac{|x_2|}{\tau_2} + Max|\delta f_2| + Max\left|0.03\left(\frac{3x_2 - \sin x_3 + v_2}{3}\right)\right|$$
$$+Max\left|0.01\left(2x_1\cos x_2 - x_3 + v_1 - \frac{1}{3}(1+e^{-x_1^2})(3x_2 - \sin x_3 + v_2)\right)\right|$$

$$\frac{d|x_3|}{dt} \le Max|\delta f_3| + |x_1| - x_2^2|x_3| - 0.4|x_3| - 0.1|\text{sat}x_3| \quad (30)$$

For

$$\tau_1 = 1, \tau_2 = 0.5 \quad (31)$$

it comes

$$\frac{d|x_1|}{dt} \le -|x_1| + Max|\delta f_1| + Max\left|0.01\left(\frac{x_2 - \sin x_3}{3}\right)\right|$$
$$+Max\left|\begin{array}{l} 0.01\left(x_1(2\cos x_2 - 1) - x_3\right) \\ -\dfrac{0.01}{3}\left((1+e^{-x_1^2})(x_2 - \sin x_3)\right) \end{array}\right|$$
$$\frac{d|x_2|}{dt} \le -2|x_2| + Max|\delta f_2| + Max\left|0.03\left(\frac{x_2 - \sin x_3}{3}\right)\right| \quad (32)$$
$$+Max\left|\begin{array}{l} 0.01\left(x_1(2\cos x_2 - 1) - x_3\right) \\ -\dfrac{0.01}{3}\left((1+e^{-x_1^2})(x_2 - \sin x_3)\right) \end{array}\right|$$
$$\frac{d|x_3|}{dt} \le Max|\delta f_3| + |x_1| - x_2^2|x_3| - 0.4|x_3| - 0.1\left|\frac{\text{sat}x_3}{x_3}\right||x_3|$$

Taking into account inequalities (26) we obtain:

$$\frac{d|x_1|}{dt} \le |x_1|\left(-1 + 0.01|2\cos x_2 - 1|\right)$$
$$+|x_2|\left(\frac{0.01}{3} + \frac{1}{3}(1+e^{-x_1^2})\right) + 0.01 + \left|\frac{-0.01\sin x_3}{3}\right|$$
$$-0.01|x_3| + \frac{0.01}{3}\left|(1+e^{-x_1^2})(\sin x_3)\right| + 0.01$$
$$\frac{d|x_2|}{dt} \le |x_2|\left(-2 + 0.01 + \frac{0.01}{3}(1+e^{-x_1^2})\right) + 0.02$$
$$+\left|\frac{0.03\sin x_3}{3}\right| + 0.01|x_3| + \frac{0.01}{3}\left|(1+e^{-x_1^2})(\sin x_3)\right| \quad (33)$$
$$+|x_1|(0.02\cos x_2 - 0.01) + 0.02$$

$$\frac{d|x_3|}{dt} \le 0.02 + |x_1| - x_2^2|x_3| - 0.4|x_3| - 0.1\left|\frac{\text{sat}x_3}{x_3}\right||x_3|$$

it comes

$$\frac{dp(x)}{dt} \le M(x)p(x) + N(x) \quad (34)$$

with

$$M(x)=\begin{bmatrix} m_{11} & m_{12} & m_{13} \\ m_{21} & m_{22} & m_{23} \\ m_{31} & m_{32} & m_{33} \end{bmatrix}$$

$$\begin{aligned}
m_{11} &= -1+0.01(2\cos x_2-1) \\
m_{12} &= \left|\frac{0.01}{3}+\frac{1}{3}(1+e^{-x_1^2})\right| \\
m_{13} &= |-0.01| \\
m_{21} &= |0.02\cos x_2-0.01| \\
m_{22} &= -2+0.01-\frac{0.01}{3}(1+e^{-x_1^2}) \\
m_{23} &= |-0.01| \\
m_{31} &= 1 \\
m_{32} &= 0 \\
m_{33} &= -0.4-x_2^2-0.1\left|\frac{\mathrm{sat}x_3}{x_3}\right|
\end{aligned} \tag{35}$$

for the linear comparison system it comes

$$M=\begin{bmatrix} -0.99 & 0.67 & 0.01 \\ 0.03 & -1.993 & 0.01 \\ 1 & 0 & -0.4 \end{bmatrix} \tag{36}$$

The conditions for M to be the opposite of an M-matrix are:

$$\begin{cases} -0.99<0 \\ (-0.99\times -1.993)-(0.03\times 0.67)>0 \\ (-1)^3\det(M)\prec 0 \Rightarrow (-1)^3\times(-0.7348)>0 \end{cases} \tag{37}$$

The overvaluation of $N(x)$

$$N(x)=\begin{bmatrix} 0.01+\left|\frac{-0.01\sin x_3}{3}\right|+\frac{0.01}{3}\left|(1+e^{-x_1^2})(\sin x_3)\right| \\ 0.02-\left|\frac{0.03\sin x_3}{3}\right|+\frac{0.01}{3}\left|(1+e^{-x_1^2})(\sin x_3)\right| \\ 0.02 \end{bmatrix} \tag{38}$$

gives:

$$N=\begin{bmatrix} 0.02 \\ 0.0367 \\ 0.02 \end{bmatrix} \tag{39}$$

It comes out:

$$\lim_{t\to+\infty} p(z)\le \begin{bmatrix} 0.0349 \\ 0.0196 \\ 0.1372 \end{bmatrix} \tag{40}$$

The following figure shows the evolution of the error between the process with and without uncertainties

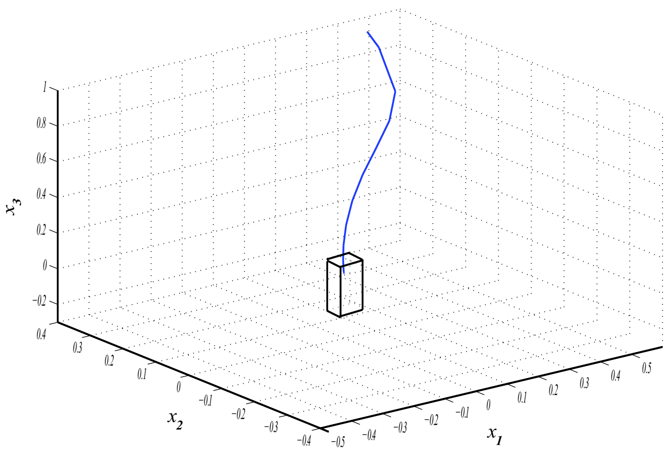

Fig. 2 Attractor D and evolution of the state vector

V. Conclusion

The use of aggregation techniques and of comparison systems enables to estimate by overvaluation the maximum error induced by the use of a non-perturbed model for the determination of the input-output decoupling of a nonlinear process in presence of uncertainties and/or bounded perturbations.

Appendix

Appendix A. Vector Norms Definition

Definition1 : Let $\mathrm{E}=\mathrm{R}^n$ and $\mathrm{E}_1, \mathrm{E}_2 \ldots \mathrm{E}_k$ be subspaces of the space E, $\mathrm{E}=\mathrm{E}_1\cup\mathrm{E}_2\ldots\cup\mathrm{E}_k$.
Let x be an n vector defined on E and $x_i=P_i x$ the projection of x on E_i, where P_i is a projection operator from E into E_i, p_i a scalar norm (i=1,2,…, k) defined on the subspace E_i and p denotes a vector norm of dimension k and with its component

$$p_i(x)=p_i(x_i)\ , \quad p(x): R^n \to R_+^k$$

Let y be another vector in space E, with $y_i=P_i y$, we have the following properties

$$\begin{cases} p_i(x_i)\ge 0, \forall x_i\in \mathrm{E}_i \forall i=1,2,\ldots,k \\ p_i(x_i)=0 \leftrightarrow x_i=0, \forall i=1,2,\ldots,k \\ p_i(x_i+y_i)\le p_i(x_i)+p_i(y_i), \forall x_i,y_i\in \mathrm{E}_i \forall i=1,2,\ldots,k \\ p_i(\lambda x_i)=|\lambda|\, p_i(x_i), \forall x_i \forall i=1,2,\ldots,k, \forall \lambda \cup R \end{cases}$$

If k-1 of the subspaces E_i are insufficient to define the whole space E, the vector norm is surjective. If in addition the subspaces E_i are in disjoint pairs, $\mathrm{E}_i\cap\mathrm{E}_j=\varnothing$, $\forall i\ne j=1,2,\ldots,k$, the vector norm p is said to be regular.

ISBN: 978-1-61804-321-4

Appendix B. Overvaluing and comparison systems

Let the differential equation $\dot{x} = A(x,t)x$. The overvaluing system is defined by the use of the vector norm $p(x)$ of the state vector x and the use of the right-band derivation $D^+ p_i(x_i)$ proposed by [13], [14] $D^+ p_i(x_i)$ is taken along the motion of x in the subspace E_i and $D^+ p(x)$ along the motion of x in E.

Definition 2: The matrix $M(x,t)$ defines an overvaluing system of S with respect to the vector norm p if and only if the following inequality is verified for each corresponding component: $D^+ p(x) \leq M(x,t)\, p(x)$

If for the same system we can define a constant overvaluing matrix M, we have $M \geq M(x,t)$ and we have $z(t) \geq p(x(t))$ for $t \geq t_0$ as soon as this property is satisfied at the origin t_0

When an overvaluing matrix $M(x,t)$ of a matrix $A(x,t)$ is defined with respect to a regular vector norm p we have the following properties:

- The off- diagonal elements of matrix $M(x,t)$ are non negative.
- If we denote by $\mathrm{Re}(\lambda_M)$ the real part of the eigenvalue of the maximum real part of $M(x,t)$ the following inequality is verified

$\mathrm{Re}(\lambda_A) \leq \mathrm{Re}(\lambda_M) = \lambda_M \quad \forall t, x \in \tau \times \mathbb{R}^n$,

whatever the eigenvalue λ_A of matrix $A(x,t)$

- When all the real parts of the eigenvalues of M (x, t) are negative this matrix is the opposite of an M-matrix and it admits an inverse whose elements are all non positive.
- When due to perturbations and/or uncertainties it is not possible to define an homogeneous overvaluing system we can define a non homogeneous overvaluing system of the form $D^+ p(x) \leq M(x,t)\, p(x) + N(x,t)$, where all the elements of vector norm nonnegative and when M and N are constant, we can define the comparison system $\dot{z} = Mz + N$

Remark 1. With $M(.) = \{m_{ij}(.)\}$ the verification of the Kotelyanski lemma by the matrix $M(.)$ prove that $M(.)$ is the opposite of an M-matrix

$$m_{1,1} \prec 0, \begin{vmatrix} m_{1,1} & m_{1,2} \\ m_{2,1} & m_{2,2} \end{vmatrix} \succ 0, \ldots, (-1)^k \begin{vmatrix} m_{1,1} & m_{1,2} & \cdots & m_{1,k} \\ m_{2,1} & m_{2,2} & \cdots & m_{2,k} \\ \vdots & \vdots & \cdots & \vdots \\ m_{k,1} & m_{k,2} & \cdots & m_{k,k} \end{vmatrix} \succ 0$$

Remark 2. A less conservative approach consists to use a vector norm of size k=n, for example $p(x) = \left[|x_1|, |x_2|, \ldots, |x_n|\right]^T$

Remark 3. If $M(.)$ is an overvaluing matrix of a matrix $A(.)$, $M(.) + M^*$ where the elements of M^* are all non negative is also an overvaluing matrix of $A(.)$. This property can be used to simplify the determination of an overvaluing matrix of $A(.)$ when some elements of $A(.)$ are ill defined or subject to uncertainties.

References

[1] B. Jakubczyk, W. Respondek, "On linearization of control systems," Bull. Acad. Pol. Sci. Ser. Sci. Math, vol. 44, no. 9-10, 1980, pp. 517-522.

[2] R. Marino, S. Peresada, and P. Valigi, "Adaptative Input-Output Linearizing Control of Induction Motors," *IEEE Tran. Oon Automatic Control*, vol. 38, no. 2, pp. 208- 221, February. 1993.

[3] H. K. Khalil, "Nonlinear Systems ,"Third edition, Prentice Hall, 2002.

[4] J. Levine, "Analyse et Commande des Systèmes Non linéaires," Centre Automatique et Systèmes, Ecole des Mines de Paris, Mars, 2004.

[5] J. K..Hedrick, and A. Girard, "Feedback Linearization," Control of Nonlinear Dynamic Systems Theory and Applications, 2005.

[6] D. D. Siljac, "Stability of large scale systems under structural perturbations," *IEEE Trans. On Syst. Manand Cyber*, vol. 2, no.5, 1972.

[7] P. Borne, J. P. Richard, and N. E. Radhy, "Stability, stabilization, regulation using vector norms, Nonlinear Systems, 2, Stability and Stabilization," *Chapman and Hall, Chapter 2*,1996, pp. 45-90.

[8] A. Gharbi , M. Benrejeb, and P. Borne, " On nested attractors of complex continuous systems determination," Proceedings of the Romanian Academy, Series A, vol. 14, no. 2, .2013, pp. 259-265.

[9] A. Gharbi , A. Catalin, M. Benrejeb, and P. Borne, " New approach for the control and the determination of attractors for nonlinear systems," Systems and Computer Science, 2013, pp. 216-221.

[10] A. Gharbi, M. Benrejeb and P. Borne, "Tracking error estimation of uncertain Lur'e Postnikov systems," International Conference on Control Decision and Information Technologies (CoDIT'14) Metz, 3, 2014, pp. 537–540.

[11] A. Gharbi, M. Benrejeb and P. Borne, "Attractors determination of uncertain nonlinear systems controlled by state feedback," Wulfenia Journal, vol. 21, no. 9, 2014.

[12] A. Isidori, "Nonlinear control systems: an introduction", Springer Verlag, 1989.

[13] M .N. Rosenbrock, "A Lyapunov function for some naturally accuring linear, homogeneous time dependent equations," Automatica, 1963.

[14] I. W. Sandeberg, "Some theorems on the dynamic response of non linear transistor network," Bell Syst. Tech. J., vol. 48, no. 35, 1969.

Amira Gharbi graduated from the "Faculté des Sciences de Tunis" in 2006. She obtained the Master degree in Automatic Control and Signal Processing in 2008 at the National Engineering School of Tunis. She has received her Ph.D. in Electrical Engineering in 2013, within the framework between the National Engineering School of Tunis and the "Ecole Centrale de Lille". She is currently Assistant Professor at the " Ecole Nationale d'Ingénieurs de Carthage". Actually, she is member of the LARA Automatic Control Research Laboratory at the National Engineering School of Tunis

Mohamed Benrejeb has obtained the Engineering Diploma in 1973. He has received the Master in 1974, the Ph.D. in Electrical Engineering in 1976 and the D.Sc. in 1980, from the University of Sciences and Techniques of Lille. Actually, he is full Professor at the National Engineering School of Tunis, since 1985, and at the "Ecole Centrale de Lille", since 2003.

Pierre Borne is Professor at the Ecole Centrale de Lille

(France). He received the Master degree of Physics in 1967, the Masters of Electrical Engineering, of Mechanics and of Applied Mathematics in 1968. The same year he obtained the Diploma of "Ingénieur IDN" (French "Grande Ecole"). He obtained the PhD in Automatic Control of the University of Lille in 1970 and the DSc of Physics of the same University in 1976. He became Doctor Honoris Causa of the Moscow Institute of Electronics and Mathematics in 1999, of the University of Waterloo (Canada) in 2006 and of the polytechnic University of Bucharest (Romania) in 2007. He is author or co-author of more than 220 Journal Articles and Book Chapters, and has presented 32 plenary lectures and more than 300 Communications in International Conferences. He is author of 26 books and has been the supervisor of 85 PhD theses, past President of the IEEE-SMC society and past President of the IEEE France Section. He is IEEE Fellow and has received distinctions from 8 countries for his research activities.

Monitoring and analysis for on/off faults in microstrip rectangular patch array antenna by means of characteristic parameters

Hassan M.Elkamchouchi, Samy H.Darwish, Yasser H Elkamchouchi, M.E.Morsy
[a] Faculty of Engineering, Alexandria University, Alexandria, Egypt
[b] Faculty of Engineering, Pharos University, Alexandria, Egypt
[c] Faculty of Engineering, Pharos University, Alexandria, Egypt
[d] Air Defense College, Alexandria, Egypt
Email: yasser.elkamshoushy@pua.edu.eg

Abstract**—**Related to the advantage of microstrips, this paper presents a regarding design and simulation of four rectangular microstrip patch array antenna working at 2.4 GHz and its characteristic parameters analysis for the on/off modeled faults that may be caused by feeding discontinuity in the antenna elements. The faults are one, two and three fault models. Some of specified antenna parameters were monitored and analysed to describe the antenna performance. The characteristic parameters are max radiation intensity, directivity, gain, returned loss and efficiency. The suggested array was analysed using Ansof/Ansys high frequency structural simulator (HFSS). The results give an obvious deviation in characteristic parameters values where operating frequency is shifted due to faulty elements, the antenna parameters are decreased, such as the directivity value (5.78, 4.40, 3.25, and 1.91dB in case of normal, one, two, and three faulty elements respectively). The final results give adequate indication to the antenna performance in normal and faulty cases.

Keywords**—**Antenna parameters, microstrip antenna, on/off faults.

I. INTRODUCTION

The microsrip patch is generally designed as square, rectangular, circular, and triangular or some other common shape. The rectangular microstrip patch antenna is the most widely used of all types of microstrip antennas. The substrate material, dimension of antenna, feeding technique will determine the performance of the antenna [2].

The substrate material is Rogers TMM4 with $\varepsilon_r = 4.5$. antenna gain and directivity can be enhanced when an array of patch elements is used instead of single patch. Hence among different feeding techniques, the inset fed technique is used for the design of rectangular patch antenna at 2.4GHz to improve input impedance [3].

Element failure as one of the on/off faults in an array antenna may occur due to the disturbance in the driving equipments, feed lines or the array elements themselves which may result in element radiation or partial failures [4],[5].

The element failure can distort the directivity of the antenna power pattern and it also leaves undesired effects on the sidelobe level of the radiation pattern, returned loss and the whole performance of the array antenna.

A. Antenna Shape

A rectangular patch is used as the main radiator. The patch is generally made of conducting material such as copper or gold and can take any possible shape as shown in Fig. 1.

For good antenna performance, a low dielectric constant (ε_r) typically in the range $2.2 < \varepsilon_r < 12$with thick dielectric substrate is desirable, as it provides better radiation and better efficiency [2].

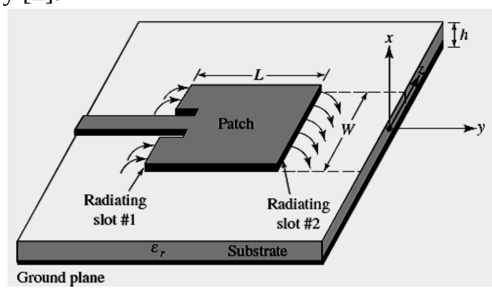

Fig. 1 rectangular microstrip patch antenna.

B. Design of Single Patch

The required specifications for a single patch are:
Resonant Frequency (f_0) = 2.40 GHz, Dielectric constant of Substrate (ε_r) = 4.5, height of the substrate (h) =1.6mm.

Using the standard formulae and the standard design considerations a single patch was designed with the following parameters [2], [5]; Fig. 2. Shows the shape of single patch:
Width of the patch (W) = 46.66 mm, Length of the patch (L) =38.765 mm, inset position (y_0) = 9.65 mm, Inset width (W_0) =3 mm, gap width(X_0) =1.15mm.

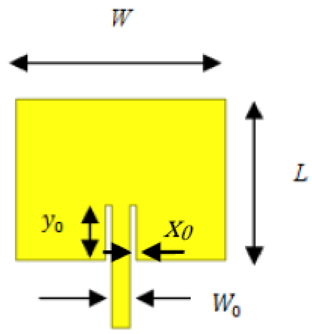

Fig. 2 single patch.

For antenna array design the physical spacing between the elements and the structure of the feed was determined using the above information. The designed array is shown in Fig. 3.

To obtain zero grating lobes we kept the inter element spacing to be λ/2. The feed length was taken to be approximately λ/4 for impedance transformation at the desired resonant frequency of 2.4GHz.

The initial width of the feed that connects the single patch to the entire feed structure was taken to be the same as inset width (W_0) [2], [6].

ISBN: 978-1-61804-321-4

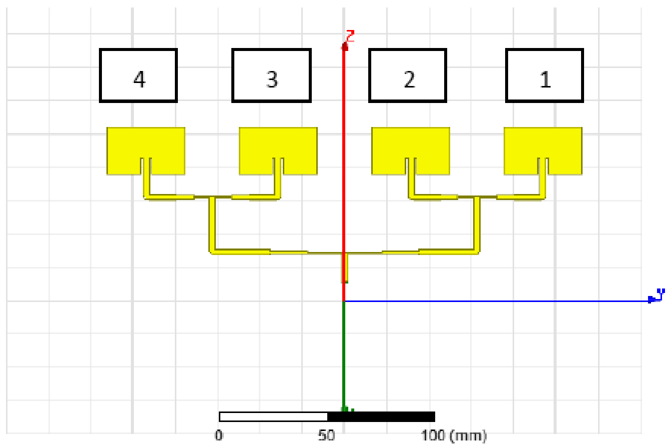

Fig. 3 designed array.

II. Fault Generation and Pattern Deviations

A single, double, and triple fault modeling with different combinations of faults in the elements antenna array were considered.

In order to generate failure in one element, it is supposed that the feed line of this element was distorted in a way that the element couldn't be fed by the directed serial feed lines (on/off fault) [7].

The corresponding radiation pattern with normal and one, two and three typically faulty elements respectively are shown in Fig .4. It can be seen evidently from the figure that element failure causes sharp variations in the sidelobe level of the radiation pattern with the increase in the number of faulty elements.

The radiation pattern of an antenna is a plot of the far-field radiation properties of an antenna as a function of the spatial co-ordinates which are specified by the elevation angle (θ) and the azimuth angle (φ). The radiation pattern shows the antenna's directivity as well as gain at various points in space.

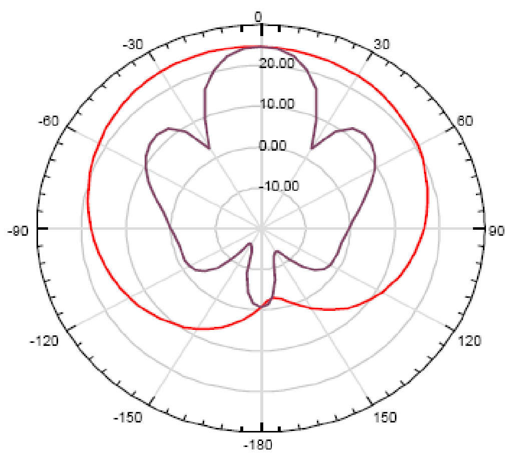

(a)

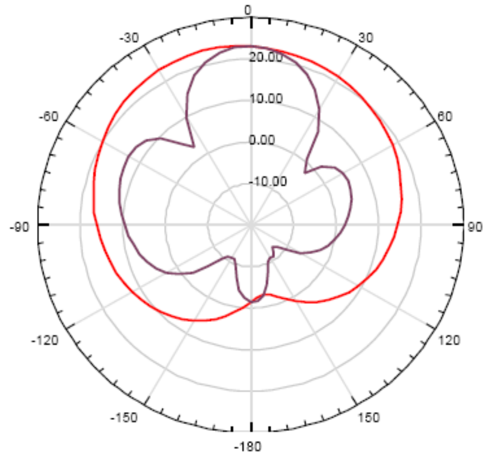

(b)

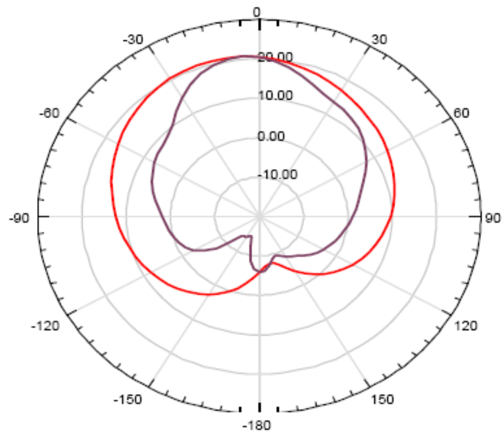

(c)

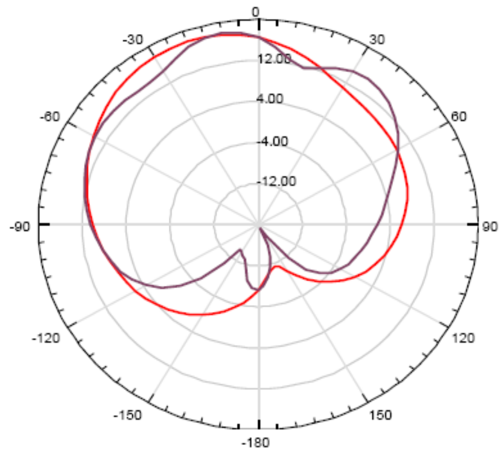

(d)

Fig. 4 the radiation patterns; (a) Normal case, (b) One element fault, (c) Two elements fault, and (d) Three elements fault.

From Fig. 4, it can be shown that the change in radiation pattern at (φ =0 degree-red curve) is clear more than at (φ =90 degree-purple curve) except in case of three element fault the change is clear at (φ =0 and 90 degree). The radiation pattern is symmetric in normal case and unsymmetrical in faulty cases. side lobe ratio is 0.5 dB for case (a) and 0.55 dB for case (b), while it can be seen that there is no side lobes for cases (c) and (d) but a low levels of directivity as compared to cases (a) and (b), and that is because of the malfunction in those cases.

III. Characteristic Parameters

To monitor and analyse the antenna performance for normal and faulty cases corresponding to its radiation pattern some parameters as; the returned loss $|S_{11}|$, max radiation intensity (Max U), directivity, gain, radiated and accepted power, efficiency, as characteristic parameters. The following section represents these parameters in figures and tabulated form.

A. Return Loss $|S_{11}|$

$|S_{11}|$ is a parameter which indicates the amount of power that is "lost" in the load and does not return as a reflection. Hence $|S_{11}|$ indicates how well the matching between the transmitter and antenna has taken place. Fig. 5, is a graph of $|S_{11}|$ of an antenna vs frequency. For optimum working such a graph must show a dip at the operating frequency and have a minimum value at this frequency.

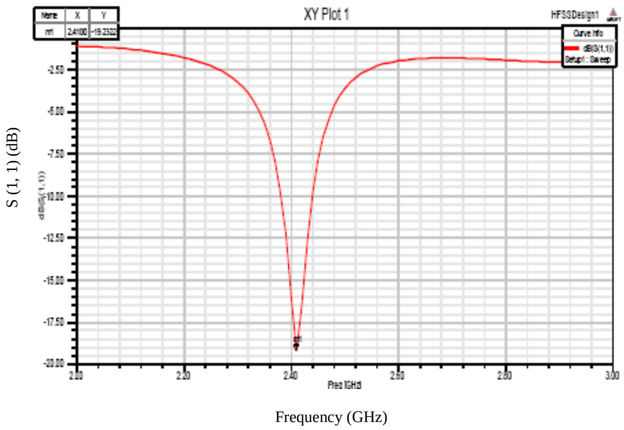

(a)

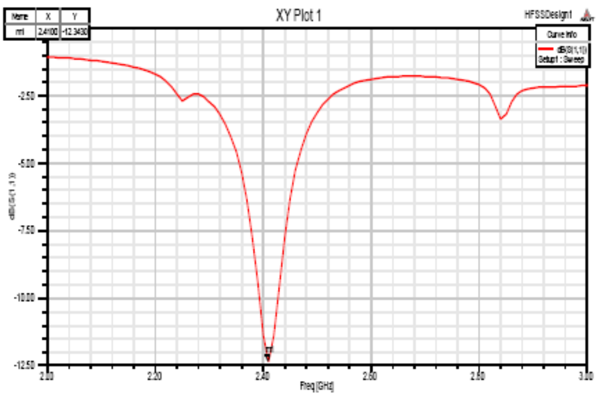

(b)

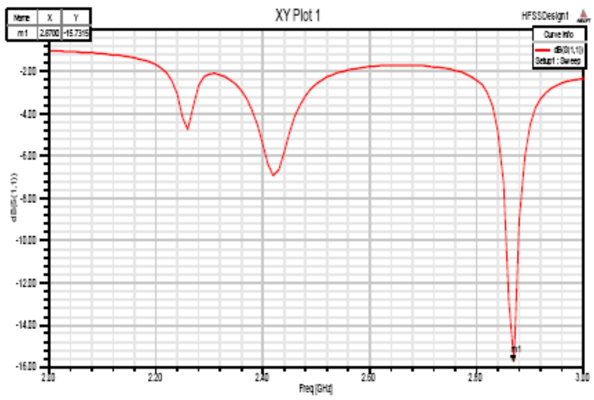

(c)

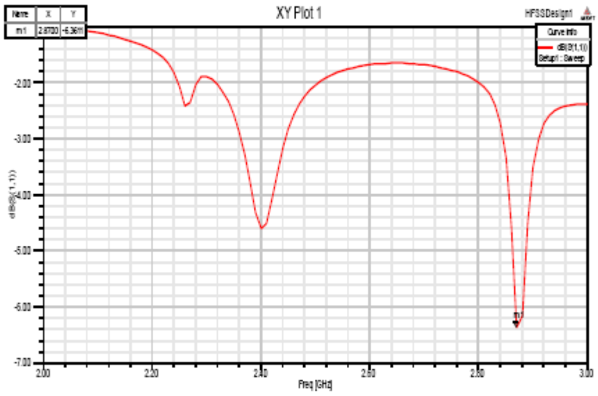

(d)

Fig. 5 the return loss; (a) Normal case, (b) One element fault, (c) Two elements fault, and (d) Three elements fault

From Fig. 5, which illustrates the return loss for the four cases, it can be seen that there is a shift in the operating frequency in normal case of 2.41 GHz, but in case of two and three fault elements the deviation in the frequency is 2.87 GHz and that is out of the tolerance value as the maximum limit of tolerance is 2% [7].

For case (a) – the normal case – the array is working from 2.38 to 2.43 GHz with more than-10 dB and maximum of -19.22 dB at 2.41 GHz. For case (b) the array is working from 2.4 to 2.42 GHz with max of -12.48 dB at 2.41 GHz. For both cases (c) and (d) a significant decrease in the return loss occur due to the faults of the elements and the antenna is not working at the operating frequency.

B. Max U, Directivity and Gain.

Another useful measure describing the performance of an antenna is the gain which is defined as the ratio of the radiation intensity, in a given direction, to the radiation intensity that would be obtained if the power accepted by the antenna were radiated isotropically.

Although the gain of the antenna is closely related to the directivity, it is a measure that takes into account the efficiency of the antenna as well as its directional capabilities.

ISBN: 978-1-61804-321-4

If an antenna is has no dissipative loss, then in any given direction, its gain is equal to its directivity [2], [8]. These parameters will be declared in table I and the bar chart.

C. Radiated Power, Accepted Power and Radiation Efficiency.

Resistive losses, due to non-perfect metals and dielectric materials, exist in all antennas. Such losses result in a difference between the power delivered to the input of an antenna and the power radiated by that antenna.

As with other electrical components, the radiation efficiency can be defined as the ratio of the desired output power to the supplied input power. In order to account for the fact that an antenna with radiation efficiency less than unity will not radiate all of its input power, so the antenna gain can be defined as the product of directivity and efficiency) [9].

Table I and its bar chart (Fig.6) give information about the maximum antenna parameters; as the values of max U, peak directivity, peak gain, radiated power, accepted power, radiation efficiency.

TABLE I
CHARACTERISITC PARAMETERS

case / parameters	Single Patch	Normal array	One element fault	Two element fault	Three element fault
Max U(w/st)	0.12	0.41	0.29	0.16	0.08
Peak Directivity (dimension less)	1.6	5.78	4.40	3.25	1.91
Peak Gain (dB)	1.5	5.32	4.02	2.93	1.70
Radiated Power (w)	0.92	0.89	0.84	0.64	0.58
Accepted Power (w)	0.98	0.97	0.92	0.71	0.65
Radiation Efficiency(%)	94	92	91	90	89

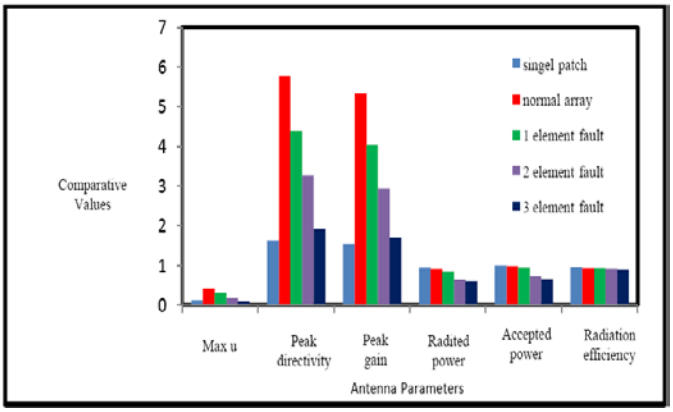

Fig. 6 the bar chart.

Table I illustrates the effect of on/off fault on the antenna performance and hence the deviations in the characteristic parameters for normal and faulty cases. The directivity and gain of the antenna array are increased more than in case of single patch, that reflects the usage of array.

The radiated, accepted power and efficiency of single patch is more than in case of normal array and that may be related to consume power in the feeding network.

The bar chart indicates a survey on antenna in various cases-normal and faulty- giving information about the variation in the maximum antenna parameters for all studying cases, hence the normal array has maximum values max U, peak directivity, peak gain otherwise the three element fault has minimum values.

IV. Conclusions

In normal case at resonant frequency there is a dip in return loss of -19.23 dB which gives very good antenna performance.

The deviation in values of return loss parameter and radiation pattern from those of fault-free case is valid.

The values of returned loss of two and three faulty elements indicate that the antenna is not working at operating frequency.

In case of the fault in three elements they work as a parasitic elements which make inter-mutual effect for working element and that is clear in the increasing of directivity parameter in comparison to a single patch.

In the future work there will be an improvement in the designed antenna based on yagi antenna to increase the directivity and gain, then the faults analysis will be based on neural networks and support vector machine.

References

[1] www.AnsoftHFSS.com

[2] Constantine A. Balanis Antenna Theory Analysis and Design 3rd ed, 2005.

[3] Sandhya Sharma, Abhishek Sharma “Variation in Inset Parameters of Microstrip Patch Antenna for Improved Performance” International Journal of Engineering Research and Applications(IJERA), Vol. 2, pp.2225-2227, 2012.

[4] A.R. Mallahzadeh and M. Taherzadeh “Element Failure Diagnosis in a Planar Microstrip Antenna Array by the Use of Neural Networks,”*IEEE Conference* on digital object identifier, pp.294-298, 2010.

[5] Fouzi Harroua and Mohamed N. Nounoua “Monitoring Linear Antenna Arrays Using an Exponentially Weighted Moving Average based Fault Detection Scheme" System Science& Control Engineering: An Open Access Journal, 2014.

[6] Rameh Garg, Prakash Bahrita ,Inder Bahl and Apisk Ittipiboon, *Microstrip Antenna Design Handbook* , Artech House, Boston London, 2001.

[7] Umesh Kumar1, Rajiv Kapoor “Patch Antenna Array Fault Modeling and its Monitoring,” IOSR Journal of Electronics and Communication Engineering, 2012.

[8] IEEE Standard Definitions of Terms for Antennas, March 18, 1993.

[9] David M .Pozar, *Microwave Engineering* 3rd ed , 2005.

ISBN: 978-1-61804-321-4

Graphical Programming for Control and Instrumentation Curses

Jorge M. Jaimes Ponce, Jesús U. Liceaga C., Irma I. Siller A. and Roberto A. Alcántara R.

Abstract**—**Normally commercial software and equipment for control and instrumentation lectureships are rather expensive for public universities reducing student's opportunities to develop important professional skills. However, different technologies have emerged which considerably reduce the costs of this learning process without using real industrial components. This paper tackles the issue of the study of control engineering and instrumentation from three different approaches applying the LabVIEW graphical programming language. The first one, based exclusively in simulation; the second, is by means of the use of Arduino; and the third, is by applying the commercial hardware from National Instrument. These strategies are well within public universities budgets.

Keywords**—**Graphical Programming, Process Simulation, Arduino.

I. Introduction

THEACHING control engineering or instrumentation using industrial devices or components may result highly costly even with the use of equipment specifically designed for educational purposes. When the lack of economic resources is a reality, a common practice to overcome the deficiency of industrial components is the use of digital simulations or the development of own software, mainly based on C language, Visual Basic, etc. Although, the development of software is an excellent alternative it may takes a considerably long time. A second option is to acquire a LabVIEW license, [1]. This software can be used for teaching purposes by creating software applications. For instance, the development of Virtual Instruments (VI) applications to simulate industrial devices such as fluid containers, pressurized tanks, furnaces, engines, etc. or temperature, flux and pressure sensors.

Another alternative is to use commercial systems based on microcontrollers like Arduino. Arduino is a very economic microcontroller for which already exist many LabVIEW applications allowing the substitution of the data acquisition hardware.

A final option is the use of the National Instruments software, from which the modulus for USB data acquisition are the cheapest and sufficient enough for many applications.

J. M. Jaimes-Ponce is with the Electronic Department of the UAM-Azcapotzalco, Av. San Pablo 180 C.P. 02200, México (e-mail: jjp@correo.azc.uam.mx).

J. U. Liceaga-Castro is with the Electronic Department of the UAM-Azcapotzalco, Av. San Pablo 180 C.P. 02200, México (phone: 52-55-53189041 ; e-mail: julc@correo.azc.uam.mx).

I. I. Siller-Alcalá is with the Electronic Department of the UAM-Azcapotzalco, Av. San Pablo 180 C.P. 02200, México (e-mail: sai@correo.azc.uam.mx).

R. A. Alcántara-Ramírez is with the Electronic Department of the UAM-Azcapotzalco, Av. San Pablo 180 C.P. 02200, México (e-mail: raar@correo.azc.uam.mx).

II. Approaches General Description

A. Simulation of Process using LabVIEW

One of the most important aspects of the use of LabVIEW for process simulation is that it is possible to implement the mathematical model of a process in a SubVI [2], such that its dynamical behavior can be simulated under different operating conditions or several parametrical configurations. Moreover, this model simulation can be used for control purposes using ON/OFF or PID controllers. In the same way, a sensor can be also simulated. With the use of several of these VI's it is possible to simulate more complex systems which can include real industrial conditions for voltages, currents, pressures and fluxes, making the simulations more realistic.

B. Control and Instrumentation of Process using LabVIEW and Arduino

Arduino has become a very popular and powerful system despite its limitations in speed and capacities for data processing compared to other microcontrollers, [3]. Nonetheless, it represents a low-cost helpful option due to all the support available to create interfaces with LabView. The A/D converters, digital E/S and PWM generation make Arduino a good device for the control and instrumentation for applications not demanding high capabilities for data processing.

Several tools or functions are available for serial connections and A/D – D/A converters linked to the generation of PWM signals, Figure 1. These functions can be used to implement different and interesting projects.

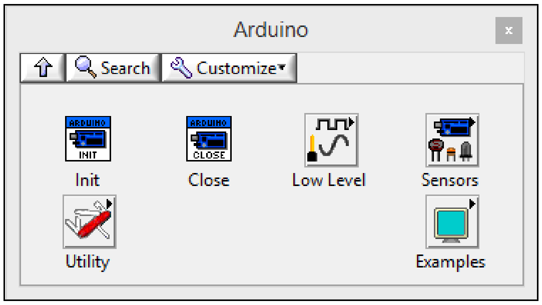

Fig. 1 Arduinos tools for LabVIEW

C. Control and Instrumentation of Process using LabVIEW

A third relatively economic option is to use National Instrument Data Acquisition Boards (NIADQ). In the market of the process instrumentation and control there are several data acquisition boards for general purposes with USB communication. In this case a real process or at least a prototype is required. A real industrial process may be really expensive; however, it is possible to construct a prototype at a considerably lower cost than a real process. The prototype of a Level process, depicted in Figure 2, consists of an acrylic tank of 50cm deep, a submerge water pump, a MPX2010DP pressure sensor -Figure 3- to indirectly measure the liquids level, and the PSV-5 proportional valve shown in Figure 3.

Fig. 2 Prototype of a Level process

Fig. 3 MPX2010DP pressure sensor

Fig. 4 PSV-5 proportional valve

III. Approaches Development

A. Simulation using Graphical Programming

The aim of creating SubVIs for the simulation of several industrial devices is to induce the students to the analysis of the dynamical models and data sheets of such devices. This will enable them to face real industrial conditions. For example, by consulting the data sheet of a humidity sensor the students must deduce that this variable depends on the environments temperature or with the dynamical model of a level system it must be also concluded that the liquids flow depends on the density and level of the liquid.

By analyzing the data sheet of the temperature sensor PT100 it can be assumed that it has linear behavior, [4]. Based on this characteristic it can be also determine how to condition its output signal using electronic components to generate measurements within industrial standards such as *0* to *5 volts* or *4* to *20 mA*. The SubVI of a PT100, in Figures 5 and 6, show the output voltage, proportional to the resistance, assuming a *1 mA* input current.

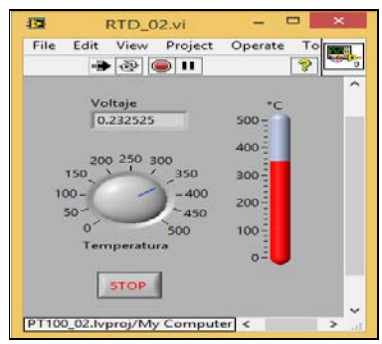

Fig. 5 SubVI frontal panel of the PT100

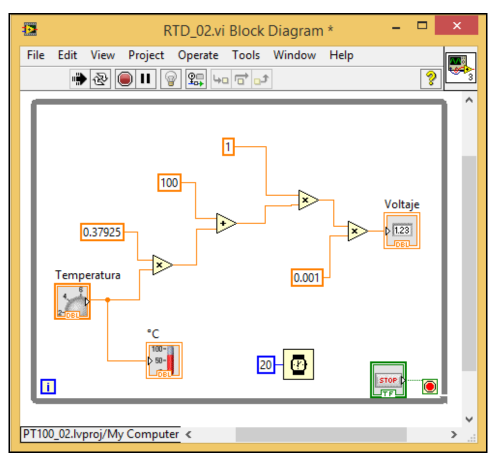

Fig. 6 PT100 SubVI program

ISBN: 978-1-61804-321-4

With the SubVI of the PT100 it is possible to use it, as a specific function, in the implementation of a block diagram of some process which requires sensing the temperature, Figure 7.

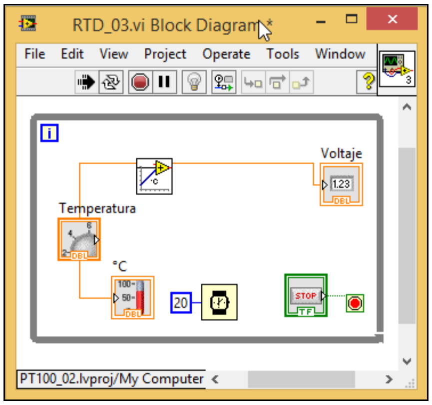

Fig. 7 Application of the PT100 SubVI

Other example consists in the implementation or simulation -Figure 8 and 9- of differential equations describing the dynamical behavior of a level system with output flow.

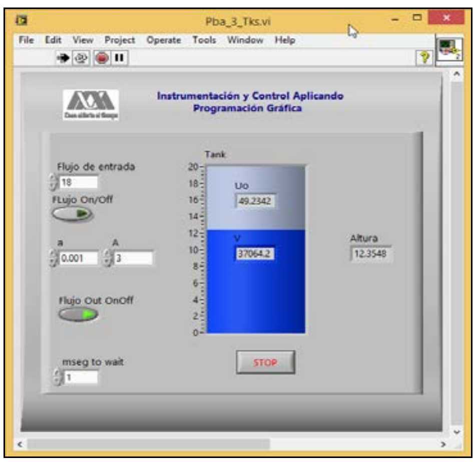

Fig. 8 Level System simulation

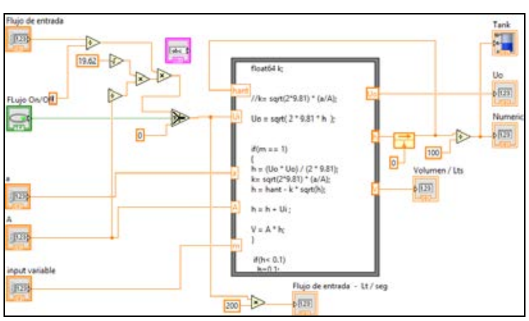

Fig. 9 Block diagram of a Level System model

Similar to the previous example, with the SubVI of the Level System it is possible to develop a VI to simulate a Level Control System which can include several interconnected tanks, Figures 10 and 11.

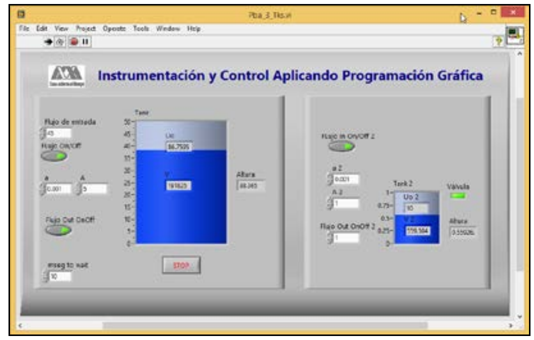

Fig. 10 Control Level System VI with two tanks

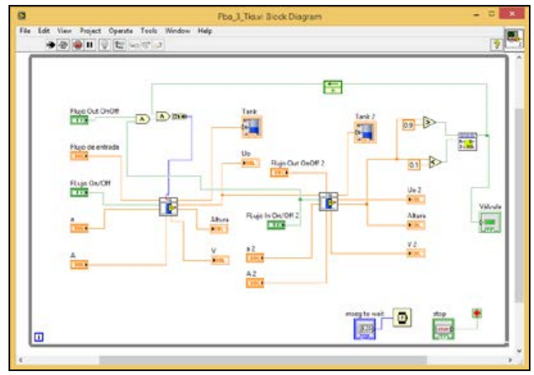

Fig. 11 Control Level System VI block diagram with two tanks

B. *LabVIEW and Arduino*

As mentioned above, Arduino includes a connecting or communication toolbox just like a typical USB data acquisition boards has, Figure 12. Obviously, Arduino doesn't have the resolution of industrial data acquisition boards; nevertheless, for some applications it is a powerful and economic alternative.

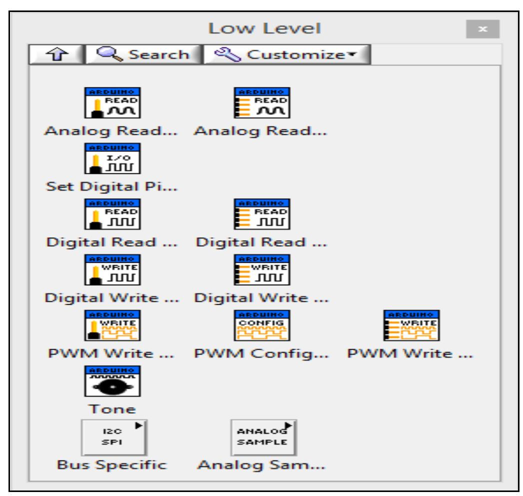

Fig. 12 Arduino communication toolbox

If a real process or a prototype is not available it is possible to emulate some simple processes using RC circuits. For example, to emulate a Level System with output flow a parallel RC circuit can be used as shown in Figure 13. In this case

ISBN: 978-1-61804-321-4

when switch S1 is off the capacitor C1 will discharge, and when switch S1 is on the capacitor will charge.

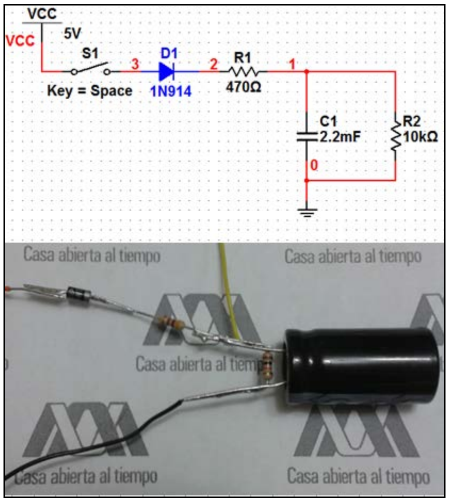

Fig. 13 RC Simulation of a Level System with output flow

Figures 14 and 15 show the charge and discharge of the capacitor showing a similar response to the level system with output flow. This VI displays the control panel from which it is possible to change the level of the liquid in the tank emulating the real tank.

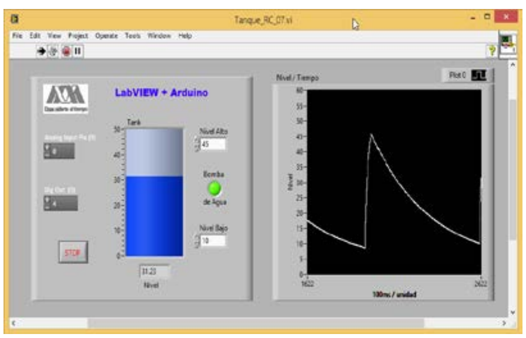

Fig. 14 VI using a RC circuit and Arduino

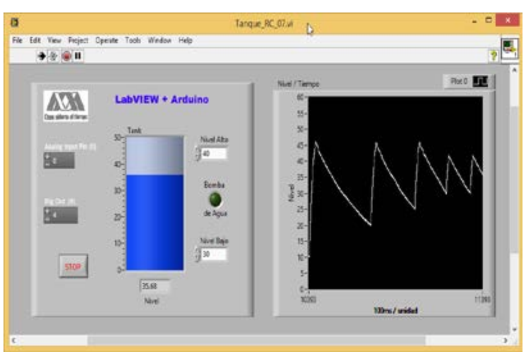

Fig. 15 VI using a RC circuit and Arduino with different control limits and hysteresis

The VI shown in Figure 16 is identical to anyone designed for a commercial data acquisition board; it only requires to substitute the Arduinos tools of data acquisition and signal generation for the specific functions of the commercial data board.

A relatively more complex application is the emulation of a Level system in which a largest tank is connected in series to two smaller tanks. This means that the largest tank feeds the two smaller tanks.

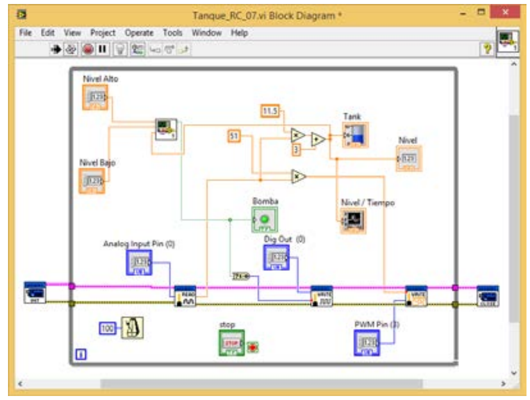

Fig. 16 Block diagram of the Level Control System with hysteresis of two tanks

Figures 17 and 18 show the diagram and the actual RC circuit that emulate the three tanks level system.

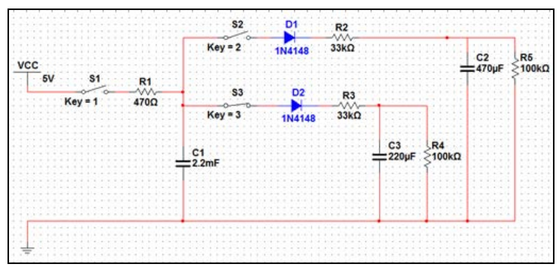

Fig. 17 Diagram of the RC circuit to emulate the three tanks system

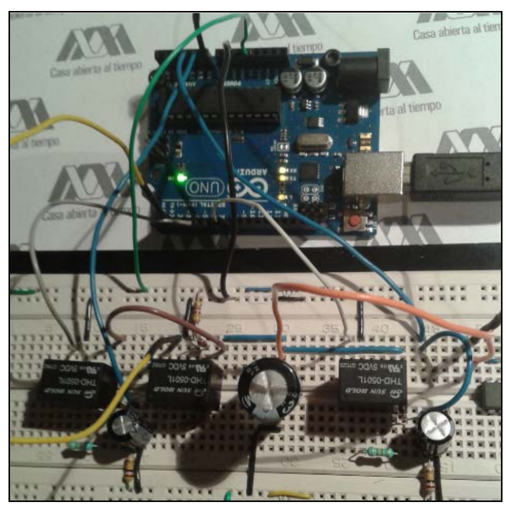

Fig. 18 Actual diagram of the RC circuit to emulate the three tanks system

The control panel of the three tank level system is shown in figure 19.

ISBN: 978-1-61804-321-4

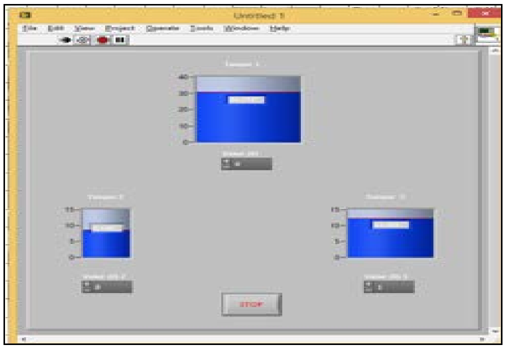

Fig. 19 Frontal Panel for the three tanks system

Finally in Figures 20, 21 and 22 three responses of the control of the level system emulated by the RC circuit are shown. In this case, the controller is based on the classical PID with a block diagram depicted in Figure 23.

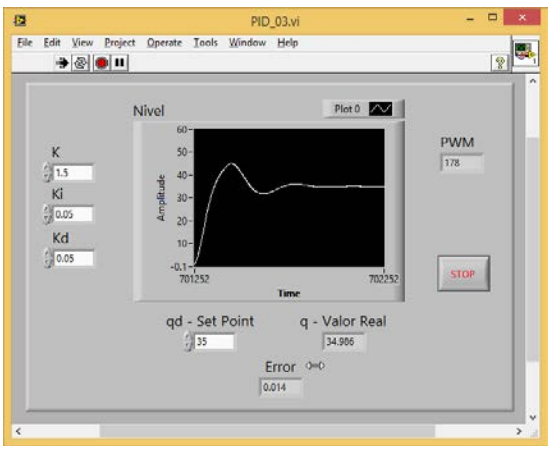

Fig. 20. Level System response with a PID controller (K_p = 1.5, K_i = 0.05 and K_d = 0.05.)

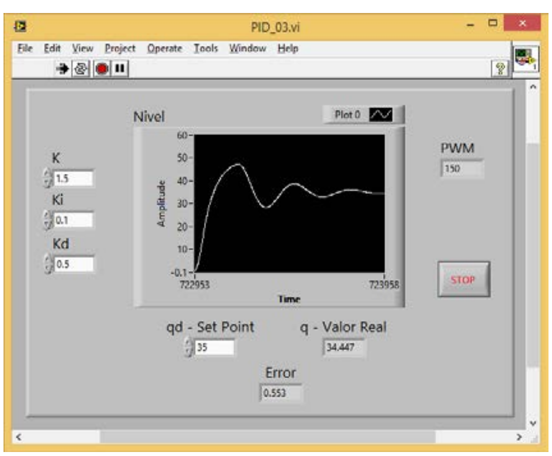

Fig. 21 Level System response with a PID controller (K_p= 1.5, K_i = 0.1 and K_d = 0.5.)

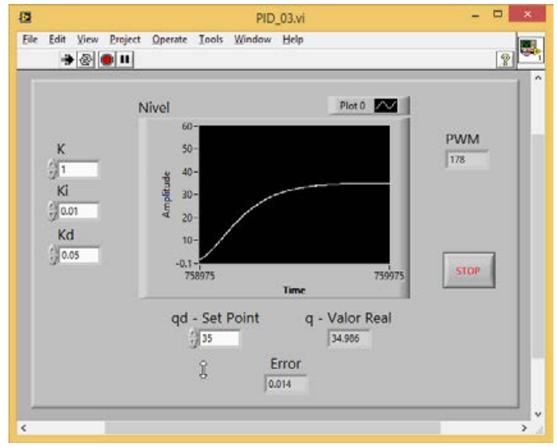

Fig. 22 Level System response with a PID controller (K_p= 1, K_i = 0.1 and K_d = 0.5.)

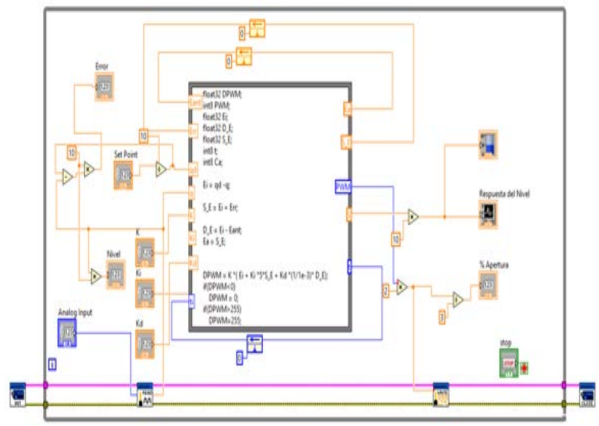

Fig. 23 Block Diagram of the PID controller

C. Instrumentation and Control using LabVIEW and the NI USB-6009 Data Acquisition Board

The electronic circuits and prototypes described in the previous sections can be controlled using the data acquisition board NI USB-6009 from National Instrument getting exactly the same results. The only difference is the exchange of the function blocks for those specifically designed to the USB-6009. For the level control of the single tank system shown in Figure 2 the PID controller programmed in the *Formula Node* to control the RC circuit tank emulator was used. It only requires a retuning using the actual parameters of the process.

Once the system or process has been characterized the PID parameters can be tuned in the *Formula Node* getting the closed loop responses shown in Figures 25-28.

ISBN: 978-1-61804-321-4

Fig. 25 Level System response with a PID controller (K_p = 5, K_i = 0.1 and K_d = 0.05.)

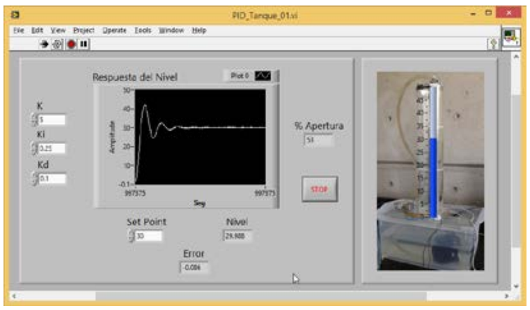

Fig. 26 Level System response with a PID controller (K_p = 5, K_i = 0.25 and K_d = 0.1.)

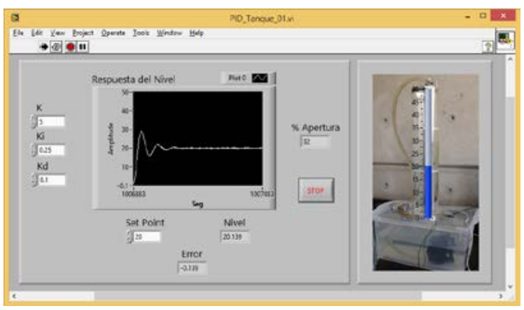

Fig. 27 Level System response with a PID controller (K_p = 5, K_i = 0.25, K_d = 0.1 and Set Point = 20.)

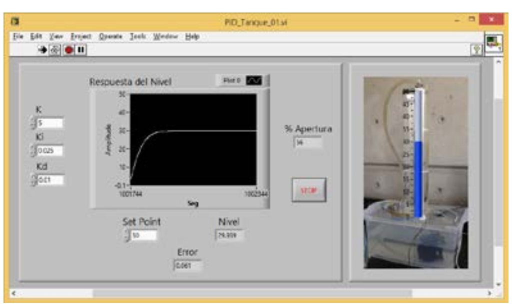

Fig. 28 Level System response with a PID controller (K_p = 5, K_i = 0.025 and K_d = 0.01.)

IV. Conclusion

In this paper three different teaching approaches that help to overcome the lack of real industrial process or components in control and instrumentation lectureships are presented. This approaches aid in the comprehension and understanding of these complex topics that otherwise must be treated in a pure theoretical context. We consider that equilibrium between practice and theory is a must. On the other hand, to get access to costly real industrial process is not always possible. In this sense the use of Arduinos represent a good alternative especially with the development of new economical sensors that can be used to construct non expensive prototypes capable to emulate real industrial processes. This has also been possible due to possibilities that LabVIEW and Arduino offer. With the use of commercial of Data Acquisition Boards the possibilities of better experiments increase.

References

[1] Ronald W. Larsen, “LabVIEW for Engineers”, E-SOURCE, Prentice-Hall, 2011.

[2] Peater A. Blume, “The LabVIEW Style Book”, Prentice Hall, 2009.

[3] Don Wilcher, “Learn Electronics with Arduino”, Technology in Action, 2013.

[4] Lawrence T. Illage, Ronald A. Roher, Chandramouli Visweswariah, “Electronic Circuits and Systems Simulation Methods”, McGraw-Hill, Inc., 1995.

Maintainability analysis of mobile robot

Panagiotis H. Tsarouhas and George K. Fourlas

***Abstract*—**Maintainability analysis is used to improve the efficiency of the robotic system based on the adequate maintenance actions. In this paper, the maintainability characteristics and the critical failure modes of the system with respect to repair frequency and duration were identified. Data collection from the robotic system and their analysis were valid for a period of thirty four months. Furthermore, the maintainability and repair rate modes for all failure modes were calculated. Moreover, maintainability for different time periods at failure level and the entire system have been estimated on the basis of fitted distribution models. This study is anticipated to serve as a valid data source for robotic systems product manufacturers, who wish to improve the design and operation of their systems.

***Keywords*—**Applied statistics, Maintainability, mobile robot, repair data.

I. Introduction

MAINTAINABILITY is a fundamental tool to estimate the operation and support costs of systems and equipment. On the other hand, maintainability is a design factor and addresses the ease, accuracy, timeliness and economy of maintenance actions [1]. In [2] reported that some of the objectives for applying maintainability engineering principles to systems are to reduce projected maintenance cost and time through design modifications directed at maintenance simplifications, to use maintainability data for estimating equipment availability, and to determine labor hours and other related resources required to perform the projected maintenance.

There is vast literature on maintainability and reliability analysis with a high number of books and articles. Research [3] and [4] describes concurrent engineering in detail and presented application examples in various industries. Work [5] has discussed the application of reliability, maintainability and risk analysis methods to minimize the life cycle cost of the system. In [6] reported a methodology for determining sample sizes for system availability on the assumption that the time between failures and the times to repair are independently and exponentially distributed. In paper [7] a guide for achieving and assessing RAM (reliability, availability, and maintainability) was developed. In [8] reported on 26 cases on reliability and maintainability and statistical techniques illustrated including modelling, reliability assessment and prediction, simulation, testing, failure analysis, regression analysis, reliability growth modelling and analysis, repair policy, availability analysis, and others. [9] presents probabilistic analysis of a system consisting of a robot and its associated safety mechanism. Expressions along with plots for the robot system availability and state probabilities are presented. Moreover, in [10] an interval method to chalk out the reliability analysis of robot was used. Authors in [11] proposed an optimal maintenance strategy on the basis of reliability engineering in fault-tolerant multi-robot systems. Paper [12] quantifies the gain in productivity of a team of repairable robots compared to a team without repair capabilities based on reliability theory.

Mobile robots and unmanned vehicles are being increasingly used (and considered for future use) in nuclear plants [13], for search and rescue [14], [15], surveillance [16], security [17] and inspection [18]. Tele-operated mobile robots are generally directed along a path using manual controls and the master system has often been a joystick although other input devices are available, for example a pointer, switches or can be custom built such as virtual reality interfaces and other more complex systems are being considered [19]. Generally, they are fitted with controllers that interface low-current input devices to high-current servo amplifiers, sometimes remotely through a radio connection or umbilical cable.

The corresponding literature related to the maintainability and reliability analysis of failure data for mobile robots is quite limited. Paper [20] describes a set of four autonomous robots used for a period of five years as full-time museum docents. Their robots reached a mean time between failures (MTBF) of 72 to 216 hours. Authors in [21] proposes a new approach, where the reliability analysis of mobile robots was studied and suggestions based on mean time between failures (MTBF), mean time to repair and downtime, for system performance, were given. In [22] the reliability analysis of a mobile robot system by applying statistical techniques based on failure data was studied. In another study [23] maximized the autonomy and interactivity of the mobile platform (with10 autonomous robots) while ensuring high robustness, reliability and performance. The result pointed out that their MTBF was

This research is implemented through the Operational Program "Education and Lifelong Learning" and is co-financed by the European Union (European Social Fund) and Greek national funds. The work is part of the research project entitled «DIAGNOR - Fault Diagnosis and Accommodation for Wheeled Mobile Robot» of the Act "Archimedes III - Strengthening Research Groups in TEI of Central Greece".

P. H. Tsarouhas, is with the Department of Supply Chain Management & Logistics, Technological Educational Institute of Central Macedonia, Katerini 60100, Greece, (phone: +30- 23510-47862; fax: +30-23510-47860; e-mail: ptsarouhas@teicm.gr).

G. K. Fourlas is with the Department of Computer Engineering, Technological Educational Institute (T. E. I.) of Central Greece, Lamia 35100, Greece, (phone: +30-22310-60186; fax: +30-22310-33945; e-mail: gfourlas@teiste.gr).

around 7 hours. Research [24] estimates mission reliability for a repairable robotic system and then extended the approach to multi-robot system design and presented the first quantitative support for the argument that larger teams of less-reliable robots can perform certain missions more reliably than smaller teams of more-reliable robots. In other study [25] surveyed failure and maintenance reports from two large automotive plants. The reports covered 200 robots representing five manufacturers over a period of 21 weeks. The robots were found to be down for repair or maintenance for 3.95 hrs per week per manufacturing line in the first plant and 1.74 hrs in the second.

In this study, the maintainability analysis of a mobile robot system for a period spanning thirty four months was carried out. The best fitness index parameters of the repair data were computed. Moreover, the maintainability and repair rate modes for all the failure modes of the robotic system were calculated. Finally, the system maintainability for different time periods has been estimated on the basis of fitted distribution models

II. Description of the Mobile Robot System

Through this research the experimental procedure was carried out using a Pioneer 3-AT mobile robot. Pioneer is a four wheel skid – steering robot driven by two motors, Fig. 1.

Fig. 1 The mobile robot Pioneer 3-AT.

One drives the wheels left and the other, the wheels on the right. The wheels on the same side are connected mechanically and consequently have the same speed. The robot is equipped with two high resolution optical quadrature shaft encoders, mounted on reversible-DC motors which provide rotational speeds of the left and right wheels respectively and an inertial measurement unit (IMU) which provides the forward linear acceleration and the angular velocity as well as the angle between the mobile robot axle and the axis of the mobile robot.

III. Repair Data

Repair data of the robotic system were collected from the files of the researchers by the end of each experimental day. The mobile robot operates continuously ten-hour during each day, five days per week. According to the records, a total of 117 failures were determined for the entire system. Thus, the repair data cover a period of 34 mounts. Thus, the total operating time of the robot is 7480 hours. The records include the failures occurring per day, the action taken to repair the failure, the down time, and the exact time of failure. Therefore, there is the exact time both for the component failure and the repair of this failure.

To describe the basic features of the repair data the *time-to-repair* (TTR) analysis is used. The TTR of system is defined as the time that elapses from the moment the equipment goes down and stops until the moment it goes up and starts operating again. The TTRs are recorded in minutes, whereas the time-between-failures (TBFs) are recorded in hours.

The currently applied maintenance policy of the robotic system is corrective maintenance; the corrective maintenance is unscheduled and carried out whenever a failure occurs, the procedure requires immediate action of the technician to restore the system into operational state. This maintenance policy may include any or all the following steps: recognition, localization & diagnosis, correction (disassemble, remove, replace, reassemble, and adjust), and operation checkout. The corrective maintenance is used during the period the robotic system is running.

There is a distinct possibility of trading-off between reliability and maintainability since availability depends only on the ratio, *a*, that is referred to as maintenance time ratio and is defined as [26]:

$$a=\frac{meanTTR}{meanTBF} \tag{1}$$

Table I: Calculation of maintenance time ratio α at failure mode level for the robotic system

	Failures	Total TBF	Total TTR	Mean TBF	Mean TTR	α
F1	53	7478.200	108	138.7	2.264	0.00027205
F2	35	7477.067	176	208	5.143	0.00041210
F3	20	7477.283	163	356.6	8.15	0.00038091
F4	7	7479.150	51	936	7.286	0.00012974
F5	2	7479.383	37	2496	30	0.00020032

In Table I, the maintenance time ratios for the robotic system were computed. From Table 1 the following observations can be made: (a) the lowest total time to repairs are at the motor (F5) and the battery (F4) with 37 minutes and 51 minutes respectively. On the other hand, the highest total time to repairs are at the gradual loss of tire pressure (F2), the loss of wireless communication (F3), and the fault in the encoder reading (F1) with 173, 163, and 108 minutes respectively. (b) The lowest maintenance time ratio are at the gradual discharge of the battery (F4), malfunction of the motor (F5), and the fault in the encoder reading (F1) with 0.00012974, 0.00020032, and 0.00027205. Therefore, the maintenance of these failure modes is satisfactory, and c) the highest maintenance time ratios are at the gradual loss of tire pressure (F2) and loss of wireless communication between the robot on-board computer and the base station (F3) with

ISBN: 978-1-61804-321-4

0.00041210 and 0.00038091 respectively. Thus, the maintenance policy of these failure modes must be reviewed immediately.

The motor (F5) has only two failures; therefore no further analysis is needed.

IV. Data Analysis

After collection, sorting and classification of the repair data, the validation of the assumption for independent and identically distributed (*iid*) nature of the TTR of each failure must be identified. The repair data are independent, meaning the data are free of trends and that each repair is independent of the preceding or succeeding repair. Identically distributed data mean that all the data in the sample are obtained from the same probability distribution. Verification of the assumption that the repairs are independent and identically distributed is critical. If the assumption that the data are independent is not valid, classical statistical techniques for reliability analysis may not be appropriate.

According to [27], there are two methods for the validation of the models, the chi-square test and the Kolmogorov–Smirnov test. In this study, the chi-square test is applied. Initially, the null hypothesis H_0: *No-trend in data* (homogeneous Poisson process), and the alternative hypothesis H_1: *Trend in data* (non-homogeneous Poisson process) is considered. Moreover, the test statistic X^2 is chi-square distributed with $2(n-1)$ degrees of freedom-*df* [28]. The X^2 statistic is calculated from the experimental repair data, whereas the $x^2_{a,df}$ can be determined from the chi-square distribution given the degrees of freedom. If the statistic $X^2 > x^2_{a,df}$ then the null hypothesis is plausible, otherwise the null hypothesis is rejected and the alternative hypothesis H_1 is accepted. The validation of the trend for the TTR at failure mode level are displayed in Table II, and at a = 5% level of significance in robot system the H_0 is not rejected.

Table II Calculation of the test statistic X^2 for TTR at failure mode level.

Failure mode	Variable	*df*	X^2 *statistic*	$x^2_{a,df}$	Decision for H_0
F1	TTR	104	96.99	81.4678	Not reject
F2	TTR	68	65.09	50.0202	Not reject
F 3	TTR	38	35.49	24.8839	Not reject
F 4	TTR	12	10.34	5.22603	Not reject

A serial correlation diagram represents the sketching of $\widehat{\rho_k}$ against lag k, where $\widehat{\rho_k}$ are the correlation coefficients and lag k are the lag-time periods separating the ordered data. Correlation coefficients, $\widehat{\rho_k}$, range in value from -1 (a perfect negative relationship) to +1 (a perfect positive relationship). A value of 0 indicates no linear relationship that is no-correlation. Figure 2 shows the serial correlation diagrams for the TTR at failure mode level that present no-correlation on repair data.

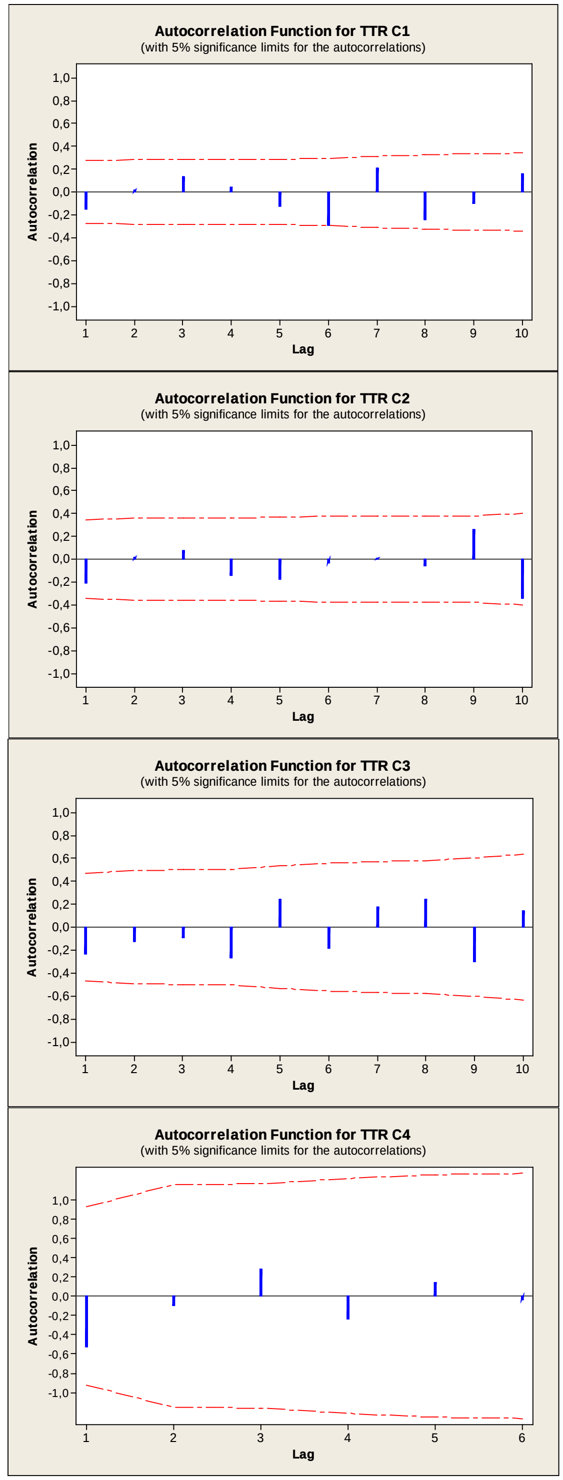

Fig. 2 Correlation diagrams for the TTR at failure mode level for the robotic system.

Thus, from the trend test and the serial correlation test, it is obvious that the repair data for all failures are free from the presence of trends and serial correlations. Therefore, an independent and identically distributed (*iid*) assumption for TTR data of the robotic system is justified.

Table III: The Anderson-Darling statistics for TTR at failure mode level. The smaller the statistic value, the better the model fitting (i.e. in system of F1 the lowest value is 2.748 which belongs to the Weibull distribution).

	T	T	R	
Failure modes	**Weibull**	**Lognormal**	**Exponential**	**Normal**
F1	2.748*	3.462	8.758	2.778
F 2	2.256*	2.278	11.288	2.272
F 3	1.147*	1.318	6.134	1.197
F 4	2.178*	2.217	3.544	2.217

**indicates the best-fit of the repair data between the candidate distributions*

To identify the distributions of the trend-free failure data between several theoretical distributions (i.e. Weibull, lognormal, exponential, and normal distribution), the maximum likelihood estimation method was used per candidate distribution and assessed its parameters by applying a goodness-of-fit test - Anderson-Darling. The Anderson-Darling statistics of several theoretical distributions for TTR based on repair data of the failure mode level are summarized in Table III. A smaller statistic value indicates that the distribution fits the data better, i.e. at all failures the TTRs follow the Weibull distribution

V. Maintainability Analysis

The Maintainability in terms of mathematics is defined as the probability that a failed system will be restored to operational effectiveness within a given period of time t when the repair action is performed in accordance with the prescribed procedures. In other words, maintainability is the probability of completing the repair at a given time. If T_r is the continuous random variable representing the time-to-repair (TTR) of the system, having a probability density function of $r(t)$, then according to [29] the maintainability is:

$$M(t) = P(T_r \le t) \quad (2)$$

The repair rate function is given by,

$$\lambda_r(t) = r(t)/(1 - M(t)) \quad (3)$$

Maintainability analysis is used to identify any weaknesses in maintenance operation on the robotic system. As mentioned above for all the failure modes, the TTR follows the Weibull distribution. The probability density function with respect to corrective maintenance times is expressed by [2]

$$r(t) = \frac{2}{\alpha^{\theta}} t^{\theta-1} \exp(-\frac{t}{\alpha})^{\vartheta} \quad (4)$$

where $r(t)$is the corrective maintenance or repair time probability density function, t is the variable repair time, θ is the distribution shape parameter, α and is the distribution scale parameter.

Substituting equation (4) into Equation (2) yields

$$M_W(t) = P(T_r \le t) = \int_0^t \frac{2}{\alpha^{\theta}} t^{\theta-1} \exp(-\frac{t}{\alpha})^{\vartheta} dt = 1 - \exp(-\frac{t}{\alpha})^{\vartheta} \quad (5)$$

where $M_w(t)$ is the maintainability function for Weibull distribution.

Having identified the repair distribution from data and estimated the Weibull parameters (see Fig. 3) then, we can calculate the maintainabilities and repair rate models for robotic system for all failure modes, as follows:

$$M_{F_1,W}(t) = 1 - \exp(-\frac{t}{\alpha})^{\vartheta} = 1 - \exp(-\frac{t}{2.5575})^{2.5928}$$

$$r_{F_1}(t) = \frac{2}{\alpha^{\theta}} t^{\theta-1} \exp(-\frac{t}{\alpha})^{\vartheta} = \frac{2}{2.5575} t^{2.5928-1} \exp(-\frac{t}{2.5575})^{2.5928}$$

$$M_{F_2,W}(t) = 1 - \exp(-\frac{t}{5.5278})^{6.0152}$$

$$r_{F_2}(t) = \frac{2}{5.5278} t^{6.0152-1} \exp(-\frac{t}{5.5278})^{6.0152}$$

$$M_{F_3,W}(t) = 1 - \exp(-\frac{t}{8.8513})^{5.1928}$$

$$r_{F_3}(t) = \frac{2}{8.8513} t^{5.1928-1} \exp(-\frac{t}{8.8513})^{5.1928}$$

$$M_{F_4,W}(t) = 1 - \exp(-\frac{t}{7.8349})^{6.3404}$$

$$r_{F_4}(t) = \frac{2}{7.8349} t^{6.3404-1} \exp(-\frac{t}{7.8349})^{6.3404}$$

In Fig. 3, the repair rates for time-to-repair (TTR) of all failures of the robotic system are shown graphically in conjunction with the appropriate distributions and their statistics. It is evident that as the time passes the repair rate is increased, meaning that the technicians get experience with time and therefore they repair the failures faster.

ISBN: 978-1-61804-321-4

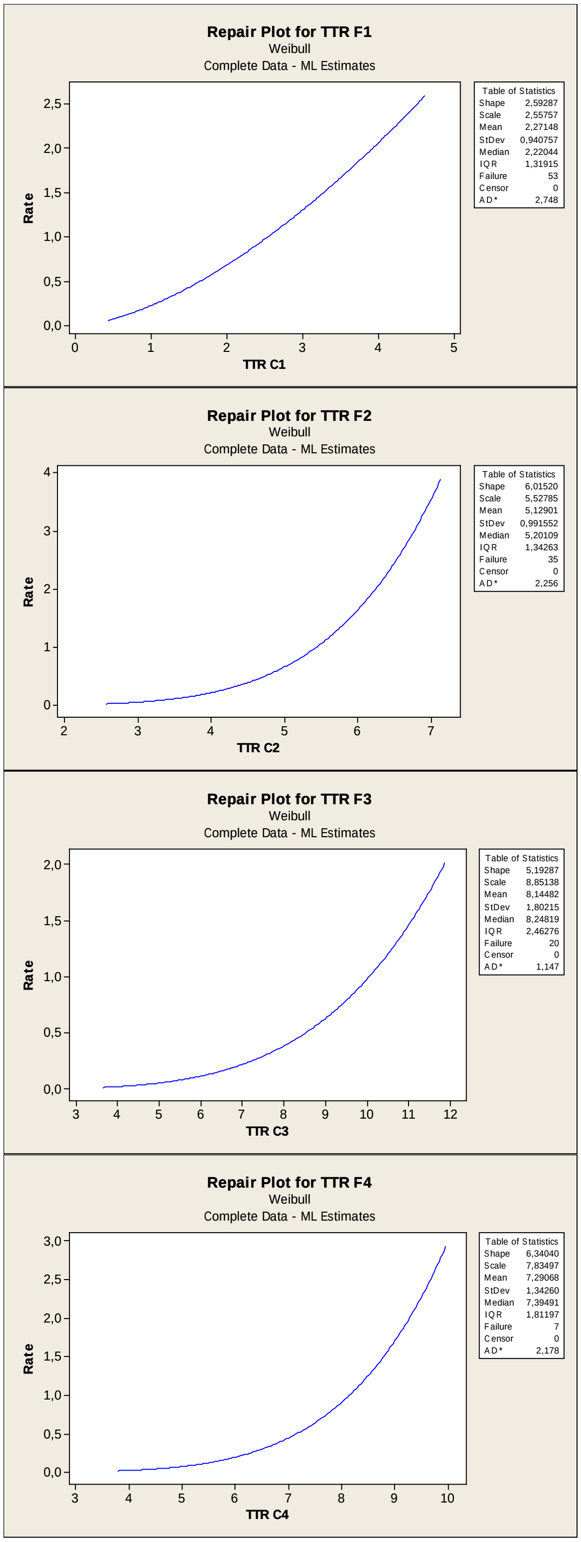

Fig. 3 Repair rate for time-to-repair (TTR) at failure mode level are shown graphically in conjunction with the appropriate distributions and their statistics.

The maintainability of different time intervals for all failures and the entire system are presented in Table IV. It is estimated that (a) the optimal repair level with the expected maintainability, that is, to achieve 95% maintainability for system, the repair must be carried out within 8 minutes. (b) For $M_{MAIN,F3}(10)=0.8480$, which means that there is a 84.80% probability that any failure in the loss of wireless communication between the robot on-board computer and the base station (F3) will be repaired within 10 minutes, and (c) there is a 100% probability that any failure in the entire system will be repaired within t=20 minutes.

In Fig. 4 the maintainabilities for the failure mode level and the system level are shown graphically, and it is observed that the maintainability must be improved on the loss of wireless communication between the robot on-board computer and the base station (F3), and on the gradual discharge of the battery (F4), and the entire robotic system as well.

Table IV. Maintainability of the robotic system at the end of different time intervals.

Time	MAIN F1	MAIN F2	MAIN F3	MAIN F4	MAIN Robot
1	0.083882	3.41486E-05	1.20863E-05	2.145E-06	0.083926423
2	0.410542	0.00220625	0.000441987	0.0001738	0.412204306
3	0.779622	0.024996106	0.003623567	0.0022703	0.786394835
4	0.958776	0.133118271	0.016040136	0.0139859	0.965328954
5	0.996611	0.421195684	0.050213055	0.0563206	0.998241736
6	0.999891	0.805483512	0.124342445	0.1682112	0.99998456
7	0.999999	0.984048229	0.255952813	0.3870334	0.999999991
8	1	0.999902862	0.446480106	0.6805930	1
9	1	0.999999993	0.663889318	0.9100380	1
10	1	1	0.848074144	0.9908797	1
11	1	1	0.954547481	0.9998151	1
12	1	1	0.992223981	0.9999997	1
13	1	1	0.999363580	1	1
14	1	1	0.999979885	1	1
15	1	1	0.999999809	1	1
20	1	1	1	1	1

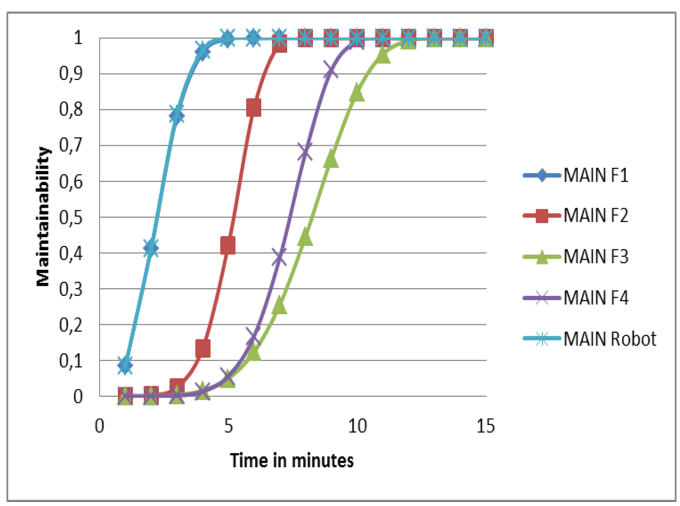

Fig. 4 Maintainability diagram for all failures and the entire robotic system.

ISBN: 978-1-61804-321-4

VI. Conclusion

The paper shows that the maintainability analysis is very useful for deciding maintenance intervals, planning and organizing maintenance. Moreover is a tool to determine "what" maintenance activities need to be taken on the event of failures occurring on the system and "how" much time is taken to carry out those maintenance activities.

The main research findings can be summarized as follows:

- The maintenance time ratios for all the failures of the robotic system were computed. The highest maintenance time ratios are at the gradual loss of tire pressure (F2) and loss of wireless communication between the robot on-board computer and the base station (F3). Thus, the maintenance policy of these failure modes must be reviewed immediately.
- From the trend test and the serial correlation test, it is obvious that the repair data for all failures are free from the presence of trends and serial correlations. Therefore, an independent and identically distributed (*iid*) assumption is justified for TTR data of the robotic system.
- A goodness-of-fit test - Anderson-Darling statistics to identity the distributions of the repair data was used. All the failure modes of the robotic system for TTRs follow the Weibull distribution.
- The maintainability and repair rate modes at failure mode level with their statistics were calculated, and
- The maintainability of different time intervals for all failures and the entire system are presented analytically.

For new similar robotic systems where data and information may be missing or unavailable, then it may be able to predict reliability and maintainability characteristics of the new one by using the repair data of this study that is anticipated to serve as a valid data source for robotic systems product manufacturers, who wish to improve the design and operation of their systems.

References

[1] A. Barabadi, J. Barabady, T. Markeset, "Maintainability analysis considering time-dependent and time-independent covariates". Reliability Engineering and System Safety, 2011, 96: 210-217.

[2] B.S. Dhillan, "Maintainability, maintenance, and reliability for engineering", CRC Press, Taylor & Francis Group, LLC, Boca Raton, FL, USA, 2006.

[3] W.R. Blischke, D.N.P. Murthy, "Reliability: modelling, prediction and optimization", 2000, Wiley, New York, USA.

[4] J.M. Usher, U. Roy, H.R. Parsaei, "Integrated product and process development", 1998, Wiley, Hoboken, NJ.

[5] T. Markeset, U. Kumar, "R&M and risk-analysis tools in product design, to reduce life cycle cost andimprove product attractiveness", Proceedings of Annual Reliability and Maintainability Symposium, IEEE, New York, NY,116-21, 2001.

[6] V.P. Singh, S. Swaminathan, "Sample sizes for system availability", Proceedings of Annual Reliability and Maintainability Symposium, 2002, IEEE, New York, NY, 51-5.

[7] Y. Jackson, P. Tabbagh, P. Gibson, E. Seglie, "The new Department of Defense (DoD) guide for achieving and assessing RAM", 2005, Proceedings of Annual Reliability and Maintainability Symposium, IEEE, New York, NY, 1-17.

[8] W.R. Blischke, D.N.P. Murthy, "Case Studies in reliability and Maintenance", 2003, pp. 351- 445, John Wiley & Sons, Inc., Hoboken, New Jersey, USA.

[9] B.S. Dhillon, A.R.M. Fashandi, "Robotic system's probabilistic analysis", Microelectronics Reliability, Vol. 37, No2, 1997, pp. 211–224.

[10] C. Carreras, I.D. Walker, "On interval methods applied to robot reliability quantification", Reliability Engineering and System Safety, Vol. 70, No3, 2000, pp. 291–303.

[11] S. Hoshino, H. Seki, and J. Ota, "Optimal Maintenance Strategy in Fault-Tolerant Multi-Robot Systems", IEEE/RSJ International Conference on Intelligent Robots and Systems September 25-30, 2011, pp. 2314-2320.

[12] C. Bererton, and P. Khosla, "An analysis of cooperative repair capabilities in a team of robots", Proc. 2002 IEEE Int. Conf Robotics and Automation, 2002, pp. 476-486.

[13] B.L. Luk, A.A. Collie, D.S. Cooke, and S. Chen, "Walking and climbing service robots for safety inspection of nuclear reactor pressure vessels", Measurement & Control, 2006, Vol. 39 No. 2, pp. 43-7.

[14] D.A. Sanders and I.J. Stott, "Analysis of failure rates with a tele-operated mobile robot between a human tele-operator and a human with a sensor system to assist", 2010, Robotica, Paper ROB-REG-08-0199 (in press).

[15] Z. Wang, and G. Hong, "A review of locomotion mechanisms of urban search and rescue robot", 2007, Industrial Robot: An International Journal, Vol. 34 No. 5, pp. 400-11.

[16] S. Urwin-Wright, D.A. Sanders, and Chen, S. (2002), "Terrain prediction for an eight-legged robot", Journal of Robotic Systems, Vol. 19 No. 2, pp. 91-8.

[17] D.A. Carnegie, D.L. Loughnane, and S.A. Hurd, "The design of a mobile autonomous robot for indoor security applications", 2004, Proc. IMechE Part B – Jnl Eng. Man., Vol. 218 No. 5, pp. 533-43.

[18] L.P. Kalra, and J. Gu, "An autonomous self contained wall climbing robot for non-destructive inspection of above-ground storage tanks", 2007, Industrial Robot: An International Journal, Vol. 34 No. 2, pp. 122-7.

[19] D.A. Sanders, "Ambient intelligence, rapid prototyping and where real people might fit into factories of the future", 2009, Assembly Automation, Vol. 29 No. 3, pp. 205-8, Invited viewpoint review paper.

[20] I. Nourbakhsh, "The mobot museum robot installations", In Proceedings of the IEEE/RSJ IROS 2002 Workshop on Robots in Exhibitions, 2002, pp. 14-19.

[21] J. Carlson, R.R. Murphy, and A. Nelson, "Follow-up analysis of mobile robot failures", Proceedings of the IEEE International Conference on Robotics and Automation, 2004, pp. 4987-4994.

[22] P. Tsarouhas, & G. Fourlas, "Reliability analysis of the mobile robot: a case study", 2014 International Conference on Mechanical Engineering (ME '14), 2014, Venice, Italy, March 15-17, Vol. 1, pp. 151-155.

[23] N. Tomatis, G. Terrien, R. Piguet, D. Burnier, S. Bouabdallah, and R. Siegwart, "Design and system integration for the expo.02 robot", In Proceedings of the IEEE/RSJ IROS 2002 Workshop on Robots in Exhibitions, 2002, pp. 67-72.

[24] S.B. Stancliff, J.M. Dolan, and A. Trebi-Ollenu, "Mission reliability estimation for repairable robot teams", International Journal of Advanced Robotic Systems, Vol. 3 No2, 2006, pp. 155-164.

[25] A. Starr, R. Wynne, and I. Kennedy, "Failure analysis of mature robots in automated production", Proceedings of the Institution of Mechanical Engineers-Part B (J. Eng. Manuf.), Vol. 213, 1999, pp. 813–824.

[26] MIL-HDBK-338B (1998). Electronic Reliability Design Handbook. Department of Defence, USA.

[27] P. Francois, D. Noyes, "Evaluation of a maintenance strategy by the analysis of the rate of repair", 2003, Quality and Reliability Engineering International 19(2):129–148.

[28] MIL-HDBK-189 (1981) Reliability growth management. Headquartes, US Army Communication Research and Development Command, ATTN: DRDCO-PT, Fort Monmouth, New Jersey.

[29] M. Ben-Daya, O.S. Duffua, A. Raouf, J. Knezevic and D. Ait-Kadi, "Handbook of maintenance management and engineering", 2009, Springer-Verlag London Limited, New York.

Dr Panagiotis Tsarouhas, Dipl. Eng., PhD is **Assistant Professor** at Technological Educational Institute of Central Macedonia (Greece), Department of Supply Chain Management & Logistics and a tutor in postgraduate course on Quality Assurance in Hellenic Open University. He received his Diploma in Mechanical Engineering from Universita degli studi di Napoli Federico II (Italy), and both Ph.D. and M.Sc. from the Department of Mechanical and Industrial Engineering from the University of Thessaly in Volos, Greece. For about 10 years he was at the Technical Department as production and maintenance operation head in food industry 'Chipita International SA' in Lamia, Greece. He has about 25 years research/teaching experience, and more than 45 research papers in international journals, book chapters and conference proceedings. He has been involved in many research and practical projects in the field of reliability analysis and maintenance engineering. His areas of interest are reliability & maintenance engineering, quality engineering, and supply chain management.

George K. Fourlas is an **Assistant Professor** at the Department of Computer Engineering of Technological Educational Institute (T.E.I.) of Central Greece, Lamia, Greece. He received his BSc in Physics from the University of Patras, Greece in 1991, MS in Control of Industrial Processes from the University Paris XII – Val de Marne, France in 1993 and PhD in Fault Diagnosis of Hybrid Systems from School of Mechanical Engineering at National Technical University of Athens (NTUA), Greece in 2003. His research interest is mainly focused on: fault diagnosis and fault tolerance of hybrid systems, failure diagnosis, robotics, air traffic management systems, hybrid control systems, embedded systems and microcontrollers, power systems.

Efficient and safe FLASH-based persistent data storage for embedded systems

Michal Bližňák, Tomáš Dulík and Tomáš Juřena

Abstracts— Nowadays, modern MCUs heavily used for embedded system design are often equipped with built-in FLASH RAM which can be used as a persistent storage container for various run-time or configuration data. However, the nature of FLASH RAM avoids users from simple and efficient multiple writes to identical memory locations so a periodic update of specific data structure cell could be difficult to implement. This paper introduces new methods and software implementations which allow users to write various data structures into the FLASH RAM in highly efficient and safe way, minimizes number of needed write and erase cycles and maximizes reliability of the overall write process.

Keywords—FLASH, RAM, write, erase, persistent, data, efficiency, MCU, embedded

I. Introduction

Modern microcontrollers used for embedded system design are often equipped with built-in FLASH RAM which can be used as a persistent storage container for various run-time or configuration data. For example, STM32F4 family of 32-bit microcontroller integrated circuits by STMicroelectronics based on ARM Cortex-M4 technology uses up to 2 MB of integrated FLASH memory used for both program instructions and data [5]. However, the nature of FLASH RAM avoids users from simple and efficient multiple writes to identical memory locations so a periodic update of specific data structure cells could be difficult to implement. This paper introduces new methods and software implementations which allow users to write various data structures into the FLASH RAM in highly efficient and safe way and minimizes number of needed write and erase cycles and maximizes reliability of the overall write process.

Before discussing the proposed methods let us to examine basic FLASH memory characteristics first.

II. FLASH memories basics

FLASH memory (also called FLASH RAM) is a type of non-volatile memory device where stored data exists even when memory device is not electrically powered. It is an improved version of electrically erasable programmable read-only memory called EEPROM. The differences between FLASH memory and EEPROM are, EEPROM erases and rewrites its content one byte at a time, i.e at byte level. On the other hand, FLASH memory erases or writes its data in entire blocks, which makes it a very fast memory compared to EEPROM [3].

Basically, there are two main types of FLASH memory: NAND and NOR types. NAND type flash memory may be written and read in blocks which are generally much smaller than the entire device. NOR type flash allows a single machine word to be written to an erased location or read independently. Another differences between NAND and NOR FLASH memories are the following:

NOR-flash NOR offers complete address and data buses to randomly access any of its memory location (addressable to every byte). This makes it a suitable replacement for older ROM BIOS/firmware chips, which rarely needs to be updated. Its endurance is 10,000 to 1,000,000 erase cycles. NOR is highly suitable for storing code in embedded systems. Most of the today's microcontrollers comes with built in flash memory [3].

NOR flash continues to be the technology of choice for embedded applications requiring a discrete non-volatile memory device. The low read latencies characteristic of NOR devices allow for both direct code execution and data storage in a single memory product [2].

NAND-flash NAND-flash occupies smaller chip area per cell. This maker NAND available in greater storage densities and at lower costs per bit than NOR-flash. It also has up to ten times the endurance of NOR-flash. NAND is more fit as storage media for large files including video and audio. The USB thumb drives, SD cards and MMC cards are of NAND type.

NAND-flash does not provide a random-access external address bus so the data must be read on a block-wise basis (also known as page access), where each block holds hundreds to thousands of bits, resembling to a kind of sequential data access. This is one of the main reasons why the NAND-flash is unsuitable to replace the ROM, because most of the microprocessors and microcontrollers require byte-level random access [3].

III. Main Limitations of FLASH memory

One limitation of FLASH memory is that, although it can be read or programmed a byte or a word at a time in a random access fashion, it can only be erased a "block" at a time. This generally sets all bits in the block to 1. Starting with a freshly erased block,

The work was performed with the financial support of the research project NPU I No. MSMT-7778/2014 by the Ministry of Education of the Czech Republic and also by the European Regional Development Fund under the project CEBIA-Tech No. CZ.1.05/2.1.00/03.0089.

Michal Bližňák is with the Tomas Bata University, Faculty of Applied Informatics, Department of Informatics and Artificial Intelligence, Nad Stranemi 4511, 76005 Zlin, Czech Republic (corresponding author to provide phone: 00420-576035187; e-mail: bliznak@fai.utb.cz).

Tomáš Dulík and Tomáš Juřena are with the Tomas Bata University, Faculty of Applied Informatics, Department of Informatics and Artificial Intelligence, Nad Stranemi 4511, 76005 Zlin, Czech Republic (e-mails: dulik@fai.utb.cz and jurena@fai.utb.cz).

any location within that block can be programmed. However, once a bit has been set to 0, only by erasing the entire block can it be changed back to 1. In other words, flash memory (specifically NOR flash) offers random-access read and programming operations, but does not offer arbitrary random-access rewrite or erase operations. A location can, however, be rewritten as long as the new value's 0 bits are a superset of the over-written values. For example, a nibble value may be erased to 1111, then written as 1110. Successive writes to that nibble can change it to 1010, then 0010, and finally 0000. Essentially, erasure sets all bits to 1, and programming can only clear bits to 0 [4].

Another limitation is that flash memory has a finite number of program-erase cycles (typically written as P/E cycles). Most commercially available flash products are guaranteed to withstand around 100,000 P/E cycles before the wear begins to deteriorate the integrity of the storage [1]. Micron Technology and Sun Microsystems announced an SLC NAND flash memory chip rated for 1,000,000 P/E cycles in 2008.

IV. Efficient and Safe FLASH Memory I/O Access

To eliminate the limitations mentioned in chapter III. a new software library aimed to STM32 microcontrollers called *PersistentData* was developed at Tomas Bata University. The library uses new approaches for accessing data written to FLASH memory integrated on the MCU's chip.

The main idea covered by the library is to store the data in internal structure similar to linked list where just real differences between old and modified data are written to the FLASH memory. Also, the library checks bit states of word to be written to determine whether the new data can be re-programmed at the current memory address location (thanks to the technology background explained in chapters II. and III.) or whether it should be stored to new empty (erased) location.

Now, let us to discuss the new write methods in more details.

A. Internal Data Structure

Main block of integrated FLASH memory available on STM32F2 and F4 families is organized into several (typically 12) sectors with variable sizes as shown in Table 1 [6].

Table 1: STM32's FLASH module organization

Name	Block base addresses	Size
Sector 0	0x0800 0000 - 0x0800 3FFF	16 Kbyte
Sector 1	0x0800 4000 - 0x0800 7FFF	16 Kbyte
Sector 2	0x0800 8000 - 0x0800 BFFF	16 Kbyte
Sector 3	0x0800 C000 - 0x0800 FFFF	16 Kbyte
Sector 4	0x0801 0000 - 0x0801 FFFF	64 Kbyte
Sector 5	0x0802 0000 - 0x0803 FFFF	128 Kbyte
...	...	...
Sector 11	0x080E 0000 - 0x080F FFFF	128 Kbyte

The *PersistentData* library uses two sectors with identical sizes to store managed data structures. The reason why two dedicated FLASH sectors are used at the same time is due to mirroring of stored data which allows the library to minimize possibility of data loss when the MCU is powered down during a data write process accidentally as discussed later in this article.

Maximum size of data stored in the FLASH by using the library is calculated in 1.

$$maxSize = \frac{sectorSize - 8}{2} \quad (1)$$

The additional memory overhead is caused by a way how the library tries to keep managed data in valid state. The validity of the data is verified by a *CRC checksum* placed behind the data section and by validity words following raw data chunks as can be seen in Figure 1.

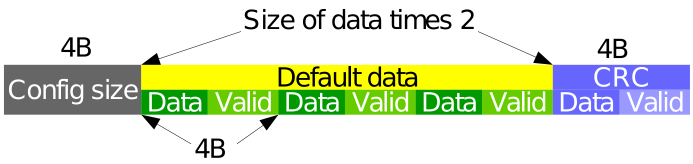

Fig. 1 default form of internal data structure

The raw data stored in the FLASH memory by using the library is divided into 16-bit words (*data chunks*) organized in the following way.

The overall length of internal data structure written as 32-bit double word is located at the beginning of the FLASH sector. The raw data interlaced by *validity words* follows. Size of the data section is doubled size of stored raw data because each data chunk is followed by its validity word with the same size (16 bits). At the end of the internal structure 16-bit *CRC checksum* of the data section followed by its validity word is placed.

The validity word's value is `0x7fff` by default which means the data chunk placed before is valid. Different validity value means relative offset in the FLASH memory where changed data chunk is stored.

B. Writing of Data

When the raw data structure is modified and the library is asked to write the modifications to FLASH memory, differences in the raw data are found. Then, the modified raw data chunks (i.e. modified 16-bits words) are written to empty (erased) FLASH memory locations after the last known (and valid) CRC checksum and the validity words associated with their previous values are updated so they point to new memory locations occupied by the new data chunks. The new data chunks are interlaced with default validity words like in the previous state. Finally, new CRC checksum is calculated and placed after the last used memory location (followed by its own validity word). Obviously, the validity word of previous CRC checksum is updated similarly to data chunk's validity word.

For minimizing of data writes into new memory locations, the library checks bit states of modified raw data chunk and writes the new value to the new memory location only when the old value cannot be re-written at the place. As mentioned in the chapter III., a content of FLASH memory can be re-written at identical memory location when bit states of the new value change just from "1" to "0". In this case, the validity word associated with the in-place modified data chunk remains unchanged (i.e. in default state) and just CRC checksum is modified (in the similar way).

ISBN: 978-1-61804-321-4

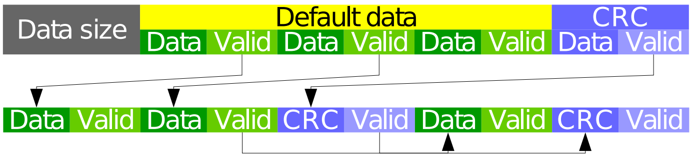

Fig. 2 modified internal data structure

Modified data structure written in FLASH memory is illustrated in Figure 2.

Remember that the write changes are mirrored in both used FLASH memory sectors so the written data can be read successfully even when one of the dedicated sectors is corrupted. All tasks done during writing of the data by using `PersistentData_Set()` API function declared in the library are shown in Figure 3.

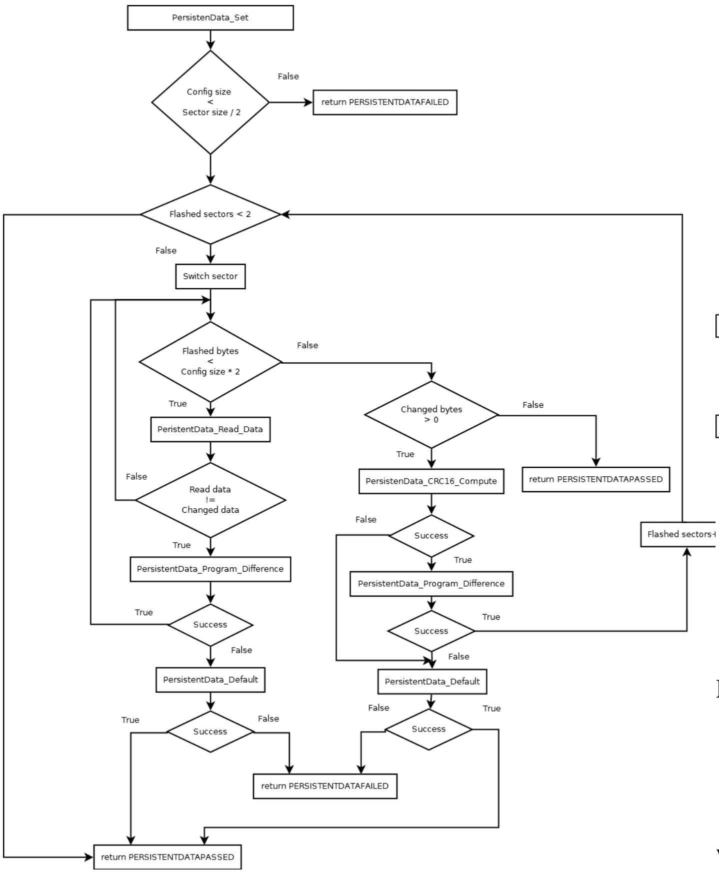

Fig. 3 activity diagram of `PersistentData_Set()` function

C. *Reading of Data*

When reading the stored raw data, the internal data structure written in FLASH memory is scanned by using content of the validity words and the data is reconstructed by joining the raw data chunks. During the scanning, the library reads values from validity words appended to data chunks and when found non-default value which means that the data chunk is outdated (as mentioned above, the default value is `0x7fff`), the library jumps to new memory location calculated as current address of examined data chunk plus offset read from its validity word. Prior to that, a validity of whole (currently active) FLASH sector is checked by reading of the last know CRC checksum. When the CRC checksum mismatches or it cannot be read, the active FLASH sector is switched to the backup one and the data reading process is repeated. If the data cannot be read successfully even from the backup sector, the reading process fails and is aborted.

Tasks performed by the library during the data reading process are illustrated in Figure 4.

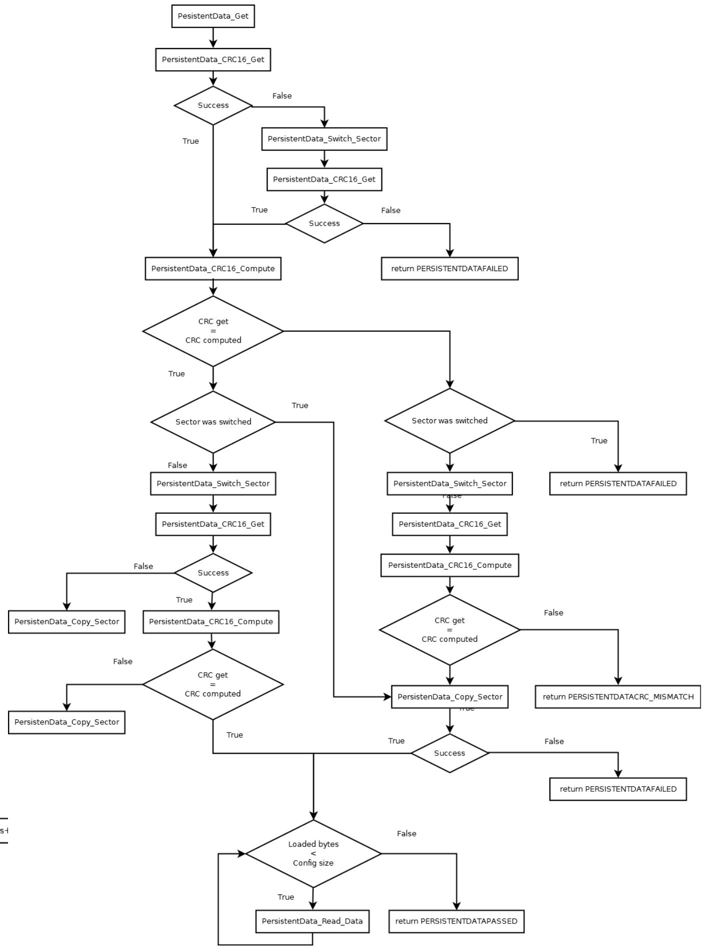

Fig. 4 activity diagram of `PersistentData_Get()` function

D. *Validation of Stored Data*

The validity of stored data is ensured by using CRC checksum which is calculated from raw data stored in the FLASH memory and it is compared with CRC value appended to the data section during the writing process as shown in Figure 1. Memory address of the first available CRC checksum can be calculated as in 2.

$$crcAddress = (2 \times dataSize) + 4 \tag{2}$$

The CRC checksum is regarded as valid itself when its assigned validity word contains the default value (`0x7fff`). If not, the up to date CRC checksum is searched in the same way like reading of data chunks described in chapter C.. During the scanning of CRCs validity words the calculated absolute memory addresses are checked to unveil possible data corruption in the following way: when the address exceeds bounds of active FLASH memory sector or when new calculated address is lower or equal to the current one, then the CRC is declared as invalid, otherwise the CRC value is regarded as valid. By the way, an integrity of validity words appended to the data chunks is ensured in the same way.

V. Solving of Possible Error States

Unfortunately, a data loss may occur when MCU's electric power supply gets down during the writing process so both data and its validation components could remain incomplete. Due to this, the CRC checksums are calculated to ensure correct writing process and to detect random errors caused by the data loss. Let us to examine several critical scenarios which may occur and let us to see how they are handled by the *PersistenData* library.

A. Accidental Power-down During the Write Process

In case of MCU's electric power supply malfunction a data being written to FLASH memory could be damaged. If happened, the CRC checksum calculated from this data mismatches CRC value stored on this affected sector. Obviously, the writing process can be aborted in any phase so the errors can involve various data structure's parts. Here are four possible critical scenarios which may occur:

- The CRC checksum is not written after the last valid data chunks followed by its validity word

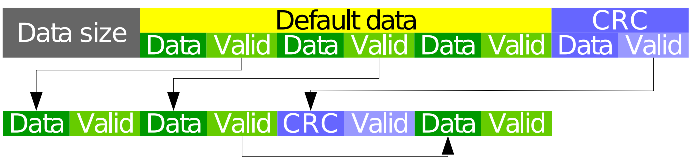

Fig. 5 CRC is not written after valid data

- Updated data chunk is not written after the update of validity word assigned to the outdated data chunk.

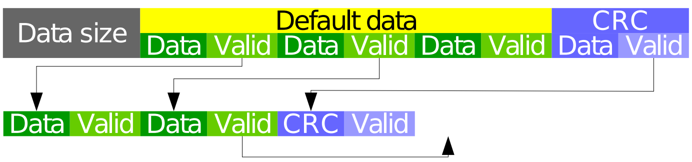

Fig. 6 new data are not written after validity word update

- Not all data chunks are written, but all the written are associated with correct validity words.

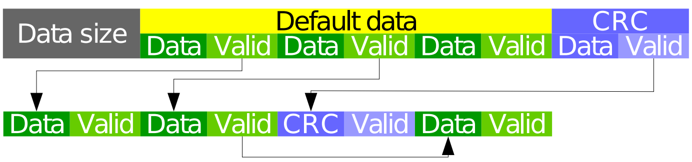

Fig. 7 data are written partially

- Not all data chunks are written; some of the written are without assigned validity word.

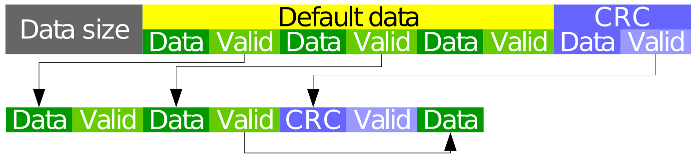

Fig. 8 data written partially, validity word is missing

All these scenarios are detected by the library and can by solved by common way: After the detection the library tries to recover the data from the backup FLASH memory sector. Of course, it is possible only when the backup sector contains valid, undamaged data.

B. Reading of Corrupted Data

During the reading, the CRC checksum could be missing or couldn't be found. Also, the calculated CRC value can mismatch the stored one. The first case occurs when the CRC's validation word is corrupted or it is missing. When both calculated and stored CRC checksums are present but they don't match then the data is corrupted or the CRC checksum hasn't been updated correctly. In this case the library tries to read requested data from the backup FLASH sector.

VI. Conclusion

All the principles discussed in this article lead to efficient and safe implementation of persistent data storage based on FLASH memory suitable for embedded systems. Based on the discussed principles, new software library called *PersistentData* has been developed and tested on STMicroelectronic's STM32F2 and STM32F4 MCU's families. Set of unit tests covering all critical functionality of the library have been created and used for testing. Also, the library has been successfully used in two commercial projects developed at the Tomas Bata University which proved its maturity.

References

[1] J. Thatcher, T. Coughlin, J. Handy and N. Ekker. (2009). NAND Flash Solid State Storage for the Enterprise. *SNIA, Solid State Storage Initiative* [Online]. Available: http://www.snia.org/sites/default/files/SSSI_NAND_Reliability_White_Paper_0.pdf

[2] C. Zitlaw. (2011). The Future of NOR flash memory. *EETimes* [Online]. Available: http://www.eetimes.com/document.asp?doc_id=1278751&page_number=1

[3] Electronics Design Magazine. (2006). Flash memory basics and its interface to a processor. *EE Herald* [Online]. Available: http://www.eeherald.com/section/design-guide/esmod16.html

[4] Wikipedia. (2015). Flash memory. [Online]. Available: http://en.wikipedia.org/wiki/Flash_memory

[5] *STM32F4 Series*, STMicroelectronics Website. (2015). [Online]. Available: http://www.st.com/web/en/catalog/mmc/FM141/SC1169/SS1577

[6] *STM32F2 Flash Programming Manual*, STMicroelectronics Website. (2015). [Online]. Available: http://www.st.com/web/en/resource/ technical/document/programming_manual/CD00233952.pdf

The CEPH cluster performance analyses in the local network with multiple independent clients

David Malanik

Abstract**—**this paper is focused to the designing, implementing and benchmarking the big data cluster based on the CEPH [1] technology. The main point of this paper is aimed to the implementation of local cluster with multiple clients. These nodes; store points of distributed data cluster; is in one location and on one specific subnet. Realized test show the dependency of number of concurrent clients connected to the cluster and cluster read/write bandwidth. These test show the potential limits of the developed solution. The article contains the recommendation for the implementation of these solution in real computer infrastructure.

Keywords**—**Distributed file system, data backup, data security CEPH, RDB, HA data cluster, storage

I. Introduction

THE problem based on the storage capacity and fail-proof run time, is one of the major problem in many companies. The first requirement, is the scalability of the storage. The Storage must be capacity flexible as soon as possible. The second and probably more important is the question of high availability an error-proof solution for data storage. These two major problem grades in the critical infrastructure.

There is the request to have the data in secure locations; especially in the geographically separated location. The purpose is clear. If there is any problem in the main data center, the company does not need any blackouts. So it is strictly recommended to have separated power part of IT infrastructure (the blade servers, rack servers, etc.) and the storage (SAN/NAS). But this scenario does not deal with geographically separated nodes, the main point of this paper is focused to the performance of the solution in the best network environment. There was only one subnet and network based on one active part (each machines was connected to one switch). The effect of the latency is minimalized. The solution is not the best practices focused to data security and high availability, but it provide the “ideal” benchmark of the technology.

This paper used different technology for the storage model. There is not the classical SAN system with FC or FCoE [4].

The work was performed with financial support of research project NPU I No. MSMT-7778/2014 by the Ministry of Education of the Czech Republic and also by the European Regional Development Fund under the Project CEBIA-Tech No. CZ.1.05/2.1.00/03.0089.

D. Malanik is with the the Faculty of Applied Informatics, Tomas Bata University in Zlín, Nad Stráněmi 4511, 760 05 Zlín, Czech Republic (e-mail: dmalanik@fai.utb.cz).

II. Used technologies

A. Storage cluster

The CEPH storage was used as a storage cluster technology. It is the object storage that provides seamless access to objects using native language bindings or radosgw, a REST interface that is compatible with applications written for S3 and Swift. The main technology for this solution is in CEPH Rados block storage device which provides access to block device images that are striped and replicated across the entire storage cluster. The CEPH also provides a POSIX-compliant network file system that aims for high performance, large data storage, and maximum compatibility with legacy applications [1].

B. Cluster node – HW/SW specification

The HW part of storage node is realized by two virtual machine with identic specification. The VM are hosted on FS-RX100 server with Proxmox VE hypervisor [1].

Specification of VM/(nodes):
CPU: 2x Intel ® Xeon ® X3320
RAM: 2GB
HDD: 50GB SATA-II
LAN: 1000BASE-T
OS: Debian 7.0.2 – 64-bit

C. Cluster client

The client for storage cluster is implement on physical server with Proxmox VE hypervisor. The hypervisor is for creating a VM for testing concurrent read/write operation to the storage cluster. The physical computer simulate the server with many virtual machines using storage cluster. The data of all virtual machine is located on Rados block storage device provided by the cluster. This solution provides the isolation between power part of the solution and the data storage.

Specification cluster client:
CPU: Intel ® i7-3770 (4 physical cores, 8 logical)
RAM: 8GB
HDD: 250GB SATA-II
LAN: 1000BASE-T
OS: Proxmox VE 3.1

D. Network model

The network model is shown on figure below.

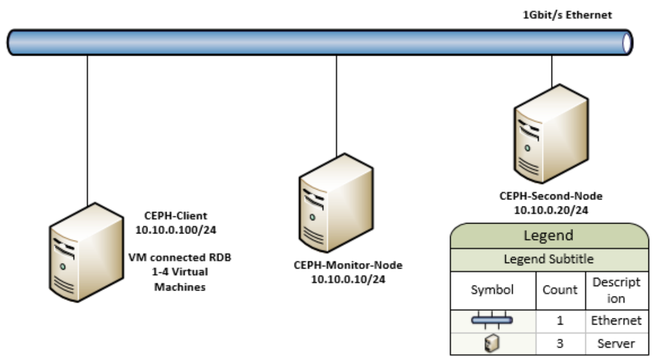

Fig. 1 Network schema

The nodes is located in one data center. The connection between nodes and CEPH-client is realized by 1 Gbit/s Ethernet [5, 6]. The network is reserved only for this cluster.

E. VM – on CEPH client

The CEPH-Client server contains 4 virtual machine that simulates the real applications running on the one physical server. Each VM is connected to share 1000BASE-T Ethernet.

Specification of VM:

CPU: Intel ® i7-3770 (2 logical cores)

RAM: 1.5GB

HDD: 15GB SATA-II

LAN: 1000BASE-T

OS: Debian 7.0.2 – 64-bit

III. NETWORK BANDWIDTH TEST

The first part of CEPH cluster testing is in local network bandwidth testing. The network is isolated from other application. The first rand of tests become from LAN testing realized by the *iperf* Linux tool [7]. Test contains 50 measurements during whole day [3]. Each measure contains 4 part; the appropriate commands are shown below.

```
#iperf –c <IP> -t 10
#iperf –c <IP> -t 30
#iperf –c <IP> -t 60
#iperf –c <IP> -t 120
```

The –t parameter from command represents the time of bandwidth test in second.

Test procedure is realize between nodes:

CEPH-Client vs. CEPH-Monitor-Node

CEPH-Client vs. CEPH-Second-Node

The measure is not be realized only for data capacity of the network; the second monitored parameter was the stability of line. Results are shown below.

A. CEPH-Client vs. CEPH-Monitor-Node

The Table I shown the maximal, minimal and average value of network bandwidth examined by the *iperf* testing procedure.

Table I CEPH-Client vs. CEPH-Monitor-Node

	Mbit/s			
	10s	30s	60s	120s
MIN.	948	940	950	949
MAX.	974	978	981	979
AVG.	959.9	960.9	964.1	965.4

The best stability of the network was with 120s time interval. The test duration was over 3 hour.

B. CEPH-Client vs. CEPH-Second-Node

The Table II shown the maximal, minimal and average value of network bandwidth examined by the testing procedure.

Table II CEPH-Client vs. CEPH-Second-Node

	Mbit/s			
	10s	30s	60s	120s
MIN.	943	940	955	952
MAX.	977	976	970	977
AVG.	960.5	957.5	963.1	966.3

The best stability of the network was with 60s time interval. The test duration was over 3 hour.

IV. CEPH STORAGE BANDWIDTH TEST

This part of paper is focused to real bandwidth in disk operation. The test is written with respect of real application.

The testing scheme is shown on **Fig. 2**. It is realized by one physical server with connection to the storage cluster. There are 4 virtual machine hosted on the physical server. The VM data is stored in the CEPH storage cluster used by Rados block device. The local storage of server is not used. The local operation system has not any SWAP device.

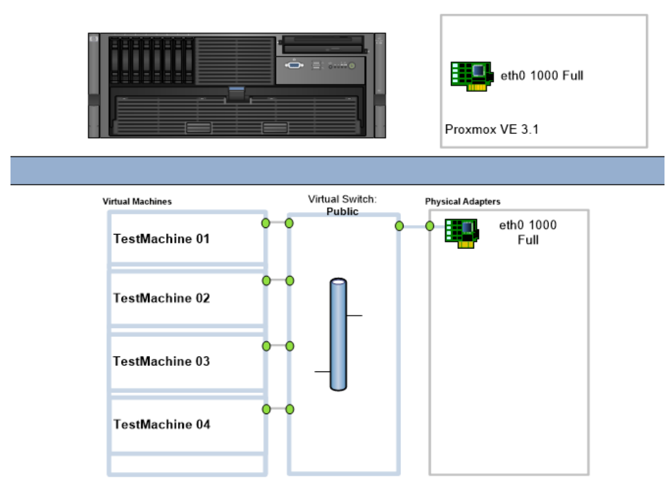

Fig. 2 VM schema

The test was realized by the Linux command *dd*; specifically by the various option of this command shown below [8].

```
#dd bs=4K count=2000 if=/dev/zero of=test conv=fdatasync
#dd bs=64K count=2000 if=/dev/zero of=test conv=fdatasync
#dd bs=256K count=2000 if=/dev/zero of=test conv=fdatasync
#dd bs=1M count=2000 if=/dev/zero of=test conv=fdatasync
```

The different size of block in set 4K, 64K, 256K and 1M represents the variability of saved data to the cluster. It simulates the variability of file size copied to the cluster. The parameter count represents the repetition of each copy tests. The test set contains 200 repetitions of *dd* commands set.

The following parts reports about testing reports. These tests were parted to 4 subcategories. The first test is realized with one VM running on cluster. Next parts describe the test result with increased number of concurrent VM on one cluster. Tests were realized for 1-4 concurrent VM.

A. One VM on cluster

The first test was realized with one active virtual machine. The testing procedure was processed on isolated local network infrastructure. The test lasted over 2 hour of continual bandwidth testing.

The Table III shows minimal, maximal and average values of realized tests with variable block size for write/read operations. The values fluctuate **from 90.0 MB/s to 130.1 MB/s**.

Table III One VM dd test

	MB/s			
	4KB	64KB	256KB	1M
MIN	41.1	106.2	98.7	108
MAX.	108	142.5	126	129.6
AVG.	90.0	130.1	108.8	119.4

The most stable bandwidth was reported by the 1 MB block size. The possible reason flowing from the latency of network interfaces. The impact of latency will be better with higher block size of data. The storage bandwidth was from 108 MB/s to 129.6 MB/s without any significant deviations.

The results from this scenario show, that there is not real bottleneck in the speed of local network/local HDD bandwidth. The examined values is close to the real limitation on 1 Gbps network interfaces. The storage bandwidth is quite similar that the real limitation. The examined average bandwidth is between 90 to 130.1 MB/s. The limit of the network is approximately 120 Mb/s. That reflect the bottleneck in the local network speed limitation.

B. Two concurrent VM on cluster

The second test was realized with two active virtual machines. The testing procedure was processed on isolated network infrastructure. The test lasted around 3 hour.

The Table IV and Table V show the comparison of bandwidth identified on each machine during the test. The bandwidth of both virtual machines are quite identical, there is no one significant difference. The cluster distributed the bandwidth to the two equivalent machines. In comparison with the one VM test; values of each machine is too close to the one VM solution.

Table IV First VM dd test

	MB/s			
	4KB	64KB	256KB	1M
MIN.	5	25	28.4	41.2
MAX.	59.6	84.4	52	57.6
AVG.	28.56	59.622	38.243	48.31

Table V Second VM dd test

	MB/s			
	4KB	64KB	256KB	1M
MIN.	4.8	25.4	28.2	37.4
MAX.	57.6	93.4	72	63.2
AVG.	28.6	58.8	37.3	48.4

The Table VI shows minimal, maximal and average values of realized tests with variable block size for write/read operations. The values of the summary average bandwidth of two concurrent machines fluctuate **from 57.5 MB/s to 118.5 MB/s**. The summary bandwidth is lower than the one VM solution. The bandwidth is consumed by the scenario of the RADOS protocol. But the lower value is in small block size. With higher block size, the bandwidth is close to the network limitation and one VM storage bandwidth test.

Table VI Two concurrent VM summary dd test

	MB/s			
	4KB	64KB	256KB	1M
MIN.	11.2	61.4	62.8	85
MAX.	112.4	163.4	120.4	107.4
AVG.	57.2	118.5	75.5	96.7

The most stable bandwidth was reported by the 1 MB block size again. The possible reason flowing from the latency of network interfaces. The impact of latency will be better with higher block size of data. The storage bandwidth was from 85 MB/s to 107.4 MB/s without any significant deviations.

The solution of two concurrent virtual machines located on one cluster shows the quite similar values of summary bandwidth than the solution with one isolated virtual machine. This assumes, that the cluster based on the designed infrastructure is able to serves the data to two concurrent machines without any problem. The bandwidth values fluctuates from **57.2 MB/s to 118.5 MB/s**.

C. Three concurrent VM on cluster

The third test was realized with three active virtual machines. The testing procedure was processed on real shared network infrastructure. The test lasted approx. 4 hour.

Tables placed below (Table VII, Table VIII, Table IX) show the comparison of bandwidth identified on each machine during the test. The test shows the distribution of available bandwidth is equally to number of active clients. The measured values is practically same on each clients.

Table VII First VM dd test

	MB/s			
	4KB	64KB	256KB	1M
MIN.	0.3	1.3	3.8	15.6
MAX.	56.4	82.6	38.6	47.2
AVG.	12.5	37.7	25.6	32.1

Table VIII Second VM dd test

	MB/s			
	4KB	64KB	256KB	1M
MIN.	1.1	2.6	4.4	9.8
MAX.	45.6	75.6	39.2	37.8
AVG.	12.9	38.0	23.9	31.0

Table IX Third VM dd test

	MB/s			
	4KB	64KB	256KB	1M
MIN.	1.7	13.8	14.8	15.2
MAX.	42.6	83.2	54	64.4
AVG.	13.8	39.8	27.5	33.7

The Table X shows minimal, maximal and average values of realized tests with variable block size for write/read operations. The values of the summary bandwidth of three concurrent machines fluctuates **from 39.3 MB/s to 115.5 MB/s**.

Table X Three concurrent VM summary dd test

	MB/s			
	4KB	64KB	256KB	1M
MIN.	6.2	35.3	43	54.4
MAX.	110.2	195.8	120.2	144.4
AVG.	39.3	115.5	77.1	96.9

The most stable bandwidth was reported by the 1 MB block size again. The possible reason flowing from the latency of network interfaces. The impact of latency will be better with higher block size of data. The storage bandwidth was from 54.4 MB/s to 144.4 MB/s.

This solution shows additional increasing of bandwidth capacity. The maximal storage bandwidth is higher than in solution with one and two concurrent virtual machines.

The bandwidth values fluctuates from **39.3 MB/s to 115.5 MB/s**. The bandwidth is limited by the examined speed limit of the network line (120 MB/s).

D. Four concurrent VM on cluster

The last test was realized with four active virtual machines. The testing procedure was processed on isolated network infrastructure. The test lasted approx. 5 hour. There is a few increasing of bandwidth speed. But the average speed is quite similar than in the one VM solution described higher.

Tables placed below (Table XI, Table XII, Table XIII, Table XIV) show the comparison of bandwidth identified on each machine during the test.

Table XI First VM dd test

	MB/s			
	4KB	64KB	256KB	1M
MIN.	0.3	1.3	8.6	15
MAX.	100.8	62.4	27.2	30.6
AVG.	6.3	27.2	19.1	25.6

Table XII Second VM dd test

	MB/s			
	4KB	64KB	256KB	1M
MIN.	1.1	8	10.2	11.4
MAX.	108	80.6	60.2	66.4
AVG.	11.3	26.3	19.8	25.7

Table XIII Third VM dd test

	MB/s			
	4KB	64KB	256KB	1M
MIN.	1.2	9	13.6	18.4
MAX.	41.4	59.2	33.4	32
AVG.	5.4	27.2	20.1	25.2

Table XIV Fourth VM dd test

	MB/s			
	4KB	64KB	256KB	1M
MIN.	1.4	8.6	10.8	19.4
MAX.	32.2	59.6	28.8	33.4
AVG.	5.4	27.5	19.3	25.5

The Table XV shows minimal, maximal and average values of realized tests with variable block size for write/read operations. The average values of the summary bandwidth of three concurrent machines fluctuate **from 28.4 MB/s to 108.2 MB/s**.

Table XV Four concurrent VM summary dd test

	MB/s			
	4KB	64KB	256KB	1M
MIN.	7.9	60.6	57.2	88
MAX.	216.4	163.4	115	133
AVG.	28.4	108.2	78.3	102.1

The best stability of bandwidth was reported by the test with 1 MB block size. The examined bandwidth was from 88 MB/s to 133 MB/s without any significant deviations.

This scenario represents the limit of usage for one 1 Gbit/s card in the network infrastructure. There is a real decreasing of bandwidth with 4 KB block and the best performance is with 64 KB blocks. The line is quite instable with small blocks.

The bandwidth values fluctuates from 28.4 MB/s to 108.2 MB/.

ISBN: 978-1-61804-321-4

V. Usability of CEPH cluster on shared network infrastructure

Test described in previous chapters show the potential usability of cluster solution based on the RADOS block device and CEPH cluster solution. The limitation of isolated network flowing from the network limitation in 1 Gbit/s line. The network bandwidth limits this solution to the approx. 120 MB/s.

The average bandwidth of solution is quite similar in each tests. The bandwidth is not affecting by the number of active clients.

Table XVI Storage bandwidth comparison

VMs/ block size	MB/s			
	4 KB	64 KB	256 KB	1 MB
1	90.0	**130.1**	108.8	119.4
2	57.2	**118.5**	75.5	96.7
3	39.3	**115.5**	77.1	96.9
4	28.4	**108.2**	78.3	102.1

The Table XVI shows that the bandwidth with the smaller block 4 KB decreasing with increasing of concurrent machines; more machines mean more scenario of the solution and the speed decreasing. Probably it is the limitation of network latency and/or RADOS scenario. The decreasing of bandwidth is observable in other block size. The highlighted columns represented the maximal average bandwidth for amount of concurrent machines. The result show that the best performance is with 64 KB block size.

VI. Conclusion

This paper contains test realized with the local isolated network between nodes of the CEPH storage cluster. The interconnection between nodes is dedicated only for these nodes. The main parts of infrastructure was tested in the chapter III-IV.

The main part of this report reflect the real usability of the data cluster stored in isolated local network. The purpose of this isolation flowing from the data security requirement. The solution has specific issues described in this paper. The main issue flowing from the network connectivity. The theoretical connection is realized by the 1 Gbit/s ethernet; but tests show, that the theoretical and practical bandwidth of the local network represents the bottleneck of this solution. The disk bandwidth of solution nodes id better than the local network bandwidth. So the CEPH storage cluster described in this paper is implementable in practice. If there is requirement of maximal bandwidth around 1 Gbit/s this solution will done it. For the higher bandwidth, there must be increasing of local network speed. It is possible with the LACP or 10 Gbit/s Ethernet. This increasing brings the other problem; 10 Gbit/s Ethernet has significantly higher bandwidth than commonly used HDD. The problem must have complex solution of each bottlenecks.

References

[1] Chen W. K., "Linear Networks and Systems," in Proceedings of the 7th USENIX Symposium on Operating Systems Design and Implementation (OSDI '06), Seattle, USA, 2006.

[2] E. Nemeth, *UNIX and Linux system administration handbook* 4ed., Upper Saddle River, NJ: Prentice Hall, 2011.

[3] B. R. Chang, H.-F. Tsai, and C.-M. Chen, "Empirical Analysis of Server Consolidation and Desktop Virtualization in Cloud Computing," *Mathematical Problems in Engineering*, 2013

[4] T. Hirofuchi, M. Tsugawa, H. Nakada, T. Kudoh, and S. Itoh, "A WAN-Optimized Live Storage Migration Mechanism toward Virtual Machine Evacuation upon Severe Disasters," *Ieice Transactions on Information and Systems*, vol. E96D, no. 12, pp. 2663-2674, Dec, 2013.

[5] L. Peterson, B. S Davie. *Computer networks: a systems approach. 5th ed.* Burlington: Morgan Kaufmann, c1999.

[6] L. Peterson, B. S Davie. *IEEE Globecom Workshops*. Anaheim, IEEE Computer Society, 2012.

[7] M. Palmer, *Guide to UNIX Using Linux*, 4 ed., pp. 697, Australia: Thomson/Course Technology, 2008.

[8] B. Djordjevic, V. Timcenko, "Ext4 File System performance Analysis in Linux Environment," in 11th WSEAS International Conference on APPLIED INFORMATICS AND COMMUNICATIONS (AIC '11), Florence, Italy, 2011.

Ing. David Malanik, Ph.D.
Born in Zlin, Czech Republic, 1. March 1984
Bacelour degree in Information technology 2006, Tomas Bata University in Zlin. Master degree in Information technology 2008, Tomas Bata University in Zlin. Ph.D. Thesis based on the user identification provided by the neural network, 2011, Tomas Bata University in Zlin
Presently SENIOR LECTURER at Tomas Bata University in Zlin, Department of Informatics and Artificial Intelligence. Main specialization: computer security, computer viruses, penetration testing, artificial neural network, computer networks.

Techniques Allowing BroadcastReceiver Malware on Android Platform

M. Oulehla, D. Malaník

Abstract**—**Currently, Android represents the most popular mobile operating system in the world. For this reason, Android security issues constitute a very important topic. Whilst the major part of published articles is focused on malware detection techniques using some anomalies such as unusual network traffic, this paper concentrates on Android malware from the hacker's point of view. It contains examples of Java as well as XML codes (representing causes) and screenshots (representing effects). Android versions 3.1 and higher contain security improvement which does not allow BroadcastReceiver malware without Activity. The research carried out in this field has discovered the procedure enabling to bypass this security protection by hiding malware Activity class bound to BroadcastReceiver. Based on revealed security weaknesses, some useful recommendations for antivirus companies as well as individual users have been raised.

Keywords**—**Android, Activity, BroadcastReceiver, camouflage, malicious activity, malicious software, mobile devices, mobile malware, mobile virus, smart phones, tablet.

I. Introduction

To be able to understand the development of malware for the Android platform better, it is necessary to explain an essential term used in this field. It is the BroadcastReceiver. It is a class that does not have a user interface and is able to run silently in the background and which processes broadcasts from the system or from other applications. For this reason the BroadcastReceiver is particularly suitable for performing malicious actions. The technique how BroadcastReceiver can be misused has been revealed.

The Android is widespread operating system nowadays. For this reason the Android OS has become primary target for malware creators on mobile platform. There are several excellent articles dealing with Android malware, for example: Kernel-based behavior analysis for android malware detection [1]. These works mostly deal with malware detection based on some anomalies. A different approach to the issue has been tried in this research. The procedures of malware writers have been used. It has posed both the study of the original Android documentation for developers on Google's web [2] and searching of security vulnerabilities allowing functioning of malware application with BroadcastReceiver and hidden Activity.

Milan Oulehla is with the Faculty of Applied Informatics, Tomas Bata University in Zlín, Nad Stráněmi 4511, 760 05 Zlín, Czech Republic (corresponding author to provide phone: +420-732118306; e-mail: oulehla@fai.utb.cz).

David Malaník is with the the Faculty of Applied Informatics, Tomas Bata University in Zlín, Nad Stráněmi 4511, 760 05 Zlín, Czech Republic (e-mail: dmalanik@fai.utb.cz).

II. Methods

This research concerns most of modern smart phones and tablets with Android operating system. Google Inc. Company [3] created a security improvement for versions 3.1 and higher of Android that no longer allows the application/malware to silently execute its tasks only via BroadcastReceiver. Nowadays each application with BroadcastReceiver must also have an Activity (If BroadcastReceiver requires some permission).

There is a technique how to create modern BroadcastReceiver malware. First of all, BroadcastReceiver class has been created and its method onReceive has been implemented. (The onReceive method should contain some malicious actions.) Then, a class has been added to the malware that is a descendant of an Activity class and then it has to be edited to AndroidManifest.xml file by adding the activity tag. The result of this modification is shown by Figure 1.

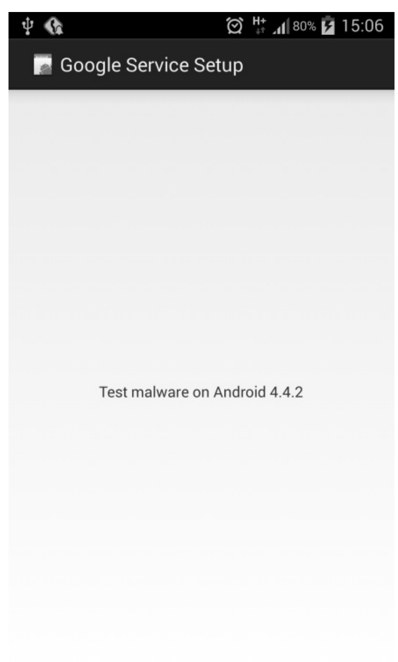

Fig. 1 Added Activity on Android 3.1 and higher versions

ISBN: 978-1-61804-321-4

As can be seen from Figure 1, Activity is now visible and that is why the malware can be easily detected by users. If the malware should work the same way as on older Android versions, it is necessary to camouflage the Activity which is now a mandatory part. It is essential to make the Activity transparent. It can be done by editing the style in .../res/values/ styles.xml file where we will add these item tags:

<item name="android:windowIsTranslucent">true</item>
<item name="android:windowBackground">@android:color/transparent</item>
<item name="android:windowContentOverlay">@null</item>
<item name="android:windowNoTitle">true</item>
<item name="android:windowFullscreen">true</item>
<item name="android:windowIsFloating">true</item>
<item name="android:backgroundDimEnabled">false</item>

Then all UI elements such as TextView from the XML layout have been removed. If we do not remove all the UI elements, Activity would not be completely transparent, as shown by Figure 2 (the highlighted part). In the XML layout file, it is important to keep only a valid tag which describes the layout, for instance RelativeLayout.

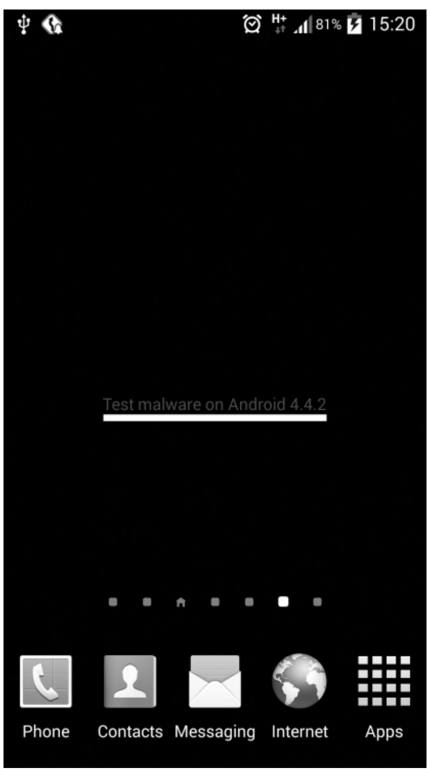

Fig. 2 UI elements cause that Activity is not completely transparent

Now the running Activity is already fully transparent. But another problem occurs if the Activity gets into the foreground. The mobile device looks "frozen" (it does not respond to any user touches on the screen). This happens because the fully transparent activity takes up the whole screen. For example, if the user pushes the software button on the screen, in fact he does not push the software button but he touches the transparent Activity located over this button. This behavior can be fixed by adding onResume method to the Activity. Then finish() is put [4] to onResume. It is not necessary to put finish() into other methods, as can be seen from Figure 3. In all cases (onStart, onRestart, Paused, Stopped), onResume method is eventually called. The calling of finish() from onResume ensures that the Activity immediately moves into the background right after it gets into the foreground. Thus the Activity releases the screen of the Android device.

There is a flash during the Activity transition from the foreground to the background. However, this flash is invisible because the Activity is transparent. The malware icon is still visible in the list of running applications (Figure 4) and in the icon list of installed applications (Figure 5). This can lead to malware uncovering. Therefore, in the end, the icon and caption camouflage is carried out.

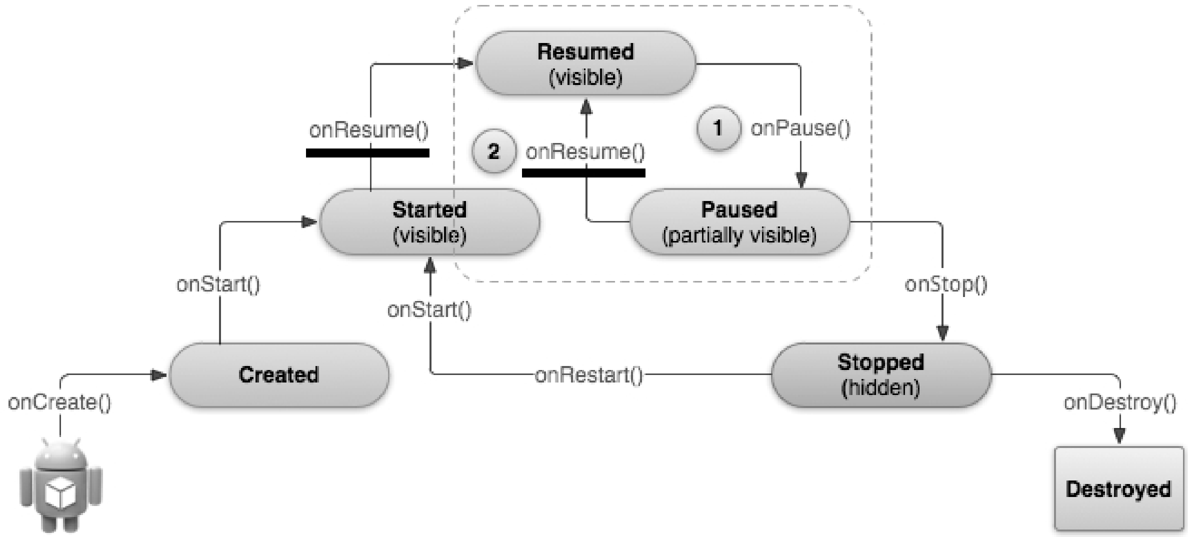

Fig. 3 Lifecycle of an Activity [5]

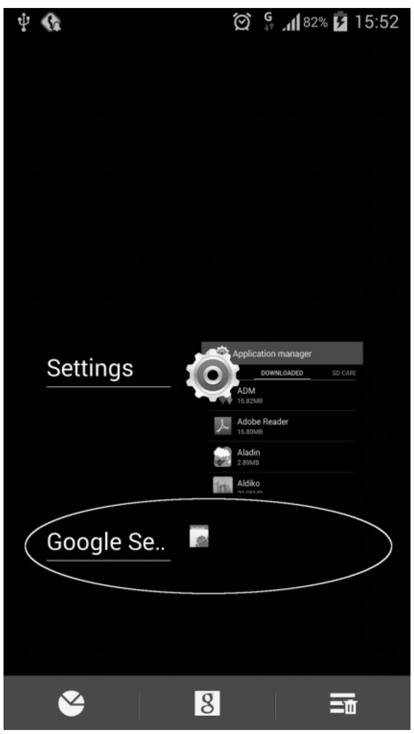

Fig. 4 The malware application is still visible in the list of running applications

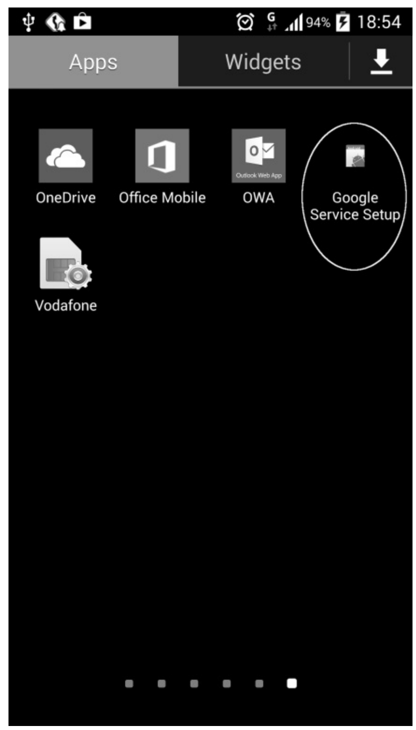

Fig. 5 The malware application is visible in the icon list of running applications

After editing the file: .../res/values/strings.xml, the value has to be changed to <string name="app_name"> </string>. Notice that the new value is not null, it is a space. Next, it is essential to ensure that the parameter android:label of the application tag, which is in the AndroidManifest.xml file, refers to this value:

android:label="@string/app_name". It is not good to edit the parameter android:label directly in AndroidManifest.xml file. The next step is replacing standard icons with transparent PNG images. It is done in the directories: .../res/drawable-hdpi, .../res/drawable-mdpi, .../res/drawable-xhdpi and

.../res/drawable-xxhdpi.

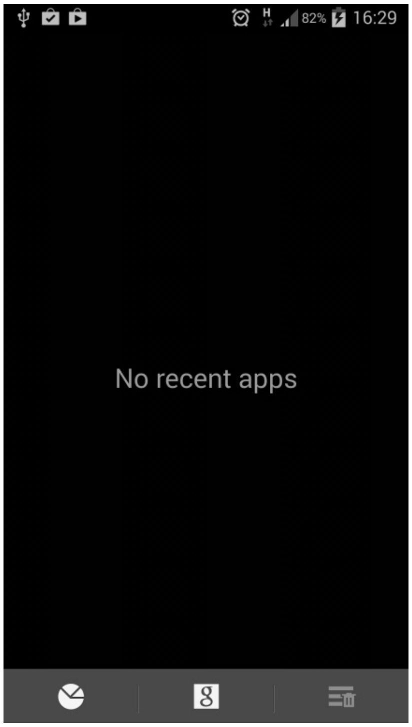

Fig. 6 The malware application is not in the list of running applications

As can be seen from Figure 6, this malware application is not in the list of running applications. However, malware application is running, as shown in Figure 7. The malware application is no longer visible in the list of installed applications either (Figure 8). If the user clicks into the place where the malware icon was, he or she does not see anything happen. The whole process of camouflage is done. The malware has the same behavior as on Android 2.3.

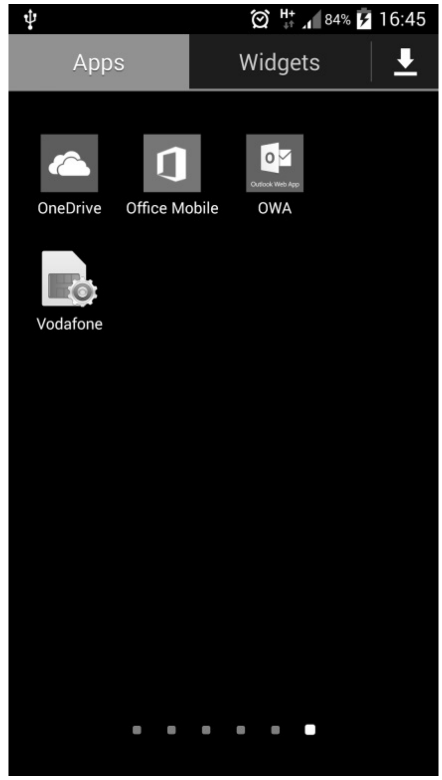

Fig. 8 The malware application is no longer visible in the icon list of installed applications

These tests have been performed on Samsung i9505 Galaxy S4 with Android 4.4.2.

Fig. 7 The log of Logcat

III. Results and Conclusion

One of the most important problems every successful malware writer has to resolve is hiding malicious software from users. If they do not know that malware is in their mobile devices, they are not able to take steps to remove it. Starting from Android version 3.1 or higher each application running with BroadcastReceiver must also have an Activity, however, this research has shown that this security protection can be avoided. As described above, it has been managed by using camouflage of Activity. Also the icon and the label of the malicious application have been hid. The results of our research are consistent with opinions of many IT security experts: "users should never allow the device to install apps from "unknown" sources" [6]. That is the only reasonable way how to prevent this type of malware to infiltrate Android mobile devices. Based on this research, we recommend antivirus companies to include in their mobile antivirus programs a repeated check whether the option to install software from unknown sources is disabled. Due to the possible presence of Clickjacking malware on Android mobile devices, it is necessary to carry out this checking repeatedly. It is also necessary for an antivirus to notify the user every time the option to install software from unknown sources is enabled. We also recommend antivirus companies to inspect the .../res/values/strings.xml file whether the string tag with the name="app_name" parameter does not contain empty string or whitespace character(s). For example:

- <string name="app_name"></string> or
- <string name="app_name"> </string> or
- <string name="app_name"> </string>
- and etc.

All our recommendations are relatively easy to implement. Running the tests created according to our recommendations is not time consuming and the tests can significantly increase the probability of finding malware with a hidden Activity. That is the reason why the plan is to carry out further research in a cooperation with selected anti-virus companies that focus on malware for mobile devices.

ACKNOWLEDGMENT

This work was supported by Internal Grant Agency of Tomas Bata University under the project No. IGA/FAI/2015/014.

REFERENCES

[1] Isohara, T., Takemori, K., Kubota, A. Kernel-based Behavior Analysis for Android Malware Detection. In: Seventh International Conference on Computational Intelligence and Security (CIS 2011). 2011. pp. 1011 – 1015, ISBN 978-1-4577-2008-6.

[2] Android. “Android Developer“, [online], 2015. http://developer.android.com/develop/index.html.

[3] Google. Company, [online], 2015. https://www.google.com/about/company/.

[4] Android. “Activity finish ()“, [online], 2015. http://developer.android.com/reference/android/app/Activity.html#finish().

[5] Android. “Lifecycle of an Activity“, [online], 2015. http://developer.android.com/images/training/basics/basic-lifecycle-paused.png.

[6] Nelson, P. “Device from Malware“, [online]. 2013. http://www.linuxinsider.com/story/79469.html..

Some aspects of the impact of building automation on energy efficiency of buildings

Pavel Drábek and Martin Zálešák

***Abstract*—** Operation of buildings is, after transport and industry, the largest consumer of energy. For this reason, efficient and sustainable energy use in buildings is an urgent necessity. This article deals with the possibility of reducing energy use in buildings by using automation and control of technologies ensuring reasonable comfort during occupancy. The purpose of this article is to describe the options which could reduce energy demands of buildings depending on the value of energy inputs in an effort to minimize them while maintaining the desired comfort level. Existing methods of reducing energy demands of the buildings are currently close to the limits and additional energy savings are achieved only by disproportionate increase of investments. Modern methods of control can use the reserves which are hidden for traditional systems.

***Keywords*—**regulation, heating system, external temperature running mean, operating temperature, regulation accuracy.

I. Introduction

IT is still a lingering practice to classify energy demands of buildings on the basis of thermal insulation properties of the building envelope, although, more aspects, which cannot be ignored, enter to the evaluation. A relatively large impact on the energy efficiency of buildings bears the quality of regulation the devices adapting internal microclimate according to the user requirements. These devices are heating, cooling and ventilation systems, as well as domestic hot water systems and lighting. Evaluation of quality of regulation must be performed both in terms of user comfort and in terms of operational cost savings.

At the workplace of Tomas Bata University in Zlin arises a team of specialist researchers, which deals with individual aspects of the impact of the implementation of automation to the environment of buildings. One of the research directions is the definition of the impact of regulation and automatic control on the energy efficiency of buildings. This article deals with the issues of regulation of heating systems in relation to the adjustment of the internal set-point temperature to marginal value, which is still within the reasonable comfort level (see Table 1).

The work was performed with financial support of research project NPU I No. MSMT-7778/2014 by the Ministry of Education of the Czech Republic and also by the European Regional Development Fund under the Project CEBIA-Tech No. CZ.1.05/2.1.00/03.0089. Work was also supported in frame of Internal Grant Agency of Tomas Bata University in Zlin, Faculty of Applied Informatics No. IGA/CEBIATech/2015/041.

All authors are with the Tomas Bata University in Zlin, Faculty of Applied Informatics, Department of Automation and Control Engineering, Nad Stranemi 4511, Zlin, Czech Republic, e-mail: (pdrabek@fai.utb.cz).

II. Parameters of regulation of the heating system

Energy consumption of heating systems in the building depends on several parameters, such as external climatic parameters, thermal insulation and storage properties of the building, the degree of utilization of internal and external gains and observance of optimum microclimatic conditions [1]. Levels of microclimate conditions described in a detailed standard EN 15251, divides the internal environment according to the level of expectations of comfort on 4 categories:

I. – High level of expectation and it is recommended for spaces occupied by very sensitive and fragile persons with special requirements like handicapped, sick, very young children and elderly persons.

II. – Normal level of expectation and it should be used for new buildings and renovations.

III. – An acceptable, moderate level of expectation and it may be used for existing buildings.

IV. – Values outside the criteria for the categories mentioned above. This category should only be accepted for limited part of the year.

The proposed parameters of the temperature range for a normal level of expectations is mentioned in Table 1.

Table I proposed parameters range of operational temperatures in winter seasons for heating (Cat. II.) [6]

Type of building or premises	**Range of operating temperature for heating, θ_0 [°C]**
Residential buildings, residential rooms (bedrooms, living rooms, etc.) Sitting activity (~ 1.2 met)	20.0 – 25.0
Residential buildings, other rooms (kitchen, etc.) Standing activity (~ 1.5 met)	16.0 – 25.0
Offices and premises with similar activities (classrooms, restaurants, etc.) Seated activity (~ 1.2 met)	20.0 – 24.0

Assumed clothing insulation ~ 1.0 clo

To reduce the energy demands, it is necessary to equip the building by the regulation device that adjusts the distribution and production of thermal energy depending on the outside temperature and other reference variables and time [4]. Therefore it is appropriate to carry out the regulation of heat supply on external temperature running mean, which includes the above parameters and interprets them as a single number. To determine the value of external temperature running mean with greater accuracy, it is necessary to know the thermal storage properties of the building, which define the thermal inertia, which determines the heat demand. The purpose of the regulation device, operating according to the outside temperature, is to save the energy by the followings functions:

1) Regulation of production and distribution of the heat in order to maintain the desired internal temperature, to ensure an acceptable thermal comfort and simultaneously in terms of energy demands, when the heat demand is determined by the external temperature and thermal storage of building [4].
2) Regulation of the heat amount is carried out according to the schedule which takes into an account the occupancy of premise.

From Table 1 above is evident that the range of operating temperature, which should comply the normal level of expectations, is relatively wide. At this time, the accuracy of regulation enters to the rate of energy efficiency fundamentally, which directly indicates the possibility of decrease of the desired internal temperature in the premises of the building and also, it ensures an acceptable thermal comfort. Accuracy should be assessed at multiple points, because the regulation also affects other dynamic components of the sensor, controller and other components of the heating system, which directly affects the results of the regulation [3]. Some influence on the energy efficiency of buildings also carries the ability to predict system of variable start/stop switches times for example between switching modes according to the time schedule of occupancy in building.

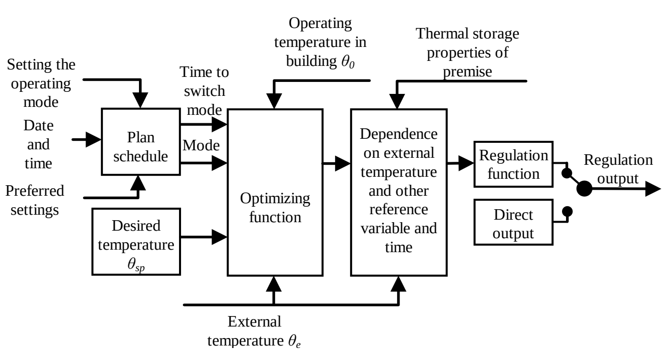

Fig. 2 block scheme of the regulation device [4]

III. Evaluation of the Impact of Regulation on Total Energy Consumption

It was created a room model for obtaining the desired outputs. This model is graphically depicted in Fig. 3. The model of the heating system consists of a heat source, heat distribution and equipment for heat transfer. Heat transfer is represented by the model of the radiator. Heat generation is simulated simply, that the output of the source of the heat is a maximum supply temperature of heating water. Dynamic behavior of system is determined by a returnable temperature of heating water. The model also includes a mixing valve and circulating pump. The position of the valve is dependent on the output signal from the controller, which is in precisely defined time steps readjusted for regulating the heat output variables. Accuracy of the regulation of this model does not depend only on the effectiveness of the internal algorithm for changes the parameters of the controller, but it also depends on the flow characteristics of the mixing valve (K_{VS} value). In the case of using regulation fitting with micro strangling system, it can minimize the rate of regulation deviation, which allows us to heat the premise on operating temperature in a range from 20.0 to 20.5 °C.

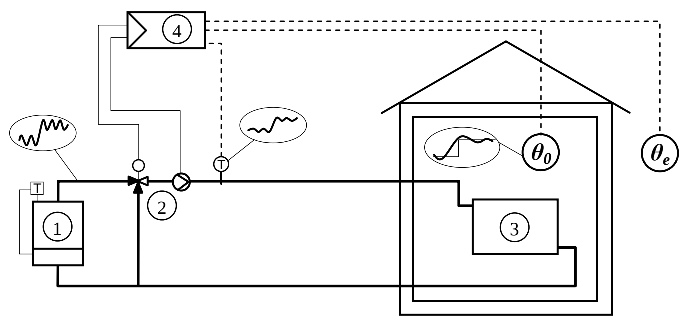

Fig. 3 model of heating system [4]
1 – Heat source, 2 – Heat distribution, 3 – Heat transfer, 4 – Controller, θ_0 – Operating temperature, θe – External temperature

Evaluation of the impact, mentioned way of regulation, on an energy efficiency of buildings can be carried out in several ways. In the case of sufficient knowledge of the managing and regulation system of heating, it can be used a detailed method, which includes the fact that controlled room and the control system interact with each other. Calculation of the impact on different aspects of regulation is necessary to perform on the basis of the thermal response of the room. Calculation relationship is based on the knowledge of energy needs for heating over a defined time period. A convenient way to determine the energy required for heating is to use the model of simple hourly methods according to EN 13790, which ensures a sufficient level of accuracy in areas, where the dynamic behavior has a significant impact on the calculated energy consumption. The standard EN 15232 shows the calculation of the energy required by following formula

$$E = L \cdot \left[\left(\theta_{sp} + \Delta\theta_c \right) - \theta_e \right] \cdot t \qquad (1)$$

ISBN: 978-1-61804-321-4

where

- E is energy consumption for a defined time period [Wh],
- L a transfer coefficient [W/K],
- θ_{sp} the set point which shall be maintained by the control system [K],
- $\Delta\theta_c$ a characteristic parameter represents the impact of actual control system [-],
- θ_e a reference temperature (outdoor temperature) [K],
- t the duration of the time period [h].

The effectiveness of the regulation system is presented by the parameter $\Delta\theta_c$. When the value of this parameter is 0, it represents the best effectiveness of regulation. Theoretically, it is possible to determine the change of energy consumption when the ambient temperature of the room change assuming that the provided time step of the calculation will be shorter than the period of change of the operating temperature.

IV. Calculating the Effect of Adjusting the Internal Temperature on Energy Consumption for Heating

The theoretical analysis of the problem preceded the creating of a model room including aground plan and compositions structures. An important consideration was to determine the particularity of the simulation. An essential part was to verify the influence of each parameter on the total energy consumption for heating. Desired output of the simulation was to determine the amount of potential savings by reducing the internal temperature on marginal value of category II (Table 1).

For calculating the annual heating energy were used the methods and procedures mentioned in the standard EN 13790, in combination with other standards for energy performance. As a source of needed climate data was used the university weather station. To determine the potential energy savings, the internal temperature served as a variable of room model. Other parameters related with the heating system and thermal insulation properties of constructions remained unchanged.

It was possible to obtain a lot of information from the simulation results. Information captured the dynamic behavior of the system and the impact of individual components on the total energy efficiency. The Fig. 4 shows graphically the percentage savings of heating costs. The percentage value is connected with a specific internal temperature and always represents saving compared to an internal temperature of about 1°C higher.

The calculation results show that the impact of accuracy of regulation not only has a positive effect on the thermal comfort of users of the building, but also reduces the unnecessary overheating of the room. Fig. 4 shows that the percentage savings in the range for residential rooms (range 20 – 23 °C) is around 7,5%. In case of high precision of regulation with a deviation about 0,5 °C is possible to reduce the temperature set point on the marginal value from 21,5 to 20,5 °C, which means a saving about 7,3%.

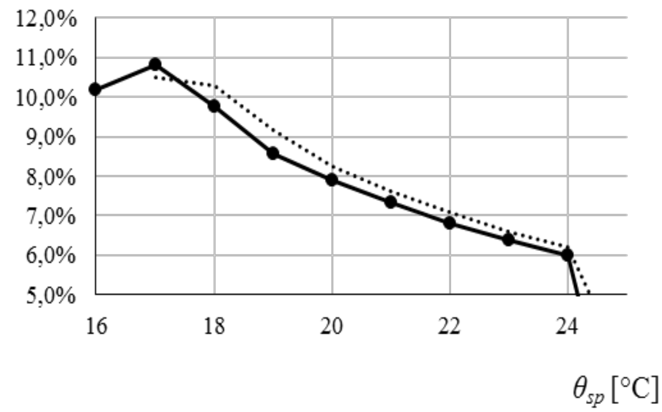

Fig. 4 potential percentage savings due to the adjustment of the internal temperature

V. Conclusion

Today, it is not desirable to build new buildings which would be insufficiently insulated, but also the buildings, which would not be equipped with the suitable control systems preventing unnecessary power consumption. Much more difficult situation is posed by the existing buildings, where it is not possible to change these buildings to the energy efficient buildings in the short term. These reasons are mainly historical and financial [7]. Therefore, for improving the energy properties, it will be better to use the implementation of the intelligent automation control system.

At the workplace of Tomas Bata University in Zlin, the simulation calculations - calculations of accurate determination of the parameters of the regulation system to improve operational and energy efficiency of buildings, will continue. The aim is to define the percentage of energy savings of the specific premise more clearly, which is characterized by various using profile and thermal storage properties.

References

[1] M. Zálešák, V. Gerlich, *In buildings as a necessary mean to achieve assumed energy savings*, TOB 2013, č. 16.

[2] EN 15232. Energy performance of buildings: *Impact of Building Automation, Controls and Building Management* Brussels: European Committee for Standardization, 2012.

[3] Siemens. Building automation: *Impact on energy efficiency*. Siemens Switzerland, 2012, 108 s.

[4] EN 12098. Controls for heating systems*: Control equipment for hot water heating systems* Brusel: European Committee for Standardization, 2013.

[5] EN 13790. Energy performance of buildings: *Calculation of energy use for space heating and cooling*. Brusel: European Committee for Standardization, 2009.

[6] EN 15251. Indoor envirinmental input parameters for design and assessment of energy performance of buildings: *Addressing indoor air quality, thermal environment, lighting and acoustics* Brusel: European Committee for Standardization, 2007

[7] EU. Directive 2010/31/EU of the european parlament and of the council: On the energy performance of buildings. In: *2010/31/EU*. 2010.

ISBN: 978-1-61804-321-4

Solved problems in the field of Integrated systems in buildings

Martin Zalesak and Vladimir Vasek

***Abstract*—**Presented article describes research problems solved in the field of Integrated systems of buildings in the Tomas Bata University in Zlin, Department of Automation and Control Engineering. The research is focused on selected aspects of optimization of the system consisted of the building and its technical systems (HVAC and lighting) including the control systems with the aim to minimize the consumption of total energy while maintaining the requirements on inner comfort parameters. There are described segments of research performed in the article – esp. thermal panel application in buildings, fotovoltaics application, control systems utilization, some aspects of artificial lighting, results of simulation of thermal properties.

***Keywords*—**Phase change materials, heat accumulation, heat simulation, environment, automation in buildings, control systems

I. Introduction

Research in the field of integrated systems in buildings is of a long term character with gradual aims and with the actualization based on development of needs and technological development. The research is focused on selected aspects of optimization of the system consisted of the building and its technical systems (HVAC and lighting) including the control systems with the aim to minimize the consumption of total energy while maintaining the requirements on inner comfort parameters.

II. Segments of research

The whole systems is described on the Fig.1. The building Of different thermal properties is supplied by energy according to the heating and cooling load by energy distribution system supplied by an energy source. The scheme is valid for both heating and cooling state. The energy requirement of the building (cooling and heating loads) depends on the building thermal parameters (both insulation and thermal accumulative properties), on the outside environment parameters and required inner parameters of the building. Energy supplied systems are designed according to the both value of the load and dynamical parameters of the building and it may employ water piping system, air conditional system or their combination. Energy source might be of classical kind, like boilers or coolers, but energy renewable sources might be employed as well (solar panels, heat pump, photovoltaics systems).

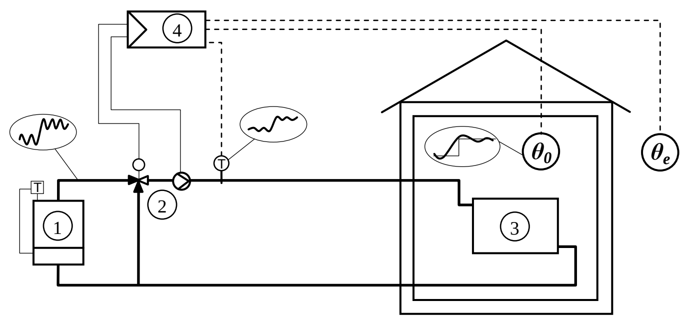

Fig. 1 Model of heating or cooling system in buildings [4]
1 – Energy source, 2 – Energy distribution system, 3 – Energy transfer equipment, 4 – Controller, θ_0 – Operating temperature, θe – External temperature

Energy distribution system is controlled by the control system in order to maintain the required inner conditions. As it can be seen on the Fig 1, the task might be reached by many ways, but only few are optimal ones for the concrete situation. The problem has a complex character and it could be divided in the particular tasks as follows

- study of comfort parameters in buildings as concerns as their levels and the impact of regulation and automatic control based on the standard EN 15 232 [1] and EN 15 251 [2]
- study of thermal parameters of buildings in relation with the energy consumption based on the standard EN 13 790 [3] and systems of heating and cooling including control system
- study thermal accumulative materials and their possible application in buildings in respect of theirs accumulative properties and derived energy consumption for heating and cooling
- application of simulation methods for prediction of thermal behavior of buildings and their structures
- possible utilization of renewable sources of energy in relation

The work was performed with financial support of research project NPU I No. MSMT-7778/2014 by the Ministry of Education of the Czech Republic and also by the European Regional Development Fund under the Project CEBIA-Tech No. CZ.1.05/2.1.00/03.0089.

M. Zalesak is a senior researcher with the Tomas Bata University in Zlín Faculty of Applied Informatics. Department of Automation and Control Engineering, Nad Stranemi 4511, 760 05 Zlín, Czech Republic. (e-mail: zalesak@fai.utb.cz).

V. Vasek is the head of CEBIA- Tech research center and the head of Department of Automation and Control Engineering in Faculty of Applied Informatics in the Tomas Bata University in Zlín Nad Stranemi 4511, 760 05 Zlín Czech Republic.: (e-mail: vasek@fai.utb.cz).

with the HVAC systems and possible energy accumulation
- optimization of artificial lighting in combination with natural lightings in buildings.

III. Impact of Regulation on Energy Consumption

According to the standard EN 15 251 [2] the thermal comfort criteria could be represented by single parameter, operative temperature $\boldsymbol{\theta_0}$ [°C], based on condition that other parameters of thermal comfort, like relative humidity, appropriate clothing, space air temperature distribution, are fulfilled. According to the allowable value range of operative temperature, there are stated I. to IV. categories of the premises in the standard. For customary premises, category II. is specified, with operative temperature range as per table 1.

Table 1 Proposed parameters range of operational temperatures in winter seasons for heating (Cat. II.) [2]

Type of building or premises	**Range of operating temperature for heating, θ_0 [°C]**
Residential buildings, residential rooms (bedrooms, living rooms, etc.) Sitting activity (~ 1.2 met)	20.0 – 25.0
Residential buildings, other rooms (kitchen, etc.) Standing activity (~ 1.5 met)	16.0 – 25.0
Offices and premises with similar activities (classrooms, restaurants, etc.) Seated activity (~ 1.2 met)	20.0 – 24.0

Assumed clothing insulation ~ 1.0 clo

It follows from the table 1, than provided the HVAC system and its control is able to keep the requirements on the lowest allowable level, there could be lowest level of energy consumption for heating for the specific building provided that regulation accuracy enables to keep the operative temperature in the range. There were performed calculations of possible energy savings according to the standard EN 15232 [1], based on the condition that precision of regulation is about 0,5%. The following formula as per standard was used in the calculation

$$E = L \cdot \left(\left(\theta_{sp} + \Delta\theta_c\right) - \theta_e\right) \cdot t \tag{1}$$

where

E is energy consumption for a defined time period [Wh],
L a transfer coefficient [W/K],
θ_{sp} the set point which shall be maintained by the control system [K],
$\Delta\theta_c$ a characteristic parameter represents the impact of actual control system [-],
θ_e a reference temperature (outdoor temperature) [K],
t the duration of the time period [h].

The result of calculation shows Fig. 2

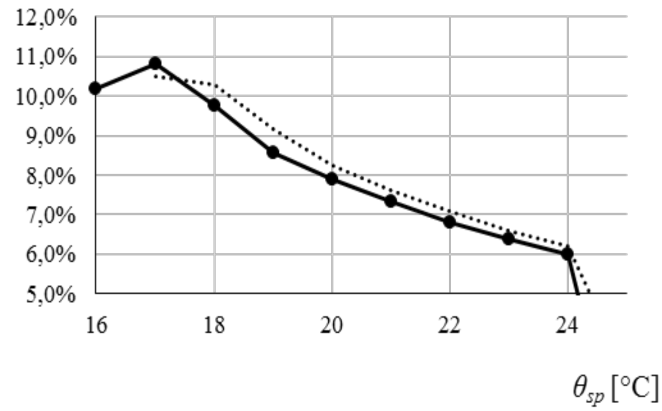

Fig. 4 Potential percentage savings due to the adjustment of the internal temperature

The research will farther be oriented to the efficient heating and cooling system including the control system, in relation with the thermal properties of building in order to reach the optimal energy consumption for heating and cooling.

IV. Study of Thermal Accumulative Materials Utilization Supplied with the HVAC Systems and Photovoltaics

From the point of view of research, the basic part of the system is the thermal panel. The thermal accumulation properties of buildings are directly and indirectly connected with energy consumption for heating and cooling of the same. The controlled thermal accumulation properties of certain systems with energy consumption like buildings could substantially decrease the energy consumption for heating and cooling and to utilize the renewable source of energy (thermal pumps, solar energy etc.). The system as designed is used as a experimental base for the above described application testing a validating the results of computer simulation of the complicated thermal systems.

The systems consists of thermal accumulative panels with active heating a cooling means - photovoltaic panels. The system is described fully in [4] and shown on the Fig. 5.

The system is supplied by AC 230 V and it is possible to supply the system by the current from the photovoltaic system. The DC generated by the panels is transformed to the parameters of the main. Both generated and consumed electricity consumption is measured. Heating of the panels is possible by two ways, either by electrical heating foils connected to the main or by water piping build in the panel. Water is heated by other laboratory device. Cooling of the panels could be allowed by water piping installed in the panels. Water could be cooled by thermoelectric heaters or by the other laboratory device. The scheme of the hydraulic circuits shows Fig. 6 and the view is shown on the Fig.7.

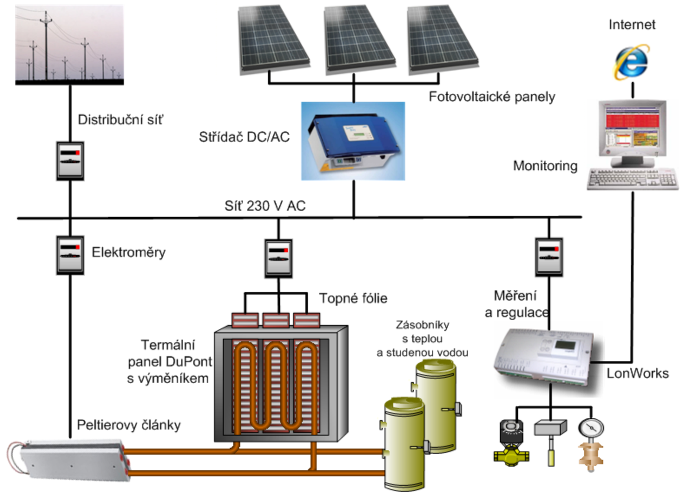

Fig. 5 Basic scheme system including thermal panels and their connection to the HVAC and electricity supply

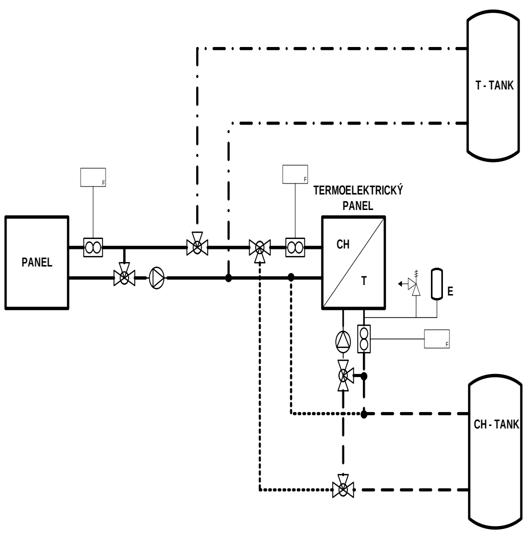

Fig. 6 The scheme of hydraulic circuits

Fig . 7 View of the hydraulic circuits and the thermal panels

The panel itself is built as a composition of set of 24 individual panels with the total size 2,4 m x 2 m. The active part of the panel is an organic PCM wax, which changes the solid state to the liquid one within the temperature range from 21 ^{o}C to 27 ^{o}C. The total thermal capacity within the temperature range is higher than 170 kJ/kg. Thermal conductivity of the wax is 0,14 - 0,18 W/(m.K).

The basic problem of using thermal panels as a heat or cold storage mean is to get the accumulated energy out from the panel in specific time by radiation and unforced convection, i.e. when the panels are installed as a part of the wall or ceiling in the room. There are being studied now thermal accumulative parameters like the time constant of the panel in relation with the radiative properties of the panel surface and the heat convection from the panel in order to optimize the utilization of the panels in light mass buildings. Such study will enable farther to simulate by the computer the thermal behavior of the specific building and based on the simulation find the optimal application of the thermal panels when buildings are designed.

Time constant was determined by several methods from measuring the cooling process of the panel. The average value of time constant as found was at value of $\tau = 6{,}8$ hours.

Based on the known time constant it was possible to simulate the temperature distribution in specific space by suitable simulation software. The preliminary results show that the research as shown might be successful. One of preliminary result of simulation is shown on the Fig. 8.

The preliminary results indicate that the method as described above might be acceptable for study and optimization of the thermal systems.

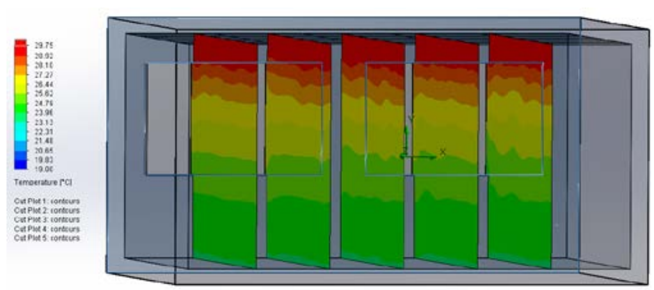

Fig.8 Preliminary result of simulation of the air temperature distribution in the room with applied thermal panels

V. Impact of the External Temperature of the Building to the Inner Environment

Due to the thermal accumulative properties of the building it is the impact of the outside air condition on the energy consumption of the building delayed. The task is to determine the time delay. Both standards CSN 06220 [5] and EN 15251 [2] are dealing with the problem.

The standard CSN 06 0220 [5] describes the heat flux through the outside walls as follows:

$$\Phi = A \cdot U\left(\theta_i(t) - \theta_e(t)\right), \tag{2}$$

A - heat transfer surface, [m^2],
U - heat passage coefficient, [W.m^{-2}.K^{-1}],
θ_i - temperature of air inside the room, [°C],
θ_e - temperature of air inside the room, [°C],
Φ - heat flux through the external wall, [W],
t – time, [s].

While the standard EN 15 251 [2] simplifies the problem by the running mean external temperature

$$\theta_{rm} = (1-\alpha)\left\{\theta_{ed-1} + \alpha \cdot \theta_{ed-2} + \alpha^2 \cdot \theta_{ed-3} \ldots\right\}. \tag{3}$$

The equation (3) can be simplified as follows:

$$\theta_{rm} = (1-\alpha) \cdot \theta_{ed-1} + \alpha \cdot \theta_{rm-1}, \tag{4}$$

where

θ_{rm} - running mean external temperature for the evaluated day, [°C],
θ_{rm-1} - running mean external temperature for the previous day, [°C],
θ_{ed-1} - daily mean external temperature for the previous day, [°C],
θ_{ed-2} - daily mean external temperature two days before the evaluated day, [°C],
θ_{ed-3} - daily mean external temperature three days before the evaluated day, [°C],
α - coefficient from 0 to 1. Its recommended value is 0.8 [1].

There were used an experiment for the case of a room with certain thermal properties in the study. Based on the experimental data the simulation was provided to find the coefficient α with relation of the time constant of the room as specified CSN 06 220 [5].

The results of simulation shows that the same might be used for the determination of the value of α, in order to use it in eq. (3). The Fig. 9 shows the relation of calculating and measured data of the heat flux based on the calculated value α.

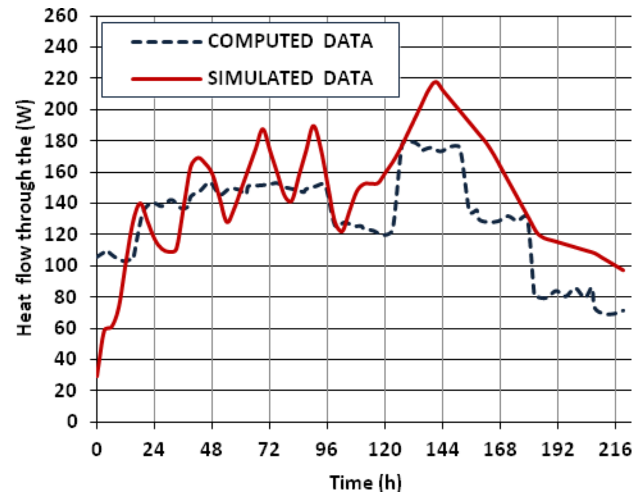

Fig. 9 Relation of calculated and the measured data of the heat flux of the room

Next research in this field will be focused on relation between time constant of the building and the running mean external temperature.

VI. Photovoltaics Systems

The aim of the task is to determine year overall efficiency of photovoltaic system based on the climatic conditions with the view of the possible accumulation of produced electricity in thermal accumulators. The laboratory system is being used for the research as shown on the Fig. 5, in combination with the university meteorological station.
The preliminary results of the efficiency of the panel during days with different climatic conditions are shown on the Fig. 10. Comparison of the accumulative possibilities of thermal panels and production of photovoltaics is shown on the Fig. 11.

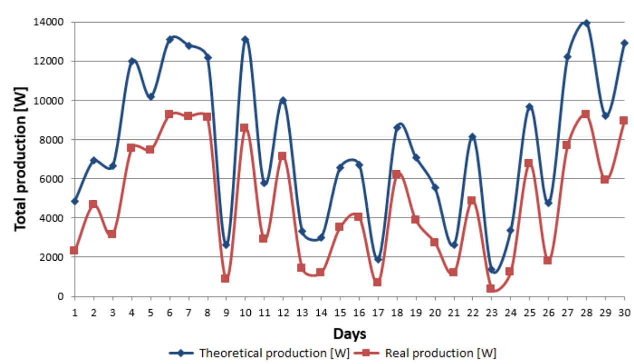

Fig. 10 Comparison of theoretical and real production of photovoltaic system

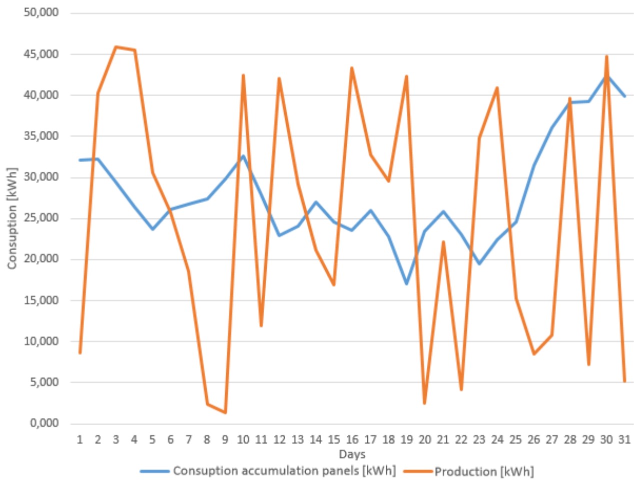

Fig 11 Comparison of the production of electricity and and accumulative capacity of thermal panels

VII. Conclusion

There are described segments of research performed in the article – esp. thermal panel application in buildings, fotovoltaics application and results of simulation of thermal properties.

References

[1] EN 15232. Energy performance of buildings: *Impact of Building Automation, Controls and Building Management* Brussels: European Committee for Standardization, 2012.

[2] EN 15251. Indoor environmental input parameters for design and assessment of energy performance of buildings: *Addressing indoor air quality, thermal environment, lighting and acoustics* Brussels: European Committee for Standardization, 2007

[3] EN 13790. Energy performance of buildings: *Calculation of energy use for space heating and cooling*. Brussels: European Committee for Standardization, 2009.

[4] Zalesak, M. Experimental backup of the field of integrated systems in uildings. Habilitation work. Zlin, 2008

[5] CSN 06 022*: Heating systems in buildings – Dynamic behaviour*. (in Czech). Prague: Czech Standards Institute, 2006.

Application of PSD controller with adaptive identification

Stanislav Plšek and Vladimír Vašek

Abstract — The article deals an implementation of modificated PSD controller for usage in 8-bit microcontroller from Freescale DZ family which is intended for general and automotive purposes. The microcontroller is a main part of control system of fast response soldering iron controller. The controlled system is identified by recursive least square method at the beginning of control process.
A hardware is designed to minimize loses on switching elements and other semiconductor parts. Due to this, the standard rectifier diodes are omitted and the switching of heater is solved by PowerTrench MOSFET transistors which has been optimized for low $r_{DS(on)}$.

Keywords—Discrete controller, microcontroller, modifications, recursive identification, thermocouple.

I. Introduction

DIGITAL PID controllers are known in a whole industry domain and they are frequently used, especially due to their easy setting and theirs favourable price. However, these controllers can be efficiently replaced by their own modifications or by the controllers based on algebraic methods, as a result of a powerful 32-bit microcontrollers boom.
The PID controllers are effective for a fast-response control [1], [2], whereas they do not provide additional functions and do not keep a control quality together. The controllers are modified for purposes of a control-quality improvement [3], [4] and several methods and procedures for their calculations and modifications have been introduced [2], [3], [5]. Modifications usually include limitations of control signal, reductions of wind-up effect, input signal filtration, restrictions of derivative part, automatic settings of controller parameters and theirs various combinations. These modifications may increase the control quality [5], prevent the oscillations of the controlled system or reduce peaks of controlled value if a step-regulation is desired. An example of the PID controller with modifications can be a fast temperature control of soldering irons with requirements of no overshoots, fast response and of depressed level of oscillations. This case of control is commonly necessitated if the high-power soldering irons are used in assembling of electronic parts onto printed circuits boards or theirs repairs. Especially, if the multi-layered boards or soldering areas with a high thermal capacity are soldered, the fast controller response is completely necessary because the high-power tips are commonly used and they can be easily overheated in the case of they are not actively used or if other type of electronic component is soldered.
The main purpose of this paper is firstly to construct an appropriate hardware for fast temperature control, and secondly to design, simulate and verify the PID controller with modifications for this process. In addition, this hardware including the controller is designed for equivalent devices, for example the device with two soldering tips. In the paper, some minor changes in settings are described for these devices.

The project was supported by Internal Grant Agency of Tomas Bata University in Zlin, IGA/FAI/2015/032 and by research project NPU I No. MSMT-7778/2014 by the Ministry of Education of the Czech Republic and also by the European Regional Development Fund under the Project CEBIA-Tech No. CZ.1.05/2.1.00/03.0089. This support is very gratefully acknowledged.

Stanislav Plšek is with the Tomas Bata University in Zlín, nám. T. G. Masaryka 5555, 760 01 Zlín, Czech Republic (phone: +420 576 035 274; e-mail: splsek@fai.utb.cz).

Vladimír Vašek is with the Tomas Bata University in Zlín, nám. T. G. Masaryka 5555, 760 01 Zlín, Czech Republic (phone: +420 576 035 254; e-mail: vasek@fai.utb.cz).

II. Controlled system

The controlled system is a solder tip in our case, but there could be used any heater up to 144W (limited by a transformer 18V/8A and by a heat sink mounted to rectifier diodes). The temperature measure is provided by a thermocouple which is internally connected direct to a heater element [6]. The heater has the 3Ω resistivity and maximum allowed power peak 192W at 24V. If 24V are applied continuously, the heater gets overheated, it begins radiate at red color and next it damages itself (melts, interrupts electric circuit, damages handle). At this condition the temperature probably exceeds 1000°C.

Due to the measurement by thermocouple and the producer does not give information about type of thermocouple, identification had been proceeded by applying 5% power in tip and by solder wrapping. The solder was selected from usually available solders which are listed in Table 1.

Tab. 1 Soft solders and melting point [7]

No.	Alloy	Melting point [°C]
1	Sn60Pb40	183 – 190
2	Sn63Pb37	183
3	Sn60Pb38Cu2	183 – 190
4	Sn99Ag0.3Cu0.7	217 – 228
5	Sn95.5Ag3.8Cu0.7	217 – 218
6	Sn96.5Ag3Cu0.5	217- 220

As can be seen at Fig. 3 and Fig. 4, the alloys No. 1 and No.5 were used for thermocouple identification.

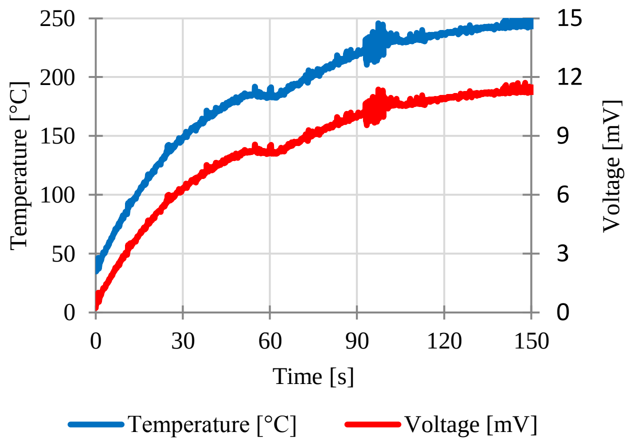

Fig. 1 thermocouple identification – alloy No. 1

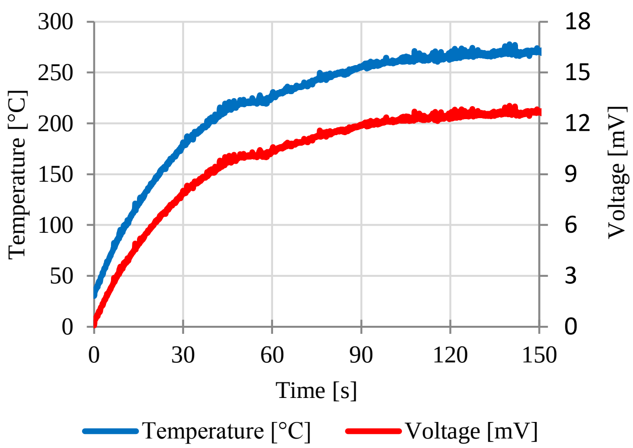

Fig. 2 thermocouple identification – alloy No. 5

Only voltages were measured during process and values at time approximately 60s when solders melted were used for comparison with table voltages of common thermocouples.

Tab. 2 Thermocouple voltages

Type	Materials	Constant at 200°C [μV/°C]
J	Fe-CuNi	55
K	NiCr-NiAl	40
S	PtRh10-Pt	8
B	PtRh30-PtRh6	2
N	NiCrSi-NiSi	33
E	NiCr-CuNi	74

Due to the nonlinearity of some type thermocouples, the table 2 is informative and exact voltage could be found in tables or calculated by appropriate equations.

The thermocouple was identified as type E, because the measured voltages were 8.15mV at 185°C and 10.08mV at 217°C.

III. Recursive Identification

The recursive identification – the least-square method [8], [11], [12] is used to unsure high stability of controlled temperature during the changing of surround conditions. This method need no huge space memory in microcontroller and complicated calculations, because two steps of controller output value and temperature are sufficient to provide identification.

It can be deduced from soldering tip knowledge, thermocouple identification and the construction [13] (the thermocouple is direct joined with the heater spiral), that system can be described by the first-order discrete function:

$$G(z)=\frac{b_1 z^{-1}}{1+a_1 z^{-1}+} \tag{1}$$

An implicit identification method is described by next equation

$$\hat{\mathbf{\Theta}}=\left(\mathbf{F}^T\mathbf{F}\right)^{-1}\mathbf{F}^T\mathbf{y} \tag{2}$$

This equation can be rewritten for $k-1$ measurements into form

$$\hat{\mathbf{\Theta}}(k-1)=\left(\mathbf{F}_{k-1}{}^T\mathbf{F}_{k-1}\right)^{-1}\mathbf{F}_{k-1}{}^T\mathbf{y}(k-1) \tag{3}$$

where:

$$\mathbf{y}^T(k-1)=\left[y(1)\quad y(2)\quad \ldots\quad y(k-1)\right] \tag{4}$$

is a vector of output variables in the interval $(1,k-1)$, and

$$\hat{\mathbf{\Theta}}(k-1)=\left[\hat{\theta}_1(k-1)\quad \hat{\theta}_2(k-1)\quad \ldots\quad \hat{\theta}_r(k-1)\right] \tag{5}$$

is vector of optimal estimates of parameter values of transfer function. A matrix

$$\mathbf{F}_{k-1}=\begin{bmatrix} f_1(1) & f_2(1) & \ldots & f_r(1) \\ f_1(2) & f_2(2) & \ldots & f_r(2) \\ \vdots & \vdots & \vdots & \vdots \\ f_1(k-1) & f_2(k-1) & \ldots & f_r(k-1) \end{bmatrix} \tag{7}$$

is modified matrix $\mathbf{F}$ for $(k-1)$ measurements. If k-measurement is done and

$$\mathbf{y}(k)=\begin{bmatrix} y(k-1) \\ y(k) \end{bmatrix} \tag{8}$$

is described, the matrix (9)

$$\mathbf{F}_k=\begin{bmatrix} \mathbf{F}_{k-1} \\ \mathbf{\Phi}^T(k) \end{bmatrix} \tag{10}$$

can be written, where

$$\mathbf{\Phi}^T(k)=\left[f_1(k)\quad f_2(k)\quad \ldots\quad f_r(k)\right] \tag{11}$$

The vector (12) can be written for k-measured variable

$$y(k)=\mathbf{\Theta}^T\mathbf{\Phi}(k)+e(k) \tag{12}$$

where $\mathbf{\Theta}^T$ is defined as:

$$\mathbf{\Theta}^T=\left[\theta_1\quad \theta_2\quad \ldots\quad \theta_r\right] \tag{13}$$

A covariance matrix $\mathbf{C}(k)$ can be defined as

$$\mathbf{C}(k)=\left[\mathbf{F}_{k-1}^T\mathbf{F}_{k-1}+\mathbf{\Phi}(k)\mathbf{\Phi}^T(k)\right]^{-1} \tag{14}$$

And it can be written as

$$\mathbf{C}(k)=\left[\mathbf{C}^{-1}(k-1)+\mathbf{\Phi}(k)\mathbf{\Phi}^{T}(k)\right]^{-1} \tag{15}$$

A general recursive algorithm can be written as

$$\hat{\mathbf{\Theta}}(k)=\hat{\mathbf{\Theta}}(k-1)+\mathbf{K}(k)\left[y(k)-\hat{\mathbf{\Theta}}^{T}(k-1)\mathbf{\Phi}(k)\right] \tag{16}$$

where $\mathbf{K}(k)$ is time changing vector of gain and can be written as

$$\mathbf{K}(k)=\frac{\mathbf{C}(k-1)\mathbf{\Phi}(k)}{1+\mathbf{\Phi}^{T}(k)\mathbf{C}(k-1)\mathbf{\Phi}(k)} \tag{17}$$

The recursive equation for covariance matrix is

$$\mathbf{C}(k)=\mathbf{C}(k-1)-\mathbf{C}(k-1)\frac{\mathbf{\Phi}(k)\mathbf{\Phi}^{T}(k)\mathbf{C}(k-1)}{1+\mathbf{\Phi}^{T}(k)\mathbf{C}(k-1)\mathbf{\Phi}(k)} \tag{18}$$

The vector of parameters $\mathbf{\Theta}^{T}(k)$ and vector of measurement data $\mathbf{\Phi}^{T}(k)$ can be written for second order transfer function as:

$$\mathbf{\Theta}^{T}(k)=\left[a_{1}\quad b_{1}\right] \tag{19}$$

$$\mathbf{\Phi}^{T}(k)=\left[-y(k-1)\quad u(k-1)\right] \tag{20}$$

IV. Discrete Controller

The modified PSD controller known as Takahashi PID controller [8] was selected due to the requirements of fast response and no overshoots of regulated value. The response is not direct affected by the controller, but the simple calculation of its parameters provides the fast response in a used 8-bit microcontroller.

The controller with modified derivative part is described by equation

$$u(k)=K_{P}\left\{e(k)-e(k-1)+\frac{T_{0}}{T_{I}}e(k)+\frac{T_{D}}{T_{0}}\cdot\right. \\ \left.\cdot\left[2y(k-1)-y(k)-y(k-2)\right]\right\}+u(k-1) \tag{21}$$

where its modified part limits action outputs if the value of w(k) changes and also limits the shifts of the action output to nonlinear zone. Changes of action outputs are also limited if the w(k) is included only by integral part of the controller which can be described as

$$u(k)=K_{P}\left\{-y(k)+y(k-1)+\frac{T_{0}}{T_{I}}\left[w(k)-y(k)\right]+\frac{T_{D}}{T_{0}}\cdot\right. \\ \left.\cdot\left[2y(k-1)-y(k)-y(k-2)\right]\right\}+u(k-1) \tag{22}$$

The equation (22) is used for in microcontroller and its parameters are calculated by next equations

$$K_{P}=0.6K_{PK}\left(1-\frac{T_{0}}{T_{K}}\right) \tag{23}$$

$$T_{I}=\frac{K_{P}T_{K}}{1.2K_{PK}} \tag{24}$$

$$T_{D}=\frac{3K_{PK}T_{K}}{40K_{P}} \tag{25}$$

where T_0 is sampling period, T_K is critical period and K_{PK} is critical gain of controlled system.

The critical period and gain may be obtained by few methods like direct finding on real device with proportional controller (usable for high order systems) or by calculation from identified systems or its model.

The calculation of critical parameters of controlled system may use Ziegler-Nichols criterion and following equations for the first-order system:

$$K_{Pk}(T_{0})=\frac{1-a_{1}}{b_{1}} \tag{26}$$

$$T_{k}(T_{0})=2T_{0} \tag{27}$$

V. Controller Hardware

The Takahashi PID controller was implemented on special hardware developed especially for this case and for control the soldering tip. The hardware includes single double-sided board with microcontroller and digital circuits, analog part for amplification voltage from thermocouple with 16-bit, 250ksps SAR analog to digital converter and galvanically isolated power switch.

MC9S08DZ60 8-bit microcontroller is intended for general purposes and automotive. The core can work at maximum frequency 40MHz and includes 4kB RAM memory for data, 60kB flash memory for program [13] and 2kB EEPROM memory which is used for save parameters of identification and of controller and user settings (temperature, times of hibernation and automatic power off).

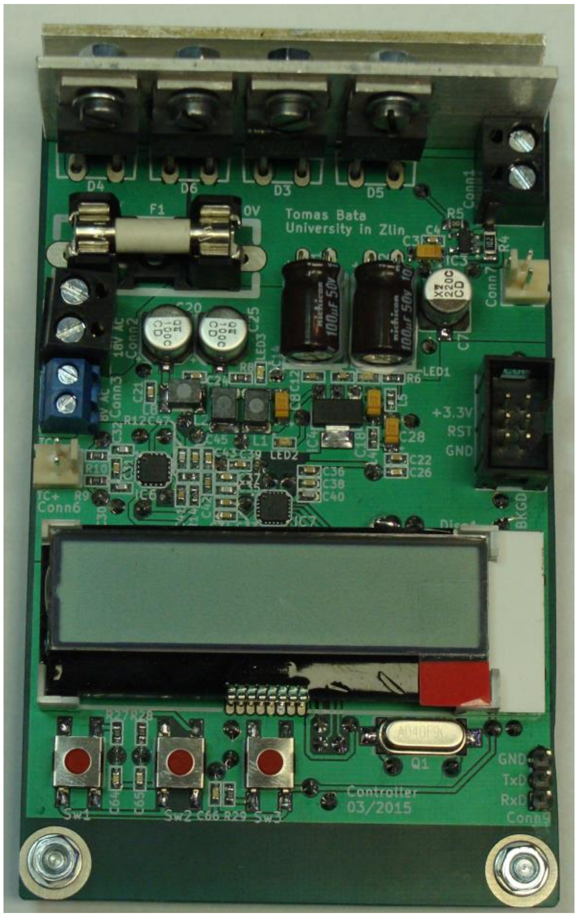

Fig. 3 controller board, dimensions 66x110mm

The analog part measuring the temperature is based on instrumentation rail-to-rail amplifier AD8231 which has digitally settings of gain (1-2-4-8-16-32-64-128) [14]. The reference voltage was set to 1.0V in case of temperature measurement under 0°C. The 16-bit AD converter 7682 was selected. It has internally switchable reference (2.5V or 4.096V) and can operate in unipolar and bipolar mode [15]. In this case it was set to unipolar mode with 2.5V reference – resolution 38.17µV. The 250ksps sampling rate provides fast temperature measurement between two periods of controller and does not influence the output power, because the soldering tip uses common wires for heater and thermocouple. The heater must be switched of before temperature measurement; on the other hand the noise and inducted voltage is measured.

VI. Verification of the Controller

The Takahashi controller and recursive identification algorithm were verified on real devices at changing ambient conditions (laboratory temperatures from 17°C to 29°C, with and without cooling by pressured air flow). First, the step responses were measured and next the controller was verified

The verification was realized by connection through serial line interface and USB converter. The actually measuerd temperature, controller output and set value were sent each period T_0=100ms. The period of PWM output signal was chosen T_{PWM}=20ms (AC line period), because the output signal was generated by PowerTrench MOSFET transistor and the lowest value of the output signal was set to 10µs.

The first time system identification was measured with $u_{OUT} = 5\%$ and $u_{OUT} = 10\%$ in order to the soldering tip not to be overheated and damaged. Step responses of both measurements are shown on Fig. 4 and Fig. 5.

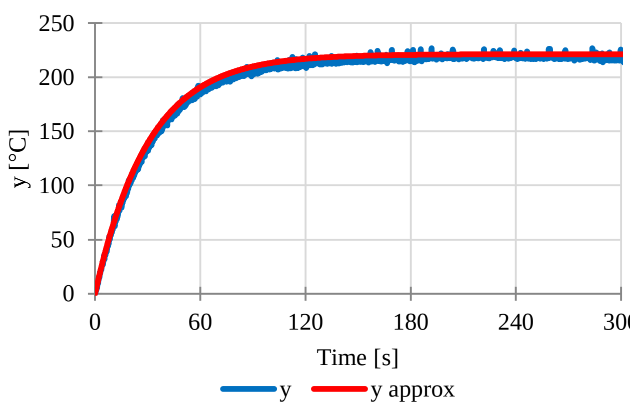

Fig. 4 system identification, u=5%

The continues step responses were calculated for these measurements and are written below (equation (28) corresponds to u=5%; equation (29) corresponds to u=10%). There can be seen some diference caused by diferent measurement conditions.

$$G(s) = \frac{221.3}{30.3s + 1} \tag{28}$$

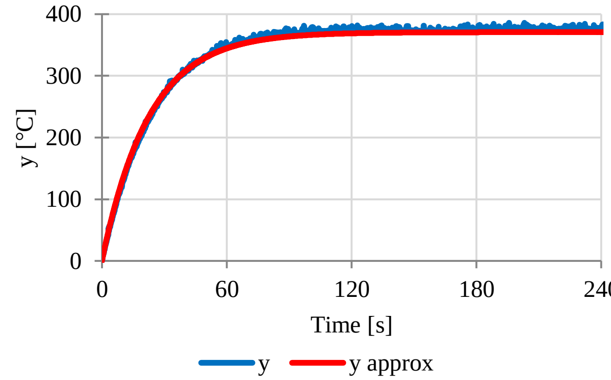

Fig. 5 system identification, u=10%

$$G(s) = \frac{370.6}{22.6s + 1} \tag{29}$$

The controll process is shown in Fig. 6 for two step changes of controlled temperature.

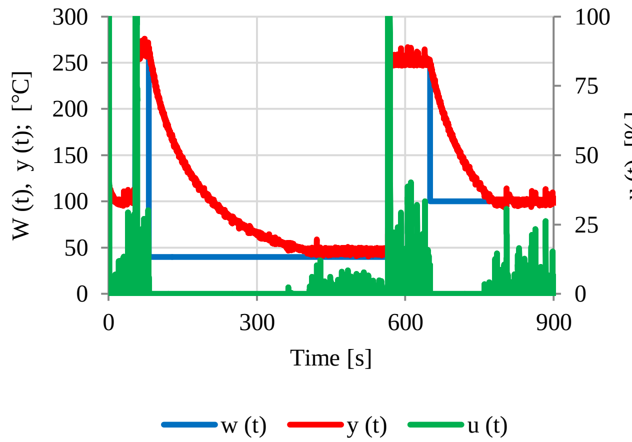

Fig. 6 controll process

As it is ploted in graph, the some noise can be seen in measured value. Due to this, the PID controller produces changing output. It can be probably removed by filtration of voltage from thermocouple. At this graph is low-pass 1.5kHz filter, but it seems that coul be used filter with 50Hz or lower frequency.

VII. Conclusion

The article deals with the application of Takahashi PID controller and recursive identification. The controller board with all circuits (digital, analog and galvanically isolated switch) was designed and manufactured and the controller implementation was verified on 8-bit microcontroller with sampling time 100ms and soldering iron.

The design of electronic circuits was universally devised for other types of heaters with thermocouples. The thermocouple type is independent, because the circuit does not includes specialized parts, but it is based on instrumentation amplifier and 16-bit, 250ksps AD converter.

ISBN: 978-1-61804-321-4

REFERENCES

[1] P. Klan, "PI regulátory s dobrým nastavením", *Automa: magazine for automation and control engineering*. Issue. 6, 2005. ISSN: 1210-9592

[2] K. Åström, J. Karl, T. Hägglund. *PID controllers*. 2nd ed., Research Triangle Park, N.C.: International Society for Measurement and Control, 1995. ISBN 15-561-7516-7

[3] K. Åström, J. Karl, R. M. Murray, *Feedback Systems*. Version v2.10b. Princeton: Princeton University Press, 2009. ISBN 978-0-691-13576-2

[4] J. Balátě, *Automatické řízení*. 2nd ed., Praha: BEN - technická literatura, 2004. ISBN 978-80-7300-148-3

[5] A. O'Dwyer, *Handbook of PI and PID controller tuning rules*, 3rd ed., London: Imperial College Press, 2009. ISBN 978-1-84816-242-6

[6] Jaume Benet Canals. JBC INDUSTRIAS S.A. *Electric soldering iron* [patent]. patent, EP 1 086 772 A2. Granted 28.3.2001.

[7] *Soft solders*, Catalogue, Kovohutě Příbram 2014. Available from http://www.kovopb.cz/products-division/soft-solders/

[8] V. Bobál, *Adaptive and predictive control*. Zlin: Tomas Bata University in Zlin, 2008, 134 p. ISBN 978-80-7318-662-3.

[9] V. Bobál, *Systems identification*. Zlin: Tomas Bata University in Zlin, 2009, 128 p. ISBN 978-80-7318-888-7.

[10] P. Navrátil, *Time-continuous identification methods for design of self-tuning controllers:* dissertation thesis. Zlín, 2007. 119 p.

[11] V. Bobál, *Practical aspects of self-tuning controllers: algorithms and implementations*. Brno: VUTIUM, 1999, 242 p. ISBN 80-214-129-92.

[12] P. Dostálek, J. Dolinay, V. Vašek and L. Pekař, "Self-tuning digital PID controller implemented on 8-bit Freescale microcontroller", *International Journal of Mathematical Models and Methods in Applied Sciences*. 2010, vol. 4, iss. 4, p. 274-281. ISSN 1998-0140

[13] Freescale Semiconductor. *MC9S08DZ60 datasheet* [online]. 2008. Freescale Semiconductor, Inc.: Freescale Semiconductor Literature Distribution Center, 2008 [cit. 2015-04-18]. Available on WWW: http:\\www.freescale.com

[14] Analog Devices. *Zero Drift, Digitally Programmable Instrumetation Amplifier AD8231*. Datasheet [online]. 2011. Analog Devices Inc. [cit 2015-04-18]. Available on WWW: http:\\www.analog.com

[15] Analog Devices. *16-bit, 4channel/8-channel, 250ksps PulSAR ADC AD7682/AD768*. Datasheet [online]. 2015. Analog Devices Inc. [cit 2015-04-18]. Available on WWW: http:\\www.analog.com

General-purpose single-chip control device

Dalibor Slovak and Stanislav Plsek

Abstract— the device includes a microprocessor unit connected to an external timer equipped firmware for the transformation of the logical values of discrete signal values into linked signal control voltages. The input of the microprocessor unit is connected via a USB port with at least one source of a control signal based on MIDI messages, while the output - respectively, outputs, of the microprocessor unit is/are connected to at least one device controlled by the continuous values states of the output voltage in the range of 0 to 5.5 V, depending on the logic values of the discrete input signal.

This general-purpose single-chip control device is designed to control electrically powered machines and equipment, such as, inter alia, lighting equipment and visual stage effects technical equipment. Firmware for the device is described in second paper. This paper is named General-purpose single-chip control device firmware. Our device is protected by CZ Patent No. 304 233 and CZ Utility Model No. 024542. Our device is registered at the European Patent Office too.

Keywords—control voltage, microprocessor, single-chip, USB

I. Introduction

COMPUTERS are very often used as main control interface for various devices. Main aim of our research was to develop small, robust, universal device for control various electrical equipment. The first area for development was usage for control devices on the stage. We have tested our device for another areas of human activities last two years. In current time we prepare interfaces for various voltage ranges such as thyristors and triacs with necessary control logic.

Usage of computers music is standard how for live performance so for music recording. MIDI protocol is the most used for the live performance. It is basic for some setting of musical instruments on the stage, e.g. sound effects too. Some musicians can use MIDI and use it. Some musicians don't know MIDI, but use MIDI too, because MIDI is standard in electronic musical instruments. MIDI is often one of inner components in keyboards, electrical string instruments or wind MIDI instruments. These MIDI components don't need human control. The base element of development was to create hardware with firmware for control variable electrical arrangement.

Dalibor Slovák Author is with the Department of Computer and Communication systems, Tomas Bata University in Zlin, Faculty of Applied Informatics nám. T.G.Masaryka 5555, 760 01 Zlín Czech republic (corresponding author to provide phone: +420 576 035 271; slovak@fai.utb.cz)

Stanislav Plšek is with the Tomas Bata University in Zlín, nám. T. G. Masaryka 5555, 760 01 Zlín, Czech Republic (phone: +420 576 035 274; e-mail: splsek@fai.utb.cz).

The device consists of a CPU, which is in this case, the PIC 18F2550 by Microchip company, 8 LEDs, crystal and necessary stabilization capacitors. An integral part is a USB type B connector for connection to a PC too.

II. Solution

General-purpose single-chip device was designed as a versatile development board for PIC18F2550 microcontroller applications with emphasis on the use of USB microcontrollers.

This hardware was created for needs of simulation without necessary to connect with real stage devices as lights or artificial smokes and water fountains too. During another research periods and test procedures was found out, that device is capable for control most of electrical devices and equipment. It is a very small cheap device. This hardware has eights simulation LEDs for controlling of Pulse Width Modulation (PWM) value. The full shine means the full value (100%) of PWM. Device has a USB connector type B and external timer and jumper for easy re-programing. The main part is MCU by American company Microchip [5].

A. General-purpose single-chip control device MCU

General-purpose single-chip control device MCU is a microcontroller PIC 18F2550 by Microchip company. It is a single chip which is compatible with USB protocol version 2.0. It also supports both USB transfer types.

The serial communication module, based on the standard RS- 232 protocol provides support for the LIN bus standard. EUSART (Enhanced Universal Synchronous/Asynchronous Receiver/Transmitter) also includes automatic detection of baud rate and 16-bit baud rate generator. If the microcontroller used in the internal oscillatory block EUSART is used in place of communication, where nurses access to unused external oscillator, avoiding mistakes in the requirements for induction.

In Run mode is controller, when running the processor and peripherals. In Idle mode runs only the peripherals. Sleep mode is set, even when is not running CPU or peripherals. The device can be connected to two external oscillator frequency up to 48 MHz. The controller has its internal oscillator too. The user can choose from a total number of eight oscillation frequencies between 31 kHz to 8 MHz [5].

Some special hardware features have been included to improve performance. Dual port memory in the device's data memory space (USB RAM) has been supplied to share direct memory access between the microcontroller core and the Serial Interface Engine. Buffer descriptors are also provided, allowing users to freely program endpoint memory usage within the USB RAM space.

ISBN: 978-1-61804-321-4

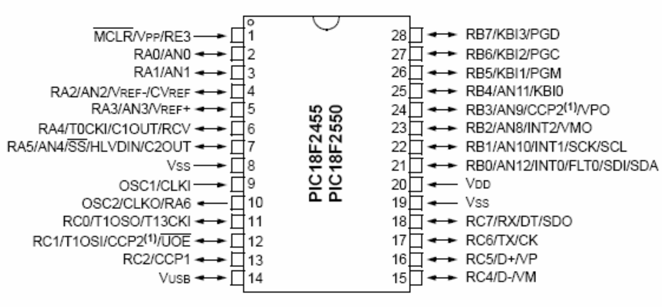

Fig.1 pins of microchip 18F2550

A Streaming Parallel Port has been provided to support the uninterrupted transfer of large volumes of data, such as isochronous data, to external memory buffers. USB Status and control the operation of the USB module is configured and managed through three control registers. In addition, a total of 22 registers are used to manage the actual USB transactions. The registers are:

- USB Control register (UCON)
- USB Configuration register (UCFG)
- USB Transfer Status register (USTAT)
- USB Device Address register (UADDR)
- Frame Number registers (UFRMH:UFRML)
- Endpoint Enable registers 0 through 15 (UEPn)

External clock input, external clock, external clock with input output interface, external clock with phase locked loop and external clock with programmed input and output oscillator modes require an external clock source to be connected to the OSC1 pin. There is not any oscillator start-up time required after a Power-on Reset or after an exit from Sleep mode. In the EC and ECPLL Oscillator modes, the oscillator frequency divided by 4 is available on the OSC2 pin. This signal may be used for test purposes or to synchronize other logic.

B. Motherboard

Motherboard is connected via the USB port, which provides a stable 5V. To filter this voltage is added inductance (ferrite seed) and 100μF electrolytic capacitor. Microcontroller also contains a stabilizer 3.3V, which is used to stabilize the output 1μF ceramic capacitor.

C. External oscillator for Microchip 18F2550

The source for generating the clock signal is 20MHz XTAL with two 15pF ceramic capacitors. The value of the crystal was chosen because of its availability, the actual microcontroller allows the use of crystal in the values (4, 8, 12, 16, 20, 24, 40, 48 MHz). Microcontroller is also equipped with an internal RC oscillator, but using the USB connection you have to use the exact source of the clock frequency crystal [3] ,[5],[7] .

1) Modes of oscillator

In previous PIC devices, all core and peripheral clocks were driven by a single oscillator source; the usual sources were primary, secondary or the internal oscillator. With PIC18F2455/2550/4455/4550 devices, the primary oscillator becomes part of the USB module and cannot be associated to any other clock source. Thus, the USB module must be clocked from the primary clock source; however, the microcontroller core and other peripherals can be separately clocked from the secondary or internal oscillators as before. Because of the timing requirements imposed by USB, an internal clock of either 6 MHz or 48 MHz is required while the USB module is enabled.

2) MULTIPLE INNER OSCILLATOR OPTIONS AND FEATURES

PIC18F2550 offer twelve different oscillator options, allowing users a wide range of choices in developing application hardware. These include:

- Four Crystal modes using crystals or ceramic resonators.
- Four External Clock modes, offering the option of using two pins (oscillator input and a divide-by-4 clock output) or one pin (oscillator input, with the second pin reassigned as general I/O).
- An internal oscillator block which provides an 8 MHz clock (±2% accuracy) and an INTRC source (approximately 31 kHz, stable over temperature and VDD), as well as a range of 6 user-selectable clock frequencies, between 125 kHz to 4 MHz, for a total of 8 clock frequencies. This option frees an oscillator pin for use as an additional general purpose I/O.
- A Phase Lock Loop (PLL) frequency multiplier, available to both the High-Speed Crystal and External Oscillator modes, which allows a wide range of clock speeds from 4 MHz to 48 MHz.
- Asynchronous dual clock operation, allowing the USB module to run from a high-frequency oscillator while the rest of the microcontroller is clocked from an internal low-power oscillator. Besides its availability as a clock source, the internal oscillator block provides a stable reference source that gives the family additional features for robust operation:
- Fail-Safe Clock Monitor: This option constantly monitors the main clock source against a reference signal provided by the internal oscillator. If a clock failure occurs, the controller is switched to the internal oscillator block, allowing for continued low-speed operation or a safe application shutdown.
- Two-Speed Start-up: This option allows the internal oscillator to serve as the clock source from Power-on Reset, or wake-up from Sleep mode, until the primary clock source is available [9].

3) Types of oscillators

In previous PIC devices, all core and peripheral clocks were driven by a single oscillator source; the usual sources were primary, secondary or the internal oscillator. With PIC18F2455/2550/4455/4550 devices, the primary oscillator becomes part of the USB module and cannot be associated to any other clock source. Thus, the USB module must be clocked from the primary clock source; however, the microcontroller core and other peripherals can be separately clocked from the secondary or internal oscillators as before. Because of the timing requirements imposed by USB, an internal clock of either 6 MHz or 48 MHz is required while the USB module is enabled.

PIC18F2455/2550/4455/4550 devices can be operated in twelve distinct oscillator modes. In contrast with previous

ISBN: 978-1-61804-321-4

PIC18 enhanced microcontrollers, four of these modes involve the use of two oscillator types at once.

Users can program the FOSC3:FOSC0 Configuration bits to select one of these modes:

1. XT Crystal/Resonator
2. XTPLL Crystal/Resonator with PLL enabled
3. HS High-Speed Crystal/Resonator
4. HSPLL High-Speed Crystal/Resonator with PLL enabled
5. EC External Clock with FOSC/4 output
6. ECIO External Clock with I/O on RA6
7. ECPLL External Clock with PLL enabled and FOSC/4 output on RA6
8. ECPIO External Clock with PLL enabled, I/O on RA6
9. INTHS Internal Oscillator used as microcontroller clock source, HS Oscillator used as USB clock source
10. INTXT Internal Oscillator used as microcontroller clock source, XT Oscillator used as USB clock source
11. INTIO Internal Oscillator used as microcontroller clock source, EC Oscillator used as USB clock source, digital I/O on RA6
12. INTCKO Internal Oscillator used as microcontroller clock source, EC [9].

D. Universal serial bus implementation in Microchip PIC 18F2550

The PIC18F2550 device contains a full-speed and low-speed compatible USB Serial Interface Engine (SIE) that allows fast communication between any USB host and the PIC® microcontroller. The SIE can be interfaced directly to the USB, utilizing the internal transceiver, or it can be connected through an external transceiver. An internal 3.3V regulator is also available to power the internal transceiver in 5V applications. Some special hardware features have been included to improve performance. Dual port memory in the device's data memory space (USB RAM) has been supplied to share direct memory access between the microcontroller core and the SIE. Buffer descriptors are also provided, allowing users to freely program endpoint memory usage within the USB RAM space. A Streaming Parallel Port has been provided to support the uninterrupted transfer of large volumes of data, such as isochronous data, to external memory buffers

Some special hardware features have been included to improve performance. Dual port memory in the device's data memory space (USB RAM) has been supplied to share direct memory access between the microcontroller core and the SIE. Buffer descriptors are also provided, allowing users to freely program endpoint memory usage within the USB RAM space. A Streaming Parallel Port has been provided to support the uninterrupted transfer of large volumes of data, such as isochronous data, to external memory buffers.

1) 3.1 USB MIDI Event packet

A 32-bit USB-MIDI Event Packet is adopted to construct multiplexed MIDI streams (MUX MIDI) that can be sent or received by each MIDI Endpoint. At the sending end, multiple individual MIDI streams are placed into constant sized packets (with cable number) and are interleaved into a single MUX MIDI stream. At the receiving end, the multiplexed stream is properly demultiplexed, the data is extracted from the 32-bit USB MIDI Event Packets, and each original MIDI stream is routed to the indicated virtual MIDI port. In this way, one endpoint can have multiple Embedded MIDI Jacks logically assigned. This method makes economical use of few endpoints but requires a mux/demux process on both ends of the pipe [11], [4].

The basis of the MIDI communication is called a MIDI message, which consists of three bytes. Each MIDI message (event) is presented as three eight-digit binary values, which are made up of zeros and ones. Each MIDI message can then contains in the each byte value from 0 to 255, for a total of 256 different values. MIDI messages are divided into two basic categories: Status messages and Data messages.

Status message determines the type of information that is sent via MIDI. Indicates a device that receives a message that the event belongs to which channel the MIDI event belongs and what it is. It may be an event: Note On, Pitch Change, Program Change (patch change) and After Touch (the last event occurs when it is developed further pressure on the already depressed note).

Data messages contain information in the device about it what values are assigned to events, which carries the Status messages.

Musical Instrument Digital Interface (MIDI) data is transmitted via USB using 32 - bit MIDI Event Packet. Data transmission is performed using the four bytes messages. USB MIDI Event Packet allows to create a virtual connection between the endpoints USB host and USB MIDI devices due to the USB MIDI Event Packet. This method of connection is advantageous for its low data flow, which does not require a large number of endpoints, like other types of USB devices. Each MIDI event has its own USB MIDI packet, which prevents creation of many mistakes.

The first four bytes starting at the MSB position contains information on the number of virtual MIDI cable, which it is transmitted by a given MIDI information. The value of CN is an indication of the range 0x0 through 0xF indicates the number of the embedded jack, through which there is a link with appropriate MIDI functionality.

Second nibl LSB is second part of MIDI message. This is the identification of MIDI message. Table 1 shows how different bytes write MIDI messages from the USB MIDI packet, which have to be submitted if it will be to communicate and receive MIDI information via the USB protocol.

Tab. 1 USB MIDI event packet

Byte 0		Byte 1	Byte 2	Byte 3
CN cable number	CIN Code Index - Number. MIDI generic classifica-tion	MIDI First byte	MIDI Second byte	MIDI Third byte

E. Usage of PWM in General-purpose single-chip device

In Pulse-Width Modulation (PWM) mode, the CCPx pin produces up to a 10-bit resolution PWM output. Since the CCP2 pin is multiplexed with a PORTB or PORTC data latch, the appropriate TRIS bit must be cleared to make the CCP2 pin an output. Figure 8 shows a simplified block diagram of the CCP module in PWM mode.
The PWM period is specified by writing to the PR2 register. The PWM period can be calculated using the following formula:

$$PWM\ Period = [(PR2) + 1] \bullet 4 \bullet TOSC \bullet (TMR2\ Prescale\ Value) \qquad (1)$$

PWM frequency is defined as 1/[PWM period]. When TMR2 is equal to PR2, the following three events occur on the next increment cycle:
• TMR2 is cleared
• The CCPx pin is set (exception: if PWM duty cycle = 0%, the CCPx pin will not be set)
• The PWM duty cycle is latched from CCPRxL into CCPRxH.

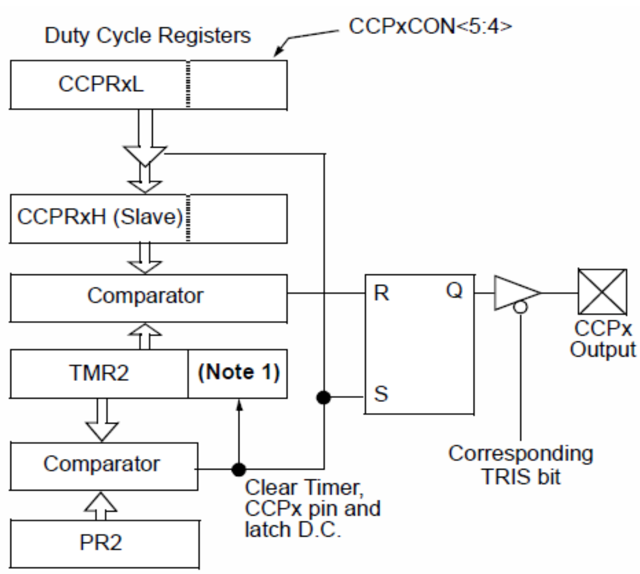

Note 1: The 8-bit TMR2 value is concatenated with the 2-bit internal Q clock, or 2 bits of the prescaler, to create the 10-bit time base.

Fig.2 simplified schema of Pulse Width Modulation

A PWM output has a time base (period) and a time that the output stays high (duty cycle). The frequency of the PWM is the inverse of the period (1/period).

The PWM duty cycle is specified by writing to the CCPRxL register and to the CCPxCON<5:4> bits. Up to 10-bit resolution is available. The CCPRxL contains the eight MSbs and the CCPxCON<5:4> bits contain the two LSbs. This 10-bit value is represented by CCPRxL:CCPxCON<5:4>.

CCPRxL and CCPxCON<5:4> can be written to at any time, but the duty cycle value is not latched into CCPRxH until after a match between PR2 and TMR2 occurs (i.e., the period is complete). In PWM mode, CCPRxH is a read-only register.

The CCPRxH register and a 2-bit internal latch are used to double-buffer the PWM duty cycle. This double-buffering is essential for glitchless PWM operation.
When the CCPRxH and 2-bit latch match TMR2, concatenated with an internal 2-bit Q clock or 2 bits of the TMR2 prescaler, the CCPx pin is cleared.

F. Setup of PWM

The following steps should be taken when configuring the CCP module for PWM operation:

1) 1. Set the PWM period by writing to the PR2 register.
2) Set the PWM duty cycle by writing to the CCPRxL register and CCPxCON<5:4> bits.
3) Make the CCPx pin an output by clearing the appropriate TRIS bit.
4) Set the TMR2 prescale value, then enable Timer2 by writing to T2CON.
5) Configure the CCPx module for PWM operation [9].

III. CONCLUSION

The paper describes only a hardware of General-purpose single-chip device. The paper is only a first part. Second part is in paper which is named Universal Single-chip Device Firmware. We created device for control lightning and water fountain systems. We tested electric motors. Our tests were successful. We have protected our device by CZ patent and CZ utility model. Our device is entered at European patent office too. Presently we develop electric voltage transducers for another forms of usage of our device.

REFERENCES

[1] D. Slovak, "General-purpose single-chip device" CZ Patent No. 304233. 15.1.2014.

[2] D. Slovak, "General-purpose single-chip device". Czech republic. Utility model No. 024542. 12.11.2012.

[3] D. Slovak, "USB MIDI Lights Device". in *Proc Recent Research in Automatic Control*. Lanzarote, Canary Islands: WSEAS Press, 2011, pp. 300-306. ISBN 978-1-61804-004-6.

[4] *Universal Serial Bus Device Class Definition for Audio Devices.pdf* [available online] http://www.usb.org

[5] D. Slovak, "Protocol MIDI and stage equipment", *Tomas Bata University, Faculty of Applied Informatics, Department of Applied Infomatics*, 2008, 64 p., Thesis supervisor prof. Ing. Vladimír Vašek, CSc.

[6] C. Poepel, D. Overholt. *Recent Developments in Violin-related Digital Musical Instruments: Where Are We and Where Are We Going?*, NIME06, *6th International Conference on New Interfaces for Musical Expression*, 2006.

[7] D. Slovak, "Pulse Width Modulation Control Voltage Interface," *in Proc. Recent Advanced in Communication, Circuits and Technological Innovations*. Paris, France: North Atlantic University Union, 2012, pp. 252-257.

[8] D. Slovak, "Universal serial bus musical instrument digital interface hardware," *International Journal of Mechanics. Journal* [online]. 5(4), pp. 294-301. T. Modegi, Shun-ichi Iisaku, Proposals of MIDI Coding and its Application for Audio Authoring, MMCS, IEEE International Conference, pp. 305 – 314 , 1998.

[9] *PIC18F2455/2550/4455/4550-datasheet.pdf*, Available: http://ww1.microchip.com/downloads/en/devicedoc/39632c.pdf

[10] *Universal Serial Bus Device Class Definition for MIDI Devices.pdf* Available: http://www.usb.org/developers/docs/devclass_docs/midi10.pdf

General-purpose single-chip control device firmware

Dalibor Slovak and Stanislav Plsek

***Abstract*—** the article connects to paper which is named General-purpose single-chip device. The main aim of our software development was to create cheap, small and robust firmware. The hardware was created for tests of software applications which will be base for controlling electrical device via electrical voltage value modulation. Paper describes elementary requirements for creation typical USB device's firmware and their connection with most of personal computers operating system such as are Windows, MacOS and Linux. Our device is protected by CZ Patent No. 304 233 and CZ Utility Model No. 024542. Our device is registered at the European Patent Office too.

***Keywords*—**control voltage, microprocessor, single-chip, USB, firmware.

I. Introduction

THE basis for the specification of the firmware is a general standard USB 2.0, followed by the standard for USB MIDI device and it is based on the actual USB Audio standard. Today this is widely used because MIDI transmission of information via the USB is more efficient than transmission of information using standard MIDI DIN jacks. DIN occupies too much space at the PC case, so the external sound cards are used most often with laptops. Placement of DIN connectors in notebooks and external sound cards are precluded due to the size of DIN connectors.

The USB connects USB devices with the USB host. The USB physical interconnect is a tiered star topology. A hub is the centre of each star. Each wire segment is a point-to-point connection between the host and a hub or universal serial bus function, or a hub connected to another hub or universal serial bus function.

II. Solution

We have developed Universal Single-chip device for control of most of electrical device. The paper describes firmware part of our solution. During our development we have lay stress on maximally universal firmware for all operating systems. Our firmware is compatible with each universal serial bus devices which enable to reconfigure their firmware. Due to precise keeping of necessary norms for all suitable kinds of universal serial bus device we created Universal Single-chip Device Firmware compatible with most of operating systems. Important USB norms for our development are:

A. Audio device USB standard

As is clear from the chosen theme, USB is entirely sufficient transmission capacity for transmission of audio data, similarly for MIDI information too. Audio equipment to the USB protocol specifications and their own appropriate set of descriptors required endpoints for transferring audio data. In most cases, it is one of several specifications of the equipment because most of them is always combined with another USB standards. A somewhat different situation is in the case of MIDI devices. MIDI USB standard is an extension of standard USB Audio. Description of the audio data flow is based on the relevant standard [10].

B. MIDI device USB standard

At the beginning it is necessary to say that the typical USB MIDI devices belonging to the USB Communication Device Class (CDC). It is the same as the audio devices are considered as communication interfaces. Class description for the USB MIDI device is one part of standard USB Audio. This happens when a USB device capable of receiving, respectively send MIDI messages. You have to specify the interface on the device interface level. USB MIDI device will have two interfaces (interface). One is an audio interface, second interface is Musical Instrument Digital Interface. This is described using the descriptors, so that the device is easily identified in the system and was particularly visible for the applications that are capable to communicate via MIDI protocol. In our case, they were software application Cubase SX 2, respectively Cubase SX 3 and SX4. Another software were Adobe Audition and Sony Soundforge 11. We created own solution and Graphic User Interface for our tests too.

1) Own test application

The application has, inter alia, one settings window. User sees all universal serial bus audio musical instruments devices at the upper-most combo box. User can choose one device for tests. After device choice, user sets values of the MIDI message third byte. The parameter is named Velocity. There is able to set Velocity parameter for up to eight channels in our device. When current control rod is moving, event "Note On" is generating. Exact values of Velocity parameter serve for check of device reaction due to control voltage value changes, respectively for check of whole controlled system reaction due to control voltage value changes. Control voltage value is

Dalibor Slovák Author is with the Department of Computer and Communication systems, Tomas Bata University in Zlin, Faculty of Applied Informatics nám. T.G.Masaryka 5555, 760 01 Zlín Czech republic (corresponding author to provide phone: +420 576 035 271; slovak@fai.utb.cz)

Stanislav Plšek is with the Tomas Bata University in Zlín, nám. T. G. Masaryka 5555, 760 01 Zlín, Czech Republic (phone: +420 576 035 274; e-mail: splsek@fai.utb.cz).

ISBN: 978-1-61804-321-4

generated via Velocity parameter. Input value of each controlled values has a form of Musical Instruments Digital Interface (MIDI) message. The second byte of MIDI message is a number identification of each MIDI note – input information for controlled device. The value of MIDI message second byte sets activity of controlled device's outputs.

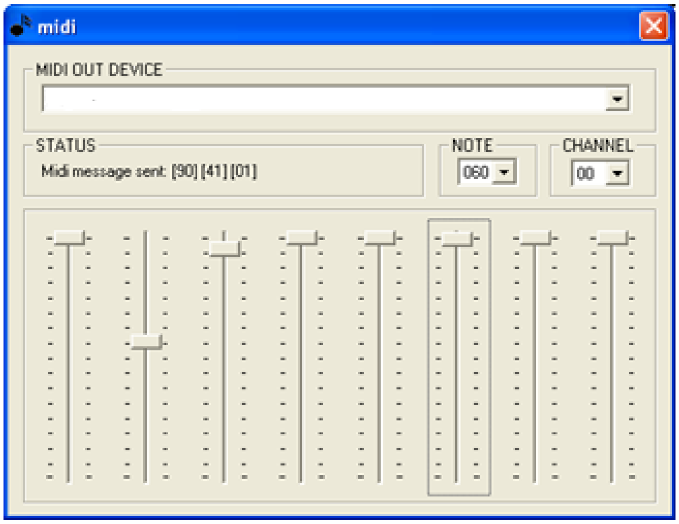

Fig. 1 test application – velocity parameter setting

The specifications of endpoints are MIDI Devices descriptors well-known as endpoints for MIDI input and output jacks. These jacks are of two kinds. Some are known as External MIDI In, respectively OUT jacks. The second groups are then Embedded MIDI In, respectively Embedded OUT jacks. Transmission of the MIDI data from the host to the MIDI device and back is following.

Information passes from Host and it is addressing to device via External MIDI OUT jack. Then information continues to Embedded MIDI IN jack to device. Now information is in device and it is treated. Treated information is send back via Embedded MIDI OUT jack of this device to External MIDI IN jack of the host.

The description is only virtual abstraction. The stave has to be programmed within the USB device. Everything is numbered via usage the descriptors and it is associated together. The relevant descriptor item shows, which connector belongs to its counterpart.

2) Universal Serial Bus Musical Instruments Digital Interface device descriptors

Now we describe main descriptors categories for our Universal Single-chip device.

1. Device Descriptor

The Device Descriptors items correspond to the standard CDC device class

2. Configuration Descriptor

Like the device descriptor with current configuration information.

3. Standard AC Interface Descriptor

Audio Control interface does not have any own endpoint. Default endpoint zero is used for communication. Class-specific Audio Control requests are sent out using default channel. It does not provide any endpoints for settings USB device interrupt.

4. Class-specific AC Interface Descriptor

It is always connected with Standard (header) descriptor, which contains basic information about audio interfaces. It contains all pointers needed to describe a group of audio interfaces in conjunction with particular audio device.

5. Standard MIDI Streaming Interface Descriptor

Standard Interface Descriptor characterizes the device as such. With this this descriptor is specified by the internal structure of the USB MIDI device, and further detailed description is contained in descriptors, which are part of the configuration structure.

6. Class-specific MIDI Streaming Interface Header Descriptor

It provides more (precise) information relating to the internal structure of the device.

7. MIDI IN Jack Descriptor

Describes MIDI IN jacks. This parameter is set in the bJackType variable.

8. MIDI OUT Jack Descriptor

MIDI OUT Jack Descriptor describes the MIDI OUT jacks, as well as MIDI IN descriptor. Its structure is added to other items that are necessary for accurate specification of the corresponding External links, respectively Embedded MIDI IN descriptor. These additional items specified each pin of the MIDI OUT connector, and his status for data transmission.

9. Element Descriptor

Element Descriptor extends structure MIDI OUT descriptor about sum input and check out data station further about setting of pertinent other ability USB MIDI arrangement .

10. Standard MIDI Streaming Bulk Data Endpoint Descriptor

The content of this descriptor is consistent with a standard endpoint descriptor as described in chapter 9.6.4 USB specification [9].

11. Class-Specific MS Bulk Data Endpoint Descriptor

The bNumEmbMIDIJack structure contains the number Embedded MIDI Jacks associated with this endpoint. In the event, that it is an input endpoint, then embedded jack should be the MIDI OUT. If this is the final endpoint, should be the Embedded MIDI IN jack. BaAssocJacks structure contains the ID of the embedded jacks.

12. Standard MS Transfer Bulk Data Endpoint Descriptor

This descriptor also agree with descriptor description from USB specifications chapter 9.6.4., then standard Endpoint descriptor. BEndpoint Adress field designates by the help of D7 parameter, if discuss input transfer endpoint or check out transfer endpoint [3].

C. Universal serial bus data flows

The USB supports functional data and control exchange between the USB host and a USB device as a set of either uni-directional or bi-directional pipes. USB data transfers take place between host software and a particular endpoint on a USB device. Such associations between the host software and a USB device endpoint are called pipes. In general, data movement though one pipe is independent from the data flow in any other pipe. A given USB device may have many pipes.

As an example, a given USB device could have an endpoint that supports a pipe for transporting data to the USB device and another endpoint that supports a pipe for transporting data from the USB device. All communication on the bus is time multiplexed into frames 1 millisecond long. Each frame can contain many transactions of different devices and different endpoints. Data transfer over the bus can be divided into 4 types:

1) Isochronous transfers

Isochronous transfers transport large amounts of data (up to 1023 B) is guaranteed delivery time, but does not ensure data integrity. Isochronous data is continuous and real-time in creation, delivery, and consumption. Timing-related information is implied by the steady rate at which isochronous data is received and transferred. Isochronous data must be delivered at the rate received to maintain its timing. In addition to delivery rate, isochronous data may also be sensitive to delivery delays. For isochronous pipes, the bandwidth required is typically based upon the sampling characteristics of the associated function. The latency required is related to the buffering available at each endpoint. A typical example of isochronous data is voice. If the delivery rate of these data streams is not maintained, drop-outs in the data stream will occur due to buffer or frame underruns or overruns. Even if data is delivered at the appropriate rate by USB hardware, delivery delays introduced by software may degrade applications requiring real-time turn-around, such as telephony-based audio conferencing. The timely delivery of isochronous data is ensured at the expense of potential transient losses in the data stream. In other words, any error in electrical transmission is not corrected by hardware mechanisms such as retries. In practice, the core bit error rate of the USB is expected to be small enough not to be an issue. USB isochronous data streams are allocated a dedicated portion of USB bandwidth to ensure that data can be delivered at the desired rate. The USB is also designed for minimal delay of isochronous data transfers.

2) Bulk transfers

Bulk transfers transport of large amounts of data to ensure integrity, but is not guaranteed delivery time. Bulk data typically consists of larger amounts of data, such as that used for printers or scanners. Bulk data is sequential. Reliable exchange of data is ensured at the hardware level by using error detection in hardware and invoking a limited number of retries in hardware. Also, the bandwidth taken up by bulk data can vary, depending on other bus activities.

3) Interrupt transfers

Interrupt transfers serve a small amount of data to ensure integrity and timely delivery. A limited-latency transfer to or from a device is referred to as interrupt data. Such data may be presented for transfer by a device at any time and is delivered by the USB at a rate no slower than is specified by the device. Interrupt data typically consists of event notification, characters, or coordinates that are organized as one or more bytes. An example of interrupt data is the coordinates from a pointing device. Although an explicit timing rate is not required, interactive data may have response time bounds that the USB must support.

4) Control transfers

They are used during initial device setup (enumeration) [9].

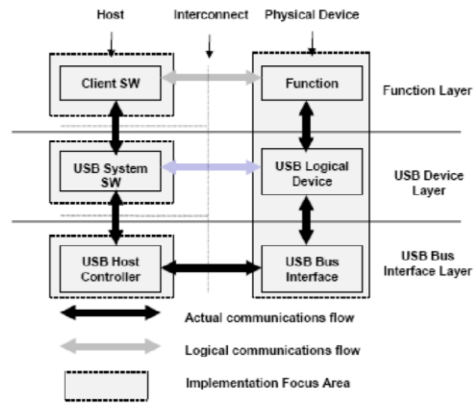

Fig. 2 layers of universal serial bus communication

D. USB-MIDI Converter

USB-MIDI converter is the kernel of every MIDI device, it provides a connection between the host and USB-MIDI interface. It is the fundamental building block. On one hand, it interfaces with the USB pipes, which are used to exchange MIDI data between the host and USB-MIDI endpoints of the device. On the other hand, there is presented an appropriate number of embedded MIDI jacks. These embedded jacks are logical interface presenting the true connectivity within a MIDI device. USB MIDI converter provides a connection between the MIDI OUT endpoint and relevant Embedded MIDI IN jack. Similarly, it provides a link between the Embedded MIDI OUT jack and the corresponding MIDI IN endpoint [11].

1) MIDI Endpoints and Embedded MIDI Jacks

The USB-MIDI Converter typically contains one or more MIDI IN and/or MIDI OUT endpoints. These endpoints use bulk transfers to exchange data with the Host. Consequently, a large quantity of USB-MIDI data can simultaneously be sent by an application without missing any MIDI events. Therefore, music applications can perform complex MIDI operations, including sending many MIDI Note On messages at the same time to more smoothly play the most complex music. The information flowing from the Host to a MIDI OUT endpoint is routed to the USB-MIDI function through one or more Embedded MIDI IN Jacks, associated with that endpoint. Information going to the Host leaves the USB-MIDI function through one or more Embedded MIDI OUT Jacks and flows through the MIDI IN endpoint to which the Embedded MIDI Out Jacks are associated. USB-MIDI converters can connect to multiple Embedded MIDI Jacks. Each MIDI Endpoint in a USB-MIDI converter can be connected to up to 16 Embedded MIDI Jacks. Each Embedded MIDI Jack connected to one MIDI Endpoint is assigned a number from 0 to 15. MIDI Data is transferred over the USB in 32-bit USB MIDI Event Packets, with the first 4 bits used to designate the appropriate Embedded MIDI Jack. A 32-bit USB-MIDI Event Packet is adopted to construct multiplexed MIDI streams (MUX MIDI) that can be sent or received by each MIDI Endpoint. At the sending end, multiple individual MIDI streams are placed into constant sized packets (with cable number) and are interleaved into a single MUX MIDI stream. At the receiving end, the multiplexed stream is properly demultiplexed, the data is extracted from the 32-bit USBMIDI Event Packets, and each original MIDI stream is routed to the indicated virtual MIDI port. In this way, one endpoint can have multiple Embedded MIDI Jacks logically assigned. This method makes economical usage of few endpoints but requires a mux/demux process on both ends of the pipe [11].

2) Transfer Endpoints

The USB-MIDI Converter can contains one or more XFR IN and/or XFR OUT endpoints. These endpoints use bulk transfers to exchange data sets between the Host and any of the Elements within the USB-MIDI function. A mechanism of dynamic association is used to link a Transfer endpoint to an Element whenever that Element needs out-of-band data sets exchanged with the Host. A typical application for this endpoint type of is the transfer of down loadable Samples to a Synthesizer Element. The same technique could be used to download program code to an Element that contains a programmable DSP core [5], [10].

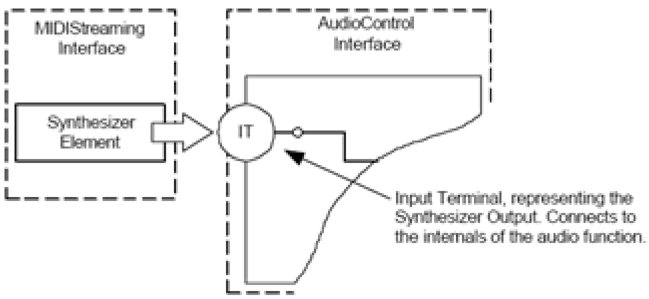

Fig. 3 Input Terminal – Output Terminal

III. Firmware – the most important modules and files

A. *User.c and user.h*

Fundamental module for user needs are two source text files user.c and user.h, that contains custom functions setting and macro. User makes pertinent modification necessary for given functionality of device firmware arrangement. There is module separated from of others in this text too. There are the adjustments made in the case of this software, which is described in this paper. All functional treatment for needs device control by the help of pulse – width modulation. Starting setting is treatment of switched and no switched states for individual arrangements, so setting of timer for connect or disconnect handled devices via pulse width of control voltage [3], [4].

B. *Other important USB communication modules*

usbctrltrf.h a .c **-** The heart of this module is routine USBCtrlEPService (void), which serves only the following three operations - EP0 SETUP EP0 OUT EP0 IN and calls the appropriate routines.

In the case of an ordinary programming of any USB classes of devices (HID, MSD, CDC) do not require any intervention without a deeper study. On the contrary any changes can be detrimental.

main.c **-** Function *main()* includes infinite program central loop *while(1)*. In this loop are procedures *USBTASKS(void)* and *void ProcessIO(void)*. All requisite tasks in programmatic succession are given through instructions in *main function* source code.

usb_compile_time_validation.h – Endpoint descriptors size verification according to standard of USB. Then descriptor reach size can be either 8, 16, 32 or 64 bytes.

usbcfg.h – By the help of this file is performed endpoint configuration of device. So it is set value and default setting of endpoint zero and further then endpoint assignment for configuration descriptor and further also values for interface descriptors and their endpoints.

IV. Conclusion

The paper is second part for paper Universal Single-chip device. We created device for control lightning and water fountain systems. We tested electric motors too. Our tests were successful. We have protected our device by CZ patent and CZ utility model. Our device is entered at European patent office too. Presently we develop electric voltage transducers for another forms of usage of our device. The description of hardware for the Universal Single-chip device firmware is in paper which is named Universal Single-chip device.

References

[1] D. Slovak, "General-purpose single-chip device" CZ Patent No. 304233. 15.1.2014.

[2] D. Slovak, "General-purpose single-chip device". Czech republic. Utility model No. 024542. 12.11.2012.

[3] D. Slovak, "USB MIDI Lights Device". in *Proc Recent Research in Automatic Control*. Lanzarote, Canary Islands: WSEAS Press, 2011, pp. 300-306. ISBN 978-1-61804-004-6.

[4] D. Slovak, "Protocol MIDI and stage equipment", *Tomas Bata University, Faculty of Applied Informatics, Department of Applied Infomatics*, 2008, 64 p., Thesis supervisor prof. Ing. Vladimír Vašek, CSc.

[5] D. Slovak, "Pulse Width Modulation Control Voltage Interface," in *Proc. Recent Advanced in Communication, Circuits and Technological Innovations.* Paris, France: North Atlantic University Union, 2012, pp. 252-257.

[6] C. Poepel, D. Overholt. *Recent Developments in Violin-related Digital Musical Instruments: Where Are We and Where Are We Going?*, NIME06, *6th International Conference on New Interfaces for Musical Expression*, 2006.

[7] D. Slovak, "Universal serial bus musical instrument digital interface hardware," *International Journal of Mechanics*. *Journal* [online]. 5(4), pp. 294-301.

[8] T. Modegi, Shun-ichi Iisaku, *Proposals of MIDI Coding and its Application for Audio Authoring*, MMCS, *IEEE International Conference*, pp 305 – 314 , 1998.

[9] *Universal Serial Bus specification.pdf*, Available: http://www.usb.org

[10] *Universal Serial Bus Device Class Definition for Audio Devices.pdf* Available: http://www.usb.org/developers/docs/devclass_docs/audio10.pdf

[11] *Universal Serial Bus Device Class Definition for MIDI Devices.pdf* Available: http://www.usb.org/developers/docs/devclass_docs/midi10.pdf

Modelling and robust stability analysis of systems with unstructured multiplicative uncertainty

Radek Matušů, Bilal Şenol, and Celaleddin Yeroğlu

***Abstract*—**This contribution is focused on linear time-invariant (LTI) systems with unstructured multiplicative uncertainty. More specifically, it presents an approach to uncertain model construction based on appropriate selection of a nominal system and a weight function followed by the fundamentals of robust stability investigation for considered sort of systems. The initial theoretical parts are accompanied by two illustrative examples in which the second and third order plants with parametric uncertainty are modelled as systems with unstructured multiplicative uncertainty and, subsequently, robust stability of feedback loops containing constructed models and chosen controllers is analyzed and obtained results are briefly discussed.

***Keywords*—**Uncertainty Modelling, Unstructured Uncertainty, Multiplicative Uncertainty, Robust Stability Analysis.

I. Introduction

ROBUSTNESS of control systems represents an attractive research topic which necessity is aroused by everyday control engineering practice. The principal problem is that the mathematical model of a controlled plant almost never exactly matches the real plant behaviour due to understandable effort to build and use simple enough LTI model in which the potential complex features are simplified or neglected and, furthermore, since the real physical parameters of the system can vary owing to a number of reasons. The popular and effective approach how to systematically study the influence of uncertainty and overcome this discrepancy in control tasks is provided by robust control.

Basically, the uncertainty can be taken into consideration by two main ways. Either one can use a model with parametric uncertainty ([1] – [5]) which structure is fixed but the parameters are assumed to lie within given bounds or a model with unstructured uncertainty ([6] – [11]) with even unknown order can be used. Both methods have their pros and cons. An advantage of the unstructured uncertainty is generally easier application of sophisticated controller design methods (based on H_∞).

This work deals with one kind of unstructured uncertainty known as the multiplicative uncertainty. Its main aim is to present an approach to construction of multiplicative uncertainty model from a single-input single-output system with real parametric uncertainty and also to show a technique for robust stability analysis. Within the scope of the presented illustrative examples, the second and third order plants with parametric uncertainty are modelled as the systems with unstructured multiplicative uncertainty (by means of suitable choice of a nominal system and a weight function), and sequentially, the robust stability of feedback loops with obtained plant models and selected controllers is investigated. Some preliminary results related to this contribution and comparison of parametric and unstructured approach to uncertainty modelling can be found in [10], [11].

II. Modelling of Uncertainty

The first and fundamental step in robust control is to respect the difference between true behaviour of control loop and its mathematical description by means of uncertain model utilization. Roughly speaking, one fixed "nominal" model is replaced by the whole family of models represented by some neighborhood of the nominal one. This neighborhood can be quantified essentially via two main approaches.

The first technique, using parametric uncertainty, supposes known structure of the system (known order), but imprecisely known real physical parameters. In practice, the parametric uncertainty is given through intervals which bound the uncertain parameters. For details see e.g [1] – [5].

On the other hand, the second, unstructured uncertainty approach does not need even knowledge of model structure and its description grounds in restriction of the frequency characteristics spread [6] – [11].

The parametric uncertainty is natural and advantageous from the viewpoint of relative simplicity, while the unstructured uncertainty is favourable especially for unmodelled dynamics or nonlinearities and furthermore, preferential for H_∞ control design methods.

The work was performed with financial support of research project NPU I No. MSMT-7778/2014 by the Ministry of Education of the Czech Republic and also by the European Regional Development Fund under the Project CEBIA-Tech No. CZ.1.05/2.1.00/03.0089. This assistance is very gratefully acknowledged.

Radek Matušů is with the Centre for Security, Information and Advanced Technologies (CEBIA–Tech), Faculty of Applied Informatics, Tomas Bata University in Zlín, nám. T. G. Masaryka 5555, 760 01 Zlín, Czech Republic (e-mail: rmatusu@fai.utb.cz).

Bilal Şenol and Celaleddin Yeroğlu are with the Department of Computer Engineering, Faculty of Engineering, Inonu University, 44280 Malatya, Turkey (e-mails: bilal.senol@inonu.edu.tr and c.yeroglu@inonu.edu.tr).

ISBN: 978-1-61804-321-4

One can distinguish among several types of unstructured uncertainty models, i.e. multiplicative and additive model and their inverse versions [6], [12]. This paper deals with multiplicative model which can be described by:

$$G(s) = \left[1 + W_M(s)\Delta_M(s)\right]G_0(s) \tag{1}$$

where $G(s)$ represents an uncertain (perturbed) model, $G_0(s)$ is a nominal model, $W_M(s)$ means a stable weight function representing uncertainty dynamics (distribution of the maximum amplitude of the uncertainty over the frequency), and $\Delta_M(s)$ stands for the uncertainty itself (uncertain information on actual magnitude and phase of perturbation), which can be represented by an arbitrary stable function fulfilling the inequality:

$$\left\|\Delta_M(s)\right\|_\infty \le 1 \quad \Rightarrow \quad \left|\Delta_M(j\omega)\right| \le 1 \quad \forall\omega \tag{2}$$

The scheme of the multiplicative uncertainty (1) is visualized in Fig. 1.

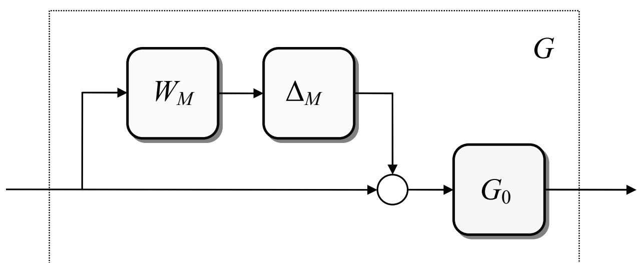

Fig. 1 system with multiplicative uncertainty

The choice of suitable weight function is the important part of the model creation as will be shown in the examples thereinafter. For the weight function the following inequality, where the left side represents normalized perturbation (relative error), must be fulfilled:

$$\left|\frac{G(j\omega)}{G_0(j\omega)} - 1\right| \le \left|W_M(j\omega)\right| \quad \forall\omega \tag{3}$$

Many theoretical tools presume that all members of the family $G(s)$ have the same amount of right-hand (unstable) poles. In other words, that $G(s)$ and $G_0(s)$ have the same amount of right-hand poles for all $\Delta_M(s)$ [6], [12].

III. Robust Stability Analysis

Under assumption of multiplicative uncertainty, the closed-loop system is robustly stable if and only if [6], [7]:

$$\left\|W_M(s)T_0(s)\right\|_\infty < 1 \tag{4}$$

where $T_0(s)$ represents a complementary sensitivity function defined by:

$$T_0(s) = \frac{L_0(s)}{1 + L_0(s)} \tag{5}$$

and where $L_0(s)$ is the open-loop frequency transfer function:

$$L_0(s) = C(s)G_0(s) \tag{6}$$

From the fundamental inequality (4), it can be derived:

$$\begin{aligned} &\left|\frac{W_M(j\omega)L_0(j\omega)}{1 + L_0(j\omega)}\right| < 1 \quad \forall\omega \quad \Rightarrow \\ &\Rightarrow \quad \left|W_M(j\omega)L_0(j\omega)\right| < \left|L_0(j\omega) - (-1)\right| \quad \forall\omega \end{aligned} \tag{7}$$

This expression means that the closed-loop system is robustly stable if and only if the envelope of Nyquist diagrams with radius $\left|W_M(j\omega)L_0(j\omega)\right|$ and centre $L_0(j\omega)$ does not include the critical point [-1, 0*j*]. The visualization of this condition is shown in Fig. 2.

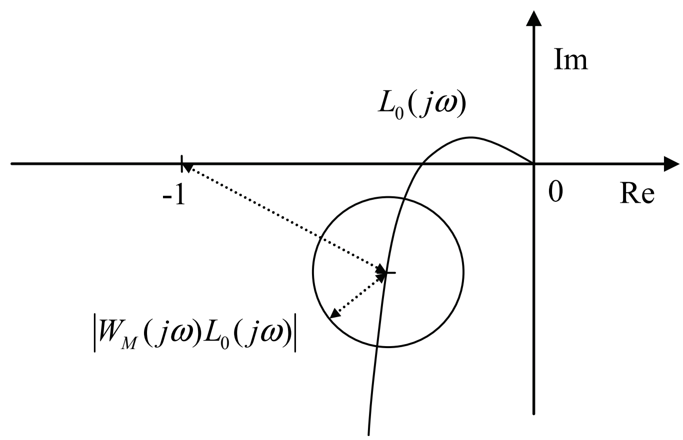

Fig. 2 graphical interpretation of the robust stability condition for multiplicative uncertainty

Furthermore, the robust stability condition (4) can have also the alternative formulation:

$$\left|T_0(j\omega)\right| < \frac{1}{\left|W_M(j\omega)\right|} \quad \forall\omega \tag{8}$$

IV. Illustrative Examples

This section presents the examples of possible construction of multiplicative uncertainty model and subsequent robust stability investigation for a closed loop with such plant model and selected feedback controller.

A. Second Order Plant

First, consider a second order system with two different time constants given by transfer function:

$$G(s)=\frac{K}{(T_1 s+1)(T_2 s+1)} \tag{9}$$

where gain and time constants are supposed to lie within intervals $K\in\langle 1.8, 2.2\rangle$, $T_1\in\langle 9, 11\rangle$ and $T_2\in\langle 0.9, 1.1\rangle$.

Remind that instead of working directly with the parametric system, the model with unstructured multiplicative uncertainty is going to be created and used in the ensuing considerations.

Firstly, the nominal model should be chosen. Here, the average values of the uncertain parameters are utilized, i.e.:

$$G_0(s)=\frac{2}{(10s+1)(s+1)}=\frac{0.2}{s^2+1.1s+0.1} \tag{10}$$

Now, the appropriate weight function, considered as the envelope of uncertainty, has to be found in order to fulfill inequality (3) and cover from the upper side the normalized perturbation of even the worst possible case of uncertainty in the model (9). In this example, such worst case is represented just by one plant with the greatest possible gain $K=2.2$ and the shortest possible time constants $T_1=9$ and $T_2=0.9$. This combination of parameters corresponds to the "uppermost" amplitude characteristics of normalized perturbation from the Fig. 3. Thus, it can be easily derived that the worst case is exactly covered by the weight function:

$$W_{M1}(s)=\frac{2.9s^2+2.2s+0.1}{8.1s^2+9.9s+1} \tag{11}$$

Nevertheless, another weight function can be found for example by using recommendation for unmodelled dynamics uncertainty from [6]:

$$W_M(s)=\frac{\tau s+r_0}{(\tau/r_\infty)s+1} \tag{12}$$

where r_0 is the relative uncertainty at steady-state (low frequencies), r_∞ represents the magnitude at high frequencies, and τ is the approximate value of frequency at which the relative uncertainty reaches 100%.

The appropriate values for this example are $r_0=0.1$, $r_\infty=0.36$ and $\tau=2$ which leads to:

$$W_{M2}(s)=\frac{2s+0.1}{5.55s+1} \tag{13}$$

The second weight function (13) is not as precise for this example as the previous one (11), but it has the lower order.

Bode magnitude plots of both weight functions (11), (13) together with "representative" set of the normalized perturbations are shown in Fig. 3. The set of relative errors is plotted for all combinations of parameters with chosen steps $K=1.8:0.02:2.2$, $T_1=9:0.2:11$ and $T_2=0.9:0.02:1.1$.

The zoomed version of the same Bode magnitude plots is depicted in Fig. 4.

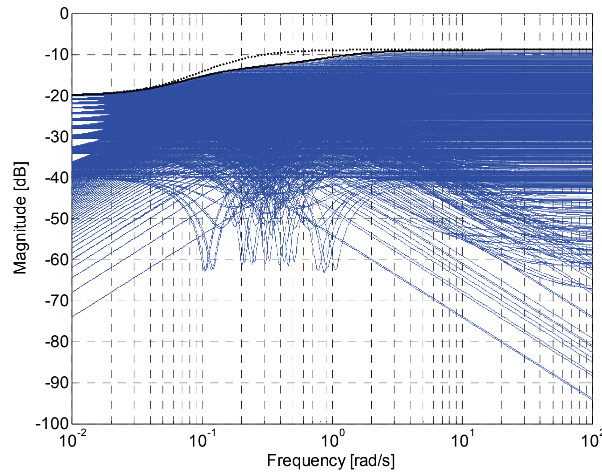

Fig. 3 bode magnitude plots – set of normalized perturbations and weight functions W_{M1} (solid line) and W_{M2} (dotted line)

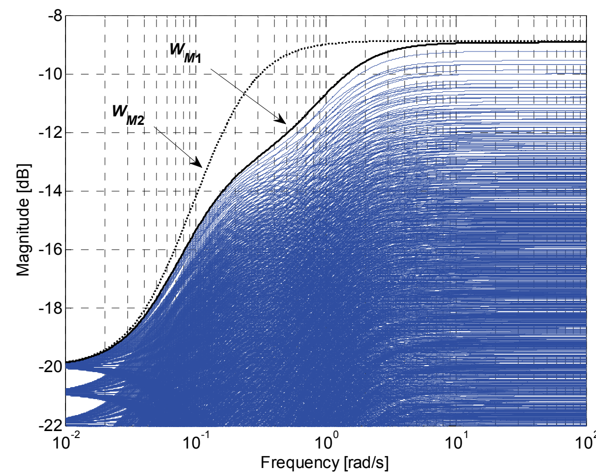

Fig. 4 zoomed version of Bode magnitude plots from Fig. 3 – set of normalized perturbations and weight functions W_{M1} (solid line) and W_{M2} (dotted line)

Thus, if the first weight (11) is considered, the final model of the plant with unstructured multiplicative uncertainty is:

$$\begin{aligned} &G(s)=\left[1+W_{M1}(s)\Delta_M(s)\right]G_0(s)\\ &\|\Delta_M(s)\|_\infty\le 1\\ &G_0(s)=\frac{0.2}{s^2+1.1s+0.1}\\ &W_{M1}(s)=\frac{2.9s^2+2.2s+0.1}{8.1s^2+9.9s+1}\end{aligned} \tag{14}$$

Now, trio of PI controllers is supposed:

$$C_1(s)=\frac{0.5s+1}{s} \tag{15}$$

$$C_2(s) = \frac{2s+1}{s} \tag{16}$$

$$C_3(s) = \frac{s+1}{s} \tag{17}$$

and robust stability of the feedback loop with one of these controllers and plant family (14) is analyzed successively.

For the first PI controller (15), the envelope of Nyquist diagrams given by circles with radius $\left|W_M(j\omega)L_0(j\omega)\right|$ around the Nyquist diagram of nominal $L_0(j\omega)$ (blue curve) is plotted in Fig. 5. It can be clearly seen that the critical point [-1, 0*j*] is included in the envelope and consequently the closed loop with controller (15) and family of systems (14) is robustly unstable.

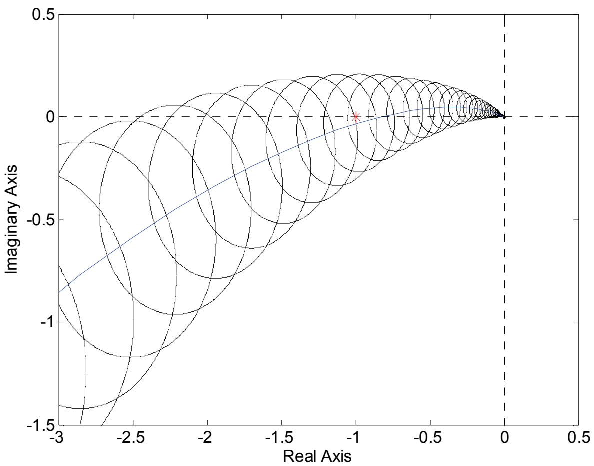

Fig. 5 envelope of Nyquist diagrams for plant family (14) and controller (15) – robustly unstable case

The similar envelope of Nyquist diagrams for the second controller (16) is shown in Fig. 6. In this case, the critical point is excluded from the envelope which entails robust stability of the closed loop with plant family (14) and controller (16).

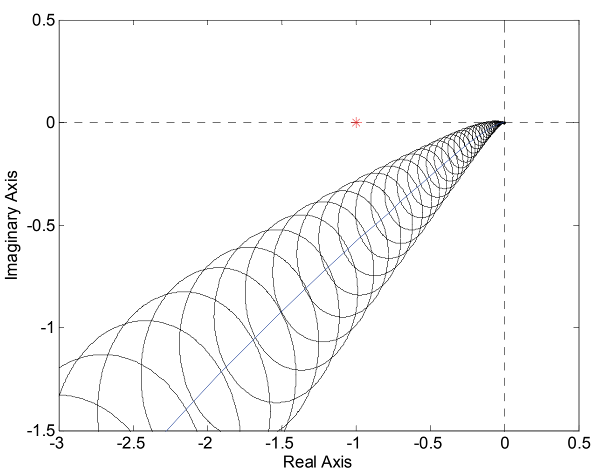

Fig. 6 envelope of Nyquist diagrams for plant family (14) and controller (16) – robustly stable case

Finally, the robust stability condition is visualized for the last PI controller (17) – see Fig. 7. Note that the point [-1, 0*j*] is included in the envelope and thus the closed-loop system is not robustly stable. However, as can be easily verified, the closed-loop system which includes the original plant model (9) with parametric uncertainty is robustly stable in fact. The robust instability holds true for constructed unstructured multiplicative uncertainty model (14), but not for the original parametric model (9). It means that even if the weight function (11) covers the normalized perturbations as tightly as possible (see Fig. 4), the family of systems (14) still can contain some members which are not stabilized by the controller (17). Consequently, one should be aware of potential conservatism in investigation of robust stability when the system with parametric uncertainty is modelled as a system with unstructured multiplicative uncertainty.

Obviously, the utilization of simpler first order weight function (13) would mean even higher level of conservatism in robust stability analysis.

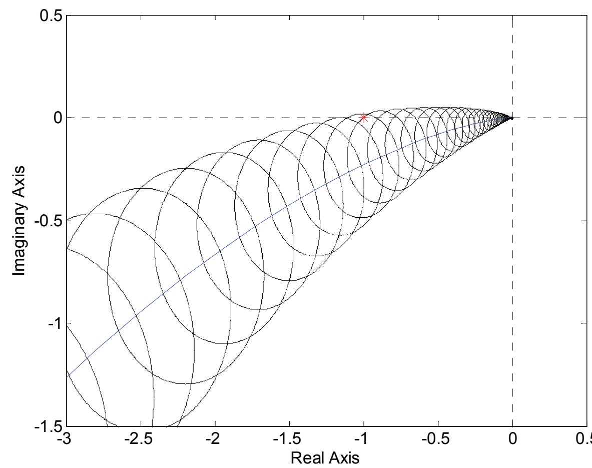

Fig. 7 envelope of Nyquist diagrams for plant family (14) and controller (17) – robustly *unstable?* case

B. Third Order Plant

Assume a third order system (inspired by Burns [13]) with integrating behaviour:

$$G(s) = \frac{1}{s\left(s^2 + a_2 s + a_1\right)} = \frac{1}{s^3 + a_2 s^2 + a_1 s} \tag{18}$$

where $a_1 \in \left\langle 3,5 \right\rangle$ and $a_2 \in \left\langle 1,3 \right\rangle$. The nominal system is considered as:

$$G_0(s) = \frac{1}{s^3 + 2s^2 + 4s} \tag{19}$$

The Bode magnitude plots of normalized perturbations for all combinations of parameters according to $a_1 = 3:0.1:5$, $a_2 = 1:0.1:3$ together with the Bode magnitude plot of the

ISBN: 978-1-61804-321-4

weight function (21) are depicted in Fig. 8. Then, the zoomed version (both frequency and magnitude axis) of the same plots is shown in Fig. 9.

The appropriate weight has been initially chosen as:

$$W_M(s) \approx \frac{0.35(s+1)}{(0.52s)^2 + 2\xi 0.52s + 1} \tag{20}$$

with damping ratio $\xi = 0.25$. Final function, after slight manual adjustment, has the form:

$$W_M(s) = \frac{0.35s + 0.35}{0.273s^2 + 0.26s + 1} \tag{21}$$

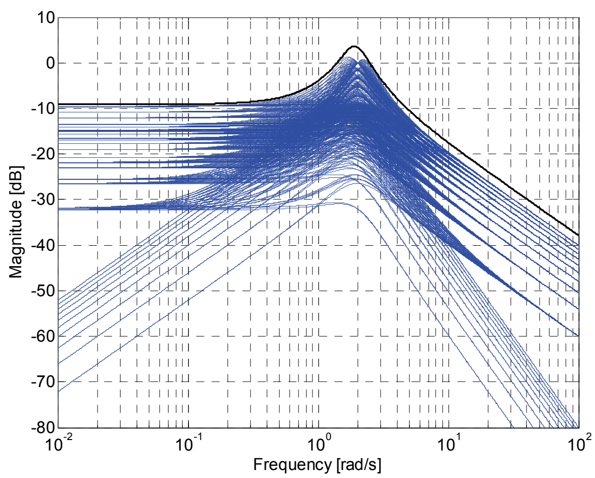

Fig. 8 bode magnitude plots – set of normalized perturbations and weight function (21)

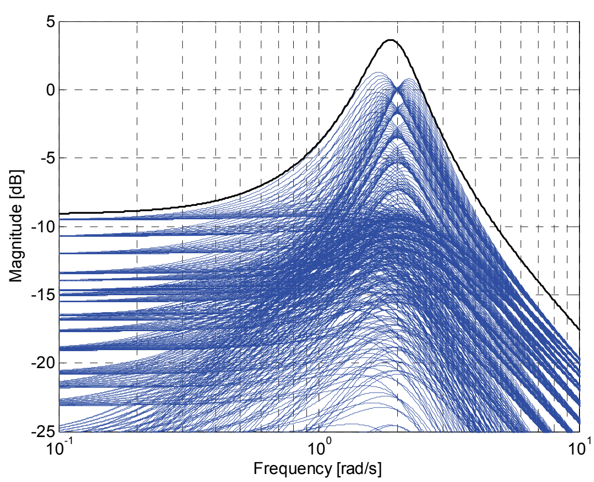

Fig. 9 zoomed version of Bode magnitude plots from Fig. 8 – set of normalized perturbations and weight function (21)

So, the final model for the second example is:

$$\begin{aligned}
&G(s) = \left[1 + W_{M1}(s)\Delta_M(s)\right]G_0(s) \\
&\left\|\Delta_M(s)\right\|_\infty \le 1 \\
&G_0(s) = \frac{1}{s^3 + 2s^2 + 4s} \\
&W_M(s) = \frac{0.35s + 0.35}{0.273s^2 + 0.26s + 1}
\end{aligned} \tag{22}$$

The critical gain of the proportional controller which brings the feedback system with the plant family (22) to the robust stability border is near the value 2.61. The envelope of Nyquist diagrams for this gain is plotted in Fig. 10. In fact, the critical gain for the original parametrically uncertain system (18) is 3.

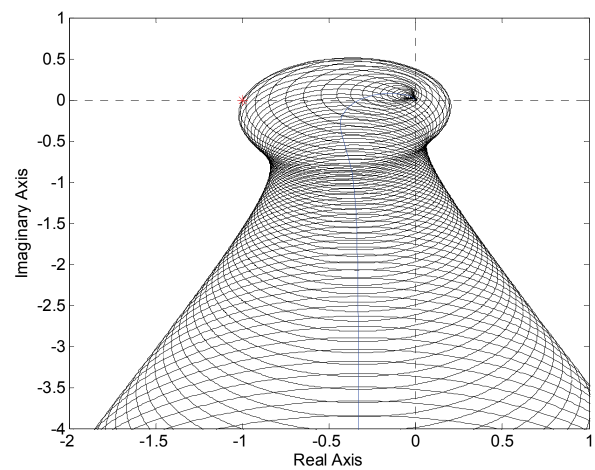

Fig. 10 envelope of Nyquist diagrams close to the robust stability border – plant family (22) and P controller with gain 2.61

V. Conclusion

The contribution has been aimed to modelling and robust stability analysis of systems with unstructured multiplicative uncertainty. The presented examples have shown the techniques for construction of multiplicative uncertainty models from the models with parametric uncertainty via the selection of suitable nominal models and weight functions. Moreover, robust stability of the feedback control loops which contains multiplicative uncertainty plants has been analyzed and their conservatism in comparison with the usage of "original" parametric uncertainty plants has been discussed.

References

[1] J. Ackermann, *et al.*, *Robust control – systems with uncertain physical parameters*, Springer-Verlag, London, UK, 1993.

[2] B. R. Barmish, *New Tools for Robustness of Linear Systems*, Macmillan, New York, USA, 1994.

[3] S. P. Bhattacharyya, H. Chapellat, L. H. Keel, *Robust control: The parametric approach*, Prentice Hall, Englewood Cliffs, New Jersey, USA, 1995.

[4] S. P. Bhattacharyya, A. Datta, L. H. Keel, *Linear Control Theory: Structure, Robustness, and Optimization*, CRC Press, Taylor & Francis Group, USA, 2009.

ISBN: 978-1-61804-321-4

[5] R. Matušů, R. Prokop, "Graphical analysis of robust stability for systems with parametric uncertainty: an overview", *Transactions of the Institute of Measurement and Control*, vol. 33, no. 2, 2011, pp. 274-290.
[6] S. Skogestad, I. Postlethwaite, *Multivariable Feedback Control: Analysis and Design*, John Wiley and Sons, Chichester, UK, 2005.
[7] J. Doyle, B. Francis, A. Tannenbaum, *Feedback Control Theory*, Macmillan, New York, USA, 1992.
[8] V. Kučera, "Robustní regulátory (Robust Controllers)", *Automa*, vol. 7, no. 6, 2001, pp. 43-45. (In Czech).
[9] V. Kučera, "Polynomial control: Past, present, and future", *International Journal of Robust and Nonlinear Control*, vol. 17, no. 8, 2007, pp. 682–705.
[10] R. Matušů, R. Prokop, L. Pekař, "Uncertainty Modelling in Time-Delay Systems: Parametric vs. Unstructured Approach", in *Proceedings of the 13th WSEAS International Conference on Automatic Control, Modelling and Simulation*, Lanzarote, Spain, 2011.
[11] R. Matušů, R. Prokop, L. Pekař, "Parametric and unstructured approach to uncertainty modelling and robust stability analysis", *International Journal of Mathematical Models and Methods in Applied Sciences*, vol. 5, no. 6, 2011, pp. 1011-1018.
[12] M. Šebek, *Robustní řízení* (*Robust Control*), PDF slides for course "Robust Control", Czech Technical University in Prague, Czech Republic, 2003, (In Czech).
[13] R. S. Burns, *Advanced Control Engineering*, Butterworth-Heinemann, Oxford, UK, 2001.

Radek Matušů was born in Zlín, Czech Republic in 1978. Currently, he is a Researcher at Faculty of Applied Informatics of Tomas Bata University in Zlín, Czech Republic. He graduated from Faculty of Technology of the same university with an MSc in Automation and Control Engineering in 2002 and he received a PhD in Technical Cybernetics from Faculty of Applied Informatics in 2007. The main fields of his professional interest include robust systems and application of algebraic methods to control design.

Bilal Şenol was born in Nevsehir, Turkey in 1985. He graduated from Electrical and Electronics in Inonu University in 2009. He recieved MSc degree in the same department in 2011 and started PhD in Computer Engineering at the same year. Currently, he is a researcher in Computer Engineering in Inonu University, Turkey.

Celaleddin Yeroğlu was born in Malatya, Turkey in 1966. He graduated from Electronics Engineering in Hacettepe University in 1991. He recieved MSc and PhD on Computer Engineering in Trakya University. He recieved his second PhD on Control Study. His research interest lies in control theory and applications. Currently, he is chairman of Computer Engineering department in Inonu University, Turkey.

ISBN: 978-1-61804-321-4

Attitude control system design using a flywheel suspended by two gimbals

Raphael W. Peres and Mário C. Ricci

Abstract**—**This work presents the attitude control system design procedures for a three axes stabilized satellite in geostationary orbit, which contains a flywheel suspended by two gimbals. The use of a flywheel with two DOFs is an interesting option because with only one device it's possible to control the torques about vehicle's three axes; through the wheel speed control and gyrotorquing phenomenon with two DOFs. If the wheel size and speed are determined properly it's possible to cancel cyclic torques using gas jets only periodically to cancel secular disturbance torques. The system, based on a flywheel, takes only one pitch/roll (earth) sensor to maintain precise attitude, unlike mass expulsion based control systems, which uses propellants continuously, beyond roll, pitch and yaw sensors. It is considered the satellite is in nominal orbit and, therefore, that the attitude's acquisition phase has already elapsed. Control laws and system parameters are determined in order to cancel the solar pressure radiation disturbance torque and the torque due to misalignment of the thrusters. Stability is analyzed and step and cyclic responses are obtained.

Keywords**—**satellite, control, attitude, flywheel.

I. Introduction

A satellite's pictorial view is shown in Fig. 1 in the orbital nominal position, with the body fixed axis x, y, z - the principal axes of inertia - aligned with the orbital reference frame. The satellite parameters as well as the requirements for the torque disturbance and pointing accuracy are given in Table 1.

The nominal orientation of the momentum wheel is shown in Fig. 2, with the spin axis coinciding with the pitch axis. The components of the angular momentum of the wheel with respect to the principal axes of inertia are obtained with help of the Fig 3.

II. Linearized Equations of Motion

Separating the environmental torques in two parts, the Euler equations of motion are given by

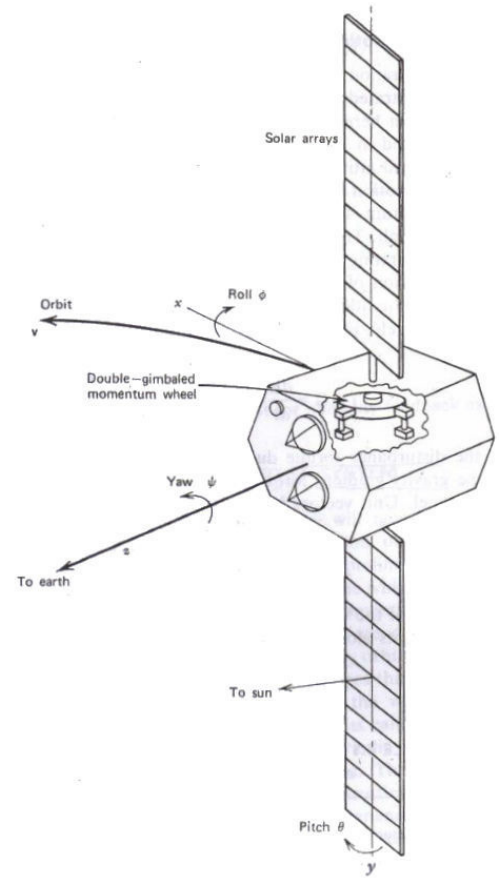

Fig. 1 Artist's conception of the three axes stabilized satellite
SOURCE: [1], p. 242

Table 1 – Parameters and design requirements

Satelitte mass	716 Kg
Moments of inertia	$I_x = I_z = 2000$ Nms^2, $I_y = 400$ Nms^2
Attitude Accuracy requirements	roll (φ) and pitch (θ) = 0,05º, yaw (ψ) = 0,40º
Solar pressure torques (t = 0 at 6 A.M or 6 P.M. orbital position)	$T_x = 2\times10^{-5}(1–2\sin\omega_0 t)$ Nm $T_y = 10^{-4}\cos\omega_0 t$ Nm $T_z = –5\times10^{-5}\cos\omega_0 t$ Nm
Thruster misalignment torque	$T_F = 8.5\times10^{-5}$ Nm

The authors acknowledge the financial support provided by FAPESP (Fundação de Amparo à Pesquisa do Estado de São Paulo) and CNPq (Conselho Nacional de Desenvolvimento Científico e Tecnológico).

Raphael W. Peres is undergraduate research scholarship from the PIBIC-CNPq program and student of control and automation engineering of the Faculdade de Tecnologia São Francisco FATESF, Jacareí, São Paulo State, Brazil (e-mail: raphael-peres@hotmail.com).

Mário C. Ricci is with the Space Mechanics and Control Division at the National Institute for Space Research, São José dos Campos, São Paulo State, Brazil (e-mail: mariocesarricci@uol.com.br).

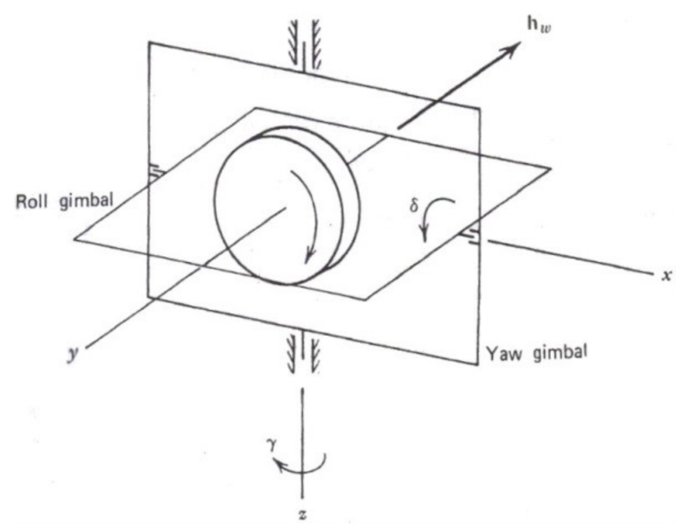

Fig. 2 Nominal orientation of flywheel with two DOFs
SOURCE: [1], p. 243

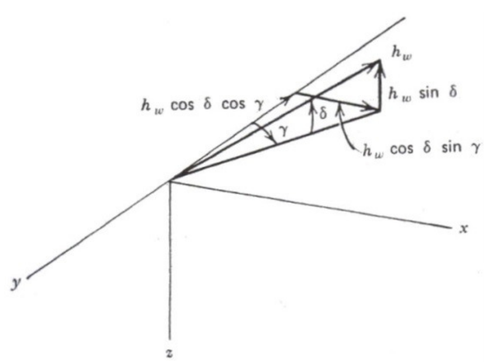

Fig. 3 Angular momentum components
SOURCE: [1], p. 243

$$\mathbf{T} + \mathbf{G} = \frac{d\mathbf{h}}{dt} = \left[\frac{d\mathbf{h}}{dt}\right]_B + \boldsymbol{\omega} \times \mathbf{h}, \tag{1}$$

where **T** are the solar radiation pressure and thrust's misalignment torques; **G** is the gravity gradient torque given by $\mathbf{G} = -3\omega_O^2(I_y - I_z)\varphi\mathbf{i} - 3\omega_O^2(I_x - I_z)\theta\mathbf{j}$; **ω** is the angular velocity vector of the satellite body. The vector **h** represents the total angular momentum of the system, $\mathbf{h} = \mathbf{h}_v + \mathbf{h}_w$, wherein $\mathbf{h}_v$ is the angular momentum of the vehicle and $\mathbf{h}_w$ is the angular momentum generated by the inertia wheel. The components of the vehicle's angular momentum vector are given with respect to the principal axis of inertia as $\mathbf{h}_v = I_x\omega_x\mathbf{i} + I_y\omega_y\mathbf{j} + I_z\omega_z\mathbf{k}$. From Fig. 3 the components of the wheel angular momentum with respect to *x*, *y*, *z* are given by

$$\mathbf{h}_w = (\cos\delta\sin\gamma)h_w\mathbf{i} - (\cos\delta\cos\gamma)h_w\mathbf{j} - (\sin\delta)h_w\mathbf{k}, \tag{2}$$

where δ and γ are the gimbals deflection angles on the roll and yaw axes, respectively.

Expanding equation (1) yields the general equation of motion

$$\begin{aligned}\mathbf{T} = \big[&I_x\dot{\omega}_x - \dot{\delta}(\sin\delta\sin\gamma)h_w + \dot{\gamma}(\cos\delta\cos\gamma)h_w + \\ &(\cos\delta\sin\gamma)\dot{h}_w + \omega_y(\omega_z I_z - h_w\sin\delta) - \\ &\omega_z(\omega_y I_y - h_w\cos\delta\cos\gamma) - 3\omega_O^2(I_y - I_z)\varphi\big]\mathbf{i} + \\ &\big[I_y\dot{\omega}_y + \dot{\delta}\,(\sin\delta\cos\gamma)h_w + \dot{\gamma}(\cos\delta\sin\gamma)h_w - \\ &(\cos\delta\cos\gamma)\dot{h}_w + \omega_z(I_x\omega_x + h_w\cos\delta\sin\gamma) - \\ &\omega_x(I_z\omega_z - h_w\sin\delta) - 3\omega_O^2(I_x - I_z)\theta\big]\mathbf{j} + \big[I_z\dot{\omega}_z - \\ &\dot{\delta}(\cos\delta)h_w - (\sin\delta)\dot{h}_w + \omega_x(I_y\omega_y - h_w\cos\delta\cos\gamma) - \\ &\omega_y(I_x\omega_x + h_w\cos\delta\sin\gamma)\big]\mathbf{k}.\end{aligned} \tag{3}$$

Whereas the vehicle's (φ, θ and ψ) and the gimbal's (δ and γ) angular deviations, with respect to the nominal frame shown in figure 1, are considerably smaller and applying the Euler angles transformation (sequence 3-2-1) in the **ω** vector components, thus yields the linearized equations of motion

$$\begin{aligned}T_x = I_x\ddot{\varphi} + \left[4\omega_O^2(I_y - I_z) + \omega_o h_n\right]\varphi + \left[-\omega_o(I_x - I_y + I_z)\right. \\ \left.+h_n\right]\dot{\psi} + \dot{h}_{xc} - \omega_o h_{zc},\end{aligned} \tag{4}$$

$$T_y = I_y\ddot{\theta} + [3\omega_O^2(I_x - I_z)]\theta + \dot{h}_{yc}, \tag{5}$$

$$\begin{aligned}T_z = I_z\ddot{\psi} + \left[\omega_O^2(I_y - I_x) + \omega_o h_n\right]\psi - \left[-\omega_o(I_x - I_y + I_z)\right. \\ \left.+h_n\right]\dot{\varphi} + \dot{h}_{zc} + \omega_o h_{xc}.\end{aligned} \tag{6}$$

III. Pitch axis control system design

For satellite specifications given in Table 1, it is observed that $I_x = I_z$ and thus, the pitch axis equation of motion given by equation (4) can be simplified to:

$$T_y = I_y\ddot{\theta} + \dot{h}_{yc}, \tag{7}$$

in which $\dot{h}_{yc}$ is the inertia wheel's angular momentum rate of change, whose aim is to impose direct torque control about the pitch axis. A pseudorate modulator is to be used, which serves to modulate the torque control $\dot{h}_{yc}$ and synthesizing the angular rate of change $\dot{\theta}$, ie, the control device makes torque being dependent on the angular rate of change. A satisfactory control form is given by

$$\dot{h}_{yc} = K_p(\tau_p\dot{\theta} + \theta), \tag{8}$$

wherein the term $\dot{\theta}$ introduces the necessary damping for the system, K_p is the pitch autopilot gain and τ_p is the pitch constant time. Substituting equation (8) into equation (7), applying the Laplace transform and rearranging the terms, the pitch axis control system transfer function results as being

$$\frac{\Theta(s)}{T_y(s)} = \frac{1}{I_y s^2 + K_p\tau_p s + K_p}. \tag{9}$$

The pitch loop root locus diagram for the variable K_p is shown in Fig. 4, and it indicates that the system is stable for all values of K_p. Adjusting the output to behave critically damped (no overshoot) and according to the attitude accuracy requirements given in Table 1, obtains the most suitable parameters pitch autopilot gain K_p = 0.275 Nm/rad and pitch constant time τ_p = 80 s. Applying the parameters found in equation (8) yields the step and cyclic disturbance torques responses, shown in Figs. 5 and 6, respectively. The step type input is due to thruster misalignment and the cyclical type input is characteristic of the solar radiation pressure torque.

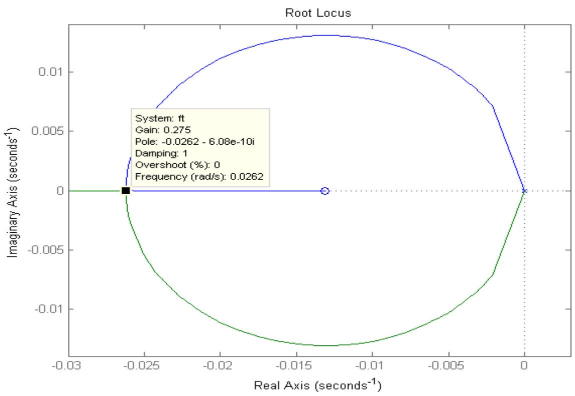

Fig. 4 pitch loop root locus diagram for variable K_p

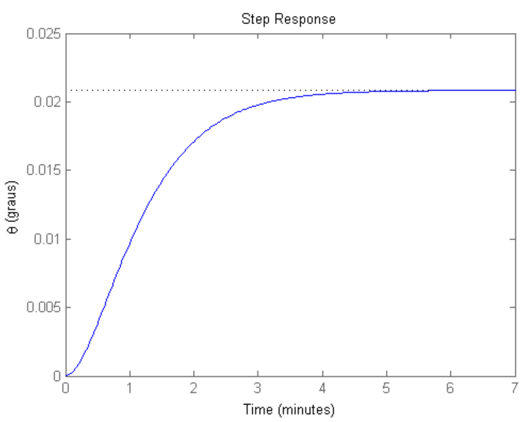

Fig. 5 pitch loop step response

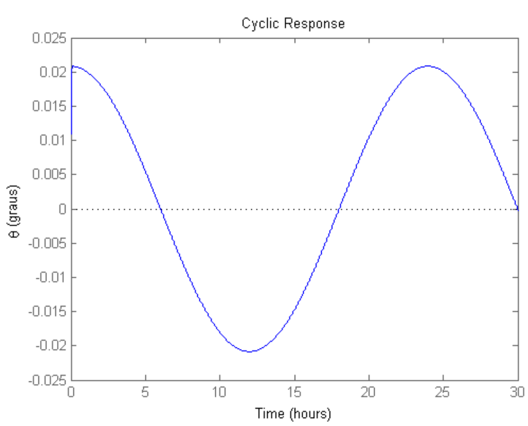

Fig. 6 pitch loop cyclical input

IV. Roll/Yaw Control System Design

In order to simplify the equation of motion for roll and yaw axis, it is assumed that $h_n \gg \max\,[I_x\omega_o, I_y\omega_o, I_z\omega_o]$, so the equation (3) and equation (5) are rewritten as

$$T_x = I_x\ddot{\varphi} + \omega_o h_n \varphi + h_n \dot{\psi} + \dot{h}_{xc} - \omega_o h_{zc}, \qquad (10)$$

$$T_z = I_z\ddot{\psi} + \omega_o h_n \psi - h_n \dot{\varphi} + \dot{h}_{zc} + \omega_o h_{xc}. \qquad (11)$$

Again using a pseudorate modulator and based on the same principles used to prepare the pitch axis control system, the used control laws are

$$M_{xc} = \dot{h}_{xc} - \omega_o h_{zc} + \omega_o h_n \phi = K(\tau\dot{\phi} + \phi), \qquad (12)$$

$$M_{zc} = \dot{h}_{zc} + \omega_o h_{xc} - h_n \dot{\phi} = -kK(\tau\dot{\phi} + \phi), \qquad (13)$$

where M_{xc} and M_{zc} represent the roll and yaw control moments, respectively, K is the roll autopilot gain, τ is the roll time constant and k is the yaw-to-roll gain ratio.

Replacing control law in equation (10) and equation (11), applying the Laplace transform and rearranging the terms, the angular responses are obtained

$$\Phi(s) = \frac{T_x(s)(I_z s^2 + \omega_o h_n) - T_z(s) h_n s}{I_x I_z s^4 + K I_z \tau s^3 + (K I_z + I_x \omega_o h_n + kK\tau h_n)s^2 + (\omega_o h_n K\tau + kK h_n)s + \omega_o h_n K}, \qquad (13)$$

$$\Psi(s) = \frac{T_z(s)(I_x s^2 + K\tau s + K) + kK(\tau s + 1)T_x(s)}{I_x I_z s^4 + K I_z \tau s^3 + (K I_z + I_x \omega_o h_n + kK\tau h_n)s^2 + (\omega_o h_n K\tau + kK h_n)s + \omega_o h_n K}. \qquad (14)$$

The roll/yaw system root locus diagram for the variable K is shown in Fig. 7. Adjusting the output to behave critically damped (no overshoot) and according to the attitude accuracy requirements given in Table 1, obtains the most suitable parameters for roll autopilot gain K = 1.56 Nm/rad, roll constant time τ = 80 s and yaw-to-roll gain ratio k = 0.054. Due to the coupling between the motions, a disturbance on one axis (roll or yaw) directly affects the motion of both axes. The Figs. 8 and 9 show the output of the roll axis due to a step disturbance in the roll and yaw axes, respectively, caused by the thrust misalignment; while the Figs. 10 and 11 show the output of the yaw axis due to a step disturbance in the roll and yaw axes, respectively, caused by the same effect. The Figs. 12 and 13 show the response of the roll and yaw axes due to a disturbance caused by the cyclic solar pressure torque type.

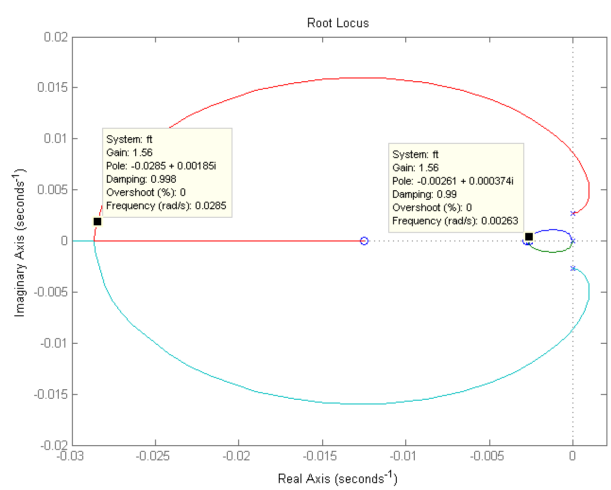

Fig. 7 Roll/yaw system root locus diagram for variable K

V. Conclusions

The linearized equation of motion for the system under consideration was obtained, which in turn separate the pitch

ISBN: 978-1-61804-321-4

motion of roll and yaw motions, thus simplifying the application of control system theory. Unlike most designs, which use three inertia wheels, one for each axis, this design has achieved successful results in accordance with any attitude of accuracy requirements only with one inertia wheel, minimizing costs, improving the dynamics and reducing satellite weight.

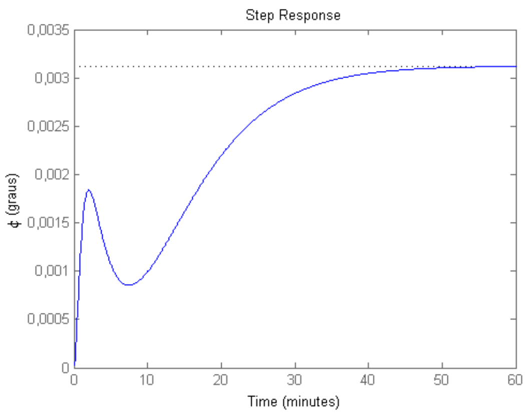

Fig. 8 Roll axis output for a step input in the roll axis

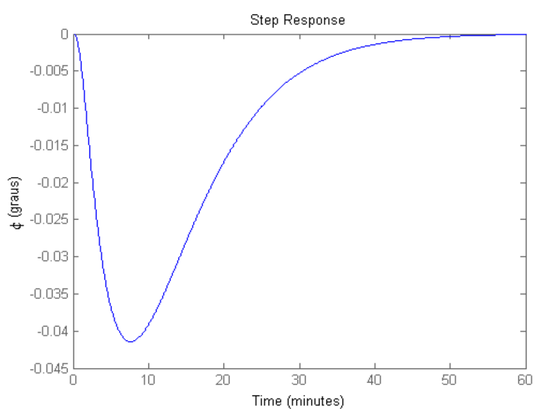

Fig. 9 Roll axis output for a step input in the yaw axis

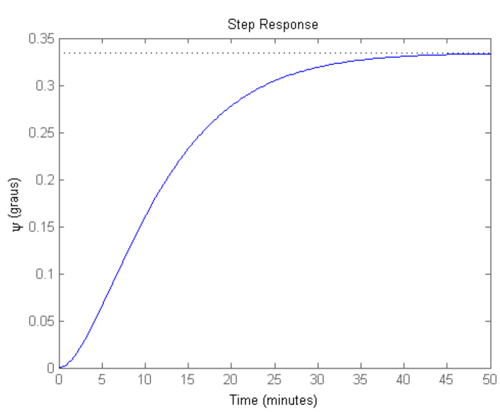

Fig. 10 Yaw axis output for a step input in the yaw axis

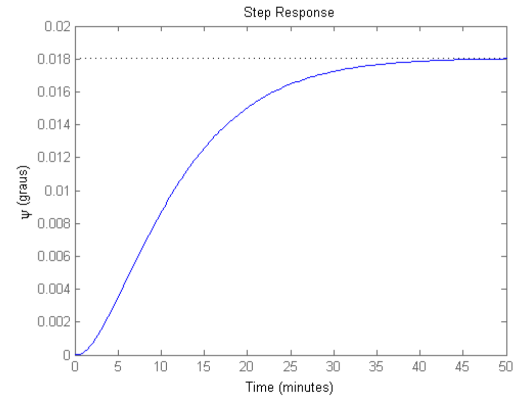

Fig. 11 Yaw axis output for a step input in the roll axis

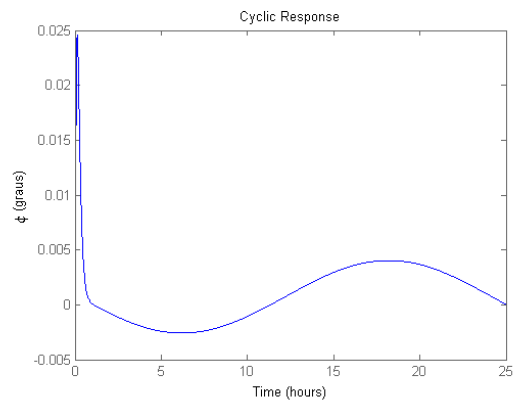

Fig. 12 Roll axis output for a cyclical input

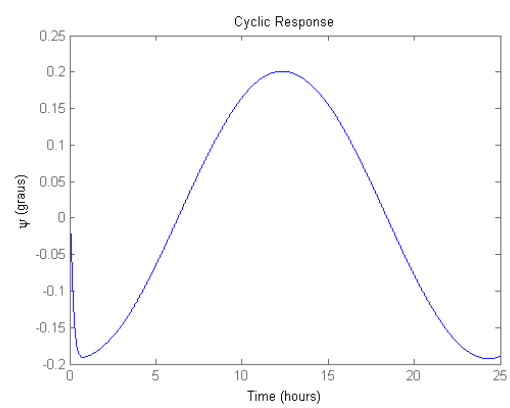

Fig. 13 Yaw axis output for a cyclical input

REFERENCES

[1] M. H. Kaplan, *Modern Spacecraft Dynamics & Control*. New York: John Wiley & Sons, 1976.
[2] K. Ogata, *Engenharia de Controle Moderno* 4ª. Ed.. Prentice-Hall, 2003.
[3] J. R. Wertz, *Spacecraft Attitude Determination and Control*. London: Kluwer Academic Publishers, 1978.

ISBN: 978-1-61804-321-4

Plant identification from relay feedback and anisochronic controller design

Milan Hofreiter

***Abstract*—**This paper presents a simple approach to parameter estimation of linear plant models. The approach enables the estimation of step responses by relay feedback. This allows the utilization of common identification methods estimating models from step responses. The introduced method can be also applied to more complicated systems with delays, latencies and after-effects, which can be described by linear anisochronic models. In this paper, the relay feedback is used for estimating five parameters of the anisochronic model and then the anisochronic controller is designed to this model using the Desired Model Method. The applicability of the suggested methodology is presented in the Matlab/Simulink programming environment.

***Keywords*—**Anisochronic control, parameter estimation, step response, relay feedback.

I. Introduction

THE basic method of control design is to first determine a model for the process dynamics and then design a controller. A linear model can describe most processes in industry when considering small changes around an operating point. The experimental relay feedback method, proposed by Åström and Hägglund [1] for determining the critical point P_c on the Nyquist curve (see Fig. 1), proved to be very useful in practice for parameter identification and controller design. Nowadays this method is frequently used for auto-tuning industrial PID controllers and more publications are devoted to system identification or controller auto-tuning using the relay feedback experiment, e.g. [1]-[10].

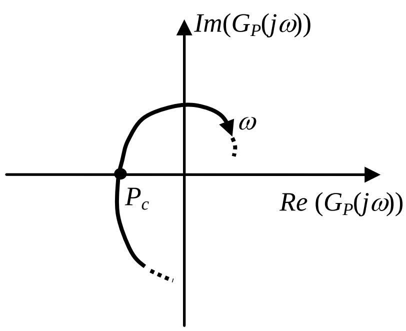

Fig. 1 The Nyquist curve of a plant

M. Hofreiter, Department of Instrumentation and Control Technology, Czech Technical University in Prague, Faculty of Mechanical Engineering, Technicka 4, 166 07 Prague 6, Czech Republic, http://fsinet.fsid.cvut.cz/~hofremil, (e-mail: milan.hofreiter@fs.cvut.cz).

The position of the critical point P_c is determined automatically from a relay feedback experiment, see Fig. 2, where e, w, u and y are the control error, the desired, manipulated and controlled variables, respectively. $G_P(s)$ is the plant transfer function, s is the complex variable in Laplace transform and u_A is the relay output amplitude.

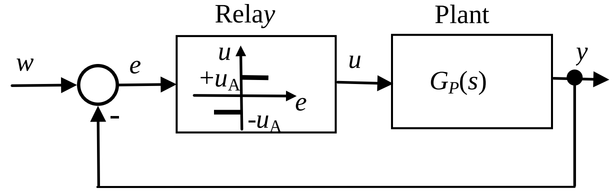

Fig. 2 Block diagram of a plant under relay feedback

It was derived [1] that it holds

$$P_c = G_P\left(j\omega_c\right) = -\frac{\pi \cdot y_A}{4 \cdot u_A}, \tag{1}$$

where y_A is the harmonic oscillation amplitude of the plant output, u_A is the relay amplitude, ω_c is the ultimate frequency. The relationship between the ultimate frequency ω_c and the ultimate period T_c is

$$\omega_c = \frac{2 \cdot \pi}{T_c}. \tag{2}$$

From one standard relay test one point P_c on the plant frequency response $G_P(j\omega)$ is obtained. This point can be used directly to calculate controller parameters or it is possible to use it for system identification [1]-[7]. This approach was also generalized for a biased relay feedback [1], [5], [10], [11].

But if a plant model has more than two unknown parameters it is necessary for system identification to find more points on a frequency response function or to add some other information. This is solved, for example by using tests with relay feedback where a known linearity is connected in series with the plant (each test for one point), by modified relay methods etc. [5], [8], [9], [11].

This paper introduces the method whereby the unit step response is determined from one relay test and model parameters are estimated from the step response using common methods.

II. Step Response Determination from Relay Feedback

The block diagram of a plant under relay feedback is shown in Fig. 2. The time courses of the relay output u and the plant output y are shown in Fig. 3 provided that the system was initially in a steady state. The manipulated variable u changes its values at the time moments t_i, $i\in\mathbb{N}$, where $\mathbb{N}$ is the set of all natural numbers.

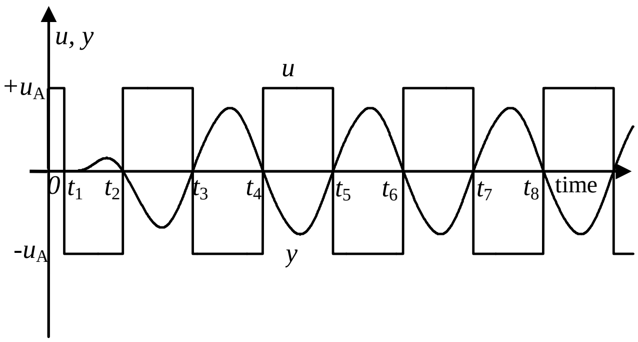

Fig. 3 The relay output u and the plant output y for a plant under relay feedback

Then the step response function $h(t)$ at the time t can be calculated recursively according to formula (3).

$$h(t)=\begin{cases} \dfrac{y(t)}{u_A} \text{ for } t\in\left\langle 0,t_1\right\rangle \\ \dfrac{y(t)}{u_1}+2\operatorname{sgn}(u_1)\displaystyle\sum_{i=1}^{n}(-1)^{i-1}\cdot h(t-t_i) \text{ for } t\in\left(t_n,t_{n+1}\right\rangle, \\ n=1,2,3,4,\cdots \end{cases} \tag{3}$$

where

$$u_1 \triangleq u(\tau),\tau\in(0,t_1) \tag{4}$$

$$\operatorname{sgn}(u_1)\triangleq\frac{u_1}{|u_1|} \tag{5}$$

The presented method of identification can be also applied using a biased (asymmetrical) relay with the hysteresis, see Fig. 4.

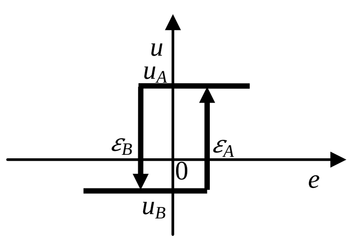

Fig. 4 The characteristic of a biased (asymmetrical) relay with hysteresis

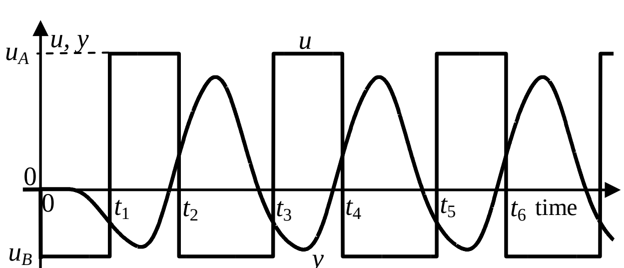

Fig. 5 The biased relay output u and the plant output y for a plant under relay feedback

The time courses of the biased relay output u and the plant output y are shown in Fig. 5 provided that the system was initially in a steady state. The manipulated variable u changes its values at the time moments t_i, $i\in\mathbb{N}$. Notice that the phase shift between the plant input and output is not $-\pi$ as it was in Fig. 3.

Then the step response function $h(t)$ at the time t can be calculated recursively according to formula (6).

$$h(t)=\begin{cases} \dfrac{y(t)}{u_1} \text{ for } t\in\left\langle 0,t_1\right) \\ \dfrac{1}{u_1}\left(y(t)+u_C\operatorname{sgn}(u_1)\displaystyle\sum_{i=1}^{t_n}(-1)^{i-1}h(t-t_i)\right) \text{ for } t\in\left\langle t_n,t_{n+1}\right), \\ n=1,2,3,\cdots \end{cases} \tag{6}$$

where

$$u_1 \triangleq u(\tau),\tau\in(0,t_1), \tag{7}$$

$$\operatorname{sgn}(u_1)\triangleq\frac{u_1}{|u_1|}, \tag{8}$$

$$u_c=u_A+|u_B|. \tag{9}$$

It is obvious that this approach to system identification can be used even for more complicated dynamical systems, where the mentioned recursive calculation is acceptable. Therefore this approach can be applied even for systems with delays, latencies and after-effects, which can be described by linear anisochronic models.

III. Example for Estimation of Five Parameters of Anisochronic Model

Example #1

A plant with the transfer function

$$G_P(s)=\frac{e^{-8s}}{(5s+1)^6} \tag{10}$$

is connected with the relay controller in the closed-loop. The biased relay with hysteresis has following parameters, see Fig. 4:

$$u_A=2, u_B=-1, \varepsilon_A=0.5, \varepsilon_B=-0.5. \tag{11}$$

The time courses of the biased relay output u and the plant output y are shown in Fig. 6 provided that the system was initially in a steady state.

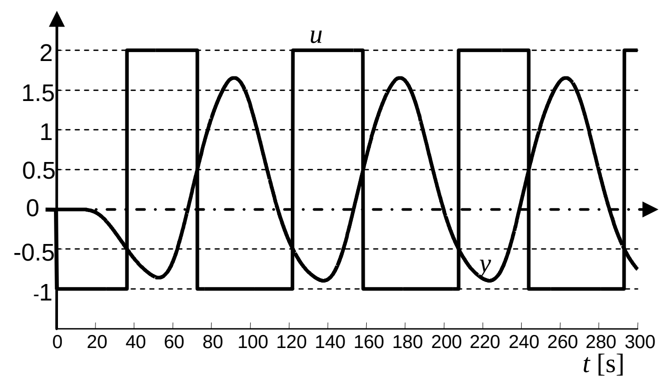

Fig. 6 The time courses of the biased relay output u and the plant output y

Anisochronic model (12) is used for plant description because this model is very universal and convenient for modeling time delay systems [12], [13].

$$G_P(s) = \frac{K \cdot e^{-s\tau_u}}{(\tau_1 s + 1)\left(\tau_2 s + e^{-s\tau_y}\right)}. \qquad (12)$$

Because the delay τ_y is in the denominator of transfer function (12), then the characteristic equation is transcendental in s and has an infinite set of roots [13], [14]. For this reason, it can be expected to be a better approximation of the dynamics of high-order systems.

Model (12) is stable if $\tau_y/\tau_2<\pi/2$, over-damped if $\tau_y/\tau_2<1/e$, critically damped if $\tau_y/\tau_2=1/e$ and under-damped if $\tau_y/\tau_2>1/e$. Therefore, model (12) may be used both for nonoscillatory and oscillatory processes [12], [13].

The task is to estimate parameters K, τ_u, τ_1, τ_2 and τ_y only from the observation data depicted in Fig. 6.

Solution:

The unit step response $h(t)$ can be determined recursively from formula (6) and the observation data depicted in Fig. 6. From Fig. 6 it follows that $u_C=3$ and the times t_i, $i=1,2,3,...$ correspond to time moments when the manipulated variable changed its value. The obtained unit step response is shown in Fig. 7.

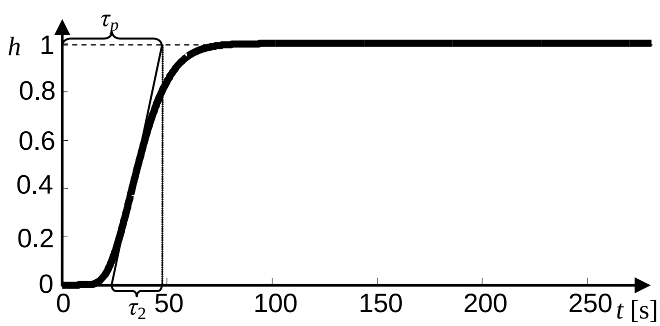

Fig. 7 The unit step response $h(t)$ determined by formula (6)

Therefore, the plant steady-state gain

$$K = 1. \qquad (13)$$

Parameter estimate of anisochronic model (12), with respect to the unit step response $h(t)$, is done here using the method of moments, see [15], [16]. The method is based on the computation two integrals (14) and (15),

$$M_0 = \int_0^\infty \left(K - h(\tau)\right) d\tau, \qquad (14)$$

$$M_1 = \int_0^\infty \tau \cdot \left(K - h(\tau)\right) d\tau. \qquad (15)$$

The values of integrals (14) and (15) are computed by a numerical integration for the given example

$$M_0 = 38 \text{ s}, \quad \mathrm{M}_1 = 797 \text{ s}^2. \qquad (16)$$

For anisochronic model (12) holds that, see [15]

$$\frac{M_0}{K} = \tau_{ar}, \qquad (17)$$

$$\frac{M_1}{K} = \frac{\tau_{ar}^2 + \tau_1^2 + \tau_2^2}{2} - \tau_2 \cdot \tau_y, \qquad (18)$$

where the average residence time

$$\tau_{ar} = \tau_1 + \tau_2 - \tau_y + \tau_u = \tau_p - \tau_y. \qquad (19)$$

The time constant τ_2 and the transient time τ_p can be determined from a graphical construction, see Fig. 7, where

$$\tau_p = 48 \text{ s}, \ \tau_2 = 24 \text{ s}. \qquad (20)$$

Due to (13), (16) and (17) the average residence time

$$\tau_{ar} = 38 \text{ s} \qquad (21)$$

and therefore with respect to (19) the delay

$$\tau_y = 10 \text{ s}. \qquad (22)$$

The time constant τ_1 can be calculated from equation (18)

$$\tau_1 = \sqrt{2 \cdot \frac{M_1}{K} - \left(\tau_{ar}^2 + \left(\tau_2 - \tau_y\right)^2 - \tau_y^2\right)} \doteq 7.4 \text{ s} \qquad (23)$$

and the apparent dead time τ_u follows from formula (19)

$$\tau_u = \tau_p - \tau_1 - \tau_2 = 16.6 \text{ s}. \qquad (24)$$

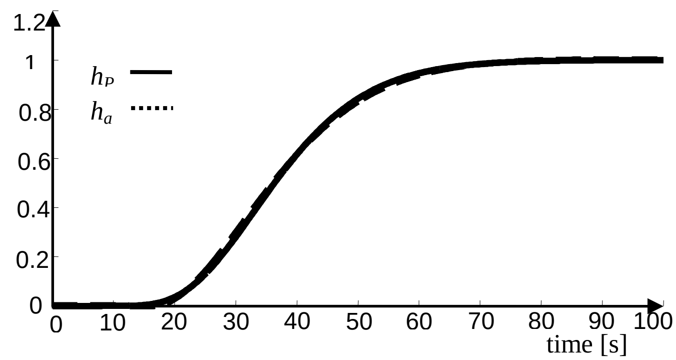

Fig. 8 The unit step response h_P of the plant with transfer function (10) and the unit step response h_a of model (25)

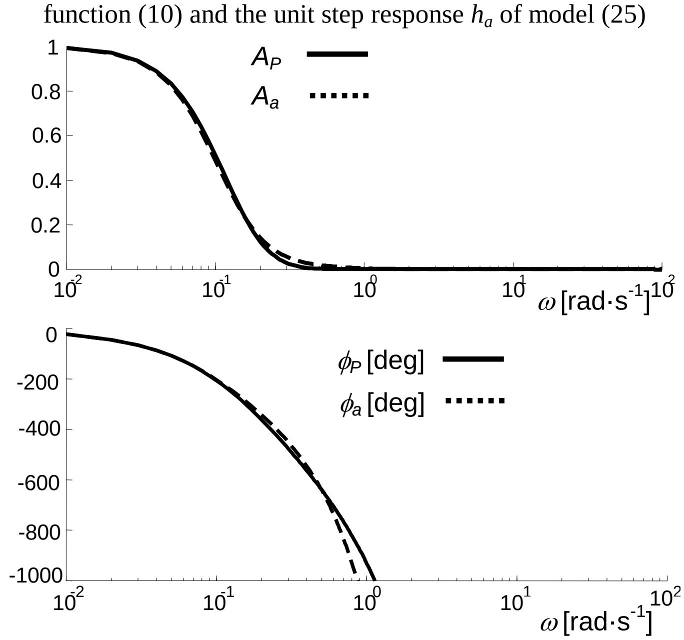

Fig. 9 The Bode diagrams for plant (10) and model (25), where $A_P(\omega)=|G_P(j\omega)|$, $\phi_P(\omega)=\angle G_P(j\omega)$ and $A_a(\omega)=|G_a(j\omega)|$, $\phi_a(\omega)=\angle G_a(j\omega)$.

ISBN: 978-1-61804-321-4

The transfer function of anisochronic model (12) is then

$$G_a(s)=\frac{e^{-16.6s}}{(7.4s+1)\left(24s+e^{-10s}\right)}. \quad (25)$$

The unit step response h_P of the plant with transfer function (10) and the unit step response h_a of model (25) are in Fig. 8. The frequency responses of plant (10) and model (25) are depicted in Fig. 9. Fig. 8 and Fig. 9 show very good conformity the step and frequency responses of identified plant (10) and anisochronic model (25) although the transfer functions $G_P(s)$ and $G_a(s)$ are different.

IV. Anisochronic controller design

Anisochronic model (12) is able to describe a broad class of time delay systems [13]. In the previous part of this paper it was shown how to estimate the model parameters by experiments with the relay feedback. The following part is devoted to the anisochronic controller design where it is used the Desired Model Method (DMM) [17].

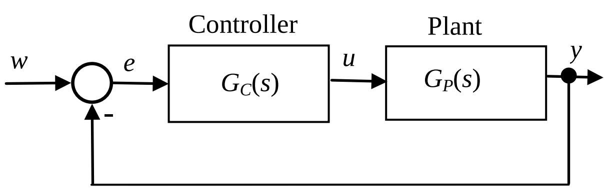

Fig. 10 Closed-loop system

The DMM uses the formula for direct synthesis (see Fig. 10)

$$G_C(s)=\frac{G_{wy}(s)}{G_P(s)\cdot\left(1-G_{wy}(s)\right)}, \quad (26)$$

where $G_C(s)$ is the controller transfer function, $G_P(s)$ is the plant transfer function, $G_{wy}(s)$ is the desired control system transfer function and it is selected in the form

$$G_{wy}(s)=\frac{k_0}{s+k_0\cdot e^{-\tau_u\cdot s}}e^{-\tau_u s}, \quad (27)$$

k_0 is the open-loop gain. The open-loop transfer function

$$G_0(s)=G_C(s)\cdot G_P(s)=\frac{k_0}{s}e^{-\tau_u s} \quad (28)$$

corresponds to desired control system transfer function (26).

After substitution of plant transfer function (12) to relationship (28) one obtains

$$G_0(s)=G_C(s)\cdot\frac{K\cdot e^{-s\tau_u}}{(\tau_1 s+1)\left(\tau_2 s+e^{-s\tau_y}\right)}=\frac{k_0}{s}e^{-\tau_u s} \quad (29)$$

hence

$$G_C(s)=\frac{k_0}{K}\cdot\frac{(\tau_1 s+1)\left(\tau_2 s+e^{-s\tau_y}\right)}{s}. \quad (30)$$

The open-loop gain k_0 can be easily determined analytically [17] assuming that the non-dominant poles and zeros of the control system have a negligible influence on its behaviour. The value of the open-loop gain k_0 can be decided according to

$$k_0=\frac{1}{\beta\cdot\tau_d} \quad (31)$$

where β is the coefficient depending on the relative overshoot κ, see Table I (copy from [17]).

Table I Values of coefficients β for given relative overshoot κ

κ	0	0.05	0.1	0.2	0.3	0.4	0.5
β	2.718	1.944	1.720	1.437	1.248	1.104	0.992

Transfer function (30) is completed by a low-pass filter with a steady-state gain of one to guarantee the physical realizable controller. The transfer function of the controller is then

$$G_C(s)=\frac{k_0}{K}\cdot\frac{(\tau_1 s+1)\left(\tau_2 s+e^{-s\tau_y}\right)}{\left(\tau_f s+1\right)^r s}, \quad (32)$$

where τ_f is the time constant of the filter and the value of $r\in\mathbb{N}$ can be chosen so that the order of the denominator is at least the same order as the numerator. The value of the time constant τ_f also allows restricting actions of the manipulated variable u.

V. Example for anisochronic controller design

Example #2

A plant with transfer function (10) is described by model (25). Design an anisochronic controller according to the DMM

Solution

The transfer function $G_C(s)$ of the controller can be selected using the DMM with respect to (25) and (32) in the form

$$G_C(s)=k_0\cdot\frac{(7.4s+1)\cdot\left(24s+e^{-10s}\right)}{(0.5s+1)\cdot s}, \quad (33)$$

where

$$K=1, \tau_1=7.4\text{ s}, \tau_2=24\text{ s}, \tau_y=10\text{ s}, \tau_f=0.5\text{ s}, r=1. \quad (34)$$

Fig. 11 shows the closed loop control for the unit step of the desired variable w and the required relative overshoot κ=0.1. Therefore with respect to Tab. 1, the value of the open-loop gain is

$$k_0=\frac{1}{\beta\cdot\tau_u}=\frac{1}{1.720\cdot 16.6}=0.035$$

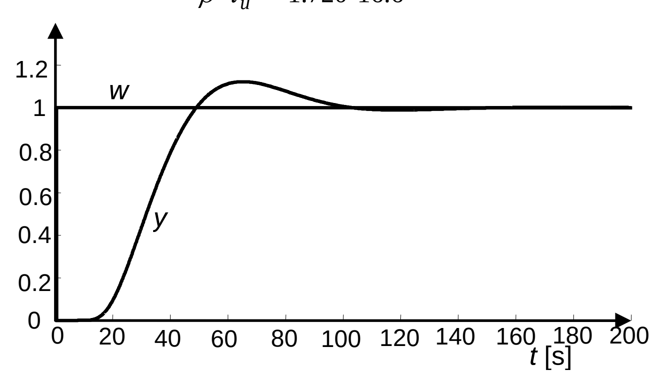

Fig. 11 Set point response for anisochronic control

VI. CONCLUSION

The presented method for plant step response identification has been developed in the context of the relay feedback test. The method has several unique features. It can estimate the whole step response of a plant with one single relay experiment. For this purpose no approximation is made. The involved computations are simple so that it can be easily implemented on micro-processors. The method allows estimating more parameters of mathematical models with various structures. Therefore, it can be used for parameter tuning both isochronic and anisochronic models. It was demonstrated on one anisochronic model in estimating five parameters. The presented identification method requires zero initial conditions and due to recursive calculation, it is sensitive to noise which can be corrected by filtration. As the aim of the identification was to design a practicably applicable controller, therefore, the anisochronic controller was derived to broad class systems describable by anisochronic model (12) using the Desired Model Method.

REFERENCES

[1] K., J. Åström and T. Hägglund, "Automatic tuning of simple regulators with specifications on phase and amplitude margins,"*Automatica,* vol. 20, issue 5, 1984, pp. 645-651.

[2] K., J. Åström and B. Wittenmark, *Adaptive Control.* Addison-Wesley Publishing Company, Inc., 1995, ch. 8.

[3] Seborg, D. E., T.F. Edgar, and D. A. Mellichamp, *Process Dynamics and Control*. John Wiley & Sons, Inc., 2011.

[4] T. Vyhlídal, P. Zitek, "Control System Design Based on Universal First Order Model with Time Dealys," *Acta Polytechnica*, vol. 41, no. 4-5, 2001, pp. 49-53.

[5] M. Vítečková, and A. Víteček, "Plant identification by relay methods," *Engineering the future* (edited by L. Dudas). Sciyo, Rijeka, 2010, pp. 242-256. Available: http://www.intechopen.com/books/engineering-the-future/plant-identification-by-relay-method

[6] R. Prokop, J. Korbel and R. Matušů,"Relay feedback identification of dynamical SISO systems-analysis and settings," in *Proc. of the 18th Int. Conf. on Systems - Latest Trends on Systems (part of CSCC'14).* Santorini Island, 2014, pp. 450-454.

[7] C. C. Yu, *Autotuning of PID Controllers.* London: Springer-Verlag, 1999, ch. 2 and 3.

[8] T. H. Lee, Q. G. Wang and K. K. Tan, "Knowledge-based process identification from relay feedback," *J. Proc.Control*, vol. 5, no. 6, 1995, pp. 387-397.

[9] Q. Bi, Q. G. Wang a nd C. C. Hang, "Relay-based estimation of multiple points on process frequency response," *Automatica*, vol. 33, no. 9, 1997, pp. 1753-1757.

[10] R. Prokop, L. Pekař, R. Matušů and J. Korbel, "Autotuning principles for delayed systems", *Int. J. of Mathematical Models and Methods in Applied Sciences,* vol. 6, no. 2, 2012, pp. 273-280. Available: http://naun.org/main/NAUN/ijmmas/17-738.pdf

[11] M. Hofreiter, "Parameter Identification of Anisochronic Models", *DAAAM International Scientific Book 2002*. Vienna: DAAAM International, Editor B. Katalanic, 2002, pp. 247-252.

[12] P. Zítek, J. Hlava, "Anisochronic Internal Model Control of Time Delay Systems," *Control Engineering Practice*, vol. 9, no. 5, 2001, pp. 501-516.

[13] P. Zítek, "Time Delay Control System Design Using Functional State Models," *CTU Reports*, CTU Prague, no. 1, 1998.

[14] M. Hofreiter, "Discretization of continuous linear anisochronic models," *Studies in Informatics and Control*, vol. 12, no. 1, 2003, pp. 69-76.

[15] M. Hofreiter, "Parameter Fitting for Anisochronic Models by Means of Moments," *Int. J.. of Mathematical Models and Methods in Applied Sciences,* vol. 8, no. 4, 2014, pp. 394-400. Available: http://www.naun.org/main/NAUN/ijmmas/2014/a262001-041.pdf

[16] P. Klán, R. Gorez, *Process Control*, FSS Public s.r.o., Prague, 2011.

[17] A. Víteček and M. Vítečková, *Closed-Loop Control of Mechatronic Systems.* Ostrava: VŠB TU Ostrava, 2013, pp. 131-141.

Options accumulation of energy from photovoltaic in thermally accumulation elements

Pavel Chrobak and Martin Zalesak

***Abstract*—**The paper discusses the possibility of using energy from photovoltaic panels for accumulation energy in thermally accumulation devices, both in the form of heat or cold. Due to increasing demands for energy autonomy in objects are of great importance accumulative substances with high the specific heat capacity. The special position of these elements in buildings thermal storage panels (PCM). The efficiency of energy production and use of photovoltaics is dependent on climatic conditions, accumulation and dynamic parameters of accumulator power.

In the paper are presented and evaluated the usability of balance in any particular case, based on real meteorological data for the winter season.

***Keywords*—**Accumulation, heat loss, photovoltaics, photodiode, semiconductor, cell, solar radiation, invertor.

I. Introduction

THE growing world population is placing ever greater demands on traditional energy sources. To be technical progress and development of human society can not continue to maintain indefinitely ever occur to increase production and consumption of energy from traditional sources (oil, coal, natural gas, uranium) that disproportionately burden the environment, and gradually exhausted. The application of these sources of energy has a negative impact on the environment, which makes mining, transport of raw materials, accident and introduce unwanted waste in the form of ash gas or highly radioactive substances. In recent years, from these sources gradually withdraws and are replaced by so-called renewable energy sources.

We in this paper will focus on the possibilities of obtaining energy from photovoltaic panels and particularly its storage in thermal storage devices for heating buildings in winter. For this purpose we use a variety of substances that have specific storage characteristics, such as water, oil and materials used for the accumulation of heat or cold thermal processes associated with phase change material.

II. Physical principle of photovoltaic conversion

Before more than 150 years ago by Alexander Edmond Becquerel discovered principle technology for the direct conversion of sunlight into electricity by using the photoelectric effect on large semiconductor photodiodes (photovoltaic cells). The individual photodiodes are called photovoltaic cells and are usually attached to larger units (photovoltaic panels).

The simplest photodiodes consists of two semiconductors with a different type of electrical conductivity. In one of the layers of material of the type N predominate negatively charged electrons, while in the second layer of material P predominate "holes" which are essentially blanks which readily accept electrons. At the point where these two layers meet with a P - N junction where there is a pair of electrons with holes, thereby creating an electric field that prevents other electrons move from the N - layer to the P - layer. Normally, the electrons in the semiconductor material are firmly bonded to the atoms of the crystal grid and the material is then nonconductive. By adding a very small amount of an element with a greater number of valence electrons to the crystal creates a region of conductivity of the type N, in which free electrons exist and they can create electrical charge. Conversely an impurity element with a reduced number of valence electrons creates a region with conductivity of the P type, in which the crystal grid range “hole are as” without electrons. If the semiconductor material capture of a photon of sufficient energy, it results in creation of an one electron-hole pair [1]. If the circuit is closed, the wearer's hub starts to move in opposite directions to the negative electrode. A positive hole is shown in Figure 1.

This work was supported in frame of Internal Grant Agency of Tomas Bata The work was performed with financial support of research project NPU I No. MSMT-7778/2014 by the Ministry of Education of the Czech Republic and also by the European Regional Development Fund under the Project CEBIA-Tech No. CZ.1.05/2.1.00/03.0089. Work was also supported in frame of Internal Grant Agency of Tomas Bata University in Zlin, Faculty of Applied Informatics, IGA/FAI/2015/022.

Pavel Chrobak is with the Tomas Bata University in Zlin, Faculty of Applied informatics, Department of Automation and Control Technologies, Zlin, 76005 Czech Republic (e-mail: chrobak@fai.utb.cz).

Martin Zalesak, is with the Tomas Bata University in Zlin, Faculty of Applied Informatics, Department of Automation and Control Technologies, Zlin,76005 Czech Republic (e-mail: zalesak@fai.utb.cz).

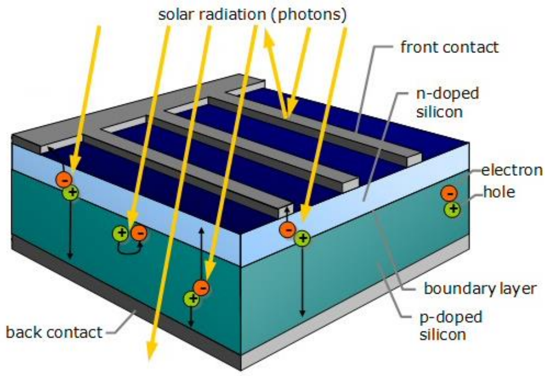

Fig. 1 the structure of the photovoltaic cell [2]

Photovoltaic cells can be divided accordingly to the type of photovoltaic cells on monocrystalline, polycrystalline and amorphous. The various types of photovoltaic cells differ from each other mainly efficiency and amount of silicon.

III. Thermal accumulation materials

For thermal energy storage are used based on physical principles of heat accumulative material, the phase change storage material, desorption of moisture from the porous materials in the range of hygroscopic sorption of moisture and dehydration crystal chemically pure substances [3]. According recovered physic-chemical principle can still be divided into thermal energy storage of several types and a sensible heat accumulation, accumulation of latent heat, absorption of water vapor and other physico-chemical processes. Currently most used for storing thermal energy, water, which has all of the commonly used materials highest specific heat capacity of 4180 J / (kg K). Further still uses a lesser extent aggregates having a higher operating temperature range but a lower heat capacity and 800 - 1000 J / (kg K). A drawback of these commonly used accumulation materials is particularly complicated construction and the demands on the heat accumulator space. The aforementioned deficiencies are largely eliminated based materials Phase Change Materials (PCM) materials or phase change of the working substance. PCM materials are used primarily for storage of latent heat and can be water, paraffin, salt hydrates. These substances are able to absorb, retain and release large amounts of heat or cold in a relatively small temperature change. This is a change such as physical state from solid to liquid. The heat that is accumulated is called latent heat. The panels are in the form of plates which are a mixture of ethylene and molecular paraffin wax closed. These boards are easily modifiable shape (easy divisibility sharp instrument) and can be easily installed on walls, bearing walls and ceilings, under plasterboard etc. These features can be used not only for storage of latent heat, but also for Sensible heat storage [4, 5].

IV. Description of the system

System described in this chapter is applied in the laboratory of environmental engineering at the FAI UTB in Zlin. The system consists of 9 photovoltaic panels with a total area of 11.25 square meters. The panels used, are of the type of polycrystalline photovoltaic cells. The producer of these panels has declared an energy efficiency of 15% (for angle of the panels surface inclined from the horizontal one of 45 ° with the southeast azimuth of the normal direction to the panel surface).Installed panels are shown in Figure 2.

Fig. 2 photovoltaics panels

Surface reaches 750 Wm-2, the electric power produced by the panels should be P = 1265 W, based on the declared efficiency by the producer. The output DC voltage of the panels is converted by the AC voltage inverter in one phase AC current with the 230 V AC. This inverter also displays information about the amount of energy produced by the various operating states of the system (fault, instantaneous power, voltage, total produced energy by the system, etc.) [6,7].

Fig. 3 inverter Sunny Boy

Figure 3 shows the inverter Sunny Boy 1700 with defined efficiency by the European standards $\eta euro$ =91.8%. This value has been measured under varying climatic conditions where maximum efficiency were reached ηmax = 93.5% with the optimal measuring conditions (stable temperature conditions, nominal DC voltage and medium values of AC power). The rest of the converted energy is lost by the electrical conversion in the form of heat [6], [7].

The last part of the system consists of two panels with a total storage area of 4.8 square meters that are placed in Laboratory of Environmental Engineering. The panels are 12 plates forming a mixture of paraffin wax and 60% copolymer of 40% ethylene. Between the layers of wax plates are always

ISBN: 978-1-61804-321-4

placed 3 Heizfolien a total power of 3600 W. Specific heat capacity of the material comes in a range of operating temperatures averaged 11,000 J / (kg K). For heating and cooling options includes panel and tube heat exchanger. The panels are coated polished galvanized sheet.

V. Methodology validation parameters

In order to exploit the latent heat panels for heating Laboratory Techniques environment in winter, we need to know the heat loss of the room, the energy manufactured by the photovoltaic panels and the average heating power accumulation panels. The heat loss of the room is determined by the relationship (1) [8]:

$$\dot{Q} = f \cdot U \cdot (\Delta\Theta) \tag{1}$$

where $\dot{Q}$ is heat loss of the room [W],
f correction factor,
U transmission heat loss coefficient [W/(m^2.K)],
A area [m^2],
$\Delta\Theta$ temperature difference [°C].

The actual amount of electricity produced by photovoltaic panels calculation based on data obtained from the sensor solar radiation (solarimetru), which is oriented in the direction of photovoltaic panels. This sensor records the total amount of solar radiation incident on the photovoltaic panels. From this value we calculate the real efficiency of a photovoltaic system according to the relationship (2) [8]:

$$\eta = \frac{P_m}{P_{rad}} = \frac{P_m}{E \cdot A_C} \tag{2}$$

where P_m is performance of a photovoltaic panel [W],
P_{rad} tower of the incident radiation [W],
E total intensity of solar radiation[W/m^2],
A_c surface of the photovoltaic cell [m^2].

Based on the efficiency of photovoltaic panels and the total amount of solar radiation incident on panels about the quantity of electricity that we are able to produce power for heat storage panels. The last step is to determine the heating output of the heat accumulation modules according to the relation (3) [8]:

$$\dot{Q} = \dot{q} \cdot A = h \cdot \Delta\Theta \cdot A \tag{3}$$

where $\dot{Q}$ is heating power panels [W],
$\dot{q}$ heat flow density [W/m^2],
A Area panels [m^2],
$\Delta\Theta$ temperature difference [°C],
h coefficient of heat transfer [W/m^2.K].

VI. Measurement

In the observed winter from October to March during the years 2013-2014 were recorded using weather station outdoor climatic conditions. The following Table 1 shows the average outdoor temperature in different months, the intensity of solar radiation and the amount of electricity produced by photovoltaic panels.

Table 1: Measurement values

Year 2013-2014			
Months	Average outdoor temperature [°C]	Average global solar radiation [W/m^2]	Energy made by PV [kWh]
October	11.17	99.12	142.372
November	5.81	39.33	52.815
December	2.4	28.62	40.033
January	2.03	31.96	41.135
February	4.46	74.24	104.283
March	8.27	138.27	180.903
Year 2014-2015			
October	11.23	81.21	111.236
November	8.17	38.51	71.63
December	2.38	29.36	57.38
January	1.62	26.35	61.22
February	0.6	73.52	78.994
March	4.95	114.81	150.101

Further, based on the construction and technical parameters calculated heat loss room temperature and heating capacity storage panels see in table 2.

Table 2: Parameters premises and accumulation panels

Premises		Accumulation panels	
Wall dimensions[m]	8,6x7,3 x3,1	Panel dimensions [m]	2x2,4
Dimensions of windows 2 [m]	4x1,9	Working temperature min. [°C]	25
External reference temperature [°C]	-15	Working temperature max. [°C]	35
Internal reference temperature [°C]	22	Consumption of heating foil [W]	3600
Heat loss wall [W]	1338,5	Heating power [W]	157,4
Heat loss window [W]	764,7		
Total heat loss [W]	2103,2		

All these values are summarized in the database. To determine the average consumption of the storage panel was modeled equation heating panel on the basis of changing the heat losses of the room, and subsequently verified in the experimental device located in the laboratory of Environmental Engineering (4):

$$\begin{gathered} y = -0{,}00003 \cdot x^5 + 0{,}0002 \cdot x^4 + 0{,}0074 \cdot x^3 \\ -0{,}0591 \cdot x^2 - 0{,}5742 \cdot x + 452{,}4 \end{gathered} \tag{4}$$

The measured values were then recalculated so that potential performance storage and photovoltaic panels correspond to real values. The results showed that the required minimum surface storage panels should be increased from the original 4.8 m^2 to about 64 m^2 and the area of photovoltaic panels from the original 11.25 m^2 to 150 m^2. The following figure 4 shows the production and consumption of electricity in December 2014.

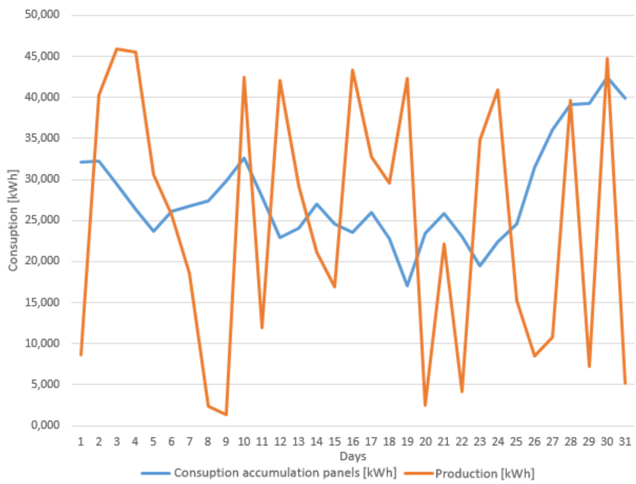

Fig. 4 production and consumption of electricity each day

From the figure it follows that in sixteen days in the month of December electricity consumption exceeds production, but in some days in the month again electricity production exceeds consumption considerably. After deducting these differences result is that only 4 days in a month's electricity production is insufficient. Overall, however, the production of electrical energy in the winter season between 2014-2015 greatly exceeds consumption, as shown in Figure 5.

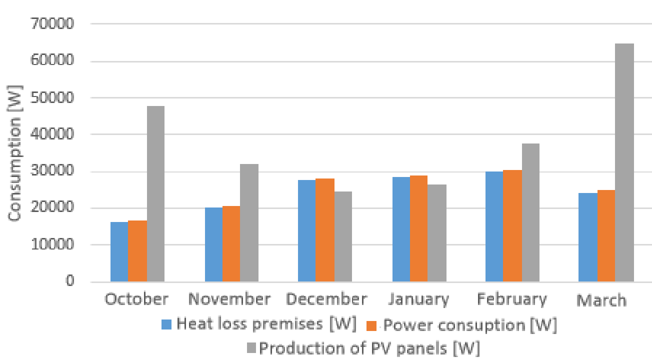

Fig. 5 comparison of production and consumption of electricity for heating

The figure shows that the photovoltaic panels are applicable to power the heat storage panels in winter. Part of the power must be backed up for periods when there is little sunlight and best selling surplus electricity to the public network and its return system in periods when production is insufficient.

VII. CONCLUSION

The aim was to verify the measurements in real conditions the possibility of using thermal storage panels (PCM) for storing electrical energy produced by photovoltaics panels in the form of heat. Thus the accumulated heat subsequently used for heating the room. Measurements showed that this concept is applicable for heating in winter. Unlike other storage materials such as water or oil based materials having nearly three times the PCM storage capacity. This can significantly increase energy autonomy objects without major structural alterations. More research will be, under what conditions would have given the latent heat panels used for room cooling in summer.

REFERENCES

[1] J. Petera and J. Herman, “Photovoltaics”. 2010 [Online]. Available: www.rescompass.org/IMG/pdf/Fotovoltaika.pdf

[2] V. Quaschining, “Renewable energy and climate change”. *Hoboken*, N.J.: Wiley, c2010, xii, 308 p. ISBN 978-047-0747-070.

[3] B. Bronislav. “Thermal energy storage – physical principles”. *TZB-info*. 2003, No. 1. Available: http://www.tzb-info.cz/1482-akumulace-tepelne-energie-fyzikalni-principy

[4] P. Zavoralova. “PCM in building“. *TZB-info* [online]. 2011, No. 2 [cit. 2015-04-15]. Available: http://stavba.tzb-info.cz/izolace-strechy-fasady/7381-pcm-ve-stavebnictvi-dil-2-pcm-jako-stavebni-material-moznosti-aplikace

[5] “Energy saving and thermal comfort in buildings” [online]. 2011 [cit. 2015-04-15]. Available: www.kerilit.cz/dokumenty/34-prezentace-energainpdf.pdf

[6] P. Chrobak, M. Zalesak, M. Oplustil, S. Sehnalek and J. Vincenec. “Return on investment in photovoltaic panels and verification their effectiveness”. *In: Proceedings of the International Conferences: Latest Trends on System*s - Volume II. 1. rel. Santorini Island, Greece, 2014, s. 581-587. ISBN 978-1-61804-244-6ISSN 1790-5117.

[7] T. Habrovansky. “Control and monitoring of heating and cooling units in laboratory of building control systems”. Available : http://dspace.k.utb.cz/handle/10563/ 6910 (accessed on 25 April 2014)

[8] CSN 73 0540. Thermal protection of buildings - Parts 1-4. Prag: Czech Standards Institute, 2005.

Data mining from radar precipitation measurement of the CZRAD network

David Šaur, Roman Žák, and Jaromír Švejda

Abstract—— This article is focused on obtaining radar data from the merged images of radar reflectivity of the Czech Radar Network System, which was implemented by the Czech Hydrometeorological Institute. Radar data mining is provided by the software developed in C#. This software tool will be used to forecasting system of local intensive precipitation in the Zlín Region, especially for the purpose of collecting radar and predictive data from resources of weather forecasting. The first part deals with an introduction to data mining on the Internet. Methodology part contains description of the basic parameters for radar precipitation measurement and the basic principle of functioning of the developed software. In conclusion, an example of selected meteorological situation is shown in terms of practical use of software tool intended for radar data mining.

Keywords—— Data mining, Radar precipitation measurement, flash floods

I. Introduction

GLOBAL warming significantly affects not only the climate of our planet, but also the development of the weather for the last 50 years. Some of the major effects of global warming is an increase of air temperature and relative humidity in the troposphere. Consequently, we can expect a higher number of extreme atmospheric phenomena inducing flash floods, such as strong thunderstorms accompanied by torrential rainfall, hail, strong wind gusts, electrical lightning discharges and tornadoes. Four flash floods occurred in the Czech Republic (Zlin Region) in 2009-2012, which caused considerable loss of life and material damage.

The current issue of crisis management of the Zlín Region are flash floods with rainfall of 10-80 mm which arise over the territory of a small size (approximately several square kilometers) and take short time interval (approximately 30-60 minutes) [1].

The essence of the problem lies in the insufficient quality and accuracy of forecasts distributed by the Czech Hydrometeorological Institute, which provides information only about the probability of storm occurrences instead of their specific locations and time of occurrences; therefore, the main objective of our research is to propose a forecasting system in the form of a software application intended to the prediction of local intense precipitation in the Zlin region and to ensure the preparedness of units of the Integrated Rescue System for 24 hours in advance. This prediction system will be part of Information, Notification and Warning System, which is an information support for crisis management in the Zlín Region.

Forecasting system will be connected to both servers on which an application with the radar, satellite and station precipitation measurement runs and outputs from aerological soundings and numerical weather prediction models. These applications provide data in only graphical formats. Consequently, part of the forecast system must be other software tools that convert data from graphical into tabular form suitable for subsequent analysis and evaluation. Subsequently, the data will be compared with selected characteristics and statistics of historical meteorological situations in order to find the characters of similarity.

Radar precipitation measurement gives us data on the current distribution and the development of precipitation over our territory. These data will have major importance in the statistics of historical meteorological situations that describe the chronological development of the thunderstorm cloud with the occurrence of the maximum values of radar reflectivity of precipitation fields.

The Czech Hydrometeorological Institute provides radar data through the interactive application JSRadView. The data is displayed in the PNG format as measurement results. However, meteorologists work only with binary form of the original measured data only, which are not publicly available. Binary form of measured data contains values of radar reflectivity of precipitation fields that are used in other calculations such as meteorological radar estimates combined with rain gauge measurement. The data in binary form are paid; therefore it was necessary to create a software tool intended to radar data mining from publicly available JSRadView.

The values of radar reflectivity of precipitation fields will be used for both statistical processing of meteorological situations and creation of prediction of torrential rainfall in the Zlin Region.

This work was supported by the Department of Security Engineering under internal grant of IGA/FAI/2015/025 (sponsor and financial support acknowledgment goes here).

First author (Ing. David Saur) is with the Department of Security Engineering, Faculty of Applied Informatics, and Tomas Bata University in Zlín (corresponding author to provide, mail: saur@fai.utb.cz). Second author (Ing. Roman Žák) is with Department of Informatics and Artificial Intelligence, Faculty of Applied Informatics, and Tomas Bata University in Zlín (corresponding author to provide mail: rzak@fai.utb.cz). Third author (Ing. Jaromír Švejda) is with Department of Informatics and Artificial Intelligence, Faculty of Applied Informatics, and Tomas Bata University in Zlín (corresponding author to provide mail: svejda@fai.utb.cz).

ISBN: 978-1-61804-321-4

II. Radar Precipitation Measurement

Radar precipitation measurement is operated by the Czech radar network of CZRAD in the Czech Republic, which consists of two meteorological radars.

Meteorological radar detects strong precipitation cloudiness (eg. thunderstorm to 250 km). Functional principle of radar is based on backscatter of microwaves (centimetres-waves) on water droplets and ice crystals in precipitation and cloud cover. The transmitter generates short high-energy pulses of electromagnetic waves which the antenna radiates in the form of a narrow beam into the atmosphere. Some of the energy is backscattered from meteorological targets (precipitation) or other targets (terrain, aircraft). Target position is determined according to the antenna position (azimuth, elevation) and the time between sending and receiving pulse. The amount of reflected energy is proportional to the intensity of precipitation (radar reflectivity) [2], [3].

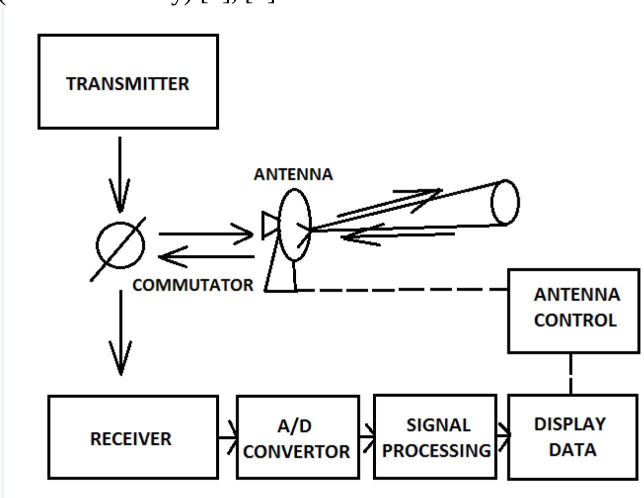

Fig. 1 scheme of meteorological radar [5]

A. Radar Precipitation Estimates

The fundamental quantity of radar precipitation measurement is radar reflectivity. This quantity is part of radar reflectivity scale shown in the bottom right of the radar picture. Radar reflectivity Z is defined as

$$Z = \sum_{i \in IV} D_i^6 = \int_0^\infty N(D) D^6 dD, \qquad (1)$$

where N (D) is a spectrum of particle size and D_i is diameter of droplet. Radar reflectivity Z is proportional to the sum of the sixth power of the particle diameters in a unitary volume (Z=SUM (D^6)). This condition applies for smaller particles than the wavelength of the radar. The unit of radar reflectivity Z is 1 mm^6/m^3 or logarithmic unit dBz, where Z [dBZ] = 10log (Z[mm^6/m^3]), thus 0 dBZ corresponds to Z=1mm^6 /m^3 [5], [6]. The measured radar reflectivity Z has a direct relation to instantaneous intensity of precipitation in a given location. Rainfall intensity I, depended on the radar reflectivity Z, is determined by Marshall-Palmer relation in the form:

$$Z = aI^b, \qquad (2)$$

where a and b are experimentally determined constants (a=200, b=1,6) for area of temperate latitudes [5], [6].

The rainfall intensity I is calculated by Marshall of Palm-relation (2) in a simplified form:

$$I = 10^{\frac{[Z - 10\log(a)]}{10b}}. \qquad (3)$$

As can be seen in Table I, the radar reflectivity Z increases exponentially depending on the rainfall intensity I [4], [8]:

Table I colour scale of radar reflectivity with the recalculated rainfall intensity [9]

Colour spectrum of radar reflectivity	Z [dBz]	I [mm/h]
	4	0,1
	8	0,1
	12	0,2
	16	0,4
	20	0,6
	24	1,2
	28	2,1
	32	3,6
	36	6,5
	40	11,5
	44	20,5
	48	36,5
	52	64,8
	56	115,3
	60	205,0

The colour spectrum is used for recalculation radar reflectivity to rainfall intensity and data processing.

III. Radar Data Mining Software

The main purpose of this software tool is to simplify the process of collecting radar data from the CZRAD network for subsequent processing, analysis and evaluation of selected meteorological situation.

The program includes the following supporting applications:

- Meteo.exe - user interface.
- Data.csv - MS Office Excel file with the extension * csv intended to the selection and location updates.

ISBN: 978-1-61804-321-4

- DataOutput.csv - MS Office Excel file with the extension * csv intended to storing the read data in the values of radar reflectivity converted from the RGB spectrum.

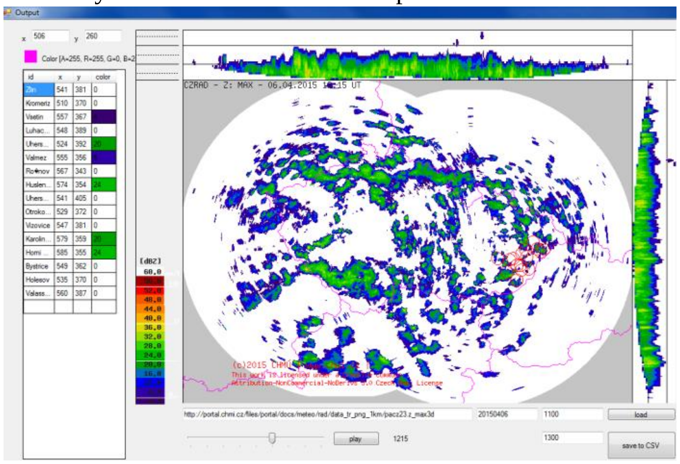

Fig. 2 the main panel of the Meteo program

The user interface of the program Meteo consists of the following parts:

- The radar picture that is loaded by pressing "load" button from JSRadView application, which runs on the server of Czech Hydrometeorological Institute (CHMI) portal.

Area under the radar images contains following parts of the program:

- Web address of CHMI portal.
- Date and time interval to retrieve the radar picture.
- Time scale for uploading radar images (the Web address).
- The "save to CSV" button intended to save the downloaded radar images to MS Office Excel.

Left of the radar output, there is a table containing these values:

a) ID - the name of the selected locality,

b) Coordinates of X and Y describing the location

c) Colour spectrum - the colour expression of the appropriate values of radar reflectivity.

```
private int color2value(int x, int y)
{
    if (loadImg)
    {
        Bitmap bitmap = (Bitmap)pictureBox1.Image;
        Color color = bitmap.GetPixel(x, y);
        int output = 0;
        if (color.R == 252 && color.G == 252 && color.B == 252) output = 60;
        if (color.R == 160 && color.G == 0 && color.B == 0) output = 56;
        if (color.R == 252 && color.G == 0 && color.B == 0) output = 52;
        if (color.R == 252 && color.G == 88 && color.B == 0) output = 48;
        if (color.R == 252 && color.G == 132 && color.B == 0) output = 44;
        if (color.R == 252 && color.G == 176 && color.B == 0) output = 40;
        if (color.R == 224 && color.G == 220 && color.B == 0) output = 36;
        if (color.R == 156 && color.G == 220 && color.B == 0) output = 32;
        if (color.R == 52 && color.G == 216 && color.B == 0) output = 28;
        if (color.R == 0 && color.G == 188 && color.B == 0) output = 24;
        if (color.R == 0 && color.G == 160 && color.B == 0) output = 20;
        if (color.R == 0 && color.G == 108 && color.B == 192) output = 16;
        if (color.R == 0 && color.G == 0 && color.B == 252) output = 12;
        if (color.R == 48 && color.G == 0 && color.B == 168) output = 8;
        if (color.R == 56 && color.G == 0 && color.B == 112) output = 4;
```

Fig. 3 sample of source code - conversion of RGB values to the radar reflectivity Z

A. *Scheme of the Program*

Initially, the user got familiar with the program, its visualization and features.

The user should follow these steps:

1) Firstly, radar data has to be loaded from the server of the Czech Hydrometeorological Institute (JSRadView application). The radar data is stored in bitmap file in the form of spectrum colour of radar reflectivity.

2) Secondly, the user sets point and the input file (name_point – name; X; Y - coordinates of the location).

3) The third step is the analysis and processing of data array.

4) Subsequently, coordinates are loaded from the file and the value from the spectrum colour of radar reflectivity is determined.

5) Further, values are converted into numerical data of the spectrum colour of radar reflectivity.

6) Finally, data is saved into output file in MS Excel.

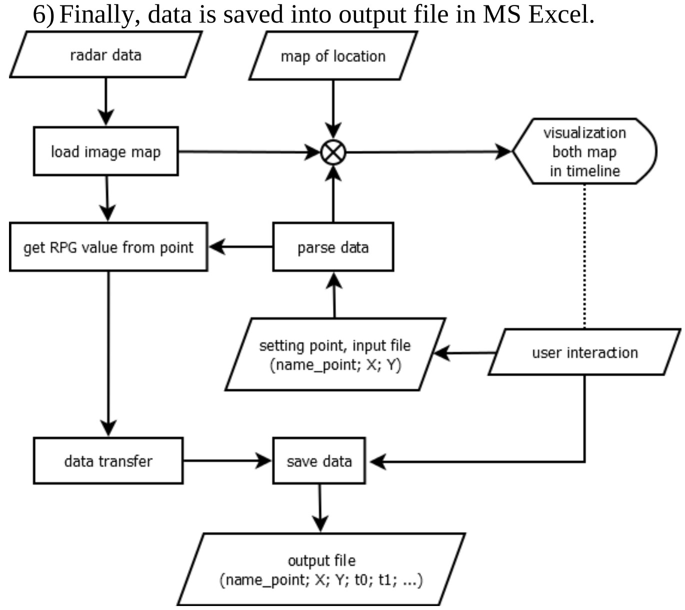

Fig. 4 scheme of the radar data mining

Controlling of the Meteo program is easy and intuitive. Firstly, the user chooses a date and a time interval for recording radar images of CZRAD network. Moreover, JSRadView the application provides a history of images for the last 87 hours. The user loads the selected radar images using the "load" button and then they can be stored using the "save to CSV" button. Selection of locations can be updated by clicking the mouse on the map radar picture, where coordinates X and Y are displayed. These coordinates are copied to a file Data.csv.

The file DataOutput.csv contains coordinates of selected locations and values of radar reflectivity loaded from radar images according to the selected time interval. The values of radar reflectivity can be calculated by formula (3) to the values of rainfall intensity for subsequent analysis and data evaluation.

ISBN: 978-1-61804-321-4

IV. Analysis of Case Study on 21.7.2014

Use of the radar data mining program is demonstrated on the analysis of the situation on July 21, 2014, when the most intense rainfall occurred in the Zlín Region in 2014. This situation showed typical features of a trough (in meteorology) passing through central Europe. Initially, the anticyclone influenced us above western Europe, which moved very quickly through central Europe to the east. Subsequently, trough influenced us from the west. Warm stable air mass was transformed into unstable air mass due to intensive warming of the Earth's surface and an increase the moisture in the atmosphere. The formation of very strong thunderstorms was significantly supported by orography terrain, especially on the windward side of the local hills and mountains [7].

Table II indexes convection calculated from aerological station Prostějov on 21.7.2014

Date	Time release radiosonde	CAPE (J/kg)	CIN (J/kg)	LI	KI	SI	SWEAT	TT index	FAUST	SHEAR (m/s)
21.7	12:00	2 077	-13	-3	36	-3	222	50	2	5

Indices of convection characterize the degree of atmosphere instability (atmospheric condition for the formation of storms). Very high value of CAPE (Convective Avalaible Potential Energy) was the main feature of the formation of very strong thunderstorms exceeding 2000 J/kg in combination with wind shear in the level of 0-6 km. The value of wind shear of 5 m/s is characteristic for the formation of convective cells and weak multicell storms, but the main parameter was the wind blowing from the southeast of the surface layer (10-100 m above the terrain) and northwest in the direction of precipitation movement (700 hPa geopotential level - 3 km above the terrain). The opposite direction of air flow in the surface and height levels of the atmosphere led to the formation of stationary convective storms, when a large amount of rainfall fell in a small area [7].

Table III shows three basic data array:

- Location - selected locations in the Zlín Region.
- Coordinates X and Y - describe the location of the selected sites.
- Time interval 2:30 p.m. to 3:15 p.m. for radar rainfall measurements.

Table III radar measurement of atmospheric precipitation on July 21, 2014-Data Output.csv

lokace	x	y	1430	1445	1500	1515
Zlin	541	381	0	0	40	36
Kromeriz	510	370	48	56	52	40
Vsetin	557	367	40	28	32	36
Hostalkova	545	365	48	56	56	52
Luhacovice	548	389	0	0	52	48
Uherske Hradiste	524	392	0	0	0	0
Valmez	555	356	40	24	8	32
Roznov	567	343	16	28	28	28
Huslenky	574	354	36	32	28	28
Uhersky Brod	541	405	0	0	0	52
Otrokovice	529	372	0	0	4	4
Vizovice	547	381	0	0	16	4
Karolinka	579	359	32	28	24	36
Horni Becva	585	355	32	28	32	32
Bystrice	549	362	20	24	24	28
Holesov	535	370	32	16	40	24
Valasske Klobouky	560	387	0	0	12	24

The result was the measured values of radar reflectivity of the most intense rainfall that occurred in the time between 14:30 and 15:15 in the Zlín Region. Maximum values of radar reflectivity were recalculated to rainfall intensity according to the formula (3) and incorporated into the statistics of the meteorological situations.

Average values of radar reflectivity Z was achieved for the locations Kroměříž (Z=48 dBz => I=37 mm/ hr) and Hošťálková (Z=52 dBz => I = 65 mm/hr).

The objective of radar data mining was to obtain the data of the maximum radar reflectivity intended to the processing of statistics of precipitation and locations for selected meteorological situation.

Result of the analysis of the meteorological situation on July 21, 2014 is the statistic of precipitation and locations listed in Table IV:

Table IV the statistic of precipitation and locations for meteorological situation on July 21, 2014

Locations	Mountains	Time of occurence	Z (dBz)	I (mm/hr)	Rainfall (mm/24h)	Station
Vsetín	**Hostýn-Vsetín Higland**	**5x 14-17; 2x 18-21**	**56**	**115**	**74**	**Maruška**
Luhačovice	Vizovice Highland	3x 14-17; 3x 18-21	56	115	49	Horní Lhota
Uh. Hradiště	Chřiby	3x 14-17; 3x 18-21	52	65	41	Staré Hutě
Rožnov p. Radhoštěm	Vizovice Highland	3x 14-17; 2x 18-21	56	115	35	Horní Bečva
Kroměříž	Litenčice Highland	3x 14-17; 2x 18-21	52	65	24	Kroměříž

Table IV expresses the relation between radar (Z of dBz) recalculated to rainfall intensity I of mm/hr and station measurements (Totals – 24 mm / hr + station). The most intense rainfall fell on the windward side of the Hostýn-Vsetín highlands due to wind shear, which prolonged the duration of the precipitation. The station Hošťálková measured the total precipitation of 65 mm/hour (between 15 and 16 hrs.), which is classified by Integrated Warning Service System of CHMI as "Very strong thunderstorms". 24-hour total precipitation was even greater (74 mm). Torrential rainfall caused considerable material damage including extensive soil erosion in the affected area [7].

V. Conclusion

The aim of this article was to provide information on new approach of radar data mining from publicly available application JSRadView of the Czech Hydrometeorological Institute (CHMI). Radar Department of CHMI currently works only with the original measured data in binary form, but these data is not publicly available yet; therefore the Meteo program was created for quick and easy radar data obtaining.

The program's output of radar data mining was presented in the analysis of the situation on July 21, 2014, when most precipitation fell in the Zlín Region in 2014 (station Hošťálková-Maruška - 74 mm / 24 hours). The results are the values of radar reflectivity of precipitation fields detected by meteorological radars of the CZRAD network obtained in tabular form. These values can also be used to calculate the rainfall intensity for the purpose of comparison with the station measured data.

The main usage consists in getting of radar data for weather forecasting system of local intense rainfall, which will be part of the Information, Notification and Warning System of the Zlín Region.

The Meteo program will be expanded to upload radar images from different servers, or satellite and predictive data mining from graphic formats on the Internet.

References

[1] Czech Meteorological Society. *“Meteorological dictionary”.* 2015. Avalaible at: http://slovnik.cmes.cz/.

[2] *“Information, notification a warning system of Zlín Region“– Integrated project, Zlín Region* [online]. Available: http://www.kr-zlinsky.cz/-informacni-vyrozumivaci-a-varovaci-system-zlinskeho-kraje-integrovany-projekt-cl-1392.html

[3] Czech Hydrometeorological Institute *“Radar network CHMI”.* [online]. 2010-2011 Available at: http:// http://www.chmi.cz/files/portal/docs/meteo/rad/info_czrad/index.html

[4] J.Kráčmar, “*Meteorological radars”.* Czech Hydrometeorological Institute. [online]. 1997-2011. Available: http:// http://www.chmi.cz/files/portal/docs/meteo/rad/info_radar/index.html

[5] D. Řezáčová, et al. “Meteorological radars” in *Physics of clouds and precipitation.* vol. 1. Prague: Academia, 2007, pp. 286-309. ISBN 978-80-200-1505-1.

[6] R.A. Houze, *“Cloud dynamics”.* International Geophysics Series, 53, Academic Press, 1993, 573 pp.

[7] D. Šaur. “*Analysis of technical resources weather forecasts and territory of the Region in terms of weather”.* Zlín, 2014.

[8] D. Šaur, S. Plšek. “Mobile Meteorological Radar Uses in Crisis Management,” *in Proc. of the 18th International Conference on Systems (part of CSCC ´14),* Santorini Island, Greece, July 17-21, 2014, s. 147-153. ISBN: 978-1-61804-243-9. ISSN: 1790-5117. Available: at: http://www.europment.org/library/2014/santorini/bypaper/SYSTEMS/SYSTEMS-00.pdf

[9] Czech Hydrometeorological Institute. “*Current radar data”.* Available at:http://portal.chmi.cz/files/portal/docs/meteo/rad/data_jsradview.html

Innovated laboratory I/O converter device

Petr Dostálek and Libor Pekař

***Abstract*—**The paper is aimed at description of the improved and extended microcontroller I/O converter unit for laboratory temperature measurement and control. Among the most significant improvements are: A more compact hardware design, increased A/D and D/A converter resolutions, added USB communication capability, better and more accurate analog circuits with more advanced operation amplifiers, the use of OLED instead of LCD display, the pulse-width modulated signal generated by the microcontroller unit itself, etc. The efficiency and functionality of the designed module is verified by dynamical responses measurements.

***Keywords*—**Converter unit, laboratory heating model, microcontroller, temperature control.

I. Introduction

A year ago, a simple and smart compact modular low-cost microcomputer input/output (I/O) laboratory module for signal converting and control of a temperature educational plant was developed and assembled at the Faculty of Applied Informatics, Tomas Bata University in Zlín, Czech Republic [1], to replace the very obsolete and dangerous appliance. The designed appliance has preserved some crucial features of the old one, and simultaneously has brought new useful functions, such as a four-line LCD panel, buttons allowing calibration of the I/O channels with saving, the RS232 interface for serial communication with PC, etc. The significant advantage of the device has been its low price, which has made the unit easily reachable for a wide range of potential users.

However, some problems and imperfections with this first evolution of the innovated converter unit persist. For instance, although the appliance can be extended with up to four converter and control boards, its modular structure is not as flexible as it should be. Some analog circuits are equipped with unsatisfactorily accurate components [2] and the used AD and DA converters are only of the 12-bit resolution [3]. Among some others, these features have brought the idea of the second evolution of the innovated unit into being. Although there are available on the market industry standard analog converters for many types of Resistance Temperature Detector (RTD) elements with unified voltage or current output signals, for our application are not suitable due to a different concept of the intelligent converter unit. Besides the basic functionality of the RTD converter we need also digital communication interface which can be directly connected to the personal computer without a special data acquisition card. Such a combined converter device including power digital output is not commonly available in the compact form which is required in the educational process.

This contribution brings about the concise description of the novel evolution of the converter unit from the functional and hardware point of view. The presented measured dynamical responses prove its applicability and functionality.

II. History Overview

Since the eighties of the last century, every single seat in the laboratory room was equipped with a central PC with Advantech PCI 1171 acquisition card connected to the I/O converter and control unit (see Fig. 1) which serves as an interface between the PC and the controlled plant. The appliance has, however, suffered from some deficiencies which have disabled to keep using it for present and future modern control and identification teaching tasks. Moreover, it has been powered by 230V AC from mains, which does not meet current working and safety conditions. Two built-in converter cards for signal processing from Pt100 sensors, have provided the user with the normalized analog signal within the range of 0-10V DC. A rheostat in the heating plant body has been warmed up by 24V AC control input.

In 2014, a modern modular unit prototype was designed and assembled [1], see Fig. 2 for its appearance and Fig. 3 for the functional block scheme. This innovation has brought the preservation of basic functional properties of the obsolete appliance, and improved many other attributes; namely, the unit has been powered by the safe 24V AC input, equipped with a central microcontroller board, LCD display, a 3x3 keyboard and the RS232 interface.

Fig. 1 the appearance of the former obsolete I/O converter and control unit

The work was performed with the financial support of the research project NPU I No. MSMT-7778/2014 by the Ministry of Education of the Czech Republic and also by the European Regional Development Fund under the project CEBIA-Tech No. CZ.1.05/2.1.00/03.0089.

P. Dostálek and L. Pekař are with the Department of Automation and Control Engineering, Faculty of Applied Informatics, Tomas Bata University in Zlín, Nad Stráněmi 4511, 760 05 Zlín, Czech Republic (e-mail: {pekar, dostalek}@fai.utb.cz.

Fig. 2 the appearance of the first evolution of the module – the front (up) and the back side (down)

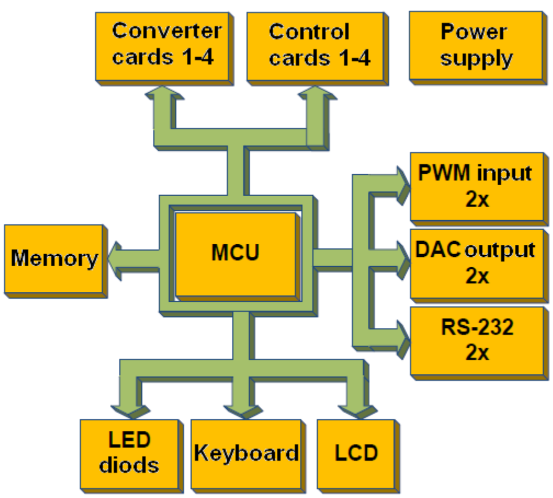

Fig. 3 a block scheme of the first evolution of the module

A firmware implementing basic input and output functions, diagnostic and peripheral services has been developed in addition, the serial interface can cooperate e.g. with MATLAB©. The unit has a modern appearance, is compact, intelligent and safe and can be easily modularly extended. Among other crucial benefits of this first evolution is its prize: Components and manufacturing on the designed device costs about 350$ in total.

There have been, however, still many features that might be improved, for instance, the unit would have processed a general unified electrical signal, such as 0-10 V DC, which may help to extend the area of its applicability, and there have been a relatively high noise and low measurement accuracy levels. The modularity of this evolution of the unit can also be better. Hence, a second evolution has been designed and the prototypal appliance assembled – its basic description follows.

III. Converter Unit Hardware Overview

Hardware design of the intelligent converter unit device for resistance temperature sensors evaluation is adapted to high accuracy and easy functionality expansion in future applications by simple adding of measurement modules with required features. Additionally, it is capable of generating power control signal which can directly drive heating elements, for example. This is achieved by splitting the converter unit into the two basic parts:

- The main board consisting of the master microcontroller (MCU), communication interfaces (COM), stabilized power supplies (PSU) and expansion connectors for input and output modules.
- Expansion modules which will be inserted into the connectors of the main board. Basically, two types of modules can be implemented: input modules converting analog signals from sensors to digital signals and output modules converting digital signals back to analog ones.

A scheme of basic blocks introduced above can be seen in Fig. 4.

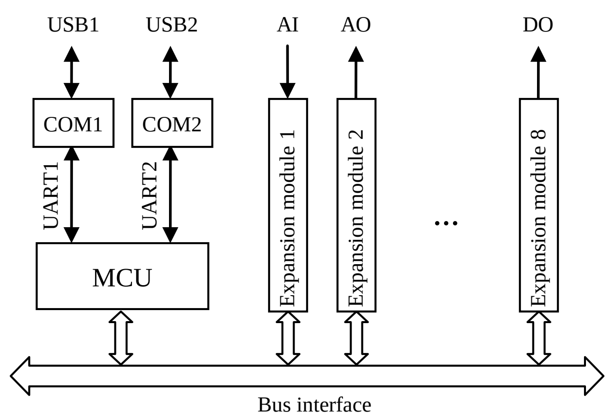

Fig. 4 block schematics of the intelligent converter unit

A. *Main board design*

Main board design is based on Freescale MCF51AC128 microcontroller [4] in the QFP64 package performing all operations of the intelligent converter unit. It is a member of Flexis 32-bit ColdFire® V1 microcontrollers' family enabling simple migration from 8-bit Flexis MCUs to 32-bit due to pin-to-pin compatibility. They are suitable for entry-level applications that do not need special features of ColdFire V2 core. Internal program loading and debugging is provided by on-chip Background Debug Module (BDM).

MCF51AC128 main features are:

- 128 KB of flash memory
- 32 KB of static RAM
- 1x Serial Peripheral Interface (SPI)
- 2x Serial Communication Interface (SCI)
- 1x Controller Area Network (CAN)
- 1x Inter-Integrated Circuit (IIC)

ISBN: 978-1-61804-321-4

- Flexible Timer Module 1 (FTM1) with 6 channels
- Flexible Timer Module 2 (FTM2) with 2 channels
- Timer Pulse-Width Modulator (TPWM) with 2 channels
- 54 general purpose I/O pins (16 pins shared with rapid GPIO (General-Purpose Input Output)
- 12-bit Analog-to-Digital Converter (ADC) with 20 analog channels
- Single-wire background debug interface

The correct program function is monitored by an integrated watchdog Computer Operating Properly (COP) system and illegal operational code and address detection with programmable reset or exception response. The Central Processor Unit (CPU) can work at the frequency up to 50.33 MHz, the maximum internal bus frequency is 24 MHz at the 2.7 to 5.5V supply voltage range.

The communication with higher control or supervision systems is provided by two FT232BM USB Universal Asynchronous Receiver/Transmitter (UART) Integrated Circuits (ICs). They are capable to communicate at TTL levels with data transfer rates up to 3 MBd. An on-chip integrated transmit and receive buffer with capacity of 128 B and 384 B enables high data throughput. FT232BM operates from the single power supply with voltage of 5 V. The USB I/O interface is supplied from an integrated 3.3V voltage regulator. Due to the integrated level converter for UART I/O signals it is possible to connect it with logic circuits operating at 3.3 V or 5 V. Both communication interfaces are realized in a manufacturer recommended wiring for a self-powered application with the 5V input/output interface. A connected EEPROM memory 93C46 is optional and can be used for storage of USB Vendor Identification (VID), the device class definition for Physical Interface Devices (PID), serial number and product description strings. The clock signal is generated externally by a crystal oscillator with frequency of 6 MHz. USB1 and USB2 UART I/O interfaces are connected to corresponding UART0 and UART1 pins of the main microcontroller.

Expansion modules can be inserted into eight 30pin double-row connectors including all necessary signals for their function. They provide all available voltage sources: 5 V for digital and +15 V, -15 V DC for analog circuits, the serial peripheral interface for communication with the master microcontroller and finally an 8 input and 8 output general purpose digital interface which can be utilized for internal logic control of the connected modules. The active expansion connector is selected by the main microcontroller in the cooperation with a 3-to-8 line decoder 74HC138 on which outputs eight board select signals (active at the low logic state) are available. Only one expansion module can be in active state at the moment and it communicates via the SPI interface with the microcontroller. Other modules must stay in the high impedance state.

The main board is supplied from a 24V AC voltage source which is commonly used in control systems for sensors and actuators power supplies. A rectified input voltage is converted by two DC-DC converters to 5 V with the output power of 6 W for logic circuits and ±15 V for analog circuits.

B. Expansion modules design

The converter unit hardware configuration is determined by installed expansion modules. Each module type has its identifier which can be read by the main microcontroller from the bus interface. During the initialization phase all expansion slots are scanned and connected modules auto-detected and correctly initialized.

The following modules are currently available:

- Analog and digital inputs
- Analog outputs
- Power digital outputs

1) Analog and digital inputs module

The module is equipped with two analog converters for Pt100 type resistance temperature sensors with range from 0 to 400 °C and two voltage analog inputs with unified range from 0 to 10 V. All analog inputs are protected against voltage overload by protection diodes. Analog signals are converted by using the 14-bit analog-to-digital converter TLC3544DW to digital values which are transferred by a SPI to the main microcontroller. High temperature stability of analog circuits is achieved by the utilization of precision operational amplifiers OPA4277. The reference voltage of 3 V for analog and digital circuits is provided by the voltage reference IC AD780ANZ. A bus interface of the module is controlled by two octal 3-state bus transceivers 74HC245.

Module parameters:

- 2x analog input for Pt100 resistance temperature sensors, 4-wire configuration, 1mA constant current
- 2x analog input from 0 to 10 V
- 2x TTL compatible digital input
- 14-bit analog-to-digital converter resolution

2) Analog outputs module

The module is based on two 16-bit digital-to-analog converters DAC8830 with a SPI communication interface. Output of the converter is amplified with a non-inverting amplifier with the gain of 4 resulting in the final output voltage range from 0 to 10 V. High temperature stability of analog circuits is achieved by utilization of precision operational amplifier OPA2277PA again. The reference voltage of 2.5 V for digital-to-analog converter is provided by the same voltage reference as for the module of analog and digital inputs.

Module parameters:

- 2x analog output with the range from 0 to 10 V
- 10mA output current per channel
- 16-bit digital-to-analog converter resolution

3) Power digital outputs module

The switching of the two resistance loads with the power supply voltage of 24V AC is the main function of this module. It utilizes power triacs T410 which are separated from sensitive digital control circuits by optotriacs MOC3063. Control signals for triacs are generated by the D-type flip-flop 74HC174 in which the main microcontroller desired value of the corresponding digital output is stored. A bus interface of the module is controlled by transceivers of the same type as for the analog and digital inputs module.

Module parameters:

- 2x power digital output 24 V AC
- 2.5A output current per channel

The overall external appearance of the appliance is pictured in Fig. 5. There can also be seen the 4-line alphanumeric OLED display WEH002004A and a simple 3-key board for moving in the menu, confirmation and cancellation in the figure.

Note that SW for the device is being developed and its description will be published in the future.

IV. Verification by Measurements

In order to verify the functionality of all HW parts and modules of the designed device its elementary firmware the measurement of dynamical (step) responses was performed. Two types of experiments were made; as first, the mean output power generated by the 24V DC PWM signal is successively increased in steps, whereas the second stage resides in the abrupt power decreasing. Graphical results of such an experiment are provided in Fig. 6.

Fig. 5 the appearance of the second (new, herein described) evolution of the module – the front (up) and the back side (down)

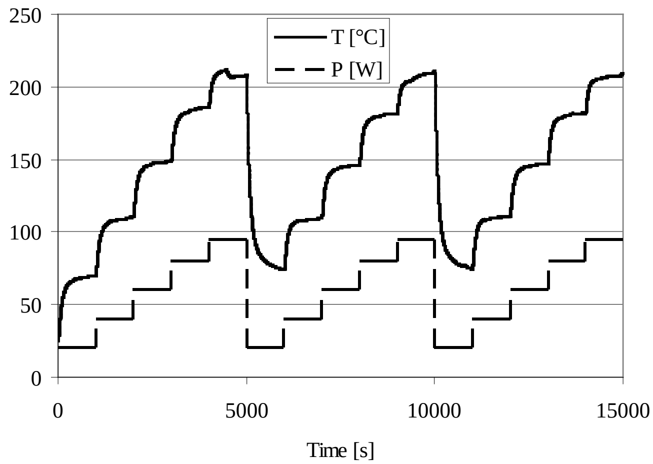

Fig. 6 the measurement of step responses by means of the new I/O converter and control device

V. Conclusion

This paper has been focused on the concise introductory description of the second evolution of the innovated I/O converter and control unit primarily given over to the laboratory measurement on heating models. The basic characteristics and main improvements compared to the previous version of the appliance can be summarized as follows:

- An innovated HW structure – the motherboard including the microcontroller, 2x USB communication interface, power supply and 8 connectors for expansion modules.
- A/D converter resolution increased to 14 bits.
- D/A converter resolution increased to 16 bits.
- More accurate operation amplifiers are mounted on analog circuits.
- The USB interface enables the better compatibility with notebooks (laptops) compared to RS232 without the necessity of an external USB to RS232 converter.
- The OLED has much better readability, response and energy consumption compared to LCD with LED backlight.

References

[1] L. Pekař, P. Dostálek, P. Navrátil, and Z. Oborný, "Low-cost intelligent educational laboratory temperature data acquisition and control device," *Int. J. Circuits, Systems and Signal Processing*, vol. 9, pp. 103-112, 2015.

[2] *LMx24, LMx24x, LMx24xx, LM2902, LM2902x, LM2902xx, LM2902xxx Quadruple Operational Amplifiers* (cited 2015, April 16), Texas Instruments Inc., Dallas, TX, 1975-2015 [Online]. Available: http://www.ti.com/lit/ds/symlink/lm324.pdf

[3] *MCP4821 - Mixed Signal - System D/A Converters – Microchip* (cited 2015, April 16), Microchip Technology Inc. [Online]. Available: http://www.microchip.com/wwwproducts/Devices.aspx?product=MCP4821

[4] *MCF51AC: Flexis 32-bit ColdFire® V1 Microcontrollers* (cited 2014, August 25), Freescale Semiconductor, Inc. [Online]. Available: http://www.freescale.com/webapp/sps/site/prod_summary.jsp?code=MCF51AC.

Heat output control in district heating system: control method

Pavel Navratil and Libor Pekar

***Abstract*— The paper deals with the description of one of possible methods to control of a heat output in district heating systems. This control method consists in simultaneous and continuous acting of two variables influencing the transferred heat output and in using the prediction of required heat output in a specific locality. The control method is called qualitative-quantitative control method of heat output with utilization of prediction of daily diagram of heat supply in hot-water piping systems of district heating. The control method should enable elimination of the influence of transport delay between the source of heat and heat consumption of individual consumers.

***Keywords*—**District heating system, heat distribution, heat output, transport delay

I. Introduction

THE district heating systems (DHS) are developed in cities in according to their growth. DHS has to ensure supply of energy to all heat consumers in quantity according to their requirements variable in time. Energy supply has always to comply with prescribed quality index. In case of hot-water piping it means to maintain prescribed temperature of hot water in intake piping. [1]

The DHS is possible to consider as technological string containing three main parts (see Fig. 1), i.e. heat production, transport + heat distribution and heat consumption. [2]

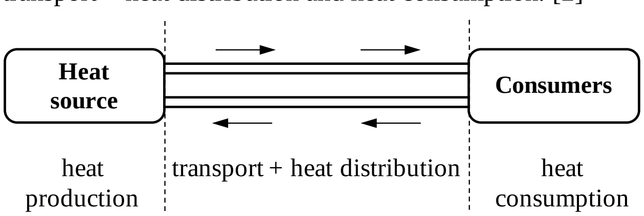

Fig. 1 technological string of district heating system, i.e. heat production, heat distribution and heat consumption

The paper deals with one of the possible approaches to control of a heat output in district heating systems. The content of paper is possible to include into all three parts of the technological string (see Fig. 1). Another possible approaches to control of district heating system can be found e.g. in [3] where the predictive approach to control is used and in [4] where the robust predictive approach to control is used. Possible approaches to solve of individual parts of technological string can be found e.g. in [5] where is solved part “heat production“, in [2] where is solved part “transfer + heat distribution“ and in [6] where is solved part “heat consumption“.

The present method of heat output control of hot-water piping heat supply is usually using the dependence on water temperature in intake piping of heat feeder or also even the dependence on outside air temperature. Two manipulated variables are available for heat output control of hot-water piping from the source of heat, i.e.

- change of difference of water temperature in intake and return piping of how-water piping which is realized by means of the change of heat input on intake to heating plant exchanger - so called qualitative control method of heat output,
- change of mass flow of hot water by means of changing speed of circulating pump - so called quantitative control method of heat output.

The above mentioned manipulated variables are usually used as independently acting, namely only one of them. If both were used it concerned a case when qualitative control method was the main method of control and quantitative method was used by means of starting and stopping pumps with different transported mass flow. These quantitative changes were used once at a change of the yearly period (winter, summer, transition period). Usually circulating pumps of two or three sizes were used for this purpose. Disadvantage of described control methods is the fact that they don’t include completely dynamic properties of the controlled system. Transport delay in intake branch of heat intake piping and the delay of inertia members of heating plant exchanger remain omitted. If the output withdrawn at any place of hot-water piping network changes, than corresponding output of sources (production) controlled by classic qualitative method adapts itself with considerable delay even when the change of hot water mass flow occurs due to self regulating properties of transport pump static characteristic caused by the change of operating point of the pump. The change of heat output withdrawal realizes by acting of autonomous controllers of temperature in secondary networks of consumer’s transfer stations. Thus non-fulfilment of some requirements for required duality indexes of heat transfer medium comes into being.

II. Qualitative-Quantitative Control Method Of Heat Output IN District Heating System

Algorithm of the qualitative-quantitative control method with utilization of prediction of heat supply daily diagram in

The work was performed with financial support of research project NPU I No. MSMT-7778/2014 by the Ministry of Education of the Czech Republic and also by the European Regional Development Fund under the Project CEBIA-Tech No. CZ.1.05/2.1.00/03.0089.

P. Navratil is with Tomas Bata University Zlin, Faculty of Applied Informatics, Department of Automation and Control Engineering, nam. T.G. Masaryka 5555, 760 01 Zlin, Czech Republic (email: pnavratil@fai.utb.cz).

L. Pekar is with Tomas Bata University Zlin, Faculty of Applied Informatics, Department of Automation and Control Engineering, nam. T.G. Masaryka 5555, 760 01 Zlin, Czech Republic (email: pekar@fai.utb.cz).

hot-water systems of district heating should enable eliminating the influence of transport delay between the heating plant exchanger in the source of heat and relatively concentrated heat consumption of all consumers. The transport delay depends on flow speed of heat transfer medium (hot water) and on the length of feeder piping. The proposed method of hot-water piping output control consists in simultaneous and continuous acting of two manipulated variables influencing transferred heat output and in using prediction of required heat output in a specific locality. The designed control method was considered for a case when the transport delay was supposed to be in the range of several hours depending on the heat output consumed by consumers.

Schematic diagram of the above mentioned qualitative-quantitative control method of heat output in district heating systems is displayed in the Fig. 2. Further information about the qualitative-quantitative control method is possible to find in [7], [8].

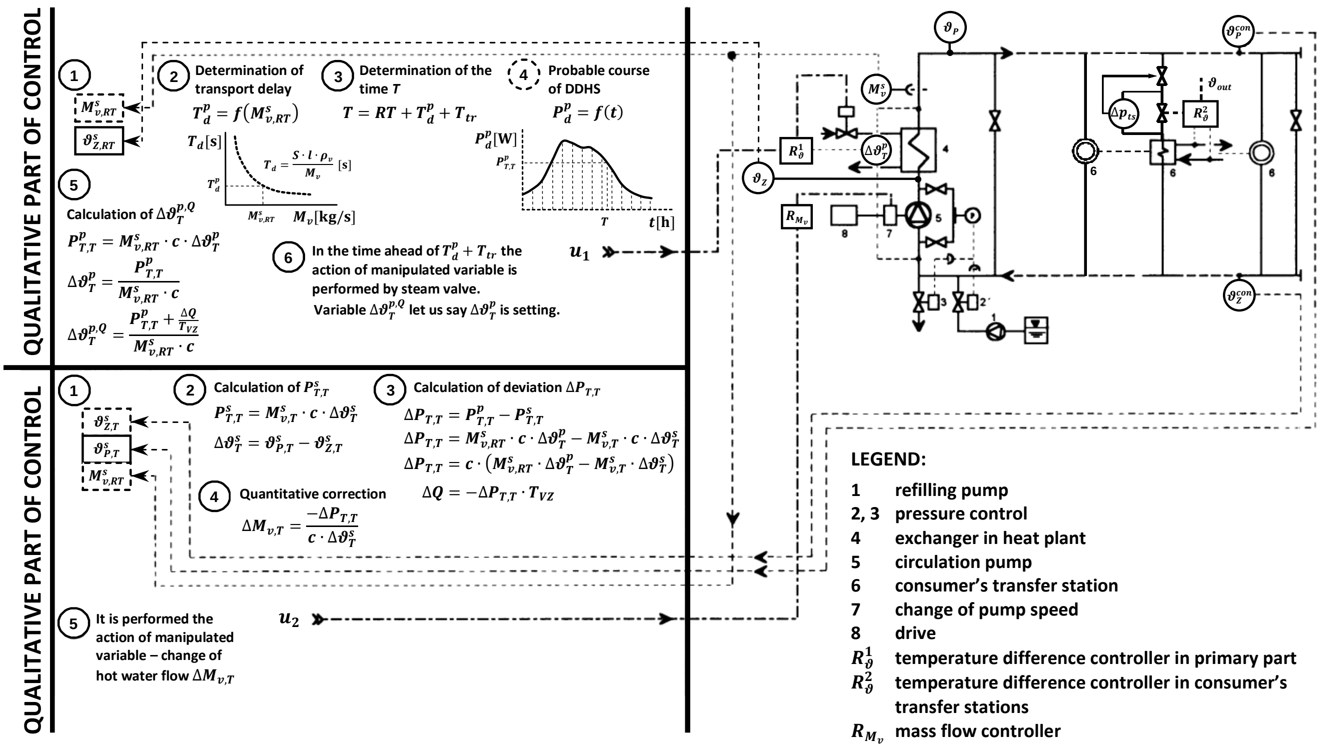

Fig. 2 schematic diagram of the qualitative-quantitative control method of heat output with utilization of prediction of daily diagram of heat supply in hot-water piping systems of district heating

Key to Fig. 2: S - cross section of intake branch of feeder, l - length of intake branch of heat feeder, ρ_v - specific mass of circulating water in intake branch of feeder, c- specific heat capacity, RT - real time, i.e time in which manipulated variable of qualitative method of control is acting on exchanger in heating plant, T - time in which acting of manipulated variable of quantitative method of control shows itself at consumers, T_d^p - presupposed transport delay, T_{tr}- time of transition of exchanger in heating plant at action of manipulated variable, T_{VZ} - sampling period (e.g. 10, 15, 30 minutes), M_v - mass flow of circulating water, $M_{v,RT}^s$ - real mass flow of circulating water in time RT, $M_{v,T}^s$ - real mass flow of circulating water in time T, $\Delta M_{v,T}$ - quantitative correction, i.e. change of mass flow of circulating water, P_T - heat output of hot-water piping, P_T^p - presupposed heat output read from predicted daily diagram of heat supply (*DDHS*), $P_{T,T}^p$ - presupposed heat output in time T, $P_{T,T}^s$ - real measured (calculated) heat output in time T, $\Delta P_{T,T}$ - deviation between presupposed and real consumed heat output in time T, ΔQ - change of heat content in intake branch of feeder caused by quantitative correction, $\vartheta_{P,RT}^s$ - real temperature in intake branch of hot-water piping in time RT, $\vartheta_{Z,RT}^s$ - real temperature in return branch of hot-water piping in time RT, $\vartheta_{P,T}^s$ - real temperature in intake branch of feeder at consumers in time T, $\vartheta_{Z,T}^s$ - real temperature in return branch of feeder at consumers in time T, $\Delta\vartheta_T^s$ - real temperature difference at consumers in time T, $\Delta\vartheta_T^p$ - presupposed temperature difference on exchanger in heating plant in time T which is calculated from $P_{T,T}^p$ and which is manipulated variable of qualitative method of control, $\Delta\vartheta_T^{p,Q}$ - presupposed temperature difference on exchanger in heating plant in time T which includes correction of heat content in intake branch of feeder ΔQ. It is necessary to bring in this heat or possibly to decrease heat admission by it in dependence on sense (sign) of quantitative correction $\Delta M_{v,T}$.

The sequence of the qualitative part of the control method is as follows

- measurement of the mass flow of heat transfer medium (hot water) $M^s_{v,RT}$ and temperature in return branch of hot-water piping $\vartheta^s_{Z,RT}$ (step 1),
- determination of the transport delay (step 2),
- determination of the time after which the action (intervention) of the qualitative control method appears at consumers - time T (step3),
- determination of presupposed heat output $P^p_{T,T}$ in time T from DDHS (step 4),
- calculation of presupposed temperature difference on exchanger in heating plant in time T, i.e. $\Delta\vartheta^{p,Q}_T$ including also correction of heat content in the intake branch of the feeder $\Delta Q/T_{VZ}$ (step 5),
- change of control signal to manipulated variable i.e. to the position of control valve of intake steam at intake to exchanger in heating plant (step 6).

The sequence of the quantitative part of the control method is as follows

- measurement of the real (actual) values of the parameters necessary for further calculations $\vartheta^s_{P,T}$, $\vartheta^s_{Z,T}$, $M^s_{v,T} \equiv M^s_{v,RT}$ (step 1),
- calculation of the real consumed heat output at the place of consumers $P^s_{T,T}$ for determined temperature difference $\Delta\vartheta^s_T$ (step 2),
- calculation of deviation between presupposed and real (actual) heat output at consumers, i.e. $\Delta P_{T,T}$ and calculation of heat content in intake branch of feeder ΔQ (step 3),
- calculation of quantitative correction of heat output $\Delta M_{v,T}$ (step 4),
- change of control signal to manipulated variable u_2 i.e. to the value of speed of circulating pump (step 5).

A. Description of the Control Algorithm

Algorithm of qualitative-quantitative control method of heat output in hot-water systems is shown in the Fig. 3. After intervention in the change of supplied heat output by applying the quantitative part of control (mass flow) it is necessary to establish the so called qualitative correction in order to maintain heat content in the intake branch of the hot-water piping system. In the control algorithm, this correction is marked $\Delta Q^{qualcorr}$ and is determined on the basis of a positive or negative deviation of expected heat output and real heat output. The consequence of this intervention is the aim that the quantitative part of control by varying the speed of the supply pump should return the resistance curve of the piping into its initial position.

Until the time $T(0)$, which is the time when the control of delivered heat output shows at the consumers´ places, the control of expected heat output is only carried out according to the forecast of the daily diagram of the heat supply. In a time lesser than $T(0)$, only the qualitative part of control is active, i.e. the quantitative part of control is not active. In a time greater than $T(0)$, they are active qualitative and quantitative part of control and correction $\Delta Q^{qualcorr}$.

As input values for the control algorithm, such variables may be considered that characterize the dimensions of the piping and properties of the heat transfer medium, i.e. cross-section of piping, length of piping, specific heat capacity and density of the heat transfer medium. Other inputs required are the daily diagram of heat supply, for determination of heat output and determination of real time (RT). Outputs of the control algorithm are two manipulated variables, i.e. first variable is temperature in the intake branch of the hot-water piping system and second variable is mass flow of hot water varies with a change of speed of the circulating pump. Additional details to this control algorithm are possible to find in [9].

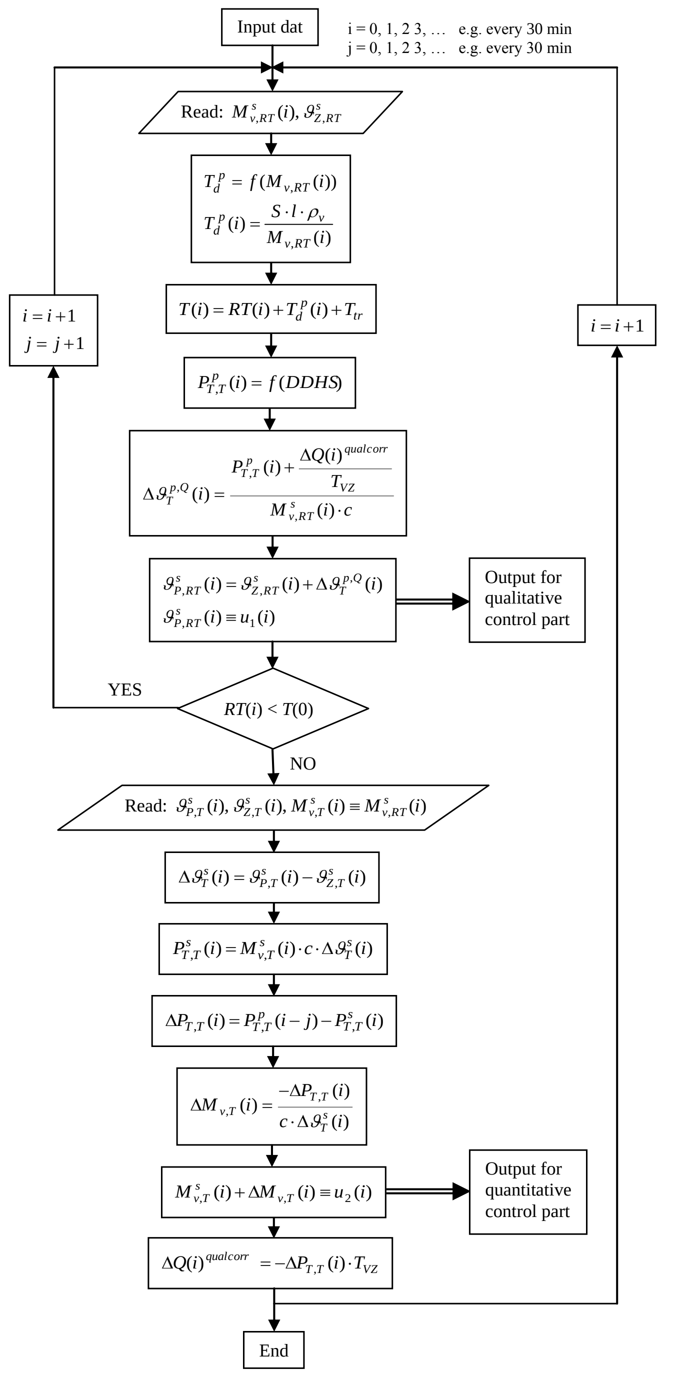

Fig. 3 algorithm of qualitative-quantitative control method of heat output in hot-water systems

Described control method is suitable in cases that the heat consumers are relatively locally concentrated. Between the heat source and the customer is usually a considerable distance and using only qualitative way of control can occur quite a large transport delay in heat supply. In such a case, when controlling the heat output delivered by the hot-water pipeline, transport delay in heat supply should be eliminated. For the control of heat output, it is necessary to use of the prediction of the course of daily diagram of heat supply (DDHS). It is possible to calculate DDHS in real time, but only for the time interval a slightly longer than current transport delay in heat supply is.

B. *Prediction of Daily Diagram of Heat Supply*

Prediction of daily diagram of heat supply (DDHS) and its use for control the district heating system was solved in many papers in the past. Most of used approaches are based on mass data processing. Methods based on these approaches have a big disadvantage that may result in out of date of real data. Therefore, it is suitable using other methods for prediction daily diagram of heat supply, e.g. statistic method of Box-Jenkins [10]. The Box-Jenkins method used fixed number of values which are continuously updated for given sampling period. It is based on the correlation analysis of time series. It works with stochastic models which enable to give a real picture of trend components and also that of periodic components. The Box-Jenkins method achieves very good results in practice.

Box-Jenkins method allows to model only stationary time series, it is therefore necessary to transform time series DDHS from a non-stationary series to stationary series. The course of time series of DDHS contains two periodic components, i.e. daily period (fluctuation during the day) and weekly period (heat consumption loss on Saturday and Sunday) (see Fig. 4).

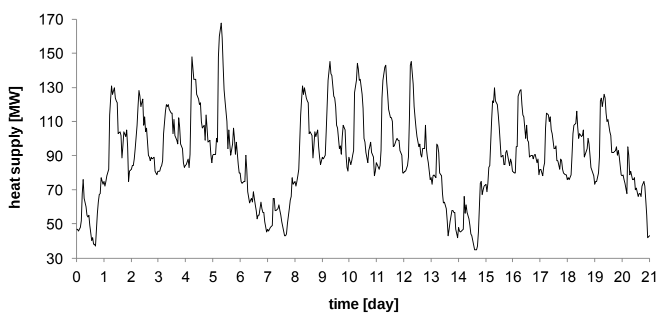

Fig. 4 course example of daily diagram of heat supply (DDHS)

General model according to Box-Jenkins (BJ) enables to describe only one periodic component. They can be proposed e.g. these two approaches to calculation of forecast of DDHS to describe both periodic components (daily period and weekly period) [11], i.e. the method using model with double filtration and the method of superposition of models. Mentioned two methods enable also to give a real picture of trend components. Trend of DDHS is attributed to fluctuation of outdoor temperature during the course of season. These methods do not describe sudden fluctuation of meteorological influences. It means that it needs to include these influences in calculation of prediction of DDHS. The greatest influence on DDHS, with respect to meteorological influences, has the outdoor temperature [12]. Other weather conditions, such as the direction and intensity of wind, sunshine and so on have less effect and are part of the stochastic component.

It is possible to say, that the forecast of energy time series has importance for control of technological process. The forecast is significant from the point of view of costs efficiency and also ecology of operation.

III. Conclusion

For large district heating networks, where is a big distance between the heat source and individual consumer systems, occur transport delay. Transport delay depends on the streaming speed of heat transfer medium and on length of the supply pipeline. The describe qualitative-quantitative control method of heat output should eliminate the influence of transport delay via the quantitative part of control. This control part is independent on transport delay unlike qualitative part of control.

The output of the described algorithm are two manipulated variables. For the qualitative part of control, it is a change of the temperature difference between the water temperatures in the intake and return branch of the hot-water piping, which is realized by changing the heat input in steam at the inlet to the heating plant exchanger. For the quantitative part of control, it is change of the mass flow of hot water realized by changing the speed of the circulation pump.

Advantage of the described approach to control of a heat output in district heating systems consists in simultaneous and continuous acting of two manipulated variables influencing the transferred heat output and in using the prediction of required heat output in a specific locality. By using the two manipulated variables, it is possible to control the heat supply to consumers more efficiently than when only one of them is used.

References

[1] B. Reetz and Ch. Halmdienst, “Witschaftliche Einsatzgrenzen kombinierter Kraft-Wärme-Kälte-Kopplungsanlagen”, in *Proc. 7th Dresden Fernwärme-Kolloquium*, Dresden, 2002.

[2] M. Princ, “Control algorithms in heat generation and distribution - software for simulation of circle heat networks operation,” Dissertation, Tomas Bata University in Zlin, 2006. (in Czech)

[3] S. Grosswindhager, A. Voigt and M. Kozek, “Predictive control of district heating network using fuzzy DMC,” in *Proc. of International Conference on Modelling, Identification and Control*, Wuhan, 2012, pp. 241-246.

[4] G. Sandou, S. Font, S. Tebbani, A. Hiret and C. Mondon, “*Predictive control of a complex district heating network*”, in *Proc. of IEEE Conference on Decision and Control*, Seville, 2005, pp. 7372-7377.

[5] P. Navratil, J. Klapka, J. Balate J. and P. Konecny, “Optimization of load of heat source described by nonlinear mathematical model,” in *Proc. of the 18th International Conference on Soft Computing MENDEL*, Brno, 2012, pp. 356-362.

[6] L. Vasek and V. Dolinay, ”Simulation and experiments on the secondary heat distribution network system,” *International Journal of Mathematics and Computers in Simulation*, vol. 6, no. 5, pp. 439-446, 2012.

[7] J. Balate, P. Jenik, B. Chramcov and P. Navratil, “The way of district heating output control by means of hydrothermal power systems – three modifications, “ in *Proc. of the IFAC Symposium on Powers Plants and Power Systems Control*, Kananaskis, 2006, pp. 395-400.

[8] J. Balate, P. Navratil and B. Chramcov, „Qualitative-quantitative control method of hot-water piping heat output for heat supply to district heating system; Basic method of control,” in *CD-ROM proc. Automation and control in theory and practice,”* Stara Lesna, 2008, pp. 2-1 - 2-10. (in Czech)

[9] J. Hurych, “Heat output control in hot-water piping systems of district heating - simulation of closed control loop,” Diploma work, Tomas Bata University in Zlin, 2006. (in Czech)

[10] G. E. P. Box, G. M. Jenkins, and G. C. Reinsel. *Time Series Analysis: Forecasting and Control*. 3rd ed. Englewood Cliffs, NJ: Prentice Hall, 1994.

[11] P. Dostal, “Elaboration of prediction of course of daily diagram of system load of district heating system,” Dissertation. VUT Brno, 1986. (in Czech)

[12] Arvastson, L. “Stochastic modeling and operational optimization in district – heating systems,” Dissertation, Mathematical Statistics, Lund University, 2001.

ISBN: 978-1-61804-321-4

On stability switching multiple delays seeking

Libor Pekař

Abstract**—**The searching of delays corresponding to leading eigenvalues that are crossing the imaginary axis represents one of tools for robust stability analysis of time-delay systems (TDS). Whenever the aim is to study the stability dependence on particular delay values, the so called delay dependent stability (DDS) task is introduced. This contribution brings the framework idea of a simple and relatively fast iterative gridding procedure for TDS with multiple delays which enables to find the leading roots via the rationalization of the characteristic quasipolynomial. Polynomial zeros are then easily computed by means of standard programs for technical computing (e.g. MATLAB®). Once the iterative procedure is finished, leading roots loci are enhanced through a simple linear interpolation method. A concise simulation example demonstrates the performance and accuracy of the proposed methodology.

Keywords**—**Delay Dependent Stability, MATLAB®, Multiple Time Delay System, Regula Falsi.

I. Introduction

THE general engineering knowledge is that (exponential) stability of time-delay systems (TDS) may depend on particular delay values [1]. Hence, if there exists a finite interval of stabilizing delays, delay-dependent stability (DDS) emerges; contrariwise, a stable operating point regardless of delays gives rise to the problem of delay-independent stability (DIS), see e.g. [2]-[6]. Moreover, fixed or varying non-delay model (system) parameters can be taken into account. These tasks go beyond the habitual stability studies for fixed-parameter TDS models as presented e.g. in [1], [7], [8].

Two basic groups of DDS methods for computing the delay stability margins prevail in the literature. The first group is based on Ljaponov-Krasovskii or Ljapunov-Razumikhin approaches and linear matrix inequalities [9]-[10], which can be computationally heavy and give purely theoretical and conservative results. The second, usually engineeringly more suitable, family includes frequency-domain approaches based on various ideas, see e.g. [8], [11]-[15]. The crucial step of these procedures consists in the determination of all characteristic roots (within the infinite spectrum) located on the imaginary axis [16]. However, only a subset of corresponding crossing delays includes critical delays that switch the system from/to stability/instability. Let us call these delays as switching.

This contribution is aimed at the novel simple gridding algorithm for the searching of multiple switching delays, initially, by performing the polynomial approximation of the characteristic quasipolynomial. Unlike many other methods for elimination of exponential terms, our procedure is not exact for imaginary roots (as, e.g., provided by the Rekasius transform [11]) and it is achieved by applying the number of iteration steps instead of a single step. This enables to reach a sufficient initial characteristic roots estimation at the vicinity of the imaginary axis. Moreover, although the number of polynomial spectrum evaluations can be very high, modern programs for mathematical and technical computing (such us MATLAB®) provide fast and accurate results; thus, the overall computing time is very short. Once the initial root loci estimation is made while the imaginary axis is crossed, it is enhanced by the linear interpolation method, namely, by the well known Regula Falsi principle.

A framework algorithm is introduced in this paper first, while two particular iterative rationalization ideas are consequently suggested. The efficiency and accuracy of the algorithm for both the substrategies is demonstrated via a concluding simulation example. The QuasiPolynomial matrix Rootfinder (QPmR) algorithm [17], which was proved to be suitable for finding the quasipolynomial roots within a selected complex plane rectangular region, is used as a benchmark tool. Note that compared to our algorithm the QPmR is relatively slow.

II. Preliminaries

A. Retarded TDS Model and Its Spectrum

Consider the frequency (Laplace) domain TDS model in the form of the transfer function

$$G(s)=b(s,\boldsymbol{\tau})/a(s,\boldsymbol{\tau}) \tag{1}$$

in $s\in\mathbb{C}$ where $a(s,\boldsymbol{\tau})$, $b(s,\boldsymbol{\tau})$ are retarded quasipolynomials

$$q(s,\boldsymbol{\tau})=s^n+\sum_{i=0}^{n-1}\sum_{j=1}^{h_i}q_{ij}s^i\exp\left(-s\sum_{k=1}^{L}\lambda_{ij,k}\tau_k\right) \tag{2}$$

where $\boldsymbol{\tau}=[\tau_1,..\tau_L]\in\mathbb{R}_{0+}^L$ represents independent delays, $\lambda_{ij,k}\in\mathbb{N}_0$ and $q_{ij}\in\mathbb{R}$.

System poles of (1), s_i, satisfy $G^{-1}(s_i)=0$.

The work was performed with the financial support of the research project NPU I No. MSMT-7778/2014 by the Ministry of Education of the Czech Republic and also by the European Regional Development Fund under the project CEBIA-Tech No. CZ.1.05/2.1.00/03.0089.

Libor Pekař is with the Department of Automation and Control Engineering, Faculty of Applied Informatics, Tomas Bata University in Zlín, Nad Stráněmi 4511, 760 05 Zlín, Czech Republic (phone: +420 57 603 5261; e-mail: pekar@fai.utb.cz).

Assumption 1. The are no common roots of $a(s,\boldsymbol{\tau})$, $b(s,\boldsymbol{\tau})$, which agrees with no distributed delays of system (1).

Under Assumption 1, system poles are given by

$$s_i \to a(s_i,\boldsymbol{\tau}) = 0 \tag{3}$$

Due to exponential terms in (2), if exists the triplet $\{q_{ij}, \lambda_{ij,k}, \tau_k\} \neq 0$, the spectrum of (1) is infinite. Basic spectral properties useful for this paper are, for instance:

1) For fixed $\beta > -\infty$, the number of poles with $\mathrm{Re}\{s_i\} > \beta$ is finite.
2) Isolated poles behave continuously and smoothly with respect to $\boldsymbol{\tau}$ on $\mathbb{C}$ [7].

Definition 1. The spectral abscissa is the function

$$\alpha(\boldsymbol{\tau}) := \boldsymbol{\tau} \mapsto \max \mathrm{Re}(s_i : a(s_i,\boldsymbol{\tau}) = 0)$$

Except for a finite set of delay vectors, $\alpha(\boldsymbol{\tau})$ of (1) behaves smoothly, see details e.g. in [18].

B. Retarded TDS Exponential Stability

Theorem 1 [1], [7], [8]. Retarded system (1) is exponentially stable if $\alpha(\cdot) < 0$.

Definition 2. The *leading pole* (or a pair), $s_{i,L}$, and the corresponding *leading delay* (vector), $\boldsymbol{\tau}_L$, satisfy

$$\mathrm{Re}\, s_{i,L} = \alpha(\boldsymbol{\tau}_L)$$

The *switching pole* and the *switching delay,* $\overline{\boldsymbol{\tau}}$, are the leading pole and delay, respectively, for which $\alpha(\overline{\boldsymbol{\tau}}) = 0$.

Hence, (exponential) stability of TDS changes only when the leading roots cross the imaginary axis at switching frequencies $\boldsymbol{\Omega} := \{\omega \in \mathbb{R}_{0+} : a(\mathrm{j}\omega, \overline{\boldsymbol{\tau}}) = 0\}$ (under Assumption 1).

III. Framework Switching Delays Searching Algorithm

As mentioned above, the task of DDS consists in the determination of open and bounded sets $\boldsymbol{\tau}_i \in (\tau_{i,\min}, \tau_{i,\max})_k^L$ in which the system remains stable. We deal with that in terms of the searching of switching delays. The framework of the algorithm can be sketched as follows:

Algorithm 1.

1) For a given $a(s,\cdot)$ select a $L \times N$ grid, and initialize the counter of found switching delays $i = 1$.
2) Find the initial leading pole $\hat{s}_0$ exactly for $\boldsymbol{\tau} = \mathbf{0}$.
3) Perform *L* nested loops for each delay in discrete steps of the grid:
   a. Within the each loop calculate iteratively the polynomial approximation $\hat{a}(s,\boldsymbol{\tau})$ and its leading root $\hat{s}_1$ near $\hat{s}_0$. Update $\hat{s}_0 := \hat{s}_1$.
   b. If the imaginary axis is crossed, perform the successive linear (Regula Falsi) interpolation $\overline{\tau}_k$ for every single delay entry τ_k of $\boldsymbol{\tau}$, and increment the value of i. Hence, the estimation of the switching delay, $\overline{\boldsymbol{\tau}}_i$, and that of the corresponding switching frequency, $\omega_i \in \hat{\boldsymbol{\Omega}}$, is obtained.
4) Eventual sets are $\{\overline{\boldsymbol{\tau}}_i\}$, $\hat{\boldsymbol{\Omega}}$.

The core of the algorithm resides in the iterative evaluation of the approximate polynomial calculated in the neighborhood of the last known leading pole estimation. This iterative procedure suppose that there exists a descending sequence

$$\left\{a_{(k)}(\hat{s}_k,\boldsymbol{\tau})\right\}_{k=1}^{\infty},\ \hat{s}_k := \left\{s : \hat{a}(s,\boldsymbol{\tau}) = 0, |s - \hat{s}_{k-1}| \to \min\right\}, \tag{4}$$

see the properties of retarded TDS poles. The problem can emerge if $|\hat{s}_k - \hat{s}_{k-1}| > \delta$ for some $\delta > 0$ and any grid step length $\Delta\boldsymbol{\tau}$ due to the spectral abscissa discontinuity; however such a case is very rare.

The second principal idea of Algorithm 1 is the successive Regula Falsi pole loci enhancement that makes the estimation more accurate reducing the gridding error. Infinitely many switching delays might be then found by the linear linkage of elements of $\{\overline{\boldsymbol{\tau}}_i\}$.

Two possible methodologies for iterative polynomial rationalization of the characteristic quasipolynomial follow.

IV. Iterative Polynomial Approximation Methods

A. Successive Taylor Series

Consider an approximating characteristic polynomial

$$\hat{a}(s,\boldsymbol{\tau} \mid \hat{s}_0) = \sum_{i=0}^{\hat{n}} \hat{a}_i(\boldsymbol{\tau}) s^i \tag{5}$$

that arises from the Taylor series expansion of $a(s,\boldsymbol{\tau})$ at $\hat{s}_0$. The proper value of $\hat{n}$ is questionable, yet a suitable choice might be $\hat{n} = n + L$ as for the Rekaius transform [11]. Once $\hat{a}(s,\boldsymbol{\tau} \mid \hat{s}_0)$ is calculated, its leading root is found and set as $\hat{s}_0$. By repeating this procedure, sequence (4) is obtained. Note that it can be proofed that

$$\delta := |s_i - \hat{s}_k| \le c \left|a(\hat{s}_k,\boldsymbol{\tau})\right|^{1/(\hat{n}+1)}, c \in \mathbb{R}_+ \setminus \infty$$

where stands for the zero of $a(s,\boldsymbol{\tau})$ for the particular fixed $\boldsymbol{\tau}$.

B. Tustin Approximation Based Linear Discretization

This second idea stems from the discretization of the characteristic quasipolynomial by means of the Tustin approximation which is closely related to delta models [19] and was proved to be suitable for delayed controller discretization [20]. More precisely, only derivatives s are subjected to the transformation

$$s \to \frac{2}{T}\frac{1-q}{1+q} \tag{6}$$

where T is the sampling period, q expresses the shifting operator that agrees with z^{-1} in the z-transform, whereas exponentials are processed by the natural shifting

$$\exp(-\eta s)X(s) \to x(t-\eta) \to q^{\eta} x(k) \tag{7}$$

Since the transformation (7) does not lead to integer z-powers in general, the following simple linear interpolation is eventually used

$$\begin{aligned} &x(t-\eta_i) \approx (1-\alpha_i)x(t-\tau_{d,i}) + \alpha_i x(t-\tau_{d+1,i}) \\ &\to \left((1-\alpha_i)q^{d_i} + \alpha_i q^{d_i+1}\right)x(k) \end{aligned} \tag{8}$$

where $\tau_{d,i} \le \eta_i \le \tau_{d+1,i}$, $\tau_{d,i} = d_i T$, $\tau_{d+1,i} = (d_i+1)T$, $d_i = \lfloor \eta_i / T \rfloor \in \mathbb{N}$, $\alpha_i = (\eta_i - \tau_{d,i})/T \in [0,1]$.

The suitable value of T is not unambiguous. With respect to delta models and derivatives discretization, the value of T in (6) should be sufficiently small which works well for delayed controller, as referred above. Contrariwise, the lower T is, the higher polynomial degree is obtained. Note that for the z-transform, the following recommendations are given

$$\begin{aligned} T &= [T_{95}/15, T_{95}/6] \approx [T_{63}/5, T_{63}/2] \\ T &= [1/(5\omega_0), 1/(2\omega_0)] \end{aligned} \tag{9}$$

for aperiodic and periodic systems [21], respectively, where T_x means the time period for which the step response reaches x % of the steady value, and ω_0 stands for the frequency of undumped oscillations. Simple algebra on (9) together with the basic knowledge of the correspondence between yields

$$T = \left[0.2|s_0|^{-1}, 0.5|s_0|^{-1}\right] \tag{10}$$

where s_0 is the leading pole. The setting (10) is performed in every single iteration in step 3a of Algorithm 1 for updating the value of T used in (6) and (8) to obtain the discrete characteristic polynomial approximation $\hat{a}(z, \boldsymbol{\tau} \,|\, T)$.

V. Illustrative Example

E.g. in [22], the following transfer function model of a skater on the swaying bow was introduced

$$G(s) = \frac{Y(s)}{U(s)} = \frac{0.2\exp(-(\tau_1+\tau_2)s)}{s^2(s^2 - \exp(-\tau_2 s))} \tag{11}$$

where $u(t)$ is the input power and $y(t)$ stands for the output angle deviation. Delays τ_1, τ_2 mean the skater's and servo latencies, respectively, with nominal values $\tau_1 = 0.3, \tau_2 = 0.1$.

Algebraic control design for the plant model (11) with a spectral optimization was solved in [23] where the following finite-dimensional linear controller was used

$$C(s) = \frac{\sum_{i=0}^{3} q_i s^i}{s^3 + \sum_{i=0}^{2} p_i s^i} \tag{12}$$

The Quasi-Continuous Shifting Algorithm [24] implemented within the spectral optimization can yield the suboptimal stabilizing solution as

$$\begin{aligned} &p_0 = 2009.2547, p_1 = 145.0583, p_2 = 95.7674, \\ &q_0 = 941.7633, q_1 = 4534.4451, q_2 = 19608.7605, \\ &q_3 = 15325.0618 \end{aligned} \tag{13}$$

One can easily obtain the characteristic quasipolynomial

$$\begin{aligned} a(s,[\tau_1,\tau_2]) = s^2(s^2 - \exp(-\tau_2 s))\left(s^3 + \textstyle\sum_{i=0}^{2} p_i s^i\right) \\ + 0.2\exp(-(\tau_1+\tau_2)s)\left(\textstyle\sum_{i=0}^{3} q_i s^i\right) \end{aligned} \tag{14}$$

By substituting parameters (13) into (14), the polynomial $a(s,[0,0])$ has the spectral abscissa $\alpha([0,0]) = 0.1323$, which indicates exponential instability and also that the control system is not DIS. A very rough use of the QPmR [17] for random delays helps to determine one of regions in which crossing delays may occur, $R := \tau_1 \times \tau_2 \in [0.05, 0.1] \times [0.05, 0.1]$.

Now let us perform Algorithm 1 with both the iterative rationalization methodologies for the grid with $\Delta\tau_{\cdot,j} = 0.01$, $j = 0,1,\ldots 5$. Set $\hat{n} = 9$ for Taylor series and choose $T = 1/3|s_0|^{-1}$ for the discretization in accordance to (10). The eventual estimations of crossing delays $\{\bar{\boldsymbol{\tau}}_i\}$ are displayed in Fig. 1 where its accuracy is graphically compared to QPmR results of the gridding $\Delta\tau_{\cdot,j} = 0.001$.

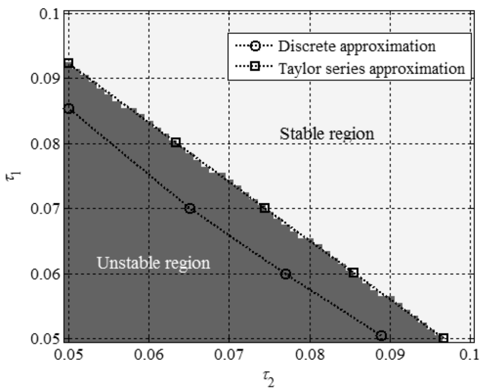

Fig. 1 results of Algorithm 1 vs. QPmR

As clear from the figure, the continuous approximation by means of the Taylor series works well and gives sufficiently accurate results. The iteration procedure concisely described in subsection IV-A converges in two steps (even for $\hat{n} \geq 2$). In the contrary, the discretization with the Tustin approximation provides not so good results; however $\hat{a}(z, \boldsymbol{\tau} \mid T)$ of the ninth order converges in four iteration cycles and the computing is approximately three times faster (in MATLAB®). This yields the necessity of the improvement of the latter methodology, for instance, via the sampling time optimization or a more advanced linearization (rather than (8)).

The significant of the Regula Falsi can be demonstrated on the calculation of the leading pole estimation, $\hat{s}_0$, e.g. in the grid nodes $\boldsymbol{\tau}_1 = [0.07, 0.06]$, $\boldsymbol{\tau}_2 = [0.07, 0.07]$, $\boldsymbol{\tau}_3 = [0.07, 0.08]$. For the continuous rationalization, we have $\hat{s}_0 = 0.00798545 \pm 3.86891283\mathrm{i}$ in $\boldsymbol{\tau}_2$, and $\hat{s}_0 = -0.00997711 \pm 3.83194106\mathrm{i}$ in $\boldsymbol{\tau}_3$, while the Regula Falsi results in $\hat{s}_0 = -0.00000556 + 3.85220963\mathrm{i}$, which interpolates the zero quite well. Regarding the discrete rationalization, one can obtain $\hat{s}_0 = 0.00708863 \pm 3.88152056\mathrm{i}$ in $\boldsymbol{\tau}_1$, and $\hat{s}_0 = -0.00677576 \pm 3.84474175\mathrm{i}$ in $\boldsymbol{\tau}_2$. The zero real part is then interpolated as $\hat{s}_0 = 0.00000006 \pm 3.86284996\mathrm{i}$.

VI. Conclusion

The main contribution of this paper has resided in the presentation of a relatively simple algorithm for the determination of crossing leading delays and corresponding crossing frequencies of time delay systems. The primary application of the result is that the found delays switch the system to exponential stability/instability, which is closely related to the notion of delay dependent stability. The leading idea stems from the gridding iterative rationalization of the characteristic quasipolynomial, the roots of which are computed simply by standard software tools. Two possible rationalization procedures have been presented, namely, the one based on Taylor series expansion in the vicinity of the current leading root estimation and the procedure that discretizes the characteristic quasipolynomial by using the Tustin approximation. The accuracy has then been enhanced by the use of the Regula-Falsi interpolation.

Note that the decision about stability or the seeking of stable/unstable regions can be performed with respect to varying delays as well as (controller) tunable parameters.

A simulation example presented in the second part of the paper has indicated a very good agreement of the algorithm results with those obtained from the quasipolynomial matrix rootfinder algorithm – if the Taylor series based approximation has been used. There are still gaps and imperfections that can be improved and several ways how to extend the algorithm, especially when using the iterative discretization procedure.

References

[1] M. Michiels and S.-I. Niculescu, *Stability and Stabilization of Time-Delay Systems*, Advances in Design and Control, vol. 12. Philadelphia: SIAM, 2007.

[2] J. Chen, D. Xu, and S. Bahram, "On sufficient conditions for stability independent of delay," *IEEE Trans. Autom. Control*, vol. 40, no. 9, pp. 1675-1680, 1996.

[3] F. Gouaisbaut and D. Peaucelle, "Delay-dependent robust stability of time delay systems," *IFAC Proc. Volumes (IFAC-PapersOnline)*, *Robust Control Design*, vol. 5, pp. 453-548, 2006.

[4] I. I. Delice and R. Sipahi, "Delay-independent stability test for systems with multiple-delays," *IEEE Trans. Autom. Control*, vol. 57, no. 4, pp. 963-972, 2012.

[5] A. F. Ergenc and B. Alikoc, "An experimental study for delay-independent state-feedback controller design," in *Preprints 19th IFAC World Congress*, Cape Town, South Africa, 2014, pp. 6074-6079.

[6] S. Sönmez, S. Ayasun, and U. Eminoglu, "Computation of time delay margins for stability of a single-area load frequency control system with communication delays*," WSEAS Trans. Power Systems*, vol. 9, pp. 67-76, 2014.

[7] J. K. Hale and S. M. Verduyn Lunel, *Introduction to Functional Differential Equations*, Applied Mathematical Sciences, vol. 99. New York: Springer, 1993.

[8] K. Gu, V. L. Kharitonov, and J. Chen, *Stability of Time-Delay Systems*. Boston: Birkhäuser, 2003.

[9] M. Wu, Y. He, J. H. She, and G. P. Liu, "Delay dependent criterion for robust stability of time varying delay systems," *Automatica*, vol. 40, no. 8, pp. 1435–1439, 2004.

[10] S. Y. Xu, J. Lam, "On equivalence and efficiency of certain stability criteria for time delay systems," *IEEE Trans. Autom. Control,* vol. 52, no. 1, pp. 95–101, 2007.

[11] Z. V. Rekasius, "A stability test for systems with delays," in *Proc. Joint Autom. Control Conf.*, San Francisco, CA, 1980, Paper No. TP9-A.

[12] K. E. Walton and J. E. Marshall, "Direct method for TDS stability analysis," *IEE Proceeding Part D*, vol. 134, no. 2, pp.101–107, 1987.

[13] J. Louisell, "A matrix method for determining the imaginary axis eigenvalues of a delay system," *IEEE Trans. Autom. Control*, vol. 46, no. 12, pp. 2008-2012, 1995.

[14] N. Olgac and R. Sipahi, "A practical method for analyzing the stability of neutral type LTI-time delayed systems," *Automatica,* vol. 40, no. 5, pp. 847-853, 2004.

[15] P. Fu, S. I. Niculescu, and J. Chen, "Stability of linear neutral time-delay systems: exact conditions via matrix pencil solutions," *IEEE Trans. Autom. Control*, vol. 51, no. 6, pp. 1063-1069, 2006.

[16] R. Sipahi and N. Olgac, "A comparative survey in determining the imaginary characteristic roots of LTI time delayed systems," *in Proc. 16th IFAC World Congress*, Prague, 2005, pp. 118-122.

[17] T. Vyhlídal and P. Zítek, "QPmR - Quasi-Polynomial Root-finder: Algorithm update and examples," in *Delay Systems: From Theory to Numerics and Applications*. T. Vyhlídal, J.-F. Lafay, and R. Sipahi, Eds. New York: Springer, 2014, pp. 299-312.

[18] T. Vanbiervliet, K. Verheyden, W. Michiels, and S. Vandewalle, "A nonsmooth optimization approach for the stabilization of time-delay systems," *ESIAM: Control, Optim., Calculus Variations*, vol. 14, no. 3, pp. 478-493, 2008.

[19] R. H. Middleton and G. C. Goodwin, *Digital Control and Estimation: A Unified Approach*. Detroit: Prentice Hall, 1990.

[20] L. Pekař and R. Prokop, "Zero-pole and Padé finite-dimensional reduction of delayed controllers: A comparative study," *Int. J. Math. Models Methods in Appl. Sci*, vol. 7, no. 7, pp. 728-735, 2013.

[21] J. Balátě, *Automatic Control* (in Czech), 2nd ed. Prague: BEN Publishing, 2004.

[22] P. Zítek, V. Kučera, and T. Vyhlídal, "Meromorphic observer-based pole assignment in time delay systems," *Kybernetika*, vol. 44, no. 5, 633-648, 2008.

[23] L. Pekař, "On the optimal pole assignment for time-delay systems," *Int. J. Math. Models Methods in Appl. Sci*, vol. 7, no. 1, pp. 63-74, 2013.

[24] W. Michiels, K. Engelborghs, P. Vansevevant, and D. Roose, "Continuous pole placement for delay equations," *Automatica*, vol. 38, no.5, pp. 747-761, 2002.

Complex wastewater treatment using membrane separation

Pavel Kocurek, Marek Šír, Zuzana Honzajková, and Karel Kolomazník

***Abstract*—**This paper deals with the application of membrane separation processes for wastewater treatment, especially for landfill leachate treatment. With its high efficiency and low costs, membrane separation seems to be a good choice of other possible progressive techniques. The landfill leachate chosen for this work contained a tremendous number of contaminants. The concentration of dissolved solids was around 10 $g.L^{-1}$ and the conductivity was 11.3 $mS.cm^{-1}$. Reverse osmosis was chosen as the most convenient separation technique for this kind of wastewater. Two-stage reverse osmosis showed the best results; nevertheless, one-stage treatment could also be sufficient. A pre-treatment step is necessary in both cases because it determines the separation level, especially the content of ammoniacal nitrogen in permeate. The total efficiency of contaminant removal exceeded 99 % for each contaminant (2 stages). The final amount of the produced concentrate was 20 % of the feed volume. The conductivity of final permeate was reduced under the conductivity level of potable water.

***Keywords*—**landfill leachate, membrane separation, pollutants removal, reverse osmosis, wastewater treatment.

I. Introduction

WASTE management is complex problematic which is bonded with almost every human activity. Landfilling belongs in the Czech Republic to the most used techniques for waste removal. Landfill leachate forms when rainwater and groundwater infiltrate the body of the landfill. The volume of the leachate depends to a large degree on the climate. The composition is very various and is depending on the total rainfall, on the kind of deposited waste and the chemical reactions taking place in landfill and on the age of landfill. Landfill leachate usually contains large quantities of dissolved solids. Over-balance volume of landfill leachate must be treated. A conventional wastewater treatment plant is designed to remove only substances of organic character, heavy metals and various forms of nitrogen. It cannot handle dissolved inorganic salts; in certain cases it even produces an increase in their concentrations [1].

Pressure driven membrane separation processes found use in many industries [2]-[6]. Reverse osmosis was used for the purification of landfill leachate. It is included to BAT (Best Available Techniques) for landfill leachate treatment [7]. Landfill leachate is probably the most complicated wastewater membrane can meet with. In this process the treated solution is separated with the help of a semipermeable membrane into two streams - the permeate and the concentrate. Permeate is formed by solvent and particles which passed through the membrane, while the concentrate contains all the chemicals that did not pass through the membrane. At higher pressures than the osmotic pressure of the treated solution, the osmotic flow of the solvent is reversed. Reverse osmosis operates at high pressure gradients at range 10-100 bar (1 MPa = 10 bar). The higher is the concentration of salts in the feed liquid, the higher is the osmotic pressure and a higher operating pressure must be applied to overcome it. Separation in the case of reverse osmosis proceeds on the ionic level, so this technique can be applied for removal of dissolved solids, heavy metals [8], pigments, total organic carbon etc. Average energy demand for 1 m^3 of permeate by achieved conversion into permeate 80 % is less than 5 kWh [9]. Using ultrafiltration as pre-treatment it is possible to extend cleaning interval of membrane modules and to increase permeate flux and total efficiency of membrane separation [10]. Successful installation of those devices is reported in many countries [11]-[13].

Focus of this work is the application of reverse osmosis for landfill leachate treatment in laboratory scale and optimization of operating conditions to achieve good quality permeate and to minimize the volume of concentrate.

II. Materials and Methods

A. Landfill Leachate

Landfill leachate was sampled in reclaimed part of landfill for municipal waste disposal. It could be characterized as a weakly alkaline brownish liquid with mild smell (pH=8.1). It

The work was supported by the project No. CZ.1.07/2.3.00/30.0035., and the project MSM6046137308. The work was performed with financial support of research project NPU I No. MSMT-7778/2014 by the Ministry of Education of the Czech Republic and also by the European Regional Development Fund under the Project CEBIA-Tech No. CZ.1.05/2.1.00/03.0089.

P. Kocurek is with the Tomas Bata University in Zlín, Faculty of Applied Informatics, Department of Automation and Control Engineering, Nad Stráněmi 4511, 76005, Zlín, Czech Republic (phone: +420576035318; e-mail: kocurek@fai.utb.cz).

M. Šír is with the University of Chemistry and Technology, Prague, Department of Environmental Protection, Technická 5, 16628, Praha 6, (e-mail: marek.sir@vscht.cz).

Z. Honzajková is with the University of Chemistry and Technology, Prague, Department of Environmental Protection, Technická 5, 16628, Praha 6, (e-mail: zuzana.honzajkova@vscht.cz).

K. Kolomazník is with the Tomas Bata University in Zlín, Faculty of Applied Informatics, Department of Automation and Control Engineering, Nad Stráněmi 4511, 76005, Zlín, Czech Republic (e-mail: kolomaznik@fai.utb.cz).

ISBN: 978-1-61804-321-4

contains high concentrations of pollutants especially with inorganic character (10 $g.L^{-1}$). Composition of landfill leachate is described in detail in Table I.

B. Analytical Determinations

Feeds and all streams were analysed using following methods. Metals concentration were measured on AAS SensAA (GBC Scientific Equipment, Australia), anions concentration were measured on capillary electrophoresis Capel 105M (Lumex, Russia), TIC and TOC on analyser Liqui TOCII (Elementar Analysensysteme GmbH, Germany), ammoniacal nitrogen using indophenol method using UV-VIS spectrophotometer Cintra 101 (GBC Scientific Equipment, Australia), conductivity on conductivity-meter GMH3430 and pH values on pH-meter GMH3530 (both Greisinger Electronic, Germany).

C. Membrane Separation Device

Separation experiments were performed on membrane separation unit LAB-M20 (Alfa Laval, Sweden). This device allows the membrane separation in laboratory scale. The device was customized for batch processing. The volume of the feed tank was ca. 12 L. The actual separation takes place on a plate-and-frame module DSS equipped with membranes for reverse osmosis RO98pHt (Alfa Laval, Sweden). Maximal number of membranes is 36 with total membrane area 0.63 m^2. A Rannie piston pump with maximum operating pressure of 60 bar was used. A separate water supply was used to maintain the pistons of the pump moist. A flow liquid-liquid heat exchanger cooled the membrane module. Water from the faucet served as the cooling agent.

The device was cleaned after every experiment using alkali and acid to allow the comparison of experiments. Permeate flux at 20 bar and 20°C using potable water as feed determines purity level of membranes.

D. Membrane Separation

Separation experiments were focused on the minimization of the feed volume to gain good quality permeate. Operating conditions were set up to achieve the stability of separation process and to minimize the negative influences (precipitation of salts, damage of membranes etc.) achieving high separation level. From these purposes pre-treatment was included and it was applied two-stage separation process too.

All experiment were carried up at operating temperature 20°C because permeate flux increases with growing temperature. Among other factors that affect reverse osmosis belong rejection R, volume reduction factor and permeate flux. Rejection indicates the separation efficiency of component or total. For calculation serve concentration values in feed c_F and in permeate c_P or conductivity values κ can be used.

$$R = \frac{c_F - c_P}{c_F} \cong \frac{\kappa_F - \kappa_P}{\kappa_F} \quad (1)$$

Volume reduction factor is defined like ratio between feed volume and concentrate volume. Permeate flux is hourly flux of permeate through the membrane with area 1 m^2. Its values are different for setting up of operating conditions of separation process and its decrease can indicate membrane fouling.

III. Results and Discussion

A. Single Stage Membrane Separation Experiments

Landfill leachate was filtered through a fabric filter to remove suspended solids. In first experiment (RUN1) it was applied operating pressure 30 bar on non adjusted landfill leachate. The first experiment served to determine whether the maximum recovery rate of the feed could be achieved at the given operating conditions. Experiment was stopped at achieved volume reduction factor equals 5 because precipitation of some salts occurred. Fig. 1 and Fig. 2 describe rejection values of dissolved components and actual volume reduction factor values during the experiment. According to the results of analyses concentration of ammoniacal nitrogen in permeate was still high.

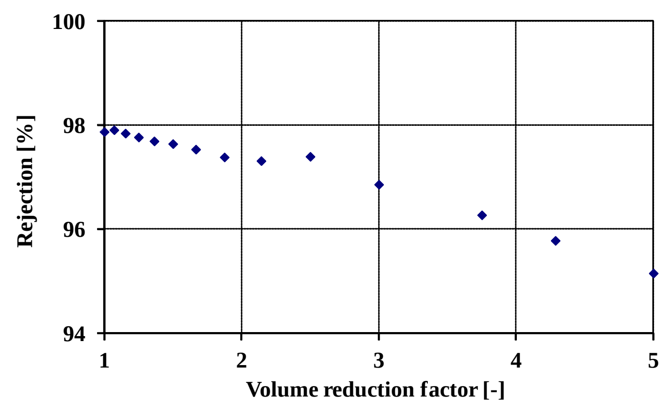

Fig. 1 RUN1 - dependence of rejection on volume reduction factor

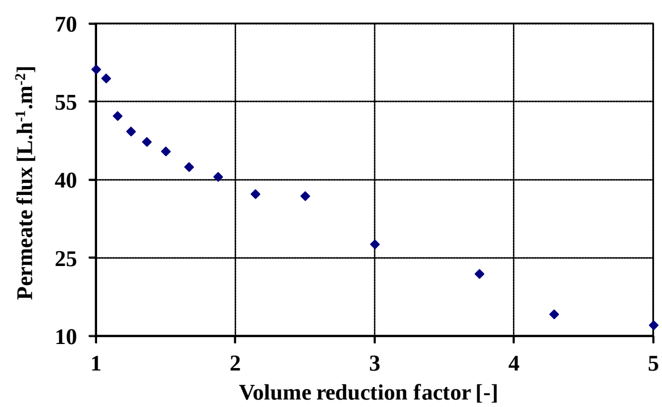

Fig. 2 RUN1 - dependence of permeate flux on volume reduction factor

Adding HCl into filtered landfill leachate pH value decreases and ammoniacal nitrogen separation level grows. Acid decomposes part of TIC and some components will not precipitate in device. From this purpose pH of feed was adjusted to 6.5 in the second separation experiment RUN2. Operating conditions stayed the same and final value of volume reduction factor equals 5 was chosen. There occurred no precipitation of salts and separation of ammoniacal nitrogen grew up. Fig. 3 and Fig. 4 describe second separation experiment RUN2.

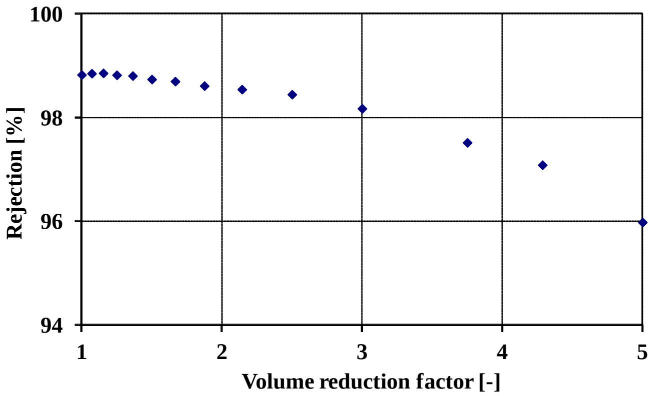

Fig. 3 RUN2 - dependence of rejection on volume reduction factor

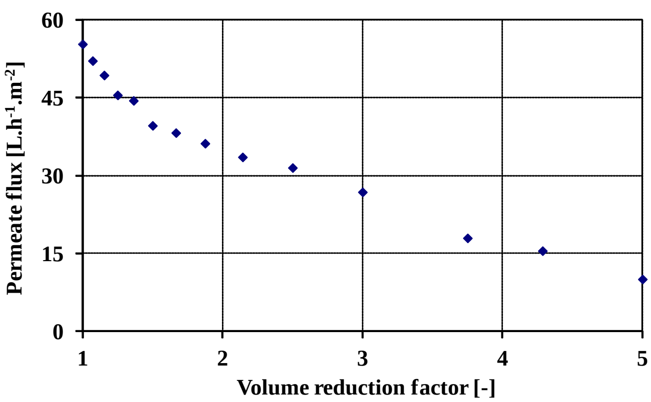

Fig. 4 RUN2 - dependence of permeate flux on volume reduction factor

As shown from previous figures it was achieved high rejection values in both single stage separation experiments. According to the decrease of permeate flux yield of permeate 80 % is ceiling at set up operating conditions. Conductivities of permeates are comparable to the values in potable water. However ammoniacal nitrogen is in most cases key parameter and in some cases simple stage treatment with pH adjustment will not be sufficient.

B. Two-stage Membrane Separation Experiment

Last experiment (RUN3) was employed as the second reverse osmosis stage, which was used to further purify the permeate that was produced in the second experiment (RUN2). There was performed no pre-treatment and operating pressure was decreased to 15 bar. Effort was made to achieve the highest recovery rate possible. From the reason of the small volume of circulating liquid in the device experiment was stopped at achieved volume reduction factor equals 10 which means yield of permeate 90 %. In Fig. 5 and Fig. 6 can we see high values of rejection and permeate flux. I could be possible to continue in this separation experiment. Conductivity of permeate is under conductivity level of potable water and composition reminds "worse distilled water". According to low pH of permeate TIC concentration is formed by CO_2xH_2O according to carbonaceous equilibrium and this form was separated by membrane by worse efficiency.

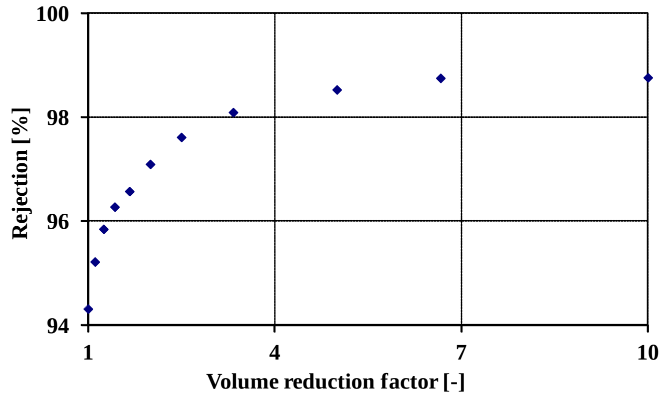

Fig. 5 RUN3 - dependence of rejection on volume reduction factor

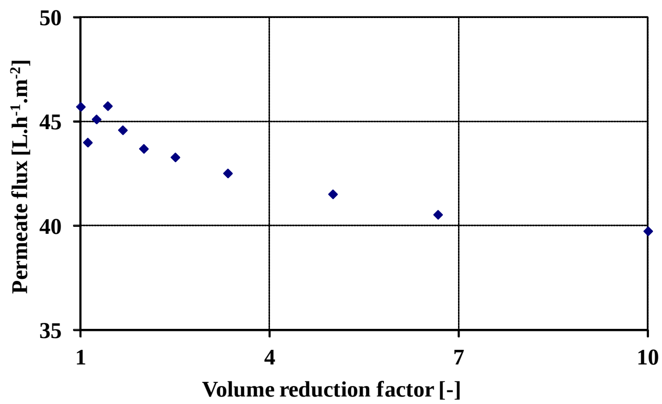

Fig. 6 RUN3 - dependence of permeate flux on volume reduction factor

Decisive criterion for number of treating stages is the quality of desired permeate which depends on its handling (using like technological water in landfill area, release into environment etc.)

The rest concentrate from firs stage must be removed the other way for example using evaporation with stabilization/solidification technology or high-pressure reverse osmosis for following decrease of its volume or other physico-chemical technology its removal. It could be possible to add the concentrate from second stage to feed into first stage.

Table I describes composition of feeds and output streams in detail in all experiments for comparison of efficiency of separation.

These data are indispensable for design of pilot plant experiment and are first step for installation of full-scale operating device in the landfill.

Table I the composition of all streams in experiments RUN1 - RUN3

parameter	unit	RUN1			RUN2			RUN3		
		feed	permeate	concentrate	feed	permeate	concentrate	feed	permeate	concentrate
Mg	$mg.L^{-1}$	145	<0.5	780	145	<0.5	712	<0.5	<0.5	8.3
Ca	$mg.L^{-1}$	85	<0.5	492	85	<0.5	402	<0.5	<0.5	26
Na	$mg.L^{-1}$	1078	26	4866	1078	19.3	4226	19.3	0.8	161
K	$mg.L^{-1}$	756	18.4	3401	756	19.5	2803	19.5	0.9	164
Mn	$mg.L^{-1}$	0.37	<0.25	1.9	0.37	<0.25	1.5	<0.25	<0.25	<0.25
Cu	$mg.L^{-1}$	0.17	<0.1	0.83	0.17	<0.1	1.1	<0.1	<0.1	<0.1
Zn	$mg.L^{-1}$	<0.2	<0.2	0.51	<0.2	<0.2	0.63	<0.2	<0.2	<0.2
Fe	$mg.L^{-1}$	8.7	<0.5	34	8.7	<0.5	27	<0.5	<0.5	<0.5
Pb	$mg.L^{-1}$	<0.1	<0.1	<0.1	<0.1	<0.1	<0.1	<0.1	<0.1	<0.1
Cd	$mg.L^{-1}$	<0.2	<0.2	<0.2	<0.2	<0.2	<0.2	<0.2	<0.2	<0.2
As	$mg.L^{-1}$	<0.4	<0.4	<0.4	<0.4	<0.4	<0.4	<0.4	<0.4	<0.4
Cr	$mg.L^{-1}$	<1	<1	<1	<1	<1	<1	<1	<1	<1
Si	$mg.L^{-1}$	12.2	<1	57	12.2	<1	41	<1	<1	<1
Cl^-	$mg.L^{-1}$	1764	47	8320	2556	124	10700	124	4.2	1030
$N_{ammon.}$	$mg.L^{-1}$	590	57	2599	573	27	2072	27	1.4	236
NO_3^-	$mg.L^{-1}$	<5	<1	<20	<5	<1	<20	<1	<1	<5
SO_4^{2-}	$mg.L^{-1}$	<2	<2	<20	<2	<2	<20	<2	<2	<2
pH		8.1	6.9	7.8	6.5	5.3	6.1	5.3	4.4	4.8
conductivity	$mS.cm^{-1}$	11.3	0.62	42.3	13.0	0.43	51.0	0.43	0.02	3.2
TIC	$mg.L^{-1}$	990	51	4151	565	93	1432	93	39	315
TOC	$mg.L^{-1}$	240	<2	1132	233	<2	929	<2	<2	16.3

IV. Conclusion

Membrane separation is modern and effective technology for treatment of almost all wastewater types including landfill leachates. Presented work describes efficiency of reverse osmosis technology using real sample of wastewater. Two-stage reverse osmosis showed the best results but one-stage treatment could be sufficient. Pre-treatment is necessary in every case because separation level especially of ammoniacal nitrogen depends on it and it particular decreases the precipitation in device. The concentration of ammoniacal nitrogen will be probably one of more limiting criteria for permeate. The total efficiency of the removal of the contaminants was over 99 % for each contaminant (2 stages). Conductivity of landfill leachate was decreased significantly in one step by 96 %, in two steps by 99.8 %. The amount of landfill leachate was reduced by 80 %.

References

[1] T. Cath, A. Childress, and M. Elimelech, "Forward osmosis: Principles, applications, and recent developments", *Journal of Membrane Science*, vol. 281, no. 1-2, pp 70-87, Sept. 2006.

[2] B. Peñate, and L. García-Rodríguez, "Current trends and future prospects in the design of seawater reverse osmosis desalination technology", *Desalination*, vol. 284, pp. 1-8, Jan. 2012.

[3] S. J. Altman, R. P. Jensen, M. A. Cappelle, A. L. Sanchez, R. L. Everett, H. L. Anderson, and L. K. McGrath, "Membrane treatment of side-stream cooling tower water for reduction of water usage", *Desalination*, vol. 285, pp. 177-183, Jan. 2012.

[4] B. Van der Bruggen, E. Curcio, and E. Drioli, "Process intensification in the textile industry: The role of membrane technology", *Journal of Environmental Management*, vol. 73, no. 3, pp. 267-274, Nov. 2004.

[5] S. S. Madaeni, and. M. R. Eslamifard, "Recycle unit wastewater treatment in petrochemical complex using reverse osmosis process", *Journal of Hazardous Materials*, vol. 174, no. 1-3, pp. 404-409, Feb. 2010.

[6] M. Catarino, A. Mendes, L. Madeira, and A. Ferreira, "Beer dealcoholization by reverse osmosis", *Desalination*, vol. 200, no. 1-3, pp. 397-399, Nov. 2006.

[7] B. Van der Bruggen, C. Vandecasteele, T. Van Gestel, W. Doyen, and R. Leysen, "A review of pressure-driven membrane processes in wastewater treatment and drinking water production", *Environmental Progress*, vol. 22, no. 1, pp. 45-56, Apr. 2003.

[8] F. Fu, and Q. Wang, "Removal of heavy metal ions from wastewaters: A review", *Journal of Environmental Management*, vol. 92, no. 3, pp. 407-418, Mar. 2011.

[9] S. Renou, J. G. Givaudan, S. Poulain, F. Dirassouyan, and P. Moulin, "Landfill leachate treatment: Review and opportunity", *Journal of Hazardous Materials*, vol. 150, no. 3, pp. 468-493, Feb. 2008.

[10] I. Even-Ezra, M. Beliavski, S. Tarre, C. Dosoretz, and M. Green, "Chemical versus biological pretreatment for membrane filtration of domestic wastewater", *Desalination*, vol. 272, no. 1-3, pp. 85-89, May 2011.

[11] K. Linde, A. S. Jönsson, and R. Wimmerstedt, "Treatment of three types of landfill leachate with reverse osmosis", *Desalination*, vol. 101, no. 1, pp. 21-30, Mar. 1995.

[12] R. Rautenbach, T. Linn, and L. Eilers, "Treatment of severely contaminated waste water by a combination of RO, high-pressure RO and NF - Potential and limits of the process", *Journal of Membrane Science*, vol. 174, no. 2, pp. 231-241, Jul. 2000.

[13] J. Wiszniowski, D. Robert, J. Surmacz-Gorska, K. Miksch, and J. V. Weber, "Landfill leachate treatment methods: A review", *Environmental Chemistry Letters*, vol. 4, no. 1, pp. 51-61, Apr. 2006.

ISBN: 978-1-61804-321-4

Determination of hexavalent chromium in products of leather industry

Pavel Kocurek, Hana Vašková, Karel Kolomazník, and Michaela Bařinová

***Abstract*—**This paper deals with practical possibilities of hexavalent chromium determination in products of leather industry. Because not every laboratory is equipped with modern devices for this pollutant measurement, this work is focused on commonly available spectrophotometric method based on the reaction with 1,5-diphenylcarbazide. Special attention was focused on the variability of the basic spectroscopic method with practical demonstration of individual variants, some critical points and moments in laboratory conditions using real samples containing hexavalent chromium.

***Keywords*—**Leather waste, hexavalent chromium determination, spectrophotometric method, 1,5-diphenylcarbazide.

I. Introduction

HEXAVALENT chromium belongs to strictly monitored pollutants in the environment and in many industrial branches. The anthropogenic sources of chromium include wastewaters from metallurgy, metal coatings, leather and textile industries, etc. From several oxidation states in which chromium can exist, the trivalent and hexavalent states are the most important from the viewpoint of the environment and commercial applications. These forms differ strongly. Whereas trivalent chromium occurs naturally in the environment and belongs to essential elements important for human body with influence on blood sugar control, hexavalent chromium compounds are toxic, carcinogenic and mutagenic and more soluble and mobile.

One of traditional application areas of chromium compounds is the leather industry. Chromium sulphate is the most popular tanning agent worldwide. This way of tanning gives leather its unique features by means of crosslinking of collagen fibers with chromium bridges. However, leather industry also ranks among major producers of potentially hazardous wastes. The processing of 1000 kg of raw hide into leather results in creating of only 200 kg of final product (leather) with chromium content of 3 kg, 250 kg of non-tanned protein waste, 200 kg of tanned wastes with chromium content of 3 kg, and 50000 kg of waste water containing 5 kg of chromium. [1] It follows from the above mentioned that both products and wastes of the leather industry contain considerable amount of chromium. In the past decades strict environmental regulations have been ordered to limit disposal of tannery waste into soil and water bodies in the developed and developing parts of the world. Before that, this chromium containing waste was mostly landfilled or merely dumped and thus distributed into the environment. [2] There are many landfills containing this kind of waste worldwide that could be a threat for sources of drinking water and local fauna and flora because it is practically impossible to predict the processes in the landfill body or the state of protection barrier in the next 50 or 100 years.

There are reports in literature that from the thermodynamic point of view there exists a possibility of spontaneous oxidation of trivalent chromium into its hexavalent form [3]. In the process of leather manufacturing this could happen for example during the tanning, post-tanning and finishing operations in the presence of various oxidation agents (e.g. hydroperoxide forming, high thermal conditions, binders, high pH value ...). The occurrence of chromium species is pH-dependent. Cr(III) is very difficult to oxidize in acid solution owing to the normal reduction potential; in alkali conditions oxidation occurs to form stable chromate. [4] Oxidation could be caused by some oxidation reagents as atmospheric O_2, O_3, UV rays, H_2O_2, peroxocompounds, MnO_2 etc. The natural oxidation of Cr(III) is extremely low, most of Cr(VI) found in soil and groundwater comes from pollution. On the other hand Cr(VI) as chromate CrO_4^{2-} is a strong oxidizing agent and unstable in acid solutions in the presence of organic molecules with oxidizable groups and electron donors as HSO_3^-, Fe^{2+} etc. This fact is exploited by remediation of pollution by $FeSO_4$ or nanoFe^0. [5] Cr(VI) can be produced at low incineration temperatures (300-600°C) which confirms impracticality of the conventional disposal methods for leather waste. [6]

For the reasons described above and due to high toxicity of Cr(VI) compounds, analytical determination of hexavalent

The work was supported by the project No. CZ.1.07/2.3.00/30.0035. The work was performed with financial support of research project NPU I No. MSMT-7778/2014 by the Ministry of Education of the Czech Republic and also by the European Regional Development Fund under the Project CEBIA-Tech No. CZ.1.05/2.1.00/03.0089.

P. Kocurek is with the Tomas Bata University in Zlín, Faculty of Applied Informatics, Department of Automation and Control Engineering, Nad Stráněmi 4511, 76005, Zlín, Czech Republic (phone: +420576035318; e-mail: kocurek@fai.utb.cz).

H. Vašková is with the Tomas Bata University in Zlín, Faculty of Applied Informatics, Department of Automation and Control Engineering, Nad Stráněmi 4511, 76005, Zlín, Czech Republic (e-mail: vaskova@fai.utb.cz).

K. Kolomazník is with the Tomas Bata University in Zlín, Faculty of Applied Informatics, Department of Automation and Control Engineering, Nad Stráněmi 4511, 76005, Zlín, Czech Republic (e-mail: kolomaznik@fai.utb.cz).

M. Bařinová is with the Tomas Bata University in Zlín, Faculty of Applied Informatics, Department of Automation and Control Engineering, Nad Stráněmi 4511, 76005, Zlín, Czech Republic (e-mail: barinova@fai.utb.cz).

chromium is of great importance not only in relation to the leather industry.

Determination of hexavalent chromium can be performed by various laboratory procedures. Some methods were described long years ago and some use the most sophisticated instrumentation. The overview of used and published methods for various samples and areas of application is described in publication [7]. Very interesting method with a low limit of detection (in the range of $\mu g.L^{-1}$) is ion chromatography combined with post column derivatization with diphenylcarbazide and photometric detection used for example for drinking water control. [8], [9] The quickest method is probably Raman spectroscopy. [10] However many technical articles mention basic photometric detection with 1,5-diphenylcarbazide as the main method. This method is very popular due to good sensitivity and feasibility.

Determination of Cr(VI) in leather is carried out for example by international standard [11] using diphenylcarbazide method and in waste using numerous EPA methods. However, many articles mention only the utilization of "method with diphenylcarbazide at wavelength 540 nm", without any description of the steps between the sample preparation and the final chromium content. The diphenylcarbazide method could be performed with various modifications. The aim of this article is to provide an overview of these modifications together with some useful information on practical Cr(VI) determination based on the international standard and laboratory experience.

II. Spectrophotometric Methods

A. *Determination with 1,5-diphenylcarbazide*

Cr(VI) in solution oxidizes 1,5-diphenylcarbazide to 1,5-diphenylcarbazone in a mineral acid environment to give a red-violet complex with chromium. Absorbance of this complex is measured mostly at the wavelength of 540 nm (maximum of the complex) or close to this value (546, 550 or 555 nm). Phosphoric or sulfuric acids are used to create the acidic conditions. Maximal coloration is achieved after 1 min. and the stability is minimally 30 min. Absorbance is measured after 15±5 min.

The reagent is prepared by dissolving 1,5-diphenylcarbazide in ethanol (0.25 g + 4 g phthalic acid anhydride in 100 mL) or in acetone (0.5%, 1% solution). [12]

B. *Determination Using CdI_2 and Starch*

The reagent is prepared by dissolving 1.1 g of CdI_2 in 34 mL of water and the mixture is boiled to remove free I_2; 0.26 g of starch is dissolved in 46 mL of water under boiling and both solutions are mixed under gentle boiling, filtered using glass frit, cooled and filled to the mark in a 100 mL volumetric flask. The prepared reagent is protected from direct sunlight. A total of 2.2 mL of 0.815M H_2SO_4 is added to a 1 mL of solution containing 0.5-5 μg Cr(VI), then water is added till the total volume of the mixture is 9 mL, and finally 1 mL of the reagent. Absorbance of blue starch-iodine complex is measured after 20 min at a wavelength of 575 nm. [11] The method presented here covers the range 0.05 to 0.5 μg. of hexavalent chromium per mL in a final volume of 10 mL as described in publication [13].

C. *Other*

Of the others method it could be mentioned the spectrophotometric determination of Cr(VI) ions using new benzothiazolyl azo compound 2-[(6-methyl-2benzothiazolyl) azo]-4-chlorophenol. This method allows the determination of Cr(VI) in the range of 0.2-9.0 $mg.L^{-1}$. Details of procedure are described in publication [14].

These methods are only mentioned for the sake of completeness of spectrophotometric determination, but were not in the center of interest of this paper.

D. *Alkali Extraction of Cr(VI)*

The extraction of Cr(VI) from waste samples is carried up under alkali conditions in order to eliminate the to Cr(III). One procedure is described in the following chapter. Literature sources mention the extraction using hot solution of a mixture of 3% $NaCO_3$ and 2% NaOH. The amount of 100 g of solid waste is mixed in a beaker with 400 mL of the extraction solution and the mixture is heated under constant stirring closely under the boiling point. After cooling and filtration the pH of the solution is adjusted under stirring with concentrated nitric acid into a range of 7-8. The solution is then filled to the mark in a 1000 mL volumetric flask with deionized water and the content of Cr(VI) is measured. [15] In publication [16] is practical comparison of mentioned alkali extraction with acid extraction using 0.2M H_3PO_4 from soil and sediment samples and following determination of Cr(VI) using method with 1,5-diphenylcarbazide and AAS.

III. Materials and Methods

The determination of Cr(VI) was carried out using real samples of cattle hide shavings, tanned sheep leather trimmings and the hydrolysate from alkali enzymatic hydrolysis of leather shavings derived from boar skins.

The reagents, calibration solutions and phosphate buffer were prepared from the following commonly available laboratory chemicals: acetone, argon, glacial acetic acid, 1,5-diphenylcarbazide, H_2SO_4, H_3PO_4, $K_2Cr_2O_7$, $Na_2HPO_4x12H_2O$.

The spectrophotometric measurements were performed using Spekol 11 (Carl Zeiss, Germany) with extension for 1 cm and 5 cm cuvettes.

The reagent was prepared by dissolving 1 g of 1,5-diphenylcarbazide in 100 mL of acetone and acidified with one drop of glacial acetic acid.

Distilled water was boiled and cooled to degas (it is possible to use an ultrasonic bath at the end of the buffer preparation).

The phosphoric acid solution was prepared by diluting of 0.7 L of phosphoric acid (w=85 %) to a 1 L flask with distilled water.

The phosphate buffer was prepared as 0.1M solution of

$Na_2HPO_4x12H_2O$ with pH adjusted to 8 using said phosphoric acid solution and finally the buffer was degassed by argon.

The calibration standards were prepared by consecutive diluting of a 1000 $mg.L^{-1}$ Cr(VI) stock solution. Final dilution was performed with phosphate buffer. The volume of sample in a 50 mL volumetric flask was 40 mL; the rest of space was intended for acid, buffer and reagent (Fig. 1).

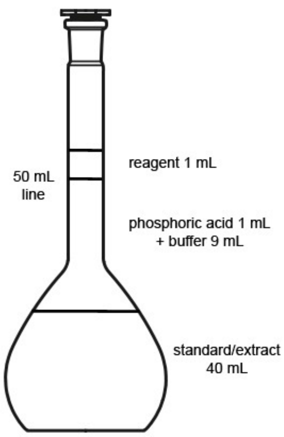

Fig. 1 composition of the volumetric flask before coloration

The Cr(VI) extraction from the samples was performed using laboratory horizontal shaker and closeable bottles. Almost no free space was left at the top of the bottle. The ratio between the solid sample and phosphate buffer was approximately 2-3 g for 100 mL of buffer. The shaking time was 3 hours. The pH value of the mixture should not change. After that the mixture was filtered using a paper filter for slow filtration and the obtained filtrate was filtered one more time through a syringe filter (0.22 and 0.45 µm).

A volume of 40 mL of the extract/calibration standard was transferred into a 50 mL volumetric flask, 1 mL of phosphoric acid was added and phosphate buffer was made up to a volume of 50 mL. After that, 1 mL of the reagent was added, unlike the common practice and the standard, above the 50 mL line and the mixture was well stirred. Using this way it is possible to add the reagent almost in one moment into all volumetric flasks. The absorbance was measured after 20 min. at the wavelength of 540 nm against a blank sample prepared from the phosphate buffer, phosphoric acid and the reagent using cuvettes with optical length of 5 cm.

The easiest procedure includes the following steps. To the solution containing Cr(VI) in a volume of 40 mL is added sulfuric acid for pH adjustment into a range of 1±0.3. In our case, 0.5 mL of concentrated sulfuric acid was added. This solution is transfered into a 50 mL volumetric flask and distilled water was added to the mark. After that, 1 mL of the reagent was added above the 50 mL line and the mixture was stirred well. The absorbance was measured after 20 min. at the wavelength of 540 nm against a blank sample prepared from distilled water, sulfuric acid and the reagent using cuvettes with optical length of 1 and 5 cm.

An InVia Basis Raman microscope (Renishaw) was used for the recording of the Raman spectra of collagen hydrolysate. A NIR diode laser with the excitation wavelength 785 nm and a maximum output power of 300 mW was used as the light source. A Leica DM 2500 confocal microscope with the resolution up to 2 µm was coupled to the Raman spectrometer. The measurements were collected at 20x magnification, with 1 second exposure time and 100 accumulations. The sample was scanned in the range from 500 to 1600 cm^{-1} with a 2 cm^{-1} spectral resolution. To avoid any interference, the Raman spectra were acquired in the absence of light. The baseline correction was applied.

IV. Results and Discussion

A. Basic Procedure with Sulfuric Acid

In this case, the easiest procedure was performed to find out the response of the device and the limit of quantification. The measurements of the solutions were carried out using cuvettes with optical length of 1 and 5 cm. Calibration solutions were prepared in the range of 0.01-3 $mg.L^{-1}$ Cr(VI). However, the response of the spectrophotometer especially for low concentrations was weak - on the second and third decimal place.

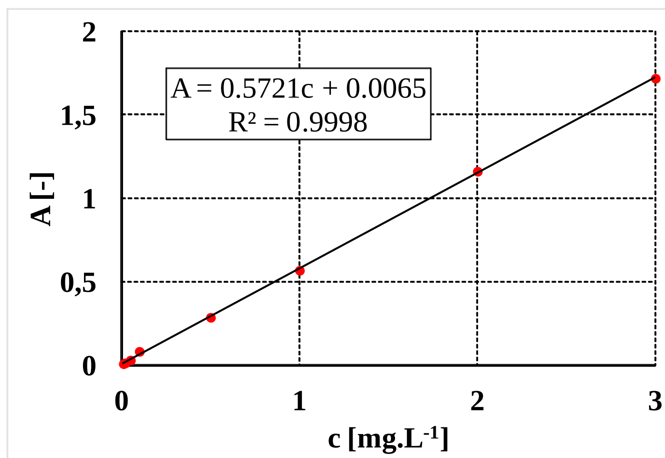

Fig. 2 basic procedure - calibration curve for 1 cm cuvette

The measurement was repeated using the cuvette with higher optical length of 5 cm to achieve better results for low concentrations. The difference is evident comparing Fig. 2 and Fig. 3. The Lambert-Beer law is valid – the slopes of the curves are in the same ratio as the cuvette lengths. The highest point of the curve was due to the high response at a concentration of 0.5 $mg.L^{-1}$. However the response for a concentration of 0.01 $mg.L^{-1}$ was weak again, so the authors recommend not to use this method for measuring Cr(VI) concentrations under 0.02 $mg.L^{-1}$.

ISBN: 978-1-61804-321-4

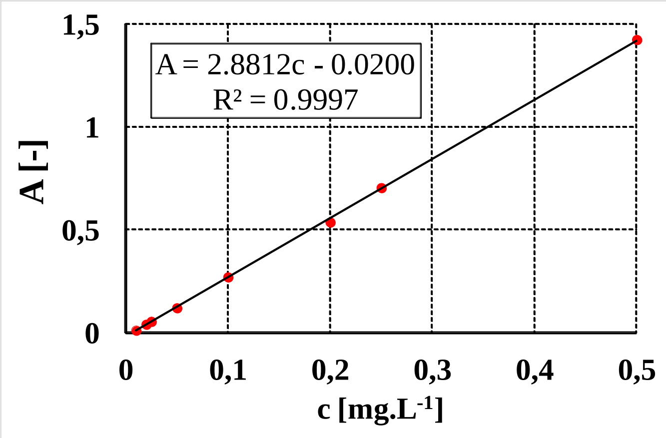

Fig. 3 basic procedure - calibration curve for 5 cm cuvette

B. Procedure Using Phosphate Buffer

The phosphate buffer was used for the extraction of real samples and for calibration solution preparation. The measurements were carried out with a cuvette with optical length of 5 cm. The resulting calibration curve is shown in Fig. 4. It is interesting that the response is twice as high compared to the basic procedure (Fig. 3). The selected picture represents one of many other measurements. According to high values of absorbance by last calibration points the range was narrowed to 0.01-0.25 $mg.L^{-1}$. The use of the lowest point is questionable and the aforementioned recommendation is valid.

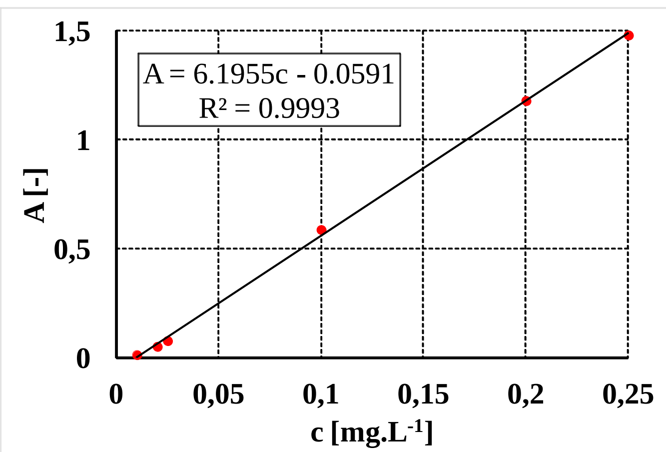

Fig. 4 procedure using phosphate buffer - calibration curve for 5 cm cuvette

Extracts from solid samples were in the case of second filtration a) non-filtered, b) filtered using a syringe filter of 0.45 µm or c) filtered using a syringe filter of 0.2 µm. During the first filtration, residual turbidity or some small particles can influence the measurement and the second filtration stage should be applied.

According to the results in the case of chromium shavings we can see small difference between the non-filtered and filtered extracts as shown in Table I, all extracts were clear. Hexavalent chromium occurred in small concentration.

But influence of the turbidity occurred by non-filtered extract from trimmings and caused difference between results (Table II). The turbidity was almost invisible by eye. The second stage of filtration was necessary and the Cr(VI) concentrations by filtered extracts are comparable. In this sample, hexavalent chromium was also detected.

A syringe filter or a comparable filtration using similar filter can remove the substances which could affect the measurement.

Table I results related to cattle hide shavings

parameter	unit	cattle hide shavings		
dry mass	%	71.8		
sample weight	g	3.10	2.99	3.20
Cr(VI) concentration	$mg.L^{-1}$	0.036	0.035	0.036
Cr(VI) content in dry mass	$mg.kg^{-1}$	**1.61**	**1.65**	**1.55**
2nd stage filtration		none	0.45 µm	0.2 µm

Table II results related to tanned sheep leather trimmings

parameter	unit	tanned sheep leather trimmings		
dry mass	%	89.6		
sample weight	g	3.11	3.10	3.13
Cr(VI) concentration	$mg.L^{-1}$	0.049	0.013	0.014
Cr(VI) content in dry mass	$mg.kg^{-1}$	**1.74**	**0.47**	**0.50**
2nd stage filtration		none	0.45 µm	0.2 µm

C. Raman Spectrometer Measurement

The content of Cr(VI) was measured in the hydrolysate obtained from alkali enzymatic hydrolysis of leather shavings derived from boar skins. Raman spectroscopy was used for qualitative measurements and the diphenylcarbazide-based method was used for quantitative measurement. As can be seen in Fig. 5, the Raman spectrum showed the presence of Cr(VI).

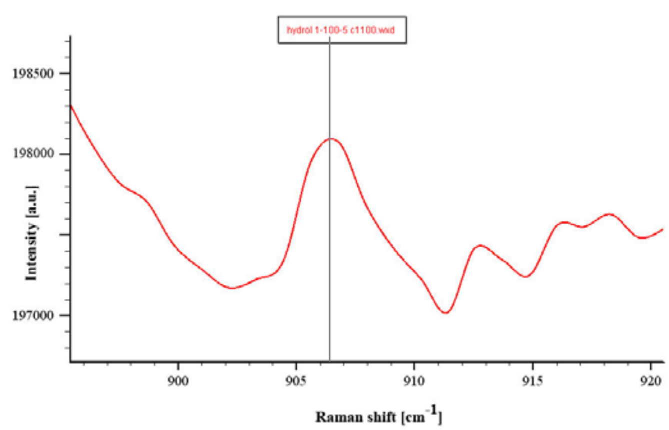

Fig. 5 Raman spectrum of dry collagen hydrolysate - detail of the peak assigned to Cr(VI)

The main interest was focused on the area around 900 cm^{-1}. The presence of Cr(VI) affects arising the peak at 907 cm^{-1} in the spectrum (Fig. 5). However, its intensity depends on the concentration of Cr(VI) in the sample.

The collagen hydrolysate was yellow liquid with dry mass content of 1.3 %. The measured concentration of Cr(VI) was 8.18 $mg.L^{-1}$ (method with phosphate buffer). Total concentration of chromium was for comparison 8.66 $mg.L^{-1}$ (AAS).

V. Conclusion

The goal of this paper was to provide an overview of available information about spectrometric determination of Cr(VI), especially spectrometric methods using 1,5-diphenylcarbazide, and evaluation of comments for real samples measurement. Even in times of modern techniques, this old method is still taking its place in laboratory analyses. It has been found that this method can detect reliably the concentrations of Cr(VI) from 0.02 $mg.L^{-1}$ for given performance. Pre-treatment of the samples could play important role in final measurement and it has to be taken into account. The performance will differ according to the nature of the measured samples. Small concentrations of hexavalent chromium were found in all measured samples. The presence of Cr(VI) in the hydrolysate was confirmed by using Raman spectroscopy.

References

[1] S. Hüffer, and T. Taeger, "Sustainable leather manufacturing - A topic with growing importance", *Journal of the American Leather Chemists Association*, vol. 99, no. 10, pp. 423-428, Oct. 2004.

[2] S. Avudainayagam, M. Megharaj, G. Ovens, R. S. Kookana, D. Chittleborough, and R. Naidu, "Chemistry of chromium in soils with emphasis on tannery waste sites", *Reviews of Environmental Contamination and Toxicology*, vol. 178, pp. 53-91, 2003.

[3] K. Kolomaznik, M. Adamek, I. Andel, and M. Uhlirova, "Leather waste-Potential threat to human health, and a new technology of its treatment", *Journal of Hazardous Materials*, vol. 160, no. 2-3, pp. 514-520, Dec. 2008.

[4] N. K. C Babu, K. Asma, A. Raghupathi, R. Venba, R. Ramesh, and S. Sadulla, "Screening of leather auxiliaries for their role in toxic hexavalent chromium formation in leather - posing potential health hazard to the users", *Journal of Cleaner Production*, vol. 13, no. 12, pp. 1189-1195, Oct. 2005.

[5] L. Di Palma, M. T. Gueye and E. Petrucci, "Hexavalent chromium reduction in contaminated soil: A comparison between ferrous sulphate and nanoscale zero-valent iron", *Journal of Hazardous Materials*, vol. 281, pp. 70-76, Jan. 2015.

[6] S. Dixit, A. Yadav, P. D. Dwivedi and M. Das, "Toxic hazards of leather industry and technologies to combat threat: A review", *Journal of Cleaner Production*, vol. 87, no. C, pp. 39-49, 2015.

[7] V. Gómez, and M. P. Callao, "Chromium determination and speciation since 2000", *Trends in Analytical Chemistry*, vol. 25, no. 10, pp. 1006-1015, Nov. 2006.

[8] P. Janoš, P. Kuráň, and M. Řídká, "Determination of Cr(III) and Cr(VI) by ion chromatography", *Chemické Listy*, vol. 101, pp. 406-410, 2007.

[9] P. E. Jackson, "Determination of inorganic ions in drinking water by ion chromatography", *Trends in Analytical Chemistry*, vol. 20, no. 6-7, pp. 320-329, 2001.

[10] K. Kolomaznik, M. Barinova and H. Vaskova, "Chromium VI issue in leather waste - A technology for the processing of used leather goods and potential of Raman spectroscopy in chromium traces detection", *International Journal of Mathematics and Computers in Simulation*, vol. 6, no. 5, pp. 447-455, 2012.

[11] International standard ISO/FDIS 17075, Leather-Chemical tests-Determination of chromium(VI) content.

[12] M. Malát, *Absorption analytic photometry*. [In Czech Absorpční anorganická fotometrie] Praha: Academia, 1973.

[13] G. Halliwell, "Colorimetric microdetermination of sexivalent Chromium", *Analytical Chemistry*, vol. 32, no. 8, pp. 1041-1042, 1960.

[14] Aqeel Mahdi . J, Kasim . H .Kadhim and Abbas. N .Al-Sharefy, "Spectrophotometric determination of Cr(VI) ions using new benzothiazolyl azo compound 2-[(6-methyl-2benzothiazolyl) azo]-4-chlorophenol", *National Journal of Chemistry*, vol. 24, pp. 608-619, 2006.

[15] J. Janků, *Analytics of Wastes*. [In Czech Analytika odpadů] Praha: VŠCHT Praha, 2010.

[16] P. Lazo, "Determination of Cr(VI) in environmental samples evaluating Cr(VI) impact in a contaminated area", *J. Int. Environmental Application & Science*, vol. 4, no. 2, pp. 207-213, 2009.

ISBN: 978-1-61804-321-4

The measurement and application of the thermal panels based on a phase change materials

Martin Kolacek, and Martin Zalesak

***Abstract*—**Presented article describes results of research of behavior and application of the thermal panels. These panels are based on the phase change materials (PCMs) under normal inner environment temperature in buildings. Measurement of parameters of thermal panels was oriented to specify heat storage capacities of the panels with the aim of their utilization possibilities in buildings. Time constant, heat transfer coefficient and their changes in different surface treatment of the panels were measured. The measurement was done in heating mode with the thermal electric foil. The article describes application of these panels in simulation environment where was created a computer model. The simulation model was validated with the parameters that were measured on the real thermal panels. In the simulation environment were created a different application of these panels to determine an appropriate use.

***Keywords*—**Phase change materials, heat accumulation, heat transfer coefficient, simulation environment

I. Introduction

THE heat storage materials start to apply for increase of the thermal accumulation parameters in buildings. The area where can be PCM materials used is so enormous and a particular uses is just in storage panels. These panels are created in form of block and there are easily recovered for increase the thermal storage parameters in lightweight construction such as wooden houses. PCM material can be created from water, paraffin and salt hydrates which allow to absorb, retain and later release a certain amount of energy. The released energy can be in form of heat or cold. The change of condition in materials occurs when the temperature difference is small. In the case of PCM materials it occurs in phase changes from solid state to liquid state. This change is accompanied by a large latent heat that can be utilized for a accumulation of heat. The ability of energy storage is called latent heat because these materials are also referred as Latent heat storage systems. The PCM materials are used in building construction and these materials can be based on organic or inorganic compounds. Among of these materials are used compounds based on modified paraffin that is used for the nucleation of large latent heat. This property is important in heat storage systems. [3],[4],[6]

The thermal storage panels are composed from mixture of ethylene based polymer 40% and 60% paraffin wax. For the crystallization of wax is necessary a large latent heat, therefore these materials are suitable as heat storage. The surface is formed on the panels by shiny aluminum cladding, thickness approximately 130μm. [2]

Measurement of parameters of PCM panels was done on the thermal panel that is located in laboratory of Faculty of Applied Informatics Tomas Bata University in Zlín in Czech Republic. System consists from two panels and in the panels are imposed 12 accumulation blocks. The rear part of panel consists of insulation and between 6 layers are imposed 3 electric heat foils on performance of 600 W. There is also water tube heat exchanger for heating or cooling. Dimensions of one panel are 1,25 x 0,083 x 2,07 m, and is covered with polished galvanized sheet. It is a specific equipment and all components are filled with thermally conductive mass.

Fig. 1 thermal panels which are located in the laboratory of Environmental Engineering

The basic problem of using thermal storage panels is heat transfer from panels. Main parameter of heat transfer is heat transfer coefficient. This parameter has two important parts, convection and radiation. The radiative heat transfer coefficient is influenced by surface emissivity. The emissivity of surface of measured equipment is about ε = 0,1, accumulation panels has polished surface and its emissivity is less than 0,1. The emissivity was measured by contact and

The work was performed with financial support of research project NPU I No. MSMT-7778/2014 by the Ministry of Education of the Czech Republic and also by the European Regional Development Fund under the Project CEBIA-Tech No. CZ.1.05/2.1.00/03.0089. Work was also supported in frame of Internal Grant Agency of Tomas Bata University in Zlin, Faculty of Applied Informatics IGA/CebiaTech/2015/002 and IGA/FAI/2015/022 References.

M. Kolacek is with the Tomas Bata University in Zlín Faculty of Applied Informatics. Department of Automation and Control Engineering. 760 05 Zlín Czech Republic. (e-mail: kolacek@fai.utb.cz, +420 576 035 642,).

M. Zalesak is with the Tomas Bata University in Zlín Faculty of Applied Informatics. Department of Automation and Control Engineering,760 05 Zlín Czech Republic. (e-mail: zalesak@fai.utb.cz).

contactless thermometer and results were around ε = 0,6. The surface of panel was oxidized and this high value of emissivity was inaccurate. The temperature distribution was measured by thermo imager. In this part of measurement was problem with an apparent reflected temperature in thermo imager.

II. The Heat transfer coefficient

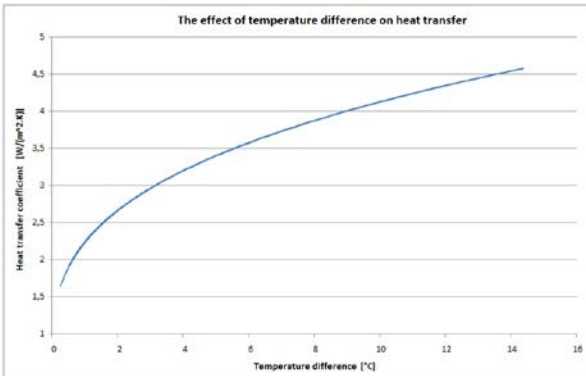

Fig. 2 the effect of temperature difference between the panel surface and surrounding environment on the heat transfer coefficient

Thermal panels were heated by electric heat foils. During the cooling process occurs changes of surface temperature (36°C - 22°C) and also the heat transfer coefficient changed.

As it is seen in Fig. 2, the value of heat transfer coefficient depends on the size of temperature difference between surface of panel and environment. During the cooling process decrease the value of coefficient, therefore it was necessary to calculate the average value. For a time constant is necessary temperature difference 27-35°C, in case of the heat transfer coefficient means average value was h = 4,1 W.m^{-2}K^{-1}. Total cooling time is very long with temperature decrease by 13 K about 40 hours, therefore the value of heat transfer coefficient is very small because the temperature difference is so small.

For gaining of parameters of panel it is difficult to maintain a stable microclimate conditions in a laboratory. Air temperature fluctuates between ± 2 K.

The heat transfer coefficient was determined by a calculation involving a natural convection and radiation, below is equation.

$$Nu = 0{,}135\left(\frac{g.\beta.l^3.\Delta\theta}{\nu^2}\frac{c_P.\eta}{\lambda}\right)^{1/3} \tag{1}$$

Where Nu is Nusselt number [-]
g gravitational acceleration [m.s^{-2}]
β thermal expansion [K^{-1}]
l characteristic dimension [m]
$\Delta\theta$ temperature difference [K]
c_p specific heat capacity [J.kg^{-1}.K^{-1}]
η dynamic viscosity [Pa.s]
ν kinematic viscosity [m^2.s^{-1}]
λ coefficient thermal conductivity [W.m^{-1}.K^{-1}]

$$Nu = \frac{h_C.l}{\lambda} \tag{2}$$

Where h_C is convective heat transfer coefficient [W.m^{-2}.K^{-1}]

$$h_T = \varphi_{12}.\varepsilon.10^8\sigma\frac{\left(\frac{T_1}{100}\right)^4-\left(\frac{T_2}{100}\right)^4}{T_1-T_2} \tag{3}$$

Where h_T is radiative heat transfer coefficient [W.m^{-2}.K^{-1}]
ε emissivity [-]
σ Stefan-Boltzmann constant [W.m^{-2}K^{-4}]
T thermodynamic temperature [K]

$$h = h_C + h_T \tag{4}$$

Where h is total value of heat transfer coefficient [W.m^{-2}.K^{-1}]

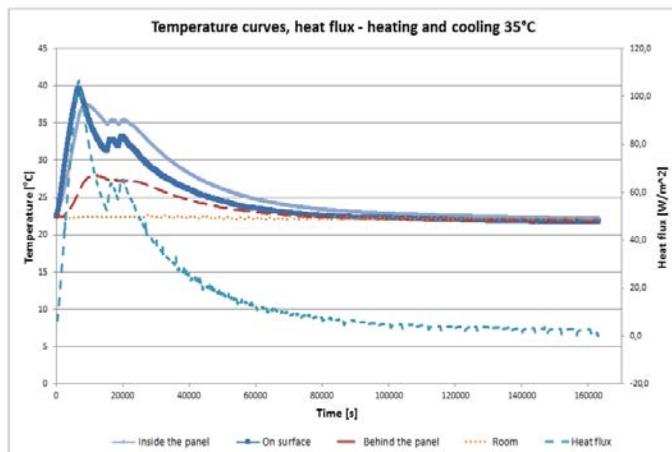

Fig. 3 temperatures in different locations of panel, the heat flux from the front surface of the panel

The surface temperatures were measured at different places of panels and these values were same almost in every point. The temperatures are shown in Fig. 3, where the temperatures are in different part of panel, heat flux and ambient temperature in the laboratory. Temperature curves are representing the average temperature.

Effects of heat accumulation are very difficult to evident from graph in Fig. 3, the reasons are that composition of panels is very extensive, but especially due to measure the impact of accumulation during the heating.

The value of Biot criterium was validated for verification thermal dynamic behavior of the panel from values in Table. 1. A specific heat capacity is the value of this system without latent heat in the temperature range 22-33 °C.

ISBN: 978-1-61804-321-4

Table 1 measured and calculated parameters panel

Name	Symbol	Unit	Value
Heat transfer coefficient	h	$[W.m^{-2}.K^{-1}]$	4.1
Specific heat capacity	c_P	$[J.kg^{-1}.K^{-1}]$	8400
Density	ρ	$[kg.m^{-3}]$	810

The value of Biot number was less than 0.1, therefore the system was possible evaluated by the thermal transient state with differential equations of the 1. order. [3]

Table 2 values of Biot number

Name	Dimensions (H,W,D)[m]	Biot number
1x PCM plate	1x1,2x0,0054	0,078
Thermal system	2,07x1,25x0,08	0,00429

III. Time Constant

Time constant was determined by several methods from measuring the cooling process, calculation or in simulation environment. The average value of time constant is τ = 6,8 hours, time constant of one PCM plate is then τ = 75 min. Calculations were carried out according to the following equations.

$$\frac{\theta}{\theta_i} = \frac{\theta - \theta_\infty}{\theta_i - \theta_\infty} = e^{(-Bi.Fo)} \tag{5}$$

Where θ is initial temperature [°C]
θ_i temperature reached [°C]
θ_∞ temperature stabilization [°C]
Bi Biot number [-]
F_o Fourier number [-]

$$\frac{\theta}{\theta_i} = e^{\left(\frac{h.L_C}{\lambda} \cdot \frac{a.\tau}{L_C^2}\right)} \tag{6}$$

Where L_C is characteristic dimension [m]
a Thermal conductivity $[m^2.s^{-1}]$
τ time constant [s]

$$\tau = \frac{\rho.V.c_P}{h.A} \tag{7}$$

Where ρ is density $[kg.m^{-3}]$
V volume $[m^{-3}]$
A area $[m^{-2}]$

IV. Surface Temperature to Measure by a Thermal Imager

The surface temperature of panel was measured by using the hermal imager. The surface of panel is made from polished galvanized sheet therefore a view of thermogram is distorted. The problem is in very low value of emissivity. The thermal imager showed a reflected apparent temperature, this temperature is shown in Fig. 4.

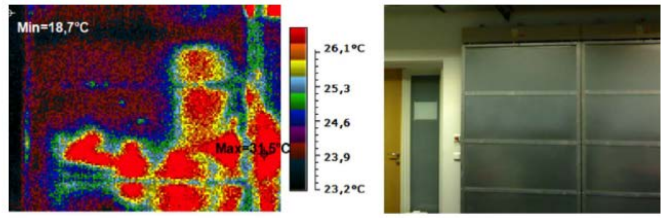

Fig. 4 thermogram of shiny surface, ε = 0,39, temperature surface θ= 32,7 °C, temperature ambient θ= 25 °C, humidity φ = 40 %, distance from panel 3,5 m

It was necessary to perform change of the surface, which shows the surface temperature without influence of inhomogeneity. One panel was painted black matte paint, than a measurements were performed again with a modified surface of panel.

On thermogram in Fig. 5 can be seen uniform distribution of surface temperature of the panel. This temperature distribution was verified by thermocouples, which confirmed uniform distribution of surface temperature as it was captured by thermo imager.

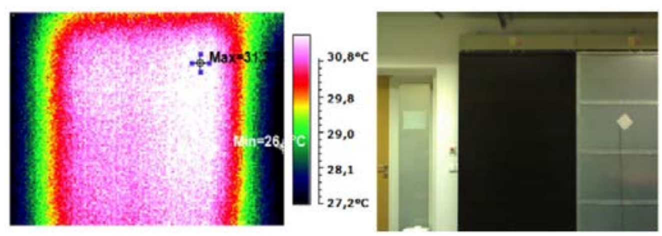

Fig. 5 thermogram of modified surface, ε = 0,97, temperature surface θ = 29,5 °C, temperature ambient θ = 24,8 °C, humidity φ= 40 %, distance from panel 5 m

The modified surface caused an increase in heat transfer by radiation, value of emissivity is ε = 0,97. This change caused the rapid cooling. Total value of heat transfer coefficient was h = 8,29 $W.m^{-2}.K^{-1}$ (increase of value). The time constant decreased to value τ = 5,5 hour.

Problems of change the surface properties of the storage panels is important in terms for heat transfer efficiency and also in terms of placement in construction. A manufacturer of storage panels guarantees a stability of paraffin wax in a higher temperature and panels are placed under the inner lining as plasterboard or wooden cladding. [2] The thickness of cover material is very important for the heat transfer efficiency. The measurement was performed on thermal panels which have a cover layer from galvanized sheet 2 mm thick. This layer minimizes thermal resistance and the surface of the

ISBN: 978-1-61804-321-4

responsibility are similar as storage plate which are placed inside the thermal panel.

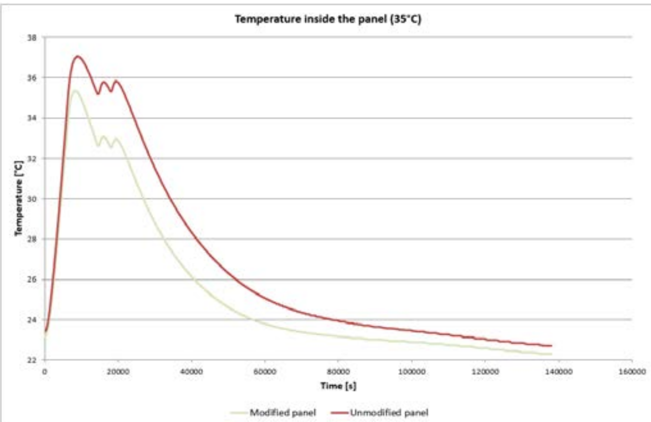

Fig. 6 compared temperatures inside the panel, modified and unmodified surface, heating 35°C

V. The Use of PCM materials

Part of the research of panel was to applicate into the upper layers of heating devices, heating wall. The research of behavior of panel was simulated and results were verified experimentally. Maximum temperature of panels is 40 °C therefore the direct application is suitable for large-scale low-temperature systems (underfloor heating, heating walls and ceilings).

The panels were heated to a temperature 35°C, maximum heat flux was 65 W.m^{-2}. Charging the panel took 85 min and this ensured surface temperature in the range 27-35°C lasting for 6,8 hour. The panels can be used under cover layer of underfloor heating. Another usage can be in heating ceiling it was applied in a simulation model.

VI. The Simulation model of the storage panel

The effective heat capacity was only used as the average value for principle of modeling phase changes in a simulation. A model of thermal panel was also created but its complexity of the composition cased difficulty in a simulation. A simple simulation caused the calculation time took almost 18 days yet it was used a powerful computing units. For a simulation model was created a simple accumulation plate and boundary conditions were used from measured values of thermal panels.

To verify the measured data was created a simple room in dimensions 3,7 x 3 x 3 m, thickness of wall and floor was 0,35 m. Under storage panel was placed 0,03 m isolation. Ambient conditions were set on constant temperature θ = 21 °C, initial temperature of panel was θ = 33 °C.

Time constant obtained from simulation was τ = 80 min, the calculated value was τ = 75 min.

The usual use is placement of these panels on wall and ceilings. The panels have an ability to accumulate an excess of heat inside the room and they can reduce the temperature peaks up to 7 °C (reduce of operating temperature).

Another simulation model was created to locate panels in the floor and its dimensions were 8,7 x 8 x 3 m. In this case was much more efficient release of energy than in the case of placement in the wall, Fig. 7. The results confirmed an appropriate use of PCM a application in underfloor heating.

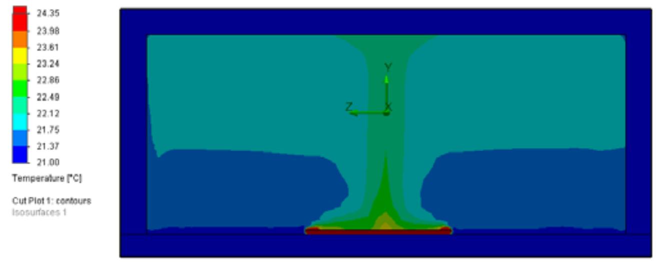

Fig. 7 the temperature of the room and panel, placement on the floor (view cut)

For the heat transfer efficiency is important a sheathing of panels. In another model was validated an application of the cover layer by drywall of the PCM materials. This application of PCM materials was done to verify of effectiveness the heating in ceiling. An important element was primarily radiation heat transfer. The dimension of simulation room were the same as in the previously model, where the panels were placed in the ceiling and 5mm thickness of drywall as cover layer. Initial conditions were set: air temperature surrounding walls and internal environment θ = 18 °C, temperature of PCM material θ = 35 °C. The experiment showed a heat discharging took 2 hours where these values were: the average air temperature increased to 24,3 °C, surface temperature of drywall 30,5 °C.

Another situation was used PCM materials without cover layer. The results were achieved as these: the average air temperature in room 26 °C, surface temperature of PCM's after 2 hours of discharging 32,3 °C. Results from these simulation showed importance to ensure an adequate cover layer of PCM panels. This cover layer must ensure an efficient heat transfer due to its minimum thickness and suitable emissivity.

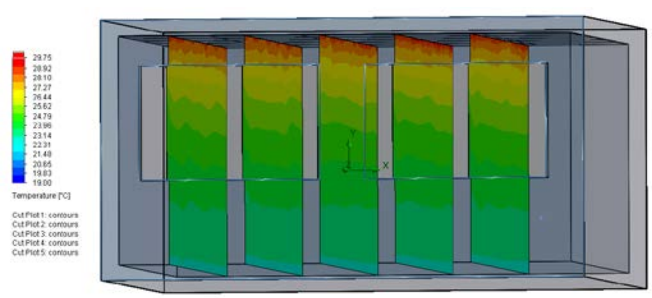

Fig. 8 the temperature distribution in the room, cover layer drywall

ISBN: 978-1-61804-321-4

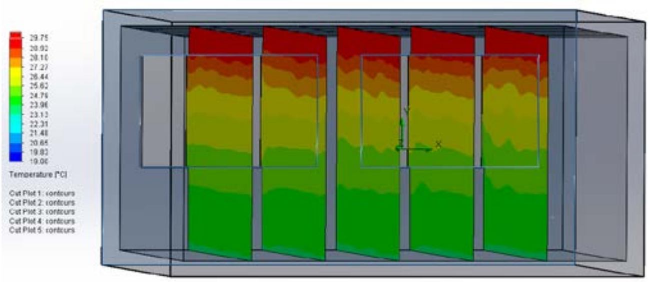

Fig. 9 the temperature distribution in the room, without cover layer

VII. Conclusion

The main activity was to measure the parameters of thermal panel based on PCM materials. Calculation and simulation validated the results. Another part of presented work was to modify the surface of thermal panel and compare it with initial properties. The obtained values were allowed to perform the simulation and the possibility of usage were checked. The parameters obtained by simulations showed good agreement and the simulation can be used to optimize the solution storage parameters of buildings. [7] The research of using the PCM materials will continue making changes to the surface convective parameters and application these materials in cooling devices.

References

[1] ASHRAE HANDBOOK. Part 1 – 4 . *American Society of Heating, Refrigeration and Air-Conditioning Engineers*, Inc. 1791 Title Circle, N.E., Atlanta, GA 30 329. ISBN 1-931862-73-7. ISSN 1549-2370..

[2] DuPont., “DuPont™ Energain® FAQs”. 2015. [online]. Available: http://energain. co.uk/Energain/en_GB/sales_support/ faq.html..

[3] P. F. Incropera, D. P. Dewit, T. L. Bergmann, A. S. Lavine, *Fundamentals of Heat and Mass transfer*. USA. 2007. ISBN: 0-471-76115-X.

[4] M. Necati, Özisik, *Heat transfer a basic approach*. Singapore: International edition, McGraw-HillBook, 1985. ISBN: 0-07- 047982-8.

[5] J. Nejmark, R. Judkoff, G. Knabe, Le. H.-T., M. Dürig, A. Glass, G. Zweifel, “Applying the building energy simulation test (BESTEST) diagnostic method to verification of space conditioning equipment models used in whole-building energy simulation programs”. *Energy and Buildings* 34. 2002. [online]. Available: https://noppa.aalto.fi/noppa/kurssi/ene-58.5181/lisatty7123/ Ene-58_5181_neymark.pdf

[6] M. Ostry, “Increase of Thermal Storage capacity of the Envelopes”. VUT FAST Brno. 2004 [online]. Available: http://www.fce.vutbr.cz/veda/dk2004texty/pdf/01_Pozemni%20stavitelstvi/1_03_Prostredi%20v%20budovach/Ostry_Milan.pdf

[7] J. Řehanek, *Thermal storage in buildings*. ČKAIT Praha 2, 2002. ISBN: 80-86364- 59-3.

[8] S. Sehnalek, M. Zalesak, J. Vincenec, M. Oplustil, and P. Chrobak, “Ground-Coupled Heat Transfer Test Cases as ranking simulation software,” *WSEAS TRANSACTIONS on INFORMATION SCIENCES and APPLICATIONS*. Volume 12, 2015. ISSN / E-ISSN: 1790-0832 / 2224-3402

[9] M. Shrestha, “PCM Application-Effect on Energy Use and IA Temperature,” *NTNU* Faculty of Architecture and Fine Arts. Project leader prof. Arild Gustavsen. Norway 2012 [online]. Available: https://www.ntnu.no/wiki/download/attachments/48431699/Master-+Shrestha.pdf?version=1&modificationDate=1343120771625.

[10] N. Soares, J. J. Costa, A. R. Gaspar, O. Santos, “Review of Passive PCM latent heat thermal energy storage systems towards buildings energy efficiency”. *Energy and Building* 59, 82-103 2013 [online]. Available: http://www.sciencedirect.com/science/article/pii/S0378778813000157

[11] M. Zalesak, J. Postava, “Implementation of Unsteady methods of measuring thermal properties of buildings materials”. *Plumbing and ventilation.* Volume 33, number 3, 1990 Prague.

Spectroscopic measuring of milk fat

Hana Vašková and Martina Bučková

***Abstract*—**Accurate monitoring of milk nutritional compositions is essential for producers of milk, dairy products and also for its quality control. This paper presents application of Raman spectroscopy as a modern tool for milk fat determination. Raman spectroscopy enables effective material identification and offers rapid, non-contact and nondestructive measurements. Reagent free determination and possibility to insert devices for automatization e.g. of production lines for milk processing are considered to the main benefits of this method comparing to traditional time-consuming techniques. Spectroscopic measurements were performed on liquid milk samples as well as on dried milk droplets with fat concentration range 0.1% to 3.5%. Main peaks in Raman spectra were assigned to appropriate milk fat components. Röse-Gottlieb gravimetric method served as a standard control method and for correlation with experimental spectroscopic data for milk fat analysis.

***Keywords*—**Milk fat, milk quality, quality control, Raman spectroscopy, rapid determination.

I. Introduction

MILK and dairy products play an important role in the human diet all over the world. These products are considered to be complex and high quality nutrient source (mainly as a calcium and protein source) well available in many countries. Moreover, current variability of produced forms and flavours of dairy products fulfils consumers' requirements in terms of different taste preferences and also demands for culinary use. Main components of milk comprise milk proteins, carbohydrates and fat. The reliable information about these main components of milk is crucial characteristic for adequate technology application. Additionally, this information has to be labelled on milk or dairy products to inform customers about their nutritional parameters and value.

Effective quality monitoring of raw milk composition and other ingredients as well as monitoring of quality confirmation of final milk products is essential especially for the producers. Common methods are based mostly on traditional laboratory techniques using usually sample pretreatment, application of many chemicals, several steps and time consuming analysis, skilled and experienced personnel. Therefore, methods allowing fast, simple, ideally nondestructive and accurate analysis need to be developed and improved. Also, methods with possibility to be connected with automatic regulation unit or small portable measuring systems are required in technology processes. However, for any automation there is a necessity to perform measuring of required physical or chemical characteristics for further evaluation and continuous evaluation.

From this point of view, new spectrometry methods (UV-visible, infrared, luminescence or Raman spectroscopy) are promising techniques. Moreover, multivariate chemometric tools coupled with spectrometric methods can significantly increase their application (not only) in food analysis and may have value for solving problems in dairy science and technology [1], [2].

The popularity of usage Raman spectroscopy related to analysis of milk and dairy product has an increasing trend as show the number of publications released lately. In contrast to many other spectroscopic methods, Raman spectroscopy does not require optical purity of the samples. Method has been applied to study molecules in different forms: liquids, fibres, thin films, powders, precipitates, gels or crystals. Raman scattering is generally a weak effect, giving signal intensity in order of $1x10^{-9}$ to $1x10^{-6}$ of those of elastic Rayleigh scattering. To obtain sufficient response signal, fairly high concentrations of target analytes are required to be contained in samples. Raman spectroscopy, therefore represent a suitable tool for direct *in situ* analysis of the major constituents of food systems [3].

The main topic studied in dairy sciences is determination of protein, carbohydrate and fat content and their change during technology or storage conditions [3] - [6]. The most known case in food chemistry and forensic toxicology was the melamin adulteration causa. In this case, Raman spectroscopy provided a very rapid screening test for melamine-adulterated dried milk [4], [7]. Additionally a portable compact Raman spectrometric system suitable for on-line analysis was constructed to determine melamine adulteration in milk powder [4]. Quantification of whey protein, a cheap by-product of cheese production added to milk powder has also been investigated [8]. Focused on milk fat, analysis of Raman spectra in combination with chemometrics methods was used to detect, classify and quantify the adulteration of butter with margarine [9].

This work is supported by the Ministry of Education, Youth and Sports of the Czech Republic, by European Regional Development Fund under the project CEBIA-Tech No. CZ.1.05/2.1.00/03.0089 and its continuing project, i.e. by Narodni program udrzitelnosti No. 1.05/2.1.00/03.0089

Hana Vaskova is with the Faculty of Applied Informatics, Tomas Bata University in Zlin, nám. T. G. Masaryka 5555, 760 01 Zlín, Czech Republic (e-mail: vaskova@fai.utb.cz)

Martina Buckova is with the Faculty of Technology, Tomas Bata University in Zlin, nám. T. G. Masaryka 5555, 760 01 Zlín, Czech Republic (e-mail: buckova@ft.utb.cz)

II. Theory

A. Milk Fat

Bovine milk is composed of 87% water, 4-5% lactose, 3% protein, 3-4% fat, 0.8% minerals and 0.1% vitamins. 98% of the contained fat in milk is in form of triacylglycerol. Other lipids forms are represent only minor content: diacylglycerol (2%), cholesterol (lower then 0.5%), phospholipids (approx. 1%), and free fatty acids (0.1%). Trace amounts of hydrocarbons, fat soluble vitamins, flavour compounds and other ingredients are arising in milk during animal feeding [10].

Determination of milk fatty acids is considered to be quite difficult due to large number of fatty acids and their structural variety. Milk fat is composed of more than 400 different fatty acids. However, most of these acids are present at only trace concentrations. Approximately 70% of fat share is comprises saturated fatty acids and 30% unsaturated fatty acids [10]. The average concentrations of the principal fatty acids in milk fats are following: 29% for oleic acid (C18:1), 26% for palmitic acid (C16:0) and 14% for stearic acid (C18:0) [11]. In the unsaturated fatty acids, also polyunsaturated fatty acids constitute only around 2,3% of total fatty acids, mainly linoleic and α-linolenic acids. Additionally, short-chain fatty acids and trans-fatty acids can be also found [10]. Quantification of minor milk fatty acids using vibrational spectroscopy becomes especially difficult in raw milk, due to the presence of other milk components, which interfere with fatty acid specific signal [12]. For instance the fat soluble vitamin fraction, mainly vitamins A, D, and E, can be included in the fat milk signal [10]. Raman spectroscopic evaluation of fatty acids contained in vegetable oils can be found e.g. in [13], [14].

B. Raman Spectroscopy

Raman spectroscopy is a vibrational spectroscopic method with a potential to answer a number of questions related to chemical details of molecular structure what makes this technique definitely proper for material identification [15]. This method becomes a valuable part of laboratories around the world in recent years.

Raman spectroscopy provides very specific chemical „fingerprint“ of every single chemical substance in the form of the Raman spectrum. The method is based on so called Raman scattering. Raman scattering is an inelastic scattering resulting from an interaction of a photon and a molecule. In inelastic scattering photons have slightly changed wavelengths that are characteristic for specific bonds in surveyed material. Since most photons are on molecules scattered elastically (Rayleigh scattering i.e. without changing the wavelength), it is necessary to filter out of the spectrum of the strongly present wavelength of laser. Diagram of the measurement using Raman spectroscopy is shown in Fig.1.

Although the fundamental phenomenon is known since thirties of the 20th century, its effective use in Raman spectroscopy occurs in about last decade. The rebirth of this method goes hand in hand with advances in a laser, detectors and computer technology. Raman spectroscopy brings many

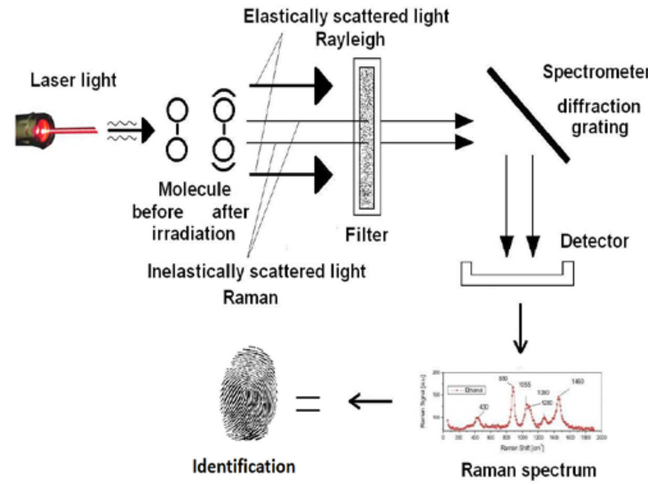

Fig. 1 laser irradiate the sample, molecules vibrate, filter eliminates intense Rayleigh scattering, the grating disperses the light onto a detector to generate a spectrum, which gives the information about molecule bonding and provides a chemical fingerprint utilizable for identification.

advantages as the method is:

- relatively rapid
- non-destructive
- contactless
- usable for measuring through transparent glass or polymeric covering layers or containers
- applicable to all states of matter and different forms
- without special requirements for sample preparation
- usable as *in situ* analysis

The greatest drawback of the method is the fact that Raman scattering is a weak effect. Luminescence as much stronger quantum effect with bigger intensity can overlap Raman spectra and mask spectral information. Another disadvantage is eventual degradation of a sensitive sample when using intense laser beam [16].

Raman spectroscopy finds many applications in recent years in a number of scientific areas such as chemistry, biochemistry, material science, mineralogy, arts, medicine, also is used for pharmaceutical or forensic and security purposes.

C. Röse-Gottlieb gravimetric method

Röse-Gottlieb method is based on extraction using a mixture of organic solvents and gravimetric determination of milk fat expressed as g of extracted fat per 100 g of milk. Before extraction, all milk samples were heated to 38±1°C to ensure complete homogenization. 100 ml milk samples were digested by NH3 solution (25% v/v) and mixed with ethanol (96% v/v). The extraction was performed 3 times using the mixture of diethyl ether and petroleum ether (1:1). Finally the solvent phase was evaporated under vacuum and fat was weighted and calculated. This method is based on European Standard EN ISO 1211 and it is considered as reference method for milk fat determination [17].

ISBN: 978-1-61804-321-4

III. EXPERIMENTAL PART

A. Samples

Samples were obtained as mixtures of commonly sold milks with 0,1%, 1,5 % a 3,5% of fat. The fat content in milk samples was calculated to 0,1 %, 0,8 %, 1,5 %, 2,0 %, 2,5 %, 3,0 % and 3,5 %. The indicated concentrations were verified for fat content using Röse-Gottlieb gravimetric method based on European Standard EN ISO 1211 and by Raman spectroscopy. Milk samples were measured in two forms: directly in liquid form in opened aluminium dishes at a laboratory temperature and in form of dried milk droplets on aluminium plates.

Table 1 fat content in milk samples

	Fat [%]	
Sample	**Calculated**	**Measured**
1	0,1	0,074 ± 0,010
2	0,8	0,872 ± 0,031
3	1,5	1,539 ± 0,009
4	2	2,015 ± 0,029
5	2,5	2,558 ± 0,016
6	3	3,048 ± 0,037
7	3,5	3,506 ± 0,002

B. Instrumentation

InVia Basis Raman microscope (Renishaw) was used to measure Raman spectra of all samples. The Raman microscope uses two lasers as light sources: argon ion laser with the maximum power 20 mW and 785 nm NIR diode laser with maximum output power 300mW. Both were tested, however, more accurate and by luminescence less affected results were those, obtained using NIR laser. A Leica DM 2500 confocal microscope with the resolution 2µm was coupled to the Raman spectrometer.

All measurements were collected with 10 s exposure time and 3 accumulations. The samples were firstly scanned in common range 100 to 3200 cm^{-1} with 2 cm^{-1} spectral resolution. After determining the principle vibrational response the spectral range was then reduced to area from 300 to 1800 cm^{-1}.

C. Results

Spectroscopic measurements were performed both on milk samples with 0,1 % – 3,5 % fat content and on dried milk droplets. Due to the appearing luminescence at milk samples, the spectra of dried milk droplets were considered for evaluation. Raman spectra of all droplets samples are displayed in Fig. 2. Several peaks show changes of intensities relating to the content of fat.

Milk fat in Raman spectra is represented by C=O stretching of the ester groups of triglycerides at 1748 cm^{-1}, whereas the 1005 cm^{-1} phenylalanine ring breathing band is indicative of protein [1]. Assuming the protein content does not alter, this peak is taken as a standard to normalise intensity values. The CH_2 deformation vibrations at 1303 cm^{-1} and 1443 cm^{-1} are specific to the saturated fatty acids, C=C at 1654 cm^{-1} for unsaturated fatty acids in *cis* configuration [6]. Raman bands of carotenoids can be found at 1008 cm^{-1}, 1150 cm^{-1}, 1525 cm^{-1} [11].

For the evaluation of fat content in samples, the attention was directed to three significant bands: 1303 cm^{-1}, 1443 cm^{-1} and 1748 cm^{-1}. The baseline correction was applied on all

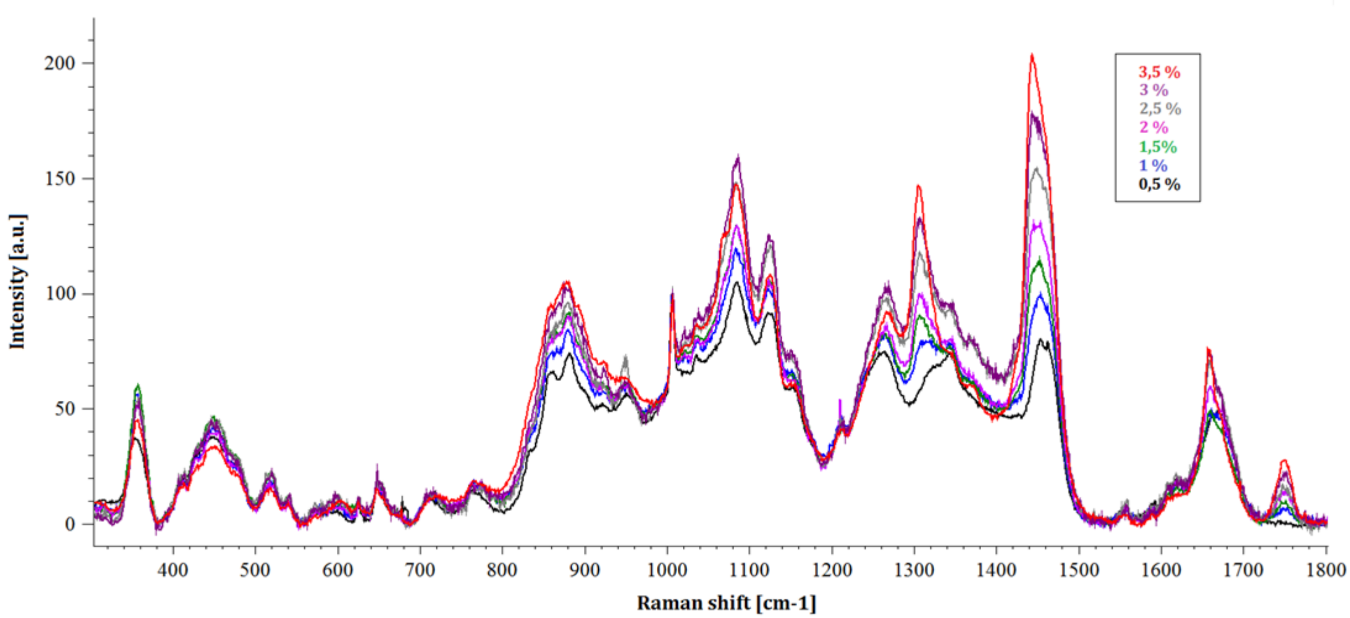

Fig. 2 Raman spectra of dried milk droplets with fat content 0,1 % – 3,5 %

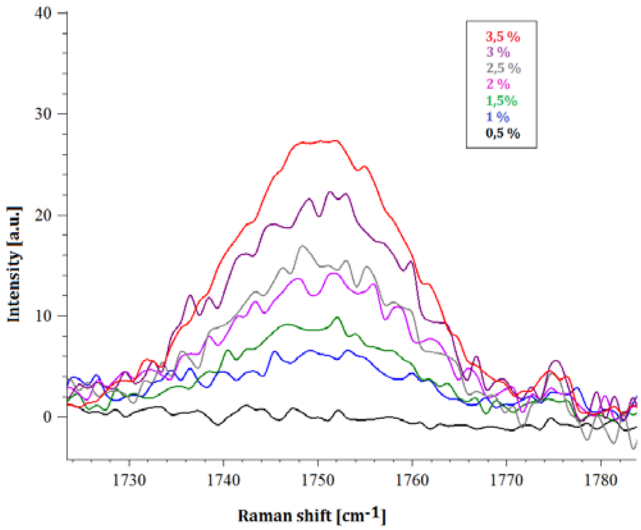

Fig. 3 Raman spectra of dried milk droplets - the increase of the normalised intensity at 1748 cm^{-1} with the content of fat

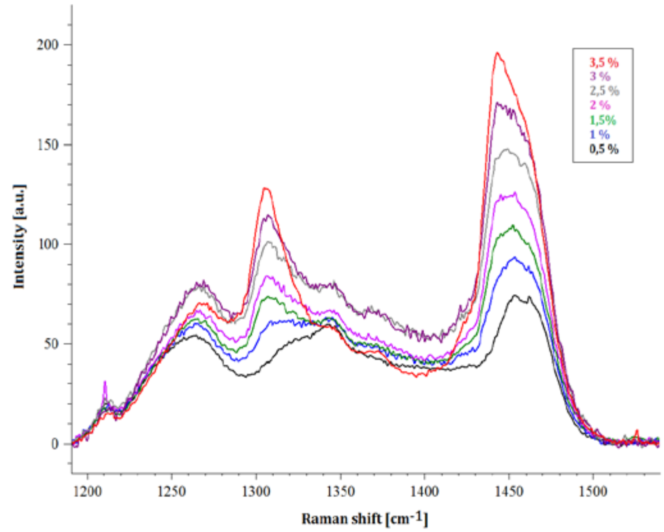

Fig. 5 Raman spectra of dried milk droplets - the increase of the normalised intensity at 1303 cm^{-1} and 1443 cm^{-1} with the content of fat

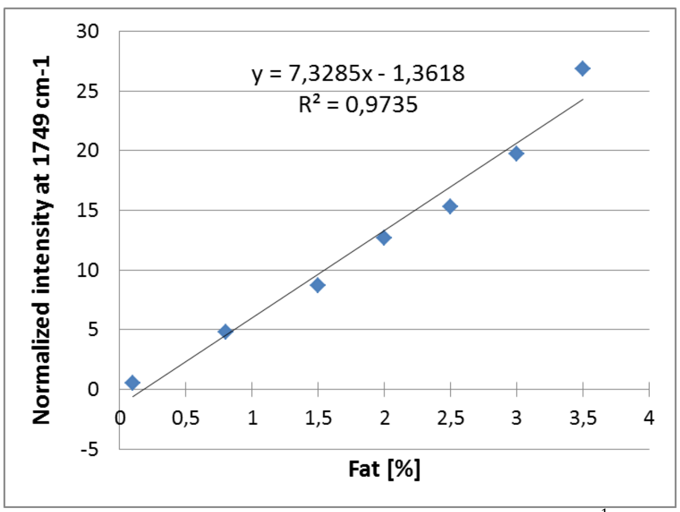

Fig. 4 dependence of the normalized intensity at 1749cm^{-1} on the fat content in dried milk droplets

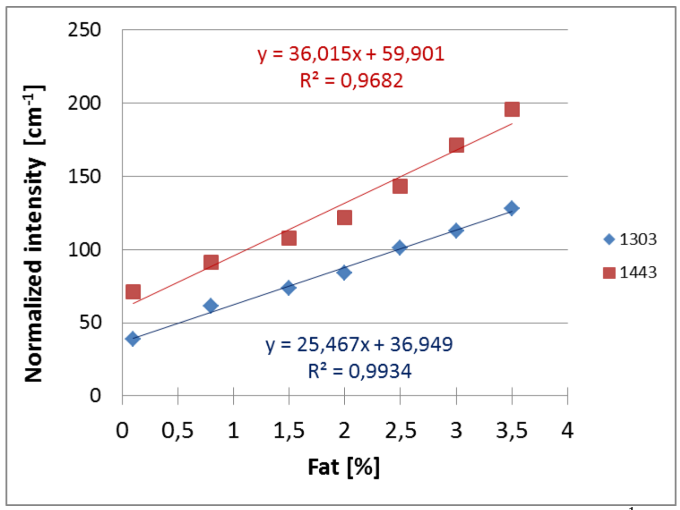

Fig. 6 dependences of the normalized intensities at 1303 cm^{-1} and 1443 cm^{-1} on the fat content in dried milk droplets

spectra and the spectra were normalized. Details of the spectral response for listed bands are displayed in Fig. 3 and Fig. 5.

The linear dependence of the normalized intensities was revealed for all three examined bands, are shown in Fig. 4 and Fig 6. In all cases the linearity exhibit quite high accuracy. Therefore based on a set of calibration data and specified procedure of data processing it is possible to determine the amount of fat in the samples. More proper for the evaluation and data processing seems to be the band 1748 cm^{-1} due to its solitary position in the spectra. However the other bands could be used for the confirmation.

IV. Conclusion

Raman spectroscopy was used as an innovative method for measuring the fat contained in milk. To obtain more precise spectral response, the measurements were performed also on dried milk droplets. Results acquired in this study show that on the basis of characteristic bands for saturated fatty acids it is possible to distinguish different fat concentrations. Raman spectroscopic evaluation brings advantages over traditional methods mainly in sense of simplicity, rapidity and no use of chemical reagents with the only need to prepare the milk droplets. These aspects of measuring mean costs and time savings.

References

[1] C. M. McGoverin, A. S. S. Clark, S. E. Holroyd and K. C. Gordon, “Raman spectroscopic quantification of milk powder constituents,” *Analytica Chimica Acta*, vol. 673, pp. 26-32, 2010.

[2] M. A. P. Rodriguez, J. Petrini, E. M. Ferreira, L. R. M. B. Mourao, M. Salvian, L. D. Cassoli, A. V. Pires, P. F. Machado and G. B. Mourao, “Concordance analysis between estimation methods of milk fatty acid content,” *Food Chemistry*, vol. 156, pp. 170-175, 2014.

[3] E. C. Y. Li-Chan, "The applications of Raman spectroscopy in food science," *Trends in Food Science and Technology*, vol. 7, pp. 361-370, 1996.

[4] D. Yang and Y. Ying, "Applications of Raman Spectroscopy in Agricultural Products and Food Analysis: A Review," *Applied Spectroscopy Reviews*, vol. 46, pp. 539-560, 2011.

[5] J. Fontecha, J. Bellanato and M. Juarez, "Infrared and Raman Spectroscopic Study of Casein in Cheese: Effect of Freezing and Frozen Storage," *Journal of Dairy Science,* vol. 76, pp. 3303-3309, 1993.

[6] S. Gallier, K. C. Gordon and H. Singh, "Chemical and structural characterisation of almond oil bodies and bovine milk fat globules," *Food Chemistry*, vol. 132, pp. 1996-2006, 2012.

[7] E. Domingo, A. A. Tirelli, C. A. Nunes, M. C. Guerreiro and S. M. Pinto, "Melamine detection in milk using vibrational spectroscopy and chemometrics analysis: A review," *Food Research International*, vol. 60, pp. 131-139, 2014.

[8] M. R. Almeida, K. S. Oliveira, R. Stephani and L. F. C. Oliveira, "Fourier-transform Raman analysis of milk powder: a potential method for rapid quality screening," *Journal of Raman Spectroscopy*, vol. 42, pp. 1548-1552, 2011.

[9] R. S. Uysal, I. H. Boyaci, H. E. Genis and U. Tamer, "Determination of butter adulteration with margarine using Raman spectroscopy," *Food Chemistry*, vol. 141, pp. 4397-4403, 2013.

[10] P. C. Pereira, "Milk nutritional composition and its role in human health," *Nutrition*, vol. 30, pp. 619-627, 2014.

[11] R. M. El-Abassy, P. J. Eravuchira, P. Donfack, B. Kammer and A. Materny, "Fast determination of milk fat content using Raman spectroscopy," *Vibrational Spectroscopy*, vol. 56, pp. 3-8, 2011.

[12] I. Stefanov, V. Baeten, B. D. Baets and V. Fievez, "Towards combinatorial spectroscopy: The case of minor milk fatty acids determination," *Talanta*, vol. 112, pp. 101-110, 2013.

[13] M. Buckova, H. Vaskova, M. Tobolova and V. Kresalek, "Spectroscopic Screening of Degradation Process in Edible Oils and Its Mathematical Evaluation," *International Journal of Mathematical Models and Methods in Applied Sciences* [online], vol. 8, pp. 319-328, 2014.

[14] B. Muik, B. Lendl, A. Molina-Diaz and M. J. Ayora-Canada, "Direct monitoring of lipid oxidation in edible oils by Fourier transform Raman spectroscopy," *Chemistry and Physics of Lipids*, vol. 134, pp. 173-182, 2005.

[15] J. M. Chalmers, G. E. Howell and M. D. Hargreaves, *Infrared and Raman spectroscopy in forensic science*. 1st pub. Chichester, West Sussex, UK: Wiley, 2012

[16] N. B. Colthup, L. H. Daly and S. E. Wiberley, *Introduction to infrared and Raman spectroscopy*. 3rd ed. San Diego: Academic Press, 1990.

[17] *Milk – Determination of fat content – Gravimetric Method (Reference method)*, European Standard EN ISO 1211:2010.

Optimization of one-stage extraction process

D. Janáčová, K. Kolomaznik, V. Vašek and P. Mokrejš

Abstract— Each industrial production needs solvent. In view of the fact that solvent sources are limited and costs for purification are ever rising, technologists search for the way how to save solvent. A substantial part of solvent is consumed in the extraction processes, and on that account, a lot of attention is pointed to that direction. There is a variety of methods how to attain the required goal, i.e. to achieve the required quality of the extracted-out substance at a minimum consumption of solvent and energy needed to drive the extraction device and to heat up the extraction solid. In this case we have used a method based on the quantification of a physical concept based on the concrete extraction process, i.e. the creation of a mathematic-physical model, its solution and computer simulation, both in different sorts of extraction process and its respective stages. The result of our process is the determination of the optimum solvent consumption and electric power needed for mixing the extracted solid; provided the pre-requisite extraction quality is attained. It was tested validity of models on the raw-hide soaking processes. In an effort to apply an automatic control system to the soaking processes, we have also elaborated a soaking process control mechanism which enables to control the process at an optimum liquid and energy consumption. The chief advantage of this work is that the optimum consumption of water and energy is determined in the course of the process.

Keywords— One-stage extraction process, optimization, mathematical modeling, diffusion model.

I. INTRODUCTION

THE quantitative description goes from the mechanism, from the individual ways of extraction process adjustment, and it is based on the weight balance of extracted component. The mechanism of the process depends on that: how the extracted substance is bound and how strong.

The work was supported with financial support of research project NPU I No. MSMT-7778/2014 by the Ministry of Education of the Czech Republic and also by the European Regional Development Fund under the Project CEBIA-Tech No. CZ.1.05/2.1.00/03.0089.

D. Janáčová, Tomas Bata University in Zlín, Faculty of Applied Informatics, Department of Automation and Control Engineering, nám. T. G. Masaryka 5555, 760 01 Zlín, Czech Republic; phone: +420 576 035 274; (e-mail: janacova@fai.utb.cz)

K. Kolomazník, Tomas Bata University in Zlín, Faculty of Applied Informatics, Department of Automation and Control Eigineering, nám. T. G. Masaryka 5555, 760 01 Zlín, Czech Republic, (e-mail: kolomaznik@fai.utb.cz)

V. Vašek, Tomas Bata University in Zlín, Faculty of Applied Informatics, Department of Automation and Control Engineering, nám. T. G. Masaryka 5555, 760 01 Zlín, Czech Republic (e-mail: vasek@fai.utb.cz).

P. Mokrejš, Tomas Bata University in Zlín, Faculty of Technology, Department of Polymer Engineering, nám. T. G. Masaryka 5555, 760 01 Zlín, Czech Republic (e-mail: mokrejs@ft.utb.cz)

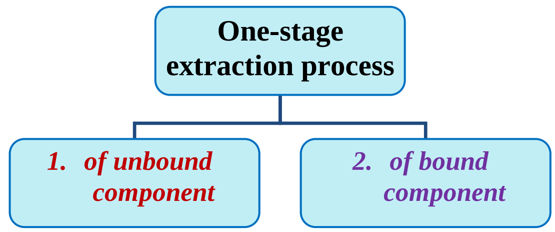

Fig. 1 Cases of one-stage extraction

II. MATHEMATIC MODELS OF ONE-STAGE EXTRACTION

1. The extraction process of unbound component

The case of extraction process of unbound component is soaking of raw hides for example. It is possible to divide the proper soaking of raw hides from the view of mechanism into two phases. In the first phase the release of the solid phase fiber structure into the inside volume of hide by water diffusion occurs. Thereby the original water content 35% (calculated for total weight of solid phase) will increase to 65%. In the second phase the removal of non-fiber parts of soluble proteins and considerable part of component occur [2, 3, 8, 11].

From the viewpoint of mathematical modeling a transport of component and water in the inside texture of hide has a great importance. Here, it is possible to describe the transport of component by diffusion model.

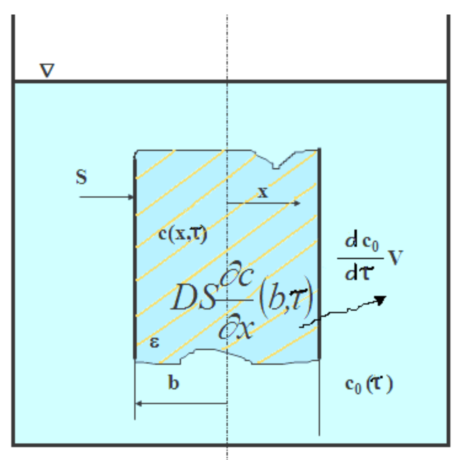

Fig. 2 Model of one-stage extraction

For the concrete case of the most used soaking technology, when hides are in contact with given volume of soaking liquid, it is possible to use the model valid for one-stage extraction of unbound component with retardative influence of diffusion-relations to [2, 15]. After solving we can obtain non-dimensional concentration field of component in hide (in solid phase)-relation. For wash process stage it is valid:

$$D\frac{\partial^2 c}{\partial x^2}(x,\tau)=\frac{\partial c}{\partial t}(x,\tau)\ , \quad \tau>0,\ 0\le x\le b \tag{2}$$

$$\frac{\partial c}{\partial x}(0,\tau)=0 \tag{3}$$

$$c(b,\tau)=\varepsilon.c_0(\tau) \tag{4}$$

$$c(x,0) = cp \tag{5}$$

$$-DS\frac{\partial c}{\partial x}(b,\tau)=V_0\frac{\partial c_0}{\partial \tau} \tag{6}$$

$$c_0(0)=0 \tag{7}$$

Equation (2) describes a non-stationary concentration field. Symmetric problem is described by equation (3). Equations (5) and (7) are initial conditions and equations (4) and (6) describe conditions of perfect matter transfer. For analytical solution we expressed non-dimensional values:

$$C=\frac{c}{c_p},\quad C_0=\frac{c_0}{c_p},\quad Fo=\frac{D\tau}{b^2},\quad X=\frac{x}{b}, \tag{8a,b,c,d}$$

Na is dimensionless consumption of extraction liquid [5, 9]

$$Na=\frac{V_0}{V} \tag{8e}$$

The mathematical model we solved by Laplace transformation and we obtained non-dimensional concentration field of component in material (in solid phase):

$$C\ (X,Fo_o)=\frac{\varepsilon}{\varepsilon+Na}-$$
$$-2Na\cdot\sum_{n=1}^{\infty}\frac{\cos\ (q_n X)\exp(-q_n{}^2F_O)}{\varepsilon\cos(q_n)-\frac{\varepsilon}{q_n}\sin(q_n)-Na\cdot q_n\sin(q_n)} \tag{9}$$

and dimensionless concentration of component in the bath:

$$C_o(Fo)=\frac{1}{Na+\varepsilon}-\frac{2Na}{\varepsilon}\sum_{n=1}^{\infty}\frac{\exp\left(-Fo\,q_n^2\right)}{\varepsilon+Na+\frac{Na^2q_n^2}{\varepsilon}} \tag{10}$$

For optimization of process is important to determine extraction process stage *y:*

$$y=\frac{V_oc_o}{Vc_p}=Na\frac{c_o}{c_p} \tag{11}$$

roots q_n we calculated from following transcendental equation:

$$\frac{-\varepsilon}{Na\,q}=\frac{\cos(q)}{\sin(q)} \tag{12}$$

Fo is the Fourier criterion (dimensionless time).
Diffusion coefficient *D* we calculated on the base experimental measurement, with using of Crank equation (which is valid for short times) [1]:

$$\frac{c_o(t)}{c_\infty}=\frac{2}{\sqrt{\pi}}\frac{1+\alpha}{\alpha}\sqrt{\lambda t} \tag{13}$$

We determined stage of extraction process *y:*

$$y=\frac{Na}{Na+\varepsilon}-\frac{2Na^2}{\varepsilon}\sum_{n=1}^{\infty}\frac{exp\left(-F_0q_n^2\right)}{\varepsilon+Na+\frac{Na^2q_n^2}{\varepsilon}} \tag{14}$$

Distribution of dimensionless concentration fields of component in material during extraction is shown on following figure 3:

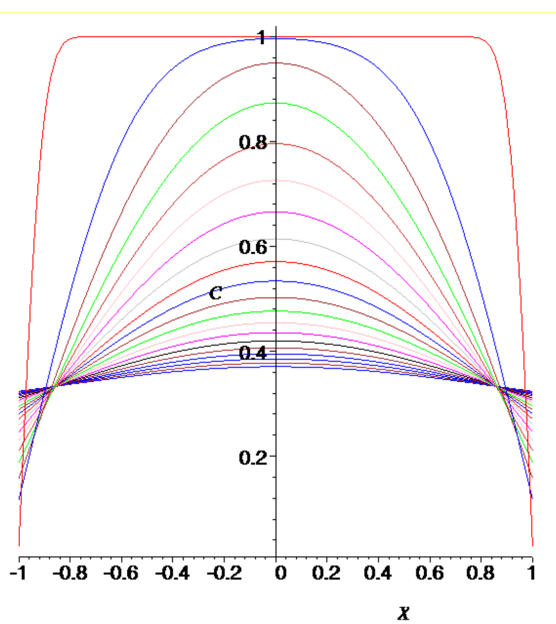

Fig. 3 Dimensionless concentration fields of component in material during extraction of unbound component for variable dimensionless time *Fo*

for input parameters:

half thickness of material b= 4 mm,
volume of material V = 1 m^3,

ratio of volume of liquid in the bath to the volume of the material Na = 1,
diffusion coefficient D =1.10^{-9} m^2.s^{-1},
porosity of the material $\varepsilon = 0.5$,
initial concentration of component c_p = 2,5 kg.m^{-3}.

Solving of mathematic model of bath extraction process enabled us to determine the operating costs-function for one-bath extraction component from material. It is possible to find the optimum of extraction liquid of process to be successful course of the process respectively, and that all from the corresponding the operating costs-function. To determine the operating costs-function for one-bath extraction we assumed that we are able to eliminate extracted component from the material by the liquid and that the main operating costs N of considered process are given by the sum of the consumed electric energy to the drive of machinery costs N_E and the consumed extraction liquid costs N_V

$$N = N_V + N_E \tag{21}$$

Whereas the consumed electric energy costs are given by the product of the electric power unit price K_E, the time τ and the electromotor input P to the drive of machinery.

$$N_E = K_E \, P \, \tau \tag{22}$$

The costs of the extraction liquid requirements N_V are given by the product of unit price of extraction liquid K_V and the extraction liquid volume V_0.

$$N_V = K_V \, V_0 \tag{23}$$

We supposed as well that the increasing liquid requirements cause the decreasing of liquid pollution during the extraction whereby the effectiveness of extraction process increases. Thereby the time interval, necessary to the drive of machinery is shorter, hence the electric energy costs are decreasing because these are linearly increasing with dependence on time. This implies that the sum of the liquid requirements costs and the electric energy in dependence on the liquid requirements keeps a minimum.

On following figure 4 is shown course of cost function for extraction process of unbound component.

Input parameters:

sorption coefficient A = 0 (unbound component),
half thickness of material b= 4 mm,
volume of material V = 1 m^3,
ratio of volume of liquid in the bath to the volume of the material Na = 1,
diffusion coefficient D =1.10^{-9} m^2.s^{-1},
porosity of the material $\varepsilon = 0.5$,
initial concentration of component c_p = 2,5 kg.m^{-3},
specific price of water K_V = 2,5 EUR.m^{-3}
specific price for electric energy K_E = 0,2 EUR.kWh^{-1},
extraction process degree y = 0,8.

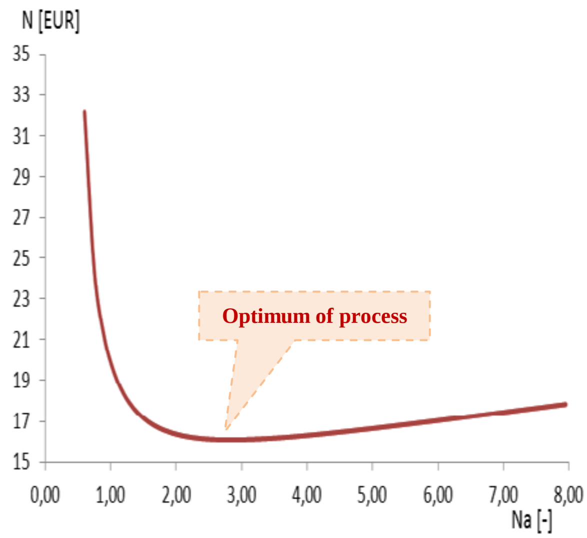

Fig. 4 Cost curve extraction process of unbound component

2. The extraction process of bound component

By formulation of mathematical model of extraction we assumed that all component will solute in extraction liquid - pure water. This diffusion process we described by one-dimensional second Fick's law [1, 3, 14]

$$\frac{D}{A+1}\frac{\partial^2 c(x,\tau)}{\partial x^2} = \frac{\partial c(x,\tau)}{\partial \tau} \quad , \ \tau > 0, \ 0 \le x \le b \tag{15}$$

Boundary balance condition (16) denotes the equality of the diffusion flux at the boundary between the solid and the liquid phases with the speed of accumulation of the diffusing component in the surrounding

$$\frac{\partial c}{\partial x}(b,\tau) = -\frac{V_0}{D\,S}\frac{\mathrm{d}c_0}{\mathrm{d}\tau}(\tau) \tag{16}$$

with conditions (3, 4, 5, 7).

Fixing power of component ions in the material represented by sorption coefficient A in diffusion equation (15) can be determined from Langmuir sorption isotherm [2, 6].

$$c_A = \frac{Ac}{Bc+1} \tag{17}$$

For very small concentrations of component ions can be written (18), where $K \approx A$.

$$c_A = Kc \tag{18}$$

Roots q_{nA} we calculated from following transcendental equation (19):

ISBN: 978-1-61804-321-4

$$-\frac{Na\, q}{\varepsilon(1+A)}=\tan(q) \tag{19}$$

Dimensionless time for extraction of bound component (Fourier criterion) is expressed by following equation:

$$Fo_{A0}=\frac{D\,\tau}{b^2\,(1+A)} \tag{20}$$

After this calculation, the concentration fields C for variable dimensionless time Fo_A is displayed on following figure 5 for following conditions:

sorption coefficient A = 5 (bound component),

another parameters are some as previous case.

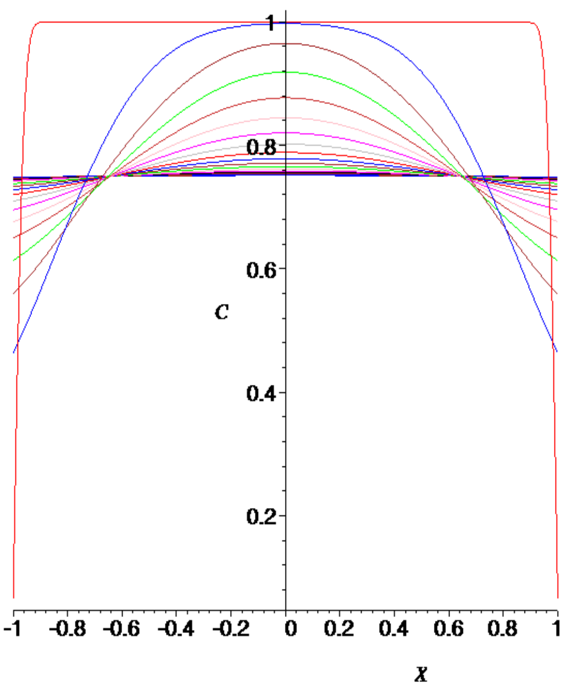

Fig. 5 Dimensionless concentration fields of component in material during extraction of bound component for variable dimensionless time Fo_A

Final solution of extraction degree for calculation cost function this case is:

$$y=\frac{C_o Na}{1+A}=$$

$$=\frac{Na}{\varepsilon\,(1+A)+Na}-2\frac{Na^2}{\varepsilon\,(1+A)}\sum_{n=1}^{\infty}\frac{\exp\left(-Fo\,q_n^2\right)}{\varepsilon\,(1+A)+\frac{q_n^2 Na^2}{\varepsilon\,(1+A)}+Na} \tag{21}$$

The determination of minimum of cost curve to reaching required extraction degree y = 0,8 on variable dimensionless volume of liquid bath Na enable to compute intersections and determine time needed for calculating of cost function points [7, 9, 13, 16].

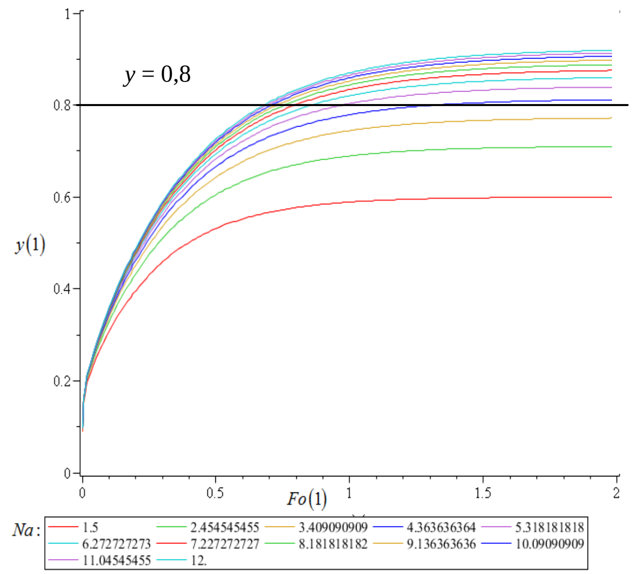

Fig. 6 Courses of extraction degree y for variable dimensionless consumption of liquid Na

On the figure 7 presents course of cost function for extraction process of bound component (**A = 5).**

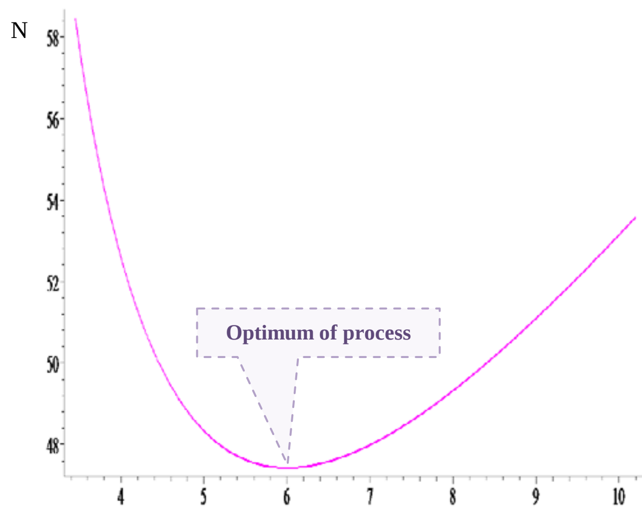

Fig. 7 Cost curve of extraction process of bound component

III. Conclusion

In this paper we determined cost function for two cases of one-stage extraction processes.

We compared two cases describing by mathematical models of extraction. From courses of concentration of fields and especially courses of cost curves is evident the higher the value sorption constant A, the higher the cost of the extraction process. Using mathematical diffusion model can be evaluated using a suitable extraction liquid with respect to consumption and cost of the process.

ISBN: 978-1-61804-321-4

By application of mathematic modelling we obtained the quality of extraction process.

It means:

- lower volume of extraction liquid for require quality of product
- to determine the extraction time
- on the base the cost function and total cost of one-stage extraction

We verified the validity of models on the raw-hide soaking processes. Technological operation soaking of raw hides was organized as a one-stage extraction. In an effort to apply an automatic control system to the soaking processes, we have also elaborated a soaking process control mechanism which enables to control the process at an optimum water and energy consumption. The chief advantage of this work is that the optimum consumption of water, and energy is determined in the course of the process, determines the optimum extraction process, independently for each particular case, as it adjusts the optimum based on the initial sequence of the soaking process.

Results of this work might be of wide using in processes which are described the same mathematical diffusion model.

LIST OF SYMBOLS

Symbol	Meaning	Unit
A	Sorption constant	1
α	Bath parameter	1
b	Half thickness of material	m
c	Concentration of component ions in material (solid phase)	$kg.m^{-3}$
c_o	Concentration of component in bath	$kg.m^{-3}$
c_A	Concentration of bound component into material	$kg.m^{-3}$
c_p	Initial concentration of component in material	$kg.m^{-3}$
$c(\tau)$	Concentration of component by diffusion into the liquid bath	$kg.m^{-3}$
c_∞	Concentration of component by diffusion into the liquid bath in infinite time	$kg.m^{-3}$
C	Non-dimensional concentration of component in material	1
C_0	Non-dimensional concentration of the component in bath	1
D	Effective diffusion coefficient	$m^2.s^{-1}$
ε	Porosity of solid phase	1
F_0	Non-dimensional time, (Fourier criterion)	1
F_{0A}	Non-dimensional time for extraction of bound component	1
K	Coefficient of fixing power of component on the material	1
K_E	Specific price for electric energy	$EUR.kWh^{-1}$
K_V	Specific price for extraction liquid	$EUR.m^{-3}$
λ	Transport parameter	$s^{-1/2}$
N	Total operating costs	EUR
Na	Non-dimensional consumption of liquid	1
N_E	Electric energy cots	EUR
N_V	Extraction liquid costs	EUR
P	Electromotor input for the stirred vessel drive	kW
q_n	Roots of transcendental equation	1
q_{nA}	Roots of transcendental equation for extraction od bond component	1
S	Surface of material	m^2
τ	Time	s
V	Volume of material	m^3
V_0	Volume of extraction liquid	m^3
x	Distance from the material center	m
X	Dimensionless space coordinate	1
y	Extraction process stage	1

REFERENCES

[1] J. Crank, "*Mathematics of diffusion*". London: Oxford University Press, 2nd Edition, 1977, ISBN 0-19-853411-6.

[2] D. Janáčová, "Modeling of Extraction Processes", (in Czech), Habilitation work, Tomas Bata University in Zlín, Zlín, 2003.

[3] D. Janáčová, et al., "Washing Processes Optimization", in *Proceedings of International Union of Material Technologists and Chemists Societies*, London, 1997.

[4] D. Janáčová, H. Charvátová, K. Kolomazník, and V. Vašek, *Creating software applications for solving diffusion problems in the MAPLE interface*. (in Czech), Zlín: Tomas Bata University in Zlin, 2012.

[5] K. Kolomazník, et al. "*Modeling of treatment processes*". (in Czech), Brno: VUT Brno, 1988.

[6] H. Charvátová, "*Modeling of Pelt Chemical Deliming*", (in Czech), Dissertation work, Tomas Bata University in Zlín, Zlín, 2007.

[7] D. Janáčová, H. Charvátová, K. Kolomazník, and V. Vašek, "*Creating software applications for solving diffusion problems in the MAPLE interface*". (in Czech), Zlín: Tomas Bata University in Zlin, 2012.

[8] D. Janáčová, V. Vašek, and K. Kolomazník, "The cost function for extraction of bound component from material", in *Latest Trends on Systems*. Volume II. Rhodes: Europment, 2014, p. 395-398.

[9] V. Grygar, "*Modeling of drying process for cylindrical bodies*". (Diploma thesis). Zlín: Tomas Bata University, Zlín, 2011. (in Czech)

[10] J. Piteľ, and J. Mižák, "Cost Effective Biomass Combustion Process Control". In: *Proceedings of the 8th PP&PSC (Power Plant and Power System Control)*, IFAC Symposium, Toulouse, France, September 02 – 05, 2012. [CD]. Toulouse: IFAC, 2012. pp. 616-620.

[11] D. Janáčová, K. Kolomazník, and V. Vašek. "Optimization of Enzymatic Digestion of Chrome Tanned Solid Waste". *In 14th International Congress of Chemical and Process Engineering CHISA*. Praha : Czech Society of Chemical engineering, 2000, ISBN 80-86059-30-8.

[12] R. Drga, "*Senzory bezpečnostních systémů na bázi elektro-magnetického záření*". (Disertation thesis). Tomas Bata University in Zlín, Zlín, 2013 (in Czech)

[13] O. Líška and J. Mihalíková, "*Modelovanie, programovanie a simulácia virtuálnej fabriky":* modelovanie v programe Cosimir Professional, (in Slovak), 2008. In: Ai Magazine. Roč. 1, č. 3 s. 74-75, 2008, ISSN 1337-7612

[14] K. Kolomazník, D. Bailey, and M. M. Taylor, "*Deliming of un-bonded and bonded lime from white hide*", Journal of American Leather Chemists Association, vol. 102, 2007.

[15] M. Fialka and H. Charvátová, "Modelling of extraction process in tannery by computer algebraic system" . In *Topical Problems of Fluid Mechanics,* 2007, AVČR, Praha, 2007, ISBN 978-80-87012-04-8

[16] D. Janáčová, et al. "Optimization of Deliming Process". In *1th International Leather Engineering Symposium "Leather Industry, Environment and Progressive Technologies"*. Izmir : Age University, 2009.

Robust stability of control systems with two feedback controllers and interval plants

Radek Matušů and Roman Prokop

***Abstract*—**This contribution deals with investigation of robust stability for closed-loop control systems with two feedback controllers and interval plants. The control design is based on the polynomial approach and subsequent robust stability analysis utilizes the combination of the value set concept and the zero exclusion condition. The presented examples illustrate design of two various sets of controllers and elucidate investigation of robust stability by means of the graphical tests. Finally, the obtained results are confirmed by the control simulations.

***Keywords*—**Two Feedback Controllers, Interval Systems, Polynomial Method, Robust Stability Analysis.

I. Introduction

THE control loop with two feedback controllers represent a relatively general structure in which the weight coefficients for two individual controllers can be selected [1], [2]. Two extreme cases of this choice then correspond either to classical one-degree-of-freedom (1DOF) control structure or (under some presumptions) to two-degree-of-freedom (2DOF) structure. Thus, this structure offers more facilities in controller tuning. However, the robustness of the loop with two feedback controllers and some family of controlled plants has not been studied in many research works so far.

The main goal of this contribution is to present utilization of a graphical robust stability analysis to closed control loops with two feedback controllers and interval plants. The applied control design method is based on the polynomial approach [1], [2] and solution of Diophantine equations [3]. Subsequent robust stability tests of the resulting closed-loop characteristic polynomials with affine linear uncertainty structure employ the well known combination of the value set concept and the zero exclusion condition [4]. The simulation examples show design and tuning of two sets of two feedback controllers, followed by graphical robust stability analysis and control simulation for several "sampled" representatives of the controlled plant family with interval parameters.

The work was performed with financial support of research project NPU I No. MSMT-7778/2014 by the Ministry of Education of the Czech Republic and also by the European Regional Development Fund under the Project CEBIA-Tech No. CZ.1.05/2.1.00/03.0089. This assistance is very gratefully acknowledged.

Radek Matušů and Roman Prokop are with the Centre for Security, Information and Advanced Technologies (CEBIA – Tech), Faculty of Applied Informatics, Tomas Bata University in Zlín, nám. T. G. Masaryka 5555, 76001 Zlín, Czech Republic (e-mails: rmatusu@fai.utb.cz and prokop@fai.utb.cz).

II. Control Systems with Two Feedback Controllers

The diagram of the control system with two feedback controllers adopted from [1], [2] with referred original inspiration in [5] is depicted in Fig. 1.

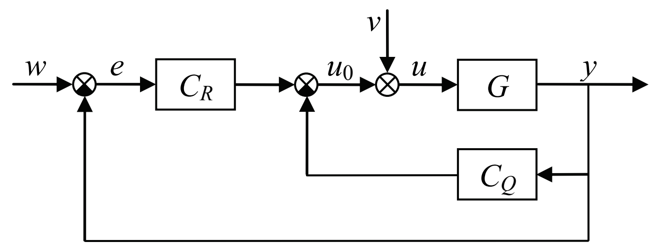

Fig. 1 control loop with two feedback controllers

The blocks C_R and C_Q represent two controllers and G stands for a controlled plant. The symbols of the signals have the following meaning: w – reference signal, e – tracking (control) error, u_0 – difference of controllers' outputs, u – control signal, y – controlled signal (output), v – load disturbance.

The controllers are supposed to be described by transfer functions:

$$C_Q(s) = \frac{\tilde{q}(s)}{\tilde{p}(s)} \tag{1}$$

$$C_R(s) = \frac{r(s)}{\tilde{p}(s)} \tag{2}$$

and controlled plant is given by:

$$G(s) = \frac{b(s)}{a(s)} \tag{3}$$

III. Control Design

A polynomial method is used for control design [1], [2]. It should fulfill the basic requirements such stability and internal properness of the control system, asymptotic tracking of the reference signal and load disturbance rejection.

Laplace transforms of basic signals from Fig. 1 can be obtained as follows [2]:

$$Y(s) = \frac{b(s)}{d(s)}\left[r(s)W(s) + \tilde{p}(s)V(s)\right] \tag{4}$$

$$E(s)=\frac{1}{d(s)}\left\{\left[a(s)\tilde{p}(s)+b(s)\tilde{q}(s)\right]W(s)-b(s)\tilde{p}(s)V(s)\right\} \tag{5}$$

$$U(s)=\frac{a(s)}{d(s)}\left[r(s)W(s)+\tilde{p}(s)V(s)\right] \tag{6}$$

where $d(s)$ is the closed-loop characteristic polynomial:

$$d(s)=a(s)\tilde{p}(s)+b(s)\left[r(s)+\tilde{q}(s)\right] \tag{7}$$

Simple substitution

$$t(s)=r(s)+\tilde{q}(s) \tag{8}$$

leads to the Diophantine equation:

$$a(s)\tilde{p}(s)+b(s)t(s)=d(s) \tag{9}$$

which is critical for control design.

Stability of control loop from Fig. 1 is guaranteed for polynomials $\tilde{p}(s)$ and $t(s)$ obtained as a solution of the Diophantine equation (9) with a stable right-hand polynomial $d(s)$.

In this paper, both reference w and load disturbance v are supposed as stepwise signals with general Laplace transforms:

$$W(s)=\frac{w_0}{s} \qquad V(s)=\frac{v_0}{s} \tag{10}$$

Under this scenario, the asymptotic tracking and load disturbance rejection are ensured by divisibility of both terms $\left[a(s)\tilde{p}(s)+b(s)\tilde{q}(s)\right]$ and $\tilde{p}(s)$ from tracking error equation (5) by the term s. Obviously, it is fulfilled for the following forms of polynomials $\tilde{p}(s)$ and $\tilde{q}(s)$:

$$\tilde{p}(s)=sp(s) \qquad \tilde{q}(s)=sq(s) \tag{11}$$

Consequently, the controllers' transfer functions (1) and (2) can be written as:

$$C_Q(s)=\frac{q(s)}{p(s)} \tag{12}$$

$$C_R(s)=\frac{r(s)}{sp(s)} \tag{13}$$

Since the transfer functions of all components of the control system are supposed to be proper, the following inequalities must hold true:

$$\begin{aligned}&\deg q\le\deg p\\&\deg r\le\deg p+1\end{aligned} \tag{14}$$

The Diophantine equation (9) can be simply rewritten to:

$$a(s)sp(s)+b(s)t(s)=d(s) \tag{15}$$

and the polynomial t (8) can be expressed as:

$$t(s)=r(s)+sq(s) \tag{16}$$

The degrees of polynomials in equations (15) and (16) can be derived (assuming their solvability) [2]:

$$\begin{aligned}&\deg t=\deg r=\deg a\\&\deg q=\deg a-1\\&\deg p\ge\deg a-1\\&\deg d\ge 2\deg a\end{aligned} \tag{17}$$

The forms of polynomials $t(s)$, $r(s)$ and $q(s)$ are:

$$t(s)=\sum_{i=0}^{n}t_is^i \qquad r(s)=\sum_{i=0}^{n}r_is^i \qquad q(s)=\sum_{i=1}^{n}q_is^{i-1} \tag{18}$$

with basic relations among their coefficients [2]:

$$\begin{aligned}&r_0=t_0\\&r_i+q_i=t_i \quad \text{for } i=1,\dots,n\end{aligned} \tag{19}$$

Coefficients of the polynomials $r(s)$ and $q(s)$ can be obtained on the basis of calculated polynomial $t(s)$ and adjustable coefficients $\gamma_i\in\langle 0,1\rangle$ according to:

$$\begin{aligned}&r_i=\gamma_it_i \quad \text{for } i=1,\dots,n\\&q_i=(1-\gamma_i)t_i \quad \text{for } i=1,\dots,n\end{aligned} \tag{20}$$

Obviously, the coefficients γ_i represent weights for numerators of transfer functions (12) and (13). The unit parameters γ_i for all i reduce the control system (Fig. 1) to standard 1DOF configuration ($C_Q(s)=0$). On the other hand, if all $\gamma_i=0$ and moreover reference and load disturbance are stepwise signals, the control system corresponds to 2DOF control structure [2].

Primarily, the control behaviour can be influenced by selection of right-hand polynomial $d(s)$ in Diophantine equation (15). In this contribution, just the simplest method with multiple real roots will be utilized.

IV. Systems with Parametric Uncertainty: Robust Stability Analysis

Systems with parametric uncertainty suppose known fixed structure but on the other hand imprecise knowledge of real physical parameters. Typically, such parameters are bounded by intervals with minimal and maximal possible values. General transfer function describing a system with parametric uncertainty has a form:

$$G(s,q)=\frac{b(s,q)}{a(s,q)} \tag{21}$$

where $b(s,q)$ and $a(s,q)$ are polynomials with coefficients depending on vector of real uncertain parameters q which is typically bounded by some uncertainty bounding set (frequently by using L_∞ norm).

A common practically used case of system with parametric uncertainty is represented by interval plant:

$$G(s,b,a)=\frac{\sum_{i=0}^{m}\left[b_i^-;b_i^+\right]s^i}{\sum_{i=0}^{n}\left[a_i^-;a_i^+\right]s^i} \tag{22}$$

with mutually independent parameters defined by means of their lower and upper limits.

The main object of interest from the viewpoint of robust stability is uncertain closed-loop characteristic polynomial:

$$p(s,q)=\sum_{i=0}^{n}\rho_i(q)s^i \tag{23}$$

where $\rho_i(q)$ are coefficient functions. Corresponding family of closed-loop characteristic polynomials can be written as:

$$P=\{p(s,q):q\in Q\} \tag{23}$$

The robust stability of this family of polynomials means that $p(s,q)$ is stable for all $q\in Q$. However, direct calculation of roots could take extremely long computation times and thus the more sophisticated methods are studied. The choice of specific technique for robust stability analysis depends mainly on the uncertainty structure. The higher level of relation among coefficients yields more complicated investigation and usually requires more powerful and effective tools. Nonetheless, there is a graphical method based on combination of the value set concept and the zero exclusion condition available [4]. It is applicable for the wide range of uncertainty structures, including the very complicated ones.

According to [4], the value set at given frequency $\omega\in\mathbb{R}$ is:

$$p(j\omega,Q)=\{p(j\omega,q):q\in Q\} \tag{24}$$

Practical creation of the value sets can be performed by substituting s for $\omega\in\mathbb{R}$, fixing $\omega\in\mathbb{R}$ and letting q range over Q.

The zero exclusion condition for Hurwitz stability of family of continuous-time polynomials (23) is defined [4]: Suppose invariant degree of polynomials in the family, pathwise connected uncertainty bounding set Q, continuous coefficient functions $\rho_k(q)$ for $k=0,1,2,\ldots,n$ and at least one stable member $p(s,q^0)$. Then the family P is robustly stable if and only if:

$$0\notin p(j\omega,Q) \quad \forall\omega\geq 0 \tag{25}$$

The detailed information on robust stability analysis under parametric uncertainty can be found in [4] and subsequently e.g. in [6], [7].

V. Simulation Examples

Suppose a controlled plant described by the second order interval transfer function:

$$G(s,b,a)=\frac{[0.4,1.6]}{[0.4,1.6]s^2+[0.4,1.6]s+[0.4,1.6]} \tag{26}$$

The nominal system, used for a controller design, is assumed to have the average values:

$$G_N(s)=\frac{1}{s^2+s+1} \tag{27}$$

so the interval family contains all parameter perturbations of the size $\pm 60\%$.

The Diophantine equation (15) takes the form:

$$\left(s^2+s+1\right)s\left(p_1s+p_0\right)+\left(t_2s^2+t_1s+t_0\right)=\left(s+m\right)^4 \tag{28}$$

i.e. it is considered as a polynomial with quadruple roots.

First, the roots are chosen as -0.85, which means $m=0.85$. Besides, the coefficients from (20) are supposed $\gamma_1=\gamma_2=0.5$. Thus, the final controllers are:

$$C_Q(s)=\frac{0.4675s+0.0283}{s+2.4} \tag{29}$$

$$C_R(s)=\frac{0.4675s^2+0.0283s+0.522}{s^2+2.4s} \tag{30}$$

The corresponding family of closed-loop characteristic polynomials (with affine linear uncertainty structure) is:

$$\begin{aligned}p_{CL}(s,a,b)&=a_2s^4+\left(2.4a_2+a_1\right)s^3+\cdots\\&+\left(2.4a_1+a_0+0.935b_0\right)s^2+\left(2.4a_0+0.0565b_0\right)s+0.522b_0\end{aligned} \tag{31}$$

where $a_2,a_1,a_0,b_0\in\langle 0.4,1.6\rangle$.

ISBN: 978-1-61804-321-4

The value sets for the family of polynomials (31) and frequency range from 0 to 1.4 with step 0.05 are depicted in Fig. 2.

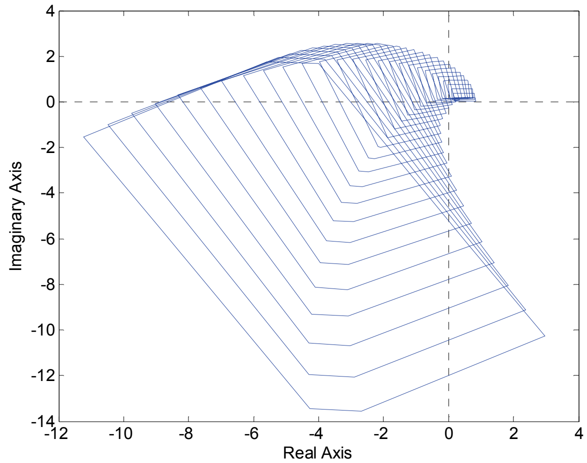

Fig. 2 value sets for family of closed-loop characteristic polynomials (31)

In spite of the fact that the view to the value sets near the origin of the complex plane is relatively distant, it is distinguishable that the zero point is included in the value sets. Consequently, the family of closed-loop characteristic polynomials (31) is not robustly stable.

The Fig. 3 shows the simulations of the output signals of 256 “sampled plants” from the interval family (26). All four interval parameters were divided into 3 subintervals of the equal size and so the obtained 4 values for 4 parameters lead to $4^4 = 256$ plants for simulation. Moreover, the red curve represents the output signal of the nominal plant (27). Besides, the stepwise reference signal changing from 1 to 2 in first third of the simulation time and step load disturbance -0.5 affecting the input to the controller plant during the last third of simulation are supposed.

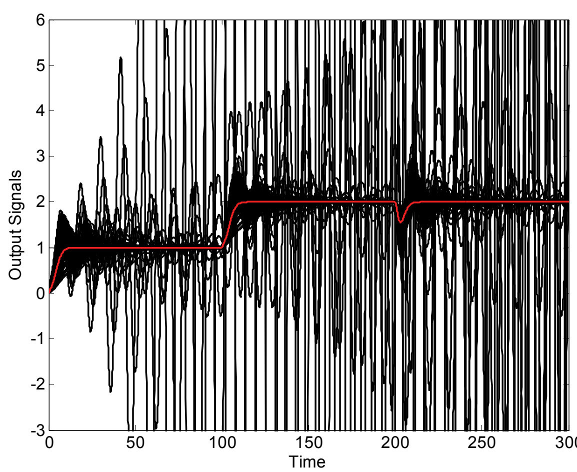

Fig. 3 control of “sampled plants” from interval family (26) by two feedback controllers (29) and (30)

As can be seen from Fig. 3, although some members of the family (26) are robustly stabilized (e.g. nominal system) by two feedback controllers (29) and (30), the other members are not so the system is really robustly unstable as had been already proven by Fig. 2.

The selection of coefficients γ_i do not influence the robust stability of the control loop with two feedback controllers. It would change “only” control performance but the system remains either robustly stable or robustly unstable for all possible γ_i.

Now, different quadruple roots are supposed, i.e. $m = 1.3$. The weight coefficients are considered again as $\gamma_1 = \gamma_2 = 0.5$. This results in controllers:

$$C_Q(s) = \frac{2.47s + 2.294}{s + 4.2} \tag{32}$$

$$C_R(s) = \frac{2.47s^2 + 2.294s + 2.8561}{s^2 + 4.2s} \tag{33}$$

and subsequently in the family of closed-loop characteristic polynomials:

$$\begin{aligned} p_{CL}(s,a,b) &= a_2 s^4 + (4.2a_2 + a_1)s^3 + \cdots \\ &+ (4.2a_1 + a_0 + 4.94b_0)s^2 + (4.2a_0 + 4.588b_0)s + 2.8561b_0 \end{aligned} \tag{34}$$

with $a_2, a_1, a_0, b_0 \in \langle 0.4, 1.6 \rangle$.

The value sets for this new polynomial family (34) (for frequency 0:0.05:1.5) are shown in Fig. 4.

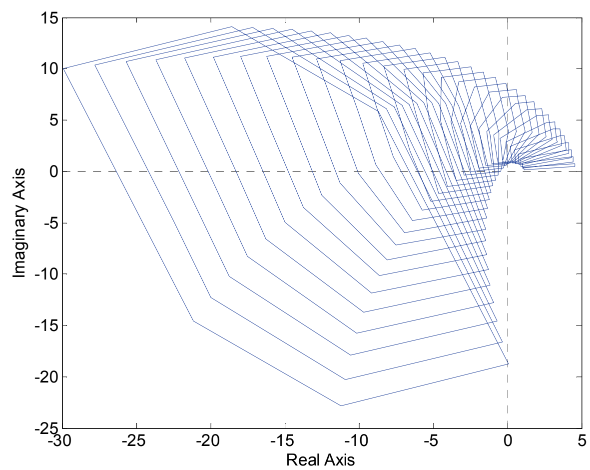

Fig. 4 value sets for family of closed-loop characteristic polynomials (34)

In this case, the Fig. 4 reveals that the complex plane origin is excluded from the value sets. Moreover, the family contains a stable member so one can conclude that the closed-loop characteristic polynomial (34) is robustly stable.

The output signals simulated under the same conditions as for the previous controller are shown in Fig. 5. As can be

ISBN: 978-1-61804-321-4

seen, all "sampled plants" are really stabilized by two feedback controllers (32) and (33).

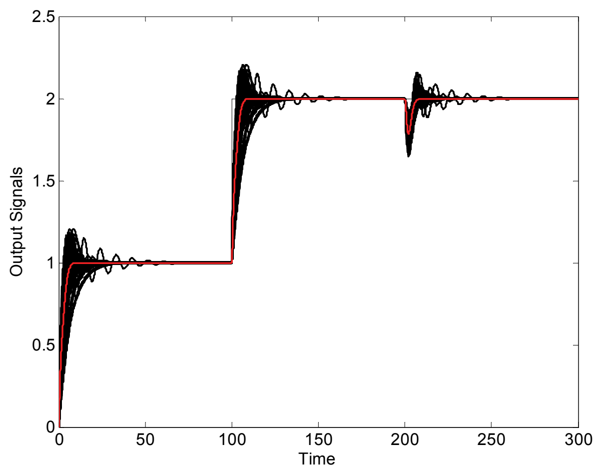

Fig. 5 control of "sampled plants" from interval family (26) by two feedback controllers (32) and (33)

Needless to say, different choice of coefficients γ_i would not influence the robust stability, again.

VI. Conclusion

The contribution has been focused on investigation of robust stability for closed-loop control systems containing two feedback controllers and interval plants by means of plotting the value sets and subsequent application of the zero exclusion condition. The controller design itself is based on the polynomial approach. The computational examples have demonstrated analysis and simulation of robustly stable or unstable control loops with second order interval plant. The paper has also shown that the choice of weight coefficients for numerators of the individual feedback controllers influences "only" control performance but has no impact on the robust stability or instability.

References

[1] P. Dostál, F. Gazdoš, V. Bobál, J. Vojtěšek, "Adaptive control of a continuous stirred tank reactor by two feedback controllers", in *Proceedings of the 9th IFAC Workshop on Adaptation and Learning in Control and Signal Processing*, Saint Petersburg, Russia, 2007.

[2] P. Dostál, F. Gazdoš, V. Bobál, "Design of Controllers for Time Delay Systems: Integrating and Unstable Systems" in *Time-Delay Systems*, D. Debeljkovic, Ed. Rijeka, Croatia: InTech, 2011, pp. 113-126.

[3] V. Kučera, "Diophantine equations in control – A survey", *Automatica*, vol. 29, no. 6, 1993, pp. 1361-1375.

[4] B. R. Barmish, *New Tools for Robustness of Linear Systems*, Macmillan, New York, USA, 1994.

[5] R. Ortega, R. Kelly, "PID Self-Tuners: Some Theoretical and Practical Aspects", *IEEE Transactions on Industrial Electronics*, vol. 31, no. 4, pp. 332-338.

[6] R. Matušů, R. Prokop, "Graphical analysis of robust stability for systems with parametric uncertainty: an overview", *Transactions of the Institute of Measurement and Control*, vol. 33, no. 2, 2011, pp. 274-290.

[7] R. Matušů, R. Prokop, "Robust Stability Analysis for Systems with Real Parametric Uncertainty: Implementation of Graphical Tests in Matlab", *International Journal of Circuits, Systems and Signal Processing*, vol. 7, no. 1, 2013, pp. 26-33.

Radek Matušů was born in Zlín, Czech Republic in 1978. Currently, he is a Researcher at Faculty of Applied Informatics of Tomas Bata University in Zlín, Czech Republic. He graduated from Faculty of Technology of the same university with an MSc in Automation and Control Engineering in 2002 and he received a PhD in Technical Cybernetics from Faculty of Applied Informatics in 2007. The main fields of his professional interest include robust systems and application of algebraic methods to control design.

Roman Prokop, born in 1952, is a Full Professor at Faculty of Applied Informatics of Tomas Bata University in Zlín, Czech Republic. He graduated from Czech Technical University in Prague in 1976 and received a PhD from Slovak University of Technology in Bratislava in 1983. He was an Associate Professor from 1996 and a Full Professor from 2004. He aims his pedagogical and research work to automatic control theory, algebraic methods in control design and optimization. The main interests of the latest period are uncertain and robust systems, autotuning of controllers and time-delay systems.

A GSM locator for security applications

Milan Adamek, Jiri Jakubec and Martin Pospisilik

Abstract **—** This work deals with the construction of a locator to determine locations using GSM technology. The locator´s design will be tailored especially for the mobile security of more expensive items. The theoretical part will discuss different ways of positioning - using GSM technology in detail. In the conclusion, the benefits of GSM localisation for security applications are evaluated and compared to satellite locations.

Keywords **—** locator, GSM, mobile security, satellite

I. INTRODUCTION

THE first mention of mobile networks, i.e. portable communications, come from the Nordic countries - Finland, Norway, Sweden and Denmark, especially. Mobile communications were used above all for maritime transport; and had two basic differing features from the existing networks. The greatest drawback was the mutual incompatibility of individual networks; while the second distinct feature was (the use of) the analogue technologies that were used for the operation of these networks.

With the advent of digitisation, GSM networks were created that allowed data transfers. Today´s widespread SMS messaging was used for the first time ever in these GSM networks. They belonged to the so-called second generation, i.e. to the 2G category. Since it involved being a digital system, it was possible to connect to the Internet; to begin with, only through using WAP protocols. As a result of the slow data-transmission speed of the GSM network, other elements were added.

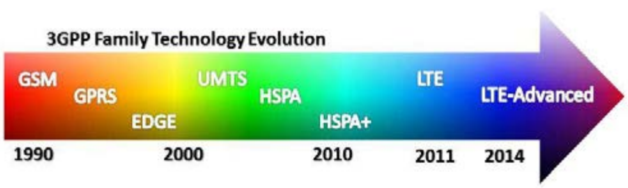

Fig. 1 the development of mobile networks [1]

This work was supported in part by the European Regional Development Fund under the project CEBIA-Tech No. CZ.1.05/2.1.00/03.0089 and by OPVK project CZ.1.07/2.3.00/30.0035.

Milan Adamek is with Faculty of applied informatics, Tomas Bata University in Zlin, Nad Stranemi 4511, 76005 Zlin, Czech Republic (corresponding author, phone: +420 606 417 702; e-mail: adamek@fai.utb.cz).

Jiri Jakubec is with Faculty of applied informatics, Tomas Bata University in Zlin, Nad Stranemi 4511, 76005 Zlin, Czech Republic (e-mail: jakubec@fai.utb.cz).

Martin Pospisilik is with Faculty of applied informatics, Tomas Bata University in Zlin, Nad Stranemi 4511, 76005 Zlin, Czech Republic (phone: +420 606 417 702; e-mail: pospisilik@fai.utb.cz)

Like, for instance, GPRS, which was followed by EDGE. These elements thus ranked GSM networks among the 2.5G generation and 2.75G category.Of course, nowadays, this network has already been superceded. On the market today, are third generation UMTS mobile networks, which allow fast data-transfers ranging in the order of Mb/s. Third-generation networks, i.e. 3G networks, have been in use for the past 10 years - with the highest achieved speed of HSPA + 28MB/s.

Their successor is the fourth generation, i.e. 4G networks for really-fast-data-transfers - in the order of 100Mb/s for moving objects, and 1 GB/s for static objects [1].

GSM networks are commonly used for voice-calls, the transmission of messages in the form of SMS, and data transmissions. The aim of this paper is to exploit other GSM network services – and that is, for the determination of a position in the field. Unlike GPS technology, line-of-sight with satellites is unnecessary in order to determine location, thus GPS technology can also be used in places where satellites are not available to determine a required location.

A proposed GPS locator is presented within the framework of this paper, and mention is made of inaccuracies in the course of determining positions.

II. GSM LOCALISATION

The main assumption of GSM localisation is the deployment of base stations across the whole structure of the GSM network. The area is divided into cells, whereby one cell is served by one BTS station or the BTS station is located at the interface and serves multiple cells – in such cases, we talk about sectors. The radius and the cell density are dependent on the estimated number of active mobile devices, or the population density in the given area. The number of BTS stations significantly affects the accuracy of the determination of a location [6].

Mobile stations communicate at any one instant with just one BTS station, but have information about other available BTS stations. BTS stations have a fixed location and are stationary, unlike mobile devices [6].

The following two identifiers important are for localisation:

1) The cell ID is the unique identifier of the BTS base station.

2) The Timing Advance (TA) is the parameter representing the signal propagation time between the mobile device and the network.

A. Cell ID

Each cell in a network has its own unique identifier. Its uniqueness is ensured within the framework of an operator in the given state. When logging into the network, the the mobile device can directly determine its location. Accuracy depends on the size of the area covered by the BTS station. Cell Sector is used for more accurate sectorisation - where the cell is divided into three sectors, which allows a two-thirds greater degree of precision [7].

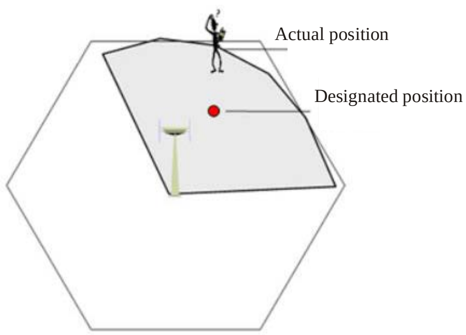

Fig. 2 the Cell ID [5]

The estimated location of the mobile device is located in the centre of the field so created. TDMA specification requires that the chain manages to travel to the BTS station and back within half of the reserved 577 µs (microseconds). After deducting time caused by losses and signal quality, 233 microseconds remain. Within this time, the signal has to travel to the BTS station and back. If we multiply this radio signal speed data, we find that the signal may cover a track of up to 70,000 meters. This also sets the maximum radius of the BTS to 35 km [2].

B. *TA Timing advance*

The TA Identifier gives us the delay value between the mobile device and the BTS station. The value can be determined directly during a telephone call, after activation of the service menu, with values from 0 to 63. The higher the value, the farther one is from the BTS station with which it is communicating. This parameter is stored in 4 bits, and if one multiplies this value by 547 m, we can ascertain the distance from the BTS station [7].

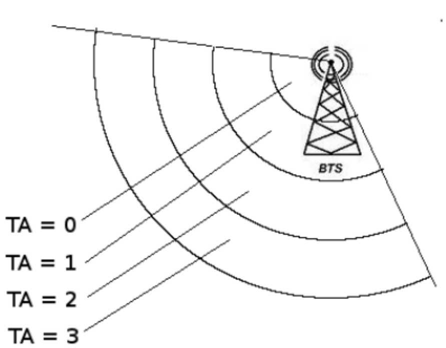

Fig. 3 TA identifier [5]

III. GSM LOCALISATION METHODS

With this knowledge of the important parameters of the GSM network and an adequate list of the greatest possible number of BTS stations, we can perform localisation itself by exploiting the GSM network.

A. *Cell of Origin*

Cell of Origin (COO) is a method based on the cellular structure of the GSM network. The top priority for this method is the Cell ID parameter, hence the accuracy of this method. In densely populated areas, the tolerance is about 200 meters; in less populated areas, the tolerance can theoretically reach up to 35 kilometers [6].

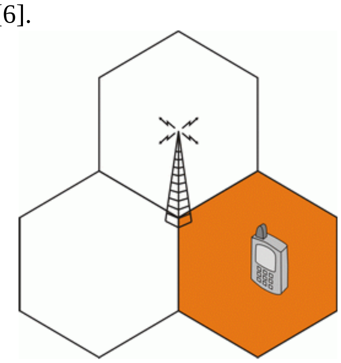

Fig. 4 the COO method [8]

B. *The TA method*

TA is a method based on the knowledge of the distance of a mobile device from at least three BTS stations. For the method to work, it is necessary to adjust the mobile device such that it will know how to provide the requested information. Usually, it is sufficient to upload new firmware or use the SIM Toolkit application. When properly used, we can refine tolerance down to 125 meters [7].

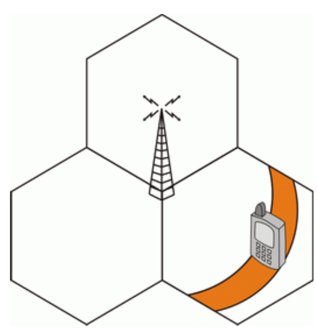

Fig. 5 TA method [3]

C. *Time-Of-Arrival*

Time-Of-Arrival (TOA) is a method based on the TA method. Its basis is the knowledge of the distances from three BTS stations. This information however, is obtained from the BTS base stations. For this, we need mutual synchronisation - which does not normally occur. The method requires additional investments; while in urban areas above all, it does not produce better results than the COO method [6].

ISBN: 978-1-61804-321-4

D. Enhanced Cell Global Identity

Enhanced Cell Global Identity (E-CGI) is a method that complements and rounds out the Cell of Origin and Timing advance methods for measuring signal levels. The E-CGI method is used for calculating the distance of the mobile device from the BTS base-station. Areas with the most likely occurrence are identified according to the measured signal levels at the site/location of the mobile device and the knowledge of the transmission peformance of the BTS base stations. The accuracy of this method is around 50-550 meters for densely populated areas, and 250 m to 8 km in rural areas with lower populations [7].

E. Enhanced Observed Time Difference

The Enhanced Observed Time Difference (E-OTD) method is based on the installation of Location Measurement Unit (LMU) reference receivers within the context of the whole GSM network.

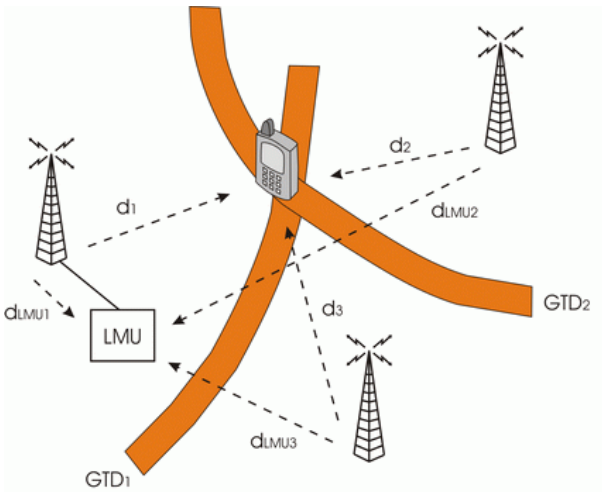

Fig. 6 the E-OTD method [4]

The reference receivers perform measurements of the real time differences in BTS stations´ broadcast signals. If the BTS stations broadcast synchronously, the RTD value would be zero. For determining the time differences in signal reception between two BTS stations, an estimate of the given area is made to determine where these all have the same distance. In the given area, the time difference of signal arrival is designated as the Geometric Time Difference (GTD) [6].

F. Angle of Arrival

Angle of Arrival (AOA) is a method that requires the use of directional antennas and knowledge of radiation characteristics. When applying this method, the angle at which the signal is received is measured. This can be performed at BTS stations as well as mobile devices. The result of these measurements is a line that intersects the BTS stations and the mobile device. With this method, the minimum number of BTS stations is set at two; the third station makes the method even more precise. The requisite location is determined by the intersection of the lines - with an accuracy of around 300m [6].

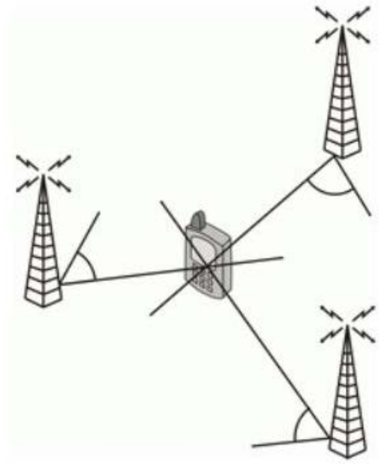

Fig. 7 the E-OTD method [9]

IV. GSM LOCATOR REALISATION

In the GSM locator design process, priority was given to two basic requirements – namely, the requirement for small dimensions of the locator, and the requirement for long battery life. The Cell of Origin (COO) method was used for localisation by the locator.

A. The GSM module

The basis of the whole system is the GSM module in which the SIM card is placed. The locator uses the smallest GSM module on the market from Enfora - the Enabler IIIG, type: GSM0308.

The module is functional both in Europe and in the USA. It does not have a screen, microphone or keyboard – there is no need for these components [10].

The module can communicate across all GSM wave-bands, including GPRS data transmission. It includes a small antenna. Energy consumption, when demanded, is around 230 mA and only 10 mA in idle mode. These values are very low and contribute to extending the overall device battery life [11].

Fig. 8 the GSM Module [12]

B. The Control module

The PCB for controlling the circuit includes an interface for communicating with the quad-band GSM/GPRS module, microcontroller and microchip, as well as an on/off switch and an SOS button.

ISBN: 978-1-61804-321-4

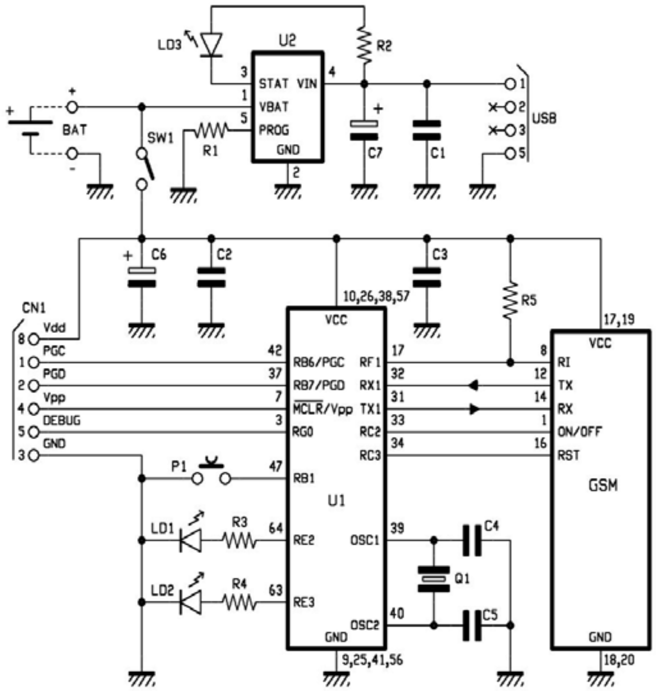

Fig. 9 control circuit scheme [13]

C. The operating principle of the GSM locator

The control circuit is programmed in a loop that waits for a certain event. This event initialises the entire programme and it starts to search for the position. Such events may include the following:

- Incoming phone calls. In this case, the device hangs up the call and starts detecting its current position. After finding it, it sends the data to the caller's number. The caller's number must be displayed correctly - it cannot be hidden, and must be on the list in the GSM locator´s memory [13].
- Incoming SMS messages. The device, when receiving SMS messages, distinguishes whether it is a configuration SMS message or a request for it to send its current location [13].
- Pressing the SOS button. This feature is optional, and allows the sending of the current location after being pressed. Its practical use is only for tracking people. The SOS button cannot be used to secure a bicycle, only for testing purposes [13].
- The last way of determining the location is automatic initialisation. This can be set with a view to the time parameter, as well as to change the location of the device. The GSM module does not contain a gyroscope, but recognises changes in location according to changes in the actual BTS station [14].

D. GSM locator configuration

All configuration of the GSM module is done through sending SMS messages to the GSM module. Table 1 provides an overview of possible settings.

V. TESTING THE PROPOSED GSM LOCATOR

The GSM locator was tested in two ways. In the first case, the locator was sited on moving object (an automobile) and the reliability of the locator was determined. In the second, the test was performed on a randomly selected location, i.e. the GSM locator had a fixed location.

A. Testing the reliability of a moving GSM locator

The proposed locator was fitted to a car which was moving around in a densely-settled area and then in an area with low population density. Fig. 13 depicts the testing of the locator in a heavily-settled area.

Fig. 10 map of a high-density settlement area

The dashed line represents the locator´s movements, the points designated by the letters A through K are then, the evaluated positions of the locator. When testing the locator in a heavily-settled urban environment, the locator´s imprecision was greater – even reaching 150 m between the actual position of the locator and its evaluated positions.

In areas with fewer buildings, the location evaluations precision was much better; in this case, the difference between the locator position and its evaluation was less than 30 m. A sample locator test is presented in Fig. 14.

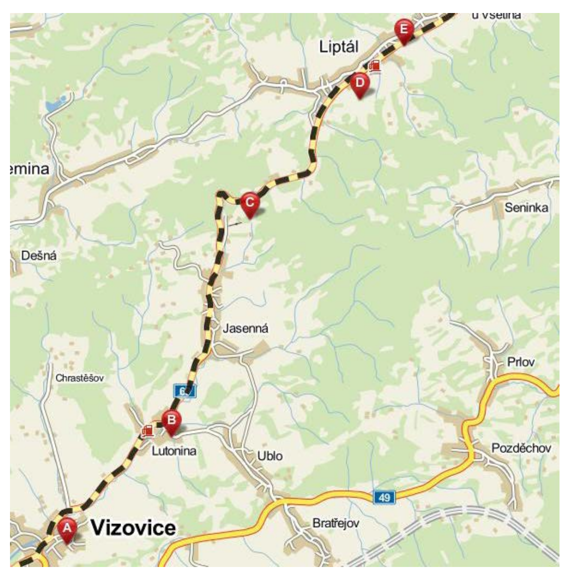

Fig. 11 map of a thinly-settled area.

B. Testing the GSM locator´s reliability while determining random locations

In view of the fact that the GSM locator can be used for securing articles against theft, it was necessary to evaluate the locator´s inaccuracy in the case where the locator is a long time in the same location, i.e. does not alter its position. In this case, the search for GSM locator locations was with the aid of SMS messages. In this case, the difference between the actual location of the locator and the evaluated location was no greater than 25 m.

Fig. 12 random location test

VI. The Evaluation of GSM Localisation Benefits for Security Applications

GSM localisation technology provides the possibility of localisation in areas where a GPS signal is unavailable - especially in dense urban areas without a direct line of sight to satellites. In contrast, in the remote places of our planet, GSM localisation is impossible, or very inaccurate. The possibility of localisation using GSM networks in buildings is the greatest benefit of this technology. Combined with low battery capacity demands and low cost, a GSM locator has the possibility of succeed in the locator market - especially for securing items.

One of the biggest disadvantages of this technology includes its inaccuracy in determining locations. Given that it is impossible to predict where stolen articles fitted with a GSM locator can end up, we cannot rely on an acceptable level of tolerance which the device indicates in densely populated areas. Unfortunately, when using a GSM locator, it can happen that when the device sends us information about its location this is so distorted that localisation is virtually impossible.

The GSM locator presented in this paper was designed with the intent to protect bicycles against theft. The locator can be placed under the seat, where both types of GSM locator can be placed. The first type of locator has a built-in battery for its operations; with the second type, the battery is located in the saddle tube, which holds the seat.

Fig. 13 installation of the GSM locator

References

[1] P. Moos, T. Zelinka, V. Malinovsky, *Telecommunication services*. Prague: CVUT, 2007, ch. 3.

[2] P. Brabenec. (2013, Januar 28). Principles of operation of the GSM network. [Online]. Available: http://www.brabenecz.wz.cz/principy_fungovani_gsm.htm

[3] O. Dudek. (2015, March 15). Structure of the GSM network. [Online]. Available: http://radio.feld.cvut.cz/personal/mikulak/MK/MK05_semestralky/Struktura_GSM_Ondrej_Dudek.pdf

[4] S. Shafi. (2015, February 2). SIM card. [Online]. Available: http://uthmag.com/wp-content/uploads/2012/07/SIM-Cards.jpg

[5] K. Karanoka. (2014, December 20). WAP push process. [Online]. Available: http://upload.wikimedia.org/wikipedia/commons/f/f2/WAP_Push_Process.jpg

[6] M. Kopp. (2014, December 10). Methods for determining the location of mobile devices in the GSM network. [Online]. Available: http://radio.feld.cvut.cz/personal/mikulak/MK/MK06_semestralky/UrceniPolohyvGSM_KoppM.pdf

[7] L. Szteffek. (2015, January 18). GSM localization. [Online]. Available: http://www.lukasszteffek.cz/files/fit/projekt_sen.pdf

[8] M. Orlich. (2014, November 19). The localization method in GSM. [Online]. Available: http://access.feld.cvut.cz/view.php?cisloclanku=2006022801

[9] L. Enfora. (2014, October 24). Enfora enabler IIIG. [Online]. Available: http://www.farnell.com/datasheets/876254.pdf.

[10] C. Srenk. (2015, January 12). Localizzatore tramite rete GSM. [Online]. Available: http://www.futuraelettronica.net/pdf_ita/7100-FT833M.pdf

[11] J. Novak. (2014, December 8). GSM localization. [Online]. Available: https://www.t-mobile.cz

[12] K. Rak. (2014. November 11). PHPBB group. [Online]. Available: http://www.futurashop.it/forum_/

[13] M. Pospisilik, L. Kouril, I. Motyl, M. Adamek, "Single and double layer spiral planar inductors optimisation with the aid of self-organising migrating algorithm", in *Proc. 11th WSEAS International Conference on Signal Processing, Computational Geometry and Artificial Vision.* Venice, 2011, pp. 104 - 108.

[14] M. Pospisilik, L. Kouril, I. Motyl, M. Adamek, "Switching power supply for an autonomous monitoring system", in *Proc. WSEAS International Conference on Systems: Latest Trends on Systems*. Greece, 2010. pp. 431-434.

Identification of dynamical systems using Levenberg-Marquardt learning algorithm for recurrent complex-valued neural networks

Edmundo P. Reynaud and Ieroham S. Baruch.

***Abstract*—**The use of the Levenberg-Marquardt learning algorithm is scarce in applications with Complex-Valued Artificial Neural Networks, mainly because of the difficulty in obtaining the correction terms for the weights to be trained with an algebraic approach. In this work, a diagrammatic based procedure is proposed for the derivation and implementation of said algorithm for a Complex-Valued Recurrent Neural Network. Furthermore, we get some comparative simulation results between the Complex-Valued Back-Propagation algorithm and our proposed Levenberg-Marquardt algorithm, for the application of a Recurrent Neural Network on a plant identification problem.

***Keywords*—**Complex-valued neural networks, Levenberg-Marquardt learning algorithm, System identification.

I. Introduction

There has been a rise in the use of Complex-Valued Artificial Neural Networks (**CVNN**) in the last decade, this is because models of certain physical phenomena have a better approach in the complex-domain than its real-domain counterparts. Examples of these are seen in the fields of electromagnetism, optics, power systems, electronic systems, and digital image processing, to name a few. ([1], [2], [3]).

Although its applications are not as spread in the field of mechanical systems, there are some works (see [3], [7]) that propose the use of **CVNN** for identification and control of mechanical plants that report quite good results.

The extension to the complex-domain of Recurrent Neural Networks enable its use for tasks that can be solved with the real-domain approach, but with better performance and less computational cost. For example, in [4], **CVNN** are used to identify analogic electric circuits; in [5] authors use a **CVNN** as a behavior predictor for a wind-powered generation system; or in [6], a **CVNN** is proposed for the design of FIR digital filters.

In [8] and [9] a method is proposed to derive a Back-Propagation learning algorithm for a **CVNN**, applied to the identification and control of a **MIMO** mechanical plant with nonlinear and oscillatory dynamics. Following that line of work, we use the diagrammatic methods presented in [10] to derive a second order Levenberg-Marquardt learning algorithm for the same proposes. We further make a comparison in performance between the complex-valued Back-Propagation used in [8], [9] and the Levenberg-Marquardt learning algorithms developed through this work.

E. P. Reynaud is a Master in Science student in the Department of Automatic Control, CINVESTAV-IPN, D.F, Mexico. E-mail: eperez@ctrl.cinvestav.mx

I. S. Baruch is with the Department of Automatic Control, CONVESTAV-IPN, D.F, Mexico. E-mail: baruch@ctrl.cinvestav.mx

II. Topology and Levenberg-Marquardt Learning of Real-Valued Recurrent Neural Networks

We consider the Real Valued Recurrent Neural Network (**RVRNN**) topology shown in Fig 1.

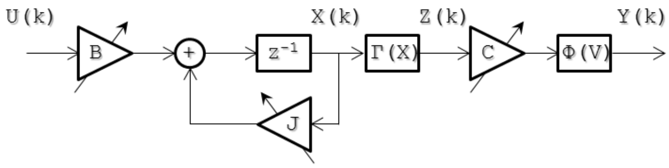

Fig.1 Block-diagram representation of a RVRNN

This network consists of an input layer, a recurrent hidden layer with linear behavior, and an output layer. The description of the network is given by the following equations:

$$X(k+1) = JX(k) + BU(k) \tag{1}$$

$$Z(k) = \Gamma[X(k)] \tag{2}$$

$$V(k) = CZ(k) \tag{3}$$

$$Y(k) = \Phi[V(k)] \tag{4}$$

Where: $X \in \mathbb{R}^n$ is the state vector, $U \in \mathbb{R}^m$ is the input vector, $Y \in \mathbb{R}^L$ is the output vector, $Z \in \mathbb{R}^n$ is the state vector of the hidden layer, $\Gamma[\cdot], \Phi[\cdot]$ are vector-valued activation functions with compatible dimensions; J, B, C are the weight state, weight input and weight output matrices with dimensions $(n \times n)$, $(n \times m)$ and $(L \times n)$ respectively.

The matrix J is a diagonal matrix with blocks J_j as its elements, which must meet the stability condition:

$$\left|J_j\right| < 1, \qquad j = 1, 2, \ldots, N \tag{5}$$

This **RVRNN** has a canonical Jordan form, which means that it has the minimum number of parameters subject to training, as well as complete parallel integration. It also presents controllability and observability properties, and

ISBN: 978-1-61804-321-4

stability conditions. The performance index to be minimized used in the training algorithm is given by the equation:

$$\zeta(k) = \frac{1}{2}\sum_j [E_j(k)]^2, \qquad \zeta = \frac{1}{N_e}\sum_k \zeta(k) \tag{6}$$

$$E(k) = Y_p(k) - Y(k) \tag{7}$$

Where equation (7) describes the identification error. The instantaneous Means Squared Error (**MSE**) $\zeta(k)$ is used in on-line applications, while the total **MSE** denoted by ζ is used for one epoch N_e in off-line applications. The general recursive real-valued Levenberg-Marquardt (**RVLM**) learning algorithm for any weight vector W is described by the following equation (see [11]):

$$W(k+1) = W(k) + P(k)\cdot DY[W(k)]\cdot E(k), \quad |W_j| < W_0 \tag{8}$$

Where: W_0 is a restricted region for the weight W_j, P can be interpreted as the covariance matrix of the weight's estimation, and $DY[W]$ is the local gradient component of the output of the network with respect to W. Applying certain diagrammatic rules (see [10]) to the **RVRNN** given in Fig.1, we obtain its adjoint topology, which is shown in Fig.2.

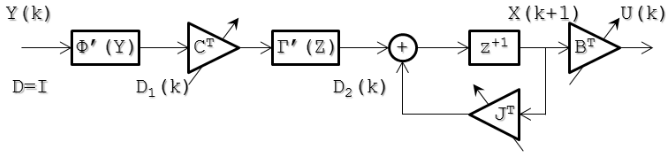

Fig.2 Block-diagram of the adjoint network for the RVRNN

Then gradient terms can be derived directly from the adjoint topology, which are described by the following equations:

$$D_1(k) = \Phi'[Y(k)]\cdot D \tag{9}$$

$$D_2(k) = \Gamma'[Z(k)]\cdot C^T \cdot D_1(k) \tag{10}$$

$$DY[C(k)] := \partial Y(k)/\partial C(k) = D_1(k)\cdot Z^T(k) \tag{11}$$

$$DY[J(k)] := \partial Y(k)/\partial J(k) = D_2(k)\cdot X^T(k) \tag{12}$$

$$DY[B(k)] := \partial Y(k)/\partial B(k) = D_2(k)\cdot U^T(k) \tag{13}$$

Where: $D = I$ is a unitary input for the adjoint topology. The matrix P is computed recursively using the following equation:

$$P(k) = \alpha^{-1}[P(k-1) - P(k-1)\cdot\Omega_{W(k)}\cdot S^{-1}_{W(k)}\cdots \cdot\Omega^T_{W(k)}\cdot P(k-1)] \tag{14}$$

Where the matrices Ω_W and S_W are given by:

$$\Omega^T_{W(k)} = \begin{bmatrix} & DY^T[W(k)] & \\ 0 & \cdots\ 1\ \cdots & 0 \end{bmatrix} \tag{15}$$

$$S_{W(k)} = \alpha\Lambda + \Omega^T_{W(k)}\cdot P(k-1)\cdot\Omega_{W(k)} \tag{16}$$

$$\Lambda^{-1} = \begin{bmatrix} 1 & 0 \\ 0 & \rho \end{bmatrix} \tag{17}$$

The matrices P and S_W have dimensions $(N_W \times N_W)$ and (2×2) respectively, where N_W is the number of weights in the vector W. The matrix Ω_W has dimension $(N_W \times 2)$, the second row of Ω^T_W consists of $(N_W - 1)$ zeroes and a unit element in the i-th position computed by:

$$i = k\cdot \mathrm{mod}(N_W) + 1 \tag{18}$$

The parameters for the algorithm should be restricted as follows:

$$10^{-6} \le \rho \le 10^{-4}, \qquad 0.97 \le \alpha \le 1.00 \qquad 10^3 \le P(0) \le 10^6 \tag{19}$$

III. Topology and Levenberg-Marquardt Learning of Complex-Valued Recurrent Neural Networks

We consider a **CVRNN** topology with real-valued input $U(k)$ and output $Y(k)$ signals, complex-valued internal state $X(k)$ and hidden state $Z(k)$ vectors, and complex-valued J, B, C weight matrices.

The matrix J is a diagonal matrix with the neuron eigenvalues as its block-elements. Complex eigenvalues come in pairs of complex conjugate numbers, while real eigenvalues come as single values. For the matrices B and C, its elements also come in pairs of complex conjugate numbers or single real numbers, and its positions are related to the positions of the elements of J.

Although the internal state and parameter matrices of the neuron are complex-valued, the complex conjugate pairs produce a real-valued output of the network, which yields a real-valued identification error signal. That way we can use the same performance index as in the **RVRNN** case to be minimized, given in (6).

Because the vector $Z(k)$ is complex-valued, the activation function $\Gamma[\cdot]$ must be also complex-valuated; not so for the activation function $\Phi[\cdot]$ given that the product $CZ(k)$ is real-valued. In this work we consider two types of hyperbolic tangents for the activation function $\Gamma[\cdot]$, one natural and one constructed, which yield two different topologies for the **CVRNN**.

A. CVRNN Topology with First Type Activation Function.

The first activation function considered is described by the following equation:

ISBN: 978-1-61804-321-4

$$f(\mathrm{z}) = \tanh(\mathrm{z}),$$
$$\mathrm{z} \in \mathbb{C} \setminus \left\{ z : \mathrm{z} = 0 \pm \frac{2n-1}{2}\pi i, \quad \forall n \in \mathbb{N} \right\} \tag{20}$$

This activation function has singularities at points $\mathrm{Re}(z) = 0$, $\mathrm{Im}(z) = \{\pm\frac{1}{2}\pi, \pm\frac{3}{2}\pi, \ldots\}$ of the complex domain. Because of this, we restrict the domain of said function near these points of singularity.

The block diagram of the **CVRNN** that uses this activation function is the same as the one shown in Fig.1. The mathematical description of this topology is the same as in equations (1)-(4) but now with some complex-valued variables. The vectors and matrices for the **CVRNN** topology are given as follows: $J \in \mathbb{C}^{n \times n}$ the feedback weight matrix, $B \in \mathbb{C}^{n \times m}$ the input weight matrix, $C \in \mathbb{C}^{L \times n}$ the output weight matrix, $X \in \mathbb{C}^{n}$ the internal state vector, $Z \in \mathbb{C}^{n}$ the hidden layer state vector, $U \in \mathbb{R}^{m}$ network input, $Y \in \mathbb{R}^{L}$ the network output, $\Gamma[\cdot]$ a complex-valued activation function given by (20), and $\Phi[\cdot]$ a real-valued activation function $f(\cdot) = \tanh(\cdot)$; n, m, L are the number of internal states, inputs and outputs respectively.

The matrix J is a diagonal matrix where its block-elements must meet the stability restriction given in (5). This type of representation allows us to apply diagrammatic rules to derive the adjoint network shown in Fig.3, and use it to derive the gradient terms needed for the learning algorithm.

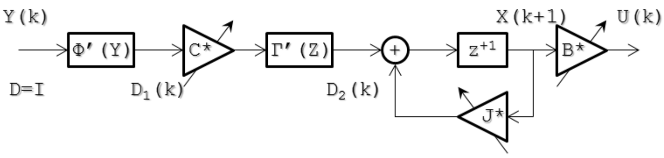

Fig.3 Block-diagram representation of the adjoint network for the CVRNN with first activation function

The complex-valued Levenberg-Marquardt (**CVLM**) algorithm for any weight vector W is described by the following equation:

$$W(k+1) = W(k) + P(k) \cdot DY[W(k)] \cdot E(k),$$
$$|W_j| < W_0 \tag{21}$$

Where: W_0 is a restricted region for the weight W_j. The gradient terms for the complex-valued network with the first type activation function are described by the following equations:

$$D_1(k) = \Phi'[Y(k)] \cdot D \tag{22}$$

$$D_2(k) = \Gamma'[Z(k)] \cdot C^* \cdot D_1(k) \tag{23}$$

$$DY[C(k)] := \partial Y(k)/\partial C(k) = D_1(k) \cdot Z^*(k) \tag{24}$$

$$DY[J(k)] := \partial Y(k)/\partial J(k) = D_2(k) \cdot X^*(k) \tag{25}$$

$$DY[B(k)] := \partial Y(k)/\partial B(k) = D_2(k) \cdot U^*(k) \tag{26}$$

Where the $(*)$ superscript denotes a complex conjugate and transposed vector, $D = I$ is a real-valued identity matrix input for the adjoint topology. The matrix P is computed recursively using the following equation:

$$P(k) = \alpha^{-1}[P(k-1) - P(k-1) \cdot \Omega_{W(k)} \cdot S_{W(k)}^{-1} \cdots$$
$$\cdot \Omega_{W(k)}^* \cdot P(k-1)] \tag{27}$$

Where the matrices Ω_W and S_W are given by:

$$\Omega_{W(k)}^* = \begin{bmatrix} & DY^*[W(k)] & \\ 0 & \cdots & 1 & \cdots & 0 \end{bmatrix} \tag{28}$$

$$S_{W(k)} = \alpha\Lambda + \Omega_{W(k)}^* \cdot P(k-1) \cdot \Omega_{W(k)} \tag{29}$$

$$\Lambda^{-1} = \begin{bmatrix} 1 & 0 \\ 0 & \rho \end{bmatrix} \tag{30}$$

Again, the matrices P and S_W have dimensions $(N_W \times N_W)$ and (2×2) respectively, where N_W is the number of weights in the vector W. The matrix Ω_W has dimension $(N_W \times 2)$, the second row of Ω_W^* consists of $(N_W - 1)$ zeroes and a unit element in the i-th position computed by (18). The parameters for the algorithm must keep the same restrictions as in (19).

B. CVRNN Topology with Second Type Activation Function.

The second activation function considered is described by the following equation:

$$f(z) = \tanh(\mathrm{Re}(z)) + i\tanh(\mathrm{Im}(z)), \qquad z \in \mathbb{C} \tag{31}$$

This activation function doesn't have any singularities, so it doesn't need any restrictions in its domain as it did the first activation function. The block diagram of the **CVRNN** that uses this activation function is shown in Fig.4.

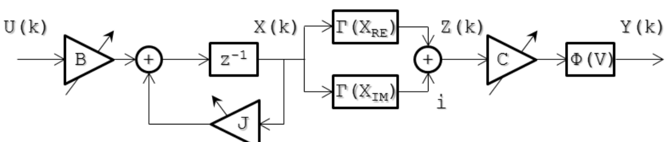

Fig.4 Block-diagram representation for the CVRNN with second activation function

The description of the RVRNN is given by the following equations:

$$X(k+1) = JX(k) + BU(k) \tag{32}$$

$$Z(k) = \Gamma[X_{\mathrm{Re}}(k)] + i\Gamma[X_{\mathrm{Im}}(k)] \tag{33}$$

$$V(k) = CZ(k) \tag{34}$$

ISBN: 978-1-61804-321-4

$$Y(k) = \Phi[V(k)] \tag{35}$$

The dimensions and domains of each vector and matrix in this **CVRNN** are the same as in the previous network. Applying the complex-valued diagrammatic rules we obtain the adjoint network, shown in Fig.5.

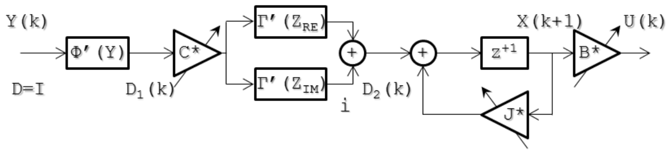

Fig.5 Block-diagram representation of the adjoint network for the CVRNN with second activation function

From this adjoint network, we derive the gradient terms needed for the **CVLM** learning algorithm, which are described by the following equations:

$$D_1(k) = \Phi'[Y(k)] \cdot D \tag{36}$$

$$\begin{aligned} D_2(k) = (\Gamma'[Z_{\mathrm{Re}}(k)] \cdot \mathrm{Re}(C^*) \cdots \\ + \Gamma'[Z_{\mathrm{Im}}(k)] \cdot \mathrm{Im}(C^*)) \cdot D_1(k) \end{aligned} \tag{37}$$

$$DY[C(k)] := \partial Y(k) / \partial C(k) = D_1(k) \cdot Z^*(k) \tag{38}$$

$$DY[J(k)] := \partial Y(k) / \partial J(k) = D_2(k) \cdot X^*(k) \tag{39}$$

$$DY[B(k)] := \partial Y(k) / \partial B(k) = D_2(k) \cdot U^*(k) \tag{40}$$

Where: $D = I$ is a real-valued identity matrix input for the adjoint topology. Then we apply the **CVLM** equations given by (18), (27)-(30) with parameters restricted by (19).

IV. Complex-Valued Neural Solution for the Nonlinear Identification Problem

We now illustrate the application of the **CVRNN** for nonlinear oscillatory system identification.

A. Description of the Nonlinear System Model.

The plant subject for identification addressed in this work is an idealized nonlinear model of a flexible-joint robot arm, illustrated in Fig.6. The flexibility at the joint is caused by a harmonic drive, which is a type of gear mechanism with high torque transmission, low backlash and compact size.

The robot joint model consists of an actuator connected to a load through a torsional spring, which represents the joint flexibility. We consider the motor torque and the angular position of the link as the input signal $u(t)$ and the output signal $y(t)$ respectively, making this a **SISO** system. The equations that describe the motion of the flexible joint are as follows:

$$J_l \ddot{\theta}_l + B_l \dot{\theta}_l + Mgl \sin\theta_l + k(\theta_l - \theta_m) = 0 \tag{41}$$

$$J_m \ddot{\theta}_m + B_m \dot{\theta}_m - k(\theta_l - \theta_m) = \mathrm{u} \tag{42}$$

Where: J_l, J_m are the link and motor inertial coefficients, B_l, B_m are the link and motor damping coefficients, k is the torsion stiffness coefficient of the harmonic drive gear, M is the mass of the link, L is the length between the shaft and the center of mass of the link, θ_l, θ_m are the angular positions of the link and the rotor of the motor respectively.

The input and output signals are discretized with a sampling period (τ) in order to use a discrete neural network approach for its identification. This is an oscillatory system, described by two nonlinear second order differential equations.

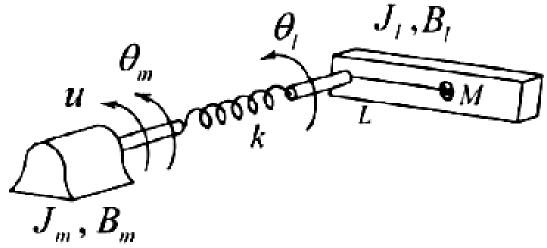

Fig.6 Flexible-joint robotic arm

B. Plant Identification.

For the plant identification, we use the scheme illustrated on Fig.7. Here, the desired output vector for our **CVRNN** is the output of the plant, with which we produce an error signal that is fed to the learning algorithm for the network. The identification objective is to adjust the weight parameters of the **CVRNN** such that its output follows the plant output, minimizing the total **MSE** given by the performance index (6).

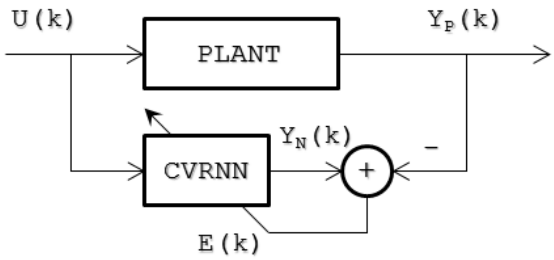

Fig.7 Identification scheme

C. Simulation and Results.

We test the **CVLM** learning algorithm applied to a **CVRNN** with the first activation function, for nonlinear oscillatory plant identification with a simulation using MATLAB.

The simulation has two stages: in the learning stage, weights are adjusted until convergence to a steady value and the **CVRNN** output matches the output of the plant; in the generalization stage, we fix the weight parameters and apply a

ISBN: 978-1-61804-321-4

different input for the plant and the **CVRNN**, to validate its learning by comparing both outputs. Next, we make a comparison between the **CVBP** and the **CVLM** learning algorithms.

As a comparison measure, we use the total **MSE** for learning and generalization stages. This section describes the simulation settings used and the results obtained. The input signals used on the learning stage $u_L(t)$ and generalization stage $u_G(t)$ are given by:

$$u_L(t) = \sin\left(\tfrac{1}{10}t\right) + 0.5\sin\left(\tfrac{1}{25}t\right) \tag{43}$$

$$u_G(t) = 0.5\sin\left(\tfrac{1}{10}t\right) + 0.8\sin\left(\tfrac{1}{20}t\right) \tag{44}$$

For the **CVRNN** we used dimensions $n=3, m=1, L=1$, with initial conditions of the internal states vector $X(0) = [0 \quad 0 \quad 0]^T$, random initial conditions for each weight parameter in the interval $[-0.5, 0.5]$; simulation time of $T = 500s$ and sampling time $\tau = 0.01$. For the **CVBP** algorithm we used the parameters: $\eta = 0.05$ and $\alpha = 0.005$. For the **CVLM** algorithm we used the parameters: $\alpha = 0.9775$, $\rho = 1\times10^{-4}$, $P_J(0) = 1\times10^{6}$, $P_B(0) = 1\times10^{4}$ and $P_C(0) = 1\times10^{5}$. For both cases, the second activation function is used.

For the **CVBP** algorithm, Fig.8, a) shows the plant and the neural network outputs, and b) the instantaneous **MSE** for the learning stage. Fig.9 a), b) shows the same signals for the generalization stage.

For the **CVLM** algorithm, Fig.10, a) shows the plant and the neural network outputs, and b) the instantaneous **MSE** for the learning stage. Fig.11, a), b) shows the same signals for the generalization stage.

For both algorithms, we observe a fast convergence of the neural network output to the plant output, while the **MSE** shows a decreasing behavior, for the learning stage. For the generalization stage, where the weight parameters are fixed and the input to the plant and neural network is changed, we observe a good performance of the output of the network and the **MSE** in general.

Table I shows the final **MSE** of the simulations for the **CVBP** and **CVLM** learning algorithms, for both learning and generalization stages.

Table I. Final MSE of both learning algorithms for the learning and generalization stages.

	CVBP	**CVLM**
Learning	6.11×10^{-4}	0.18×10^{-4}
Generalization	25.44×10^{-4}	20.84×10^{-4}

We observed from the total **MSE** for both stages that the **CVLM** learning algorithm has a better performance compared to the **CVBP** learning algorithm.

We also observe that the **CVLM** learning algorithm tends to be more sensible to the initial conditions of its weight parameters. Nevertheless, this sensibility doesn't affect the performance and convergence of the learning stage for the **CVRNN**.

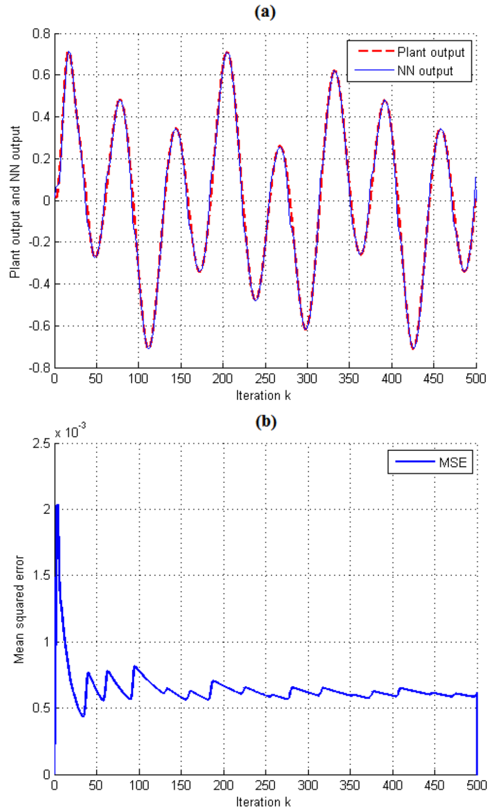

Fig.8 CVBP learning stage, a) Plant output and NN output signals, b) Instantaneous MSE

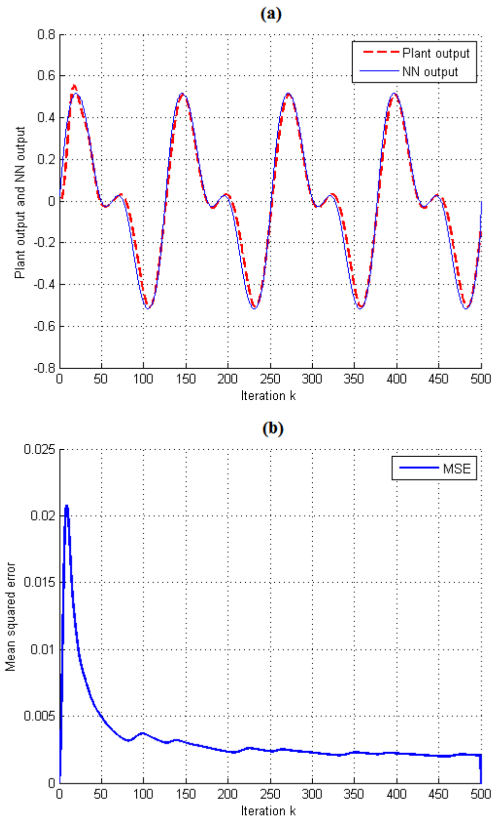

Fig.9 CVBP generalization stage, b) Plant output and NN output signal, b) Instantaneous MSE

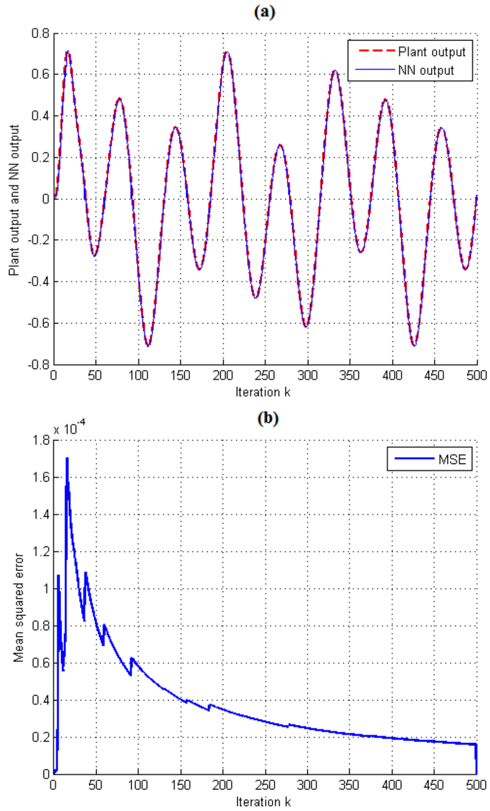

Fig.10 CVLM learning stage, a) Plant output and NN output signals, b) Instantaneous MSE

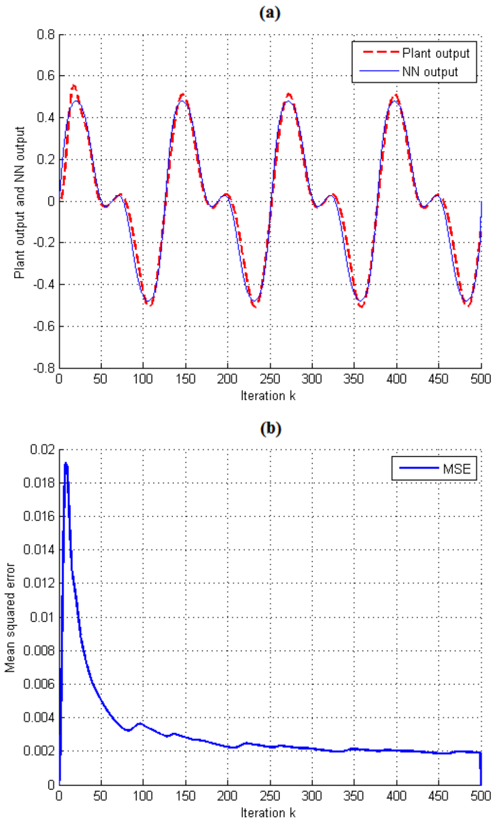

Fig.11 CVLM generalization stage, (b) Plant output and NN output signal, (b) Instantaneous MSE

V. Conclusions

In the present article we proposed a Complex-Valued Levenberg-Marquardt learning algorithm for a Recurrent Neural Network, using a diagrammatic approach to derive the gradient terms and recursive calculations of the weight's covariance matrix, needed for the full implementation of said algorithm. We then applied the Recurrent Neural Network in the complex domain for identification of a dynamic, nonlinear, and oscillatory mechanical plant. The comparative results obtained between the Levenberg-Marquardt and Back-Propagation learning algorithms show a better performance of the neural network for the former algorithm, both in the learning and generalization stages.

Acknowledgment

Master Degree student Edmundo Pérez Reynaud would like to thank CONACyT, Mexico, for the student grant received during his studies at the Department of Automatic Control, CINVESTAV-IPN, Mexico (grant number: 364197, holder number: 295620).

References

[1] A. Hirose. "Complex-Valued Neural Networks." 2nd ed., S.i.C. Intelligence, Springer-Verlag, vol. 400, 2012.

[2] A. Minin, Y. Chistyakov, E. Kholodova, H.G. Zimmermann, A. Knoll. "Complex-Valued Open Recurrent Neural Network for Power Transformer Modeling." *International Journal of Applied Mathematics and Informatics*, vol. 6, no. 1, pp. 41-48, 2012.

[3] L. Ferariu, "Nonlinear System Identification Based on Evolutionary Dynamic Neural Networks." *Proc. Of European Control Conference*, Cambridge, UK, paper no. 432, 2003.

[4] A. Luchetta, S. Manetti, M. C. Piccirilli. "Analog System Modeling Based on a Double Modified Complex-Valued Neural Networks." *The 2013 International Joint Conference on Neural Networks*, 2013.

[5] T. Kitajima, T. Yasuno. "Output Prediction of Wind Power Generation System Using Complex-Valued Neural Network." *Proc. Of SICE Annual Conference*, 2010.

[6] L. Zheng, Z. Wang. "Design of FIR Digital Filters in Complex Domain by Complex-Valued Neural Networks." *2010 2nd International Conference on Information Science and Engineering*, Hangzhou, China, 2010.

[7] A. Hirose. "Motion Controls Using Complex-Valued Networks with Feedback Loops." *Proc. Of IEEE International Conference on Neural Networks*, vol.1 San Francisco, CA, pp. 156-161, 1993.

[8] V. M. Arellano-Quintana, I. S. Baruch. "Identification of Dynamical Systems Using Recurrent Complex-Valued Neural Networks." In *Proc. Of the 18th International Conference on Circuits, Systems, Communications and Computers*, Santorini, Greece, pp. 74-79, 2014.

[9] I. S. Baruch, V. M. Arellano-Quintana. "Identification and Control of Oscillatory Dynamical Systems Using Recurrent Complex-Valued Neural Networks." In *Proc. Of the 18th International Conference on Circuits, Systems, Communications and Computers*, Santorini, Greece, pp. 534-539, 2014.

[10] E. A. Wan, F. Beaufays. "Diagrammatic Methods for Deriving and Relating Temporal Neural Network Algorithms." *Neural Computation*, pp. 182-201, 1996.

[11] I. S. Baruch, C.R. Mariaca-Gaspar. "A Levenberg-Marquardt Learning Applied for Recurrent Neural Identification and Control of Wastewater Treatment Bioprocess." *International Journal of Intelligent Systems*, no. 24, pp.1094-1114, 2009.

ISBN: 978-1-61804-321-4

Control of measuring the positioner using virtual instruments

Rudolf Drga, and Dagmar Janáčová

Abstract**—** The work deals with control of the positioner using the LabView programming environment. There is used graphical programming, which is based on the creation of subroutines, known as virtual instruments. The work presents the implementation of a workplace for PIR detectors, where is preferably used technique graphical programming with virtual instruments.

Keywords**—** Spatial characteristics, security detector, LabView.

I. Introduction

To ensure correct operation of safety devices that handle electromagnetic signal or wave thermal radiation from space in their vicinity, it is important to know the spatial characteristics of the device. According to this feature, you can specify the maximum range of the device or its sensitivity to a certain distance and direction. For example, Fig. 1 shows the characteristics of the fire flame detector S200 and S300. The detector S200 represents classic flame detector, which uses a radiation sensor of the flame. It consists of further filter lets through the radiation generated during combustion particular material. The detector S300 represents the flame detector, which consists of the sensor array of 16 x 16 points, and as shown in the figure, the characteristic is less than 90 ° coverage.

This work was financially supported by the research project NPU I no. MSMT-7778/2014 of the Ministry of Education of the Czech Republic and the European Regional Development Fund under the project CEBIA Tech-no. CZ.1.05 / 1.2 00 / 03,0089..

R. Drga, Tomas Bata University in Zlín, Faculty of Applied Informatics, Department of Security Engineering, nám. T. G. Masaryka 5555, 760 01 Zlín, Czech Republic (e-mail: rdrga@fai.utb.cz)

D. Janáčová, Tomas Bata University in Zlín, Faculty of Applied Informatics, Department of Automation and Control Engineering, nám. T. G. Masaryka 5555, 760 01 Zlín, Czech Republic (e-mail: janacova@fai.utb.cz)

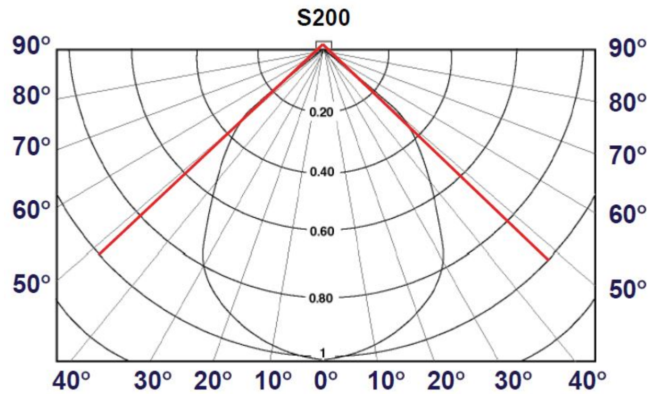

Fig. 1 Characteristics of the flame detector type S200 and S300

Moreover, there is the possibility of determining the position used in the flame space using polar coordinates, and the system then marks this region in the camera image, which is part of the detector, as shown in Fig. 2. This is very advantageous in the case that the actual flame emits radiation, which is outside the visible spectrum, and thus invisible to the human eye. In this example it is clear that for the purposes of use in security technology is important to exactly determine the spatial characteristics of the particular device, in this case the flame detector. In the lower part of the figure is a table for flame range of 0.1 m^2 area for various types of burning material. As is evident from the table, the maximum distance of the detected flame is relatively large, it is from 35 m to 60 m. This can be a relatively large problem for implementing a workplace where we want to measure this characteristic.

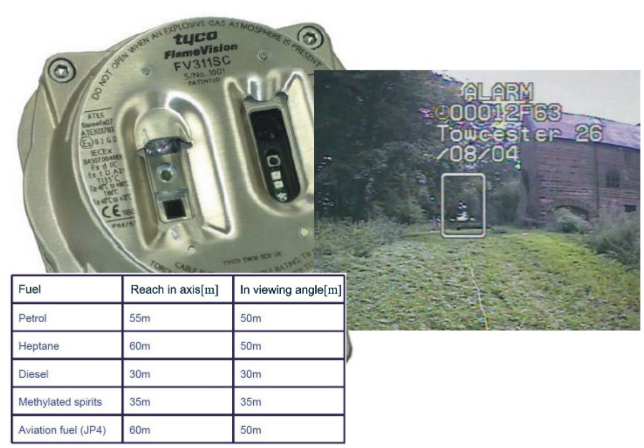

Fuel	Reach in axis[m]	In viewing angle[m]
Petrol	55m	50m
Heptane	60m	50m
Diesel	30m	30m
Methylated spirits	35m	35m
Aviation fuel (JP4)	60m	50m

Fig. 2 Fire alarm detector S300 and the image of the camera by specifying the place of burning

II. Methods of Measurement of the Spatial Characteristics

One of the simplest methods, how to measure the spatial characteristics, is to create a workplace whose dimensions correspond to the real ranges of device, as shown in Fig. 3. Shining object 1 is moving in polar coordinates, and after reaching the new position occurs when the impact of radiation on the measured device 2 and performs measurements using measuring instruments 3. The disadvantage of this solution is the fact that the dimensions of the workplace are large, in the case of flame detectors then we need to create a grid of lines with an area of 60 m x 40 m with the fact that characteristics are the spatial and must therefore reckon with height in the range 10-20 m. Another problem is the exact movement of the source of radiation after the desktop workstation, or the ability to change its height from the floor. In this case, the radiation source moves after the desktop manually. Another way to move the source of radiation in space, is the use of a robot that moves in Cartesian coordinates after the desktop. In this way, the measurement is performed by PIR detectors in Belgium according to the standard T 014: 2014, as shown in Fig. 4.

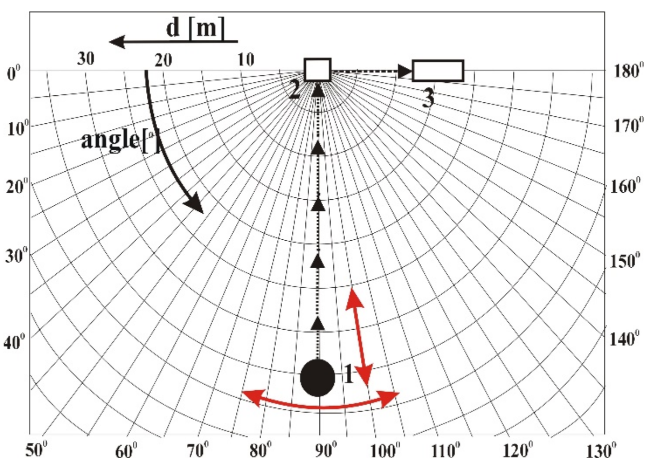

Fig. 3 Classical concept of measuring workplace

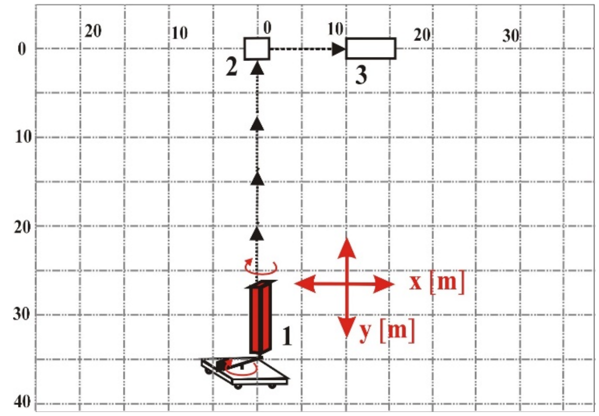

Fig. 4 Robotic concept of a measuring workplace

Source 1 is located on the chassis, which is moving exactly along the floor of the test room. The chassis is located the source of the radiation, that represents a prism, warmed to a specific temperature, this rotates around the vertical axis and is around the second axis, which is placed on the chassis, as shown in the figure. Radiation then turns on its own MOTION detector, and his response is measured using measuring instruments 3.

III. New Method for the Measuring Spatial Characteristics

Of the reasons referred to in the previous chapter, it was realized the workplace, where the function was changed due to the motion of the source of radiation scanning device. In this case the source of radiation 1 is static and moving the actual measurement device 2 measuring instruments 3. The measuring devices 3 are located in its vicinity, as shown in Fig. 5. Devices whose characteristic measured is placed on a very accurate multiaxial manipulator 4 that is programmatically controlled by special programs for positioning.

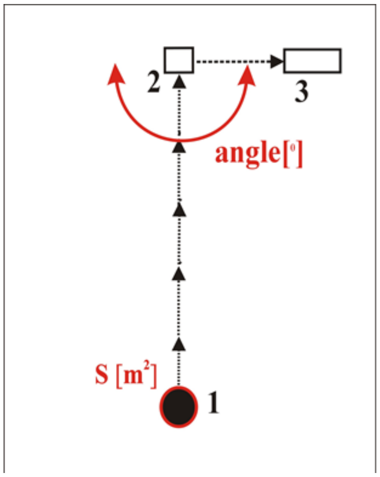

Fig. 5 New concept of measuring workplace

ISBN: 978-1-61804-321-4

The distance of the source of radiation is simulated, the size of the object, or a broadcast performance. In the case of thermal radiation is changing the size of the surfaces of the heater.

IV. Libraries of Programs for the Control of Motors

For testing drives the manipulator is provided a special program, which the user interface is shown in Fig. 6. This program can be used with advantage for the initial position of the manipulator. Linear drives have end points, from which you can then roll on a specific desired position. Also, rotating movements have their own hardware starting position from which it can be moved in steps at a specific desired position.
For the further development of the control of the program has been recovered, the program of the Development kit from the manufacturer of the manipulator, that has included the drivers of drives and their calls using global variables. Their part shown in the LabView is shown in Fig. 7 and Fig. 8 as Default parameters, and Run-Time parameters. The default parameters are used to set the default properties for the drive and Run-Time parameters commands to the control unit, thus the immediate control of the actuator.

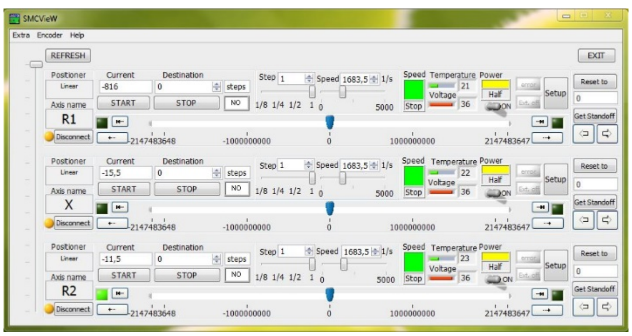

Fig. 6 The geometric layout of the situation

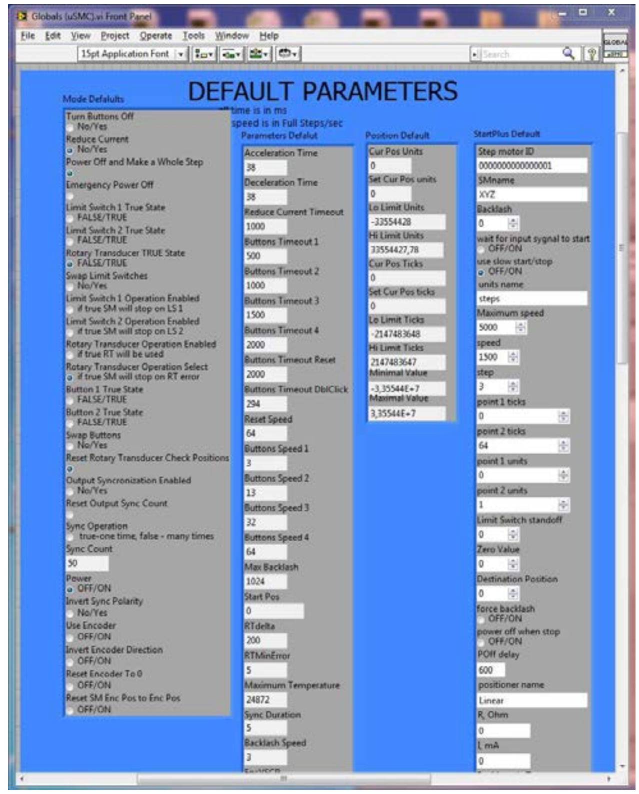

Fig. 7 Default parameters of the program for the measurement characteristics

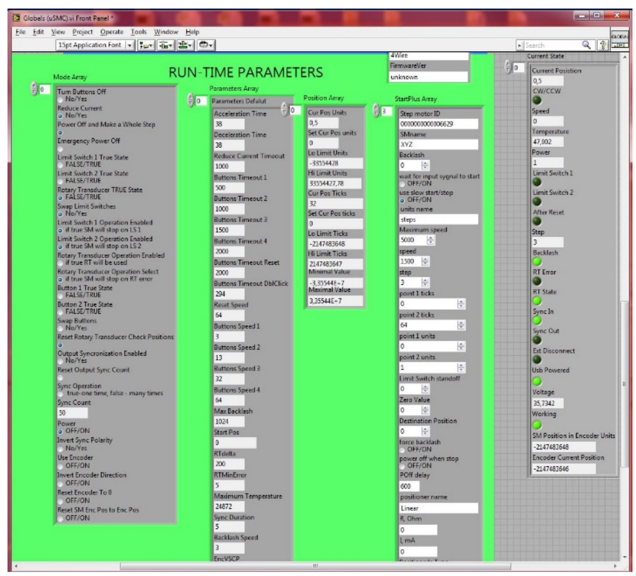

Fig. 8 Run-Time parameters of the program for the measurement characteristics

V. Program for the Measurement Control

Fig. 9 shows a simplified full functionality. In Fig. 10 is shown a specific user interface for the measurement of the PIR detector. After the start of the program are initialized control values, it means setting all the defaults Run-Time Default parameters from the default parameters After starting step "Find Devices" will be loaded physically connected drives. Button from the group "Movement" may serve to set the initial

ISBN: 978-1-61804-321-4

position of the manipulator to its initial position measurement device. It is then necessary to make "set range", set restrictive conditions for mechanical drives or other devices. After calling the "start measurement" is started measurement and at each position measurement is performed, the values are stored in a database and simultaneously displayed on the chart. Then step is performed at a new position and the measurement is repeated until reaching the limit position specified in step "set range", then the measurement is finished.

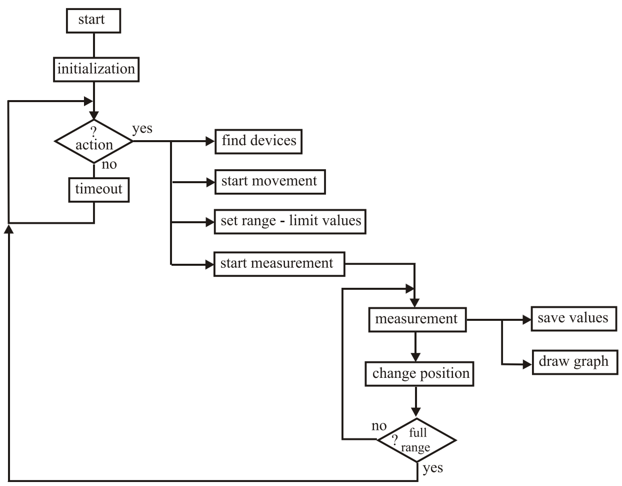

Fig. 9 Simplified flowchart of the measurement programme

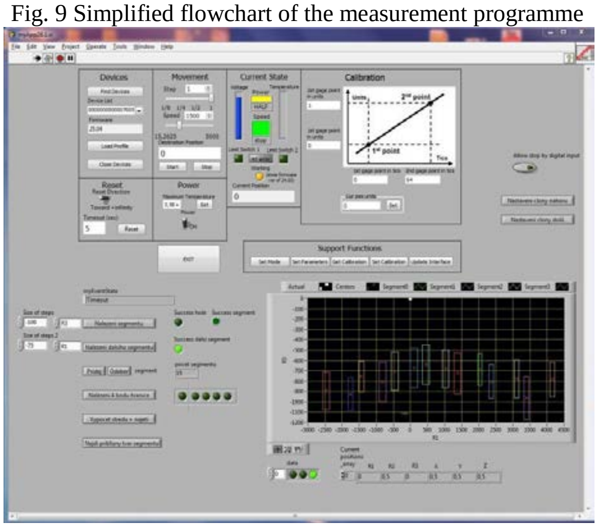

Fig. 9 Sample application user interface for measurement of the PIR detector

From the graphs it is evident that the heat treatment for 1-5 seconds for incident radiation having a density of 0.75 W/m^2 temperature pyroelement increased about 0.015 °C, while for incident radiation having a density of 0.02 W/m^2, the temperature hardly increased pyroelement. The calculations and simulations, the temperature distribution in the heated pyroelement also shows that even at low values of the density of heat flux at a given time, the surface temperature pyroelement nearly the same temperature throughout its thickness (no steep temperature field). This proves that pyroelement is flawed. It can be said that in the early stages of measurement evaluates pyroelement right temperature and laboratory measurements is therefore in the initial stages sufficiently accurate.

VI. Summary

Of the work, it was proposed a new solution to the measurement of the spatial characteristics of the installations, which are used mainly in the security industry. Here is the developed HW solutions utilizing precision manipulator and SW solutions, which you can use to link the modules control actuators with laboratory instruments from different manufacturers using LabView from National Instruments. It brings great advantages in the use of measuring instruments that use GPIB bus and source libraries to each measuring device. Using the graphical programming, you can then create a unified interface for automated and rapid measurement of the spatial characteristics of the various devices. A large problem measuring disturbances and also owns its own electromagnetic radiation manipulator. This must be solved individually for a specific type of measurement. However, this problem occurs even when you use measurement for classical departments of large dimensions, however, these problems are much larger and shading the large space is more difficult.

References

[1] J. D. Vincent, *Fundamentals of infrared detector operation and testing.* USA, Texas: WILEY, 1990.

[2] G. F. Knoll, *Radiation detection and measurement*. USA, Texas: WILEY, 2000.

[3] B. Saleh, *Fundamentals of photonics*. USA, Texas: WILEY, 2007.

[4] *CSN EN 50132: Alarm systems - CCTV surveillance systems for use in security applications Part 7: Application guidelines*. Prague: Office for Standards, Metrology and Testing, 2011.

[5] *CSN EN 54-10 Fire detection and fire alarm systems - Part 10: Flame detectors - Point detectors*, Prague: Office for Standards, Metrology and Testing, 2002.

[6] Tyco Fire & Security, *datasheet Flame detector S300*, 2008.

[7] Tyco Fire & Security, *datasheet Flame detector S200*, 2008.

[8] A., R. Jha, . *Infrared technology*. USA – Texas: WILEY, 2006

[9] *CSN 50131-2-2 Alarm systems - Intrusion and hold-up systems - Part 2-2: Intrusion detectors - Passive infrared detectors*, Prague: Office for Standards, Metrology and Testing, 2008.

[10] C. Hotz, *Přenos tepla zářením* (in Czech), Prague: SNTL, 1979.

[11] K. Kolomazník, *Modelování zpracovatelských procesů* (in Czech), Brno: University of Technology in Brno, 1990.

[12] M. Feriančik. O. Líška. M. More. “Navigation of industrial manipulator based on computer vision”. *Transfer inovácií*. vol. 28. 2013. pp. 140-142.

[13] R. Makovník and O. Líška, ”Contribution to experimental identification and simulation problems of dynamic systems”, *Ovidius University Annual Scientific Journal*. vol. 9, No. 1, 2007.

Autonomous system monitoring space by infrared camera with the possibility of detection and evaluation of combustible materials

Martin Struška, Jan Struška, and Miroslav Popelka

Abstract— Motion detection is wide spread action in video systems to discover objects, potential fire or people in images. A number of methods and algorithms have been proposed for estimating 2D motion detection in images. Some of these methods may be classified as matching methods, other as methods of differentials, spectral methods like Fourier methods. Article deals with proposal of intuitive fire system detection in a scene using the infrared camera.

Keywords— Thermo Vision Systems, Thermal Image Sequence, Fire Detection

I. Introduction

Thermo vision is branch of science which analyzes the distribution of temperature field on the surface of the body using non-contact manner. The main task of thermography is analyze infrared energy radiated by the body. Using thermographic measurement system can be viewed temperature field of measured object, but only on its surface. The main advantages of using Thermal images is the ability to see objects, people and potential fire even in total darkness. The applications of thermal imaging technology is quite wide: military or police systems, security systems, industrial control systems, medical systems, etc. [1] The idea of motion detection or potential fire in a building can be analyzed in several ways, such as: methods of differentials, matching methods, spectral methods like Fourier methods. [2] All of these methods can be applied also in thermo visual systems for motion detection with some modifications typical for thermal images. The choice of a concrete method of motion detection in a real working thermos visual system can be made analyzing the advantages and disadvantages of the well known motion detection methods for visible images. For a more accurate analysis is discussed in this article method of algorithm for fire detection thermography image in a mathematical and simulation program MATLAB/Simulink.

This work was supported by Internal Grant Agency of Tomas Bata University under the project No. IGA/FAI/2015/040, IGA/FAI/2015/028, and No. IGA/FAI/2015/027.

Martin Struška is with Department of Automation and Control Engineering, Faculty of Applied Informatics, Tomas Bata University in Zlín, Czech Republic (corresponding author, e-mail: mstruska@fai.utb.cz).

Miroslav Popelka is with Department of Automation and Control Engineering, Faculty of Applied Informatics, Tomas Bata University in Zlín, Czech Republic (corresponding author, e-mail: popelka@fai.utb.cz).

Jan Struška is with Department of Automation and Control Engineering, Faculty of Applied Informatics, Tomas Bata University in Zlín, Czech Republic (corresponding author, e-mail: jstruska@fai.utb.cz).

II. Measurement system

A. Fire characteristics of combustible materials and building products division by class flammability and reaction to fire.

1) The flash point

Flashpoint is the lowest temperature at which a flammable under normal pressure develops so much flammable vapor that these mixed with air in the short approach precisely defined open clematis briefly ignite, but do not afire anymore.

At temperatures below the ignition temperature of the ignition is not possible, because the vapor pressure of the substance is too small to create a flammable mixture of vapors with air. This does not mean that at temperatures below the flashpoint fire hazards exist. The source of ignition substance can be rapidly heated to its flash point.

2) The burning temperature

The burning temperature is the lowest temperature of the flammable substance at which the flammable vapor form so that these pairs when approaching open clematis themselves ignite and continue to burn.

Upon reaching the combustion temperature evaporation rate is at least as large as the combustion rate, so that the steam is further formed in sufficient quantity and self-combustion is further maintained.

3) Ignition temperature

The ignition point is the lowest temperature at which, under defined test conditions of flammable mixtures with air alone without initiation ignites. As ignition is called start the chemical reaction of gas or vapor mixtures with air under discovery open flame. When determining the ignition temperature of the ignition activated only by heat rather than an open flame or spark.

Reaction to fire according to flammability
A1,2 - non-flammable
B – flammable with difficulty
C – heavily flammable

ISBN: 978-1-61804-321-4

D – medium flammable
E,F – lightly flammable

Table I class of reaction to fire

Class A1

Products no-contributing to fire in any of its stages, automatically deemed to comply with all requirements of the lower classes.

Class A2

Natural building stone (Slate, marble, sandstone, granite), concrete heavy, light porous (aerated concrete, foam concrete) as lightweight aggregates (agloporitem, diatomaceous earth, perlite), building materials made of clay (bricks, blocks, tiles) etc.

Class B

Slabs of inorganic materials with surface finish (drywall) rigid polyvinyl chloride (PVC).

Class C

Grown deciduous wood (beech, oak), plates of laminated wood (plywood) hardened paper (ecrona, formica), organic-fiber (felt boards the hair), cast polyester laminated flooring.

Class D

Chipboard for general use (PCB stamped) wood-fibre board (duplex), plates of vegetable matter (SP-type cork boards, cork parquet).

Class E

Products capable of withstanding exposure to a small flame for a short period of time without significant flame spread rubber isolation foil, foil coverings of plastics and rubber (rubber floor pattern, rubber isolation carpet for electronics).

Class F

Products that do not fit into any of the previous classes.

Ignition temperature of certain substances			
Title	**°C/°F**	**Title**	**°C/°F**
Wood	270/518	Paper	Over 185/365
PVC	370/698	Cloth	Over 290/554
Perspex	460/860	Petrol	470/878
Cotton	450/842	Disel	250/482
Straw	310/590	Hard coal	350/662
Tabacco	175/347	Lignite	260/500

Table II ignition temperature of certain substances

4) Auto-ignition temperature

Auto ignition temperature is the lowest temperature at which the starting substance without external heat supply exothermic processes that lead to auto-ignition. The heat required to ignite the substances arises from the substance itself as the result of chemical, physical or biological processes.

For a safe temperature at which a substance can be heated, is considered the temperature, the value of which does not exceed 90% of the auto-ignition temperature.

5) Glowing temperature

The glowing temperature of solids is the lowest temperature at which the flames without the action occurs incandescence. Glowing may occur especially in dust and fine bulk materials. Glowing temperature is dependent on the thickness of the dust layer.

Sources of ignition may be free hot surfaces (pipes, radiators, etc.).

B. Image Processing of thermal images using mathematical and simulation program MATLAB

Load the image, store it in a 2D array. The next step is thresholding thermal image. Aside from our interest in those pixels that are below our defined value that is subtracted from the warmest found pixel, which is larger than the brightest pixel calibration (the ones that are so cold compared to the warmest pixel that are not interesting for us). Now get rid thermal image noise. Remove those areas of pixels that make up the least square (pixels are square in shape), which define as the noise floor. It can happen (and it happens almost always) that the scene will have more potential targets. If we now calculate the surface center of gravity, it may be outside an object in the scene left (if one not significantly greater will be very close to each other, the scene will be in one plane in an odd number). Filter out the scene that the field of view of a 2D matrix remained only one object -> greatest = closest, most dangerous. After this selection can already be calculate the center of gravity of the area that represent the coordinates of the remaining pixels.

Center of gravity in the individual coordinates calculate by following equation:

$$Tx = \frac{\sum_{i=1}^{n} x_i * m_i}{m} \qquad Ty = \frac{\sum_{i=1}^{n} y_i * m_i}{m} \tag{1}$$

Where n is the number of remaining pixels, x_i is the i-th coordinate x, y_i is the i-th coordinate y, mi is the i-th value of the gray level am the sum of the level of the entire area. (1) If we know the size of the thermal image (resolution matrix detector), can be determined deviations from the centers of gravity of the optical axis, as follows:

$$O_x = T_x - \frac{x}{2} \qquad O_y = T_y - \frac{y}{2} \tag{2}$$

Where x is the size in the x-coordinate (image width) and y is the size in the y-coordinate (height of the image). The minus sign means are at the center of gravity is located on the optical axis of the IR camera left (x-coordinate) or the top (y coordinate). For the plus sign is reversed (right down to the x coordinate for the y coordinate). (2) While watching the object, we will try to achieve zero deviation.

Image processing of two thermo images to determine the distance objectives:

It is virtually the same procedure as given above with the difference that a pair of thermal process, whose center of gravity compared with each other. According to their mutual position passively determine the object's distance from the plane of the objective lens. Sensors are placed in the frame in the same horizontal position but different vertical position. We have to use the same IR cameras with identical computational algorithm of gravity of the object. The small difference in these parameters takes a big mistake to determine the actual distance of the object being tracked. We adjust the relationship of the equation for the calculated pixel values of the centroid, with which we find the distance at which the tracked object is:

$$z = \frac{b * f}{|T_{x1} - T_{x2}| * k} \tag{3}$$

Where (3) b is the distance between optical axes IR cameras, f is the distance between the plane of the lens and the sensor, T_{x1} is x-coordinate of the center of gravity of the object pursued by the first IR camera, T_{x2} is x-coordinate of the center of gravity of the object observed IR camera and the other is the size of one IR detector from which is formed by the IR chip.

III. THERMO VISION IMAGE PROCESSING FOR FIRE DETECTION

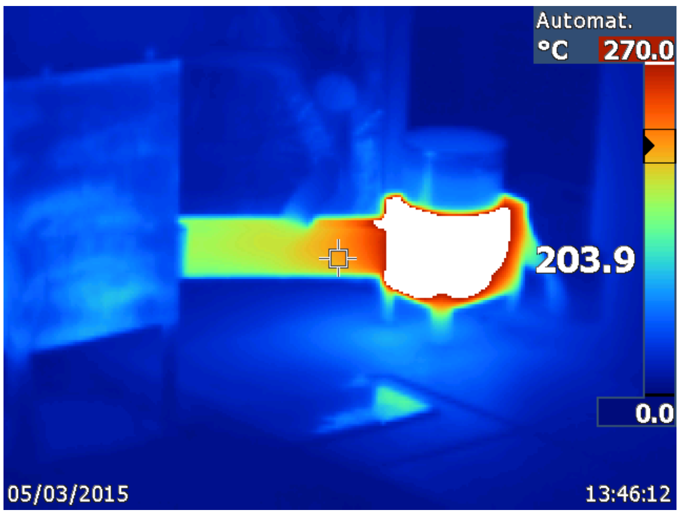

Fig. 1 thermo vision image processing 1st stage

Load the image and convert it to grayscale palette. Each pixel is represented by a pair of coordinates defining its position, and a numeric value in the range 0-255, corresponding gray level (0 represents black, 255 white). Save the image into a 3D array (x-coordinate, y-th coordinate, gray level). For converting color image to grayscale image conversion method we used standard CIE (gray = R * G * 0.2126 + 0.7152 + 0.0722 * B), where R is the red component palette, G (green) and B (blue). At the same time also saves the value of the gray levels hottest pixel in the scene, from which we subtract thresholding value, and thus we find the value of the coldest yet crediting pixel.

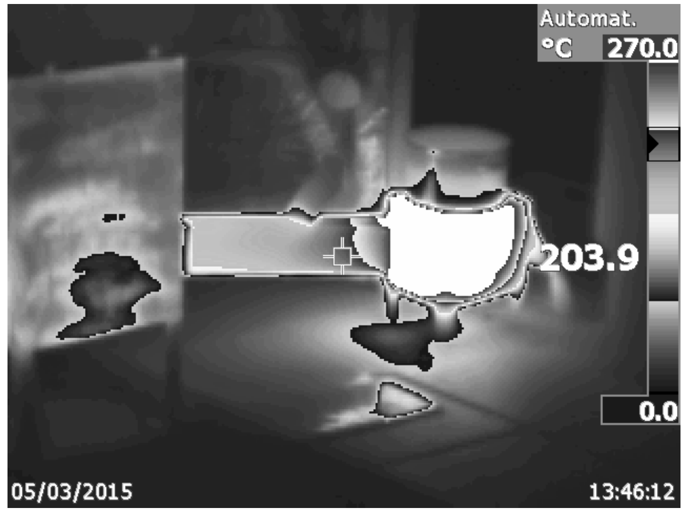

Fig. 2 thermo vision image processing 2nd stage

Using warmest pixel values from the previous stage and specified threshold (threshold gray level indicates the interval from the warmest pixel to the cooler, which will still be included in the calculation) shows how many pixels will be stored in the field and according to this data it will create for us crawled still field the size of the entire image. Now we focus on the entire field and record only those pixels that are satisfactory to us.

The range of individual components:

- Red <128, 255>, weight representation corresponding to this interval is ramping <0; 254>
- Blue <0; 127>, weight representation corresponding to this interval is linearly decreasing <254; 0>
- Green <31; 223>, the corresponding weight representation is ramping <0; 255> interval <31; 127> and linearly decreasing <255; 0> interval <128; 223>

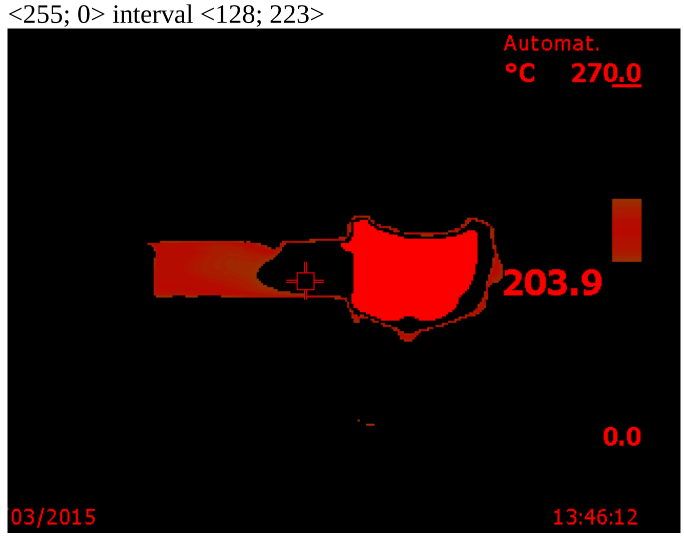

Fig. 3 thermo vision image processing 3th stage

Filter out noise from the image. Size noise specify using a number which tells us that the square of the size of the part number entered will still be considered as noise. This square will not be included in the calculation. The first is tested the levels of gray in row coordinates. If is find next to each other (in columns in the same row) more pixels than the size specified noise data we leave, otherwise erasing. Then is going to be tested field in the column coordinate. First rank array by

ISBN: 978-1-61804-321-4

rows, then by column. To test whether the pixels above the other (in the same column and row increasing by 1), need to sort array conversely (sort by columns first, followed by rows). While it's sorted, tested similarly as in the previous case, if the superimposed pixels more than the noise value. If so, leave them, otherwise discarded.

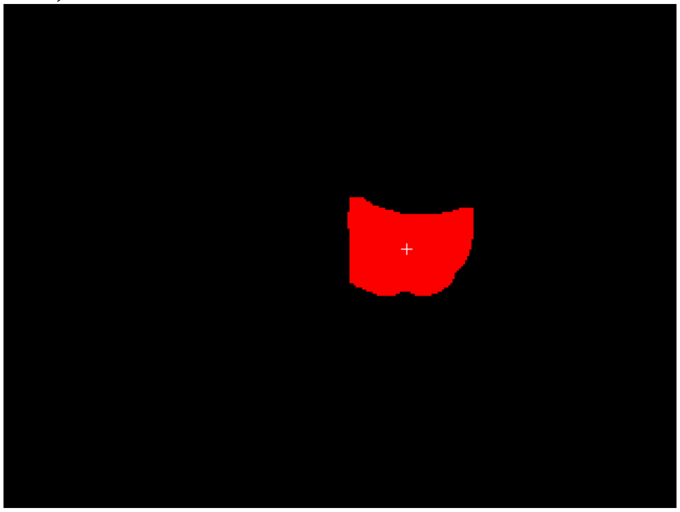

Fig. 4 thermo vision image processing 4th stage

From the filtered image, select the largest, in most cases the closest object and focus on it. We set the maximum variance that is allowed for one continuous object. In other words, unless the row (column) coordinates are remote from the previous row (column) coordinates more than the specified maximum variance, consider these pixel by pixel one object. We will continue in the first row coordinates, therefore, we will examine whether the row coordinates increases up to a specified maximum variance. Consider another cluster of pixels as a new object. Always store the start and end of row coordinates, we can evaluate at the end of which object is the coordinate of the largest (highest).

After evaluating the supreme object we only work with this area. In the column coordinate it may be more objects, as in the previous case, we will be working here. Field have to sort that we have ranked first column. After finding the largest object in the column coordinate (widest), again everything outside this area aside from the calculations. Now, it could happen that the exclusion of some areas from the column are created multiple objects in a row coordinates. Therefore, this cycle repeats until the scene has less than a single object.

From the final field that left is necessary calculate the center of gravity of the area and the center of gravity deviation from the optical axis. In the final image, the position of the center of gravity plotted cross.

IV. Results and Conclusion

The proposed algorithm for thermo vision images fire detection programed in a mathematical and simulation program MATLAB/Simulink is examined with a lot of test thermal images sequences. The time of the calculation is moving on the applicable resolution (640x480 pixels) thermal images around 20-30ms. These results are of practical use more than the other one is sufficient. With increasing resolution, with respect to the used method, times grow linearly. For brevity here in this article are presented only some parts of input (Fig. 1) and outputs (Fig. 4) sequence of frames from a whole used in one of the experiments test thermal images sequence. All experiments are carried out with test thermal images sequences from a real working thermal image camera Fluke Ti9.

Acknowledgment

We thank Zdeněk Úředniček, Tomas Bata University in Zlin, for his support and helpful advice. Thanks go to Tomáš Dulík for borrowed thermal camera Fluke Ti9.

References

[1] L.J. Kozlowski, K. Vural, J. Luo, A. Tomasint, T. Liu, W. E. Kleinhans, *Low-noise infrared and visible focal plane arrays*. Rockwell science Center, CA: Camino dos Rios, 1999, pp 259–269.

[2] M. Andriluka, S. Roth, B. Schiele, *Monocular 3D Pose Estimation and Tracking by Detection*. CA: San Francisco, 2010, pp 623-630.

[3] M. Vollmer, S. Henke, D. Kartadt, K. Mollmann, F. Pinno, *Identification and Suppression of Thermal Reflections in InfraredImaging*. Cambridge, MA: Broadway, 2004, pp 7-12.

[4] H. R. Sheikh, M. F. Sabir, A. C. Bovik, *A Statistical Evaluation of Recent Full Reference Quality Assessment Algorithms*. Department of electrical and computer engineering TX: Austin, 2006, pp. 3440-3451.

[5] H. Kaplan, *Practical applications of infrared thermal sensing and paging equipment*. 3rd ed. Bellingham, Wash.: SPIE Press, 2007, pp 120-146.

[6] M. Netopilová, D. Kačíková, A. Osvald, *Reakce stavebních výrobků na oheň*. Praha: Edice SPBI spectrum, pp. 25-57.

[7] H,-D. Steinleiter, *Tabulky hořlavých a nebezpečných látek*. Praha: Svaz PO ČSSR, 1980, pp 7-25.

[8] G. C. Holst, *Electro-optical paging system performance*. 2nd ed. Winter Park, FL: JCD Pub., 2000, pp 320-336.

[9] G. C. Holst, *Testing and evaluation of infrared imaging systems*. 3rd ed. Winter Park, FL: JCD Pub, 2008. pp 73-92.

[10] A. Ess, B. Leibe, K. Schindler, L. V. Gool. *Robust Multi-Person Tracking from a Mobile Platform.* PAMI, 2009.

Martin Struška studied at the Tomas Bata University in Zlin, Czech Republic, where he obtained his master degree in Computer and Communication Systems in 2013. He now attends PhD. study in the Department of Automation and Control Engineering of the Tomas Bata University in Zlin. His research interest focus on digital signal and image processing of thermal cameras for fire detection.

Miroslav Popelka studied at the Tomas Bata University in Zlin, Czech Republic, where he obtained his master degree in Computer and Communication Systems in 2013. He now attends PhD. study in the Department of Automation and Control Engineering of the Tomas Bata University in Zlin. His research interest focus on ultrasonic signal processing. He is currently working on programming ultrasound imaging for mobile robot systems.

Jan Struška studied at the Tomas Bata University in Zlin, Czech Republic, where he obtained his master degree in Computer and Communication Systems in 2013. He now attends PhD. study in the Department of Automation and Control Engineering of the Tomas Bata University in Zlin. His research interest focus on motion control manipulator autonomous service robotic system for image scanning.

He is currently working on completion of the project management of physical condition and its security, including physical simulation model performance and interaction.

Temperature stratification in the passage space of the shaft type

Stanislav Sehnalek, and Martin Zalesak

Abstract—Glazed vertical communication areas (stairs and elevators), which often form an independent fire escape unit, are usually poorly ventilated and due to large glazed areas exposed to excessive heat loss in the winter, but also considerable heat gain during the summer may occur. This heat load leads to the high temperatures of air in the head space. The paper presents the results of measurements of the temperature distribution in the summer time in a particular case and compare these results with model simulations using the software, which has been verified using the method IAE BESTEST. The simulation showed good agreement with measurements and can be used to design technical solutions providing convenient climatic conditions in these areas.

Keywords—Heat gains, simulation software, glazing space, temperature distribution.

I. Introduction

THE share of glass used as a construction material in building's faades has increased during the last 1000 years. Particularly thanks to its specific features, such as transparency, low weight and an ability to separate different environments. As glass is so popular for use in faades, there is one important question that should be always taken into account temperature gains caused by internal and external heat sources. A special attention should be paid to habitability of these plant house buildings. A long-term research of people's comfort was executed in 26 office buildings in five European Union states. [1] Interior comfort can be achieved by ventilation systems, shading systems or by their combination. In recent years, a particular emphasis is put on sustainability of glass buildings. [2],[3],[4] Regardless of our experience and knowledge, the risk of constructing a discomfortable building is always present. Such a building is the subject of investigation in this article. The main reason for selection of this building were excessive heat gains in the glazed area, which is used for stairs and also disposes of gazed elevator shaft. The excessive heat gains were measured in immediate distance of this shaft. The process of measurement and computer simulation are described in the methods section, while gathered data are summarised in the results section.

The work was performed with financial support of research project NPU I No. MSMT-7778/2014 by the Ministry of Education of the Czech Republic and also by the European Regional Development Fund under the Project CEBIA-Tech No. CZ.1.05/2.1.00/03.0089. Work was also supported in frame of Internal Grant Agency of Tomas Bata University in Zlin, Faculty of Applied Informatics No. IGA/CebiaTech/2015/002

Stanislav Sehnalek is with the Tomas Bata University in Zlin, Faculty of Applied Informatics, Department of Automation and Control Engineering, Nad Stranemi 4511, Zlin, Czech Republic, e-mail: (sehnalek@fai.utb.cz).

Martin Zalesak is with the Tomas Bata University in Zlin, Faculty of Applied Informatics, Department of Automation and Control Engineering, Nad Stranemi 4511, Zlin, Czech Republic, e-mail: (zalesak@fai.utb.cz).

Fig. 1 block B of the VTP-ICT Park

II. Methods

The measurement took place in the staircase area of VTP-ICT Parks building, displayed in Fig. 1. Building is situated next to Faculty of Applied Informatics (FAI) of Thomas Bata University in Zlin. The staircase area is 17 meters tall and stands on the south hillside. The building consists of two symmetrical parts called Block A and Block B. The results of this study are restrained to Block B, even though Block A has the same staircase area. But in the morning hours Block A is shadowed by FAI building, which means that such a marginal fluctuation as in Block B is not possible. The measurement was done in the staircase area from 0^{th} to 4^{th} floor. Its construction is as follows: the east side and 2 meters of the north and the south sides are made of glass combined with supportive aluminium matrix and they are exploited to outside weather conditions; the rest of the area is surrounded by rooms and is adjacent to regulated inside conditions. The 4^{th} floor is completely embosomed by glass and supportive aluminium matrix. A weather station was used for the measurement of the outside climatic conditions, which are air temperature, humidity, climate pressure, global sunshine, wind speed, wind direction and precipitation. This weather station is placed on the roof of the FAI building. The weather station was created as a Master thesis and its detailed description can be found here [5]. For the measurement itself, 5 temperature sensors were used, each surrounded by aluminium foil, which eliminates effects of radiation heat as shows Fig. 2. Sensors were placed approximately 1.5 meters above the floor and 0.3 meters away from elevator door. A temperature sensors working radius was limited by the length of the cable. An emergency ventilation system was shut down during the measurement, in order to simulate the worst possible conditions.

Fig. 2 shilded thermometer

The measurement started at 7 a.m. on 28^{th} of July and finished at 7 p.m. This day, was the hottest day in the whole year.

The adaptive thermal comfort approach, applying the indoor operative temperature in relation to the running mean outdoor air temperature as the main performance indicator. For the mean temperature of the outside air is typical regular, periodic fluctuations in both daily and annual cycle. It is the average daily temperature and its value is given by the average values of the clock cycle. Adaptive comfort temperatures are based on outside mean air temperature during the preceding several days. Mean air temperature can be calculated as is in (1). The weighting or influence given to the outside temperature is largest for the previous day, reducing for the preceding day, reducing again for the day preceding that and so on. A weighted running mean of outdoor temperatures θ_{rm} is calculated as follows (2). The α is a constant between 0 and 1 which defines the speed at which the running mean temperature responds to the outdoor air temperature and the characteristic time period of the relationship. The larger the value of α the more important are the effects of past temperatures. [6] The calculation is described more in czech translation of Europien standard CSN EN 15 251. [7]

$$\theta_{ed} = \frac{\theta_{7am} + \theta_{2pm} + \theta_{9pm} + \theta_{9pm}}{4} \quad (1)$$

Where is	θ_{ed}	mean air temperature	$[°C]$
	θ_{7am}	air temperature at 7 am	$[°C]$
	θ_{2pm}	air temperature at 2 pm	$[°C]$
	θ_{9pm}	air temperature at 9 pm	$[°C]$

$$\theta_{rm} = (1 - \alpha)\left\{\theta_{ed-1} + \alpha\theta_{ed-2} + \alpha^2\theta_{ed-3} + ...\right\} \quad (2)$$

Where is	θ_{rm}	running mean air temperature	$[°C]$
	θ_{ed-1}	mean air temperature from previous day	$[°C]$
	θ_{ed-2}	mean air temperature from previous two days	$[°C]$
	α	constant between 0 and 1 recomended value is 0.8	[-]

A. Building simulation in environmental engineering

In Environmental Engineering is now increasingly used methods of computer simulation for design, research, and evaluation of the dynamic behaviour of a buildings. Many manufacturers also enables customers to freely use various design of simulation environment. Larger environments serving designers and professionals, allow to use a much wider range and more accurate calculations. Thanks to the ever-increasing power of computers, these methods are used much more frequently. BESTEST or The Building Energy Simulation Test, is a project developed by the International Energy Agency (IEA), based on empirical validation, analytical validation and comparison analyses, which are tested on a variety of simulation software. [8] Around the world, there are developed many software tools that use different approaches to calculate the energy behaviour. There are exist several ways with which to assess the accuracy of simulation programs. Empirical validation enables comparison of calculations with data from the program monitored on a real building. Analytical validation on contrary compares calculations with the already known analytical solution, or generally accepted numerical methods with limited boundary conditions. Comparative testing already presents itself comparison with other simulation programs, which can be considered accurate. As test cases used different models, such as specifically set system environment, which is subsequently applied to the adiabatic shell of the building for a longer time horizon, or even years. All parameters that comparative model poses are defined by ANSI ASHRAE Standard 140: 2011 [9], which is approved as a standard test method for assessing computer program.

Simulated model used in this study was created to by most reliable around investigated staircase area, the rest of the model was retain inaccuracy. Computation was executed only in steady-state set. Boundary conditions of the computational model was set from measured data, outside air temperature $\theta_e = 34.7°C$, temperature of the surrounded rooms with regulated conditions $\theta_i = 32.7°C$. Time of calculated model was set to 2 p.m., because at this time was most extreme conditions during the measurement.

III. Results

Fig. 4 illustrates the temperature behaviour in Block B and solar radiation during the measurement period. As can be seen,

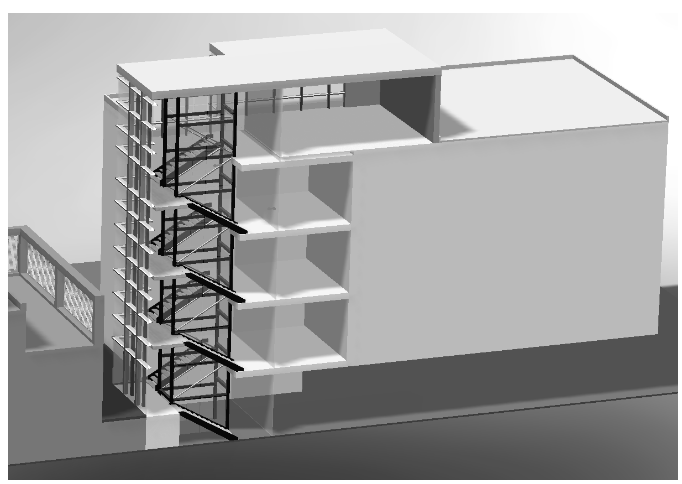

Fig. 3 model of the block B in simulation software

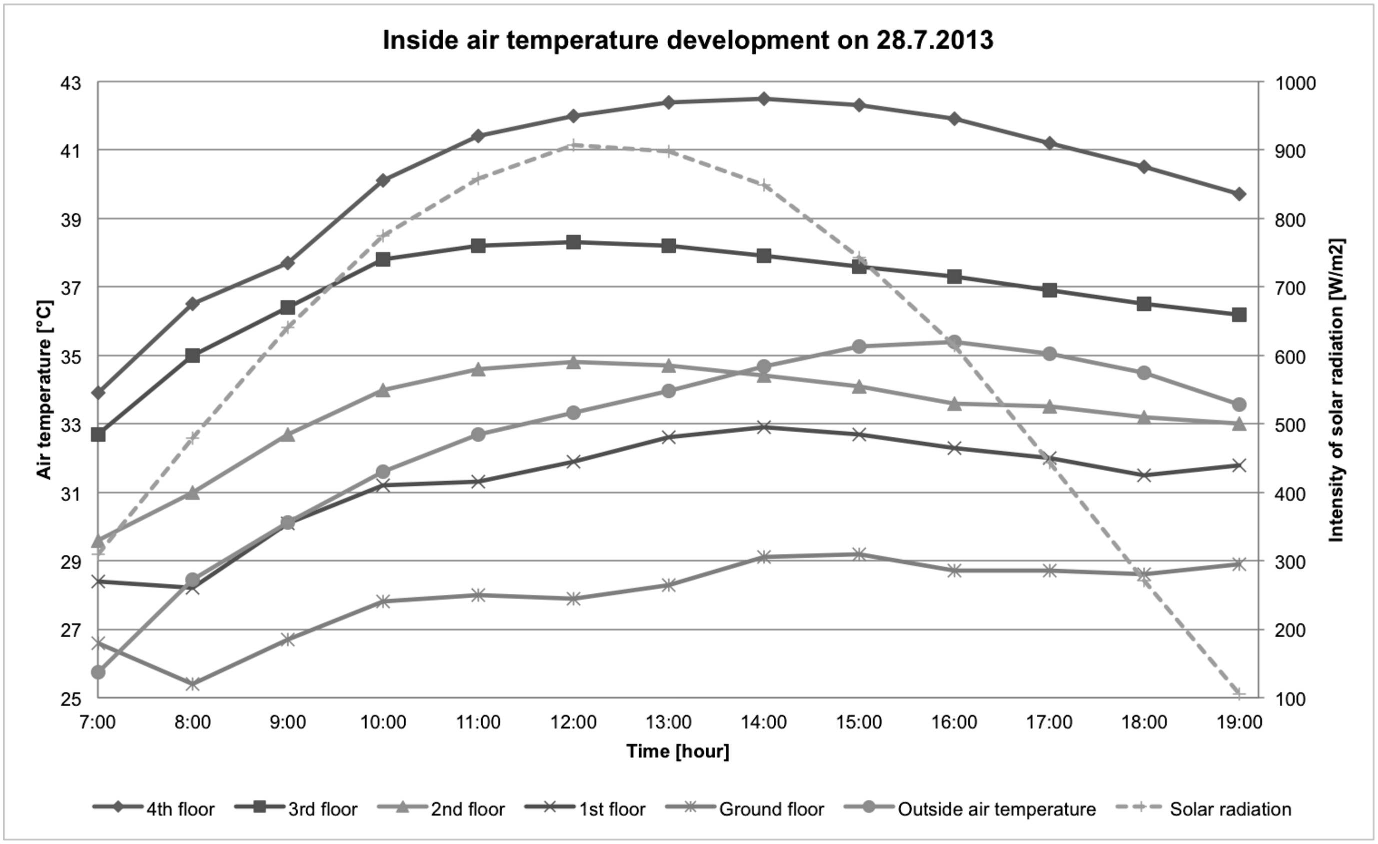

Fig. 4 air temperature distribution and solar radiation distribution on the day of measurement

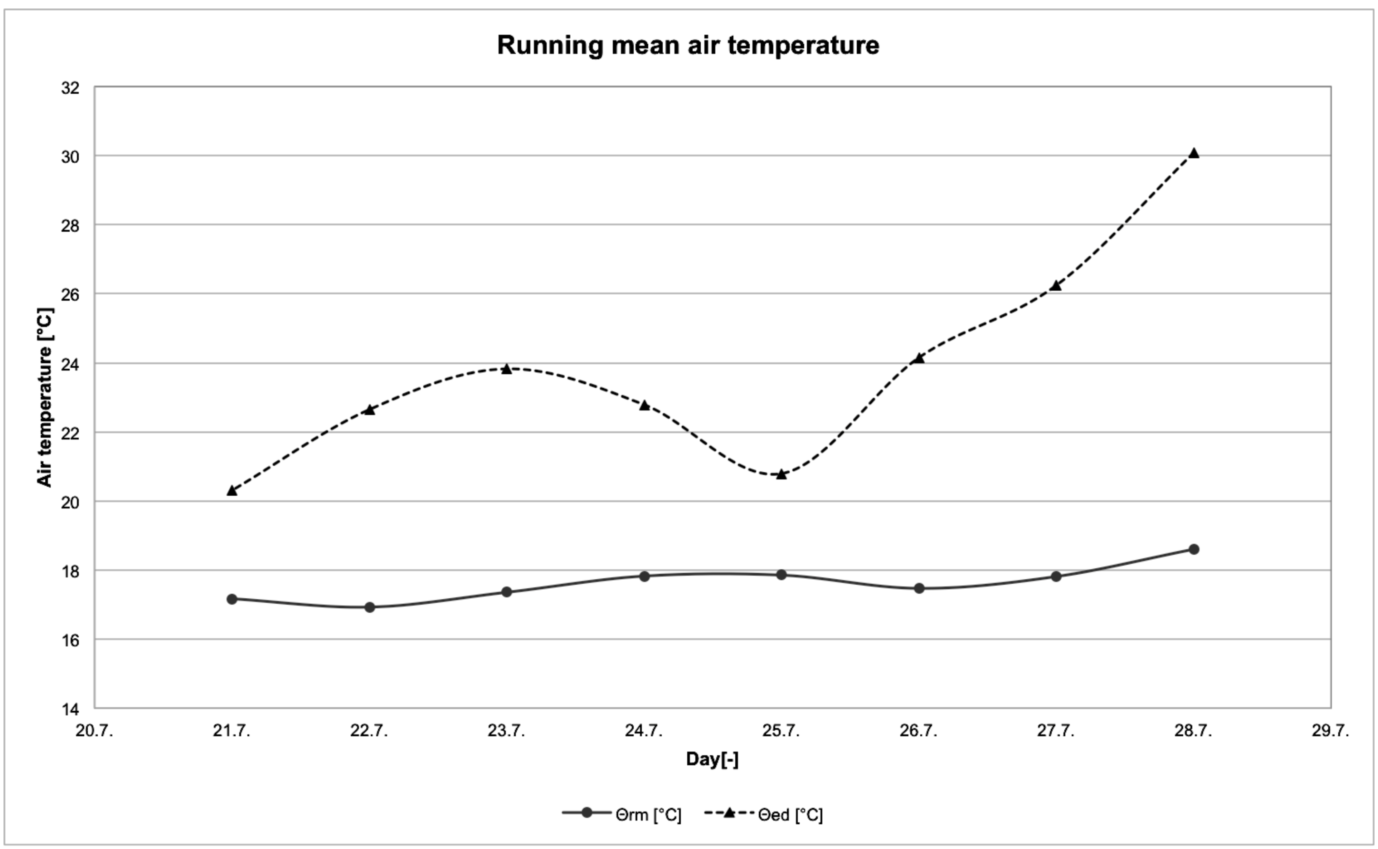

Fig. 5 development of running mean temperature and mean temperature 7 day before measurement the temperature progress is homogeneous at all floors of the staircase. The highest outside temperature was above $35°C$ and this value was measured at 2 p.m. This occurred two hours after the solar radiation peak, which is nothing unusual in this time of the year. The solar peak was slightly above $900\,W\,m^{-2}$, containing both global and diffusion beaming. The sky was clear during the whole day, as illustrated by the smooth curve of solar radiation. The temperature progress inside the building was completely different. As predicted, the highest temperatures were collected on the 4^{th} floor, on the contrary to the lowest temperatures, which occurred on the 0^{th} floor. This development is due to the sunshine, which was beaming whole day on the entire 4^{th} floor, in contrast to the 0^{th} floor, where the sun shined on inside walls for two hours from 8 a.m. and then one hour before sunset. The air temperature on the 0^{th} floor reached its bottom at 8 a.m. after a slight decrease, as clarified in Fig. 4. It is worth to mention, that at 8 a.m., 9 a.m. and almost at 10 a.m. the outside temperature had the same progress as the air temperature on the 1^{st} floor. The highest degrees on the 2^{nd} and the 3^{rd} floor were achieved at 12 a.m. A marginal hike on the 0^{th} and the 1^{st} floor occurred between 12 a.m. and 2 p.m. It can be assumed, that it was caused by temperature increase on the upper floors, especially on the 4^{th} floor, where temperature had reached almost $43°C$. Fig. 5 shows development of running mean air temperature and mean temperature for seven days before measurement of indoor air conditions. As can be seen running mean air temperature had periodic character. At the day of the measurement was on its rising path.

IV. Conclusion

The results indicate, overall, that the temperature gains are steep above the limit value for the daily rise in air temperature specified in Czech standard for indoor climatic conditions. [10] There is a high probability that inattention at the planning stage or under development could be the reason for such high heat gains. Disputation can be seen in a fact, that the standard was overrun because the measurement was done on the hottest day of the year. On the contrary, this is an advantage for further research, that data were collected under the worst possible conditions. Notwithstanding the limitations, this work suggests to take precautions against solar gains in Block B. A computer model of block B was created for the use of computer simulation. The simulation is performed by simulation software that has proven its credibility in the area through IEA BESTEST. [11],[12] On Fig. 6 is a preliminary result of simulation using coarse resolution computational grid. Currently, the calculations with a finer resolution are computed and results will be presented. Furthermore, the simulation will be compared with the measured data, then the model will be used to simulate the modifications to the least expensive customisation of the block B.

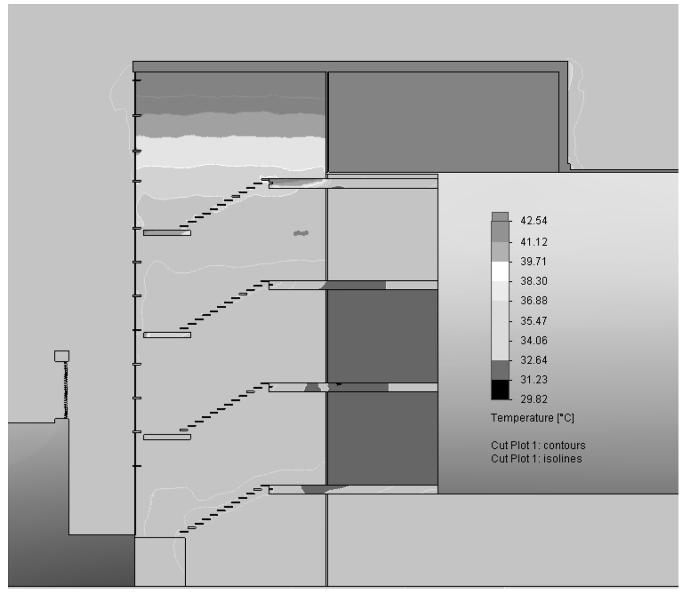

Fig. 6 air temperature stratification using coarse grid

References

[1] F. Nicol and M. Humphreys, “Maximum temperatures in European office buildings to avoid heat discomfort,” *Solar Energy*, vol. 81, no. 3, pp. 295–304, Mar. 2007.

[2] F. M. Butera, “Glass architecture : is it sustainable ?” in *Passive and Low Energy Cooling for the Built Environment*, no. May 2005, Santorini, 2004, pp. 161–168.

[3] H. Poirazis, “Double Skin Façades for Office Buildings Literature Review,” Lund, Tech. Rep., 2004.

[4] A. GhaffarianHoseini, N. D. Dahlan, U. Berardi, A. GhaffarianHoseini, N. Makaremi, and M. GhaffarianHoseini, “Sustainable energy performances of green buildings: A review of current theories, implementations and challenges,” *Renewable and Sustainable Energy Reviews*, vol. 25, pp. 1–17, Sep. 2013.

[5] J. Manasek, “Utilization of university weather station for creation of commercial information system,” Ph.D. dissertation, Tomas Bata University in Zlín, 2008. [Online]. Available: http://dspace.k.utb.cz/handle/10563/5269

[6] J. Nicol and M. Humphreys, “Adaptive thermal comfort and sustainable thermal standards for buildings,” *Energy and Buildings*, vol. 34, no. 6, pp. 563 – 572, 2002, special Issue on Thermal Comfort Standards. [Online]. Available: http://www.sciencedirect.com/science/article/pii/S0378778802000063

[7] V. Zmrhal and F. Drkal, “Indoor environmental input parameters for design and assessment of energy performance of buildings - addressing indoor air quality, thermal environment, lihting and acoustics,” Czech Technical Standard, Standard, February 2011.

[8] J. Neymark, R. Judkoff, G. Knabe, H.-T. Le, M. Dürig, a. Glass, and G. Zweifel, “Applying the building energy simulation test (BESTEST) diagnostic method to verification of space conditioning equipment models used in whole-building energy simulation programs,” *Energy and Buildings*, vol. 34, no. 9, pp. 917–931, Oct. 2002. [Online]. Available: http://linkinghub.elsevier.com/retrieve/pii/S0378778802000725

[9] R. Judkoff and J. Neymark, “Model validation and testing: The methodological foundation of ashrae standard 140,” ANSI/ASHRAE, Standard, 2011.

[10] J. Tywniak, Z. Svoboda, and T. Matuska, “Thermal protection of buildings,” Czech Technical Standard, Standard, October 2011.

[11] D. B. Crawley, S. J. Rees, M. J. Witte, S. D. Kennedy, H. F. Crowther, R. G. Baker, M. F. Beda, K. W. Cooper, S. D. Cummings, K. W. Dean, R. G. Doerr, E. P. Howard, and H. M. Newman, “Standard Method of Test for the Evaluation of Building Energy Analysis Computer Programs,” vol. 4723, 2008.

[12] S. Sehnalek, M. Zalesak, J. Vincenec, M. Oplustil, and P. Chrobak, “Ground-Coupled Heat Transfer Test Cases as ranking simulation software,” *WSEAS Transactions on Iinformation Sscience and Applications*, vol. 12, pp. 11–21, 2015.

New development kit for teaching microcontroller programming

Jan Dolinay, Petr Dostálek and Vladimír Vašek

***Abstract*—**This paper describes new platform for teaching microcontroller programming at our faculty. This platform replaces older board with Freescale HCS08 microcontroller and is based on new microcontroller with ARM core. Main component of the kit is low cost evaluation board with Arduino-compatible pin layout FRDM-KL25Z.

***Keywords*—**Arduino, FRDM-KL25Z, hcs08, Kinetis, microcontroller.

I. INTRODUCTION

THE hardware for teaching microcontroller programming is very diverse in general. There are hundreds of types of microcontrollers from many manufacturers and no common standard which would be accepted as the right tool for education. Typically, each school makes its own choice about the platform. Some schools use factory-made evaluation boards, some create their own custom boards.

However, in recent years more and more schools started to use Arduino. Arduino is a prototyping platform with microcontroller which allows very easy programming. The platform is composed of the hardware (board with microcontroller), program library for this microcontroller and integrated development environment (IDE) [1]. The Arduino has become de facto standard for prototyping and is very popular in the do-it-yourself community. It is also increasingly popular as a tool for teaching programming of embedded systems. The opinions whether this platform is suitable for such purpose are varied, from very positive to very negative [2], [3], [4]. In summary, it can be said that the platform is very easy to use and has wide community of users worldwide which makes it easy for students to write their programs and see the results quickly. This greatly improves the motivation to learn and the students are more likely to become really interested in the subjects and create their own projects [2]. On the other hand, the skills the students obtain are not easily transferable to other microcontroller platforms [4]. The Arduino programming interface (API) is very easy to use, but does not adhere to any consistent standard or design pattern. We also believe that given the current state of the industry, a successful graduate who intends to work with embedded systems needs to understand and handle microcontroller (MCU) programming at the level of peripheral registers, which is still the only common denominator for controlling peripherals of any MCU from any vendor. The knowledge of specific software library or graphical configuration tool is applicable only as far as this library or tool is widespread in the industry. Generally, there is no such library or tool with really broad appeal except perhaps the CMSIS standard for ARM microcontrollers [5], which is currently not fully supported by many MCU vendors, but which can become such a standard in near future.

As already mentioned, the Arduino can be considered a standard of its own, but it only applies to the do-it-yourself community. It is seldom used (and usable) in industrial applications.

However, it is true that Arduino represents sort of a standard in the hardware layout of a microcontroller prototyping board and microcontroller vendors now often provide their evaluation boards with pin layout compatible with the Arduino boards. This is also the case of the FRDM-KL25Z board used in our design [6].

The above mentioned facts play key role in considering what tools to use when planning MCU programming course, together with the purpose of the course, i.e. the intended future career of the course participants.

At our faculty we have two courses which deal with microcontroller programming for two different study programs. First course is for students who specialize in security technologies and management and the second course is for students of information technology. For the first course Arduino platform is suitable according to our opinion. It offers the right tools to fulfill the aim of the course, which is to introduce the students into embedded systems and show them the possibilities. With easy-to-use platform like Arduino students can quickly build projects which have interesting, real-world outputs and motivate them to learn more.

The second course should produce future software engineers

This work was supported by the European Regional Development Fund under the project CEBIA-Tech No. CZ.1.05/2.1.00/03.0089)

Jan Dolinay is with the Department of Automation and Control Engineering, Tomas Bata University in Zlin, Faculty of Applied Informatics, nám. T. G. Masaryka 5555, 76001 Zlín, Czech Republic (e-mail: dolinay@fai.utb.cz).

Petr Dostálek is with the Department of Automation and Control Engineering, Tomas Bata University in Zlin, Faculty of Applied Informatics, nám. T. G. Masaryka 5555, 76001 Zlín, Czech Republic (e-mail: dostalek@fai.utb.cz).

Vladimír Vašek is with the Department of Automation and Control Engineering, Tomas Bata University in Zlin, Faculty of Applied Informatics, nám. T. G. Masaryka 5555, 76001 Zlín, Czech Republic (e-mail: vasek@fai.utb.cz).

able to deal with microcontrollers at more general level. For such course we believe more traditional approach with C language is more suitable. We needed to create hardware tool for this course which would allow such approach while keeping up with the latest developments in the industry. The results are discussed in the next section.

II. Hardware for microcontroller programming lessons

As mentioned in the introduction, we have two different courses of microcontrollers programming at our faculty with two different purposes. Recently, a decision has been made to update the equipment and contents of these courses to reflect new trends in the industry. Previously, we used the same tools in both courses. While this has obvious advantages of easy maintenance of the equipment and course materials, it was also clear that the lessons suitable for students with strong programming background are too difficult for the students of the non-programming, security-technology program. These students were often put off by the difficulties of working with the full-featured IDE and programming in C language. Even though we provide supporting libraries which simplify access to the peripherals, for many students this was not sufficient and their motivation to learn was low.

A. *Evaluation kit with HCS08 microcontroller*

In previous years we used evaluation kit M68EVB908GB60, which can be seen in figure 1. It contains microcontroller with 8-bit HCS08 core [7], to be exact it uses HCS08GB60 MCU. The kit is out of production for several years, but the MCU itself was discontinued only recently, so we were able to repair the kits damaged during the course by replacing the MCU. However, it is clear that our supply of the MCUs would not last long and the kits would need to be replaced just for this reason in a year or two anyway. In the following section this older kit will be briefly described to provide better understanding of the requirements on the new kit.

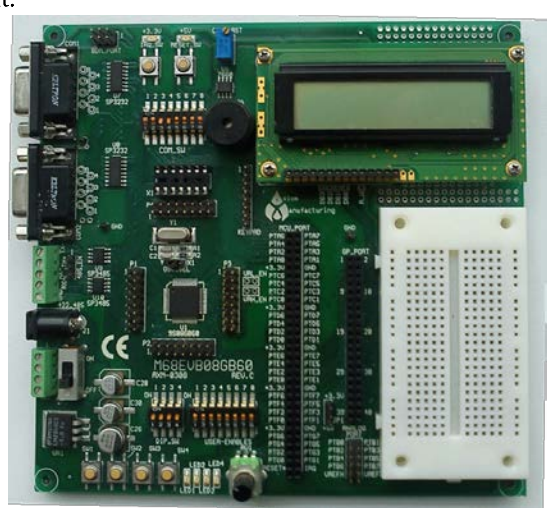

Fig. 1 evaluation kit with Freescale HCS08GB60 microcontroller

As already mentioned, the core of the kit is 8-bit microcontroller HCS08GB60 with 60 kB of flash and 4 kB of RAM memory. The MCU itself contains many internal peripherals such as two timers, two asynchronous serial interfaces (UART), analog-to-digital converter and others. The board adds external peripherals useful for education, such as LCD display (2 lines by 16 characters), four push buttons and four LEDs, potentiometer and a buzzer. There is also a so-called MCU port, which provides access to all the GPIO pins of the MCU and together with the breadboard (in the bottom right part of the picture) allows easy prototyping of students own circuits. We also use the MCU port as a means for connecting expansion modules which can offer other peripherals. These modules include, for example, a stepper motor, heat plant, graphical LCD display, digital-to-analog converter, etc. Some of the modules were described in [8]. As a part of the course we also teach programming with simple real-time operating system (RTOS). We have developed such simple system for the older kit [9].

The kit is connected to the development PC through serial port. The MCU contains monitor program which allows downloading the program to MCU memory and debugging.

B. *Requirements for the new board*

When defining desired features of the new educational board, the experience with the old board was also taken into account, besides the latest trends in the industry.

The main points for the new design can be summarized as follows:

- Microcontroller with 32-bit ARM core
- LCD display on board
- Several push buttons and LEDs
- MCU connector compatible with previous kit
- Low cost
- Easy repairs

Reasons for the above points are given here. ARM architecture has become a standard in the industry and is replacing 8-bit microcontrollers even in simple, low-cost applications.

LCD display, push buttons and LEDs are the basic means of communication of the MCU with the outside world. We prefer to include these directly on the evaluation board as opposed to a “minimalistic” approach known, for example, from the Arduino boards. Such approach means that the board contains minimal number of external peripherals, basically just the power supply, MCU, programming interface and connectors for accessing the MCU pins. This results in lower price and allows students to learn about the hardware together with software. For example, to see a blinking LED, one has to connect the LED and resistor. This is certainly good for understanding the topic better. On the other hand, for courses focused mainly on programming, this hardware interaction may be unnecessary and distracting and it also makes the course difficult to maintain – the equipment such as LEDs, push buttons, resistors, wires etc. has to be dealt with. For

ISBN: 978-1-61804-321-4

these reasons we prefer to have the basic peripherals on-board. Obviously, this does not limit the possibility to connect external peripherals if desired.

On the old kit with HCS08 there is a so-called MCU port which allows access to the MCU pins. As mentioned earlier we have several educational modules which connect to this connector. It was desirable to make it possible to use these modules also with the new kit. This means that a connector with physically compatible layout and functionally compatible pins of the MCU connected is required. It presented rather complicated task to connect the pins as required to maintain functional compatibility with the older kit's connector, but it was solved successfully.

Low cost was not a topmost priority, but naturally, it was also considered. Together with requirement for easy repair of damaged kits this lead to the decision to use factory-made MCU board which will be attached to the printed circuit board (PCB) of the kit, rather than using the MCU directly. There are many low-cost boards with ARM MCUs on the market nowadays. With cost starting even below $10, it is economically more suitable to use such factory-made board with the MCU and supporting electronics including programming interface than trying to use these small parts directly on PCB. We chose Freescale FRDM-KL25Z board [6] as the main part of the new educational kit. The board is shown in figure 2.

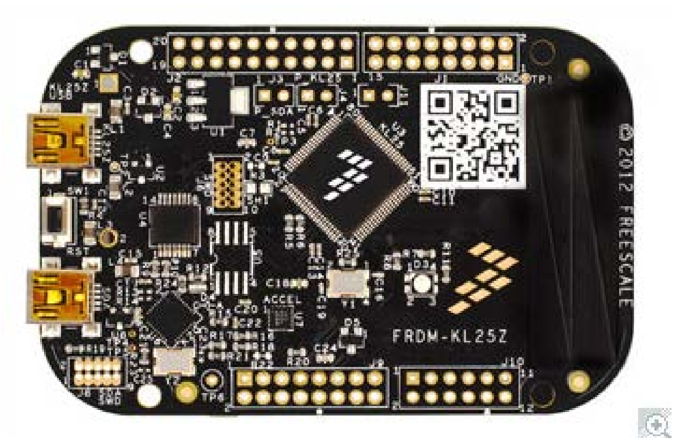

Fig. 2 freescale FRDM-KL25Z board used in the kit [6]

This board is member of a family of low cost evaluation boards called Freedom platform [10]. The board we used contains KL25Z128VLK4 microcontroller with ARM M0+ core, 128 kB of Flash and 16 kB of RAM. The board includes programming and debugging interface (openSDA). Layout of the board is compatible with the layout of the Arduino platform [1].

The compatibility with Arduino was not a requirement but seems advantageous. The platform is extremely popular in the community of do-it-yourself users and often used also for education. There are also numerous expansion boards (shields) available for this platform, which follow the same pin layout. Therefore, it is nice feature of the new kit, that the main board has Arduino-compatible layer and allows connecting the expansion boards designed for Arduino. Also the FRDM-KL25Z board can be detached from the kit and used separately and vice-versa another board with Arduino-compatible board could theoretically be connected to the educational kit as a new MCU component.

III. New educational kit

Main features of the new development kit were already mentioned in the previous chapter. Block diagram in figure 3 shows the key components. Actual physical layout of the kit can be seen in figure 4.

As can be seen in the figures, central component of the kit is the FRDM-KL25Z board with microcontroller and programming interface. This board connects to the host computer via USB cable. It is attached to a connector on the main board of the kit, so it can be easily replaced in case of damage. The FRDM-KL25Z board itself contains several interesting peripherals – an RGB LED, touch slider and three-axis accelerometer. On the main board there are many other peripherals useful for education:

- LCD display
- MCU port
- Four push buttons
- Three LEDs
- Potentiometer
- Rotary encoder
- RS-232 port
- RS485 port
- Real-time clock circuit PCF8583P
- Temperature sensor LM75AD
- Humidity sensor HIH6130
- EEPROM memory 25LC640A, connected via SPI bus, 64 kbit.

The text LCD display has two lines with 16 characters per line. MCU port allows connecting our educational models developed for the previous development board used in the lessons. There is also one serial port available on the board in addition to the virtual serial port provided by the programming interface over USB and also one RS-485 port. This way all three UART modules available in the microcontroller are utilized.

For learning about analog-to-digital converter there is a potentiometer connected to one of the input pins of the MCU. There is also rotary encoder connected to a timer channel, which makes it possible to experiment with input capture function of the timer module in the MCU.

The temperature and humidity sensor together with real-time clock (RTC) circuit are connected to the MCU via I2C bus; and there is also external EEPROM memory connected via SPI bus. Thus students can learn both about the communication via these busses and also about working with the connected devices and sensors.

ISBN: 978-1-61804-321-4

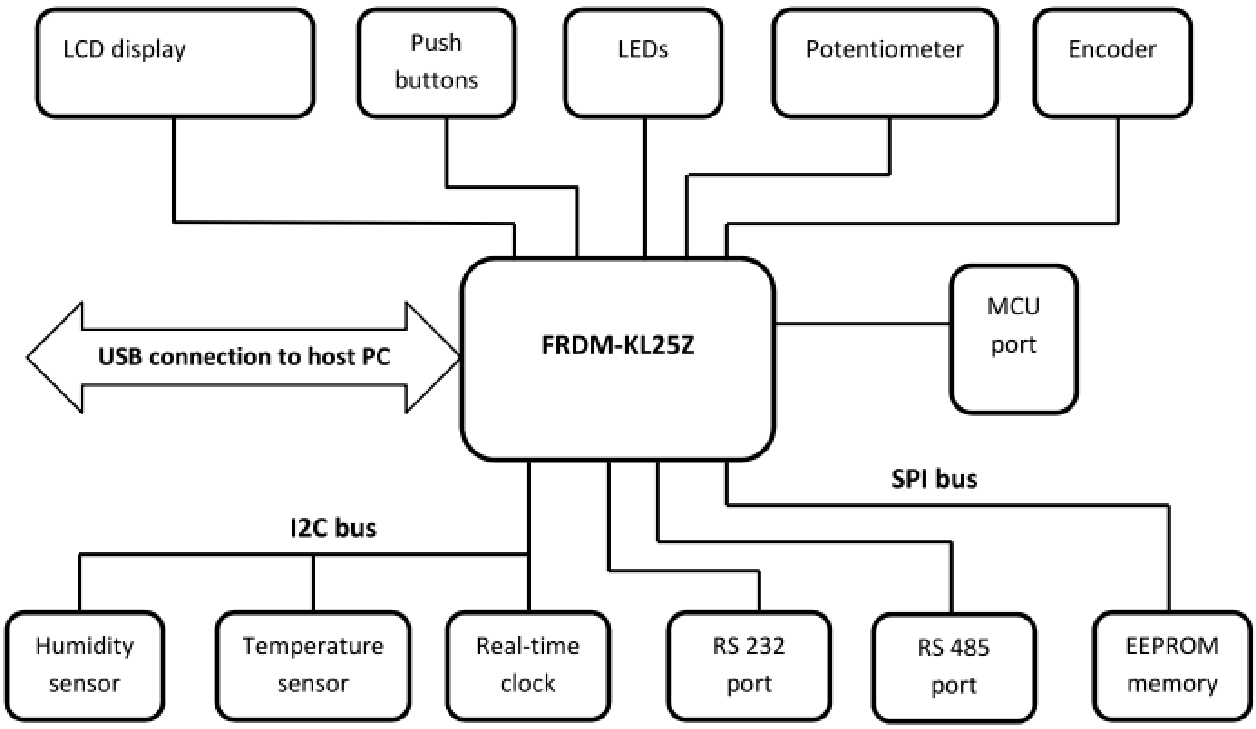

Fig. 3 main components of the new kit

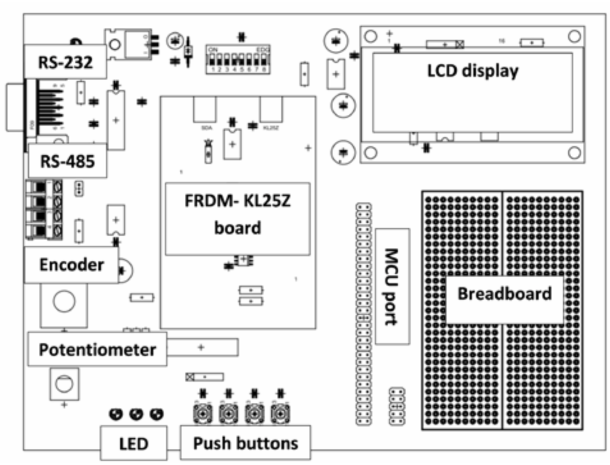

Fig. 4 physical layout of the kit

IV. CONCLUSION

This article described our development kit for teaching microcontroller programming. This kit was developed to update the equipment used for courses of microcontroller programming at our faculty. It replaces older board with Freescale HCS08 microcontroller. This new board is based on 32-bit microcontroller with ARM M0+ core from Freescale's Kinetis family. The microcontroller is used in the form of a low-cost board FRDM-KL25Z which is the main component of the kit. It is attached to our custom printed circuit board with other peripherals, such as display, push buttons, LEDs, external EEPROM memory, etc. Currently, a prototype of the kit is being assembled and the board will undergo final testing. We plan to introduce this kit into the courses which start in the winter semester in September 2015. In the meantime course documentation and example programs will be prepared.

REFERENCES

[1] *Arduino, Open-source electronics prototyping platform*, Available: http://www.arduino.cc.

[2] P. Jamieson, Arduino for Teaching Embedded Systems. Are Computer Scientists and Engineering Educators Missing the Boat?. [Online]. Available: http://www.users.muohio.edu/jamiespa/html_papers/fecs_11.pdf.

[3] P. Bender, K. Kussmann, "Arduino based projects in the computer science capstone course," *Journal of Computing Sciences in Colleges*, vol. 27, no. 5, pp. 152-157, May 2012.

[4] *Why Arduino is not the right educational tool*, Available: http://www.hackvandedam.nl/blog/?p=762.

[5] *ARM Ltd., CMSIS - Cortex Microcontroller Software Interface Standard*. Available: http://www.arm.com/products/processors/cortex-m/cortex-microcontroller-software-interface-standard.php

[6] *Freescale Semiconductor, FRDM-KL25Z: Freescale Freedom Development Platform for Kinetis KL14/15/24/25 MCUs.* Available: http://www.freescale.com/webapp/sps/site/prod_summary.jsp?code=FRDM-KL25Z

[7] *Freescale Semiconductor, CPU08 Central Processor Unit Reference Manual, rev.4.* Available: http://www.freescale.com

[8] J. Dolinay, P. Dostálek, V. Vašek, "Educational models for lessons of microcontroller programming", in *Proc. 11th International Research/Expert conference TMT 2007*, Hammamet 2007, pp. 1447-1450.

[9] J. Dolinay, V. Vašek, P. Dostálek, "Implementation and Application of a Simple Real-time OS for 8-bit Microcontrollers," in *Proc. 10th WSEAS International Conference on ELECTRONICS, HARDWARE, WIRELESS and OPTICAL COMMUNICATIONS (EHAC '11)*, Cambridge 2011, pp. 023-026.

[10] *Freescale Semiconductor, Freescale Freedom Development Platform.* Available: http://www.freescale.com/webapp/sps/site/overview.jsp?code=FREDEVPLA

The proposal motion of manipulator for active monitoring of luggage compartment and description of its dynamic behavior

Jan Struška, Martin Struška, and Miroslav Popelka

Abstract— Article deals with design autonomous service robotic system with ability of scanning and identification suspicious objects in luggage compartments of transport vehicles. The basis is a complete project control of motion states, derived and calculated by based on the equations of motion. Following these are determined effects of inertia of the moving object, their interaction and subsequent effect on individual homogenous moving arms including the dynamic load drives. Equations of motion are derived and calculated from kinetic and potential energy of motion systems. Based on calculations and chosen concept of manipulator is created 3D structural model.

Keywords— Robotics, manipulator, motional equations, kinematics, dynamics

I. Introduction

AUtonomous serviced robotic systems can be used in particular scanning and identification of suspicious objects in cabin luggage compartments of vehicles. Such spaces, as in vehicles type train, plane located above the passenger's heads and require viewing, where possible, identify and remove dangerous objects.

Based on the structure of this type of service robot, is primarily implemented manipulator, allowing the movement of the camera and a distance sensor as an element of external sensory system. Also for supporting any sensors of chemical compounds or explosives for the autonomous movement of the effector on the premises. Inner sensory system is commonly formed beside the angular position sensor of any electrical or hydraulic actuators mobile system, especially a system of sensors for controlling the movement of possible states of the manipulator.

This work was supported by Internal Grant Agency of Tomas Bata University under the project No. IGA/FAI/2015/027, IGA/FAI/2015/040, and No. IGA/FAI/2015/017.

Jan Struška is with Department of Automation and Control Engineering, Faculty of Applied Informatics, Tomas Bata University in Zlín, Czech Republic (corresponding author, e-mail: jstruska@fai.utb.cz).

Martin Struška is with Department of Automation and Control Engineering, Faculty of Applied Informatics, Tomas Bata University in Zlín, Czech Republic (corresponding author, e-mail: mstruska@fai.utb.cz).

Miroslav Popelka is with Department of Automation and Control Engineering, Faculty of Applied Informatics, Tomas Bata University in Zlín, Czech Republic (corresponding author, e-mail: popelka@fai.utb.cz).

Give cause for the emergence of this project was the absence of potential manipulator arm, allowing the dimensions and design integration directly into the luggage space.
The main general aim of the works, one of which this text the first part, is methodology of motional equations derivation of manipulator and achieved results, necessary for motion system proposal and the control.

Next works will be dedicated to complete manipulator movement, its motional equations and created 3D structural model based on the obtained parameters.

II. Manipulator Body Motional Equations

A. Statement of a problem

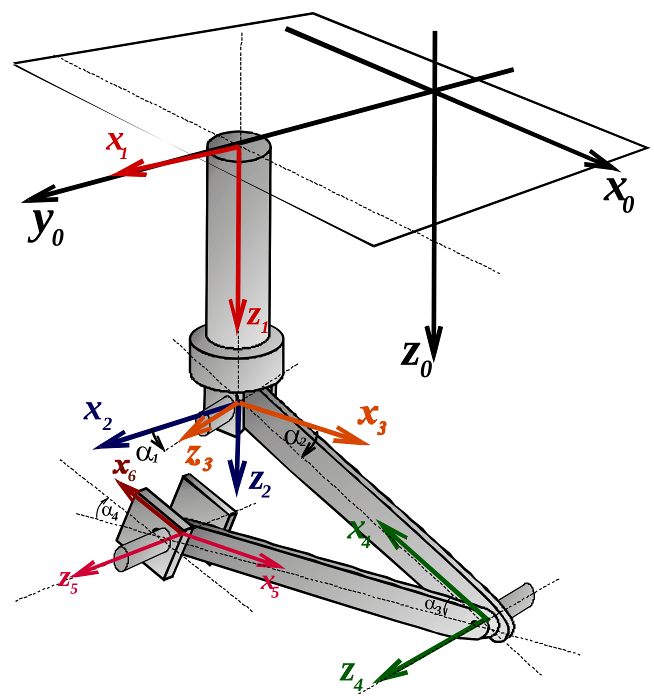

Fig. 1 manipulator parameters in the framework the coordinate system

On Fig.1 manipulator body presented, situated in plane as a system with six freedom degree.
Task is to derive the motional equations depending on the position of the arms towards the origin of the coordinate system, forming angles $\boldsymbol{\alpha_1}$, $\boldsymbol{\alpha_2}$ and $\boldsymbol{\alpha_3}$. The end effector with the momentum of inertia relative to the axis $\mathbf{Z_5}$ is neglected in this case.

B. Determination transformation and kinematic matrix

For the compilation equations of motion is first necessary to find kinematic transformation matrix $^{\mathbf{i-1}}\mathbf{T_i}$ for **i=1,2,3,4** equation of physical element **dm1** first arm and for **i=1,2,3,4,5** of physical element **dm2** by second arm, where basic matrix is:

$$^{i-1}\mathbf{T}_i = \begin{bmatrix} \cos\theta_i & -\cos\alpha_i \sin\theta_i & \sin\alpha_i \sin\theta_i & a_i\cos\theta_i \\ \sin\theta_i & \cos\alpha_i\cos\theta_i & -\sin\alpha_i\cos\theta_i & a_i\sin\theta_i \\ 0 & \sin\alpha_i & \cos\alpha_i & d_i \\ 0 & 0 & 0 & 1 \end{bmatrix}; \quad (1)$$

Following matrix, and calculations demonstrates the procedure for first arm element **dm1.** In the second arm of physical element **dm2** is procedure similar. After substitution:

$$^{0}\mathbf{T}_1 = \begin{bmatrix} \cos 90^0 & -\cos 0^0 \sin 90^0 & \sin 0^0 \sin 90^0 & y_T \cos 90^0 \\ \sin 90^0 & \cos 0^0 \cos 90^0 & -\sin 0^0 \cos 90^0 & y_T \sin 90^0 \\ 0 & \sin 0^0 & \cos 0^0 & 0 \\ 0 & 0 & 0 & 1 \end{bmatrix} = \begin{bmatrix} 0 & -1 & 0 & 0 \\ 1 & 0 & 0 & y_T \\ 0 & 0 & 1 & 0 \\ 0 & 0 & 0 & 1 \end{bmatrix} \quad (2)$$

$$^{1}\mathbf{T}_2 = \begin{bmatrix} 1 & 0 & 0 & 0 \\ 0 & 1 & 0 & 0 \\ 0 & 0 & 1 & h \\ 0 & 0 & 0 & 1 \end{bmatrix}; {}^{2}\mathbf{T}_3 = \begin{bmatrix} -\sin\alpha_1 & 0 & \cos\alpha_1 & 0 \\ -\cos\alpha_1 & 0 & -\sin\alpha_1 & 0 \\ 0 & -1 & 0 & 0 \\ 0 & 0 & 0 & 1 \end{bmatrix}$$

The resulting transformation matrix $^{\mathbf{3}}\mathbf{T_4}$ is:

$$^{3}\mathbf{T}_4 = \begin{bmatrix} -\cos\alpha_2 & -\sin\alpha_2 & 0 & \ell_1\cos\alpha_2 \\ \sin\alpha_2 & -\cos\alpha_2 & 0 & -\ell_1\sin\alpha_2 \\ 0 & 0 & 1 & 0 \\ 0 & 0 & 0 & 1 \end{bmatrix} \quad (3)$$

Coordinates physical element **dm1** of first arm in his coordinate system $\mathbf{O_{x4y4z4}}$ is:

$$[x \quad 0 \quad 0 \quad 1]^T$$

Following the determination of absolute coordinates physical element **dm1** of first arm, in global coordinate of systém $\mathbf{O_{x0y0z0}}$

Global position of element $\mathbf{dm_1}$:

$$\begin{bmatrix} X_{dm1} \\ Y_{dm1} \\ Z_{dm1} \\ 1 \end{bmatrix} = {}^{0}\mathbf{T}_4 \cdot \begin{bmatrix} x \\ 0 \\ 0 \\ 1 \end{bmatrix} = \begin{bmatrix} \ell_1\cos\alpha_1\cos\alpha_2 \\ y_T - \ell_1\sin\alpha_1\cos\alpha_2 \\ h + \ell_1\sin\alpha_2 \\ 1 \end{bmatrix} \quad (4)$$

Vector absolute speed of element $\mathbf{dm_1}$ is then:

$$\vec{v}_{dm1} = \begin{bmatrix} (\ell_1 - x)\cdot(\omega_1 \cdot \sin\alpha_1\cos\alpha_2 - \omega_2 \cdot \cos\alpha_1 \sin\alpha_2) \\ v_y + (\ell_1 - x)\cdot(\omega_2 \sin\alpha_1 \sin\alpha_2 - \omega_1\cos\alpha_1\cos\alpha_2) \\ (\ell_1 - x)\cdot\omega_2\cos\alpha_2 \\ 0 \end{bmatrix} \quad (5)$$

Quadrat of size speed $\mathbf{dm_1}$:

$$\begin{aligned} |\vec{v}_{dm1}|^2 &= (\ell_1 - x)^2 \cdot \{\omega_2^2 + \omega_1^2 \cdot \cos^2\alpha_2\} + \\ &+ 2(\ell_1 - x)\cdot v_y \cdot (\omega_2 \cdot \sin\alpha_1 \sin\alpha_2 - \omega_1 \cos\alpha_1 \cos\alpha_2) + v_y^2 \end{aligned} \quad (6)$$

Then apply for the first drive:

$$\begin{aligned} |\vec{v}_{p1}|^2 &= \ell_1^2 \cdot \{\omega_2^2 + \omega_1^2 \cdot \cos^2\alpha_2\} + \\ &+ 2\ell_1 \cdot v_y \cdot (\omega_2 \cdot \sin\alpha_1 \sin\alpha_2 - \omega_1\cos\alpha_1\cos\alpha_2) + v_y^2 \end{aligned} \quad (7)$$

The kinetic energy of swing:

$$W_{k1} = \frac{1}{2}\cdot m \cdot \dot{y}^2 + \frac{1}{2}\cdot J_m \cdot \dot{\alpha}_1^2 \quad (8)$$

The kinetic energy of element $\mathbf{dm_1}$ by first arm is:

$$dW_{km1} = \frac{1}{2}\cdot\frac{m_1}{\ell_1}\cdot|\vec{v}_{dm1}|^2 \cdot dx$$

The kinetic energy of first arm W_{km1}:

$$W_{km1} = \frac{1}{2}\cdot m_1 \cdot \left[\begin{aligned} &\frac{1}{3}\cdot(\dot{\alpha}_2^2 + \dot{\alpha}_1^2 \cdot \cos^2\alpha_2)\cdot\ell_1^2 + \ell_1 \cdot \dot{y} \cdot \\ &.(\dot{\alpha}_2 \cdot \sin\alpha_1 \sin\alpha_2 - \dot{\alpha}_1 \cos\alpha_1 \cos\alpha_2) + \dot{y}^2 \end{aligned} \right] \quad (9)$$

Resulting kinetic energy of first drive W_{kp1}:

$$W_{kp1} = \frac{1}{2}\cdot m_{p1} \cdot \left[\begin{aligned} &\ell_1^2 \cdot (\dot{\alpha}_2^2 + \dot{\alpha}_1^2 \cdot \cos^2\alpha_2) + 2\ell_1 \cdot \dot{y} \cdot \\ &(\dot{\alpha}_2 \cdot \sin\alpha_1 \sin\alpha_2 - \dot{\alpha}_1 \cos\alpha_1 \cos\alpha_2) + \dot{y}^2 \end{aligned} \right] \quad (10)$$

After determining the kinetic energy of the system, we can compile the equations of motion (13). But first, a description of the dynamics of the system using lagranger function (11).

Lagrangian:

$$\begin{aligned} L &= \overbrace{(m + m_1 + m_{p1} + m_2 + m_{p2} + m_e)}^{M}\cdot\dot{y} + \left(m_{p1} + \frac{1}{2}m_1\right)\cdot \\ &\ell_1[\dot{\alpha}_2^2 \cdot (\sin\alpha_1 \cdot \sin\alpha_2) - \dot{\alpha}_1^2 \cdot (\cos\alpha_1 \cdot \cos\alpha_2)] + m_2 . \\ &.\left\{ \begin{aligned} &\frac{1}{2}\ell_2 \left[\begin{aligned} &\dot{\alpha}_1 \cdot \cos\alpha_1 \cos(\alpha_2 - \alpha_3) + \dot{\alpha}_2 \cdot \sin\alpha_1 \sin(\alpha_2 - \alpha_3) - \\ &- \dot{\alpha}_3 \cdot \sin\alpha_1 \sin(\alpha_2 - \alpha_3) \end{aligned} \right] - \\ &- \ell_1(\dot{\alpha}_1 \cos\alpha_1 \cos\alpha_2 - \dot{\alpha}_2 \sin\alpha_1 \sin\alpha_2) \end{aligned} \right\} + \\ &+ (m_{p2} + m_e)\cdot\left\{ \begin{aligned} &\ell_2 \left[\begin{aligned} &\dot{\alpha}_1 \cdot \cos\alpha_1 \cos(\alpha_3 - \alpha_2) + \dot{\alpha}_2 \cdot \sin\alpha_1 \sin(\alpha_3 - \alpha_2) - \\ &- \dot{\alpha}_3 \cdot \sin\alpha_1 \sin(\alpha_3 - \alpha_2) \end{aligned} \right] - \\ &- \ell_1(\dot{\alpha}_1 \cos\alpha_1 \cos\alpha_2 - \dot{\alpha}_2 \sin\alpha_1 \sin\alpha_2) \end{aligned} \right\} \end{aligned} \quad (11)$$

Where $\frac{\partial L}{\partial y} = 0$

C. Motion equations by manipulator object

The most important step for the dynamic analysis of the manipulator is a derivation equations motion of system, describing the dynamic behavior of the manipulator. The equations of motion derived from a lagranger function (11).

Motion equation for **y**:

$$\frac{d}{dt}\left(\frac{\partial L}{\partial \dot{y}}\right)-\frac{\partial L}{\partial y}=F_{ext}$$

Substituting then:

$$\begin{aligned}
F_{ext} &= \overbrace{\left(m+m_1+m_{p1}+m_2+m_{p2}+m_e\right)}^{M}\cdot \ddot{y}+\\
&+\ddot{\alpha}_1\cdot\left\{\begin{array}{l}\left[\left(m_{p2}+m_e\right)+\dfrac{m_2}{2}\right]\ell_2\cos\alpha_1\cos\left(\alpha_3-\alpha_2\right)-\\ -\left[\left(m_{p2}+m_e+m_2+m_{p1}+\dfrac{m_1}{2}\right)\cdot\ell_1\cos\alpha_1\cos\alpha_2\right]\end{array}\right\}+\\
&+\ddot{\alpha}_2\cdot\left\{\begin{array}{l}\left[\left(m_{p2}+m_e\right)+\dfrac{m_2}{2}\right]\ell_2\sin\alpha_1\sin\left(\alpha_3-\alpha_2\right)+\\ +\left[\left(m_{p2}+m_e+m_2+m_{p1}+\dfrac{m_1}{2}\right)\cdot\ell_1\sin\alpha_1\sin\alpha_2\right]\end{array}\right\}+\\
&-\ddot{\alpha}_3\cdot\left\{\left[\left(m_{p2}+m_e\right)+\dfrac{m_2}{2}\right]\ell_2\sin\alpha_1\sin\left(\alpha_3-\alpha_2\right)\right\}+\\
&+\dot{\alpha}_1^2\left\{\begin{array}{l}\left(m_{p2}+m_e+m_2+m_{p1}+\dfrac{m_1}{2}\right)\ell_1\sin\alpha_1\cos\alpha_2-\\ -\left(m_{p2}+m_e+\dfrac{m_2}{2}\right)\ell_2\sin\alpha_1\cos\left(\alpha_3-\alpha_2\right)\end{array}\right\}+\\
&+\dot{\alpha}_2^2\left\{\begin{array}{l}\left(m_{p2}+m_e+m_2+m_{p1}+\dfrac{m_1}{2}\right)\ell_1\sin\alpha_1\cos\alpha_2-\\ -\left(m_{p2}+m_e+\dfrac{m_2}{2}\right)\ell_2\sin\alpha_1\cos\left(\alpha_3-\alpha_2\right)\end{array}\right\}-\\
&-\dot{\alpha}_3^2\left(m_{p2}+m_e+\frac{m_2}{2}\right)\ell_2\sin\alpha_1\cos\left(\alpha_3-\alpha_2\right)\\
&+2\dot{\alpha}_1\cdot\dot{\alpha}_2\left[\begin{array}{l}\left(m_{p2}+m_e+\dfrac{m_2}{2}\right)\ell_2\cos\alpha_1\sin\left(\alpha_3-\alpha_2\right)+\\ +\left(m_{p2}+m_e+m_2+m_{p1}+\dfrac{m_1}{2}\right)\ell_1\cos\alpha_1\sin\alpha_2\end{array}\right]-\\
&-2\dot{\alpha}_1\cdot\dot{\alpha}_3\left(m_{p2}+m_e+\frac{m_2}{2}\right)\ell_2\cos\alpha_1\sin\left(\alpha_3-\alpha_2\right)+2\dot{\alpha}_2\cdot\\
&.\dot{\alpha}_3\left(m_{p2}+m_e+\frac{m_2}{2}\right)\ell_2\cos\alpha_1\sin\left(\alpha_3-\alpha_2\right)
\end{aligned}\tag{12}$$

Example motion equation for **Mα1**, **Mα2** and **Mα3** are:

$$\begin{aligned}
&\frac{d}{dt}\left(\frac{\partial L}{\partial \dot{\alpha}_1}\right)-\frac{\partial L}{\partial \alpha_1}=M_{\alpha_1},\ \frac{d}{dt}\left(\frac{\partial L}{\partial \dot{\alpha}_2}\right)-\frac{\partial L}{\partial \alpha_2}=M_{\alpha_2}\\
&\frac{d}{dt}\left(\frac{\partial L}{\partial \dot{\alpha}_3}\right)-\frac{\partial L}{\partial \alpha_3}=M_{\alpha 3}
\end{aligned}\tag{13}$$

Following is a sample derivation of the equation for **Mα3**. Pro **Mα1** and **Mα2** is similar process. The first step is an equation (11) into these derivatives $\frac{\partial L}{\partial \dot{\alpha}_3}\ a\ \frac{\partial L}{\partial \alpha_3}$.

After substituting is expressed **Mα3**:

$$\begin{aligned}
M_{\alpha 3} &= -\ddot{y}\cdot\left\{\left(\frac{m_2}{2}+m_e+m_{p2}\right)\cdot\ell_2\cos\alpha_1\sin\left(\alpha_3-\alpha_2\right)\right\}+\\
&+\ddot{\alpha}_2\cdot\left[\left(m_{p2}+m_e\right)\left(\ell_1\ell_2\cos\alpha_3-\ell_2^2\right)-\frac{m_2}{3}\ell_1^2\right]+\\
&+\ddot{\alpha}_3\cdot\left[\left(m_{p2}+m_e\right)\ell_2^2-\frac{m_2}{3}\ell_1^2\right]+\\
&+\dot{\alpha}_1^2\left[\left(m_{p2}+m_e\right)\ell_2^2+\frac{m_2}{3}\ell_1^2\right]\cos\left(\alpha_3-\alpha_2\right)\sin\left(\alpha_3-\alpha_2\right)+\\
&+\dot{\alpha}_1^2\left[\left(m_{p2}+m_e\right)\right]\ell_1\ell_2\cos\alpha_2\sin\left(\alpha_3-\alpha_2\right)-\\
&-\dot{\alpha}_2^2\left(m_{p2}+m_e\right)\cdot\ell_1\ell_2\sin\alpha_3
\end{aligned}\tag{14}$$

D. *The structural design of the manipulator*

Based on the equations of motion within the simulation was performed complete project management of physical states, and were created by the physical and simulation models information interaction. This was detected effects inertial masses whole moving object, their interaction and its effects on individual homogenates moving arms including the dynamic loading drives. On that basis, was created by 3D design of one of the possible forms of the manipulator (Fig.2), including the selection of appropriate materials and drives.

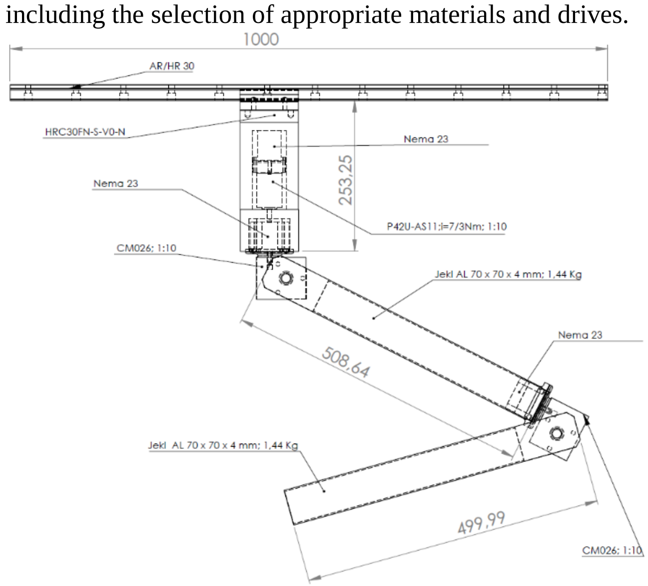

Fig. 2 proposal body of manipulator manned movable elements

III. CONCLUSION

The paper is concerned with utilization equations of motion on based on which are obtained kinematic and dynamic properties of an object usable for subsequent simulations.

ISBN: 978-1-61804-321-4

This contribution forms the first part of the works concerned on created manipulator autonomous serviced robotic system for luggage compartments. 3D graphic model on Fig. 3 shows one possible form of the final construction of the manipulator.

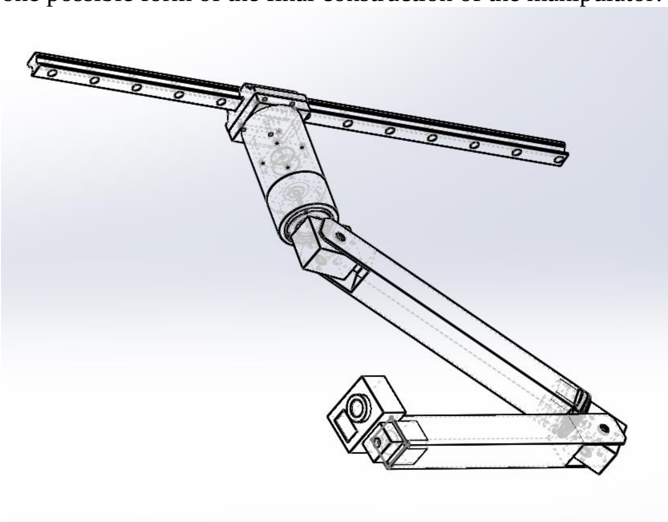

Fig. 3 the final form 3D graphic form of the manipulator systems

ACKNOWLEDGMENT

We thank Zdeněk Úředníček, Tomas Bata University in Zlin, for his support and helpful advice.

REFERENCES

[1] I.Astrov, M. Pikkov, R. Paluoja, “Motion Control of Vectored Thrust Aerial Vehicle for Enhanced Situational Awareness (Published Conference Proceedings style),” *in Proc. WSEAS International Conf. Mathematical Applications in Science and Mechanics*, Dubrovnik, Croatia, June 25-27, 2013,pp. 59-64.

[2] Z. Úředníček, *Robotika* (Book style with paper title editor), Thomas Bata Unverzity in Zlin: Zlin, 2012, pp. 184-212.

[3] S. H. Crandall, D. C. .Karnopp, E. F. Kurz, *Dynamics of Mechanical and Electromechanical Systems* (Book style). NewYork: McGraw-Hill, 1968, pp. 164-182.

[4] D. C. Karnopp, R. C. Rosenberg, “*System dynamics:* A Unifies Approach (Book style),” Wiley & Sons, 1975, pp. 279-305.

[5] S. Hubalovsky, P. Kadlec, L. Mitrovic, P. Hanzalova, “Computer simulation model of static mechanical properties of real technical device - elevator cab (Published Conference Proceedings style),”. In Proc. *3th International Conf. Mathematical Models for Engineering Science (MMES 2012)*, Paris, France, December 2-4, 2012, pp. 252-257.

[6] H. M. Trent, “Isomorphism between oriented linear graphs and lumped. physical systems,”. J.Acoust. Soc. Am., vol. 27 ,pp. 500-505, 1955.

[7] H.A. Darweesh, M. Roushdy, H. M. Ebied, B. M. Elbagoury, “Design a Cost Effective Non-Holonomic Vehicle for Autonomous Driving Applications (Published Conference Proceedings style),” in Proc. *WSEAS International Conference Mathematical Applications in Science and Mechanics*, Dubrovnik, Croatia, June 25-27, 2013, pp. 91-96.

[8] P. Pilay, R. Krishnan, “Modeling, Simulation and analysis of permanent Magnet Motor Drive, Part II: The Brushless D.C. Motors Drives (Published Conference Proceedings style),” IEEE Trans. Industry Application, vol. 25, no 2, pp. 274-279, April 1989.

[9] J. U. Liceaga-Castro, I. I. Siller-Alcalá., J. Jaimes-Ponce, R., Alcántara-Ramírez, A. Ferreyra-Ramírez, “Information and Communication Technologies Applications in Control Theory Courses. Case of study: Speed Control (Published Conference Proceedings style),” in Proc. *11th WSEAS International Conference on Circuits, Systems, Electronics, Control & Signal Processing (CSECS '12)*, Montreux, Switzerland, December 29-31, 2012, pp. 110-115.

Jan Struška studied at the Tomas Bata University in Zlin, Czech Republic, where he obtained his master degree in Computer and Communication Systems in 2013. He now attends PhD. study in the Department of Automation and Control Engineering of the Tomas Bata University in Zlin. His research interest focus on motion control manipulator autonomous service robotic system for image scanning.
He is currently working on completion of the project management of physical condition and its security, including physical simulation model performance and interaction.
Martin Struška studied at the Tomas Bata University in Zlin, Czech Republic, where he obtained his master degree in Computer and Communication Systems in 2013. He now attends PhD. study in the Department of Automation and Control Engineering of the Tomas Bata University in Zlin. His research interest focus on digital signal and image processing of thermal cameras for fire detection.
Miroslav Popelka studied at the Tomas Bata University in Zlin, Czech Republic, where he obtained his master degree in Computer and Communication Systems in 2013. He now attends PhD. study in the Department of Automation and Control Engineering of the Tomas Bata University in Zlin. His research interest focus on ultrasonic signal processing. He is currently working on programming ultrasound imaging for mobile robot

Optimal Automatic System for Controlling the Concentration of Carbon Dioxide in Tomato Greenhouse Based on a Dynamic System

J. E. Moisés Gutiérrez Arias Member BUAP, Nubia Ilia Ponce de León Puig Student BUAP, Gabriela Pérez Osorio Member BUAP, Eladio Flores Mena Member BUAP, Josefina Castañeda Camacho Member BUAP and José Rodellar Member UPC

***Abstract*—From the dynamic model of tomato crop and greenhouse a model is obtained , which is formed by the tomato crop mass balances and the carbon dioxide concentration. This model allow to get an optimal control for the carbon dioxide enrichment in a tomato greenhouse which gives benefits, because it is possible to achieve a saving for energy consumption and more tomato production. The optimal control theory is applied to the crop-greenhouse integrated system, which is based on four state variables: the consumption of nutrients, the fruits and leafs growth and the carbon dioxide concentration. This work contributes with the optimal control law that gives the desired CO_2 concentration behaviour during the growth time for the crop. This behaviour will be a reference signal for the controller implementation in the electronic device that will be made in a future work. In this paper a classical PI controller is designed to follow the reference signal that was obtained from optimal control theory. The parameters used for the simulations are taken from the Puebla region, in Mexico, in order to bring the system closer to reality for its application. The results shown in this paper are the simulations for a time of two weeks.**

***Index Terms*—Greenhouse, carbon dioxide, structural biomass of leaves, structural biomass of fruit, optimal control, functional, state space, controller, reference signal.**

I. Introduction

In past years, researches have proposed different optimal climate control methods for greenhouse systems. These efforts have not been applied in practice because it is difficult for real application [1,2,3,9,12]. The difficulty lies in that the crop growth is based in many different variables and the mathematical analysis with all variables is complicated. In this work, the variable that has our interest is the carbon dioxide.

The carbon dioxide enrichment is practised in the greenhouse crops in order to increase the yield and the benefit. There are studies that demonstrate the CO_2 enrichment improves the net photosynthesis in the plants achieving the increase of the total weight, height, and the number of leaves and branches [9]. Other research has demonstrated that the CO_2 enrichment makes physic-chemical changes in the crop, like color and firmness [8].

Optimization problems with two or more objectives are very common in engineering and many other disciplines. The process of optimizing a collection of objective function is called multi-objective optimization and it is difficult because of the large number of conditions and variables involved in the system [4]. In this work the optimization problem has two objectives, first, decrease the energy consumption for carbon dioxide enrichment and second, increase the tomato production. The search process can be accomplished in two ways: deterministic and stochastic search algorithms [6].

Optimal strategies for CO_2 enrichment can be deduced experimentally or analytically. Experimentation is not able to produce a valid result for all condition set. The mathematical analysis gives us a better option to obtain an optimal strategy because it considers all the variables involved in the system. This method is based on ventilation, photosynthesis, dry matter and production rate models.

One of the main objectives is to contribute with the optimal control problem and its implementation in real time. The tomato crop has been chosen because it is one of the most important crop in our country and is the second farm product consumed in the world. To achieve the objective, we start from the tomato and greenhouse mathematical set model considering the following variable: plant and fruit dry weight, the nutrients amount and the CO_2 concentration.

J. E. Moisés Gutiérrez, Eladio Flores y Josefina Castañeda is with the Faculty of Electronics, University Autonomus of Puebla, México

Nubia Ilia Ponce de León Puig master student of Faculty of Electronics, BUAP, MÃ©xico

Gabriela Pérez is with the Faculty of Chemistry, BUAP, México

José Rodellar is with Deparment of Applied mathematics, UPC, España

ISBN: 978-1-61804-321-4

In this paper, we obtained the behaviour of CO_2 concentration inside the greenhouse that is necessary for growth during two weeks. We start from the fact that this behaviour is a reference signal that a classic controller will have to follow for each time instant. In future work, all results in this paper help us to design an electronic device that could be used in real tomato greenhouses.

II. General Formulation of the Optimal Control Problem

Optimal control problems appeared as essential tools in modern control theory. Several authors have proposed different basic mathematical formulations of fixed time problems [5].

The optimal control of any system has to be based on three concepts: the dynamic model of the system, a functional and the system restrictions. In matrix notation the state equation is represented as follows:

$$\dot{x} = f\left(x(t), u(t), t\right). \tag{1}$$

Where $x(t)$ is the state vector, $u(t)$ is the control vector and t is the time. A criterion is required to evaluate the performance of the system, normally, the functional is defined by:

$$J = \phi\left(x(t_f), t_f\right) + \int_{t_0}^{t_f} L\left(x(t), u(t), t\right)\, dt, \tag{2}$$

Where t_0 and t_f are the initial and final time, ϕ and L are scalar functions, t_f can be fixed or free. Starting at the initial state $x(t_0) = x_0$ and applying the control signal $u(t)$ for $t \in [t_0, t_f]$, it makes that system follows some trajectory of states, then the functional assigns a unique real number for each trajectory of the system.

The fundamental problem of optimal control is to determine an admissible control u^* which makes that equation (1) follows one admissible trajectory x^* that minimize the value of the functional in equation (2). Then, u^* is named optimal control and x^* is an optimal trajectory.

Necessary conditions for a solution

Restrictions (1) are added to the functional (2) with a Lagrange multipliers vector time variant$\Psi(t)$ and the functional is rewritten as follows:

$$\begin{aligned} J = \phi(x(t_f)) + \int_{t_0}^{t_f} [L(x(t), u(t), t) \\ -\Psi^T f(x(t), u(t), t) - \dot{x}]dt, \end{aligned} \tag{3}$$

Then, the Hamiltonian scalar function is defined, which depends on the variable state vector, the control signal and the new vector $\Psi(t)$

$$\begin{aligned} H(x(t), u(t), \Psi(t), t) = \\ = L(x(t), u(t), t) + \Psi(t) f(x(t), u(t), t) \end{aligned} \tag{4}$$

Then, it is possible to write an auxiliary system starting from a new auxiliary vector that depends on time $\Psi(t)$. The new system is formed from Hamiltonian function, as follows:

$$\dot{\Psi}^T = -\frac{\partial H}{\partial x} = -\frac{\partial L}{\partial x} - \Psi^T \frac{\partial f}{\partial x} \tag{5}$$

The auxiliary system allows to know the final conditions of the general system, which can be written as follows:

$$\Psi^T(t_f) = \frac{\partial \phi}{\partial x}(t_f) \tag{6}$$

An infinitesimal variation in $u(t)$ denominated $\delta u(t)$ produces a variation in the functional J like δJ. For a stationary solution it is required that arbitrary variation is equal to zero, $\delta J = 0$. This is true when

$$\frac{\partial H}{\partial u} = \frac{\partial L}{\partial u} + \Psi^T \frac{\partial f}{\partial u} = 0 \tag{7}$$

Note that from the Hamiltonian function (4) it is possible to get the control form. Then, to find the vector function of control $u(t)$ that produces a stationary value of the functional we must solve the following differential equation system:

$$\begin{cases} \dot{x}(t) = f\left(x(t), u(t), t\right), \\ \dot{\Psi}(t) = -\frac{\partial H^T}{\partial x}, \end{cases} \tag{8}$$

The boundary conditions for this differential equations are separated, it means that some of them are defined in $t = t_0$ and the others in $t = t_f$. This is a *problem with boundary values of two points*. Note the equations that describe the states $x(t)$ and the auxiliary states $\Psi(t)$ in the equation (8) are coupled, for this reason $u(t)$ depends on $\Psi(t)$ through the stationary condition and the auxiliary states depend on $x(t)$ and $u(t)$. And the first system in (8) has the initial conditions of he system while the last system in (8) has the final condition of the system.

III. Dynamic Models of the Crop and of the Greenhouse

A. Dynamic model of the Crop

The model in space states of the tomato crop has three principles states (Van Straten et al., 2011)[13]:

- Non-structural Biomass (Nutrients).
- Leaves Structural Biomass.
- Fruits Structural Biomass.

ISBN: 978-1-61804-321-4

1) Biomass balance of nutrients: Nutrients are being produced by photosynthesis. The gross canopy photosynthesis rate in dry matter per unit area is P. Nutrients are converted to leaf and fruits, this is known as growth. Leaf and fruits have a demand for nutrients, which will be honored if there are sufficient nutrients available. We denote W_B as the total nutrients in the plant and it is expressed as dry weight per area unit. The biomass balance equation of nutrients is the following [13]:

$$\begin{aligned}\tfrac{dW_B}{dt} &= P - h\{\cdot\}\left(\tfrac{(1+\theta_V)}{z}G_L^{dem} + (1+\theta_F)\,G_F^{dem}\right) - \\ &-h\{\cdot\}\left(\tfrac{R_L}{z} + R_F\right).\end{aligned} \tag{9}$$

The biomass balance equation of nutrients (9) can take two values depending on the nutrients abundance $h\{\cdot\}$, where the first expression is taken when $h\{\cdot\} = 1$ (abundance of nutrients) and the second one is taken when $h\{\cdot\} = 0$ (lack of nutrients).

$$\frac{dW_B}{dt} = \begin{cases} P - \frac{(1+\theta_V)}{z}G_L^{dem} - (1+\theta_F)\,G_F^{dem} - \\ -\frac{R_L}{z} - R_F, \\ P, \end{cases} \tag{10}$$

R_F.- Respiration needs of fruits
θ_V.- Additional amount of nutrients needs for one unit of structural vegetative parts.
G_L^{dem}.- Unit area growth demand of leaves.
θ_F.- Additional amount of nutrients needs for one unit of structural fruit parts.
G_F^{dem}.- Unit area growth demand of fruit.
z.- Total vegetative parts.
$h\{\cdot\}$.- Nutrients abundance.

2) Biomass balance of leaves: The leaf growth is equal to the amount of nutrients converted to structural leaf biomass in the plant and it is given by $h\{\cdot\}G_L^{dem}$. The model does not incorporate an extra state for stem and roots, but the factor z assumes that each increment in leaf will be accompanied by an increment in stem and roots. If there are no sufficient assimilates (nutrients), growth stops, normally the assimilates are used for the maintenance, but in lack of nutrients, maintenance in the model goes at the expense of structural parts (leaves and fruit). The biomass balance of leaves is expressed in the form [13]:

$$\frac{dW_L}{dt} = h\{\cdot\}G_L^{dem} - (1 - h\{\cdot\})\,R_L - H_L, \tag{11}$$

Depending on the abundance of nutrients $h\{\cdot\}$, the biomass leaf balance equation (11) can take two values:

$$\frac{dW_L}{dt} = \begin{cases} G_L^{dem} - H_L, & \text{if } h\{\cdot\} = 1, \\ -R_L - H_L, & \text{if } h\{\cdot\} = 0. \end{cases} \tag{12}$$

where
H_L is the leaf picking rate.

3) Biomass balance of fruit: Similarly to the biomass of leaf case, the growth of fruits in the plant from the nutrients is given by $h\{\cdot\}G_F^{dem}$. The term G_F^{dem} depends principally on the pivotal temperature, cultivation temperature level and the reference temperature [13].

$$\frac{dW_F}{dt} = h\{\cdot\}G_F^{dem} - (1 - h\{\cdot\})\,R_F - H_F, \tag{13}$$

Finally, the equation (13) of biomass balance of fruits can take two different values depending on nutrient abundance $h\{\cdot\}$, where H_F is the fruit harvest rate:

$$\frac{dW_F}{dt} = \begin{cases} G_F^{dem} - H_F, & \text{if } h\{\cdot\} = 1, \\ -R_F - H_F, & \text{if } h\{\cdot\} = 0. \end{cases} \tag{14}$$

B. Dynamic Model of the Greenhouse

1) Balance of CO_2 energy in the greenhouse: The balance of carbon dioxide energy within greenhouse is given by the equation [13]:

$$\begin{aligned}\tfrac{V_g}{A_g}\tfrac{dC_{CO_2}}{dt} &= -\eta_{CO_2/dw}P + \eta_{CO_2/dw}R - \\ &-\varphi_{CO_2,g\_o}^{vent} + u_{CO_2},\end{aligned} \tag{15}$$

Then each term is described.

* Carbon dioxide taken from the greenhouse air for plant photosynthesis:

$$\eta_{CO_2/dw}P,$$

* Carbon dioxide returned to the greenhouse air for plant respiration:

$$\eta_{CO_2/dw}R,$$

The term $\frac{V_g}{A_g}$ is the reason of the volume of greenhouse per unit of area.
R is the total respiration plant per unit of time.

* Lost of carbon dioxide mass by ventilation:

$$\varphi_{CO_2,g\_o}^{vent} = u_V(C_{CO_2} - C_{CO_2\_o}),$$

where: u_V is the ventilation flow rate per unit of area.
C_{CO_2} (kgm^{-3}) is the carbon dioxide concentration within greenhouse.
$C_{CO_2,o}$ (kgm^{-3}) is the carbon dioxide concentration on the outside greenhouse.

* Carbon dioxide supply:

$$u_{CO_2} = u_{CO_2}^{Vp}\varphi_{CO_2,in\_g}^{max},$$

where $u_{CO_2}^{Vp}$ is the opening supply valve.
$\varphi_{CO_2,in\_g}^{max}$ $\left(kg[CO_2]m^{-2}[gh]s^{-1}\right)$ is the maximum flow rate of carbon dioxide.

In this greenhouse model, the position of the carbon dioxide supply valve is the control input. For this reason, the valve relates directly to the actuator that is present on a physical way in the greenhouse.

ISBN: 978-1-61804-321-4

C. Integrated Model Crop-Greenhouse

From previous description of greenhouse and crop models is possible to get a complete system formed by three crop equations and greenhouse equation. This new equation system describes the complete system behaviour and it is important to note that all of the equations are related principally by the P element and the state variables of the crop. It is important to say that the three equations related to the crop are taken with the assumption that there is an abundance of nutrients ($h\{\cdot\} = 1$). Therefore, general system is as follows:

$$\begin{cases} \dot{W}_L(t) = G_L^{dem} - H_L, \\ \dot{W}_F(t) = G_F^{dem} - H_F, \\ \dot{W}_B(t) = P - \frac{1+\theta_v}{z} G_L^{dem} + (1+\theta_F) G_F^{dem} - \frac{R_L}{z} + R_F, \\ 3\dot{C}_{CO_2}(t) = -\eta CO_{2/dw} P + +\eta CO_{2/dw} R - \varphi_{CO_{g-0}}^{vent} \\ \qquad +uCO_2, \end{cases} \tag{16}$$

IV. Synthesis of Optimal Control

We consider the system (16). The terms for the equation system are substituted using the equation table of the mathematical model (table 1) and the values are substituted using the table of physical parameters (table 2). The resulting model is:

$$\begin{cases} \dot{W}_L(t) = 2.2996 \times 10^{-6}\ W_L(t), \\ \dot{W}_F(t) = 4.3925 \times 10^{-6}\ W_F(t), \\ \dot{W}_B(t) = P(t) - 5.39 \times 10^{-6} W_L(t) - 5.92 \times 10^{-6} W_F(t), \\ 3\dot{C}_{CO_2}(t) = 1.0266(R(t) - P(t)) + 0.155 \times 10^{-10} u_{CO_2}^{v_p}, \end{cases} \tag{17}$$

P and R are the following:

$P(t) = \frac{3.7192 \times 10^{-11}\ W_L^{2.511}(t)}{1.6353 \times 10^{-9} + 4.0439 \times 10^{-5}\ W_L^{2.511}(t)}$,

$R(t) = 1.5942 \times 10^{-6} W_F(t) + 0.4856 \times 10^{-6} W_L(t) + 1.668 \times 10^{-7}$.

It is important to note that the terms P(t) and R(t) have involved two of the three state variables of the crop and they are time dependent functions, so the entire system is connected and it can be solved simultaneously.

We consider the following functional, which has the same form shown in (3):

$$J = \frac{1}{2}[W_L^2(tf) + W_F^2(tf) + W_B^2(tf) + C_{CO_2}^2(tf) + \\ + \int_{t_0}^{t_f} [W_L^2(t) + W_F^2(t) + \\ + W_B^2(t) + C_{CO_2}^2(t) + (u_{CO_2}^{v_p})^2(t)] dt] \tag{18}$$

The first term involves the three first variables at the end time, they are related to the final production and the nutrients, and the integral contains the control input in order to avoid the risk for big control inputs. The idea is to minimize the functional (18), related with the equations system (17).

A. Solution Method Description

The Hamiltonian scalar function is obtained considering the relation (4) with the Lagrange multipliers and the functional (17):

$$H(\mathbf{x}, \mathbf{u}, \mathbf{\Psi}, t)) = \\ = \frac{1}{2}[W_L^2(t) + W_F^2(t) + W_B^2(t) + C_{CO_2}^2(t) + (u_{CO_2}^{v_p})^2(t)] + \\ + 2.2996 \times 10^{-6} W_L(t)\Psi_1(t) + 4.3925 \times 10^{-6} W_F(t)\Psi_2(t) + \\ + \left[P - 5.39 \times 10^{-6} W_L(t) - 5.92 \times 10^{-6} W_F(t)\right] \Psi_3(t) + \\ + \frac{1}{3}\left[1.0266(R - P) + 0.1554 \times 10^{-10} u_{CO_2}^{v_p}\right] \Psi_4(t). \tag{19}$$

The system of auxiliary variables is formed using the expression (5) and has the following form:

$$\begin{cases} \dot{\Psi}_1 = W_L + 2.2996 \times 10^{-6}\ \Psi_1 + \frac{\partial P}{\partial W_L}\Psi_3 - \\ \quad -5.39 \times 10^{-6}\Psi_3 + \frac{1}{3}\frac{\partial (R-P)}{\partial W_L}\Psi_4(1.0266) \\ \dot{\Psi}_2 = W_F + 4.3925 \times 10^{-6}\ \Psi_2 - \\ \quad -5.92 \times 10^{-6}\ \Psi_3 + \frac{1}{3}\frac{\partial R}{\partial W_F}\Psi_4(1.0266), \\ \dot{\Psi}_3 = W_B, \\ \dot{\Psi}_4 = C_{CO_2}, \end{cases} \tag{20}$$

The stationary condition give us the following control form, which was obtained from equation (7) and depends on fourth appended state:

$$u_{CO_2}^{v_p} = -\frac{1}{3} 0.1554 \times 10^{-10} \Psi_4(t). \tag{21}$$

It is necessary to solve the equation systems (17) and (20), in this way we can know the Ψ_4 value and finally we will get the control form. The system (17) has initial condition and the system (20) has final conditions. The systems are coupled because the control form (21) has been substituted. To solve the complete system like a system with initial conditions, the auxiliary equations are considered in reverse time, then the behaviour of the auxiliary variables is returned to the direct time. When we solve the appended equation system in reverse time the system becomes a system with initial conditions. It is important to note that the equation (21) depends on the fourth state but this state depends on the other three states. Using MatLab tools we solve the equation systems (17) and (20).

V. Simulation of Control Law

The MatLab tools were used to elaborate the program that solve the differential equations system formed by equations (17) and (20). The simulation period is for two weeks. The results obtained are described below. It is important to know that in the following results, the temperature and solar radiation are time varying, in order to make the simulation more real. Figures 1 and 2 show the temperature and solar radiation varying in a time of two weeks.

TABLE I
GREENHOUSE AND CROP MATHEMATICAL MODEL EQUATIONS

Term	Description
$P = P^{max}\left(\frac{I^{PAR}}{I^{PAR}+K_I}\right)\left(\frac{C_{CO_2}}{C_{CO_2}+K_C}\right)f_m\{\cdot\}$	Production of assimilates by photosynthesis.
$R = h\{\cdot\}\left(\frac{\theta_V}{z}G_L^{dem} + \theta_F G_F^{dem}\right) + \frac{R_L}{z} + R_F$	Total amount breathed plant per unit of time.
$I^{PAR} = f_{PAR/I}\tau_r I_o$	The PAR light intensity at the crop level.
$f_m\{\cdot\} = \frac{(W_L/p_m)^m}{1+(W_L/p_m)^m}$	Maturity factor.
$G_L^{dem} = f_{L/F}(T)k_{GF}^{ref}f_{TG}(T)f_D\{\cdot\}W_L$	Growth leaves demand.
$G_F^{dem} = k_{GF}^{ref}f_{TG}(T)f_D\{\cdot\}W_F$	Growth fruits demand.
$f_{L/F}(T) = f_{L/F}^{ref}e^{v_2(T-T_{L/F}^{ref})}$	Temperature-dependent ratio.
$f_{TG}(T) = Q_{10R}^{T-T_G^{ref}/10}$	Temperature dependent with a Q_{10G} relation.
$f_{TR}(T) = Q_{10R}^{T-T_R^{ref}}$	Function of temperature with a Q_{10G} relation.
$f_D\{\cdot\} = \frac{c_{f1}-c_{f2}D}{c_{f1}-c_{f2}}$	Correction factor for the fruit growth rate.
$R_L = k_{RL}^{ref}f_{TR}(T)W_L$	Respiration demand of the leaves.
$R_F = k_{RF}^{ref}f_{TR}(T)W_F$	Respiration demand of the fruits.
$H_L = k_{HL}W_L$	Leaf picking rate.
$H_F = k_{HF}W_F$	Harvest rate.
$K_{HL} = C_{yL}K_H$	Coefficient of harvest.
$K_{HF} = C_{yF}K_H$	Coefficient of harvest.
$K_H = Cd1 + Cd2ln(T/Cd3) - Cd3 - Cd4e_D$	Harvest rate.
$u_V = \left(\frac{p_{V1}u_V^{A_{plsd}}}{1+p_{V2}u_V^{A_{plsd}}} + p_{V3} + p_{V4}u_V^{A_{pwsd}}\right)v + p_{V5}$	Ventilation flow rate.

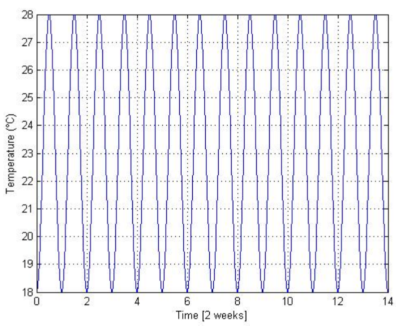

Fig. 1. Time varying temperature for two weeks.

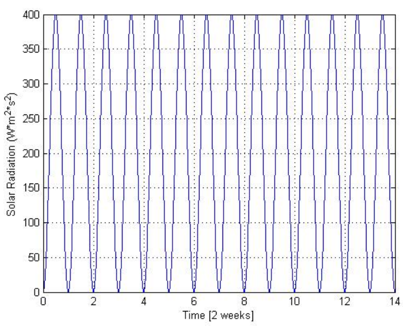

Fig. 2. Time varying solar radiation for two weeks.

A. Analysis with a Step Input.

In a first simulation we use a step function as control input ($u_{CO_2}^{v_p} = 1$). We solved the equation system and later we got the graphics that represent the behaviour of most important variables of the system. Figure 3 shows the behaviour of three crop state variables. The red line shows the fruit behaviour which has acceptable growth just like the leafs (green color line). The black line represents the nutrients behaviour which is acceptable

ISBN: 978-1-61804-321-4

TABLE II
PHYSIC PARAMETERS.

Variable	Value	Description
z	0.6081	Fraction leaf of total vegetative mass
θ_v	0.23	Surplus assimilate requirement factor per unit fruit increment.
θ_F	0.2	Surplus assimilate requirement factor per unit vegetative increment.
p_h	2.7×10^{-3}	Parameter of switching function, $[m^2\ kg^{-1}]$
p_m	1.8×10^{-2}	Parameter in maturity factor, $[kg\ m^{-2}]$
m	2.511	Parameter in maturity factor
p^{max}	2.2×10^{-6}	Maximum gross canopy photosynthesis rate, $[kg\ m^{-2}\ s^{-1}]$
K_1	577	Monod constant for PAR, $[W\ m^{-2}]$
K_c	0.211	Monod constant for CO_2, $[kg\ m^{-3}]$
$f_{PAR/I}$	0.475	PAR fraction of global radiation
τ_r	0.7	Transmittance of the roof
k_{GF}^{ref}	3.8×10^{-6}	Reference fruit growth rate coefficient, $[s^{-1}]$
T_{GF}^{ref}	20	Reference temperature, $[^0C]$
Q_{10G}	1.6	Temperature function parameter growth
$f_{L/F}^{ref}$	1.38	Reference leaf-fruit partitioning factor
v_2	-0.168	Parámetro de partición de fruta-hoja, $[K^{-1}]$
$T_{L/F}^{ref}$	19	Fruit-leaf partitioning reference temperature, $[^0C]$
k_{RL}^{ref}	2.9×10^{-7}	Maintenance respiration coefficient leaf, $[s^{-1}]$
Q_{10R}	2	Temperature function parameter respiration
T_R^{ref}	25	Reference temperature for respiration, $[^0C]$
k_{RF}^{ref}	1.2×10^{-7}	Maintenance respiration coefficient leaf, $[s^{-1}]$
η	0.7	Absorbed in relation to the total energy of the net radiation heat received.
$Cd1$	$2.13x10^{-7}$	Parameter in development rate function, s^{-1}
$Cd2$	$2.47x10^{-7}$	Parameter in development rate function, s^{-1}
$Cd4$	$7.50x10^{-11}$	Parameter in development rate function, s^{-1}
C_{yL}	1.636	Parameter in harvest function (fruit)
C_{yF}	0.4805	Parameter in harvest function (leaf)
$C_{CO_{2,0}}$	1.6637	
$C_{CO_{2/dw}}$	1.4667	Ratio CO_2 per unit dry weight, $Kg[CO_2]Kg^{-1}[dw]$
$C_{CO_{2,ing}}$	$2.10x^{-6}$	Ratio CO_2 per unit dry weight, $Kg[CO_2]m^{-2}[gh]s^{-1}$
$\frac{V_g}{A_g}$	3	Volume per unit greenhouse area
p_{v1}	$7.17x10^{-5}$	Parameter.
p_{v2}	0.0156	Parameter.
p_{v3}	$2.71x10^{-5}$	Parameter.
p_{v4}	$6.32x10^{-5}$	Parameter.
p_{v5}	$7.40x10^{-5}$	Parameter.

because it is observed that the crop is consuming the available nutrients during the growth time. Figure 4

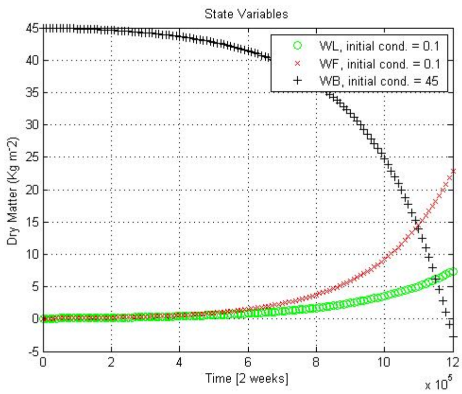

Fig. 3. Behaviour of fruits, leaves and nutrients dry matter with an input step.

shows the carbon dioxide behaviour. Note the CO_2 concentration increases up to 9000 ppm. This is very high and it means so much energy consumption.

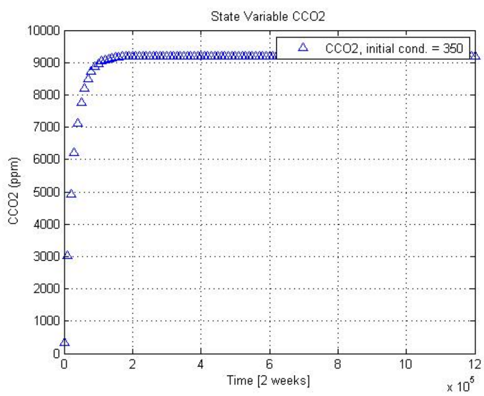

Fig. 4. Behaviour of CO_2 concentration a step as input control.

B. Analysis with the Synthesized Control

For the next simulation, we got results using the variable parameters, but now we simulated the control law

ISBN: 978-1-61804-321-4

(21) deduced in this paper. Figure 5 shows the results. Note thet the behaviour of the three crop state variables are similar to the previous cases, but in this case the carbon dioxide behaviour is different. In Figure 6 we can note that CO_2 concentration decreases and it reaches 450 ppm, which is very acceptable because it means low energy consuption and an acceptable quantity of carbon dioxide for clean air.

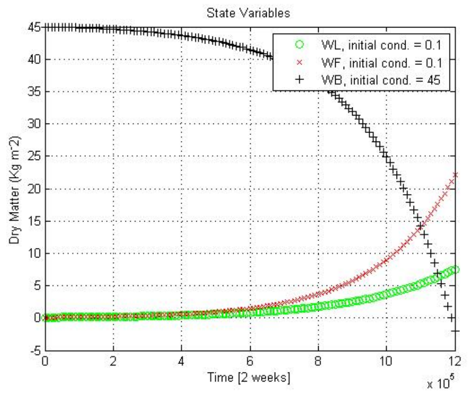

Fig. 5. Behaviour of fruits, leaves and nutrients dry matter with the control deduced.

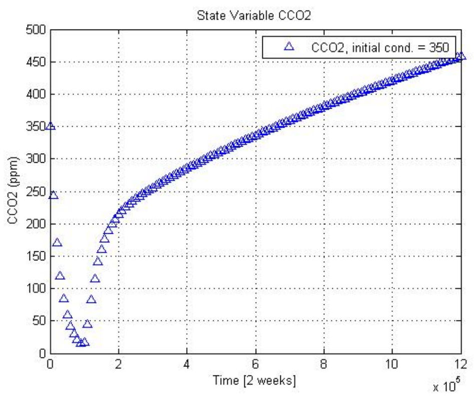

Fig. 6. Behaviour of CO_2 concentration the control input deduced.

VI. Automatic Control Sistem for the Concentration of Carbon Dioxide Inside the Greenhouse

Figure 7 shows the complete automatic system which will control the carbon dioxide concentration. The valve and supply tank are the pneumatic system. And the CO_2 sensor will make the reading of current carbon dioxide inside de greenhouse.

A. Mathematical Model of Pneumatic Pressure System

The pressure system that will do the carbon dioxide enrichment is formed by a valve and a storage tank, Figure 8. In it, the flux through the restriction is a

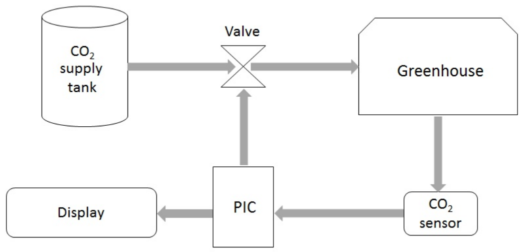

Fig. 7. Automatic control system for concentration of carbon dioxide inside the greenhouse.

function of the difference of pressure. This kind of system is characterized in terms of a resistance and a capacitance. The resistance is defined like the change in the differential pressure to make a change in the mass flux [15]:.

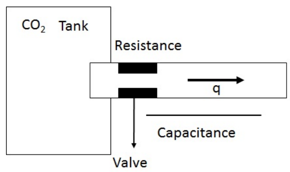

Fig. 8. Pressure system with tank and restriction.

$$R = \frac{d(\Delta P)}{dq} \tag{22}$$

where ΔP is a small change in the pressure of the gas and dq is a small change in the flux of the gas.

By the other hand, the capacitance is defined like:

$$C = \frac{dm}{dp} = V\frac{d\rho}{dp} \tag{23}$$

where
$C =$ Capacitance, $lbfth^2/lb$
$m =$ Gas mass in the tank, lb
$p =$ Pressure of gas, lb/fth^2
$V =$ Volume of tank, fth^3
$\rho =$ Density, lb/fth^3

From the general law of gases, the capacitance is expressed as [15]:

$$p(\frac{V}{m})^m = \frac{p}{\rho - n} = constant \tag{24}$$

where n is the politropic exponent. The expression for ideal gases is:

$$pv = \frac{p}{\rho} = \frac{\overline{R}}{M}T = R_{gas}T \tag{25}$$

where:
$p =$ Absolute pressure, lb/fth^2
$\overline{v} =$ Volume occupied by one mole of gas, $fth^3/lbmol$

ISBN: 978-1-61804-321-4

$\overline{R} =$ Universal constant gas, $fthlb/lbmolR$
$v =$ Specific volume of the gas, fth^3/lb
$M =$ Molecular weight of the gas, $lb/lbmol$
$R_{gas} =$ Constant of the gas.

Therefore, the capacitance is obtained as:

$$C = \frac{V}{nR_{gas}T} \tag{26}$$

For the system in this paper, the capacitance was got from the formula (26) using the parameters in Table VI-A. The calculated value was $0.0013447Kgm^2/N$

Description	Value	Units
V- Tank volume	0.17657	pie^3
n- Politropic exponent	1	
R_{gas}- Gas constant		$pielb/lbR$
$\overline{R}$- Universal constant of gases	10.73158	$pielb/lbmolR$
M- Molecular weight CO_2	44.01	g/mol
T- Absolut temperature	538.47	R

TABLE III
VALUES TO CALCULATE THE CAPACITANCE OF THE SYSTEM.

The formula to calculate the resistance is

$$R = \frac{8\eta L}{\pi r^4} \tag{27}$$

where:
ΔP is the pressure difference.
η is the viscosity of the gas, N/m^2.
r inner radius of the pipe in meters.
L length of the pipe expressed in meters.

For our particular system we use the values in table VI-A and the result is 171817.0426 pneumatic ohmnios.

Description	Value	Units
Viscosity of CO_2	$1.3711e^{-5}$	N/m^2
Inner of pipe	0.003175	m
Lenght of pipe	0.50	m

TABLE IV
VALUES TO CALCULATE THE RESISTANCE FOR THE SYSTEM

To obtain the mathematical model of the system small variations are considered and the system is considered linear. The following terms are defined:

$\overline{P} =$ Pressure of the gas in stable state, lb/pie^2
$p_i =$ small change in the gas that enter ld/pie^2
$p_o =$ small change in the pressure gas in the thank lb/pie^2
$V =$ volume of the thank pie^3
$m =$ mass of the gas in the thank, lb
$q =$ flux gas, ld/seg
$\rho =$ density gas, lb/pie^3

The resistance is $R = (p_i - p_o)/q$ and the capacitance is obtained from (24), in this way:

$$Cdp_o = qdt \quad \text{or}$$
$$Cdp_o = \frac{p_i - p_o}{R} dt$$

which is written like $RC\frac{dp_o}{dt} + p_o = pi$

If p_i and p_o are the input and output, respectively, the transfer function is:

$$\frac{P_o(s)}{P_i(s)} = \frac{1}{RCs + 1} \tag{28}$$

And, with the values of resistance and capacitance calculated previously, the transfer function can be written as follows:

$$\frac{P_o(s)}{P_i(s)} = \frac{1}{231.0423s + 1} \tag{29}$$

B. Characterization of the Reference Signal

In previous result, the behaviour of the CO_2 concentration in the greenhouse was obtained , this result is the amount of CO_2 required by the crop at each time instant for two weeks. Now it is necessary to obtain a mathematical expression that represents the CO_2 behaviour, in order to use the expression for simulation and get the controller which will be used in an electronic device for a future work. Making use of MatLab tools was possible get the mathematical expression for polynomial approximation. From now, this expression will be named the signal reference for the system, because we expect the output of the complete system will be equal or similar to this reference signal. Figure 9 shows two graphics, the blue line (o) represents the behaviour of CO_2 concentration which was got from optimal control and was showed in previous section. And the red line (+) shows the curving fit made by MatLab tool and it is a polynomial fit of ninth degree.

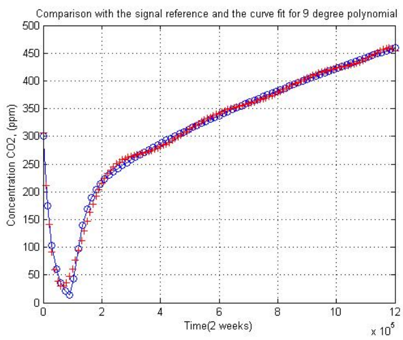

Fig. 9. Comparison with the signal reference and the curve fit for 9 degree polynomial.

The mathematical expression obtained from de curve fit is:

$$\begin{gathered} C^{ref}_{CO2} = -25.7776z^9 + 39.134z^8 + 116.96z^7 - \\ -176.26z^6 - 148.88z^5 + 218.42z^4 + 63.944z^3 - \\ -90.64z^2 + 77.471z + 342.05 \end{gathered}$$

Where $z = (t - 6x10^5)/3.529x10^5$ and t is the time crop, in this case this time is for two weeks.

C. Simulation of a PI Controller

The PI controller is used because, by itself, the plant reaches to the reference signal, but it is for a long time. The proportional component of controller PI will make the system reaches the reference signal in less time and the integral component will minimize the stable state error. From the transfer function and its open-loop analysis it is possible to design a classical PI control, which causes the system follows the reference signal at each time instant of the tomato crop. To design the control the rules of Ziegler and Nichols were used. A blocks diagram was simulated in Simulink in order to know the response of the system with the designed control. The diagram is represented in Figure 10.

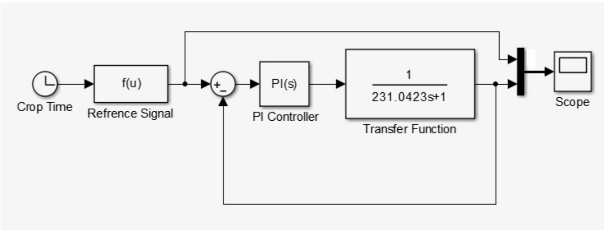

Fig. 10. Simulation block diagram of the controller PI.

Next simulations were made with the purpose of observing that the system response follows the reference signal and knowing in what time achieves this. Also, it is possible to study the overshoot of the response. Figure 11 shows the response, the red line is the input reference and the green line is the response of the system. Figure 12 is a zoom in the first seconds. Note the response is equal to the input in second 15.

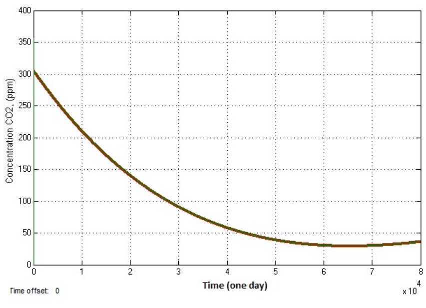

Fig. 11. Response of the system with PI control.

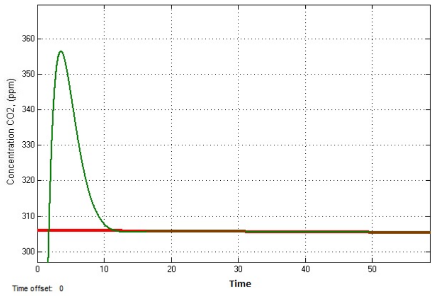

Fig. 12. Response of the system with PI control.

VII. Conclusion

From the integrated tomato-greenhouse model it is possible to do the optimization of all variables. In this case, the most important variable is the carbon dioxide concentration. In a first step, the optimal control theory was used to determine the desired behaviour of the variables over a prescribed time period. In a second step, a classical PI control was designed to make the system follow this behaviour at each time instant.

All the results obtained in this paper are the base to create an electronic device able to make the automatic control of carbon dioxide concentration inside a real tomato greenhouse.

References

[1] Aikman D. P., 1996. A procedure for optimizing carbon dioxide enrichment of a glasshouse tomato crop. Journal of agricultural engineering research 63, No. 2, 171–183.

[2] Ioslovich I., Gutman P. and Linker R., 2009. Hamilton-Jacobi-Bellman formalism for optimal climate control of greenhouse crop. Automatica, 1227–1231.

[3] Ioslovich I. and Seginer I., 1995. Normalized co-state variable for seasonal optimization of greenhouse tomato production. Acta horticulturae 417, 87–94.

[4] Alexander Zemiliak, Tatiana Markina (2013) . Preliminary Structure of Quasi Optimal Algorithm of Optimization of Analog Circuits. WSEAS Transactions on CIRCUITS and SYSTEMS ISSUE 7, volume 12.

[5] Hull D.G., 2013 Optimal control theory for applications, Springer-Verlag, New York, USA.

[6] B. Fahimnia, R. Molae, M. Ebrahimi(2008) . Genetic Algorithm Optimization of Fuel Consumption in Compressor Stations. WSEAS Transactions on CIRCUITS and SYSTEMS ISSUE 1, Volume 3.

[7]Ioslovich I. and Seginer I., 1998. Approximate seasonal optimization of the greenhouse environment for a multi-state-variable tomato model. Transactions of the ASAE 41.

[8] Md. Shahidul I., Toshiyuki M., Yuichi Y., 1996. Effect of carbon dioxide enrichment on physico-chemical and enzymatic changes in tomato fruits at various stages of maturity. Scientia horticulturae 65, 137–149.

[9] Mortensen M. L., 1987. CO2 enrichment in greenhouse. Sci. Horticulturae 33, 1–25.

[10]Seginer I. and Ioslovich I., 1998. Seasonal optimization of the greenhouse environment for a simple two-stage crop growth model. Journal of agricultural engineering research 70, 145–155.

[11]Tchamitchian M. and Ioslovich I., 1998. Equivalence of

ISBN: 978-1-61804-321-4

the temperature integral and the carbon dynamics concepts in plants: Utility for controll. Acta horticulturae 519, 171–180.
[12] Van Straten G., Challa H. and Buwalda F., 2000. Towards user accepted optimal control of greenhouse climate. Computers and electronics in agriculture 26, No. 3, 221–238.
[13] Van Straten G., van Willigenburg L. G., van Henten E. and van Ooteghem R., 2011. Optimal control of greenhouse cultivation. CRC. Press, United States of America.
[14] Van Henten E. J., 1994. Greenhouse climate management: An optimal control approach. Doctorate dissertation. Agricultural University, Wageningen.
[15] Robert L. Mott, Mecánica de Fluidos, 6ta edición.

Nubia Ilia Ponce de León Puig *Born on July 23, 1989 in Puebla, Mexico. Graduate in Mecatronics Engineer from the Autonomus University of Puebla (BUAP). Student in Master of Electronic Engineering (MIE) of the Autonomus University of Puebla (BUAP).*

J. E. Moisés Gutiérrez Arias *He received the titles of the Bachelor of Mathematics and the Master of Sciences Mathematics in 1997 from the Autonomous University of Puebla, the Doctorate in Mathematical Sciences also he received from the same institution in 2003.*

José E. Flores Research fellow in *Faculty of Science of the Electronics (FCE)* of the *Benemérita Universidad Autónoma de Puebla (BUAP)*

Josefina Castaẽda Camacho Research fellow in *Faculty of Science of the Electronics (FCE)* of the *Benemérita Universidad Autónoma de Puebla (BUAP)*

José Rodellar Teacher in Politecnical University of Cataluña and director of the team CoDAlab in the UPC.

Smart building control algorithm check out device

Tomas Sysala and Petr Neumann

***Abstract*—** The article concerns control possibilities and smart building partial component control algorithm check out. There are two simplified models of real devices described. The first one is a more complex five-floor lift model composed from two cages linked up for control. The second one is a family house simplified model where the centralized and decentralized control of smaller systems is supposed. Concerning the examples of those smaller systems, heating, lighting, controlled access, security and air condition system are taken into account. The assumption for control algorithm check out is a programmable logical controller controlling the whole system and exploiting all feasible communication variants.

***Keywords*—** lift model, real model, smart building.

I. Introduction

AUTOMATION and modern control methods are accompanying every step of ours nowadays. While couple of years ago the device control methods were absolutely prevailing in big industrial facilities applications and processes, these methods are spreading to household, to our flats and to our family houses.

First efforts to design houses with a comprehensive related parameters control possibilities can be traced back to the fifties of the last century and the same effort has started in Japan in early sixties of the last century. That concept was not accepted in Japan at that time eventually unlike Europe, especially in Germany where the company Siemens was the leading innovator in developing relevant concept and devices for that application area.

For mastering and controlling any device, we need relevant wiring. Such wiring formerly served for lighting control. The current ground breaking information and communication technologies development offers an efficient possibility to control a wide range of devices like various appliances whose control would have been inconceivable about thirty or twenty years ago.

The work was performed with financial support of research project NPU I No. MSMT-7778/2014 by the Ministry of Education, Youth and Sports of the Czech Republic and also by the European Regional Development Fund under the project CEBIA-Tech No. CZ.1.05/2.1.00/03.0089.

Tomas Sysala is with Tomas Bata University in Zlin, Faculty of Applied Informatics, nam. T.G.Masaryka 5555, 760 01 Zlin, Czech Republic (corresponding author to provide phone: +420 57 603 5260; fax: +420 57 603 2716; e-mail: sysala@fai.utb.cz).

Petr Neumann is with Tomas Bata University in Zlin, Faculty of Applied Informatics, nam. T.G.Masaryka 5555, 760 01 Zlin, Czech Republic (e-mail: neumann@fai.utb.cz).

The lighting control, heating optimization, air condition and similar living environment parameters adaptation tasks have been already elaborated for decades. The TV and radio set control via WIFI or by a control unit via an IR signal, the voice control of all devices seen only in movies so far has to become reality nowadays.

II. Common versus Smart Wiring

As far as we solve a simple task, or the task is a small scope project, we are going to exploit a common wiring. Only when the project scope in relation to devices and peripherals extends, we start to consider if we can use the different way of communication or generally, the way of signal transmission between controlling unit and a controlled devices. An “smart wiring” offers interesting qualities. Nevertheless, each way has its advantages and disadvantages.

The first project outcome attribute is economical aspect which is very often the most important one. As already mentioned above, the price for common wiring at small scale tasks is remarkably lower. The basic configuration cost of intelligent wiring is high because of expensive control unit what represents disadvantage in comparison to the common wiring. However, the cost difference decreases in relation to increasing number of connected devices what fact tends to deciding choice of intelligent wiring at certain project complexity level. That choice has number of advantages.

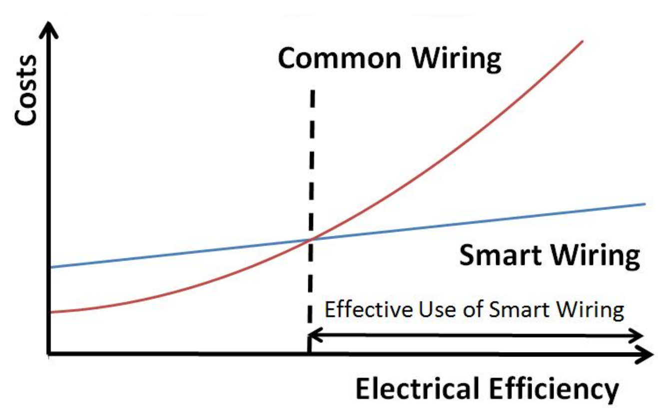

Fig. 1 costs for common and smart wiring

A. Automation and comfort

- Simple one touch (or voice command) lighting control (gradual lighting run-up, predefined light scenes, etc.)
- One stimulus may initiate a lot of functions and activities.

For instance, the arrival home initiates the temperature increase, light scene setting, slats draw and the like.

- Temperature can be adjusted according to predefined programs.
- The whole system can be controlled by desk top computer, tablet, or by other mobile device including a remote control via internet.

B. *Security and Protection*

- The realisation of protection system against an unauthorized intrusion is very simple.
- The failure and unexpected event occurrence messaging is very easy to be accomplished with SMS transfer.
- It is possible to simulate a standard house functions operation during resident absence period for the house does not give impression of a deserted place.

Appreciable aspect represents the energy economy concerning electricity and gas supply influenced by heating and other functions optimization.

III. Way of Control

The wiring type is closely related to the way of control.

A. *Centralized*

All inputs and outputs are star like conducted to the central unit. That unit is most frequently a programmable logic controller (PLC).

B. *Hybrid*

Some devices are connected to the control unit via bus system, some others via a star wiring topology like at the centralized way of control.

C. *Decentralized*

Each device has its own intelligence (it mostly incorporates microcontroller). All those devices are interconnected with bus. The whole system can or cannot comprise a control unit. Even if the system comprises a control unit, that is not for controlling but for command handing over, like for instance lighting command – “activate the scene arrival home”, or the heating command – “there is a holiday, heat as on Sunday”. The control unit puts out a command a it does not care for “how the device will perform that”. Device contains control algorithms.

IV. The Control Software Verifying

In case of project creation, we need to verify control algorithms for hardware control. The algorithm verifying is often not possible to verify with a real device because of controlled object destroying or damaging eventuality, alternatively involved persons (users) injury or putting them in danger.

Couple of models for functionality and safety of designed algorithms have been created at our faculty so far.

Further those models exploitation way of import represents their application PLC programming education and training. Students learn to program a real device which they may encounter in their successive professional life without any above mentioned danger.

V. Smart Family House Model

A Family house model (Fig. 2) consists of three main parts – a house building, a programmable controller and a control panel [1].

Fig. 2 family house model

There are hallway, living room, two bedrooms, toilets and kitchen in the family house model. The house top view is shown in Fig.3.

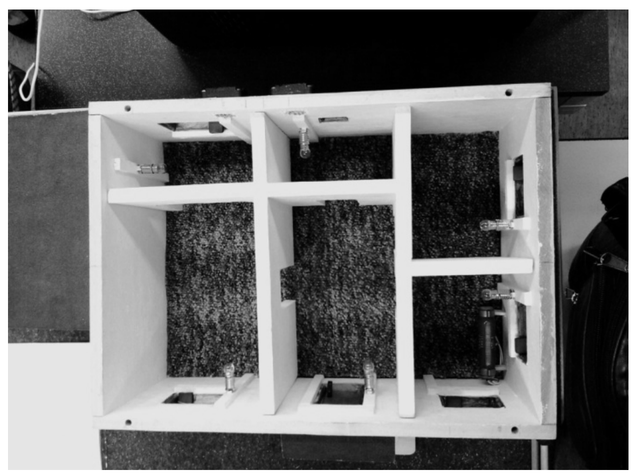

Fig. 3 top view on the house model

The whole smart building functionality depends on control device stored program complexity. We can control lights in every room, fans in the toilet and in the kitchen. The garden entrance gate and also garage gate can be manipulated remotely. There is a small pool in the garden. It is possible to fill it with water or drain it according to user requirements.

Owing to window and door sensors, we can easily set up a security system.

The control panel contains a small keyboard with ten numerical keys (Fig. 4). We can pre-set arbitrary function for each key, but we mostly use all keys for security system control.

That part is massively exploited in educational process. Each student can program his own security system. The security option makes possible to use that model in educational process not only for students with “Automation and process control” specialization, but also for our faculty students with specialization aimed at “Security technologies and systems”.

23 binary inputs *(from the model to PLC)*
• light switches
• ventilator switches
• limit switches
• open window detectors
• open door detector
• doorbell switch
• contact sensor in front of door
2 analog inputs
▪ reference temperature
▪ real temperature
31 binary outputs *(from PLC to the model)*
• lights in all rooms
• alarm lights
• ventilator
• doorbell
• heating
• motor door opening
• motor windows opening
• LED indicators of all inputs and outputs on the control panel
1 analog output
▪ signal to the potentiometer on the control panel

Table 1 active elements in family house model

The whole smart building is controlled with a PLC we can access to from anywhere in the world. Either via a web portal or via a mobile device.

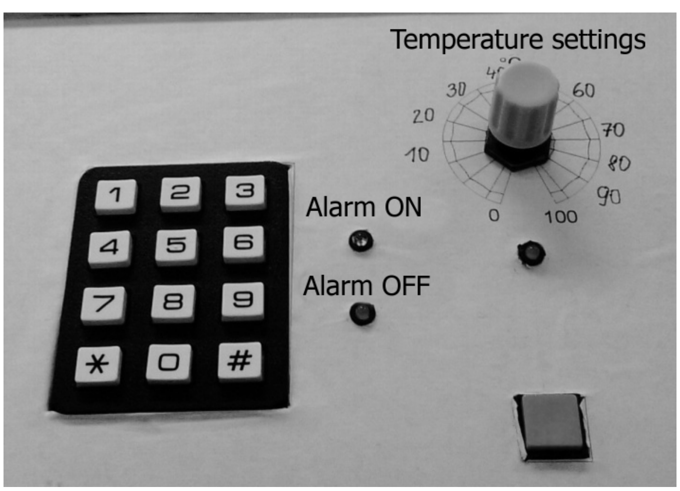

Fig. 4 small keyboard for security control system

VI. LIFT CONTROL

Majority of smart buildings has lift(s). There is mostly not only one lift but a lift group. It is not an easy task to originate a control program for the lift control.

Determinative factors for pinpointing a right lift control methods are primarily the following ones:

- Lift category (personal, freight lift, etc.)
- Building category (flat, administrative, hotel, etc.)
- Way of operation (self-service, lift operator assisted, etc.)

On the combinational basis of these determinative factors, there exists plenty of various control ways different operation and control automation levels.

A. Simple Control

The lift system can always accept and perform only one ride request. The moment a request is registered and being served, there is no opportunity for another user´s request to be served until the first request is fully attended to. There is a control button for cage call in at each lift stop. In case more buttons are pressed at the same time, the lower floor has priority [5].

B. Collective Control

The disadvantage of simple control is limitation to only one ride request to be served at the time. From the most effective transportation performance point of view, especially at higher lifting capacity elevators, is that way of operation very disadvantageous because of very low average cage occupancy rate. For the most effective lift utilization, the collective control is the right solution. It enables the registration of multiple requests from stops and cage at the same time. The requests are served with aim at the highest possible number of requests (transport of as many passengers as possible) to be served in the shortest possible time period.

C. Unidirectional Collective Control

Unidirectional collective control is used in economically advantageous cases like in buildings where the traffic from default stop (ground floor) to individual floors and from individual floors back to ground floor stop prevails. The mentioned way of transportation occurs in overwhelming cases in flat buildings where the traffic from individual upper floors further up is very rare. Unlike the Simplex control (bidirectional collective control), there is only one push control button with light indicator at all lift stops which is possible to stop with the not fully occupied cage passing the stop in down direction, or it is possible to call in the empty cage [6].

D. Bidirectional Collective Control

It is a most common collective control lift system design termed as SIMPLEX. That way of control is characterized by two control buttons with signal light at each lift stop. One control button is for the lift up, and the second one is for the lift down. By pressing one of those two buttons, the user sends to the control system the stop identification from where and in what direction is the transport requested.

There is possible to record an arbitrary number of ride requests in cage or at stops. Requests are served successively in order considering requests in direction of cage current moving first determined by a first recorded request. When there are no more requests in current moving direction, the serving of opposite direction requests is executed.

E. Group Control

Large buildings have a much higher need of vertical traffic so that single elevators are insufficient solution there. That is why they are equipped with groups of several elevators. In such a case, it is necessary to have elevator entrances as close as possible to each other and also the common control system is shared for all elevators. Only an appropriate group control system can ensure that the elevator group total transporting performance is higher than the a mere sum of individual elevators performance [5].

VII. Lift Model Description

We have designed and realized a 2 cages five floor elevator system model for control algorithm verification at our department (Fig. 5).

Fig. 5 workplace with an elevator model [2]

The whole workplace consists of following parts:

- computer table
- computer for PLC programming or for elevator monitoring
- elevator model
- separated panel for cab control panel simulation
- PLC control Tecomat FOXTROT

Basic characteristic of the elevator model is as follows:

- 2 capsules
- 5 levels
- 2 electric motors for each capsule
- 10 small electric motors for each door
- 2 buttons and 2 LED indicators (cab annunciator) on each floor,
- 12 buttons and 12 LED indicators on personal control panel,
- 18 sensors indicating the cage position
- 10 closed door indicators.

The whole system is controlled with a PLC Tecomat FOXTROT by Czech company Teco. That system enables slight modification of any function, and above all, it offers also a remote access [2].

The lift operation can be visualized in any SCADA/HMI system. The InTouch systems by American company Wonderware and ControlWeb system by Czech company Moravian Instruments are used in our application predominantly.

VIII. Conclusion

The main project goal was to design and create a functional equipment for the verification of smart building components control algorithms. By such a verification performed on a real installation model, it is possible to prevent damages and destruction of the controlled object, the real object closure because of tests and the last but not least reason for such approach is to prevent user injury at an incorrect functionality.

Two models for algorithms verification are representing the outcome of our project.

Also students are making use of those systems in course of their educational process and their preparation for future jobs and for situation they may encounter in praxis.

References

[1] J. Dvořáček, "Model domku monitorovaný a ovládaný programovatelným automate" (A Family House Model controlled by PLC), diploma work (in czech), Tomas Bata University in Zlin, Faculty of Aplied Informatics, 2007.

[2] O. Vrzal, "Sekvenční řízení modelu výtahu programovatelným automate" (Sequence control of elevator model by programmable logic controller), diploma work (in czech), Tomas Bata University in Zlin, Faculty of Aplied Informatics, 2010.

[3] A. Qamar, J. Iqbal, I. Javed, Ishaque, H. Rehan, "Design and manufacturing of a real time imitation based robotic arm using low cost microcontroller", *Proceedings of the 6th WSEAS International Conference on Applied Informatics and Communications*, Elounda, Greece, August 18-20, 2006 (pp363-368).

[4] T. Sysala, P. Neumann, J. Pribyslavsky, M. Adamek, "Tutorial development kit for 32-bit ARM microcontrollers with a focus on multimedia", *International Journal of Circuits, Systems and Signal Processing*, Issue 2, Vol. 7, 2013, North Atlantic University Union.

[5] L. Janovský a J. Doležal, "Výtahy a escalatory" (Lifts and escalators – in Czech). Praha: SNTL –Nakladatelství technické litaratury, 1980.

[6] G. Barney, Elevator Traffic Handbook: *Theory and Practise*. 2011. London: Spon Press, 2011, ISBN 978-0415274760.

[7] J. Navratil, M. Stanek, M. Manas, D. Manas, K. Kyas, V. Senkerik, A. Skrobak, "Recyclation of irradiated HDPE - influence on tensile toughness", *in Proc. 17th WSEAS International Conference on Systems*, Rhodes Island, Greece, 2013, pp. 186-189.

[8] D. Manas, M. Ovsik, M. Manas, M. Stanek, P. Kratky, A. Mizera, M. Bednarikl, "Effect of Beta low irradiation doses on the microhardness of PA 66," *in Proc. 17th WSEAS International Conference on Systems*, Rhodes Island, Greece, 2013, pp. 190-195. ISBN 978-960-474-314-8.

[9] V. C. Petre, „Microcontroller based measurements : how to take out the best we can of them", *Proc. of the 8th WSEAS Int. Conf. on Mathematical Methods and Computational Techniques in Electrical Engineering*, Bucharest, October 16-17, 2006.

[10] P. Navratil, L. Pekar, "Combined production of heat and electric energy – linear mathematical model", *Proc. of the 16th WSEAS International Conference on Circuits*, Kos Island, Greece, July 14-17, 2012.

Real time processing of electrooculographic signal to type with a virtual keyboard

Karim Ben Si Saïd, Noureddine Ababou and Amina Ababou

Abstract— When a disabled person loses the ability to speak, he or she becomes private of all his or her usual communication tools. Several methods and techniques of communication were developed to offer new supports of communication using alternative methods. Among them the movement of eyes can be considered as an interesting technique. Because of its efficiency, electrooculographic signal (EOG) has been a widely used technique to detect human eye activity. Several applications used eye tracking as a primary source input or consign generator. In this paper, a method for writing text using EOG eye tracking on a virtual keyboard is proposed. It was developed using a new type of keyboard with 5x6 pads, eyes blinking as well as left/right saccades. Data acquisition and analysis software were developed using LabVIEW language. Different digital filters were applied and compared and a derivative method was used. Typing speed test and accuracy of the system's response are discussed.

Keywords— *electrooculography, eye tracking, speech disabled, virtual keyboard*.

I. Introduction

When people are motor disabled, they become dependent on others and usually need assistance. So, during the last decades several systems were developed with the aim of offering them certain autonomy. In the case these people cannot control their upper limbs, alternative methods are usually used. They consist in generating commands and instructions to some developed systems using their physiological signals like electroencephalography (EEG) or electromyography (EMG) [1], and even electrooculography (EOG) [2].

Usually, a motor disabled person can still control his eyes movements, thus these movements have been used in several devices and systems as a source of control or instructions. To track the movements of the eyes, two methods are generally used, (i) Video-occulography (VOG) which consists essentially on using a camera with an image processing algorithms to detect the eye gaze rotations, (ii) EOG where five surface Ag-AgCl electrodes placed around the eyes and a conditioning circuit are generally used.

Among the existing systems, in the prototype proposed by Arai and Mardiyanto [2] an eye tracking device based on VOG was proposed in the aim to control an electric wheelchair, by placing a camera at 15cm from the face, in order to follow the eye gaze movements and to generate four commands (left, right, forward, and stop).

Other systems are based on electrooculography (EOG), like the application described in [3-5], where five surface electrodes were used with a conditioning card to control a wheelchair with eyes for quadriplegic disabled people. Sung et al. [6] proposed another device based on EOG eye tracking using just vertical movements of the eyes (three surface electrodes), to control an android application in a tablet. The principal aim was to help musicians to turn pages when playing with their musical instruments. Other authors [7] presented a low cost device that can control some home appliances using only the left-right eye movements. Martinez et al. [8] combined between EOG and voice recognition to control a robotic arm, and showed a comparison results between the two used methods (voice recognition and EOG).

Recently, some applications aimed to offer a communication support for paralyzed people by using the EOG eye tracking to type text on virtual keyboards using different methods. Tangsuksant et al. [9] proposed a method where a square virtual keyboard with (5x5) buttons was developed, the saccadic movements of the eyes were used to navigate between buttons, and the voluntary eyes blinking was used to select the letters. Soltani et al. [10] proposed a wearable eye tracking system based on EOG communicating with a Human Computer interface (HCI) using a Bluetooth unit. The keyboard developed was a classic phone keypad with nine buttons, each button could be selected using eye blinks with opening a second page containing characters on each button.

In this work, a new system which based on EOG eye tracking that enables the user to control a virtual keyboard is presented. The aim of this system was to offer an easy and fast channel of communication for people suffering from motor disable and unable to speak, by using their eyes' movements via a human computer interface (HCI). A new type of virtual keyboard with 5x6 pads containing usual characters was proposed. Horizontal saccadic movements have been used to select each character. Data acquisition and analysis software were developed using LabVIEW language. Different digital filters were applied and compared, then a derivative method was used.

Research supported by MESRS JO200220140002 CNEPRU.

K. Ben Si Said, N. Ababou and A. Ababou are with the Instrumentation laboratory, University of Science and Technology Houari Boumediene, Algiers, Algeria.

N. Ababou is the corresponding author (e-mail: nababou@ usthb.dz).

ISBN: 978-1-61804-321-4

II. Experimental

A. EOG analog conditioning

Electrooculography is the measure of the resting potential (potential difference), arising from hyperpolarization and depolarization existing between the cornea and the retina. This potential varies as the eyeball rotate. Therefore the human eyeball can be considered as a spherical battery. The EOG amplitude varies from 50 to 3500 µV (around 20 µV per degree) in a frequency range from DC to 100 Hz [11]. To record the EOG signals, five Ag-AgCl surface electrodes were used, two of them for the horizontal movements (Blue) and two others for the vertical (Red) movements as shown in Fig.1. The last one (purple) was used as a reference electrode.

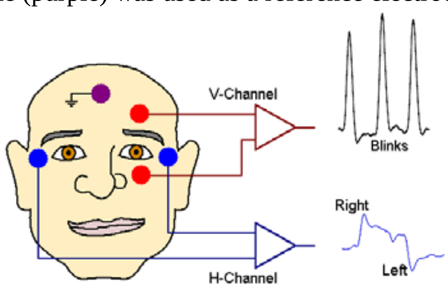

Fig.1. Electrodes placement and resulting signals

The raw emerged signals from electrodes had low magnitude and were noisy. To get better signal output, the conditioning circuit shown in Fig. 2 was used for horizontal as well as for vertical electrodes. It contains five stages: the pre-amplification stage (a) consisting of an instrumentation amplifier with a gain equal to 1000. When using EOG to track the movements of the eyes, the resulting signals contain a low frequency noise caused by luminance, EEG, head movements, electrode placement, etc. So, it is necessary to eliminate the shifting resting potential (mean value) because this value changes [4]. This was accomplished by the second order high-pass active filter (b) with a cutoff frequency equal to 0.5 Hz. The third part of this circuit (c) is a third order, active, low-pass filter with a cut off frequency of 30 Hz. The block (d) is an inverting amplifier with an amplification of 3.

The resulting signal after amplification and filtering has negative and positive values depending on eyeball movements. To convert it into digital signal, a summing amplifier (e) has been added. The output signal of the conditioning circuit has a maximal magnitude equal to 4V, so it can be processed using a USB acquisition card (See Fig.2.2) based on PIC18f2550 microcontroller which was configured and programmed in this application as a slave. Analog EOG signals were converted into digital data with a sampling frequency of 50 Hz, and sent to the host (computer) using the USB 2.0 protocol.

The movements of human eyes can give three informational signals using EOG: right-left, high-low eyeball movement, and eyes blinking. It is proposed in this paper a method to control a virtual keyboard using only two signals: the first one from eye blinking and the other from right-left eyeball movements. A virtual keyboard with five green bars (1 to 5) with six characters on each one is proposed to the user. To control the keyboard, he must look at first to the middle bar. Then, he can start by using his right-left eye movements to select one bar among the five existing. The selected bar becomes light green colored. Then he uses his voluntary eye blinking to select the desired character among the six existing on the chosen bar (see Fig.3.).

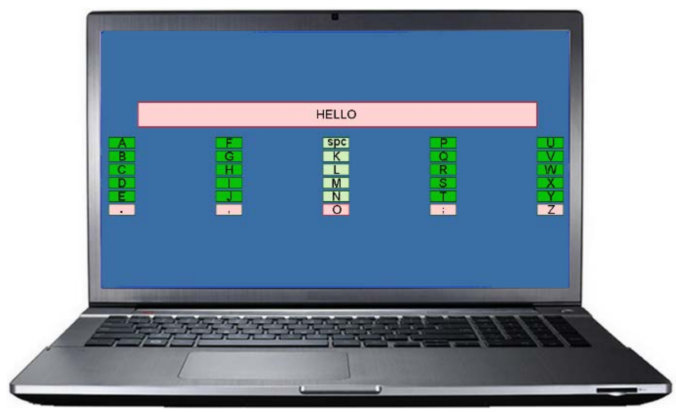

Fig.3. Virtual keyboard 5x6 pads: five columns positions, each one containing six different characters in six rows.

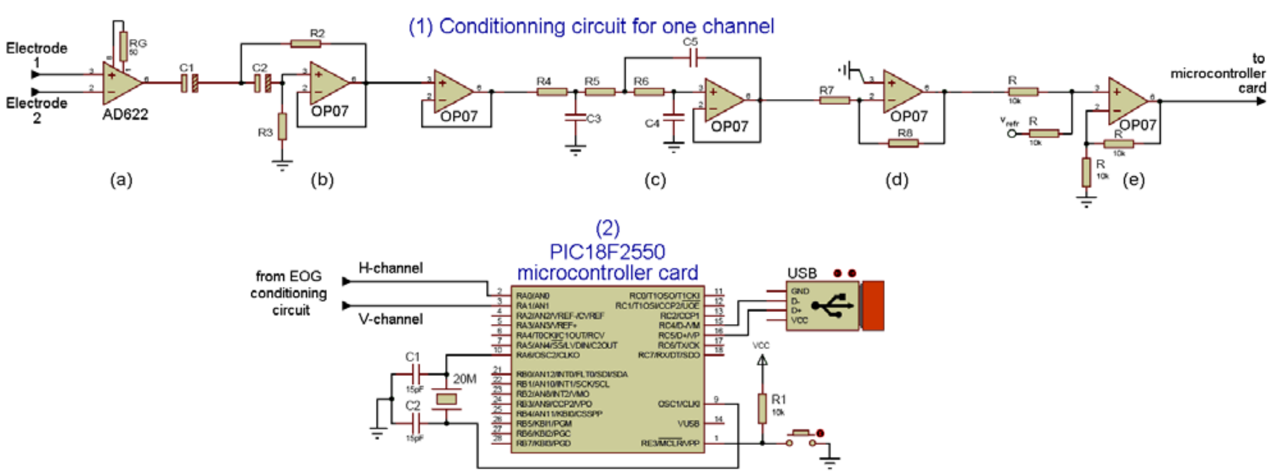

Fig. 2. Hardware parts of the system: (1) EOG conditioning circuit, (2) microcontroller-based USB acquisition card

B. Signal processing on LabVIEW

The main code of the virtual keyboard developed on LabVIEW was executed in a loop as represented in Fig.4. It deals with opening the USB communication with the acquisition card via the bloc (A), then receiving the data of the converted horizontal and vertical EOG in the reception buffer (B). The block (C) separates the data into two parts, one for the horizontal and the other for the vertical EOG channel. Each channel signal was upgraded via block (D) then the two signals were digitally filtered in block (E) with low-pass filter (fc = 3Hz).

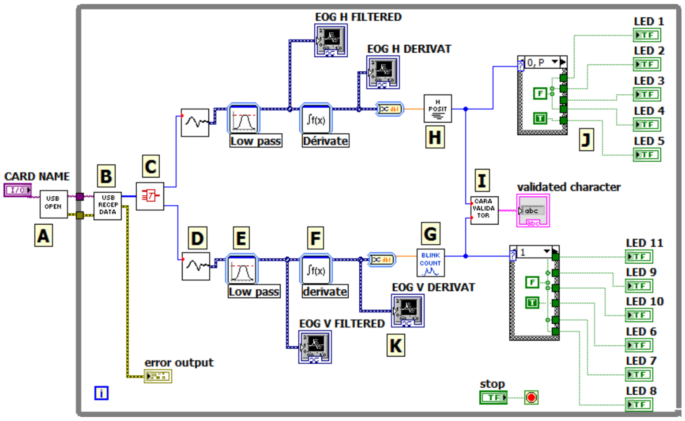

Fig.4. Diagram of the virtual keyboard developed on LabVIEW

To detect saccadic movements (rapid movement) of the eyes, a first order central difference numeric derivative method was used to eliminate the shift dc value; this was performed by the block (F). The resulting values were compared to thresholds by the block (G) for vertical EOG channel resulting in the determination of the number of blinks, and block (H) for horizontal EOG channel resulting in determining which pad the user looked at. The block (I) determined when a character was validated using the method described in the next sub-section, then displayed in the text box (See Fig.3). The next block (J) is a switch-case structure that lights up the horizontal (1-5), and vertical (6-11) LEDs, on the front face of the interface. The next part (K) is a graphical representation of the filtered and derivate signals associated with vertical and horizontal EOG. All the treatments were done in real time at sampling frequency of 50Hz.

C. Using the virtual keyboard

The distance between the user's eyes and the screen must range between 30 and 40cm. Two different lights from red and light green LEDs indicate the current position (letter 'O' in Fig.3.). red color the selected raw (which increases progressively depending on eye blinks from the first to the last raw), and light green for the selected column (which changes from the middle (3) to left (1, 2), or to right (4, 5) positions, depending on horizontal eyes movements. In Fig.3, the last raw which has been selected is red, and the middle column is light green as it has also been selected. The intersection of the selected raw and column corresponds to the character selected by the user. The text box above the keyboard contains the chosen and validated character. To validate a character, the user has to select a horizontal position (indicated by light green color) then he blinks his eyes resulting in a move of the red light position from the first raw to that containing the desired character.

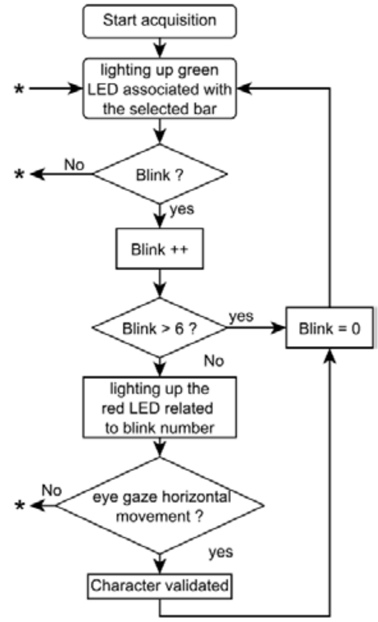

Fig.5. flowchart describing the typing steps

Fig.5 represents the flowchart describing the different steps to validate a character on the virtual keyboard. The selected bar is indicated by light green color. If no blink is detected the character cannot be selected nor displayed. If one blink is performed and its related signal detected, a light red LED lightens on the first row of the active bar. As the blinks' number increases the next pads lighten successively depending on the number of blinks. If this number exceeds 6, the blinks counter returns to zero. If the eye gaze changes horizontally, the character is validated then displayed in the text box.

III. Results and Discussion

A. Selecting a convenient filter

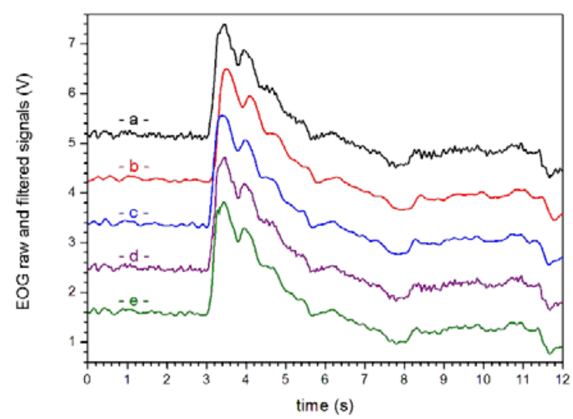

Fig.6. EOG signals after applying analog and digital filters
-a- Raw data after applying analog low-pass filter (fc=3Hz);
-b- Third-order Butterworth filter; -c- FFT filter;
-d- Haar wavelet filter; -e- Savitzky-Golay filter.

Four different digital filters have been tested in order to select the most efficient one for EOG signals. The results associated with analog filtered data are represented by the black curve -a- in Fig.6. Curves -b- to -e- are associated to the same data filtered by four different digital filters: Butterworth low-pass filter, FFT filter, Haar wavelet filter and Savitzky-Golay filter. From the curves' shapes one can consider that in first approximation the digital third-order Butterworth filter shows better results than the three others.

Considering the effect of the four precedent different filters on time derivative of EOG signals shown in Fig.7, the third-order Butterworth filter (red curve -b-) seems also in this case to be the filter that gave the best results with the highest value of the signal to noise S/N ratio.

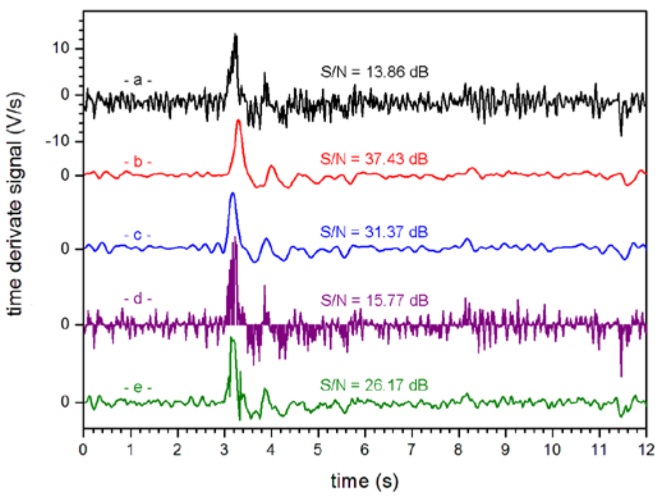

Fig.7. Filter effect on time derivative of EOG signal

B. *Derivative method efficiency*

A graphical representation of the signals was made to show the efficiency of the derivate method to detect saccadic movements of the eye gaze. This was done in our laboratory. A subject with five Ag-AgCl electrodes placed on his face as shown in Fig.1 performed a test. First, he was asked to look at the middle of the keyboard (position 3 in Fig.3) for a time. Then, he was asked to look at the position (5) before returning to the middle position (3), then looking successively at position (1), (3) and so on, during a succession of times. The resulting signal illustrated in Fig.8 shows a random variation of the filtered signal (blue curve) magnitude corresponding to the same eye gaze direction, because the current magnitude depends on the precedent one (corresponding to the last eye gaze direction).

But the same magnitude can be noted in the derivate curve (See Fig.8) for the same horizontal eye movement (1-3, 3-5, 5-3, etc.) because the derivate eliminates the dc-shift component of the signal. So, only the signal associated with saccadic horizontal movement of the eyes remains. Thus, the difference of the signals magnitude related to eye saccades becomes significant and can be easily compared to thresholds to determine the eye gaze direction angle.

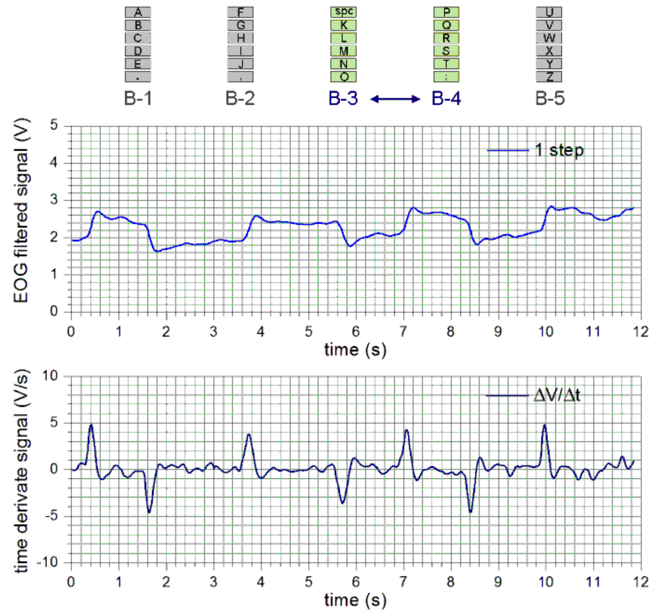

Fig.8. Horizontal EOG signals & derivative for one-step saccade

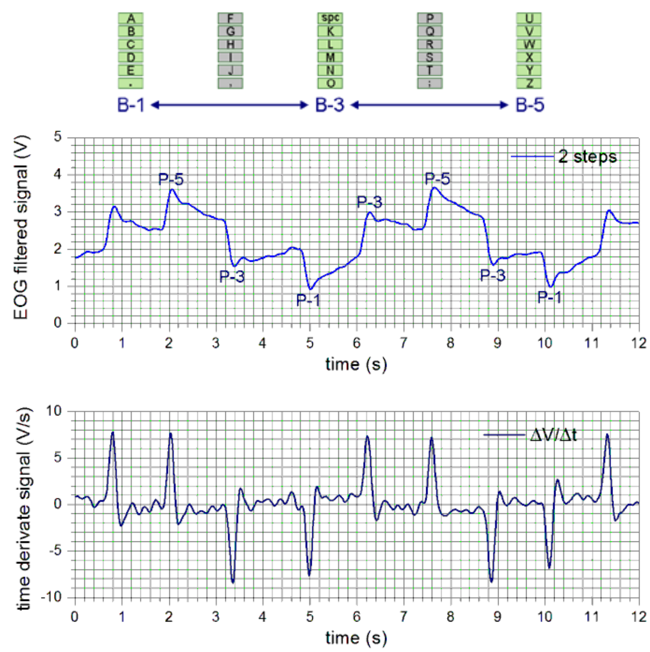

Fig.9. Horizontal EOG signals and related time derivative signal for two steps saccades

C. *Calibration*

For EOG horizontal calibration a subject was asked to sit down in a manner to have his eyes and the virtual keyboard displayed on the PC monitor spaced approximately by 30 to 40 cm. Then, EOG signals were recorded for different eye saccadic movements. For each horizontal position (1-5), six points of the derivate signals have been used to plot the experimental data and the trend line (Linear fit line) as well as the thresholds for each column as represented in Fig.10.

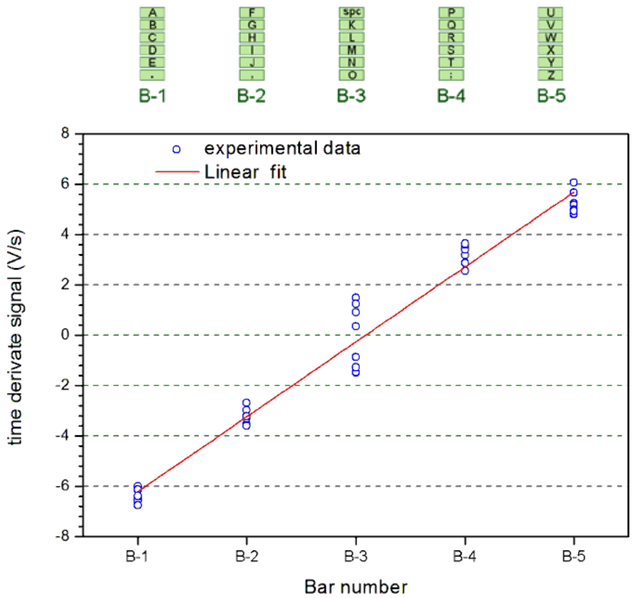

Fig.10 Scatter plot, trend line, and thresholds (blue dash dot lines) of horizontal EOG calibration

D. Performance evaluation

To evaluate the performance of our system two tests we carried out. The first one concerned the typing speed and the second one was relative to the accuracy of the system's response.

- Typing speed test

Two subjects aged 24 and 23 participated in this test procedure. They were asked to seat as in the calibration experience, and to train first for five minutes with the system trying to write some words. After that, they were asked to type the "HELLO" word three times. At each experiment the time was recorded. The obtained results are shown in the table 1 below where the average typing speed for the two subjects were respectively 8.25 character/min and 8.65 character/min.

TABLE I: TYPING TIME FOR "HELLO" WORD

	Typing time (s) for "HELLO"			
Users	Test 1	Test 2	Test 3	**Average**
1	40	35	34	36.33
2	37	32	35	34.67

- Accuracy of system's response:

To determine the accuracy of the virtual keyboard, a test was carried out by a subject who sat as in the calibration procedure, and performed saccades 25 times between the middle button (3) and each position. The right detection of the system (RP) was considered when the right LED lighted up. In the other cases it was considered as a wrong detection (WP). The table II contains the different results as well as the success ratio. The columns 1 and 5 were reached from the middle column 3 by performing eye rotation amplitude of two steps, and one step is performed for the columns 2 and 4.

TABLE II: ACCURACY OF THE SYSTEM 'S RESPONSE

Accuracy of typing					**Success ratio**
Tests	Test 1		Test 2		
positions	CP	WP	CP	WP	
Pos.1	20	05	19	06	78%
Pos.2	23	02	22	03	90%
Pos.4	22	03	23	02	90%
Pos.5	21	04	20	05	82%
Success ratio for tests	86 %		84 %		

The results of the test show that the typing accuracy of the system was around 85%. Several factors could influence on the typing accuracy, namely the electrode placements, the tiredness of the user, and his practice in using this system. This accuracy can certainly be improved by training.

IV. CONCLUSION

The aim of this paper was to present a communication system for people who are simultaneously motor and speech disabled. The system was based on EOG eye gaze tracking to write on a virtual keyboard developed using LabVIEW. Using their left-right eye movements, and their eye blinks, the results showed that the derivative method applied to EOG filtered signals was efficient to detect the saccades of eye gaze movements that result in writing on the virtual keyboard.

V. REFERENCES

[1] A. Ferreira, R.L. Silva, W.C. Celeste, T.F. Bastos , and M . Sarcinelli, "Human-Machine Interface Based on Muscular and Brain Signals applied to a Robotic Wheelchair," IOP Publishing Ltd., vol.7, pp. 1541-1672, 2007.

[2] K. Arai and R. Mardiyanto, "A Prototype of Electric Wheelchair Controlled by Eye-Only for Paralyzed User," Journal of Robotics and Mechatronics vol. 23, pp. 66-74, 2011.

[2] R. Barea, L. Boquete, M. Mazo, and E. López, "Guidance of a wheelchair using electrooculography," *Proceeding 3rd IMACS Int. Multiconference Circuits, Syst. Commun. Comput.*, 1999.

[3] R. Barea, L. Boquete, M. Mazo, E. López, and L. M. Bergasa, "electrooculographic guidance of a wheelchair using eye movements codification 3 eye model based in eog (bidim-eog)."

[4] R. Barea, L. Boquete, J. M. Rodriguez-Ascariz, S. Ortega, and E. López, "Sensory system for implementing a human-computer interface based on electrooculography," *Sensors*, vol. 11, no. 1, pp. 310–328, Jan. 2011.

[5] W. T. Sung, J. H. Chen, and K. Y. Chang, "ZigBee based multi-purpose electronic score design and implementation using EOG," *Sensors Actuators, A Phys.*, vol. 190, pp. 141–152, Feb. 2013.

[6] A. R. V and K. R. V, "EOG Based Low Cost Device for Controlling Home Appliances," vol. 3, no. 3, pp. 708–711, 2014.

[7] P. A. Ratna, C. N. S. Murty, K. R. Sekhar, and V. D. Raj, "An Interface of Human and Machine with Eye Blinking," vol. 1, no. 7, pp. 429–434, 2012.

[8] J. a., A. Ubeda, E. Ianez, J. M., and C. Perez-Vidal, "Multimodal System Based on Electrooculography and Voice Recognition to Control a Robot Arm," *Int. J. Adv. Robot. Syst.*, p. 1, 2013.

[9] W. Tangsuksant, C. Aekmunkhongpaisal, P. Cambua, T. Charoenpong, and T. Chanwimalueang, "Directional eye movement detection system for virtual keyboard controller," *The 2012 Biomed. Eng. Int. Conf. BMEiCON-2012*, pp. 1–5, 2012.

[10] S. Soltani, "Design of a Novel Wearable Human Computer Interface based on Electrooculograghy," 2013.

[11] H. Singh and J. Singh, "Human Eye Tracking and Related Issues : A Review," vol. 2, no. 9, pp. 1–9, 2012.

ISBN: 978-1-61804-321-4

Generalizing Topological Relations of loose

Lejdel Brahim, Kazar Okba

***Abstract*—** In GIS, we use principally three features, such as PolyLine, Point and loose region to represent the geographic object. The loose region is used to represent the area objects as building or green area. Loose regions can be seen as an extension of simple regions described in Egenhofer model. In this paper, we treat the mutation of the topological relations into others relations, when we need to change the scale the map. A new topological model is presented based on simple regions which are defined in *Egenhofer* model and also on the assertions of mutation of the topological relationships according certain criteria.

***Keywords*—**Loose region, generalization, visual acuity, loose topological relations.

I. INTRODUCTION

To represent exactly the reality in GIS, we have to use the loose region to represent the area object. We can define loose region as the extension of simple region represented in the *Egenhofer model*. In this new configuration, the topological relationships between the regions can be different.

In different situations, we need to change the scale of certain detailed representation because the demanded representation doesn't exist in the geographic Database. When applying this process, various changes have been held in the representation contents; as geometry, topology, etc. the loose region can be mutate to a simple region, to point or will be disappear , also the topological relationships can be mutate into others relationships according to certain measurements and thresholds. So, we will develop the mathematical assertions which guide these mutations.

This paper will be organized as follows. First, definitions and a state of the art review for generalization process will be given (Section 2). Also, definitions and a state of the art review for topological relations will be given (Section 3). Then, loose regions and topology model will be defined (Section 4). Finally, we present a conclusion and future work (Section 5).

II. GEOGRAPHIC OBJECT GENERALIZATION

The generalization process can be defined as a process of abstraction of represented information subject to the change of the scale of a map. The purpose of generalization is to produce a good-looking map, balancing the requirements of accuracy, information content and legibility [1]. It encompasses the modification of the information in such a way that it can be represented on smaller surfaces, retaining the geometric and descriptive characteristics. The essence of the original map should be maintained at all smaller scales. Figure 1 gives an example of generalization of a map at the same place: shapes are simplified, some points disappear, etc.

Figure 1. Generalization process (left: 1:100,000, middle: 1:200,000, right: 1:500,000), Source: Swisstopo.

A. *Definition*

Many definitions have been given for the generalization process, The International Cartographic Association [12] has defined it as "the selection and simplified representation of detail appropriate to scale and/or the purpose of a map". The geographic object generalization is a very complex process. In order to reduce its complexity, the overall process is often decomposed into individual sub-processes, called operators [16], such as simplification, displacement,...etc. Each operator defines a transformation that can be applied to a single spatial object, or to a group of spatial objects.

B. *State of the art for geographic object generalization*

Historically speaking, the first algorithm for generalizing polylines was published in [4]. Then, several variants were published, essentially to improve the results of the initial algorithm. However, this algorithm does not take into account many aspects, such as the topological relationships between objects.

Now, several methods and concepts proposed to model and implement the generalization process but a framework for their combination into a comprehensive generalization process is still missing [9].

The first generalization process appeared in the early of 1990s [17]. It involved only a few geographic areas.

Ruas and Plazanet [19] proposed a framework controlled by a set of constraints. The dynamic generalization model is

ISBN: 978-1-61804-321-4

based on avoiding constraint violations and on the local qualification of a set of objects, represented by means of an object situation. A situation is described by the geographical objects involved, their relationships, and the constraint violations. Ruas and Plazanet [19] concentrated only on constraints related to objects and not the constraints between objects, such as the topological constraints.

Many other works use the least squares adjustment theory to solve the generalization problems, such as [10], [23], [24], whose works aim to globally reduce all spatial conflicts. The idea is to solve spatial conflicts by modeling different constraints using mathematical expressions. Moreover Harrie [10] proposed to formulate the geometric and topological constraints as linear functions of the object coordinates. The least squares adjustment seems to be an interesting technique but these constraints are difficult to express by a linear equation.

In the same context and for reducing the spatial conflicts in the map, many interesting methods were proposed in [27] and [26]. In those approaches, a cost function (fitness) must be defined for validating statements. However, it is questionable whether it is realistic to define such a function that integrates all the constraints of generalization, such as the topological constraints.

Then several works model the spatial objects by agents such as the works of [5], [20] and [21]. In the agent-based model, the spatial objects are modeled by the decisional entities in the generalization system. These entities are software agents the goal of which is to satisfy their cartographic constraints the more as possible. The constraints are subdivided into four types, metric, topological, structural and procedural constraints [20]. The topological constraints ensure that any topological relationship between objects is maintained or modified consistently, for example, self-intersections of an object or any intersection between two objects must be avoided.

Also to improve the map generalization process, another approach was proposed in [22] which are based on a new concept called SGO (Self-generalizing object). An SGO is able to generalize a cartographic object automatically using one or more geometric patterns, simple generalization algorithms and spatial integrity constraints, but this approach does not define a pattern for topological constraints.

In the EuroSDR project, cartographic experts of four NMAs (National Mapping Agencies) were called to evaluate the results of the automation generalization process according to certain constraints [25]. The objective of this project consists to illustrate the state of the art of automated generalization in practice, exchange of knowledge between research community, NMAs and software vendor and to contribute to development of constraint specification. Four test cases that were selected, provided by the participated NMAs. NMAs defined their map specifications for automated generalization in template which were developed by the EuroSDR team [25]. These map specifications were formalized as a set of cartographic constraints to be followed. They distinguished between two main categories of constraints: legibility constraints and preservation constraints. After the analysis of constraints composition, the EuroSDR project team derived a list of generic and specific cartographic constraints which must respected in generalization process.

Lejdel and Kazar [14] proposed an approach for optimizing the automatic generalization process by satisfying cartographic constraints. This approach consists in providing agents geographic genetic properties to enable them to choose the optimal actions, so giving the concept of genetic agent. Each geographic agent is equipped with an optimizer, and each one executes a genetic algorithm to determine the optimal action to be executed according to its current state, in order to satisfy cartographic constraints the most possible. The genetic algorithm follows the classical steps as selection, crossover and mutation. The solution is refined gradually over the iterations until to reach convergence to a solution that approaches the optimal solution and a certain degree of imperfection is acceptable. The solution here is a set of algorithms with adapted parameters which minimize conflicts. The model of the topological constraints of this approach is not addressed in this paper.

In the recent paper, Lejdel et al. [15] define a mathematical model of the generalization of topological relationships between two rectangular ribbons or between ribbons and simple regions. Thus, two rectangular ribbons or two simple regions can be disjoint or intersect. The disjunction is defined by a distance separating the two ribbons. The intersection between two simple regions can be Point (0D), Line (1D) or area (2D) according to certain criteria. In this work, they get formally the mathematical description for each topological relationship between objects when we use thresholds and metric measurements; as area, distance, etc. These topological relationships can be: disjoint, meet, merge and crossing. When downscaling, these topological relations can be mutated into other topological relations according to certain criteria. In this paper, we developed a topological model to define a good generalization process. It based on the Egenhofer model which describes the topological relationships between simple regions.

III. TOPOLOGICAL RELATIONS

Topological relationships describe relationships between all objects in space, the points, lines and areas for all possible kinds of deformation.

A. *Definition*

Topology is defined as mathematical study of the properties that are preserved through deformations, twistings, and stretchings of objects. Topology is foremost a branch of mathematics, but some concepts are of importance in cartographic generalization, such as topological relationships [11]. Several researchers have defined topological relationships in the context of geographic information [2] ,[7] and [29].

B. *State of the art for topological relations*

From an historical point of view, different topological models were proposed. First, Max Egenhofer with his colleagues proposed the first topological model for two-dimensional objects and then a second model family named RCC was proposed. Let us examine them rapidly.

1) *Egenhofer topological relationship*

To define a model of topological relationships, Egenhofer and Herring [8] proposed a spatial data model based on topological algebra. The algebra topological model is based on geometric primitives called cells that are defined for different spatial dimensions 0-D, 1-D, and 2-D. A variety of topological properties between two cells can be expressed in terms of the 9-intersection model [6]. The 9-intersection model between two cells *A* and *B* is based on the combination of six topological primitives that are interiors, boundaries, and exteriors of A $(A^{\circ}, \partial A, A^{-})$ and $B(B^{\circ}, \partial B, B^{-})$.

These six topological primitives can be combined to form nine possible combinations representing the topological relationships between these two cells. These 9-intersections are represented as one 3×3 matrix [3].

$$R(A,B) = \begin{pmatrix} A^{\circ} \cap B^{\circ} & A^{\circ} \cap \partial B & A^{\circ} \cap B^{-} \\ \partial A \cap B^{\circ} & \partial A \cap \partial B & \partial A \cap B^{-} \\ A^{-} \cap B^{\circ} & A^{-} \cap \partial B & A^{-} \cap B^{-} \end{pmatrix}$$

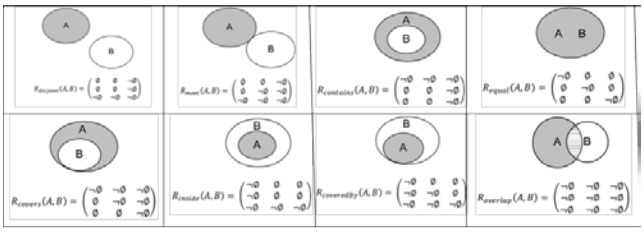

Figure 2. The eight topological relations between two regions A and B.

2) *Other models RCC*

Independently developed, the RCC (Region Connection Calculus) is an alternative topological approach to qualitative spatial representation and reasoning where spatial regions are subsets of topological space [18]. The RCC model distinguishes eight topological relationships between two simple regions, which are in fact exactly the same as those identified by 9-intersection (see Figure 2).

The RCC-8 uses a set of eight pairwise disjoint and mutually exhaustive relations, called base relation denoted as EQ, DC, EC, PO, TPP, NTPP, TPP-1, NTPP-1, with the meaning of EQual, DisConnected, Externally Connected, Partial Overlap, Tangential Proper Part, Non-Tangential Proper Part, and their converses. In this model, sometimes one does not want to distinguish between DC and EC, and between TPP and NTPP. So, a set of five relations are derived, called RCC-5. Other refinements have been developed, taking into account the convex hulls of region, so twenty-three topological relationships are obtained, called RCC-23. Also, [28] presents a statistical model for quantitative assessment of uncertain topological relations between two imprecise regions. This model based on a morphologic distance function to determine the type of topological relations.

C. *Mutation of topological Region-Region relations*

In this section, the Egenhofer's relations [6] are treated mainly. After generalization, the object geometries are adapted to the perceptual limits imposed by the new (smaller) scale [13]. We present in following the different mutations of topological relationships between loose regions.

1) *Mutation Disjoint-to-Meet*

The relation "Disjoint" mutates to relation "Meet" (Figure 3), according the following assertions.

$$\forall \mathrm{O}^1, \mathrm{O}^2 \in \mathrm{GeObject}, (\forall \sigma \in \mathrm{Scale}) \wedge (O^1_\sigma = 2Dmap(O^1, \sigma)) \wedge (O^2_\sigma = 2Dmap(O^2, \sigma)) \wedge$$
$$(Disjo\,\mathrm{int}(\mathrm{O}^1, \mathrm{O}^2)) \wedge (Dist(\mathrm{O}^1, \mathrm{O}^2) < \varepsilon)$$
$$\Rightarrow Meet(O^1_\sigma, O^2_\sigma).$$

But a smaller object can disappear or be eliminated if its area is too small to be well visible. So in this case, the initial relation does not hold anymore.

$$\forall O \in \mathrm{GeObject}, \forall \sigma \in \mathrm{Scale} \wedge (O_\sigma = 2Dmap(O, \sigma)) \wedge (Area(O_\sigma) < (\varepsilon_{lp})^2)$$
$$\Rightarrow O_\sigma = \phi.$$

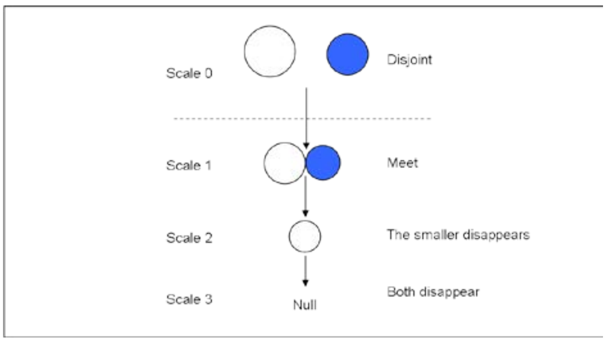

Figure 3. The mutation of Disjoint-to-Meet.

2) *Mutation Overlap-to-Meet*

The relation "overlap" can mutate to "meet" relation according to the following condition (Figure 4):

$$\forall \mathrm{O}^1, \mathrm{O}^2 \in \mathrm{GeObject}, (\forall \sigma \in \mathrm{Scale}) \wedge (O^1_\sigma = 2Dmap(O^1, \sigma)) \wedge (O^2_\sigma = 2Dmap(O^2, \sigma)) \wedge$$
$$(Overlap(\mathrm{O}^1, \mathrm{O}^2)) \wedge (Area(\mathrm{O}^1 \cap \mathrm{O}^2) < Area(\neg(\mathrm{O}^1 \cap \mathrm{O}^2)))$$
$$\Rightarrow Meet(O^1_\sigma, O^2_\sigma).$$

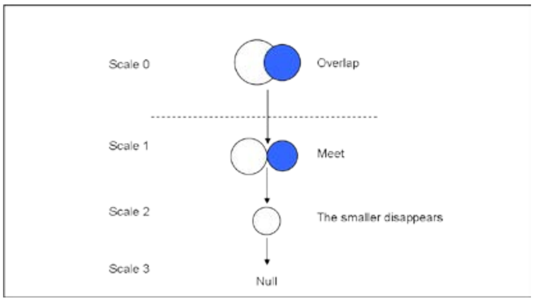

Figure 4. The mutation of Overlap-to-Meet.

In addition, similarly, the smaller object can disappear.

3) *Mutation Overlap-to-Cover*

Also, the relation “overlap” may be mutate to relation “cover”, to formulate this mutation, one use the following assertion (Figure 5):

$$\forall\, \mathrm{O}^1, \mathrm{O}^2 \in \mathrm{GeObject}, (\forall \sigma \in \mathrm{Scale}) \wedge (O^1_\sigma = 2Dmap(O^1, \sigma)) \wedge (O^2_\sigma = 2Dmap(O^2, \sigma)) \wedge (Overlap(\mathrm{O}^1, \mathrm{O}^2)) \wedge (Area(\mathrm{O}^1 \cap \mathrm{O}^2) > Area(\neg(\mathrm{O}^1 \cap \mathrm{O}^2))) \Rightarrow Cover(O^1_\sigma, O^2_\sigma).$$

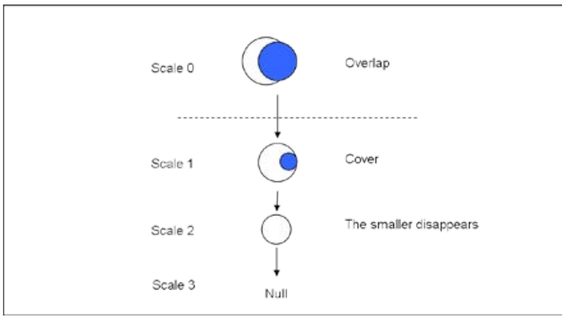

Figure 5. The mutation of Overlap-to-Cover.

4) *Mutation Contains-to-Cover*

The mutation of relation “contains” to “Cover”, was expressed by the following assertion (Figure 6):

$$\forall\, \mathrm{O}^1, \mathrm{O}^2 \in \mathrm{GeObject}, (\forall \sigma \in \mathrm{Scale}) \wedge (O^1_\sigma = 2Dmap(O^1, \sigma)) \wedge (O^2_\sigma = 2Dmap(O^2, \sigma)) \wedge (Contains(\mathrm{O}^1, \mathrm{O}^2)) \wedge (Dist(\mathrm{O}^1, \mathrm{O}^2) < \varepsilon_1) \Rightarrow Cover(O^1_\sigma, O^2_\sigma).$$

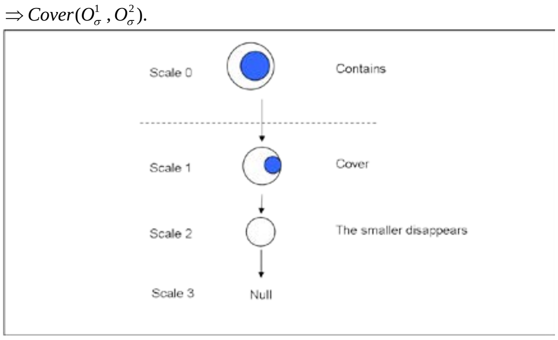

Figure 6. The mutation of Contains-to-Cover.

IV. SCALING MUTATION OF TOPOLOGICAL RELATIONS

As previously told according to scales, geographic objects can mutate according to two rules. As scale diminishes: Loose region will mutate to simple region, to a point and then will disappear,

A. *General Process*

The generalization process is very complex. As we treat in this context, the generalization of the topological relations during downscaling, we would simplify it. So, the complete process can be modeled as follows:

- Step 0: original geographic features only modeled as loose region,
- Step 1: as scale diminishes, loose regions will be generalized and possibly can mutated into simple region,
- Step 2: as scale continues to diminish, small simple region mutate to point,
- Step 3: as scale continues to diminish, points can be disappear.

Let us call this process “generalization-reduction-disappearance” (GRD process).

B. *Visual acuity applied to geographic objects*

It is well known that “*Cartographic representation is linked to visual acuity*”. Thresholds must be defined. In classical cartography, the limit ranges from 1 mm to 0.1 mm. If one takes a road and a certain scale and if the transformation gives a width more that 1 mm, this road is an area, between 1 mm and 0.1mm, then a line and if less that 0.1mm the road disappears. The same reasoning is valid for cities or small countries such as Andorra, Liechtenstein, Monaco, etc. In these cases, the “holes” in Italy or in France disappear cartographically. With the thresholds previously defined, we can formally get (in which *2Dmap* is a function transforming a geographic object to some scale possibly with generalization , in the 2-dimension domain) [15]:

a/ Disappearance of a geographic object (O) at scale σ:

$$\forall O \in \mathrm{GeObject}, \forall \sigma \in \mathrm{Scale} \wedge O_\sigma = 2Dmap(O, \sigma) \wedge Area(O_\sigma) < (\varepsilon_{lp})^2 \Rightarrow O_\sigma = \phi.$$

b/ Mutation of an loose region into a point (for instance the centroid of the concerned object, for instance taken as the center of the minimum bounding rectangle):

$$\forall O \in \mathrm{GeObject}, \forall \sigma \in \mathrm{Scale} \wedge O_\sigma = 2Dmap(O, \sigma) \wedge (\varepsilon_i)^2 > Area(O_\sigma) > (\varepsilon_{lp})^2 \Rightarrow O_\sigma = Centroid(O).$$

C. *Granularity of interest*

The previous remarks are not only valid for cartography, but also for any type of reasoning. Beyond thresholds of visual

ISBN: 978-1-61804-321-4

acuity which is a fundamental concept in cartography, let us define “granularity of interest”: this is the minimum level of interest for a geographic user. For instance a nationwide politician will be interested at state level whereas an urban will be concerned only at the level of the city for which he works.

In the sequel to simplify the presentation, we will continue to use the thresholds for visual acuity instead of granularity of interest.

V. GENERALIZING TOPOLOGICAL RELATIONS OF LOOSE REGION

The generalization of spatial data implied the generalization of the topological relations according to certain accurate rules. We considered here the GRD process described in section IV.A. The objective of this section is to formulate the list of these rules, between loose regions.

A. *Mutation of loose topological relations*

Often, due to measurement errors and independent processing or generalizations, geographic objects do not coincide exactly. Eghenhofer (2009) investigate the possible connections between the topological relationships and metrics.

When one wants to evaluate the topological relations between them, he needs to take this aspect into account. Within the context of granularity of interest, when downscaling, this characteristic will disappear. Let define loose topological relations when dealing in such cases. By considering the conventional topological relations, let us immediately say that the disjoint relation is not concerned, except when the regions are very close. (See figure 7)

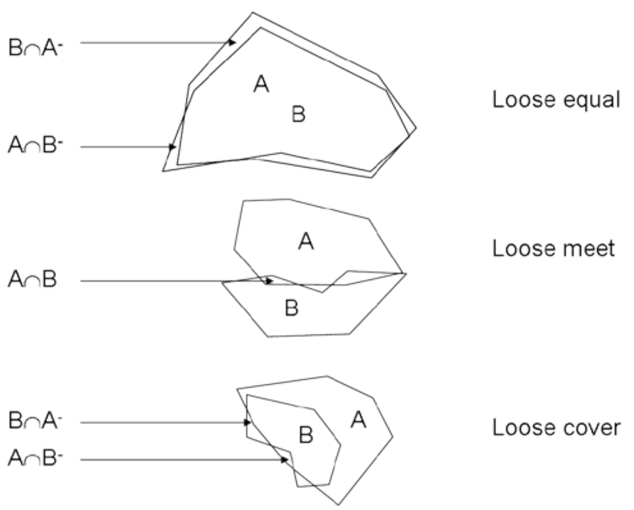

Figure 7. Loose topological relations.

1) *Loose meet*

The criterion to define a loose meet is based on the area of the intersection of two regions, *A* and *B*. For instance, given a threshold ε_{LM}:

$$\frac{Area(A \cap B)}{Area(A \cup B)} < \varepsilon_{LM} \Rightarrow Lmeet(A, B)$$

When downscaling from σ_1 to σ_2, this mutation Lmeet-to-meet can be defined:

$$Lmeet(A_{\sigma_1}, B_{\sigma_1}) \wedge (\sigma_2 < \sigma_1) \wedge (\mathrm{A}_{\sigma_1} = 2Dmap(A, \sigma_1)) \wedge$$
$$(\mathrm{A}_{\sigma_2} = 2Dmap(A, \sigma_2)) \wedge (\frac{Area(A_\sigma \cap B_\sigma)}{Area(A_\sigma \cup B_\sigma)} < \varepsilon_2{}^2)$$
$$\Rightarrow Meet(A_{\sigma_2}, B_{\sigma_2})$$

2) *Loose cover*

Here one has to evaluate the area of the sliver polygons. This area is composed of two parts, $A \cap B^-$ and $A^- \cap B$. In other terms, this is a symmetric difference defined as follows: $A \oplus B = (\mathrm{A} \cap B^-) \cup (A^- \cap B)$. Therefore by defining another threshold, the corresponding criterion can be:

$$\frac{Area(A \oplus B)}{Area(A \cup B)} < \varepsilon_{LC} \Rightarrow \mathrm{Lcover}(A, B)$$

So, the mutation Lcover-to-cover when downscaling:

$$Lcvr(A_{\sigma_1}, B_{\sigma_1}) \wedge (\sigma_2 < \sigma_1) \wedge (\mathrm{A}_{\sigma_1} = 2Dmap(A, \sigma_1)) \wedge$$
$$(\mathrm{A}_{\sigma_2} = 2Dmap(A, \sigma_2)) \wedge (\frac{Area((A \cap B^-) \cup (A^- \cap B))}{Area(A \cup B)} < (\varepsilon_4)^2)$$
$$\Rightarrow \mathrm{Cover}((A_{\sigma_2}, B_{\sigma_2})).$$

3) *Loose equal*

The loose-equal relation can be defined from the loose-cover relation, but the area in the intersection must not be far from the union. So two criteria must be used with another threshold:

$$\frac{Area(A \oplus B)}{Area(A \cup B)} < \varepsilon_{LC} \wedge \frac{Area(A \cap B)}{Area(A \cup B)} < 1 - \varepsilon_{LE} \Rightarrow Lequal(A, B) \cdot$$

Similarly, this relation can mutate to an Equal relation when downscaling:

$$Lequal(A_{\sigma_1}, B_{\sigma_1}) \wedge (\sigma_2 < \sigma_1) \wedge (\mathrm{A}_{\sigma_1} = 2Dmap(A, \sigma_1)) \wedge$$
$$(\mathrm{A}_{\sigma_2} = 2Dmap(A, \sigma_2)) \wedge (\frac{Area((A \cap B^-) \cup (A^- \cap B))}{Area(A \cup B)} < (\varepsilon_5)^2)$$
$$\Rightarrow Equal((A_{\sigma_2}, B_{\sigma_2}))$$

ISBN: 978-1-61804-321-4

VI. CONCLUSION AND FUTURE WORKS

In this paper, we develop a topological model of loose regions. This Model principally based on the Eghenhofer model. Also, we treat the mutation of the topological relations which can hold between the loose regions into others relations, when downscaling. To assure the topological consistency, topological conditions are used to mutate the relationships in terms of meeting, overlapping, disjunction, and merging between map objects into others relationships.

This work can open various future works, such as:

- Integration of this topological model in the automatic generalization process or on-the-fly web map generation.
- Use these basic topological relations to model the other relations which can be between the complex regions.

REFERENCES

[1] Cecconi, A. 2003. “Integration of Cartographic Generalization and Multi-scale databases for Enhanced Web Mapping”, PhD Thesis, University of Zurich.

[2] Clementini, E., Di Felice, P., Van Oosterom,P. 1993. “A Small Set of Formal Topological Relationships Suitable for End-User Interaction”. In Abeland, B. C. (ed), Advances in Spatial Databases, Lecture Notes in Computer Science. Springer,692: 277-295.

[3] Clementini, E., Sharma J., Egenhofer M. 1994. “Modeling Topological Spatial Relations : Strategies for Query Processing, In Journal of Computers and Graphics”, 18 (6): 815-822.

[4] Douglas D., Peuker T. 1973. “Algorithms for the Reduction of the Number of Points Required to Represent a Digitized Line or its Caricature”, The Canadian Cartographer. 10(2): 112-122.

[5] Duchêne, C. 2003. “Automated Map Generalization using Communicating Agents”. Proceedings of the 21st International Conference of Cartography (ACI/ICA), Durban, Afrique du Sud , 160-169.

[6] Egenhofer, M. 1991. “Topology and Reasoning: Reasoning about Binary Topological Relations”. In Second Symposium on Large Spatial Databases, In O. Gunther and H.-J. Schek (Eds.), LNCS in Advances in Spatial Databases, Springer-Verlag, 141-160.

[7] Egenhofer, M., and Franzosa, R. 1991. “Point-Set Topological Spatial Relations. International Journal of Geographical Information Systems”. 5(2): 161-174.

[8] Egenhofer, M.,Herring J. 1990. “A Mathematical Framework for the Definition of Topological Relationships”. In Proceedings of the 4th International Symposium on Spatial Data Handling, 803-813.

[9] Galanda, M. , Weibel R. 2002. “An Agent-Based Framework for Polygonal Subdivision Generalization”, in Richardson D. and van Oosterom P. (eds.), Advances in Spatial Data Handling. 10th International Symposium on Spatial Data Handling, Berlin Heidelberg: Springer, 121–136.

[10] Harrie, L. 1999. “The Constraint Method for Solving Spatial Conflicts in Cartographic Generalization”, Cartography and Geographic Information Science, 26(1), 55-69.

[11] Harrie, L. 2001. “An Optimisation Approach to Cartographic Generalisation”, PhD. Thesis, Lund University, Sweden.

[12] ICA, 1973. “International Cartographic Association: Multilingual Dictionary of Technical Terms in Cartography”. Wiesbaden, F. Steiner.

[13] Laurini, R. 2014. “A Conceptual Framework for Geographic Knowledge Engineering”, Journal of Visual Languages and Computing. 25(1):2-19.

[14] Lejdel, B., Kazar, O. 2012. “Genetic Agent for Optimizing Generalization Process of Spatial Data, International Journal of Digital Information and Wireless Communications” (IJDIWC), 1(3) : 729-737.

[15] Lejdel, B., Kazar,O., Laurini R. 2015. “Mathematical Framework for Topological Relationships between Ribbons and Regions”, Journal of Visual Languages and Computing. 26(1):66-81.

[16] McMaster, B., and Shea, S. 1992. “Generalization in Digital Cartography”. Association of American Geographers, Wahington D.C.

[17] Müller, J., and Wang, Z. 1992. “Area-Patch Generalization: A Competitive Approach”. The Cartographic Journal, 29(2) : 137–144.

[18] Randell, D., Cui Z., Cohn A. 1992. “A Spatial Logic based on Regions and Connection. In: 3rd International Conference on Principles of Knowledge Representation and Reasoning”. Morgan Kaufmann Publisher , 165–176.

[19] Ruas, A, Plazanet, C. 1996. “Strategies for Automated Generalization”. In: Proceedings of the 7thInternational Symposium on Spatial Data Handling, Advances in GIS ResearchII, 1-6.

[20] Ruas, A. 1999. “Modèle de généralisation de Données Géographiques à Base de Contraintes et d‘Autonomie”. PhD thesis, Université de Marne-la-Vallée.

[21] Ruas, A. , Duchêne C. 2007. “A Prototype Generalisation System Based on the Multi-Agent System Paradigm”. In W.A.Mackaness, A.Ruas and L.T. Sarjakoski, editor: Generalisation of Geographic Information: Cartographic Modelling and Applications, Elsevier Ltd, chapter 14, 269-284.

[22] Sabo, N. 2007. “Généralisation et des patrons géométriques pour la création des objets auto-generalisants (SGO) afin d’améliorer la généralisation cartographique à la volée”. PhD thesis, Université de laval , Quebec.

[23] Sarjakoski, T. , Kilpelainen, T. 1999. “Holistic Cartographic Generalization by Least Squares Adjustment for Large Data Sets”. Proceedings of 19th International Cartographic Conference, Ottawa, Canada, 1091–1098.

[24] Sester, M. 2000. “Generalization Based on Least Squares Adjustment”. International Archives of Photogrammetry and Remote Sensing , 33 (B4/3) : 931-938.

[25] Stoter, J., D. Burghardt, C. Duchêne, B. Baella, N. Bakker, C. Blok, M. Pla, N. Regnauld, G. Touya, S. Schmid. 2009. “Methodology for Evaluating Automated Map Generalization in Commercial Software”. Computers, Environment and Urban Systems 33 (5) : 311-324.

[26] Ware, M., Thomas, N., Jones, C. 2003. “Resolving Graphic Conflicts in Scale Reduced Maps: Refining, the Simulated Annealing Technique”. Proceedings of 11th Annual GIS Research UK Conference (GISRUK) , City University, 244-248.

[27] Wilson, D., Ware, M., Ware, A. 2003. “Reducing Graphic Conflict in Scale Reduced Maps Using A Genetic Algorithm”. ICA Map Generalization Workshop, Paris ,01-11.

[28] Winter, S. 2000. “Uncertain Topological Relations between Imprecise Regions”. International Journal of Geographical Information Systems. 14 (5) : 411- 430.

[29] Winter, S., Frank A. 2000. “Topology in Raster and Vector Representation”. GeoInformatica. 4(1) :35-65.

Multi-Length Directional Interpolation Filter based on Color Correlation for Bayer Pattern Demosaicking

Yonghoon Kim, Dokyung Lee, and Jechang Jeong

***Abstract*—**In this paper, we proposed a multi-length directional interpolation filter (MLDIF) for color filter array interpolation, where the green channel is interpolated using directional filters which have different filter lengths. In the MLDIF, the filter length is determined using the green pixel correlation between the center and outside regions, and the whole process is non-recursive. To increase the performance of the green channel interpolation, we used a calibration term to compensate for the misguided green pixel values caused by the mismatch between the color channels. Furthermore, we avoided recursive processes, and every interpolation process exploits only one set of weights. By doing this, the complexity burden can be reduced. Experimental results demonstrate that the proposed algorithm shows great improvement in the objective and subjective image quality for 18 images of the IMAX dataset; the proposed algorithm, in particular, successfully suppresses the demosaicking artifacts.

***Keywords*—**- Color filter array (CFA) interpolation, multi-length directional interpolation filter, demosaicking, Bayer pattern.

I. Introduction

NOWADAYS, the single-sensor digital camera is widely used in many devices. The single-sensor records only one color spectrum among the red (R), green (G), and blue (B) channels with a color filter array (CFA) at each pixel position. The most famous CFA pattern is the Bayer pattern introduced by its inventor, Bayer [1]. It consists of the G component on a quincunx grid, and other color components, R/B, on a rectangular grid, as shown in Fig.1. The G pixels have a higher sampling rate than the other two because the human visual system is sensitive in the medium wavelengths. The reconstruction process of the three color components is called CFA interpolation or demosaicking [2].

In the past few years, many demosaicking algorithms have been proposed to enhance the interpolation performance and image quality [3-15]. Most demosaicking algorithms exploit the color correlation between G and R/B to obtain better estimation results. In [3], Gunturk et al. proposed an alternating projections (AP) algorithm and Lu et al. improved the AP algorithm by adopting fast one-step implementation [4]. In [6], a hard decision algorithm based on color variance is used to preserve details in texture regions. Dengwen et al. proposed color demosaicking with directional filtering and weighting (DDFW) [7]. They exploit a hard decision algorithm for G channel interpolation. Zhen et al. proposed another hard decision technique called voting direction interpolation (VDI) [8]. Paliy et al. introduced adaptive filtering based on local polynomial approximation (LPA) [9].The gradients of the color difference are integrated and exploited as weights for non-directional interpolation [10] and directional interpolation methods [11-16]. Other approaches tried to solve the demosaicking problem at the frequency domain [17-18].

	j-2	j-1	j	j+1	j+2
i-2	B	G	B	G	B
i-1	G	R	G	R	G
i	B	G	B	G	B
i+1	G	R	G	R	G
i+2	B	G	B	G	B

Fig. 1. Bayer color filter array pattern.

The weight technique obtained from the gradient provides high accuracy for direction interpolation, and the hard decision algorithms also help to select the direction of interpolation. These algorithms achieve great improvements in demosaicking performance. However, conventional demosaicking methods have sticking demosaicking artifacts. In addition, the demosaicking process is becoming heavier due to complex weight calculations and iterative processes. To solve these issues, we introduce a new interpolation concept called a multi-length directional interpolation filter (MLDIF). This method is based on [19]. Instead of exploiting a two direction

"This research was supported by the MSIP(Ministry of Science, ICT & Future Planning), Korea, under the "Establishing IT Research Infrastructure Projects" supervised by the NIPA(National IT Industry Promotion Agency)(I2221-14-1005)

Y. Kim is with the Department of Electronics and Computer Engineering, Hanyang University, Haengdangdong, Sungdonggu, Seoul, South Korea (e-mail: hoonykim85@gmail.com).

D. Lee is with the Department of Electronics and Computer Engineering, Hanyang University, Haengdangdong, Sungdonggu, Seoul, South Korea (e-mail: dky1006@gmail.com).

J. Jeong is with the Department of Electronics and Computer Engineering, Hanyang University, Haengdangdong, Sungdonggu, Seoul, South Korea (corresponding author, e-mail: jjeong@hanyang.ac.kr).

ISBN: 978-1-61804-321-4

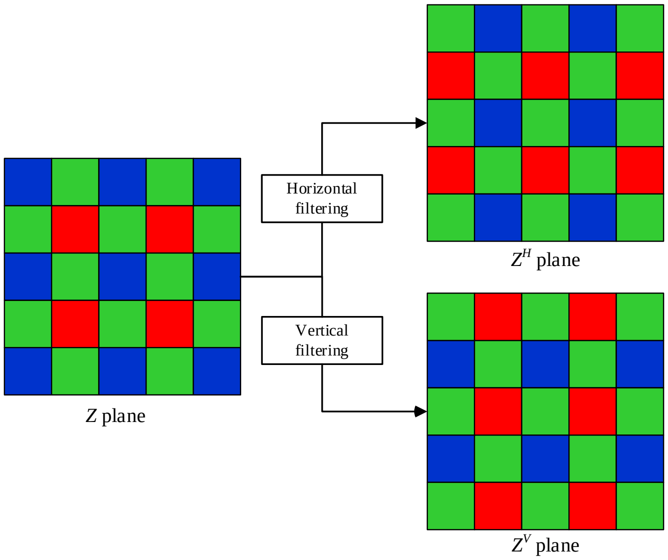

Fig. 2. Original bayer plane (Z), filtered plane of vertical direction (Z^V) and horizontal direction (Z^H)

interpolation [19], we adopt four direction interpolation using two filters which have different lengths.

The remainder of this paper is organized as follows. Section I gives the details of the proposed multi-length interpolation algorithm, and Section II presents the objective and subjective experimental analysis. Section discusses the parameter choice problem. Finally, a conclusion is given in Section III.

II. Proposed Algorithm

The G channel contains more spatial information than other color channels due to the characteristics of the Bayer CFA pattern. Therefore, most demosaicking algorithms reconstruct the G channel in advance. To interpolate the G channel accurately, 4-way directional interpolation is utilized based on the weights of each direction.

The proposed weighting algorithm uses two kinds of planes, original bayer plane Z, and reconstructed bayer planes Z^H and Z^V, shown in Fig. 2. The reconstructed planes are calculated as follows:

$$\begin{aligned} Z^H &= Z * f, \\ Z^V &= Z * f', \end{aligned} \tag{1}$$

where f=[1/4,1,-1/2,1,1/4] and Z^H and Z^V denote a reconstructed Bayer plane using horizontal and vertical filtering, respectively. The f is the filter that Hamilton and Adam's formula [12] used in conventional demosaicking algorithms. After filtering, the R/B position transforms to G and the G position is changed to R/B depending on the direction of the filter. Using original and reconstructed planes, the gradient is calculated as follows:

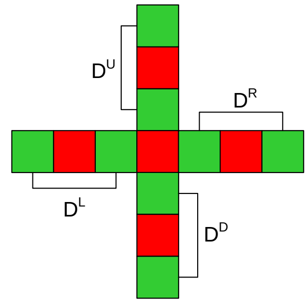

Fig. 3. G pixel correlation of four directions

$$\begin{aligned} \Delta^H_{i,j} &= \left| Z_{i,j-1} - Z_{i,j+1} \right|, \\ \Delta^V_{i,j} &= \left| Z_{i-1,j} - Z_{i+1,j} \right|, \\ \tilde{\Delta}^H_{i,j} &= \left| Z^H_{i,j-1} - Z^H_{i,j+1} \right|, \\ \tilde{\Delta}^V_{i,j} &= \left| Z^V_{i-1,j} - Z^V_{i+1,j} \right|, \end{aligned} \tag{2}$$

where suffixes I and j represent the pixel coordination, Δ^H and Δ^V denote the vertical and horizontal gradients obtained from the original Bayer plane, and $\tilde{\Delta}^H$ and $\tilde{\Delta}^V$ denote the vertical and horizontal gradients obtained from the reconstructed Bayer plane of each direction. From (2), we can see that the gradients are estimated using the difference of same color channel, and sum of both gradients are exploited to make the directional weight. In the proposed algorithm, four directions, up, down, left and right (U, D, L, and R), are exploited for the three channel interpolations. The weights are calculated as follows:

$$\begin{aligned} w^U_{i,j} &= 1 / \left(\left\{ \sum_{a=-2}^{0} \sum_{b=-1}^{1} (\Delta^V_{i+a,j+b} + \tilde{\Delta}^V_{i+a,j+b}) \right\}^2 + \varepsilon \right), \\ w^D_{i,j} &= 1 / \left(\left\{ \sum_{a=0}^{2} \sum_{b=-1}^{1} (\Delta^V_{i+a,j+b} + \tilde{\Delta}^V_{i+a,j+b}) \right\}^2 + \varepsilon \right), \\ w^L_{i,j} &= 1 / \left(\left\{ \sum_{a=-1}^{1} \sum_{b=-2}^{0} (\Delta^H_{i+a,j+b} + \tilde{\Delta}^H_{i+a,j+b}) \right\}^2 + \varepsilon \right), \\ w^R_{i,j} &= 1 / \left(\left\{ \sum_{a=-1}^{1} \sum_{b=0}^{2} (\Delta^H_{i+a,j+b} + \tilde{\Delta}^H_{i+a,j+b}) \right\}^2 + \varepsilon \right), \end{aligned} \tag{3}$$

where w^U, w^D, w^L, and w^R denote weights for the up, down, left, and right directions, and small number ε is added to avoid division by zero. We try to reduce the weight calculation process while preserving the accuracy of the estimation performance, because conventional demosaicking methods exploit multiple complex weight sets and cause a heavy complexity burden. By using only one set of weights for the whole interpolation process, we can reduce the complexity of the weight calculation.

A. Green channel interpolation

The proposed G channel interpolation exploits the color difference. To calculate the color difference, we used 3 and 5-tap interpolation filters. To determine the length of the

ISBN: 978-1-61804-321-4

interpolation, we simply calculated the G correlation of the four directions at the R location, as shown in Fig. 3; the G correlation at the B position is the same. The G correlation of the four directions (D^U, D^D, D^L, D^R) is calculated as follows:

$$
\begin{aligned}
D_{i,j}^{U} &= \left|Z_{i-1,j} - Z_{i-3,j}\right|, \ D_{i,j}^{D} = \left|Z_{i+1,j} - Z_{i+3,j}\right|, \\
D_{i,j}^{L} &= \left|Z_{i,j-1} - Z_{i,j-3}\right|, \ D_{i,j}^{R} = \left|Z_{i,j+1} - Z_{i,j+3}\right|.
\end{aligned} \tag{4}
$$

If the G correlation is larger than threshold T, the 3-tap directional interpolation filters are exploited, if not, the 5-tap directional interpolation filters are used. The estimation of the G pixel is the combination of the directional color difference which is calculated using a filter. The four directional 3 and 5-tap filters are given as follows:

$$
\begin{aligned}
& f_3^L = [1,-1,0], \quad f_3^R = [0,-1,1], \\
& f_3^U = (f_2^L)', \quad f_3^D = (f_2^R)', \\
& f_5^L = [-\tfrac{1}{2},1,-\tfrac{1}{2},0,0], \ f_3^R = [0,0,-\tfrac{1}{2},1,-\tfrac{1}{2}], \\
& f_5^U = (f_5^L)', \quad f_5^D = (f_5^R)'.
\end{aligned} \tag{5}
$$

The length of the filter for the four directions is then determined as follows:

$$
f^X = \begin{cases} f_3^X & if\ D^X < T \\ f_5^X & otherwise \end{cases}, \ where\ X \in \{U, D, L, R\}, \tag{6}
$$

where f^X denotes the directional interpolation filters that are finally determined. Our assumption is that less correlated pixels cause degradation of the interpolation performance. Therefore, using the G channel correlation we control the length of the interpolation filter. The missing G pixel is calculated as follows:

$$
\tilde{G} = \left\{ Z_{i,j} + \frac{\sum_{X \in \{U,D,L,R\}} w^X \times (Z_{i,j} * f^X)}{w^T} \right\} \alpha + \hat{G}(1-\alpha), \tag{7}
$$

where $\hat{G}$ denotes the calibration term for the G channel interpolation defined as:

$$
\hat{G} = \frac{w^U \times Z_{i-1,j} + w^D \times Z_{i+1,j} + w^L \times Z_{i,j-1} + w^R \times Z_{i,j+1}}{w^T}. \tag{8}
$$

We use α as the control factor of the calibration term, and it is empirically set to 0.7. The proposed weights exploit the color difference of not only G gradient but also R and B gradient therefore, these weights sometimes misleads the pixel value when the G channel has less correlation to the R/B channels; in this case, the G pixel value lies far from the neighboring G pixels value. Thus, we adopt the calibration term, which is calculated using only the original neighboring G pixels and

Fig. 4. IMAX test images (500 × 500)

which compensates for the wrongly estimated $\tilde{G}$ which can be changed to a more natural value compared to the neighboring pixels.

B. R/B channel interpolation

After the G pixels are fully reconstructed, the missing R/B pixels are interpolated. The R/B pixels can be divided into two cases: R/B pixels at the B/R pixel location and R/B pixels at the G pixel location. These two cases have different available reference pixels. Therefore, we should use different approaches for each case. Firstly, the R/B pixels at the B/R pixel location are interpolated. In this step, we don't have many choices, because only the diagonal pixels are available. Thus, 7 ×7 filter f_{RB} is exploited without any weights:

$$
f_{RB} = \frac{1}{32} \times \begin{bmatrix}
0 & 0 & -1 & 0 & -1 & 0 & 0 \\
0 & 0 & 0 & 0 & 0 & 0 & 0 \\
-1 & 0 & 10 & 0 & 10 & 0 & -1 \\
0 & 0 & 0 & 0 & 0 & 0 & 0 \\
-1 & 0 & 10 & 0 & 10 & 0 & -1 \\
0 & 0 & 0 & 0 & 0 & 0 & 0 \\
0 & 0 & -1 & 0 & -1 & 0 & 0
\end{bmatrix}. \tag{9}
$$

The R/B pixel at the B/R pixel location is calculated as follows:

$$
\begin{aligned}
\tilde{R}_{i,j} &= \tilde{G}_{i,j} + D_{i,j}^{GB} * f_{RB}, \\
\tilde{B}_{i,j} &= \tilde{G}_{i,j} + D_{i,j}^{GR} * f_{RB},
\end{aligned} \tag{10}
$$

where $D^{GB} = \tilde{G} - B$ and $D^{GR} = \tilde{G} - R$.

The R/B interpolation at the G pixel location can use four vertical and horizontal neighboring pixels. Thus, we reuse the four directional weights calculated using (3). The R/B channel interpolation is calculated as follows:

$$
\begin{aligned}
\tilde{R} &= \tilde{G} - \frac{w^U \times D_{i-1,j}^{GR} + w^D \times D_{i+1,j}^{GR} + w^L \times D_{i,j-1}^{GR} + w^R \times D_{i,j+1}^{GR}}{w^T}, \\
\tilde{B} &= \tilde{G} - \frac{w^U \times D_{i-1,j}^{GB} + w^D \times D_{i+1,j}^{GB} + w^L \times D_{i,j-1}^{GB} + w^R \times D_{i,j+1}^{GB}}{w^T}.
\end{aligned} \tag{11}
$$

ISBN: 978-1-61804-321-4

TABLE I
COMPARISON OF CPSNR (dB) MEASURE FOR DIFFERENT DEMOSAICKING METHODS

No.	ESF	DDFW	MSG	LPA	EDAEP	VDI	MLDIF
1	26.38	27.14	27.05	26.82	27.60	28.01	28.65
2	33.48	33.54	33.67	33.84	33.99	34.18	34.51
3	32.56	32.63	32.93	32.47	32.07	32.64	32.41
4	34.97	34.72	35.49	34.94	34.36	36.00	36.35
5	30.64	31.11	31.12	31.39	32.10	32.63	33.58
6	32.57	33.75	33.56	34.37	35.03	35.63	37.24
7	39.10	38.98	39.17	39.20	36.22	36.03	34.78
8	37.85	37.33	37.61	37.88	37.12	37.41	37.29
9	34.39	34.78	34.69	35.07	35.23	35.95	37.14
10	35.78	36.93	36.47	37.02	37.01	37.28	38.03
11	36.61	37.50	37.28	37.72	37.83	37.98	38.46
12	36.16	36.83	36.80	36.97	37.16	37.09	37.56
13	38.67	38.64	38.83	39.29	39.34	39.40	40.38
14	37.21	37.14	37.13	37.54	37.65	37.32	38.38
15	37.01	37.32	37.19	37.66	37.76	37.86	38.73
16	29.24	30.05	30.18	29.48	31.39	31.40	32.42
17	28.57	29.79	29.30	29.27	30.59	31.15	32.73
18	33.69	33.81	34.10	33.96	34.05	34.23	34.40
Avg	34.16	34.55	34.59	34.72	34.81	35.12	35.73

TABLE II
COMPARISON OF S-CIELAB ΔE^* MEASURE FOR DIFFERENT DEMOSAICKING METHODS

No.	ESF	DDFW	MSG	LPA	EDAEP	VDI	MLDIF
1	3.784	3.190	3.170	3.414	2.903	2.620	2.459
2	1.453	1.296	1.252	1.267	1.246	1.144	1.083
3	2.076	2.083	1.825	2.103	2.290	1.893	1.691
4	1.461	1.253	1.086	1.169	1.484	1.113	0.917
5	1.771	1.551	1.551	1.518	1.526	1.374	1.223
6	1.857	1.464	1.502	1.410	1.278	1.127	0.894
7	0.944	0.932	0.897	0.877	1.228	1.199	1.339
8	0.659	0.632	0.589	0.584	0.723	0.613	0.638
9	1.396	1.217	1.203	1.199	1.305	1.058	0.877
10	1.192	0.976	1.025	0.968	0.999	0.932	0.831
11	0.907	0.765	0.783	0.745	0.725	0.675	0.640
12	1.257	1.067	1.081	1.057	0.940	0.956	1.039
13	0.739	0.707	0.692	0.667	0.683	0.650	0.609
14	0.860	0.796	0.784	0.758	0.789	0.742	0.712
15	0.913	0.822	0.836	0.807	0.819	0.773	0.715
16	2.839	2.295	2.317	2.594	1.673	1.499	1.672
17	3.090	2.352	2.577	2.757	2.290	1.960	1.504
18	1.601	1.522	1.460	1.506	1.451	1.287	1.396
Avg	1.600	1.384	1.368	1.411	1.353	1.201	1.124

By the end of this process, every missing pixel is fully reconstructed.

III. EXPERIMENTAL RESULTS

To evaluate the performance of the proposed multi-length directional interpolation filter (MLDIF), the MLDIF is compared conventional algorithms such as LPA [9], ESF [10], DDFW [7], EDAEP [14], MSG [11], and VDI [8]. The experiments are performed using MALTAB with an Intel® Core(TM) i7 CPU K4770 at 3.5 GHz and with 4 GB of RAM. We use an IMAX dataset consisting of 18 images with a size of 500 × 500 pixels (shown in Fig. 4).These images have low spectral correlation and highly saturated color which has similar characteristics to images captured by digital cameras of today [20].

TABLE III
COMPARISON OF FSIMC MEASURE FOR DIFFERENT DEMOSAICKING METHODS

No.	ESF	DDFW	MSG	LPA	EDAEP	VDI	MLDIF
1	0.9906	0.9936	0.9924	0.9918	0.9927	0.9935	0.9955
2	0.9959	0.9969	0.9964	0.9966	0.9966	0.9968	0.9976
3	0.9973	0.9986	0.9978	0.9975	0.9970	0.9975	0.9985
4	0.9985	0.9993	0.9988	0.9986	0.9982	0.9987	0.9994
5	0.9960	0.9972	0.9967	0.9969	0.9971	0.9974	0.9985
6	0.9971	0.9984	0.9980	0.9983	0.9984	0.9985	0.9992
7	0.9987	0.9992	0.9989	0.9988	0.9978	0.9978	0.9979
8	0.9978	0.9981	0.9979	0.9981	0.9979	0.9981	0.9986
9	0.9968	0.9980	0.9973	0.9976	0.9976	0.9978	0.9988
10	0.9981	0.9988	0.9985	0.9986	0.9984	0.9985	0.9990
11	0.9980	0.9986	0.9984	0.9985	0.9984	0.9984	0.9990
12	0.9981	0.9986	0.9984	0.9985	0.9984	0.9983	0.9990
13	0.9977	0.9980	0.9979	0.9982	0.9983	0.9983	0.9990
14	0.9977	0.9981	0.9980	0.9982	0.9983	0.9985	0.9989
15	0.9977	0.9982	0.9980	0.9981	0.9980	0.9981	0.9986
16	0.9955	0.9972	0.9969	0.9961	0.9977	0.9977	0.9986
17	0.9937	0.9966	0.9952	0.9949	0.9958	0.9958	0.9982
18	0.9976	0.9984	0.9979	0.9978	0.9977	0.9980	0.9985
Avg	0.9968	0.9979	0.9974	0.9974	0.9975	0.9977	0.9985

Three metrics, Color Peak Signal-to-Noise Ratio (CPSNR), S-CIELAB ΔE^*[21], and feature-based image quality assessment algorithm Feature Similarity Index for Image Quality Assessment (FSIMc) [22], were exploited as the objective measures for comparing the demosaicking performance. The CPSNR is a metric widely used as a performance evaluation method; to analyze the performance from different views, we use an additional two metrics which consider the human visual system. Ten pixels from the boundary are excluded for the objective performance evaluation, and threshold T of the G correlation is set to 15.

The CPSNR results of the 18 images are presented in Table I and ordered in ascending order of the average CPSNR values. It is clearly seen that the proposed MLDIF achieves an approximately 0.6 dB higher average CSPNR than VDI, which gives the best performance among the reference algorithms, and an about 0.9dB higher average CSPNR than EDAEP. In terms of individual images, the proposed algorithm outperforms 15 of the 18 images. The S-CIELAB ΔE^* are summarized in Table II. If the S-CIELAB ΔE^* values are close to zero, the performance is better. From the results, the proposed algorithm produces the best performance of the average S-CIELAB ΔE^* with 0.077 higher than VDI and 0.129 higher than EDAEP.

The FSIMc method is a recently proposed performance evaluation metric that can measure the feature similarity. By using this metric, we can see the different aspects of the demosaicking algorithms which the CPSNR cannot distinguish. It can be seen in Table III that the proposed MLDIF also outperforms the other demosaicking algorithms. The ESF exhibits the worst results, and MSG and LPA produce the same results even though they have different CPSNR and S-CIELAB ΔE^* results. It is remarkable that DDFW produces the second best results, nevertheless it produces the second worst CPSNR results. Both DDFW and VDI have the hard decision for direction, and the direction decision techniques have the

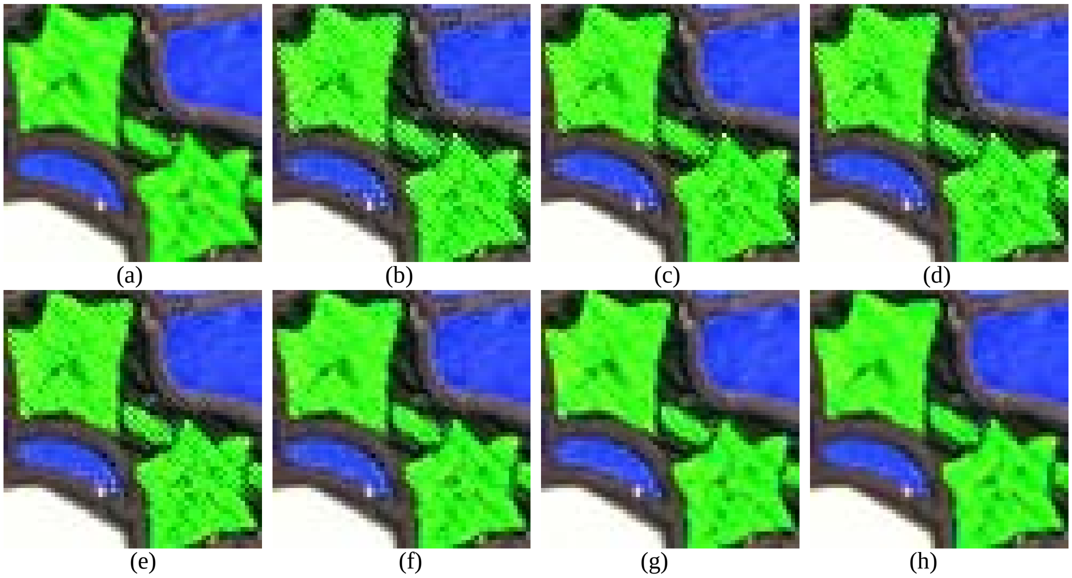

Fig. 5. (a) Cropped region of original image #1 and the demosaicking results. (b) ESF. (c) DDFW. (d) MSG. (e) LPA. (f) EDAEP. (g) VDI. (h) MLDIF.

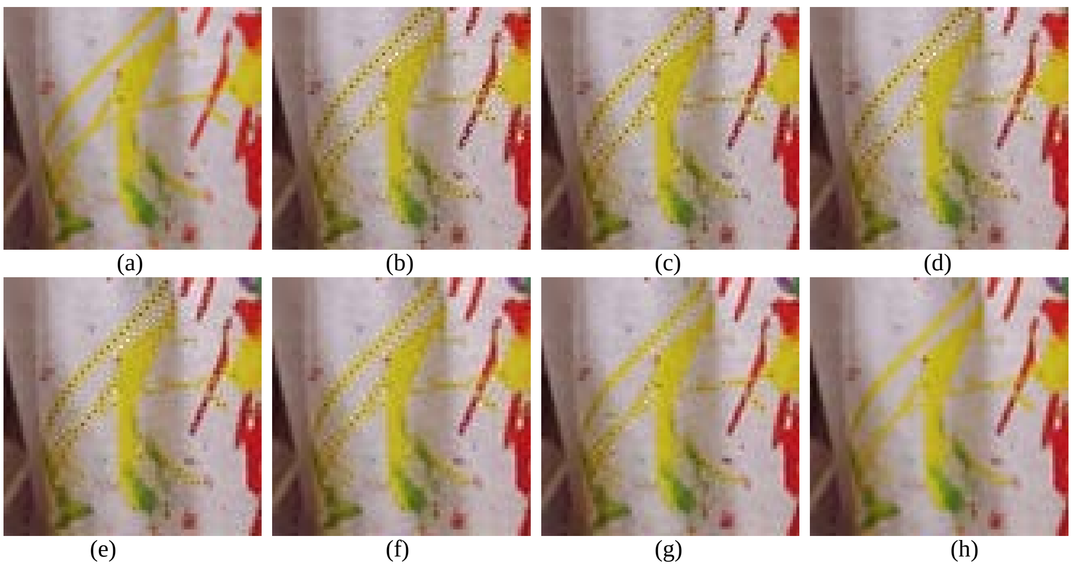

Fig. 6. (a) Cropped region of original image #5 and the demosaicking results. (b) ESF. (c) DDFW. (d) MSG. (e) LPA. (f) EDAEP. (g) VDI. (h) MLDIF.

advantage of improving the FSIMc performance.

For the subjective performance comparison, images #1 and #5 are selected from the IMAX dataset for the visual comparison. Figure 5 shows a partially zoomed area of image 1; it can be seen that the proposed algorithm provides the best image quality. Except for the proposed MLDIF, the other demosaicking algorithms produce demosaicking artifacts which make the images appear to have noise in the G star region. The proposed algorithm does not produce any demosaicking artifacts and appears to be closest to the original image. Figure 6 shows a cropped region of image 5. It is obvious that the proposed algorithm also outperforms the others. We find that the proposed multi-length filter technique significantly improves the image quality. The MLDIF reconstructs an image while preserving the original color without any interference. VDI provides a relatively better image quality than EDAEP and LPA, however the false coloring effect still exists. A more complex region is shown in

From Figures 5-6, it is concluded that the proposed algorithm greatly improves the visual quality, and solves the most demosaicking problems by exploiting the MLDIF. The proposed scheme preserves any edge direction well and produces the closest images with fewer demosaicking artifacts compared to the state-of-art algorithms. The proposed algorithm also has an advantage in terms of complexity. The MLDIF consumes approximately 0.2 seconds per image, but VDI, EDAEP, LPA, and MSG take 4.3, 0.5, 0.7, and 8.3 seconds, respectively. The proposed directional weight strategy and non-iteration interpolation process make our demosaicking algorithm have lower complexity than the others. From the objective and subjective comparison results, the proposed DLMIF outperforms the state-of-the-art demosaicking algorithms.

IV. Conclusion

In this paper, we have proposed an MLDIF for color image demosaicking. The proposed MLDIF exploits the two lengths of the directional filter, where the length is determined based on the G correlation between the center and outside region. The experimental results indicate that the proposed method achieves an outstanding objective performance, and also provides the greatest improvement in visual quality without demosaicking artifacts. Furthermore, we achieve low complexity by exploiting only one set of weights for the whole interpolation process and by simplifying the interpolation process.

References

[1] B. E. Bayer, "Color imaging array," U.S. Patent *3 971 065*, Jul. 1976.

[2] B. K. Gunturk, J. Glotzbach, Y. Altunbasak, R. W. Schafer, and R.M. Mersereau, "Demosaicking: Color filter array interpolation," *IEEE Signal Process. Mag.*, vol. 22, no. 1, pp. 44–54, Jan. 2005.

[3] B. K. Gunturk, Y. Altunbasak, and R. M. Mersereau, "Color plane interpolation using alternating projections," *IEEE Trans. Image Process.*, vol. 11, no. 9, pp. 997–1013, Sep. 2002.

[4] Y.M. Lu, M. Karzand, M. Vetterli, 'Demosaicking by alternating projections: theory and fast one-step implementation', IEEE Trans. Image Process., vol. 19, no. 8, pp. 2085–2098, Aug. 2010.

[5] D. Menon, S. Andriani, and G. Calvagno, "Demosaicing with directional filtering and a posteriori decision," *IEEE Trans. Image Process.*, vol. 16,no. 1, pp. 132–141, Jan. 2007.

[6] K. H. Chung and Y. H. Chan, "Color demosaicing using variance of color differences," IEEE Trans. Image Process., vol. 15, no. 10, pp. 2944–2955, Oct. 2006.

[7] Z. Dengwen, S. Xiaoliu and D. Weiming, "Colour demosaicking with directional filtering and weighting," *IET Image Process.*, Vol. 6, no. 8, pp. 1084–1092, Nov. 2012.

[8] X. Chen, G. Jeon, and J. Jeong, "Voting-based directional interpolation method and its application to still color image demosaicking," *IEEE Trans. Circuits Syst. Video Technol.*, vol. 24, no.2, pp. 255-262, Feb. 2014.

[9] D. Paliy, V. Katkovnik, R. Bilcu, S. Alenius, and K. Egiazarian, "Spatially adaptive color filter array interpolation for noiseless and noisy data," *Int. J. Imaging Syst. Technol.*, vol. 17, no. 3, pp. 105–122, Oct. 2007.

[10] I. Pekkucuksen and Y. Altunbasak. "Edge strength filter based color filter array interpolation," *IEEE Trans. Image Process.*, vol. 21, no. 1 pp. 393–397, Jan. 2012.

[11] I. Pekkucuksen and Y. Altunbasak, "Multiscale Gradients-Based Color Filter Array Interpolation," *IEEE Trans. Image Process.*, vol. 22, no. 1, pp. 157–165, Jan. 2013.

[12] J. Hamilton and J. Adams, "Adaptive color plan interpolation in single sensor color electronic camera," U.S. Patent *5 629 734*, May. 1997

[13] D. Menon, S. Andriani, and G. Calvagno, "Demosaicing with directional filtering and a posteriori decision," *IEEE Trans. Image Process.*, vol. 16, no. 1, pp. 132–141, Jan. 2007.

[14] W. Chen, P. Chang, "Effective demosaicking algorithm based on edge property for color filter arrays," *Digit. Signal Process.*, vol. 22, no. 1, pp. 163–169, Jan. 2012.

[15] D. Menon and G. Calvagno, "Regularization approaches to demosaicking," *IEEE Trans. Image Process*., vol. 18, no. 10, pp. 2209–2220, Oct. 2009.

[16] Y. Kim and J. Jeong, "Subdivided Weight Interpolation based on Multiscale Gradients for Color Filter Array," *in Proc. Int. Conf. on Communications, Signal Processing*, 2014, pp 32-35

[17] N. X. Lian, L. Chang, Y. -P. Tan, and V. Zagorodnov, "Adaptive filtering for color filter array demosaicking," *IEEE Trans. Image Processing*, vol.16, no. 10, pp. 2515?2525, Oct. 2007.

[18] B. Leung, G. Jeon and E. Dubois, "Least-squares luma-chroma demultiplexing algorithm for Bayer demosaicking," *IEEE Trans. Image Process*., vol. 20, no. 7, pp. 1885–1894, Jul. 2011.

[19] Y. Kim, G. Jeon and J. Jeong, "Colour interpolation using adaptive window for Bayer colour filter array," *IET Electronics Letters.*, vol 50, no. 23, pp. 1689-1691.

[20] X. Li, B. Gunturk, and L. Zhang, "Image demosaicing: a systematic survey," *in Proc. of SPIE*, vol. 6822, pp. 68221J, 2008.

[21] X. Zhang and B. A. Wandell. "A spatial extension of cielab for digital color image reproduction," *Journal of Society for Information Display*, vol. 5, no. 1, pp. 61–63, March 1997.

[22] L. Zhang, L, Zhang, X. Mou, and D. Zhang, "FSIM: a feature similarity index for image quality assessment," *IEEE Trans. Image Process.*, vol. 20, no. 8 pp. 2378–2386, Aug. 2011.

ISBN: 978-1-61804-321-4

Implementation of filter with membership function into control system of biomass combustion process

Ján Piteľ and Jana Mižáková

***Abstract*—**The control system of biomass combustion process was designed and installed for control of the medium-scale biomass-fired boilers. The problem with strong interferences of some measured process variables occurred. It was solved using special filter with membership function. In the paper there are described some properties of such filter and some results of its implementation into control system.

***Keywords*—**biomass combustion, process control, filtering, membership function

I. Introduction

ACCEPTABLE operation, economic and ecological conditions (combustion efficiency, pollutants production under emission limit) have to be considered in biomass combustion, because biomass and especially woodchips is fuel with very unstable composition in comparison with fossil fuels. Uncontrolled or badly controlled biomass combustion can have similar impact on the environment as coal or oil combustion [1]. It was presented in [2], [3], that considering inconstant characteristics of the fuel it is necessary to control the amount of combustion air during woodchips supply into furnace and during the combustion too. If the amount of air is less than optimum one, incomplete combustion occurs and flue gas contains a part of combustible components. There is necessity to divide the supplied air into primary and secondary air too. Next it is necessary to provide high enough temperature and time to complete biomass combustion occurs [4]. So there is need to achieve simultaneously controlled values of the required heat output and optimal conditions for the combustion process from both the emissions and efficiency point of view [5], [6]. That is why operation of such devices has to be properly controlled using classical cascade [7] and also advanced control techniques [8] with possibility of on-line monitoring [9].

This work was supported by the Project of the Structural Funds of the EU, Operational Programme Research and Development, Measure 2.2 Transfer of knowledge and technology from research and development into practice and it is supported by grant of Scientific Grant Agency of the Ministry of Education, Science, Research and Sport of the Slovak Republic and the Slovak Academy of Sciences.

J. Piteľ is with Department of Mathematics, Informatics and Cybernetics, Faculty of Manufacturing Technologies, Technical University of Košice, Bayerova 1, 080 01 Prešov, Slovakia (corresponding author to provide phone: +421 905 524605; fax: +421 421 51 7733453; e-mail: jan.pitel@tuke.sk).

J. Mižáková is with Department of Mathematics, Informatics and Cybernetics, Faculty of Manufacturing Technologies, Technical University of Košice, Bayerova 1, 080 01 Prešov, Slovakia (e-mail: jana.mizakova@tuke.sk).

II. Control System of Biomass Combustion Process

As result of solution of the project „Research and development of intelligent control systems for biomass based heat production and supply" the control and monitoring system of biomass combustion process was designed (Fig. 1) with these basic requirements [10]:

1) Industrial control system for application also in real technical practice.

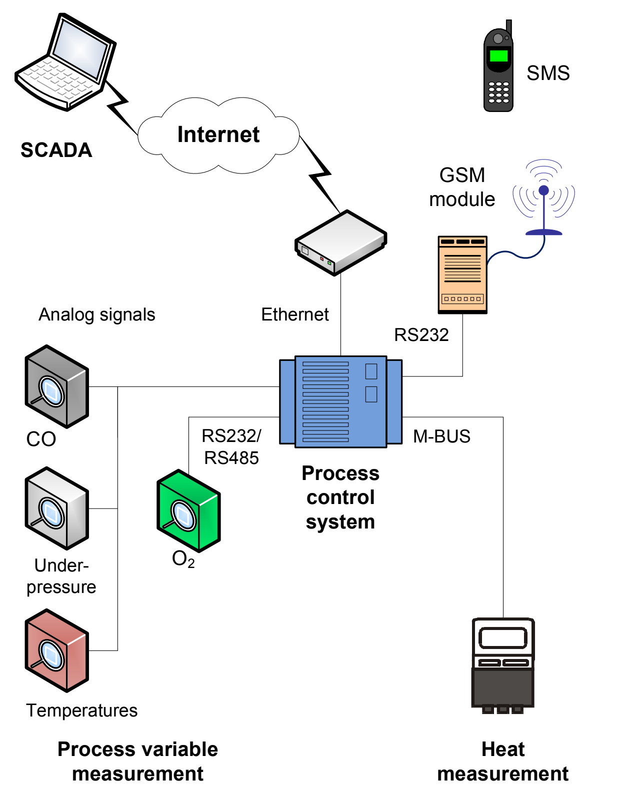

Fig. 1 Structure of control and monitoring system of biomass combustion process [10]

ISBN: 978-1-61804-321-4

2) Free programmable system for possibility of testing and implementation of new control algorithms.
3) Cost effective sensors for possibility of using in control of small-scale biomass-fired boilers too.
4) On-line monitoring of biomass process control system with a possibility to visualize technological process (graphical schemes, diagrams, trends and reports), evaluate quality of combustion process and change control parameters with access via internet.

The basis of the realized control and monitoring system is free programmable industrial modular process control system ADiS which is monitored by SCADA system Promotic also with the possibility of free programming. The process control system communicates with heat meter via M-BUS for measurement of power of boiler and produced heat. The important parts of system with high influence on combustion quality are oxygen (O_2) and carbon monoxide (CO) sensors and sensor for furnace temperature measurement [11]. The main their selection criterion was an achievement of required technical parameters under minimal costs for possibility of using also in control systems of the small-scale biomass-fired boilers [12].

The wide band Lambda probe LSU 4.2 with converter LC-1 was used for O_2 concentration measurement in flue gas and it communicates with process control system via RS232/485 interface by Innovate Serial Protocol 2 (ISP2). For CO concentration measurement in flue gas there was used low cost gas sensor TG816 which conductivity increases depending on the gas concentration [13]. This gas sensor was connected to the analog input of process control system via simple electrical circuit converting the change in sensor conductivity to an analog output signal which corresponds to the gas concentration. The thermocouple of type K was used for furnace temperature measurement and it was also connected to the analog input of process control system with 10 bits A/D converter.

The designed control and monitoring system was installed for control of the medium-scale biomass-fired boilers of different types and different manufactures. The new control algorithms based on the information not only about oxygen concentration in flue gas but also about trend of carbon monoxide emissions were implemented into control systems with aim to reach the complete combustion with minimum excess of combustion air. It was proved that low cost wide band Lambda probe and simple CO sensor can be used for biomass combustion control in medium-scale and after some simplification also in small-scale biomass-fired boilers. But due to the problem with strong interferences in one type of boiler the task how to define a trend function of measured variables (especially O_2 concentration and CO emissions in flue gas) and correctly use the measured data for biomass combustion process control has occurred. The measured values were influenced by various disturbances, transfer errors and external interferences, for that reason measured data have to be appropriately smoothed and filtered.

III. Filtering Based on the Membership Function

A lot of digital filters are used for signal filtering [14]. Some of them are not convenient because stochastic elements have influence on the output of filter. The others are useful only with mathematical model of system (e.g. Kalman filter) [15]. There are also known filters based on the moving average or moving average with exponential forgetting, but they are not useful for combustion process control due to algorithm of weight counting.

The basic demand on filtering of combustion process variables is that random changes have lowest weight and not have influence on filter output. Long-lasted changes out of supposed interval must have influence on filter output and must be signified on trend of measured variable. To satisfy these demands the specific method for weights calculation based on the membership function can be used, as for example with normal distribution function in the form:

$$f(x) = \frac{1}{\sigma\sqrt{2\pi}} e^{-\frac{(x-\mu)^2}{2\sigma^2}} . \tag{1}$$

Then after some simplifications this can be derived for weight calculation:

$$w(x) = e^{-\frac{(x-\mu)^2}{s}} , \tag{2}$$

where s is defined as sensitivity and μ is last weighted average.

Sample of non-filtered signal $u(t_i)$ includes deterministic $u_d(t_i)$ and stochastic $u_s(t_i)$ elements:

$$u(t_i) = u_d(t_i) + u_s(t_i) , \tag{3}$$

Stochastic signal element can be suppressed by substitution for counted moving weight average from last k samples of non-filtered signal:

$$\bar{u}(t_i) = \frac{\sum_{j=1}^{k} u(t_j) \cdot w_j}{\sum_{j=1}^{k} w_j} \tag{4}$$

where $j = 1,\ldots,k$ and k is chosen number of samples, $u(t_j)$ is last k signal samples which have deterministic and stochastic element, w_j are counted weights from $(0, 1\rangle$ for k last obtained signal samples. For membership function based on normal distribution function the weights are counted using (2).

Filter with membership function (Fig. 2) consists of blocks 1 for sampling of non-filtered signal, block 2 for sampling of filtered signal, blocks 3 for weight assignment of non-filtered samples according to membership function (2) and blocks 4 (multiplication), 5 (summation) and 6 (division) for calculation of filter output according to (4).

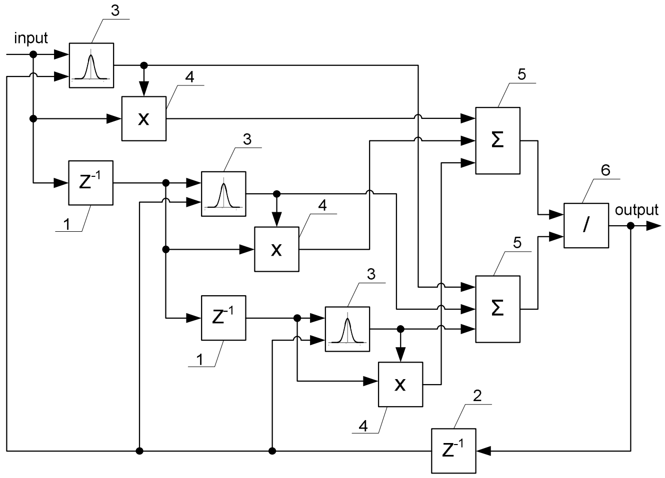

Fig. 2 Basic principle of filter operation for last three samples of non-filtered signal

Testing result of using a filter based on the membership function for filtering of continuous variable with external interference is in Fig. 3. As we can see the interference was successfully suppressed without substantial effect on the course of the measured signal.

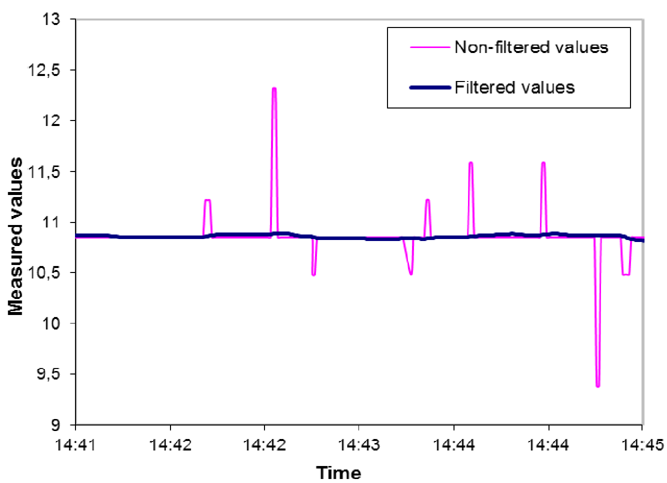

Fig. 3 Testing result of filtering based on the membership function

IV. Implementation of Filter into Process Control System

The designed filter with membership function was simulated in MATLAB Simulink environment and next it was created in C programming language (weights are counted on the base of normal distribution function) and implemented into process control system of biomass combustion which was on-line monitored by SCADA system Promotic. The graphical scheme of monitored technological process is shown in Fig. 4. In the Fig. 5 we can see an example of process variables remote monitoring. As it can be seen some of them are strongly interfered. Especially quality of O_2 concentration sensing (yellow course in Fig. 5) was unable to use for effective control of combustion process. The correct values of O_2 concentration in flue gas are very important for combustion

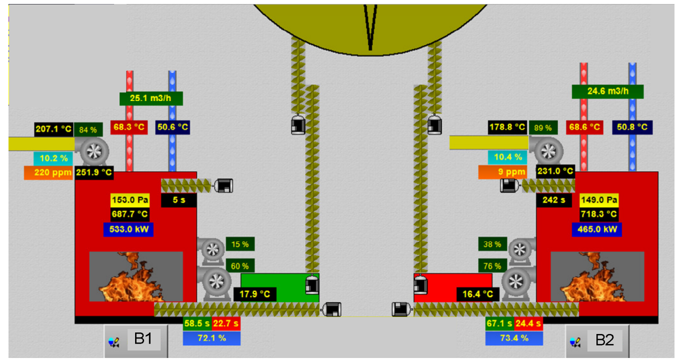

Fig. 4 Monitored technological process of biomass combustion by SCADA system

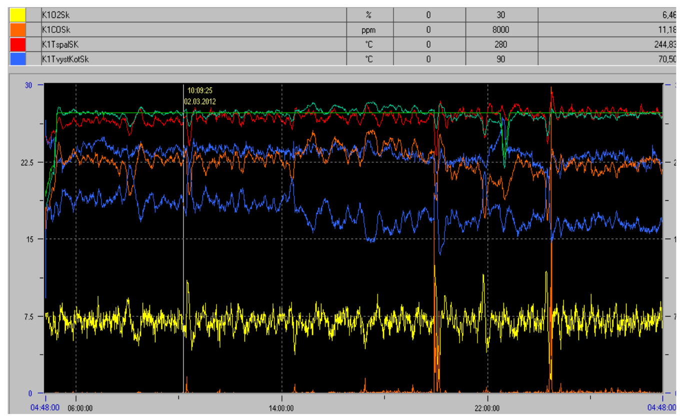

Fig. 5 Remote monitoring of biomass combustion process variables by SCADA system

process control because efficiency of the biomass combustion depends on the excess air ratio λ, which can be obtained from the measured O_2 concentration as follows [10]:

$$\lambda = \frac{21}{21 - O_{2\,\%}}. \tag{5}$$

That is why firstly the new filter with membership function was applied for filtering of O_2 concentration measured data and result of filtration is shown in Fig. 6.

The optimal range of excess air ratio λ for biomass combustion is usually in interval <1,4; 2> and its optimal value depends on the type of wood, the moisture content in wood, combustion chamber construction and so on. However the most optimal biomass combustion operating conditions are when the compromise between maximal combustion efficiency and minimal CO emissions is achieved [16], [17]. One of the control algorithms tasks is to find such value of excess air ratio λ so that CO emissions would be minimal although the fuel parameters have been changed. To fulfill this task it is necessary to continuously monitor a trend between CO emission and excess air ratio and consequently to change the set point of O_2 concentration in flue gas. That is why this filter was also applied for filtering of CO emissions measured data and result of filtration is shown in Fig. 7.

ISBN: 978-1-61804-321-4

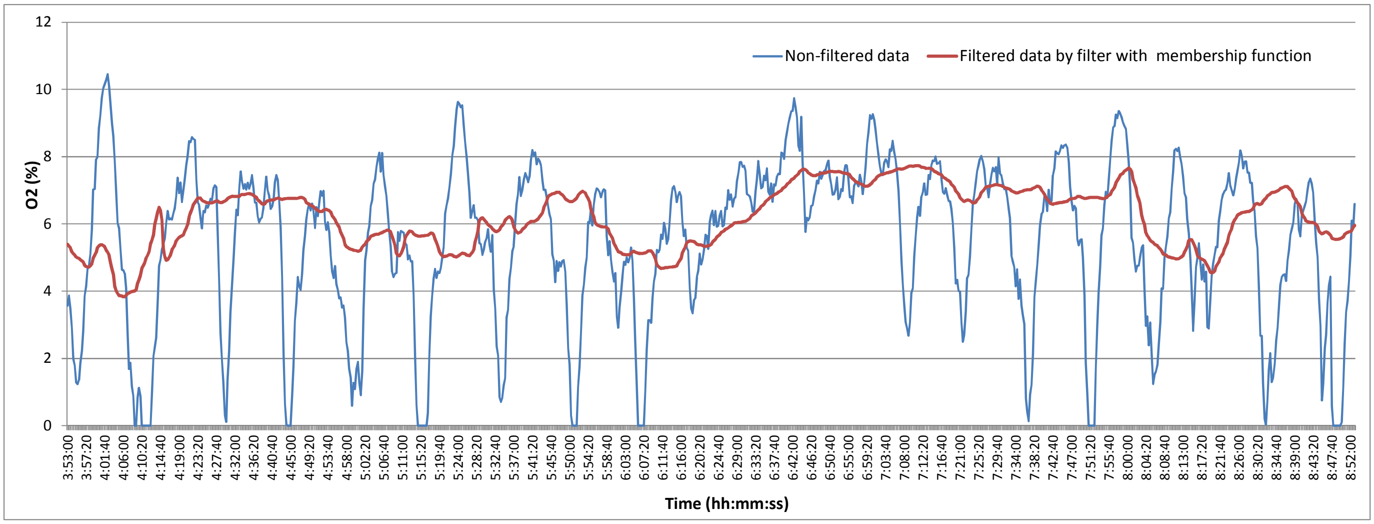

Fig. 6 O_2 concentration filtering of using filter with membership function

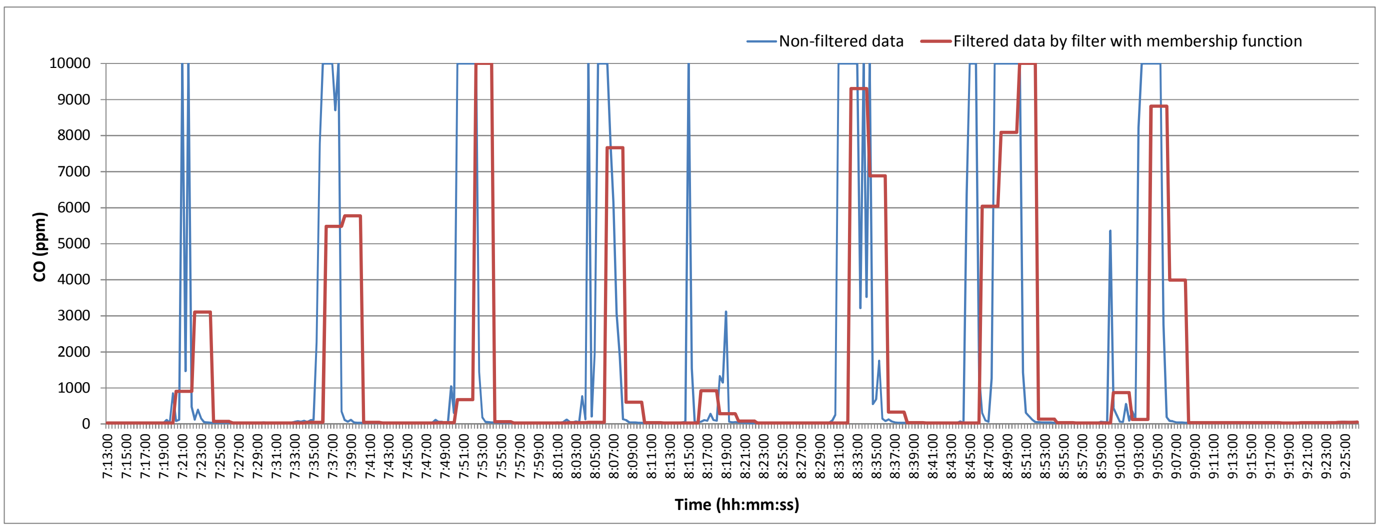

Fig. 7 CO emissions filtering of using filter with membership function

V. Conclusion

It was proved by implementation of the designed special filter based on the membership function into control system of biomass combustion process that it can be useful for signal filtering of O_2 concentration and CO emissions process variables and it can very good reduce signal interferences arising in biomass combustion. Further research will be focused on testing of various membership functions with different sensitivity of filter.

VI. Acknowledgment

The research work was supported by project "Research and development of intelligent control systems for biomass based heat production and supply", ITMS code: 26220220030 and also it is supported by grant VEGA 1/0881/13 „Research of Algorithms and Methods for Predictive Control of Biomass Combustion Processes".

References

[1] J. Hrdlička, B. Šulc, S. Vrána, and V. Plaček, "Ecological aspects of small-scale biomass combustion control", *in Develepment, Energy, Environment, Economics*, Puerto De La Cruz, Tenerife, 2010, pp. 388-393.

[2] J. Piteľ, J. Boržíková, and J. Mižák, "Biomass combustion process control using artificial intelligence techniques", *in Proceedings of XXXV. Seminar ASR'2010 Instruments and Control,* Ostrava, 2010, pp. 317-321.

[3] P. Skok, M. Rimár, and J. Mižák, "Woodchip combustion process quality and the amount of combustion air", *Applied Mechanics and Materials*, vol. 308, pp. 115-119, 2013.

[4] Z. Pastorek, J. Kára, and P. Jevič, *Biomasa – obnovitelný zdroj energie*. Praha: FCC PUBLIC, 2004.

[5] A. Hošovský, "Genetic optimization of neural networks structure for modeling of biomass-fired boiler emissions", *Journal of Applied Science in Thermodynamics and Fluid Mechanics*, vol. 9, no. 2, pp. 1-6, 2011.

[6] J. Hrdlička, B. Šulc, V. Plaček and S. Vrána, "Impact of control solutions on ecology and economy of small-scale biomass boilers", *International Journal of Circuits, Systems and Signal Processing*, vol. 5, no. 3, pp. 247-254, 2011.

[7] M. Tóthová, M. Balara, and J. Dubják, “Simulation model of cascade control of the heating system (Accepted for publication)”, *Key Engineering Materials*, to be published.

[8] A. Hošovský, “Biomass-fired boiler control using simulated annealing optimized improved Varela immune controller”, *Acta Polytechnica Hungarica*, vol. 12, no. 1, pp. 23-39, 2015.

[9] J. Boržíková, J. Piteľ, and J. Mižák, “Monitoring of operational states of biomass combustion process”, *Applied Mechanics and Materials*, vol. 308, pp. 153-158, 2013.

[10] J. Piteľ and J. Mižák, “Cost effective biomass combustion process control”, *in Proceedings of the 8th PP&PSC (Power Plant and Power System Control) IFAC Symposium*, Toulouse, 2012. pp. 616-620.

[11] R. Drga, D. Janáčová, and H. Charvátová, “Infrared radiation, sensor, source and infrared camera measurement”, *International Journal of Circuits, Systems and Signal Processing,* vol. 5, issue 6, pp. 581-588, 2011.

[12] J. Piteľ and J. Mižák, “Computational intelligence and low cost sensors in biomass combustion process”, *in Proceedings of the 2013 IEEE Symposium Series on Computational Intelligence (SSCI): 2013 IEEE Symposium on Computational Intelligence in Control and Automation (CICA)*, Singapore, 2013. pp. 165-168.

[13] R. Padinger, *Regelungstechnik für die Haustechnik der Zukunft*. Graz: Joanneum Research Institut für Energieforschung, 2002.

[14] P. Sovka, R. Čmejla, and L. Šmejkal, “What about... digital filters I.”, *Automatizace*, vol. 48, no. 7-8, pp. 495 – 497, 2005.

[15] K. Židek, T. Saloky, and V. Maxim, “Global navigation and its specification using Kalman filter”, Transfer inovácií, no. 9, pp. 159-162, 2006.

[16] C. Oswald, V. Plaček, B. Šulc, and A. Hošovský, “Transfer issues of control optimizing combustion from small-scale to medium-scale biomass-fired boilers”, *in Proceedings of the 8th PP&PSC (Power Plant and Power System Control) IFAC Symposium*, Toulouse, 2012. pp. 207-211.

[17] J. Mullerová, S. Hloch, and J. Valíček, “Reducing emissions from the incineration of biomass in the boiler”, Chemické listy, vol. 104, no. 9, pp. 876-879, 2010.

Ján Piteľ is an Associate Professor and Vice-dean in Faculty of Manufacturing Technologies of the Technical University of Košice with a seat in Prešov. His research activities include modeling, simulation and automatic control of machines and processes.

Jana Mižáková is a Doctor in Faculty of Manufacturing Technologies of the Technical University of Košice with a seat in Prešov. Her research activities include modeling and simulation of dynamic systems and technological processes.

Extension to fat X-rays of uniqueness results for the grid model in discrete tomography

Stefano Brocchi [a], Paolo Dulio [b], Silvia M.C. Pagani [b]*

***Abstract*—In some circumstances it is preferable, instead of modeling the real world as a continuous space, facing directly the discrete problem. It may happen in the framework of Tomography, where we can employ several tools relying on discrete models: this is Discrete Tomography.**

In this work we start our investigation from a limit case of the discretization process, namely the grid model, and then show how we can extend our approach to a more general framework. It turns out that, if we employ X-rays in the strip model whose width is under a given threshold, uniqueness of reconstruction, which came from exploiting the line structure of X-rays in the grid model, is still achieved. Moreover, we wrote a program which enumerates all possible sets of four valid directions which ensure uniqueness of reconstruction in a given lattice grid.

***Index Terms*—Binary tomography, computerized tomography, discrete tomography; lattice grid; projection; uniqueness of reconstruction.**

I. Introduction

SINCE its early beginning, Computerized Tomography (CT) has been based on the pioneering paper by J. Radon in 1917 [5], where the inversion formula for line integrals was presented and proved. This supplied the theoretical background for uniqueness of reconstruction, which can be achieved in the ideal case when projections in all directions, and no noise, are considered. However, in order to be efficiently applied in the *real world*, Radon theory needs to be matched with several mechanical, physical, and technical constraints. For instance, X-ray projections cannot be considered in the whole range $[0, \pi)$, X-rays are not continuous, do not travel along straight lines, there can be dispersion, diffraction, refraction, scattering or some other noise effects during data collection. In particular, employing a limited number of projections implies that the injectivity of the Radon Transform is lost, so that *ghosts* appear in its null-space which are responsible of ambiguous reconstructions.

It turns out that the continuous Radon inversion formula must be reconsidered from a different perspective, which reflects in a discretization of the whole reconstruction process. As a consequence, the reconstructed image is the result of a long sequence of discretization, interpolation and filtering operations performed by a CT-scan in collecting and reprocessing the available data. The discretization of the reconstruction procedure provides the output in form of a digitalized image $\mathbf{x}$.

This suggests a different approach to the tomographic problem, which can be considered from an algebraic point of view. Here, the digital image $\mathbf{x}$ to be reconstructed is represented as a column vector of unknowns in $\mathbb{R}^n$, being n the total number of involved pixels. If projections are taken in d different directions, then the collected data consist of d different arrays, whose lengths change according to the direction. If L_i is the length of the data array corresponding to the i-th projection, then a column vector $\mathbf{p} \in \mathbb{R}^m$ is formed, where $m = \sum_{i=1}^{d} L_i$, representing the total number of collected measurements. This allows the tomographic reconstruction problem to be modeled as the linear system of equations

$$W\mathbf{x} = \mathbf{p}, \tag{1}$$

where W is an $m \times n$ matrix, and

$$\sum_{j=1}^{n} w_{ij} x_j = p_i \quad \text{for all } i = 1, ..., m. \tag{2}$$

The generic entry w_{ij} of W is related to the discrete contribution of the j-th pixel to the i-th ray integral, and its evaluation depends on the specific discrete model that is considered. Reconstructing $\mathbf{x}$ is equivalent to solving the linear system (1) obtained from the collected projections.

In this paper we investigate the tomographic reconstruction problem from the algebraic point of view. In Section II we briefly outline the main discretization approach that can be considered. In Section III we discuss the uniqueness result obtained in [3], concerning a kind of limit case of discretization. Then we assume to know in advance a suitable lattice grid $\mathcal{A}$ containing the object to be reconstructed. An algorithm is presented that finds all possible sets of four projections which allow perfect reconstruction in $\mathcal{A}$. In Section IV we show how the model can be adapted to the case where X-rays have a non zero width. In Section V we give some experimental results concerning the reconstruction of images by means of four no-noisy fat projections, comparing different reconstructions of a same image and showing how the quality of the output changes according to the width. We end the paper in Section VI with a few concluding remarks.

II. Discrete models for tomographic algebraic reconstruction

When the tomographic reconstruction problem is approached by means of the linear system (1), the number of involved equations and unknowns is, in general, extremely

[a] Dipartimento di Matematica e Informatica “U. Dini”, Università di Firenze, viale Morgagni 67/A, 50134 Firenze, Italy

[b] Dipartimento di Matematica “F. Brioschi”, Politecnico di Milano, Piazza Leonardo da Vinci 32, I-20133 Milano

* Corresponding author

Email addresses: stefano.brocchi@unifi.it, {paolo.dulio, silviamaria.pagani}@polimi.it

high (of order 65.000, for a 256×256 image). Therefore, a direct approach to the resolution is unaffordable, and iterative algorithms are usually employed, such as ART and SART, which, however, lead to accurate results only if m is large, namely, only if the number of available projections is sufficiently wide.

On the other hand, in several applications only a limited number of projection can be employed, or it is desirable to exploit, to avoid high doses of radiation. In this cases system (1) is highly under-determined, and consequently, in order to select an admissible output among all the feasible solutions, one tries to incorporate some possible prior knowledge in the reconstruction algorithms. This is the typical case of Discrete Tomography, where it is assumed to know in advance that the object to be reconstructed consists of a small number (2-5) of different materials, corresponding to different constant grey levels of the image $\mathbf{x}$ to be reconstructed; such prior knowledge is exploited for instance in DART, which iteratively alternates continuous and discretization steps (see [2]). As a special case one can consider Binary Tomography, where only of two gray levels are involved, which is largely applied in reconstructing industrial objects.

A quality measure for the reconstruction, with respect to the unknown original image, is desirable; in [1] it has been shown that all the binary solutions of the linear system (1) are equally distant from the real-valued solution with minimal Euclidean norm, i.e., the solution obtained by pseudo-inverting the matrix W, provided it has full rank. From now on, we focus on the reconstruction of binary images.

A main point is to decide how the entries w_{ij} of W must be computed. According to different possible choices, various discrete models are obtained, which we briefly discuss below. In particular, for an $N \times N$ image, the size of a pixel is $1/N^2$ the size of the whole image. Therefore, any computation concerning distances must be normalized accordingly, once we assume as unit lengths the horizontal and the vertical dimensions of the whole image. However, usually, the unit length is instead assumed to be the pixel size, so that no normalization is required.

A. The strip model

Probably, from an applicative point of view, the *strip model* is the natural one, since pixels are represented by continuous squares, and *fat* X-rays are employed, namely X-rays are continuous strips of some width w. In this model w_{ij} is the portion of normalized area intercepted by the i-th ray in the j-th pixel (see Figure 1(a)).
Note that there are many zeros entries in the matrix W, since any strip corresponding to a fat X-ray intersects only a small number of pixels containing the object to be reconstructed.

B. The line model

As a limit case of the strip model one can assume X-rays as represented by perfectly continuous straight lines (Figure 1(b)). This is the typical case of Geometric Tomography, where uniqueness of reconstruction by a limited number of available projections can be sometimes achieved by exploiting some

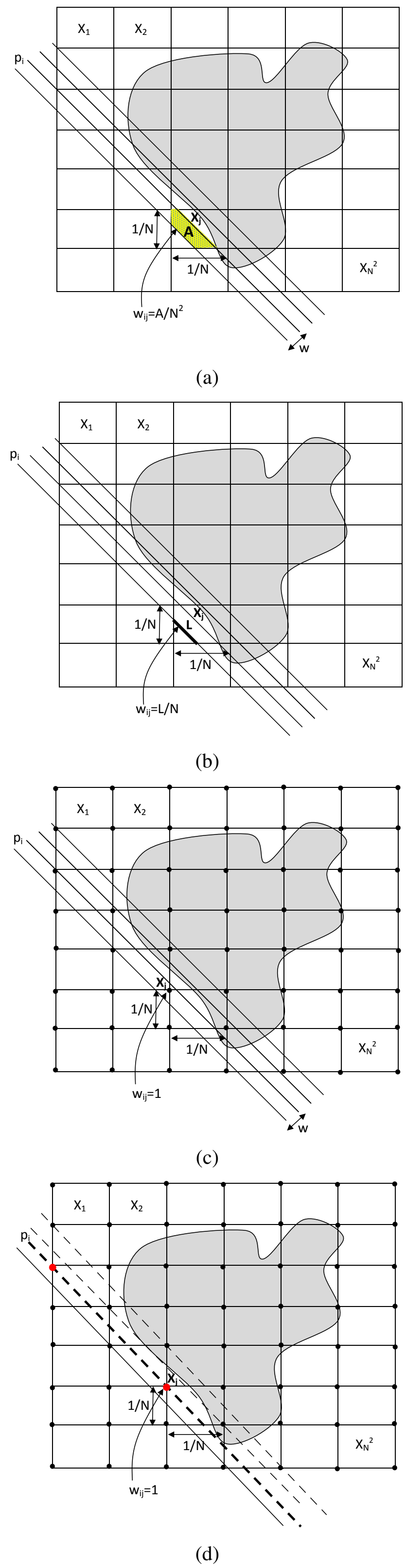

Figure 1. Different models for ART. (a) The strip model. (b) The line model. (c) The discrete strip model. (d) The discrete line model, or grid model.

geometric a priori information. In this case, the algebraic approach to Radon inversion leads to compute w_{ij} as the normalized length of the segment intercepted by the i-th line in the j-th square-shaped pixel.

C. The discrete strip model

Starting from the strip model, a second kind of discretization can be introduced (Figure 1(c)), by assuming the square grid of the form

$$\mathcal{A} = \{(i,j) \in \mathbb{Z}^2 \ : 1 \leq i, j \leq N\},$$

for some integer number $N \geq 1$. In this case pixels are lattice points with integer coordinates, so that $w_{ij} = 1$ if the pixel x_j belongs to the i-th strip of width w, and $w_{ij} = 0$ otherwise. Therefore, in (2), p_i counts the number of lattice points falling in the corresponding strip.

D. The grid model

The same kind of discretization introduced in the strip model can be also considered in the line model, which leads to a discrete line model, also known as *grid model* (Figure 1(d)). In this case we have the limit case of discretization, since pixels are lattice points with integer coordinates, and X-rays are discrete straight lines, namely, sets of lattice points belonging to a continuous straight-line. Consequently, $w_{ij} = 1$ if the pixel x_j belongs to the i-th line, and $w_{ij} = 0$ otherwise. This model can also be interpreted as a limit case of the discrete strip model as $w \to 0$, and, in this sense, it can be considered as the basic discrete theoretical model. As a consequence, it seems to be of applicative interest trying to extend uniqueness results holding in the grid model to different approaches to the tomographic reconstruction problem.

III. A UNIQUENESS RESULT IN THE GRID MODEL

The incorporation of some a priori knowledge can lower the number of allowed solutions of the linear system (1), and, in some cases, also uniqueness can be achieved. An assumption, that is frequently employed in the grid model, is the prior knowledge of the size of the grid where the object to be reconstructed is confined (see for instance [3], [4], [6], [7]).

A *(lattice) direction* is a pair (a, b) of coprime integers such that $a = 1$ if $b = 0$ and conversely $b = 1$ if $a = 0$. Without loss of generality we can assume $a \geq 0$. Let $S = \{(a_r, b_r)\}_{r=1}^d$ be a set of d lattice directions. We say that S is *valid* for a finite grid $\mathcal{A} = \{(i,j) \in \mathbb{Z}^2 \ : \ 0 \leq i < M, \ 0 \leq j < N\}$, if

$$\sum_{r=1}^{d} a_r < M, \qquad \sum_{r=1}^{d} |b_r| < N. \tag{3}$$

Let $S = \{u_1, u_2, u_3, u_4 = u_1 + u_2 \pm u_3\}$ be a valid set of four directions for $\mathcal{A}$, where $u_r = (a_r, b_r)$, $r = 1, \ldots, 4$, and set

$$\sum_{r=1}^{4} a_r =: h, \quad \sum_{r=1}^{4} |b_r| =: k.$$

We also consider the set $D = \pm S \cup \hat{S}$, where $\hat{S} = \{\pm(u_1 - u_4), \pm(u_2 - u_4), \pm(u_1 + u_2)\}$. Split D into two disjoint sets A, B, defined as follows:

$$\begin{aligned} A &:= \{(a,b) \in D : \ |a| > |b|\}, \\ B &:= \{(a,b) \in D : \ |b| > |a|\}. \end{aligned}$$

Moreover, if $|a| = |b|$, for some $(a, b) \in D$, we then include (a, b) in A if $\min\{M - h, N - k\} = M - h$, while $(a, b) \in B$ otherwise. Thus we have $D = A \cup B$, where one of the sets A, B may be empty.

In [3], the following result has been obtained for the grid model.

Theorem 1. Let $S = \{u_1, u_2, u_3, u_4 = u_1 + u_2 \pm u_3\}$ be a valid set for the lattice grid $\mathcal{A} = \{(i,j) \in \mathbb{Z}^2, 0 \leq i < M, 0 \leq j < N\}$. Suppose that $g : \mathcal{A} \to \{-1, 0, 1\}$ has zero line sums along the lines with direction in S. Then g is identically zero if and only if

$$\min_{(a,b) \in A} |a| \geq \min\{M - h, N - k\}, \tag{4}$$

$$\min_{(a,b) \in B} |b| \geq \min\{M - h, N - k\}, \tag{5}$$

and

$$\begin{aligned} M - h < N - k \ &\Rightarrow \ \forall (a,b) \in B : \\ &|a| \geq M - h \ \text{ or } \ |b| \geq N - k, \end{aligned} \tag{6}$$

$$\begin{aligned} N - k < M - h \ &\Rightarrow \ \forall (a,b) \in A : \\ &|a| \geq M - h \ \text{ or } \ |b| \geq N - k, \end{aligned} \tag{7}$$

where, if one of the sets A, B is empty, the corresponding condition (4) or (5) drops.

Starting from the above theorem, we can derive an algorithm which provides all sets of four lattice directions which allow uniqueness of reconstruction of a given $N \times N$ image. An online program exploiting such an algorithm is available at http://www.dsi.unifi.it/users/brocchi/dev/unique4d.html. The algorithm works as follows.

1) For a given integer number N, all sets $S = \{u_1, u_2, u_3, u_1 + u_2 \pm u_3\}$ of four distinct directions, such that $a_r < N, |b_r| < N$, $r = 1, 2, 3, 4$, are computed.
2) For each set S, it is verified whether it is valid for an $N \times N$ grid.
3) If so, the corresponding set $D = \pm S \cup \hat{S}$ is computed.
4) A consistency test for D is applied in order to check whether conditions (4)-(7) hold.
5) All consistent outputs are provided.

IV. FAT X-RAY ALGEBRAIC RECONSTRUCTIONS BASED ON UNIQUENESS RESULTS

Our purpose is to adapt to fat X-rays the uniqueness result provided by Theorem 1, holding in the grid model. To this, we propose a few steps which allow a progressive change of the reconstruction model. We also assume the pixel size as unit length.

First of all we must move from the continuous strip model to its discrete version, so, as a starting step, we assume to work with continuous strips of width w formed by union of

ISBN: 978-1-61804-321-4

lines in given lattice directions. This means that a line has a rational slope, and, consequently, the width of a fat X-ray cannot be arbitrarily small. The limit case is represented when strips are bounded by neighboring lattice lines. Let us compute the maximal width $w(v)$ allowed for a lattice direction $v = (a, b)$. If $a = 0$, then v is the vertical direction, and $w(v) = 1$. Otherwise, neighboring lattice lines L_1, L_2 have equations $ay - bx = t - 1$ and $ay - bx = t$, respectively, for some $t \in \mathbb{Z}$. Consequently, $w(v)$ equals the distance of the point $P = (0, t-1) \in L_1$ from L_2, namely

$$w(v) = \frac{1}{\sqrt{a^2 + b^2}}. \tag{8}$$

From easy geometric argument it follows that any pixel is intersected by $|a| + |b|$ consecutive strips of minimal width. For instance, in case $a > 0$ and $b < 0$, the pixel bounded by lines $x = i - 1$, $x = i$, $y = j - 1$ and $y = j$ is intersected by the consecutive strips between the lattice lines $-bx + ay = t - 1$ and $-bx + ay = t$, for $(i-1)(-b) + (j-1)a \le t \le -bi + ja$ (see also [8]). The number of corner points (vertices of pixels) falling in each strip equals the number of corner points belonging to the two lattice lines bounding the strip. The number of corner points on a lattice line precisely equals the projection along that line in the grid model. Also, note that any corner point belongs to two adjacent strips. Coming back to the original continuous strip model, assume to work with strips of width $w < w(v)$ centered on lattice lines having the same direction. In these cases the number of corner points belonging to a given strip is completely determined on the median line of the strip, and equals the projection along the same line according to the grid model.

Reconstructing a digital image from fat projections needs the strip model to be considered in its discrete version, by introducing an $N \times N$ lattice grid whose size depends on the required resolution. Consequently, digital image reconstructions with fat X-rays of width $w < w(v)$ can be interpreted as grid model based reconstructions. If $S = \{u_r = (a_r, b_r) : 1 \le r \le 4\}$ is a set of four directions of uniqueness for an $(N \times N)$-sized lattice grid, then the corresponding minimal width is

$$w(S) = \min_r \frac{1}{\sqrt{a_r^2 + b_r^2}}. \tag{9}$$

It follows that sets S of four directions, providing uniqueness of reconstruction of a digital image according to the grid model, also lead to perfect reconstruction by means of fat X rays, whenever strips of width $w < w(S)$ are employed.

In particular, we could have several sets S of uniqueness for a same $N \times N$ grid $\mathcal{A}$, so that we can compute the maximal width allowed for uniqueness of reconstruction in $\mathcal{A}$ by computing

$$w(\mathcal{A}) = \max_S w(S) = \max_S \min_r \frac{1}{\sqrt{a_r^2 + b_r^2}}. \tag{10}$$

V. Experimental results

In this section we want to show how the previous results can be exploited for algebraic tomographic reconstructions.

First of all, for any given integer N, our algorithm computes, according to Theorem 1, all the sets S of four directions that ensure uniqueness of reconstruction in an $(N \times N)$-sized lattice grid. In Table I we list the number of different sets S for increasing sizes (5-19) of the lattice grid. The numbers are obtained by exploiting an online program, available at http://www.dsi.unifi.it/users/brocchi/dev/unique4d.html. It is worth underlying that the number of sets of uniqueness is an exponential function in the odd and even sizes, separately, and that the number of sets of uniqueness for an even size of the grid is always less than the number regarding the previous odd size. This is due to the fact that, by the formulation of our problem, h and k are always even, so $\min\{N-h, N-k\} \ge 2$, while for odd sizes we have $\min\{N-h, N-k\} \ge 1$. It would be desirable to write explicitly the function giving the number of the sets of uniqueness.

In Table II the resulting sets S for $N = 10$ have been pointed out explicitly.

Size of the grid	5	6	7	8	9
number of sets of uniqueness	6	0	30	0	132
Size of the grid	10	11	12	13	14
number of sets of uniqueness	8	510	80	1100	270
Size of the grid	15	16	17	18	19
number of sets of uniqueness	2868	838	6018	2104	10800

Table I
NUMBER OF SETS S OF FOUR DIRECTIONS OF UNIQUENESS FOR LATTICE GRIDS OF INCREASING SIZE.

u_1	u_2	u_3	u_4
$(1, -4)$	$(1, 2)$	$(2, 1)$	$(4, -1)$
$(1, -4)$	$(3, 1)$	$(3, -1)$	$(1, -2)$
$(1, -3)$	$(1, 3)$	$(2, -1)$	$(4, -1)$
$(1, -3)$	$(1, 3)$	$(2, 1)$	$(4, 1)$
$(1, -2)$	$(1, 4)$	$(2, -1)$	$(4, 1)$
$(1, -2)$	$(3, 2)$	$(1, 2)$	$(3, -2)$
$(1, 2)$	$(3, 1)$	$(1, 4)$	$(3, -1)$
$(2, -3)$	$(2, 3)$	$(2, -1)$	$(2, 1)$

Table II
LIST OF SETS OF FOUR DIRECTIONS ENSURING UNIQUENESS OF RECONSTRUCTION IN A 10×10 GRID.

For any given size N, the structure of the different sets S of uniqueness can change greatly. However, some regularities can be discovered. In particular, when N is odd, we always get the set

$$S = \left\{(1,0), (0,1), \left(\frac{N-1}{2}, \frac{N-3}{2}\right), \left(\frac{N-3}{2}, \frac{N-1}{2}\right)\right\},$$

which is in accordance with [3, Corollary 16]. For instance, if $N = 51$, then $S = \{(1,0), (0,1), (24,25), (25,24)\}$, and computing $w(S)$ as in (9) we find that

$$w(S) = \frac{1}{\sqrt{24^2 + 25^2}} = 0.02885549284,$$

so that any tomographic reconstruction with fat X-rays of width $w < w(S)$ can be interpreted as a tomographic reconstruction in the grid model, and consequently, due to the

ISBN: 978-1-61804-321-4

nature of the set S, it is a perfect reconstruction. In Figure 2 we show the reconstructions of a random 51×51 image with fat X-rays of decreasing width. Note that for $w = 0.025$ we get a perfect reconstruction.

VI. Conclusion and comments

In this work we proposed an extension from the limit-case line model to the discrete strip model, under the condition that the width of the X-rays does not exceed a given threshold. This enables us to create a connection between the ideal world of line X-rays and the real world, where the rays have a certain size. The proposed paper can be useful in order to apply the theoretical results, obtained for the grid model, in a more general framework.

A further extension will be the translation of the same argument for noisy data. In this case there is no uniqueness result, neither in the grid model, so we will argue in such a limit case. Another possible extension to our work could be the explicit enumeration of all sets of four directions ensuring uniqueness of reconstruction in the considered grid.

References

[1] K.J. Batenburg, W. Fortes, L. Hajdu, R. Tijdeman, *Bounds on the quality of reconstructed images in binary tomography*, Discrete Applied Mathematics, 161 (15) (2013), pp. 2236-2251.

[2] K.J. Batenburg, J. Sijbers, *DART: a Practical Reconstruction Algorithm for Discrete Tomography*, IEEE Trans. Image Processing, 20 (9) (2011), pp. 2542-2553.

[3] S. Brunetti, P. Dulio, C. Peri, *Discrete Tomography determination of bounded lattice sets from four X-rays*, Discrete Applied Mathematics, 161 (15) (2013), pp. 2281-2292.

[4] S. Brunetti, P. Dulio, C. Peri, *Discrete Tomography determination of bounded sets in $\mathbb{Z}^n$*, Discrete Applied Mathematics, 183 (2015), pp. 20-30.

[5] J. Radon, *Über die Bestimmung von Funktionen durch ihre Integralwerte längs gewisser Mannigfaltigkeiten*, Ber. Verh. Sächs. Akad. Wiss. Leipzig Math.-Phys. Kl. 69 (1917), pp. 262-277.

[6] L. Hajdu, *Unique reconstruction of bounded sets in discrete tomography*, Electron. Notes Discrete Math., 20 (2005), pp. 15-25.

[7] L. Hajdu, R. Tijdeman, *Algebraic aspects of discrete tomography*, J. reine angew. Math. 534 (2001), pp. 119-128.

[8] J. Zhua, X. Lia, Y. Yeb, G. Wang, *Analysis on the strip-based projection model for discrete tomography*, Discrete Applied Mathematics, 156 (12) (2008), pp. 2359-2367.

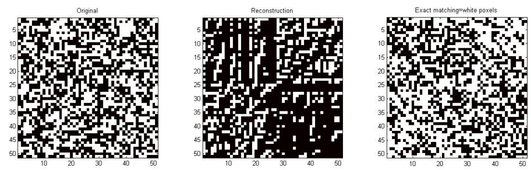

(a)

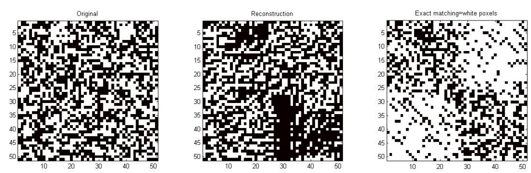

(b)

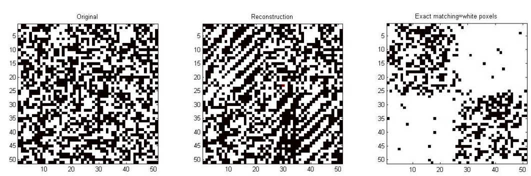

(c)

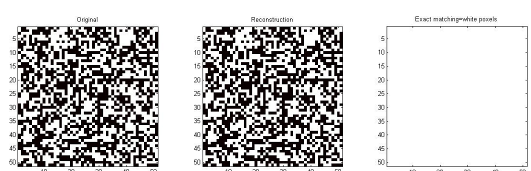

(d)

Figure 2. Reconstruction of a 51×51 random binary image with $S = \{(1,0),(0,1),(24,25),(25,24)\}$ and width ranging from $w = 0.1$ (a) to $w = 0.05$ (b), $w = 0.033$ (c) and $w = 0.025$ (d). In every sub-figure, the leftmost image represents the original phantom, the central image is the reconstruction and the rightmost image shows the difference between the previous images (black pixels mean different values of the two images). The last choice of w provides a perfect reconstruction. All figures are plotted by MATLAB.

ISBN: 978-1-61804-321-4

Control of nonlinear dynamical systems using Levenberg-Marquardt learning algorithm for recurrent complex-valued neural networks

Ieroham S. Baruch and Edmundo P. Reynaud

Abstract—The present work follows the obtained results in the development of a Complex-Valued Recursive Levenberg-Marquardt learning algorithm, applied in the training of Complex-Valued Recurrent Neural Networks. These networks are used in two proposed adaptive neural control schemes, applied to a nonlinear, mechanical plant with multiple inputs and outputs to validate the quality of the learning algorithm. Furthermore, we make a comparative test between this and a Complex-Valued Back-Propagation learning algorithm for the same control schemes, which yields good results.

Keywords—Complex-valued neural networks, Adaptive control, Nonlinear control, Levenberg-Marquardt learning algorithm, System identification.

I. Introduction

THE use of Artificial Neural Networks is fundamental in the field of adaptive control, mainly because of its application in a wide range of dynamical systems of different nature, robustness, high-scale integration and popularity. Even so, the use of Neural Networks in the complex domain for control tasks is still low in comparison to its real-valued counterparts.

The use of Complex-Valued Neural Networks is preferred in systems with an oscillatory behavior, or systems where its nature can be better codified in the domain of complex numbers, such as electromagnetic and optical phenomena, electric power systems, electronic and information systems to name a few (see [1], [2], [3]).

Nonetheless their use is not limited to these fields. For example, in [4] the authors use a Complex-Valued Recurrent Neural Network (**CVRNN**) to generate cooperative motion trajectories for a pair of robots. In [5], a High-Dimension Complex-Valued Neural Network is used to control the end effector of a three-dimensional robotic manipulator. In a previous work (see [6]) we used **CVRNN** in the identification of a nonlinear mechanical system. The present article follows the works of [7] and [8], where a Complex-Valued Back-Propagation (**CVBP**) learning algorithm is devised for a **CVRNN**, which is used for the identification and control of a nonlinear oscillatory plant. In the same way, we developed a second order recursive Complex-Valued Levenberg-Marquardt (**CVLM**) learning algorithm in the complex domain, applied to the training of Recurrent Neural Networks used in the identification and control of a nonlinear mechanical plant. Furthermore, we used simulation results to validate our algorithm and to make a comparison with the **CVBP** algorithm proposed in [7].

I. S. Baruch is with the Department of Automatic Control, CONVESTAV-IPN, D.F, Mexico. E-mail: baruch@ctrl.cinvestav.mx

E. P. Reynaud is a Master in Science student in the Department of Automatic Control, CINVESTAV-IPN, D.F, Mexico. E-mail: eperez@ctrl.cinvestav.mx

II. Complex-Valued Recurrent Neural Network Topology and the Recurrent Levenberg-Marquardt Learning Algorithm

Let us consider a **CVRNN** with a constructed activation function given by the following equation:

$$f(z) = \Gamma(\mathrm{Re}(X)) + i\Gamma(\mathrm{Im}(X)), \quad z \in \mathbb{C} \tag{1}$$

This function has no singular points in its domain and is similar to the one used in [7], [8]. The **CVRNN** with this activation function has a diagrammatic representation shown in Fig 1.

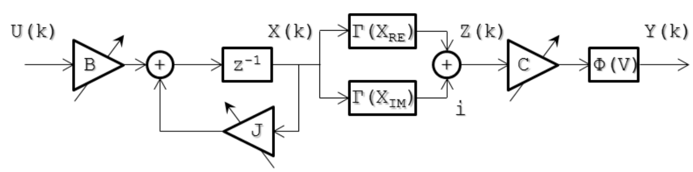

Fig.1 Block-diagram representation of a CVRNN

And its mathematical description is given by the following equations:

$$X(k+1) = JX(k) + BU(k) \tag{2}$$

$$Z(k) = \Gamma[X_{\mathrm{Re}}(k)] + i\Gamma[X_{\mathrm{Im}}(k)] \tag{3}$$

$$V(k) = CZ(k) \tag{4}$$

$$Y(k) = \Phi[V(k)] \tag{5}$$

Where: $X \in \mathbb{C}^n$ is the state vector, $Z \in \mathbb{C}^n$ is the state vector of the hidden layer, $U \in \mathbb{R}^m$ is the input vector, $Y \in \mathbb{R}^L$ is the output vector; n, m, L are the number of internal states, inputs and outputs respectively.

$J \in \mathbb{C}^{n\times n}$, $B \in \mathbb{C}^{n\times m}$ and $C \in \mathbb{C}^{L\times n}$ are the feedback, input and output weight matrices respectively, and they constitute the weight parameters from the neural network subject to training. The matrix J is a diagonal matrix with the neuron eigenvalues as its block-elements. Complex eigenvalues come in pairs of complex conjugate numbers, while real eigenvalues come as single numbers. For the matrices B and C, its elements also come in pairs of complex conjugate numbers or single real numbers, and its positions are related to the positions of the elements of J.

The diagonal block-elements J_j of the J matrix must meet the stability condition:

$$\left|J_j\right| < 1, \qquad j = 1, 2, \ldots, N \tag{6}$$

The map $\Gamma : \mathbb{R}^n \to \mathbb{R}^n$ is a real-valued vector function. Given that the product $CZ(k)$ is a real-valued vector, the map $\Phi : \mathbb{R}^L \to \mathbb{R}^L$ is also a real-valued vector function.

This **CVRNN** has a canonical Jordan form; this means that it has the minimum number of parameters subject to training, as well as complete parallel integration. It also presents properties of dynamical systems such as controllability, observability, and stability conditions.

Although the internal state and parameter matrices of the neuron are complex-valued, the complex conjugate pairs produce a real-valued output of the network, which yields a real-valued identification error signal. The performance index to be minimized used in the training algorithm is given by the equation:

$$\zeta(k) = \frac{1}{2}\sum_j [E_j(k)]^2, \qquad \zeta = \frac{1}{N_e}\sum_k \zeta(k) \tag{7}$$

$$E(k) = Y_p(k) - Y(k) \tag{8}$$

Where equation (8) describes the error between the desired output Y_p and the real output Y of the network. The instantaneous Mean Squared Error (**MSE**) $\zeta(k)$ is used in on-line applications, while the total **MSE** denoted by ζ is used for one epoch N_e in off-line applications.

The **CVLM** algorithm for any weight vector W is described by the following update equation (see [6],[10]):

$$W(k+1) = W(k) + P(k)\cdot DY[W(k)]\cdot E(k), \qquad \left|W_j\right| < W_0 \tag{9}$$

Where: W_0 is a restricted region for the weight W_j, P can be interpreted as the covariance matrix of the weight's estimation, and $DY[W]$ is the local gradient component of the output of the network with respect to W.

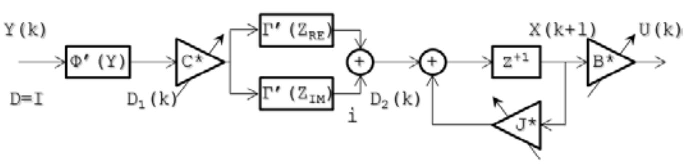

Fig.2 Block-diagram of the adjoint network for the CVRNN

Applying certain diagrammatic rules (see [9]) to the **CVRNN** given in Fig 1, we obtain its adjoint topology, which is shown in Fig 2. Then gradient terms can be derived directly from the adjoint topology, which are described by the following equations:

$$D_1(k) = \Phi'[Y(k)]\cdot D \tag{10}$$

$$D_2(k) = (\Gamma'[Z_{\mathrm{Re}}(k)]\cdot \mathrm{Re}(C^*) + \Gamma'[Z_{\mathrm{Im}}(k)]\cdot \mathrm{Im}(C^*))\cdot D_1(k) \tag{11}$$

$$DY[C(k)] := \partial Y(k)/\partial C(k) = D_1(k)\cdot Z^*(k) \tag{12}$$

$$DY[J(k)] := \partial Y(k)/\partial J(k) = D_2(k)\cdot X^*(k) \tag{13}$$

$$DY[B(k)] := \partial Y(k)/\partial B(k) = D_2(k)\cdot U^*(k) \tag{14}$$

Where: $D = I$ is a unitary input for the adjoint topology. The matrix P is computed recursively using the following equation:

$$P(k) = \alpha^{-1}[P(k-1) - P(k-1)\cdot\Omega_{W(k)}\cdot S^{-1}_{W(k)}\cdot \Omega^*_{W(k)}\cdot P(k-1)] \tag{15}$$

Where the matrices Ω_W and S_W are given by:

$$\Omega^*_{W(k)} = \begin{bmatrix} & DY^*[W(k)] & & \\ 0 & \cdots & 1 & \cdots & 0 \end{bmatrix} \tag{16}$$

$$S_{W(k)} = \alpha\Lambda + \Omega^*_{W(k)}\cdot P(k-1)\cdot \Omega_{W(k)} \tag{17}$$

$$\Lambda^{-1} = \begin{bmatrix} 1 & 0 \\ 0 & \rho \end{bmatrix} \tag{18}$$

The matrices P and S_W have dimensions $(N_W \times N_W)$ and (2×2) respectively, where N_W is the number of weights in the vector W. The matrix Ω^*_W has dimension $(2\times N_W)$, and its second row consists of $(N_W - 1)$ zeroes and a unit element in the i-th position, which is computed by:

$$i = k\cdot \mathrm{mod}(N_W) + 1 \tag{19}$$

The parameters for the algorithm should be restricted as follows:

$$10^{-6} \le \rho \le 10^{-4}, \qquad 0.97 \le \alpha \le 1.00, \qquad 10^3 \le P(0) \le 10^6 \tag{20}$$

The **CVRNN** topology presented in (1)-(5) with the **CVLM** learning algorithm (9)-(20) can be used in identification (see [6]) and control problems applied to nonlinear, oscillatory dynamical systems.

ISBN: 978-1-61804-321-4

III. Complex-Valued Adaptive Neural Control

We illustrate the application of **CVRNN** in the design of neural control for a multiple-input multiple-output (**MIMO**) nonlinear plant by proposing a neural adaptive controller scheme with a feedforward term, state feedback term, and an integral term, in two different control schemes.

We further make a comparison between the **CVLM** learning algorithm developed in this work and the **CVBP** learning algorithm presented in [7], [8], using the total **MSE** of the control error as performance index. The plant model is given in continuous time so, in order to use discrete-time **CVRNN** in a control scheme, the input and output signals of the plant are discretized with a sampling time τ .

A. Direct Feedforward Adaptive Neural Control with State Feedback.

For the first adaptive neural controller, we use the control scheme represented in the diagram shown in Fig 3.

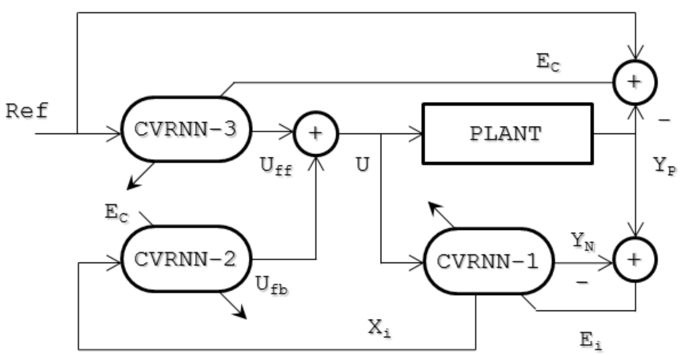

Fig.3 Diagram for the feedforward adaptive neural controller with state feedback

In this control scheme we use three different **CVRNN**, each with a specific task:

- *CVRNN-1*: Is used as a plant model identifier. It has the control signal U that is fed to the plant as its input and produces an identification output Y_N , which is compared to the plant output Y_P to produce the identification error signal used for the training of its own weight parameters. The identification error is described by the following equation:

$$E_i(k) = Y_P(k) - Y_N(k) \tag{21}$$

- *CVRNN-2*: This neural network is fed the internal state vector X_i of the identification network **CVRNN-1** to produce a state feedback control signal U_{fb} . This network is trained with the control error signal E_C , which is produced by comparing the reference signal R to the output of the plant, described by the following equation:

$$E_C(k) = R(k) - Y_P(k) \tag{22}$$

- *CVRNN-3*: This neural network is trained with the control error signal so it converges to the inverse model of the plant. The network is fed the reference signal R to produce a feedforward control signal U_{ff} .

Except for the dimensions of each of the **CVRNN**, the three present the same topology. The control signal is the sum of the feedforward and state feedback control signals, and is described by the following equation:

$$U_1(k) = U_{ff}(k) + \mathrm{U}_{fb}(k) \tag{23}$$

B. Direct Feedforward Adaptive Neural Control with Integral Term and State Feedback

This control scheme is described by the diagram shown in Fig 4.

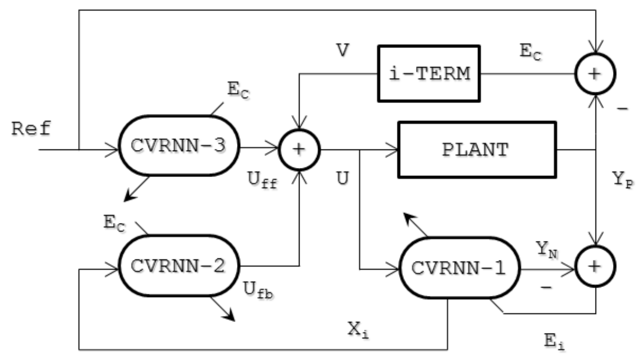

Fig.4 Diagram for the feedforward adaptive neural controller with integral term and state feedback

We used three **CVRNN** for this control scheme: one as a plant model identifier, one as a state feedback controller, and one as a direct feedforward controller. We add an integral term U to the control signal to eliminate the steady-state error present in the plant output. This integral term is given by the following equation:

$$V(k+1) = V(k) + \tau \cdot K_i \cdot E_C(k) \tag{24}$$

Where: K_i is the integral-action gain and τ is the sampling time. The control signal for this scheme is the sum of three terms and is described by the following equation:

$$U_2(k) = U_{ff}(k) + \mathrm{U}_{fb}(k) + \mathrm{V(k)} \tag{25}$$

This control scheme forces the plant to follow the reference signal with zero steady-state error. The stability of the whole system, for both control schemes, is assured by the restriction in the weight parameters of the matrix J of the **CVRNN** and the boundedness of its activation functions.

C. Nonlinear Plant Model Description

The nonlinear plant proposed for this work is a flexible-joint robotic arm with two degrees of freedom (**DOF**) as shown in Fig 5. Each joint consists of an actuator connected to a load through a torsional spring representing its flexibility. We make the following assumptions to get a simplified mathematical model of the plant:

- The rotor inertia of each joint is symmetric about its rotation axis so that the gravitational terms of the model, the rotor velocity, and the center of mass of each link are independent of the rotor position.
- The kinetic energy acting on the rotor is due to its own rotation, and the motion of the rotor is a pure rotation with respect to the inertial frame.

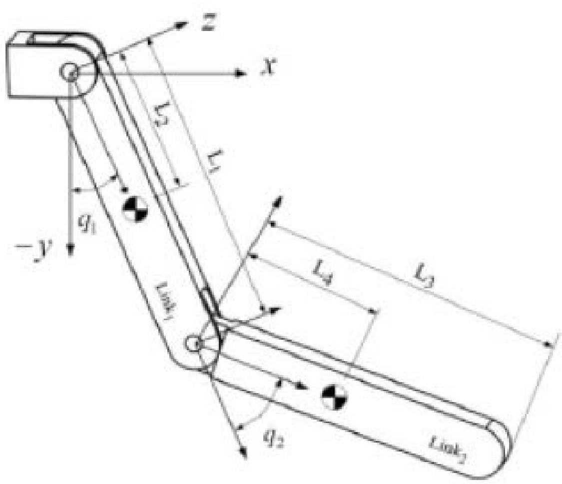

Fig.5 Two-DOF robotic arm with flexible joints

The flexibility at the joint is caused by a harmonic drive, which is a type of gear mechanism with high torque transmission, low backlash and compact size (Fig 6).

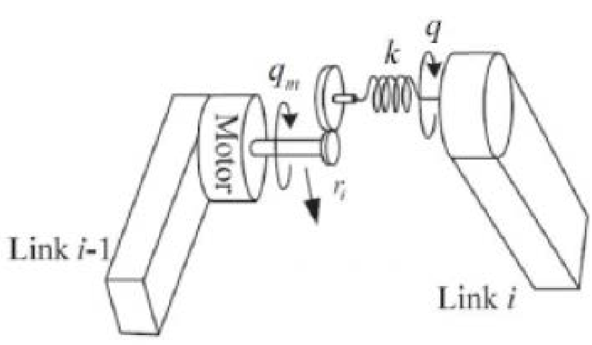

Fig.6 Idealized model of the i-th flexible joint

Under these assumptions, we obtain the equations of motion of our plant, which are given by:

$$D(q)\ddot{q} + C(q,\dot{q})\dot{q} + G(q) + K(q - q_M) = 0 \tag{26}$$

$$J_M \ddot{q}_M - K(q - q_M) = u \tag{27}$$

Where: $q, q_M \in \mathbb{R}^n$ are the links and motor shafts angular displacement respectively; $\mathrm{D(q)}: \mathbb{R} \to \mathbb{R}^{n\times n}$ is a positive definite inertia matrix, $C(\mathrm{q},\dot{\mathrm{q}}): \mathbb{R}^{n\times n} \to \mathbb{R}^n$ is a matrix containing all the Coriolis and centrifugal force terms, $G(\mathrm{q}): \mathbb{R}^n \to \mathbb{R}^n$ is the gravitational force vector, $K \in \mathbb{R}^{n\times n}$ is a diagonal, positive definite spring constant matrix of the flexible joints; $J_M \in \mathbb{R}^{n\times n}$ is the inertia matrix of the motors of each joint, and $u \in \mathbb{R}^n$ is the input torque vector.

Defining an extended vector $q_f := \begin{bmatrix} q^T & q_M^T \end{bmatrix}^T$, we rewrite equations (26)-(27) in the following matrix form:

$$D_f(q)\ddot{q}_f + C_f(q,\dot{q})\dot{q}_f + G_f(q) + K_f q_f = u_f \tag{28}$$

Where:

$$D_f(q) = \begin{bmatrix} D(\mathrm{q}) & 0 \\ 0 & J_M \end{bmatrix}, \qquad C_f(q,\dot{q}) = \begin{bmatrix} C(q,\dot{q}) & 0 \\ 0 & 0 \end{bmatrix}$$

$$G_f(q) = \begin{bmatrix} G(q) \\ 0 \end{bmatrix}, \quad K_f = \begin{bmatrix} K & -K \\ -K & K \end{bmatrix}, \quad u_f = \begin{bmatrix} 0 \\ I \end{bmatrix} u$$

The plant is a sub-actuated, oscillatory, nonlinear system described by four second order ordinary differential equations. More properties of this model are mentioned in [11].

D. Simulation and Results.

We test the **CVLM** learning algorithm applied to the two control schemes proposed in this work, for a nonlinear plant with a simulation using MATLAB. Next, we make a comparison between the **CVBP** and the **CVLM** learning algorithms. As a comparison measure, we use the total **MSE** of the control error signal. This section describes the simulation settings used and the results obtained.

The reference signals used is given by the following vector:

$$R(\mathrm{k}) = \begin{bmatrix} 0.25 \\ -0.45 \end{bmatrix} \mathrm{rad} \tag{29}$$

For every simulation, a total time of $T = 100s$, a sampling time of $\tau = 0.01$, and activation function $\Gamma[\cdot] = \Phi[\cdot] = \tanh(\cdot)$ were used. For the simulations using the **CVBP** learning algorithm, the learning rate parameter $\eta = 0.1$ and the momentum parameter $\alpha = 0.04$ were used for each one of the neural networks. For the simulations involving the **CVLM** learning algorithm, the parameters $\alpha = 0.98$, $\rho = 1\times 10^{-4}$, and $P_J(0) = P_B(0) = P_C(0) = 1\times 10^5$ were used for each one of the neural networks.

For the first control scheme, the dimensions used for the **CVRNN-1** and **CVRNN-3** were $n_{1,3} = 3, m_{1,3} = 2, L_{1,3} = 2$, for the **CVRNN-2** were $n_2 = 3, m_2 = 3, L_2 = 2$ with initial conditions of the internal state vector $X(0) = \begin{bmatrix} 0.1 & 0.1 & 0.1 \end{bmatrix}^T$, and random initial conditions for each weight parameter in the interval $[-0.1, 0.1]$ for each neural network.

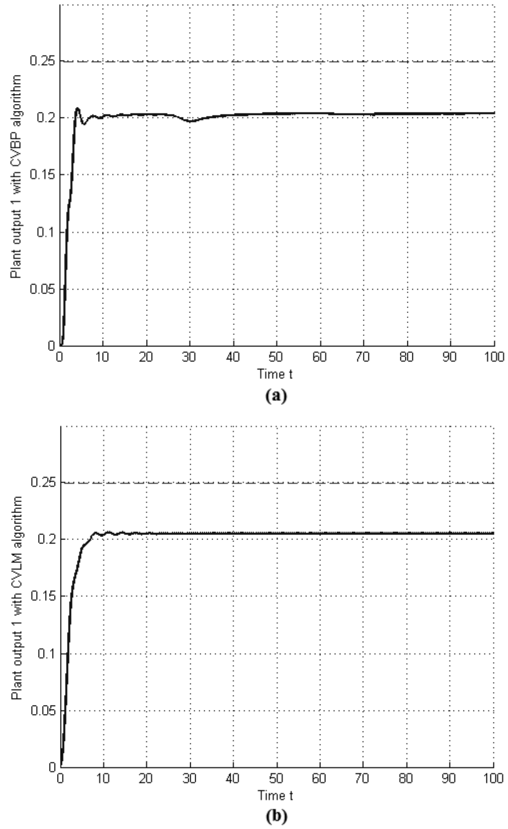

Fig.7 Output 1 of the plant without integral term, for (a) CVBP algorithm and (b) CVLM algorithm.

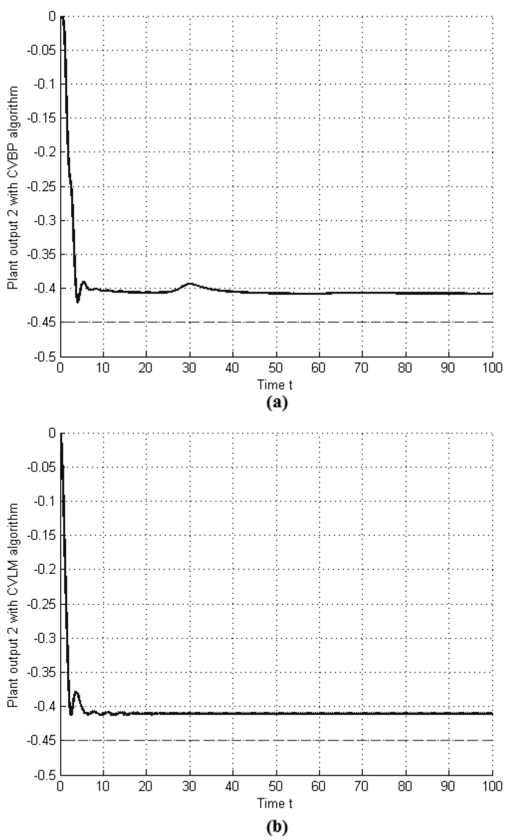

Fig.8 Output 2 of the plant without integral term, for (a) CVBP algorithm and (b) CVLM algorithm.

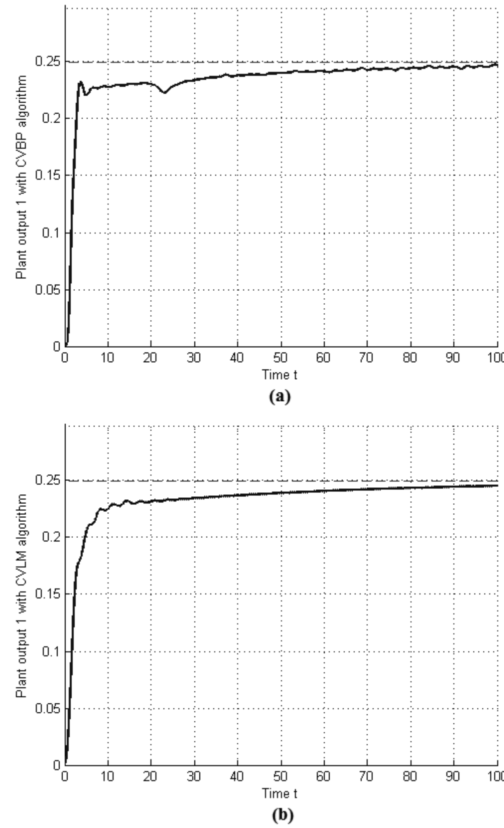

Fig.9 Output 1 of the plant with integral term, for (a) CVBP algorithm and (b) CVLM algorithm.

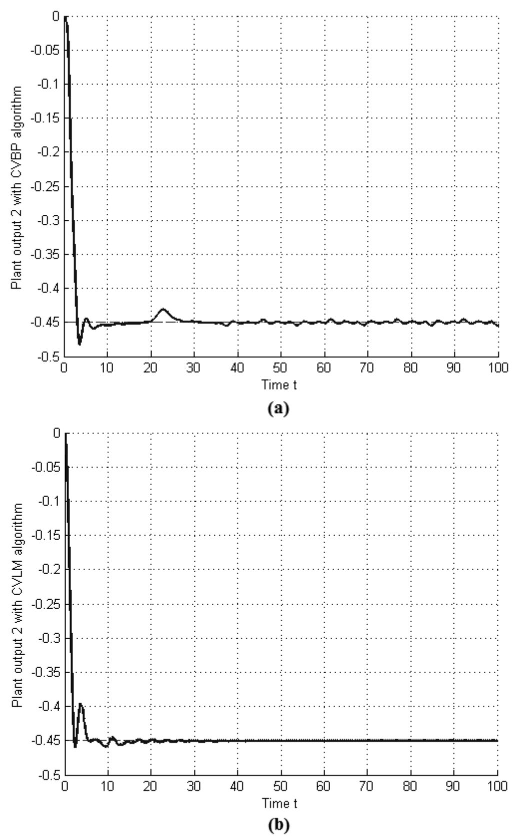

Fig.10 Output 2 of the plant with integral term, for (a) CVBP algorithm and (b) CVLM algorithm.

ISBN: 978-1-61804-321-4

The outputs of both **DOF** of the plant for this control scheme are shown in Fig7 for the **CVBP** learning algorithm and Fig 8 for the **CVLM** learning algorithm.

For the second control scheme, the dimensions used for the **CVRNN** were the same as the ones used in the first control scheme, with initial conditions of the internal state vector $X(0) = \begin{bmatrix} 0.1 & 0.1 & 0.1 \end{bmatrix}^T$, random initial conditions for each weight parameter in the interval $[-0.1, 0.1]$ and integral-action gain $K_i = 5$. The outputs of both **DOF** of the plant for this control scheme are shown in Fig 9 for the **CVBP** learning algorithm and Fig 10 for the **CVLM** learning algorithm.

From these graphs we observe that the adaptive neural control schemes are effective for taking the plant outputs to the desired positions when using both learning algorithms for the training of the **CVRNN**.

As it was expected, the control scheme with no integral term presents steady-state error, which is eliminated for the control scheme with integral term. An overshoot can be observed in both control schemes, being smaller for the controller trained with the **CVLM** algorithm.

The controllers trained with the **CVLM** learning algorithm have a better time-response than its **CVBP** counterparts. They also present more oscillations throughout the transient state but, unlike the **CVBP** trained controllers, the oscillations attenuate in the steady state.

The final **MSE** for each of the control schemes trained with both learning algorithms are presented on Table I.

Table I. Final MSE for the CVBP and CVLM learning algorithms applied to the three control schemes

	CVBP	**CVLM**
Scheme 1	6.18×10^{-3}	4.67×10^{-3}
Scheme 2	3.44×10^{-3}	1.64×10^{-3}

From the final **MSE** we observe that both control schemes trained with the **CVLM** learning algorithm have a better performance compared to their training with the **CVBP** learning algorithm. Furthermore we observe that the control scheme where the integral term is added has a better performance than when it is not added.

IV. Conclusions

In this article we proposed three adaptive neural control schemes in the complex domain, applied to a nonlinear, sub-actuated mechanical plant.

A second order Recursive Levenberg-Marquardt learning algorithm was obtained to train the Complex-Valued Recurrent Neural Networks that were used in the control schemes, using diagrammatic methods to derive the gradient terms, and calculating in a recursive way the covariance matrix, needed for the update equations of its weight parameters.

The control schemes shown through this article present good behavior, and the comparative results obtained while using the Complex-Valued Back-Propagation algorithm and the Levenberg-Marquardt algorithm show that the later presents a much better performance than the former.

Acknowledgment

Master Degree student Edmundo Pérez Reynaud would like to thank CONACyT, Mexico, for the student grant received during his studies at the Department of Automatic Control, CINVESTAV-IPN, Mexico (grant number: 364197, holder number: 295620,).

References

[1] A. Hirose. "Complex-Valued Neural Networks." 2nd ed., S.i.C. Intelligence, Springer-Verlag, vol. 400, 2012.

[2] A. Minin, Y. Chistyakov, E. Kholodova, H.G. Zimmermann, A. Knoll. "Complex-Valued Open Recurrent Neural Network for Power Transformer Modeling." *International Journal of Applied Mathematics and Informatics*, vol. 6, no. 1, pp. 41-48, 2012.

[3] L. Ferariu. "Nonlinear System Identification Based on Evolutionary Dynamic Neural Networks." *Proc. Of European Control Conference*, Cambridge, UK, paper no. 432, 2003.

[4] H. Suzuki, T. Yasuno, A. Kuwahara, S. Urushihara, E. Yasuno. "Control characteristics of cooperative conveyance system for multiple mobile robots using complex-valued neural networks." *Proceedings of SICE Annual Conference 2010*, Taipei, Taiwan, pp. 3581-3585, 2010.

[5] T. Fujiwara, Y. Maeda, H. Ito. "Learning of inverse-kinematics for robot using high dimensional neural networks." *Proceedings of SICE Annual Conference 2013*, Nagoya, Japan, pp. 2743-2748, 2013.

[6] E. P. Reynaud, I. S. Baruch. "Identification of dynamical systems using Levenberg-Marquardt learning algorithm for recurrent complex-valued neural networks." *19th International Conference on Circuits, Systems, Communications and Computers*, Zakynthos Island, Greece, 2015. (accepted for presentation).

[7] V. M. Arellano-Quintana, I. S. Baruch. "Identification of Dynamical Systems Using Recurrent Complex-Valued Neural Networks." In *Proc. Of the 18th International Conference on Circuits, Systems, Communications and Computers*, Santorini, Greece, pp. 74-79, 2014.

[8] I. S. Baruch, V. M. Arellano-Quintana. "Identification and Control of Oscillatory Dynamical Systems Using Recurrent Complex-Valued Neural Networks." In *Proc. Of the 18th International Conference on Circuits, Systems, Communications and Computers*, Santorini, Greece, pp. 534-539, 2014.

[9] E. A. Wan, F. Beaufays. "Diagrammatic Methods for Deriving and Relating Temporal Neural Network Algorithms." *Neural Computation*, pp. 182-201, 1996.

[10] I. S. Baruch, C.R. Mariaca-Gaspar. "A Levenberg-Marquardt Learning Applied for Recurrent Neural Identification and Control of Wastewater Treatment Bioprocess." *International Journal of Intelligent Systems*, no. 24, pp.1094-1114, 2009.

[11] S. S. Ge, T. H. Lee, C. J. Harris, "Adaptive Neural Network Control of Robotic Manipulators." C. J. Harris, Ed. UK: World Scientific Publishing Co. Pte. Ltd., 1998, vol. 19.

Dissolved oxygen control strategy for an activated sludge wastewater treatment process

Gabriel Harja, Grigore Vlad and Ioan Nascu

***Abstract*—**Nowadays the optimization of wastewater treatment plants (WWTP) has received great emphasis because of the strict regulations applied for the discharged waters. Many of the plants in this category are manually operated, causing high costs and inefficient operation in order to meet the regulations. The most complex part of wastewater treatment is the activated sludge process where the *sewage* is biologically treated by means of a microorganism culture in the *presence of air* or oxygen. This paper shows a simple way of decreasing the operation costs, together with an increased performance and disturbances rejection using PI controllers on the dissolved oxygen concentration and air pressure generated by the air blower. The controllers are designed and simulated on the mathematical model of the WWTP of Romanofir, Talmaciu.

***Keywords*—**wastewater treatment, PI control, modeling, costs;

I. Introduction

Waste Water Treatment Plants (WWTP) are complex processes which present strong nonlinearities and are exposed to major perturbations. These perturbations are due to the complexity of the physical, chemical and biological phenomena that take place, the influent flow variations and the large variations of the time constants (from few minutes to even days) which follow with these processes. A WWTP is divided in multiple parts according to the specific substances that need to be dealt with: mechanical, chemical and biological treatment processes. In the mechanical treatment stage the water is treated form the physical residue point of view and requires processes like screening and removal of grit and sediments. In the chemical stage some substances are neutralized using different chemical compounds. In the last stage, biological treatment takes place and the typical procedure is to use the activated sludge technology. It requires the reduction or removal of the organic matter present in the waste water using bio-reactions or by making use of a microorganism culture present in the aeration tank of the plant. This is the most complex process that takes place in a WWTP. The activeness of the microorganism culture is strongly related to the quantity of the dissolved oxygen in water controlled by the blowers which bubbles the air in the tank. Oxygen consumption could indicate the condition of the whole biological treatment process. Monitoring and controlling the dissolved oxygen concentration is a convenient way to monitor and control the treatment process. Furthermore, a very low dissolved oxygen concentration in the aeration tank results in biomass die-off, while an excessively high dissolved oxygen level increases energy consumption and may degrade the sludge quality. Thus, optimizing and maintaining the dissolved oxygen set point define important objectives for researchers in WWTP control. Optimization of the dissolved oxygen set point is out of the purpose of this paper. In practice, an appropriate dissolved oxygen set point is determined either manually by experienced operators or automatically through optimization algorithms. In this paper we assume the appropriate set point is given and a control system will be proposed to maintain this set point.

The consumed energy management was applied in the case of many industrial applications as a method of decreasing the costs and raising the profit. However, in the case of WWTP this concept didn't represent a subject of intense study as these kind of plants are not delivering a profitable finite product from the commercial point of view. Simultaneously, the strict regulations of the European Union (European Directive 91/271 "Urban wastewater") imposed in the year 2005 regarding the permitted limits for the organic matter in the effluent water lead to an increase in the energy consumption and also to greater penalties. In this context, an improvement in the WWTP is mandatory for being able to meet the standards of the future.

The transfer of the dissolved oxygen from gaseous to liquid form requires a great quantity of energy, the Activated Sludge Process being therefore the most energy consuming process of the Waste Water Treatment Plants. According to [1], the aeration process of the bioreactor is responsible of approximately 40-50% of the total consumed energy in a WWTP. Some facts need to be considered regarding the level of aeration. For example, an over dosage of aeration is unwanted because it brings increased costs and just little or even none gain in the quality of water. Using the blowers in manual operation at constant flow rates in the periods of reduced wastewater intake will produce a loss of energy.

Among the main goals of a WWTP, as stated in [2], one can number the followings: (i) to meet the requirements for discharged water, (ii) to keep biological sustainability of activated sludge in the treatment plant, (iii) to reduce the operational costs (especially the ones related to energy and

The research was developed under the PCCA CASEAU Project nr. 274/09.09.2014.

G. Harja and I. Nascu are from Technical University of Cluj-Napoca, Department of Automation, Romania (e-mail: Gabriel.Harja@ aut.utcluj.ro, Ioan.Nascu@aut.utcluj.ro).

G. Vlad, is from ICPE Bistrita, Romania (e-mail: gvlad@icpebn.ro).

chemicals used), (iv) to minimize the load of untreated sewage discharged to the receiving waters.

For decades the PID controller has been the most common control algorithm because of its evident advantages: having a simple and clear structure and also being adequate for most control loops. K.J. Astrom states in one of his articles [3] that PID controllers are used in more than 90% of the control loops in the industrial applications. The emphasis in this paper falls on the DO concentration in the WWTP of Romanofir, Talmaciu for keeping the microorganism culture at the right level of activity and fulfilling the discharged water regulations. It is shown that the manual operation can be replaced by the popular PI controller, tuned using a model of the WWTP, and results in lowering the costs and providing better performance.

The paper is organized as follows: the description of the WWTM of Romanofir and the modeling results are presented in the next section. Section III describes the control methodologies that have been used in this work. The results and simulations of the closed loop control are described in Section IV while last section summarizes the conclusions.

II. Case Study

A. Description of the Romanofir WWTP

In a wastewater treatment plant the system includes multiple stages for removing the unwanted substances from residual water. The plant from Romanofir, Talmaciu is dealing with the residual water coming from the process of painting cotton, from a factory that processes milk and also residual domestic wastewater. In a prior chemical stage the industrial residual wastewater is treated with sulfuric acid and fume in order to neutralize the chemical substances. The next stage of biological treatment is indispensable because the colloidal and dissolved carbonaceous organic matter does not meet the admissible values. The outlet of the first stage is combined with residual domestic wastewater and pumped in the biological process whose configuration is schematically presented in Figure 1.

The biological treatment diagram consists of: homogenization compartment, aerated bioreactor, secondary settler, open channel for water flow rate measurement, sludge drying stand.

The biological treatment stage is a complex process that requires a microorganism population that feeds with the colloidal and dissolved carbonaceous organic matter from the wastewater and break down organic and biodegradable compound. Then the minerals resulted are allowed to settle down.

The maximum water intake is 1000 m^3 and enters the first compartment of the tank, the homogenization tank, in order to smooth the wastewater flow variations. In the second compartment, the biological treatment takes place. The secondary settler is making use of gravity for separating the clear water and the sludge. A part of the sludge is entering the sludge drying stand and then exits the plant and another part is recycled using sludge pumps.

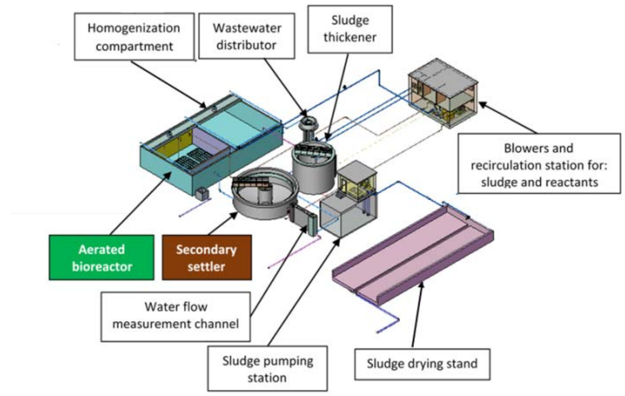

Figure 1. Biological treatment stage

In the biological treatment stage the main goal is to control the activity of the microorganisms so the reaction sustenance level is maintained. This is made in two ways. The first one is by increasing or decreasing the dissolved oxygen concentration in the aeration section and the second is by recirculation of the activated sludge from the settler to the aeration tank. The biological treatment tank contains an aeration network composed of disk diffusers with elastic membranes with the air being provided by a blower. The same blower also delivers air for maintaining wastewater mixing in the homogenization tank and for two air-lift pumps providing both aeration tank inflow and recycled sludge transportation. At the moment, the air flow that enters the diffusers is manually controlled with a valve.

B. Modeling the biological process

Physical (hydrodynamic and mass transfer), chemical (direct oxidation of inorganic compounds) and biochemical (dependant on the nature and metabolism of the microorganisms) factors influence the biological treatment process. Consequently, a proper correlation between these parameters is required in order to operate the process at maximum efficiency point. For the correlation, measurements are required to deliver information regarding the aerated bioreactor, wastewater (composition) and activated sludge (age, biological state and composition).

In Fig. 2 we present a simplified version of the biological treatment stage, where, in principle the process is constituted of an aerated bioreactor and a settler.

The best known models for the biological treatment process are the activated sludge family models (ASMs) developed by the International Water Association (IWA) [4]. However for control purposes proposed in this paper, a complete and detailed description of the physical, chemical and biochemical processes within the biological treatment stage model is not necessary. A set of simplifying assumptions will be thus considered: the aeration tank is continuously stirred, in the settler there are no bio reactions, the activated sludge being the only component recycled to the aerated bioreactor, the concentrations of oxygen and substrate are neglected along the recycling path, the output flow from the aerated bioreactor is equal to the sum between the output flow of the settler and the recycled activated sludge flow.

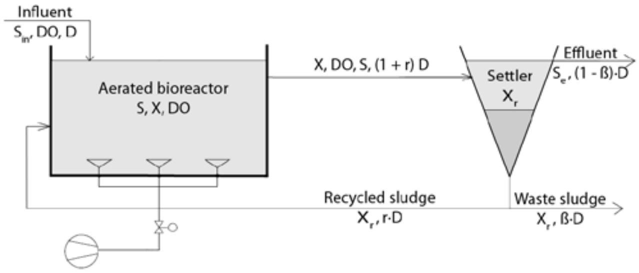

Figure 2. Biological treatment stage

In these conditions the mathematical model of the biological treatment process will be composed of a set of four non-linear differential equations, three equations for the aerated bioreactor and one for the settler.[5][6].

The first equation is related to the material balance of the activated sludge in the aerated bioreactor:

$$\frac{dX(t)}{dt} = \mu(t)X(t) - D(t)(1+r)X(t) + rD(t)X_r(t) \quad (1)$$

The second one describes the mass balance of the substrate in the aerated bioreactor:

$$\frac{dS(t)}{dt} = -\frac{\mu(t)}{Y}X(t) - D(t)(1+r)S(t) + D(t)S_{in} \quad (2)$$

The third equation is related to the mass balance of the dissolved oxygen in the aerated bioreactor:

$$\begin{aligned}\frac{dDO(t)}{dt} &= -K_0\frac{\mu(t)}{Y}X(t) - D(t)(1+r)DO(t) + \\ &+ D(t)DO_{in} + \alpha W[DO_{max} - DO(t)]\end{aligned} \quad (3)$$

The last of the four equations is related to the balance of the activated sludge in the settling tank:

$$\frac{dX_r(t)}{dt} = D(t)(1+r)X(t) - D(t)(\beta + r)X_r(t) \quad (4)$$

In the above equations, the following notations were used: $X(t)$, $S(t)$, $DO(t)$ - biomass, substrate and dissolved oxygen concentrations in the aerated bioreactor, $X_r(t)$ - recycled biomass concentration, $D(t)$ - dilution rate (the ratio of influent flow to the aerated bioreactor's volume), S_{in} and DO_{in} - substrate and dissolved oxygen concentrations in the influent, W - aeration rate, DO_{max} - maximum dissolved oxygen concentration, Y - biomass yield factor, α - oxygen transfer rate, K_0 - model constant, r - the ratio of recycled sludge flow to influent flow, β - the ratio of waste flow to influent flow. The biomass growth rate μ – is a complex function of many physical, chemical and biological factors. Many different analytical laws have been suggested for modelling this parameter. The most common one is the Monod law [7] but here we assume that μ depends on substrate, dissolved oxygen concentrations and several kinetic parameters (Olsson model[8]):

$$\mu = \mu_{max}\frac{S(t)}{K_S + S(t)} + \frac{DO(t)}{K_{DO} + DO(t)} \quad (5)$$

where μ_{max} represents the maximum specific growth rate, K_S - affinity constant, expressing the dependency of the degradation rate on the concentration of pollutant S and K_{DO} - saturation constant.

The model parameters were selected such that the model best fits the experimental data collected at the waste water treatment plant. These are: r=0.8, μ_{max}=0.07, Y=0.54, K_0=0.46, β=0.015, DO_{max}=10 (mg/l), α=0.017.

C. *Modeling the blower and air pipes*

Considering the final goal of this paper, that of designing good control strategy for the plant presented, it is required a comprehensive and well tuned model. The most used controlled variable for meeting the requirements for a WWTP discharged water is the concentration of dissolved oxygen (DO). According to [9], where a RGA analysis is made and the dependencies between manipulated and controlled variables are revealed, the aeration flow rate is considered as the manipulated variable having the most influence on the dissolved oxygen concentration as controlled variable. Thus, in this paper the activated sludge model will incorporate also the aeration model by introducing the calculation of valve positioning, blower speed and pressure losses over the pipes.

In the current state, a manual valve is controlling the air flow rate that supplies the aeration tank. Therefore, an improvement is required to be done in the proposed simulation model of the physical setup by replacing the manual valve with a control valve that is going to be controlled electrically. The control valve chosen for this purpose is a knife gate valves that is driven by an electric motor. The input of the valve is the percentage from the total opening.

The blower provides the airflow for the aeration system. For this paper the blower is modeled such as the output of the blower is computed as a percentage of the nominal flow rate. In the physical setups the blower is usually controlled by an inverter which also introduces a rate limitation avoiding shocks on the blower motor, this aspect being modeled as well.

The pressure system is presented in Fig. 3 and is modeled based on the equilibrium equation of flows described in (6):

$$\frac{dp(t)}{dt} = \frac{p(t)}{V}\left(F_a(t) - F_{e_i}(t)\right) \quad (6)$$

where V is the total volume of the pipes, $p(t)$ is the actual value of the pressure, F_a is the flow rate from the blower and F_{e_i} is the total effluent flow. The former consists of summing up all the flows needed for aeration, homogenization and for air-lift pumps, each being computed using the nonlinear flow equation:

$$F_{e_i} = k_i\sqrt{p(p - p_c)} \quad (7)$$

where p_c is the downstream pressure, in this case the atmospheric pressure, and k_i is a constant determined by the pneumatic resistance of the discharge flow course. These constants were determined experimentally for steady state conditions. Note that k_1 embodies also the pneumatic resistance of the control valve fully opened. Even though the different valve positions are defining a nonlinear behavior of k_1, it was used its linear approximation for the sake of simplicity. So, it is multiplied by a factor that represents the valve degree of opening when 1 if the fully opened state.

ISBN: 978-1-61804-321-4

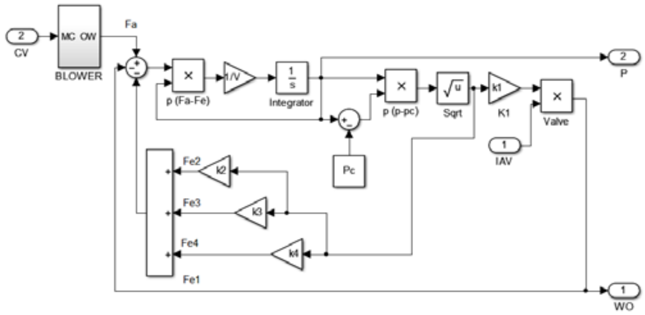

Figure 3. Simulink model of the blower and piping

III. Control Methodologies

This section describes the control strategy that was used in this work. Control techniques in current use in wastewater treatment plants include simple PLC-techniques, time control, manual control, rules of thumb or simple proportional-integral-derivative (PID) control. The PID controller is well known and is used on large scale in control systems and has three major components as proportional, integral and derivative. Though, PI controller is sufficient in the purpose of this paper. The algorithm is described by the equation that follows:

$$u(t) = K\left(e(t) + \frac{1}{T_i}\int_0^t e(t)dt\right) \tag{8}$$

where u is the control signal, e is the error (the difference between setpoint and process output), K is the proportional gain and T_i is the integral time.

Reminding the final goal of the paper, that to assure a controlled DO concentration, some aspects need to be considered. It is a common practice in industry to tune the PID parameters by experience through trial and error experiments. In this case due to the complex structure, interaction between various subsystems and process constraints (saturation and rate limitations) the discussed approach will result in poor performances of the plant. Thus, the controller design for this paper was performed using a linearized process model and the simulation data around an operating point.

It is universaly accepted that every pressure systems is required to have a safety valve that prevents the pressure to increase above a maximum imposed limit. When working with a blower at constant speed, the air pressure in the pipes will vary according to the control valve position. Opening the valve will produce a pressure drop and closing it will result in an increase of pressure. If the pressure reaches the safety valve limit will cause it to open and loose all the pressure in the pipes. In this case the human factor will need to intervene to close back the safety valve.

The DO concentration is controlled by using the control valve to manipulate the total air flow reaching the aeration tank through diffusers. It is obvious that the pressure fluctuations act as disturbances on the output air flow. In order to reject these disturbances a second control loop is necessary to stabilize the air pressure, especially in our case where four different consumers are supplied from the same source of pressure. Other works also emphasis the use of air pressure control loop as in [9]. This section presents two control loops for DO concentration and air pressure that are illustrated in the form of Simulink block diagram in Fig. 4.

The AIR MODEL block represents the Simulink model of the blower and piping (Fig. 3), the WWTP block represents the biological treatment process Simulink model (ec. 1-5) and the AIR VALVE block represents the air valve and positioner model.

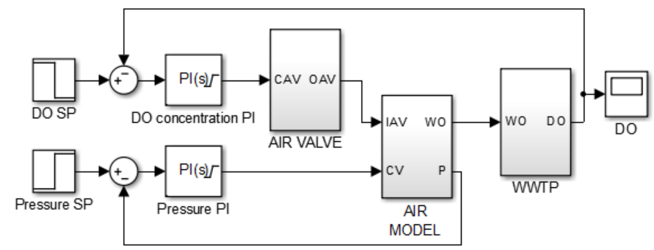

Figure 4. Control loops for pressure and DO

A. Pressure control

Tuning the parameters of the PI controller is straight forward by imposing the settling time of the desired closed loop system dynamics. Considering the time required for the motor to drive the blower at a constant speed (settling time) having a value of 2.5 sec [11] will result in a time constant of 0.8 sec. Linearizing the equation (6), the time constant from the blower flow to the pressure in the volume of the pipes can be determined. For the operating point of 80% of nominal blower speed this time constant is 2.5 sec.

Moreover the motor is controlled through an inverter that is having a ramp-up of 40 seconds. This means that reaching the maximum speed of the motor from 0 initial conditions requires 40 sec. This is a frequent way to control high power motors. It is used to prevent shocks and damage and it is acting as a rate limiter. It is evident that a small settling time imposed on the closed loop system will produce an aggressive controller and will bring the inverter in limitation, thus, the settling time is carefully chosen, larger than the ramp-up time.

B. Control of the DO

As in the case of pressure control where some limitations occurred so is in the DO concentration case. The control of the DO is done by manipulating the flow of air that enters the aeration zone by means of control valve. The control valve has also some limitations in its dynamics. Being a positioning system it has an opening time from 0 to 100% given by the datasheet. Electric multi-turn actuators are used for the automation of knife gate valves. The actuator runs at nominal output speed up to the set tripping point. The time interval to moves the valve from one to other of the two end positions OPEN and CLOSED is 50 seconds. But this is not so important because large inertia in the DO dynamics. The open loop settling time for DO, in WWTP Simulink block is about 1 hour. Therefore, the time response of the closed loop system should be carefully designed to match with the valve opening/closing rate limitations.

The two control loops presented are linked together by the fact that the manipulated variable in the DO control loop acts as a disturbance in the air pressure control loop. By changing the position of the valve, the air pressure modifies and the controller attempts to reject the disturbance. The time constant of the pressure control loop should be kept considerably faster in order to properly reject these disturbances.

IV. Simulations And Results

Based on the model aforementioned in this paper, process model identifications were performed for both DO and air pressure model. Then the resulted data was used to tune the PI parameters. For the DO model a closed loop with a settling time of 0.5 hour was imposed, which means a time constant of 0.25 h and PI controller parameters $K_p = 0.2, T_i = 0.28$. Usually, in the WWTP simulations the time is measured in days because of the large time constants of the process. This work also presents simulations where the time constants are of the order of seconds (air pressure control). Thus, a compromise was made and the time was chosen to be measured in hours.

From the analysis of the measurements has been concluded that the plant is operating with air excess and a large DO concentration (about 6 mg/l), based on operators reasoning that in this way the plant will tackle the variations of the organic charge and of the influent flow rate. For the first simulation, the inputs to the system have been considered constants and equal to the mean values of the measurements: S_{in} = 600mg/l, D = 0.7h^{-1}, DO_{in} = 0.5mg/l. Also the considered initial conditions are W = 270m^3/h for the air flow rate and the resulted value for DO = 6.4mg/l. In Fig. 5 are presented the simulation results for a step in the DO reference form 6.4 to 3 mg/l at time 0.2 h and a step from 3 to 1.3 mg/l at time 1.2 h. This situation happens on rare occasions because of the large variation but this hypothetical example was given to show the stability and good behavior of the DO control loop even in such changes of the reference. As can be seen the response for the two steps has no over or undershoot but the closed loop settling time is changing as the process gets to different operating conditions. The control signal is also relevant as it can be seen that the control valve doesn't suffer shocks and doesn't enter in its limitations.

From the analysis of the measurements has been concluded that the plant is operating with air excess and a large DO concentration (about 6 mg/l), based on operators reasoning that in this way the plant will tackle the variations of the organic charge and of the influent flow rate. For the first simulation, the inputs to the system have been considered constants and equal to the mean values of the measurements: S_{in} = 600mg/l, D = 0.7h^{-1}, DO_{in} = 0.5mg/l. Also the considered initial conditions are W = 270m^3/h for the air flow rate and the resulted value for DO = 6.4mg/l. In Fig. 5 are presented the simulation results for a step in the DO reference form 6.4 to 3 mg/l at time 0.2 h and a step from 3 to 1.3 mg/l at time 1.2 h. This situation happens on rare occasions because of the large variation but this hypothetical example was given to show the stability and good behavior of the DO control loop even in such changes of the reference. As can be seen the response for the two steps has no over or undershoot but the closed loop settling time is changing as the process gets to different operating conditions. The control signal is also relevant as it can be seen that the control valve doesn't suffer shocks and doesn't enter in its limitations.

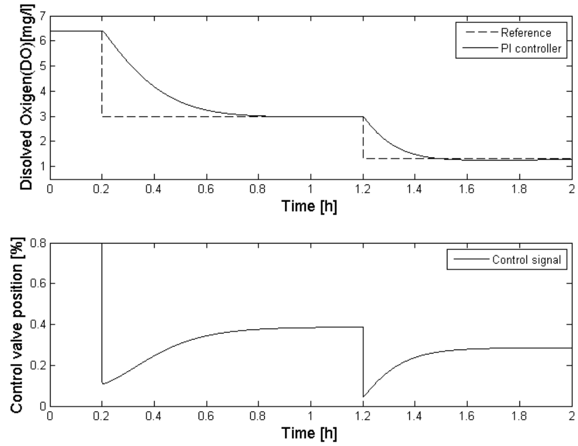

Figure 5. Evolution of the DO and control signal

The secondary control loop is tuned based on the air pressure model of the blower and piping for an imposed settling time of 0.01 hours which is comparable with the blower ramp-up time, so in most cases the saturation of the blower control signal is prevented. The imposed settling time is chosen to be smaller than the time response of the control valve (composed of valve and positioning system) which will help to reject pressure disturbances caused by the control valve without large changes in the pressure. The resulted PI parameters are the following: $K_p = 6.349$, $T_i = 0.0008$. Fig. 6 (up) shows how the secondary control loop is rejecting the disturbances of pressure produced by the air control valve position. The pressure is kept near the setpoint with a small variation at the moment of abrupt closure of the valve. The air piping design is favorable to prevent high pressure values because of the multiple pipes fed by the blower. In the moment of valve closing, the pipes for the air-lift pumps and for homogenization zone are receiving the excess flow produced by the blower. This prevents the pressure to increase rapidly and significantly. The summed output flow used for the homogenization zone and air-lift pumps is depicted in Fig.6 (middle), where an increased flow appears until the pressure is stabilized back to the setpoint.

As seen above, the secondary control loop is maintaining the pressure at 1.32 bar, excepting the moment of the sudden and significant change in the DO reference. Fig. 6 (down) shows how the air flow entering the aeration tank follows, at constant pressure, the same signal trajectory as the control valve. As can be seen, the air flow doesn't reach the saturation zone because the blower limitation is avoided.

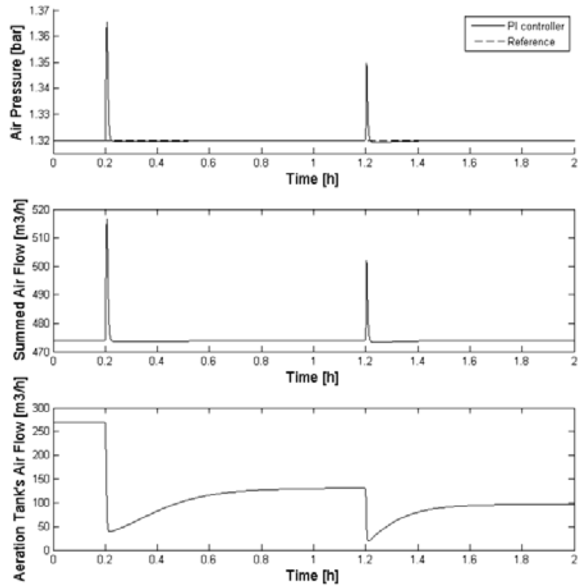

Figure 6. Evolution of the Air Pressure (up); Evolution of the summed Air Flows: Air-Lift pumps and homogenization tank (middle); Evolution of the Air Flow in the aeration tank (down)

The above simulation was made considering a constant value of 600 mg/l for S_{in}. As initial operating point for the following simulations was chose W = 130.5 m^3/h and different values for the organic load (S_{in}: 400 and 800mg/l). Because of the modified S_{in} the initial DO concentration changes. Fig. 7 shows how DO concentration evolves when applying a setpoint of 3mg/l for the different values of the influent organic load (S_{in}). It can be observed that the DO response signal keeps the same shape but the time response changes as the dynamics of the biological treatment process modifies according to the operating point.

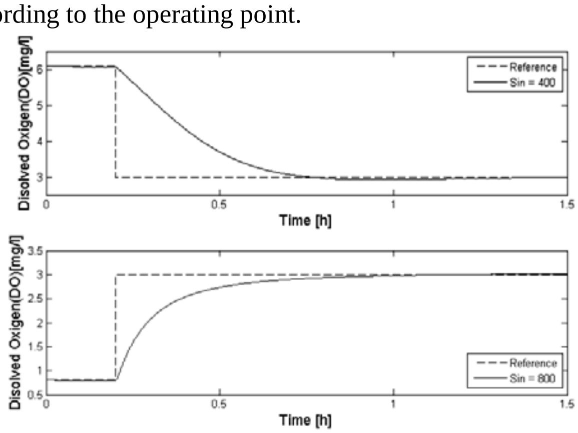

Figure 7. Evolution of the DO for a step to 3mg/l with different values for S_{in}

The validation of the controller is done by applying real measured data (as in Fig. 8) on the influent organic load (S_{in}) (middle) and dilution (D) (down) thus, simulating the most usual perturbations that can occur in a WWTP. Fig.8 (up) presents the DO concentration for a comparison between the plant with and without controller under the action of perturbations presented in the same figure. Process without controller oscillates ±1mg/l around the setpoint while adding the controller lowers the oscillations below ±0.1mg/l around the setpoint. There is a visibly better performance gained due to the use of the simple PI controller.

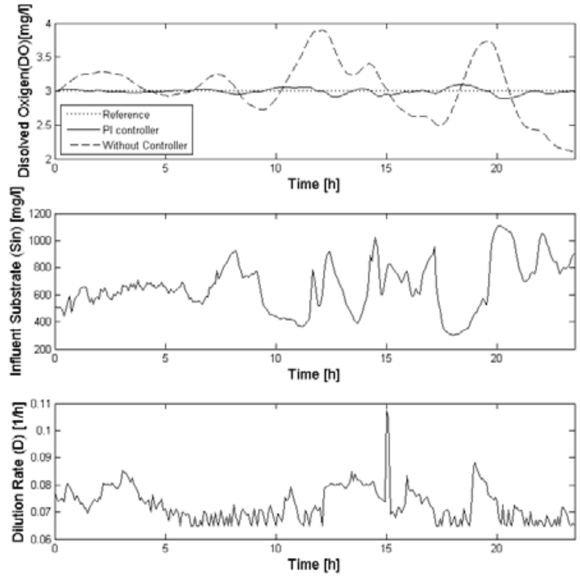

Figure 8. Comparison between plant with controller and without controller when maintaining the setpoint under action of D and S_{in} real perturbations.

V. Conclusion

The wastewater treatment is a complex process that requires several stages in order to meet the regulations for the discharged water. The most complex stage is the activated sludge process that is nonlinear and is subject of many perturbations. Many WWTP are still operated manually causing large operational costs.

The purpose of this paper was to demonstrate that a well tuned model of the WWTP can lead to very simple control strategies like the well known PI controller. The controller was used to maintain the DO concentration on the specified reference and to reject disturbances that appear in the system by manipulating the flow of air that enters in the aeration tank. In manual operation the blower is working on constant speed providing excess of air in order to meet the regulations for the discharged water and tackle the variations of the influent organic load and flow rate. By introducing the automated control of the DO, the blower's speed is allowed to be lowered when the operating conditions of the WWTP permits. As a result the total costs of the plant are reduced.

The blowers operate under a predictable set of laws concerning speed, power and pressure. In accordance with affinity laws, flow is proportional to motor speed; and power is proportional to the cube of motor speed. This means that already minimal reductions in blower air flow can provide savings in energy consumption. Reducing the blower air flow by 10% decreases the power requirement by 27%.

It was also emphasized that a secondary PI control loop for the air pressure helps to maintain the desired pressure in the piping regardless of the control valve position so a more precise control can be achieved avoiding the effects of the pressure disturbances.

REFERENCES

[1] M. Henderson, "Energy Reduction Methods in the Aeration Process at Perth Waste Water Treatment Plant.", *University of Strathclyde, Renewable Energy Systems and the Environment MSc Individual Theses, 2001-2002*

[2] M. A. Brdys, M. Grochowski, T. Gminski, K. Konarczak and M. Drewa, "Hierarchical predictive control of integrated wastewater treatment systems.", *Control Engineering Practice*, 16 (6), 751-767, 2008.

[3] K. J. Astrom and T. Hagglund, "The future of PID control", *Control Engineering Practice*, Volume 9, Issue 11, pp. 1163-1175, 2001.

[4] M. Henze, W. Gujer, T. Mino and M. Van Loosdrecht, "Activated Sludge Models Asm1, Asm2, Asm2d And Asm3." *Padstow: Iwa Task Group On Mathematical Modelling For Design And Operation Of Biological Wastewater Treatment, 2000.*

[5] F. Nejjari, B. Dahhou, A. Benhammou and G. Roux, "Non-Linear Multivariable Adaptive Control." *International Journal Of Adaptive Control And Signal Processing* 347-365, 1999.

[6] G. Vlad, R. Crisan, B. Muresan, I. Nascu and C. Darab, "Development and application of a predictive adaptive controller to a wastewater treatment process." *Automation Quality and Testing Robotics (AQTR), 2010 IEEE International Conference on (Volume:1).* Cluj-Napoca: IEEE. 1-6. doi:10.1109/AQTR.2010.5520886.

[7] D. Herbert, "Some principles of continuous culture." *Recent Progress in Microbiology* 381-396, 1958.

[8] G. Olsson, "State of the art in sewage treatment plant control." *A.I.Ch.E. Symp. Ser. 72* 52 – 76, 1976.

[9] I. Muntean, R. Both, R. Crisan and I. Nascu, "RGA Analysis and Decentralized Control for a Waste Water Treatment Plant."

[10] S. Kestel, T. Stahl and M. Gray, "Process Simulator Evaluates Blower and Valve Control Strategies for WWTP Aeration." http://www.airbestpractices.com/

[11] T. Giampaolo, "Compressor Handbook: Principles and Practice." The Fairmont Press, 2013, ISBN-13: 978-1439815717

Miniaturized Flexible CPW-Microstrip Antenna Array for Microwave Radiometry

Amal Afyf, Larbi Bellarbi, Fatima Riouch Abdelhamid Errachid, and M.Adel Sennouni

***Abstract*—** A novel flexible slotted antenna array printed on a Kapton Polyimide substrate for microwave radiometer is proposed. The design consists of two element coupled with a T-junction using a co-planar waveguide (CPW) feed to transmit power to the array patches. The proposed antenna is very suitable for breast cancer detection using microwave radiometer also for wearable applications due to its miniaturized size (53X50mm²) and its low profile, low weight and very thin substrate, which is enabling a certain level of flexibility and a good robustness against different external influences. The developed antenna array can operate in S-Band and provides a bandwidth of 480MHz around operatinf frequency of 3 GHz with a total gain of about 6dBi. The antenna array prototype has been built and carried out using both CST Microwave Studio and HFSS Softwares.

***Keywords*—**Wide-Band, Flexible Antenna, Antenna Array, Kapton Substrate, Microwave Radiometer, Co-planar Waveguide, Breast Cancer Detection, CST Microwave Studio, HFSS.

I. Introduction

Recent years have witnessed a great deal of interest from both academia and industry in the field of flexible electronics. In fact, this study tops the pyramid of research priorities requested by many national research agencies. According to market analysis, the revenue of flexible electronics is estimated to be 30 billion USD in 2017 and over 300 billion USD in 2028 [1]. Their light weight, low-cost manufacturing, ease of fabrication, and the availability of inexpensive flexible substrates (i.e.: papers, textiles, and plastics) make flexible electronics an appealing candidate for the next generation of consumer electronics [2]. Moreover, recent developments in miniaturized and flexible energy storage and self-powered wireless components paved the road for the commercialization of such systems [3]. Consistently, flexible antennas operating in specific frequency bands to provide wireless connectivity are highly demanded by today's information oriented society.

Breast cancer is a significant health issue affects one in every seven women [4]. Early diagnosis and treatment are the hot keys to survive from breast cancer. The present "golden" standard screening technology for detecting early-stage breast cancer is X-rays mammography. However, it has several limitations [5-12].There is a need for complementary, safe, and reasonably priced method [13]. Microwave Thermography for breast cancer detection has been introduced as a complementary non-invasive method for breast cancer detection. Where the receiving antenna is one of the most crucial components in a microwave radiometer and based on the above references, we propose a flexible antenna array with two elements, having I-shaped slots and a tuning stub which is designed as an RF receiver. This paper is organized as followed: Section II and III respectively introduce, Design Procedures and Simulation Results for both elementary and antenna array. Conclusion is shown in Section IV. As described in subsequent sections, the optimization of antenna structures was carried out by simulations with CST Microwave Studio [14], and Ansoft HFSS [15].

A. Afyf and L. Bellarbi are with Higher National School of Technical Education (ENSET)/ Rabat/ Morocco.
Riouch is with National Institute of Post and Telecommunications (INPT))/ Rabat/ Morocco.
M.A. Sennouni is with LITEN Laboratory of FST-Settat/Morocco.
A. Errachid is with Institute of Analytic Sciences (ISA) Lyon University /France.

II. Elementary Antenna

A. Antenna Design

The elementary antenna is a thin rectangular patch printed on a Kapton Polyimide substrate having a thickness of HS=0.125mm, a dielectric constant of εr=3.4 with a tangent loss of 0.02. To preserve the flexibility of the antenna, the rectangular radiator with two symmetrical I-slots is feeded by a coplanar waveguide transmission line ensuring 100Ω characteristic impedance. Figure.1 presents the geometry shape of the proposed design.

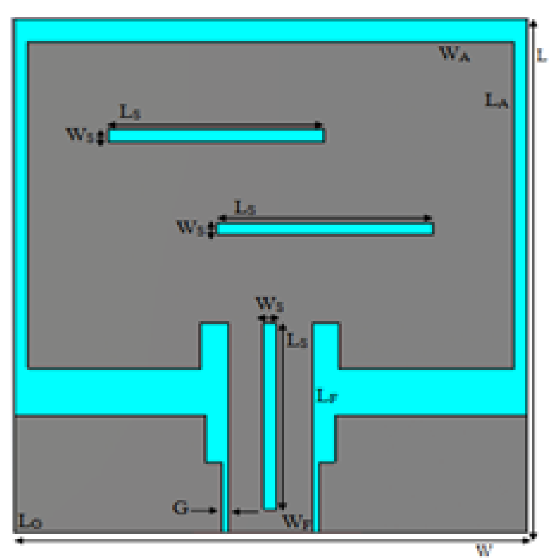

Figure 1. The elementary flexible CPW antenna

ISBN: 978-1-61804-321-4

Hence the main goal is to develop a receiving antenna with good performances working in S-band at 3 GHz which can provides a good penetration into the breast tissue. Then to achieve the goal, several optimisation processes were applied by using an optimization solver in CST Microwave Studio. Table 1 below presents the various optimized parameters of the proposed elementary antenna.

TABLE. 1 PHYSICALS DIMENSIONS OF THE ELEMENTARY ANTENNA

Parameters	**Values (mm)**	**Parameters**	**Values (mm)**
W	15	$\mathbf{L_S}$	9
L	20	$\mathbf{W_S}$	0.5
$\mathbf{W_A}$	14	$\mathbf{H_S}$	0.125
$\mathbf{L_A}$	12	$\mathbf{T_M}$	0.035
$\mathbf{L_G}$	5	**G**	0.25
$\mathbf{W_F}$	3.122	$\mathbf{L_F}$	7

B. Simulation Results

It is reported in literature that abnormal both tissues and it surrounding area are warmer than normal's [7], which mean a self radiation with a weak power. This report overviews the design and optimization of a novel microwave receiver antenna which must serve as an element in a radiometry system for early breast cancer detection. According to Nyquiest low (Equation.1) and for getting the emitted difference of temperature generated by a tissue located at a depth of about 3cm, the microwave radiometer can indicate a previous anomaly at operating frequency around 3GHz [8].

$$T = \frac{P}{K \times \Delta F} \qquad (1)$$

Where P is the power available at antenna port, K is the Boltzman constant, T is the tissue temperature and ΔF is the antenna bandwidth. As shown in Figures 2 and 3, the return loss of the elementary antenna is about -22.58dB with a large bandwidth of 480 MHz at center frequency of 3.09 GHz, which means a good matching input impedance is achieved at the operating frequency, also the VSWR obtained, for 3GHz it's 1.16 (less than 2), which is within the recommended range. Then the obtained result indicates that the antenna is well matched at 3.09GHz and a maximum possible amount of energy is absorbed at the input terminal with a minimum reflected power.

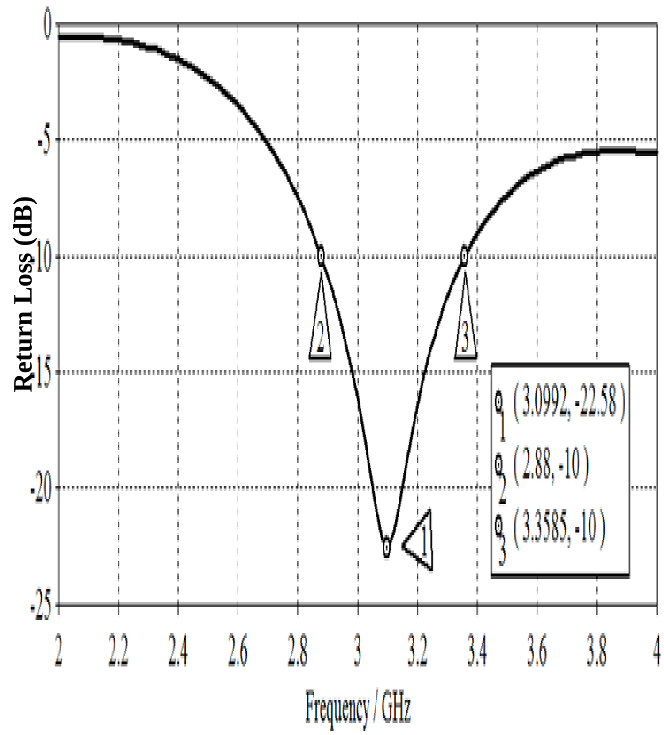

Figure 2. Simulated Return Loss of the elementary antenna

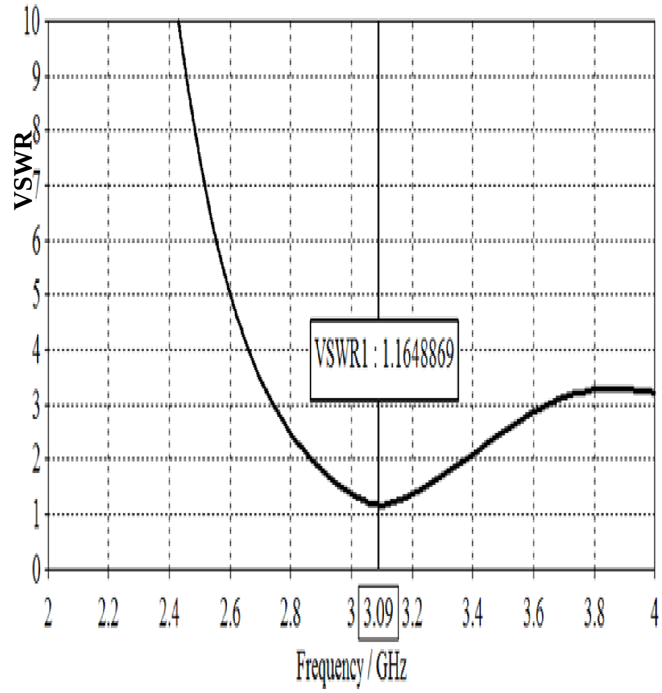

Figure 3. Simulated VSWR of the elementary antenna

Fig.4 presents the 3D-radiation pattern with the structure below at 3.1GHz. Further Fig.5 depicts the gain versus frequency that is almost around 3 GHz with a peak gain of about 1dB which is not sufficient for microwave thermography using microwave radiometery.

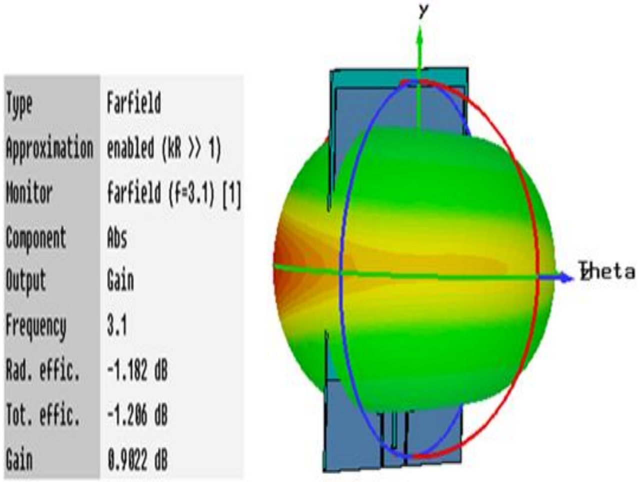

Figure 4. 3D radiation pattern @3GHz

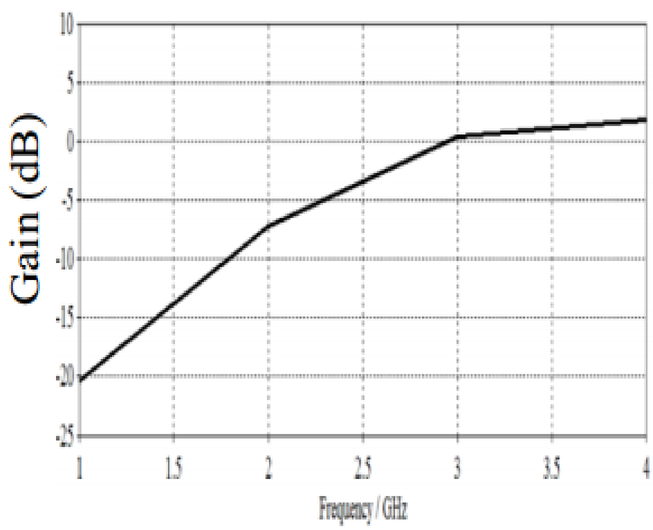

Figure 5. Antenna gain versus frequency of the elementary antenna

III. TWO-ELEMENT ANTENNA ARRAY

A. Design process

In order to increase the antenna gain and directivity by preserving the operating frequency in S-band at 3 GHz, we have started from the elementary antenna optimized before and we have modeled an array of two-Element printed on the top layer of the same substrate used for the elementary antenna presented above, with the arrangement shown in Fig.6. We have chosen this arrangement to minimize the effects of coupling and the generation of higher modes, also to reduce the array occupation area. A T-power junction has been used to transmit power to the array elements, in addition the CPW feed line with a characteristic impedance of 50 Ω is also used to excite the global antenna array. Further a tuning stub with an optimized dimensions and position is added to the CPW feed to improve the antenna array performances. The proposed antenna array has an overall size of about 5.3x5 cm^2 with the geometry along with the parameters of the antenna array which are shown in Fig.6(c).

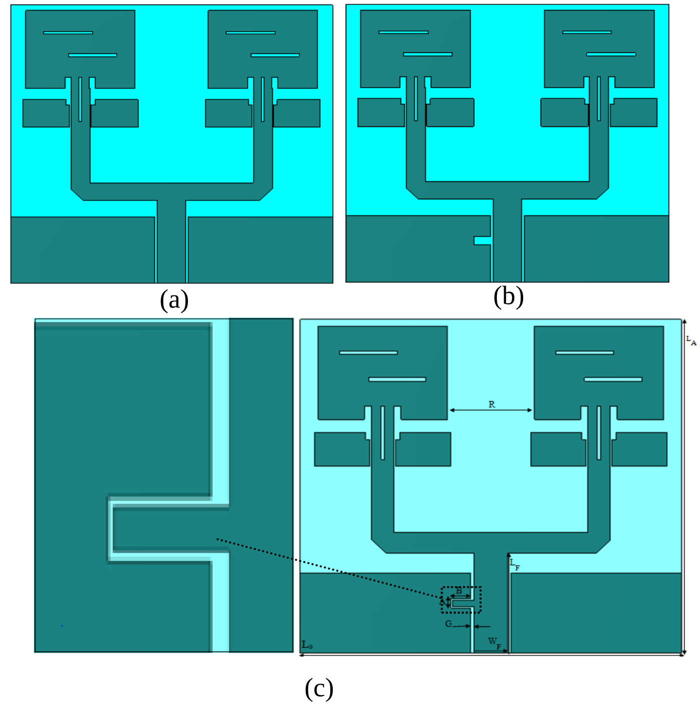

Figure 6. Proposed antenna array (a) with simple ground, (b)with shaped ground, and (c) with a tuning stub. (G= 0.15mm, W_A= 53mm, L_A= 50mm, R=10mm, $W_F \times L_F$=4.8×12.5mm, A×B=2×4mm)

B. Simulation Results and Discussion

To show the effect of the tuning stub, a comparative study has been applied. It is seen that the tuning stub can shift the operating frequency from 3.4 GHz to 3 GHz providing a good impedance matching for the antenna array with a return loss of about −35 dB at the operating frequency of 3GHz and an important bandwidth of 480MHz which is from 2.72 GHz to 3.2 GHz. Fig. 7 shows the simulated return loss of the proposed design.

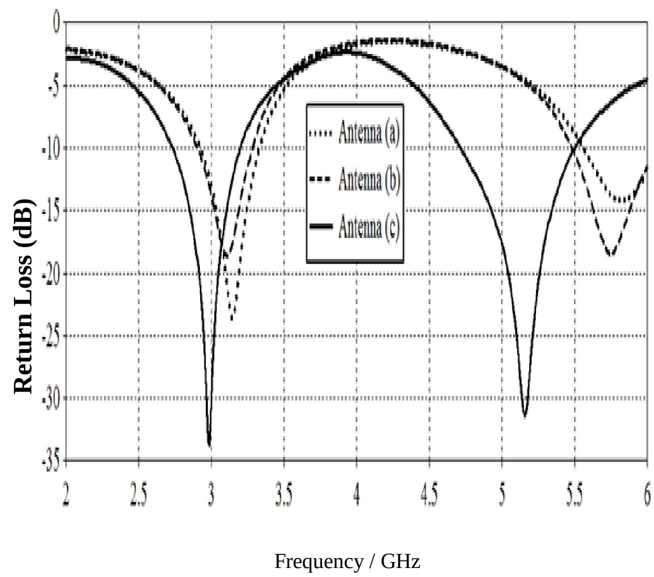

Figure 7. Return Loss vs. Frequency for the three antenna structures: (a), (b), and (c)

We have applied another method to prove the antenna array results by using the FEM (Finite Element Method) introduced by HFSS software. Figures 8 and 9 shows the comparison results with the two methods. The results show that the proposed antenna array is operating at the same frequency range (S -band, 2-4GHz) for both softwars with a good input matching and approximately the same bandwidth.

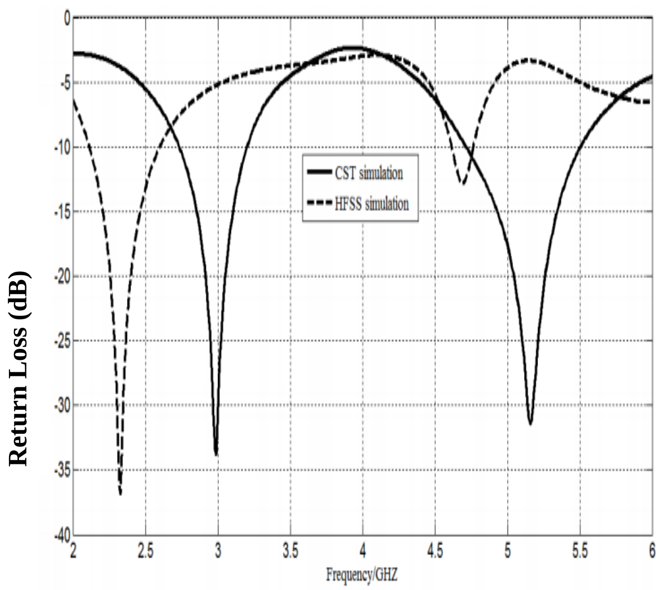

Figure 8. The return loss of the proposed antenna array with CST&HFSS

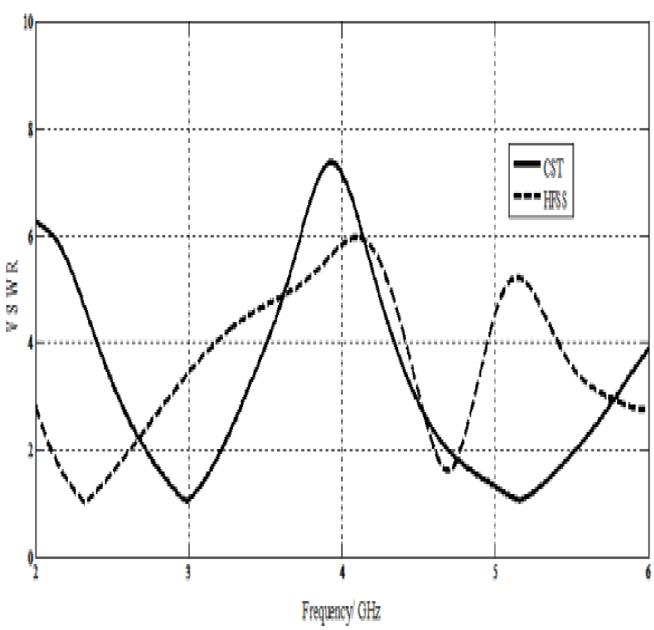

Figure 9. VSWR of the proposed antenna array with CST&HFSS

The radiation pattern taken for the far-field at 3GHz is indicated in Figures 10 and 11. The results indicate that the antenna array provides a directional behavior in E-plan (for PHY=0°) and omnidirectional's behavior in H-plan (for THETA=0°). Furthermore Fig.12 presents the normalized gain against frequency of the developed antenna array. The results show that the design provides an important gain that is almost around 5 dB in the frequency range below 2.7 GHz. However at the operating frequency of 3 GHz the design exhibits a gain of about 5.3 dB which is perfectly sufficient and suitable for microwave thermography.

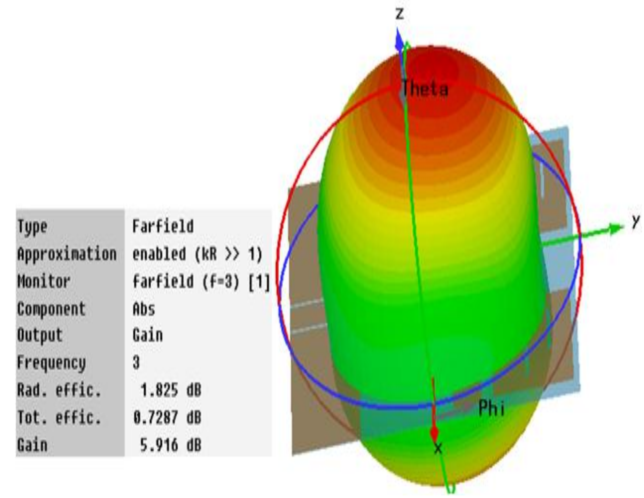

Figure 10. 3D radiation pattern for the antennas array @ 3GHz

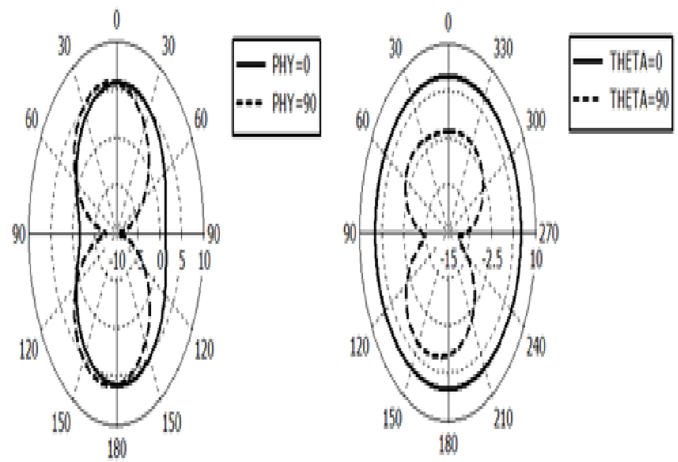

Figure 11. 2D polar radiation pattern @ 3GHz for the antenna array; (a) E-Plan, and (b) H-Plan.

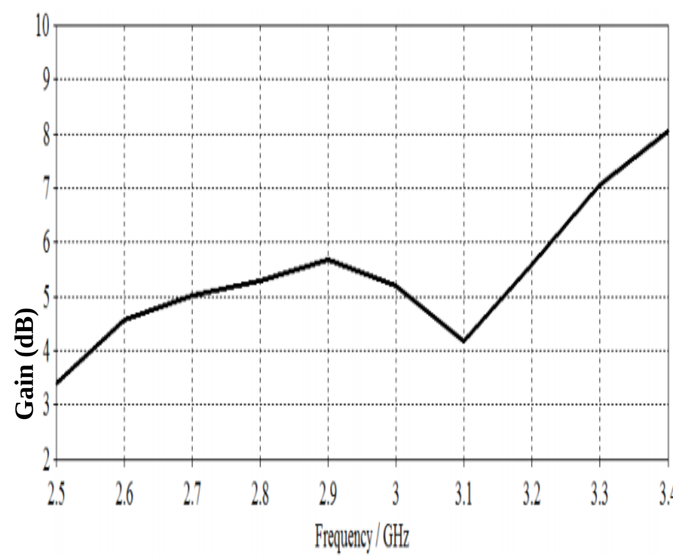

Figure 12. Antenna gain versus frequency

Current distribution determines how the current flows on the patch of the antenna array. Fig. 13 demonstrates these results at 3 GHz. We observe a high strength of current radiates along the transmission lines, at the tuning stub and in the edges of the array patches.

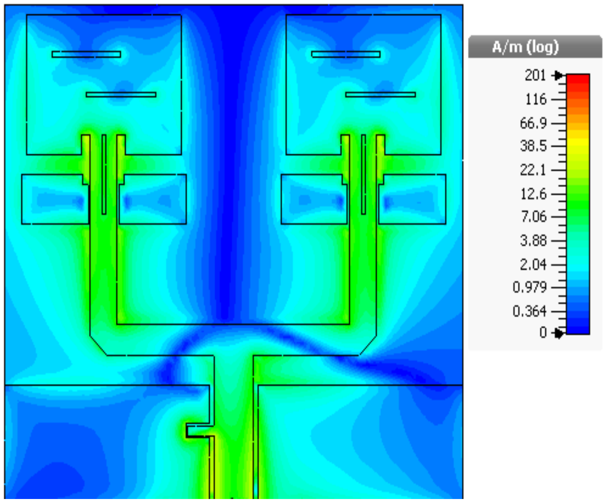

Figure 13. Simulated surface currents at 3GHz of antenna array

IV. CONCLUSION

A novel CPW microstrip antenna array has been successfully designed and simulated using CST Microwave Software. The performance criteria extracted from the software includes return loss, VSWR, radiation pattern, and surface currents provide clear indication that the proposed design, has the required performances to be investigated in a microwave radiometry system as well as for wearable applications, due to its miniature size (5.3x5 cm^2), low profile and weight and very thin substrate. Also the an increased gain of about 6dBi have been achieved and the important bandwidth of 480MHz around the center frequency of 3 GHz provided by the developed antenna are good features to improve the radiometer sensivity at very low power densities transmitted by the self-radiation of abnormal breast tissue. Future work will be focused to validate the simulated results of the developed antenna array by measurement and associate it with a synchronous detector to complete the microwave radiometer system.

ACKNOWLEDGMENT

I acknowledge the contribution by my colleagues and students in this work and all members of the GE Laboratory, ENSET/ENSIAS, Rabat, Morocco for providing facility and technical assistance in this research.

REFERENCES

[1] Hu, J.: Overview of flexible electronics from ITRIs viewpoint. VLSI Test Syposium (VTS), 2010 28th, 19-22 April , 84.

[2] Nathan, A.,Chalamala, B. R.: Special Issue on Flexible Electronics Technology, Part 1: Systems and Applications. Proceedings of the IEEE, 93(7), 1235-1238, 2005.

[3] Huang, Y., Jiankui, C., Zhouping, Y., Youlun, X.: Roll-to-Roll Processing of Flexible.

[4] Heterogeneous Electronics With Low Interfacial Residual Stress. Components, Packaging and Manufacturing Technology, IEEE Transactions on Sept., 1(9), 1368-1377, 2004.

[5] Afyf, A., Bellarbi, L.: A Novel Miniaturized UWB Antenna for Microwave Imaging, 978-1-4799-3824-7/14/$31.00 ©2014 IEEE.

[6] Brown, M., Houn, F., Sickles, E., Kessler, H.: Screening Mammography in community practice, Amer. J. Roentgen, Vol. 165, pp 1373-1377, Dec 1995.

[7] Ellis, H., GL, Colborn., J.E, Skandalakis.,: Surgical embryology and anatomy of breast and its related anatomic structures, Surgical Clinic North America, vol. 73, pp. 611-32, 1993.

[8] CE, Jacobi., B, Siegerink., van, Asperen CJ.: (2009) Differences and similarities in breast cancer risk assessment models in clinical practice: which model to choose? Breast Cancer Res Treat, 115: 381–90.

[9] Collaborative Group on Hormonal Factors in Breast Cancer. Familial breast cancer: collaborative reanalysis of individual data from 52 epidemiological studies including 58,209 women with breast cancer and 101,986 women without the disease, Lancet. (2001), 358 (9291):1389-99

[10] Saving Women's Lives: Strategies for Improving Breast Cancer Detection and Diagnosis. Washington, DC: Inst. Med., Nat. Academy Press, 2004.

[11] S. P., Poplack., K. D., Paulsen, A., Hartov Meaney.: (2004) Electromagnetic breast imaging: average tissue property values in women with negative clinical findings, Radiology, 571-580.

[12] Wellman P. S., Dalton E. P., Krag D., Kern K. A., Howe R. D.,: Tactile imaging of breast masses (2001) Archives of Surgery, 136, 204-208.

[13] Fear, E., Li, X, Hagness, S. Stuchly, M.: Confocal microwave imaging for breast tumor detection: Localization in three dimensions, IEEETrans. Antennas Propag., vol. 49, no. 8, pp. 812-822, 2002.

[14] Mohammed, B.,Abbosh, A., Bialkowski, M.: Design of tapered slot antenna operating in coupling liquid for ultrawideband microwave imaging systems, APS URSI, Washington, USA, pp. 145-148, July 2011.

[15] CST Microwave Studio Suite 2011, www.cst.com.

[16] Ansoft HFSS Software, http://www.ansys.com.

Test of electromagnetic susceptibility of a digital camera

Martin Pospisilik, Tomas Riha, Milan Adamek, and Rui Muguel Soares Silva

***Abstract*—** With the increasing number of electronic devices, the issues of electromagnetic compatibility became important. An important part of the electromagnetic compatibility field is the electromagnetic susceptibility that studies how a tested device can withstand the external interferences that affect its circuitry. The authors of this paper processed a test of electromagnetic susceptibility on a DSLR photo camera Nikon D40 that employs a CCD sensor, converting the captured image to the electrical signal, in order to discover how much the quality of the scanned image will be affected by external electromagnetic field, which the camera is exposed to. This paper describes the configuration of the experiment as well as the obtained results.

***Keywords*—**Electromagnetic susceptibility, Electromagnetic compatibility, Photo camera, Semianechoic chamber

I. Introduction

IN 1968, H. M. Schilke, one of the founder of the field of science related to the electromagnetic compatibility, claimed: "The system itself may be perfectly reliable, but practically worthless in operation unless it is not electromagnetically compatible at the same time." [1]. Since that time, the constructers had to face many problems raising at the field of mutual electromagnetic compatibility of devices that had to be in a concurrent operation. For example, as described in [2], in 1984 the NATO airplane "Tornado" crashed in Germany after its circuits interfered with a powerful transmitter in Holkirchen. In 1982, the British cruiser Sheffield was sunk by Argentine aircraft in the Falklands War, partly because its defense system abetting the enemy rockets was switched. Due to its electromagnetic incompatibility, it interfered with radio communication, crucial for the cruiser's crew. According to [3], there were several accidents reported in the Czech Republic, for example a pileup of mining equipment failures in Náchod that was caused by an incompatible mining machine with a power of 3.4 MW.

The above mentioned examples demonstrate how the field of electromagnetic compatibility is important. Because this paper focuses mainly to the electromagnetic susceptibility, it is worth describing how the electromagnetic susceptibility is included in the field of electromagnetic compatibility. It can simply be said that the electromagnetic compatibility is divided into two groups that studies the interaction between the devices. These groups are as follows:

- **Electromagnetic interference** – describes how the tested device disturbs other devices. It is focused on measurement of the disturbing electromagnetic fields or currents emitted to the connected cables. It identifies the source of disturbances, describes the disturbing signals and focuses on elimination of the disturbances.
- **Electromagnetic susceptibility** – describes how the operation of the device can be affected by external disturbing signals, either spread by electromagnetic field, capacitive or inductive coupling or directly over the conducting line. It is focused on measurement of the device's ability to resist the disturbances, describes the consequences of the interferences, identifies the locations at which the disturbances penetrate the device and focuses on elimination of the consequences.

In this paper a test of the susceptibility of the camera Nikon D40 is described. The measurement was processed according to the requirements of the standard EN 61000-4-3. It is obvious that it is only a part of a complex set of tests that must be performed in order to check the electromagnetic susceptibility of the device. However, complex testing of the camera would exceed the framework of one paper. The most common susceptibility tests and standards are enlisted in the subchapter below.

A. Basic European standards for susceptibility tests

The set of standards for electromagnetic susceptibility has developed into a complex system that covers almost all possible situations that can occur during the operation of the tested device. The system of standards is created as follows: there are basic (root) standards to define basic requirements on all devices tested for the electromagnetic susceptibility. On their basis more complex groups of standards are created, defining the requirements for certain groups of devices (for example computers, lighting devices, etc.). If the device cannot be

This work was supported in part by the European Regional Development Fund under the project CEBIA-Tech No. CZ.1.05/2.1.00/03.0089 and by OPVK project CZ.1.07/2.3.00/30.0035.

Martin Pospisilik is with Faculty of applied informatics, Tomas Bata University in Zlin, Nad Stranemi 4511, 76005 Zlin, Czech Republic (corresponding author, phone: +420 606 417 702; e-mail: pospisilik@fai.utb.cz)

Tomas Riha is a student of Faculty of applied informatics, Tomas Bata University in Zlin, Nad Stranemi 4511, 76005 Zlin, Czech Republic

Milan Adamek is with Faculty of applied informatics, Tomas Bata University in Zlin, Nad Stranemi 4511, 76005 Zlin, Czech Republic (corresponding author, phone: +420 606 417 702; e-mail: adamek@fai.utb.cz)

Rui Miguel Soares Silva is with Polytechnic Institute of Beja, Campus do Instituto Politécnico de Beja Rua Pedro Soares, 7800-295 Beja, Portugal (e-mail: ruisilva@acm.org)

assigned to any group, the tests are run according to the root standards. A shortened list of the basic standards is provided in the Table I.

Table I. Basic standards for electromagnetic susceptibility tests [1] (shortened)

Standard code	**Description**
EN 61000-4-1	List of the susceptibility tests
EN 61000-4-2	Electrostatic discharge
EN 61000-4-3	Radiated electromagnetic field
EN 61000-4-4	Fast transients and/or set of pulses
EN 61000-4-5	Surge pulse
EN 61000-4-6	Interferences induced by the high frequency fields, conducted by wires
EN 61000-4-7	Harmonic and interharmonic frequencies in power supply mains – general
EN 61000-4-8	Magnetic field of the power supply mains
EN 61000-4-9	Magnetic field pulses
EN 61000-4-10	Damped oscillations of the magnetic field
EN 61000-4-11	Short-time decreases in supply voltage, short voltage drops and slow voltage changes
EN 61000-4-12	Oscillating waves
EN 61000-4-14	Voltage ripples

B. Principle of CCD sensor operation

The motivation for processing of the test was triggered by the statement published in [9], where the authors claimed that the "CCD sensors are susceptible to modest electromagnetic environments". This announcement can be considered as expectable, when studying the principle of the CCD sensor operation.

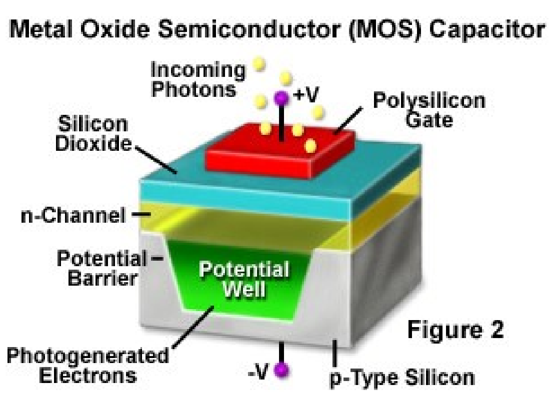

Fig. 1 visualisation of an individual CCD sense element [8]

According to [7], the technology of charged-couple devices was developed in 1969 in the Bell laboratories, but it was expected to serve for other purposes than for digital picture scanning. The visualisation of an individual CCD sense element is provided in Fig. 1. Generally it can be said, that the elements respond to incident photons by absorbing much of their energy in the form of an electrical charge. This charge is linearly proportional to the light flux incident on a sensor pixel. [8] On the CCD sensor the sense elements are organized in a matrix and the obtained pieces of charge are sequentially moved to the amplifier (charge to voltage converter) and, sub sequentially, to the A/D converter. This process is stimulated by electrodes producing electrical field that attract the charger through the mass of the sensor. More information on this topic can be found in [7]. The principle of processing of the charges can be compared to a bucket brigade, as depicted in Fig. 2.

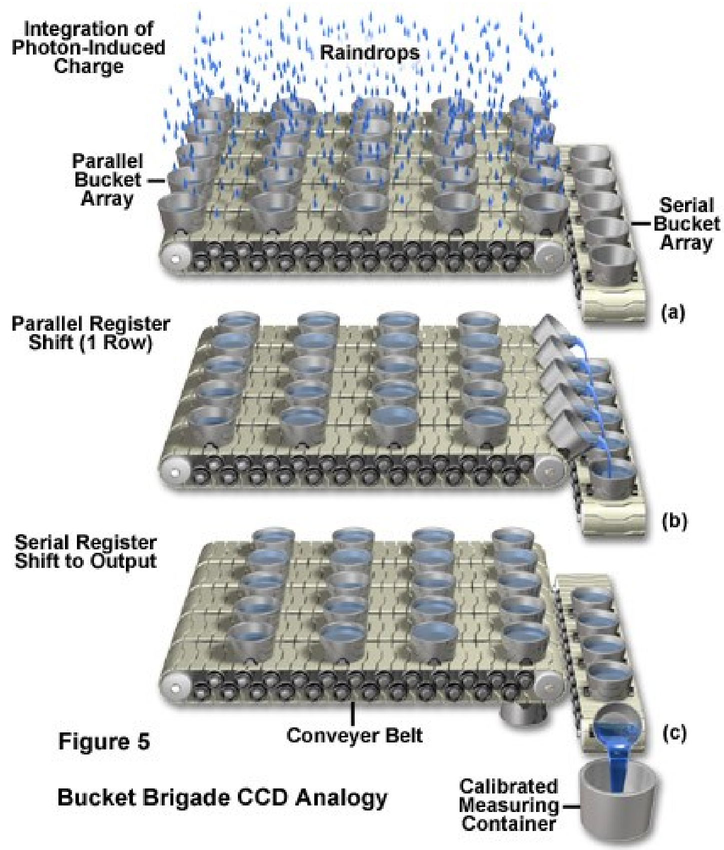

Fig. 2 principle of the sequential processing of the sensed charges on the CCD matrix [8]

Once the CCD sensor operates with electrical charges and transports these charges by means of electrical field, it can be expected that this device will be affectable by external electrical fields.

II. Experiment Description

The experiment was run in the laboratory of the electromagnetic compatibility under the conditions and with the equipment described in this chapter.

A. Tested camera

As the equipment to be tested, an older DSLR Nikon D40 was chosen. The camera was frequently used for 7 years and suffered from minor wear. Nikon D40 is an entry-level single lens reflex camera that employs a sensitive CCD sensor with the resolution 3,008 x 2,000 pixels. The dimensions of the sensor are 23.7 x 15.5 mm and the basic sensitivity is ISO 200 and with the use of an internal amplifier, it can be increased up to ISO 3200. This is possible because on the area of the chip there is a low number of pixels. The pixels occupy larger area and thus the sensor reaches high sensitivity.

B. Equipment

The experiment was held in a shielded semi anechoic chamber Frankonia SAC 3 plus in which the camera and the transmitting antenna were placed. The signal was generated by Rohde & Schwarz SMF 100 A and amplified by a set of amplifiers Amplifier Research 150W1000 and 80S1G4. The signal was transmitted with the antenna Rohde&Schwarz HL046E. The frequencies and the modulation were set in accordance with the standard EN 61000-4-3. The power of the amplifiers was set by means of a feedback field probe ETS Lindgren HI-6005 that was located as close to the camera as possible. The instruments were driven by EMC 32 software.

C. Arrangement of the experiment

The tested camera was placed on a wooden table located on a rotatable surface. Its rotation was controlled by means of the EMC 32 software. Close to the camera the feedback field probe was placed, being connected to the instruments in the rack by means of an optical cable. In the distance of 3 m, the transmitting antenna was placed. The measurement was run in both antenna polarizations – the vertical and the horizontal one. The camera was connected by a shielded USB cable to a computer placed outside of the semi anechoic chamber. The cable was threaded through a waveguide in the penetration panel. Inside the chamber, non-radiating halogen lamps were used to ensure enough light for taking the photos. For each polarization of the antenna, the camera was exposed to the electromagnetic field produced by the transmitting antenna, the intensity of which was defined and controlled by the feedback probe.

According to the possibilities of the laboratory equipment, in order to reach higher field intensities than 10 V/m in the whole frequency range, the distance between the tested camera and the transmitting antenna had to be reduced proportionally to the demand of the increase in the field intensity.

A diagram describing the whole arrangement of the experiment is depicted in Fig. 3. A description to the Figure is provided in Table II.

D. Requirements of the Standard EN 61000-4-3

This standard requires to process the measurements in the frequency range from 80 to 1,000 MHz. The amplitude of the testing signal is modulated with the frequency of 1 kHz. The depth of the modulation is 80 %.

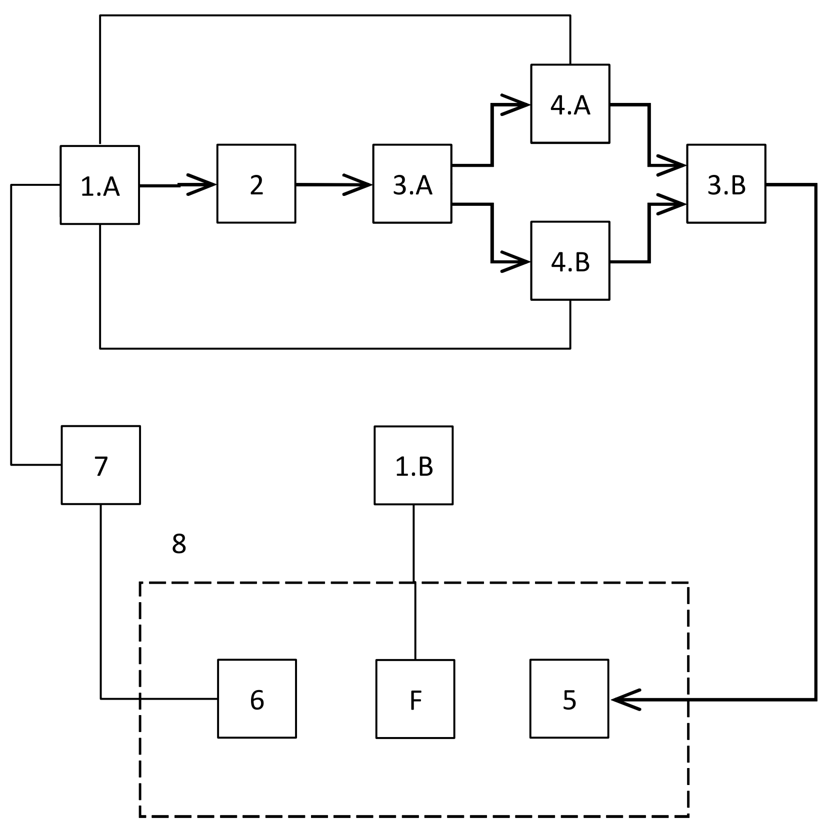

Fig. 3 arrangement of the experiment described in this paper [10]

Table II. Description of the elements depicted in Fig. 3

Element	Description
1.A	Computer running EMC 32 controlling software
1.B	Laptop running Nikonkontrol 3k, a software for communication with the tested camera
2	Signal generator Rohde & Schwarz SMA 100 A
3.A	Path switches Rohde & Schwarz OSP 130
3.B	Path switches Rohde & Schwarz OSP 150
4.A	Power amplifier Amplifier Research 150W1000
4.B	Power amplifier Amplifier Research 80S1G4
5	Antenna Rohde & Schwarz HL 046
6	Electrical field isotropic probe ETS Lindgren HI 6105
7	Converter from optical connection to USB ETS Lindgren HI 6113
8	Semianechoic chamber Frankonia SAC 3 plus
F	Tested digital camera Nikon D40

According to the class of the tested device, the device should stay in operation up to the intensities defined in Table III.

Table III. Test intensities of the electromagnetic fields

Class	Intensity [V/m]	Description
1	1	Device is operated in the area with low interferences, the radio and TV transmitters are in the distance higher than 1 km.
2	3	Device is operated in the area with moderate interferences, the transmitters in its neighbourhood does not exceed the output power of 1 W.
3	10	Device is operated in the area with high interferences, close to powerful transmitters or scientific, medical or industrial appliances.
X	-	Device is operated under specific conditions, described by other documents.

E. Experiment conditions

The experiment conditions were chosen according to the requirement of EN 61000-4-3 for the first set of measurements. The intensity of the fields was set according to Table III Class 2 and Class 3.

In the second set of measurements, more challenging conditions were used:

- The modulation depth was increased to 100 %,
- The intensity of the electrical field was increased to 30 V/m or 50 V/m respectively by shortening the distance between the transmitting antenna and the tested camera.

F. Functional criteria

When the electromagnetic susceptibility of any device is tested, it is important to classify the influence of the received electromagnetic field on the operation of the device. The unified set of functional criteria is therefore defined by EN 50082 in order to enable the evaluation of the test. The list of basic functional criteria according to EN 50082 is provided in Table IV.

Table IV. Functional criteria according to EN 50082

Criterion	Description
A	The operation of the tested device is not affected by the external electromagnetic field.
B	The operation of the tested device is affected by the external electromagnetic field, but once the external field is eliminated, the tested device will operate normally. The external electromagnetic field does not change data stored in the memory of the device as well as the device's parameters.
C	The operation of the tested device is affected by the external electromagnetic field, but once the external field is eliminated, the normal operation of the device is recovered either automatically or by means of the remote controlling system or by the operator according to the steps defined in the user's manual of the device.
D	The operation of the tested device is permanently affected, even when the external electromagnetic field was eliminated. The device is destroyed or damaged.

III. EXPERIMENT PROGRESS AND RESULTS

The experiment was held in two phases. In both of them, the frequency range and type of modulation were chosen according to the requirements of EN 61000-4-3 and the tested camera was rotated on a turntable controlled by the EMC32 software in order to find such mutual position of the transmitting antenna and the tested camera, in which the susceptibility of the camera reaches the worst results. The configuration of the experiment was always done according to the diagram depicted in Fig. 3.

A. Phase I

In the first phase, the intensity was set to 3 V/m and 10 V/m respectively, according to the values defined in Table III. In all positions and both, horizontal and vertical polarization of the transmitting antenna, the results of the experiment was evaluated according to the Table IV and the operation of the device was not affected. The result was, according to Table IV, classified by the grade A.

B. Phase II

On the basis of the results of the first phase of the experiment, more challenging conditions were set as described in the text above. The modulation depth of the transmitted signal was increased to 100 % and the intensity of the electrical field was increased to 30 V/m and 50 V/m respectively. Several malfunctions of the tested camera were detected. Most of them consisted in loss of the connection between the camera and the controlling laptop, which occurred always on the frequencies above 112 MHz. On the lower frequencies of the disruptive electromagnetic field, several changes in the colour and quality of the captured image were observed, as depicted in Fig. 4. Generally, it can be stated, that for the intensity of electromagnetic fields between 10 V/m and 50 V/m, the tested camera complied with the functional criterion B according to the list in the Table IV.

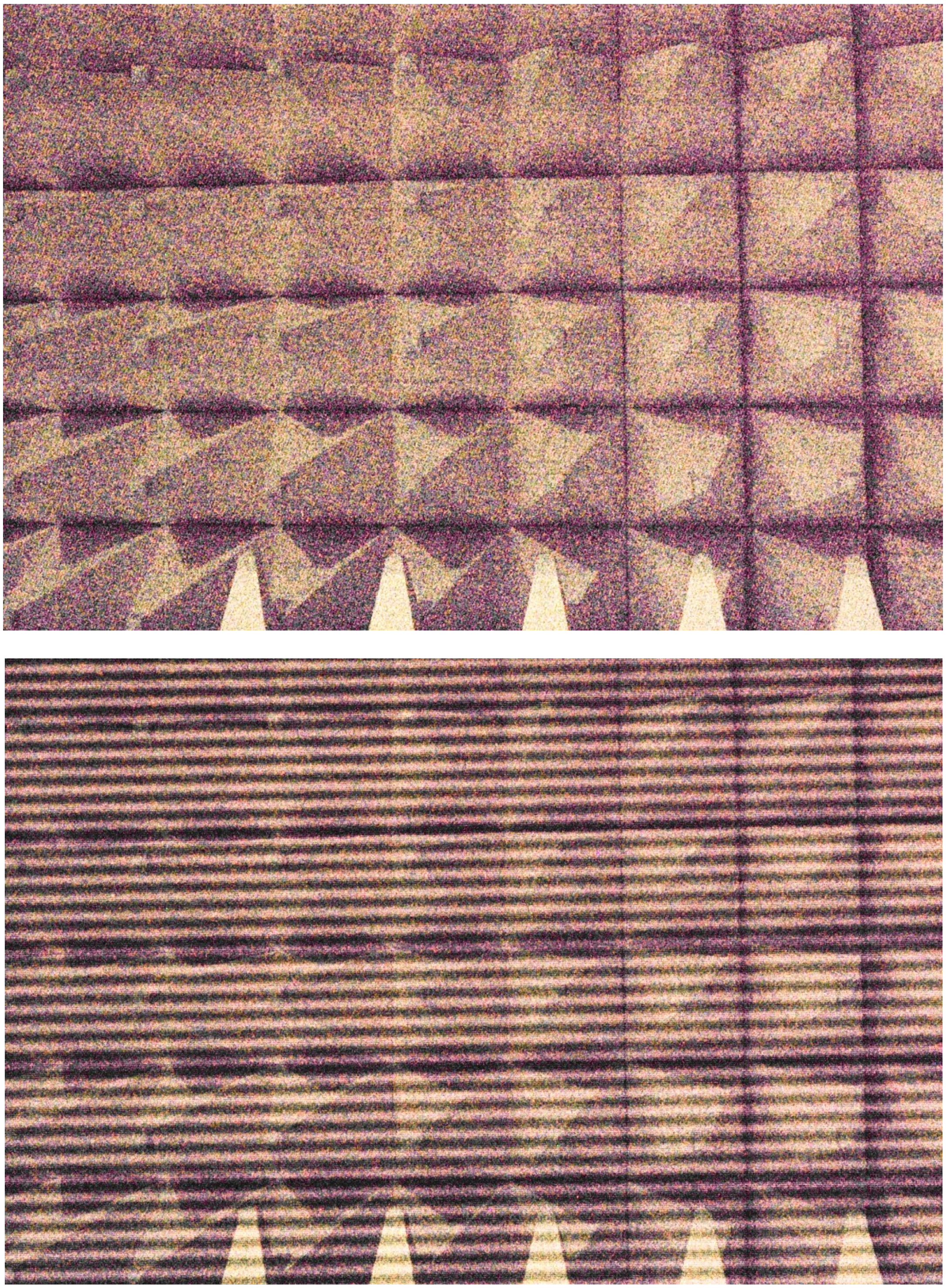

Fig. 4 comparison of the quality of the captured image without disruptive electromagnetic field (upper) and with disruptive electromagnetic field (lower)

ISBN: 978-1-61804-321-4

C. Effects of the disruptive electrical field to the quality of the captured image

The disruptive electrical field resulted in black lines occurring in the captured image. In order to achieve the highest visibility of these lines, the signal from the CCD sensor of the tested camera was amplified by means of the internal amplifier by setting the ISO sensitivity to 1,600. The comparison of a picture captured in the area without intensive electromagnetic field and the picture captured in the area with intensive electromagnetic field is provided in Fig. 4. The conditions under which the pictures were taken, are described in Table V.

Table V. Conditions under which the pictures in Fig. 5 were captured

Field settings	Frequency of the disruptive field	82 MHz
	Modulation frequency	1 kHz
	Modulation depth	100 %
	Intensity of the disruptive field	50 V/m
Camera settings	ISO sensitivity	1,600
	Time of exposition	1/640 s
	Focal length	31 mm
	Aperture	F 8.0
Position	The camera is in the same height as the transmitting antenna, the transmitting antenna is in horizontal position, the angle between the transmitting antenna and the camera lens is 90 °	

IV. CONCLUSIONS

This paper describes the experiment that consists in testing of a digital camera Nikon D40 susceptibility to the disruptive electromagnetic field according to EN 61000-4-3.

According to the obtained results, the camera is fully operational without a malfunction within the external electromagnetic fields the intensity of which does not exceed 10 V/m. At higher intensities, the quality of the captured image is affected, which is documented by a comparison provided in Fig. 4. As it can be seen, the black lines emerging in the picture due to the effect of interfering electromagnetic fields are observable at a certain frequency of the field (82 MHz) and are not parallel to the edge of the picture. The authors of the paper assume that this effect is formed directly on the CCD chip of the camera, which is expected to be sensitive to disruptive electrical fields and which is scanned gradually within the period of the sensing, as depicted in Fig. 2. Within the framework of this assumption it can be stated, that what is actually observed, is directly the effect of the electrical field on the CCD sensor.

The susceptibility of the camera was tested up to the intensity of the electrical field of 50 V/m which is rather high value. Even thus the functionality of the camera complied with the functional criterion B according to EN 50082.

Further tests are planned to be performed inside a GTEM cell. The achieved results will be compared to the results presented in this paper.

REFERENCES

[1] J. Svacina, *Electromagnetic compatibility [Elektromagneticka kompatibilita]*. Brno: Brno University of Technology, Brno, 2002

[2] C. R. Paul, *Introduction to Electromagnetic Compatibility*. New York: John Wiley, New York 1992

[3] P. Vaculik, "Uvod do problematiky EMC", in *Proceedings of Radio-Komunikace '94*, Pardubice, Czech Republic, 1994

[4] P. A. Chatterton, M. A. Houlden, *EMC – Electromagnetic Theory to Practical Design*. New York: John Wiley, 1991.

[5] J. A. Cartrysse, "Measuring method for the characterization of shielding gaskets", in *8th International Conference on Electromagnetic Compatibility*, pp 251 – 253, Heriot-Watt University, Edinburgh, UK, September 1992.

[6] Z. Trnka, *Theory of Electrical Engineering [Teoretická elektrotechnika]*. Bratislava: SNTL Alfa, 1972

[7] Vision Doctor – Solutions for Industrial Machine Vision: *CCD Sensors* [online]. Available: http://www.vision-doctor.co.uk/camera-technology-basics/ccd-sensors.html

[8] Microscopy for you: *Introduction to Charge-Coupled Devices*. [online]. Available: http://www.microscopyu.com/articles/digitalimaging/ccdintro.html

[9] J. K. Daher, G. H. Champion, M. F. Seifert, "Susceptibility of charge-coupled devices to RF and microwave radiation", In *IEEE Symposium on Electromagnetic Compatibility*, Anaheim, USA, 1992

[10] T. Riha, *Testing of electromagnetic susceptibility of a camera*, Diploma thesis, Tomas Bata University in Zlin, 2015. Supervisor: M. Pospisilik

Computer aided TDT interpretation

Florentina A. Pintea, Dan L. Lacrama, Florin Alexa, and Tiberiu M. Karnyanszky

***Abstract*—**This paper aims to advocate the use of image processing techniques for Tree Drawing Test interpretation. The proposed method is thought to be especially useful during the screening of large groups when psychologists & psychiatric doctors have to quickly evaluate many TDT tests. The proposed algorithm detects the tree position inside the drawing space and the ratio between its size and the drawing paper's dimensions. The results are compared with the evaluation made by a professional psychologist. The recognition rate for the location of the tree is 92.035% while the recognition rate for the tree size is 97.06%

***Keywords*—**Projective tests, image processing.

I. Introduction

THE information technology has become a vital part of people's everyday life. Thus one can hardly imagine any current activity without computers' involvement. In health care the computerized systems are used both to storage large collections of patients' personal and medical data and to process the medical imagery. All these records are included in the subject's electronic folder and thus they are instantly accessible to doctors. Moreover the system can generate reports, tables and graphs showing valuable information on the evolution of one's state of health. Therefore, nowadays medical software is implemented in order to be able to assist both anamneses and diagnosis.

During last two decades, the computer aided processing of medical imagery has undergone a spectacular development. There are two main categories of procedures: a. image correction & enhancement b. feature extraction & parameters measurement.

The first type contains pre-processing techniques applied to an image in order to increase its quality and to enhance the visibility of significant details: pseudo – coloring, histogram adjustment, mask filters, morphological transforms etc. [12]

This work was partially supported by the strategic grant POSDRU /131/5.1/G/125380 of the Ministry of Labor, Family and Social Protection, Romania, co-financed by the European Social Fund – Investing in people.

Florentina A. Pintea, was Ph.D. student in "Politehnica" University of Timisoara, Romania. She is now with the Computers Science Department, "Tibiscus" University of Timisoara, Romania (e-mail: fpintea@tibiscus.ro).

Dan L. Lacrama, is with the Computers Science Department, "Tibiscus" University of Timisoara, Romania (corresponding author phone: +40732808851; fax: +40256220690; e-mail: dll1962@gmail.com).

Florin Alexa is with the Telecommunications Department, "Politehnica" University of Timisoara, Romania (e-mail: florin.alexa@etc.upt.ro).

Tiberiu M. Karnyanszky, is with the Computers Science Department, "Tibiscus" University of Timisoara, Romania (e-mail: mtk@tibiscus.ro).

The second category contains a range of software environments able not only to enhance the visibility of interesting details from the raw image, but also to extract its significant features and provide a description vector useful for the latter pattern recognition. Such expert systems provide to the physician a potential diagnosis of the analyzed subject. Usually if the automatic decision is "ill patient", supplemental tests are performed in order to validate this decision.

This paper aims to demonstrate that image processing techniques can be useful in psychology & psychiatry too - namely in projective tests.

Psychological investigations are grouped in two main classes:

- Objective tests based on a multiple choice quiz (i.e. a list of question with a set of given alternative answers);
- Projective tests based on free drawings of a required theme (e.g. subject's family, a certain member of subject's environment, a tree etc.)

The projective tests are used to investigate hidden personality features. They where elaborated in order to let a patient respond to ambiguous stimuli, disclosing his unseen emotions and internal conflicts. During the psychological evaluations they are used solely or as a supplement to the multiple choice quiz. The resulting drawing is content analyzed for detecting its features significance. Projective tests where conceived by psychoanalysts, bearing in mind the fact that humans have both conscious and unconscious attitudes and motivations which are frequently concealed from conscious awareness [7].

Scientific literature proves that individual's drawings are the best way to interpret subject's hidden thoughts and behavior [14]. Still there is a major setback, these tests take a lot of time and great effort to learn how to accurately apply them and a long practice until a specialist can feel the test and have good intuitions.

Drawings are investigated to spot certain behavioral and emotional disorders. Among these projective tests used for the detecting mental diseases the most popular are: Tree Drawing Test, Rorschach Test, House–Tree–Person Test and Kinetic Family Drawing.

The authors of this paper selected the TDT because the trees' sketches are best fitted to be processed through image processing technique. Furthermore TDT model is currently systematized and adapted as a datasheet protocol. It is structured for each topic: clues for assessing the design, interpretation for the parameters' taxonomy, comments etc.

ISBN: 978-1-61804-321-4

The Tree Drawing Test (also named “Baum test”) is a projective method proposed by Emile Jucker, who began to apply it in 1928. The selection of the tree as the sketched item was motivated by the fact that trees are non-threatening elements. They are also an important symbol in many cultures worldwide and there is a broad range of alternatives in drawing them [14].

Later, after a systematic statistical study, the Swiss psychologist Charles Koch standardized the management of quotation and interpretation of indices. Further studies showed that the results of the test can be used as evidence of children’s personality and intellectual progress. More than fifty years of experience proved that the type and features of the patient’s outlined tree relates to the structure of his psyche. The TDT is the most frequently used personality test in school. Nowadays it is widely used to investigate the patient’s personality and reveal his emotive history.

When TDT is used, subjects are demanded to draw a wide-leaved tree using a pencil on a blank sheet of standard A4 paper in portrait orientation. Some practitioners allow the use of the rubber gum too. No time limit is imposed. After the drawing is finished, the clinician makes a set of measurements, apply a standard algorithm and extract conclusions from the way results are placed inside or outside the normal values domain [6].

The TDT image is examined in terms of:

- Morphological analysis – emphasizes the drawing’s quality and distinctive features. (e.g. if the pressure on the pencil was high or low, if many erasures where done, if the ground & roots are present in the sketch, if the crown is figured as a simple ellipse or as a crowd of brunches with just a few leaves etc.);
- Structural analysis concentrates over the ratios computed from direct measurements of size and position (e.g. the position of the tree on the A4 paper as revealed in Figure 1, its slant, the its main parts’ dimensions etc.) [9].

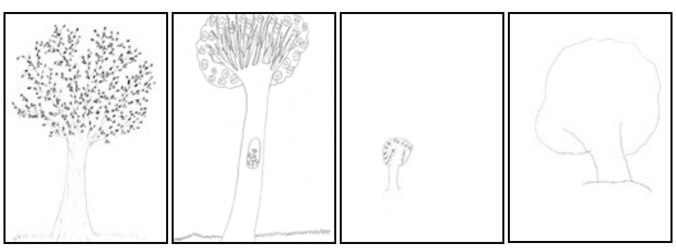

Fig. 1 The drawing position and size related to the A4 paper

a. Normal;
b. Oversized & exceeding the top;
c. Too small;
d. Slant & decentered.

The Structural analysis is concerned with the tree’s main parts measurements as shown in Figure 2 and the computation of the next three quotients used to quantify the test’s results:

- $\mathbf{R_{TC} = B/A}$ (trunk to crown ratio = trunk’s length /whole tree’s length);
- $\mathbf{R_{LR} = D/C}$ (left to right side ratio = trunk’s left half-width /whole trunk’s width);
- $\mathbf{R_{T} = C{\times}A/E{\times}F}$ (total tree’s size to page space ratio = whole length of tree*whole width of tree /paper area).

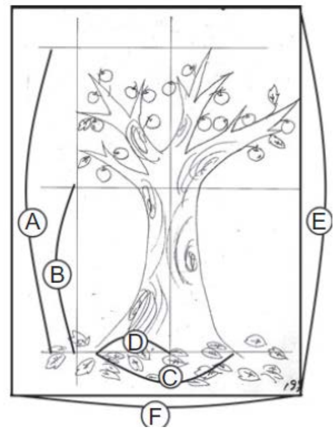

Fig. 2 TDT: Calculation of structural analyses [8]

These quotients are in fact the tree’s structure descriptors and thus can be used in an algorithm of decision. They are the leading criteria in the psychologist’s judgement over the patient’s cataloguing as normal or affected by psychic illnesses [10].

For example, the literature, based on statistics over a long clinic experience, show that if the tree is oversized – the patient is extraverted while if the tree is undersized – the patient is introverted and potentially anxious. If the tree is placed more on the left from the paper center – subject is clinging with the past and fears of involvement in relationships with others while if it is drawn mainly on the right - subject is sentimental and has environment predisposition [13].

As described in the above, this is a quite long and difficult procedure, thus during a screening with many subjects it tends to be very tiresome. Therefore during last few years, the efforts to implement an expert system for the automatic interpretation of TDT grew considerably.

Furthermore, interpretation of many tests successively, was psychologically proved wrong because the perception of the TDT previously evaluated may influence the perception of the next one (e.g. an evaluator assesses a group of successive oversized trees, and then he may perceive a normal sized tree as undersized) [11].

The objective is not only to gain speed by helping doctors get rid of the routine work to measure, compute and compare, but also to automatically eliminate normal subjects and left the clinicians to examine more carefully only the potentially problematic ones.

The authors also expected that the computer should be able to better weight the geometrical dimensions and the visual framing than the psychologist’s human eye whose precision is limited. Of course, the expert system cannot replace the human evaluation, but it aims to be a helpful aid in measuring

ISBN: 978-1-61804-321-4

parameters, computing rations and automatically signaling the normal limits exceeding.

II. The Proposed Method for Feature Extraction

We have adopted the standard TDT procedure described in [11] and obtained a set of drawings which were analyzed by a professional psychologist using the above described features to evaluate the sketches. Each subject's indicators are recorded in a protocol sheet inserted in our database.

Considering the features employed by psychologists to process TDT and classify a person's mental state & feelings the authors of this paper decided to concentrate at this stage on the automatic estimation of the tree's positioning related to the paper center and on computing R_T the total tree's size to page space ratio. In order to measure these characteristics we executed the succession of steps showed in Figure 3.

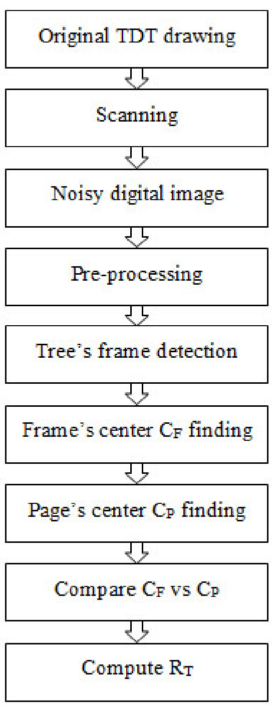

Fig. 3 The operational diagram

First, in order to obtain the drawings' digital images, the paper sheets were scanned and consequently noise appeared even if a good quality scanner was used. This noise occurred as isolated pixels that are not part of the original drawing's lines & curves. Still it is harmful information affecting the digital image's quality. Therefore we need to pre-preprocess the initial scanned image to reduce noise and to obtain a segmented black & white one.

The detection of the drawing region cannot be simply made by standard image thresholding. This is not recommended while variable illumination produces a non-uniform background [3].

To circumvent these problems, a Canny edge detector was used [1]. It was applied by employing a high sensibility threshold thus no detail should be missed in the sketch's image. This leaded to the detection of false edges, mostly generated by noise.

The removal of these false edges was done tacking advantage of the fact that they are made of isolated or low connected pixels. Thus, if discontinuous and winding lines are detected, their pixels connectivity is examined. Low connectivity pixels are erased and consequently both noise and false edge occurrence is reduced. [2]

Once the image has been pre-processed, the rectangle framing the tree can be detected. In order to realize this, it was marked on each row x_{min} and x_{max}, representing the first and respectively the last pixel on the row different from the background. The same operation is done on every column, thus y_{min} and y_{max} represent the first and respectively last black pixel in the column.

The framing rectangle F corners' coordinates are:

$$\begin{aligned}
(X_{min},Y_{min}) &= (\min(x_{min}),\min(y_{min}))\\
(X_{min},Y_{max}) &= (\min(x_{min}), \max(y_{max}))\\
(X_{max},Y_{min}) &= (\max(x_{max}), \min(y_{min}))\\
(X_{max},Y_{max}) &= (\max(x_{max}), \max(y_{max}))
\end{aligned} \quad (1)$$

After computing these coordinates it is straightforward to find the tree's frames geometrical center CF. Its (X_{CF},Y_{CF}) coordinates are:

$$\begin{aligned}
X_{CF} &= (X_{min} + X_{max})/2\\
Y_{CF} &= (Y_{min} + Y_{max})/2
\end{aligned} \quad (2)$$

The gravity center of the A4 page is computed using its geometrical dimensions H = height and W = width.

Therefore, the coordinates of the A4 sheet's center are:

$$\begin{aligned}
X_{CP} &= W/2\\
Y_{CP} &= H/2
\end{aligned} \quad (3)$$

Thus the distance (Diff) between CF and CP is computed using the two axis coordinates:

$$\begin{aligned}
Diff_x &= X_{CF}-X_{CP}\\
Diff_y &= Y_{CF}-Y_{CP}
\end{aligned} \quad (4)$$

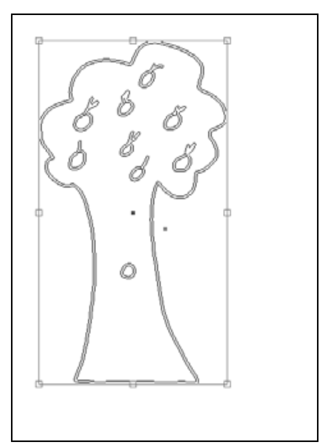

Fig. 4 Representation of the tree's frames geometrical center and the gravity center of the A4 page

Using these results and clues from the psychological literature [4] [5], the decision on the position is summarized as follows:

ISBN: 978-1-61804-321-4

- $|Diff_x| < 15\%$ of W and $|Diff_y| < 15\%$ of H - the verdict is “central position”;
- $|Diff_x| > 15\%$ of W and $Sign(Diff_x) = -1$ - the verdict is “shift to left”;
- $|Diff_x| > 15\%$ of W and $Sign(Diff_x) = 1$ - the verdict is “shift to right”;
- $|Diff_y| > 15\%$ of H and $Sign(Diff_y) = -1$ - the verdict is “shift down”;
- $|Diff_y| > 15\%$ of H and $Sign(Diff_y) = 1$ - the verdict is “shift up”.

To decide if the tree’s drawing exceeds the paper space, the difference between x_{max} and x_{min} in the first five rows from the top and bottom of the image is examined. The same investigation can be done over y_{max} and y_{min} in the first five columns from the left and right of the image. If the difference is greater than a given threshold the computer concludes that the tree’s sketch exceeds the paper space.

The last step of the analysis is to compute the ratio RT between the size of the drawn tree and the size of the A4 paper. Taking into account the page height H, the tree’s height:

$$H_T = X_{max} - X_{min} \tag{5}$$

and the thresholds Pn=0.7H and, Ps=0.85H given by the literature[4] [5], the final classification is:

- $P_n > H_T < P_s$ the verdict is “The tree’s size is normal”
- $H_T > P_s$ verdict is The tree is oversized”;
- $H_T > P_n$ verdict is “The tree is undersized”.

After all these calculations are done, the index of the TDT drawing, the computed parameters’ values and the verdict are written in a text file that is displayed on the screen and stored in the database.

III. Experimental results

During the expert system testing stage, 100 TDT drawings of 8 to 14 years old school pupils were used. For each test, an experienced psychologist filled in a standard protocol sheet containing the subject’s diagnosis, all the main features’ measurements (as described in section I) and the manually computed three ratios R_{TC}, R_{LR} and R_T.

Each individual test was scanned and processed using the above algorithm. The experimental results are displayed in Table 1 to 4.

Both the automatic evaluations and the results provided by the psychologist were compared to the exact measurements performed on the screen with pixel precision The human missed the geometrically exact position in 9 cases (two trees with “central position”, one tree with “shift up”, five trees with “shift to down”, and one tree with “shift to the left”) while the expert system was wrong only 8 times (two trees was wrong assessment the “central position”, a tree was wrong interpretetion in the “shift to right” and five trees was wrong evaluated in “shift to left”). This is due to the fact that psychologist cannot measure features exactly.

A significant aspect to detect is whether the paper was place in portrait layout or not. If the subject turns the paper to landscape layout, it is a sign of his opposition and rebelliousness. The paper layout can be simply determined by comparing the H to W. If W is bigger, than the paper was rotated to landscape.

In Table I the recognition rate for each predominant feature is displayed and Table II shows the confusion matrix.

Table I. Recognition rate

Position	Recognition rate
Centered	88,88%
Shift Up	100%
Shift Down	100%
Shift to Right	80%
Shift to Left	83.33%
Exceeding the paper	100%
Total recognition rate	**92.035%**

Table II. The confusion matrix for each predominant feature of the tree position on the sheet of paper

Position	Centered	Shift Up	Shift Down	Shift to Right	Shift to Left	Exceeding the paper
Centered	88.88	0	5.56	5.56	0	0
Shift Up	0	100	0	0	0	0
Shift Down	0	0	100	0	0	0
Shift to Right	20	0	0	80	0	0
Shift to Left	10	0	0	6.67	83.33	0
Exceeding the paper	0	0	0	0	0	100

Some of the errors are caused by the ground line, which was not evaluated and processed by the presented algorithm. This impediment will be resolved later through an algorithm able to deal with the drawing’s lines and curves.

Nevertheless, the implemented software was more accurate in detecting the tree position due to the good measurements of $Diff_x$ and $Diff_y$, while the psychologist couldn’t quantify with pixel precision.

Table III shows the recognition rate for the tree size (R_T good evaluation) and Table IV presents the confusion matrix for each predominant type (undersized, oversized or normal size).

Table III. Tree’s size recognition rate

Size	Recognition rate (R_T good evaluation)
Normal	97.30%
Oversized	100%
Undersized	96.43%
Total recognition rate	**97.06%**

Again the automatic and human results were compared to exact measurements performed on screen with pixel precision and once more the human was less accurate.

Table IV. The confusion matrix for tree's size

Size	Normal	Oversized	Undersized
Normal	97.30	2.70	0
Oversized	0	100	0
Undersized	3.57	0	96.43

IV. Concluding Remarks

This paper presents an expert system able to extract useful features from a TDT drawing. The software proved reliable for detecting the position of the tree on the A4 paper and to compute the total size ratio R_T. The good recognition rate for the position in the page was 92.035% and R_T evaluation was correct in 97.06% cases.

The described technique is a very useful tool for psychologists when they have to investigate large number of TDT drawings during short time. Automation is also useful for avoiding errors of interpretation due to tiredness or routine.

Thus using an expert system is a promise for gaining speed and to help clinicians escape from routine work. The software is also able to eliminate normal subjects from the start and left psychologists to concentrate over the potentially ill patients.

Acknowledgment

The authors of this paper express their gratitude for the constant help received from Veronica Violeta Fejes, a special education teacher (psycho) to School Center for Inclusive Education "Dumitru Ciumageanu" Timisoara, expert in projective test analysis experimented psychologist in using TDT. We would also like to thank to the professors of Psychology Department of "Tibiscus" University of Timisoara for their useful advices.

References

[1] J. Canny, "A computational approach to edge detection", *IEEE Transactions on Pattern Analysis and Machine Intelligence* (6), 1986, pp. 679-698.

[2] C. C. Cheng, G. J. Peng, and W. L. Hwang, "Pixel Connectivity", *IEEE transactions on image processing: a publication of the IEEE Signal Processing Society*, 18(1), 2009, pp. 52-62.

[3] R. C. Gonzalez, and R. E. Woods, "*Digital Image Processing (2nd Edition)*", Prentice Hall, 2002.

[4] H. Inadomi, G. Tanaka, and Y. Ohta, "Characteristics of trees drawn by patients with paranoid schizophrenia", Psychiatry and Clinical Neurosciences, 57(4), 2003, pp. 347-351.

[5] H. Inadomi, G. Tanaka, Y. Kikuchi, Y. Ohta, and H. Ozawa, "Ability of Procedural Learning and Gestalt Cognition in Patients with Schizophrenia Assessed by Push-Button Task and Tree-Drawing Test", *Acta medica Nagasakiensia*, 50(4), 2005, pp. 155-160.

[6] A. Kaneda, N. Yasui-Furukori, M. Saito, et al, "Characteristics of the tree-drawing test in chronic schizophrenia", *Psychiatry and Clinical Neurosciences*, 64(2), 2010, pp. 141-148.

[7] C. Koch, *Testul arborelui (Trans.S. Mocanu - 3rd ed.)*, Ed. Profex 2006.

[8] D. L. Lacrama, F. A Pintea, T. M. Karnyanszky, and D. S. Codat, "Computer Aided Analysis of Projective Tests", *Proceedings of the 12th Seminar on Neural Network Applications in Electrical Engineering(NEUREL)*, 2014, pp. 135-138.

[9] D. L. Lacrama, F. A. Pintea, T. M. Karnyanszky, and C. Musuroi, "Automatic Pre-Classification Of Baum Test Images", *Proceedings of the 17th International Conference on Computers part of CSCC '13* WSEAS Press., 2013, pp. 65-68.

[10] I. Mizuta, Y. Inoue, T. Fukunaga, R. Ishi, A. Ogawa, and M. Takeda, "Psychological characteristics of eating disorders as evidenced by the combined administration of questionnaires and two projective methods: The Tree Drawing Test (Baum Test) and the Sentence Completion Test", *Psychiatry and Clinical Neurosciences*, 56(1), 2002, pp. 41-53.

[11] A. Rozorea, and M. Sterian, "*Testul Arborelui*", Bucuresti Ed. Paidea 2000.

[12] M. Tarata, "*Informatica Medicala*, Cap. Analiza si prelucrarea imaginilor medicale", (Vol. I- II), Craiova: Ed. Sitech, 2010.

[13] Z. A. Vass, "*Psychological interpretation of drawings and painting. The SSCA Method: A systems analysis approach*", Ed. Alexandra, 2012.

[14] K. Yoshikawa, and K. L. Mutharayan, "*Cultural Ecology through Tree Test*", Tokyo: Tokai University Press, 2012.

Low cost home management system

Florin Alexa, Dan L. Lacrama, Florentina A. Pintea and Tiberiu M. Karnyanszky

***Abstract*—**This paper present the design and the implementation of a low-cost, home management system based on SNMP (Simple Network Management Protocol) standard protocol. The scope of a home network management system is to monitor and control different type of devices from different location which sets up the bases of a home automation system. Now the SNMP protocol is widely supported by device such as routers, bridges and printers and could be easily integrated to any networks. The message exchange between SNMP agents is done via Ethernet and wireless networks. The protocol is implemented in an optimized way in order to reuse the existing local communication network and to support most of the software applications**.** The proposed system is flexible and secure.

***Keywords*—**SNMP protocol, home management system.

I. Introduction

THE migration from proprietary hardware and software platforms for distributed monitoring and control in favor of open standardized approaches is the trend in home and building management systems. Open source programming, Internet technologies and mobile communication interfaces influence the development of today's distributed systems.

A network management system (NMS) is a system comprising software and hardware that is responsible for the direct monitoring and controlling of the hardware, software and communication in the network [1].

With efficient development process and low cost electronic components the home management systems and automation become key features in all modern houses. The home automation represents the control of all type of home devices from a central location.

The connection between the server and devices can be established using wireless or non-wireless networks. X10 becomes a good choice for non-wireless communication and for the wireless devices infrared (IR), radio frequency (RF) or ZigBee, thus it was extensively agreed on. Except with minor differences in timing, the protocol that X-10 uses for RF devices is identical to the NEC IR (NEC Infrared) protocol. In terms of wireless communications between devices there are automation systems based on ZigBee without the Internet controllability [2].

In this paper it is presented a SNMP protocol based wireless home automation system with wireless access points, SNMP managers and different type of devices configured as SNMP agents.

II. Data communication protocol

The networks in different buildings include equipments from multiple vendors, and therefore, the need for network management tools that can be used across of various product types, including end systems, bridges, routers, printers, multimedia and telecom equipment increases.

The SNMP is an application layer protocol that offers network management services in the TCP/IP protocol stack. It is based on a client/server architecture in which the client issues requests to the server and the server processes requests and responds to the client.

The SNMP protocol includes the following basic commands:

- read - the management station retrieves the value of objects from the agent.
- write - the management station sets the value of objects at the agent.
- trap - agent notifies the management station about significant events (status changes) [3].

Resources in the network are managed as objects, which are essentially data variables that represent different states of the managed agent. This collection of objects is referred to as a Management Information Base (MIB). All of the values that are stored in the MIB are dynamic and are not stored in any file or registry key. The MIBs must be located at both the agent and the manager to work effectively.

A management station (SNMP manager) can monitor and control remote elements by retrieving or changing the value of MIB objects of the management agent via the SNMP protocol. The SNMP agent synchronously responds to requests from the manager and may further asynchronously provide important but unsolicited information (e.g., the alarm conditions) to the management station in the monitoring and control center.

Information stored by agents is made available to the management system by means of the following two techniques: SNMP pooling and SNMP traps. Pooling is a request-response interaction between a manager and agent. The manager can query any agent and request the values of various information elements; the agents respond with information from their MIB.

Florin Alexa is with the Telecommunications Department, "Politehnica" University of Timisoara, Romania (e-mail: florin.alexa@etc.upt.ro).

Dan L. Lacrama, is with the Computers Science Department, "Tibiscus" University of Timisoara, Romania (corresponding author phone: +40732808851; fax: +40256220690; e-mail: dll1962@gmail.com).

Florentina A. Pintea, was Ph.D. student in "Politehnica" University of Timisoara, Romania. She is now with the Computers Science Department, "Tibiscus" University of Timisoara, Romania (e-mail: fpintea@tibiscus.ro).

Tiberiu M. Karnyanszky, is with the Computers Science Department, "Tibiscus" University of Timisoara, Romania (e-mail: mtk@tibiscus.ro).

The SNMP messages (Fig. 1) formats are variable in length and are complex. To describe SNMP message structure we use ASN.1 (Abstract Syntax Notation) language.

```
SNMP-message::= SEQUENCE
{
  version       INTEGER,
  community OCTET STRING,
  data            ANY
}
```

Fig. 1 Structure for SNMP messages

The field version indicates the version number of message format. Community is a string value that is sent in every SNMP message. An agent receiving an SNMP message checks the community name against its configured community name value. If there is a match, the operation requested in the SNMP message is performed. If there is no match, the SNMP agent will ignore the requested operation [4].

An SNMP data PDU (Protocol Data Unit) contains the body of the SNMP message. There are five types of PDUs: GetRequest, GetNextRequest, GetResponse, SetRequest and Trap.

The agent reports the events using traps and the manager is in the role of a listener, waiting for incoming information. An agent may generate a trap periodically to transmit the current status to the manager.

Because the SNMP based system is focused on SNMP traps, the structure of SNMP trap message is presented in Fig. 2.

```
TRAP_PDU::= implicit sequence
{
   enterprise      Object identifier,
   agent_addr    Network address,
   generic_trap  Integer
  {
   coldStart (0),
   warmStart (1),
   linkDown (2),
   linkUp (3),
   authentificationFailure (4),
   egpNeighborLoss (5),
   enterpriseSpecific (6)
  }
   specificTrap          Integer,
   timeStamp            TimeTicks,
   variableBindings   VarBindList
}
```

Fig. 2 Structure for SNMP Trap message

The SNMP agents transmit this type of messages to signal abnormal conditions to the management station (SNMP manager).

In order to demonstrate the SNMP usage in an IP based network, Fig. 3 shows the TCP/IP protocol suite which is the basis for any Internet communication.

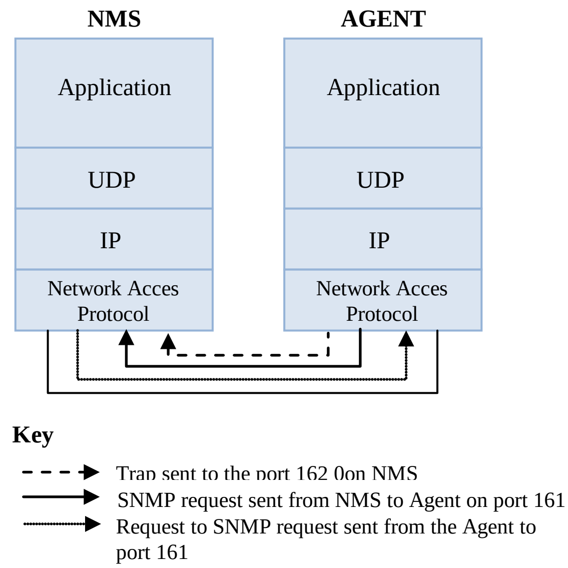

Fig. 3 SNMP IP based communications

SNMP employs the User Datagram Protocol (UDP) as the transport protocol for passing data between managers and agents. Because it is connectionless and unreliable it is up to the SNMP application to determine if datagrams are lost and retransmit them if it so desires. This is typically accomplished with a simple timeout flag set up at the manager.

When either a manager or an agent wishes to perform an SNMP function (e.g. a request or a trap), the following events occur in the protocol stack:

- Application – the SNMP application decides what action is needed to be performed, alone as configured or under the control of an user through the services support offered at this layer;
- UDP – allows the hosts to communicate between each other. Beside other things, the UDP header contains the destination port of the device: 161 – query; 162 – trap;
- IP – tries to drive the packets through the network to their destination based on the IP address;
- Network Access Protocol – the layer where the data is handed off to the physical network.

III. Case of Study

In this section an example implementation of the SNMP agent is presented with the possibility of extending this approach to other type of equipment monitoring.

In Fig. 4 it is a proposed architecture of a home automation system, which would be able to monitor and control most of the home devices which have SNMP capable software installed.

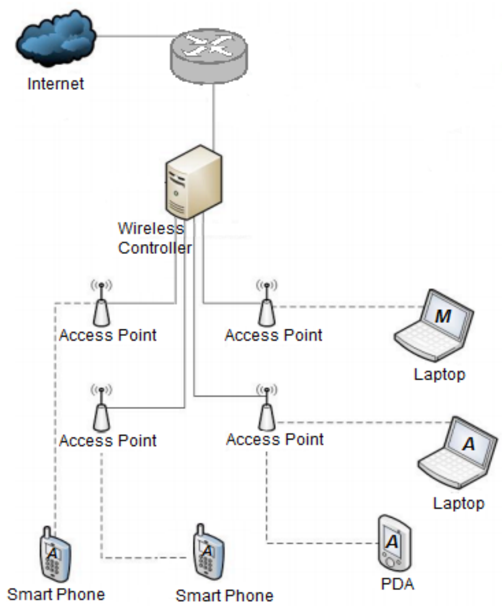

Fig. 4 Network management system SNMP-based

The testing environment is composed of a wireless controller and a couple of access points that form a wireless distribution system (WDS). At different access points we will connect laptops, tablets and smart phones, all SNMP capable as the figure shows.

We will use only one SNMP manager installed on one laptop, the architecture becoming centralized, so, with just one device capable of gathering all the SNMP-related information.

In order to be able to extend this type of management architecture to a fully compatible and usable home automation system that could involve any type of equipments, such as smoke detectors, indoor lights, indoor temperature controllers or other types of sensors that can provide alarms, we intend to test different cases regarding coverage, configuration, protocol or security, in order to obtain a valid conclusion for the feasibility of the proposed system.

A. *Access point coverage testing*

Various types of antennas can be used for site survey testing, including: directional, semi-directional and omni-directional. For indoor applications the omni-directional antennas are recommended. After positioning the access points AP1, AP2, AP3 … APn, the coverage area and the data speeds should be measured.

There are different opinions about where measuring coverage and data speeds should begin. Some experts recommend starting in the corner, while some say staring in the middle of the room is best. After choosing the starting point in the room, the following data depending on the distance from AP were recorded:

- Data rate – measured in Mbps
- Signal strength – measured in dBm
- Signal-to-noise-ratio – measured in dB

Table 1 AP coverage measurements

Distance[m]	Signal Strength		Speed [Mbps]
	[dBm]	[%]	
1	- 28	78	36
5	- 50	52	32
10	- 61	41	30
20	- 82	10	30

B. *WDS configuration*

All AP’s installed in the WDS should have the same SSID (Service Set Identifier), channel and encryption type and key.

There are different types of WDS configurations, like star, chain and their combinations. In the star WDS configuration, the root AP needs “n” WDS ports enabled for “n” different links, while the other satellite APs have only one WDS port enabled.

In the chain WDS configuration, the APs are chained together, while the end of the chain needs one WDS port enabled, the APs in the middle of the chain require two WDS ports enabled for the left and right AP in the chain.

Fig. 5 shows a representation of the two configurations.

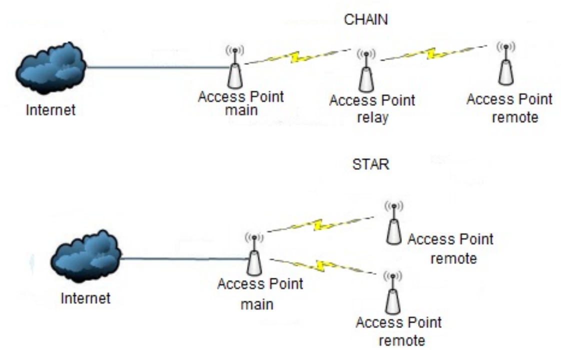

Fig. 5 WDS topologies

The choice of the WDS configuration is being done taking into account the number of the objects that are needed to be managed and the spatial distribution of those on floors and rooms.

The communication between access points that are interconnected by a WDS link works exactly the same way as for cells that are interconnected via Ethernet. The relocation of a station from one cell to the other is done by the request messages that are part of the IAPP (Inter Access Point Protocol) offering more flexibility and load balancing to the system [5].

C. *Security*

The network offers strong 802.11i/WPA2 wireless LAN security. So the WPA2 + AES (Wi-Fi Protected Access II + Advanced Encryption Standard) key was used as security and access control. This security protocol offers better security than the older implementations currently available and

ISBN: 978-1-61804-321-4

supports more speed on Wi-Fi, which is about 150Mbps [6]. Additionally a RADIUS server based authentication can be used to improve the system security.

D. *SNMP query monitoring*

The SNMP manager can be instructed to periodically query remote SNMP agents, filter the collected data, process, analyze and take certain management decisions.

Several applications exist for executing a SNMP query – some of them with graphical user interface others as command line tools. We will use the command-line tool SnmpWalk [7] that can be started from a simple Windows command line by navigating to the folder where the exe file is located.

The SNMP queries are more used for debugging and troubleshooting, ensuring that a device correctly replies to the queries it receives from the manager or for testing the communication link between the entities.

The following simple SNMP query is presented:
>>snmpwalk –c:[community] –v:[version] –r:[agent_IP] –Os:[OID_start] –Op:[OID_stop]
where parameters represent [8], [9]:

- community – the manager and the agents must have the same community string set as it defines a workgroup for the entire SNMP system;
- version – the SNMP packet versions:v1, v2c, v3;
- agent_IP – IP address of the agent device;
- OID – object ID which is read from the MIB of the agent. If it is omitted the query will return all the database information from the client;
- Os – start_oid – it is added to start from the first possible variable of the ID and return all the data regarding that object in one response (eg.1.3.6.1.2.1.1.* will start from .0 up to the value set in the Op field).

As an example in Fig. 6 we will read the system description object (sysDescr) from the MIB of one agent trying to check if the response is, as expected, details regarding the operation system of one agent.

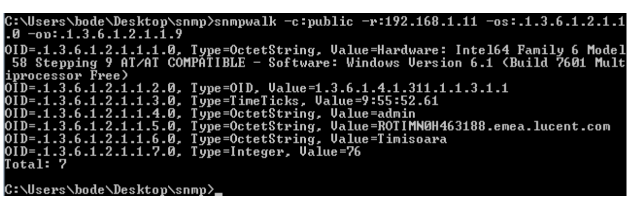

Fig. 6 SNMP Query for system description MIB

After getting a valid reply from a SNMP enabled device we need to figure out the values which are of interest, this being the most difficult part as the values are stored in a tree similar to folders on the hard drive. Each vendor may implement a private branch with specific information about its hardware or the generic one could be used according to RFC 1156 [10].

A response from a device that doesn't support SNMP or is unreachable would result in a timeout.

After passing all these first tests we can conclude that the agents were installed correctly. If required, the manager could be instructed to perform automatically query polls at a precise timestamp in order to check that all the agents are running.

E. *SNMP trap monitoring*

The advantage of this method is that it doesn't require the periodical scanning of the agents in the network. Messages are only delivered when the agent status is changed (for example: smoke or broken window detected).

For the purpose of this trap monitoring, we set one of the SNMP agents to generate traps when their batteries are bellow one value (e.g. 30%), in order to receive this trap at the management level and to check whether we can extract useful information from it.

Agent: 192.168.1.101:35071		
Enterprise: 1.3.6.1.4.1.1.0		
Uptime: 2638809440		
Timestamp: 22/04/2015 19:03:50		
1.3.6.1.4.1.1.0.1	Octet string	SmartPhone
1.3.6.1.4.1.1.0.3	Octet string	28
1.3.6.1.4.1.1.0.4	Octet string	30
1.3.6.1.4.1.1.0.5	Octet string	100
1.3.6.1.4.1.1.0.12	Octet string	SmartPhone

Fig. 7 SNMP low battery trap

In Fig. 7, we can see a trap message sent by one of the agents when the battery dropped down 30%. We can distinguish the lower and upper values of the condition as 30% and 100%, and when the current value exceeds the limits (28%), the agent will send traps to the manager once at a predefined timestamp.

The SNMP trap could be interpreted as an alarm that can trigger actions at the management level or could just be checked as important status information coming from the agents. Same as the manager, the agent can be instructed to send traps at certain moments in time or when predefined conditions are no longer accomplished.

F. *Extension of the system*

As proposed at the beginning of this section, this type of management system could be extended to a home automation system that could involve other types of equipments different than PCs, such as smoke detectors, indoor lights, temperature controllers, etc.

While the sensors and actuators are not directly SNMP capable, they need to be connected to the GPIO (General-purpose input/output) pins of Digi-Connect Wi-ME modules that have an SNMP agent installed. The solution can be designed for hotels or companies with multiple floors in which the existing wireless Internet network could be reused easily [11].

At every floor of the building we have access points that form a WDS. The networks with sensors are build in every room and are connected through Digi-Connect module, being accessed through UDP based SNMP communication protocols, as proposed in system architecture (Fig. 8).

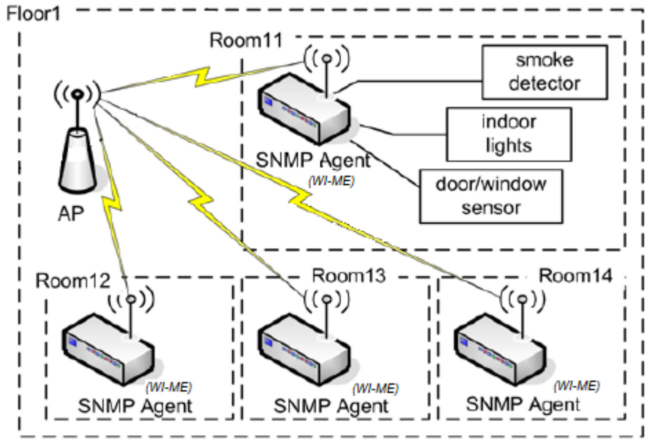

Fig. 8 Home automation system architecture

IV. Conclusions

In this paper we introduced a low cost, flexible, scalable and secure SNMP protocol based wireless solution for the home automation. A basic criterion for this architecture is that the device must be IP-enabled and SNMP protocol supported.

SNMP in Ethernet and Wireless networks can be used in the home automation systems without any constraints, because this is not required to be in real time. The measured delay between the request and the response is not significant (<20ms).

A drawback for this solution can be the testing, which can be time consuming. Also, the installation and deployment of this type of management architecture is not very simple because it combines a lot of equipments from different vendors that need to be configured to work together.

Regarding the bandwidth used, one SNMP poll can be up to 1KB (for request and reply), which is very low compared to the data rates of the nowadays communications. Although, by reducing the polling frequency and sending traps every time when the agent status is changed we have optimized the SNMP protocol bandwidth usage.

References

[1] Hill2Dot website: Network Management System Description.

[2] Ali Ziya Alkar, Umit Buhur, "An INTERNET Based Wireless Home Automation System for Multifunctional Devices", *Consumer Electronics, IEEE Transactions*, Volume 51(4), Nov. 2005, pp.1169 – 1174, ISSN: 0098-3063, DOI: 10.1109/TCE.2005.1561840

[3] Steven T. Karris, "*Orchard Publications Networks Design and Management*", 2nd Edition, 2009.

[4] Douglas Mauro, Kevin Schmidt, "*Essential SNMP*", 2nd Edition, O'Reilly Media, 2005.

[5] Allied Telesis publications – *How to configure a Wireless Distribution System*

[6] SpeedGuide website: *Selecting the Best Wi-Fi Security Options for Homes*, Available: http://speedguide.net.

[7] SNMP Soft, Available website: www.snmpsoft.com

[8] Net-SNMP, Available website: http://www.net-snmp.org

[9] *Simple Network Management Protocol (SNMP)* v.4.11, Reference Manual, Available Erlang website.

[10] RFC 1156 – *Management Information Base for Network Management of TCP/IP-based internets*.

[11] Digi, Wired and Wireless Device Server Modules, Available: http://www.digi.com/pdf/prd_ds_digiconnectme.pdf.

New Standard Test Routines for Reliability Evaluation in Fault Indicator Devices

Ivan N. Silva, Rogerio A. Flauzino, and Danilo H. Spatti

Abstract-- **Fault indicators are devices used to signal the passage of faulty current in power distribution lines, allowing a significant reduction in the time needed by maintenance teams to locate the respective defective sector. However, there is a high operational failure rate associated with this device, which affects its performance and, consequently, its reliability. This paper presents a new methodology for laboratory tests, in order to complement those standard tests used by manufacturers, aiming to identify factors and circumstances that cause fault indicator failure. The results showed that the method developed is efficient in identifying operational failures, undetectable by applying just standard tests performed by manufacturers.**

Index Terms-- **Fault indicator, power distribution protection, fault currents, testing facilities.**

I. Introduction

The outages in power distribution systems are caused by a variety of situations, such as atmospheric turbulence, contact with trees, defective equipment and accidents, which may affect the power quality. Finding the faulty sector is the biggest problem encountered by power distribution utilities, since line inspection time can be extremely costly [1-2].

If information about a fault is available, the faulty sector identification process and its subsequent restoration then become faster. As a result, electricity supply can be restored in a more efficient and agile way [3]. In the light of this fact, it is of paramount importance that the elements responsible for detecting and signaling faults be sensitized immediately after the occurrence of a fault, thus helping to avoid fatal accidents and to minimize financial losses [4].

The use of Fault Indicators (FI) in primary circuits enables distribution utilities to improve both reliability and quality, since they aid in locating faulty sectors. They are also small (portable), easy to install, and can effectively help in service restoration procedures. Moreover, these devices help to reduce total outage time originating from permanent faults, decreasing the inspection time spent by maintenance teams in order to locate and isolate a faulty sector. In this case, service restoration procedures can also be easier and faster [5-7].

Studies indicate that the presence of FIs at strategic points in the distribution system can reduce total outage time by up to 60%, helping to improve the performance indices associated with both the duration and frequency of outages in which customers are without service [8].

Most of the investigations presented in the correlated literature handle FIs as drivers for automating the restoration of faulty sectors. In this context, the methodologies proposed in [9]-[12] present relevant contributions for automatic management purposes.

Despite the numerous benefits in installing FIs along power distribution lines, many utilities are detecting problems related to high failure rates observed in these devices, reaching over 20% for models mounted on cables and 40% for those used on poles. If fault indicators fail to detect every fault as it occurs, there is then a possibility that those undetected faults will occur again until the system fails without any warning.

In fact, since such devices are an essential element in service restoration guides adopted by many utilities, it is crucial that they should work within acceptable levels of failure. However, there is a lack of studies into the circumstances that impair proper operation of these devices in distribution lines.

We therefore formulated an experimental methodology in order to test fault indicators in the laboratory. These tests complement standard tests performed by manufacturers, which are insufficient to treat several fault situations, with particular characteristics, similar to those observed in field.

II. Principal Features of Fault Indicators

FIs can be used both in overhead and in underground networks. The test methodology proposed in the present study focuses on FIs installed in overhead distribution systems. This section presents the main features of these devices when used in overhead lines.

A. Functional Description

The detection of a faulty situation by an FI is performed by sensors that monitor the passage of current through the primary distribution system. This device is designed to distinguish between normal operational conditions and faulty situations, which are sensed from the magnetic field produced by the current flowing through the circuit.

B. Fault Indication

If the current flowing through a monitored circuit exceeds the FI trip current previously adjusted, the indicator then signals the existence of a fault situation. Various forms of

I. N. Silva, D. H. Spatti and R. A. Flauzino are with the University of São Paulo, USP/EESC/SEL, São Carlos, SP, CEP 13566-590, Brazil (e-mail: insilva@sc.usp.br, raflauzino@sc.usp.br, danilospatti@gmail.com).

ISBN: 978-1-61804-321-4

signalization can be employed to indicate a fault, such as electromechanical flags, discharge lamps (flashlights) or LEDs.

C. Resetting Procedure

Once a faulty sector has been located, its circuit repaired and power supply restored, the FI needs to be reset.

This resetting procedure can be performed either manually or automatically, in accordance with various manufacturer parameters, such as programming mechanism and model characteristics. Automatic resetting can usually be established, triggered by load current, voltage level or time period. These resetting categories may be summarized as follows:

- Automatic resetting by current: requires a minimum reset current (from 3% to 80% of the tripping current), flowing through the conductor cable on which the FI is mounted, in order to change from faulty to normal condition indication.
- Automatic resetting by voltage: requires a minimum reset potential to be restored to the conductor cable on which the FI is mounted in order to change from faulty to normal condition indication.
- Automatic resetting by time: after a time period required for resetting, which should be specified by the manufacturer, the FI should move from faulty to normal condition indication.
- Manual resetting: requires use of a resetting tool, specified by the manufacturer, which effects the change from faulty to normal condition indication. This procedure is normally performed by approximating a permanent magnet (mounted on a hot stick) to the FI sensor, reverting its magnetic field and, consequently, resetting the indicator.

From the operational point of view, automatic resetting procedures are more reliable than manual resetting and, moreover, they dispense the use of hot line tools. For this reason, several investigations into the automatic resetting procedures of these FI types were presented in [13], focused on improving reliability.

D. Battery

The FI power supply is derived from an internal battery which, as source independent of the monitored circuit, has brought a great evolution in the operation of these devices. Some FI devices have a low battery indication, i.e., indicating when the battery should be replaced, since correct operation of the FI depends on an adequate battery charge level.

E. Communication

Some models of FI have a communication function, enabling the device to be integrated with the Distribution Operation Center (DOC) and other protection equipment. This communication function informs the DOC supervisory system of the operational status of the FI. There are also FI models that generate a signal, via radio frequency or GSM (Global System for Mobile Communication), when a fault indication occurs. This signal immediately helps maintenance teams to locate, by means of georeferenced maps, the FI that signaled a fault occurrence [14].

F. Programming

An FI detects a faulty circuit when the current exceeds the tripping current previously programmed by means of keys (switches) or software. In order to avoid an indication as a result of system switching situations, or inrush currents due to transformer energization, the device is programmed to automatically signal a normal condition during the time necessary to energize a circuit.

G. Maintenance

For maintenance purposes, FIs should be inspected periodically. Usually, manufacturers recommend intervals of one year. The typical maintenance procedure just consists of replacing the internal battery. Replacement of an FI can also be necessary when the response from an appropriate test, performed by approaching a magnet or key to the sensor, is considered to be unsatisfactory.

H. Placement Points of Overhead Fault Indicators

FIs are placed at strategic points in the power distribution system, either on a conductor cable or on a pole. These points are typically located at main feeder junctions, and also along extended rural distribution lines. Some optimization methods for the selection of the most appropriate points for placing FIs have also been developed, which have already presented promising results by using intelligent system approaches, such as those proposed in [15, 16].

I. Fault Indicators Installed on Conductor Cables

An FI mounted directly on a power conductor cable is also known as a cable/line indicator or fault flag, where a device is needed to monitor each phase circuit (Fig. 1). In the event of a service outage, caused by a protection device sensitized by a fault situation, the FI will signal the existence of a permanent fault by means of the previously mentioned luminous mechanism. In this case, it can easily be seen by the maintenance team patrolling the line in search of the respective faulty sector.

For this type of FI, the faulty current detection is made through a sensor that measures the change of current with respect to time, i.e., di/dt, making it possible to distinguish between a faulty condition and a normal operating condition.

J. Indicators Installed on Poles

In this category, a FI is mounted on a pole by means of a metal band and, in contrast to those devices mounted on conductor cables, a single pole indicator can monitor the three phases simultaneously (Fig. 1). Pole indicators are also used to detect both phase-phase and phase-ground faults, using the same principle of current variation adopted by indicators mounted on conductor cables.

Although the three phases are simultaneously monitored using a single device, they are subject to interference, such as that caused by the presence of a secondary network on the same pole or by metallic structures, e.g. cross arm and surge arrester conductors, which make the cable indicator more suitable for power distribution systems.

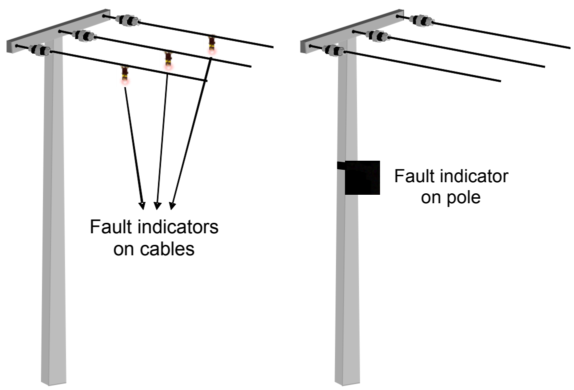

Fig. 1. Cable- and pole-mounted fault indicators.

III. Structuring of Experimental Tests

In order to carry out a more detailed study of FI operating principles, several tests were performed in a laboratory in order to detect the possible causes of FI failure. The tests were conducted using an automated test methodology, developed especially for the evaluation of cable-type FIs.

The objective was to simulate normal, faulty and reset operations conditions for FIs. The tests here proposed are complementary to those covered by the guide IEEE 495-2007 [17], which only considers the design tests that should be performed by the manufacturer on a sufficient number of FIs, such as temperature cycle test, water submersion, immersion corrosion, salt spray, electric cord pull-out, impact resistance and outdoor weathering of plastics.

In general terms, we can consolidate the goals of this new methodology as covering those types of routine experimental tests in which the FI should fully operate in a suitable way, i.e., without producing failures. The developed tests were planned in order to allow inferences about FI functionality, taking into account manufacturer design characteristics as the respective reference guides informing the operating conditions under which they must operate.

The elements used for building the laboratory structure were based on those employed in real distribution systems. Installation and configuration were also similar to those found in the field. The structure was specifically mounted in order to simulate a single-phase power distribution system as shown in Fig. 2.

The equipment and materials needed to make the laboratory setting were the following:

- Current Transformer (CT): An ALSTOM instrument was adopted with a conversion ratio of 30:5. However, the equipment was assembled for the purpose of increasing the current to a level used in medium-voltage distribution lines (reverse link).
- Potential Transformer (PT): An ALSTOM instrument with a conversion ratio of 70:1 was utilized. The equipment was likewise installed to raise the voltage to those values used in distribution systems (reverse link).

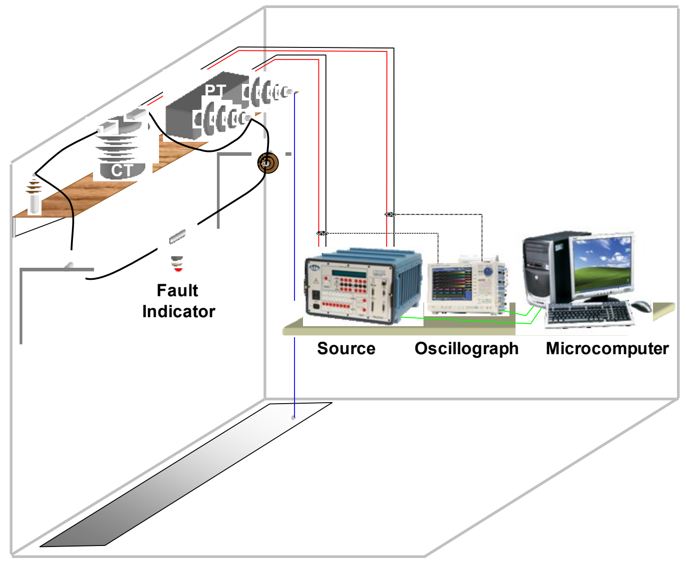

Fig. 2. Laboratory structure for testing fault indicators.

- Source: A DOBLE/F6150 power system simulator was used to generate simulated events in order to test FI operational conditions, such as short-circuit, steady-state, dynamic-state, and transient simulation tests.
- Oscillograph: A Yokogawa DL750 instrument was responsible for measuring and recording all waveforms produced during the experimental tests, which enabled all electric signals to be monitored in real time.
- Microcomputer: This was used to run the communication, configuration, monitoring and analysis applications, and also to generate simulated events for those instruments responsible for the injection (source) and acquisition (oscillograph) of electric signals.
- Software: Customizable computational templates (ProTest and F6-Test), available for the implementation of automated tests using a DOBLE/F6150 simulator and for controlling power system events, such as sources, inputs, outputs and timers, were used to guide all testing practices. However, the test routines here developed were generic and can therefore be implemented in any power system simulator.
- Other materials were used to compose the laboratory structure, such as galvanized steel plate, suspension isolators and cables.

In order to automate and to standardize the test procedures for fault indicators, some specific routines (macros) were developed (using ProTest) to simulate the following situations:

- Indication by current change;
- Resetting by presence of voltage on the line;
- Automatic resetting after restoring the system;
- Sensitivity to current transients;
- Operational test during primary network powering.

To address the above situations, four routine tests, presented in Section IV, were drawn up by using the LRAMPI and PRAMPI macros available from the ProTest template. The LRAMPI macro was implemented to apply an ascending or descending current, like a step function (piecewise), whose behavior is illustrated in Fig. 3. The parameters related to the pre-fault conditions and to the current steps are the following:

- Pre-fault voltage;
- Pre-fault current;
- Pre-fault duration in cycles;
- A – Initial current;
- B – Duration of the initial current;
- C – Increase/Decrease of current considering the magnitude of the previous current;
- D – Duration of the current step;
- E – Maximum value of the current.

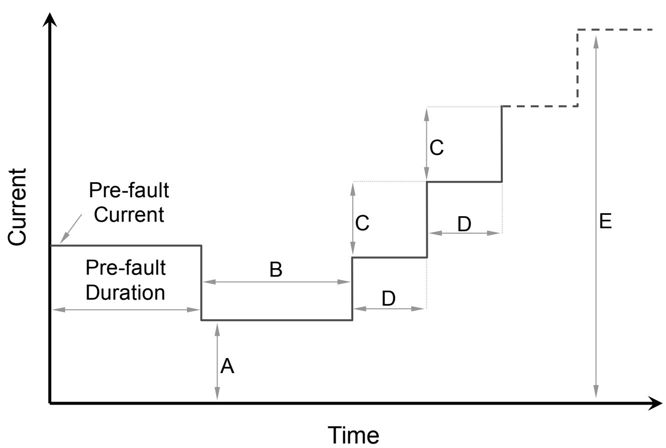

Fig. 3. Parameters of the LRAMPI macro.

The PRAMPI macro was implemented to apply a pulsating current in an increasing or decreasing way, as illustrated in Fig. 4.

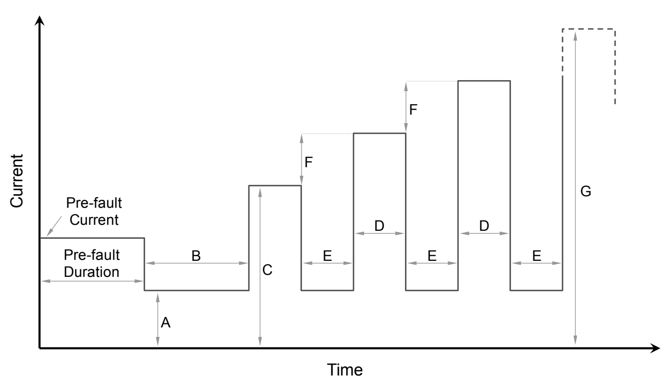

Fig. 4. Parameters of the PRAMPI macro.

The parameters relating to pre-fault conditions and to current pulses were defined by:

- Pre-fault voltage;
- Pre-fault current;
- Pre-fault duration in cycles;
- A – Initial current;
- B – Duration of the initial current;
- C – Magnitude of the first current pulse;
- D – Duration of the current pulse;
- E – Time interval between pulses;
- F – Increase/Decrease of current considering the pulse magnitude of the previous current;
- G – Maximum value of the current.

IV. Automated Test Routines

Four automated test routines were defined using LRAMPI and PRAMPI macros, which contemplated the pre-fault conditions, simulating the powering periods, and also the non-tripping periods of the FI in this situation.

The automated routine idea arose from the need for test repeatability, combining one or more macro, in order to characterize the full functioning of the distribution system in situations involving faults or normal operational situations.

A. Current Evolution

To check the FI behavior under a normal increase in load, we designed a scheme using the LRAMPI macro (Fig. 3), which simulates a current rise (in steps) as illustrated in Fig. 5. This current evolution must not be high and fast enough to generate a range of d*i*/d*t*, which would sensitize the FI device to trip on, since the purpose of the test is only to check for improper indications under situations of load increase considered normal.

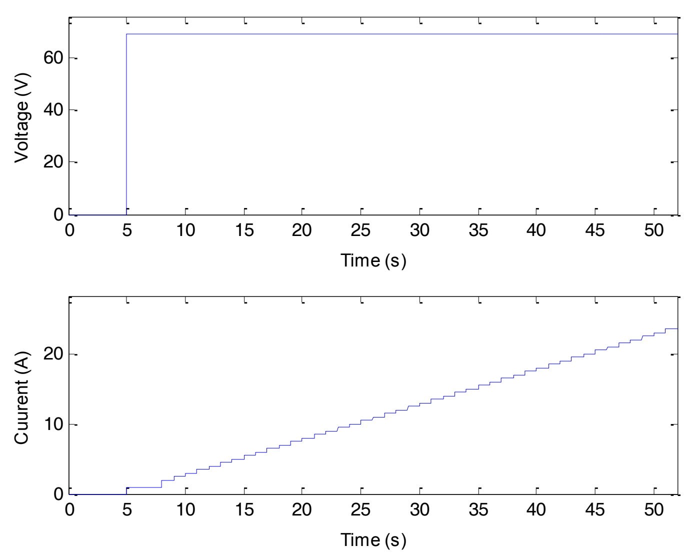

Fig. 5. Current evolution test.

B. Pulsating Currents

The second routine test includes, as shown in Fig. 6, the application of pulsating currents with increasing amplitude for each time interval.

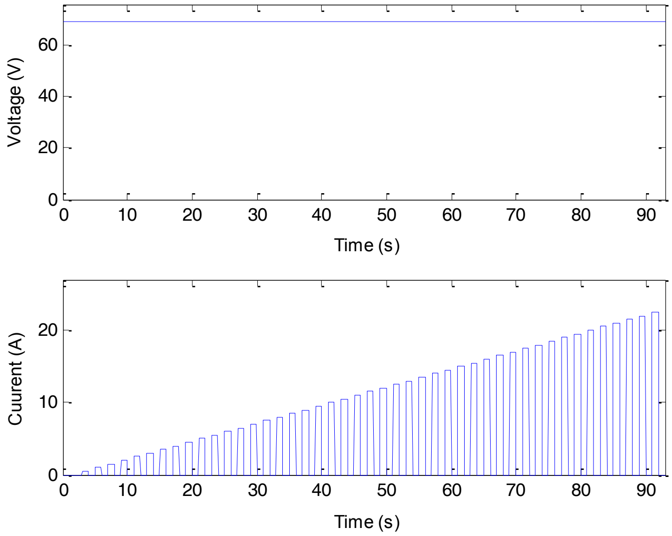

Fig. 6. Pulsating currents with increasing magnitude.

The purpose of this test is to check whether pulsating currents sensitize the FI to trip on, determining at what level of current variation the fault indication occurs. Through this test, it is possible to verify the status of the FI when the current tripping value (as specified by the manufacturer) is reached.

C. Unsuccessful Reclosing

In this scheme, a permanent fault situation in the distribution line is simulated. We considered three attempts to restart the system with no success, after which the fault was then removed and the power supply restored.

The objective of this test was to check whether the devices work properly when transient and permanent faults occur. Another important verification refers to the resetting capacity of the FI normal service is restored.

In this test, after the powering period, a fault was generated which should normally sensitive the FI device, whose current goes to 15A. It is important to highlight that normal operating current values are higher than the CT used here in a proportion of 5:30; therefore, a load current of 7A in the simulator output would be elevated in the line to 42A.

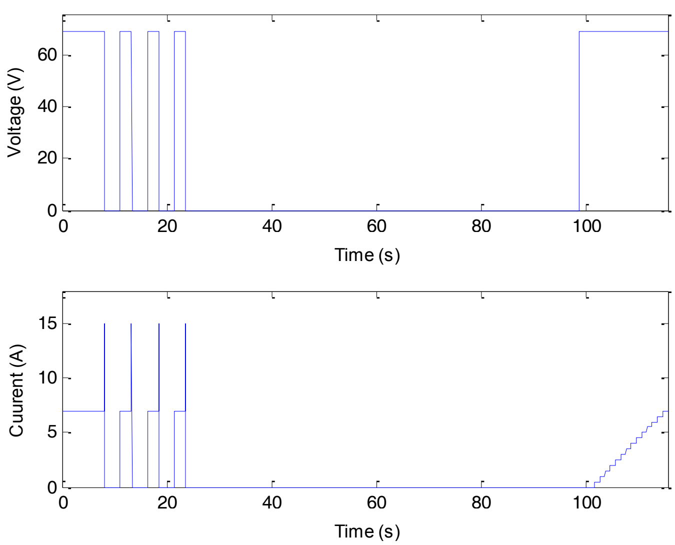

Fig. 7. Simulation of a fault condition and unsuccessful attempts at reclosing.

In this case, the PRAMPI macro only gives an increase of 8A in relation to the previous pulse, i.e., varying from 7A to 15A, the simulation being completed when this set current maximum is reached.

For this purpose, we used five PRAMP macros (in sequence) in order to produce the test routine illustrated in Fig. 7.

D. Successful Reclosing

A transient fault condition was simulated in this test, was followed by reclosing the distribution system at the second attempt. After restarting the system, there was then a load evolution. The test scheme consisted of using four macros carried out sequentially. The test is presented in Fig. 8. The purpose of the test was to verify FI response in faulty situations, followed by successful reclosing from the protection system. The FI should sensitize on the occurrence of the first fault and, after reclosing of the distribution system, it should indicate a transient fault occurrence, whose resetting action is expected in some cases.

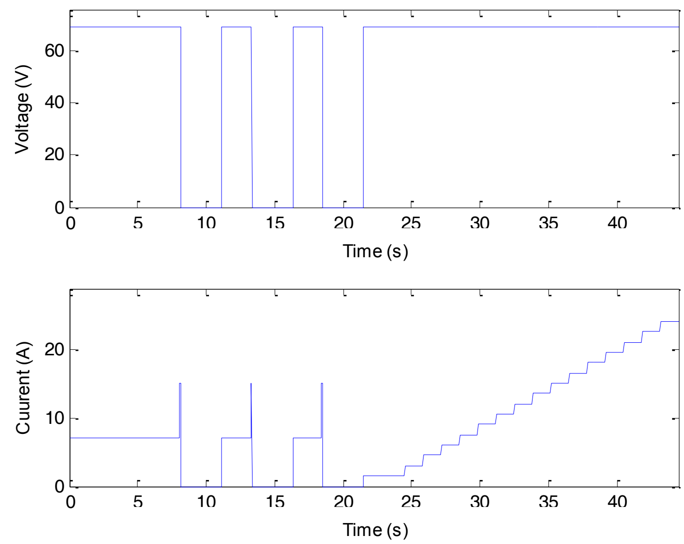

Fig. 8. Situation of fault followed by successful reclosing.

V. Experimental Results

For the purpose of validating experimental tests, we chose 4 commercial models of FI device, which are typically used in power distribution systems, and which also cover a wide range of properties involving operating characteristics, bands and types of indication. Table I provides the main features relating to the indication bands for each device tested. The number of samples for each model is proportional to the device types installed on the field. Table II describes the test plan schemes adopted for the experimental evaluation of these models.

Table I
Indication Bands

Model	Indication bands d*i*/d*t* (A)
# 1 (29 samples)	6, 12, 25, 60 and 120
# 2 (26 samples)	30
# 3 (21 samples)	6, 12, 25 and 60
# 4 (21 samples)	Automatic

ISBN: 978-1-61804-321-4

TABLE II
TEST PLAN SCHEMES

Model	Operation
#1	1 – Line powered for at least 5s 2 – Extremely fast variation of current (20ms) 3 – Voltage off
#2	1 – Line powered for 5 minutes and load current above 25A 2 – Current variation of 30A maintained for 167ms 3 – Voltage off
#3	1 – Line powered for the minimum time of 0, 3, 30 or 60s 2 – High current variation maintained for 30ms 3 – Voltage off
#4	1 – Line powered for at least 5 minutes 2 – Current variation of at least 24 ms 3 – Voltage off 2 minutes after the fault

In order to be able to take into consideration the different operating principles of the FI models chosen for evaluation, the test plan was adapted to the specifications of model to be tested. These adjustments included the setting of parameters, such as minimum time for enabling or minimum load current, for each band available for indicating faults.

Model #2 presents a fixed setting (single indication band), which means that each experimental repetition (total of 4 tests per repetition according to Section IV) was sufficient to cover all the operational possibilities.

In relation to models #1 and #3, they have 5 and 4 indication bands, respectively, which necessitated for each experiment a repetition of 20 and 16 tests, respectively.

Model #4 provides automatic adjustment of the indication bands, with up to 8 different adjustment levels. Each of these 8 levels required 4 automated tests, considering only one experimental repetition. In this case, 32 tests were then needed to cover all operational possibilities. Only 4 bands were utilized, since the remaining 4 applied to levels of current not supported in the simulated circuits.

In fact, prior preparation arrangements for each test can be extremely time-consuming when using non-automated routines, while the adjustments performed from the developed methodology were quickly and accurately implemented for each device being evaluated.

The possibility of experimental repeatability is another advantage in using automated routines to detect defects in FI lots, because it is possible to carry out various tests with the same model. In this case, an experimental repetition was composed of those 4 tests defined in Section IV. A total of 10 repetitions was assumed for testing each sample, which meant that 40 tests were performed for each sample of model #2, a total of 160 tests for each sample of models #3 and #4, and 200 tests for samples of model #4.

The overall FI operational success/failure rate is shown in Fig. 9, which reveals numbers very close to those observed in the field, i.e., an efficiency of 80%.

The results reported in Fig. 9 thus confirm that the standard tests recommended by manufacturers alone are insufficient to verify the correct functioning of FIs when installed in the field, since most models showed no operational problem in relation to the application of these standard tests. Moreover, the failure rate of 17% obtained in the course of the laboratory procedures is close to that observed by utilities, which is close to 20%.

Fig. 9. Overall FI operational success/failure rate.

It is worth highlighting the efficiency of this new test methodology in detecting defective devices very quickly, which makes it possible to reject unreliable FI devices, even where they have passed manufacturers' standard tests.

Other additional tests were also executed in order to verify if the distance between adjacent fault indicators can affect their operation, and so discover if there is a minimum separation distance for the installation of fault indicators to guarantee correct functioning. Fig. 10 illustrates the experimental arrangement involving distance variations between 4 fault indicators.

Fig. 10. Experimental arrangement analyzing varying separation distance between fault indicators.

Several experimental tests were carried out for different distances between the fault indicators, demonstrating that undue proximity between them provokes deformation in the magnetic field to be monitored. The tests indicated that a minimum distance of 50 centimeters is sufficient to guarantee adequate functioning.

Another interesting test analyzed the angular position between fault indicators, whose experimental arrangement is illustrated in Fig. 11.

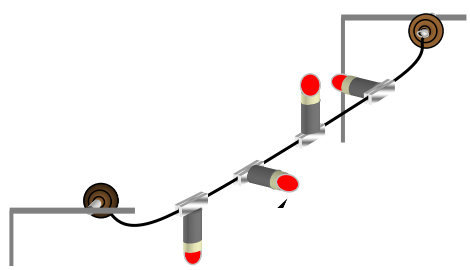

Fig. 11. Experimental arrangement considering angular variation between several fault indicators.

Additionally, various other tests involving angular variation between voltage and current signals were also executed. In this test, every fault indicator provided correct responses irrespective of its angle of installation.

ISBN: 978-1-61804-321-4

Finally, by way of complementary tests for validation purposes, the test methodology was applied to 24 samples that had been removed from the field, out of which 11 were operating correctly and 13 were faulty. The tests successfully differentiated between healthy samples and faulty ones. In contrast, most of the samples considered faulty were not found to be so when tests recommended by the manufacturers alone were applied.

VI. CONCLUSIONS

The aim of this study was to develop and to validate an automated methodology for experimental tests involving FIs, since there is known to be a high failure rate of these devices when installed in the field. Four FI models, with different indication bands and operating principles, were chosen for evaluation. These models cover the most common devices used in distribution feeders.

The overall rate of correct responses (83%) was very close to that observed in the field, which is about 80% according to the utilities that use this type of device. The efficiency of this test methodology, obtaining failure rates similar to those found in the field, leads us to the conclusion that several improvements need to be made in the design of FI devices.

In general terms, the new methodology here developed, composed of 4 experimental test routines, has confirmed that standard tests recommended by manufacturers are insufficient to certify the correct functioning of FI devices when installed in distribution feeders.

The reliability of these devices is only assured when they are tested under real conditions of voltage, current and repeatability. Furthermore, most manufacturers omit to mention in their reference guides to what extent correct functioning of FIs is dependent on battery charge level.

In addition, the speed with which experimental tests can be performed using this new methodology should also be highlighted, since it is possible to verify the behavior of each fault indicator prior to installation.

ACKNOWLEDGMENT

The authors gratefully acknowledge to the FAPESP (Process 2011/17610-0) by the financial support for the development of this research.

REFERENCES

[1] T. Baldwin, F. Renovich, L. F. Saunders and D. Lubkeman, "Fault locating in ungrounded and high-resistance grounded systems," *IEEE Trans. on Industry Applications*, vol. 37, no. 4, pp. 1152-1159, 2001.

[2] T. Baldwin, F. Renovich and L. F. Saunders, "Directional ground-fault indicator for high-resistance grounded systems," *IEEE Trans. on Industry Applications*, vol. 39, no. 2, pp. 325-332, 2003.

[3] Y. Tang, H. F. Wang, R. K. Aggarwal and A.T. Johns, "Fault indicators in transmission and distribution systems," in *Proc. Electric Utility Deregulation and Restructuring and Power Tech.*, pp. 238-243, 2000.

[4] G. Baker, J. P. Steiner and D. Rockwell, "Performance of on-line fault distance monitor for distribution cable circuits," in *Proc. IEEE Transmission and Distribution*, vol. 2, pp. 979-981, 2001.

[5] F. J. Muench and G. A. Wright, "Fault indicators: types, strengths & applications," *IEEE Trans. on Power Apparatus and Systems*, vol. PAS-103, no. 12, pp. 3688-3693, 1984.

[6] H. Falaghi, M. R. Haghifam and M. R. O. Tabrizi, "Fault indicators effects on distribution reliability indices," in *Proc. International Conf. and Exhibition on Electricity Distribution (CIRED)*, pp. 1-4, 2005.

[7] H. F. Zhang, Z. C. Pan and Z. Z. Sang, "Fault locating in ungrounded and compensated systems," in *Proc. 8th IEE International Conf. on Developments in Power System Protection*, vol. 2, pp. 469-472, 2004.

[8] D. J. Krajnak, "Faulted circuit indicators and system reliability," in *Proc. Rural Electric Power Conference*, pp. A4/1-A4/4, 2000.

[9] A. Shahsavari, S. M. Mazhari, A. Fereidunian, and H. Lesani, "Fault indicator deployment in distribution systems considering available control and protection devices: a multi-objective formulation approach," *IEEE Transactions on Power Systems*, vol. 29, no. 5, pp: 2359-2369, 2014.

[10] F. Peng, Y. Qincheng, and Y. Liu, "Research and application of new type fault indicator in smart distribution grid," 2014 China International Conference on Electricity Distribution, pp. 67-69, 2014.

[11] A. Vukojevic, P. Frey, and M. Smith, "Making a smart grid case: fault circuit indicators", *IEEE PES – General Meeting*, pp. 1-5, 2013.

[12] C. Gonzalez, T. de Rybel, de Miguel, and J. Driesen, "Implementation of a digital directional fault passage indicator," *39th Annual Conference of the IEEE Industrial Electronics Society*, pp. 2075-2080, 2013.

[13] H. Thomas and J. Kalmuck, "Reset characteristics of automatic resetting type fault indicators on three-phase URD systems," *IEEE Trans. on Power Apparatus and Systems*, vol. PAS-101, no. 8, pp. 2439-2442, 1982.

[14] E. Bjerkan, "Efficient fault management using remote fault indicators," in *Proc. International Conf. and Exhibition on Electricity Distribution (CIRED)*, pp.1-4, 2009.

[15] D. M. B. S. Souza, A. F. Assis, I. N. Silva, and W. F. Usida, "Efficient fuzzy approach for allocating fault indicators in power distribution lines," in *Proc. IEEE Transmission and Distribution*, pp. 1-6, 2008.

[16] C. Y. Ho, T. E. Lee, and C. H. Lin, "Optimal placement of fault indicators using the immune algorithm," *IEEE Trans. on Power Systems*, vol. 26, no. 1, pp. 38-45, 2011.

[17] IEEE Std. 495-2007, *IEEE Guide for Testing Faulted Circuit Indicators*, pp. 1-17, 2007.

Ivan Nunes da Silva was born in São José do Rio Preto, Brazil, in 1967. He received both M.Sc. and Ph.D. degree in electrical engineering from the State University of Campinas, Brazil, in 1995 and 1997, respectively. Currently he is an Associate Professor at the USP. His research interests are within the fields of power system automation. He is also associate editor of the Journal of Control & Automation (Brazil). He has published more than 250 papers in congress proceedings, international journals and book chapters.

Danilo Hernane Spatti was born in Araras, Brazil, in 1981. He graduated in electrical engineering and received Ph.D. degree in electrical engineering from the University of São Paulo (USP), Brazil, in 2011. Currently he is conducting a postdoctoral study at the USP. His research interests are within the field of power system protection, intelligent systems, computation complexity and optimization.

Rogerio Andrade Flauzino was born in Franca, Brazil, in 1978. He graduated in electrical engineering and received Ph.D. degree in electrical engineering from the USP, Brazil, in 2007. Currently he is an Assistant Professor at the USP. His research interests are within the field of power system protection, nonlinear optimization, and intelligent systems. He has published more than 80 papers in congress proceedings, international journals and book chapters.

Intelligent Speed Adaptation For Highways In Egypt

M. A. Massoud

Abstract **—**This paper represents a new technique for safety highways. This system is designed to maintain and limit speed on highways in Egypt. This system consists of two units a transmitter unit which is fixed at an entrance of highway, and a car receiver unit which locates in the vehicle. The system allows the efficient adaptation of the speed of the vehicle to the circumstances of the road to avoid the speed accidents. Moreover the system can apply in special regions as schools, hospitals, and government buildings.

Keywords— Speed limiter, throttle position sensor, Transmitter unit, car receiver unit.

I.INTRODUCTION

By official statistics of the ministry of transport in Egypt revealed that the total accidents on highways in 2011 were 2000 accidents. There were 1000 dead and 4400 injured persons. The statistics showed that 58.4% of accidents were caused by the human element; 30.6% as a result of defects in the car, the rest distributed to environmental factors and weather conditions. In the cities the 90-95% of the traffic accident is occurred by the driver errors [1]- [3].

Human errors occur by many factors such as; high speed, careless drive, overweight trunk, Overhight trunk, and bad driver attitudes [4].

Education, mass media campaigns, and police enforcement are very important factors which lead to minimize road accident by changing the driver behaviors[5]- [7].

The ministry of transport statistical and many other statistical spotted the technical opinion of the passage about the causes of accidents, and the outcome that came speeding in the first place [8].

Accident caused by high speed has become a serious health problem [9].So that the speed limiter plays the main function that can eliminate high speed accidents.

M. A. Massoud is with Faculty of Engineering, El-Minia University, Egypt (Mobil: 01008186983; e-mail: Massoud300@yahoo.com).

There are many researches in the speed limiter field. The driver behavior improved when speed is limited by using Automatic Speed Control [10]-[12] and Intelligent Speed Adaptation (ISA) systems. Automatic Speed Control is reduced and adaptive speed. The ISA can separate into three types of system; advisory, advisory intervention, and mandatory intervention[13]-[20]

Cruise control system (CCS) and adaptive cruise control (ACCS) are the systems belong to ISA. In ACCS a constant speed and the safe distance from the preceding vehicle can be taken [21], [22].

This introduced system belong to ISA system which is maintain and limit speed at highways in Egypt.

II. METHODOLOGY

The proposed technique was designed to decrease highway accidents and enhance the driving safety. According to traffic department rules in Egypt, the maximum speed of desert ways are; 60 km/h to tractor and semi trailer cars, 80km/h to transport cars, 90 km/h for passenger cars, and 100 km/h for the rest types of cars [23]. Therefore the setting of maximum speed is 100km/h.

The system consists of a transmitter (TX) unit and a car receiver (RX) unit. The TX unit is designed to establish at highway entrance. It composed of sensor, controller, and transmitter module. In the car receiver (RX) unit, the receiver module receives RF signal and sends it to Arduino controller. Fig. 1 shows the block diagram of transmitter unit.

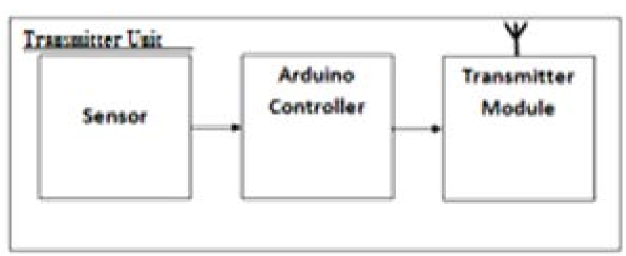

Fig. 1 The block diagram of the transmitter unit.

ISBN: 978-1-61804-321-4

The prototype of introduced system shows in Fig. 2(a). It uses a photoelectric sensor to detect the car and send signal to Arduino controller which sends the signal to NRF24L01 TX module. The TX unit transmits radio frequency (RF) signal to car RX unit. Fig. 2(b) shows the proposed highway entrance.

Fig. 2 The prototype system and proposed entrance.

Modern cars use engine control unit (ECU) as a new control system. ECU is a type of electronic unit that controls a series of actuators on an internal combustion engine to get optimal engine performance. Air/fuel mixture, idle speed, electronic valve, and ignition timing are controlled by ECU. In the engine fuel injection, ECU determines the quantity of the air/fuel injection. Fig. 3 shows the block diagram of the proposed technique.

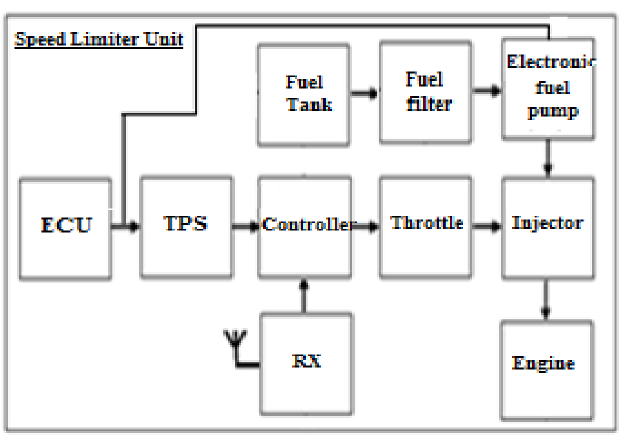

Fig. 3 The block diagram of the proposed technique.

ECU sends a signal to throttle position sensor (TPS) which uses to control the throttle opening or closed depending on gas pedal. The TPS is a simple electronic potentiometer device. Fig. 4 shows the TPS and wire connection.

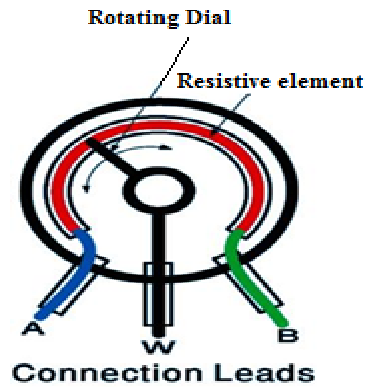

Fig. 4 The TPS and wire connection.

Fig. 4 shows three wires connected to potentiometer namely A, B, and W. Wire A is related to a reference voltage (5 volt), B is a ground (0 volt), and W is a control signal. The control signal is a signal which controls the throttle to open or closed. A throttle is a butterfly valve that is controlled in air flow to mix with fuel. The throttle is wide open at high speed and vice versa. Fig. 5 shows the throttle and TPS in the car engine

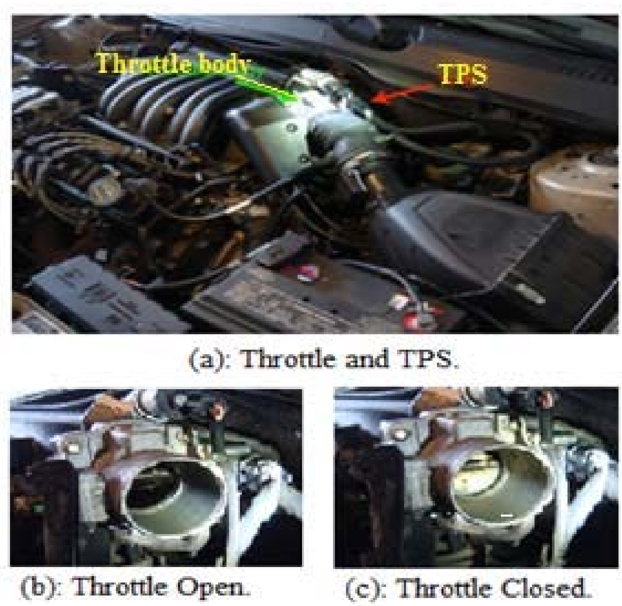

Fig. 5 The Throttle and TPS

ISBN: 978-1-61804-321-4

The system is design to control in the throttle by Arduino controller. At the entrance of the desert way, the TX sends thesignal then the car RX receives this signal.

The Arduino controller works by the RX signal as illustrated in Fig. 3. If car speed is less than or equal permissible speed the Arduino applies TPS voltage, otherwise the Arduino voltage applies following equation:

$$\text{Arduino output voltage} = 5\text{V} \times \alpha/\zeta \qquad (1)$$

where:

α is a permissible speed of highway,

ζ is a maximum car speed.

The throttle is controlled by Arduino output voltage. Fuel mixes with throttle air in the carburetor (injector) to feed an engine and reduce the car speed. The RX prototype system illustrates in Fig. 6.

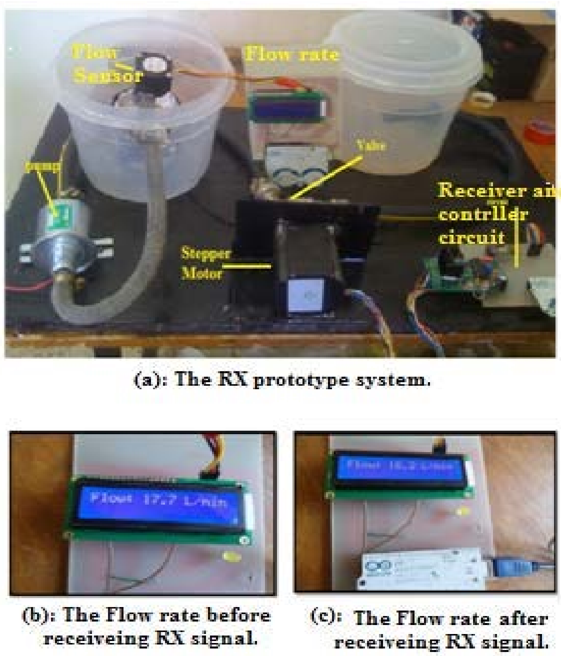

(a): The RX prototype system.

(b): The Flow rate before receiveing RX signal.

(c): The Flow rate after receiveing RX signal.

Fig. 6 The RX prototype system and Flow rate before and after RX signal .

The electric circuit of the prototype stepper motor shows in Fig. 7.

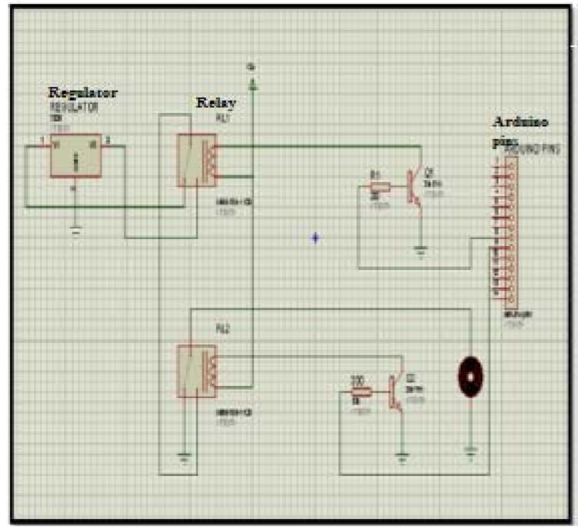

Fig. 7 The electric circuit of the prototype stepper motor.

III RESULTS

The system had been tested to measure the performance and accuracy. The prototype system was tested 30 times, a half of them without using TX signal. Twelve of fifteen were success to maintain a desire speed without using TX signal. By using TX signal all tested conditions were success to maintain a desire speed. So that the accuracy increase from 80% to 100% to limit speed by using introduced system. TABLE 1 illustrates the results of testing system and Fig. 8 shows the accuracy of the system.

TABLE 1. The results of tested system.

	Testing Without TX signal	Testing With TX signal
Number of testing system	15	15
Maintain a desire speed	12	15
System accuracy	80%	100%

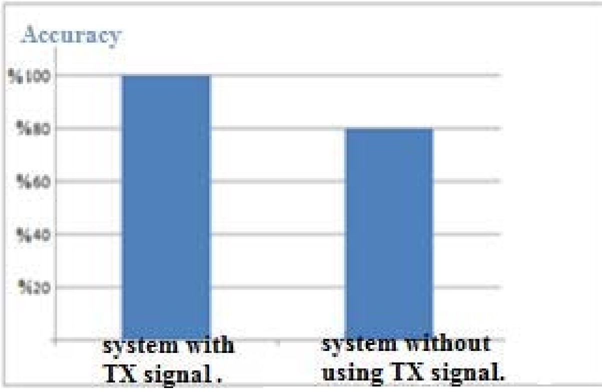

Fig. 8 The accuracy of the system.

IV. CONCLUSIONS

Speed limiter can improve the driving safety in Egypt. It suffers from high way accidents. The prototype study evaluated speed limiter control in terms of TX and RX signals. The vehicle's speed was successfully changed as a result of the detection of the signals, increasing the driver's safety. The technique can assist human drivers in difficult road circumstances. This ensures that the safety is done effectively. This system can be applied and considered as a possibility for future speed management in Egypt

REFERENCES

[1] http://www.eip.gov.eg/ Upload/ Documents/ 522/ SUM/Intro.pdf

[2] DETR , "New directions in speed management," A review of policy, Eland House, London, UK, 2000.

[3] http://www.almasryalyoum.com/ node/ 1015861

[4]- Mohamed A. Massoud, " Over-Height Vehicle Detection System in Egypt," WCE 2013, ICEEE2013, London, U.K., 3 - 5 July, 2013.

[5] Carstensen, G., "The effect on accident risk of a change in driver education in Denmark," Accident Analysis & Prevention 34(1), 2002, page 111-121.

[6] Delaney, A., Lough, B., Whelan, M., Cameron, and M., "Review of mass media campaigns in road safety," Monash University Accident Research Centre, Melbourne, Australia, 2003.

[7] Armour, M. "A review of the literature on police traffic law enforcement Australian Road", Australia, 1984, Research Board: 17-25.

[8] Rumar, K. "The role of perceptual and cognitive filters in observed behavior," VTI särtryck 111 A, VTI, Linköping, Sweden, 1986.

9] Omaima Bamasak, Ghadah Al Mehmadi, Amal Al-Ghamdi , Arwa Al-Mutawa, and Mashael Al-Ghamdi,"Monitored Intelligent Car Speed Adaptation (MISA) System," International Journal of Electrical & Computer Sciences IJECS-IJENS Vol: 11 No: 03 1, 113203-7575 IJECS-IJENS © June 2011 IJENS I J E N S.

[10] Nilsson, L., Berlin, M. "Driver attitudes and behavioral changes relatedto presentation of roadside information inside the car," A pilot study of the CAROSI system, VTI-meddelande 689 A, Linköping, Sweden, 1992.

[11] Carsten, O.,and Comte, S. "UK Work on Automatic Speed Control," Proceedings of the ICTCT 97 conference, 5-7 November 1997, Lund, Sweden, 1997.

[12] Comte, S., "Intelligent Speed Adaptation: Evaluating the possible effects of an innovative speed management system on driver behavior and road safety," University of Leeds, Leeds, UK, 2001.

[13] Päätalo, M., Peltola, H., Kallio, M.,"Intelligent speed adaptation –effects on driving behaviour," Traffic safety on three continents, Moscow, Russia, 2001.

14] Persson, H., Towliat, M., Almqvist, S., Risser, R., Magdeburg, and M.,"Speed-limiters in cars. On-road study on speeds, behavior, conflicts and drivers comments when driving in built up areas, In Swedish," Lund University, Lund, Sweden, 1993.

[15] Duynstee, L., Katteler, H., Martens, G., "Intelligent Speed Adaptation: Selected results of the Dutch practical trial," Proceedings of the 8th ITS world congress, Sydney, Australia, 2001.[16] Päätalo, H. Peltola and M. Kallio. "Intelligent Speed Adaptation-Effects on driving behavior,_, in Proc.7th European Congress on ITS, 2001, pp. 1-10.

[17] Lahrmann, H., Runge, J., and Boroch, T. "Intelligent Speed Adaptation – Development of a GPS based ISA-system and field trail of the system with24 test drivers," Aalborg University, Aalborg, Denmark, 2001.

[18] Joshué Pérez, Fernando Seco, Vicente Milanés, Antonio Jiménez, Julio C Díaz, and Teresa De Pedro, "An RFID-Based Intelligent Vehicle Speed Controller Using Active Traffic Signals," MDPI Publishing, Sensors 2010, Volume: 10, Issue: 6, Pages: 5872-5887

19] Hsieh, W.H., Ho, C.J. Jong, and G.J.,"Vehicle Information Communication Safety Combined with Mobile RFID," International Conference on Intelligent Information Hiding and Multimedia Signal Processing, Harbin, China, August 15–17, 2008.

[20] Sato, Y. "Makane, K. "Development and Evaluation of In-Vehicle Signing System Utilizing RFID Tags as Digital Traffic Signals," Int. J. ITS Res. 2006, 4, 53–58.

[21] Lusetti , B. Nouveliere, L. Glaser, S. Mammar ,and S., "Experimental Strategy for A System Based Curve Warning System for A Safe Governed Speed of A Vehicle", IEEE Intelligent Vehicles Symposium. Eindhoven, the Netherlands, June 2008; pp. 660–665.

[22] Van Nes, N.; Houtenbos, M.; Van Schagen, I. "Improving Speed Behavior: the Potential of In-Car Speed Assistance and Speed Limit Credibility", IET Intel. Transp. Syst,no2. 2008, page 323–330.

[23] http:// www.moiegypt.gov.eg/ Arabic/ Departments%20Sites/ Traffic/ QandA/ Sor3atMokarara

M. A. Massoud was born in Alexandria, Egypt on September 8th, 1964. He was graduated from Alexandria University Faculty of Engineering Electrical and Electronics department class 1987. He published many papers in Electrical and biomedical application. Dr. Mohamed Ahmed Massoud's major field is Biomedical, Electrical engineering and instrumentation, he had his B.Sc. in 1987, and then he had his Master degree in 1999 and then he had his Ph.D. degree in 2004. From 1987 to 2004 he worked as a control engineer Alexandria-Egypt, and from 2004 to now he worked as a lecture, El -Minia University -Faculty of Engineering-BED, El-Minia-Egypt.

Pertaining Classification for Decision Support System in the Form of Decision Tree for Disseminated Database

Bineet Kumar Gupta, Neeraj Kumar Tiwari, Noopur Srivastava

Abstract: Classification plays major role in an organization for decision making. Classification is useful in areas like customer segmentation, business modeling, credit analysis, and numerous applications. Sometimes there is not an easy model for an organization to enhance the performance based on decision making. In this paper we proposed a model of classification to build a decision tree for the purpose of decision making to enhance availability of useful information for decision support system. It is a combined approach of classification and information system. Decision making is also an approach of extracting useful information from the database. Proposed model stores information from disseminated database and creates a new database named decision tree database. Decision tree is built with the help of decision tree algorithm of classification. A decision tree has decision nodes and leaf nodes after when entropy becomes zero. IS can interact with decision tree database for the extraction of useful information

Keywords: Decision Tree, Information Retrieval, Information System, Database.

I. INTRODUCTION

Data Mining is the arrangement of patterns which can be mined in useful pattern. Two kinds of functions are involved in data mining on the basis of the data to be mined. First one is descriptive function which deals with general properties of data in the database. Second one is classification and prediction and classification deals with the procedure of finding a model which defines the data classes or concepts. The main tendency is to make able to use this model to predict the class of objects whose class label is unknown.

A. Classification

Classification is function of the data mining which is responsible to assign items in a group to target categories or classes. The objective of classification is to accurately predict the target class for each case in the data like classification model can be applied to identify whether to increase rates of particular procedure as low, medium, or high credit risks

There are two values in classification, first one is called values of predictor and second one is called values of target [1] [3] [4]. We use classification to find relationships between the values of the predictors and the values of the target. Classification algorithms like distance based algorithm using KNN and distance tree algorithm using ID3 Approach are used to build the decision tree [5] [6] [7].

B. Decision Tree

Decision trees are produced by an algorithm that identify various ways of splitting a data set into branch-like segments and is an important model to realize the classification. These segments form an inverted decision tree that is responsible to originate with a root node at the top of the tree. The object of analysis is reflected in this root node in the form of one dimensional display in the decision tree interface. The display of nodes reflect all the data set records, fields and field values that are found in the object of analysis.Decision trees are able to handle both categorical and numerical data.

The final result is in the form of a tree which has decision nodes and leaf nodes that means a decision node has two or more branches and leaf node characterizes a classification or decision. Therefore leaf is an important part of classification for decision making. The topmost decision node is called root node accountable to the best predictor called root node.

C. IS and DSS

An information system is a system that collect, process, store and distribute information to support decision making in an organization or we can say an information system which is responsible for tasks like planning, controlling and decision making with the help of providing summary repots and exception reports as output. Gathering of useful information is part of decision making process that includes obtaining of complete and accurate information and to point out what data suggest for the decision [9] [10] [12]. Decision support system is part IS and it enables authorities to support decision making process for special purpose in addition to get values of inputs essential to accomplish a desired level of output. Decision trees are helpful in a way of applying Information system for decision making. It is a class of computer based information system which includes knowledge based system to support decision making activities [11]. DSS is a computerized system which supports indecision making in addition DSS can assist decision suggestion or solution. It allow the decision maker to modify, complete or refine the decision suggestion provided by the system, before sending them back to the system for validation.

II. PROPOSED STUDY

Retrieval of useful information is the semi-automatic exploration of immense quantities of data to find out useful patterns that can be helpful in research or expansion of business in addition can be extremely precious for a user if done in the right way. Data extraction techniques are therefore, gearing up to use algorithms, analysis and implementation that are easy to fetch result automatically otherwise not possible to locate manually for decision making. To retrieve information from various database locations at dissimilar places for decision making, a methodology for finding the n most similar documents across multiple databases for any given query and for any positive integer n is needed. Proposed study works on disseminated database for the creation of decision tree. The decision tree is made by applying algorithms that identify ways of splitting a data set into branch like segments. These segments form a decision tree that originates with a root node at the top of the tree. Decision trees are trees that arrange instances by sorting them based on feature values. Each node in a decision tree represents a feature in an instance to be classified and each branch shows a value that the node can assume. Instances are classified starting at the root node and sorted based on their feature values. Finally a database of decision trees is created to interact with information system for desired set of operations to make decision.

Name	Gender	Height
Krishna	F	1.6 m
Jay	M	02 m
Madhvi	F	1.9 m
Mansi	F	1.88 m
Shrishti	F	1.7 m
Bhola	M	1.85 m
Triveni	M	1.95 m

Fig. 1 Database1

Name	Gender	Height
Daud	M	1.7 m
Waqar	M	2.2 m
Shakeel	M	2.1 m
Darshi	F	1.8 m

Fig. 2 Database 2

Name	Gender	Height
Khuma	F	1.9 m
Arti	F	1.8 m
Wardha	F	1.75 m

Fig. 3 Database 3

A. K nearest neighbors (KNN)

The K Nearest neighbors (KNN) in one common classification scheme based on the use of distance measures is that of. The KNN technique assumes that the entire training set includes not only the data in the set but also the desired classification for each item. In consequence, the training data become the model [4] [22] [23]. Its distance to each item in the training set must be determined when a classification is to be made for a new item. Only the K closest entries in the training set are considered further the new item is then is placed in the class that contains the most item from this set K_n closest item. Here the points in the training set are shown and K_n=3. The three closest items in the training set are shown; t will be placed in the class to which most of these are members [26], [25].

2 m ≤ Height	Tall
1.7 m < Height<2 m	Medium
Height ≤ 1.7m	Short

Fig. 4 Classified Data

B. Classification Based on Distance Based Algorithm Using KNN

We classify the tuple <Krishna F, 16> as the training data set the sample data from fig. 1 and the Output 1, for distance calculation only height will be used so that the same result is obtained for both distance for Lucknow and Jaipur. Let us consider Kn = 5, the neighbors of Kn to input tuple

Name	Height	Classification
Madhvi	1.9 m	Tall
Mansi	1.88 m	Tall
Shakeel	2.1 m	Tall
Triveni	1.95 m	Medium
Khuma	1.9 m	Tall

Fig. 5 Selected data for classification

C. Classification Based on Distance Tree Algorithm Using ID3 Approach

A decision tree is constructed top down from a root node and contains dividing the data into subsets that surround instances with similar values. ID3 algorithm practices entropy to calculate the homogeneity of a sample. It is represented as, if the sample is completely homogeneous the entropy is zero and if the sample is an equally divided it has entropy of one
To construct a decision tree

Primarily there are 10 medium and 5 tall people in the table 4.2 while considering the output 2 column. We have to produce a DT for the heights with the help of ID3 algorithm.

D. Information Gain

The information gain is a process to gain the most homogeneous branches of the entropy based on attributes therefore constructing a decision tree is finding the attribute that returns the highest information gain. The datasets are divided to smaller and smaller datasets which results the decrease in entropy after a dataset is split on an attribute.

Steps to Calculate Information Gain

Step 1: Calculate entropy of the target

Step 2: Split the dataset on the different attributes.

- 2.1 The entropy for each branch is calculated.
- 2.2 It is added proportionally, to get total entropy for the split.
- 2.3 The resulting entropy is subtracted from the entropy before the split.
- 2.4 The result is the Information Gain, or decrease in entropy

Step 3: Select the attribute with the largest information gain as the decision node

Step 4: Calculate Leaf/Split

- 4.1 leaf node → A branch with entropy of 0 is a

4.2 Again Split→ A branch with entropy more than 0 needs

Step 5: Apply The ID3 algorithm is run recursively on the non-leaf branches till classified of all data

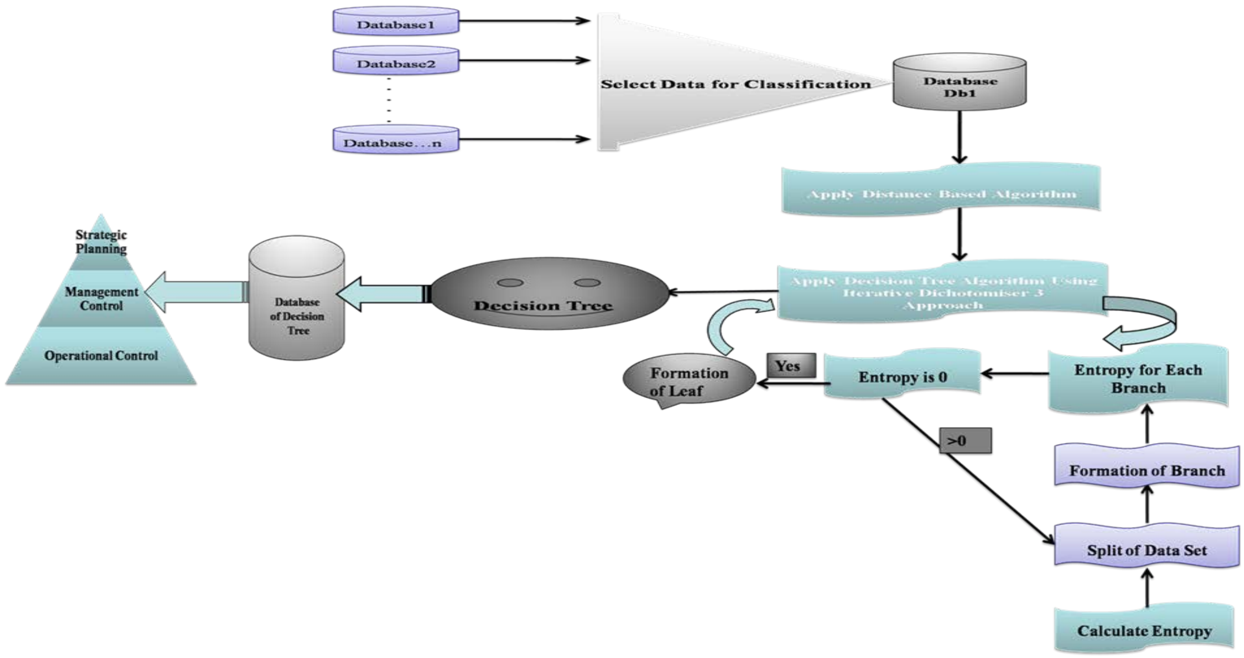

Fig. 6 Process of Decision Making

III. RESULT

In today's digital world and service on demand scenario it is commonly feel hard with handling uncertain future scenarios of corporations, institution, organizations and government agencies. It is need to plan for a multiplicity of outcomes to remain competitive for shifting business climate to executives. Very sensitive and hard decisions are made based on instant input and most of the time the proposed approach implements quantitative and logical decision to confirm expertise and experience. Our approach is combination of classification theory and information theory resulting high performance of organization for decision making. Moreover management information system can receive input in the form of classified data as well.

Abbreviation:
IS: Information System
DSS: Decision Support System
KNN: K Nearest Neighbour.

REFERENCES

[1] A. Ahmad, and L. Dey, "A k-Mean Clustering Algorithm for Mixed Numeric and Categorical Data .Data & Knowledge Engineering", 2007, 63(2), pp. 503-527.

[2] M. N. Anyanwu, and S. G. Shiva, "Comparative Analysis of Serial Decision Tree Classification Algorithms. International Journal of Computer Science and Security", 2009, 3(3), pp. 230-240.

[3] A. K. Choudhary, J. A. Harding, and M. K. Tiwari, "Data Mining in Manufacturing: A Review Based on the Kind of Knowledge. Journal of Intelligent Manufacturing", 2009, 20(5), pp. 501-521.

[4] R. Cooley, B. Mobasher, and J. Srivastava, "Web Mining Information and Pattern Discovery on the World Wide Web. Tools with Artificial Intelligence". Proceedings. Ninth IEEE International Conference, 1997, 3(8), pp. 558 – 567.

[5] T. L. Daniel, "Discovering Knowledge in Data: An Introduction to Data Mining", John Wiley & Sons, Inc., 2005, 0-471-66657-2.

[6] G. Forman and E. Kirshenbaum, "Extremely Fast Text Feature Extraction for Classification and Indexi". Conference on Information & Knowledge Management (CIKM), 2008, pp 1-15.

[7] M. Guojun, "the Principle and Algorithm of Data Mining". Tsinghua University Press, 2007.

[8] N. Gustafson, and Y. K. Ng, "Augmenting Data Retrieval with Information Retrieval Techniques by Using Word Similarity. Natural Language and Information Systems", Springer, 2008, pp. 163-174.

[9] S. Lee, S. Nat, and U. Seoul, "Challenges and Opportunities in Information Quality". E-Commerce Technology and the 4th IEEE International Conference on Enterprise Computing, E-Commerce, and E-Services, 2008, pp. 481 – 481.

[10] X. Li, "A Supervised Clustering and Classification Algorithm for Mining Data with Mixed Variables". IEEE Transactions on Systems, Man, and Cybernetics, Part A: Systems and Humans, 2006, 6(2), pp. 376-406.

[11] M. Mrunalini, T. V. S. Kumar, and K. R. Kanth, "Simulating Secure Data Extraction in Extraction Transformation Loading (ETL) Processes". IEEE Computer Modeling and Simulation Conference. EMS'09. Third UKSim European Symposium, 2009, pp. 142–147.

[12] A. Ladra, Nieves R. Farina, and G. Navarro, "Implicit Indexing of Natural Language Text By Reorganizing Bytecodes Springer Information Retrieval Journal", 2012, 15(6), pp. 527-557

[13] P. Ogilvie, and J. Callan, "The Effectiveness of Query Expansion for Distributed Information Retrieval". Proceedings of the tenth International Conference on Information and Knowledge Management, ACM, 2001, pp. 183-190.

[14] S. Ozmutlu, H. C. Ozmutlu, and A. Spink, "Automatic New Topic Identification in Search Engine Transaction Logs Using Multiple Linear Regressions". Proceedings of the 41st Annual International Conference on System Sciences, 2008, 140.

[15] B. Parhami, "Introduction to Parallel Processing Algorithms and Architectures", Kluwer Academic Publishers New York, 2002, pp. 111-112.

[16] B. Parhami, and D. Kwai, "Parallel Architectures and Adaptation Algorithms for Programmable FIR Digital Filters with Fully Pipelined Data and Control Flows", Journal of Information Science and Engineering, 2002 19, pp. 59-74.

ISBN: 978-1-61804-321-4

[17] T. N. Phyu, “Survey of Classification Techniques in Data Mining”. Proceedings of the International Multi Conference of Engineers and Computer Scientist (IMECS), 2009, 1, pp. 1-5.

[18] Yu. Qing, M. Zhengke and W. Gang, “Algorithms for Computing Google’s Pagerank and Its Derivative, with Attention To Unreferenced Nodes”, Springer Information Retrieval Journal, 2009, 15(6), pp. 503-52.

[19] E. Rahm, and H. Do, “Data Cleaning: Problems and Current Approaches”. IEEE Bulletin of the Technical Committee on Data Engineering, 2010, 23(4).

[20] S. Ramaswamy, R. Rastogi, and K. Shim, “Efficient Algorithms for Mining Outliers from Large Data Sets”. ACM SIGMOD Record, 2000, 29 (2), pp. 427-438.

[21] S. Reddy, A. Lavanya, V. Khanna, and L. S. Reddy, “Research Issues on Data Warehouse Maintenance”. International Conference on Advanced Computer Control, ICACC, 2009, pp. 623-627.

[22] E. Storti, “Semantic-Driven Design and Management of KDD Processes”. International Symposium on Collaborative Technologies and Systems (CTS), 2010, pp. 447-449.

[23] G. Wang, “A Study of Classification Algorithm for Data Mining Based on Hybrid Intelligent Systems”. Ninth ACIS International Conference on Software Engineering, Artificial Intelligence, Networking, and Parallel/Distributed Computing (SNPD), 2009, pp. 371 – 375.

[24] C. Yu, K. L. Liu, W. Meng, Z. Wu, and N. Rishe, “A Methodology to Retrieve Text Documents from Multiple Databases. Knowledge and Data Engineering”, IEEE Transactions, 2002, 14(6), pp. 1347-1361.

[25] W. Zheng, X. Wang, H. Fang and H. Cheng, “Coverage-based search result diversification”. Springer Information Retrieval Journal, 2011, 15(5), pp. 433-457.

[26] D. Zhou, S. Lawless and V. Wade, “Improving Search via Personalized Query Expansion Using Social Media”, Springer Information Retrieval Journal, 2012, 3(4), pp. 218-242

1- Dr. Bineet Kumar Gupta, an Assistant Professor in Faculty of CSE, Shri Ramswaroop Memorial University, UP, India. His area of specialization is Information Science.

2- Dr. Neeraj Kumar Tiwari (M.Tech, PhD, EACCME-Italy), an Astt. Professor in Faculty of CSE, Shri Ramswaroop Memorial University, UP, India. His area of interest includes Green Communication & E-Health.

3- Ms Noopur Srivastava , completed her M.Tech (CSE) from Shri Ramswaroop Memorial University, UP, India. Her are of interest is software development.

ISBN: 978-1-61804-321-4

Concepts of Instrumentation Scheme for Thought Transfer

Rai Sachindra Prasad

Abstract— Thought is physical force. This has been well recognized but hardly translated visually or otherwise in the sense of its transfer from one individual to another. In the present world of chaos and disorder with yawning gaps between right and wrong thinking individuals, if it is possible to transfer the right thoughts to replace the wrong ones, it would indeed be a great achievement in the present situation of the world. If a proper instrumentation scheme containing appropriate transducers and electronics is designed and implemented to realize this thought transfer phenomenon, this would prove to be extremely useful when properly used. Considering the advancements already made in recording the nerve impulses in the brain, in Aura extraction through the human bio-field measurements using GDV/EPI techniques, and the latest top most of research finding in proving the existence of an invisible physical body of human beings, it is conceivable that this may be used to very good effect in society's transformation. So far only clinical aspects in instrumentation for 'brain-to-brain transfer' have been explored which are hardly of any worth in bringing a permanent change in the society's mind-set for peace and tranquility in the present world. Presently, recording of EEG relies on capturing thought waves in the so called meditation mode where the meditation procedure means closing eyes in rest position in half-sleep conditions, while completely ignoring the roles played by pineal body, pituitary gland and 'association' areas which have profound influence in generating 'quality meditation'. In this paper, the ideal procedure of meditation is defined and then the concepts of possible instrumentation scheme for brain–to-brain transfer, irrespective of the distance of separation of the donor and recipient individuals, are discussed.

Keywords— Meditation, EEG, Neurophysiology, GDV/ EPI techniques, Biofield measurement, 'Aura' extraction.

I. Introduction

THIS is well known that human beings are the highest form of evolution of life. The knowledge of the functions of brain and nervous system greatly facilitate the understanding of biological and evolutionary basis of human behaviour considering that it is the brain alone which is the source of all actions that follow. However, because of the lack of proper motivations and directions, the mystery of human behaviour vis-à-vis brain's working has hardly been unravelled even to the extent of ten percent. In the Hindu mythology, and in their sacred scriptures like Vedas and other Holy books, it is stated that in the ages past it was an easy task to materialize instantly any thought that emerged in the human brain. It was quite an easy task to accomplish anything by mere concentration of thought. Every thought that one sends out is a vibration which never perishes. It goes on vibrating every particle of the universe whether the thoughts are noble or not. They resonate in vibration every sympathetic mind. Unconsciously, all people who are alike will take the thought one has projected and in accordance with the capacity that they have, they send out similar thoughts. This is what some call it the phenomenon of telepathy. The result is that, without our knowledge of the consequences of our own work, we will be setting in motion great forces which will work together [1]. In sharp contrast, in today's world of chaos and disorder to the utmost, such possibilities are generally dismissed as figment of imagination or a fantasy. A massive arsenal of destructive weapons including nuclear war-heads, biological and chemical weapons, together with a completely wanton society devoid of moral values are all pointers to the negative aspects in the development of science and technology. What roles the scientists and technologists have to play to stem the rot that has set in? Should we avoid the problem and set it for the nature to react or should we undertake an endeavour for a scientific research to devise some instruments or mechanisms to deliver the goods following Einstein's ideas as quoted by Marx Plank "Einstein talks about the development of our faculties of perception as science goes on. He says, scientists will arise who will have much keener perception than the scientists of today. They will also have more delicate instruments". It is with this perspective that the author was motivated to search for some innovative ideas to effect thought transfer from one individual to another. This paper discusses the concepts of instrumentation scheme using the advances already made. Components constituting proposed Instrumentation scheme are as follows:

1 Thought waves- their characteristics, 2 Current practices in extracting brain wave- limitations and suggested improvements 3 Hardware for storage of brain waves/ biofield images 4 Transmission of stored brain-waves in specially erected electromagnetically shielded enclosure 5 Tests and validation.

This paper is organized as follows: the next section deals with review of literature on brain-to-brain transfer where we cover specifically components 1 and 2 stated above; section III discusses hardware design for storage of brain wave- highlighting the specific needs for storage on an external memory device; section IV deals with the experimental procedure for exposing stored brain wave of a subject to another subject who is the candidate for thought 'correction'; section V briefly highlights the need for further advanced research and the novelty in our proposed instrumentation scheme. However, before concluding this section, the notion of ideal meditation procedure of the subject (donor) is

R. S. Prasad is Ex-Professor Graphic Era University, Dehradun, India. (Phone +91 135 2666763; Mob: +91 9997790418) email drsachpd@yahoo.com).

ISBN: 978-1-61804-321-4

described as the foundation on which this paper is built upon.

What is Ideal Meditation Procedure?

There are several important functions which are absolutely crucial to the behaviour and character pattern of an individual, despite the fact that complete understanding of the functions of the brain has remained distant proposition so far. Among the most complicated and hitherto least understood by the neurophysicists are the joint working of the two vital organs of human brain, viz., the pituitary gland and the pineal body. While the physiological psychologists are greatly interested in the roles pituitary glands play in behaviour, it has been well established that the hormones generated from these glands play a vital role in learning and memory [2]. The pineal body on the other hand has hardly been known to neuroscientists with regard to its hidden power to change the course of an individual's behaviour and character. As stated in [3] "do we realize that our body actually has three physical eyes? Our mysterious 'third eye' was pondered by mystics through the ages, and has long been believed to be the source of a higher inner vision. One may be surprised to learn that such a 'third eye' actually does exist. It is a tiny gland in our brain – the pineal gland. The pineal gland is located in the exact geometric center of the brain. Interestingly, this correlates to the exact location of the ancient Great Pyramid that sits in the center of our physical planet". The pineal gland is about the size of a pea, and sits in a tiny cave behind and above the pituitary gland. It is located directly behind our eyes, and is attached to our brain's third ventricle. And yes, it's real! The true function of this mysterious gland has long been contemplated by philosophers and spiritual adepts. The ancient Greeks believed the pineal gland was our connection to the "Realms of Thought." The great philosopher Descartes called it the "Seat of the Soul." The pineal gland has many characteristics of our exterior eyes, including a lens. It contains a complete map of the visual field of the eyes. It is activated by light, and controls our body's various natural biorhythms. The pineal body works in direct harmony with the hypothalamus gland – the director of thirst, hunger, sexual desire, and the biological clock controlling our aging process. The pineal gland secretes melanin when we are relaxed and visualizing, and also responds to electromagnetic energy. At certain brainwave frequencies such as deep Theta, a sense of our ego boundary often vanishes. Our consciousness is then less concerned with our "physical" state. According to many ancient traditions, this is when our "third eye" begins to exhibit special powers." Studies made on the effects of meditation by some researchers [4]-[6] suggest that during meditation the heart rate slows down a little, the breathing rate goes down and even cease for periods greater than thirty seconds. Other physiological changes also occur as seen in the EEG [7]. The important changes noticed in the EEG records, before and after meditation, are the decrease in frequency and the waves become more coherent.

Although no biological study or proof has been furnished as yet on the role played by pineal body, the very process of meditation is to concentrate on this pineal body so as to excite it from a 'normally' (or 'abnormally') existing 'dormant' state. One can find several books and literature on this aspect, particularly originating from India. In existing practices for obtaining basic brain patterns of individuals in the so called meditation mode, subjects are instructed to close their eyes and relax.

In this paper, the EEG waves in ideal meditation state and extraction of 'Aura' using the Gas Discharge Visualization (GDV) / Electrophotonic Imaging (EPI) techniques of biofield measurements, discussed in great details by Dr Korotkov in several papers and books [8], [9], of the individual who is capable to generate the attributes of ideal meditation are represented by templates $Temp_{EEG}$, $Temp_{GDV}$, and $Temp_{EPI}$ respectively. (The book [9] is a survey of research papers on electrophotonic imaging (EPI)). In a comparison mode, these templates will be used to compare the status of the recipient' mental health (an ordinary individual whose thought waves are desired to be replaced by the donor's thought waves non invasively). Then, we suggest the possible instrumentation hardware and software design for correction of the recipient's thought waves using the present day advancements in designing a hybrid of analog-digital circuit for simulating a given EEG wave and GDV/EPI image (aura).

II. Literature review

Electroencephalography (EEG) is a diagnostic measure that records the changes in electrical potentials (brain waves) in various parts of the brain. As an important diagnostic tool it aids in management of various types of diseases and disorders, including in the diagnosis of brain damage due to several causes. This has been discussed adequately in numerous texts and papers [10]. EEG is still in very active research in determining its scope in the diagnosis and management of mental mal function, sleep disorders , degenerative diseases and in other mental disorders. The EEG recording is conducted only by specially trained professionals and its interpretation is a matter of serious research by neurologists. The EEG recording is conducted using extremely sensitive instrument, and its findings can be greatly influenced by the mental status of the patient. It is important that the patient be properly prepared physically and psychologically in order to obtain an accurate and reliable record. Brain wave samples with dominant frequencies belong to beta, alpha, theta, and delta band. The best-known and most extensively studied rhythm of the human brain is the normal alpha rhythm. As stated in [10], Alpha can be usually observed better in the posterior and occipital regions with typical amplitude about 50 μV (peak-peak). Other conclusions drawn by the experts are stated as follows. Alpha activity is induced by closing the eyes and by relaxation, and abolished by eye opening or alerting by any mechanism (thinking, calculating). Most of the people are remarkably sensitive to the phenomenon of "eye closing", i.e. when they close their eyes their wave pattern significantly changes from beta into alpha waves. The precise origin of the alpha rhythm is still not known. EEG is sensitive to a continuum of states ranging from stress state, alertness to resting state, hypnosis, and sleep. During normal state of wakefulness with open eyes beta waves are dominant. In relaxation or drowsiness alpha activity rises and if sleep appears, power of lower frequency bands increase. Various regions of the brain do not emit the same brain wave frequency simultaneously. An EEG signal between electrodes placed on the scalp consists of many waves with different characteristics. A large amount of data received from even one single EEG recording presents a difficulty for interpretation. Individual's brain wave patterns are unique. In some cases, it is possible to distinguish persons only according to their typical brain activity. As the EEG procedure is non-invasive, it is being widely used to study the brain organization of cognitive processes such as perception, memory, attention, language, and emotion in normal adults and children. For this purpose, the most useful application of EEG recording is the ERP (event related potential) technique [11].

Brain wave characteristics:

Several texts are available which discuss the brain wave characteristics related to EEG recordings [10]. We briefly state some salient features. The rate, height, and length of brain waves vary depending on the part of the brain being studied, and every individual has an unique and characteristic brain-wave pattern. Age and state of consciousness also cause changes in wave patterns. Several wave patterns have been identified:

- Alpha waves: Most of the recorded waves in a normal adult's EEG are the occipital alpha waves, which are best obtained from the back of the head when the subject is resting quietly with the eyes closed but not asleep. These waves, occurring typically in a pattern of eight to 13 cycles per second, are blocked by excitement or by opening the eyes.
- Beta waves: These waves, obtained from the central and frontal parts of the brain, are closely related to the sensory-motor parts of the brain and are also blocked by opening the eyes. Their frequency is in the range of 8–30 hertz (cycles per second).
- Delta waves: These are irregular, slow waves of 2–3 hertz and are normally found in deep sleep and in infants and young children. They indicate an abnormality in an awake adult.
- Theta waves: These are characterized by rhythmic, slow waves of 4–7 hertz.

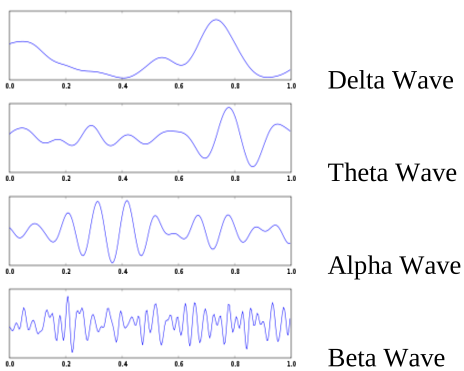

Fig. 1 Brain waves patterns

Modifications in current practice of EEG recording:

For the purpose of this paper, the EEG representing brain wave in meditation mode requires to be implemented when the ideal meditation procedure, defined earlier, is carried out. However, this would be possible when the donor of the EEG wave is an ideal person who is capable to perform in ideal mode. This is important since the extracted wave would be the template for comparison with the EEG wave of the recipient. We use a template EEG of the donor-an ideal person- and not of a patient for clinical analysis. The EEG waves featuring in our study would resemble brain wave of a person in 'real' meditation. The procedure of meditation as taken in clinical study in neuroscience is not the meditation we intend to use in our study.

III. Instrumentation Scheme (Hardware):

The details of the Instrumentation scheme design tools will be dependent upon the following basic requirements.

(i) EEG Recording and Analysis

In nature no two things are exactly similar; it is much less so in human beings. This uniqueness emanates from the different behavioral pattern of each individual. Therefore, if a continuous record of brain waves of several persons is available, a minute observation would reveal that each wave is positively different from others. Yet, if the pattern of wave of each individual is compared, it would be found that in a majority of cases of common types of human beings, a great deal of similarity exists. Let us call this type of wave pattern as pattern B. However, in case of some rare individuals whom we call Ideal, the wave pattern is strikingly different-rich in theta wave and low in other wave bands. Let us call it wave A. Obviously, pattern A is obtained through EEG under our definition of meditation state. However, in this paper, the main emphasis is on the study of the effect of imposition or impression of wave A on the receptors who have wave B on their EEG records and biofield measurement parameters templates $Temp_{GDV}$/ $Temp_{EPI}$. As a consequence, the observed changes in the various parameters of interest after exposition on individuals (type B) form the focal points of study. In this study of comparison of wave patterns (type B) and templates (type A), we do not include those who suffer from any kind of disease. Once the EEG wave patterns and GDV/EPI images are captured on storage oscilloscopes/ special cameras, their comparison would reveal glaring differences in the characteristics of the thought waves reflecting wide gap in the thinking of two sets of individuals. If an ordinary individual of type B (recipient) is subjected/ exposed to donor's wave patterns (templates) non-invasively, the behavior of B would change and if several such exposures on frequent intervals are implemented, there would be similarity of wave patterns to those of donor (A). The urgency of developing suitable instrumentation for the purpose of transmission of wave A to any distance, if needed, and its reception by an individual in need of it, without allowing corruption/ attenuation of original signal during transmission is absolute necessity for the success of the experiment. This may be achieved with the advances already made in communications, e.g., in satellites related navigation. However, an alternative to this scheme, and perhaps more useful, is the design of analog-digital hybrid circuit which can generate the same EEG wave as actually obtained during EEG recording (type A). This hybrid circuit then can be physically carried and placed in an electromagnetically (EMI) shielded room at a different location.

The analysis of brain-waves is concerned with identifying the following:

1 What is the nature of waves- periodic, aperiodic, or a mixture of the two?

2 Is there any relation of wave from one channel with that from the other, i.e., what is the relationship among the waves?

There are well developed techniques to deal with the above two cases and we do not consider it necessary to discuss this.

System Parameters for Evaluation of Experiment:

It is important that the experiment, in which a subject has been exposed to the brain-waves A in a specially shielded room, must be evaluated against some undisputed parameters. Detailed precautions for EEG recordings can be found in literature. The following procedures for experiment are proposed:

(a) Extraction of EEG wave B and its comparative analysis before and after exposition of subject to wave A. If the features noticed are contrastingly different from its original

ISBN: 978-1-61804-321-4

(before exposition) wave B, and nearly similar to wave A, the experiment is to be graded as satisfactory. The degree of nearness is subjective, however, and this is left for further study.

(b) A second parameter, as important as the EEG wave pattern and in fact more essential, is the bio-field measurement (described next) of the subject under study for extraction of aura (image). For this experiment, it is necessary to have the clinical records of the bio-field measurement of the subject before exposing to the wave A, and again after exposition in the shielded room. If the difference in bio-field measurements indicates much improved clinical features, the experiment would be graded as satisfactory.

(ii) *Measurement of the Human Biofield:*

The following text is quoted heavily from Rubik's paper [12]. The human body emits low-level light, heat, and acoustical energy; has electrical and magnetic properties; and may also transduce energy that cannot be easily defined by physics and chemistry. All of these emissions are part of the human energy field, also called the biologic field, or biofield. However, no agreement has been reached in the scientific community on the definition of the biofield. Various approaches have been submitted by several authors [9]. Most researches have focused on electromagnetic aspects of the biofield. We restrict our choice on the electromagnetic portion of the human biofield where the main scientific focus has been. In the absence of adequate funding, scientific advances in biofield research have been few, and biofield science remains a frontier area ripe for exploration. The biofield is also elusive. The biofield travels outwards to infinity, interacts with other fields by superposition, and interacts with matter along the way. Additionally, phenomena such as resonance can occur, involving an energetic coupling of, or oscillation within, matter. The fields of the human body may also be influenced by the fields of nearby organisms, the biosphere, and even the earth and cosmos, especially geo-cosmic rhythms. From a theoretical perspective, we cannot calculate the human biofield from first principles because of its dynamic aspects and enormous complexity. Nonetheless, we can measure certain aspects of the biofield and observe its footprints via novel technologies, and this is what is proposed in this paper since there are strong evidences to support this.

Conventional Measures of the Human Biofield used in Science and Medicine:

Some of the field emissions from the body are the basis of many technologies commonly used in clinical diagnosis and research. Thus a significant number of conventional medical tests already provide windows into the human biofield such as the electrocardiogram (ECG) and the electroencephalogram (EEG) to assess physiologic function of heart and brain, respectively. The human body is a strong emitter of infrared radiation, of the order of 100 watts, and visualization of this emission is used in medical imaging.

TABLE 1 Biological Effect on different frequency spectrum

Frequency Range (Hz)	Classification	Biological Effect
0	Direct Current	Non-ionizing
0-300	Extremely low frequency	Non-ionizing
$300\text{-}10^4$	Low frequency	Non-ionizing
$10^4\text{-}10^9$	Radio frequency	Non-ionizing
$10^9\text{-}10^{12}$	Microwave and Radar bands	Non-ionizing
10^{12} - 4×10^{14}	Infrared band	Non-ionizing
4×10^{14} - 7×10^{14}	Visible light	Weakly ionizing
7×10^{14} - 10^{18}	Ultrviolet band	Weakly ionizing
10^{18} - 10^{20}	X-ray films	Strongly ionizing
$>10^{20}$	Gamma rays	Strongly ionizing

Recent Approaches in Human Biofield measurements

If it would be possible to measure all of the electromagnetic components of the human biofield, with adequate funding, we would mny teams of scientists from diverse disciplines to measure the emissions of radiation from human beings at the various frequency bandwidths using a plethora of detectors and measurement devices. This effort would involve measuring different frequency bands within the electromagnetic spectrum emanating from the body as shown in Table 1. It includes the full range of non-ionizing energies, as well as visible and ultraviolet light, which are ionizing radiation. This spectral range is enormous. In some of these spectral regions, such as the infrared, as mentioned previously, the human body emits relatively high- intensity radiation, whereas in other regions, such as the visible spectrum, the body emits extremely low-intensity light radiation of the order of a few hundred photons per second per square centimeter surface area. Figure 2, given below, shows the power spectrum of human emission [12].

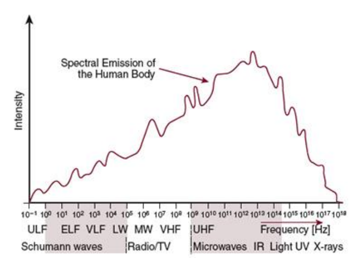

Fig. 2 Power spectrum of the human body radiation

Measuring Devices and Techniques:

Despite the claim of using various devices to identify some features of the biofield, which are essentially electromagnetic in nature, research is still in its primary stage. Therefore, several issues remain to be resolved. 'Theoretical considerations suggest that the Gas Discharge Visualization (GDV) images of some organs of the body are a complex mixture of a correlate of the biofield plus additional effects' as stated in [8]. The human subject is considered as part of a

ISBN: 978-1-61804-321-4

large electrical circuit in the GDV technique. A major contributor to the field of biofield measurement is Dr Korotkov [8], [9], who together with colleagues, has published several experimental research papers using the GDV technique on a wide range of applications to humans, including on different stages of consciousness, and in cosmetology. Some researchers advocated the utility of the GDV technique as a medical screening method. The GDV technique has been used for clinical studies mainly in Russia. Dr. Korotkov has hosted a series of annual international scientific conferences in Russia since year 2000, inviting scientists from several countries to participate and present their research findings in a variety of research areas, utilizing EPI protocols, including some significant studies involving early cancer diagnosis. Several studies by other researchers have explored the usefulness for whole body assessment of human subjects [12]. Unfortunately, there is no standard set for interpretation of the GDV data yet. However, with tremendous interest generated in this exciting area of research it would be soon when we find a very reliable measurement parameter to assess the benefits of the GDV/ EPI techniques. One limitation is that it measures induced light produced by electrifying, for example, the person's finger. A second limitation is that, for the human being, the GDV can measure emission only from the fingertips. The accumulated experience of the past years supports a conclusion [8] that the concept of spirituality and physiology can be usefully reflected by study of the biological field. The electrophoton imaging (EPI) method is one of the several possible ways of studying a biological field. For the time being a reasonable approximation would be to view the aura as an energy field, more properly a field that can be represented by a stress-energy tensor which is not in Einstein-Minkowsky space-time [8], it is to form structures in physical reality but only partly in physical space-time. Numerous publications by scientists from different countries have shown that the analysis of electrophotonic images allows registering the radiation activity from the biofield of any organism. As stated by Korotkov [8], the biofield emitted by the organism has a holographic structure but it does not represent a constant rigid formation-rather it is a living, fluctuating, breathing cloud, concentrated to a particular area of space, but not limited by any rigid borders. They are like clouds –on a gloomy day clouds are stable, but we can detect changes even within the stability. Therefore, the biological energy of humans reacts to ideomotor images and mental pictures, and an EPI-gram can be useful for psycho-physiological diagnostics of an individual's state and/or the state of mind (thought waves).

Biophoton Measurements

This type of energy is extremely low level, but it can today be accurately measured with sophisticated instrumentation that is generally customized [13],[14]. Systematic measurements of this extremely weak light emission from the body, the waveband of which is in the visible range from 400 to 720 nm in wavelength, represent one approach to assessing the radiant non-thermal human biofield. This range might be correlated, as expected, to changes in health, disease, healing, and altered states of consciousness, according to the biofield hypothesis. organism. Three types of systems are presently used to measure biophotons: (1) photomultiplier tubes, cooled down to minimize their noise, which register photon counts over time; (2) a spectral analysis system, using a set of cut-off optical filters to determine the wavelength characteristics of the emitted light; (3) and a two-dimensional system of sensitive photon-counting devices, including arrays of cooled photomultipliers and CCDs that produce biophoton images [12]. In 1992, Popp and colleagues [15] created a special darkroom with a cooled photomultiplier that could be moved around to scan the whole body of a subject lying on a bed below. The biophoton emission from humans in studies on consciousness has also been investigated. In eight subjects, Vekaria [16] investigated the influence of intention to change one's emission on the measured biophoton emission and found that the mean photon count decreased in some, but not all. Similar conclusions were drawn in experiments in [17] after meditation. One wonders if the meditation procedure followed in the experiments means closing eyes and half-sleeping-which is not the real meditation mode as discussed earlier. The handling of subjects is also problematic for these studies. Collecting the spatial data on humans is difficult, which requires that they remain still for a long time, with the risk that their blood flow may decrease in the process, affecting the biofield that researchers hope to measure. Studies also show the importance of subjects' states of consciousness, which should also be analyzed along with biophysical and physiologic correlates of photon measurements. Also at the cutting edge of biofield research is the question of how the biofield may shift as a result of shifts in consciousness. In all the above experiments if meditation procedure follows as defined earlier the nature of results would be drastically different and surprising! Fortunately, technology is advancing at a rapid speed in this area since it has now been possible to demonstrate beyond any shadow of doubt (described below) that there exists an invisible physical body [18] which theosophists and Indian sacred texts have long ago claimed. This very latest development of the proof of an invisible physical body, which in effect is the aura of the body, completely revolutionizes the present day concept of consciousness and spirituality. It gives a firm foundation to materialize instrumentation for comparing the thinking and mind-set of right and wrong thinking individuals in society. What is now left to be discovered is that each invisible physical body is unique, and that it emits colors of different shades which represent the type and nature of the individual, each being different from the other. Sooner than later this would also be demonstrated which will then help all including the neurophysiologists and neuroscientist in their efforts to diagnose the physical and mental health.

(iii) Invisible Physical Body (Aura) Experiments:

As reported on April 26, 2015, [18], and which we quote "in a first, scientists have created a perceptual illusion of having an invisible body among humans in the lab and found that the feeling of invisibility changes our physical stress response in challenging social situations. The experiment on 125 participants, neuroscientists from Sweden's Karolinska

Institute involved participants standing up and wearing a set of head-mounted displays. They were then asked to look down at their bodies, but instead they only saw empty space. Researchers then explored the psychological effects of invisibility – just as H G Wells did in his 1897 novel 'The Invisible Man' about a power mad scientist who makes himself invisible and is eventually driven insane. To evoke the feeling of having an invisible body, a scientist touched a participant's body in various places with a large paintbrush while, with another paintbrush exactly initiating the movements in mid-air in full view of the participant. 'Within less than a minute, the majority of the participants started to transfer the sensation of touch to the portion of empty space where they saw the paintbrush the paintbrush move and experienced an invisible body in that position,' said Arvid Guterstam, author of the study. 'The study demonstrates that the 'invisible hand illusion' can, surprisingly be extended to an entire invisible body,' said Arvid Guterstam. To demonstrate feasibility of the illusion, the Swedish researchers made a stabbing motion with knife towards the empty space that represented the belly of the invisible body. The participants' sweat response on seeing the knife was elevated while experiencing the illusion, but absent when the illusion was broken, which suggested the brain interpreted the threat in empty space as a threat directed towards one's own body. In another part of the study, the researchers examined whether the feeling of invisibility affected by placing the participants in front of an audience of strangers. ' We found that their heart rate and the self-reported stress level during the 'performance' was lower when they immediately experienced the invisible body illusion compared to when they experienced having a physical body,'Guterstam said. The researchers hope that the results of the study will be of value to clinical research, for example in the development of therapies for social anxiety disorder".

The primacy of the aura, the invisible physical body, over the material body, a belief held by all saints and seers and in Indian sacred books since ancient times, means that the material aspect of the body is subordinate to the physical body-in the death of human body the physical body dies immediately but not the invisible body which lasts on an average 1200 years in space, although the invisible body is also made of material such as the ether as claimed by C.W. Leadbeater-a highly reputed and well known theosophist of nineteenth century. This view is equally shared today by Rubik in [12] where she adds that "all disease may show first via imbalances in the biofield (aura). Self-healing involves changing the biofield, which then organizes changes in the tissues at the deepest levels of the biochemistry". This is a complete departure from the view that in death everything perishes.

Steps Involved in Design of Instrumentation Scheme:

(a) Search for Ideal men/women who are acknowledged to be real lover of humans, for whom the lust for worldly desires, the feeling of belonging to any particular nation or race or society are totally absent and who are directly or indirectly engaged for the upliftment of individuals of the entire world. (Note: A few persons are available and no problem exists on this score). Care must be taken to ensure proper protection against external EM radiation entering the experiment room, i.e., the experiment must be performed under electromagnetically shielded enclosure.

(b) Capture the thought waves (Brain-waves) of the selected ideal person using (i) EEG recording techniques, (ii) Biofield measurement using the techniques of GDV/ EPI-gram. Call the captured images as waves A_{EEG} and $A_{Biofield}$ and preserve them on computer hard disk.

(c) Using both linear and non linear circuit elements like R, L, C, diodes, transistors, etc., design an electrical circuit which can match the wave A_{EEG}.

(d) Design the appropriate transmission circuit for transmitting the A_{EEG} and $A_{Biofield}$ to a distant location where these waves are to be used by another individual in need of the 'treatment'

(e) As outlined in step (a) obtain record brain waves $B_{EEG(1)}$ and biofield images $B_{Biofield(1)}$ of a subject who is recipient of these images.

(f) Place the recipient at the desired location in a electromagnetically shielded enclosure and expose him/her to the transmitted waves/images A_{EEG} and $A_{Biofield}$ separately for a duration of an hour (optional).

(g) Capture the brain waves of the recipient, say $B_{EEG(2)}$ and biofield image $B_{Biofield(2)}$.

(h) Compare $B_{EEG(2)}$ and biofield image $B_{Biofield(2)}$ with $B_{EEG(1)}$ and $B_{Biofield(1)}$. If these are similar to the extent of more than sixty percent, grade the experiment 'satisfactory', else repeat the step (f) for extended duration, and repeat comparisons

(i) Extract the virtual (invisible) physical body (aura) of the ideal person (donor) and that of the recipient subject. After repeated exposure of the EEG and Biofield waves of the ideal person to the recipient subject obtain the aura of the subject. This may be continued until the patterns of EEG , biofield, and aura of the subject under study match those of the ideal person.

The following items are essential for EEG recording experiments [10]:

Electromagnetic Sensor/ Electrode cap with conductive jelly or Ag-AgCl disc electrodes with conductive paste, Amplifiers with overall amplification gain between 100-100,000, with input impedances at least 100 M Ohms, and common-mode rejection ratio at least 100 dB, Analog filters integrated in the unit with high pass filter with cut-off frequency in the range of 0.1-0.7 Hz and low pass filter with cut-off frequency less than one half of the sampling rate. Frequencies above 50 Hz are rarely involved as they contribute negligibly to power spectrum of EEG. A 12 bit or more A/D converter with accuracy lower than overall noise (0.3-2 μV pp.), and sampling frequency usually between 128 – 1024 Hz. A sophisticated PC capable to record and analyze online, with large volume external memory, Digital high pass filter with similar cut-off frequency as analog high pass. The sensor detects the brainwave signal. Once the signal is detected it passes through the DC gain. The next stage is AC coupling to remove the DC component and output a straight AC signal which will be amplified with an AC gain so a functional signal can be filtered. The Anti-Aliasing Filter (e.g., a fourth order Butterworth filter) removes any distortion and the clean signal is sent to the micro controller for processing. The micro controller is responsible for the Analog to Digital Conversion, the FFT and is also responsible for storing the data about the brainwave frequencies being detected. The signal is sent to the transmitter antenna which sends that signal wirelessly to a receiver. The second micro controller is used as a pass through which is USB interfaced with a computer.

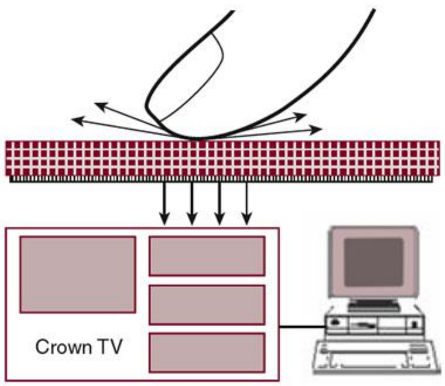

Fig. 3 Schematic set up of the GDV camera [12]

The GDV / EPI techniques would require the GDV camera and associated equipments. The GDV camera uses pulses (10-microsecond) of high-frequency (1024 Hz), high-voltage electricity (10-15 kV) that is selectable from several ranges. The time exposure of the sample is selectable from 0.5 to 30 seconds. In addition to still digital photography, recording digital video is also possible for up to 30 seconds. A charge-coupled detector (CCD), which is a standard detector of low-level visible light used in telescopes and other scientific instruments, detects the pattern of photons emitted from each fingertip. This information is sent by cable to a computer for analysis [12].

IV. EXPERIMENTAL PROCEDURE

As outlined in previous section, the first step in the experiment would be to capture the EEG wave of an ideal person (we suppose this individual is available.). It is emphasized that the experiments must be conducted in an electromagnetically shielded chamber in order to avoid any interference or corruption from external signals. For this, all necessary precautions and instructions must be taken /followed as detailed in [19]. The captured EEG wave would be then be stored in a sophisticated high resolution storage oscilloscope. Each of the four components of brain waves, viz., Theta, Beta, Alpha, and Delta would be subjected to Fourier transform to analyze the properties of the EEG wave captured. The procedure for extraction of EEG wave of an ideal person would be obtained when the person enters in meditation mode; no instructions need be given by the experimenter since the person concerned would be well aware of the real meaning of meditation. The captured wave, $Temp_{eeg}$, is then required to be simulated by an analog-digital circuit. When this is successfully implemented a prototype of this hybrid circuit would be utilized at any distant location for exposition of wave A using transmitter to the recipient as described earlier. We do not consider it necessary to discuss the design of transmitting circuit and antenna design except that the success of the experiment would be dependent upon how well the design has been perfected. Specialists performing the experiment need to be careful so that the recipient (type B wave) enters into a calm and quiet posture in the mode of so called ‘meditation’ mode as practiced today by the neuroscientists. The other alternative is to transmit directly the EEG wave A to a distant location, where the recipient is confined in a EM-shielded enclosure, right from the experiment room using the advances in transmission of signal without corruption as in satellite navigation.

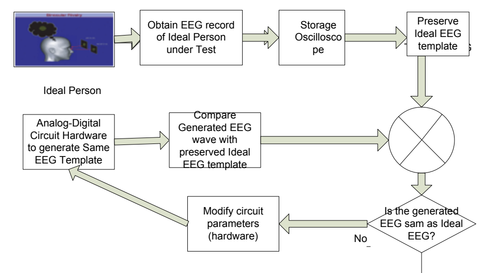

Fig. 4 Flow chart for EEG recording and Hybrid circuit simulation for EEG Generation (Wave A)-see text

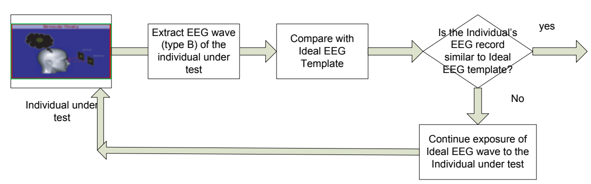

Fig 5 Flow chart for Comparing Individual's EEG wave with Ideal EEG Template

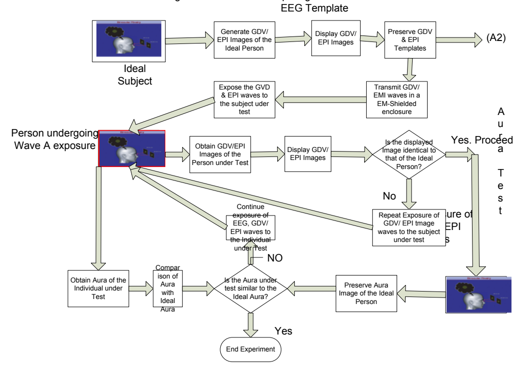

Fig 6. Flow chart of experiment processes obtaining and comparing GDV/ EPI and Aura Tests

Figs. 4, 5 and 6 represent the Flow chart of the experiments.

Before exposing (radiating) wave A on to the recipient, however, EEG wave of the recipient would be captured (wave B) and with the help of the template for EEG of wave A it would be compared at regular intervals. The comparison parameters for EEG wave would come from Fourier transform analysis and its power spectrum. The experiment would be

ISBN: 978-1-61804-321-4

completed in more than one sitting until a marked similarity with $Temp_{eeg}$ occurs. Simultaneously, neuropsychologists would determine the 'significant' change in the behavior and thinking process of the recipient. This would determine the degree of success of the experiment and would conclude when the transform parameters match and psychologists' findings agree.

Validation of the proposed concept

With the latest research on the existence of an invisible physical body [18] it is now easily possible to verify the logic of the proposed instrumentation scheme. The invisible body of common human beings of type B wave would not be distinctly different from each other except when some of them are suffering from some disease. However, when their aura (invisible physical body) would be compared with that from the ideal person (type A wave) this would be distinctly different from the group of ordinary or normal persons. With further advancements in research in near future when colours emitted by the invisible physical body are clearly visible it would be then possible to identify the gradual positive effect of exposition of radiations transmitted by the wave A and/ or image generated by GDV/ EPI. No quantitative figure can be possible as of now but visual proof of positive effect can be easily determined.

V. Conclusions

This paper outlines a novel approach of an instrumentation scheme for thought transfer. The use of EEG, GDV/EPI techniques, and the latest research on the existence of an invisible physical body open up a huge area of application of the proposed concepts in designing the instrumentation platform for benefits to the society as a whole. The implementation of this proposed concept would still take time since it would require crossing the final frontier of research in detecting the colours emitted by the invisible physical body by a team of dedicated brilliant scientists and engineers of all shades. Hope is eternal but now this hope is based on solid foundation because of finding of the existence of invisible physical body which the scientists had been dismissing as figment of imagination.

References

[1] Sri Swami Sivananda, "Thought Power," A Divine Life Society Publication, Eleventh Edition 1996, WWW Edition 1999, available on line http://www.dlshq.org/.

[2] De Wied, "Hormonal influences on motivation, learning, memory and psychosis", In D. T. Krieger and J. C. Hughes (Eds.); Neuroendocrinology, Sunderland, MA. Sinauer Associates.

[3] J. Ammon-Wexler, "Could the Mysterious Pineal Gland be the Third Eye?, Available on line BuildMindPower.com.

[4] H. Benson, J. B. Kotch, and K. D. Crassweller, "Historical and Clinical Considerations of the relaxation responses", Am Sci 1977;65:441-5

[5] M. A. Tanner et al, "The effects of transcendental program on mindfulness", JOURNAL OF CLINICAL PSYCHOLOGY, Vol. 65(6), 574--589 (2009) & 2009 Wiley Periodicals, Inc. Published online in Wiley InterScience (www.interscience.wiley.com). DOI: 10.1002/jclp.20544.

[6] C.K. Peng et al, "Heart rate dynamics during three forms of meditation," International Journal of Cardiology 95 (2004) 19 – 27 Elsevier publication.

[7] P. A. Balaji, S. R. Verne, and S. S.Ali,"Physiological Effects of Yogic Practices and Transcedental Meditation in Health and Disease", N Am J Med Sci. 2012 Oct; 4(10): 442–448.

[8] K. G. Korotkov, "Energy of Space", GDV eBooks available on line, http://www.korotkov.eu/gdv-books/.

[9] E. Jakovleva, K. G. Korotkov, "Electrophotonic Analysis in Medicine" GDV eBooks available on line, http://www.korotkov.eu/gdv-books .

[10] M.Teplan, "Fundamentals of EEG Measurement", Measurement Science Review, Vol. 2, Section 2, 2002, pp 1-11.

[11] Arvid Guterstam T.W. Picton et al," Guidelines for using event-related potentials to study cognition: Recording, standards and publication criteria", Psychophysiology , vol.37, 2000, pp 127-152.

[12] B. Rubik, "Measurement of the Human Biofield and Other Energetic Instruments," Chapter 20 of the Book *Energetics and Spirituality* by Lyn Freeman, available on-line http://www.faim.org/energymedicine/measurement-human-biofield.html.

[13] Lin S et al: "Measurement of biophoton emission with a single photon counting system", J Altern Complement Med 12:210, 2006.

[14] Van Wijk E P A, Ackerman J, Van Wijk R:" Effect of meditation on ultraweak photon emission from hands and forehead", Forsch Komplementarmed Klass Naturheilkd, 12:107, 2005.

[15] F.A. Popp, K H Li, GuQ, eds: "Recent advances in biophoton research and its applications, Singapore and New York", 1992, World Scientific Publishing

[16] M. Vekaria:" Biophoton emission and intentionality (doctoral dissertation)", Encinitas, Calif, 2003, California Institute for Human Science.

[17] E P A Van Wijk et al, "Anatomic characterization of human ultraweak photon emission in practitioners of transcendental meditation and control subjects", J Altern Complement Med 12(1):31, 2006.

[18] A. Guterstam," 'Invisible Man' is fact now, not just fiction",news item in Times Of India Daily newspaper dated April 26, 2015.

[19] "EMI Shielding Theory", available on line www.parker.com/chomerics

Automatic Focus Control of Microscope for Leukocyte Detection and Recognition System

Lina
Faculty of Information Technology
Tarumanagara University
Jl. Letjen. S. Parman No.1, Jakarta 11440, Indonesia
lina@untar.ac.id

Agus Budi Dharmawan
Faculty of Information Technology
Tarumanagara University
Jl. Letjen. S. Parman No.1, Jakarta 11440, Indonesia
agusd@fti.untar.ac.id

***Abstract*—This paper describes an automatic focus control of microscope for leukocyte detection and recognition system. The developed system consists of hardware components with servo motors and application programs for detecting leukocyte areas and identifying leukocyte types. The hardware components are integrated with the microscope to capture images of leukocytes automatically after adjusting its image focus using the Modulation Transfer Function method. Then, the Rotation-Invariant Local Binary Pattern method is implemented to recognize the leukocyte type. The experimental results show that the auto focus system could give 85% improvements of the captured image quality, and high accuracy of 94.43% and 100% were achieved for the leukocyte detection and the recognition system.**

Keywords—automatic focus control; leukocyte detection; leukocyte recognition.

I. Introduction

There are numerous works in the literature on the separation of leukocytes from eritrocytes and platelets [1-4] as analysis of leukocyte is important for understanding human body immune. The checking of leukocyte is usually conducted by calculating the number of white blood cells in one sample and comparing them to the normal leukocyte numbers. In general the counting of the human blood cells is done manually by a human operator by putting the microscope slides onto the microscope. Then, the operator will shift the microscope slides slowly from the top left area to the bottom right. During the shifting process, the operator has to identify the leukocyte type, calculate the number of each leukocyte type, and at the same time try to maintain the microscope lense focus by controlling the microscope micromanipulator gear. Since this process is highly rely on human operator, it has a high potential to human error when processing a huge number of slides continuously.

In this paper, we propose hardware components that are integrated with the microscope to adjust image focus and capture images of leukocytes automatically. The proposed hardware system moves the microscope slides smoothly, then a special camera will be used to capture the blood cell images. Finally, a leukocyte detection for separating the leukocyte areas from the images and a leukocyte recognition for identifying leukocyte types are developed.

This work is supported by the Indonesian Ministry of Education – Directorate General for Higher Education (Hibah Penelitian Unggulan Perguruan Tinggi, 2015).

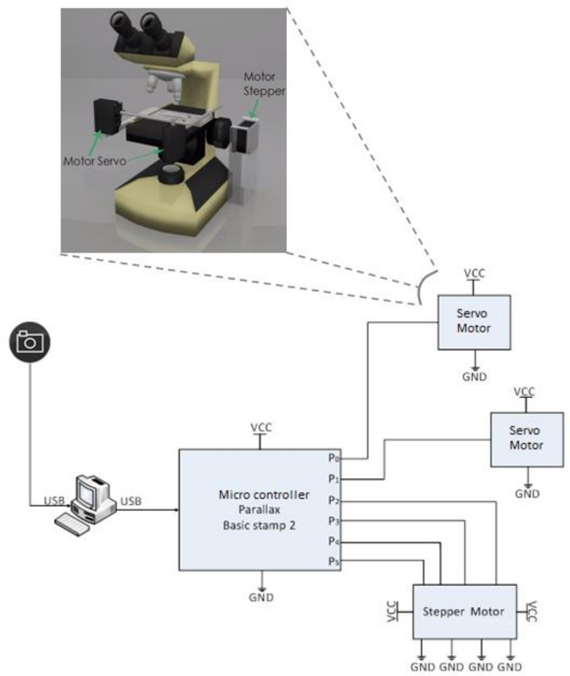

Fig. 1. The design of the customized hardware tools of the microscope.

II. Proposed System

The proposed system consists of a customized hardware components for controlling the microscope lense focus using servomotors and a software system for calculating focus value of the input image using Modulation Transfer Function (MTF) and Binary Search method, followed by the Local Binary Pattern (LBP) for the leukocyte detection and recognition system. The design and process of the developed hardware components are shown in Figure 1 and Figure 2, respectively.

A. Hardware Components

The system starts when the human operator put the microscope slide onto the microscope. The developed hardware will then smoothly shift the microscope slides from top left area to the bottom right using servo motors. For each servo motor step, a digital microscope camera will capture the

ISBN: 978-1-61804-321-4

blood cell image automatically. A digital microscope AM4023X Dino-Eye camera is used for capturing the images. The captured blood cell image will be processed using the MTF method. In general, the Modulation Transfer Function (MTF) is a method for calculating image quality [5]. The high MTF value represents the better focus of the image. The image samples of a low focus value and a high focus value are depicted in Figure 3(a) and Figure 3(b), respectively. The MTF value can be used also to estimate the best focus position from the images. Therefore, the MTF values of black and white contrast could be define as:

$$MTF = \frac{\frac{H-L}{2}}{\frac{H+L}{2}} = \frac{H-L}{H+L} \qquad (1)$$

where H is the average of the grayscale mean value (µ-255) and L is from 0 to the grayscale mean value (0-µ).

If the MTF value of the input image is less than a certain threshold, calculate the focus value using the Binary Search method and the motor stepper will control the micro manipulator gear on the microscope to change the focus of the microscope lense. This process is repeated until the input image already has the best focus value. Then the system will capture the image and proceed to the next step for leukocyte detection and recognition.

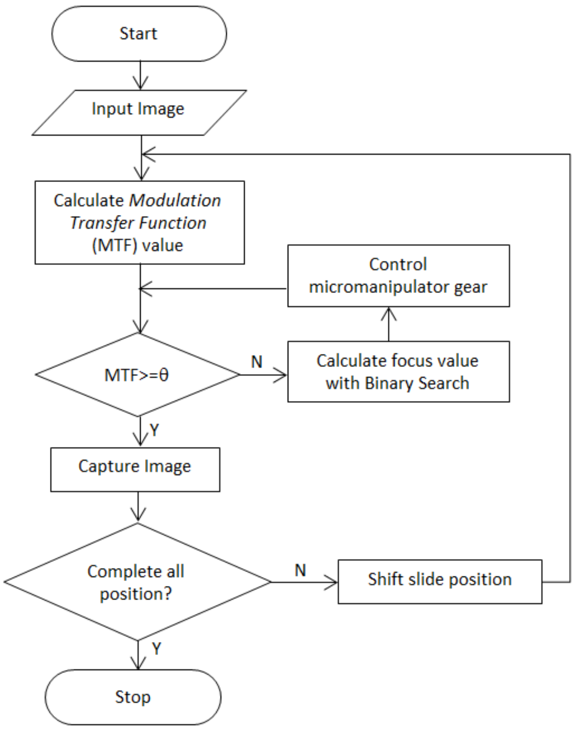

Fig. 2. The example of calculating the LBP value.

B. Leukocyte Detection and Recognition System

After capturing the images from the previous stage, the system will automatically detect the leukocyte areas in the captured image and then recognize the leukocyte types from the microscopic images. The detection process is conducted by transforming the RGB microscopic images into the grayscale image domain. Then, a simple thresholding method is used to determine the cropping area of the leukocyte. The threshold value is determined by previous learning of the leukocyte grayscale values.

For leukocyte recognition process, the cropped images which contain only the leukocyte area are processed through the system. The Local Binary Pattern (LBP) method is implemented in the recognition process to find local texture patterns in an image. In LBP, small odd size windows are constructed from the original image, such as 3x3, 5x5, etc. Then, a threshold value is determined to obtain image matrices with binary values. After the thresholding stage, the image matrix will be multiplied with a binomial weight matrix which has 1, 2, 4, ..., 128 values. The multiply results from the matrix after thresholding with the binomial weight is called the LBP value [6]. The ilustration of the process of determining the LBP value can be seen in Figure 4.

After obtaining the LBP value, a histogram is constructed from the LBP values. Finally, the Euclidean Distance of the histogram of the testing (input) image and the training images will be calculated using:

$$d(A,B) = \sqrt{\sum_{j=1}^{n} (T_j - I_j)^2} \qquad (2)$$

where *d(A,B)* is a similarity value, *I* is histogram value of the input, and *T* is the histogram value of the training image.

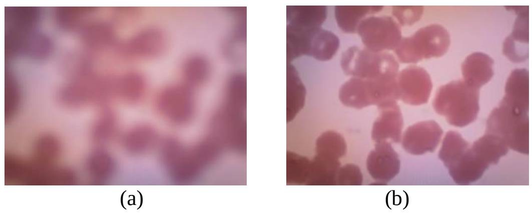

Fig. 3. The samples of the captured image with (a) low focus with MTF=0.168458, (b) high focus with MTF=0.195729.

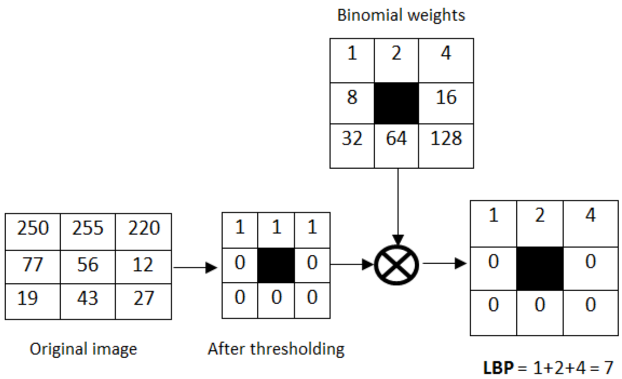

Fig. 4. The example of calculating the LBP value.

ISBN: 978-1-61804-321-4

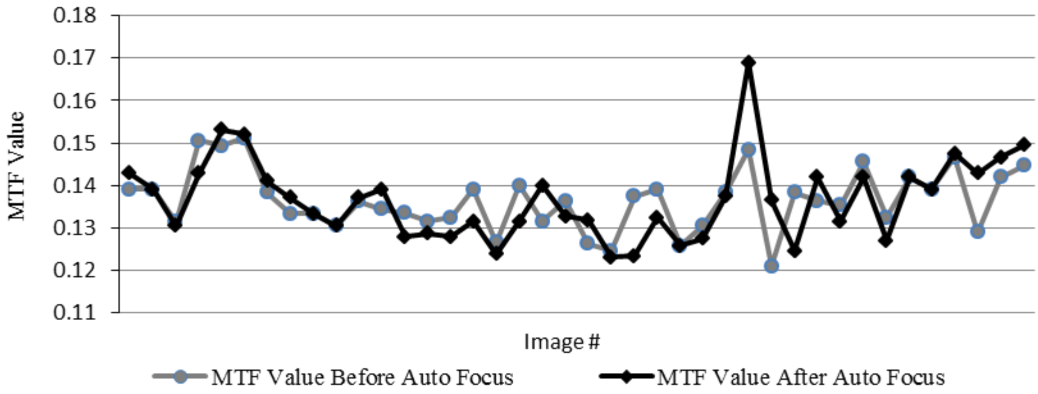

Fig. 5. The samples of MTF values of 40 images used in the experiments using the proposed auto focus system.

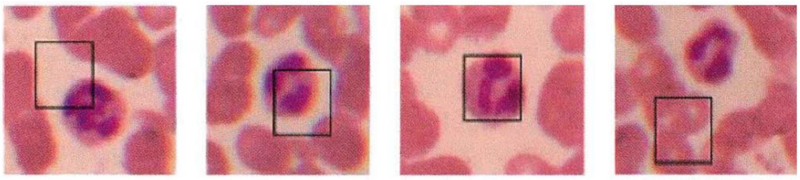

(a) (b) (c) (d)

Fig. 6. The samples of three categories of detection used in the experiments: (a) S category which contains 0.1-33% of leukocyte area, (b) M category which contains 34-66% of leukocyte area, (c) L category which contains 67-100% of leukocyte area, and (d) Background area.

TABLE I. THE EXPERIMENTAL RESULTS OF THE LEUKOCYTE DETECTION SYSTEM

Leukocyte types	Σ images	Detection Accuracy (%)			Failed (%)
		S	M	L	
Basophyl	24	0	1.64	6.23	0
Monocyte	25	0	0.98	4.26	2.95
Neutrophyl	94	0.33	1.64	28.85	0
Lymphocyte	69	0	0	20.66	1.96
Eosinophyl	93	0.33	9.84	19.67	0.66
TOTAL	**305**	**0.66**	**14.10**	**79.67**	**5.57**

III. EXPERIMENTAL RESULTS

The experimental results were conducted using three testing modules, i.e. the auto focus test, the leukocyte detection test, and the leukocyte recognition test. We developed our own database of blood cell images of 305 images with bmp format. The database consists of 24 basophyl images, 93 eosinophyl images, 69 lympocyte images, 25 monocyte images, and 94 neutrophyl images. These images were captured using a microscope camera with 1000x optical microscope lense.

For the auto focus system, the experiments were conducted by calculating the focus values using the MTF method, then finally capturing the image. Figure 5 shows the samples of MTF values of 40 images used in the experiments. It can be seen from Fig. 5, that only 15% of the data samples that were not having changes in their MTF values from the proposed auto focus system. Thus, the captured images received 85% improvements of their image focuses, which means the system gave better input images for the detection and recognition processes.

For leukocyte detection system, the experiments were conducted by autocropping the leukocyte area from the captured image. We defined 3 criteria for evaluating the performance of the detection system, i.e. S category is when 0.1-33% of the leukocyte area is correctly cropped by the system, M category is when 34-66% of the leukocyte area is correctly cropped by the system, and L category is when 67-100% of the cropped image contains the leukocyte area. Figure 6 shows the samples of images with three categories of detection (S, M, and L), and a background image without any leukocyte area. Table 1 shows the detail detection results of each leukocyte types. The total detection accuracy of the detection system is 94.43%, which contains 0.66% of S category, 14.10% of M category, and 79.67% of L category. The total failure rate of the detection system is 5.57%. From Table 1, it can be seen that the system could detect areas of basophyl and neutrophyl correctly from all the captured images, while monocyte areas was the hardest to detect by the proposed system.

TABLE II. THE EXPERIMENTAL RESULTS OF THE LEUKOCYTE RECOGNITION SYSTEM (MANUAL CROPPING OF THE TRAINING IMAGES, AUTOCROPPING OF THE TESTING IMAGES)

Leukocyte Type	Recognition Accuracy (%)		
	Dataset 1 Train:Test = 70:30	Dataset 2 Train:Test = 60:40	Dataset 3 Train:Test = 40:60
Basophyl	52.94	64.29	66.67
Neutrophyl	52.94	50	66.67
Monocyte	47.06	21.43	33.33
Eosinophyl	17.65	7.14	0
Lympocyte	100	100	100
AVERAGE	**54.12**	**48.57**	**53.33**

TABLE III. THE EXPERIMENTAL RESULTS OF THE LEUKOCYTE RECOGNITION SYSTEM (AUTOCROPPING OF THE TRAINING IMAGES, AUTOCROPPING OF THE TESTING IMAGES)

Leukocyte Type	Recognition Accuracy (%)		
	Dataset 1 Train:Test = 70:30	Dataset 2 Train:Test = 60:40	Dataset 3 Train:Test = 40:60
Basophyl	100	100	100
Neutrophyl	100	100	100
Monocyte	100	100	100
Eosinophyl	100	100	100
Lympocyte	100	100	100
AVERAGE	**100**	**100**	**100**

Finally, the leukocyte recognition system is conducted to automatically identify the leukocyte type of the input image. For the recognition system 288 images were used for testing, which consists of 24 basophyl images, 16 monocyte images, 94 neutrophyl images, 63 lymphocyte images, and 91 eosinophyl images. Table 2 shows the experimental results of the leukocyte recognition system with manual cropping of the training images and autocropping of the testing images, while Table 3 shows the results of the leukocyte recognition system with autocropping for both the training and the testing images.

From Table 2, it can be seen that for manual cropping of the training images, the higher ratio of the number of training to testing images, the recognition accuracies of the leukocytes were more evenly distributed. It is shown in Table 2 for Dataset 1 with 52.94% recognition accuracy for basophyl, 52.94% for neutrophyl, 47.06% for monocyte, and 17.65% and 100% for eosinophyl and lympocyte, respectively. However, the average values of the recognition accuracies of each dataset were not significantly changed eventhough the ratio of training and testing images were modified up to 40%. The highest recognition accuracy of the leukocyte recognition system with manual cropping of the training images and autocropping of the testing images was achieved by Dataset 1 with 54.12%. Meanwhile, Table 3 shows the recognition accuracy of the leukocyte recognition system using both autocropping technique for the training and the testing images. The proposed system could achieve 100% accuracy for every leukocyte types in all Datasets.

IV. CONCLUSION

We have presented the development of an integrated system (hardware and software) for automatic focus control of microscope for leukocyte detection and recognition system. The Modulation Transfer Function method of the auto focus system gave 85% improvements of the captured image quality. This result leads to a high detection and recognition accuracy of the leukocytes. For the detection results, the system could give a satisfying result with 94.43%, while 100% recognition accuracy could be obtained from the proposed system. In the future, we will focus on improving the detection accuracy by considering the use of other parameters, such as color and texture information.

ACKNOWLEDGMENT

The authors thank Arlends Chris from the Faculty of Medicine, Tarumanagara University, and Gunawan for their help in preparing the blood cell microscope slides and applications used in the experiments.

REFERENCES

[1] D. M. Garge and V.N. Bapat, "Application of multiwavelet transform in determining ratio of blood cells for leukemia detection," Int. Journal of Engineering and Innovative Technology, vol. 3, no. 6, pp. 205-209, December 2013.

[2] M. Adjouadi, N. Zong, and M. Ayala, "Multidimensional pattern recognition and classification of white blood cells using support vector machines," Particle & Particle System Characterization, vol. 22, no. 2, pp. 107-118, May 2005.

[3] Lina, A. Chris, and B. Mulyawan, "A combination of feature selection and co-occurrence matrix methods for leukocyte recognition system," Journal of Software Engineering and Applications, vol. 5, no. 12B, pp. 101-106, December 2012.

[4] M.C. Colunga, O.S. Siordia, S.J. Maybank, "Leukocyte recognition using EM-algorithm," Proc. 8th Mexican Int. Conference on Artificial Intelligence, pp. 545-555, November 2009.

[5] C.F.J. Kuo, C-H. Chiu, "Improved auto-focus search algorithms for CMOS image-sensing module," Journal of Information Science and Engineering, vol. 27, pp. 1377-1393, July 2011.

[6] M. Topi, P. Matti, O. Timo, "Texture classification by multi-predicate local binary pattern operators," Proc. 15th Int. Conference on Pattern Recognition, pp. 939-942, September 2000.

Lina received a B.Eng. degree in computer science from Tarumanagara University, Indonesia in 2001, and got a M.Sc. degree in computer science from the University of Indonesia in 2004. In 2009, she got her doctoral degree from Nagoya University, Japan. Currently she is working as a lecturer at Tarumanagara University, Indonesia. Her research interest is in pattern recognition and computer vision field. She is also a member of IEEE and IEICE.

Agus Budi Dharmawan received the MSc degree from the Departement of Electrical Engineering, FachbereichEIT, University of Applied Sciences Hochschule Darmstadt(hda) Germany in 2011 and the MT degree from the Departement of Electrical Engineering, ITS Surabaya, Indonesia, in 2011. He has been with the Tarumanagara University, Jakarta, Indonesia, since 2008. His research interests include robotics, computer vision, machine learning, and pattern recognition

Adjustment of the harvester parameters through fuzzy decision-making

Lyudmila V. Borisova, Inna N. Nurutdinova, and Valery P. Dimitrov

Abstract—This paper considers the problem of choosing the values of the adjustable parameters of working units of the combine harvester. Models describing dependence of the quality indicators of the harvesting on external factors have been analyzed. We justify the necessity of a new approach to modeling of technological adjustment of the combine in the field, which takes into account fuzzy information about environmental factors, its approximate character, as well as an expert method of forming information. To describe environmental factors and quality indicators we have introduced linguistic variables, developed their membership functions and formulated production rules. The process of fuzzy logic inference was illustrated by the example of choosing rotational speed value for the threshing drum. A knowledge base and an inference engine forming the basis of the expert system have been created. We have implemented the software that uses our fuzzy model for the automation of the harvester technological adjustment in the field.

Keywords—Combine Harvester, technological adjustment, fuzzy knowledge, linguistic variable, expert system..

I. Introduction

THE implementation of the potentialities included in the design of the combine harvester, achievement of the high quality performance harvesting and productivity and only possible with correct technological adjustment of working units and observance of operating rules. Complex and changing environmental conditions grain harvesters operate under require the operator to find optimal solutions promptly. Non-optimal decisions, made in the field, downtime due to technical and technological reasons result in substantial loss of resources and potentialities [1].

To develop optimal algorithms of technological adjustment it is necessary to know accurate values of environmental factors and also regularities between adjustable parameters and environmental factors. These interrelationships are quite often known approximately. As a result of the operator's inability to perform technological adjustment the harvester operates with unregulated working units and with the exceeded level of grain loss.

There are some investigations where the problem of technological adjustment is solved with the help of mathematical modeling, in particular, using regression models [2 – 4]. These models have a narrow area of the adequacy and are used only for evaluation procedures.

Among formal approaches of developing models the experimental and statistical approaches using correlation and regression analyses have got greater distribution. To eliminate the drawbacks of the traditional approach they use empirical formulae developed as a result of processing experimental data [2, 3, 5, 6]. The feasibility of empirical formulae for forecasting the values of quality indicators of operation is a positive property of the given approach. However the accuracy of the forecast is determined by the accuracy of the values of input factors, fluctuations of which in the experiment are reduced to a minimum, Therefore changes in output characteristics are stipulated, in great extent, by uncontrolled inputs and this calls into question the adequacy of the mathematical problem itself. Moreover, in these models it is necessary to take into account correlation factors, and to determine the influence of one of the factors with the fixed values of others is rather a difficult problem in the experiment. All this results in that the available correlation-regression models represent rather bulky mathematical constructions (and they don't always adequately reflect reality), and their real-time application in complex practical conditions is complicated.

At present grain harvesters rather widely use the facilities of control and management automation. Harvesters are also included into the automated system of "precision agriculture". Although application of a number of automatic control systems by important working units, devices and systems of the harvester is certainly effective, it should be noted that the available automatic systems mainly solve the problems of the harvester movement control and don't provide decision-making support for the operator when performing

.

This work was supported by the Ministry of Education and Science of the Russian Federation under the project 1.12.12 – registration number 01201255338.

Lyudmila V. Borisova is with the Department of Economics and Management in Engineering, Don State Technical University, Rostov-on-Don, Russia (phone: +7(863)258-92-10, e-mail: borisovalv09@mail.ru).

Inna N. Nurutdinova is with the Department of Applied Mathematics, Don State Technical University, Rostov-on-Don, Russia (phone: +7(863)258-91-45, e-mail: nurut.inna@yandex.ru).

Valery P. Dimitrov is with the Department of Quality Management, Don State Technical University, Rostov-on-Don, Russia (phone: +7(863)238-15-10, e-mail: kaf-qm@donstu.ru).

,

ISBN: 978-1-61804-321-4

technological adjustment of the harvester working units.

At present grain harvesters rather widely use the facilities of control and management automation. Harvesters are also included into the automated system of "precision agriculture". The available automatic systems mainly solve the problems of the harvester movement control and don't provide decision-making support for the operator when performing technological adjustment of the harvester working units.

II. PROBLEM DEFINITION

Complexity of the system of the harvester operation results in that its mathematical model is difficult to be constructed in the traditional sense, and the available approximate models are not practically suitable in the field. This causes us to turn to fuzzy modeling the methodology of which is directed to fuzzy information, its approximate character and also an expert method of forming solutions. A linguistic approach is used for the purpose of formalizing real systems, and the relationship among the sets of input and output variables is described on the quality level in the form of statements by way of production regulations. Fuzzy models have already proved to be good in very different areas [7 – 9].

The problem of choice of the adequate formal language is very important, therefore we should note the advantages of the decision-making process description in a complex multi-level hierarchy system on the basis of the theory of fuzzy sets. This language makes it possible to reflect adequately the essence of the decision-making process itself in fuzzy conditions for the multi-level system, to work with fuzzy limitations and aims and also to set them with the help of linguistic variables. Therefore a mathematical apparatus of the theory of fuzzy sets is expedient to be used as the main tool for describing a multi-level hierarchy system – a grain harvester, processes of decision-making and control of technological processes in complex systems. The suggested approach of the decision-making processes modeling when performing technological adjustment and updating of technological adjustments of the harvester working units on the basis of fuzzy models meets the requirements of the system analysis – consistency of consideration of the complex hierarchy system (harvester) on the basis of accounting basic elements and processes in the system of relations between them and the sufficient degree of simplification during modeling allowing to reflect adequately a real process and take into account the determining factors in this system.

III. PROBLEM SOLUTION

The technique of modeling the decision-making process while performing technological adjustment of the harvester is based on application of mathematical apparatus of the theory of fuzzy sets and contains the stages of fuzzification, composition and defuzzification [10, 11].

At the stage of fuzzification it is necessary to give the conditions of solving the problem in a linguistic form. At the stage of composition all the fuzzy sets specified for each term of each input variable unite and the sole fuzzy set is formed – a value for each output linguistic variable (LV). As a result of application of the rule set – fuzzy knowledge base – we calculate the truth value for supposition of each rule on the basis of certain fuzzy operations corresponding conjunction or disjunction of terms in the left part of the rule. The main point of the defuzzification stage is in working out, on the basis of fuzzy logic output, recommendations on determining certain values of the adjustable parameters of the machine.

Let us consider the problem when depending on possible values of the input situation (A_j) an expert draws a conclusion about the output situation (B_j) (about the values of the adjustable parameters). Let $\{X\}$ denote a set of values of input parameters i.e. value part of environmental factors which substantially influence the value of the output parameter V (adjustable parameter). To solve the given problem it is necessary to solve the questions of modeling expert information about relations of characteristics under consideration and also about the decision-making procedures.

According to logic-linguistic approach [12, 13] we have developed the models of input and output characteristics X, V in the form of semantic spaces and corresponding them membership functions (MF):

$$\{X_i, T(X_i), U, G, M\}, \qquad \mu_R(x_1, x_2, \dots, x_i) \in [0; 1],$$
$$\{\beta_v, T_v, V, G_v, M_v\}, \qquad \mu_R(v_1, v_2, \dots, v_j) \in [0; 1],$$

where β is a name of the linguistic variable, T - set of its values, or terms, which are the names of the linguistic variables defined over the set U, G - syntactic procedure describing the process of deriving the new values of linguistic variables from the set T, M - semantic procedure, which allows one to map new value generated by procedure G into fuzzy variable, μ - membership functions.

The result of the analysis is a generalized model of domain "preliminary adjustment of the harvester" in the form of composition of fuzzy relations of the semantic spaces under consideration:

$$\mathrm{R} = X \to V,$$

where R is a fuzzy relation between environmental factors and adjustable parameters:

$$R\{X_i, T(X_i), U, G, M\} \times \langle \beta_v, T_v, V, G_v, M_v \rangle \; \forall (x, v) \in X \times V.$$

Relation R can be regarded as a fuzzy set on the direct product XV of the complete space of suppositions X and the complete space of conclusions V.

As a result of fuzzification of the studied characteristics, MF of the adjustable parameters and external factors have been plotted. For this normal fuzzy sets for which upper bound of the membership function is equal to 1 ($\sup_{x \in E} \mu_A(x) = 1$) have been used. Fuzzy sets can be both unimodal, i.e. only on one *x* of *E*, and possessing an area of tolerance. To describe the terms we used typical functions of triangle and trapezoidal type [14].

Solution of the problem of choosing adjustable parameter values is considered by an example of selecting the values of rotational speed of the threshing drum. It is known that this parameter is greatly influenced by the following environmental factors: crop yield, grain humidity, rough straw, grain dockage [5]. The analysis of the subject domain allowed us to define linguistic description of the external factors under consideration and values of the MF parameters [12]:

LV tuple «Crop yield - 50» has the form:

<CROP YIELD, q/ha {Less 50, Approximately 50, More 50}, [44 – 56] >

CY ={CYL50, CYA50, CYM50}.

LV tuple «Stand of grain humidity» has the form:

<STAND OF GRAIN HUMIDITY, % {Dry, Normal, Humid}, [0 – 30]>

SGH ={DrSG, NorSG, HumSG}.

LV tuple «Rough straw» has the form:

<ROUGH STRAW, % {Small, Normal}, [40 – 70]>

RS ={SmRS, NorRS}.

LV tuple «Stand of grain dockage» has the form:

<STAND OF GRAIN DOCKAGE, % {Low, Large}, [0 – 40] >

SGD ={LwSGD, LgSGD, %}.

The tuple of the output LV “Rotational speed of the threshing drum for wheat-50” (i.e. for crop yield approximately 50 q/ha) has the form:

<ROTATIONAL SPEED OF THRESHING DRUM, rev/min {Very low, Low, Lower than nominal, Nominal, Higher than nominal, High, Very high}, [620 – 940] >

RSTD = {VLRSTD, LRSTD, LNRSTD, NRSTD, HNRSTD, HRSTD, VHRSTD, rev/min} (fig. 1).

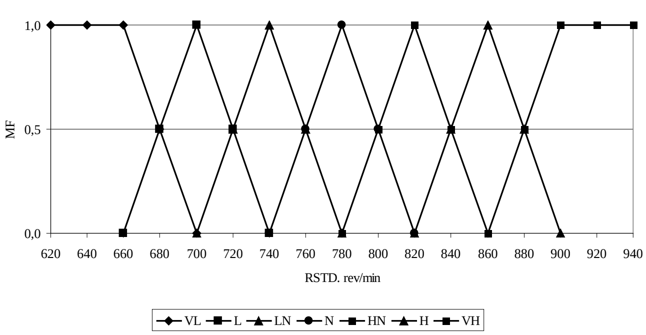

Fig/ 1 Membership functions of LV terms “Rotational speed of the threshing drum for wheat”

In the basis of the solutions output mechanism of intelligence information system there is a model of the given subject domain representing a composition of fuzzy relations of semantic spaces of input and output parameters.

An expanded form of the fuzzy logic inference for the system of knowledge is received by standard procedure [15].

As a result of the analysis of the subject domain a knowledge base has been created. A logic inference of the solution is based on it.

At the stage of defuzzification accurate values of the resulting LV are calculated. For these calculations a “center of gravity” method is used [16]. This method is implemented in Matlab with the help of Fuzzy Logic Toolbox application package [17].

Fuzzy inference is an application of a maximin composition as a compositional rule of fuzzy inference and the operation of taking minimum as a fuzzy implication:

Fuzzy inference is an application of a maximin composition as a compositional rule of fuzzy inference and the operation of taking minimum as a fuzzy implication.

Figure 2 presents surfaces “inputs-output”, and figure 3 presents graphs, corresponding synthesized fuzzy system of production rules.

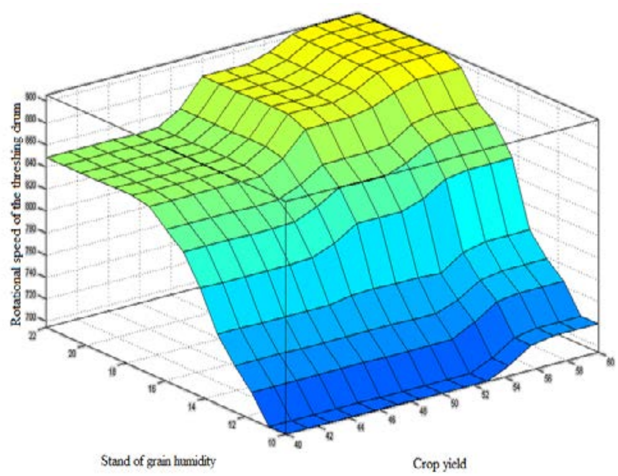

a)

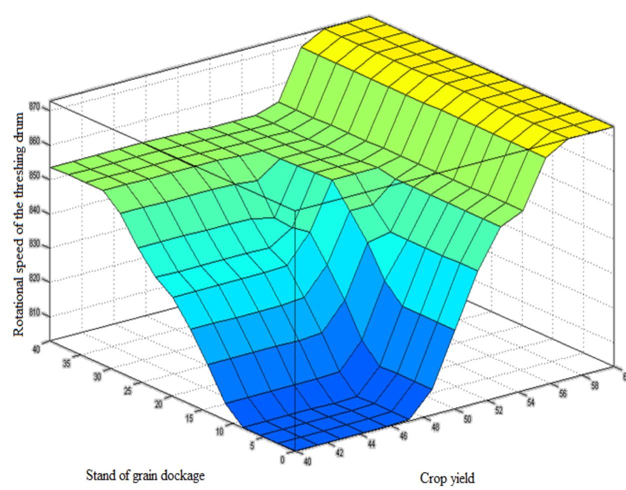

b)

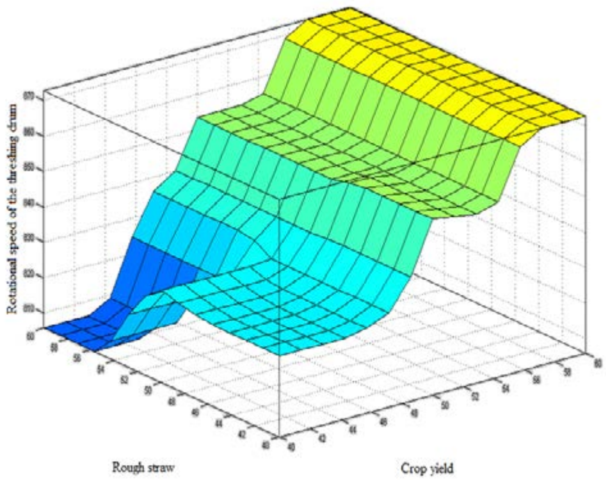

c)

Fig. 2 Response surfaces of rotational speed of the threshing drum vs a) humidity and crop yield; b) dockage and crop yield; c) rough straw and crop yield

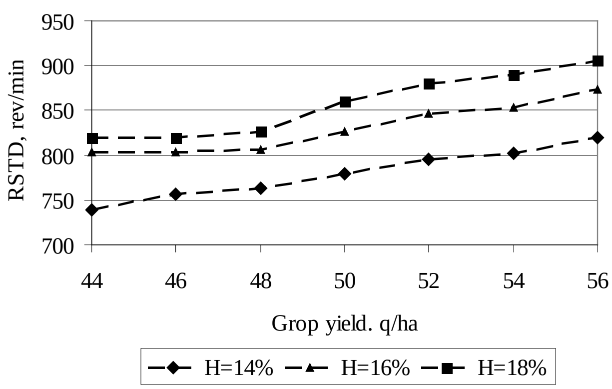

a)

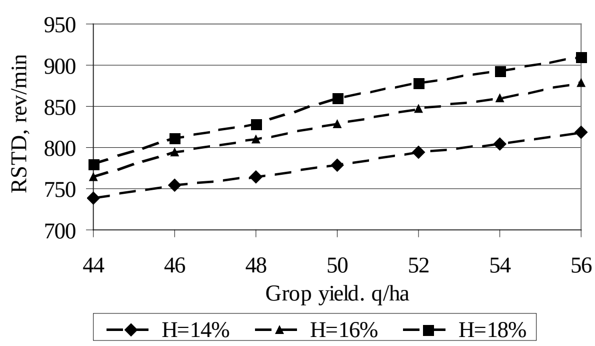

b)

Fig. 3 Dependency of rotational speed of the threshing drum on crop yield and grain humidity a) if rough straw is 50%, dockage is 10%; b) if rough straw is 40%, dockage is 0%

From figures 2 and 3 we can see that the system of fuzzy expert statements adequately describes relations: adjustable parameter – input factors.

IV. Conclusion

The analysis of papers on theoretical and applied aspects of the theory of fuzzy sets shows that application of fuzzy models makes it possible to represent the properties of the initial system properly and to simplify the process of its analysis. The accepted degree of abstraction is the most reasonable as wider generalization will be fruitless from the point of view of practice. And an insufficient degree of abstractness will result in impossibility of solving the problem – it will be too difficult. In the context of the considered example the possibility of applying fuzzy inference has been displayed. They represent ascending conclusions from suppositions to conclusions while solving the problem of the harvester technological adjustment. Modeling of relations “external factor – value of the adjustable parameter” is carried out by the way of maximum-minimum composition and also by calculating center of gravity of inference results according to each rule. On the basis of this approach the formalization of the subject domain has been performed and the mechanism of fuzzy inference of the expert system solutions has been constructed for solving the mentioned problem under the conditions of uncertainty.

Created on the basis of the model the knowledge base and the solutions output mechanism make up the basis of the expert system. Application of this system in field allows reducing time for technological delays and decreasing the yield loss. Practical implementation of the developed algorithms is creation of software tools for automatic problem solution. Application of the expert system in practice while performing technological adjustment made it possible to reduce this period 2- 5 times compared to the traditional methods.

V. References

[1] A.G. Rybalko, *Some features of harvesting high-yield crops*. Moscow: Agropromizdat, 1988.

[2] E.F. Vetrov, M.D. Genkin, L.M. Litvin and others, “Optimization of technological process according to statistic data,” *Mashinovedenie*, no. 5, 1986, pp. 48 – 55.

[3] E.F. Vetrov, V.P.Tchernyavskaya, G.F Bobrineva and others, “Optimal adjustment of combine harvester (Electronic journal «Sovetchik kombainera»),” *Proceedings*, 4/89, Moscow: NPO VISHOM, 1989, pp,. 80 – 85.

[4] L.M. Litvin, E.V. Zhalkin, E.F. Vetrov, “Generalized estimation of zone operational performance of combine harvesters,” *Machinery in agriculture*, no. 5, 1989. pp. 41 – 45.

[5] S.N. Yerokhin, A.S. Reshetov, “Influence of technological adjustments on grain loss behind the thresher of the combine Don-1500,” *Mechanization and electrification in agriculture*, no. 6, 2003, pp. 18 – 19.

[6] Y.A. Tsarev, A.V. Kharkovsky “The prospects of using electronic control system in combine harvesters “Don” and “Niva”, Tractors and agricultural machines, no. 1, 2005, pp. 37 – 38.

[7] A. N. Averkin, I. Z. Batyrshin, A. F. Blishun, V. B. Silov, V. B. Tarasov, *Fuzzy sets in the models of management and artificial intelligence*, Nauka, Moscow, 1986.

[8] K. Asai, D. Vatada, S. Sugeno, *Applied fuzzy systems*, Moscow: Mir, 1993.

[9] A. K. Tugengold. A.S. Tishin, A.F. Lysenko, “On the problem of forming knowledge system with intelligence electronic documenting of mechanotronic objects,” *Vestnik DSTU*, no. 3, pp. 30-36, 2012.

[10] L. Zadeh, “Fuzzy sets,” *Information and Control*, vol. 8, 1965, pp. 338 – 353.

ISBN: 978-1-61804-321-4

[11] L. Zadeh, "Knowledge representation in fuzzy logic," in *An Introduction to Fuzzy Logic Applications in Intelligent Systems, The Springer International Series in Engineering and Computer Science,* R.R. Yager, L.A. Zadeh Eds, vol. 165, – New York: Springer, 1992, pp. 1 – 27.
[12] V. P. Dimitrov, L. V. Borisova, *Theoretical and applied aspects of developing expert systems for machines maintenance*, Rostov-on-Don: DSTU Publishing center, 2007.
[13] L. V. Borisova "Modeling technique of the subject domain "technological adjustment" in a fuzzy formulation,"in *Proceedings RASHN*, no. 6, 2005, pp. 62 – 65.
[14] L. Kofman, *Introduction in the theory of fuzzy sets*, Moscow: Radio and communication, 1982.
[15] N.G. Malyshev, L.S. Bershtein, A.V. Bozhenyuk, *Fuzzy models for expert systems in CAD*, Moscow: Energoatomizdat, 1991.
[16] I.M. Makarov, V.M. Lokhin, S.V. Manko, M.P. Romanov, Artificial intelligence and intelligence control systems, Moscow: Nauka, 2006.
[17] S.D. Shtovba *Designing fuzzy systems with MATHLAB facilities*, Moscow: Hot line – Telecom, 2007.

Lyudmila V. Borisova graduated in 1990 with a degree in agricultural machinery at the Rostov-on-Don State Academy of Agricultural Engineering, Rostov-on-Don, Russia. She received her degree of doctor of Engineering from the Don State Technical University (DSTU), Rostov-on-Don, Russia in 2007. She is now Head of Department of Economics and Management in Engineering, DSTU, Rostov-on-Don, Russia. Her research interests include information systems of decision making support, quality management systems. She developed Expert Systems of Decision Making in the operation combine harvests. Dr. Borisova is Honorary Worker of Higher Professional Education of Russia, member of the Dissertation Council of DSTU, Rostov-on-Don, Russia. She has been involved in technical committees for several conferences.

Inna N. Nurutdinova graduated in 1982 with a degree in physics at the Rostov State University, specialty physics, Rostov-on-Don, Russia. She received her PhD in physical and mathematical sciences from the Institute of Semiconductors of Academy of Science of Ukraine, Kiev, Ukraine in 1992. She is now associate professor at the Department of Applied Mathematics, DSTU, Rostov-on-Don, Russia. Her research interests include mathematical modeling of systems and processes, application the theory of fuzzy sets, information systems of decision making.

Valery P. Dimitrov graduated in 1975 with a degree in design and production of agricultural machines at the Rostov institute of agricultural engineering, Rostov-on-Don, Russia. He received his degree of doctor of Engineering from DSTU, Rostov-on-Don, Russia in 2002. He is now head of Department of Quality Management, DSTU, Rostov-on-Don, Russia. His research interests include information systems of decision making support, operation of agriculture machines, quality management systems. He developed Expert Systems of Decision Making in the operation combine harvests. Dr. Dimitrov is Honorary Worker of Higher Professional Education of Russia, Chairman of the Dissertation Council of DSTU, Rostov-on-Don, Russia. He has been involved in technical committees for several conferences

ISBN: 978-1-61804-321-4

Harnessing Power of NVIDIA CUDA for Parallelizing the Motion Estimation Part in Video Encoding

Darshan Pawar[1], Sagar Karwande[2], Renuka Joshi[3], Kochmuriyil Jancy James[3], Chandrama Thorat[4]
Department of Computer Engineering
JSPM's Rajarshi Shahu College of Engineering
Pune, India
darshanp40@gmail.com, sagar_karwande123@yahoo.com, renu.joshi4@gmail.com, janamy.16793@yahoo.com, chandrama1684@gmail.com

Abstract*— Video compression is a very important aspect of how video streaming websites like Youtube, Netflix and Hulu etc. works. There are many video compression standards available over the internet which claims to have the best features and compression ratios, but the one being most popular is H.264. H.264 standard gives a very good compression ratio as well as quality, but it is very slow. As parallel computing is a solution to many time complex tasks, so it can also be used for video compression. This paper combines the two concepts of video compression and parallel computing to devise an approach which ultimately gives a parallel solution to the problem of slowness of H.264 standard based video compressor. This paper uses CUDA parallel computing platform to perform the task of motion estimation in parallel. This paper shows that upto 6X speedups can be achieved if parallelism is applied for video compression.

***Keywords*—Compute Unified Device Architecture (CUDA), General Purpose Graphics Processing Unit (GPGPU), H.264 Video Coding Standard, Codec, Motion Estimation, Block Matching Algorithms**

I. Introduction

Nowadays, the most widely used and followed standard for video encoding is H.264. It is known for its compression efficiency and quality of the encoded video. Though video encoding is a necessary process to have practical storage and streaming of videos, there are some factors which become a bottleneck to it. The most appealing feature is the time required for encoding. The encoders designed using H.264 standard take a lot of time for encoding a single video file. This is because of the motion estimation process which is done to encode a frame in a video. Motion Estimation is the process, which takes about 70-90 % of the total encoding time of a video. This paper proposes an approach which overcomes the drawback of time consumption of video encoding process by introducing the concept of parallelism. To achieve parallel computation task, the experiments make use of CUDA and a reference encoder very close to the H.264 standard. The experimentation has resulted in about 600% efficiency in terms of speed of video encoding.

II. Literature Survey

A. *Natural Scene*

A real world or natural video scene is typically composed of multiple objects each with their own characteristic shape, depth, texture and illumination [5]. It is spatially and temporally continuous. To process the natural scene using normal computation, digitization of the natural scene is required. So the natural scene is sampled spatially and temporally to get a digital sequence. The basic and smallest unit for representing this digital sequence is called a pixel. The spatial sampling of natural scene gives rise to pixels, whereas the temporal sampling of natural sequence gives rise to frames.

B. *Issues with uncompressed video and need for compression*

An uncompressed video scene which is also called as raw video scene is practically impossible to store for each case. The reason behind this can be simply explained by a small example. Let us say, a raw video is having a resolution of 1920 X 1080; that means for a single frame we would be having almost two million pixels. Considering 30 frames per second, we would be having almost sixty two million pixels per second. If each pixel requires 24-bit or 3-bytes of data, then we would be looking at approximately 178 mega-bytes for a video of just one second. Assuming an uncompressed video of five minutes, it will go upto 52 gigabytes. As it's clearly observed that these types of uncompressed videos are really impractical for storage purpose, as such we need video compression or encoding methods.

C. *Redundancy Removal*

The basic work which is done in any compression technique for any type of data is the removal of redundancy. The same case is applied to video encoding. Video encoding works on eliminating redundancy present in the video in two forms [5]:

1) Spatial Redundancy
2) Temporal Redundancy

Spatial redundancy is concerned with the redundancy involved in a single frame of the video. The removal of such kind of redundancy is called as spatial compression or intra-prediction. The concept of removal of data is similar to that of still image compression. One of the methods applied over here include chroma subsampling, transformation and quantization etc.

Temporal redundancy is concerned with the redundancy involved temporally, i.e. among many frames. The removal of such kind of redundancy is called temporal compression or inter-

ISBN: 978-1-61804-321-4

prediction. The inter-prediction methods are the most time expensive methods and that too the process which takes maximum time is the process of motion estimation.

D. Motion Estimation

Each video frame which is to be encoded is divided into 8x8 or 16x16 blocks of pixels which are also called as macroblocks. The inter-prediction involves predicting the best position of these macroblocks in the reference or previously encoded frame. The motion estimation process which is a part of inter-prediction defines a search area in the previously encoded frames commonly known as reference frames. In that search area the current macroblock of the current frame which is to be encoded, is searched and its best position is found.

The calculation of the best position involves calculation of Sum of Absolute Differences (SADs). The formula applied here can be given as:

$$SAD = \sum_{i=0}^{m-1} \sum_{j=0}^{n-1} |C[i,j] - R[i,j]|$$

In the equation, C is one candidate MB (Macro block); R is the original Reference MB (Macro block); m & n are the dimensions of the MB in samples.

E. Motion Compensation

Once the macroblock's best position is predicted, it is then subtracted from the reference macroblock. This process of finding the difference is called as motion compensation. This subtracted data then undergoes transformation and quantization, which again reduces the bits of the sequence. This type of encoded sequence is suitable for transmission and storage.

III. Proposed System

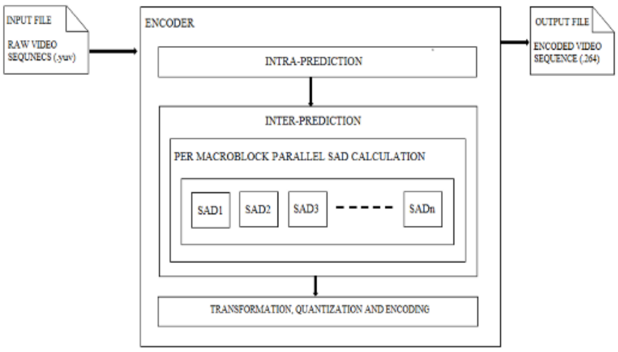

Fig. 1. Proposed System Architecture

The system architecture presents the overview of the experiment performed. The basic video encoding of video undergoes many stages before the raw video in the form of .yuv file being converted to compressed video in the form of .264. These stages can be merely listed as:

1) Configuring Video Parameters

2) Prediction of Each Frame

3) Transformation

4) Quantization

5) Encoding

The configuring of video parameters is the phase where the input video is analyzed and verified with a configuration file. The configuration file involves setting the macroblock size, resolution of input and output sequences, search range for macroblock prediction, the sampling format, number of frames to be encoded, etc. These values are read first from the .cfg (configuration) file and then set to the corresponding parameters of the video.

The scope of the implementation is limited to only the prediction phase of the video encoding. The prediction as explained comprises of inter-frame and intra-frame prediction. The implementation gives a parallel approach to the prediction process, which itself is naturally parallelizable. Based on our research we found that the biggest percentage of complexity is involved in predicting the candidate picture in the reference picture. As shown in Fig. 1, the process which is parallelized using CUDA is the calculation of Sum of Absolute Differences. This process of SAD calculation is done for each macroblock of the given candidate frame.

The phases of the transformation, quantization and encoding are left to the implementers of the encoder [5].

IV. Implementation

As the paper exploits the area of motion estimation, we shall not go into details of other parts such as intra-prediction, transformation etc. Here, for the purpose of specific experimentation, we have used already developed encoder libraries which follow the H.264 standard. These libraries are present in JM reference encoder. This implementation extends the code of JM by adding extra libraries for CUDA.

On profiling one of the existing encoders i.e. JM reference encoder it was found that negligible amount of time is taken if the prediction is intra-prediction, but for inter-prediction almost 97% of the total time is consumed. This was verified as shown in the fig. 2.

Function Name	Inclusive Samples %	Exclusive Samples %
code_a_plane	97.55	0.00
encode_one_slice	97.47	0.00
encode_one_macroblock_high	97.31	0.02
submacroblock_mode_decision_p_slice	**51.51**	**0.04**
PartitionMotionSearch	**34.96**	**0.01**

Fig. 2. Execution Path of most time consuming functions in JM

This straight away approach motivated us towards the parallelization of computeSAD function used in JM reference encoder.

The serial approach for SAD calculation can be best explained by the following pseudocode with search range of 16:

```
for ( MB = 0; MB < 1089; MB++ ) {
    for ( pixel = 0, SAD = 0; pixel < 256; pixel++ ) {
```

```
            SAD += abs ( MB [ pixel ] - SA [ pixel ] ) ;
        }
        if ( SAD < bestSAD ){
            bestSAD = SAD;
        }
    }
```

Where, MB is the current macroblock which is to be searched in a given search area (SA).

The above pseudocode clearly gives an exhaustive approach for calculating the SAD. This can be done in parallel for each macroblock using the cores available in CUDA enabled GPGPUs. The abs function in the algorithm can be mapped to iabs in computeSAD. The iabs function itself takes almost 44% of the encoding one macroblock.

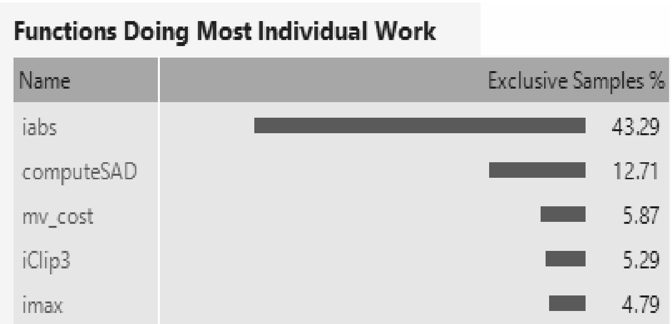

Fig. 3. Percentage comparison of function doing computationally expensive task

The implementation of computeSAD in parallel involves launching the threads on GPGPU which ultimately puts light on the launch of the kernel function. Also, implementation of computeSAD in parallel means generating the best position for a given macroblock using a single search area in parallel. So the demand of generation of threads comes to core part that is calculating the search area. The search area used in the implementation is given by the following formula:

$$SearchArea = (2 * SearchRange + 1)^2$$

Where, SearchRange is the maximum width of the macroblock.

Thus, we can say that we have to generate $(2 * SearchRange + 1)^2$ threads on the GPU (As shown in Fig. 4).

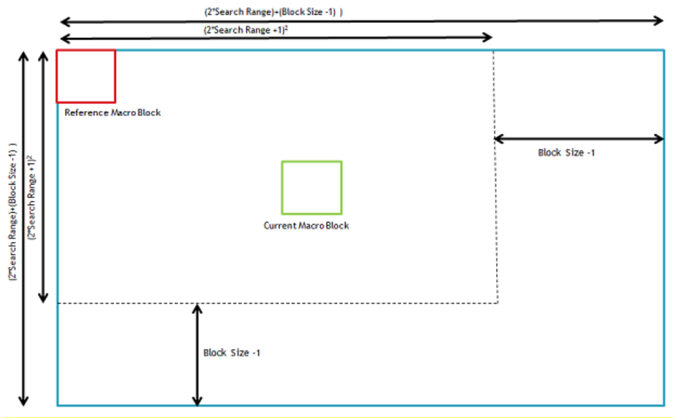

Fig. 4. Calculating Search Area

V. Experimentations and Results

The serial execution was carried out on a Quad Core Intel Core i5 2.50 GHz processor with 4GB RAM.

For the experimentation involved in parallel execution we used three different GPGPUs with different configurations on three different machines. The different GPUs used are:

GeForce GT-630M

GeForce GTX 480

Tesla C2075

Fig. 3 and Fig. 4 show the plots of results obtained from testing of 352X288 and 176X144 resolution videos respectively. The horizontal axis shows different kinds of video sequences taken whereas the vertical axis shows time taken in seconds to encode 30 frames of each of the video. The colored bars indicate the baseline serial execution and parallel executions on different GPUs.

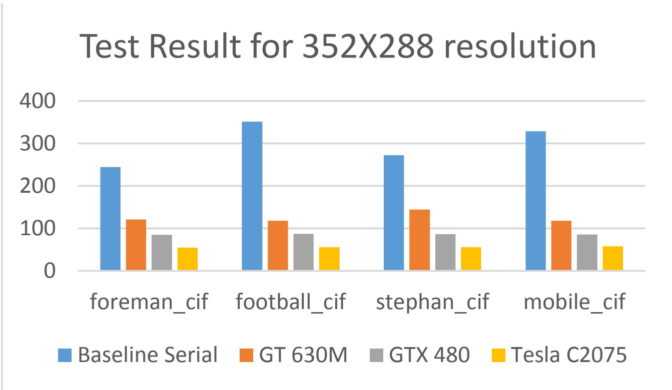

Fig. 5. Results obtained for 352X288 resolution videos

The experimentations were performed on videos of two different resolutions on the mentioned GPUs which showed that up to 6X performance can be achieved for motion estimation from CPU to GPU.

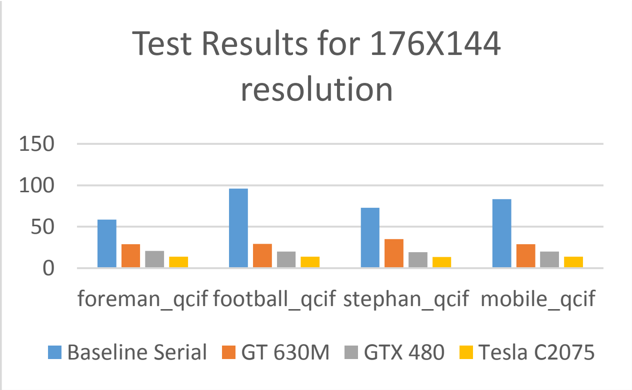

Fig. 6. Results obtained for 176X144 resolution videos

VI. Conclusion and Future Scope

Video processing is considered as an extreme smart work because a little change in the code can hamper the compression as well as the quality of the results. The research work involved an in-depth study of video compression and the tradeoffs present in it. The literature survey itself concentrated the focus towards the choice of parallel approach for video encoding. The results obtained from parallel approach were very amazing and showed upto 6X speedup as compared to the traditional sequential approach.

This experimentation has involved use of only global memory of the GPU. This can be further improved if shared memory and registers are used extensively. Also, the bottleneck in the performance is the memory transfer between the CPU and GPU memory which takes most of the time of parallel approach. The future scope would be the reduction mechanisms for memory transfers. This paper is based on H.264 standard whose predecessor H.265 has now come into the global market for experimentation. So the future area of research would be to have some parallelism in H.265.

Acknowledgment

With this paper, we present the research work carried out by us as a part of our final year curriculum of BE Computer Engineering. Through our research, we implemented H.264 on CUDA platform in the CUDA research centre available at RSCOE, University of Pune. This project would not have been possible without the unstinted support, dedication and constructive suggestion by our project guide Prof. C.G. Thorat and Project co-ordinator Prof. V.M. Bharkade, during the course of the project. We owe our immense gratitude to them. We also wish to put on record our sincere thanks to Prof. Dr. A.B. Bhgwan, Head of Computer Engineering Department, for his support and providing us with necessary facilities.

References

[1] Joint Video Team (JVT) of ISO/IEC MPEG and ITU-T VCEG, "Draft ITU-T recommendation and final draft international standard of joint video specification (ITU-T Rec. H.264/ISO/IEC 14 496-10 AVC)", Std. JVTG050, 2003.

[2] W. Chen, H. Hang, "H.264/AVC motion estimation implementation on Compute Unified Device Architecture(CUDA)", pp – 697 -700, IEEE 2008.

[3] Aleksandar Colic, Hari Kalva, Borko Furht , "Exploring NVIDIA-CUDA for Video Coding", Dept. of Electrical and Computer, Engineering and Computer Science, Florida Atlantic University, Boca Raton, FL 33431, pp- 13-22, ACM, 2010

[4] Youngsub Ko, and Youngmin Yi, Soonhoi Ha, "An Efficient Parallel Motion Estimation Algorithm and X264 Parallelization in CUDA", Dept. of Electrical and Computer, Engineering and Computer Science, Florida Atlantic University, Boca Raton, FL 33431, pp- 1-8, IEEE, 2011.

[5] I. Richardson. "H.264/AVC and MPEG-4 Video Compression – Video Coding for Next-Generation Multimedia". Chichester: John Wiley and Sons. 2003.

[6] The H.264 Advanced Video Compression Standard, second edition, http://as.wiley.com/WileyCDA/WileyTitle/productCd-0470516925.html

[7] Parallel computing, http://en.wikipedia.org/wiki/Parallel_computing

[8] CUDA, http://www.nvidia.com/object/cuda_home_new.html.

[9] http://www.videomaker.com/article/15362-video-formats-explained

[10] http://www.videomaker.com/article/15374-the-current-state-of-codecs

[11] H.264/MPEG-4 AVC, http://en.wikipedia.org/wiki/H.264/MPEG-4_AVC

[12] NVIDIA CUDA Programming Guide version 4.0 (5/6/2011), http://www.shodor.org/media/content//petascale/materials/UPModules/matrixMultiplication/cudaCguide.pdf

Parameterization of RBF Neural Networks via Combination of Unsupervised Procedures and a New Way of Scaling Parameters

Carlos Alberto Murari Pinheiro, Flavia Aparecida Oliveira Santos, Pedro Paulo Balestrassi, and Benedito Isaias Lima Lopes

***Abstract*—**This paper addresses a procedure for the selection of parameters in Radial Basis Function Neural Networks. The approach consists of the combination of unsupervised procedures and a new way to scale parameters associated to the values of widths of the radial functions. The application of the approach will be illustrated with examples of approximation of functions and time series forecasting.

***Keywords*—**Approximation of functions**,** Artificial neural networks**,** parameter adjustment, Radial basis function networks.

I. Introduction

RADIAL Basis Function (RBF) neural networks are effectively utilized in time series forecasting [16, 8], approximation of functions [14], control systems [7], pattern classification [1], among other applications.

In its most basic form, RBF networks have only one hidden layer, while Multilayer Perceptron (MLP) neural networks present one or more hidden layers, according to its specifications [6].

Hidden layers in RBF networks have activation functions modeled by radial-basis functions, where the more usual are Gaussian functions defined by their centers and widths. The output layer has weights that aggregate the outputs of the radial functions, providing the output information of the network (which can have more than one output, according to the corresponding application).

C.A.M.P. Author is with the Institute of Systems Engineering and Information Technology, Federal University of Itajubá, Itajubá, Brazil (corresponding author to provide phone: (55) 35 3629-1875; e-mail: pinheiro@unifei.edu.br).

F.A.O.S. Author is with the Institute of Systems Engineering and Information Technology, Federal University of Itajubá, Itajubá, Brazil (corresponding author to provide phone: (55) 35 3629-1875; e-mail: flaviaoliveira@unifei.edu.br).

P.P.B. Author is with the Institute of Production Engineering and Management, Federal University of Itajubá, Itajubá, Brazil (corresponding author to provide phone: (55) 35 3629-1875; e-mail: ppbalestrassi@gmail.com).

B.I.L.L. Author is with the Institute of Electrical Systems and Energy, Federal University of Itajubá, Itajubá, Brazil (corresponding author to provide phone: (55) 35 3629-1875; e-mail: isaiasdlima@gmail.com).

There are some strategies used to adjust the parameters (centers, widths and weights) in RBF networks, typically classified as empirical, auto-organized and supervised. In empirical strategies, the centers of the functions are adjusted randomly, and the width values are given by the relationship between the positions of the centers [6]. The objective is to obtain uniform distributions for the radial functions in order to enable a good capacity of generalization of the network. The weights of the output layer are calculated by the least squares method based on the output values of the established Gaussian functions, with a set of input training data and the corresponding pattern for the network output in question. Auto-organized strategies [6] use data clustering algorithms (K-means, for example) to select the values of the centers of each radial basis function. The values of the widths are adjusted empirically, and the weights of the output layer are adjusted by the least squares method. The paper of [16] uses an optimized data partitioning method which is based on the distance between the centers of the data clustering. An additional cost function is associated with an optimization method with the objective of adjusting the centers and widths of the radial basis functions. Supervised strategies [6, 10, 15] employ methods such as gradient descent to adjust all parameters of a determined RBF network, where the error information between the information network output concerned and its desired pattern are used in the training process.

In reference [5] it was shown the algorithm Output Value-Based Initializer, which calculates the initial values for the centers and widths of the radial functions according to the output values of the target function. In paper [17] also suggested the use of supervised learning, where a new discrete-continuous algorithm is proposed for the construction of a RBF model. First, the orthogonal least squares is used for an initial model, and the Levenberg–Marquardt method is used to optimize the hidden nodes and output weights in the continuous space.

This paper addresses a procedure for the selection of parameters in RBF neural networks. The approach consists of the combination of unsupervised procedures and a new way to scale parameters associated to the values of widths of the radial functions. Applications in approximations of functions and time series forecasting will be exemplified.

This paper is organized as follows. Section 2 contains a basic review of the RBF networks and the description of typical unsupervised methods for setting parameters. Section 3 describes the methodology proposed in this paper. Application examples are illustrated in Section 4. And in Section 5 is the conclusion of the paper and suggestions for future work.

II. Basic Review

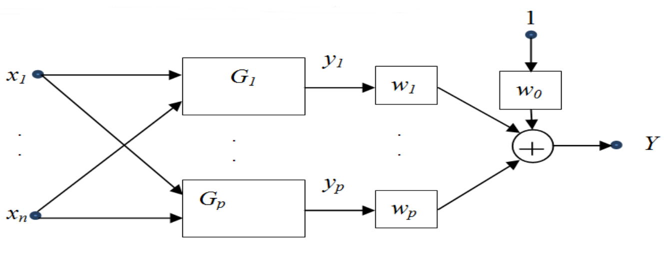

Fig. 1 Typical RBF neural network structure.

A typical structure of RBF networks is shown in Figure 1.

There are no weights in the first layer of the neural network. The input variables are the data of the activation functions (G_j), which are themselves nodes of the hidden layer of the network. The typical expression of a radial basis function is given by (1), where c_j denotes its central value of the function in question, and σ_j is the width of the RBF.

$$Y_j = G_j(x) = e^{-\left(\frac{(x1-c1)^2}{2\sigma_2^1}+\ldots+\frac{(xn-cn)^2}{2\sigma_n^2}\right)} \quad (1)$$

The weights (w_i) of the output layer of the network multiply the values (y_j) supplied by radial basis functions of the model, and the aggregation of these values results in output information Y of the network, which is added to a unitary bias value multiplied by the associated weight w0. RBF neural networks can have other outputs associated with other corresponding weights. The information for each output of a given neural network is modeled by equation (2).

$$Y_j=\sum_{j=1}^{p} W_j G_j(x) \quad (2)$$

A. Typical Unsupervised Methods for Setting Parameters

This item addresses typical procedures unsupervised, often used for adjusting parameters of RBF networks.

B. Values of the Centers of the Gaussian Functions Randomly Selected

1) The central value of each radial basis function of a network is randomly chosen from the training data, and the justification of this procedure is explained in [9].

2) The value of width (standard deviation) of each radial basis function network is given by expression (3), where N_c is the number of functions used in the hidden layer and D_{max} is the maximum distance between selected pairs of values of the centers in question.

$$\sigma = \frac{D_{\max}}{\sqrt{2N_c}} \quad (3)$$

A common width value ($\sigma_{kj} = \sigma$) for all network functions can be used when the input data have a uniform distribution, unusual condition in most practical applications. A more feasible procedure is expressed by (4), where c_{ij} are values in the neighborhood of the corresponding c_{kj} center associated with the radial function in question, a suggested value for p is 2 [11].

$$\sigma_{kj} = \frac{1}{p}\sqrt{\sum_{m=1}^{p}\left\|c_{kj} - c_{ij}\right\|^2} \quad (4)$$

Another approach [13] uses the data related to the Euclidean distance between the center value of each RBF and its immediate vicinity, which information is multiplied by a constant K as expressed in (5) in order to establish an overlap appropriate between adjacent network functions in question, whose purpose is to improve the interpolation of the resulting model.

$$\sigma_{kj} = K \cdot \min\left(\left\|c_{kj} - c_{ij}\right\|\right) \quad (5)$$

[2] suggested the use of a scaling factor K_e as expressed in (6) to jointly adjust the values of the deviations of RBF, whose values can be estimated by one of three expressions mentioned above, allowing a better modeling capability of the resulting network.

$$\sigma_{kj} = K_e \cdot \sigma_{kj} \quad (6)$$

3) The values of the weights of the output layer are calculated using the pseudo-inverse method (7), where G+ is the corresponding values associated with $G_j(x)$ of RBF functions and Y_d are the values of the output desired in the neural network. When there are no problems of matrix inversion, the conventional least squares method is used.

$$W_j = G^{+} \cdot Y_d \quad (7)$$

ISBN: 978-1-61804-321-4

C. Values of the Centers Determined by Methods of Data Clustering

1) The central value of each radial basis function is determined by clustering techniques, processing the network data and providing values of the centers of clusters in question. The K-means algorithm is usually employed in the context of RBF networks [12], and alternatively more elaborate methods can be applied, for example, via the self-organizing map or other techniques.

2) The values of the widths of the RBF can be adjusted by information of distances related to centers of the functions and data in the neighboring regions, similarly to the procedures mentioned above. Other approaches processing the values of standard deviations associated with the RBF information covariance matrices resulting from elliptical data clustering algorithms, such as the algorithm of Kessel-Gustafson [12], for example, but that tends to be computationally expensive due to the complexity of the algorithm involved.

3) The values of the weights of the hidden layer are calculated by the methods of least squares.

III. Methodology

This section details the approach suggested in this paper to adjust the parameters of RBF networks, compiled from combinations of unsupervised procedures and with and a new way to scale parameters.

IV. Procedure for Setting Parameters in RBF Neural Networks.

1- The number of nodes is chosen for the hidden layer of the RBF neural network in question;

2- Network training data are processed by a clustering algorithm Fuzzy-Cmeans [3] in order to optimize the clusters of the corresponding data. The information of the clusters will be used to select the parameters of the activation functions, and the number of clusters defines the number of nodes in the network hidden layer;

3- Centers (c_j) of the Gaussian functions are the core values of the clusters determined by the Fuzzy-Cmeans algorithm;

4- The widths of the functions are initially estimated with (8), calculating the standard deviation (σ_j*) on the range of data (x_j) of each variable associated with the cluster identified by the algorithm.

$$\sigma_j^* = \sqrt{\frac{\sum_j^m = 1X_j^2 - \frac{1}{m}\left(\sum_j^m = 1x_j\right)}{m-1}} \quad (8)$$

5- A new way to scale parameters associated to the initial values of widths of the radial functions and intervals of data clusters, is proposed via equation (9). The purpose is to establish appropriate values of widths to improve the characteristic of generalization of network. In the case of a null value resulting from the application of equation (8) or (9), is repeated the value of the deviation of the nearest cluster;

$$\sigma'_j = \frac{1}{2}\frac{\left|\max(x_j) - \min(x_j)\right|}{\sigma_j^*} \quad (9)$$

6- A common multiplicative factor Km (10), with values between 1 and 10, serves as the additional adjustment of the parameters (widths) in question;

$$\sigma_j = K_m \sigma'_j \quad (10)$$

7- The weights wj of the output layer are then calculated by the least squares method (11), where "T" denotes transposed matrix and "-1" inverse matrix, using the regressor Fr, output values of Gaussian functions (y1 through yp), and the corresponding expected pattern for the output information (Y) of the network;

$$\begin{aligned} F_r &= [y_1 y_2 \ldots y_p 1]; \\ W_j &= [F_r^T F_r]^{-1} F_r^T Y. \end{aligned} \quad (11)$$

8- Verify the precision achieved by the neural network. If necessary, vary the value of the multiplying factor of step 6, or increase the number of network nodes in step 1, and repeat the procedure.

V. Examples of Applications

Initially some simple examples are shown in order to illustrate the procedure outlined in this paper, and afterwards more elaborate applications will be presented. Comparisons with results obtained with standard procedures for setting parameters will be provided.

A. Example 1 – Approximation of Function

This example is didactic, serving to illustrate the application of the approach and illustrate the calculations. The RBF network in question is applied to model the nonlinear function expressed by (12).A data set of twenty-one samples represents the original function: x1 = [0; 0.05; 0.1; 0.15; 0.2; 0.25; 0.3; 0.35; 0.4; 0.45; 0.5; 0.55; 0.6; 0.65; 0.7; 0.75; 0.8; 0.85; 0.9; 0.95; 1]; y = [0; 0.0025; 0.01; 0.0225; 0.04; 0.0625; 0.09; 0.1225; 0.16; 0.2025; 0.25; 0.3025; 0.36; 0.4225; 0.49; 0.5625; 0.64; 0.7225; 0.81; 0.9025; 1].

$$y = x_1^2; \qquad x_1 \subset [0,1]. \quad (12)$$

Three experiments were conducted and are described below: i) Initially it was considered the unsupervised procedure with the values of the centers of the radial functions randomly selected; ii) The same example was run using a clustering algorithm as shown in previous works; iii) The proposed algorithm was then considered.

B. Unsupervised procedure (with randomly centers)

It was assumed a network with three nodes in the input layer, and the values of the centers were randomly chosen from the vector data x1. Table 1 contains the values of the centers of Gaussians functions.

Using the expression (3) follows the common value of the widths: $\sigma = \sigma11 = \sigma12 = \sigma13 = 0.26$. With the expression (7) or (11), the values of the weights of the output layer of the network are calculated. The simulation of the network model and the comparison with the data of the original function resulted in the sum of the squared error (SSE = ∑[y - Y]2/2) of 7.0*10-2.

Adjusting now the values of the widths individually by expression (5), the values are obtained for K = 1.Now the SSE was modified to 2.8*10-2, resulting in improved accuracy of the corresponding neural model.

Now adopting a scaling factor given by (5) or (6) for $K = K_e = 3$, whose data was tested to achieve better accuracy in modeling, follow the values of the widths of the functions of the network and weight values of the output layer. The SSE was modified to 7.7*10-5, resulting in better accuracy of the corresponding neural model.

c_{11}	0.2		
c_{12}	0.6		
c_{13}	0.85		
σ_{11}	0.26	0.4	1.2
σ_{12}	0.26	0.25	0.75
σ_{13}	0.26	0.25	0.75
w_0	0.3299	1.3901	7.1102
w_1	-0.2448	-1.408	-8.8043
w_2	-0.2815	0.0585	4.1214
w_3	0.6421	-0.3285	-2.6859
SSE	$7.0*10^{-2}$	$2.8*10^{-2}$	$7.7*10^{-5}$

Table I Values of centers, widths and weights of the radial functions (Case 1).

C. Clustering algorithm

Figure 2 illustrates the clusters obtained via Fuzzy C-Means on data from the original system. The resulting clusters are represented by three colors, and their centers are indicated by circles in black. The values of the centers of the clusters are (0.1728; 0.0435), (0.5707; 0.3354) and (0.8945; 0.8063), respectively, for the vectors x1 and y of the nonlinear function. In Table 2there are the corresponding values of the centers of the clusters associated with the vector data x. Using the procedure defined by equation (5) with K = 3, are also in Table 2 the values of the widths of the radial functions and the values of the weights of the output layer of the network. Now the SSE (related to the error estimates between the RBF and the original data of the system) was modified to 4.4*10-5, resulting in improved accuracy of the corresponding neural model compared to previous network.

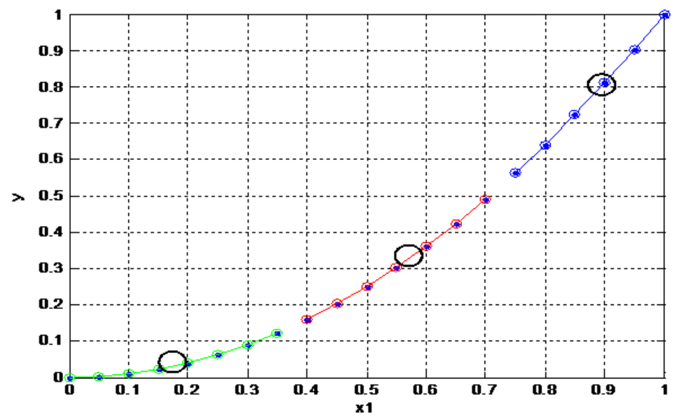

Fig. 2 Data from equation (12) and the respective clusters.

c_{11}	0.1728
c_{12}	0.5707
c_{13}	0.8945
σ_{11}	1.19
σ_{12}	0.97
σ_{13}	0.97
w_0	8.7252
w_1	-14.7917
w_2	-0.2815
w_3	-8.5432
SSE	$4.4*10^{-5}$

Table II Values of centers, widths and weights of the radial functions with K = 3 (Clustering algorithm).

D. Proposed algorithm

For the same data clusters (Figure 2), derived from the application of Fuzzy-Cmeans algorithm, there are the intervals associated to the vector data x1:[0; 0,05; 0,1; 0,15; 0,2; 0,25; 0,3; 0,35], [0,4; 0,45; 0,5; 0,55; 0,6; 0,65; 0,7] and[0,75; 0,8; 0,85; 0,9; 0,95; 1].Calculating by (8) the variances associated with each cluster, we have σ_11^*=0.1225, σ_12^*=0.1080 and σ_13^*=0.935.

Using (9), we have the values appropriately scaled:
σ1'=0.5*(0.35−0)/0.1225=1.4286;
σ2'=0.5*(0.7−0.4)/0.108=1.3889;
σ3'=0.5*(1−0.75)/0.0935=1.3369.
For the same value of the scale factor $K = K_e = K_m = 3$ (10) used in the previous neural models. In Table 3 are the final values of the widths of the radial functions.

c_{11}	0.1728
c_{12}	0.5707
c_{13}	0.8945
σ_{11}	4.2857
σ_{12}	4.1667
σ_{13}	4.0107
w_0	33.8119
w_1	−369.0504
w_2	672.7098
w_3	−339.8387
SSE	$8.6*10^{-8}$

Table III Values of centers, widths and weights of the radial functions with K = 3 (Proposed algorithm).

With the values y1, y2, and y3calculated for the three Gaussian functions corresponding to the vector x1 from the input data of the system in question, using (11) with the vector y(data expected for the network output) the weights of the RBF are calculated by (11).

Figure3 shows the data of the original function (".") and the estimated data ("+") for the neural network with the parameters determined with the approach suggested in this paper. The SSE was modified to 8.6*10-8, resulting in better accuracy of the corresponding neural model.

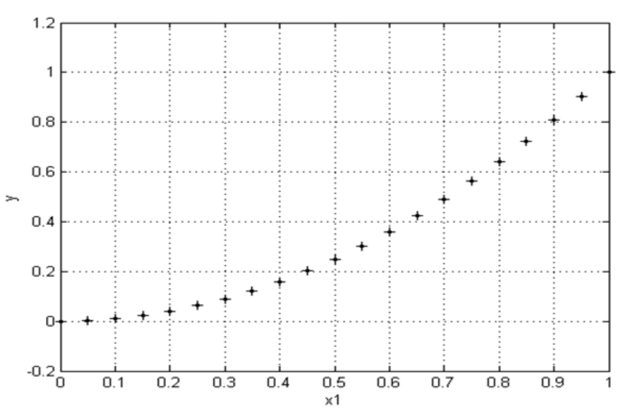

Fig. 3 Data from equation (12) and the values estimated with the corresponding RBF.

E. Example 2 – Application in Prediction of Time Series

Figure 4 contains data related to prices of a particular commodity, with records of prices for seventy-three months. A RBF neural network will be used as model for the corresponding time series. The network model was obtained with data of the first sixty-two months, and the data of the next eleven months was used to verify the generalizability of the model.

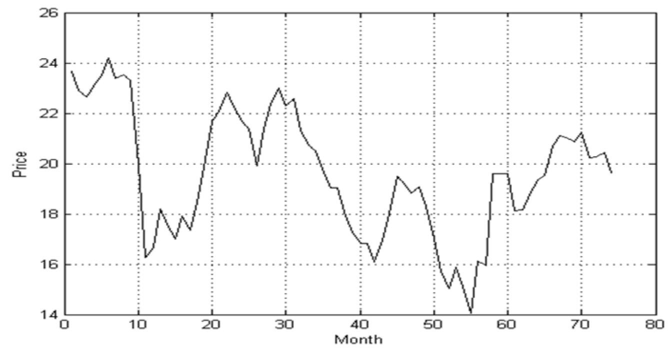

Fig. 4 Time series data.

A current price value (k) and the previous value (k-1) were used in order to estimate the price of the following month (k+1). The basic structure of RBF neural network will be similar to Figure 5, where the modeling variables are: x1 =

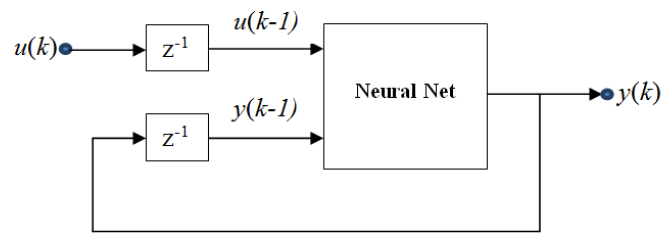

Fig. 5 Example of neural network used for system modeling.

Previous Price; x2 = Current Price; y =Following Month Price.

The following experiments described below were considered.

F. Initially was considered a RBF network obtained via supervised training.

Using a neural network toolbox (MATLAB), a model (newrb) was generated with a good accuracy for the training data. But was noted that with a higher accuracy in the resulting model via training data, was obtained a larger error in the predictions with the test data. For comparison, the mean absolute percentage error (MAPE) was used between the values given for the data test and output data estimated by RBF:$\sum |(Ytest - Yestimated)/Ytest|/N$, where N is the number of samples. With the model obtained the value of error was: MAPE = 3.8%.

G. Now using the approach proposed in this paper

For the hidden layer network six nodes were adopted. The six clusters of data processed by the Fuzzy-Cmeans algorithm are illustrated in Figure 6, where the values of the centers of the Gaussian are shown in Table 4.

ISBN: 978-1-61804-321-4

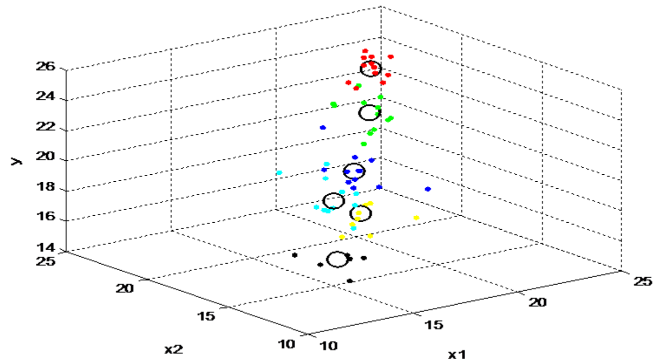

Fig. 6 Time series data and respective clusters.

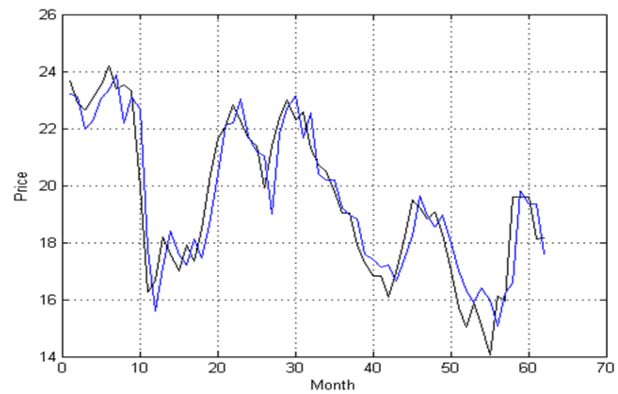

Fig. 7 Time series data and values estimated with the neural network.

c_{11}	23.1373	σ_{11}	18.6332	w_0	-5.5924
c_{12}	19.2555	σ_{12}	19.5991	w_1	-3.2244
c_{13}	21.7906	σ_{13}	16.7311	w_2	-55.8650
c_{14}	15.5351	σ_{14}	14.8883	w_3	122.6187
c_{15}	18.2458	σ_{15}	15.4140	w_4	1.5879
c_{16}	16.8230	σ_{16}	15.1891	w_5	-282.6299
c_{21}	23.1892	σ_{21}	17.0218	w_6	246.7825
c_{22}	19.2246	σ_{22}	18.3433		
c_{23}	21.5552	σ_{23}	18.1947		
c_{24}	15.3847	σ_{24}	13.7824		
c_{25}	17.4568	σ_{25}	15.3732	SSE	35.66
c_{26}	17.3302	σ_{26}	16.7565	MAPE	2.46%

Table. IV Values of the centers of the radial functions with Km = 10 related to Example 4.

Applying the approach proposed in this paper and using a scale factor with Km=10 (value tested to achieve better accuracy in the neural model), we have the values of the widths and the values of the weights of the output layer.

Figure 7 shows the training data (black line) and the values estimated (blue line) with the RBF network, where the SSE was 35.66.

Figure 8 shows the test data (black line) and the prices estimated (blue line) with the RBF network for eleven consecutive months (N = 11), where the MAPE was 2.46% (with some improvement in the accuracy of the model in relation to the previous neural network).

Other tests were considered through changes in the structure of the neural networks adopted, such as the use of more nodes in the hidden layers, larger numbers of input variables, more previous samples to model dynamic systems and time series. Applications in pattern recognition were also tested. These results will be presented in later publications.

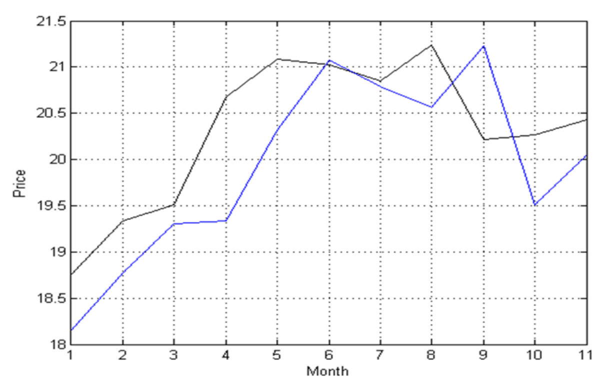

Fig. 8 Time series data and the values estimated by the neural network.

VI. Conclusion

The procedure proposed in this paper, for adjusting of the parameters in RBF neural networks, is efficient and easy to use in different contexts of applications. The results obtained in examples of approximation of functions, modeling of systems with nonlinear characteristics and time series forecasting suggest promising potential for various applications in areas such as pattern recognition, control systems, signal processing, among others. The accuracy obtained in the approximations and estimations used in the examples suggest that the approach is an interesting alternative for the strategies of setting parameters for RBF neural networks.

The following suggestions are proposed for future investigations:

-The use in the first step of the procedure proposed in this paper of an approach to determine the number of minimal clusters for a particular application, for example, with the use of a criterion such as Fuzzy Silhouette [4], or others cited in the literature;

- The use of the procedure proposed in this paper as an initial parameter adjustment for a RBF neural network, which later (after the last stage of the procedure), will be refined by training techniques based on the gradient descent method, genetic algorithms, etc.

REFERENCES

[1] BABU G.S., SURESH S. Sequential Projection-Based Metacognitive Learning in a Radial basis Function Network for Classification Problems. IEEE Transactions on Neural Networks and Learning Systems. 2013, 24(2), pp. 194-206, doi: 10.1109/TNNLS.2012.2226748.

[2] BENOUDJIT, N., VERLEYSEN, M. On the kernel widths in Radial Basis Function Networks. Neural Processing Letters. 2003, 18(2), pp. 139-154, doi: 10.1023/A:1026289910256.

[3] BEZDEK J.C. A convergence theorem for the fuzzy isodata clustering algorithms. IEEE Trans. On Pattern Analysis And Machine Intelligence. 1980, 2(1), pp. 1-8, doi:10.1109/TPAMI.1980.4766964.

[4] CAMPELLO RJGB, HRUSCHKA ER. A fuzzy extension of the silhouette with criterion for cluster analysis. Fuzzy Sets and Systems. 2006, 157(21) pp. 2858-2875, doi:10.1016/j.fss.2006.07.006.

[5] GUILLÉN A, ROJAS I, GONZÁLES J, POMARES H, HERRERA L.J, VALENZUELA O, ROJAS F. Output value-based initialization for radial basis function neural networks. Neural Processing Letters. 2007, 25 (12):209–225, doi: 10.1007/s11063-007-9039-8.

[6] HAYKIN S. Neural Networks: A comprehensive Foundation. Prentice Hall, 2nd ed. 1999, Englewood Cliffs.

[7] JAFARNEJADSANI H, PIEPER J, EHLERS J. Adaptive Control of a Variable-Speed Variable-Pitch Wind Turbine Using Radial Basis Function Neural Network. IEEE Transactions on Control Systems Technology. 2013, 21(6):2264-2272, doi: 10.1109/TCST.2012.2237518.

[8] KEBRIAEI H, ARAABI BN, KIAN A.R. Short-Term Load Forecasting with a New Non symmetric Penalty Function. IEEE Transactions on Power Systems. 2011, 26(4):1817-1825, doi: 10.1109/TPWRS.2011.2142330.

[9] LOWE, D. Adaptive radial basis function nonlinearities, and the problem of generalization. First IEEE International Conference on Artificial Neural Networks, 1989, p. 171-175, London.

[10] MAHDI, R.N., ROUCHKA, E.C. Reduced Hyper BF Networks: Regularization by Explicit Complexity Reduction and Scaled Rprop-Based Training. IEEE Transactions on Neural Networks. 2011, 22(5):673-686, doi: 10.1109/TNN.2011.2109736.

[11] MOODY, J., DARKEN, C. J. Fast learning in networks of locally-tuned processing units. Neural Computation, 1989, n. 1, p. 281-295, doi:10.1162/neco.1989.1.2.281.

[12] NELLES, O. Nonlinear System Identification. Springer-Verlag, Berlin, 2001, doi: 10.1007/978-3-662-04323-3.

[13] SAHA, A., KEELER, J. D. Algorithms for better representation and faster learning in Radial basis Function Networks. Advances in Neural Information Processing Systems 2, edited by DavisS. Touretzky, 1989, p. 482-489.

[14] SHI Y, CHAN C.H. Comparison of Interpolating Functions and Interpolating Points in Full-Wave Multilevel Green's Function Interpolation Method. IEEE Transactions on Antennas and Propagation. 2010, 58(8):2691-2699, doi: 10.1109/TAP.2010.2050448.

[15] SU S.F, CHUANG C.C, TAO C.W, JENG J.T, HSIAO C.C. Radial basis Function Networks with Linear Interval Regression Weights for Symbolic Interval Data. IEEE Transactions on Systems, Man and Cybernetics – Part B: Cybernetics. 2012, 2(1):69-80, doi: 10.1109/TSMCB.2011.2161468.

[16] SUN YF, LIANG YC, ZHANG WL, LEE HP, LIN WZ, CAO L.J. Optimal partition algorithm of the RBF neural network and its application to financial time series forecasting. Neural Comput. & Applic. 2005, 14:36-44, doi: 10.1007/s00521-004-0439-7.

[17] ZHANG L, LI K, HE H.B. A New Discrete-Continuous Algorithm for Radial Basis Function Networks Construction. IEEE Transactions On Neural Networks And Learning Systems. 2013, 24 (11):1785-1798, doi:10.1109/TNNLS.2013.2264292.

Novel Design of Array Multiplier

Seyed Masoud Razavi, Seyyed Reza Talebiyan

***Abstract*—** In this paper by using array multipliers and return technique, a new array multiplier has been proposed, Which has better operation than the regular array multipliers. This technique has been applied on two conventional and leapfrog array multipliers. In the formation of a 8×8 multiplier all designs proposed in this paper have been implemented using the HSPICE by the use of 180 nm TSMC technology at a supply voltage 1v. To verify the performance of the proposed structures, structures have been simulated in 130 nm & 65 nm PTM technologies. The simulation results show that applying the return technique in the array structures causes power consumption reduction and consequently PDP reduction. This improvement for 180 nm technology in the conventional array structure is 13.32 % and in the leapfrog array structure is 23.27 %. It should be noted that this technique substantially makes the number of transistors less and as a result area reduction.

***Keywords*—**Array multiplier, delay, power, return technique, return leapfrog array multiplier.

I. Introduction

Many application systems such as digital signal processing systems require the processing of large amounts of digital data [1-5]. To implement algorithms such as convolution and because of various filters, multiplication operation unit is placed in digital signal processor systems. In many algorithms, multiplication is considered as the critical path and consequently the most critical operations [1]. In recent years, researchers have put emphasis on three fields of power, speed, and area [4]. The need for specific design causes the increase of consumption power and the number of transistors on chip as well. Therefore, power is the most important field among those three. In order to achieve the high operating speed the most suitable structure is array multipliers which are in good order and lead to the ordered arrangement of layout [1]. This paper focuses on power consumption and a new method for array multipliers has been proposed which can reduce the power and the area as well. In the second section, the mathematical relationships and the multiplication algorithm of two 8-bit numbers have been explained. In the third section, two conventional array multiplier and leapfrog structures have been analyzed and in the fourth section, by applying return technique on two structures, a new design has been done. In the fifth section, how to perform the simulation process about the best selection and result presentation is examined and finally in the sixth section, a general conclusion has been made about the work done.

The authors are with the Electrical Engineering Department, Imam Reza International University, Mashhad, Iran (e-mail: masoudrazavi96@yahoo.com; talebiyan@imamreza.ac.ir).

II. Parallel Multiplier

A serial multiplier consumes less power but due to ripple, delay will be more. In parallel multiplier delay is less but high complex circuitry it consumes more power.

Consider the multiplication of two unsigned n-bit numbers, where $X= x_{n-1},x_{n-2},...x_0$ is the multiplicand and $Y= y_{n-1},y_{n-2},...y_0$ is the multiplier. The product of these two bits can be written as [1, 3, 4].

$$X = x_{n-1}x_{n-2}....x_0 = \sum_{i=0}^{n-1} x_i 2^i \tag{1}$$

$$Y = y_{n-1}y_{n-2}....y_0 = \sum_{j=0}^{n-1} y_j 2^j \tag{2}$$

$$P = XY = \left(\sum_{i=0}^{n-1} x_i 2^i\right)\left(\sum_{j=0}^{n-1} y_j 2^j\right) = \sum_{i=0}^{n-1}\sum_{j=0}^{n-1} x_i y_j 2^{i+j} \tag{3}$$

In the example discussed in this paper are 8-bit multiplicand and multiplier. Using equation (3), 8 rows of partial product as shown in figure 1 has been shown to be produced.

$$\begin{array}{ccccccccccccccc}
 & & & & & & & X_7 & X_6 & X_5 & X_4 & X_3 & X_2 & X_1 & X_0 \\
 & & & & & & * & Y_7 & Y_6 & Y_5 & Y_4 & Y_3 & Y_2 & Y_1 & Y_0 \\
\hline
 & & & & & & & P_{07} & P_{06} & P_{05} & P_{04} & P_{03} & P_{02} & P_{01} & P_{00} \\
 & & & & & & P_{17} & P_{16} & P_{15} & P_{14} & P_{13} & P_{12} & P_{11} & P_{10} & \\
 & & & & & & & \vdots & & & \vdots & & & & \\
P_{77} & P_{76} & P_{75} & P_{74} & P_{73} & P_{72} & P_{71} & P_{70} & & & & & & & \\
\hline
S_{15} & S_{14} & S_{13} & & & \cdots & & & & & & & S_2 & S_1 & S_0
\end{array}$$

Fig. 1 8×8 array multiplication algorithm

III. Array Multiplier

In this section conventional and leapfrog array multipliers will be reviewed briefly. It will be a point for our design in section 4.

A. Conventional Array Multiplier

The block diagram of a 8×8-bit conventional array multiplier is shown in Figure 2. In the conventional array multiplier [4-6], output signals (Sum and Carry) of the carry save adders (CSAs) are directly connected to the next row of CSAs. Finally, in order to produce an 8-bit value most significant bit (MSB) of the ripple carry adder (RCA) n-bits is used.

B. Leapfrog Array Multiplier

The block diagram of a 8×8-bit leapfrog array multiplier is shown in Figure 3. In the leapfrog array structure [5, 6], on the other hand, the interconnections of the CSAs are rearranged such that the propagation delay of the CSAs is better synchronized within the intermediate rows. This potentially results in higher speed and lower spurious switching (lower power dissipation) because the carry signal of the full adder is generally generated earlier than the sum signal of the same full adder. To take advantage of this, instead of connecting the sum outputs of the CSAs in row 1 to the CSAs in row 2 (as in a general array structure), the sum outputs of the CSAs in row 1 are instead connected to the CSAs in row 3. The carry signals of the CSAs in row 1, however, remain connected to the CSAs in row 2. Put simply, in a leapfrog array structure, the arrival times of carry (from row 2) and sum signals (from row 1) are better synchronized to the CSAs in row 3. Consequently, this results in higher speed (for data propagation) and lower spurious switching (less power dissipation) [5, 6].

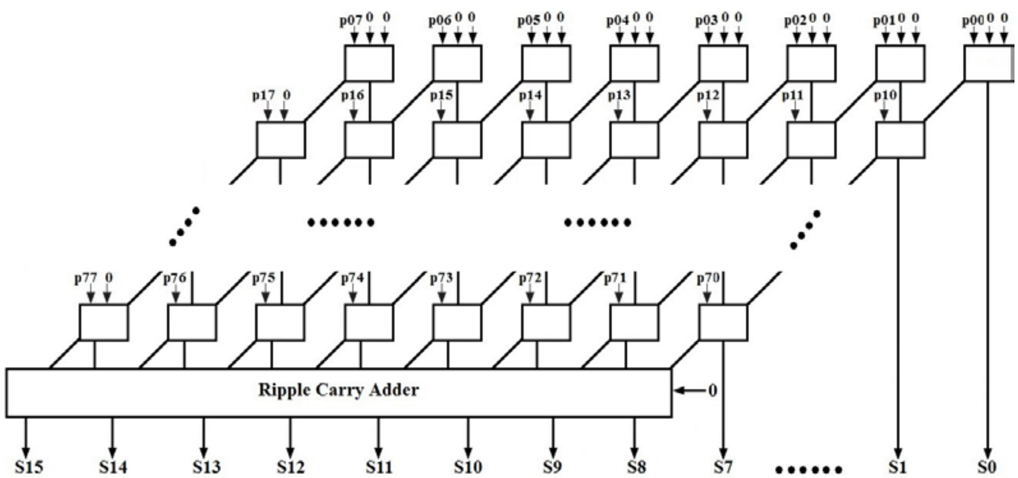

Fig. 2 block diagram of conventional array multiplier

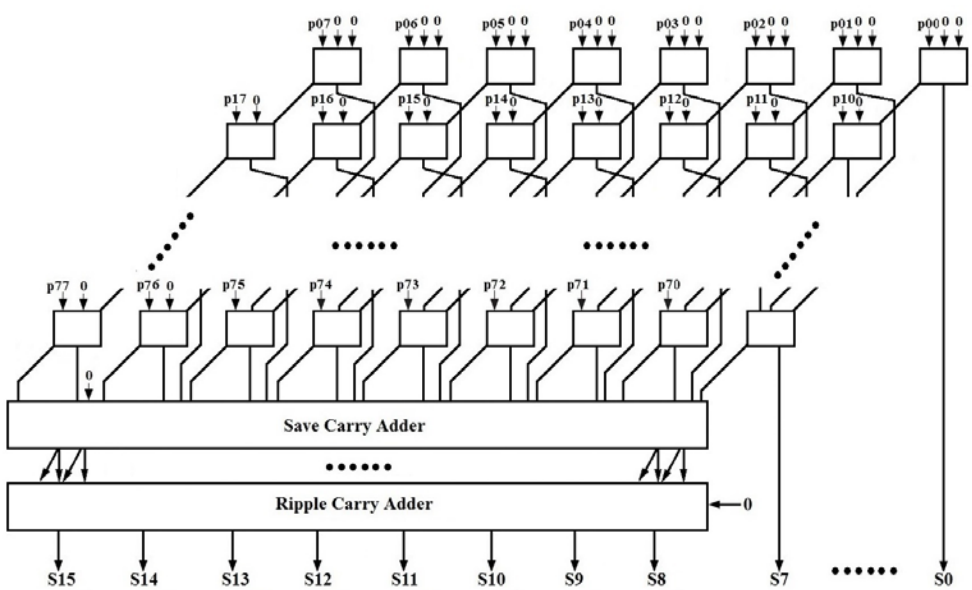

Fig. 3 block diagram of leapfrog array multiplier

IV. RETURN TECHNIQUE

By using return technique in these structures, addition operation is done through two cycles. For the first cycle, the addition operation on the first four rows of partial products is also done and for the second cycle, the addition operation on the second four rows of partial products and on the final result of the first cycle is done. In figure 4, the multiplication algorithm of two 8-bit numbers is shown by applying return technique.

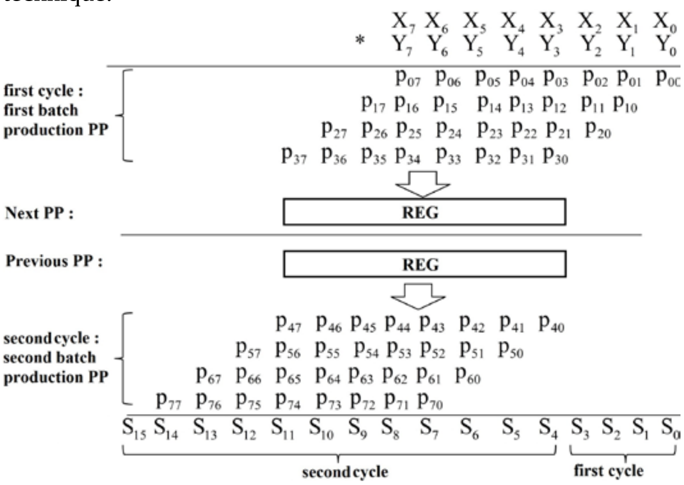

Fig. 4 8-bit multiplication algorithm by applying a return technique

A. Return Conventional Array Multiplier

The block diagram of the return conventional array multiplier is shown in figure 5. In the structure the number of full adder rows is reduced to half than conventional array multiplier and a row of registers for saving the outputs of the last full adder row for the first cycle and returning them for the second cycle to the input of the first full adder row, are used. T-1…T-4 are 1-bit registers and T-0…T-7 are 2-bit registers. T-1…T-4 registers for every two cycles include the 8-bit least significant bit (LSB) of the final product. In this structure, if the 8-bit LSB are considered as two groups, for first cycle, First 4 bit of the final product are produced and saved in T1…T4 registers, and the sum of the first 4 rows partial product are saved in the T0…T7 registers, and are returned to the input of the first row of full adder for the second cycle, and they are added to the second 4 rows of partial product. The second 4 bit of the LSB of the final product are produced for the second cycle and saved in the T1…T4 registers. The saved bits on T0…T7 registers are applied to the final stage of full adder (CRA). So that the 8 bit MSB of the final product are produced.

B. Return Leapfrog Array Multiplier

The main structure presented in this paper which has the lowest consumption power is the return leapfrog array multiplier structure. In figure 6, block diagram of the return leapfrog array multiplier is shown. In this structure, the length of the first adder row is n-bit which is equal to the length of multiplicand, and the length of the next three rows is n+1bit. The addition of a full adder to these three rows is for adding the output of previous row sum and the leapfrog sum of the previous two rows as well. Because of leapfrog, in this structure two register rows are used. The number of these registers in the first row is 3/2n, which T1-1…T1-4 registers are single-bit and T10…T17 registers are two-bit and include output carry of the last row of adder and the sum output of penultimate row. The length of these registers in the second row is n-bit which includes T20….T27 and consists of the first registers, carry of single adder in the fifth row, and the rest of registers consist of the sum output of the last row (fourth row) adder.

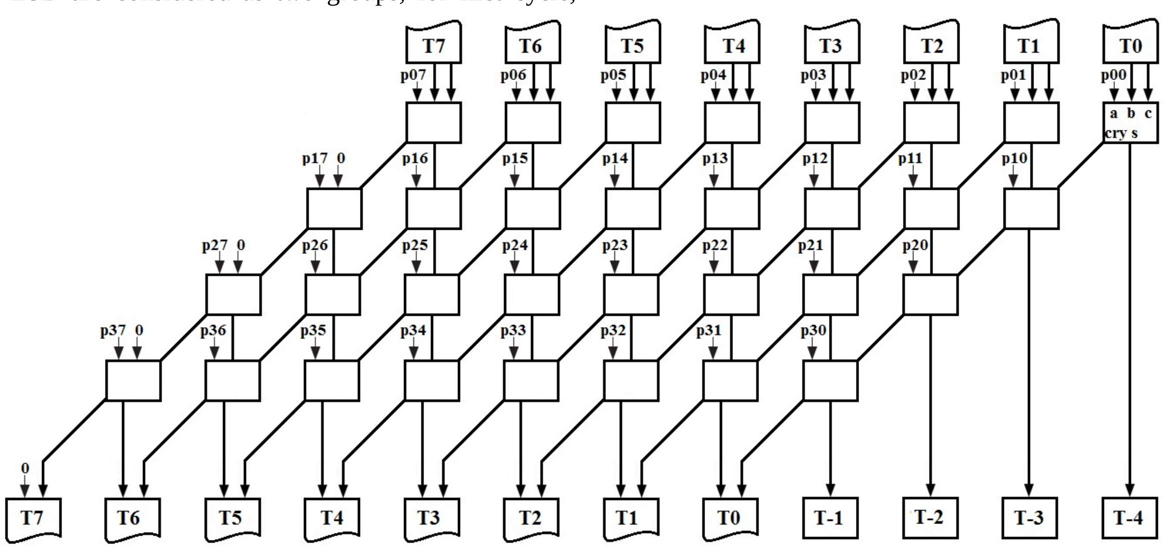

Fig. 5 block diagram of return conventional array multiplier

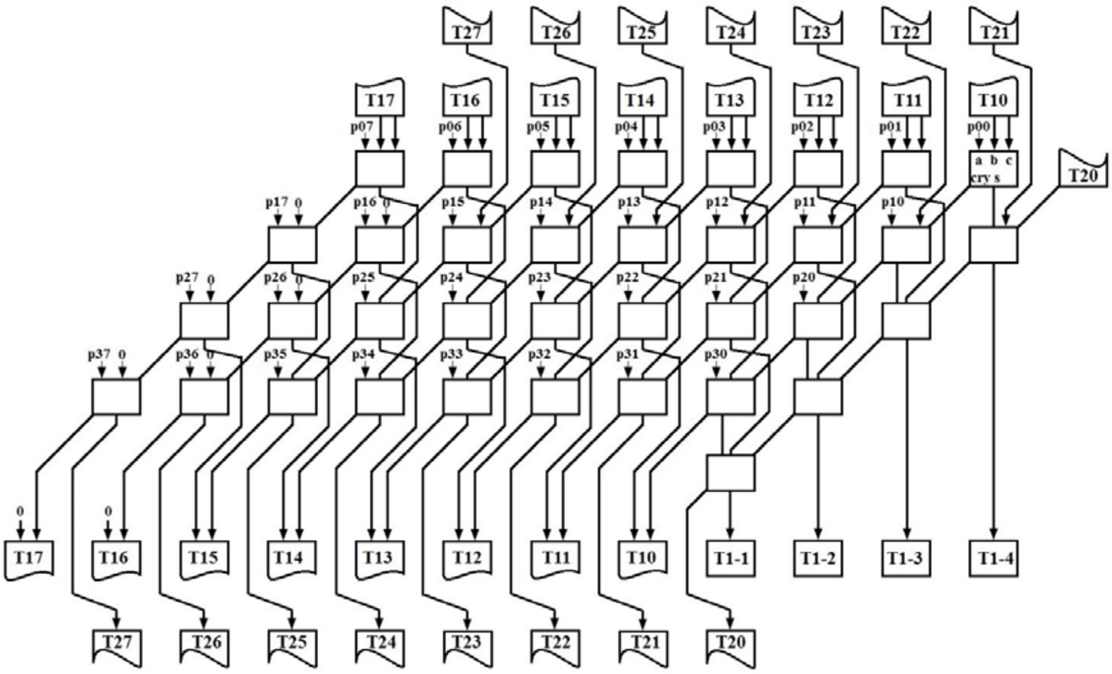

Fig. 6 block diagram of return leapfrog array multiplier

The performance of this structure the same as the previous one, stands for two cycles. For the first cycle 4-bit of first LSB and for the second cycle 4-bit of second LSB are also produced in the output of T1-1…T1-4 registers. For the first cycle, sum output of the third row and the fourth row carry of adders are saved in T10…T17 registers and will be returned to the first row of adder. The sum output of adder last row will be saved in T21…T27 registers and fifth row carry will be saved in T20 and will be returned to the adder second row to be also added with the second category of partial product rows for the second cycle. The last stage of this structure, the same as the structure of current leapfrog array multiplier, consists of a row of CSA and a row of CRA. For the second cycle, T10…T17 and T21…T27 registers output are applied in a row of CSA in order to decrease the number of product rows. Finally a CRA row is used to produce the final result.

The full adder and register architecture used in this paper are shown in figures 7 and 8.

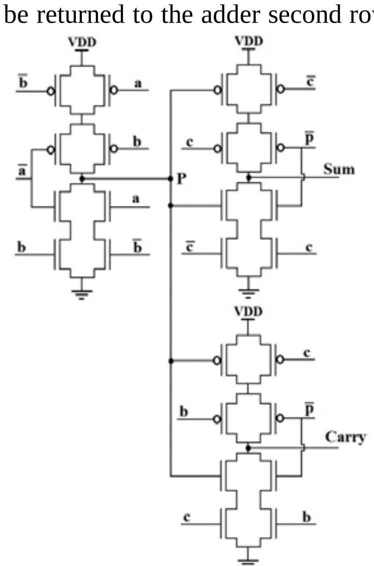

Fig. 7 full adder architecture

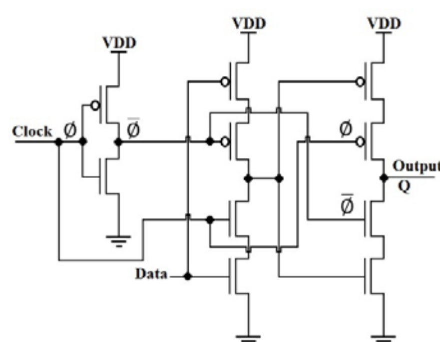

Fig. 8 C2CMOS flip flop architecture [7]

In fact, in these two structures, due to the reduction of the number of full adder rows, area and consequently consumption power also decrease.

V. SIMULATION RESULTS

The simulation in this paper was performed by HSPICE software and by means of 180nm TSMC and 130nm & 65nm PTM libraries and in the form of multiplying two 8-bit

ISBN: 978-1-61804-321-4

numbers. In order to show the suitable performance and very low consumption power of the designed return leapfrog array multiplier structure, this structure along with the return conventional array multiplier structure were designed and simulated by full adder cell and register which is presented in figures 7 and 8 of this paper.
The results of simulation have been shown in the following tables by means of different libraries. In all technologies, the related results of the performance of each structure are presented in front of it first Real values and then, normalized values. It should be noted that, the normalization process was performed separately for each structure. Since the main discussion in this paper is on the array structure, in this simulation assuming that all individual bits of partial product have been previously produced, delay and consumption power are only related to the array structure and were calculated. In all technologies, the return leapfrog array multiplier structure in comparison to the rest of proposed structures has the least PDP.

Table 1: The results of the simulation of array and return array multiplier by using the 180 nm technology

Multipliers (180nm)	**Parameters**	**Avg.Power (E-6)**	**Delay (E-9)**	**PDP (E-15)**	**No. of Transistors**
CAM	Real	3.1260	1.4806	4.6283	2736
	Normalized	1	1	1	1
CAM_{Return}	Real	1.6524	2.4279	4.0119	1760
	Normalized	0.5285	1.6398	0.8668	0.6432
LAM	Real	2.3131	1.7486	4.0447	3344
	Normalized	1	1	1	1
LAM_{Return}	Real	1.6601	1.8696	3.1037	2350
	Normalized	0.7176	1.0691	0.7673	0.7027

Table 2. The results of the simulation of array and return array multiplier by using the 130 nm technology

Multipliers (130nm)	**Parameters**	**Avg.Power (E-4)**	**Delay (E-10)**	**PDP (E-14)**	**No. of Transistors**
CAM	Real	2.8774	2.6334	7.5775	2736
	Normalized	1	1	1	1
CAM_{Return}	Real	1.6507	4.4419	7.3324	1760
	Normalized	0.5736	1.6867	0.9676	0.6432
LAM	Real	2.1033	4.4923	9.4487	3344
	Normalized	1	1	1	1
LAM_{Return}	Real	1.5959	3.5190	5.6161	2350
	Normalized	.07587	0.7833	0.5943	0.7027

Table 3: The results of the simulation of array and return array multiplier by using the 65 nm technology

Multipliers (65nm)	**Parameters**	**Avg.Power (E-4)**	**Delay (E-10)**	**PDP (E-14)**	**No. of Transistors**
CAM	Real	1.7218	1.4746	2.5390	2736
	Normalized	1	1	1	1
CAM_{Return}	Real	0.9972	2.3547	2.3482	1760
	Normalized	0.5791	1.5968	0.9248	0.6432
LAM	Real	1.2867	2.5073	3.2261	3344
	Normalized	1	1	1	1
LAM_{Return}	Real	0.97995	1.8475	1.8104	2350
	Normalized	0.7615	0.7368	0.5611	0.7027

The frequency of return structures by means of different libraries are as follows:

F_{max_180nm} = 2 Mhz

F_{max_130nm} = 266,66 Mhz

F_{max_65nm} = 400 Mhz

VI. CONCLUSIONS

The simulation results show that applying the return technique in the array structures cause power consumption reduction and consequently PDP reduction. This improvement for 180 nm technology in the conventional array structure is 13.32 % and in the leapfrog array structure is 23.27 %. It should be noted that this technique substantially makes the number of transistors less and as a result area reduction. This reduction, for leapfrog array structure is 29.73 % and for conventional array structure is 35.68 %.

REFERENCES

[1] K. Mathew, S. A. Latha, T. Ravi, and E. Logashanmugam, "Design and Analysis of Array Multiplier using an Area Efficient Full Adder Cell in 32nm CMOS Technology," International Journal of Engineering and Science, vol. 2, pp. 8-16, 2013.
[2] P. Srivastava, V. Vishant, R. K. Singh, and R. K. Nagaria, "Design and implementation of high performance array multipliers for digital circuits," in Engineering and Systems (SCES), 2013 Students Conference on, 2013, pp. 1-5.
[3] N. Ravi, Y. Subbaiah, T. J. Prasad, and T. S. Rao, "A novel low power, low area array multiplier design for DSP applications," in Signal Processing, Communication, Computing and Networking Technologies (ICSCCN), 2011 International Conference on, 2011, pp. 254-257.
[4] N. Ravi, D. T. Rao, and D. T. Prasad, "Performance Evaluation of Bypassing Array Multiplier with Optimized Design," International Journal of Computer Applications (0975–8887) Volume, 2011.
[5] K.-S. Chong, G. Bah-Hwee, and J. S. Chang, "A low power 16-bit Booth Leapfrog array multiplier using Dynamic Adders," in Circuits and Systems, 2004. ISCAS '04. Proceedings of the 2004 International Symposium on, 2004, pp. II-437-40 Vol.2.
[6] S. S. Mahant-Shetti, P. T. Balsara, and C. Lemonds, "High performance low power array multiplier using temporal tiling," Very Large Scale Integration (VLSI) Systems, IEEE Transactions on, vol. 7, pp. 121-124, 1999.
[7] R. V. Tambat and S. A. Lakhotiya, "Design of Flip-Flops for High Performance VLSI Applications using Deep Submicron CMOS Technology," 2014.

ISBN: 978-1-61804-321-4

Biomass boiler model for estimation of unmeasurable process quantities

Viktor Plaček, Bohumil Šulc and Ján Piteľ

***Abstract*—**Automatic biomass boilers are of significant importance for future achievement of strict flue gas emissions limits for small-scale boilers in the European Union. For this achievement economic-ecological optimization of combustion process must be implemented in a boiler control algorithm. The further improvement of optimization needs information about quantities that are not commonly measured because of high price or unreliability of their sensors. The paper introduces a mathematical model intended for estimation of the important unmeasurable quantities.

***Keywords*—**biomass, small-scale boiler, process control, quantities estimation

I. Introduction

THE European Union has decided to go the green way with sustainable alternative energy sources. One of important local energy sources mainly for residential heating are small-scale automatic biomass boilers. These devices usually combust properly prepared fuel in a form of pellets or wood chips with a minimal need of user interaction. There are two criterions that the combustion device has to fulfill to really have positive impact on living environment. It is criterion of minimum flue gas emissions and criterion of maximal combustion efficiency. The optimum fulfilling both criterions can be attained by a proper device construction and advanced device control algorithms. The construction of automatic small-scale biomass burning boilers is based on long time experience with manually operated boilers and during last decade probably has reached its optimum. With coming of automatic boilers the task of proper combustion process control has been taken over by boiler control algorithms.

This work was supported by Technology Agency of the Czech Republic and it is supported by grants of Scientific Grant Agency of the Ministry of Education, Science, Research and Sport of the Slovak Republic and the Slovak Academy of Sciences, Ministry of Education, Youth and Sports of Czech Republic and Slovak Research and Development Agency.

V. Plaček is with Department of Instrumentation and Control Engineering, Faculty of Mechanical Engineering, Czech Technical University in Prague, Technická 1902/4, 166 07 Praha 6, Czech republic, (e-mail: viktor.placek@fs.cvut.cz).

B. Šulc is with Department of Instrumentation and Control Engineering, Faculty of Mechanical Engineering, Czech Technical University in Prague, Technická 1902/4, 166 07 Praha 6, Czech republic, (e-mail: bohumil.sulc@fs.cvut.cz).

J. Piteľ is with Department of Mathematics, Informatics and Cybernetics, Faculty of Manufacturing Technologies, Technical University of Košice, Bayerova 1, 080 01 Prešov, Slovakia (corresponding author to provide phone: +421 905 524605; fax: +421 421 51 7733453; e-mail: jan.pitel@tuke.sk).

Although the problem of homogenized biomass combustion control seems like an easy task the opposite is true. The combustion of solid fuels with gaseous oxidant (non-homogenous combustion) is from the modeling and control point of view quite difficult task. It is mainly due to non-linear behavior of chemical processes taking part during the combustion, dependence of the process on many variables simultaneously, internal coupling of processes, time delay or non-minimal phase behavior of some processes etc. The measurement is weighted by a strong noise resulting from chaotic basis of a combustion process.

Due to difficult controllability of a combustion process contemporary control algorithms of automatic small-scale biomass boilers are based on long experience of manufacturers with the devices operation. The manufacturers often prefer direct control only with some inevitable usage of a feedback. Their goal is an algorithm with the highest reliability with the optimality of combustion process at a second place.

In Fig. 1 is an example of a typical direct control algorithm. The feedback from a measured temperature of hot water and its set-point determine the boiler heat output demand. On the basis of the heat output demand the control algorithm sets the fuel and air inflow using preprogrammed curves by a manufacturer. The reason for such a simple direct control algorithm is simplicity. By avoiding of feedback control the manufacturers get around problems with stability of closed-loop control that is a significant issue with such difficultly controllable processes.

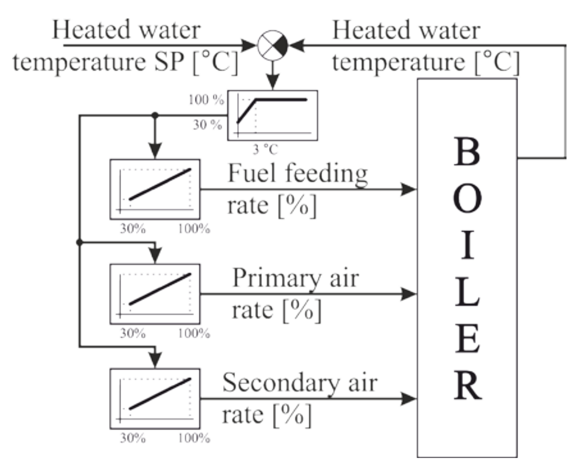

Fig. 1 Scheme of the simplest and the most common control method used at small-scale biomass boilers

A weak point of direct control algorithm is a sensitivity of a controlled process to a change of conditions for which the algorithm was tuned. That change of conditions can be for example heat exchanger surface sooting, clogging of a grate by ashes, failure of some control member or a sensor flaw. But the main source of conditions changes is the quality of used fuel. The range of biofuel parameters is very wide (wood or herbal origin, density, calorific value, water content etc.) and without a knowledge of at least some of the parameters it is not possible to effectively control the combustion process with just a direct control method.

Currently the manufacturers solve the problem of unknown fuel parameters by requesting this information from the boiler operator via a control unit. This solution may be unsatisfactory as the small-scale boilers operators are usually end-users with only marginal knowledge of combustion process. End-users often consider an automatic boiler as fully autonomous home appliance and neglect the necessity to provide the information about used fuel quality.

One of our goals was to find a method that would allow to estimate at least some of the fuel quality parameters without necessity of operator cooperation. Main parameter influencing combustion process control process is calorific value of a used fuel. During our experiments the quality of biomass fuels ranged from 6 MJ/kg for wet wood waste to 17 MJ/kg for a wood chips from crushed wood pallets. Often we observed the variability in biomass calorific value even within one batch of fuel (probably due to a way of storage). Although it is possible to measure water content as most influential parameter to a calorific value it is practically impossible to ask an end-user to measure it in a common end-user household.

The estimation of fuel calorific value can be obtained by using information from existing measurement of other variables and their relation with the calorific value. The most transparent way of relation description is usage of mathematical model.

II. Mathematical Model of Combustion Process

During a bibliographic search we have not found any mathematical model simple and transparent enough to be used for process control. The main reason we avoided to create our own mathematical process model was the lack of a practically usable relation describing release of heat from in a combustion chamber. Breakthrough was discovery of empirical equation published by prof. Havlena in [3]. The rest of the mathematical model is based on analytical power balances of the boiler functional parts. The scheme of modeled heat transfers inside a boiler is in Fig. 2.

A boiler heat source is burning fuel layer on a grate inside a combustion chamber. The heat output is dependent on a fuel surface that is proportional to a weight of a fuel. A weight balance of the fuel can be described by a difference between inflow of fed fuel and its drop due to burning out:

$$\frac{\mathrm{d}}{dt} m_b(t) = M_{bi}(t) - M_{bo}(t)\,, \tag{1}$$

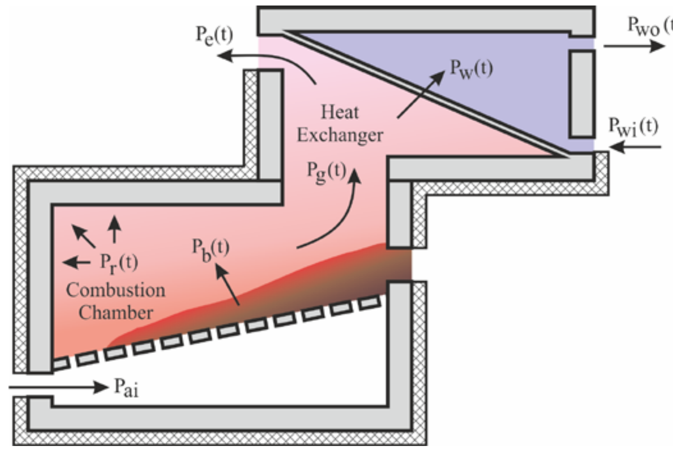

Fig. 2 Scheme of power balance inside a grate firing boiler with adiabatic combustion chamber.

where $m_b(t)$ [kg] is burning fuel mass on a grate, $M_{bi}(t)$ [kg·s^{-1}] is mass flow of the fuel fed to the combustion chamber and $M_{bo}(t)$ [kg·s^{-1}] is fuel mass drop rate due to its combustion.

The fuel mass drop rate caused by the fuel combustion $M_{bo}(t)$ is calculated by the equation:

$$M_{bo}(t) = \frac{P_b(t)}{H(t)}\,. \tag{2}$$

where $P_b(t)$ [kW] is power generated by fuel burning out and $H(t)$ [kJ·kg^{-1}] is fuel caloric value.

The heat balance of the flue gas in the combustion chamber describes the power balance:

$$c_g V_g \frac{\mathrm{d}}{dt} \vartheta_g(t) = P_b(t) + P_{ai}(t) - P_r(t)\,, \tag{3}$$

where $P_{ai}(t)$ [kW] is heat of the combustion air inflow, $P_r(t)$ [kW] is heat flow to the combustion chamber refractory, $P_g(t)$ [kW] is heat flow leaving the combustion chamber to the heat exchanger, c_g [kJ·m^{-3}·K^{-1}] is volumetric specific heat capacity of flue gas, V_g [m^3] is internal volume of the combustion chamber and $\vartheta_g(t)$ [ºC] is temperature of the flue gas leaving combustion chamber to the heat exchanger.

Expressing the powers in (3) as the heat flows we get the equation for computing the temperature of the flue gas:

$$\begin{aligned} c_g V_g \frac{\mathrm{d}}{dt} \vartheta_g(t) &= P_b(t) + c_a Q_a(t) \vartheta_{ai} \\ &\quad - k_r\big(\vartheta_g(t) - \vartheta_r(t)\big) - c_g Q_g(t) \vartheta_g(t) \end{aligned} \tag{4}$$

where k_r [kW·K^{-1}] is flue gas to the combustion chamber refractory heat transfer coefficient, $\vartheta_r(t)$ [ºC] is temperature of the combustion chamber refractory, $Q_a(t)$ [m^3·s^{-1}] is volumetric flow rate of the primary and secondary air together and $\vartheta_{ai}(t)$ [ºC] is temperature of the combustion air inflow.

The boiler refractory is a significant heat accumulator which influences dynamics of the boiler in a cardinal way. In derivation of the model, so called adiabatic combustion chamber is considered, it means that the refractory exchanges heat with the combustion chamber only, and there are no heat losses to the boiler surrounding. Considering that fact, the heat balance of the refractory expresses the equation:

$$\frac{\mathrm{d}}{dt}\vartheta_r(t)=\frac{k_r}{c_r m_r}\left(\vartheta_g(t)-\vartheta_r(t)\right), \tag{5}$$

where c_r [kJ·kg^{-1}·K^{-1}] is mass heat capacity of the refractory and m_r [kg] is mass of the refractory.

The flue gas having the temperature $\vartheta_g(t)$ leaves the combustion chamber for the heat exchanger where it transfers a part of heat to water and the remaining departs unused. The heat balance on the flue gas side of the heat exchanger is:

$$\frac{\mathrm{d}}{dt}\vartheta_e(t)=\frac{1}{c_g V_e}\left(P_g(t)-P_w(t)\right), \tag{6}$$

where $P_g(t)$ [kW] is flue gas heat flow the from combustion chamber to the heat exchanger, $P_w(t)$ [kW] is heat flow from the flue gas to water, $\vartheta_e(t)$ [ºC] is temperature of flue gas at the stack entrance and V_e [m^3] is volume of the flue gas side of the heat exchanger.

For description of the heat transfer from the flue gas to the water a very simplified linear model has been used in which the arithmetical mean of the inlet and outlet temperature is applied:

$$\begin{aligned}\frac{\mathrm{d}}{dt}\vartheta_e(t)&=\frac{c_g Q_g(t)}{c_g V_e}\left(\vartheta_g(t)-\vartheta_e(t)\right)\\&-\frac{k_w}{2c_g V_e}\left(\left(\vartheta_g(t)-\vartheta_{wo}(t)\right)+\left(\vartheta_e(t)-\vartheta_{wi}(t)\right)\right)\end{aligned} \tag{7}$$

where k_w [kW·K^{-1}] is heat transfer coefficient flue gas to water, $\vartheta_{wi}(t)$ [ºC] is temperature of the return water and $\vartheta_{wo}(t)$ [ºC] is temperature of the heated water.

In the similar way it is possible to formulate the heat balance for the water side of the heat exchanger and after substituting powers by heat flows we get the differential equation describing the temperature changes of the heated water:

$$\begin{aligned}\frac{\mathrm{d}}{dt}\vartheta_{wo}(t)&=\frac{M_w(t)}{m_w}\left(\vartheta_{wi}(t)-\vartheta_{wo}(t)\right)\\&-\frac{k_w}{2c_w m_w}\left(\left(\vartheta_g(t)-\vartheta_{wo}(t)\right)+\left(\vartheta_e(t)-\vartheta_{wi}(t)\right)\right)\end{aligned} \tag{8}$$

where c_w [kJ·kg^{-1}·K^{-1}] is water heat capacity and $M_w(t)$ [kg·s^{-1}] is mass flow rate of the heated water.

III. Usage of Kalman Filter

The model introduced in previous chapter is intended only for approximate prediction of variables trend. The reason is a lot of unmeasurable disturbances that influence a combustion process. Many of the constants used in the model are in a real process partially dependent on other variables (like specific heat capacity dependence on a temperature) and usually time-variant (like heat transfer coefficient change due to sooting of heat transfer surfaces in a heat exchanger). These influences cause a gradual increasing of a model error in comparison with real process behavior. Because the introduced model is intended for continuous calorific value estimation, the model will be operated side by side with real process run. Due to this fact we could take advantage of Kalman filter for continuous correction of internal states of the model. Kalman filter is one of methods used for correction of model internal states in a way to minimize the model error with preserving physical relations of modeled variables.

One of the input variables of the model is a fuel calorific value $H(t)$. However, this value is unknown for an algorithm and our goal is to estimate it. For the purpose of continuous calorific value estimation was the variable $H(t)$ changed to model state value modelled as a constant:

$$\frac{\mathrm{d}}{dt}H(t)=0\,. \tag{9}$$

In a model alone the calorific value never changes. But Kalman filter can change its state value in a way to minimize the model error (a difference of the model output variables from their measured counterparts on a real process).

IV. Model verification

The model and its ability to estimate fuel calorific value were verified on data acquired during experiment with a real biomass boiler of Fiedler company with nominal heat output 100 kW. During eight hours long experiment the boiler was first stabilized to a steady-state heat output of 50 % of its nominal value. Then a fuel inflow was step raised to reach heat output of 80 % of nominal value. Then the heat output was lowered back to 50 % of nominal value again.

The comparison of the boiler and model behavior is in Fig. 3. The solid line is time record of variables measured on a real boiler and the dashed lines are their respective modeled values. In Fig 4 values of unmeasured variables are estimated by a Kalman filter using the model. These are fuel mass on a grate and fuel calorific value. It can be seen from the picture that an estimation shows calorific value around 13 MJ/kg. The real fuel calorific value was batch measured by drying a sample in a laboratory to be 13.2 MJ/kg. A fluctuating value of estimation may be due to inaccuracy of the estimation or by a real fluctuation of fuel calorific value fed during the experiment.

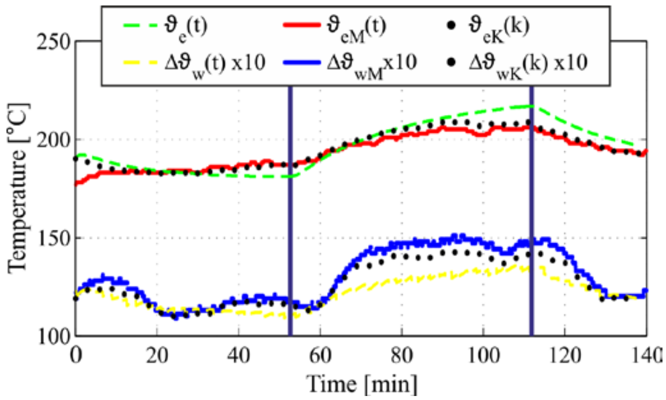

Fig. 3 Comparison of real boiler measured variables with its model output. Dashed lines are modeled variables, solid lines are measured variables and discrete points are Kalman estimations of variables.

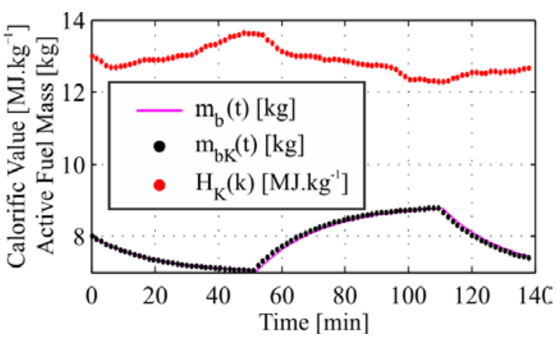

Fig. 4 Estimation of unmeasured variables using a Kalman filter and a process model. Upper dotted line is fuel calorific value estimation and lower line is estimation of a fuel mass actively burning on grate.

V. Conclusion

One of parameters that crucially affect process control algorithm abilities is a used fuel calorific value. This parameter is not possible to measure in common household environment by an economically affordable way. The fuel calorific value changes not only between batches of a fuel but even within one batch and with reference to a way of storing it can change with time.

The contribution introduces simplified mathematical model that is able to estimate fuel calorific value using a comparison of real boiler measured variables with the corresponding variables of simultaneously simulated reference model.

The usage of Kalman filter corrected model for calorific value estimation is the only one possibility of boiler model utilization. A process model may be used for wide range of other applications using model such as device failure detection, sensors credibility loss, control methods using a model like MPC (Model Predictive Control) etc.

Acknowledgment

The research work was supported by project TA02020836 cofinanced by Technology Agency of the Czech Republic and also it is supported by grant VEGA 1/0881/13 „Research of Algorithms and Methods for Predictive Control of Biomass Combustion Processes“ and by grant SK-CZ-2013-0095 “Research of the Optimal Ecological Biomass Combustion Algorithms Using Intelligent and Statistical Methods of Process Control”

References

[1] J. Mullerová, S. Hloch, and J. Valíček, “Reducing emissions from the incineration of biomass in the boiler”, Chemické listy, vol. 104, no. 9, pp. 876-879, 2010.

[2] V. Plaček and C. Oswald, “Methods of small and medium-scale biomass combustion”, *International Journal of Power and Energy Systems*, vol. 34, issue 1, pp. 20-25, 2014.

[3] V. Havlena and D. Pachner, “Model-based predictive control of a circulating fluidized bed combustor”, *in Power Plant Applications of Advanced Control Techniques,* Verlag ProcessEng Engineering, 2010.

[4] S. Loob and J. Koppejan, *The handbook of biomass combustion and co-firing*, Earthscan, 2008.

[5] P. Skok, M. Rimár, and J. Mižák, “Woodchip combustion process quality and the amount of combustion air”, *Applied Mechanics and Materials*, vol. 308, pp. 115-119, 2013.

[6] A. Hošovský, “Genetic optimization of neural networks structure for modeling of biomass-fired boiler emissions”, *Journal of Applied Science in Thermodynamics and Fluid Mechanics*, vol. 9, no. 2, pp. 1-6, 2011.

[7] J. Mižáková, “Monitoring of biomass-based heat production system”, *Applied Mechanics and Materials*. vol. 616, pp. 143-150. 2014.

[8] J. Haapa-Aho, T. Korpela, T. Bjorkqvist, J. Hrdlička, V. Plaček, S. Vrána, and B. Šulc, „Continuous control issues concerning operation improvement of small-scale biomass boilers“, *in: Proceedings of 18th IFAC World Congress*, Milano, 2011. pp. 7035-7042.

[9] J. Piteľ and J. Mižák, “Cost effective biomass combustion process control”, *in Proceedings of the 8th PP&PSC (Power Plant and Power System Control) IFAC Symposium*, Toulouse, 2012. pp. 616-620.

[10] C. Oswald, V. Plaček, B. Šulc, and A. Hošovský, “Transfer issues of control optimizing combustion from small-scale to medium-scale biomass-fired boilers”, *in Proceedings of the 8th PP&PSC (Power Plant and Power System Control) IFAC Symposium*, Toulouse, 2012. pp. 207-211.

[11] T. Korpela, T. Bjorkqvist, and A.-P. Lautala, “Control strategy for small-scale wood chip combustion”, *in Proceedings of 6th IFAC Symposium on Power Plants and Power Systems Control*, Tampere, 2009. pp. 119-124.

[12] Y. Chungen, L.-A. Rosendahl, A. Søren, K. Kær, “Grate-firing of biomass for heat and power production”, *Progress in Energy and Combustion Science*, vol. 34, issue 6, pp. 725–754, 2008.

[13] K. Židek, T. Saloky, and V. Maxim, “Global navigation and its specification using Kalman filter”, Transfer inovácií, no. 9, pp. 159-162, 2006.

[14] A. Hošovský, “Biomass-fired boiler control using simulated annealing optimized improved Varela immune controller”, *Acta Polytechnica Hungarica*, vol. 12, no. 1, pp. 23-39, 2015.

[15] A. Hošovský, M. Tóthová, and K. Židek, “Comparison of performance of optimized Varela immune controller and PID controller for control of time-delay process (Accepted for publication)”, *Key Engineering Materials*, to be published.

Viktor Plaček is a PhD student in Faculty of Mechanical Engineering of the Czech Technical University in Prague. His research activities include modeling, simulation and automatic control of small-scale biomass-fired boilers.

Bohumil Šulc is a Professor in Faculty of Mechanical Engineering of the Czech Technical University in Prague. His research activities include automatic control of technological processes and its modeling and simulation of real operational conditions, focusing on discrete algorithms.

Ján Piteľ is an Associate Professor and Vice-dean in Faculty of Manufacturing Technologies of the Technical University of Košice with a seat in Prešov. His research activities include modeling, simulation and automatic control of machines and processes.

The FLEHAP device

Corrado Boragno , Gregorio Boccalero

Abstract**—**In this paper, we present a device which can autonomously power small sensors and wireless nodes as required in the developing Internet of Things. This device is based on the fluttering effect: when a fluid in motion impacts on an elastic structure, a part of the mechanical energy is transferred to the structure, inducing large amplitude vibrations. Via an electromagnetic coupling, these oscillations produce electric energy which can be stored in a rechargeable battery or a (super) capacitor.

Keywords**—**Energy harvesting, Internet of Things, Network of Wireless Sensors

I. INTRODUCTION

THE Internet of Things IoT is the next big evolution of electronics. It is based on the concept of omnipresent connectivity among different objects which in a large part are Networks of Wireless Sensors NWS. Such a complex system requires sensors, microcontrollers and radio devices enabling the transmission of the collected information to the Internet (the Cloud). These sensors cannot be wired, especially when the network is intended to be used on very large areas or placed in difficult-to-reach places (i.e. buried or in harsh or hazardous locations). A common solution is to provide all nodes of the network their own energy source, usually a battery; but for a large number of application domains, also a battery is not a reliable solution. In fact, installation and replacement costs can become too high if the network involves hundreds or thousands nodes.

For this reason the possibility for an application to stay reliable and economically viable on the long term (10 yrs or more) will more and more depend on the node's capability to recover energy from the node's environment (energy harvesting), either to prevent the battery from discharging or, much better, to get rid off the battery itself.

Among other available sources (mechanical vibrations, light, temperature difference …), a fluid in motion (air, water) can represent a useful resource of energy if a specialized device is constructed. Windmills are commonly used to get energy from a wind, but this system cannot be scaled-down in a centimeter-sized device, as necessary for typical IoT applications.

This work was supported by Fondazione Carige and by PRIN 2012 project n. D38C1300061000 funded by the Italian Ministry of Education.

C.Boragno is Associate Professor at the Dipartimento di Fisica, Università di Genova, Italy (corresponding author, phone: +39 010 353 6229, fax: +39 010 314218, e-mail: corrado.boragno@unige.it)

G.Boccalero is PhD student at the Dipartimento di Fisica, Università di Genova, Italy.

An alternative method to harvest energy from a wind is based on the fluttering effect: after the seminal work of McKinney and J. DeLaurier [1], in recent years many devices have been proposed [2] [3] [4] .

In the present contribution, we describe a device called FLEHAP (Fluttering Energy Harvester for Autonomous Powering) which can be used in a NWS system.

II. EXPERIMENTAL

The FLEHAP device is schematically presented in Fig. 1 .

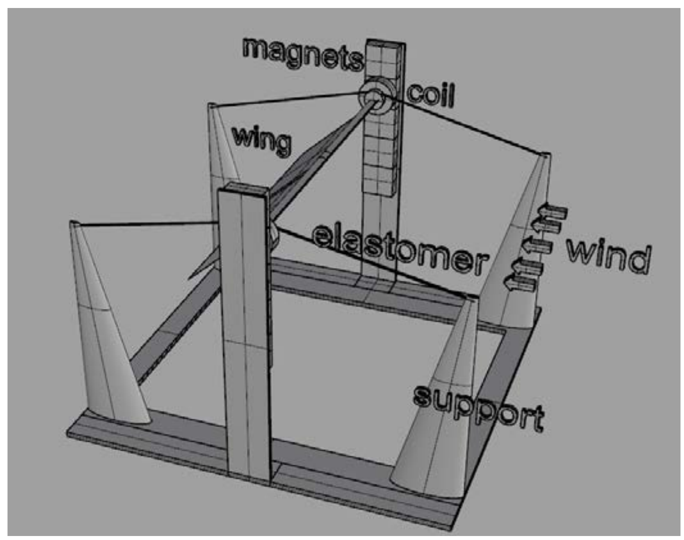

Fig.1 – A schematic representation of the FLEHAP device

At the ends of a rigid axis, two coils are placed close to a series of permanent magnets. Two elastomers connect the rigid axis to a support and a wing can freely rotate around it.
Under the wind action, the system oscillates and the rigid axis follows a periodic vertical trajectory, then an e.m.f. is induced in the coils due to Faraday effect.

Since we are interested to apply the device to NWS systems, the typical dimensions of the structure are in the centimeter range. A sheet of polyvinyl acetate of 0.2 mm thickness is used for the wings; the wing span (i.e. the dimension perpendicular to the wind) is in the range 50 - 90 mm, while the chord is within 20 - 40 mm. With these dimensions, the

ISBN: 978-1-61804-321-4

wing can be considered rigid. The global mass of the system (rigid axis + coils + wing) is around 4 g. The elastomers are made by natural rubber, with a diameter of 1.3 mm and a length at rest L_0 = 60 mm. During the device assembly procedure, the elastomers are pre-stretched in order to tune the elastic force acting on the wing.

To test the performance of the device, it is inserted in an open circuit wind tunnel, able to produce a wind in the range 2 – 16 m/s . A fast camera, positioned outside the tunnel, is used to record the wing trajectory and a digital oscilloscope is used to measure the e.m.f induced in the coils.

III. FLUID DYNAMICS

First, the aeroelastic response of the system is studied as function of the wind velocity U and the mechanical parameters of the system.

In Fig.2 we report some images extracted from a typical movie.

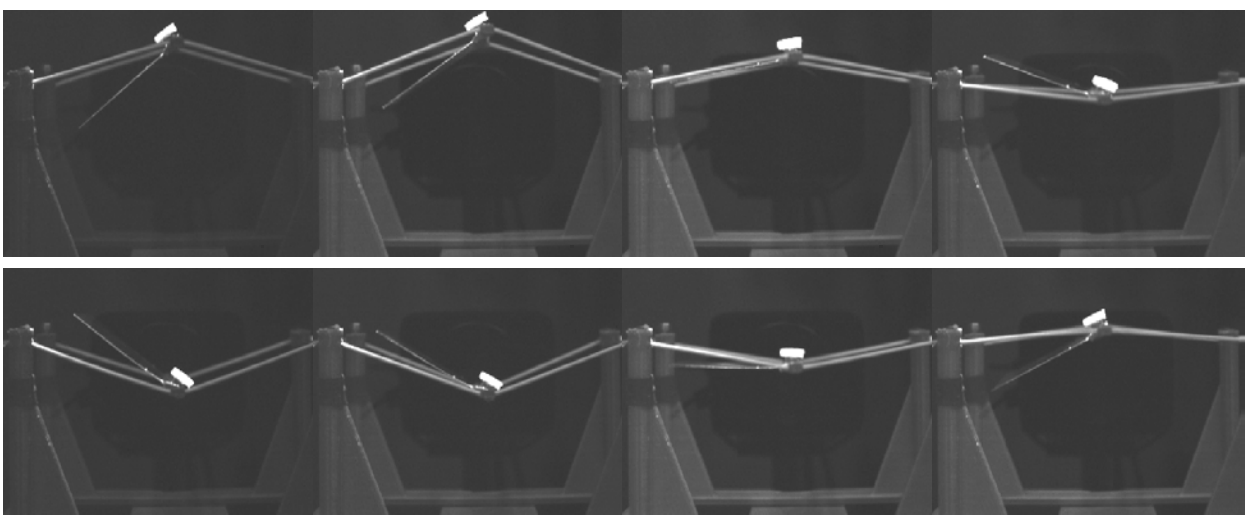

Fig. 2 – Some snapshots showing the wing motion under the wind action. In this case, chord = 40 mm, span = 60 mm, U = 3.8 m/s

It is evident that the rigid axis (where the elastomers are fixed) moves along a periodic trajectory in the vertical direction, while the wing oscillates in angle.

This behaviour is due to the aeroelastic interaction of the wind with the system. When the wing assumes a positive angle (counter clockwise) a lift force is generated, inducing the wing to move up. When the elastic force counterbalances this lift force, the wing rotates around the axis, the angle becomes negative then reverting the direction of the lift force. CFD simulations and smoke fluid visualization (not reported here) show that a vortex is created at the Leading Edge LE when the wing reaches an angle (positive or negative) larger than 30° . These vortices are responsible of the instability that triggers the wing movement, inducing the transition to a stable Limit Cycle Oscillation LCO.

Many parameters influence the shape of LCO: mass and shape of the wing, elastomer strength, position of the rigid axis along the wing side. Acting on these parameters, it is possible to tune the system in order to maximize LCO amplitude and frequency in a particular wind range.

As an example, we show in Fig. 3 the LCO amplitude vs. U for a wing with chord = 20 mm and span in the range 50 – 90 mm.

The system oscillates if the wind velocity is in the range 2 – 6 m/s, reaching a maximum at 3 m/s. About the wing angle, it is around 50° (in absolute value) at low velocity, reaches a maximum around 90° at a velocity of 3.5 m/s, then it decreases at higher velocities.

For U > 6 m/s, the movement stops and the wing assumes a horizontal position.

In order to extract energy from such a system with an electromagnetic coupling, it needs to maximize the oscillation frequency. The measured frequency f is always larger than the natural frequency f_n of the system:

$$f_n = \sqrt{K/m}$$

where K is the effective elastomer strength along the vertical direction and m is the system mass; f grows with the wind velocity as $U^{1/2}$, as shown in Fig.4 . We notice that because of this relation the FLEHAP device can be used as an autonomous sensor to measure wind velocity.

IV. ENERGY HARVESTING

In order to harvest energy from the wing fluttering, then transforming part of the mechanical energy in electrical energy we use an electromagnetic coupling: two series of magnets are placed in front of the coils that are fixed at the ends of the rigid axis (Fig. 1).

The magnets (NdFeB) have dimensions 10 mm x 10 mm x 5 mm and are arranged with alternate polarity N-S-N-S-N . The coils have L = 10 mH , R = 150 Ω , 1500 turns and external diameter 10 mm.
A typical e.m.f. measured during the wing oscillation is reported in Fig. 5 .

When a resistive load R_L is inserted at the ends of the coils, the induced current acts as an electromagnetic brake, lowering the frequency oscillation and eventually stopping the wing movement, if R_L is low enough and the wind velocity is not high. Of course, this effect depends also on the other parameters of the system and then it is necessary to tune the resistive load for a fixed wind velocity or to choice a R_L value as a compromise useful for a larger wind velocity range.

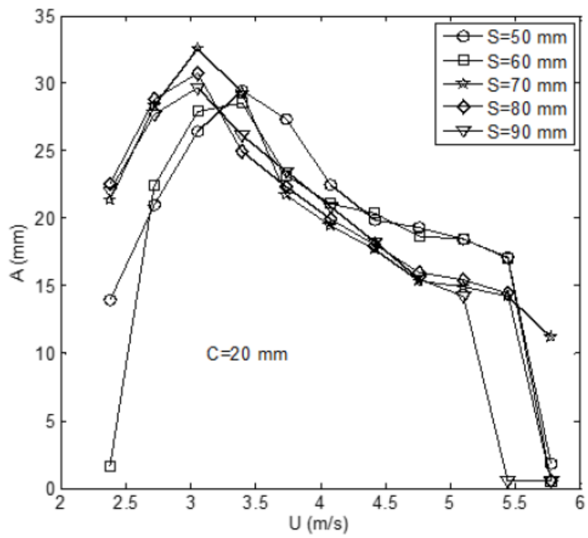

Fig. 3 – Amplitude of the vertical motion as function of U

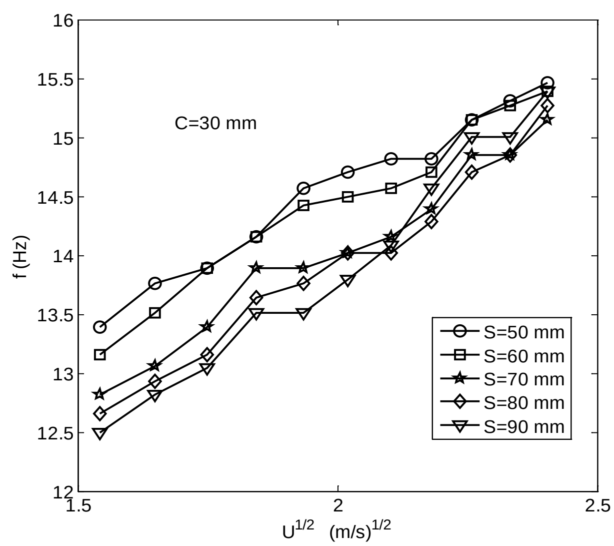

Fig. 4 – Oscillation frequency as function of wind velocity

In Fig.6 we report the power dissipated on the optimized load for a wing having chord = 40 mm and span = 80 mm. R_L varies from 10 kΩ at low wind velocity to 1 kΩ .

The maximum power (32 mW) is obtained for U = 5.5 m/s with R_L = 1 kΩ : this value is high enough to power a wireless sensor, demonstrating that the present device can be used in WNS systems.

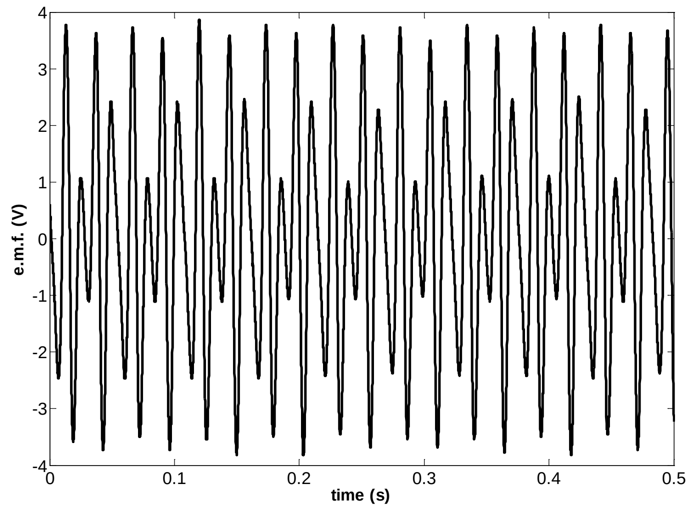

Fig. 5 – e.m.f. measured with a wing of chord = 40 mm and span = 70 mm in a wind of 5 m/s (no load).

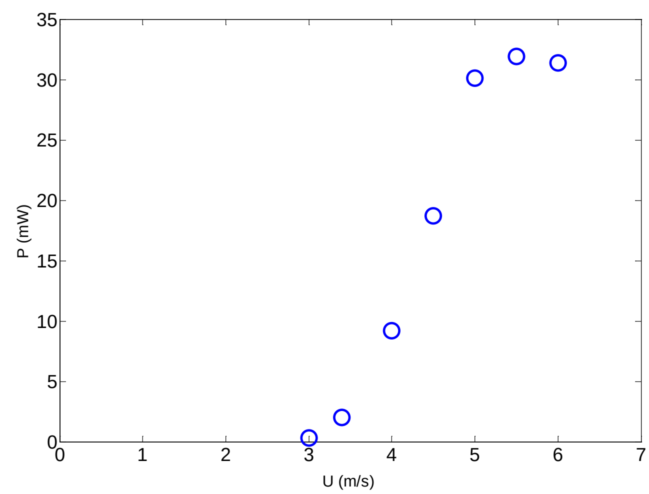

Fig. 6 – Power dissipated in the optimized load as function of wind velocity

In order to obtain a DC output and to charge a battery or a capacitor, a simple diode bridge is not convenient since the power loss on these components can be a relevant part of the harvested energy. Today are present on the market specialized circuits that efficiently convert a poor regulated voltage input into a stable DC output. Linear Technologies, Texas Instruments, Maxim Integrated and other companies produce IC specifically designed to operate with electromagnetic

ISBN: 978-1-61804-321-4

energy harvester.

Actually, we are testing our device in conjunction with an IC prototype developed by ST Microelectronics.
This IC contains three blocks: an Adaptive Scanvenger Interface (ASI), a single inductor quadruple output Buck DCDC Converter (DCDC) and a digital communication and configuration block (DIG). The converter is able to provide four independent and regulated power supply outputs each of them with a selectable voltage between 1V and 2.5V .

V. CONCLUSIONS

We developed a new energy harvester based on the aeroelastic interaction between a fluid in motion and a wing elastically connected to a support. Under the wind action, the system oscillates periodically in the vertical direction. Via an electromagnetic coupling, more than 30 mW can be produced in a wind around 5 m/s.

.

REFERENCES

[1] McKinney,W. and DeLaurier,J. “Wingmill: An Oscillating-Wing Windmill” , J. Energy **5**, 109 (1981)

[2] Bryant, M. and Garcia, E. “Modeling and Testing of a Novel Aeroelastic Flutter Energy Harvester” , J. Vib. Acoust **133** , 011012 (2011)

[3] Fei,F. , Mai,J.D. and Li,W.J. “A wind-flutter energy converter for powering wireless sensors “ , Sensors & Actuators A – Physical **173** , 163 (2012)

[4] Boragno,C. , Festa,F. and Mazzino,A. “Elastically bounded flapping wing for energy harvesting” , App.Phys.Lett. **100**, 253906 (2012)

Traction control algorithm development for energy regeneration subway - ACTREM: energy efficiency improvement of traction rail systems

Sergio L. Pereira, Carlos A. de Sousa and Eduardo M. Dias

Abstract— This paper presents the development and the tests of the control algorithm called ACTREM - Traction Control Algorithm for the Generation of Subway Power whose main objective is to enable the synchronization of train traffic in subway systems so that the energy from regenerative braking can be reused in the traction system. The ACTREM algorithm is based on the control of the train stops and departures throughout its trip for the optimization of power consumption. The ACTREM requires the application of the Genetic Algorithm (GA) for setting the best traffic of trains. This article also presents the modeling of the traction system, and the development of the traction simulator of a subway system. To analyze the performance of the ACTREM control algorithm in increasing the power (energy) efficiency a simulation of the application was conducted by applying the ACTREM in the São Paulo METRÔ Line 4 - Yellow, and the results were compared with the measurements in substations and trains of the line in question. The proposed model and the solutions found by the ACTREM control algorithm is discussed, contemplating the possibility of its use in solving this same problem in similar subway systems such as those covered by the case study addressed herein.

Keywords— Subway, power (energy) efficiency, numerical optimization, rectifier substation, power regeneration.

I. Introduction

In the subway system of São Paulo approximately 77% of the electric power is consumed by the traction systems, i.e., movement of the trains. In 2012, this represented a consumption of 561,341 MWh, equivalent to an average of more than 3.5 million residential consumers [1].

The results of the Metrô's Inventory on Greenhouse Gas Emissions showed that the subway transportation emits about 50 times less greenhouse gases per kilometer of passenger transported than the equivalent transported by car and 25 times less than the bus.

According to the APTA - American Public Transportation Association [2], the public transport prevents the use of 4.2 billion gallons of gasoline per year in the United States. The APTA attributes the reduction of about 223 liters of gasoline per family per year in the US, and easy access to the subway system in the large cities of the country.

The subway systems provide a great benefit to the communities, however, the subway rail systems require a lot of power to operate. [3]

According to Pires, to reuse the energy produced by the regenerative braking produced by trains of a subway system is essential for increasing the energy efficiency of the system, but difficult to apply in the São Paulo subway due to the small interval between consists and frequent departures and braking [4].

In terms of energy efficiency, the operation of the São Paulo subway can be divided into two levels. At the first level, the operation engineering sets to the traffic operators of CCO a time diagram, which regulates the departure and arrival times of the trains, i.e., the time travelled between the stations and the time spent at the stations. The second level, the operation engineering programs an efficient speed profile in terms of energy during travel time. The distance between trains can vary in the signaling systems, according to their speed, thus, it is possible to generate various speed profiles for trains, among which it must be selected the one that minimizes the energy consumption in accordance with the safety restrictions. In line 4 Yellow of the São Paulo subway, the purpose of this study was to implement a CBTC – (Communications Based Train Control).

According to Xiang [5] the control studies on conventional trains separately optimize the speed profile in each section between stations. According to Ghoseiri [6] the studies of the train traffic control optimization are based on the assumption that the trains have constant speed, and the power consumption is determined by the energy required to overcome the resistance to movement during the travelled section.

Optimizations of the train speed profiles and the train traffic optimization are dependent on each other. However, the travel time between stations as defined by the train traffic control is a major obstacle to the implementation of the energy

S. L. Pereira is professor at the Polytechnic School of University of São Paulo and a researcher of GAESI - Grupo de Automação Elétrica em Sistemas Industriais, a research group of the Electrical Energy and Automation Department, Polytechnic School of University of São Paulo, Av. Prof. Luciano Gualberto, trav. 3, n. 158, São Paulo/SP, Brazil, CEP 05508-970 (sergioluizpe@uol.com.br)

C. A. de Sousa is a professor at the Universidade Nove de Julho - UNINOVE, an engineer at the São Paulo Subway Company and a PhD student at Polytechnic School of University of São Paulo (carlos.as@usp.br).

E. M. Dias is full professor at the Polytechnic School of University of São Paulo and coordinator at GAESI (emdias@pea.usp.br).

regeneration control algorithm to improve energy efficiency.

On the other hand, the energy consumption determined by the speed profile is the basis for the train traffic control optimization. Thus, studies, which analyzed the speed profile and the optimization of train traffic separately, cannot get the best overall solution for energy savings. In order to achieve a better performance in energy efficiency, this paper presents the development of a control algorithm called ACTREM to increase the coincidence time between the acceleration and braking cycles through the control of the stop time of the trains at the stations, for the case study we used the data from the subway line Yellow 4 of São Paulo subway..

II. Comtrole do Trafego de Tres

The synchronization of the acceleration and braking of different trains through the optimization of the subway train time diagram is a solution with low implementation cost, but effective to implement a train traffic control algorithm to maximize the use of the regenerative braking in the urban subway systems. This solution not only saves traction energy, but also helps to reduce power surges caused by simultaneous acceleration of several trains in the system. The effect of this measure will be more noticeable in dense urban networks such as the São Paulo subway, where there is a higher probability of matching the phases of acceleration and braking with less nfluence in the service schedules. The optimization of the time diagram to enhance the recovery of the energy from braking the trains in urban subway system has been proposed by several studies. The main ones are

a) Nasri developed in 2010 an optimization method that based on a genetic algorithm determines the optimal values of the reservation time which maximizes the use of the regenerative braking [7];
b) In 2011 the Pena research group proposed a new time diagram to line 3 of the Madrid subway, solving a linear programming optimization problem. After a week applying the system, an average energy saving of 3% was obtained, although the authors state that this number can be 7% if operating restrictions were to be decreased [8];
c) In 2011 the study of Boizumeau, Leguay, and Navarro showed that in the subway system Rennes an annual savings of 12% was achieved by optimizing the time diagram [9];
d) Xin Yang proposed a model that considers both the energy savings and the quality of the service rendered [10].

To obtain better energy savings rates by optimizing the time diagram it is necessary an implementation in real time of a control system to determine the best train driving strategies.

A real time control system should automatically recalculate the schedule in case of unforeseen events, such as delays and minor incidents.

The ACTREM algorithm coordinates the movement of the trains increasing the overlapping time intervals of acceleration and braking of trains, increasing the use of energy from the braking of trains. The algorithm to increase the overlap of the braking and acceleration times will change the time diagram, changing downtime at the station.

III. Math Modeling of the Traffic Control Optimization

In the mathematical development of the ACTREM control algorithm, the concepts of linear programming were used due to the problem with the synchronization of the train acceleration and braking cycles involving limitations or restrictions of resources.

According to Goldbarg and Luna the formalization and mathematical modeling of linear programming problems can be expressed by the set of equations 1, 2 and 3. [11]

Minimum
$$Z = c_1.x_1 + c_2.x_2 + \cdots + c_n.x_n \qquad (1)$$

Subject to
$$\left.\begin{aligned} a_{11}.x_1 + a_{12}.x_2 + \cdots + a_{1n}.x_n\{\leq,=,\geq\}b_1 \\ a_{21}.x_1 + a_{22}.x_2 + \cdots + a_{2n}.x_n\{\leq,=,\geq\}b_2 \\ a_{m1}.x_1 + a_{m2}.x_2 + \cdots + a_{mn}.x_n\{\leq,=,\geq\}b_m \end{aligned}\right\} \qquad (2)$$

$$x_{1,}\, x_2, \ldots, x_n \geq 0 \qquad (3)$$

Where $a_{ij}(i = 1, \ldots, m; j = 1, \ldots, n)$ are the technical or technological coefficients $b_1, b_2, \ldots, b_m$ are the independent terms, containing restrictions or second members $c_1, c_2, \ldots, c_n$, are the coefficients of the objective function, and $x_1, x_2, \ldots, x_n$ are the decision variables, either main or controllable.

Since equation 1 is the objective function, equation 2 is the restriction functions and equation 3 is the non negativity condition.

A. *Definition of the model parameters*

In order to define the model variables it is necessary to define the four train driving cycles that are the acceleration cycle, constant speed cycle, inertial motion cycle and braking cycle as shown in Figure 1.

These times can be extrapolated to all line trains because the frequency of the train trips can be considered constant for the subway system trains with high passenger demand.

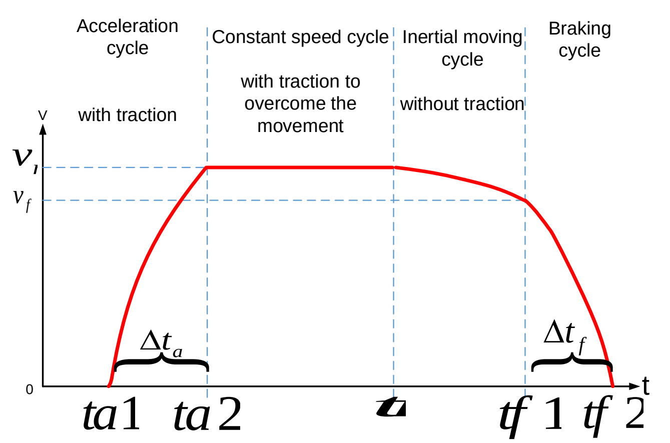

Fig. 1. Cycles of electric power traction.

Where ta1indicates the start of the acceleration cycle, ta2indicates the changing time from the acceleration cycle to the constant speed cycle t_i indicates the changing time from the constant speed cycle to the inertial cycle, tf1indicates de chanting time from the inertial cycle to the braking cycle, ta2

ISBN: 978-1-61804-321-4

indicates the end time of the braking cycle, v_c is the cruise speed, and v_f is the braking speed.

The parameters for the development of the mathematical model to optimize the time diagram used in this article are:

E – total number of stations;

NT – total number of trains;

Δtv_n – travel time period between stations n e n + 1;

Δt_a – the train acceleration time period;

Δt_f - the train braking time period;

ts_a –overlap time period in sector 1;

ts_f -overlap time period in sector 2;

In this article the decision variables defined for developing the model are:

h intervals between trains, known in railroad transportation companies as headway;

$ta1_{in}$ start time of the acceleration of train "I" starting from station "n";

$tf1_{in}$ start time of the braking of train "I" arriving at station "n";

tp_n time of stay required at station n.

The intermediate variables used in this article are:

a) $ta2_{in}$ acceleration end time of train "i" after the departure from station "n", which is defined as $ta2_{in} = ta_{1in} + \Delta t_a$;
b) $tf2_{in}$ braking end time of train "i" before arriving at station "n", which is defined as $tf1_{in} = tf1_{in} - \Delta t_f$;

In this article, all parameters and variables are considered integers to meet the engineering requirements and simplify the programming process.

B. *Assumptions adopted for developing the model*

According to the operating characteristics of the São Paulo subway system, the assumptions adopted in the preparation of the model are:

a) Only a small part of the braking power regeneration is used by the auxiliary services on board of the train, most of the energy is sent to the energy distribution circuit;
b) All trains share a common time diagram, lagging by the interval between trains;
c) The train stopping time on the platform is determined for each station;
d) The travelling time between stations will be considered constant, which means that the time diagram is cyclic.
e) The recovery of energy generated by the train braking can return to the DC distribution line and be immediately ready to the other train in the acceleration cycle. If the braking energy cannot be used, the exceeding energy will be dissipated through resistances.
f) Losses of electric power transmission are not considered due to short distance for the transmission of the power between two successive trains.
g) The train is powered only from the rectifier substations adjacent its position;
h) The region between two rectifier substations in this article is defined as an electrical zone;
i) The power from the braking energy of a train can be absorbed by trains, which belong to the same power zone. For example, in Figure 2, the power generated by the regenerative braking of train j can be used to the acceleration of train i, and the power generated by the regenerative braking of train j + 1 can be used to the acceleration of train i - 1. Arrows indicate the direction of the current.

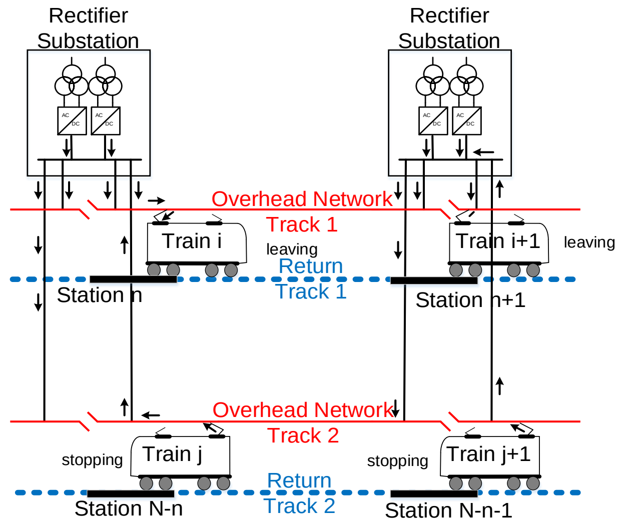

Fig. 2. Electric power distribution zone to subway systems

j) All trains are moving in the same direction and share the same time diagram, which means that the interval between trains and the travel time in each section is the same for all trains, except for the stay time at the station that can be differentiated.
k) In all sections between two stations, the acceleration and braking times of the trains are known parameters, which are used by ACTREM control algorithm to increase the energy efficiency of the subway system based on the current time diagram.

C. *Description of the train traffic*

Due to the operating characteristics of the subway systems, the trains depart from the first station and move along the subway track up to terminal station N. Then, they move back to the first station. This process is shown in Figure 3.

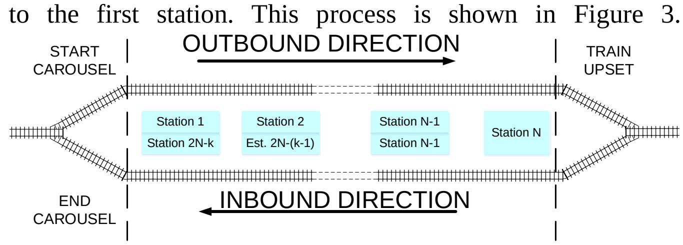

Fig. 3. Nomenclature of stations

In this article, it was adopted that the movement of the trains is similar to the movement of a carousel. Thus, it was agreed that the stations:

a) in the outbound direction as $n = \{1, 2, 3, \ldots, N - 1, N\}$;
b) in the inbound direction as $n = \{N, N - 1, \ldots, 2N - (k - 1), 2N - k\}$;

Where $k = \{1, 2, \ldots, 2N - 1\}$ is a growing indication of the stop for boarding of users on the subway line under study. In

ISBN: 978-1-61804-321-4

practice, for $1 \le k \le 2NE$, stop station k and stop station 2N - k are the same subway station at a physical location.

In this research it was adopted $kt = \{1, 2, \ldots, NT\}$ as a growing prefix of the trains, in order to prepare the formulation of the mathematical model the set of prefixes of the trains was divided in two, i.e., outbound as i and inbound as j: Thus it was agreed that the trains:

a) in the outbound direction as $i = \{1, 2, 3, \ldots, I - 1, I\}$ where i is the prefix f the last outbound train;
b) in the inbound direction as $j = \{ I + 1, \ldots, kt - 1, NT\}$;

To prepare the ACTREM train traffic control algorithm, two conditions were set:

a) Condition 1: Train arriving at station "n" and a train leaving station "n";
b) Condition 2: Train arriving at station "n" and a train leaving station "n+1";

Figure 4 illustrates the movement of arrival and departure of trains to condition 1, where in track 1, train i, in the outbound direction, departs from stop station k and train i+1 arrives at stop station n + 1. In track 1, train j, in the inbound direction, arrives at stop station $2N - k$and train j-1 departs to stop station $2N - (k + 1)$.

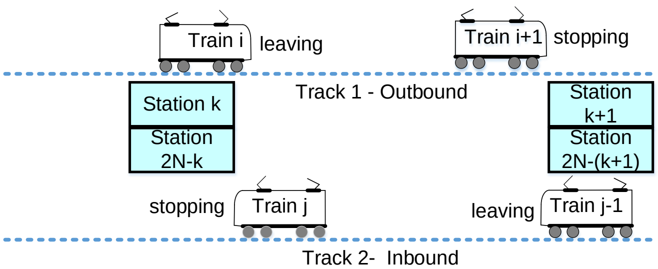

Fig. 4. Moving of the arrival and departure of trains to condition 1.

Note that the k and $2N - k$stations are the same subway station with relation to the physical location, this rule also applies to stations k+1 and $2N - (k + 1)$, which means that train i can absorb the generated energy from the regenerative braking of train j and that train i+1 can absorb the energy enerated from the regenerative braking of train j-1.

Figure 5 illustrates the movement of arrival and departure of trains to condition 2, where in track 1 train i is leaving stop station k, and in track 2, train j is stopping at stop station $2N - (k + 1)$. This means that the recovery of energy generated from train j can be absorbed by train i.

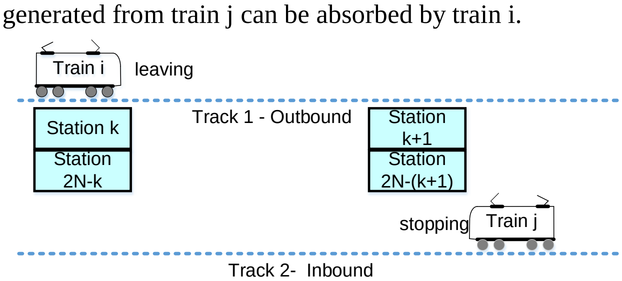

Fig. 5. Movement of the arrival and departure of trains to condition 2.

In a subway system with a high user demand as the one of São Paulo, it is impossible to coordinate all acceleration and braking interval times for all trains at all stations individually. The goal of the algorithm developed in this article is to improve the synchronization of acceleration and braking at the same electric section so that the use of the energy recovery is improved.

D. Description of the objective function

The purpose of the model developed in this research is to maximize the total time of coincidence between the acceleration and braking cycles of trains that are within the area of operation of the rectifier substation. For simplification purpose, this thesis adopted $a = \{\Delta ta_{in}, 1 \le i \le I, 1 \le n \le N\}, f = \{\Delta tf_{in}, 1 \le i \le I, 1 \le n \le N - 1\}$ and the coincidence of time as$\Delta ts(a, f) = \sum \Delta ta \cap \Delta tf$. Figure 6 illustrates the overlapping time of the acceleration and braking cycles.

To simplify, in this research it is defined $tp = \{tp_n , n = 1, 2, \ldots, 2NE - 2\}$ and $tv = \{tv_n,\ n = 1, 2, \ldots, 2NE - 2\}$. In this research it is adopted that the first train should stop at station 1 at the initial time t = 0.

For the outbound direction when $1 \le i \le NT$ and $1 \le n \le NE - 1$, the start time $ta1_{in}$ indicates that train i departs to station n is given by equation 4.

$$ta1_{in}(i, n) = (i - 1).h + \sum_{k=1}^{NE} tp_n + \sum_{k=1}^{NE-1} tv_n \qquad (4)$$

In the inbound direction, when train i arrives at station N, an extra time is required for changing of direction, called transposition time. Therefore, for $N \le n \le 2NE - 2$ and $N \le n \le 2NE - 2$, the start time $ta1_{in}$, determined by equation 5, indicates that train i departs to station NE-1.

$$ta1_{in}(i, n) = (i - 1).h + \sum_{k=NE}^{2NE} tp_n + \sum_{k=NE}^{2NE-1} tv_n + t_t \qquad (5)$$

Then, for $1 \le n \le 2N$-1:

a) the time for changing the acceleration cycle to the Constant speed cycle is defined by $ta2_{in}(i, n) = ta_{in}(i, n) + \Delta ta$;
b) the time for changing the inertial cycle to the braking cycle is defined by $tf1_{in}(i, n) = ta2_{in}(i, n) + \Delta tv$;
c) the arrival time at station n+1 is defined by $tf2_{in}(i, n) = tf1_{in}(i, n) + \Delta tf$.

This article stipulated that the set of the acceleration cycle time $ta = \{ta \in \Delta ta_{in} \mid 1 \le i \le NT \text{ e } 1 \le n \le NE\}$, the set of the braking cycle times $tf = \{tf \in \Delta tf_{in} \mid 1 \le i \le NT \text{ e } 1 \le n \le NE - 1\}$, and the time of coincidence of cycles should be $\Delta ts(ta, tf) = \sum \Delta ta \cap \Delta tf$

For each 1 <i <NT-1 and 1 <n <n-1, there are two conditions for maximizing the overlap time $\Delta ts(ta, tf, i, n)$:

a) Condition 1: Train arriving at station "n" and a train leaving station "n". The overlap time is the difference between the end of the braking cycle of train j minus the beginning of acceleration of train i, defined by $\Delta ts_n(ta, tf, i, n)$;
b) Condition 2: Train arriving at station "n" and a train departing from station "n+1". The overlap is the difference between the end of the acceleration of train j

ISBN: 978-1-61804-321-4

minus the beginning of the braking cycle of train i, defined by $\Delta ts_{(n+1)}\,(ta, tf, i, n)$.;

Figure 6 illustrates the overlap time of the acceleration and braking cycles.

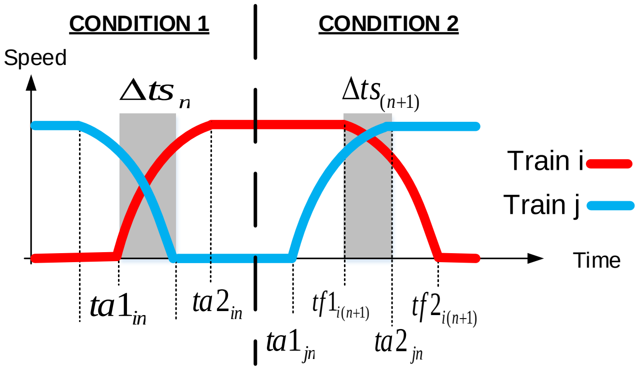

Fig. 6. Overlap of the acceleration and braking cycles

For the overlap time Δts_n in condition C1 to be the maximum, the difference should be minimum between:

a) the initial time of the acceleration and braking cycles expressed by the time interval $\Delta ts1_n$ expressed as: $\Delta ts1_n = ta1_{in} - tf1_{jn}$, se $tf1_{jn} \leq ta1_{in} \leq tf2_{jn}$

b) the initial time of the acceleration and braking cycles expressed by the time interval $\Delta ts2_n$ expressed as: $\Delta ts2_n = ta2_{in} - tf2_{jn}$, se $ta1_{in} \leq tf2_{jn} \leq ta2_{in}$

In the C1 condition there is no overlap of the acceleration and braking cycle when. $ta2_{in} < tf1_{jn}$ and $tf2_{jn} < ta1_{in}$.

For the overlap time $\Delta ts_{(n+1)}$ in condition C2 to be the maximum, the difference should be minimum between:

a) the initial time of the acceleration and braking cycles expressed by the time interval $\Delta ts1_{(n+1)}$ expressed as: $\Delta ts1_{(n+1)} = tf1_{i(n+1)} - ta1_{jn}$, se $ta1_{jn} \leq tf1_{i(n+1)} \leq ta2_{jn}$

b) The initial time of the acceleration and braking cycles expressed by the time interval $\Delta ts2_{(n+1)}$ expressed as: $\Delta ts2_{(n+1)} = tf2_{i(n+1)} - ta2_{jn}$, se $tf1_{i(n+1)} \leq ta2_{jn} \leq tf2_{i(n+1)}$

In condition, C1 there is no overlap of the acceleration and braking cycle when. $ta2_{jn} < tf1_{i(n+1)}$ and $ta2_{jn} < tf1_{i(n+1)}$.

The total time of the overlap of all trains in all stations is expressed by equation 6, considering $\Delta ta \cong . \Delta tf$.

$$\Delta ts = \mathrm{NT}.\Delta tf.k - \sum_{i=1}^{NT-1}\sum_{n=1}^{NE-1} \Delta ts1_n + \Delta ts2_n + \Delta ts1_{(n+1)} + \Delta ts2_{(n+1)} \quad (6)$$

D. *Objective function restrictions*

For a cyclic time diagram, the time interval between trains indicates the train density in service is defined by the total travel time and the number of trains, the restriction capacity imposed by the signaling system and the passenger flow. This requires that the headway time should meet the restrictions set out in equations 7, 8 and 9.

$$\mathrm{h}_{\min} \leq \mathrm{h} \leq \mathrm{h}_{\max} \quad (7)$$

For subway trains it is necessary to save a downtime at the station for passengers entering and leaving the train; thus, the waiting time window is required at each station. For every $1 \leq n \leq 2N\text{-}2$, we have the following restrictions:

$$tp_{min} \leq tp_n \leq tp_{max} \quad (8)$$

According to the operating demand, each train must satisfy the total travel time restriction

$$\Delta tcv_{min} \leq t_t + \sum_{n=1}^{2NE-2} (tp_n + tv_n) \leq \Delta tcv_{max} \quad (9)$$

E. Objective function of the traffic control.

For each $1 \leq \mathrm{i} \leq \mathrm{NT}$, $1 \leq \mathrm{n} \leq 2\mathrm{NE}-2$ and $\mathrm{ta1_{in}} \leq \mathrm{t} \leq \mathrm{tf1_{in}}$ the electric power needed for moving train i is defined by equation 10, where η_{ec} is the motor yield.

$$\mathrm{ec(t)} = \mathrm{m}.\frac{\left(\mathrm{v_{in}}^2(\mathrm{t}+1) - \mathrm{v_{in}}^2(\mathrm{t})\right)}{2.\eta_{ec}} \quad (10)$$

Where for each $\mathrm{tf1_{in}} \leq \mathrm{t} \leq \mathrm{tf2_{in}}$ the recovery of power generated from train i , and defined by equation 11, where $.\eta_{eg}$ is the engine yield when operating as a generator.

$$\mathrm{eg(t)} = \mathrm{m}.\frac{\left(\mathrm{v_{in}}^2(\mathrm{t}+1) - \mathrm{v_{in}}^2(\mathrm{t})\right)}{2}.\eta_{eg} \quad (10)$$

According to the analysis of the coordination process, for train i to complete the full course of the movement of station 1 up to station 2N - 1, the total energy consumed by the system is determined by equation 12.

$$\mathrm{E} = \sum_{\mathrm{k}=1}^{2\mathrm{NE}-1}\sum_{\mathrm{i}=1}^{\mathrm{NT}} \mathrm{e_c(t)} - \mathrm{e_g(t)} \quad (12)$$

The formalization and mathematical modeling of the train traffic control for the optimization of energy consumption can be expressed by the set of equations.

$$\begin{cases} \text{Minimum} & \mathrm{E} = \sum_{\mathrm{k}=1}^{2\mathrm{NE}-1}\sum_{\mathrm{i}=1}^{\mathrm{NT}} \mathrm{e_c(t)} - \mathrm{e_g(t)} \\ \text{subject to} & \\ & \mathrm{h} = \left(\sum_{\mathrm{k}=1}^{2\mathrm{NE}-2} (\mathrm{tp_n} + \mathrm{tv_n}) + \mathrm{t_t}\right) \Big/ \mathrm{NT} \\ & \mathrm{h_{min}} \leq \mathrm{h} \leq \mathrm{h_{max}} \\ & \mathrm{tp_{min}} \leq \mathrm{tp_n} \leq \mathrm{tp_{max}} \\ & \mathrm{tv_{min}} \leq \mathrm{t_t} + \sum_{\mathrm{k}=1}^{2\mathrm{NE}-2} (\mathrm{tp_n} + \mathrm{tv_n}) \leq \mathrm{tv_{max}} \end{cases} \quad (13)$$

IV. CONTROL ALGORITHM DEVELOPMENT - ACTREM

During the development of the Traction Control Algorithm for Subway Power Generation - ACTREM to improve the energy efficiency of the traction systems, it was decided to use the concepts of genetic algorithms, due to their characteristic of combining targeted and random search procedures in order to get the optimum point of a particular function, even when this has nonlinear characteristics, multiple peaks and discontinuities. [12]

ISBN: 978-1-61804-321-4

Genetic algorithms are iterative algorithms, where each iteration the population is modified by using the best features of the previous generation elements, and subjecting them to the three basic types of operators to produce better results.

To achieve these objectives, initially, the initial population is generated, i.e., an initial set of strings called in AG by chromosomes, which is generated randomly. Then, the populations evolve in generations, basically through three operators [13]:

a) Selection;
b) Crossover;
c) Mutation.

The three operators are the basic flowchart of a genetic algorithm that is shown in Figure 7.

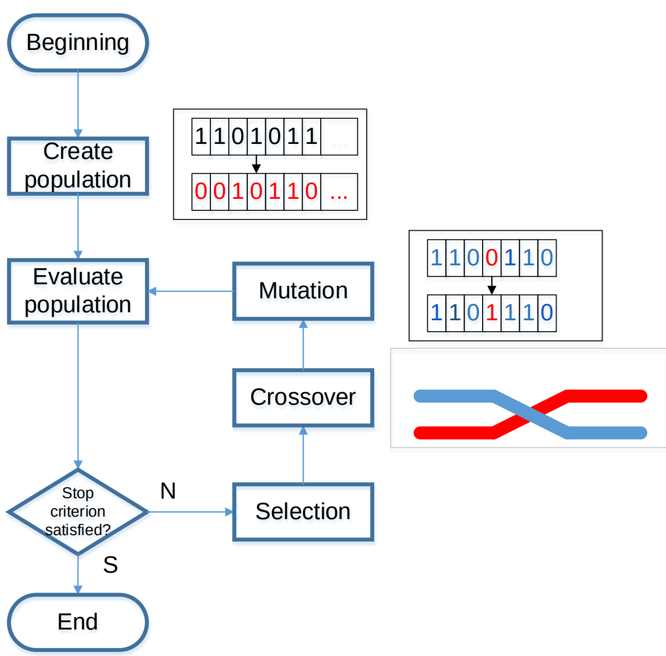

Fig. 7. Basic flowchart of a genetic algorithm

Table 1 contains the definition of the AG terms adopted for the control algorithm development ACTREM.

Table 1: AG Nomenclature

AG Terminology	Model
Gene	Stopping time at the station
Chromosome	Set of all downtime at stations of the line under study
Individual	A complete solution, downtime, result of the evaluation function and the genetic operator to apply.
Generation	A set of all currently active individuals

Source adopted: [14]

The development of the Traction Control Algorithm for Subway Power Regeneration - ACTREM was divided into four macro steps:

a) Macro step - data input;
b) Macro step - generation of the first population;
c) Macro step - assessment of the population;
d) Macro step - genetic operators.

A. Structure of the chromosome of the control algorithm ACTREM

The chromosome is formed by a set of genes and each gene represents a variable of the function that will be optimized.

In case of optimizing the control of the train traffic of line 4 Yellow the chromosome consists of 22 genes representing the downtime at the stations. $tp = (tp_1, tp_2, tp_3, tp_4, tp_5, tp_6, tp_7, tp_8, \ldots, tp_{21}, tp_{22})$.

Therefore, gene tp_k must have at least m_i bits according to equation 14.

$$m_i > \frac{\log(tp_{max} - tp_{min}).10^p}{\log 2} \qquad (14)$$

Therefore, gene tp_k must have at least m_i bits.

$$m_i > \frac{\log(28s - 18s).10^0}{\log 2} \qquad (15)$$

$$m_i > 3{,}32\ bit's$$

According to equation 15 the size of the gene adopted in this study is 4 bits for each tp_k as shown in Figure 8.

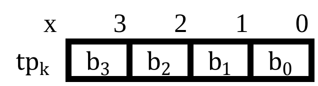

Fig. 8. Representation of the gene

Figure 9 illustrates the generation of a chromosome, where C is the chromosome and C_N the gene. The tp is the set of train stoppage times at the station where tp_{2NE} is the decoding of the tp_{2NE} genes of chromosome C.

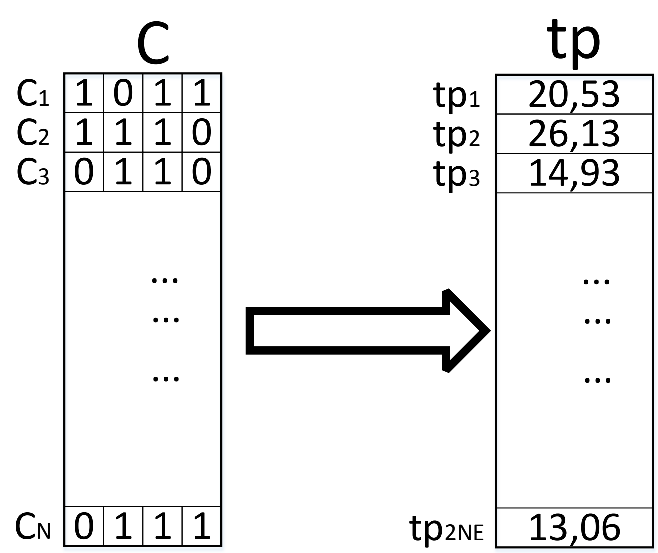

Fig. 9 Generation of the chromosome

B. Macro step - evaluation of the population of the control algorithm ACTREM

For each station, the representation of an element chosen randomly. Then you need to determine whether the chosen stop time at the station meets the operational constraints.

A generation consists of a number of individuals, formed randomly. In this study, the chromosomes are composed of a sequence of characters k, where k is equal to twice the number of stations of the line in study. Each position is a representation of a down time in the station.

In order to achieve these goals initially it is necessary to generate the starting population established randomly. Then the populations evolve into generations, basically through four operators [13]:

a) Copy;
b) Crossover;
c) Mutation;
d) Give out.

The genetic operators found are shown in Table 2. In this table, the column indicates the percentage of each operation (Generation %) based on Hetem [15], Flake [16], Goldberg [12] and Rojas [17].

Table 2: Description of the genetic operators used

Operator	Symbol (S)	% in the ACTREM
Copy	e	10
Crossover	c	80
Mutation	x	2
Give out	k	18

V. ANALYSIS OF CONTROL ALGORITHM – ACTREM RESULTS

After a large number of simulations, it is observed that the results of downtime converge at the station. It is also noticeable that the optimized solution shows a small increase in the transport capacity of system users.

It is possible to ascertain that the optimized solution is reached around the 22nd generation; in some cases, the convergence occurs from the 12th generation; in others around the 42nd. However, the final solution always results in the optimized solution, confirming the convergent feature of the AG. The final result is shown in Figure 10.

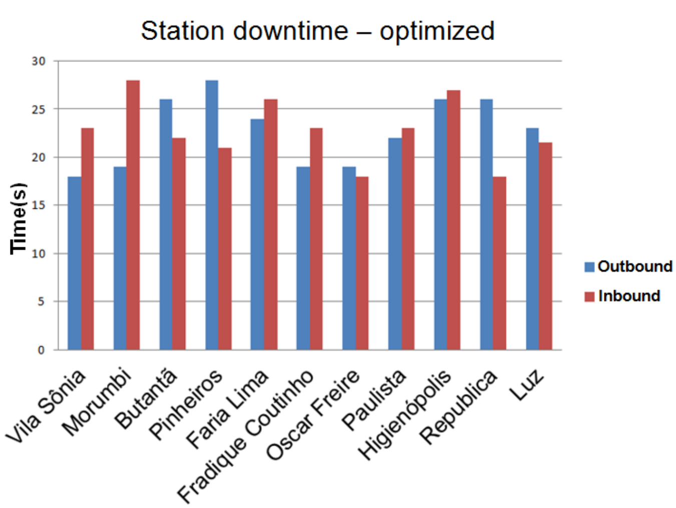

Figure 10. Station downtime - Optimized

From the optimized solution, it was obtained the table 3, which shows the result of using the ACTREM control algorithm, the outcome results were compared with the data obtained by the traction simulation.

Table 3: Energy generated and consumed on line 4 - yellow

Rectifier Substation	Power consumed	Braking Power available		Braking power reused – without algorithm		Braking power reused – without algorithm	
	[kWh]	[kWh]	[%]	[kWh]	[%]	[kWh]	[%]
Pátio Vila Sônia	5526.31	2616	100	922	35.28	1498	57.29
Caxingui	5967.14	2824	100	996	35.29	1329	47.07
Pinheiros	6643.73	3145	100	1080	34.34	1828	58.14
Fradique Coutinho	6897.05	3265	100	1121	34.34	1479	45.31
Paulista	7089.85	3356	100	1120	33.37	2249	67.02
República	5611.09	2656	100	886	33.36	1493	56.24
Luz	4746.74	2247	100	751	33.46	998	44.45

Source: (Author)

By using the ACTREM control algorithm it was possible to obtain 9.5% power reduction, without the algorithm 16,16% of the energy consumed came from the braking energy, by using the control algorithm this value increases to 25.6 %, as shown in Figure 11.

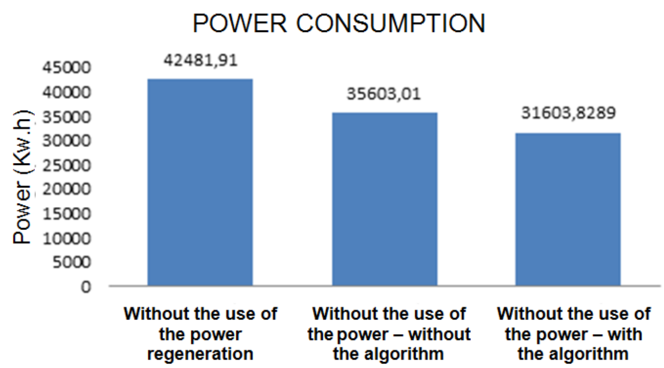

Fig. 11. Comparison of energy consumption.

IV. VI. CONCLUSIONS

This article presents a proposal and the development of a Traction Control Algorithm for Subway Power Regeneration - ACTREM to allow the use of train regenerative braking power to improve the energy efficiency of subway traction systems.

To develop the Traction Control Algorithm for Subway Energy Regeneration - ACTREM the research included four steps:

a) In the first step, the field measurements were carried out to obtain values of voltage, current and energy consumed in the substations and trains of Line 4 - Yellow of São Paulo METRÔ.

b) In the second step, the traction system simulator was developed for the purpose of analyzing the performance of the control algorithm ACTREM.
c) In the third step the control algorithm ACTREM was developed to increase the energy efficiency by applying the theories of genetic algorithms.
d) In the fourth step, the contribution of the ACTREM control algorithm was analyzed as to the increase of energy efficiency in comparison with the actual values of line 4 - Yellow.

For the development of the ACTREM control algorithm the programming language C++ was chosen, which proved to be efficient due to an information processing time shorter than 2 seconds:

The choice to implement the ACTREM control algorithm using the concepts of genetic algorithms is justified by its characteristics:

a) Be a robust algorithm for the treatment of data and specific information related to the problem;
b) It is an interactive method and has some intelligence in the search process to get solutions that would not stop at the first great spot found.

To determine the efficiency of the proposed algorithm based on the data from the São Paulo Subway Line 4 – Yellow 15 simulations were performed. The results show that the proposed algorithm can save 9.5% of energy, and without relevant impacts in the transportation of passengers of the system.

The simulations for the application of the ACTREM control algorithm demonstrated the efficiency to automatically generate time diagrams optimized for energy savings in subway systems, taking into account the system's operational constraints such as maximum capacity of each train, total wait time, total travel time, and interval between trains.

The main contribution of this paper was to propose a new control algorithm called ACTREM that optimizes the use of energy produced by the application of train brakes without causing significant impacts in the transportation of passengers of the system.

The results suggest the continuity of the research and the expansion of its functionality. As a suggestion for the continuity of this research and the improvement of the algorithm, the following may apply:

a) study the use of a control algorithm for energy recovery that also controls the travel time between stations;
b) consider the energy savings throughout the energy supply system, including transmission losses and the efficiency of the rectifier substations.
c) improvement in the development of the simulator for reducing the calculation errors.
d) study of the processing requirements for the application of the ACTREM to a subway line in Brazil.
e) development of a graphical interface for the ACTREM control algorithm

.

References

[1] EPE, "Resenha mensal do mercado de energia elétrica,," 2013.

[2] APTA, "Public Transportation Saves Energy and Helps Our Environment," 2009.

[3] R. A. H. d. Oliveira, L. S. Mattos, A. C. Ferreira and R. M. Stephan, "Regenerative braking of a linear induction motor used for the traction of a maglev vehicle," *Eletrônica de Potencia,* pp. 241-251, jun./ago. 2014.

[4] C. L. Pires, S. I. Nabeta and Cardoso, "Simulação de composição ferroviária acionada por motores de indução e inversores de tensão," *Revista Controle & Automação,* vol. 16, Jan.,Fev. e Março 2005.

[5] X. Li, T. Tang and Z. Gao, "A Subway Train Timetable Optimization Approach Based on Energy-Efficient Operation Strategy," *IEEE TRANSACTIONS ON INTELLIGENT TRANSPORTATION SYSTEMS,* vol. 14, pp. 833-893, JUNE 2003.

[6] K. Ghoseiri, F. Szidarovszky and M. J. Asgharpour, "A multi-objective train scheduling model and solution," *Transp. Res. B, Methodol,* vol. 38, p. 927–952, DEC 2004.

[7] A. Nasri, M. Fekri Moghadam and H. Mokhtari, "Timetable optimization for maximum usage of regenerative energy of braking in electrical railway systems," *International Symposium on Power Electronics, Electrical Drives, Automation and Motion – SPEEDAM 2010, Pisa, Italy,* 2010.

[8] M. Peña-Alcaraz, A. Fernandez, A. P. Cucala and Ramos, "Optimal underground timetable design based on power flow for maximizing the use of regenerative-braking energy," *Proceedings of the Institution of Mechanical Engineers, Part F: Journal of Rail and Rapid Transit,* pp. 397-408, 2011.

[9] J. R. Boizumeau, P. Leguay and E. Navarro, "Braking energy recovery at the Rennes metro," *Workshop on Braking Energy Recovery Systems – Ticket to Kyoto Project, Bielefeld, Germany,* 2011.

[10] X. Yang, B. Ning, X. Li and T. Tang, "A two-objective timetlable Otimization Model in Subway Sustem," *IEEE Transactions on intelligente transportation systems,* vol. 15, 5 October 2014.

[11] M. C. Goldbarg and H. P. L. Luna, Otimização combinatória e programação linear modelos e algoritmos, 2º ed., Rio de Janeiro: Editora Campus, 2005.

[12] D. E. GOLDBERG, Genetic Algorithms in Search, Optimization, and Machine Learning, New York: ADDISON-WESLEY PUBLISHING COMPANY, INC., 1989.

[13] N. KAGAN, H. P. SCHMIDT, C. C. BARIONI and H. KAGAN, Métodos de Otimização Aplicados a Sistemas Elétricos de Potência, 1º ed., São Paulo: Blucher, 2009.

[14] R. Burian, Algoritmos genéticos na alocação de dispositivos de proteção de distribuição de energia elétrica, São Paulo: Universidade de São Paulo, 2009, p. 190.

[15] A. Hetem Jr. and J. G. Hetem, "The use of genetic algorithm to model protoplanetary discs," *Fundação*

Santo André- FAFILe Universidade de São Paulo, IAG-USP, Dezembro 2007.

[16] G. W. Flake, The computational beauty of nature: computer explorations of fractals, chaos, complex systems, and adaptation, Bradford Book, 1998.

[17] G. Rojas, J. Gregorio-Hetem and A. Hetem Jr., "Towards the main sequence: detailed analysis of weak line and post-T Tauri stars.," *Monthly Notices of the Royal Astronomical Society*, pp. 1335-1343, 2008.

[18] S. LU, "Optimising Power Management Strategies for Railway Traction Systems," Birmingham, 2011.

ISBN: 978-1-61804-321-4

The experience of discrete event simulation robotic technology of mining

Vasily V. Sinoviev, Victor V. Okolnishnikov, Alexy N. Starodubov, Mihail U. Dorofeev

Abstract— A number of models of various robotic technologies of coal mining were developed. The models were developed using GPSS World. These models were used for comparing various robotic technologies on the selected criteria and justification their effective structure and parameters through the computer experiments.

Keywords— discrete event simulation, queuing system, robotic mining technology.

Mining is carried out by drilling and blasting or by a combine. The main works are carried out in the mine when blasting and drilling are charging, rock mass loading and support fixing.

The drill rig 1 first enters the heading face (Fig. 1) and bores a specified number of holes. After charging of holes and blasting cargo transport vehicle 2 exports mountain range to the distance depending on the distance of the face. Then anchors installer 3 enters the face and fixes support by anchors. Simultaneously ancillary works are performed

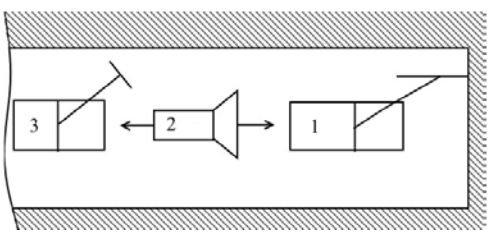

Fig. 1 mapping schemes of gallery driving by drilling and blasting

(installation of drainage, building ventilation pipes and others).

The combine, simultaneously, (Fig. 2) drives in gallery executing unit 1 for a given program, and loads the rock mass when unit 2 is loaded with its transportation conveyer bridge 3 to haulage unit 4. After gallery driving to a predetermined depth the combine is off and the support is installed by robotic anchors installer 5, located on the frame of the combine. Then gallery-driving cycle repeats.

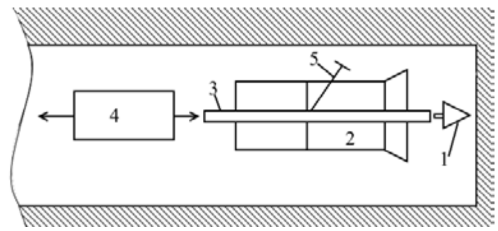

Fig. 2 mapping schemes of gallery driving by combine

A variety of proposals for robotics technology of mining and its high cost, the difference between the conditions at coalfield and mining, multivariate methods of work organization are available at the design stage while comparing the options of mining on computer models [1].

Most of the operations during mining are discrete with a finite number of variables. Such operations include the beginning and ending of drilling, loading and unloading of coal, the beginning and the end of a combine cycle.

It is exigent to use the mathematical apparatus of queuing systems (QS) for the simulation of such works [2].

The models of robotic technology of mining in the form of multi-channel multi-phase closed QS, where requests were the moments the equipment was ready for the next cycle, were developed.

Requests service implies their delay for the time of duration of processes of the gallery driving execution in devices that simulate the appropriate equipment. The duration of the process of technological cycle is displayed by entering random time delays in the devices QS. The length of the ongoing gallery driving is specified in the QS by the amount of the requests at the input of system (1)

$$m = L/l \tag{1}$$

where L - length of tunnel; l - face advance per cycle.

In actual practice equipment may start execution of the next gallery driving after the previous cycle, the time interval between the beginning and the end of the gallery driving depends on the random cycle time process operations. This feature is displayed in the model by the feedback input through another request, which is input after the QS application has

This work was supported in part by the Russian Foundation for Fundamental Research, project number 13-07-98023 "Design and simulation of unmanned technologies for underground mining of solid minerals"

V.V. Sinoviev, Institute of coal of Siberian branch of the Russian academy of Sciences, Kuzbass State Technical University, Kemerovo, Russia (zinovyev@kemsc.sbras.ru).

V.V. Okolnishnikov, Design Technological Institute of Digital Techniques of Siberian Branch of the Russian Academy of Sciences, Novosibirsk, Russia, (okoln@mail,ru).

A.N. Starodubov, Institute of coal of Siberian branch of the Russian academy of Sciences, Kemerovo, Russia (stan@kemsc.sbras.ru).

M.U. Dorofeev, Institute of coal of Siberian branch of the Russian academy of Sciences, Kemerovo, Russia (dorofeev@kemsc.sbras.ru).

ISBN: 978-1-61804-321-4

been handled at the system output. Thus, feedback forms the input stream requests. Speed of the applications receipt is the speed of their services, therefore the queue on the entrance is not formed and the objectives of the study are to assess the overall service time of the application and utilization of the equipment.

The average duration of the gallery driving is defined in the model as the sum of random variables (2)

$$t_{\mu} = \left(\sum_{i=1}^{m} t_{di} + \sum_{i=1}^{m} t_{li} + \sum_{i=1}^{m} t_{si}\right)/m \quad (2)$$

where t_{di}, t_{li}, t_{si} - random values of the simulating equipment service time for a request, where the equipment simulates the devices for the destruction of the rock mass, rock mass load and support at the *i*-th cycle.

For example, the robotic technology of gallery driving by drilling and blasting method is presented in the form of a two-channel polyphase closed queuing system (Fig. 3).

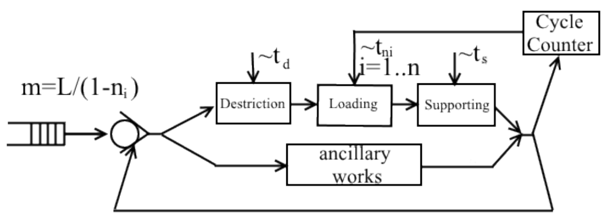

Fig. 3 mapping model of the robotic technology of production drilling and blasting as QS

Request is the time when the equipment is ready for the next driving cycle, and devices are tunnelling machines, execution of requests for a random time; the rate of receipt of requests in the system is determined by the speed of their service. The request is served by robotic drilling rigs, loaders and support installer using one channel. Another channel is to perform ancillary works. At the end of the gallery driving the serviced request changes the value in cycle counter and allows unserved request to enter the system as an input. Service time requests devices are presented as functional dependencies (3)

$$\begin{aligned} t_d &= f(n_h, l_h, P^d, f_s, S, n^d) \\ t_l &= f(S, f_s, l_h, \eta, P^l, n^l, k_l, V) \\ t_s &= f(S, l_s, n_m) \end{aligned} \quad (3)$$

where t_d, t_l, t_s - random variables of the time of destruction of the rock mass, rock mass loading and supporting; S - cross-section of heading; f_s- coefficient of hardness of rocks; n_h- number of holes per cycle; l_h - the length of the drill hole; η - utilization of holes; k_l - coefficient of loosening rocks; P^d, P^l - performance drilling and loading machines; n^d, n^l - number of drilling and loading machines; V - volume haulage unit; l_s - the length of the supported gallery driving during one cycle; n_m - number of miners busy in supporting.

To account for changes in trip times of haulage unit cycle counter that increases the delivery time, depending on the number of driving cycle is mounted (4)

$$t_{li} = f(l_d), i = (1, m) \quad (4)$$

where l_d - the length of the path for delivery of the rock mass; *m* - the number of cycles required for gallery driving.

The current version of the simulation language GPSS - GPSS World best fits as the means of software implementation models of mining technology. GPSS language is one of the most effective and common software tools for modeling complex discrete systems on the computer and is successfully used for the simulation of various branches of industry [3, 4], including mining operations [5], formalized as queuing systems.

There are two basic types of objects: transacts and blocks, - in GPSS World. Blocks define the operation logic of the model and determine the path of transacts on it. Blocks analogous are QS devices showing the combine, drilling machines, loaders, and support installer. Transacts, moving from block to block, simulate mining works: snapping-distilled drilling rigs, load haulage unit, support etc. Transacts are analogous of QS requests to perform operations of the gallery-driving cycle. The modeling system transacts interact with blocks, resulting in a change of their attributes, as well as converted arithmetic or logical values. Such transformations are called events.

Using GPSS World model, we have developed software modules in order to build models of the excavation technology, "cut with loading", "drilling", "charging", "loading", "supporting". Fig. 4 shows an example of the module "loading."

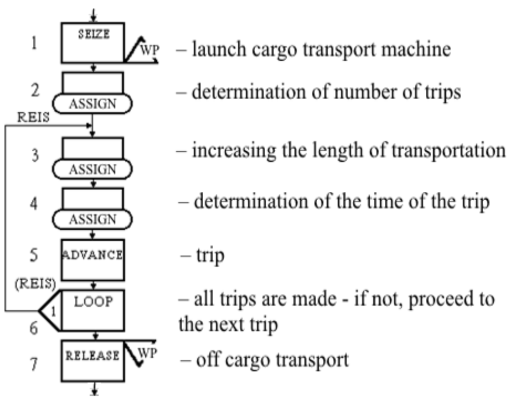

Fig. 4 mapping block diagram of module "Loading"

In block 2 (ASSIGN) is determined by the desired number of trips for removal of separated rock mass (5)

$$\begin{aligned} Q &= S l_h k_s \\ n &= Q / V k_f \end{aligned} \quad (5)$$

where Q - separate volume of the rock mass; S - cross-section of heading; l_h - the length of the drill hole; k_s - coefficient of softening; n - the number of required trips of haulage unit for removal of the separated rock mass; V – capacity of haulage unit; k_f - fill factor.

Duration of cargo transporting is modeled by delay in ADVANCE block (6)

$$t_{Li} = 2\left(\frac{l_i}{v}\right) + t_l + t_{un} \tag{6}$$

where t_{Li} – duration of the i-th cycle of loading; l_i – length of gallery driven at i-th cycle v – velocity of haulage unit; t_l - the time of filling; t_{un} - unloading time.

Increasing the distance of transportation of rock mass l_i is determined in block 4 (ASSIGN) the expression (7)

$$l_i = l_{i-1} + l \tag{7}$$

where l_i - length of gallery driven at i-th cycle; l - face advance per cycle.

Turning off the cargo transport vehicle by block RELEASE occurs when all the trips that are defined by a block LOOP, which reduces the required number of flights per unit and checks the condition n_i=0, are performed. If not, it repeats the cycle of loading.

The developed model can be used to select the optimal volume of the loading and transport vehicles buckets; the maximum length of the rock mass transportation when the performance of the gallery driving is limited; the desired volume of haulage vehicles; the effectiveness of robotic technology and others evaluations.

For example, operating time for cargo transport machine depends on the distance from the place of unloading to the face. During the development, this distance increases with each cycle the value of face advance. The problem arises of assessing the impact of transport on the length of the key indicators of the gallery driving.

In the mines several sizes of cargo transport vehicles with different volumes of the bucket (1 to 7.5 m^3) are used. To select a machine it is necessary to determine the dependence of the duration, the gallery driving on the capacity of cargo transport machine. Fig. 5 is a graph of the cycle time of the length of production for different bucket capacity of cargo transport machine obtained from the results of simulation experiments.

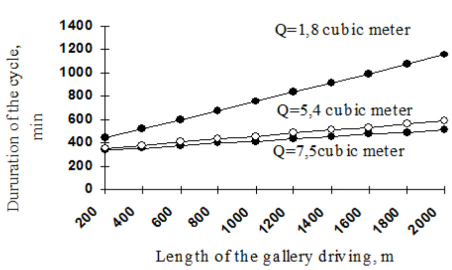

Fig. 5 mapping effect of the length of output per cycle at different bucket capacity of cargo transport machine

It was found during the development of robotic technology of individual machines that average cycle time increases linearly with the length of the production from 200 to 1800m. A reduction of capacity bucket loading and transport vehicles from 7.5 to 1,8m^3 increases the gallery driving to 24-56% depending on the length of the driven working.

Conclusion

Discrete event simulation displaying the mining technology as the QS, followed by software implementation on a specialized simulation language GPSS World allows comparing various robotic technologies and justifying their effective structure and parameters through the computer experiments. This opens up new choices of technological options and allows avoiding significant loss of investment during the design stage of the mine.

References

[1] V. Konyukh, "Simulation of mining in the future," in *Proc. of the IASTED International Conference on Automation, Control, and Information Technology - Control, Diagnostics, and Automation, ACIT-CDA*, Novosibirsk, Russia, 2010, pp. 1–6.

[2] Kleinrock L. *Queuing theory*, Moscow, Russia, Mashinostroenie, 1979 (in Russian).

[3] V.A. Poletayev, V.V. Sinoviev, A.N. Starodubov, I.V. Chicherin, *Design of the computer integrated production systems*, Moscow, Russia, Mechanical engineering, 2011 (in Russian).

[4] A.N. Starodubov, V.V. Sinoviev, and M.U. Dorofeev "Simulation of the technological complex for deep coal processing", *Ugol*, no. 2, pp. 8–12, 2010 (in Russian).

[5] V. V. Sinoviev, "Modeling multi face gallery tunneling using a simulation approach", *Mining Informational and Analytical Bulletin*, Moscow, Russia, vol. 6, pp. 138–144, 2013.

An Experimental Analysis of Vehicle Exhaust Noise Signals by Means of Order Tracking Approach

D. Siano [1] , M. A. Panza [2]

Abstract**—**Exhaust noise represents one of the major noise sources in vehicles powered by internal combustion engine, and consequently an important noise pollution contributor in urban environment. Experimental measurements of exhaust noise emissions is often necessary for implementing a subsequent refinement process aimed to reduce noise levels, as established by the new EU Regulations, and to improve perceived sound quality. This work presents the results of an experimental campaign carried out on a gasoline passenger car in order to measure exhaust noise levels and analyze frequency spectra. Specifically, experimental tests were conducted by using a microphone located at a proper distance from the exhaust termination. Acquiring exhaust noise signal in engine rapid run up condition, a depth order tracking analysis has been performed. Different stationary operating conditions have been investigated, too. Of course, all the acquired signals have been triggered with the tachometer signal containing the information about the engine rotational speed. The analysis of the exhaust noise frequency content reveals a predominant noise emission at low frequency range up to 250 Hz, and a particular behavior of the engine orders peak values at some of the investigated operating conditions.

Keywords**—**Exhaust Noise, Frequency Spectrum, Gasoline Car, Order Tracking, Tachometer Signal.

I. Introduction

Noise pollution represents one of the most important environmental issues, for the rapid increase of the number of vehicles which surely give a considerable noise contribution, especially in urban environment. Among all vehicle external noise sources, exhaust system is considered one of the major sound emitting source, and therefore an important research and development subject. Exhaust design process is a very complex task mainly driven by restrictive EU Regulations, which impose to increasingly attenuate noise levels through the employment of proper silencing elements, that in turn have not to negatively affect engine performances. At the same time, in addition to comply with environmental legislation requirements, cars manufacturers are interested in satisfying customer's expectations too, which could be even a loud and exciting note from the exhaust. Thus, exhaust refinement process does not merely involve noise attenuation, but increasingly involves sound quality engineering in molding the aural excitement of a new car.

Generally, broadband noise can be desirable or objectionable depending on the frequency content, amplitude and structure-borne versus airborne content [1]. Pure tones are almost always objectionable. Resonances, either structural or acoustical, also cause pure tones.

Of course, all these aspects have to be taken into account for undertaking a noise and vibration refinement process of a vehicle exhaust system. In this regard, experimental measurements play a key role in the identification of possible critical behaviors of the system.

This work explains results coming from an experimental campaign carried out on a gasoline car, in order to assess exhaust radiated noise and verify the presence of any unexpected noise to be eliminated. Firstly, an order tracking analysis has been performed on the exhaust noise signals acquired during a rapid engine run-up condition. For a better characterization of the noise frequency content, also exhaust signals referred to stationary operating conditions have been then analyzed in depth.

Hence in the paper, after the description of the experimental setup and a detailed overview about the main principles of order tracking method, experimental results in terms of frequency spectra and Overall Noise Level will be reported and discussed in depth.

II. Experimental setup

Experimental tests were carried out on a gasoline passenger car in order to carefully evaluate vehicle exhaust noise. In particular, data were acquired in free field conditions through the employment of a microphone positioned at a proper distance from the exhaust termination, according to the European Regulations adopted for measuring noise levels of stationary motor vehicles. EU Regulations specify that microphone should be located to the exhaust outlet at a distance of 0,5 m ± 0,01 m from the reference point of the exhaust pipe, at an angle of 45°(± 5°) to the exhaust

[1] D. Siano is with the National Research Council (Istituto Motori- CNR), Italy (corresponding author to provide phone: +39-081-7177108; e-mail: d.siano@ im.cnr.it).

ISBN: 978-1-61804-321-4

flow axis of the tail pipe (Fig. 1). Moreover, the pressure transducer should be at the height of the exhaust orifice, but not less than 0.2 m from the ground surface in order to avoid ground reflective effects.

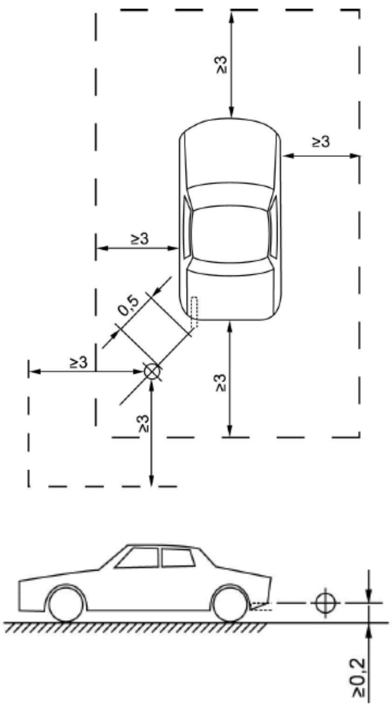

Fig 1. Microphone's position according to EU Regulations for measurement of noise emitted by stationary vehicles.

Since the aim of the work was not the vehicle certification and its silencing system technical requirements for the EU type-approval, the microphone was positioned at the height of the tail pipe, at a distance of 0.20 m from the exhaust termination and at an angle of 45° to the pipe axis, in order to avoid acoustic field influence on acquired data. Specifically, measurements accuracy was ensured thanks to the use of a BSWA MK series 200V polarized 1/4" free-field microphone characterized by good stability and high temperature resistant capacity. Being a small size transducer, it allows a lower interference and reverberation influence of its presence in the sound field, too.

Acoustic signals were acquired by LMS SCADAS III multi-channel acquisition system, and subsequently post-processed by using LMS Test.Lab software. The acquired signals were properly triggered by using the tachometer signal. In this way the signals were related to the rotational speed and its harmonics.

Exhaust acoustic data were firstly acquired during a rapid engine run-up from about 1000 to 3500 rpm in approximately 23 sec, with a 25 rpm step. For a better understanding of the exhaust noise frequency content, different stationary operating conditions were also tested and analyzed.

III. Order tracking analysis

A. Theory

Rotating machines produce repetitive vibrations and acoustic signals related to rotational speed. These relations are not immediately attained through a standard dynamic signal analysis, particularly with variations in the rotational speed. In this sense the measurement technique called *order tracking* represents an effective method for sorting out all the many signal components that a rotating machine can generate. Specifically, order tracking is a special type of frequency analysis which consists in tracking RMS levels of time-varying sine tones resulting from the periodic forces acting on the machine, as a function of rotational speed [2],[3].

On rotating machines, vibrations, directly or indirectly caused by the rotation itself, are of particular interest as they can become large without any resonance amplification. The main causes in these cases are attributable to imbalances, axle deformation or misalignment, defects in bearing races, defects in teeth on gears, etc. Each of these vibration sources produces vibration at a particular factor times the rotational speed of the machine. Of course, rotational speed dependent vibrations in rotating machines could occur at a frequency which coincides with a resonance of the structure, producing very high vibration levels and even failures. In general, a factor times the rotational speed is called an *order*, where the rotation speed is referred to as the 1st order, two times the rotation speed is the 2nd order , and so on. Orders are not necessarily integer numbers. Note that order value of the dominant vibration can be very useful for understanding from where the vibration originates and if it is due to either an order or a resonance frequency.

Rotating machines analysis is mostly based on investigating the vibrations during a speed sweep, where the machine is either run up from a low to a high RPM, or run down from a high to a low RPM. The time data measured during the speed sweep and sampled with a fixed frequency are divided into smaller segments, each of which is processed by FFT to find the spectrum. It is a particular case of non-stationary signals which shift up or down in frequency, as the machine speed is changing. It is important to take into account that in the analysis of a time-varying signal, there is a difficulty due to the bandwidth-time product limitation [4]. Ideally the RPM should not vary within the timeframe ΔT of each small segment, so ΔT should be made as small as possible, [1]. However, the frequency resolution ΔF of the FFT corresponds to $1/\Delta T$ (being unity the bandwidth-time constant for FFT analysis), therefore with conventional FFT analysis a compromise must be found between RPM and frequency resolution. A constant block length ΔT yields a constant frequency resolution ΔF. This corresponds to a varying order resolution ΔO, because the order frequency increases with RPM. So for low RPM the order resolution

ISBN: 978-1-61804-321-4

might become critical. This can be improved by adapting the frequency resolution $\Delta F = 1/\Delta T$ to be proportional to the actual RPM. Surely, as long as the data are sampled with a fixed frequency, this cannot be possible. The problem can be overcome only if the signal is re-sampled synchronously to the actual rpm. For this reason, in order analysis the synchronization of data collection with the machine's rotational speed represents a fundamental step [5]. In most cases synchronization is realized by using a rotational speed transducer, a tachometer, which provides a pulse or an integral number of pulses for each revolution. This signal indicates that the machine has finished one cycle and is beginning the next. A single tacho pulse points out when the rotating machine has reached a particular angular position. Capturing two tacho pulses, it is possible to determine rotating speed by counting clock cycles between the tach pulses. A third pulses gives information about an eventual speed change. The target is to collect a set of points evenly spaced by shaft position, not by time, keeping constant the number of points per cycle. In this way, the measurement rate tracks the rotational speed of the machine.

It is well known that the FFT process transforms time domain data to the frequency domain, creating a spectrum. Signals that are periodic (repetitive) in the time domain appear as peaks in the frequency domain. Similarly, in order analysis the FFT transforms the revolution domain data into an order spectrum. Signals that are periodic in the revolution domain appear as peaks in the order domain. An order spectrum gives the amplitude or the phase of the signal as a function of harmonic order of the rotation frequency. The harmonic or sub-harmonic order components remains in the same analysis lines independently from the speed of the engine.

The set of spectra produced by processing the time signal measured from the run-up or coast-down can be plotted in several formats, [2]. A common way is the waterfall plot, which is a three-dimensional diagram with frequency, amplitude and rotation speed on the three axes. In this type of plot, order-related spectrum-components, which occur at locations proportional to the rotation speed, can be visible as peaks on a straight line, and structural resonances can often be visible as peaks at fixed frequencies. Thus, in the diagram it is possible to appreciate which peaks are highest, at which speed the maximum occurs, and if they are caused by resonances or rotation-speed-dependent phenomena. As sometimes in the waterfall plot smaller peaks are difficult to distinguish, an alternative plot is the so-called color map plot, in which the different colors correspond to different noise signal amplitudes.

A key application of order tracking is the analysis of vibrations generated in vehicle drivetrain components, as many vibrations are related to engine rotational speed and in particular to engine ignition frequency. Also the exhaust noise spectrum always contains harmonic responses that are multiple of the rotation frequency, that is called the first engine order, [6]. Generally in the exhaust spectrum the strongest tone is the engine ignition frequency, which for a four-stroke four-cylinder engine is called the second order (as it is two times the engine rotation frequency), and can be obtained multiplying the firing rate of each cylinder for the number of cylinders.

B. Results Discussion

In the present work order tracking analysis has been applied on the exhaust noise signal acquired during an engine rapid run-up condition from approximately 1000 to 3500 rpm.

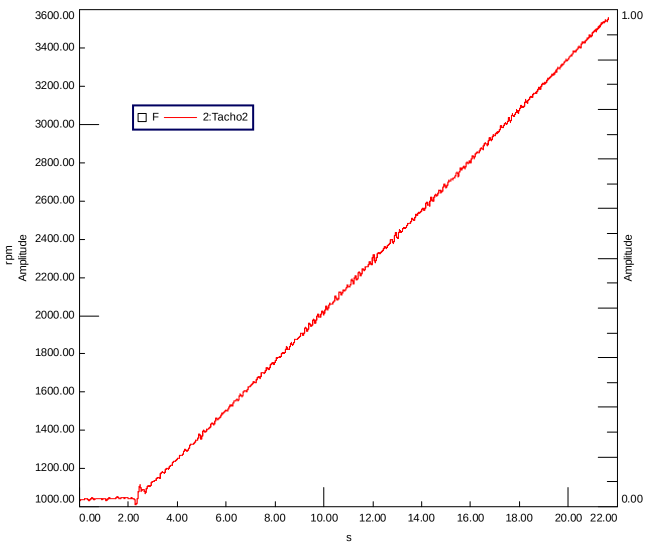

Fig. 2. RPM profile vs time

In figure 2 the acquired RPM profile during acquisition time, is reported. The goodness of the tachometer signal is, as well known, very important for order tracking analysis. In fact, the quality of the order track is therefore very sensitive to the stability to the rpm profile. This becomes significant where the effect of engineering changes needs to be established with reference to set rpm points.

ISBN: 978-1-61804-321-4

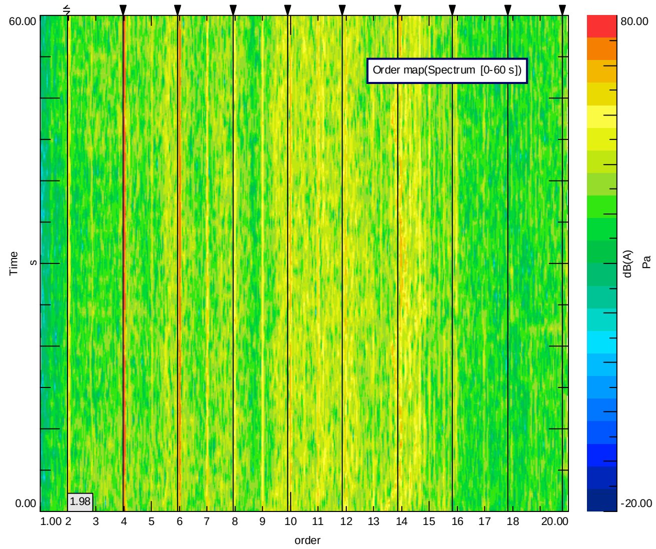

Fig. 3a. Order Spectrum vs. time

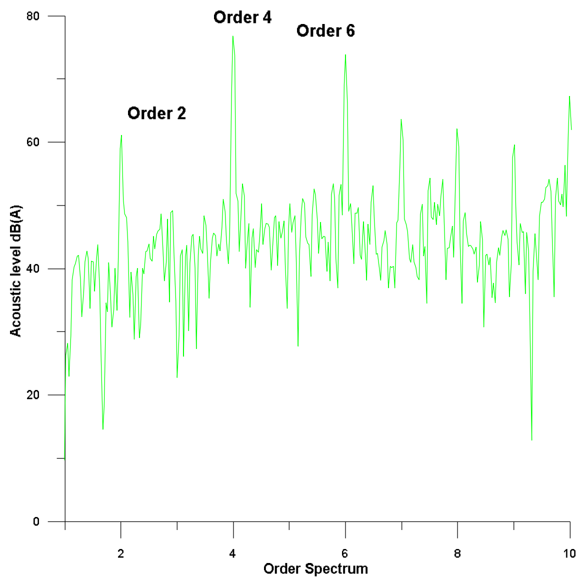

Fig. 3b. Order Spectrum of acoustic level

The acoustic levels in an order analysis can be represented in different ways. In fact, in figures 3a is shown the order map level versus time and in figure 3b the average level versus rpm order. In both cases, it is evident that the major contribution to the average acoustic level is the engine order 4 for which about 80 dB(A) of acoustic level is reached.

Figures 4-5 show respectively color-map and waterfall plots of the acquired noise signal.

The waterfall map is a 3 dimensional diagram representation. In this case the X-axis corresponds to frequency, Y-axis to engine speed and the Z-axis represents the amplitude value (Pa) of the exhaust microphone.

It is possible to observe, in both figures, a predominant noise content at low frequency range up to approximately 350 Hz, with more pronounced peak values up to 100 Hz for engine rotational speeds above 2700 rpm.

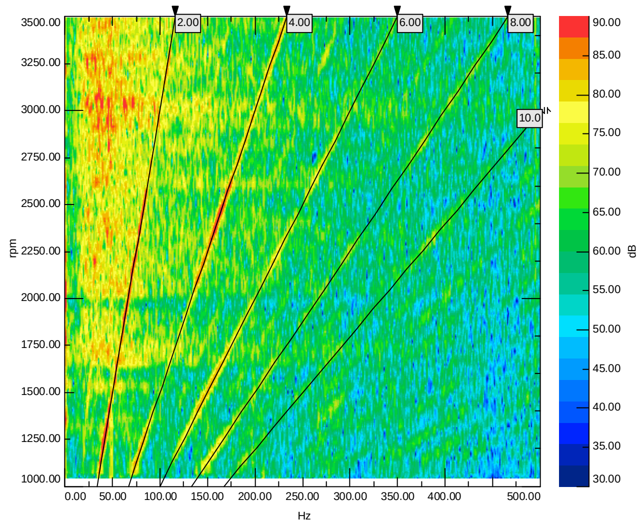

Fig. 4. 3D acoustic map in engine run up condition (1000 to 3500 rpm), FFT vs. rpm.

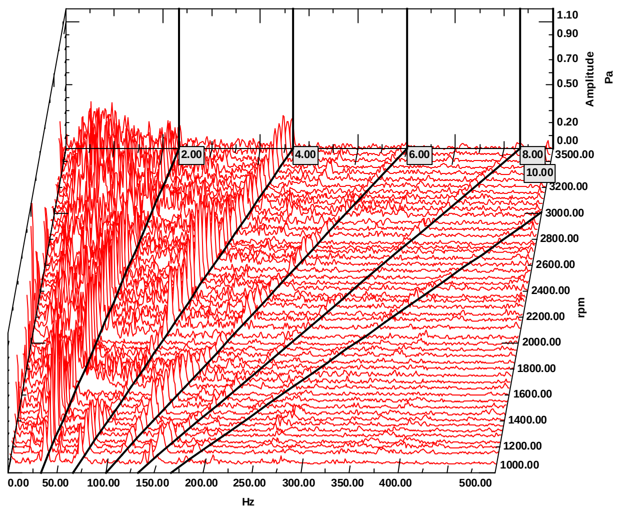

Fig. 5. Waterfall diagram in engine run up condition from approximately 1000 to 3500 rpm.

The magnitude peaks of the spectrum are lined up with the orders spectrum lines. As it is a four-cylinder four-stroke engine, the dominant frequency, namely the firing frequency, corresponds to the “second engine order”. Nevertheless, in the range between 2200 to 2600 rpm, the 4th engine order presents peak values more dominant than the second one. For this reason, a deeper analysis aimed to a steady state condition, is also investigated and following discussed.

IV. Steady-states Analysis

Steady-state tests were performed by varying engine rotational speed from about 1500 to 3800 rpm, by using vehicle gas pedal. For a better accuracy of the measure, tests were carried out twice for each considered condition. Thus, results are here reported in terms of mean values over the two different acquisitions and for all the acquisition time (60 seconds).

In Fig. 6 a bar plot of the exhaust overall noise levels, expressed in decibel (dB) and according to A-Weighting human ear perception (dB(A)) for all the tested operating conditions, is depicted.

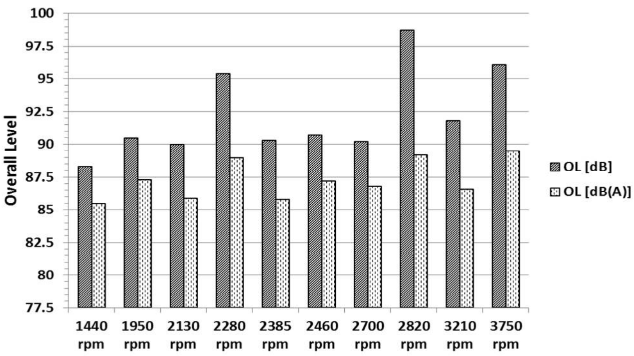

Fig. 6. Exhaust Overall Noise Level in dB and dB(A) for the tested operating conditions.

As expected, both overall levels in dB and dB(A) seem to have a rising trend with increasing engine speed values. However, it is possible to identify two particular conditions (@ 2820 rpm and @ 2280 rpm) which depart from the expected trend. Hence, it could be interesting to analyze exhaust noise frequency content in the two identified critical conditions.

For a better comprehension, in Fig. 7 the frequency spectrum up to 350 Hz of the exhaust signal acquired @ 2820 rpm, is reported. It is possible to immediately note a not-negligible noise contribution at low frequencies (up to about 100 Hz), as previously observed in the spectrograms of Fig. 3-4. Note that this considerable noise level occurs at frequencies below the engine firing frequency (94 Hz) and it is characterized by amplitude peaks even higher than the second engine order pressure amplitude value. This could depend on a resonance effect with exhaust natural frequencies and it has to be investigated to avoid possible noise increment in the vehicle cabin.

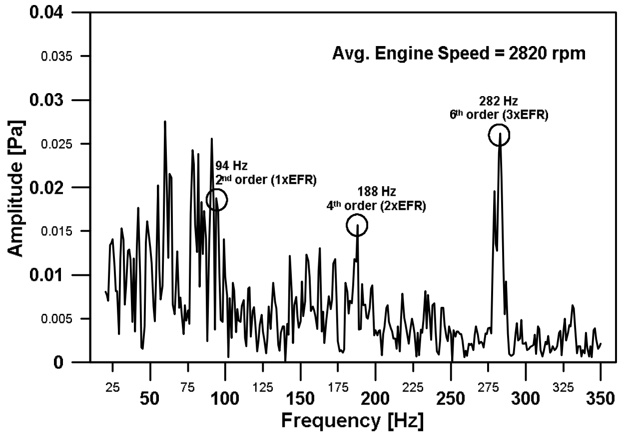

Fig. 7. Noise frequency spectrum of exhaust microphone signal @ 2820 rpm.

Engine test @ 2280 rpm has been also analyzed in terms of frequency spectrum, as it can be observed in Fig. 8. The high overall noise level value, in this case, is mostly due to the fourth engine order noise amount which results predominant in frequency spectrum among the other engine orders contributions. This confirms what has been previously observed in order tracking analysis.

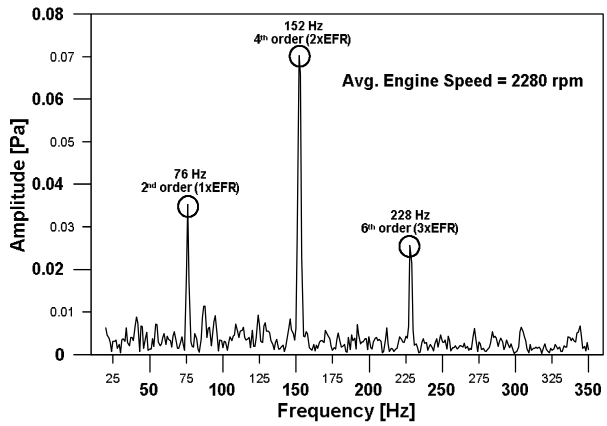

Fig. 8. Noise frequency spectrum of exhaust microphone signal @ 2280 rpm.

With this regard, other engine operating conditions characterized by the same particular orders behavior, have been identified. Plots of their spectra are reported in Fig. 9, where a dashed rectangle allows to point out that the fourth engine order is almost the dominant frequency band with respect to the second one, in the range of about 150 ÷ 250 Hz, as clearly reported in figure 2a. Therefore, this latter is most likely to represent a frequency range in which natural resonances, either structural or acoustical, of the tailpipe exhaust system may be present.

ISBN: 978-1-61804-321-4

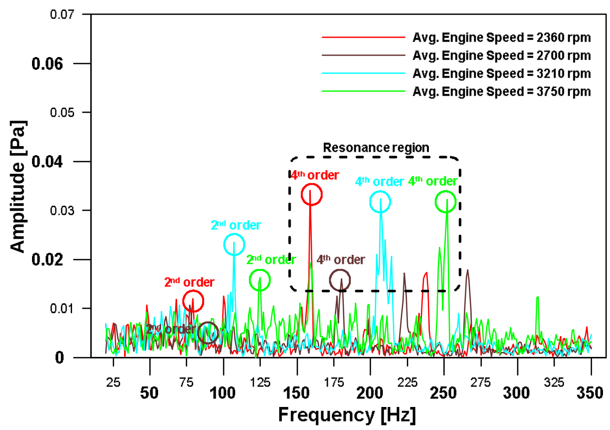

Fig. 9. Noise frequency spectrums of exhaust microphone signal in some of the tested operating conditions.

In conclusion, in order to better understand such behaviour in all the investigated engine operating conditions, future analysis could regard the implementation of an experimental Operational Modal Analysis (OMA) in order to identify possible structural resonances of the exhaust system. At the same time, the definition of an accurate and reliable system numerical model could be useful for the identification of its acoustic performances.

V. Conclusion

In this work vehicle exhaust noise signals, acquired by a microphone located at a proper distance from the pipe termination, have been deeply analyzed by means of order tracking technique. Results obtained from the performed order analysis have been also confirmed by processing exhaust signals in stationary operating condition. More in detail, a considerable radiated noise level in the frequency range up to 100 Hz is occurred for rpm engine speed above 2700 rpm. Moreover, an unusual orders noise content distribution has been observed, allowing to identify a probable resonance frequency region in which possible acoustical or structural resonance effects of the whole tailpipe exhaust system could occur. In this regard, future developments could concern the possibility to study the system dynamic behavior at the most critical engine operating conditions through the implementation of an Operational Modal Analysis (OMA). In addition to identify possible system structural resonances, a numerical analysis could be helpful in finding out any acoustical resonance of the exhaust system. Then a refinement process of the system for improving overall sound quality could be desirable.

References

[1] Xu Wang, *Vehicle noise and vibration refinement*, Woodhead Publishing, 2010.

[2] A. Brandt, *Noise and Vibration Analysis: Signal Analysis and Experimental Procedures*, Wiley, 2011, ISBN: 978-0-470-74644-8.

[3] Brandt A., Lago T., Ahlin K., Tuma J., "Main principles and limitations of current order tracking methods", *Sound and Vibration* (2005), pp. 19–22.

[4] Shao W., Wang X., Liu D., Shao Z., "An Analysis of Vehicle Engine Vibration Signals with Digital Order Tracking Approaches", *Proceedings of the FISITA 2012 World Automotive Congress*, doi: 10.1007/978-3-642-33832-8_45, Springer-Verlag Berlin Heidelberg 2013.

[5] Hewlett-Packard Application Note, “Order Analysis”, Realtime Update / Fall 1996 - Winter 1997.

[6] M.V. Prati, D. Siano, M. A. Costagliola, M.A. Panza, “An experimental evaluation of pollutants and noise exhaust emissions of a Bi-Fuel SI car in urban driving conditions”, to be published at *SAE 12th International Conference on Engines & Vehicles*, September 13-17, 2015, Capri, Naples.

D. Siano was born in Naples in 06/01/1969 Italy, and graduated in Aeronautical Engineering at the University of Naples “Federico II”, Italy in 1994.
Until 2001, she was researcher in acoustic and vibration department at C.I.R.A. (Italian aerospace Research Center). From 2001 until now,she is a Researcher at National Research Council of Italy (CNR) in the field of Acoustic and Vibration in transport field. She is responsible of Acoustic and Vibration Laboratory in her Institution. Expert evaluator within the EU 6th and 7th Framework Research Programme, in Transport-Aeronautics in 2006 and 2007. Project expert evaluator in Ministry Economic Development, Italy.
Referee for some International Journals and session organizers collaborating with SAE conferences. She is author of about 75 Scientific Papers published on International Journals and Conferences Proceedings and editor of two Scientific Books. She is tutor of several thesis and PhD thesis, as well.

M. A. Panza was born in Cosenza in 23/06/1986 Italy, and graduated in Mechanical Engineering at the University of Calabria, Italy in 2012.
She is currently a PhD Student in Industrial Engineering at University of Naples “Federico II”, Italy, in collaboration with CNR - Istituto Motori, Italy. She is dealing with acoustic and vibration in automotive field.

Semantics of the knowledge and competency levels applying probabilistic logic

Mikhail M. Kucherov, Nina A. Bogulskaya, Dmitry A.Starenkov

***Abstract*—** We propose a framework for probabilistic modeling where binary classification trade-offs arise when there is some set of subjects we wish to classify into two categories. We adopt probability theory as the mathematical formalism for data manipulation. An agent can express the probability in its knowledge about an element of information in the form of a confidence level, consisting of a pair of intervals of probability, one for each of two categories. The space of confidence levels naturally leads to the notion of a trilattice. Intuitively, the points in such a trilattice can be ordered according to knowledge, amount of information, or competency. While the trilattice structure offers the truth-ordering [5], our choice of semantics is based on knowledge-competency ordering, which we find to be closest to the classical framework for testing based assessment. We show that our results can be used after technology of pattern recognition as the structures on which may be based an effective testing of personnel at the enterprise.

***Keywords*—** module-rating system of knowledge assessment, many-valued logic, partial order

I. Introduction

During last decades many investigations were undertaken for knowledge and skills estimation. Most of them were focused on development of automated tests providing immediate feedback. The general disadvantage of such tests is first order logic usage in the process of decision making. While first order logic seems adequate for most daily reasoning, it is, however, not able to provide with meaningful results in the condition of inconsistent and/or incomplete input [1].

System model was described earlier [3]. Here we will mainly emphasize on semantic problems of assessment levels (Section 4).

The rest of the paper is composed with the following divisions. Basic terms and definitions are shown in the Section 3. A simple example adopted from [4] shows functioning of the model. It is described in Sections 2 and 5. The paper ends with general description of designed system (Section 6).

Nina A. Bogulskaya is an associate professor in the Institute of Space and Information Technologies of the Siberian Federal University, Krasnoyarsk, Russia (e-mail: NBogulskaya@sfu-kras.ru).

Mikhail M. Kucherov is an associate professor in the Institute of Space and Information Technologies of the Siberian Federal University, Krasnoyarsk, Russia (e-mail: MKucherov@sfu-kras.ru).

Dmitry A.Starenkov is a student of the Chair of Applied Mathematics and Computer Security of the Siberian Federal University, Krasnoyarsk, Russia (e-mail: nomad1408@rambler.ru).

II. Analysis example

A group of students of Institute of Space and Information Technology (ISIT) is planning a trip to see the Pillars Nature Sanctuary (Stolby). Normally, it takes 1.5 hours to get to Right Bank by car, but the students know that Kopylovski Bridge Expressway is not called by the locals “the longest parking lot” for nothing.

The students consult a traffic service, which integrates information from several independent information sources to provide traffic advisory along various travel routes. Let us assume that these sources are:

- weather forecast (rain, snow, fog);
- social activity (parades, motorcades, marathons);
- police activity (accidents, emergencies);
- road reparation.

The service uses the following rules to generate advisories:

If the weather is bad, and there is road reparation along the route, the probability of a delay is 0.9.

If there is road reparation, and social activities along the route, the likelihood of a delay is 0.8.

If there is road reparation, and police activities along the route, the likelihood of a delay is 0.99.

These rules are expressed as levels of evaluation, as [0.9, 1], [0.8, 1] and [0.99, 1].

The service generates advisories expressed as the likelihood of delays along the routes of interest. Students do not want to miss the excursion due to traffic, but they also have conference deadlines and so do not want to leave too early.

They decide that if the advisory says that the likelihood of delays is between 0.2 and 0.4, then they add one extra hour to the trip time. If the likelihood is between 0.4 and 0.6, then they add two hours, and if the likelihood is over 0.6 then they take a river-train. In Section 5, we will return to this example and show that our approach improves the quality of the advisory and could have helped the students avoid unnecessary trouble.

III. Preliminaries

Let P be a non-empty ordered set. If $sup\{x, y\}$ and $inf\{x, y\}$ exist for all $x, y \in P$, then P is called a *lattice* [2]. In a lattice the logic conjunction is identified with meet operation and the logical disjunction with the join operation.

Denote by E[0,1] the set of all closed subintervals over [0,1]. Let $Cl(A) = \langle[\alpha, \beta], [\gamma, \delta]\rangle$ be an element of $E[0,1] \times E[0,1]$. The element $Cl(A)$ is required to assess the knowledge and competency levels respectively of the object A. The object A is the set of functional characteristics acquired during learning.

Definition 1.

Denote the following orders. Let $\langle[\alpha_1, \beta_1], [\gamma_1, \delta_1]\rangle$, $\langle[\alpha_2, \beta_2], [\gamma_2, \delta_2]\rangle$ be any two elements of $E[0,1] \times E[0,1]$.

$\langle[\alpha_1, \beta_1], [\gamma_1, \delta_1]\rangle \leq_s \langle[\alpha_2, \beta_2], [\gamma_2, \delta_2]\rangle$, iff $\alpha_1 \leq \alpha_2$, $\beta_1 \leq \beta_2$ and $\gamma_2 \leq \gamma_1$, $\delta_2 \leq \delta_1$;

$\langle[\alpha_1, \beta_1], [\gamma_1, \delta_1]\rangle \leq_v \langle[\alpha_2, \beta_2], [\gamma_2, \delta_2]\rangle$, iff $\alpha_1 \leq \alpha_2$, $\beta_2 \leq \beta_1$ and $\gamma_1 \leq \gamma_2$, $\delta_2 \leq \delta_1$;

$\langle[\alpha_1, \beta_1], [\gamma_1, \delta_1]\rangle \leq_f \langle[\alpha_2, \beta_2], [\gamma_2, \delta_2]\rangle$, iff $\alpha_1 \leq \alpha_2$, $\beta_2 \leq \beta_1$ and $\gamma_2 \leq \gamma_1$, $\delta_1 \leq \delta_2$.

Definition 2.

Let $\langle E[0,1] \times E[0,1], \leq_s, \leq_v, \leq_f\rangle$ be as defined in Def. 1. Then the meet and join corresponding to the knowledge, amount of information, and competency are defined as follows. The symbols $\otimes$ and $\oplus$ denote meet and join, and subscripts s, v, and represent knowledge, amount of information (precision), and competency, respectively.

1. $\langle[\alpha_1, \beta_1], [\gamma_1, \delta_1]\rangle \otimes_s \langle[\alpha_2, \beta_2], [\gamma_2, \delta_2]\rangle = \langle[\min\{\alpha_1,\alpha_2\}, \min\{\beta_1, \beta_2\}], [\max\{\gamma_1,\gamma_2\}, \max\{\delta_1,\delta_2\}]\rangle$.
2. $\langle[\alpha_1, \beta_1], [\gamma_1, \delta_1]\rangle \oplus_s \langle[\alpha_2, \beta_2], [\gamma_2, \delta_2]\rangle = \langle[\max\{\alpha_1,\alpha_2\}, \max\{\beta_1, \beta_2\}], [\min\{\gamma_1,\gamma_2\}, \min\{\delta_1,\delta_2\}]\rangle$.
3. $\langle[\alpha_1, \beta_1], [\gamma_1, \delta_1]\rangle \otimes_v \langle[\alpha_2, \beta_2], [\gamma_2, \delta_2]\rangle = \langle[\min\{\alpha_1,\alpha_2\}, \max\{\beta_1, \beta_2\}],[\min\{\gamma_1,\gamma_2\},\max\{\delta_1,\delta_2\}]\rangle$.
4. $\langle[\alpha_1, \beta_1], [\gamma_1, \delta_1]\rangle \oplus_v \langle[\alpha_2, \beta_2], [\gamma_2, \delta_2]\rangle = \langle[\max\{\alpha_1,\alpha_2\}, \min\{\beta_1, \beta_2\}], [\max\{\gamma_1,\gamma_2\}, \min\{\delta_1,\delta_2\}]\rangle$.
5. $\langle[\alpha_1, \beta_1], [\gamma_1, \delta_1]\rangle \otimes_f \langle[\alpha_2, \beta_2], [\gamma_2, \delta_2]\rangle = \langle[\min\{\alpha_1,\alpha_2\}, \max\{\beta_1, \beta_2\}],[\max\{\gamma_1,\gamma_2\},\min\{\delta_1,\delta_2\}]\rangle$.
6. $\langle[\alpha_1, \beta_1], [\gamma_1, \delta_1]\rangle \oplus_f \langle[\alpha_2, \beta_2], [\gamma_2, \delta_2]\rangle = \langle[\max\{\alpha_1,\alpha_2\}, \min\{\beta_1, \beta_2\}], [\min\{\gamma_1,\gamma_2\}, \max\{\delta_1,\delta_2\}]\rangle$.

Definition 3.

Let $\langle E[0,1] \times E[0,1], \leq_s, \leq_v, \leq_f\rangle$ be a trilattice. Than we can introduce the following unary operations with the following properties:

1. *S-inversion* ($\sim_s$):
$\langle[\alpha_1, \beta_1], [\gamma_1, \delta_1]\rangle \leq_s \langle[\alpha_2, \beta_2], [\gamma_2, \delta_2]\rangle \Rightarrow \sim_s \langle[\alpha_2, \beta_2], [\gamma_2, \delta_2]\rangle \leq_s \sim_s \langle[\alpha_1, \beta_1], [\gamma_1, \delta_1]\rangle$,
where $\sim_s \langle[\alpha, \beta], [\gamma, \delta]\rangle = \langle[1-\beta, 1-\alpha], [1-\delta, 1-\gamma]\rangle$.
2. *V-inversion* ($\sim_v$):
$\langle[\alpha_1, \beta_1], [\gamma_1, \delta_1]\rangle \leq_v \langle[\alpha_2, \beta_2], [\gamma_2, \delta_2]\rangle \Rightarrow \sim_v \langle[\alpha_2, \beta_2], [\gamma_2, \delta_2]\rangle \leq_v \sim_v \langle[\alpha_1, \beta_1], [\gamma_1, \delta_1]\rangle$,
where $\sim_v \langle[\alpha, \beta], [\gamma, \delta]\rangle = \langle[1-\gamma, 1-\delta], [1-\alpha, 1-\beta]\rangle$.
3. *F-inversion* ($\sim_f$):
$\langle[\alpha_1, \beta_1], [\gamma_1, \delta_1]\rangle \leq_f \langle[\alpha_2, \beta_2], [\gamma_2, \delta_2]\rangle \Rightarrow \sim_f \langle[\alpha_2, \beta_2], [\gamma_2, \delta_2]\rangle \leq_f \sim_f \langle[\alpha_1, \beta_1], [\gamma_1, \delta_1]\rangle$,
where $\sim_f \langle[\alpha, \beta], [\gamma, \delta]\rangle = \langle[1-\delta, 1-\gamma], [1-\beta, 1-\alpha]\rangle$.

The partial order $\leq_s$ can be considered the knowledge and competency ordering: “truth” relative to expert’s knowledge increases as *knowledge* goes up (if $a \leq_s b$ then b can be characterized at least the same amount of knowledge as a). The order $\leq_v$ is the *variation* ordering: precision of information supplied increases as the probability intervals become narrower. *Normative* ordering $\leq_f$ means that if $a \leq_f b$ then maximally a has equal amount of procedural skills as b, and b has at least the same amount of knowledge as a. Intuitively, a confidence level increases according to this *f*-ordering, when the variation of the knowledge component of a confidence level goes up, while that of the competency component goes down.

Let define *read* ($A \leftarrow B$) as operation $\oplus$, and *write* ($A \rightarrow B$) as operation $\otimes$, and indices s, v and f are referred to appropriate orderings then test execution is described as a sequence of write operations. Eventually it causes to changing of *normative* assessment in the order $\leq_f$.

IV. Combining answers

We can learn levels for compound events, which include basic objects, having the confidence levels for basic objects. We need rules of combining in terms of probability theory.

Definition 4 (*Semantics of Assessment Levels*).

According to the expert’s knowledge, an event A can be true, false, or unknown. Let 1, 0 и $\perp$ respectively denote true, false, and unknown. Let S_i denotes the case where the truth-value of A is i, $i \in \{0, 1, \perp\}$. Let s_i denotes the probability of the case S_i. Then the assertion that the confidence level of A is $\langle[\alpha, \beta], [\gamma, \delta]\rangle$, written $Cl(A) = \langle[\alpha, \beta], [\gamma, \delta]\rangle$, corresponds to the following constraints:

$$\begin{aligned} &\alpha \leq s_1 \leq \beta \\ &\gamma \leq s_0 \leq \delta \\ &s_i \geq 0, \quad i \in \{1, 0, \perp\} \\ &\Sigma_i s_i = 1 \end{aligned} \tag{1}$$

where α and β are the lower and upper bounds of the knowledge, and γ and δ are the lower and upper bounds of the competency in A.

The scope of the possible interaction between A and B can be characterized as follows. According to the expert’s knowledge, each of answers A, B can be true, false, or unknown. This gives rise to 9 possible cases. Let S_{ij} denote the case where the truth-value of A is i and that of B is j, $i,j \in \{1,0,\perp\}$. E.g., S_{10} is the case where the answer A is true and B is false, while $S_{0\perp}$ is the case where A is false and B is unknown. Suppose s_{ij} denotes the probability associated with the case S_{ij}. Then the possible scope of interaction between A and B can be characterized by the following constraints which must be satisfied for all modes:

$$\begin{aligned} &\alpha_1 \leq \Sigma_j s_{1j} \leq \beta_1 \\ &\gamma_1 \leq \Sigma j\, s_{0j} \leq \delta_1 \\ &\alpha_2 \leq \Sigma_j s_{j1} \leq \beta_2 \\ &\gamma_2 \leq \Sigma_j s_{j0} \leq \delta_2 \\ &s_{ij} \geq 0 \quad i, j \in \{1, 0, \perp\} \\ &\Sigma_{i,j} s_{ij} = 1 \end{aligned} \tag{2}$$

Case 1: Independence.

Independence of events A and B can be characterized by the equation $P(A|B) = P(A)$, where $P(A|B)$ is the conditional probability of the event A given event B. More specifically, since in our model an event can be true, false, or unknown, (i.e., we are modeling knowledge and competency independently) we have:

$$Cl_2 (A \otimes_s B) = \langle[\alpha_1\alpha_2, \beta_1\beta_2], [1-(1-\gamma_1)(1-\gamma_2), 1-(1-\delta_1)(1-\delta_2)]\rangle.$$
$$Cl_2 (A \oplus_s B) = \langle[1-(1-\alpha_1)(1-\alpha_2), 1-(1-\beta_1)(1-\beta_2)], [\gamma_1\gamma_2, \delta_1\delta_2]\rangle \tag{3}$$

Case 2: Positive Correlation

Two events A and B are positively correlated if they overlap as much as possible. This happens when either (i) occurrence of A implies occurrence of B, (ii) occurrence of B implies occurrence of A. One can obtain that the solution can be shown to be

$$Cl_2 (A \otimes_s B)=\langle[\min\{\alpha_1,\alpha_2\}, \min\{\beta_1, \beta_2\}], [\max\{\gamma_1,\gamma_2\}, \max\{\delta_1,\delta_2\}]\rangle.$$
$$Cl_2(A \oplus_s B)=\langle[\max\{\alpha_1,\alpha_2\}, \max\{\beta_1, \beta_2\}],[\min\{\gamma_1,\gamma_2\},\min\{\delta_1,\delta_2\}]\rangle \tag{4}$$

V. Example for analysis (cont’d)

Returning to the example in Section 2, suppose that our information sources predict 50% chance of bad weather, parades with 50% certainty, roadwork along the Kopylovski Bridge (KB) with certainty 80%, and police activity with the probability of 40%. This information is expressed in this way:

– roadwork: ⟨[0.8, 0.8], [0.2, 0.2]⟩;
– social_act: ⟨[0.5, 0.5], [0.5, 0.5]⟩;
– bad_weather: ⟨[0.5, 0.5], [0.5, 0.5]⟩; and
– police_act: ⟨[0.4, 0.4], [0.6, 0.6]⟩.

The traffic service fetches the above information from four different information sources and integrates them independently using these rules as in Eq. (3):

– delay, if there are roadworks and bad weather:

Cl (roadwork $\otimes_s$ bad_weather) =⟨[0.9×0.8×0.5,0.8×0.5], [0.6,0.64]⟩. Eventually, one can obtain Cl (roadwork $\otimes_s$ bad_weather) = ⟨[0.36,0.4], [0.6,0.64]⟩. (5)

– delay, if there are roadworks and the marathon:

Cl (roadwork $\otimes_s$ social_act) = ⟨[0.8×0.8×0.5,0.8×0.5], [0.6,0.68]⟩ = ⟨[0.32,0.4], [0.6,0.68]⟩. (6)

If there are road works and traffic accident:

Cl(roadwork $\otimes_s$ police_act) = ⟨[0.99×0.8×0.4,0.8×0.4], [0.68,0.68]⟩ = ⟨[0.32,0.32], [0.68,0.68]⟩. (7)

Using the second rule of Eq. (3) one can obtain from Eqs. (5) and (6) Cl_{tot} [(roadwork $\otimes_s$ bad_weather) $\oplus_s$ (roadwork $\otimes_s$ social_act)] = ⟨[0.56,0.64], [0.6×0.6, 0.64×0.68]⟩ = ⟨[0.56,0.64], [0.36, 0.44]⟩. (8)

Adding Eq. (7) one has Cl_{tot} [… $\oplus_s$ (roadwork $\otimes_s$ police_act)] = ⟨[0.7,0.76], [0.36×0.68, 0.44×0.68]⟩ = ⟨[0.7, 0.76], [0.24, 0.3]⟩. (9)

The key observation here is that the three rules used in generating the advisory are not independent – they all rely on the roadwork information from Department of Transportation. Our intuition suggests that predictions based on the independence assumption might cost our students an excursion, a few hours of sleep, or a conference paper. When correlation is not taken into account, the confidence level of delay(KB) is [0.36, 1], which means that the available information predicts traffic delay with certainty 0.36 and smooth traffic with certainty [0, 0.64]. Taking into account the possibilities of parades and accidents, it is reasonable to up the expectation of delays. In contrast, our method computes the confidence level for traffic delays to be [0.7,0.76], which is more narrow then the certainty factor according BLP theory [0.63,1] [4].

We thus see that our theory is able to better predict confidence levels of the combined information.

VI. Testing System Implementation

Model of evaluation described in the paper [3] provide rules, which will be used in intelligence e-learning system of self-education support. With each learned skill the student is offered the minimal number of questions obtained as described in [3]. Every answer has its confidence level $Cl(A)$ = ⟨[α, β], [γ, δ]⟩. In the case of multiple answers, the result is the product of evaluations. For each test dichotomy the characteristic, which it verifies, is known beforehand: theoretical knowledge vs. competency; certainty or the volume of information; normative evaluation of knowledge and competency; since it defines the choice of one of three writing operations: $\otimes_s$, $\otimes_v$, or $\otimes_f$ for current evaluation. For example, the system can be implemented as considered in a typical three-tiers Web deployment paradigm: an Apache front end web-server; a Python based application middleware for dynamic content, integration of data and users' programming agents which is based on Python; back end SQLite database (DB) for storage static and dynamic data.

Every user has her own database to store session data and the data of the present state of the system. The authenticated user receives a unique session key, which is used for the user identification in the system for current session. Documents subsystem for dynamic publication compiles the page which will be presented to the user. The documents and subjects templates are read from public documents database. Test questions are read from a public tests database.

The authentication subsystem verifies an user during login and creates the first session contact in this system, if the user logs in with correct authentication data. Also this subsystem provides the user with authorized access during the session and it deletes the session when the user logs out.

A stack profiler subsystem tracks down the chronology of user's actions in a stack as the data structure in the user database. The tutor subsystem provides the student with intellectual diagnostics and optimal educational data stream based on his current profile. Since the system is built from weekly linked subsystems, any unique subsystem can be supported and improved independently. All the subsystems are bound with the information stored in multiple databases.

References

[1] N.J. Belnap A useful four valued logic // Modern Uses of Multiple-Valued Logic, Dunn, J.M., Epstain, G. (eds.). – D. Reidel Publishing Company, Dordrecht, 1977. – PP. 8–37.

[2] B.A. Davey, H.A. Priestley: Introduction to lattices and order. Cambridge University Press, Cambridge, 2005.

[3] M.M. Kucherov Knowledge evaluation model and competencys with usage of probabilistic logic and image recognition theory / N. A. Bogulskaya, M. M. Kucherov, E. A. Kresan // Acta universitatis Pontica Euxinus, Special number, TU-Varna, 2014, PP. 383–388.

[4] H. Wan, M. Kifer Belief Logic Programming: Uncertainty Reasoning with Correlation of Evidence. LPNMR 2009: Potsdam, Germany. – PP. 316–328.

[5] Ya. Shramko, J. M. Dunn, T. Takenaka The trilattice of constructive truth values. // J. Logic Computat., Vol. 11, No. 6, 2001, PP. 761–788.

The problem of automatic generation of educational tests based on a vector-based semantic classification

Dmitry V. Lichargin, Mikhail M. Kucherov, Mikhail V. Rybkov, Roman Yu. Tsaryov, Ekaterina A. Chzhan

Abstract— The problem of generating grammatically and semantically meaningful phrases and texts on natural languages is discussed. The observation of a vector-based semantic classification over the words and notions of the English language is given. The test generating software, that can be applied by teachers of English to prepare the tests for their students, is developed and described.

Keywords— Computational linguistics, educational tests, natural and machine languages, semantic classification.

I. Introduction

ONE of important problems of the modern computational linguistics is the problem of automatic generation of the educational tests. In respect to the study of the natural and machine languages structure the problem of generating the natural language is very topical, including the problem of generating grammatically and semantically meaningful phrases and texts on natural languages, satisfying definite criteria of meaningfulness, for the purpose of contributing to the Turing test passing. The latter is topical today, because of the importance of such applied tasks as building natural-language interfaces, developing expert systems, electronic translators, electronic summarizing systems, e-learning systems, advertisement software of dialogue with the user, etc. The problem of generating educational tests is important due to wide usage of tests in education, and universities need to have a big amount of different version of the tests of several types in order to avoid the risks of the tests to be similar and not individual enough.

A great number of researchers now work at the problem of generating the meaningful subset of the language: philologists, programmers, mathematicians, semantics experts, philosophers and many others. [1-3, 5-7]. Especially surprising results for today are presented in the sphere of natural language grammatically meaningful phrases generation. The programs of text editors, electronic translators and other systems effectively carry out generation of language grammatically meaningful structures. However, the generation of semantically meaningful speech is a less investigated topic. Although many systems based on semantic nets, ontologies and other methods show a good efficiency in the dialogue with the user in the natural language. The most popular method of supporting the dialogue with the user is reduced to the application of databases on the natural language dialogues.

In general, this problem can be expanded to an issue of semi-automatic textbook generation. Today almost all the teachers and tutors have to compose textbooks for students. They usually have theoretical material, some tasks and methodical recommendations, but it is quite a difficult and routine process to gather all the materials together, forming original texts without involving materials breaking the copyright law and to perform text formatting. Therefore, developing semi-automatic textbook generation software, where the user can compose a textbook by adjusting a set of parameters (type of formatting, extension of output document, etc.) is a topical problem.

In this paper, it is necessary to assume that *a task* is a question with four or five, for example, possible answers, only one of which is right. A test is a set of tasks of different type. The purpose of the work is to develop a test generator description and algorithms that are used for generating big amount of different English grammatical tasks. The basic task includes determining of the types of questions, developing a special way of generating wrong answers, creating the algorithms of meaningful speech generation based on the a specific semantic classification. The novelty of the work is reduced to the application of a vector based semantic classification over the words and notions of the English language for developing a test generator.

Nowadays there are a lot of different test generators that can produce quite a big amount of different English tests. But they usually use a database of complete tasks that was not generated, but prepared by people in advance. Therefore, the diversity of tests depends only on the size of this base. Algorithm of tests generation, for example, of 10 tasks includes just choice of 10 questions from the base and input to user in a random way. Besides, the possible answers in every

Dmitry V. Lichargin is with the Siberian Federal University, Krasnoyarsk, Russia (e-mail: orderist@yandex.ru).

Mikhail M. Kucherov is with the Siberian Federal University, Krasnoyarsk, Russia (e-mail: MKucherov@sfu-kras.ru).

Mikhail V. Rybkov is with the Siberian Federal University, Krasnoyarsk, Russia (e-mail: mixailrybkov@ya.ru).

Roman Yu. Tsaryov is with the Siberian Federal University, Krasnoyarsk, Russia (e-mail: rahatamatahata@mail.ru).

Ekaterina A. Chzhan is with the Siberian Federal University, Krasnoyarsk, Russia (e-mail: ekach@list.ru).

ISBN: 978-1-61804-321-4

task are mixed every time as well. A new algorithm of generating tasks that uses a vector based semantic classification over the words and notions of the English language is proposed in this paper.

II. Semantic classification over the words and notions

Let's consider a semantic classification of natural language words and notions, reduced to 16 classes of language semes (semantic, meaning «atoms»). Based on the natural language semes classification a natural language notions classification vector of five coordinates is offered. The values of the G vector coordinates are assigned by means of a generative grammar of the following form:

1. The first level of the notions classification corresponds to the coordinate G_1 of the vector G. Let G_1 = {SOMETHING, RELATION, MIND, IDEA, INFORMATION, PLACE, THING, CREATURE}.
2. The second level of the notions classification is presented by the coordinate G_2. A set G_2 of the coordinates value for the classification is assigned by a set of generative grammar rules: {S→Fd, S→Fx, d→ALIVE, d→NOT ALIVE, x → WHICH ALIVE, x → WHICH NOT ALIVE, F→OF, F→IN, F→ON, F→AT}, where notion AT means any nonzero distance between objects.
3. The third level of the notions classification is determined by the coordinate G_3, G_3={X-y (*ESSENCE*), X-X-y (*ESSENCE OF ESSENCE*), RELATION-X-y (*PROPERTY*), RELATION-X-X-y (*CONNECTION*), RELATION-CREATURE-X-y (*ACTION*), RELATION-CREATURE-X-X-y (*JOINING*), RELATION-CREATURE- CREATURE-X-y (*PRESENTING*), RELATION-CREATURE-CREATURE-X-X-y (*EXCHANGE*)}, where X is any of the basic semes, determined on the first level of the classification, while y is any sequence of such semes. X is determined as the seme, main by its meaning. Sign «-» is used in the given case for concatenation notation. Essential explanations are shown in the round brackets.
4. A set of G_4 values of the coordinate G is assigned by a set of generative grammar rules: {$S \to P_1 \cdot P_2 \cdot P_3 \cdot P_4 \cdot P_5 \cdot P_6 \cdot P_7 \cdot P_8$, $P_1 \to$ g·QUANTITY, $P_1 \to \lambda$, $P_2 \to$ g·STABILITY, $P_2 \to \lambda$, $P_3 \to$ g·POSITIVITY, $P_3 \to \lambda$, $P_4 \to$ g·SPECTRUM, $P_4 \to \lambda$, $P_5 \to$ g·INFORMATION CONTENT, $P_5 \to \lambda$, $P_6 \to$ g·LOCATION, $P_6 \to \lambda$, $P_7 \to$ g·SIZE, $P_7 \to \lambda$, $P_8 \to$ g·BEING ARTIFICIAL, $P_8 \to \lambda$}, where g is a linguistic scale value like: {minimal, … ,little, …, medium, …, big,…, maximal, λ}. Here λ is an empty symbol.
5. A set G_5 of the coordinate values G is assigned by a set of generative grammar rules: {S→x, x→(xFx), x→xFx, x→1 (*EXISTING*), x→0 (*NON-EXISTING*), x→◊ (*POSSIBLE*), x→$\Box$ (*NECESSARY*), F→INCLUDES, F → IS INCLUDED IN, F → INCLUDES AND IS INCLUDED IN, F → PARTIALLY INCLUDES, F → MORE THAN, F → LESS THAN, F → EQUAL TO, F → SIMILAR TO, F → BECOMES, F → IS DERIVED FROM, F →IS SIMULTANEOUS WITH, F → IS NOT SIMULTANEOUS WITH, F → IMPLIES, F →IS DETERMINED BY, F → CORRESPONDS TO, F → IS CONNECTED WITH}.
6. All further levels of the classification are formed by means of the recursive repetition of the offered five levels of classification. The index of the level can be calculated by the formula $Gi=G_{mod(i,5)}$, where i belongs to the set of natural numbers. Any notion or class of notions for the natural language corresponds to a definite classification vector.

For example, the group of words {take, give, buy, sell, accept, present, …} correspond to the such a vector as [THING\\RELATION-CREATURE-CREATURE-X]. The group of words {shop, kiosk, supermarket, …} correspond to such a vector as [THING\IN WHICH ALIVE\X]+[THING\\RELATION-CREATURE-CREATURE-X]. The word «transport» corresponds to a vector: [THING\IN WHICH ALIVE\X]+[PLACE\\RELATION-CREATURE-X]. Each word corresponds to a set of semantic notions – points of the notions space. However, using the five coordinates of the multidimensional classification vector is a definite simplification. In the most complete form, the classification can be based on 16 coordinates of a recursively repeating vector of values.

The structures of different levels are formed over the given semantic classification of words and notions of the natural language. On the first level there are word groups of the language, on the second level they are united into word combinations – pairs of words linked semantically and grammatically, on that level the combinations of words more or less useful as word combinations are assigned. On the second level the words are united into patterns for example: *«Determiner + Attribute + Subject + Modality + Predicate + Determiner + Attribute + Object + Link + Determiner + Attribute + Nominal Group (Modifier of Time) + Link + Determiner + Attribute + Nominal Group (Modifier of Place) + Link + Determiner + Attribute + Nominal Group (Modifier of Purpose) + …»*. Semantic chains of the type are presented in the following way: *«this/that/… + hungry/full/… + vegetarian/gourmand/… + can/wants to/… + eat/have a bite with/… + the/a/… + tasty/aromatic/… + pie/salad/… + after/before/… + five/six/… + hours + in/for/… five/six/… + minutes + … + in + a + big/beautiful/… + restaurant/canteen/… + on + a + big/beautiful/… + street/square/… named after Smith/Brown/… + in + a + big/beautiful/… + city/village/… + Ababa/Acaca/… + in order to/to/… + taste/know/… + a + pungent/spicy/… + taste/aftertaste/… + …»*. On the forth level words are separated into subsets of these patterns: *«I/he/… + have eaten/tasted/… + on a street/square/… + named after + Smith/Brown/…»*. On the fifth level the fragments of the patterns are united into semantic patterns of the second rank: *«the taste of a pie surprised me in the morning»* (pattern type: Relation-Attribute_of_Object-Time), *«The restaurant gladdened me with a crunching crust»*. (pattern class: Relation-Place-Part_of_Object). Generation and ordering the semantic patterns of the second rank is an important task determining the success of the system for natural speech generation by software means.

ISBN: 978-1-61804-321-4

III. Test generator development

According to this classification a database of words that was programmed in Delphi was created. The database has a structure of a tree of words, and it is possible to move between the branches of the tree in semantic-based classification criteria, because firstly, all the notions are ordered by basic semes. Secondly, the words are separated into topics, so this separation into semantically combinable classes is very useful with respect to test generating. The general algorithm of task generation is mainly based on the traversal of the tree of words (the database) and creating sentence patterns, while it consists of the following sequential steps:

STEP 1. Load from the file the database of words and database of patterns into the program.

STEP 2. Select the topic that is necessary for the task generating. As a rule, the topic is chosen by user.

STEP 3. Select the type of task (for example, "choose the best word or phrase to complete the sentence", "arrange the words to make sentences", "answer the following question").

STEP 4. Select the pattern of generating phrase according to the type of task chosen at step 3.

STEP 5. Generate grammatically and semantically meaningful phrase using selected pattern.

STEP 6. Compose a task question from the phrase obtained at step 5.

STEP 7. Generate possible answers taking into account the chosen topic and the most common mistakes of students.

STEP 8. Write a task ready to be used into the file. The ready task should include description of the task, question and possible answers.

The above algorithm was carried out in the program "English test generator", where tests can be generated on more than 10 topics (Food, Clothes, Place, etc) and three types of tasks are implemented.

Let's consider a software interface that allows generating the tasks in English to foreign language lessons (the software program is described in), shown in Fig. 1.

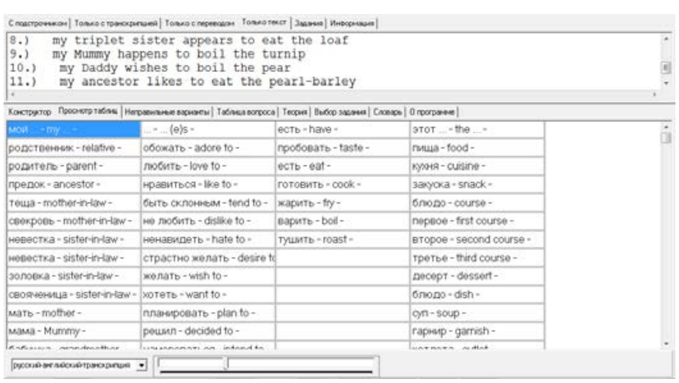

Fig.1. The system for generation of meaningful phrases and tasks in English based on the semantic classification of words

IV. Task generation example

Several examples of tasks that were generated by "English test generator" are given below:

Task 1. Put the words in the right order.
my publish client plans to the book
(The right answer is: My client plans to publish the book).

Task 2. Insert the proper word into the following sentence:
My boss ___________ correct the price list.
a) wants to
b) becomes to
c) amends to
d) feels to
(The right answer is a)

Task 3. *Insert the proper word into the following sentence:*
I happen to play ___________
a) Hockey
b) Mollusk
c) People
d) Pest

(The right answer is A)

Task 4. *Insert the proper word into the following sentence:*
We hate to go in for ___________
a) Pet
b) Human
c) Alien
d) Football

(The right answer is D)

Task 5. *Select the right variant of phrases.*
a) I need to go in for basketball
b) They hate to go in for a person
c) I love to play an animal
d) I love to play a cat

(The right answer is A)

Task 6. *Put the words in the right order.*
Need to go in for basketball I

(The right answer is: I need to go in for basketball)

Task 7. *Put the words in the right order.*
Have to attend hockey they

(The right answer is: «they have to attend hockey»)

It is necessary to notice that there can be several right answers on the first question (except the latter, «The client plans to publish my book» is possible too). Therefore, in this case we face the problem of several suitable answers when it should be only one according to the test description [4].

ISBN: 978-1-61804-321-4

When generating task 2 and similar tasks, the software selects two different topics: the one is for the question and the right answer and another (one or more) is for the wrong answers. So sometimes when these two topics are situated «far» from each other in the semantic classification tree, it is very easy to find out the right answer and the difficulty of the task is rather low. This problem can be solved by using not full database of words but its *clone* in the program. The clone of database is a reduced version of full database, where we retain only those topics that are situated «close to» each other in the semantic classification tree. The usage of database clones has shown the efficiency of this approach.

V. SEMI-AUTOMATIC TEXTBOOK GENERATION

Having developed the test generator, now the purpose is to expand its interface and create multifunctional integrated system that includes the following capabilities:

– handling the dictionary (the database, which is implemented as a tree of words);

– test generating (herewith there should be implemented generation of different types of task: grammatical, lexical, etc.);

– accumulating and saving all the tests and materials in standard file format, which were generated by the system or were downloaded by a user;

– operating a tree of text formatting;

– generating a complete textbook by multiplying the textbook tree and the tree of text formatting (by using a special algorithm).

These capabilities can be implemented by means of imperative programming language and relational database managing system application. Although performing a presentation of a text in the form of a tree is the most complicated problem. When building a text parsing algorithm, some key features should be taken into account such as type of a text, text structure (chapter, section, paragraph) and table of contents. The program module that performs a text tree parsing algorithm is supposed to have a user-friendly interface, because textbook generation is a semi-automatic procedure and the usability plays very important role. All the actions such as applying a pattern to a text, creating a new chapter, adding some tasks into a section should be carried out. After the tree of textbook having been composed, it is necessary to perform the formatting of the text in order to all the headlines, paragraphs, references and other “parts” of the document have the necessary format. This problem can be solved by creating a tree of text formatting. This tree contains formats of every element of the general text structure, i.e. every node of the tree includes specific pattern of text formatting that, for example, can be written in tags of the HTML markup language:

 <i> the chapter headline </i>

The tree of text formatting is fulfilled or exported by the user, in this way it will be very useful to develop some standard trees that can be downloaded and then possibly edited in the program. Obviously, the tree editor should allow changing formats using some buttons or menus, because users do not usually know HTML language. Therefore, having fulfilled the tree of text formatting and the textbook tree, complete textbook generating system is reduced to the «multiplication» of these trees. During this procedure the program sets specific text format from the first tree for every element from the second tree. Thus, the user gets a ready textbook on the output of the program.

The authors analyzed the problem of the generation and synthesis of high quality training tasks and tests based on classification of false possible answers for the most frequent types of topics. It is necessary to draw a conclusion about the need to systematize the possible errors in a single classification.

It should be noted that it is recommended to review the generated tasks in order to eliminate stylistic uncertainty.

Therefore, an experiment showing the possibility to generate this type of tests has been successfully carried out.

VI. CONCLUSION

In this paper the observation of a vector based semantic classification over the words and notions of the English language is given. It is quite effective to apply semantic vector-based classification of words and notions to build generators of semantically and grammatically meaningful phrases. Particularly, this classification was used in the real test mode to develop a test generator that can be applied by teachers of English to prepare the tests for their students. Nowadays, this program can generate tasks of only several types, so the main purpose now is to expand its possibilities in order to build a more expanded test generator. For reaching the purpose, important factors should be taken into consideration, including classification of errors, word compatibility and patterns multiplication to expand the diversity of patterns.

REFERENCES

[1] H. Avancini, A. Lavelli, F. Sebastiani, R. Zanoli., “Automatic Expansion of Domain-Specific Lexicon by Term Categorization” *ACM Translation on Speech and Language Processing*. 2006.Vol. 3. No. 1, p. 1-30.

[2] R. Higashinaka, N. Miyazaki, M. Nakano, K. Aikawa, “Evaluating Discourse Understanding in Spoken Dialogue Systems” *ACM Translation on Speech and Language Processing*. 2004. Vol.1. P. 1-20

[3] D. V. Lichargin, “Generation of tree of states based on generative grammars over the trees of string” *Vestnik SibGAU*. 2010, Vol.1 (27), p. 57-59

[4] Lichargin D.V., Taranchuk E.A. The hierarchical structure of the educational e-learning and its variability for learning a foreign language. // Journal "Distance and Virtual Learning", 2011 – №4 – pp. 56-75.

[5] Lichargin D.V., Sumaneeva J.A., Yuryeva E.V. Method of substitution tables and its application in the field of teaching Russian to foreigners // Bulletin of the Surgut State Pedagogical University, 2012 – № 6.

[6] Lichargin D.V. "Methods and tools for the generation of semantic constructs of the natural language interface of software systems." Thesis. Candidate of technical sciences: 05.13.17. / D.V. Lichargin. Protected 05.07.2004, approved. 10.12.2004; №137428. Krasnoyarsk, 2004, 154 p.

[7] Safonov K.V. The possibility of computational recognition of context-free grammars // Computational Technologies. 2005. Vol. 10. № 4. p. 91-98 (In Russ.).

Developing an approach for combining generated semantic patterns and multidimensional data arrays

Dmitry V. Lichargin, Alexandra A. Usova, Valentina V. Sotnikova,

Viktor V. Butovchenko, Elena P. Bachurina

Abstract— The purpose of the work is reduced to the need to formulate some principles of generating the learning tasks that can be used for creating educational tests to check the knowledge in order to improve the process of composing the educational materials. For solving this problem it is proposed to apply the method of multidimensional analysis of semantically vectorized data. Software for text analysis and visual representation of the text semantics, as well as automatic generation of training materials based on is successfully developed. A conclusion should be made about the need to expand this method using generated semantic templates.

Keywords— computational linguistics, generation of educational tasks, generation of meaningful speech

I. Introduction

THIS paper addresses the problem of improving the method of generating learning materials based on multi-dimensional analysis of semantic data by using the patterns of the natural language automatic generation.

Nowadays, a variety of foreign language learning systems are widely spread and developed. The problem of the development of larger amounts of learning materials is relevant due to the implementation of creative, flexible and individual learning paths.

This problem is solved in the interdisciplinary fields of sciences such as discrete mathematics, mathematical logic, theory of formal languages and grammars. The purpose of this work is to develop a hybrid approach for using the methods, like generative grammar and the method of multidimensional data.

The tasks of this work are the following:

- development of the generative grammars for creating generation patterns;
- development of a rule-base for these generative grammars;

The basic idea is to extend the functionality of the program "Generator of educational tasks", that uses multidimensional analysis of data for the analysis of the English text and that generates test materials by providing facilities of automatic generation of special patterns that refer to sections of a multidimensional database.

The novelty of this work is reduced to the hybridization of the method of multidimensional data analysis, according to the analysis of the English text with the method of generative grammars, concerning to the generation patterns, referring to sections of a multidimensional database, in order to generate a variety of learning materials.

This paper considers the problem of generating educational tasks, as well as multidimensional analysis of the data for the modeling of an abstract text in English. The problem of e-learning and the creation of autonomous programs and foreign language courses for a long time are widely studied by various authors, in particular, in the works of V.V. Kruchinin, it refers to the creation of educational software and modern control methods of learning, and he suggests ways for automatic generation test tasks in a foreign language. The solution may be the analysis of phrases, and the generation of individual phrases and texts on the basis of the account of pairs of words as the feature vectors of the multidimensional space of words as points and sentences as functions in this space. Today, a variety of programs for learning a foreign language are widely spread and developed. Therefore, the generation of educational tasks is an urgent problem.

II. Semantic classification

Let's consider a semantic classification of natural language words and notions, reduced to 16 classes of language semes (semantic, meaning «atoms») and further to four gene-semes (elementary particles of meaning), and further to a notion of link (meaning «quantum»), that can be shown based on the notional apparatus of the semantic nets. The definition based on the meaning quantum is a semantic net with arcs baring the semantics of the notion of equivalence of some elements, which means a link between objects.

Based on four elementary particles – gene-semes such as {SYSTEM, CLASSIFICATION, LOCALIZATION IN SPACE AND PERCEPTION} it is possible to determine the

Dmitry V. Lichargin is with the Siberian Federal University, Krasnoyarsk, Russia; e-mail: orderist@yandex.ru).

Alexandra A. Usova, is with the Siberian Federal University, Krasnoyarsk, Russia; e-mail: 2723434@mail.ru).

Valentina V. Sotnikova, is with the Siberian Federal University, Krasnoyarsk, Russia; e-mail: KrokoZyablik_i@mail.ru).

Viktor V. Butovchenko, is with the Siberian Federal University, Krasnoyarsk, Russia; e-mail: vbutovchenko@mail.ru).

Elena P. Bachurina is with the Siberian Federal University, Krasnoyarsk, Russia (e-mail: hellenb@mail.ru).

ISBN: 978-1-61804-321-4

semes of the natural language. LOCALIZATION IN SPACE is determined as an object, where subsystems of all the levels are similar. For example, a triangle between stars of a galaxy is similar to any proportional triangle between the houses on a planet of the star system. PERCEPTION is determined as an object, where all the subsystems (perceived) are similar to the super-systems (perceiving). For example, an image of a vase in reality, in the light flow, on the pupil of the eye, in the brain and in the consciousness will form the pyramid of information similarity. The structure is determined as an object with heterogeneous systems and super-systems. For, example, the structure of a body and the wheels of an automobile are heterogeneous. CLASSIFICATION is determined as an object with the similarity of all subsystems to the super-systems. For example, crab apples include all the properties of apples, while apples include all the properties of fruits.

Based on four gene-semes it is possible to determine 16 classes of semes. Let's show examples of such a definition for the semes class: «Basic semes».

CREATURE – perceiving and localized in space;

THING – not perceiving and localized in space;

MIND – perceiving and not localized in space;

ABSTRACTION – not perceiving and not localized in space;

IDEA – perceived and not localizing in space;

PLACE – not obligatory perceived and localized in space;

INFORMATION – perceived and localizing;

ABSTRACTION – not obligatorily perceived and not localizing.

The following basic classes of meaning atoms are determined as semes of the natural language.

Basic semes: CREATURE, PLACE, INFORMATION and others;

Semes of probability: EXISTING, NON-EXISTING, NECESSARY, POSSIBLE and the derived ones;

Semes-predicates: RELATION-X, RELATION-X-X, RELATION-CREATURE-X and others;

Semes-arguments: SUBJECT, OBJECT, RECIPIENT, INSTRUMENT and others;

Semes of localization: OF, IN, ON, AT and others;

Semes-relations: INCLUDES, IS INCLUDED IN, INCLUDES and IS INCLUDED IN, PARTIALLY INCLUDES, IS MORE THAN, IS LESS THAN and others;

Semes-numbers: digits from 0 to 15;

Semes of indefinite number: ALL, MANY, SOME, FEW, NO and others;

Semes of the language stylistics: POSITIVE – NEGATIVE, LOW – HIGH and others;

13-16. Semes, characterizing the description of images and forms: WIDE – NARROW, STABLE – UNSTABLE and others.

The problem of drawing up possible answers to the test is relevant in connection with the students' knowledge test in electronic form.

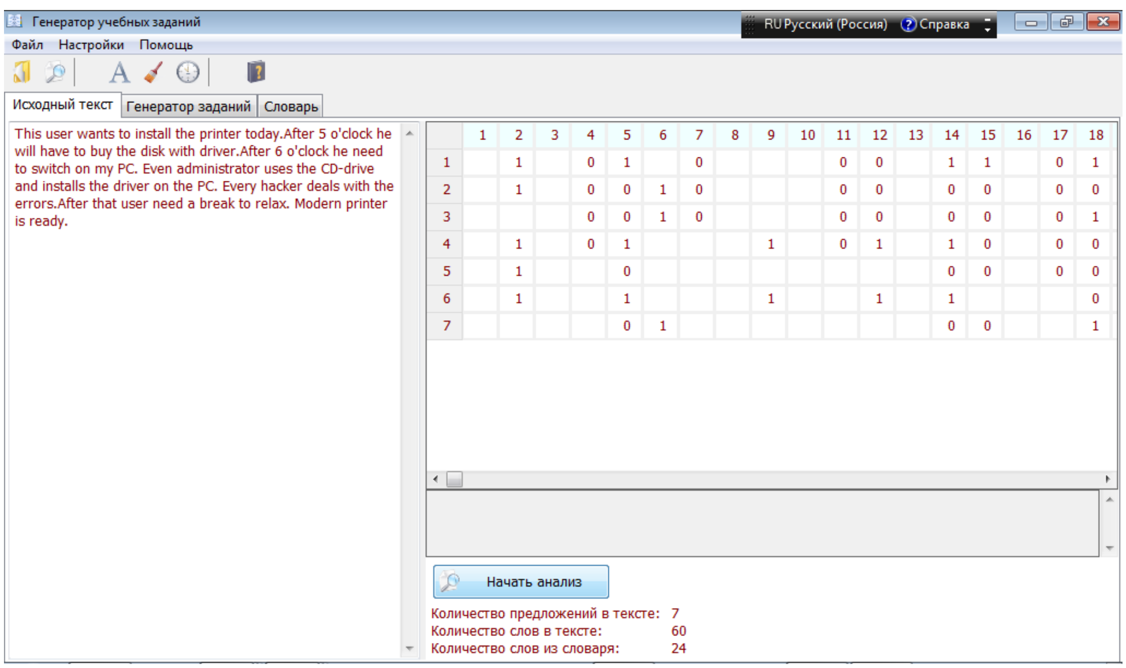

Fig. 1. The main window of program with loaded text and its visualization

The development of IT-technologies allows teachers to attempt automating the process of multi-variant tasks creation for their courses.

It is important to develop a hybrid usage of methods: generative grammar and the method of multidimensional data.

"Educational tasks generator" is a software product that will help teachers to automate the process of creating educational tests saving their time. Within the software, patterns for creating tasks and phrases are generated to match different

ISBN: 978-1-61804-321-4

cells of a multidimensional hyper-cube of words and phrasal units.

Let’s view the "Generator of educational tasks" software. A random English text is loaded in this program for analysis and generating learning tasks. The teacher finds a matching text on the lesson and puts it in the program.

Therefore, the following formula will show the method of projecting inclusion of words in a sentence onto the multidimensional and relational data subset:

$$K = F\left(\log_2 \frac{q(A)}{h}\right) \cdot F\left(\log_2 \frac{q(B)}{h}\right) \cdot F\left(\log_2 \frac{q(C)}{h}\right) \cdot F'\left(\sum_{i=1(A,B)}^{q(A,B)} \frac{1}{|S_i(A,B)\cdot k - S'(A,B)\cdot k'| + m}\right) \cdot F'\left(\sum_{i=1(B,C)}^{q(B,C)} \frac{1}{|S_i(B,C)\cdot k - S'(B,C)\cdot k'| + m}\right) \cdot F'\left(\sum_{i=1(A,C)}^{q(A,C)} \frac{1}{|S_i(A,C)\cdot k - S'(A,C)\cdot k'| + m}\right),$$

where q (A, B) is the number of pairs of words (A, B), occurring at a short distance in the proposed text corpora, h is the total number of sentences in the corpus, S_i (A, B) is the distance interval between words A and B in the i-th sentence without considering the homogeneous parts of the sentence in the body of the text, S'(A, B) is the distance between the words in the pattern of generation, k and k' are factors for increasing the value of the final small probabilities, m is a factor to avoid division by zero, K is an index that defines the acceptability of the generated phrases. The proposed formula is very different from the traditional formula of the statistical estimation of the acceptability of the generated phrases.

F and F 'are functions, such as the normal distribution of the form f (x):

$$f(x) = \frac{1}{\sigma\sqrt{2\pi}} e^{-\frac{(x-\mu)^2}{2\sigma^2}},$$

F and F 'can be expressed as other distributions, depending on the style and features of the text.

Another distributions can be as follows:

- Average;
- Linear function;
- The power function;
- Mexican Hat, etc.

In this respect after application of the formula it should be possible to process different sentences projection on the multidimensional data or the phrases generation pattern.

It is necessary to implement the various forms of software system data presentation, in particular, based on presentation of multidimensional data sets of the foreign language sentences.

III. Generated patterns

Generated patterns are the design patterns that abstract the process of inheritance. They allow making the system independent of the method of creation, composition and presentation of the syntax elements and be based only on the markers addressing the multidimensional space of words and phrasal units.

Action + -ing + Link + -(e) s + Noun (Manner);

Action + -ing + the + Object + Link + -(e) s + Noun (Manner);

Action + -ing + was + Done + Time;

Surely, + Action + -ing + was + Done + Time.

Markers such as Action, Object address to the appropriate cells of the three-dimensional data space.

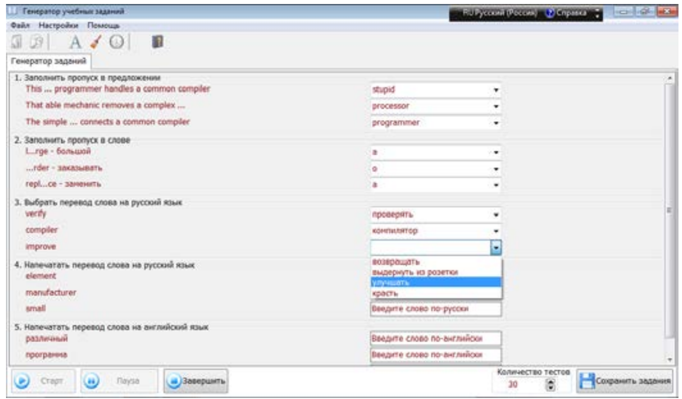

Fig.3. Passing tasks, generated by the software

On the basis of the generated generative grammar patterns modified version of the "generator of educational tasks" should give the phrase the following form:

- Eating the cake implies good appetite.
- Building means accuracy.
- Driving the bus presupposes interruptions.
- Driving the bus was carried out this morning.
- Obviously, knitting the coat was performed on Monday.

This approach will allow making a great number of tasks sets for a single text.

The approach will allow teachers to save time because this program is adopted for the user with any level of PC skills.

IV. Conclusion

This paper considers the approach for combining generated pattern and multidimensional data sets by example of a corresponding software, which can automate the work of teachers, as well as accelerate the process of test development.

References

[1] R. Goodfellow, “CALL Programs for Vocabulary Instruction / R. Goodfellow”/ Computer Assisted Language Learning Journal, Vol.8, №2, 1995. - P. 205-226.

[2] B. Ingraham, T. Chanier, C. Emery “Language Training for Various Purposes in Several Languages on a Common Hypermedia Framework” Computer & Education, Vol.23, Iss. 1 2, 1994. - P. 107-115.

[3] G. Jones, “Computer Simulations in Language Teaching - the Kingdom Experiment” System, Iss.17, 1986. – P. 35-47.

[4] D. V. Lichargin, “Generation of tree of states based on generative grammars over the trees of string” Vestnik SibGAU. 2010, Vol.1 (27), p. 57-59.

[5] D. V. Lichargin, E. P. Bachurina, “Generalized hierarchical structure of the educational e-learning course and base principles of e-learning in teaching English” Informatiztion of Education and Science. 2012. № 3 (15), p.20-36.

[6] D. V. Lichargin, A. Y. Maglinets, M. V. Ribkov, E. P. Bachurina, “Statistical methods for the analysis of natural language as a way to improve the efficiency of its generation based on semantic templates” Informatiztion of Education and Science. 2014. №4 (24), p. 92-103.

Recursive generative grammars system development for transcription automatic generation

Dmitry V. Lichargin, Mikhail M. Kucherov, Mikhail V. Rybkov, Roman Yu. Tsaryov, Ekaterina A. Chzhan

Abstract— In work the problem consisting in the development of a new class of the generative grammars is considered, it has the higher quality of strings generation capacity due to specific structure of the rules set. A model is proposed to build and use a "recursive generative grammars", which should allow solving a wider class of problems in computational linguistics.

Keywords— Computational linguistics, generative grammars with parallelism, phonetic transcription generation, recursive generative grammars.

I. Introduction

In this paper a problem of the development of a generative grammars new class providing the best quality of generating strings in terms of generating strings state trees needed for modeling subsets of the natural language is considered.

The problem of increasing the computer linguistics tools efficiency is being successfully solved by various authors referred to such sciences as discrete mathematics, software development methodology, mathematical logic, artificial intelligence techniques, etc.

This problem is conducted by various authors for a long time, in particular by A.V.Gavrilov, F. Harary, D.V.Gaskarov and others. In papers of Russian and foreign authors the question of analysis, improving, classification and hybridization of various intelligent systems is considered [1,2].

However, the issue of GG rules structure and string state trees generation regulated by generative grammars requires extra researches regarding application of command syntax elements. The purpose of this paper is to develop the model of a Recursive GG system, which allows realizing strings generation for such tasks as:

Dmitry V. Lichargin is with the Siberian Federal University, Krasnoyarsk, Russia (e-mail: orderist@yandex.ru).

Mikhail M. Kucherov is with the Siberian Federal University, Krasnoyarsk, Russia (e-mail: MKucherov@sfu-kras.ru).

Mikhail V. Rybkov is with the Siberian Federal University, Krasnoyarsk, Russia (e-mail: mixailrybkov@ya.ru).

Roman Yu. Tsaryov is with the Siberian Federal University, Krasnoyarsk, Russia (e-mail: rahatamatahata@mail.ru).

Ekaterina A. Chzhan is with the Siberian Federal University, Krasnoyarsk, Russia (e-mail: ekach@list.ru).

- words and sentences transcription generation of the natural language,
- generation of meaningful phrases of the natural language
- considering the criteria of language subsets meaningfulness, etc.

This principle will allow using the generation of meaningful language phrases more effectively with a high probability based on semantic vector-based word classification of the natural language, which is provided in paper [1].

II. Making the Case

Generative grammar allows deriving the language chains starting from some kind of initial chain by specific replacement rules (substitution rules).

It is well known that, standard generative grammars on strings have a form of four elements:

G<S, T, N, R>, where S is a generative grammars initial symbol, T is a set of terminal symbols, N is a set of non-terminal symbols, R is a set of transformation rules from one string to another.

In turn, Recursive GG will have the form of five elements: G<S, T, N, R, C>, where C is a set of substrings interpreted by its own syntax as command to string tree generation system within generative grammars.

Generation is a step-by-step process, where each step provides generating a new chain by replacement and substitution of rules being applied to the previous chain.

Software of generating correct and false transcriptions and creating a set of tasks with correct and false answers for training tests was created. This software allows choosing the language from the list; translate the chosen word or text in correct or incorrect transcription, which can be used for creating tests for more simple education control process among students and schoolchildren, who study foreign language, in particular English.

At the same time the generative grammars rules of the form of «substring$_1$» + «substring$_2$» + … + «substring$_n$» → «substring$_{1'}$» + «substring$_{2'}$» + … + «substring$_{n'}$» will have the following inclusions of the internal rules description syntax: after any string there may be a command of the form: «string$_i$» + «string$_{i+1}$» + … {rule_base_name, generation_depth, amount_of_strings}.

The example of using the proposed type of Recursive GG

ISBN: 978-1-61804-321-4

rules is shown below:

«The» + «tasty» + «cake» + «cook»+ «is … -(e)d»{constructions,4,2} + «to» + «~celebrate» + «~celebration». Wherein the «~» symbol defines words as a class of definitions, forming generative grammars non-terminal symbol.

The result of the applied set of rules of generative grammar on the second level of recursion will be the following string:

«The» + «tasty» + «cake» + «is» + «cooked» + «to» + «dance» + «at» + «Christmas».

The second example of generative grammars rules of the considered class is shown below:

«The» + _ «tasty» + / «cake» + «~tend to» {modality,2,1} \ «be cooked» + «to» + / «dance» + _ «at» \ «Christmas».

Next, we have the string: *«The» + _ «tasty» + / «cake» + «should» {modality,2,1} \ «be cooked» + «to» + _ «dance» + _ «at» \ «Christmas».*

Or: *«The» + _ «tasty» + / «cake» + «has to» {modality,2,1} \ «be cooked» + «to» + _ «dance» + _ «at» \ «Christmas»* and etc.

The method of defining semantic and grammar structure of the rules is applied on one of the levels of the natural language string tree generation, from the other side the substitution of semantic equivalents takes place for: synonyms, emotional synonyms and other types of words. The substitutions of grammatical and morphological transformations variants are used and further grammar and other categories in words meaning description often refer to different parts of the sentence, parts of speech and deeper semantics. For the final stage using one more type of generative grammars is offered: generative grammars with parallelism. These grammars allow creating parallel substitution in two parts of the string. The string *«I» [1] + «cook» + «the» + «cake» + «myself» [1]* after using the rule *~someone [1] → I [1]* and *~oneself [1] → myself [1]* is transformed into the *string «I» + «cook» + «the» + «cake» + «myself»*. The next generation stage removes symbols of type *[1]*, *[2]*, etc.

The English language, the German language and other languages should be supported by the functionality of the software viewed below.

Some fragments of the schemes of algorithmic realization for solving phonetic transcription generation problems are shown below:

- rb ++rb   rd ++rd
- rsch ++rʃ   rsh ++rʃ
- rcy ++rsy   tch ++tʃ

III. Software Realization

The following practical advantages of the viewed software «Transcription Generator» with a module for interpreting command substrings and parallel processed substrings can be designated:

• the principal possibility of generating teaching materials by using the transcription with the opportunity to view and remember string generation stage, connected to the application and such semantic phenomenon as matching personal and reflexive pronouns in English and many other;

• The possibility of generation of phonetic descriptions, combining transcription symbols and special symbols of orthography or intonation patterns.

The current program should support creating phrases like *«I need to cook the pizza» → «We managed to cook the pizza» → «We managed to fry the cutlets»* in the form of sentence classification tree.

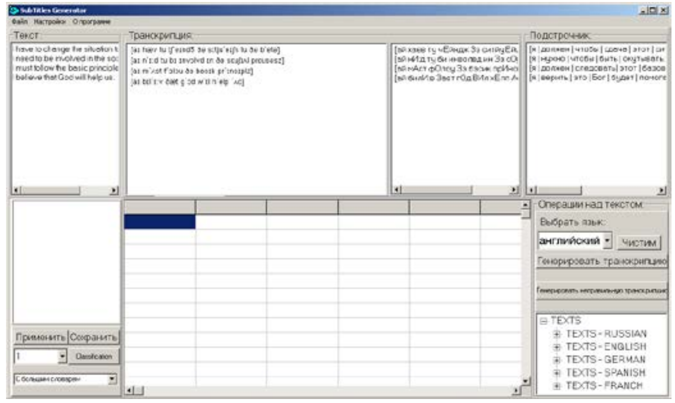

Pic 1.The resulting text after transcription in English

The algorithms providing the RGG and GGP can be supported by especially created software, i.e. generative grammars which generate command substrings for specific stages of strings tree generation up to the target strings, and then process them on the following generation stage. The software (see Pic. 1) allows working with a subtitle, allows generating learning materials for Open-and-Read method, allowing reading a text in English without preliminary knowledge of the language, in particular, due to a mini-dictionary for all words of each sentence it can be applied for creating different e-learning courses.

IV. Conclusion

Therefore, in this paper a model of RGG for increasing the efficiency of the natural language string generation rules and of the process ordering and the flexibility of generated strings tree, divided into levels – generation stages, is offered. The principles of syntax formalization, which allow forming the principle of another class of generative grammars – generative grammars with parallelism – (GGP) are offered. Examples of using RGG rules were shown.

References

[1] D. V. Lichargin, “Generation of tree of states based on generative grammars over the trees of string” *Vestnik SibGAU*. 2010, Vol.1 (27), p. 57-59

[2] Lichargin D.V. "Methods and tools for the generation of semantic constructs of the natural language interface of software systems." Thesis. Candidate of technical sciences: 05.13.17. / D.V. Lichargin. Protected 05.07.2004, approved. 10.12.2004; №137428. Krasnoyarsk, 2004, 154 p.

The time tree structure of the educational e-learning course and its variability for foreign language teaching

Ekaterina A. Chzhan, Elena P. Bachurina, Olga I. Zavyalova

***Abstract*—** In the work the problem of developing a flexible system for e-learning courses generation on the discipline "Foreign Languages" is considered. A model of building an e-learning course is offered, based on time tree, allowing arranging educational material, which should be studied within an individual trajectory – a function of parameters for the system of e-learning courses generation. The question of distributing materials within a modern e-learning course is viewed. A conclusion about the profit from ordering the e-learning course structure and the possibilities of its automatic generation is made concerning the educational system parameters, based on the primary principles of methodical science.

***Keywords*—** computer linguistics, electronic education, educational process time tree, self-directed education.

.

I. Introduction

TODAY variety of remote and self-study education including the field of foreign languages is widespread. Problems of developing the structure of e-learning course are relevant because of wide spreading of information technology.

II The hierarchical structure of the educational e-learning

The problem of developing a single hierarchical structure for e-learning courses is achieved at the junction of such sciences as linguistics, methodology, pedagogy, mathematics, logic and computer science.

The problem of creating e-learning courses is widely studied by different authors, in particular [1-3]. Electronic textbook, like any other, is designed to manage the activities of teachers and students, to reflect the conceptual approach to learning process, objectives, principles and content of studying; which in turn determines the strategy and tactics, instruction system in general. The following terms are used in the titles of many modern electronic courses:

Ekaterina A. Chzhan V. is with the Siberian Federal University, Krasnoyarsk, Russia (e-mail: ekach@list.ru)
Elena P. Bachurina is with the Siberian Federal University, Krasnoyarsk, Russia (e-mail: hellenb@mail.ru)
Olga I. Zavyalova with the Siberian Federal University, Krasnoyarsk, Russia (e-mail: zav.olga8888@mail.ru)

in education, as well as the transition to a module-rating education system, which requires a high level of academic autonomy and students independence. Properly built e-learning course provides a high awareness and motivation of students in the learning process of foreign languages, allowing students to apply the methods of self-learning and gradually move on to manage their own educational activities through self-scheduling, management, monitoring and evaluation of studying, the implementation of the results. The variable structure of e-learning courses helps students to have sufficient self learning skills; they learn to plan and organize their own learning process to do tests and examinations in time, to cope with a large amount of educational material to be learned:

- "Educational course";
- "Educational software" (software designed for use in education);
- "Computer- aided multimedia interactive learning environment";
- "Courseware" (software used for learning);
- "Hypermedia courseware" (hypermedia course);
- "Hypermedia learning system";
- "Automated training system" (ATS);
- "Automated training course" (ATC);
- "Means of computer support of learning", "electronic textbook" and others.

The following terms can be also given to refer to programs of foreign language learning:

- "CALL software package" (package of computer language learning programs);
- "Language learning system";
- "Computer learning program";
- "Computer learning system";
- "CALL system" (system of computer language learning);
- "Dedicated language learning program";
- "Computer software for language learning";
- "Computer language course";

ATS to study the language (some aspects of the language);

- "Hypertext textbook";
- "Multimedia program" and others.

However, the issue of constructing flexible models to study academic disciplines, such as foreign languages, has to be

ISBN: 978-1-61804-321-4

investigated further. It requires further research within, in particular, graph theory, system analysis, multidimensional databases [4] and the theory of classifications.

The purpose of this study is to develop a flexible model which will generate training courses in English according to the method of vectorization of large systems.

The tasks of this work are:

1. Analysis of some basic aspects of modern methods of teaching foreign languages;
2. Constructing a model of the educational process according to the time tree;
3. Constructing a model of the studying content based on multidimensional databases;
4. Description of the principle of matching fragments of the educational process time tree and multidimensional study materials databases to construct flexible electronic systems which will generate tasks, lessons and courses.

The basic idea is to construct a single hierarchical structure of educational e-learning course on the basis of modern requirements and to apply this structure to the process of learning a foreign language.

The novelty of this work is to use the model of the traditional curriculum and lesson, based on the generation of educational process time tree based on the database of study materials which applied to the development of electronic textbooks and their content with the use of the classification of natural language words and sentences proposed in work [3].

Let's look at the model of the educational process on the basis of the time tree, taking into account that it was built as a complex flexible system.

Vector of time tree

[Institution level {Nursery, kindergarten, junior school, high school, college, bachelor and specialists courses, graduate school, postgraduate, doctoral school, life-long education},

year of study {First, second, third, fourth, ...},

semester {First, second} / quarter {first, second, ...}

course structure {Introductory lesson, entrance test, Module 1, Module 2, ...},

module structure {Introduction, Lesson 1, Lesson 2, Lesson 3, ..., conclusion}

lesson structure {organization, setting, motivation, speech exercises, Exercise 1 [aspect of language {Vocabulary, grammar, ...} stages of study {Presentation, drilling, skill development, practice / project, repetition}]}

tasks block structure{Process 1 Process 2, ...},

task structure{logical progression, purpose, reminder, representation of supports / means, explanation, an example, assignment cycles (1 ... n), error analysis, estimation},

speech act structure {sentence in language 1, translation into the language 2, explanations, corrections, motivation / evaluation},

complex sentence structure {sentence 1, sentence 2}, simple sentence structure {introductory word / modifier / question word, auxiliary word, subject {determinant, adverb of degree, definition, nominal part}, predicate {compliment, adjective, verbal part}, object {determinant, adverb of degree, adjective, nominal part} nominal group {link, determinant, adverb of degree, adjective, nominal part}} verb group {}, ..., modifier},

phrase unity,

word,

morpheme,

letter,

bit of information].

In square brackets the vector defining time stages tree in learning process of foreign languages is given, value options of time tree nodes are given with a slash and in braces are the possible values of the vector coordinate that defines the tree.

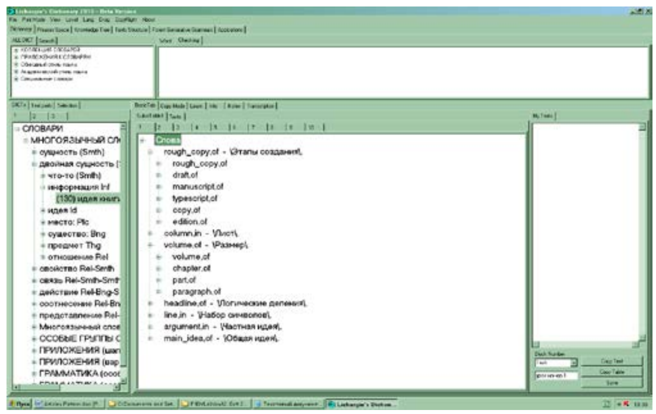

Fig. 1

General view of the interface of an "Electronic Dictionary" software system

The principles of linguistic database fragments projection on the educational process time tree does not exclude the creative activity of the developer while preparing the training courses or lessons. Therefore, the program "Electronic Dictionary" function in the mode of semi-automating generation of training materials, which allows generating a substitution table that is used for the generation of educational tasks or as a support for the method of substitution tables.

The process of filling the educational process time tree with phrases from the pattern created by the software is defined as random-automatic or human-assisted process.

The patterns form the subsets of multidimensional spaces of data. They are structured by topics: People, Food, Clothes, Transport, by word order of a classical type of a sentence: The Attribute + Doer + Modality + Action + The + Attribute + Recipient. The variants of words like: the / this + cook / vegetarian + cooks / eats + salad / apples form meaningful phrases generation patterns.

The software should generate training materials that have been proposed in the paper [5], where, in particular, the principles and algorithms of generating the learning tasks based on the natural language phrases generation are considered.

ISBN: 978-1-61804-321-4

III The processes with tubular structure

Let's consider the educational e-learning course as a process with tubular structure [6]. The tubular processes feature is in the stochastic dependence between the components of input vector.

Let the components of the input variables be linked by some unknown stochastic dependence [7]. The case where the input vector components are independent can be illustrated by the following figure:

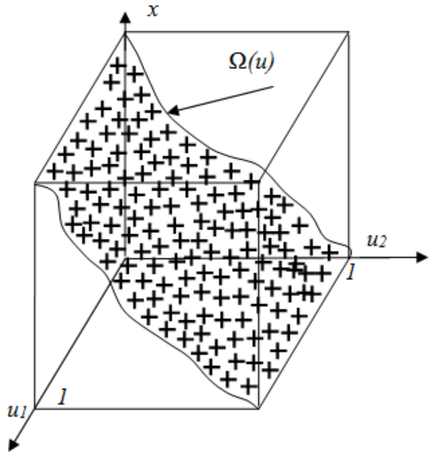

Fig.2
Sample based on observations for the case of independent components of $u(t)$ input vector

The three-dimensional case is considered for simplicity, when $x = f(u_1, u_2)$, $u_1, u_2 \in [0;1]$. The elements of the sample are shown as sign "+" in the fig. 2. It can be seen from fig. 2, the one value of $u_1(t)$ component corresponds to a set of values $u_2(t)$ component, and vice versa. If there is dependence upon different components of the input, then the process has a "tubular" structure. Such type of processes is presented in Figure 3.

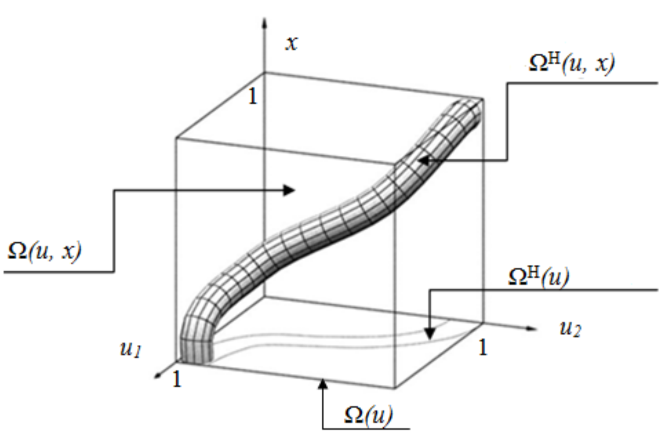

Fig.3
Object with "tubular" structure

Without loss of generality the space of the process $\Omega(u, x)$ is the unit hypercube where $u = (u_1, u_2) \in R^2$, $x \in R^1$ as can be seen from the figure 3. The hypercube space $\Omega(u, x)$ is always known in practice. For example, for the technological process values of input and output variable is limited by the technological regulations concerning the technological process. However, if the investigated data has a "tubular" structure, i.e. its input variables are linked by stochastic dependence, the process runs not in all space of a hypercube $\Omega(u, x)$, but in some of its subspace $\Omega^H(u, x) \in \Omega(u, x)$, which we have no explicitly information about. Since the subspace $\Omega^H(u, x)$ is not known, we do not know if the process is "tubular" or not. This is the main complexity modeling of this kind of processes [8, 9].

The complexity of the H-processes control is reduced to proper selection of the input $u(t)$ values. The input action $u(t)$ should belong to subspace $\Omega^H(u)$, only in this case the output variable $x(t)$ would take an appropriate value.

Otherwise, the value of the output $x(t)$ can be beyond technological regulations and can not physically be implemented (for example, the quality of chemical element in a definite material can conditionally be presented by a negative number) or be out of the "tube-shaped" distribution. It is not critical for calculations because if the output value does not belong to technological regulations, this sample element can be eliminated [10].

References

[1] D. V. Lichargin, "Generation of tree of states based on generative grammars over the trees of string" Vestnik SibGAU. 2010, Vol.1 (27), p. 57-59

[2] D. V. Lichargin, E. P. Bachurina, "Generalized hierarchical structure of the educational e-learning course and base principles of e-learning in teaching English" Informatiztion of Education and Science. 2012. № 3 (15), p.20-36

[3] D. V. Lichargin, A. Y. Maglinets, M. V. Ribkov, E. P. Bachurina, "Statistical methods for the analysis of natural language as a way to improve the efficiency of its generation based on semantic templates" Informatiztion of Education and Science. 2014. №4 (24), p. 92-103

[4] Agamdjanova V.I. Contextual Redundancy of the Lexical Meaning of a Word. –Moscow: Higher School, 1977. – 150 pp.

[5] Apresyan Yu.D. Ideas and Methods of Modern Structural Linguistics. – Moscow: Science, 1966.

[6] Medvedev A.V. Analysis of the data in the identification problem // Computer analysis of modellinf data. 1995. Vol. 2. P. 201-206.

[7] Korneeva A.A., Sergeeva N.A., Chzhan E.A. About data analysis in nonparametric identification problem // Proceedings of the tenth international conference «Computer data analysis and modeling. Theoretical and applied stochastics», Minsk. Vol. 2. 2013. P.56-60.

[8] Korneeva A.A., Sergeeva N.A., Chzhan E.A. About nonparametric data analysis in the identification problem // Vestnik TGU. Control, Computer Science and Informatics. Vol.1 (22). 2013. P.86-96.

[9] Korneeva A.A., Sergeev A.N., Chzhan E.A. Investigation of nonparametric models of tubular type processes. Vestnik SibGAU. 2012, No 5 (45). 44-49 pp.

[10] Korneeva A. A., Mihov, E. D., Chzhan, E. A. About H-models Of Noninertial System // Proceedings of the tenth international conference «Computer data analysis and modeling. Theoretical and applied stochastics», Minsk. http://elib.bsu.by/handle/123456789/111871

A New Approach on Elimination of Noise from Electrogastrogram Signals: Singular Spectrum Analysis-Wiener Filter

Ç.G. ACER, F. LATİFOĞLU, E. ÇELİKZENCİR, G. C. SEZGİN, A. YURCİ

***Abstract*—**Electrogastrogram (EGG) is cutaneous measurement for obtaining electrical activity of stomach. Filtering of EGG signals is difficult. There is no much work about filtering EGG signals. In this study, SSA with Wiener methodology was applied to EGG signals for reduction of noise. Comparison SSA-Wiener and SSA methods were carried out with results of computed variances. Also to define which electrode replacement is beter, two channel EGG signals were used and compared according to hunger and satiety stage EGG signals variance. Consequently, this study is inferred that SSA-Wiener filter is more successful than SSA and 1-4 electrode placements is more appropriate for feature extraction from EGG signals.

***Keywords*—** Singular Spectrum Analysis, Wiener Filter, Electrogastrogram, Signal processing

I. Introduction

Electrogastrogram (EGG gives information about the electrical activity of the stomach. EGG signals were obtained with surface electrodes placed on the surface of abdomen skin. First studies on EGG are reviewed by Alvarez in 1922 [1]. There are several techniques for measuring myoelectrical activity of stomach. Myoelectrical activity of stomach measured by serosal, intraluminal or electrodes placed skin of abdomen. Serosal and intraluminal records are more accuracy; also noise of these records is less but the studies are limited because of the difficulty of implementation. EGG is harmless and noninvasive method that never gives electrical stimulation to subjects. Through new developments in methodology and the measurement is noninvasive, EGG has become more widely used practice, but its clinical application is limited [2].

Diagnosis of stomach disease such as stomach cancer, ulcers, gastritis, reflux is diagnosed by invasive methods which are biopsy, endoscopy and Ph-meters. Patients are applied anesthetic during Endoscopy imaging. Ph-meter method is applied sending catheter to the stomach for measuring acid from escaping into the esophagus from stomach. For implementation of ph-meter method mounted on the nose catheter remains with individual for 24 hours. Also diagnosis of gastric emptying is performed by scintigraphic imaging. Patients are applied radionuclide for scintigraphic imaging. These are disadvantages of invasive methods. EGG signals obtained from abdominal skin is harmless and short time process.

There are slow waves giving information about stomach contraction in EGG signal and the waves have highest frequency (3 cycles per minute). Frequency range of normal electrical activity is 2.4-3.7 cpm (cycle per minute). Arrhythmia that may occur in the stomach will cause a change in the frequency spectrum of EGG signal. Bradygastria (0.2-2.4 cpm), and tachygastria (3.7-9.0 cpm) arrhythmias are the abnormality of slow waves. Using gastric dysrhythmias and motility disorders of stomach for diagnosis of many syndromes associated vomiting, nausea, stomach bloating, early satiety, reflux, it is diagnosed with EGG signal [3]-[4]-[5].

Because of there is no gold standard for placement cutaneous electrodes, different points and leads are used in scientific studies [6]-[7]-[8]-[9]. Literature shows that, studies on the acquisition and analysis of EGG signals are limited.

Main problem of EGG records is weakness of real stomach signals. Breaths, movement, cardiac artifact, electrical activity of originate other organs, such as random noise is introduced easily to the EGG signals. Respiratory artifact frequency which occurs during abnormal activities in the abdominal area is very close to frequency of the real stomach signals. Therefore filtering of EGG signals is difficult. Liang has succeeded in separating the stomach signals from noisy EGG signal with adaptive method that is achieved with a new Independent Component Analysis (ICA) [10]. Similarly, Hubka et al. have implemented ICA to 4 channels EGG signals that obtained from EGG recorder designed by them. They proved that this method was successful in noise removing [11]. Liang et al. have achieved successful elimination of artifacts from the EGG signal using Empirical Mode Decomposition [12].

Elimination noise from EGG signals is very important to extract feature from these signals. However EGG signals have low frequency and filtering of the signals is difficult. In our study, we introduced a novel SSA and Wiener methodology for elimination of noise from EGG signals. To obtain wiener filter impulse response, noise must be extracted from EGG signal. Firstly, we applied SSA algorithm for decomposition of the original EGG signal into seven components. Secondly, these components were reconstructed according to %98 representation of data. Thirdly residue signals were used for noise signals. Finally, Wiener filters were realized for filtering of EGG signals. Also EGG signals that obtained 2 channels were compared with variances and appropriate electrode placement was tried to find. Consequently we performed analysis of EGG signals from hungry and satiety stage of human.

II. Methodology

In this study, Singular Spectrum Analysis (SSA) method has been applied to EGG signals. As a result of SSA, residual data have been used to obtain noise component for Wiener Filter input. Wiener filter frequency response and a general filter transfer function has been obtained using this residue signal.. The details of the study are presented in below.

A. *Data Set*

EGG signals were obtained from 12 healthy volunteers. Volunteers were between 18-60 years old. Signals were recorded at Erciyes University Medical Faculty Hospital through a physician. EGG signals were obtained 2 channels Biopac MP-150 system using Ag-Cl cutaneous electrode as noninvasively seen in Fig. 1. First channel was recorded with 1-4 electrodes placement. Second channel was recorded with 2-3 electrodes placement.

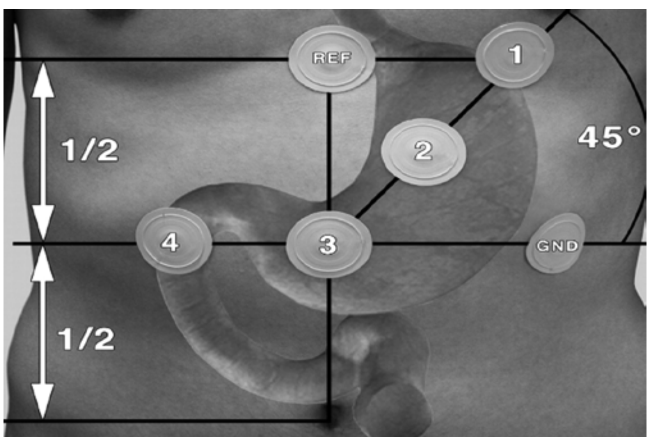

Fig. 1: Placement of Electrodes to abdomen skin.

Recordings were done with two stage during 1 hour while volunteers were relaxed and lying down. The first stage of recording was that, the volunteers were hungry. They did not eat anything up to 8 hours. The EGG signals were recorded for 30 minutes at this stage. The second stage of recording was that, the volunteers were satiated. They ate 536 kcal cheese (or turkey) sandwich and 200 ml juice. Also, the EGG signals were recorded for 30 minutes at the second stage. All calculations of this study are performed by Matlab software.

B. *Singular Spectrum Analysis (SSA):*

SSA is a new and powerful method. It is used in many fields including economics, finance, biomedical time series analysis, image processing, system identification, and modeling [14]-[16].

In literature studies, SSA has been used for filtering or forecasting process. Elimination of high frequency components without requiring the cut off frequency is reported as advantage of SSA. Therefore it is called universal filter [17].

In this study SSA method was used for two aims. The first aim is to obtain residual signals for noise input of Wiener Filter. The second aim is to obtain reconstructed signal using SSA for comparisons of SSA- Wiener methodology according to filtering performance.

SSA is a method that separates signal to associated parts using time information. This method generally consists of two main processes: decomposition and reconstruction stage.

Embedding and Singular Value Decomposition is performed at decomposition stage. Process of SSA are shown in Fig.2

X (t) signals seen in equation 1, is embedded with L length window as seen in equation 2.

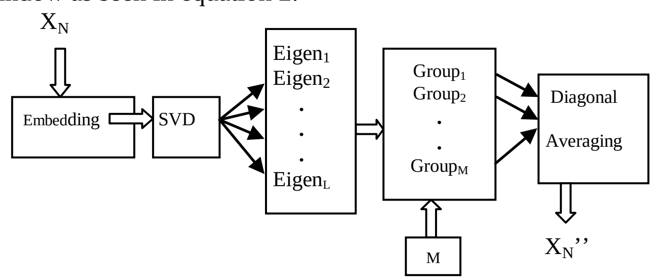

Fig. 2: Stages of Singular Spectrum Analysis Method

$$X= [X_1,X_2,X_3,\ldots\ldots,X_N] \tag{1}$$

$$X = \begin{bmatrix} X_1 & X_2 & \cdots & X_L \\ X_2 & X_3 & \cdots & X_{L+1} \\ \vdots & \vdots & \ddots & \vdots \\ X_K & X_{K+1} & \cdots & X_N \end{bmatrix} \tag{2}$$

The X (t) signal as a matrix form is named with Hankelization matrix. KxL-dimensional matrix obtained with embedding process is called as trajectory matrix. The window length is defined as half of period for periodic signals. In this study, window length L is chosen seven.

After embedding step, Singular Value Decomposition (SVD) is applied. SVD is a linear algebra method. In this step, decomposed trajectory matrices T_i are obtained for i = 1…L. Trajectory matrix T_x is decomposed three matrices called by eigentriples $T_x=USV^T$. U_i for $1 < i < L$ is a KxK orthonormal matrix. V_i for $1 < i < L$ is LxL orthonormal matrix. S_i for $1 < i < L$ is LxK diagonal matrix. The diagonal elements of the S matrix are called the singular values of T_x matrix [13]-[14]. Grouping process decomposes the LxK matrix Ti into subgroups according to the trend, seasonal, monthly components, and white noises. In the last step of SSA algorithm, the diagonal averaging step transforms the grouped matrices T_{gi} into a new time series of length N [15].

In this study, Reconstructed and residual signals using SSA in hungry stage is shown in Fig. 3 and Fig. 4.

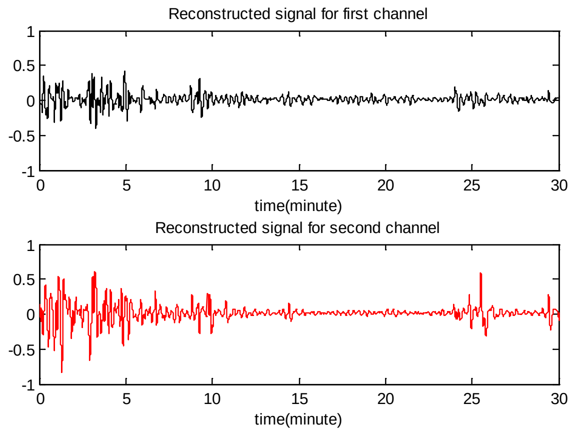

Fig. 3: Reconstructed EGG signal with SSA

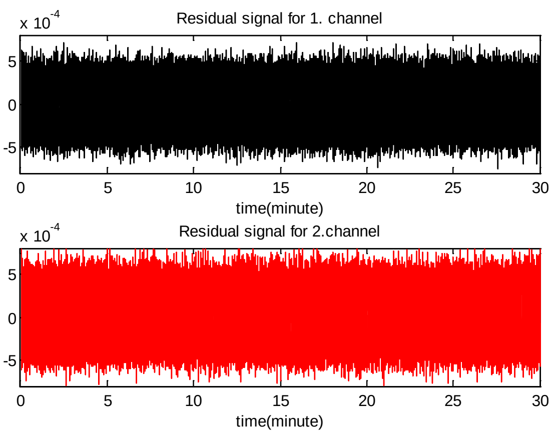

Fig. 4: Residue signal obtained by SSA

C. *Wiener Filter:*

Wiener theory, presented by Norbert Wiener, depends on minimizing difference between desired signal and filter output. This method tries minimizing mean square error. Wiener filters are used in wide range of applications such as linear prediction, echo cancellation, signal restoration, channel equalization, noise removing and system identification [18].

Important step of Wiener filtering is obtaining a noise and noise free (optimal) signal estimation. The signal and the (additive) noise are assumed to be stationary linear stochastic processes with known spectral characteristics or known autocorrelation and cross-correlation. [18].

Frequency domain formulation has been used for Wiener Filter frequency response. Residual signal obtained by SSA is assumed as noise (n(t)) for Wiener filter input. Steps of process are shown in Fig. 5.

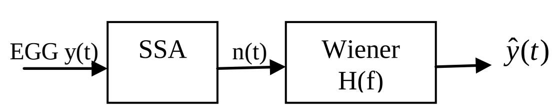

Fig. 5: Steps of study

In the frequency domain, Wiener filter output $\hat{Y}(f)$ is product of the input signal $N(f)$ and filter frequency response $H(f)$:

$$\hat{Y}(f) = H(f).N(f) \tag{3}$$

Error signal $E(f)$ is equal to difference between the desired signal $Y(f)$ and the filter output $\hat{Y}(f)$:

$$E(f) = Y(f) - \hat{Y}(f) \tag{4}$$

$$E(f) = Y(f) - H(f)N(f)$$

The mean square error at a frequency f is given by equation (5)

$$E\left[\left|E(f)\right|^2\right] = E\left[\left(Y(f) - H(f).N(f)\right)^*\left(Y(f) - H(f).N(f)\right)\right] \tag{5}$$

E[.] is expectation function and * symbol is meaning of complex conjugate.

Wiener filter frequency response is obtained with minimized mean square error:

$$\frac{\partial E\left[\left|E(f)\right|^2\right]}{\partial H(f)} = 2H(f)P_{nn}(f) - 2P_{yn}(f) = 0 \tag{6}$$

$P_{nn}(f) = E\left[N(f)N^*(f)\right]$ and $P_{yn}(f) = E\left[Y(f)N^*(f)\right]$ are power spectrum of N(f), and cross-power spectrum of Y(f) and N(f) [18]. From equation (6) the least mean square error Wiener filter in the frequency domain is given as:

$$H(f) = \frac{P_{yn}(f)}{P_{nn}(f)} \tag{7}$$

If y(t) is considered noisy EGG signal, consist of a signal x(t) (desired) and noise $y(t) = x(t) + n(t)$. Here, signal and noise are assumed as uncorrelated. The autocorrelation matrix of noisy signal is sum of the autocorrelation matrix of the signal x(t) and the noise n(t):

$$R_{yy} = R_{xx} + R_{nn} \tag{8}$$

And because of signal and noise are uncorrelated;

$$r_{xy} = r_{xx} \tag{9}$$

Equation (9) can be written. In the equation r_{xy} is the cross-correlation vector of the noisy signal and the noise-free signal.

$$h = R_{yy}^{-1} r_{yx} \tag{10}$$

Substitution of Equations (8) and (9) in the Wiener filter, Equation (10), yields

$$h = \left(R_{xx} + R_{nn}\right)^{-1} r_{xx} \tag{11}$$

Equation (11) is the optimal linear filter for removal of noise. In the frequency domain, the noisy signal *Y(f)* is sum of *X(f)* and *N(f)* that are the signal and noise spectra.

In additive random noise, the frequency-domain Wiener filter is obtained as

$$H(f) = \frac{P_{XX}(f)}{P_{XX}(f) + P_{NN}(f)} \tag{12}$$

$P_{XX}(f)$ *and* $P_{NN}(f)$ are the signal and noise power spectra [18].

Traditionally, Burg's, Welch and Fast Fourier Transform (FFT) methods are used to obtain Power Spectral Density. The FFT method is very sensitive to noise. The Welch method has windowing problem. The Burg's method does not apply window to data and not very sensitve to noise. Therefore Burg's method was used for calculation of Power Spectral Density in this study.

General Wiener Filter was applied to above equations. The Wiener Filter implemented to all EGG signals. Result of filter is shown in Fig. 6.

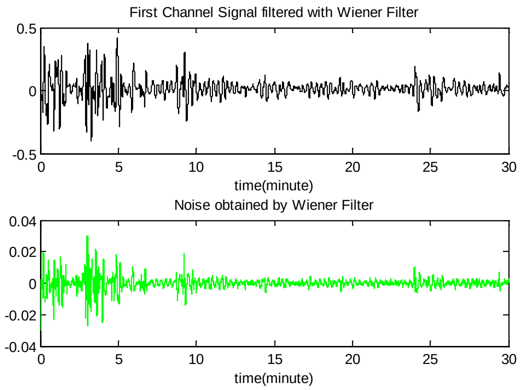

Fig. 6: Result of Wiener Filter

III. Results and Discussion

To the best of our knowledge, there aren't any studies about application of SSA and Wiener methodology together to the EGG signals. General Wiener filter transfer function was obtained with proposed process. After that the EGG signals were filtered using Wiener filter. Therefore filtered signals and noisy signals (noisy signals= EGG signals- filtered signals) obtained using proposed process.

Variance gives information about distribution of the data. Zero variance indicates that all values are identical in the data. In this study, filtered and noisy signals using Wiener filter variance were calculated. Also recontructed and residual signals using SSA variances were calculated for comparison. Table I- IV show raw EGG, reconstructed using SSA and filtered using Wiener signals variances for hungry and satiety stage for first and second channel. Table V shows noisy signals variances derived from Wiener and SSA method for hungry stage. Table VI shows noisy signals variances derived from Wiener and SSA method for satiete stage.

Table I: Variances for *first channel* data of *Hungry Stage*

	Raw	SSA	Wiener
1	0.005767663	0.005767595	0.005754461
2	0.000695801	0.000695769	0.000694819
3	0.008862517	0.008862437	0.008844062
4	0.001746156	0.001746120	0.001743291
5	0.008304796	0.008304709	0.008285162
6	0.000343096	0.000343066	0.000342421
7	0.007354663	0.007354605	0.007344266
8	0.000280684	0.000280655	0.000280189
9	0.000595678	0.000595646	0.000594445
10	0.008229863	0.008229798	0.008210896
11	0.000944295	0.000944261	0.000942589
12	0,001227819	0,001227785	0,001225957

Table II: Variances for *first channel* data of *Satiety Stage*

	Raw	SSA	Wiener
1	0.007948941	0.007948878	0.007937027
2	0.001353996	0.001353960	0.001351194
3	0.186685174	0.186684576	0.186496731
4	0.078018781	0.078018547	0.077950087
5	0.011488313	0.011488243	0.011474474
6	0.001863977	0.001863940	0.001860643
7	0.011569886	0.011569813	0.011554159
8	0.002257378	0.002257339	0.002253828
9	0.001439715	0.001439678	0.001437071
10	0.030896897	0.030896746	0.030854896
11	0.010519856	0.010519786	0.010506137
12	0,001882740	0,001882701	0,001879318

Table III: Variances for *second channel* data of *Hungry Stage*

	Raw	SSA	Wiener
1	0.014646013	0.014645897	0.014619466
2	0.002721200	0.002721156	0.002717312
3	0.007159323	0.007159252	0.007147134
4	0.002128677	0.002128637	0.002126009
5	0.001108390	0.001108347	0.001105427
6	0.599207539	0.599207503	0.599567577
7	1.309163782	1.309163548	1.309210835
8	0.666675623	0.666675581	0.667344586
9	0.000107201	0.000107167	0.000106961
10	0.003809854	0.003809800	0.003804869
11	0.000340399	0.000340361	0.000339829
12	0,000703605	0,000703566	0,000702199

Table IV: Variances for *second channel* data of *Satiety Stage*

	Raw	SSA	Wiener
1	0.004023796	0.004023741	0.004017446
2	0.003068585	0.003068531	0.003061660
3	0.021107761	0.021107603	0.021024459
4	0.012208304	0.012208229	0.012194765
5	0.001542481	0.001542436	0.001539500
6	0.068360302	0.068360258	0.068830979
7	3.968475297	3.968475188	3.968367363
8	0.704702109	0.704701859	0.705240456
9	0.000205547	0.000205512	0.000205147
10	0.034374009	0.034373868	0.034338305
11	0.005908115	0.005908056	0.005900412
12	0,001637588	0,001637545	0,001635215

Table V: Variance values for *noise signals* of *Hungry Stage*

	First Channel		Second Channel	
	SSA noise	Wiener Noise	SSA noise	Wiener Noise
1	2.58E-08	1.54E-05	3.31E-08	3.13E-05
2	2.56E-08	1.15E-06	2.98E-08	4.28E-06
3	2.46E-08	2.17E-05	3.16E-08	1.42E-05
4	2.50E-08	3.18E-06	2.94E-08	3.03E-06
5	2.48E-08	2.29E-05	3.09E-08	3.51E-06
6	2.54E-08	8.04E-07	3.22E-08	1.58E-05
7	2.39E-08	1.22E-05	7.20E-08	1.09E-04

ISBN: 978-1-61804-321-4

8	2.46E-08	5.92E-07	3.37E-08	4.12E-06
9	2.55E-08	1.41E-06	3.02E-08	2.78E-07
10	2.59E-08	1.43E-05	3.49E-08	5.91E-06
11	2.59E-08	1.61E-05	3.29E-08	6.75E-07
12	2,52E-08	2,12E-06	3,17E-08	1,59E-06

Table VI: Variance values for *noise signals* of *Satiety Stage*

	First Channel		Second Channel	
	SSA noise	Wiener Noise	SSA noise	Wiener Noise
1	2,61E-08	1,39E-05	3,29E-08	7,36E-06
2	2,59E-08	3,13E-06	3,07E-08	8,11E-06
3	2,60E-08	2,19E-05	3,28E-08	8,84E-05
4	2,55E-08	8,11E-05	3,00E-08	1,61E-05
5	2,55E-08	1,64E-05	3,16E-08	3,55E-06
6	2,47E-08	3,88E-06	3,34E-08	3,18E-04
7	2,57E-08	1,75E-05	3,04E-08	3,95E-05
8	2,54E-08	4,15E-06	1,86E-07	3,27E-04
9	2,57E-08	3,13E-06	3,04E-08	4,52E-07
10	2,59E-08	4,79E-05	3,32E-08	4,09E-05
11	2,59E-08	1,61E-05	3,26E-08	9,11E-06
12	2,55E-08	4,00E-06	3,20E-08	2,72E-06

When Table I and Table II are analyzed, variance in satiety is always higher than hunger stage. This shows that signal is similar when stomach is empty. The feature of variance at hunger and satiety stage can be descriptive for stomach diseases. In future studies comparisons can be done by including disease group.

Variance changes are not distinct at hunger and satiety stage, when Table III-IV are examined. According to this result, 1-4 electrode placement is more appropriate for feature extraction from EGG signals.

Table V and Table VI show that noise obtained by SSA has always lowest variance than noise obtained by Wiener filter. Also Wiener filter reduces variance of signal better than SSA. Signal has low frequency with Wiener filter. This means SSA-Wiener methodology is better than SSA for noise reduction of EGG signals.

ACKNOWLEDGMENT

This study was approved by the Erciyes University Ethical Committee with the registration number of 2015/115.

IV. REFERENCES

[1] WC. Alvarez, The electrogastrogram and what it shows. JAMA, 1922, vol. 78, pp. 1116–8.

[2] K.L Koch, R.M Stern, W.R Stewart, MW. Vasey, Electrogastrography: current issues in validation and methodology, Psychophysiology, 1987, vol. 24, pp. 55–64.

[3] P. Camborova, P. Hubka, I. Sulkova, I. Hulin, The pacemaker activity of interstitial cells of Cajal and gastric electrical activity, Physiol Res, 2003, vol. 52, pp. 275-284.

[4] J.D. Huizinga, T.L. Robinson, L. Thomsen, The search for the origin of rhythmicity in intestinal contraction; from tissue to single cells, Neurogastroenterol. Motil, 2000, vol. 12, pp. 3-9.

[5] Electrogastrogram: Wikipedia, the free encyclopedia.

[6] J.H. Szıjrszewskı, T.Y. El-Sharkawy, K.G., Morgan, Intracellular Electrical Activity of Canine and Human Gstric Smooth Muscle, J. Physiol., 1978, vol. 279, pp. 291-307.

[7] H. P. Parkman, W. L. Hasler, J. L. Barnett, E. Y. Eaker, Electrogastrography: a document prepared by the gastric section of the American Motility Society Clinical GI Motility Testing Task Force, Neurogastroenterol Motil, 2003, vol. 15, pp. 89–102.

[8] B.E. Bellahsene, J.W. Hamilton, J.G. Webster, P. Bass, M. Reıchelderfer, An Improved Method for Recording and Analyzing the Electrical Activity of tie Human Stomach, IEEE Transactions on Biomedical Engineering, vol. 32(11), 1985.

[9] T. J. Contreras, M. A. Mayen , A. Servin, L. I. Garay, System for acquisition and analysis of multichannel electrogastrogram, 7th International Conference on Electrical Engineering, Computing Science and Automatic Control, 2010, pp. 220-224.

[10] H. Liang, Adaptive independent component analysis of multichannel electrogastrograms, Medical Engineering & Physics, 2001, vol. 23, pp. 91–97.

[11] P. Hubka, V. Rosík, J. Ždiňák, M. Tyšler, I. Hulín, Independent Component Analysis of Electrogastrographic Signals, Measurement Science Review, vol. 5(2), 2005,pp. 21-24.

[12] H. Liang, Z. Lin, R.W. McCallum, Artifact reduction in electrogastrogram based on empirical mode decomposition method., Med Biol Eng Comput, 2000, vol. 38(1), pp. 35-41.

[13] G. Stewart, On the early history of the singular value decomposition, *SIAM Review*, vol. 35(4), pp. 551–566,1993.

[14] H. Hassani, Singular Spectrum Analysis: Methodology and Comparison ,*Journal of Data Science*, vol. 5, pp. 239-257,2007.

[15] N. Golyandina, V. Nekrutkin, A. Zhigljavsky, Analysis of Time Series Structure: SSA and Related Techniques. Chapman & Hall/crc, 2001.

[16] S. H. Iranmanesh, A. Miranian, M. Abdollahzade, Signal processing using singular spectrum analysis for nonlinear system identification, Information Science Signal Processing and their Applications (ISSPA) 11th International Conference on, 2012, pp. 722-727.

[17] C. Mert, A. Milnikov, Singular Spectrum Analysis Method as a Universal Filter, Application of Information and Communication Technologies (AICT), pp. 1-5, 2011.

[18] SV. Vaseghi, Advanced Digital signal Processing and Noise Reduction, Second Edition", John Wiley & Sons Inc, USA, 2000.

Adaptive Multivariable Continuous-Time 2DOF Control

Marek Kubalcik, Vladimir Bobal

Abstract— The paper is focused on a design and implementation of a 2DOF (two degree of freedom) multivariable controller. The controller was designed in continuous-time version. The control algorithm is based on polynomial theory and pole – placement. The controller integrates an on – line identification of an ARX model of a controlled system and a control synthesis on the basis of the identified parameters. Since derivatives of input and output variables of continuous – time systems can not be directly measured, differential filters and filtered variables are established to substitute primary variables. The filtered variables are then used in a recursive identification procedure where the classical recursive least squares method is used to identify the system.

Keywords— multivariable control, control algorithms, adaptive control, polynomial methods, pole assignment, recursive identification

I. Introduction

TYICAL technological processes require the simultaneous control of several variables related to one system. Each input may influence all system outputs. The design of a controller for such a system must be quite sophisticated if the system is to be controlled adequately. There are many different methods of controlling MIMO (multi input – multi output) systems [1]. Several of these use decentralized PID controllers [2]. The classical approach to the control of multi-input–multi-output (MIMO) systems is based on the design of a matrix controller to control all system outputs at one time. The basic advantage of this approach is its ability to achieve optimal control performance because the controller can use all the available information about the controlled system. Controllers are based on various approaches and various mathematical models of controlled processes. A standard technique for MIMO control systems uses polynomial methods [3], [4], [5] and is also used in this paper. Controller synthesis is reduced to the solution of linear Diophantine equations [6].

One controller, which enables control of TITO (two input-two output) systems, is presented. The proposed control algorithm is based on the 2DOF (two degree of freedom) configuration [7]. The controller was realized in continuous-time version. The controller was realized both with fixed parameters and as a self-tuning controller [8], [9] with recursive identification of a model of the controlled system. The recursive least squares method was used in the identification part.

Marek Kubalčík is with Tomas Bata University in Zlín, Faculty of Applied Informatics, Nám. T. G. Masaryka 5555, 760 05 Zlín (corresponding author to provide phone: +420 57-603-5198; e-mail: kubalcik@ fai.utb.cz).

Vladimír Bobál is with Tomas Bata University in Zlín, Faculty of Applied Informatics, Nám. T. G. Masaryka 5555, 760 05 Zlín (e-mail: bobal@fai.utb.cz).

II. Model Of the Controlled system

A general transfer matrix of a two-input–two-output system with significant cross-coupling between the control loops is expressed as

$$\boldsymbol{G}(s)=\begin{bmatrix} G_{11}(s) & G_{12}(s) \\ G_{21}(s) & G_{22}(s) \end{bmatrix} \tag{1}$$

$$\boldsymbol{Y}(s)=\boldsymbol{G}(s)\boldsymbol{U}(s) \tag{2}$$

Where $\boldsymbol{U}(s)$ and $\boldsymbol{Y}(s)$ are vectors of the manipulated variables and the controlled variables.

$$\boldsymbol{Y}(s)=[y_1(s), y_2(s)]^T \quad \boldsymbol{U}(s)=[u_1(s), u_2(s)]^T \tag{3}$$

It may be assumed that the transfer matrix can be transcribed to the following form of the matrix fraction:

$$\boldsymbol{G}(s)=\boldsymbol{A}^{-1}(s)\boldsymbol{B}(s)=\boldsymbol{B}_1(s)\boldsymbol{A}_1^{-1}(s) \tag{4}$$

where the polynomial matrices $\boldsymbol{A}\in R_{22}[s]$, $\boldsymbol{B}\in R_{22}[s]$ represent the left coprime factorization of matrix $\boldsymbol{G}(s)$ and the matrices $\boldsymbol{A}_1\in R_{22}[s]$, $\boldsymbol{B}_1\in R_{22}[s]$ represent the right coprime factorization of $\boldsymbol{G}(s)$ .The further described algorithm is based on a model with polynomials of second order. This model proved to be effective for control of several TITO laboratory processes [10], where controllers based on a model with polynomials of the first order failed.

$$\boldsymbol{A}(s)=\begin{bmatrix} s^2+a_1s+a_2 & a_3s+a_4 \\ a_5s+a_6 & s^2+a_7s+a_8 \end{bmatrix} \tag{5}$$

$$\boldsymbol{B}(s)=\begin{bmatrix} b_1s+b_2 & b_3s+b_4 \\ b_5s+b_6 & b_7s+b_8 \end{bmatrix} \tag{6}$$

Differential equations describing dynamical behavior of the system are as follows

$$\begin{aligned} & y_1'' + a_1 y_1' + a_2 y_1 + a_3 y_2' + a_4 y_2 = \\ & = b_1 u_1' + b_2 u_1 + b_3 u_2' + b_4 u_2 \end{aligned} \tag{7}$$

$$\begin{aligned} & y_2'' + a_5 y_1' + a_6 y_1 + a_7 y_2' + a_8 y_2 = \\ & = b_5 u_1' + b_6 u_1 + b_7 u_2' + b_8 u_2 \end{aligned} \tag{8}$$

III. Design of the 2DOF Controller

The 2DOF configuration of the closed loop system is depicted in Fig. 1. It was presented in [7] for SISO control loop.

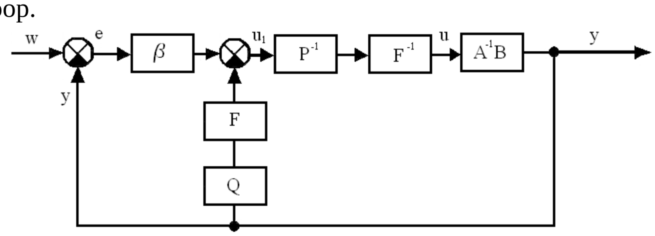

Fig. 1 Block diagram of 2DOF configuration

Generally, the vector of input reference signals $\boldsymbol{W}$ is specified as

$$\boldsymbol{W}(s) = \boldsymbol{F}_w^{-1}(s)\boldsymbol{h}(s) \tag{9}$$

Further the reference signals are considered as step functions. In this case $\boldsymbol{h}$ is a vector of constants and $\boldsymbol{F_w}$ is expressed as

$$\boldsymbol{F}_w(s) = \begin{bmatrix} s & 0 \\ 0 & s \end{bmatrix} \tag{10}$$

The compensator $\boldsymbol{F}$ is a component formally separated from the controller. It has to be included in the controller to fulfil the requirement on the asymptotic tracking. If the reference signals are step functions, then $\boldsymbol{F}$ is an integrator.

It is possible to derive the following equation for the system output

$$\boldsymbol{Y} = \boldsymbol{A}^{-1}\boldsymbol{B}\boldsymbol{U} = \boldsymbol{A}^{-1}\boldsymbol{B}\boldsymbol{F}^{-1}\boldsymbol{P}^{-1}\boldsymbol{U}_1 \tag{11}$$

Where

$$\boldsymbol{U}_1 = \boldsymbol{\beta}(\boldsymbol{W} - \boldsymbol{Y}) - \boldsymbol{Q}\boldsymbol{F}\boldsymbol{Y} \tag{12}$$

The corresponding equation for the controller's output, as shown in the block diagram in Fig. 1, follows as

$$\boldsymbol{U} = \boldsymbol{F}^{-1}\boldsymbol{P}^{-1}\boldsymbol{U}_1 \tag{13}$$

The substitution of $\boldsymbol{U}_1$ and $\boldsymbol{Y}$ results in

$$\boldsymbol{U} = \boldsymbol{F}^{-1}\boldsymbol{P}^{-1}\left[\boldsymbol{\beta}\left(\boldsymbol{W} - \boldsymbol{A}^{-1}\boldsymbol{B}\boldsymbol{U}\right) - \boldsymbol{Q}\boldsymbol{F}\boldsymbol{A}^{-1}\boldsymbol{B}\boldsymbol{U}\right] \tag{14}$$

The equation (12) can be modified using the right matrix fraction of the controlled system into the form

$$\boldsymbol{U} = \boldsymbol{A}_1\left[\boldsymbol{P}\boldsymbol{F}\boldsymbol{A}_1 + (\boldsymbol{\beta} + \boldsymbol{F}\boldsymbol{Q})\boldsymbol{B}_1\right]^{-1}\boldsymbol{\beta}\boldsymbol{W} \tag{15}$$

The determinant of the matrix in the denominator $\boldsymbol{P}\boldsymbol{F}\boldsymbol{A}_1 + (\boldsymbol{\beta} + \boldsymbol{F}\boldsymbol{Q})\boldsymbol{B}_1$ is the characteristic polynomial of the MIMO system. The roots of this polynomial matrix determine the behaviour of the closed loop system. They must be placed on the left side of the Gauss complex plane for the system to be stable. Conditions of BIBO stability can be defined by the following Diophantine matrix equation:

$$\boldsymbol{P}\boldsymbol{F}\boldsymbol{A}_1 + (\boldsymbol{\beta} + \boldsymbol{F}\boldsymbol{Q})\boldsymbol{B}_1 = \boldsymbol{M} \tag{16}$$

where $\boldsymbol{M} \in R_{22}[s]$ is a stable diagonal polynomial matrix. If the system has the same number of inputs and outputs, matrix $\boldsymbol{M}$ can be chosen as diagonal, which allows easier computation of the controller parameters. Correct pole placement of the matrix $\boldsymbol{M}$ is very important for good control performance.

$$\boldsymbol{M}(s) = \begin{bmatrix} \begin{array}{l} s^4 + m_1 s^3 + \\ + m_2 s^2 + m_3 s + m_4 \end{array} & 0 \\ 0 & \begin{array}{l} s^4 + m_5 s^3 + m_6 s^2 + \\ + m_7 s + m_8 \end{array} \end{bmatrix} \tag{17}$$

The degree of the controller polynomial matrices depends on the internal properness of the closed loop. The structures of matrices $\boldsymbol{P}$, $\boldsymbol{Q}$ and $\boldsymbol{\beta}$ were chosen so that the number of unknown controller parameters equals the number of algebraic equations resulting from the solution of the Diophantine equation (16) using the method of uncertain coefficients:

$$\boldsymbol{P} = \begin{bmatrix} s + p_1 & p_2 \\ p_3 & s + p_4 \end{bmatrix} \tag{18}$$

$$\boldsymbol{Q} = \begin{bmatrix} q_1 s + q_2 & q_3 s + q_4 \\ q_5 s + q_6 & q_7 s + q_8 \end{bmatrix} \tag{19}$$

$$\boldsymbol{\beta} = \begin{bmatrix} \beta_1 & \beta_2 \\ \beta_3 & \beta_4 \end{bmatrix} \tag{20}$$

The solution of the Diophantine equation results in a set of algebraic equations with unknown controller parameters. Using matrix notation, the algebraic equations are expressed in the following form.

$$\begin{bmatrix} 1 & a_1 & a_2 & 0 & 0 & a_3 & a_4 & 0 \\ 0 & a_5 & a_6 & 0 & 1 & a_7 & a_8 & 0 \\ b_1 & b_2 & 0 & 0 & b_3 & b_4 & 0 & 0 \\ 0 & b_1 & b_2 & 0 & 0 & b_3 & b_4 & 0 \\ b_5 & b_6 & 0 & 0 & b_7 & b_8 & 0 & 0 \\ 0 & b_5 & b_6 & 0 & 0 & b_7 & b_8 & 0 \\ 0 & 0 & b_1 & b_2 & 0 & 0 & b_3 & b_4 \\ 0 & 0 & b_5 & b_6 & 0 & 0 & b_7 & b_8 \end{bmatrix} \begin{bmatrix} p_1 \\ p_2 \\ q_1 \\ q_2 \\ q_3 \\ q_4 \\ \beta_1 \\ \beta_2 \end{bmatrix} = \begin{bmatrix} m_1 - a_9 \\ m_2 - a_{10} \\ m_3 \\ m_4 \\ -a_{11} \\ -a_{12} \\ 0 \\ 0 \end{bmatrix} \tag{21}$$

$$\begin{bmatrix} 1 & a_1 & a_2 & 0 & 0 & a_3 & a_4 & 0 \\ 0 & a_5 & a_6 & 0 & 1 & a_7 & a_8 & 0 \\ b_1 & b_2 & 0 & 0 & b_3 & b_4 & 0 & 0 \\ 0 & b_1 & b_2 & 0 & 0 & b_3 & b_4 & 0 \\ b_5 & b_6 & 0 & 0 & b_7 & b_8 & 0 & 0 \\ 0 & b_5 & b_6 & 0 & 0 & b_7 & b_8 & 0 \\ 0 & 0 & b_1 & b_2 & 0 & 0 & b_3 & b_4 \\ 0 & 0 & b_5 & b_6 & 0 & 0 & b_7 & b_8 \end{bmatrix} \begin{bmatrix} p_3 \\ p_4 \\ q_5 \\ q_6 \\ q_7 \\ q_8 \\ \beta_3 \\ \beta_4 \end{bmatrix} = \begin{bmatrix} -a_{13} \\ -a_{14} \\ 0 \\ 0 \\ m_5 - a_{15} \\ m_6 - a_{16} \\ m_7 \\ m_8 \end{bmatrix} \tag{22}$$

The control law is defined as:

$$\boldsymbol{FPU} = \boldsymbol{\beta E} - \boldsymbol{FQY} \tag{23}$$

where $\boldsymbol{E}$ is a vector of control errors. This matrix equation can be transcribed to the differential equations of the controller

$$\begin{aligned} & u_1'' + p_1 u_1' = \\ & = \beta_1 e_1 + \beta_2 e_2 - q_1 y_1'' - q_2 y_1' - q_3 y_2'' - q_4 y_2' - p_2 u_2' \end{aligned} \tag{24}$$

$$\begin{aligned} & u_2'' + p_4 u_2' = \\ & = \beta_3 e_1 + \beta_4 e_2 - q_5 y_1'' - q_6 y_1' - q_7 y_2'' - q_8 y_2' - p_3 u_1' \end{aligned} \tag{25}$$

For purposes of simulation, the controller was realized in the Matlab/Simulink environment as an S-function. It was then necessary to obtain its state equations. Further there it is introduced a conversion of the first differential equation (24) to the state equations. The second differential equation (25) was converted similarly. Equation (24) can be itemized as follows

$$\begin{aligned} u_{1A}'' + p_1 u_{1A}' &= e_1 \beta_1 \\ u_{1B}'' + p_1 u_{1B}' &= e_2 \beta_2 \\ u_{1C}'' + p_1 u_{1C}' &= -q_1 y_1'' - q_2 y_1' \\ u_{1D}'' + p_1 u_{1D}' &= -q_3 y_2'' - q_4 y_2' \\ u_{1E}'' + p_1 u_{1E}' &= -p_2 u_2' \end{aligned} \tag{26}$$

Equation (26) can be transcribed to transfer functions. It is also possible to establish auxiliary variables Z_1, Z_2, Z_3, Z_4 and Z_5.

$$\begin{aligned} G_1(s) &= \frac{\beta_1}{s^2 + p_1 s} = \frac{U_{1A}}{E_1} = \frac{U_{1A}}{Z_1}\frac{Z_1}{E_1} \\ G_2(s) &= \frac{\beta_2}{s^2 + p_1 s} = \frac{U_{1B}}{E_2} = \frac{U_{1B}}{Z_2}\frac{Z_2}{E_2} \\ G_3(s) &= \frac{-q_1 s^2 - q_2 s}{s^2 + p_1 s} = \frac{U_{1C}}{Y_1} = \frac{U_{1C}}{Z_3}\frac{Z_3}{Y_1} \\ G_4(s) &= \frac{-q_3 s^2 - q_4 s}{s^2 + p_1 s} = \frac{U_{1D}}{Y_2} = \frac{U_{1D}}{Z_4}\frac{Z_4}{Y_2} \\ G_5(s) &= \frac{-p_2 s}{s^2 + p_1 s} = \frac{U_{1E}}{U_2} = \frac{U_{1E}}{Z_5}\frac{Z_5}{U_2} \end{aligned} \tag{27}$$

By means of the variables Z_1, Z_2, Z_3, Z_4 and Z_5 it is possible to define following equations

$$\begin{aligned} & \beta_1 z_1 = u_{1A} \\ & \beta_2 z_2 = u_{1B} \\ & -q_1 z_3'' - q_2 z_3' = u_{1C} \\ & -q_3 z_4'' - q_4 z_4' = u_{1D} \\ & -p_2 z_5' = u_{1E} \end{aligned} \tag{28}$$

and

$$\begin{aligned} & z_1'' + p_1 z_1' = e_1 \\ & z_2'' + p_1 z_2' = e_2 \\ & z_3'' + p_1 z_3' = y_1 \\ & z_4'' + p_1 z_4' = y_2 \\ & z_5'' + p_1 z_5' = u_2 \end{aligned} \tag{29}$$

Equations (29) can be converted to a set of differential equations of the first order (state equations). Choice of the state variables is as follows

$$\begin{aligned} x_1 &= z_1 \\ x_2 &= z_1' \\ x_3 &= z_2 \\ x_4 &= z_2' \\ x_5 &= z_3 \\ x_6 &= z_3' \\ x_7 &= z_4 \\ x_8 &= z_4' \\ x_9 &= z_5 \\ x_{10} &= z_5' \end{aligned} \tag{30}$$

And the state equations are

$$\begin{aligned} x_1' &= x_2 \\ x_2' &= e_1 - p_1 x_2 \\ x_3' &= x_4 \\ x_4' &= e_2 - p_1 x_4 \\ x_5' &= x_6 \\ x_6' &= y_1 - p_1 x_6 \\ x_7' &= x_8 \\ x_8' &= y_2 - p_1 x_8 \\ x_9' &= x_{10} \\ x_{10}' &= u_2 - p_1 x_{10} \end{aligned} \tag{31}$$

On the basis of the state variables, which are substituted to equations (28), it is possible to derive particular parts of the manipulated variable u_1

$$\begin{aligned} u_{1A} &= \beta_1 x_1 \\ u_{1B} &= \beta_2 x_3 \\ u_{1C} &= -q_1 (y_1 - p_1 x_6) - q_2 x_6 \\ u_{1D} &= -q_3 (y_2 - p_1 x_8) - q_4 x_8 \\ u_{1E} &= -p_2 x_{10} \end{aligned} \tag{32}$$

ISBN: 978-1-61804-321-4

The manipulated variable we obtain as sum (33)

$$u_1 = u_{1A} + u_{1B} + u_{1C} + u_{1D} + u_{1E} \tag{33}$$

An expression for computation of the manipulated variable u_2 is obtained similarly on the basis of differential equation (25).

IV. Recursive Identification

The controller was realized as a self-tuning controller with recursive identification of a model of the controlled system. Self-tuning controllers are suitable for control of nonlinear systems or systems with variable parameters. The recursive least squares method [9] proved to be effective for self-tuning controllers and was used as the basis for our algorithm. For our two-variable example we considered the disintegration of the identification into two independent parts.

As the regression model we considered the ARX (AutoRegressive model with Exogenous input) [11]. Usually the ARX model is tested first and more complex model structures are only examined if it does not perform satisfactorily. Linear continuous time ARX model is

$$\begin{aligned} &y_1^{//}(t)+a_1 y_1^{/}(t)+a_2 y_1(t)+a_3 y_2^{/}(t)+a_4 y_2(t)= \\ &=b_1 u_1^{/}(t)+b_2 u_1(t)+b_3 u_2^{/}(t)+b_4 u_2(t)+n_1(t) \end{aligned} \tag{34}$$

$$\begin{aligned} &y_2^{//}(t)+a_5 y_1^{/}(t)+a_6 y_1(t)+a_7 y_2^{/}(t)+a_8 y_2(t)= \\ &=b_5 u_1^{/}(t)+b_6 u_1(t)+b_7 u_2^{/}(t)+b_8 u_2(t)+n_2(t) \end{aligned}$$

where n_1 and n_2 are non - measurable random signals, which are assumed to have zero mean value and constant covariance.

It is not possible to measure directly input and output derivatives of a system in case of continuous – time control loop. One of the possible approaches to this problem is establishing of filters and filtered variables to substitute the primary variables. This approach is described in detail in [12], [13], [14]. The filtered variables are then used in the recursive identification procedure.

$$\begin{aligned} &C(\sigma)u_{1f}(t)=u_1(t) \\ &C(\sigma)u_{2f}(t)=u_2(t) \\ &C(\sigma)y_{1f}(t)=y_1(t) \\ &C(\sigma)y_{1f}(t)=y_1(t) \end{aligned} \tag{35}$$

where σ is the derivative operator and $C(\sigma)$ is a stable polynomial in σ. The degree of $C(\sigma)$ must be equal or greater than polynomials of the highest order in the matrix $\boldsymbol{A}$. The time constants of the filters must be smaller than the time constants of the model. Since the latter are unknown at the beginning of the estimation procedure, it is necessary to make the filter time constants, selected a priori, sufficiently small.

It can be easily proved that the transfer behaviour between the filtered and between the non – filtered variables is equivalent. This fact enables to employ the filtered variables for the model parameter estimation. If these are computed via filters (46) in discrete time intervals $t_k = kT_s$, $k = 0,1,2, \ldots$, where T_s is the sampling period, then the parameters of the model can be recursively estimated from the equations

$$\begin{aligned} y''_{1f}(t_k) &= -a_1 y'_{1f}(t_k) - a_2 y_{1f}(t_k) - a_3 y'_{2f}(t_k) - a_4 y_{2f}(t_k) + \\ &+ b_1 u'_{1f}(t_k) + b_2 u_{1f}(t_k) + b_3 u'_{2f}(t_k) + b_4 u_{2f}(t_k) + \varepsilon_1(t_k) \end{aligned} \tag{36}$$

$$\begin{aligned} y''_{2f}(t_k) &= -a_5 y'_{1f}(t_k) - a_6 y_{1f}(t_k) - a_7 y'_{2f}(t_k) - a_8 y_{2f}(t_k) + \\ &+ b_5 u'_{1f}(t_k) + b_6 u_{1f}(t_k) + b_7 u'_{2f}(t_k) + b_8 u_{2f}(t_k) + \varepsilon_2(t_k) \end{aligned} \tag{37}$$

The regression vectors have the form

$$\begin{aligned} \phi_{1,2}{}^T(t_k) = [&-y'_{1f}(t_k), -y_{1f}(t_k), -y'_{2f}(t_k), -y_{2f}(t_k), \\ &-u'_{1f}(t_k), -u_{1f}(t_k), -u'_{2f}(t_k), -u_{2f}(t_k)] \end{aligned} \tag{38}$$

and the parameter vectors are

$$\boldsymbol{\Theta}_1{}^T(t_k) = [a_1, a_2, a_3, a_4, b_1, b_2, b_3, b_4] \tag{39}$$

$$\boldsymbol{\Theta}_2{}^T(t_k) = [a_5, a_6, a_7, a_8, b_5, b_6, b_7, b_8] \tag{40}$$

Considering the order of the system, the filters for all variables were chosen to have the second order. A right choice of the coefficients of the filter's polynomials and choice of the sampling period are the ruling factors for the speed of the parameter's convergence.

$$\begin{aligned} &y''_{1f}(t) + c_1 y'_{1f}(t) + c_0 y_{1f}(t) = y_1(t) \\ &y''_{2f}(t) + c_1 y'_{2f}(t) + c_0 y_{2f}(t) = y_2(t) \\ &u''_{1f}(t) + c_1 u'_{1f}(t) + c_0 u_{1f}(t) = u_1(t) \\ &u''_{2f}(t) + c_1 u'_{2f}(t) + c_0 u_{2f}(t) = u_2(t) \end{aligned} \tag{41}$$

The recursive least squares method was then used for the estimation of the parameters.

V. Simulation Verification

Verification by simulation was carried out on a range of plants with various dynamics. The control of the model below is given here as an example.

$$\boldsymbol{A}(s) = \begin{bmatrix} s^2 + 2s + 0{,}7 & 0{,}2s + 0{,}4 \\ -0{,}5s - 0{,}1 & s^2 + 2s + 0{,}7 \end{bmatrix} \tag{42}$$

$$\boldsymbol{B}(s) = \begin{bmatrix} 0{,}5s + 0{,}2 & 0{,}1s + 0{,}3 \\ 0{,}5s + 0{,}1 & 0{,}3s + 0{,}4 \end{bmatrix} \tag{43}$$

Figure 2 shows the plant's step response

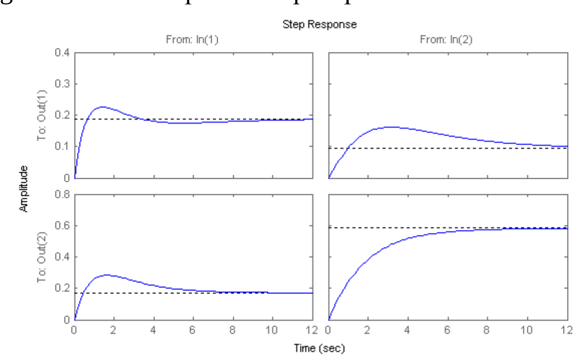

Fig. 2 Step response of the controlled system

The matrix $\boldsymbol{M}(s)$ on the right side of diophantine equation (16) obtained from experiments is

$$\boldsymbol{M}(s)=\begin{bmatrix} s^4+2s^3+ \\ +9s^2+6s+2 & 0 \\ 0 & s^4+2s^3+ \\ & +9s^2+6s+2 \end{bmatrix} \tag{44}$$

The time responses of the control are shown in Fig 3. and Fig. 4.

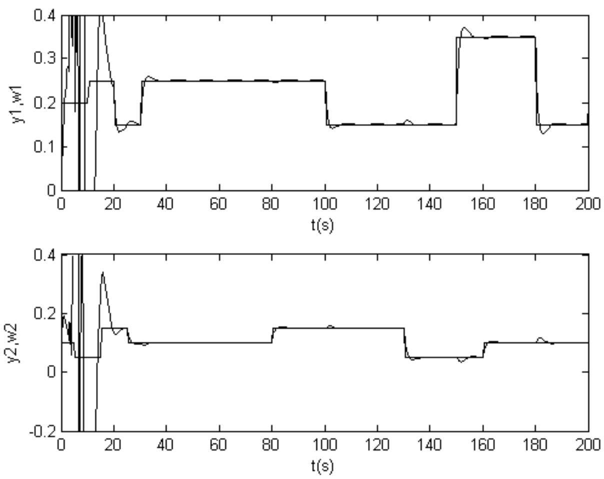

Fig. 3 Adaptive control with 2DOF controller

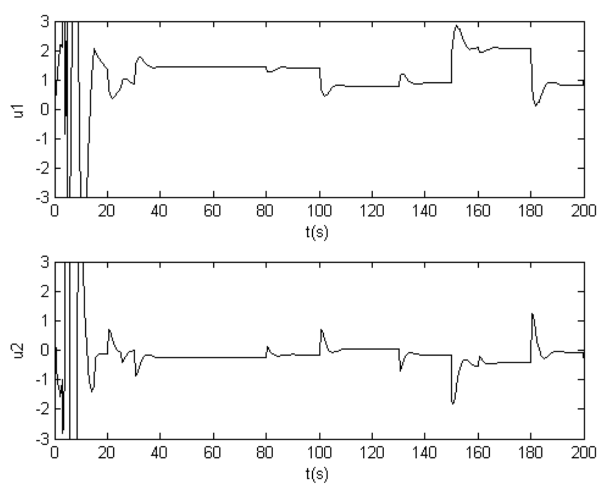

Fig. 4 Adaptive control with 2DOF controller-manipulated variables

From the courses of the variables in Fig. 3 and Fig. 4 it is obvious that the basic requirements on control were satisfied. The system was stabilized and the asymptotic tracking of the reference signals was achieved.

VI. Conclusion

The 2DOF TITO controller was designed and implemented in the continuous-time version. General principles were elaborated on a specific system with two inputs and two outputs that is often applicable in industrial practice. Control law based on specific model was derived in the form of self-contained expressions that is especially useful for practical applications of control on common industrial devices. An advantage of the proposed strategy lies in its simplicity and applicability.

It is necessary to recognize that self-tuning controllers do not work satisfactorily in the initial adaptation phase if the initial parameter estimates are chosen without a priori information. However, the most important property for practical use of self-tuning controllers is their performance after the adaptation phase. The described method of continuous – time models parameters estimation proved to be effective. A right choice of the filter’s constants and the sampling period improves convergence of the parameters. The method is suitable for the identification part of continuous – time self – tuning controllers.

References

[1] W. L. Luyben, “Simple Method for Tuning SISO Controllers in Multivariable Systems”, *Ing. Eng. Chem. Process Des. Dev.*, Vol. 25, pp. 654 – 660, 1986.

[2] I.L. Chien, D.E.Seborg and D. A. Mellichamp, “Self-Tuning Control with Decoupling”, *AIChE J.*, Vol. 33, No. 7, 1079 – 1088, 1987.

[3] V. Kučera,“ Stochastic multivariable control: a polynomial approach“, *IEEE Trans. of Automatic Control*, 5, pp. 913–919,1980.

[4] V. Kučera, V., *Analysis and Design of Discrete Linear Control Systems*. Prentice Hall, Englewood Cliffs, New Jersey, 1991.

[5] Vidyasagar, M., *Control System Synthesis: A Factorization Approach*. MIT Press, Cambridge MA, 1985.

[6] V. Kučera, “Diophantine Equations in Control – a Survey”. *Automatica*, 29, pp. 1361 – 1375, 1993.

[7] R. Ortega, and R. Kelly, PID self – tuners: Some theoretical and practical aspects, IEEE Trans. Ind. Electron., IE - 3, pp. 332 – 338, 1984.

[8] I. D. Landau, R. Lozano, M. M’Saad, *Adaptive Control*, Springer - Verlag, Berlin, 1998.

[9] V. Bobal, J., Bőhm , J., Fessl, J., Machacek, *Digital Self-Tuning Controllers*, Springer - Verlag, London, 2005.

[10] Kubalčík, M. and V. Bobál „Adaptive Control of Coupled Drives Apparatus Based on Polynomial Theory”. In Proc. IMechE Vol. 220 Part I: *J. Systems and Control Engineering*, 220(I7), pp. 641-654, 2006.

[11] O. Nelles, Nonlinear System Identification, Springer-Verlag, Berlin, 2001.

[12] Wahlberg, B., On the identification of continuous – time dynamical systems, *Report LiTH-ISY-I-0905*, Linköping, 1990.

[13] Unbehauen, H., Rao, G.P., *Identification of Continuous Systems*, North Holland, Amsterdam, 1987.

[14] Gawthrop, P. J., *Continuous – Time Self – Tuning Control*, John Willey, Chichester, 1987.

Utilization of cellular network data for road traffic prediction

Vasileios Asthenopoulos, Ioannis Loumiotis, Pavlos Kosmides, Evgenia Adamopoulou and Konstantinos Demestichas

Abstract — This paper focuses on the use of data originating from cellular networks in an attempt to predict road traffic. Real data acquired from cellular and road network operators are used to investigate whether the proposed approach is plausible, and which of the two evaluated machine learning techniques, namely the Multi-Layer Perceptron and the General Regression Neural Network, performs better for this particular purpose. Real-world use of the proposed approach could potentially reduce the number of road sensors used to measure traffic parameters such as speed, allow the prediction of road traffic solely through the use of anonymous cellular network performance data and even provide road incident alerts in near real-time, without the need for implementing sensor infrastructures.

Keywords—Intelligent Transport Systems, cellular data, traffic prediction, Multi-Layer Perceptron, General Regression Neural Network, Vehicle Detection System, mobile network.

I. Introduction

INTELLIGENT transportation systems (ITS)[1] have made significant advances in improving everyday life and reducing the cost and environmental impact of transportation. The current research trends aim for the concept of smart cities, where an entire city would coordinate and optimize every operational aspect in order to improve overall efficiency. According to this approach, viewing all available data sources as potentially useful information provides a very interesting research area.

Acknowledging that services used by citizens in everyday life (such as the cellular and road networks in our case) are not totally isolated from each other, but rather are more or less affected by one another, can lead to the conclusion that information about one system can be deduced from data provided by other systems. The study of the exact relationships among these “interlaced” systems can provide useful information about how to make use of data fusion to make reasonable assumptions about one system solely by using data originating from other systems. One simple example that helps better understand the described concept is suddenly noticing a significant increase in outgoing calls or data traffic from a specific cellular base station that is near a large highway and reaching the conclusion that there is probably some sort of traffic related incident in progress, as that would be a major reason for the drivers to stop driving and start using their mobile devices. To this end, this paper assesses the feasibility of using data originating from cellular networks in order to reach conclusions about traffic conditions and, more specifically, to predict vehicle speeds on an adjacent motorway.

The rest of the paper is organized as follows. In Section II, the proposed problem is described in detail. The dataset that was employed is presented in Section III. In Section IV we present the evaluation techniques that we used, while in Section V we provide the results and discuss on the performance of the proposed algorithms. Finally, future work and conclusion of the paper are presented in Sections VI and VII respectively.

II. Problem Description

One of the most challenging tasks of road network monitoring is the management of road sensors. The cost of planning, installing and maintaining a complete set of often heterogeneous road sensors is quite significant, and can increase further, if the vast size and complexity of dense urban road networks is taken into consideration. On the other hand, in the domain of cellular communications there is the problem of creating a network dense enough to provide adequate coverage. This paper attempts to assess the relationship between the performance figures of cellular network base stations and the traffic conditions in the adjacent road network. If close ties can be found between the two, there would be a significant benefit in utilizing data originating from the cellular network in order to analyze and/or predict road traffic and road network conditions in general. This would eventually lead to more road traffic data being available indirectly to aid in optimizing transportation, without the requirement for expensive sensor networks to be setup and maintained, but rather by simply making better use of data that is already available from the existing cellular network base stations.

III. Dataset Description

In order to assess the problem described, heterogeneous data are required, on which to validate the proposed solution. Specifically, there are two discrete data sources involved;

V. Asthenopoulos, I. Loumiotis, P. Kosmides, E. Adamopoulou and K. Demestichas are with the Institute of Communication and Computer Systems of the National Technical University of Athens, Iroon Polytechneiou 9, 15772 Greece (phone: +30-210-772-1493; e-mail: asthen@ cn.ntua.gr).

cellular network traffic data and road traffic data. These must be properly combined in order to create a dataset which correlates the operational conditions of the cellular network with the conditions on the road network in its vicinity. The key variables of each data source used in this study is cell-to-cell handover count and road speed.

The cellular data used in this paper originate from the cellular network of Vodafone Greece and the relevant road data are provided by Attikes Diadromes, a major Greek highway operator. In particular, a set of base stations located near key interchanges "Metamorfosi" and "Koropi" of Attiki Odos were selected. The selection of cells was made so that their antennas point as accurately as possible towards the adjacent highway lanes. This way, it is expected that the vast majority of cellular network subscribers associated with these particular cells at any time are actually driving on the motorway. Once the cells to be involved in the study were specified, the relevant road traffic data source had to be found. Attikes Diadromes operates a dense Vehicle Detection System (VDS) which is used to acquire data in real time, allowing both prompt incident response and offline statistical traffic analysis. Using their VDS, the specific induction loops that measure traffic parameters on the aforementioned interchanges were specified and monitored. Given the geospatial correlation, from the timestamps of both data sources, a temporal correlation between the two data sources can be deduced.

The metric of interest for cellular network data is the hourly handover count. This metric refers to the number of subscribers that were disassociated from Cell A and associated ("handed over") to Cell B within one hour. This metric can provide a quantitative figure for the directional flow of subscribers from one geographical area to the next. On the other hand, the metric taken into consideration for the road network is the average speed of the vehicles driving on that part of the road.

In more detail, the dataset used consists of the following fields:

- *Month;* The month id. The dataset includes records for February and March 2015.
- *Day of week;* The day id (1...7).
- *Hour of day;* The hour id (0...23).
- *Cell1;* The ID of the cell the handovers originate from.
- *Cell2;* The ID of the cell the handovers are destined to.
- *Handovers;* The hourly handover count in the direction Cell1→ Cell2, as measured from the cellular network.
- *Speed;* The hourly average speed over the part of road pointed to by the cells in the direction Cell1→ Cell2, as measured by the VDS.

Last but not least, it is worth making clear that all data used in these experiments, from both sources, are real-world data, not simulated or expanded from a small set of real data. The full dataset used consists of about 4200 records.

IV. Evaluated Techniques

The essence of the problem lies in discovering how input data (cellular network data) affect the target variable, in our case road speed. While a strict mathematical model would provide us with a well-defined relationship between these entities, a great deal of time, effort and validation would be required to successfully reach one. Therefore, a different approach is quite often used for such problems, namely machine learning techniques. The Multi-Layer Perceptron (MLP) and the General Regression Neural Network (GRNN) are two very popular and proven techniques in the field of machine learning.

The Multi-Layer Perceptron [2] is one of the simplest yet most effective machine learning methods utilized these days. Being a special case of an artificial neural network (ANN), it is designed to closely mimic the structure of the human brain and its learning abilities. An artificial neural network consists of neurons, which are formed by three elementary entities: a set of connecting links (synapses), each carrying a weight, an adder used to compute the weighted sum of the inputs carried by the synapses and an activation function which controls the output of the neuron. In an MLP, sets of neurons are structured to form layers, as depicted in Fig. 1.

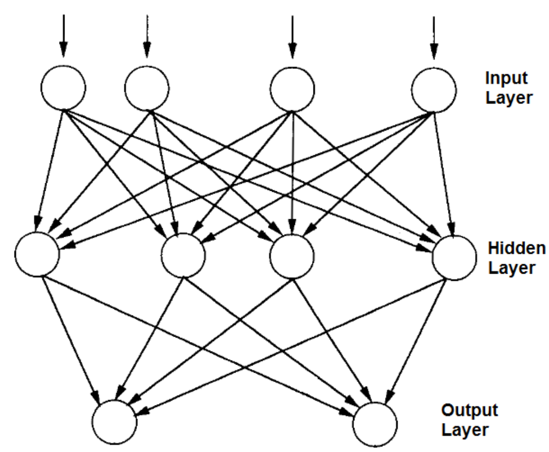

Fig. 1 A Multi-Layer Perceptron with four inputs, one hidden layer with 4 neurons and two outputs.

The first layer, called the input layer, consists of as many neurons as the number of inputs to the network, while the final, called the output layer consists of as many neurons as there are outputs. Between these layers, one or more so-called hidden layers are formed, which are fully connected with synapses to the outputs of the previous layer. Using an MLP with just one hidden layer of sufficient neurons, a large variety of functions can be approximated fairly accurately [3], while adding more hidden layers results in the system being able to mimic more complex functions. However, there is a tradeoff between the complexity of the system and the accuracy of the results it provides; increasing the number of neurons or hidden layers for a given problem could lead to worse performance and less accuracy when feeding the MLP with new, unseen data. Therefore, the architecture of the network plays a significant role in the results to be expected from it.

The General Regression Neural Network (GRNN) [4] is a single-pass neural network often utilized for the estimation of continuous variables. Its main characteristics are its quick learning ability as well as its ability to converge to the optimal regression surface as the training samples become large enough. In addition, because the regression surface is instantly defined everywhere, the GRNN is a very suitable candidate for real-time problems that provide sparse data. One of the most challenging issues with the GRNN is the proper selection of the smoothing parameter σ that corresponds to the relevant Gaussian function used in the estimation process. In all, the structure of the GRNN is presented in Fig. 2.

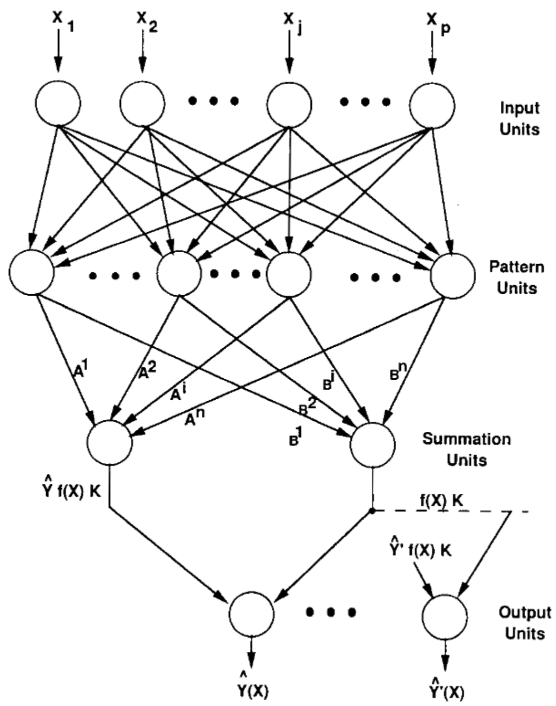

Fig. 2 Structure of a General Regression Neural Network [4].

This paper evaluates the performance of both MLPs and GRNNs for the purpose of utilizing cellular network data to predict road traffic conditions. The software used to this end is DTREG[5], a popular modelling tool. DTREG allows for an exhaustive evaluation of a machine learning technique by also finding the optimal value for some of the technique's parameters, such as the hidden layer neuron count in the case of MLP.

Taking a look at the dataset, Fig. 3 depicts the relationship between hourly handover count and road speed versus the "hour of the day" variable. As can easily be seen, road speed is roughly periodic with a period of one day, while the hourly handover count presents some repetitive patters which are not as clear as those for road speed. We expect the techniques evaluated to succeed in finding the mathematical relationship between these two variables.

V. Tests And Results

The metric used to evaluate the performance of the techniques is the Mean Absolute Percentage Error (MAPE) of the target variable (road speed). For both the MLP and the GRNN, 10-fold cross validation was defined as the validation procedure. According to this popular validation procedure, the dataset is split into 10 equally sized subsets and training is performed using 9 of them as the training set and the remaining subset as the validation set. Then, the process is repeated 9 more times, rotating the subsets so that each subset is used for validation only once. This way, validation is performed on unseen data each time.

As far as the MLP run is concerned, the settings defined in DTREG were to use just 1 hidden layer, find the best performing number of neurons in the hidden layer, use the Logistic function as an activation function for the hidden layer and Linear for the output layer. The optimization performed by DTREG showed that 7 neurons in the hidden layer would be the most efficient architecture for this problem, therefore it was this specific setup (6 input neurons, 7 hidden neurons, 1 output neuron) that was tested. Regarding the GRNN, we requested that the optimal sigma values be computed for each input variable and defined a Gaussian kernel function. The

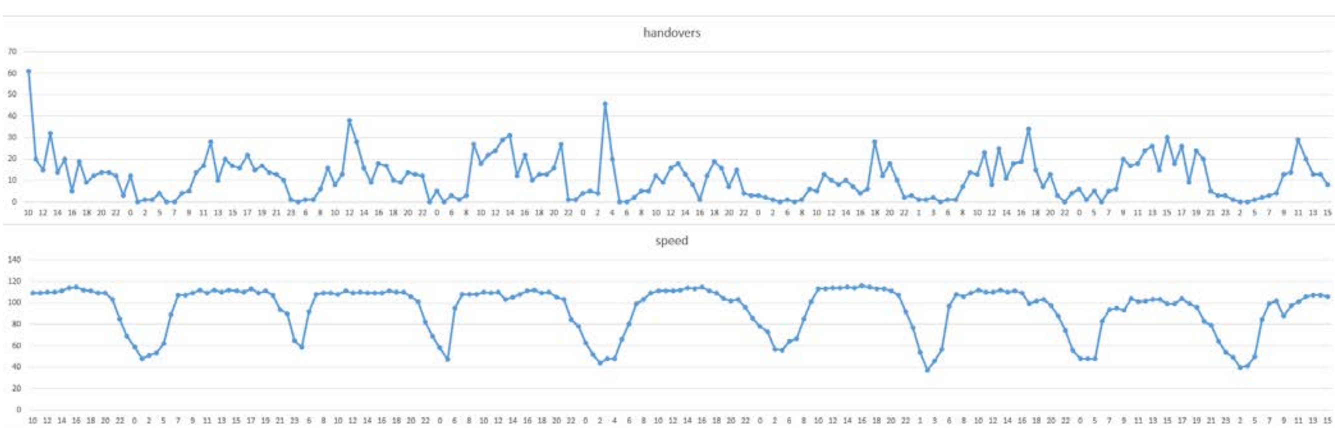

Fig. 3 Temporal relationship between hourly handover count and hourly average speed.

ISBN: 978-1-61804-321-4

results of the evaluations are presented in the following table.

Table I. Accuracy scored by evaluated techniques.

Technique	MAPE
GRNN	4.47%
MLP (6-7-1)	9.32%

As can be seen from the results, the GRNN has a significantly smaller Mean Absolute Percentage Error than the MLP. This shows that for this particular problem, the GRNN approach is much more appropriate. Furthermore, this level of accuracy (about 4.5%) is high enough to show that over-fitting to this specific dataset did not occur, but at the same time low enough to present usable results. This leads to the conclusion that handover data can indeed be associated with traffic conditions on the nearby road network. As a result, this kind of data can successfully be used to assess and predict road traffic parameters.

VI. Future Work

This paper evaluated the relationship between two specific variables, namely the hourly handover count from the cellular network and the average hourly speed on the motorway beside the base stations considered. It would be very interesting to also take other variables, such as road traffic flow, density and data traffic or outgoing call rate into consideration for the same purposes. Furthermore, fusion of data from more than one cellular network operator could potentially provide more accurate results or better validation of the model. Finally, an expansion of the research to more complex road networks than just the adjacent highway, potentially also evaluating more machine learning techniques, would provide a generalization of the results for urban road networks which often lack road sensors.

VII. Conclusion

This paper evaluated the concept of using cellular network performance data for the purpose of estimating and predicting road traffic parameters. Two popular machine learning techniques, namely the Multi-Layer Perceptron and the General Regression Neural Network were used to test the feasibility and accuracy of the proposed system. The results of applying these techniques to a real-world dataset showed that the GRNN provides significantly better accuracy in predicting road speed than the MLP. Further work on this research area could greatly decrease the number of road sensors needed to gain a complete view of road traffic conditions in an urban network by utilizing performance data collected from cellular network base stations.

Acknowledgment

This work has been performed under the Greek National project CARMA (11ΣΥΝ_10_877), which has received research funding from the Operational Programme “Competitiveness & Entrepreneurship” of the National Strategic Reference Framework NSRF 2007-2013. This paper reflects only the authors’ views, and the Operational Programme is not liable for any use that may be made of the information contained therein.

References

[1] A. Sheng-hai, L. Byung-Hyug and S. Dong-Ryeol, “A Survey of Intelligent Transportation Systems” in *Proceedings of the 3rd International Conference on Computational Intelligence, Communication Systems and Networks*, Bali, July 2011, pp. 332-337.

[2] S. Haykin, *Neural Networks, A Comprehensive Foundation*, Prentice Hall, 2nd edition, 1999.

[3] T. M. Mitchell, *Machine Learning*, McGraw-Hill, 1997.

[4] D. F. Specht, “A General Regression Neural Network”, *IEEE Transactions on Neural Networks*, vol.2(6), 1991, pp.568-576.

[5] DTREG, Predictive Modelling Software, retrieved May 2015 from https://www.dtreg.com/.

A Performance Oriented Approach for Energy Efficient Routing

Pavlos Kosmides, Vasileios Asthenopoulos, Evgenia Adamopoulou and Konstantinos Demestichas

Abstract— Over the past decades, the research community has focused on reducing the energy consumed in every aspect of our everyday life. One of the most significant factors of energy consumption is transportation, thus a great deal of work in the field of Intelligent Transport Systems focuses on maximizing energy efficiency. Eco-routing refers to the choice of the most energy efficient route towards a destination and seems very promising for reducing everyday energy consumption. In this paper, we present a novel method for predicting energy consumption levels, based on machine learning techniques. Specifically, we formulate the problem as a classification problem and propose a Probabilistic Neural Network, which is compared against two other types of neural networks.

Keywords—Intelligent Transport Systems, energy efficiency, energy consumption levels, machine learning.

I. Introduction

THE The concept of green growth and the resulting rise of environmental awareness in all aspects of everyday life have undoubtedly made their way into the transportation domain these days. Meanwhile, technological advances and maturity over the past decade have led to an increasing number of the so called "green" passenger vehicles, being widely available in the market. Plug-in hybrid electric vehicles (PHEVs) and fully electric vehicles (FEVs) are presenting increased figures of market penetration, partially owing to recharging infrastructure steadily expanding to serve ever growing geographic areas. Energy efficient routing, also called "eco-routing", addresses the problem of suggesting routes for reaching specific destinations, based on the optimization criterion of minimizing the energy or fuel consumption, instead of applying traditional optimization criteria, such as trip distance or time. Eco-routing can systematically reduce the consumed energy without tampering with the powertrain of the vehicles, and thus boost driving range of vehicles, especially of those with limited energy reserves, such as FEVs. The main issue of eco-routing is how to estimate the cost of each segment in the route graph, so that a routing algorithm can be applied to it. One of the most promising approaches in estimating these costs involves a machine learning process fed with data acquired by vehicles travelling on the road network.

P. Kosmides, V. Asthenopoulos, E. Adamopoulou , K. Demestichas are with the Institute of Communication and Computer Systems of the National Technical University of Athens, Iroon Polytechneiou 9, 15773 Greece (phone: +30-210-7721495; e-mail: pkosmidis@ cn.ntua.gr).

On the problem of predicting the energy consumption of a vehicle over a journey, several models have been described, each having its advantages and drawbacks. The most "traditional" approach would be to find a formula that describes fuel consumption as a function of all relevant variables, such as the one presented in [1], and then attempt to estimate the values of these variables for each road segment. This approach is followed in [2], where traffic and geographic information as well as vehicle parameters are taken into consideration in order to predict the driving pattern of a route and compute the relevant variables. This model produces fairly accurate results, but assumes a standard driving style and cannot take into account fluctuating driving conditions unless real-time traffic information is provided.

Other studies, such as [3] and [4] combine machine learning techniques with information about the vehicle in an attempt to predict its average fuel consumption figures over different transit modes such as city, highway etc. This approach ignores driver- and route-specific parameters, so the provided rough accuracy is not adequate for the purpose of eco-routing, although the techniques are used successfully. Another set of papers [5],[6] take the approach of predicting acceleration and deceleration patterns based on static map data and historical traffic data to calculate speed profiles and then estimate consumption. This method typically applies for given routes, therefore is not suitable for populating a road network graph with the associated costs and then finding the optimal route to be followed. Previous work tailored for routing algorithms [7],[8] follows a similar approach, but requires real-time traffic and weather data for varying road conditions consideration; although in [8] the use machine learning techniques provides accurate results. Finally, [9] uses regression methods to estimate a set of energy and emissions operational parameters from historical and real-time data, achieving good accuracy, but, as stated by the authors, data errors from the fusion process and other sources can accumulate.

In this paper, following the above trend, we propose a system architecture for collecting and elaborating useful data from vehicles. In order to provide drivers with eco-friendly route suggestions, we formulate a classification problem and use machine learning techniques in order to estimate the energy consumption level that is necessary for the vehicle to pass through a specific route segment. Specifically, we present a performance comparison between a Probabilistic Neural Network (PNN), a Support Vector Machine (SVM) and a

ISBN: 978-1-61804-321-4

Multilayer Perceptron (MLP).

The rest of this paper is organized as follows. In Section II, we describe the architecture of the proposed system for collecting data from the vehicles and for processing them using machine learning mechanisms. In Section III, we present the three different approaches that we use based on machine learning. The dataset that was employed is presented in Section IV, while in Section V we provide the results and discuss on the performance of the three proposed algorithms. Finally, the paper is concluded in Section VI.

II. System Description

The conceived system's primary goal is to present the most energy efficient route to the driver, just as a traditional navigator would do with the shortest or quickest route. This would allow the driver to conveniently access energy efficient routes from inside his car. The architecture designed to implement this, consists of both on-board and back-office infrastructure, namely the Integrated In-vehicle Energy Management – Advanced Driver Assistance System (IIEM-ADAS) and the Services Control Platform (SCP).

The IIEM-ADAS consists of an application for mobile devices (smartphones, tablets etc) and the On-Board Unit (OBU). The mobile app is mainly responsible for presenting a graphical interface to the driver, providing the routing functionality and communicating with the SCP, while the OBU is responsible for the integration with the vehicle's CAN bus and the collection of tracking data to feed the machine learning mechanism. In the back-office, the SCP communicates with the IIEM-ADASes, acquires and stores tracking data, processes them to create the relevant machine learning engines and supports the functionalities provided by the in-vehicle components when needed.

In more detail, raw tracking data are gathered by the OBUs of vehicles travelling on the road network. These data typically include vehicle and driver ID, timestamp, geographic coordinates, speed and instantaneous energy/fuel consumption. Upon being uploaded to the SCP, they are processed to obtain per-segment data, where a segment is defined as a part of road that does not contain any junctions (i.e. only intersects with other segments at its endpoints). Per-segment data consist of timestamp, segment ID with its direction, average speed, travel time and energy/fuel needed to drive through the specific segment. These data are accumulated to create per-segment training sets, which are used to train machine learning engines for energy/fuel or travel time prediction.

In the architecture presented in Fig. 1, tracking data are collected by the OBUs and uploaded to the SCP, which processes them and generates the training data. After that, the training data are forwarded to the MLE training component, which is responsible for creating and training the corresponding MLEs. It is these MLEs that are in turn supplied to the mobile app in order to predict the required trip parameters (energy/fuel or time) for each segment and finally compute the optimal route towards the trip destination.

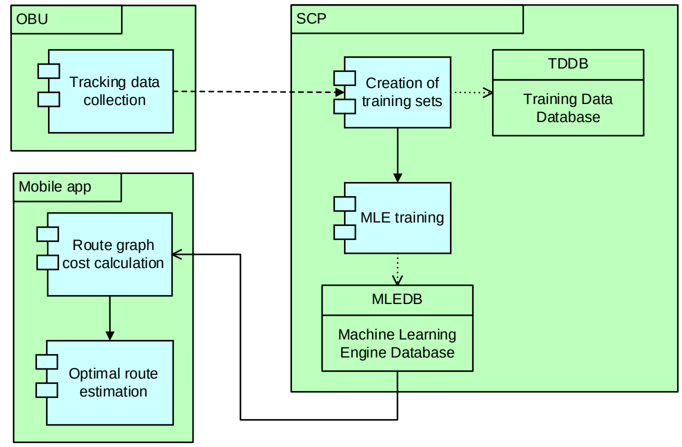

Fig. 1 System Architecture

III. Prediction Models

In order to provide recommendations to users about energy efficient routes that they can follow so they can arrive to a specified location, we use three different approaches based on machine learning techniques, namely Multilayer Perceptron, SVM and PNN.

A. *Multilayer Perceptron*

The first approach used as a prediction model is the Multilayer Perceptron Network. Multilayer Perceptrons form one type of feed-forward Artificial Neural Networks (ANNs) according to the taxonomy of neural network architectures presented in [10].

The Multilayer Perceptron's architecture consists of an input layer, a number of hidden layers and an output layer. The number of the necessary hidden layers depends on the problem formulation. However, it has been proved that using more than two hidden layers rarely improves the model, while it introduces a risk of converging to local minima [11]. The nodes are connected by weights and output signals which are a function of the sum of the inputs to the node.

B. *Support Vector Machine (SVM)*

SVM is a learning machine that is closely related to neural networks. It is based on statistical learning theory and uses linear, polynomial and radial basis kernel. An SVM, unlike common ANNs, is characterized by the absence of local minima. In addition, the computational complexity of SVMs does not depend on the dimensionality of the input space [12].

The SVM algorithm takes as input an n dimensional vector, $\boldsymbol{X} = \{x_1, x_2, \dots, x_n\}$. The data vector is mapped into a higher dimensional space. Afterwards, the algorithm finds a hyperlane in the space that separates the training data by maximal margin. In case there is no linear separation in the dataset, SVM is using kernel operators to project the original training data to a higher dimensional feature space. The vectors near the hyperplane are the support vectors.

C. *Probabilistic Neural Network (PNN)*

PNNs are used to perform classification where the target variable is categorical. Compared to the Multilayer Perceptron networks, a PNN is usually much faster to train and more accurate. This is mainly due to the fact that the PNN uses the radial basis function as kernel and interprets the network structure in the form of probability density function. It is noteworthy that PNNs are based on the Bayes' theory, resulting to classifications that approach Bayes' optimal classification [13].

As it can be seen from Fig.2, a PNN takes as input an n dimensional feature vector, $\boldsymbol{X} = \{x_1, x_2, \ldots, x_n\}$. The inputs are passed to the neurons in the Hidden Layer, where the distance of the test case from the neuron's centre point is computed and then a radial basis function is applied, using a smoothing parameter (σ). The number of units in this layer is equal to the number of samples in the training set. The Summation Layer is responsible for summing the input from the hidden layer and produces a vector of probabilities that represent the probability of each feature to belong to a specific class. Finally, the Output Layer provides the classification decision, following Bayes' decision rule. It is worth mentioning that the smoothing parameter (σ) is the only parameter of the network that needs to be fixed at the beginning of the training.

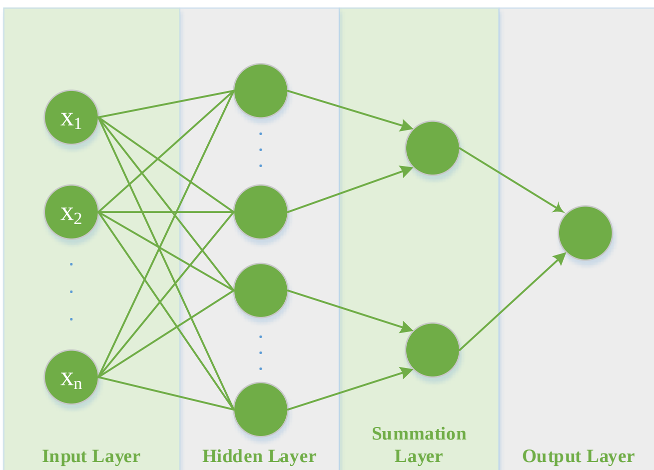

Fig. 2 Architecture of a Probabilistic Neural Network

IV. Data Analysis

The dataset used in this paper is based on a data acquisition campaign that was conducted for research purposes in [14]. The campaign was performed by a FEV [15] in the town of Chieri, Turin area, Italy. The variables of the dataset that were used for this paper are described in Table I.

TABLE I. VARIABLES AND VALUES USED

Variable	Description
segmentId	Segment's unique id {total 269 segments}
direction	The direction of the vehicle within the segment
averageSpeed	The average speed of the vehicle within the segment
length	The length of the specific road segment
energyClass	Each energy class corresponds to the energy consumption level that is requires for the vehicle to travel over a road segment {3 classes used; minimum consumption, medium consumption, high consumption}

Using the described variables, the input set for the proposed algorithms can be defined as:

$$\boldsymbol{x} = (segmentId, direction, averageSpeed, length, energyClass) \tag{1}$$

V. Results

As previously described, we compare the results of the validation process of the PNN, with two other types belonging to the family of neural networks. The proposed learning algorithms were used in order to estimate the expected energy consumption level of each road segment. By estimating the consumption level that is needed for each road segment, we can provide "green" route recommendations to drivers.

First, we assess the PNN by analysing its performance against the smoothing parameter (σ). In Fig. 4, we present the effect of the smoothing parameter with values that range from 0.05 to 1, using 10-fold cross-validation method. It can be observed that in our case PNN performs better for σ = 0.6.

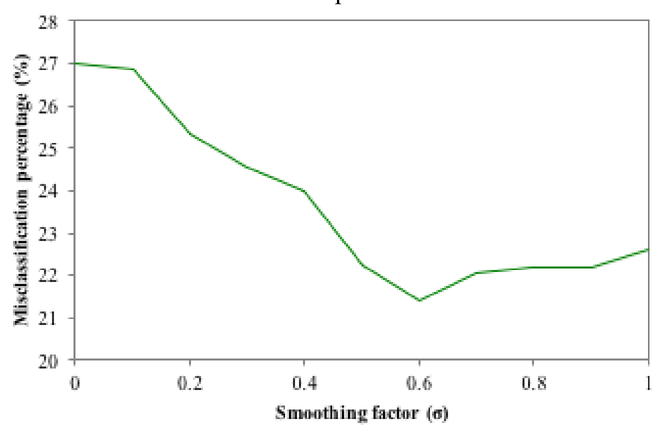

Fig. 3 Misclassification percentage for PNN with respect to σ values.

In Table II, we present the misclassification percentage that was derived from the other two learning methods evaluated. Specifically, the Multilayer Perceptron was formulated as a 4-7-3 three-layered feed-forward neural network, while the SVM was constructed with an RBF kernel function. It can be clearly seen that PNN with (σ = 0.6) provides the lowest misclassification percentage.

TABLE II. RESULTS OF VALIDATION PROCESS

Learning Method	Misclassification percentage (%)
3-layered MLP	22.645
SVM	22.039
PNN (σ = 0.6)	21.405

VI. Conclusions

In this paper, we have presented our work on the topic of energy efficient routing. More specifically, we described an architecture for the use of machine learning techniques to

ISBN: 978-1-61804-321-4

compute optimal routes based on energy consumption. The overall process involves collecting tracking data from vehicles travelling on the road network, processing them and finally using them in order to predict energy consumption levels for future journeys. Three different learning algorithms based on neural networks, namely MLP, SVM and PNN were used in order to predict the energy consumption level of each road segment. The dataset used includes real world measurements from a FEV.

ACKNOWLEDGMENT

This work is performed under the FP7 314151 project EMERALD, which has received research funding from the EU Seventh Frame- work Programme. This paper reflects only the authors views, and the Community is not liable for any use that may be made of the information contained therein.

REFERENCES

[1] T. Oguchi, M. Katakura, and M. Taniguchi, "Carbon dioxide emission model in actual urban road vehicular traffic conditions," *Journal of Infrastructure Planning and Management*, vol. 695, Jan. 2002, pp. 125─136.

[2] T., Kono, T., Fushiki, K., Asada, and K., Nakano, "Fuel consumption analysis and prediction model for eco route search," *In 15th World congress on intelligent transport systems and ITS America's 2008 annual meeting*, Nov. 2008.

[3] J. D., Wu, and J. C., Liu, "Development of a predictive system for car fuel consumption using an artificial neural network," *Expert Systems with Applications*, vol. 38(5), May 2011, pp. 4967–4971.

[4] J. D., Wu, and J. C., Liu, "A forecasting system for car fuel consumption using a radial basis function neural network." *Expert Systems with Applications*, vol. 39(2), Feb. 2012, pp. 1883–1888.

[5] D., Karbowski, S., Pagerit, and A., Calkins, "Energy consumption prediction of a vehicle along a user-specified real-world trip," *In Proceedings from the Electric Vehicle Symposium (EVS26)*, Los Angeles, California, May 2012.

[6] C. F., Minett, A. M., Salomons, W., Daamen, B., Van Arem, and S., Kuijpers, "Eco-routing: comparing the fuel consumption of different routes between an origin and destination using field test speed profiles and synthetic speed profiles," *In 2011 IEEE Forum on Integrated and Sustainable Transportation System (FISTS)*, Vienna, Austria, June 2011.

[7] K., Kraschl-Hirschmann, and M., Fellendorf, "Estimating energy consumption for routing algorithms," *In 2012 IEEE Intelligent Vehicles Symposium (IV)*, Alcala de Henares, Madrid, Spain, June 2012.

[8] M., Martínez, A., Gardel, A. M., Wefky, F., Espinosa, J. L, Lázaro, I., Bravo, and P. Revenga, "Electric Vehicle Consumption Estimation based on Heuristics and MLP Artificial Neural Network," *In European Electric Vehicle Congress (EEVC)*, Brussels, Belgium, Nov. 2012.

[9] K. Boriboonsomsin, M. J., Barth, W., Zhu, and A., Vu, "Eco-routing navigation system based on multisource historical and real-time traffic information," *IEEE Transactions on Intelligent Transportation Systems*, vol. 13(4), July 2012, pp. 1694–1704.

[10] A. K., Jain, J., Mao, and K. M., Mohiuddin, "Atrificial neural networks – a tutorial," *IEEE Computer*, vol. 29, March 1996, pp. 31-44.

[11] G., Panchal, A., Ganatra, Y. P., Kosta, and D., Panchal, "Behaviour analysis of multilayer perceptrons with multiple hidden neurons and hidden layers," *International Journal of Computer Theory and Engineering*, vol. 3, 2011, pp. 332–33.

[12] N., Cristianni, and J., Shawe-Taylor, *An Introduction to Support Vector Machines and other kernel-based learning algorithms*, Cambridge University Press, 2000.

[13] D. F., Specht, "Probabilistic neural networks," *Neural Networks*, vol. 3, 1990, pp. 109-118.

[14] M., Masikos, K., Demestichas, E., Adamopoulou, and M., Theologou, "Reliable vehicular consumption prediction based on machine learning", *Neural Network World*, vol. 24, 2014, pp. 333–342.

[15] Pininfarina Nido EV, retrieved on May 2015 from URL: http://www.pininfarina.com/en/nido_ev

INPUT: A Distributed Cloud Infrastructure for Intelligent Transportation Systems

George Lyberopoulos, Eleni Theodoropoulou, Ioanna Mesogiti and Konstantinos Filis
COSMOTE Mobile Communications S.A.
E-mail: {glimperop, etheodorop, imesogiti, cfilis} @cosmote.gr

Roberto Bruschi,
CNIT, Consorzio Nazionale Interuniversitario per le Telecomunicazioni
E-mail: roberto.bruschi@cnit.it
Paolo Lago and Chiara Lombardo
Telecommunication Networks and Telematics (TNT) Lab, University of Genoa and CNIT
E-mail: {paolo, chiara}@tnt-lab.unige.it

***Abstract*— Future Internet denotes the continuous increase in the number and "intelligence" of end-devices, which poses however, a number of requirements with regard to processing power, storage space, network connectivity, etc. At the same time, Cloud Computing addresses the effective utilization of centralized processing and storage resources. In this landscape, the INPUT project introduces a novel infrastructure and paradigm to support Future Internet cloud services going beyond classical service models (i.e., IaaS, PaaS, SaaS), and even replacing physical Smart Devices (SD) with their virtual images, providing them to users "as a Service". This paper presents the INPUT concept and its applicability in Intelligent Transport Systems as a representative example of Future Internet.**

***Index Terms*— distributed cloud, intelligent transportation systems, device virtualisation**

I. Introduction

Nowadays, two of the major trends that drive forward the Information Technologies (IT) evolution are: (1) Future Internet (FI) focusing on the expansion of IT intelligence to the greatest possible number of end-user devices, and (2) Cloud Computing addressing the continuously growing requirements for storage space, processing and energy of the IT sector. Although a lot of research and development effort has been put on each of these two focus areas, the integration of these two into a common framework has not been adequately investigated. This paper presents a distributed cloud-based solution with innovative added-value capabilities, as defined in the context of the H2020 project INPUT, that aims at supporting FI cloud services in a more scalable and sustainable way compared to existing state-of-the-art (SoA) solutions.

In section II, the INPUT concept is presented leveraging SoA solutions. An overview of the INPUT system architecture is given in section III. The cloudification of Intelligent Transport Systems (ITS) and the applicability of the INPUT concept on specific ITS services are discussed in sections IV and V. Finally, conclusions along with insights about the envisioned future work within the INPUT project are provided in section VI.

II. State of the Art and the INPUT Concept

Nowadays, intelligence is present at numerous end-user devices, the types and the number of which is continuously growing. The continuous growth of Internet content, applications and services has resulted in ever more demanding requirements related to data transfer speed, storage capacity, processing power and energy consumption.

In order to cope with the limited resources of relatively "small" end-user devices, there have been significant developments towards the migration of applications and services to "Cloud" paradigms ([1],[2]), which move most of the computational and storage weight to large-scale powerful datacenters. The potential of these new paradigms is limited by weaknesses deriving from the utilization of too ossified and obsolete networking technologies and infrastructures ([3], [4]). In this context, ITU-T [5] suggests that a radical change in networking technologies is necessary to achieve the performance scalability levels needed to cope with this hyper connected world, while significantly reducing the energy consumption and footprint of next-generation Internet service infrastructures. To this end, several EU funded projects are dealing with cloud infrastructures and in-network programmability solutions, such as IDEALIST [7] and SMARTEN-IT [8] focusing on cross-layer network optimization (at transport and management levels, respectively) and SASER [9] and G-LAB [10] focusing on Software Defined Networks, GREEN-NET [11], TREND [12] and ECONET [13] dealing with Green Networking, UNIFY [14] dealing with Network Function Virtualization and PAASPORT [15] focusing on cloud services. On the other hand, major telecommunication network equipment vendors are focusing on taking advantage of idle storage space and processing resources of network infrastructure for the support of applications/services exhibiting locality [6].

In this landscape, the INPUT Project aims at designing a

ISBN: 978-1-61804-321-4

novel infrastructure and paradigm to support Future Internet personal cloud services in a more scalable and sustainable way than existing SoA solutions - further extending the EU projects' results- including also innovative added-value capabilities. The INPUT technologies will enable next-generation cloud applications to go beyond classical service models (i.e., IaaS, PaaS, SaaS), and even to replace physical Smart Devices (SDs), usually placed in users' homes (e.g., set-top-boxes, video recorders, etc.) or deployed around for monitoring purposes (e.g., sensors), with their virtual images, providing them to users "as a Service".

Virtual and physical SDs will be made available to users at any time and at any place by means of virtual cloud-powered Personal Networks, which will constitute an underlying service model. These Personal Networks will provide users with the perception to be always connected to their own smart digital (virtual and physical) devices.

INPUT will overcome current limitations in the cloud service design due to the underlying obsolete network paradigms and technologies, by:

- Using the computing and storage capabilities of network infrastructure to allow users create private clouds "in the network"
- Exploiting the energy consumed in network infrastructure more efficiently than in traditional cloud computing scenarios
- Moving cloud services much closer to end-users and smart devices, thus avoiding useless network infrastructure overloading.

III. INPUT System Overview

The primary goals of a high-level system architecture supporting the INPUT concept are the following:

- To enable Telecommunication Operators' Edge Networks to host cloud services, e.g., to host virtualized SDs providing them to users "as a Service" and
- To provide the users with the perception of always having access to their own (virtual and physical) SDs independently from their location.

To this end, INPUT considers a telecommunication network infrastructure with full technological convergence between the mobile and the wireline accesses. The network infrastructure is meant to be constituted by the Core Network (CN) and the Access Network (AN) parts. In SoA network infrastructures traffic from the AN to the CN is aggregated and routed by the Edge Nodes (EN) located in the edge network segment of the telco network. In order to move cloud services much closer to the end-users, SoA Private Cloud paradigms at ENs are considered and extended with novel capabilities and functionalities to support next-generation personal network and cloud services. In particular, the INPUT reference platform shall be capable of providing:

- Standard EN functionality to provide L2/L3 connectivity between AN and CN segments and user authentication.
- Computing and storage capabilities for running both application-level (e.g., providing virtual video decoder services, NAS, smart meter management) and network function services (e.g., IP forwarding/routing, firewall, deep packet inspector, NAT, DHCP).
- Flexible manageability and vertical integration between application-level services and network-specific functions.

INPUT logic spans over three complementary axes, namely "Smart Network Programmability Support", "Smart Personal Cloud Services" and "Network and Service Abstraction and Virtualization Interfaces".

More specifically, at the telecommunication network side and concerning the "Smart Network Programmability Support" axis, the INPUT Platform is meant to replace legacy telco EN with a distributed architecture composed by computing and storage appliances and by physical/virtual SDN switches providing SDN/NFV (Software Defined Networking/ Network Functions Virtualization) and orchestration capabilities.

"Smart Personal Cloud Services" will replace existing smart end-user devices' functionalities and processes with an "in-network" programmable part concerning the INPUT Cloud services. The latter will take advantage of the ground-breaking nature and features of the "in-network" programmability paradigm at the network edge, as well as the extended set of innovative network-integrated primitives.

The "Network and Service Abstraction and Virtualization Interfaces" axis will implement the intermediate level between the other two providing the core of the INPUT framework by:

- Defining the interfaces towards both the "in-network" programmable devices and the Personal Cloud Services, and
- Developing the management logic to drive the long- and the short-time optimal configurations of the network infrastructures and of "in-network" cloud services in order to meet the workload and user's QoE, while minimizing the energy consumption.

Fig. 1 outlines the high level INPUT concept architecture.

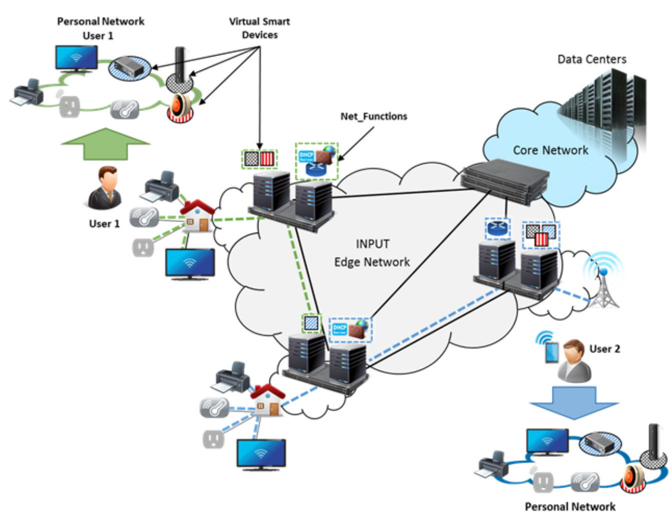

Fig. 1. INPUT System Overview [ref]

IV. The INPUT Concept on ITS

ITS applications aiming at the provision of safety,

ISBN: 978-1-61804-321-4

energy/cost efficient driving, fleet management services, etc. is a typical example of FI services that require system intelligence and operation on a wide number of devices. Such services are posing significant capacity, processing power, latency, etc. system requirements related to data acquisition, processing and storage regarding user/vehicle location, traffic, consumption, direction, driving profiles, etc. received by a wide number of vehicles usually via their in-vehicle systems and/or through users' handheld devices. At user level, the common requirements of ITS users are the need for ubiquitous, efficient access to transport data wherever they are, possibly using different vehicles each time, as well as the need to update this data/information timely with low latency.

Considering the ITS case , the INPUT concept proposes the "cloudification" of part of Advanced Driver Assistance System (ADAS) devices and/or mobile devices' functionality so that part of ITS processing is performed on their virtual image and provided "as a ITS service" to the aforementioned lightweight devices. At next stage, this virtual image can be duplicated or distributed over the network so as to become available to different end-user devices. In this context, the necessary transportation–related data collected from multiple sources will become instantly available upon their creation to the interested, authorized, authenticated users. At the same time the need to download multiple copies of the same data and perform sophisticated, energy-, time- and processing power- consuming functions incurring delays and linking applications/services with specific vehicles, etc. is minimized.

The primary storage and distribution of work data can be determined by a variety of factors such as: special application/service prerequisites, QoS restrictions (especially low latency), available resources at the edge data center/ conventional data center/nano/micro data center. In this context, the image can be stored/placed at a far network end/location, e.g. in order to save storage space when it is required to be accessible by multiple users scattered over a large geographical area. In the opposite case, when customers are spread over a small geographical area it can be stored near the network edge, near the location of the user. Therefore, a management functionality that monitors service, resources and network is required.

Besides Telecom Operators, Cloud infrastructure/services providers and system integrators, interest in ITS over cloud may originate from existing business sectors such as ITS applications/services developers and providers and/or manufacturers of in-car devices (e.g. ADAS).

V. Applicability of INPUT on Specific ITS Services

Multiple services considered under the umbrella of ITS can benefit from the ITS cloudification approach such as:

- Map and collaborative navigation services (personalized time-of-arrival based on driving profile and current traffic conditions, road conditions or other useful information received by other vehicle drivers)
- Intelligent public transport services (incl. collaborative public transport optimization, smart intersection for intelligent priorities)
- Collaborative co-modal route planning
- Cooperative logistics services.

More specifically, in the cases of "map and collaborative navigation services" and "cooperative logistics services", collecting, monitoring and filtering a huge amount of data, as well as storing and presenting it to the end-user device requires a lot of storage and processing power, while more than one user can be interested in the same content. The processes of these services are performed at the ADAS/end-user device side, while their cloudification at remotely located cloud infrastructure may insert quite high delay. Under the INPUT concept, part of the ADAS/end-user device functionality will be substituted by its virtual image, located at a distributed cloud infrastructure utilising telecom edge and core network.

Indicatively, instead of having map information stored at each ADAS/in-vehicle device, it can be stored at a core network point, efficiently accessible by a large number of users. General traffic information can be stored/ processed at a point of the edge network covering a wide area, while specific logistics information can be stored/ processed also at the edge network, especially when it concerns local logistics services. Finally, sophisticated ITS services processing triggered either by the end-user or by the system, such as route optimisation based on various conditions and algorithms, can be performed on the virtual image of the ADAS/in-vehicle device.

Likewise, sophisticated processing required in the case of "Intelligent public transport services" can be performed at the virtual images of the smart end-devices (i.e. the smart intersections devices) located at the INPUT distributed cloud infrastructure.

VI. Conclusion

The INPUT project leverages SoA solutions in order to deliver flexible, distributed FI cloud services, towards even replacing physical Smart Devices with their virtual images, providing them to users "as a Service". The INPUT reference platform is envisioned primarily over Edge Network Nodes providing computing and storage capabilities for running application-level services along with standard L2/L3 connectivity functionality. SDN/NFV and orchestration capabilities for providing flexible manageability and vertical integration between application-level services and network functions are also necessary.

Considering ITS, INPUT envisions the partly "cloudification" of ADAS devices and/or mobile devices' functionality/applications. The INPUT concept is primarily applicable to ITS applications with high storage and processing requirements such as "map and collaborative navigation services" as well as "cooperative logistics services". In such cases, sophisticated processing and, , data storage (map, traffic, etc. data) can be performed at the virtual images of the smart devices located at the distributed cloud infrastructure.

Future R&D efforts will focus on the development of a prototype of the INPUT system.

ISBN: 978-1-61804-321-4

ACKNOWLEDGMENT

The research leading to these results has received funding from the European Commission under the Horizon 2020 - Research and Innovation Framework Programme, Research and Innovation action, Grant Agreement No. 644672 and project name "INPUT: In-Network Programmability for next-generation personal cloUd service supporT" (http://input-project.eu).

REFERENCES

[1] W. Vogels, *A head in the clouds the power of infrastructure as a service*, in: Proc. of the 1st Workshop on Cloud Computing and Applications (CCA'08), Chicago, IL, USA, Oct. 2008.

[2] M. Armbrust, et al., *Above the clouds: a Berkeley view of cloud computing*, Technical Report UCB/EECS2009-28, 2009.

[3] K. W. Cameron, *Energy Oddities, Part 2: Why Green Computing Is Odd*, IEEE Computer, vol. 46, no. 3, pp. 90-94, Mar. 2013.

[4] P.M. Corcoran, *Cloud Computing and Consumer Electronics: A Perfect Match or a Hidden Storm?*, IEEE Consumer Electronics Magazine, vol.1, no.2, pp.14-19, Apr. 2012.

[5] D. Matsubara, T. Egawa, N. Nishinaga, V. P. Kafle, M.K. Shin, A. Galis, *Toward Future Networks: A Viewpoint from ITU-T*, IEEE Communications Magazine, vol. 51, no. 3, pp. 112-118, Mar. 2013.

[6] Nokia, Liquid Net, Product website http://networks.nokia.com/portfolio/liquidnet

[7] EU 7th Framework Program, Cooperation ICT, IDEALIST (Industry-Driven Elastic and Adaptive Lambda Infrastructure for Service and Transport Networks) Project website, http://www.ict-idealist.eu/

[8] EU 7th Framework Program, Cooperation ICT, SMARTEN-IT (Socially-aware Management of New Overlay Application Traffic combined with Energy Efficiency in the Internet) Project website, http://www.smartenit.eu/

[9] Celtic Plus, SASER Project website, https://www.celticplus.eu/project-saser/

[10] G-LAB (German-Lab) Project website, http://www.german-lab.de/index.html

[11] EU 7th Framework Program, GREENET (An Initial Training Network on Green Wireless Networks) Project website, http://www.fp7-greenet.eu/default.php

[12] EU 7th Framework Program, Cooperation ICT, TREND (Towards Real Energy-efficient Network Design) Project website, http://www.fp7-trend.eu/

[13] EU 7th Framework Program, Cooperation ICT, ECONET ((low Energy COnsumption NETworks) Project website, http://www.econet-project.eu/

[14] EU 7th Framework Program, Cooperation ICT, UNIFY (Unifying Cloud and Carrier Networks) Project website, https://www.fp7-unify.eu/

[15] EU 7th Framework Program, Cooperation ICT, PAASPORT (A European initiative on semantically-enhanced marketplace of interoperable Platform-As-A-Service offerings) Project website, http://paasport-project.eu/

Traffic Simulation Platform for Technical Validation and Decision Making in different fields of application

D. Fuentes, I. Luengo, R. Santos, and E. Muelas

***Abstract*—** This paper introduces the capabilities that a novel Traffic Simulation Platform can bring in the technological validation and the decision making procedures in different fields of application. Particularly, it is intended to point up the advantages that the use of the traffic simulation capabilities supposes in two completely different contexts: the first of them, when support to decision making procedures is needed by introducing traffic monitoring, control and prediction policies and infrastructures in the context of a Smart City; and the second one, when support to technical validation is needed by being extremely difficult to reproduce the increasingly complex driving situations with highly automated vehicles in real environments. Thereby, it is intended to put in evidence the wide range of fields of application where a Traffic Simulation Platform can be used. The results which are presented in this paper are the outcomes of research activities which are being performed under the framework of the following JTI Artemis projects: ACCUS and EMC2.

***Keywords*—**Fully Electric Vehicles, Highly Automated Vehicles, Smart City, Traffic Simulation Platform

I. Introduction

THIS paper aims at introducing the advantages that the use of traffic simulation capabilities can suppose in a wide range of fields of application: from the technological validation and decision making both in the context of a *Smart City* and in *highly automated vehicles*. For this reason, a *Traffic Simulation Platform* is currently under development.

The concept of *Traffic Simulation Platform* was born from the FP7 project ECOGEM (whose full title is "Cooperative Advanced Driver Assistance System for Green Cars") [1] and continues its evolution under the FP7 Project EMERALD (whose full title is "Energy Management And Recharging For Efficient Electric Car Driving") [2]. Within the framework of ECOGEM and EMERALD, the platform was designed and developed based on open source SW and focused on supporting *fully electric vehicles* simulation. So, the purpose was to support the verification of the service performance for synthetically generated traffic scenarios with the aim of validating the advantages of using energetically efficient routing vs. traditional (e.g., shortest route, minimized time) routing for *fully electric vehicles*.

The *Traffic Simulation Platform* continues under additional evolution within the framework of the following JTI Artemis projects: ACCUS (whose full title is "Adaptive Cooperative Control in Urban (sub) Systems") [3], where the platform is being incorporated within a real time traffic information platform in the context of a *Smart City* with the purpose of generating historical simulated data to be used to generate traffic models and predictions for a *Smart City*; and EMC2 (whose full title is "Embedded Multi-Core systems for Mixed Criticality applications in dynamic and changeable real-time environments") [4], where it is being adapted to support *highly automated vehicles* and facilitate their associated decision making mechanisms.

As a result of these two projects, the *Traffic Simulation Platform* will, once it is fully operational, feature the following characteristics: (i) high performance, (ii) modular design and open interfaces that allow easy integration into third party systems; (iii) cloud–based services; (iv) easiness of access and operation; (v) high customization in terms of simulation parameters; inclusion of environmental values, and different types of vehicles (vehicles with internal combustion engines, *fully electric vehicles*, or even, *highly automated vehicles*); (vi) multi-criteria route optimization; (vii) schedule through a easy-to-use User Interface; (viii) ability to incorporate real world features in order to predict future situations; (ix) ability to simulate recharging point infrastructure demand and planning recharging points locations in case of *fully electric vehicles*.

II. Concept

A. Functionalities

Although the *Traffic Simulation Platform* was initially designed and developed under the scope of ECOGEM and evolved and improved under EMERALD, the final objective was to develop a market product not only focused on fully

This work was supported in part by the European Commission 7th Frame Programme for ICT under Grant Agreement n° 314151 (EMERALD), by the EU ARTEMIS Joint Undertaking under Grant Agreement n° 333020 (ACCUS) and Grant Agreement n° 621429 (EMC2), and by the Ministry of Industry, Energy and Tourism of Spain (MINETUR) .

D. Fuentes is with the HI-IBERIA Ingeniería y Proyectos S.L. 28036 Madrid, Spain (dfuentes@hi-iberia.es).

I. Luengo is with the HI-IBERIA Ingeniería y Proyectos S.L. 28036 Madrid, Spain (iluengo@hi-iberia.es).

R. Santos is with the HI-IBERIA Ingeniería y Proyectos S.L. 28036 Madrid, Spain (rsantos@hi-iberia.es).

E. Muelas is with the HI-IBERIA Ingeniería y Proyectos S.L. 28036 Madrid, Spain (emuelas@hi-iberia.es).

ISBN: 978-1-61804-321-4

electric vehicles. Nowadays those specific functionalities developed for ECOGEM and EMERALD have been or are being applied to other fields of application, as observed in ACCUS and in EMC2. Also, other new functionalities are currently being incorporated in order to complement the operation of the above-mentioned ones in such fields of application. So, the full set functionalities of the *Traffic Simulation Platform*, once it is fully operational, are described as follows:

- To provide a means for synthetic traffic scenario generation on the basis of different network topologies and context information (e.g. different types of vehicles, different weather conditions, etc.).
- To serve as a validation service to assess the performance of energy efficient route planning technologies with respect to normal route planning and, at the same time, to provide large scale simulations in order to gather insights on the efficiency of the novel optimal route calculation solutions.
- To enable the calculation of the estimated energy consumption and, consequently, to predict the power demand needed from the utility providers. For that, it collects information about past recharging schedules per geographical area and uses it to predict the power demand for the available grids per geographical area, taking into account both past recharging schedules and past recharging history.
- To support recharging station planning by optimally locating the recharging points' into the network topology. Starting from the predicted power demand per geographical area (provided by the above functionality), the platform provides information on where locating the recharging stations, on the basis of the data on historical recharges and calculated predicted power demand.
- To reinforce the city infrastructure planner offering the possibility of locating new recharging points (deployment strategies for recharging points and queuing considerations) based on the currently existing recharging points in the city, and on the particular features of *fully electric vehicles* and historic recharges.
- To conduct simulations in order to predict urban changes caused by variations and events in the urban subsystems. Such predictions are performed by the simulation platform taking into account *fully electric vehicles* capabilities (such as energy consumption and specific features affecting these type of vehicles like slopes, vehicle type or car electric auxiliaries) and real world features available through the urban subsystems with the aim of considering situations based on current road status (such as information from cars obtained from RFID, cameras and sensors installed in the streets and so on). As a result, the platform intends to provide information about possible traffic events or traffic jam prediction that serves as input for other routing applications.
- To allow bidirectional connectivity between the *Traffic Simulation Platform* and routing applications, so routes are generated based on the predicted traffic models (that is, the above-mentioned predictions), which are obtained from ad-hoc simulations for the specific smart city provided by the simulation platform.
- To integrate real-time information from the Smart City in the simulation, so results, predictions and models are more accurate and adapted to the city conditions.
- To allow bidirectional connectivity between the *Traffic Simulation Platform* and ADAS (Advanced Driver Assistance Systems) simulator with frequent updates. Thereby, the *highly automated vehicle* and its surrounding relevant elements will be generated by the platform, whose local dynamic behavior will be updated according to the ADAS simulator feedback.
- To integrate external modules such as DR (Dynamic Ridesharing) and IPM (Intelligent Parking Management) in the traffic simulation, allowing to parameterize their behavior through a GUI coupled to SUMO.To allow monitoring features on top of the simulation environment to visualize the behavior of DR and IPM functionalities.

B. Baseline infrastructure and summary of extensions

The *Traffic Simulation Platform* relies on an *Adapted Traffic Simulator* built starting from an open source traffic simulator named as SUMO ("Simulator of Urban Mobility") [5]. In a few words, using SUMO provides the following relevant advantages to this platform:

1) It is a purely microscopic traffic simulation where each vehicle is given explicitly, defined at least by an identifier (name), the departure time, and the vehicle's route through the network.
2) It allows to simulate different types of vehicles
3) The simulation is space-continuous and time-discrete with a default simulation step length of 1s.
4) It allows to import many road network formats like OpenStreetMap, VISUM, Vissim, or MATsim.

However, such advantages are not enough for the intended purpose and additional features are needed. So, different extensions have already been or are being introduced; the main ones are explained below:

- Adaptation of a theoretical model for *fully electric vehicles*. SUMO introduces the concept of "vehicle devices", such as an emissions control device or a person device for advanced person *interchange*, e.g. from private vehicle to bike or bus. Therefore, an additional "vehicle device" for *fully electric vehicles* has already been created to manage the simulation of common battery measures, and features such as efficiency ratios and weight and torque parameterization; the calculation of energy consumption by car, by area or by time; the consideration of car electric auxiliaries like lights, air conditioner, heating, etc; the consideration of different car driver behavior; and the consideration of different types of vehicles like cars, van or buses, among others.
- Extension of the theoretical model for *fully electric vehicles* to *highly automated vehicles*. Another "vehicle device" is currently being created to manage the

ISBN: 978-1-61804-321-4

simulation of the specific information provided by the sensors on board the vehicle such as cameras, LIDARS (Laser Imaging Detection and Ranging), IMU (Inertial Measurement Unit), V2V (vehicle-to-vehicle) routers, wheel odometer and steering position sensor, among others.

- Ability to read and write XML extended simulation scenario input/output files which are produced/consumed by the *Simulation Web Interface*.
- Inclusion of three-dimensional slopes in maps in order to simulate how they affect the energy consumption of *fully electric vehicles*.
- Inclusion of additional parameters that could influence the traffic conditions such as weather conditions (i.e., rain), day of the week, hour of the day, etc.

The *Traffic Simulation Platform* is being designed in order to be accessed remotely as a web service, and additionally, the majority of the features, which have been or are being added, are developed within an ad-hoc middleware in order to reduce development complexity, isolate critical features and comply with GPL license restrictions which apply for the usage of SUMO.

III. USE CASES

A. The Traffic Simulation Platform in the context of a Smart City

The use of a *Traffic Simulation Platform* which is able to support decision making processes by introducing traffic monitoring, control and prediction policies and infrastructures can bring about a great effect within the context of a *Smart City*.

Chiefly, it could help in solving the some of the main challenges of Sustainable and Green Mobility by providing a means to assess the existing Smart Mobility services and Smart Environment solutions.

In this context, the *Traffic Simulation Platform* can be a traffic information provider for existing Intelligent Transport Systems by providing means for massive and rapid evaluation of traffic and energy consumption scenarios. This is a crucial aspect in *Smart Cities*, as it would contribute in enabling real time online services for traffic management and control, offering a greater flexibility and performance of the current functions of today's traffic management. So, this would enable direct vehicle-to-traffic system interaction, and would allow new possibilities for local, sector and wide area traffic optimization.

Furthermore, the platform can be a means to support the municipalities when it comes to apply urban policies which fosters the introduction of the *fully electric vehicles* with the aim to solve several constraints which affect the today's cities. So, its use can help to the municipalities to make decisions based on transport indicators, efficiency ratios and their impact in the city environment. Among other advantages, the use of the platform for the prediction of energy demands and for the optimization of recharging infrastructures planning is quite relevant for Regional or National Public Authorities to assess and evaluate the wider impact of adoption of *fully electric vehicles* in the cities.

Anyway, the *Traffic Simulation Platform* is not only beneficial for the city authorities, but also for the citizens, as observed in the Fig. 1, where the citizen can request several alternative routes depending on the traffic situation in the city through a mobile application.

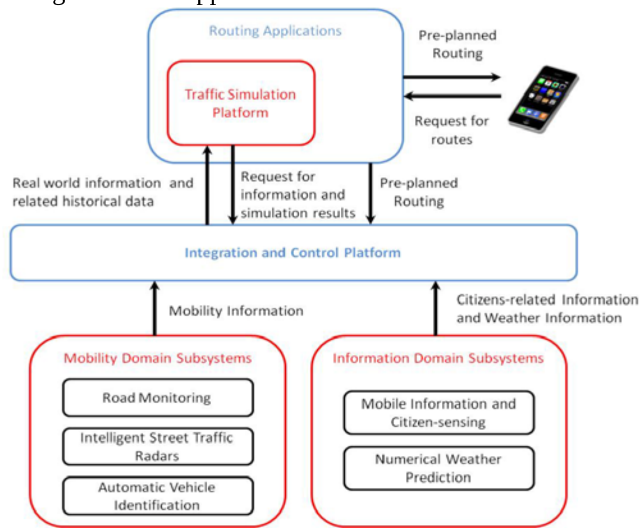

Fig. 1 Potential use of Traffic Simulation Platform in a Smart City

Specifically, the Fig. 1 illustrates a scenario in which the citizen wants to know if there is any problem on the traffic flow for his/her route, and he requests information to the routing mobile application which informs him about the conditions in real time. In order to obtain this kind of information, a procedure is started:

1) The information related with the traffic is provided to the Integration and Control Platform through the Road Monitoring and the Intelligent Street Traffic Radar Subsystems which monitor the weather conditions and their impact on the road surface as well as the traffic flow using wired and wireless sensors.
2) On the one hand, these data are processed by the Route application which analyzes the traffic conditions with the aim of obtaining the best possible route for a user by means of detecting incidents such as congestions, traffic jams and vehicle collisions.
3) On the other hand, these data are also processed by the *Traffic Simulation Platform* which makes traffic predictions on multiple variants of scenarios created mixing real-life city events obtained by Information Domain Subsystems and a number of frequent possibilities that might affect the outcomes in order to provide decision-making information to Routing Application to generate the best possible route.
4) If a traffic jam is detected or predicted, the city management authorities receive through a traffic event application information regarding the traffic situation and possibilities of rerouting the cars involved. At the same time, the citizen who made the request through the Routing Application receives information about the traffic status and alternative routes to avoid the traffic jams and

reach their destination saving time and gasoline consumption.

Of course, this is only one use case of the many that there could be in the context of a *Smart City*.

B. The Traffic Simulation Platform for Highly Automated Vehicles

The evolution towards *highly automated vehicles*, zero-accident driving and associated improved road utilization accelerate the trend towards integrated and dependable ADAS systems. In this sense, preventing accidents and automating tasks in progressively more complex driving situations requires innovation in perceiving the environment, the driver-state, the vehicle-state, and the reasoning/interacting about these tasks. However, human intervention is still necessary in specific situations, so advanced human machine interfaces have to be considered not only for safety-related feature, but also for other purposes such as navigation or web services.

In this context, a seamless integrated simulation environment, which is composed of a *Traffic Simulation Platform* and ADAS simulator, can be a valuable help to support the technical validation of the system, since it is not at all easy to reproduce the increasingly complex driving situations with *highly automated vehicles* in real environments. Additionally, not only the embedded functionalities are evaluated, but also the aspects related to the connectivity with the world such as DR and IPM functionalities. Therefore, the two main reasons which support the development of this simulation environment are as follows:

- To carry out complete and reliable simulators, since it is a must to validate the proper behavior of such complex systems at different levels in the development cycle.
- To simulate external modules such as DR and IPM, since it is extremely hard to cope realistically with these modules in real environments.

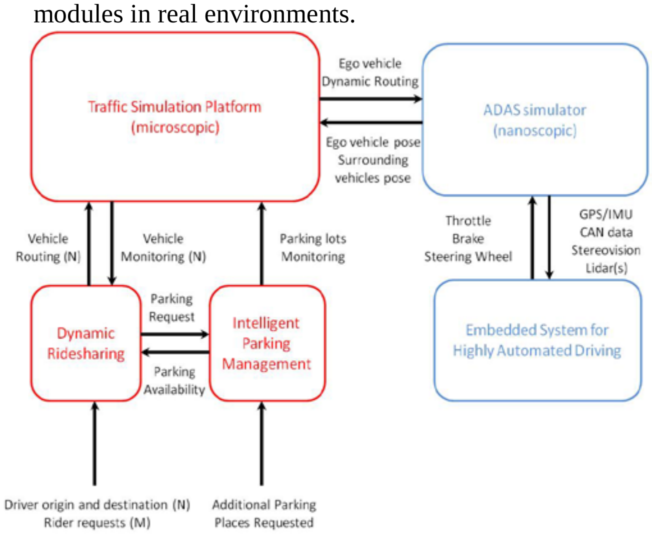

Fig. 2 Use Case of Traffic Simulation Platform for highly automated vehicles

Specifically, the Fig. 2 illustrates a scenario in which the *Traffic Simulation Platform* provides a dynamic vehicle routing to the ADAS simulator according to the ego and surrounding vehicles evolution provided by the ADAS simulator itself in a given time. So, the procedure to calculate such dynamic vehicle routing is as follows:

1) The ADAS simulator reproduces the different behavior of the sensors on board vehicle such as stereo cameras, LIDARS, IMU and GPS, among others, as well as the road simulation environment in a given time.
2) On the one hand, these data are sent to an embedded system which is used to make decisions on the *highly automated vehicles*, and which acts on different actuators such as throttle, brake and steering wheel in a real environment.
3) On the other hand, these data are processed by the ADAS simulator itself with the aim of providing the ego and surrounding vehicles positions to the *Traffic Simulation Platform*.
4) The *Traffic Simulation Platform* provides the ego vehicle routing to ADAS simulator dynamically considering, on the one hand, the ego and surrounding vehicles positions previously sent by the ADAS Simulator; and on the other hand, the potential vehicle routing provided by the DR module in case of the vehicle is shared by several passengers, and the free parking lots in case of the vehicle needs a parking space. As a result, the ego and surrounding vehicles evolution will be part of a frequently updated closed-loop system between both simulation platforms.

Therefore, although the perception and localization needs to be evaluated in real experimentation, risk assessment and decision-making mechanisms can be validated to some degree at the simulation level, where traffic and infrastructure connectivity features can be more pertinently tested.

IV. Conclusions

This paper presented the advantages that the use of a *Traffic Simulation Platform* can bring in the technological validation and decision making procedures in the context of a *Smart City* and for *highly automated vehicles*, as well as the full set functionalities that the *Traffic Simulation Platform* will feature and the summary of extensions brought in SUMO, once it is fully operational.

Acknowledgment

Authors thanks EMERALD, ACCUS and EMC2 Consortia their cooperation along the lifecycle of both projects.

References

[1] EcoGem Project Official website retrieved in May. 2015 under http://www.ecogem.eu
[2] EMERALD Project Official website retrieved in May. 2015 under http://www.fp7-emerald.eu/
[3] ACCUS Project Official website retrieved in May. 2015 under http:/www.projectaccus.eu
[4] EMC2 Project Official website retrieved in May. 2015 under http://www.artemis-emc2.eu/
[5] SUMO Simulation for Urban Mobility - website: http://sumo-sim.org/

Source code security of web-based hybrid mobile applications

Radek Vala, Roman Jasek, and David Malanik

***Abstract*—**HTML5 hybrid mobile application (HMA) development is considered as a cross-platform solution in world of mobile application. Therefore, this development approach is relatively popular and competes with the native approach, but both one and the second are suffering from inability to achieve sufficiently secured source code of product application. Whereas the mobile application package is distributed from distribution channel to end mobile phone, developers have to consider this mobile phone as a client device, with fully access to the application package. Preventing reverse engineering of application source code seems to be almost impossible. While source code of the native application is converted into byte code, application resources, which form the application logic of HMA, remain unchanged and it is possible to get it very easily. This paper focuses on increasing security level of these resources, because in case of HMA, there can be revealed very valuable information about application architecture, or they can be extracted for a purpose to create malicious copy of the application.

***Keywords*—** Source code security, mobile application, native application, HTML5 mobile application, hybrid mobile application, encryption

I. Introduction

MOBILE application development is in recent years one of the most active area of software development. With the rapid growth and changes in the mobile market also developers are facing a lot of options and challenges within the process of mobile application development. Development teams are trying to publish applications for all major platforms on the market, which means to prepare at least three different versions in these days. Recently, it can be stated that three different approaches in mobile application development are used in general. The first one is native development approach, which is the basic way of mobile development, which occurred after introduction of software development kit (SDK) within individual mobile platform. Advantage of this method is especially existence of mature development tools and methods or platform guidelines, which are maintained directly by the platform vendor. The main disadvantage is the fact that there has to be separate development project for each mobile platform. The main purpose of second two methods (so called hybrid mobile application development methods) is to bring solution for cross-platform development in mobile world. The diversification of various mobile operating systems is at very high level, therefore the cross-platform solutions are not able to offer developers to various mobile platforms. But these solutions allow reusing as much source code as possible in process of development mobile application for more platforms. One of these method is based on cross-compilation from some common language to native language (Xamarin) [1] and the other is based on HTML5 technologies [2] running in integrated web browser used as a runtime environment.

This paper focuses on the web-based (HTML5) hybrid mobile application development method, especially on the security of application source code.

The source code security is a highly discussed topic in the area of mobile applications, because of mobile application package insufficient security level. The possibility of extracting the application package brings up security challenges, also in context of web-based hybrid mobile applications, because getting source code and sensitive business logic is in this scenario feasible also by moderately experienced user.

Extracted source code could be an inspiration for a rival company or complex template for creating fraudulent application or other kind of malware. Moreover, it often reveals valuable know-how or sensitive data, such as complex access to web services and other network data sources.

First section of this paper introduces the types and architecture of web-based mobile applications. Then the research is focused in security concerns of mobile application packages, which are used on the major platforms. Chapter III shows the principle of encrypted source runtime decryption for achieving the higher security level. In chapter IV, there can be found the proposal implementations with different encryption key storage. These methods are compared, and limitations are discussed here.

II. Introduction to Web-based mobile applications

This chapter introduces the web-based hybrid mobile application architecture and appropriate development methods, because they are in main focus of this paper.

A. Web-based mobile application types

In 2007 at the WWDC, Apple announced that the iPhone would run web apps, which will be created for Safari and there would be no need for any SDK. “The full Safari engine is inside of iPhone. And so, you can write amazing Web 2.0 and Ajax apps that look exactly and behave exactly like apps on the iPhone.” (Steve Jobs, Apple WWDC 2007).

The research work was performed to financial support by the European Regional Development Fund under the Project CEBIA-Tech No. CZ.1.05/2.1.00/03.0089.

The idea of cross-platform web based mobile applications has the same basics. The web browser can be used as a runtime environment for the application and all of the major platforms offer modern web browser with capability to run such an application.

Web-based mobile application can be divided into these types: Mobile web, Standalone mobile web application and Web-based (HTML5) hybrid mobile application.

Mobile web is common web site, which is adapted for mobile devices (especially in area of displaying on small screens, or supporting touch gestures). Standalone mobile web application is an Apple customization of common mobile friendly website [3], which can be saved to desktop and provides some desktop icon. Both of these types of applications are available through mobile browser and are hosted on the Internet with specific URL. On the other side, Web-based (HTML5) hybrid mobile application could be locally hosted directly in the mobile device and behave like typical native application. The runtime environment - web browser - and also the HTML5 source code of the application is packed inside the native application package. This package can be distributed using official distribution channels (App Store, Google Play and Windows Phone Store) and the application is able to cooperate with native mobile device APIs within the native container.

B. Architecture of web-based hybrid mobile applications

The idea of cross-platform mobile application is directly connected with cross-platformity of web pages. If there is native web browser on each mobile platform, than web technologies are the only source code, which is possible to interpret on each mobile device.

The most simple web-based hybrid application could be implemented using native application wrapper, which contains web view (view component for displaying websites).

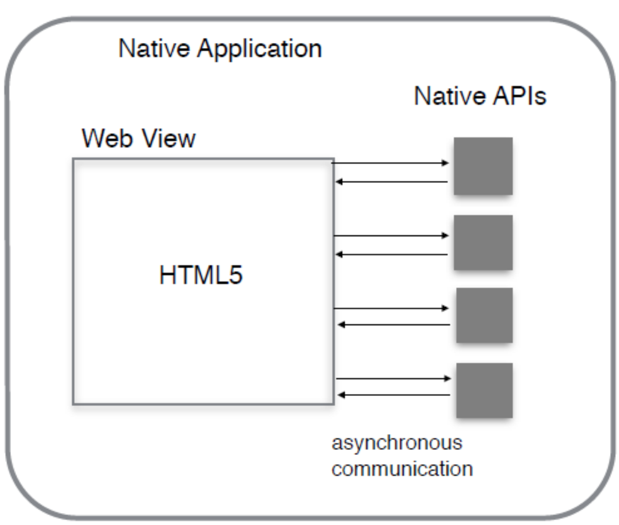

Fig. 1 web-based HMA architecture

In real scenarios this implementation is more complex (see Fig. 1, because it is necessary to resend native application's life cycle events to the web-based application logic.

Mobile devices in these days are also equipped with various hardware peripherals such as GPS, Accelerometer, Camera etc. and HTML5 specification do not define API for accessing all of these hardware. Therefore there is a need for technology called native bridge, which creates the communication link from native APIs (which are able to access hardware peripherals) to web-based source code (application logic written in JavaScript). Typical representative of this technology is open-source project Apache Cordova [4], or its commercial branch Phonegap [5].

C. Decomposing of application package

Application package is possible to extract and decompose. Therefore there is no safety mechanism by default. This statement is true for all major platforms (Android, iOS, Windows Phone). Android platform is using for the application package the format APK, iOS platform IPA and Windows Phone XAP or APPX. All of these formats are basically ZIP containers, which is possible to decompress and obtain the content. Overall Android application structure is described [6].

Getting the native source code from the extracted package into readable form is more complicated, but also possible. The source code is presented in compiled form and therefore it is not readable. In case of Android applications also native source code is possible to obtain with proper tools using static analysis methods discussed in [7], [8],[9].

If we consider iOS applications, it is more complicated because part of application content is encrypted using per-device unique key, but the source code, could be particularly obtained from jailbroken device as well. The hacker is than able to get all of the method names and its parameters, frameworks used, property lists and also variable names [10].

In case of web-based hybrid mobile applications, the main application logic is usually kept in JavaScript, which can be found with other application resources (HTML, CSS, images, fonts, etc.) in resources folder. Because there is no obfuscation by default and no need for compilation, these sources are fully readable regardless of platform. This weakness could be very easily misused and so-called repackaged attacks against web-based HMA on the Android platform are described in [11].and application package structure (APK). The main application logic and valuable know-how is fully accessible to everyone in few steps:

1) Downloading some mobile app from store
2) Changing the extension to zip
3) Extracting the package
4) Navigating to the resource folder to folder www
5) Viewing the source code

III. Securing of web-based HMA application logic

From the chapters above it is obvious, that obtaining whole readable source code of web-based HMA is possible also for mid experienced user, therefore severity of this security issue is bigger than in case of native applications.

ISBN: 978-1-61804-321-4

Level of security could be considered the same as in case of common web application, where the user is also able to see the source code. However, due to reduction of network data flow, in case of mobile devices, maximum of application logic is transferred to client side (to mobile device) and only web services or some sensitive information are kept on the server side.

From these reasons web-based HMA could be the easiest target for some hacker to create a spoofed application (using slightly modified version of obtained source code) and spread this malware application, which will mimic the original one.

The following text presents available options for increasing the level of the source code security and brings also considerations of its limitations.

A. Minification, uglyfication and obfuscation

Terms minification and uglification are well known for JavaScript developers. The first one means cropping white spaces and combining source files and the second means shortening function names etc. to reduce the code footprint. Obfuscation is not so widely used in case of web-technologies, because critical parts are usually kept on the server side. But obfuscation is growing in importance especially in context of week security level of mobile application packages, because it is can be used for source code transformation into unreadable and understandable form. Application of these methods can improve the base level of security of source code, but with proper tools and effort, the original source code could be also regain. Practical application of JavaScript deobfuscator in context of JavaScript malware detection is shown in [12].

B. Encryption of source code

The only way to protect the source code of web-based HMA, which is held in unprotected resource folder of application package, is to encrypt it by the build process and provide decryption at run time (Fig. 2).

In this scenario, the source should be still obtained from the application package resource folder, but as far as it is encrypted, it is not possible to decrypt it without knowledge of encryption key by simple extraction of application package.

IV. Implementation and Technology Challenges of Source Code Encryption

This chapter focuses on implementation options, limitations and challenges arising from contemporary architecture of mobile operation systems.

A. Cryptographic function

The first implementation issue is, which of cryptographic function is appropriate to use in case of mobile application. One of the most used encryption method in desktop development is Advanced Encryption Standard (AES). According to US National Security Agency (NSA) 256 bit keys in AES are suitable for top-secret materials. [13] With the advert of native crypto functions in mobile operation systems, AES is also suitable in mobile environment without significant performance impact.

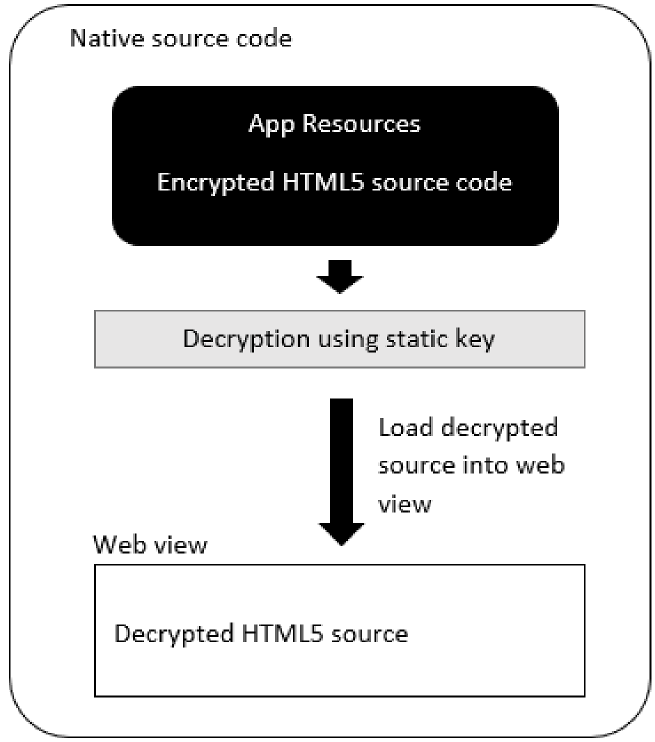

Fig. 2 runtime source code decryption process

B. Key storage

The main security is how to store encryption key securely on client device. In source code (neither native nor web-based), there is no secure place for storing sensitive information (e.g. crypto key) on the client. Therefore, one of the main challenges is, where and how to save crypto key, which will be used for source code decryption.

C. Types of secured source implementations

After the research of security principles and distribution process of mobile application packages, several possibilities of source code securing using encryption were identified and are listed and described below. All solutions are based on fact, that application logic - JavaScript and CSS source code is minimalized, combined into one file with HTML, encrypted and then embedded into application package. The source code encryption key is static and never changes because encryption has to be completed before build of the product application. Therefore all clients have to use the same crypto key for source decryption. Sharing one static key between more client applications is usually considered as serious weakness. But this issue arises, from the application package distribution process, which is uniform, with no possibility to change source code per client. Moreover, if main goal of encryption is source code protection in this scenario, then if the encryption key is revealed, the secret is revealed, no matter if for one specific application build, or more. Therefore the most important task should be the encryption key protection.

ISBN: 978-1-61804-321-4

1) Static key embedded in native source code

Encryption key could be basically embedded right into native part of application source code, but with the risk of disclosure. Especially longer strings are noticeable by in-depth analysis of source code. Although obfuscation may be reverted, it has to be provided to the embedded static key, to ensure at least basic security level of the key.

2) Static key requested using HTTPS request

This approach attempts to eliminate the main disadvantage of the previous one. Encryption key is not presented directly on device, but it can be send there from the server-side by starting process of the application. In this scenario, the weak point is transferred to the server-side and especially into moment of proper authorization of client device. The attacker could try to analyze application's network traffic and pretend the authorized application and create fake HTTP(S) request to the server to obtain the encryption key.

3) Client-server composite key

Higher level of security could provide the partial key, which is embedded directly in native source code. Although it could be obfuscated it is still possible to get it by the attacker using static source code analysis. However this string is looking like an encryption key, it is just a part of the complete key, therefore is not possible to use it for encryption. As can be seen in Fig. 3, the second part of the key is on the server-side, therefore there is also need for request to the server. Within this request, unique identifier of device and timestamp could be sent to the server.

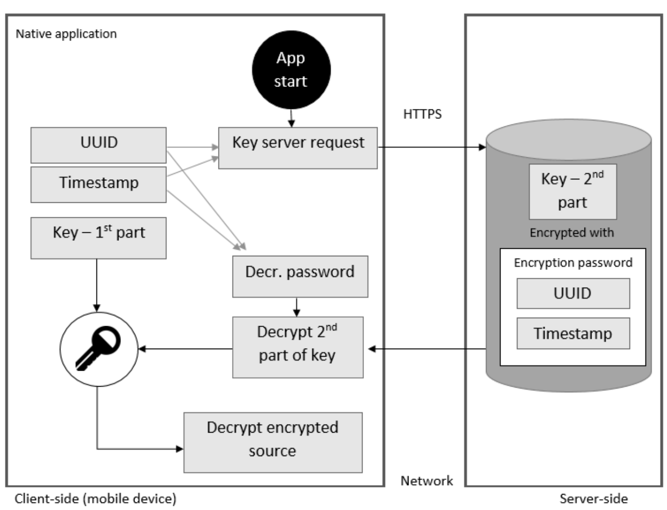

Fig. 3 process of decryption using client-server composite key

On the server-side, the second part of the key is encrypted also using AES-256 and dynamically changing password, which can be obtained from the combination of device identifier and timestamp string. Encrypted second part of key is sent then via server response over HTTPS. Client application decrypts the second-part of the key using own unique identifier and stored timestamp and connects the two parts of the key. Encrypted source code, could be decrypted then.

D. Security comparison and limitations

Provided approaches for encryption key storing in context of web-based HMA with encrypted source code, was compared using DREAD threat model [14] and also security limitations are discussed in following text.

DREAD threat model was used for evaluation and relative comparison of security level gained using particular implementation method. The DREAD threat model is commonly used in case of web applications, but for simple comparison it is applicable also in this scenario, where the vulnerability of getting the application resources with encrypted source code, was evaluated. Evaluation of parameter D (Damage potential) and A (Affected user) was evaluated in the same manner for all application types. It is assumed here, that getting of the encrypted source code can cause an average damage and also for an average count of users. For example, unlike web applications, malicious mobile application is not possible to distribute among all users centrally.

As can be seen from Table 1, the most vulnerable type is the default type of HMA application package without any further encryption. The threat rate decreases with added security mechanism and encryption.

Table 1 DREAD threat model

Application type	D	R	E	A	D	Rate
No encryption	5	10	10	5	10	8
Static key embedded in native source code	5	5	5	5	5	5
Static key requested	5	4	4	5	5	4.6
Client-server composite	5	1	0	5	1	2.4

The most important limitation of the encryption approach in context of HMA in general is the possibility of live debugging of encrypted JavaScript source code. Live debugging can be normally done only against application running in browser, but in case of rooted or jailbroken devices it is possible to debug also native application's web view.

V. Further Research

During examining the security of mobile application packages, there emerge several areas for further research. Especially the problem of secure key storage could be at least for iOS devices solved using implementation of Keychain. In further research, pentesting of Keychain could be performed and security level and limitations could be considered. Also secure storage within other major platform could be studied.

VI. Conclusion

Security issues of mobile application packages were considered in the first part of the paper. The security research revealed, that current technology available to developers suffers from serious lack of security mechanism for application content protection. In case of all major mobile platforms, the application package is possible to extract and reveal application resources with almost no effort and only the basic knowledge. This is especially critical for web-based HMA application where the main application logic and valuable know-how is stored directly in application resources without any encryption. However, also in case of native application, the reverse engineering of source code is possible, but while the source code is compiled, higher level of effort and knowledge is required.

In chapter IV countermeasures against insufficient source code security in HMA were proposed. These countermeasures are based on source code encryption and subsequent decryption in runtime. Encryption disables obtaining source code using application package extracting, however, it overlaps another security issues such as the problem of storing encryption key.

Limitations of proposed security countermeasures are based on current technology concepts, used within mobile platforms. The most serious issue of proposed implementations is the possibility of live source code debugging via rooted or jailbroken device.

This research of mobile application packages highlights serious weaknesses and security concerns connected with possibility of source code reverse engineering. Fundamentally identical types of attacks are applicable on all of major mobile platforms. Only the level of effort required differs here in behalf of closed source platforms.

The main conclusion is not very optimistic. In these days, there is no possibility to secure the know-how, intellectual property, or sensitive parts of source codes in case of mobile application. Almost all security mechanisms are breakable using proper knowledge, tools and effort. However, protection against low and moderately sophisticated attacks is feasible and possible implementation concepts were designed.

REFERENCES

[1] Xamarin Inc., “Build apps in C# for iOS, Android and Windows Phone. - Xamarin,” 2015; [Online]. Available: http://xamarin.com/platform.

[2] S.S. Freed Ned, Abel Yang, “RFC 2045 - Multipurpose Internet Mail Extensions (MIME) Part One: Format of Internet Message Bodies,” 2012; https://tools.ietf.org/html/rfc6532.

[3] Apple Inc., “Mac Developer Library - Safari Web Content Guide,” 2014; [Online]. Available: https://developer.apple.com/library/mac/documentation/AppleApplications/Reference/SafariWebContent/ConfiguringWebApplications/ConfiguringWebApplications.html.

[4] The Apache Software Foundation, “About Apache Cordova™,” 2013; [Online]. Available: https://cordova.apache.org/.

[5] Adobe Systems Inc., “PhoneGap Home,” 2015; [Online]. Available: http://phonegap.com/.

[6] D. Shivarudrappa, et al., “COFA : Automatic and Dynamic Code Offload for Android,” University of Colorado.

[7] A. Bartel, et al., “Dexpler: converting Android Dalvik bytecode to Jimple for static analysis with Soot,” *Proc. SOAP '12 Proceedings of the ACM SIGPLAN International Workshop on State of the Art in Java Program analysis*, 2012, pp. 27-38.

[8] É. Payet and F. Spoto, “Static analysis of Android programs,” *Information and Software Technology*, vol. 54, no. 11, 2012, pp. 1192-1201; DOI http://dx.doi.org/10.1016/j.infsof.2012.05.003.

[9] N. Raboy, “Extract An Android APK And View Its Source Code,” 2014; [Online]. Available: https://blog.nraboy.com/2014/11/extract-android-apk-view-source-code/.

[10] M. Renard, “Practical iOS Apps hacking,” *Proc. The 2nd International Symposium on Research in Grey-Hat Hacking*, 2012, pp. 15-26.

[11] H. Heitkötter, et al., “Evaluating Cross-Platform Development Approaches for Mobile Applications,” *Proc. 8th International Conference, WEBIST 2012, Porto, Portugal, April 18-21, 2012, Revised Selected Papers*, Springer-Verlag Berlin Heidelberg, 2013, pp. 120-138.

[12] G. Blanc, et al., “Term-Rewriting Deobfuscation for Static Client-Side Scripting Malware Detection,” *Proc. New Technologies, Mobility and Security (NTMS), 2011 4th IFIP International Conference on*, 2011, pp. 1-6.

[13] National Security Agency, “NSA Suite B Cryptography,” 2009; [Online]. Available: https://www.nsa.gov/ia/programs/suiteb_cryptography/.

[14] OWASP Foundation Inc., “Threat Risk Modeling,” 2015; [Online]. Available: https://www.owasp.org/index.php/Threat_Risk_Modeling.

ISBN: 978-1-61804-321-4

HTML5 hybrid mobile application development in comparison with native approach

Radek Vala, and Roman Jasek

Abstract**—**The main trigger for HTML5 hybrid mobile application development was the rise of multiple mobile platforms. In recent years there were relatively large changes in the market distribution of particular platforms and it is not possible to forecast, if this trend will continue. Developers are tending to support all of the major mobile operational systems, but in case of native development, there is often need for extra development team for each platform. Therefore, the native development is usually the most expensive way. Moreover, new and promising platforms are appearing in area of open-source operational systems (OS) and low cost devices and adding support to these new platforms can be time and financial demanding. The key idea of mobile hybrid application development is in maximization of common source code, which could be executed on different mobile platforms. And with consideration of mobile OS market distribution changes, it is also possible to create mobile application supporting new platform quickly and with less expenses, than in case of native development approach. And this is the main reason, why hybrid mobile application development is a popular approach. However, this development approach has also a lot of opponents and it is very important to identify its strengths and weaknesses. This paper focuses on the comparison of HTML5 hybrid mobile and native application development in connection with the latest trends and support development technologies, which appeared in recent years.

Keywords**—**mobile application, native, HTML5, development process, cross-platform, comparison.

I. Introduction

In recent years, the mobile market has been rapidly changing. We have seen new mobile platforms emerging and taking a substantial part of the current market. Also developers are facing a lot of options and challenges within the process of mobile application development. Some of the established mobile platforms have very quickly lost significant market shares. In some aspects, different mobile platforms are getting closer, especially in case of user experience, design or ergonomics. But in fact, the diversification of software development tools and development or production concepts, increases.

These differences in development concepts lead to the effort to form new cross-platform development methods and therefore the principle of transformation native application to web-based application appeared also in mobile world. This idea is based on same basics - each mobile OS provides some Internet browser (so called Web View) and therefore, the web-based source code is possible to consider cross-platform within all mobile platforms.

Very interesting is the fact that the idea of creating web-based applications firstly appeared in mobile context at the Apple Inc. company. In 2007 at the WWDC, Steve Jobs announced that the iPhone would run web apps, which will be created for Safari without need for any Software Development Kit (SDK). These applications should provide the same look and functionality as build-in iPhone apps, but technically they could be written using Web 2.0 and AJAX technology. But in the same year beta of Android OS was released followed by the own native SDK. In 2008 Android 1.0 with SDK and also iOS 1.x with SDK were introduced and gave the third party developers the possibility of creating native applications. The native application development becomes almost the only trend especially within Android platform, where the implementation of native Internet browser was, in comparison with desktop browsers, insufficient and with slow performance. But the great divergence between major mobile platforms still keeps the web-based cross-platform solution popular. Moreover, this popularity of cross-platform solutions has started to grow.

In 2011 Adobe Inc., acquired Nitobi, developer of PhoneGap technology, which is basically a native mobile wrapper for running web-based applications (so called hybrid mobile applications - HMA). The popularity of HMA have peaked probably just in this year. In 2012, few well-known companies from the IT world announced the transition from HMA to native applications, which started the loss of HMA's popularity.

This paper is focused in real comparison of the pros and cons of hybrid or native mobile applications and especially in context of latest development trends, tools and current technology state.

II. Related work

The most serious limitation of research in the field of mobile application development is, that the studies are highly relevant only in short term and for specific technologies or development tool versions, or in context of specific mobile platform versions.

Currently, there is possible to find research papers focusing on the basic comparison of native and hybrid development [1] - [3] or the challenges of hybrid approach [4] - [8].

The main limitation of majority of the revisited comparative studies is the fact, that lot of information there is outdated.

The research work was performed to financial support by the European Regional Development Fund under the Project CEBIA-Tech No. CZ.1.05/2.1.00/03.0089.

Introduction of new OS version releases, within iOS and Android platform, greatly changed important aspect of web-based HMA development. These aspects are discussed in the following text.

Other limitation of some studies and research papers lie in high generalization of the problem and solutions. For example authors from IBM Software Lab propose in [9] new approach for reusing web or desktop based server Java applications on mobile platforms. This approach deals with translators for application business logic. Source code can be automatically translated from Java to .NET (or Objective-C) for porting to other mobile platform, where only UI needs to be designed from the scratch. However, the paper shows only very simple example of translating one-class source code and there can be a very serious limitation in case of complex-source code translating. Post-processing of such automatically translated code, to eliminate possible syntax error, could be very demanding.

III. Mobile Application Types

Mobile applications can be divided into two main types – native and hybrid applications. The native apps are developed with proper platform SDK using native programming language. In context of cross-platform applications (so called hybrid mobile applications), another two types may be found in mobile development. First solution is based on web technologies and the second on cross-compilation or interpretation of another common programming language. Also standard web applications can be adapted to mobile browsers, to bring more complex app-like behavior within the mobile Internet browser.

A. *Native mobile applications*

The most platform specific are the native mobile applications. Mobile platform vendors issue SDKs using which is possible to develop platform dependent application, designed for specific hardware or device capability. Within SDKs, there are native libraries for GPS, camera, accelerometer and other device's peripheral.

B. *Hybrid mobile applications*

The name of this development method is based on architecture of the development approach, which combines native technologies for creating the runtime application wrapper with non-native language for application logic development. In recent year, Xamarin technology [10] appears to get one of the leading technologies in cross-platform mobile development. It creates whole new development platform, ecosystem with mature development tools and possibility to use one programming language, at least for application logic part [11]. But the heterogeneity of specific platform projects, which is relatively large, shows the advantage of web-based HMA, where most of the source code can be shared.

Web-based (HTML5 [12]) hybrid mobile application could be locally hosted directly in the mobile device and could behave like typical native application. The runtime environment - native web browser classes - and also the HTML5 source code of the application are packed inside the native application package. This package can be distributed using official distribution channels (App Store, Google Play and Windows Phone Store) and the application is able to cooperate with native mobile device APIs within the native container. Probably the most known wrapper technology for web-based HMA is the open-source project Apache Cordova [13] and its commercial branch Phonegap [14], owned by Adobe Inc.

IV. Comparison of Native and HMA Development Process

Following comparison is based on key findings of few research papers focusing on this topic and real experiences from the field of mobile development. According to identifying strengths and weaknesses, SWOT analysis [15] of each approach is provided in following text.

A. *SWOT analysis of native approach*

As can be seen in Fig. 1, the strengths of native approach are especially the application performance and the actuality of framework (fast adaptation on mobile operating system updates or new features). Native applications also provide full access to native libraries (APIs) for working with various sensors or hardware peripherals of mobile device. One of the most significant advantages for end-user is the design of application, which is created using native user interface objects, with full support of native animations and hardware acceleration. This leads to smooth and consistent user experience.

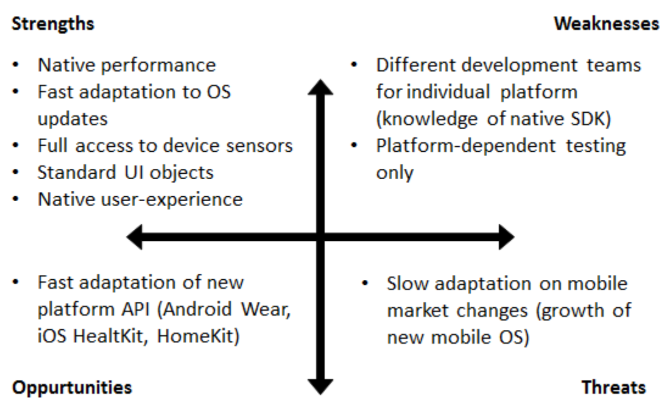

Fig. 1: SWOT analysis of native mobile development

If we consider the opportunities of native approach, in contrast of hybrid development, there is the possibility to fast adaptation on new platform API. We can mention few of newly introduced technologies in recent years. E.g. Android Wear [16], iOS HealthKit [17], iOS HomeKit [18], etc.

In a bigger project, there is usually the need for different development teams for individual platform, which is probably the most significant weakness of the native development approach. The development team should provide specific know how for specific platform. In case of testing, there is no possibility to test some parts (e.g. business logic) platform independently.

ISBN: 978-1-61804-321-4

The native approach has also one serious thread, which is the slow project adaptation on mobile market changes. As the history has shown, rapid changes on mobile platform penetration are possible and new mobile operating systems could appear. Porting the application to another platform using new SDK could be costly and time challenging.

B. SWOT analysis of web-based HMA approach

Fig. 2 shows, that there are following strengths within HMA development. The build process could be set up to build once and deploy to all target platform. While the business logic is almost reusable across different platforms, the maintenance costs, are lower than in case of native approach. There are also lower demands on technical know-how within HMA, because there is no need to have deep knowledge of single mobile platform and its SDK and different programming languages.

Within the opportunities, there can be found the possibility of fast adaptation to market changes. E.g. when new mobile platform occurs, it is possible to port the application easily, without need to create new separate project (if the platform is supported by the wrapper technology).

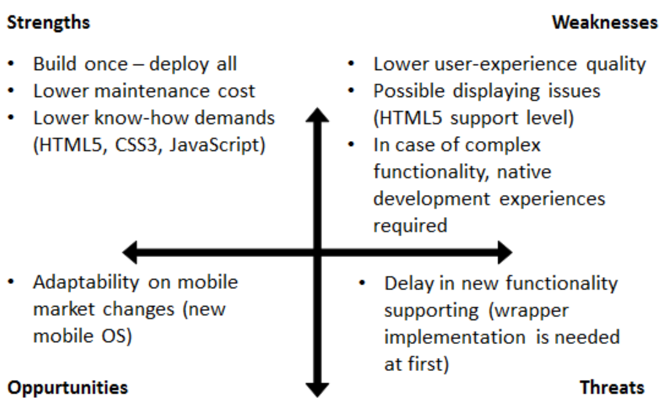

Fig. 2: SWOT of HMA development

HMA development approach also brings following weaknesses. It is very common, that the user-experience is worst as in case of native applications. This is due the way of creating application UI, which is built using web technologies instead of native UI components. Also displaying issues often occur. Moreover, if the application should provide lower level or other complex functionality, native development experiences could be required for implementing the functionality, which is not provided by offered plugins.

The most significant threat is the delay in new functionality support. For example if the new mobile OS version is introduced and the wrapper technology do not fully support it.

C. Skillset comparison

Both native and web-based HMA development approaches requires different set of skills. For following comparison, an application development for three major platforms (Android, iOS, Windows Phone), were considered. As can be seen from Table 1, within the native development approach, at least 12 different skills are needed within the development team, in contrast with web-based HMA, where only 4 skills are needed. Moreover, if we consider finding developers with desired knowledge, the resource pool is significantly bigger in case of programmers with web technology know how in contrast with experts on specific native platform.

Table 1: Native and HMA development skillset comparison

Native approach				
Platform	**Business logic**	**User interface**	**IDE**	**SDK**
Android	Java	Android XML	Android Studio	Android SDK
iOS	Objective-c	Storyboards	Xcode	iOS SDK
WP	C#	XAML	Visual Studio	WP SDK
Web-based HMA approach				
Platform	**Business logic**	**User interface**	**IDE**	**SDK**
All	JS	HTML5	arbitrary	HTML5 API

D. Criteria comparison

For comparison purposes 22 criteria from 6 categories of development and preparation process for more mobile platforms were identified.

The criteria from the Table 2 were rated from 1 to 5, which means from the least suitable to the most suitable. Each criterion evaluation is based on real experiences from mobile application development. Rating justification and clarification of the criteria is shown in following text.

Table 2: Criteria comparison of native and HMA development

Criteria	Native	Hybrid
Category: Costs		
Development cost	3	4
Support cost	3	4
Cost/Time-to-market	3	5
Category: Development process		
Code reuse and duplication	2	4
Off-line Support	5	3
Leveraging existing web apps	2	4
Updates/Enhancements	2	4
Store publish guidelines compatibility	5	4
Mature development tools	5	3
Access to devices hardware peripherals	5	4
Category: General		
Multi-platform support	N/A	5
Resource Pool	2	4
Usage Statistics/Analytics	3	4
Security	4	3
Category: Performance		
Response time	5	4
App counting power	5	3
Application startup time	5	4
Category: Testing		
Platform dependent testing	5	3
Platform independent testing	N/A	4
Category: User-experience		
User Experience	5	3
Platform design guideline compatibility	5	4
Addapting to design guideline changes	5	2

1) Costs criteria

In this criteria section, overall cost of certain project stages are considered. It is arguably cheaper to develop, support and

ISBN: 978-1-61804-321-4

maintain hybrid apps, especially in context of more platform versions. Different platform versions are using as much common business logic source code, as possible, in contrast with native applications, where different development projects need to be maintained.

2) Development process criteria

Especially in area of source-code development process we can found criteria according to which the native application development seems to be the ideal method. We can mention Off-line support, smoother compatibility with store publication guidelines, availability of mature development tools and direct access to hardware peripherals. Abilities of web-based HMA are in these points considerably lower and it is necessary to pay special attention to them.

3) General criteria

This category contains some of the criteria, which are not directly connected with any project development stage. Here can be found the criterion of multi-platform support, where in case of native apps, no support is available. However, web-based HMA received full rating, because they can be built for various platforms. Very interesting, especially for the project-planning phase, is the resource pool criterion. This criterion expresses the availability of developers with required knowledge. Current market shows that web developers are more easily retrievable, than mobile-platform-specific developers.

4) Performance criteria

Very important point of evaluation especially in case of mobile hardware is the question of performance. Three different performance criteria were evaluated and results clearly speaks in favor of native mobile applications. This is primarily due to the fact that web-based hybrid applications business logic is written in JavaScript and needs to be interpreted in native mobile browser (web view). The performance of mobile application is directly proportional to the performance of native Web View.

5) Testing criteria

Testing is one of the most important software development project stage in general. Both native and hybrid mobile applications are offering routine testing tools, like a functional testing, unit testing, user interface testing, etc. But for the comparison purpose, there is an area, where the two approaches differ. If we consider the possibility of platform independent testing (business logic testing without depending on the end platform) only web-based HMA is possible to test in this way. Business logic of native application needs to be tested separately for each platform.

6) User experience criteria

In the criteria of user experience, native applications are logically the leading technology. Especially in terms of look and feel, web-based HMA need extra effort to simulate a native app. But it is possible using some of third-party UI frameworks. Also compatibility with platform design guidelines needs to get extra attention in case of web-based HMA. Other week point of this development method is slower adaptation of design guideline changes. We can mention in this context the significant design change from iOS 6 rich design to iOS 7 flat design. This week point was not in practice a real threat, because few hybrid mobile UI frameworks offered the new iOS 7-like UI before the official deployment of new OS version.

V. Web-based HMA limitations

Recent studies often conclude, that cross-platform development solutions are necessary in mobile environment of these days. [5]

Some of the researchers exceeded the theoretical level of the research and presented development of real application using cross-platform methodology. Authors of the paper [19] and [20] are pointing to real limitations of web-based HMA approach but only on the general level. Generally known fact about performance and user experience issues of HMA are discussed here.

During the real implementation, more severe limitations and problems of HMA were discovered. These problems were studied in detail to analyze their source and specific countermeasures were found.

The most severe limitation of web-based HMA lies in implementation of the native web browser (Web View). This Web View creates the runtime environment for the application logic and user interface written using HTML5. Let us consider developing of HMA for Android. In real scenario, there is often the requirement for support Android versions from 2.3.7 to 5. It means, that the HTML5 part of the app may be running in 4 different main versions of web view (WebKit [21]). Moreover, each of these versions has different level of HTML5 support.

Table 3: Android WebKit versions market penetration [22] and HTML5 support

Android version	WebKit version	Market penetration	HTML5 support
Android 2.3.3 - 2.3.7	533.1	6.4%	162
Android 3.0 - 3.2	534.13	<1%	N/A
Android 4.0.3 - Android 4.3	**534.3**	**46.4%**	**220-228**
Android 4.4.x - 5.0	**537.36**	**46.8%**	**379-452**

As can be seen from the Table 3, the HTML5 support differs from roughly 220 points to 452 points (scored using html5test.com) in case of the most spread versions of Android. With regard to the version 2.3.3 – 2.3.7 the HTML5 support score is around 160 points. It creates great variance causing inability to use widely all of the modern HTML5 properties.

If we consider iOS platform, the situation here is similar, but considerably more optimistic. It is due to the fact, that lot of iOS users are periodically updating their mobile OS to the newest version, which provides also new Web View rendering engine.

This problem with different HTML5 functionality support can be solved using feature detection technique [23], known from desktop web application, but this usually leads to source code tweaking for different Web View versions, which requires deep knowledge of concrete mobile browser and its HTML5 support.

Of the foregoing, it is necessary to test HMA on real devices with different Android OS version installed, because the real behavior can be observed only in the real runtime environment (Web View).

ISBN: 978-1-61804-321-4

VI. Future of web-based HMA

Previous section discussed the real limitations of HMA development approach, which contain especially displaying, behavior and application inconsistency through different versions of runtime environment (Web View). Practical testing has shown, that Web Views do not differ only through different platforms, but also within one platform, through its versions. This finding disputes many optimistic opinions about suitability of web-based HMA development approach. The real application also show, that the costs, which are saved in the development phase, in contrast with native development, could be again increased in the testing and debugging and fixing phase.

However, the future of web-based HMA technology seems to be not so pessimistic. In contrast of ongoing diversification of native development, differences in Web View implementation are in newer mobile OS versions reduced and the support of HTML5 increases. Also performance of JavaScript implementation is rapidly growing and more complex calculations could be conducted within mobile web view. Therefore web-based HMA development could become in the coming years very suitable cross-platform technology, which needs to be taken seriously.

VII. Conclusion

This paper brings the overview of current mobile development approaches and focuses especially in comparison of native and web-based HMA development. The chapter Related work provides an overview of recent research papers from this topic, and points to the limitation of this research, which is especially in high level of generality.

Within the comparison of mentioned technologies SWAT analysis and criteria comparison is used. Criteria are divided into categories, which are related to specific development stage. Ratings of these criteria are clarified and current experiences from development area are taking into account.

Also limitations of HMA development approach are discussed more in detail, and the real shortcomings resulting from different implementation of native Web View, are mentioned.

Last part of this paper is focused on the future of web-based HMA, in context of recent development of mobile platforms. After it has been greatly improved support of HTML5 in native Web View, it is possible, that web-based HMA will again strengthen its position within mobile app development approaches.

References

[1] S. Amatya and A. Kurti, "Cross-Platform Mobile Development: Challenges and Opportunities," *ICT Innovations 2013*, Advances in Intelligent Systems and Computing 231, V. Trajkovik and M. Anastas, eds., Springer International Publishing, 2014, pp. 219-229.

[2] I. Dalmasso, et al., "Survey, Comparison and Evaluation of Cross Platform Mobile Application Development Tools," IEEE, 2013, pp. 323 - 328.

[3] D. Gavalas, et al., "Development Platforms for Mobile Applications: Status and Trends," IEEE, 2011, pp. 77-86.

[4] H. Heitkötter, et al., "Evaluating Cross-Platform Development Approaches for Mobile Applications," *Proc. 8th International Conference, WEBIST 2012, Porto, Portugal, April 18-21, 2012, Revised Selected Papers*, Springer-Verlag Berlin Heidelberg, 2013, pp. 120/138.

[5] H. Ng Moon, et al., "Cross-platform mobile applications for android and iOS," *Proc. Wireless and Mobile Networking Conference (WMNC), 2013 6th Joint IFIP*, 2013, pp. 1-4.

[6] J. Ohrt, et al., "Cross-Platform Development Tools for Smartphone Applications," IEEE, 2012, pp. 72-79.

[7] N. Nishanth and R.K. Bhandar, *Building Mobile Applications Using Kendo UI Mobile and ASP.NET Web API*, Packt Publishing Ltd., 2013.

[8] M. Palmieri, et al., "Comparison of cross-platform mobile development tools," IEEE, 2012, pp. 179 - 186.

[9] P. Gokhale and S. Singh, "Multi-platform strategies, approaches and challenges for developing mobile applications," *Proc. Circuits, Systems, Communication and Information Technology Applications (CSCITA), 2014 International Conference on*, 2014, pp. 289-293.

[10] "Xamarin Inc., "Build apps in C# for iOS, Android and Windows Phone. - Xamarin," 2015; [Online]. Available: http://xamarin.com/platform.

[11] B. Anderson, "Introduction to Xamarin," 2013. [Online]. Available: http://www.slideshare.net/brian0anderson/ost-xamarin/.

[12] "W3C," 2014, [Online]. Available: http://www/w3c.org/.

[13] The Apache Software Foundation, "About Apache Cordova™," 2013; [Online]. Available: https://cordova.apache.org/.

[14] Adobe Systems Inc., "PhoneGap Home," 2015; [Online]. Available: http://phonegap.com/.

[15] M.H. Marilyn and N. Judy, "Exploring SWOT analysis – where are we now?," *Journal of Strategy and Management*, vol. 3, no. 3, 2010, pp. 215-251; DOI 10.1108/17554251011064837.

[16] "Android Wear," 2015; Available: http://www.android.com/wear/.

[17] "HealthKit - Apple Developer," 2015; Available: https://developer.apple.com/healthkit/.

[18] "HomeKit - Apple Developer," 2015; Available: https://developer.apple.com/homekit/.

[19] Z. Yanyan, et al., "Tradeoffs in cross platform solutions for mobile assistive technology," *Proc. Communications, Computers and Signal Processing (PACRIM), 2013 IEEE Pacific Rim Conference on*, 2013, pp. 330-335.

[20] R. Raj and S.B. Tolety, "A study on approaches to build cross-platform mobile applications and criteria to select appropriate approach," *Proc. India Conference (INDICON), 2012 Annual IEEE*, 2012, pp. 625-629.

[21] D. Golubovic, et al., "WebGL implementation in WebKit based web browser on Android platform," *Proc. Telecommunications Forum (TELFOR), 2011 19th*, 2011, pp. 1139-1142.

[22] A. Inc., "Dashboards | Android Developers," 2015; Available: https://developer.android.com/about/dashboards/index.html?utm_source=suzunone.

[23] Microsoft, "HTML5 - Browser and Feature Detection," 2015; Available: https://msdn.microsoft.com/en-us/magazine/hh475813.aspx.

ISBN: 978-1-61804-321-4

The proposal of the holonic control for the district heating systems

Lubomir Vasek and Viliam Dolinay

Abstract— This paper shows possibilities of distributed control systems, in our case holonic system, in processes inside the district heating (DHC). It shows basic ideas of Holonic control and describes steps necessary to incorporate it inside the DHC. The steps are based on analysis of the DHC processes and aimed at the formulation of the suitable holarchy for it. The individual holons and its function will be shown as well as services that provide their mutual cooperation. The example at the end of this article will show implementation for one of the system parts – CHP source.

Keywords—Distributed control system, district heating, holon, holarchy, smart thermal grid.

I. Introduction

THE key objective of European Union in the field of energy efficiency is to lower consumption of primary energy as much as EU's economic performance allows [1]. This is also the objective of most countries outside the EU who want to behave ecologically. To reduce primary energy means:

- Modernize and improve the efficiency of technological equipment for heat production (improving the combustion process, development of modern boilers, etc.)
- Use broader engagement of energy from RES, which is not be ranked among primary energy
- Use of secondary heat sources - waste heat from industrial processes, low-potential sources and municipal waste incineration
- Insulation - reduce losses in the distribution network and heated objects
- Heat management optimization

Addressing heat management optimization together with wider use of RES and waste heat is included in the Smart Thermal Grid (STG) concept [9]. In fulfilling this concept is also trying to contribute our proposal distributed district heating control system, which should be built on the idea of holonic structure. The primary idea is however distributed concept itself, which may not necessarily be called holonic, we can understood it as a system of cooperating agents with which is usually a general reader more familiar.

This article will try to show how such a system should be designed - how to divide tasks for individual Holons, how to build a holarchy and what services must be implemented to ensure the optimal performance of the entire system. Because control, or more appropriately management of STG is a huge field and each location can also offer other possibilities, the article will not try to cover the entire field but focus on one sub-area which are CHP sources.

II. District Heating And Cooling

Classical District energy systems produce steam, hot water or chilled water at a central plant [10]. The steam, hot water or chilled water is then piped underground to individual buildings for space heating, domestic hot water heating and air conditioning. As a result, individual buildings served by a district energy system don't need their own boilers or furnaces, chillers or air conditioners. The district energy system does that work for them, providing valuable benefits including:

- Improved energy efficiency
- Enhanced environmental protection
- Fuel flexibility
- Ease of operation and maintenance
- Reliability
- Comfort and convenience for customers
- Decreased life-cycle costs
- Decreased building capital costs
- Improved architectural design flexibility

In addition, district energy systems can use the "reject heat" that results from burning fuel to produce electricity at a power plant, dramatically increasing the overall efficiency with which useful energy is extracted from the fuel.

The reject heat can be used to spin turbines and generate electricity. This arrangement, called "combined heat and power" (CHP). A CHP system may have double the fuel efficiency of an electric generation plant and can also lower the emissions typically associated with conventional fossil-fuel powered electrical production. The less energy used, the less sulfur dioxide and carbon dioxide and other emissions are expelled into the environment [2].

This work was supported by the European Regional Development Fund under the project CEBIA-Tech No. CZ.1.05/2.1.00/03.0089) and project CZ.1.07/2.3.00/20.0035.

Viliam Dolinay is with the Department of Automation and Control Engineering, Tomas Bata University in Zlin, Faculty of Applied Informatics, nám. T. G. Masaryka 5555, 76001 Zlín, Czech Republic (e-mail: vdolinay@fai.utb.cz).

Lubomir Vasek is with the Department of Automation and Control Engineering, Tomas Bata University in Zlin, Faculty of Applied Informatics, nám. T. G. Masaryka 5555, 76001 Zlín, Czech Republic (e-mail: vasek@fai.utb.cz).

ISBN: 978-1-61804-321-4

Comparison of CHP and standard power plant energy efficiency presented by International District Energy Association is shown in fig. 1.

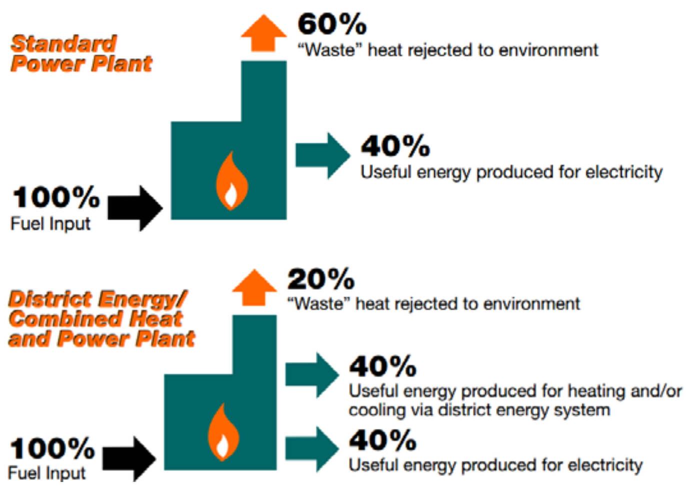

fig. 1 Energy-efficiency comparisons [2]

A. Smart Thermal Grid

Do not waste energy is the fact that humanity is aware for several decades. Above mentioned concept of CHP is very important, but the effort to optimize the use of energy sources continues. Currently it is the concept of Smart Thermal Grid (STG), which efforts to use all the energy produced but also seeks the way to make this use the most optimal. An example might be the use of the sources that are in particular moment the most efficient and also effort to accumulate energy that can be produced profitably and there is no consumer for it at a given moment. This is especially applicable for the energy produced from the sun, wind and other renewable sources.

For STG is also important the role of buildings that should not be considered as simple consumers but as the objects that are able to cooperate with sources for optimum performance of the entire smart system [3].

STG can play an important role in the future Smart Cities by ensuring a reliable and affordable heating and cooling supply to various customers with low-carbon and renewable energy carriers like waste heat, waste-to-energy, solar thermal, biomass and geothermal energy.

Smart thermal grids allow for adapting to changing circumstances in supply and demand in the short, medium and long term, and facilitate participation of end-users, for instance by supplying heating or cooling back to the network. To do so, they need to be spatially integrated in the whole urban energy system and interact with other urban infrastructure, such as networks for electricity, sewage, waste, ICT, etc. Optimizing the combination of technologies and enable a maximum exploitation of available local energy resources through cascade usage, smart thermal grids can contribute to improving the efficiency of urban heating and cooling, while increasing the cost efficiency and increasing the security of supply at a local level by using local sources of energy. The scale of smart thermal grids can range from neighbourhood-level systems to city-wide applications, depending on heating and cooling demand and urban context.

Technical elements of smart thermal grids cover thermal generation like small-scale low-carbon heating and cooling systems, CHP and new approaches for producing domestic hot water, thermal storage technologies and innovative network improvements such as new piping materials new piping layouts and non-invasive construction and maintenance of thermal networks. Network-integrated sensors and smart heat meters allow for more effective and efficient use of the separate components, supported by overarching energy management [4].

Possible components of STG are shown in fig. 2.

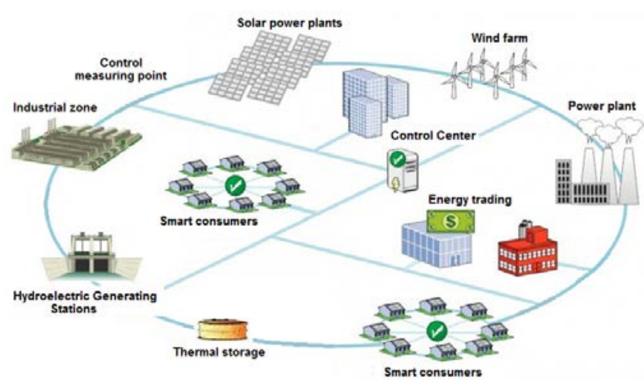

fig. 2 Components of the STG [5]

III. Holonic System

The term "holon" and “holonic system” appeared more than 40 years ago, it was introduced by Herbert Simon and Arthur Koestler [6]. In recent years the concept of holonic systems expanded, elaborated and applied inter alia in the field of production systems, especially in discrete manufacturing. It is one of the concepts applicable to distributed systems and their management, but it has also potential for use in other industrial areas.

The term holarchy refer to a set of holons including their mutual relations. Holarchy is a system of holons that can co-operate to achieve a goal or objective. The holarchy defines the basic rules for co-operation of the holons and thereby limits their autonomy [7]. The concept of holarchy is illustrated in the following fig 3.

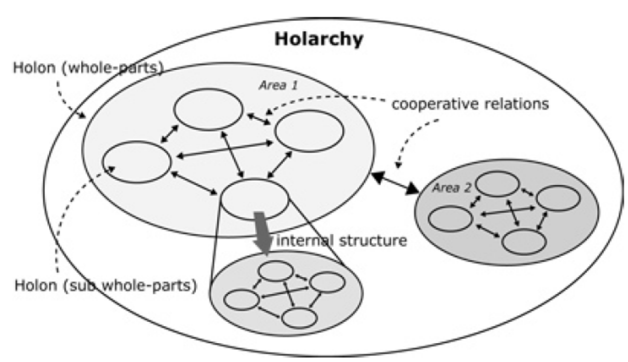

fig. 3 Holarchy

Holon, in this context, could be defined as an autonomous and co-operative building block of a production system for transforming, transporting, storing and/or validating information and physical objects. The holon consists of an information processing part and often a physical processing part. A holon can be part of another holon. It is also possible to see it as a model of a particular element, i.e. part of the model of the entire system. In this sense is holon used in this article.

The internal structure of holons can be made up of a group of other holons, which can be described as "subholons". Any such subholon is, of course, full holon. This allows a very flexible way to define entire holonic system.

The most important features of holon are autonomy and co-operation. Autonomy is characterized by its ability of self-regulation, i.e. the capability to apply the flexible strategy which allows holon to respond differently to changes in its relevant environment. This ability to respond individually to changing conditions in which holon work, must be connected with a certain degree of intelligence to its reaction to change and adapt to the demands of the environment to be efficient and effective. Cooperation takes place between holons using the corresponding parts "subholons" of each holon - the parts that have the ability to implement relevant cooperation.

Good co-operation requires good communication between holons. Holon exchange information with other holons throughout holarchy. This direct, mutual communication between holons manifests an important distinction between distributed systems management and centralized management systems. In centralized systems, all communication takes place via a central element of the control system.

IV. Holonic Model Of DHC

Creating a holonic model the system comprises a series of specific steps - for the DHC system as follows:

A. *Split system into Holons and the creation of Holarchy*

This is based on an analysis of the modelled system in which it is necessary to carefully and thoroughly assess the structure of the modelled system, carefully identify individual holons including their internal structure exploits the use subholons. It is also necessary to analyse the relationships and bindings between holons. All of these steps should result into a suitable split of the system into holons and creation of appropriate holarchy.

B. *Specification of particular properties of holons*

The aim of this step is to specify particular properties of individual holons and, if relevant, also define their inner structure.

When specifying the properties of individual holons, it is necessary to take into account the nature of the modeled system, i.e. what characteristics of the behavior of the system will be with the support of the prepared model analyzed. For each of these characteristics must every holon associated with such characteristic contain a set of methods, techniques and algorithms that allow to quantify this characteristic as accurately and completely as possible.

In the case of the DHC will be typically monitored and analyzed the ongoing processes on both, the technical and economic terms.

From the technical point of view the model, and thus holons modeling the individual elements of DHC, will usually contain mathematical and physical description of the involved processes. On this basis will be determined the characteristics of the individual elements. Also will be determined the operating ranges limits of various physical quantities associated with these characteristics. These are e.g. limits of the thermal energy delivered by the source, depending on factors affecting the production (e.g. irradiation with solar thermal energy), or limits for the amount of thermal energy transferred by the distribution elements.

In terms of economy, the model will include a description of the economic variables and their calculation, depending on the value of the influencing factors. It is e.g. the determination of prices of produced thermal energy unit by the source (of course as time function), determination of the heating costs for the particular consumers (again as a function of time), etc.

C. *Specification of services*

This step focuses on the specification of individual holon services which are offered to all others holons.
Each holon performs within the system some specific, clearly defined activities and the results of these activities are offered to other holons as a specific services. Supply and use of these services is closely related to the implementation of essential holon characteristics - autonomy and a cooperative.

To guaranty administration of these offered services is a need to be developed and used appropriate communication system. Such system has to allow holonic model to: Communicate between any holons which may be located anywhere on a computer network

- Initiate communication between two holon to any of them. This is due to the requirement of strict compliance with the principles of distributed systems, where all elements are "equal", at the same level. Each holon, which offers its service can make such offer to others holons either on its own initiative (e.g. when it is able to carry it out) or on demand from the potential user of this service.

One possible solution is to use a standardized mechanism for Web services, respectively semantic Web services or WCF framework [8].

An example of model preparation will be demonstrated on CHP source, see schematic diagram in fig. 4. Next figure shows holarchy and particular services for supply (offer) and demand for the selected system.

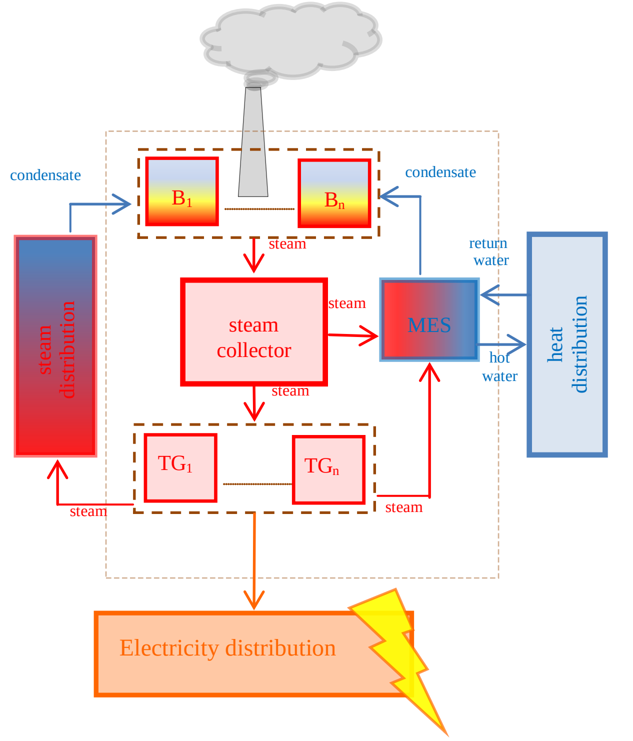

fig. 4 Simplified diagram of the basic elements of the CHP plant

Where $B_{i\ ..\ n}$ are boilers, $TG_{i\ ..\ n}$ are turbo generators, MES .. main exchange station.

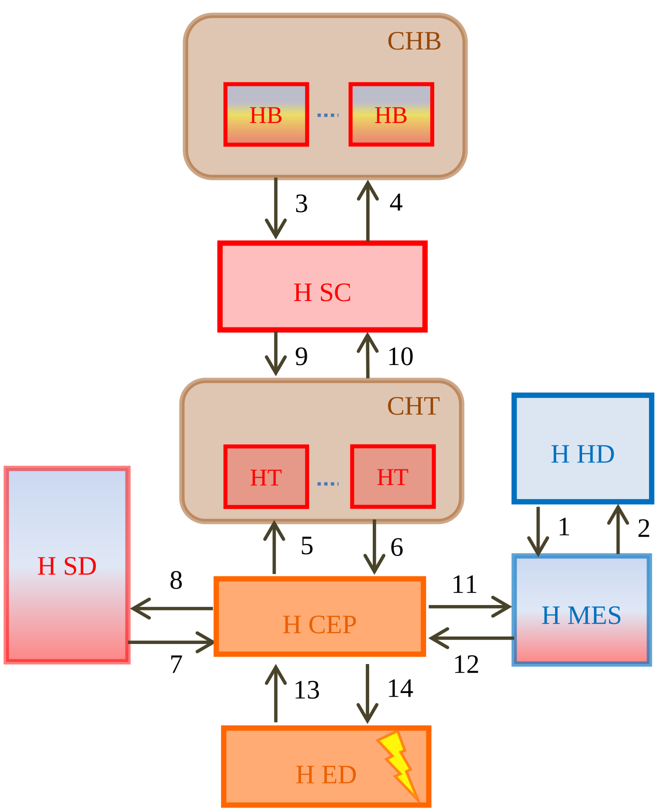

fig. 5 Holarchy of the control system

Where:
CHB …container of boiler holons
CHT …container of turbines holons
HB …holon of the boiler
HT …holon of the turbine
HSD …holon of the steam distribution
HSC …holon of the steam collector
HHD …holon of the heat distribution
HMES …holon of the main exchange station
HCEP …holon of the cogeneration electricity production
HED …holon fo the electricity distribution

Description of individual services in figure 5:

1 – Demand on predicted amount of "primary" steam for direct distribution

2 – Offer achievable (free) amount of "primary" steam for direct distribution

3 - Offer achievable (free) amount of "primary" steam for steam collector

4 - Demand on predicted amount of "primary" steam for steam collector

5 - Offer achievable (free) amount of "primary" steam for heat exchanger

6 - Demand on predicted amount of „primary“ steam for heat exchanger

7 – Demand on predicted amount of steam for direct distribution

8 - Offer achievable (free) amount of steam for direct distribution

9 - Offer achievable (free) amount of steam from the steam collector for cogeneration

10 - Demand on predicted amount of steam from the steam collector for cogeneration

11 - Offer achievable (free) amount of steam for main exchange station

12 - Demand on predicted amount of steam for main exchange station

13 – Offer achievable (free) amount of electricity for direct distribution

14 – Demand on predicted amount of electricity for direct distribution

V. Method For Controlling DHC

The processes associated with the production, distribution and consumption of thermal energy in DHC, especially if the system included a large dominant source, have in terms of their timing a specific behaviour. They are reacting relatively slowly and between their individual parts is quite various and non-negligible delay - traffic delays. This significantly affects the way of control of the entire DHC. On the one hand this simplifies the implementation of control actions (there is "enough time" to make it), but on the other hand it complicates the control strategy - it is necessary extensively to predict the behaviour of system (e.g. when the heat is produced, it is already necessary to predict its amount, what will be needed in order a few hours, which will last transfer of heat media to the point of its consumption.

In view of the above, it is possible to specify a three-stage

ISBN: 978-1-61804-321-4

process of DHC control:

- *Prediction phase*. At this stage, applies inter alia, the technical characteristics of the individual parts of the system. For their determination is usually used a combination of the above mentioned mathematical and physical models, and analysis of historical operational data. Prediction context must be understood sufficiently broad, because it involves all parts of DHC:
  a) The most important is the prediction of heat consumption in individual consumers in time and depending on a number of external factors - climatic conditions, the nature of the operation of individual consumers, etc.
  b) Very important is also the prediction of the amount of heat possible to be produced by individual sources, again depending on the time and range of internal and external factors - energy from renewable sources, depending on the sunlight, wind strength, the configuration of the technological equipment and the dynamics of their changes in the classical sources using combustion processes, etc.
  c) It is considerable important to predict time possibility of the heat distribution, respectively its ability to transfer the required amount of thermal energy in required time.

- *Optimization phase*. At this stage, it is necessary on the basis of the whole complex of predicted data to determine the best division of supply of heat between different producers and consumers. Here are mostly applied above mentioned economic variables. The objective function to optimize is the cost function whose minimum is searched.

  At this stage of the control considerably appear the benefits of the holonic concept, i.e. distributed system. Optimization can be very easily divided to solution at different levels - individual holon, suited holons groups and for the entire holarchy. For the optimization in higher level it is possible to use results from lower level, which are easily calculable.

  Algorithm optimization calculations is based on the fact that individual consumers are demanding at all (technically possible) producers whether they are able to meet its requirements for heat supply in quantity, or even the quality spread over time. Quality means the temperature of the heat transfer medium - however, this option is very limited by distribution network layout. Contacted suppliers will evaluate and weigh their possibilities and make an offer to consumers - under what conditions, usually economic, or with which restrictions may be quoted energy supplied. In the simplest variant, the consumer compares each relevant offer and chooses the one, which is most suitable for its needs. Suppliers then have the opportunity to influence their profit through their offerings. In more complicated cases, the optimization is conducted with respect to the specified groups of holons or to whole holarchy. Disclosed algorithm in this case is supplemented by iterative procedures for finding the optimal value of the more complex formulated objective function.

- *Implementation of control actions*. At this stage of the control process has been ongoing for quite classical approach when control interventions determined by the prediction and optimization phase are applied using the appropriate technical means.

For the practical implementation of DHC control is necessary to resolve the issue of time synchronization of the phases of the control process. This is relates to the fundamental specific problem, that prediction, eventually optimization takes place at a different time of the controlled system long before the application of control interventions. The time difference, which is due to the time needed to transfer the required amount of heat exchange medium from the point of production to point of consumption. This is the dynamic variable that has a large divergence, depending on the number of internal state variables of the system.

VI. CONCLUSION

Building and deploying Smart Thermal Grids into practice requires a number of steps. Besides upgrading hardware and improve communication and measurement is necessary to ensure that elements of the system together and collectively came to the efficient use of resources. The article tried to show that in such a heterogeneous environment, it is advisable to implement a distributed system management. And one of the options is to use holonic concept – concept of independent but also cooperative agents in the environment of the joint information network.

REFERENCES

[1] *European Commision, Research & Innovation,* Available: http://ec.europa.eu/research/participants/portal/doc/call/h2020/common/1632649-part_10_energy_v2.1_en.pdf

[2] *International District Energy Association*, Available: http://www.districtenergy.org/what-is-district-energy/

[3] *Johansson, C., Smart Heat Grids, Sustainable district heating and cooling for the future,* Available: http://innoheat.eu/wp-content/uploads/2012/04/Guest-Writer-NODA.pdf

[4] *AnsversTM,* Available: http://www.answers.com/topic/log-mean-temperature-difference

[5] *B:TECH*, Available: http://www.btech.cz

[6] Koestler A., “The Ghost in the Machine”, Penguin Books (reprint 1990), ISBN-13: 978-0140191929

[7] Kwangyeol, R., “Fractal-based Reference Model for Self-reconfigurable Manufacturing Systems”. Ph.D. dissertation, University of Science and Technology. Pohang, Korea, 2004.

[8] *Microsoft, What Is Windows Communication Foundation*, Available: https://msdn.microsoft.com/en-us/library/ms731082%28v =vs.110%29.aspx

[9] Lund, H., Werner, S., Wiltshire, R., Svendsen, S., Thorsen, J. E., Hvelplund, F., Mathiesen, B. V., “4th Generation District Heating (4GDH): Integrating smart thermal grids into future sustainable energy systems”, Energy, Volume 68, 15 April 2014, ISSN 0360-5442.

[10] Chramcov B. “Identification of time series model of heat demand using Mathematica environment”. In Recent Researches in Automatic Control: Proceedings of 13th WSEAS Int. Conference on Automatic Control, Modelling & Simulation. Lanzarote: WSEAS Press, 2011. pp. 346-351. ISBN 978-1-61804-004-6.

Energy requirements of light sources

Jiří Vincenec, Martin Zálešák, Pavel Chrobák, and Stanislav Sehnálek

***Abstract*—**This paper focuses on energy requirements of light sources mostly used in administrative and residential buildings. In buildings for which are properly treated thermally insulating properties, constitute heat gains from light sources proportion of the total heat gains. With the expansion of new technologies there are new light sources, which could lead to a reduction in energy requirements for lighting. Energy requirements for lighting are not only requirement. There are also demands for the quality of the luminous environment. These parameters means the color rendering respectively color temperature and glare requirements. These parameters may not be meet when the lighting design is wrong. This paper summarizes the basic requirements for lighting in buildings, means requirement for environmental quality and energy requirements.

***Keywords*—**Energy requirements, light sources, lighting requirements, quality of the luminous environment.

I. Introduction

LIFE as we know it could not exist without the light. It is necessary for photosynthesis or for visual perception of world by mankind or other living beings. The best known light source is the Sun, which provide us with daylight. During the day there is possibility to use this daylight for lighting work environment. With respect to the requirements for lighting, specifically uniformity illuminance is necessary to regulated daylight eventually complete it with artificial light. For correct completing luminous environment with artificial light is needed to know characteristic of artificial lights, which are used. With this characteristic it is possible to set the right level of artificial light to achieve right luminous environment with minimal energy requirements. Also with the right daylight regulation there are minimal heat grains from the Sun radiation.

The work was performed with financial support of research project NPU I No. MSMT-7778/2014 by the Ministry of Education of the Czech Republic and also by the European Regional Development Fund under the Project CEBIA-Tech No. CZ.1.05/2.1.00/03.0089. Work was also supported in frame of nternal Grant Agency of Tomas Bata University in Zlin, Faculty of Applied Informatics IGA/FAI/2015/003, IGA/FAI/2015/022 and IGA/CebiaTech/2015/002 References.

Jiří Vincenec is with the Tomas Bata University in Zlín Faculty of Applied Informatics. Department of Automation and Control Engineering. 760 05 Zlín Czech Republic. (e-mail: vincenec@fai.utb.cz)

Martin Zalesak is with the Tomas Bata University in Zlín Faculty of Applied Informatics. Department of Automation and Control Engineering., 760 05 Zlín Czech Republic. (e-mail: zalesak@fai.utb.cz).

Stanislav Sehnalek is with the Tomas Bata University in Zlín Faculty of Applied Informatics of specialization in the Department of Automation and Control Engineering. 760 05 Zlín Czech Republic.: (e-mail: sehnalek@fai.utb.cz).

Pavel Chrobak is with the Tomas Bata University in Zlín Faculty of Applied Informatics of specialization in the Department of Automation and Control Engineering. 760 05 Zlín Czech Republic.: (e-mail: chrobak@fai.utb.cz).

II. Standard requirements

Lighting is revise by several standards, which maintain requirements for quality of the luminous environment and energy requirements for lighting [1], [2], [5].

A. Luminous environment requirements

Requirements for illuminance are well known and with uniformity illuminance in place of visual task and its close area have effect on speed, safety and comfort. Measured illuminance and uniformity illuminance depends on specified network. The network is a set of points in which is illuminance calculated and measured. Square network is favors. Maximal dimension of cell is given by [2]:

$$p = 0{,}2 \cdot 5^{\log_{10} d} \tag{1}$$

where d is the longer dimension of the area
p maximal dimension of cell

Luminance requirements means especially the luminance distribution that gives eye adaption and also effect task visibility. Balanced eye adaption luminance is important for improve of the visual acuity [2].

Color temperature and color rendering give color quality of artificial sources or daylight. Color temperature is related with apparent color of light. This color of light could be replaced with color temperature T_{cp}. Daylight during the day change its color temperature. Artificial light may be sort in one of three categories of white light. Warm white with color temperature under 3300 K, neutral white with color temperature between 3300 K and 5300 K and cold white with color temperature above 5300 K. Color rendering means that color of subjects and mankind skin are seen in true color. Color rendering is described with index R_A. Maximal value of R_A index is 100 [2].

Bright surfaces in field of view, for example illuminated surfaces, parts of light sources or windows cause glare. For avoiding fatigue, work accidents it is necessary to minimize the glary [2].

These requirements for lighting could be achieved by using daylight, artificial lighting or integrated lighting [2], [3], [4].

In buildings with are determined for people reside during the day is required adequate daylight. In new constructed buildings is required adequate daylight for living quarters, bedrooms, rooms for preschools, health care facilities. Sources of daylight in buildings are windows, skylight and light pipe. This daylight sources must be designed effectively. The requirements for daylight must by achieved with the smallest area of glazing. The spectral composition must not be change by the glazing [3].

Integrated lighting is more comfortable instead of using only artificial lighting. In newly constructed buildings or theirs parts could be integrated lighting used only in justified cases. In indoors with integrated lighting must be maintained required part of daylight. This part depends on difficulty of view task. There are seven difficulties of view tasks. The spectral composition of artificial light sources must be comparable with the daylight spectral composition. The spectral composition of the artificial sources must be also continuous or at least maintain significant continuous component. This artificial lighting could be regulated depending on exterior illuminance.

B. Energy requirements for lighting

Standard ČSN EN 15193 [5] describe energy requirements for lighting in buildings. It also provides procedures for energy consumption calculation in buildings. For appropriate calculation of energy consumption is required lighting system, which design is consistent with ČSN EN 12646-1 [2] standard.

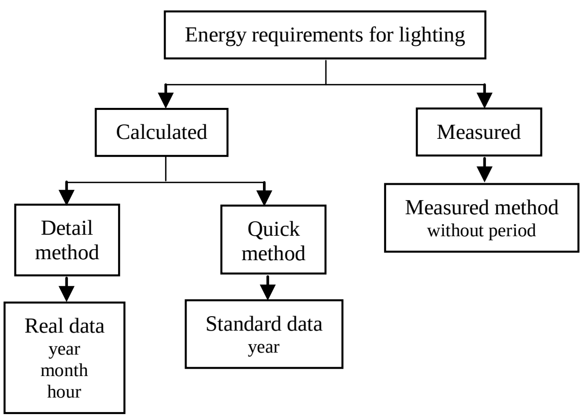

Fig. 1 methods of determining energy requirements [5]

The estimated total electricity consumption of a lighting for room or zones for calculated time is given by [5]:

$$W_t = W_{L,t} + W_{P,t} \tag{2}$$

where $W_{L,t}$ is estimated consumption of electricity in the building to meet the purpose and function of lighting and is given by [5]:

$$W_{L,t} = \sum \frac{\{(P_n \cdot F_C) \cdot [(t_D \cdot F_O \cdot F_D) + (t_N \cdot F_O)]\}}{1000} \tag{3}$$

and $W_{P,t}$ is estimated loss of electricity in the building, caused mainly by charging emergency lighting and standby lighting control system and is given by [5]:

$$W_{P,t} = \sum \frac{\{\{P_{pc} \cdot [t_y - (t_D + t_n)]\} + (P_{em} \cdot t_{em})\}}{1000} \tag{4}$$

where
- P_n is the total power consumption for lighting in a room or area in watts;
- P_c total power dissipation control devices in a room or area in watts;
- P_{em} total charging power for emergency lighting luminaries in watts;
- t_D hours of daylight in hours;
- t_N time without the use of daylight in hours;
- t_y standard time of year, fixed at 8760 h;
- t_{em} charging time emergency lighting in hours;
- F_C constant illuminance factor;
- F_O factor depending on the occupation;
- F_D factor depending on daylight.

Lighting Energy Numeric Indicator (LENI), indicate year consumption for lighting in building for 1 m^2 floor surface. LENI indicator is given by [5]:

$$LENI = \frac{W}{A} \tag{5}$$

According to Fig. 1 there are two methods for calculating energy consumption. Detail method provides energy consumption for different time schedule. Otherwise quick method calculates data only for one year. Data calculated by one of these methods could be compared with data measured on installed lighting system. Measuring must be done by one of methods described in standard [5].

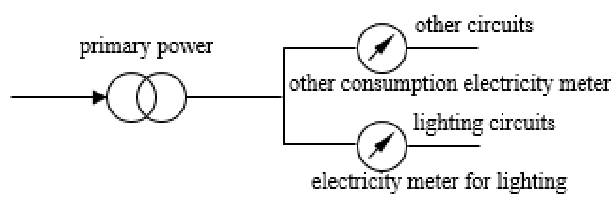

Fig. 2 example of energy consumption measuring [5]

III. Lighting sources characteristics

For comparison of light sources characteristics were determined the most used lighting sources. The first is bulb 75 W, 2700 K, 940 lm, the second is Classic ECO Halogen 53 W, 2700 K, 840 lm, the third is LED Premium 14 W, 2700 K, 995 lm, and the last is Compact fluorescent light 20 W, 2700 K, 1200 lm. All light sources are dimmable and it is possible to determine regulation influence on characteristics.

Fig. 2 shows schematic circuit for measuring electric parameters of light source regulation. For regulation was used KNX/EIB system, universal dimming actuator specifically. Regulation level was set by push buttons; level of regulation was determined on 0 %, 25 %, 50 %, 75 % and 100 %. For each level of regulation and light sources was made several measurements. For characteristics were used only current in regulated circuit. Voltmeters were used only as control devices. [2]

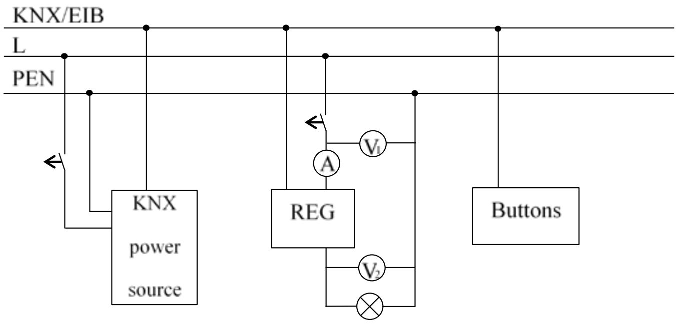

L	-	Phase	V_1,V_2	-	Voltmeter
PEN	-	Protective earth, neutral	A	-	Ammeter
REG	-	Regulation element			

Fig. 3 schematic circuit regulation of light sources with measurement electrical values

This paper does not compare measured values but compare percentage values due to different technologies of light sources. For each light source and level of regulation is calculated percentage level. With regulation set on 100 % the value is 100 % and for others levels of regulation is calculated theirs percentage value based on this 100 % regulation value.

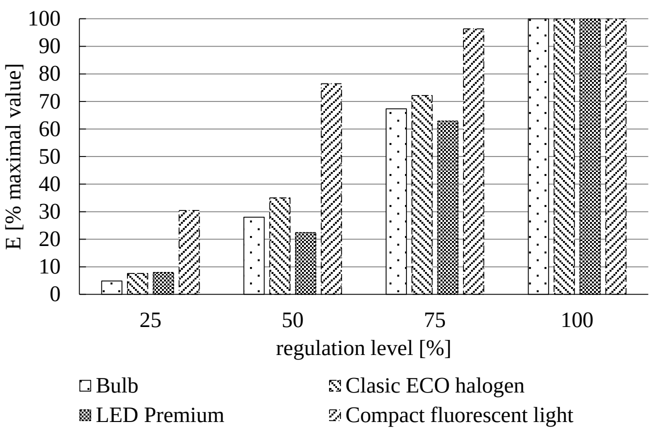

Fig. 5 dependence percentage illuminance on the set regulation

On the Fig. 4 is shown percentage illuminance and its dependence on the regulation level. As could be seen none of the light sources were regulated effectively. In case of bulb, classic ECO halogen and LED light sources percentage illuminance was always under required level. But compact fluorescent light had percentage illuminance above required level.

Fig. 5 provides percentage current and its dependence on regulation level. Instead of Fig. 4 there is obvious opposite problem. The current in regulated circuit is almost in every case above regulation level. Only LED light sources current at 50 % and 75 % regulation level were under regulation level.

In Fig. 6 are depicted dependences between percentage current and percentage illuminance. These dependences provide basic knowledge of what percentage of current is needed for required percentage illuminance.

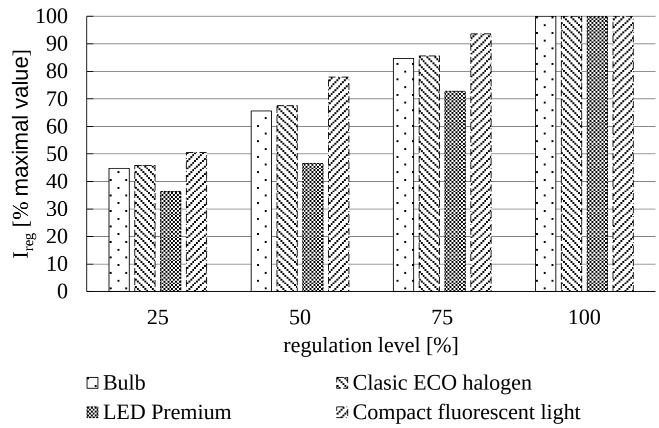

Fig. 7 dependence percentage current on the set regulation

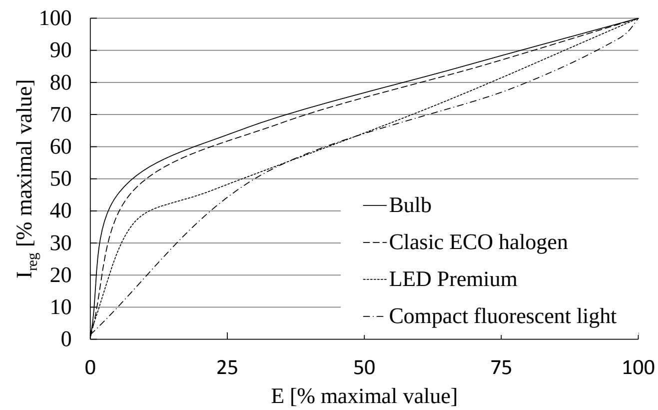

Fig. 6 dependence percentage current on the set regulation

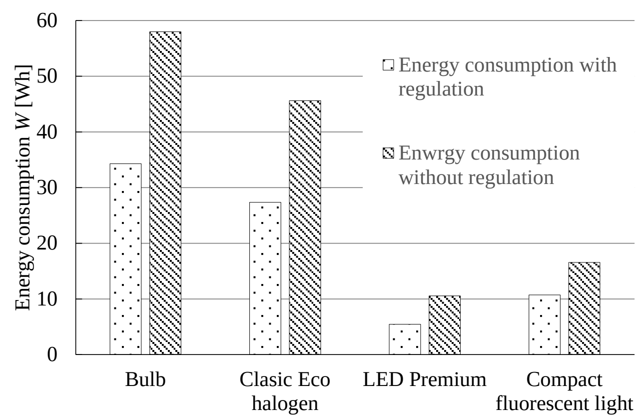

Fig. 4 energy consumption with and without regulation

Fig. 7 and Table 1 show energy consumption during fifty minutes cycle for each light source. First cycle was calculated for regulated light source. Second cycle was calculated as energy consumption without regulation.

Using Table 1 could be assumed that LED premium light source was able to save 48.8 % energy during the cycle with regulation. Instead compact fluorescent light was able to save only 35.3%. Explanation could be found in Fig. 5 which shows percentage current and it is obvious that percentage current of compact fluorescent light was in every step over percentage regulation level.

Table 1 energy consumption with and without regulation

	Bulb	Clasic Eco halogen	LED Premium	Compact fluorescent light
Energy consumption with regulation [Wh]	34.3	27.3	5.4	10.7
Energy consumption without regulation [Wh]	58.0	45.6	10.5	16.6
Percentage savings [%]	40.9	40.1	48.4	35.3

IV. Conclusion

This paper summarized standards used for lighting solutions. Energy consumption optimization required knowing characteristics of used light sources. Regulation system could be adapted according these characteristics.

The next step of the research is identifying light sources used in administrative buildings. Also the different regulation will be tested.

References

[1] ČSN EN 15251. *Indoor environmental input parameters for design and assessment of energy performance of buildings- addressing indoor air quality, thermal environment, lighting and acoustics*. Prague: Czech office for standards, metrology and testing, 2011.

[2] ČSN EN 12464-1. *Light and lighting - Lighting of work places - Part 1: Indoor work places*. Prague: Czech office for standards, metrology and testing, 2012.

[3] ČSN 73 0580-1. *Daylighting in buildings - Part 1: Basic Requirements*. Prague: Czech office for standards, metrology and testing, 2007.

[4] ČSN 36 0020. *Integral lighting - Basic requirement*. Prague: Czech office for standards, metrology and testing, 2015.

[5] ČSN EN 15193. *Energy performance of buildings - Energy requirements for lighting*. Prague: Czech office for standards, metrology and testing, 2008.

[6] DILAURA, David L. The lighting handbook: reference and application. 10th ed. New York, NY: Illuminating Engineering Society of North America, 2011, p. cm. ISBN 9780879952419.

Interoperability among Electro Mobility Service Providers and Charging Infrastructure Operators: A Clearinghouse Roaming Approach

Valentín Sánchez, Gonzalo Lázaro, Aurelio Díaz de Arcaya and David García-Pardo

***Abstract* —** One of the main concerns of the Electric Vehicle (EV) users is the availability of public charging infrastructure and the associated services like reservation and charge point dynamic information. This paper presents a novel clearinghouse based solution that facilitates the provision of electro mobility services in roaming, allowing a customer to use the charging infrastructure and services of different infrastructure providers in a transparent way.

***Keywords*—** Electro mobility services, Roaming, Clearinghouse

I. Introduction

One of the main concerns of the Electric Vehicle (EV) users is the availability of public charging infrastructure and the associated services like reservation and charge point dynamic information.

ICT4EVEU (http://www.ict4eveu.eu/) is a project born with the aim of developing an innovative set of ICT services for electric vehicles (EV) users in different and complementary pilots across Europe: United Kingdom (Bristol), Spain (Pamplona and Vitoria-Gasteiz) and Slovenia (Ljubljana and Maribor).

From this point of view, the main challenge has been to overcome the different conditions and infrastructures existing in each pilot at the beginning of the project, making possible a real interoperability of the final technical solutions and services between the three pilots.

The services in the Vitoria – Pamplona Pilot have been focused on providing transparent roaming functionality for the final EV users.

This paper presents a novel clearing house based solution that facilitates the provision of electro mobility services in roaming, allowing a customer to use the charging infrastructure and services of different infrastructure providers in a transparent way, designed and developed by the ICT4EVEU Spanish pilot.

ICT4EVEU is a project co-funded by the European Commission within the ICT Policy Support Programme.

V. Sánchez (Tecnalia Research & Innovation, Spain (e-mail: valentin.sanchez@tecnalia.com).
G. Lázaro (Tecnalia Research & Innovation, Spain e-mail: gonzalo.lazaro@tecnalia.com).
A. Diaz (Tecnalia Research & Innovation, Spain (e-mail: aurelio.diazdearcaya@tecnalia.com).
D. García-Pardo (IBERDROLA CLIENTES, Avenida San Adrián 48, 48003 Bilbao. Email: dgpardo@iberdrola.es)

.

II. Roaming concept and Pilot scenario

A. Roaming concept in the Electric Vehicle context

The Stakeholders related to the EV deployment include the following roles:

- **EVSE operator**: a party that operates the charging infrastructure from an operational technical point of view.
- **EMSP**: A party that sells e-mobility services to e-mobility customers. It may include electricity supply and other services such as roaming, EV location, parking, charge point reservation, etc. It is the "legal entity that the customer has a contract with for all services related to the EV operation".
- **E-mobility customer (EV user)**: someone consuming e-mobility services.
- **Clearinghouse**: A global platform between EVSE operators and EVSP to organise and process their exchange of data to allow any e-mobility customer of any EVSP charge at any EVSE.

A roaming agreement is defined as a contract between an EMSP and an EVSE operator. From the point of view of management and communication the roaming agreements can be managed in a one by one basis or in a centralized way, using a clearinghouse.

Figure 1 shows an example of a direct roaming scenario.

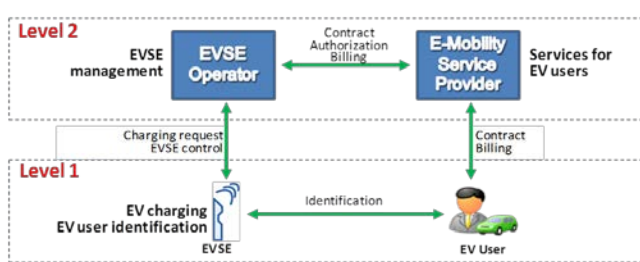

Figure 1 Roaming scenario (without clearinghouse)

The next figure shows the Spanish pilot roaming scenario that uses a clearinghouse to manage and facilitate the services provision in roaming.

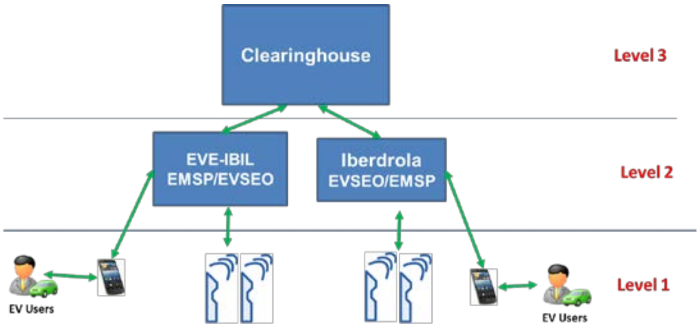

Figure 2 Spanish roaming scenario (with clearinghouse)

B. Roaming in Pamplona – Vitoria Pilot

EVE-IBIL and IBERDROLA are the "recharge managers" for the Pilot. Within the scope of the project EVE-IBIL operates in Vitoria Region and Iberdrola in Pamplona region. Both Iberdrola (Pamplona region) and EVE-IBIL (Vitoria region) act as Charging Service Provider (CSP), combining the role of E-Mobility Service Provider and EVSE Operator. So each Integrated Manangement System (IMS) manages and operates Charge Point Infrastructure, customer's contracts and provides Charging Services to the EV-User.

Iberdrola's and IBIL's systems manage and operate Charge Points from different Manufacturers. INGETEAM is one of these manufacturers and provides to EVE-IBIL and Iberdrola all Charge Points that will be part of the pilot.

The specification and design of the clearinghouse was made jointly by Iberdrola, EVE-IBIL and TECNALIA.

The general approach of the pilot is defined by the following general criteria:

- **Clearinghouse based roaming**: Relationships between different IMSs are established and managed through a Global Management System (**GMS**) or Clearinghouse.
- **Unique entry point for the value added services**: It means that users always access the services through the mobile applications provided by their charging service provider.

Figure 3 shows the Spanish pilot architecture and the different new modules developed. Both Charging Service Providers have adapted their internal management systems in order to communicate with the clearinghouse. Furthermore a GUI has been developed to manage the clearinghouse allowing the registration of new EMSPs or EVSEOs.

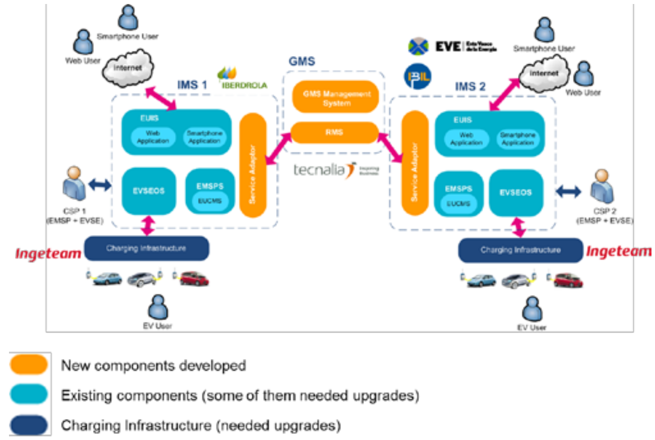

Figure 3 Spanish pilot architecture

Tecnalia has been responsible of the development and deployment of the Clearinghouse (Global Management System: GMS in Figure 3) that provides roaming services to both EVE-IBIL and Iberdrola.

III. Proposed Solution Approach

A. Existing solutions

There are several platforms that have each established their own eRoaming solutions and service offerings in different European countries including e-clearing.net, GIREVE, MOBI.E, Enel and Hubject.

eRoaming platforms are a link connecting different market participants in the emobility sector. These business and IT platforms enable charge point operators to conveniently and cost-efficiently open their own networks to additional users and thus get additional revenues by making contracts with emobility providers. These connected networks allow EV drivers to seamlessly recharge their vehicles at charging stations operated by connected charging operators, delivering value to users and all emobility providers and service providers, namely EV electricity suppliers, vehicle manufacturers as well as other market participants.

Besides, e-Clearing.net has published the open clearing house protocol (OCHP: http://www.ochp.eu/) as an open protocol available and free to use it in a commercial way.

However none of the existing solutions provides the level of business and service flexibility we require and only offers the basic charging service in roaming.

In order to provide the desired interoperability our objective has been to define a clearinghouse model and platform with the following characteristics:

- Provision of a comprehensive initial set of roaming services.
- Flexible definition of the roaming agreements allowing accommodating to different business models and strategies.
- Open to the inclusion of new e-mobility services

ISBN: 978-1-61804-321-4

B. Clearinghouse design issues

The clearinghouse developed has the following main roles:

- Manage roaming agreements among EMSP and EVSEOs
- Manage EV user roaming contracts
- Facilitate the provision of services in roaming
- Provide audit capabilities.

One of the main issues regarding the specification of the clearinghouse was to provide the level of business and service flexibility required by the two Charging Service Providers involved in the pilot.

This flexibility was taken into account in the definition of the roaming agreement, the EV user contract models and in the clearing house based services provision model.

1) Roaming agreement flexibility

A roaming agreement among EMSPs and EVSEOs include information about the specific services offered in roaming and the specific Charge Points included in the agreement.

This way an EMSP can stablish a roaming agreement with a EVSEO only for a set of services (e.g. charging and static visualization of charging points) and in a specific geographic area.

2) EV user contract flexibility

An EV user contract includes information about the services included in the roaming contract by EVSEO.

This is very important from the business point of view because the same service could have different prices and conditions depending on the specific EVSEO.

3) Services provision model flexibility

The way in which the clearinghouse facilitates the provision of services in roaming is also very flexible and includes the following options:

- The clearinghouse is used to interchange information between the EVSEO and the EMSP so that it is not necessary to call the clearinghouse to provide the service.
- The clearinghouse stores the information needed to provide the service.
- The clearinghouse is just a gateway that redirects the service request to the appropriate company and returns the answer.

IV. SERVICES IN ROAMING

In order to cover a full roaming management, a set of four categories of services have been included in the clearinghouse:

- **Charge Process**: Covering the process of charging in a Charging Point (authorization and later storing of the charge data)
- **Exchange of authorization data**: Covering the process of inserting new authorized users in the interoperability platform.
- **Charging Point Management**: Covering the process of management of Charging Points (insert/update/ delete, status information)
- **Reserve**: Covering the process of making a reserve for a Charging Point.

A. Functionalities for Charging Process

This set of services covers the process of charging in a Charging Point (authorization and later storing of the charge data)

Each time a customer wants to charge in a Charging Point that doesn´t belong to his service provider, the owner of the Charging Point needs to ask the CLEARINGHOUSE to obtain authorization for this customer.

Sometimes a service provider may want to be asked before giving authorization to a customer. In this case, or if the customer is of type prepayment, the Clearinghouse will ask the service provider for authorization. Otherwise, the Clearinghouse will allow/deny the charge process itself checking the authorization data stored.

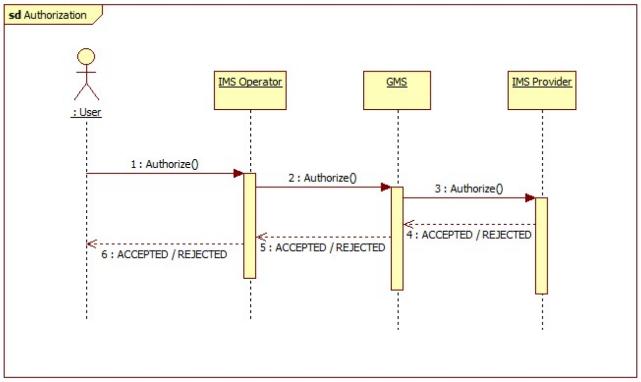

Figure 4 Authorization sequence diagram

When the charge is finished, the Clearinghouse will receive and store all the data related with the charge process (SDR - Service Detailed Record) and will also send it to the service provider of the Customer.

ISBN: 978-1-61804-321-4

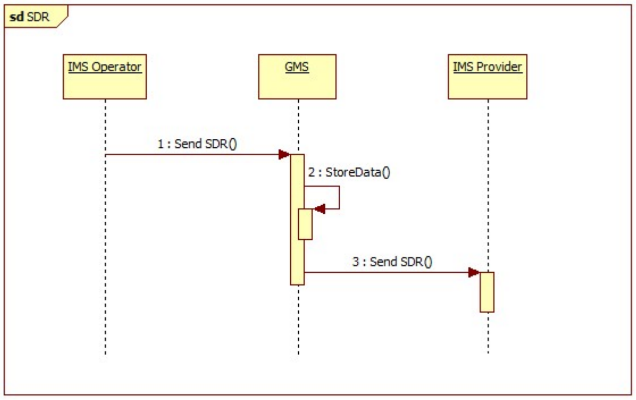

Figure 5 SDR Forward sequence diagram

B. Functionalities for exchanging Authorization Data

This service covers the process of inserting new authorized users in the interoperability platform

Each IMS will upload its own Customer authorization data to the Clearinghouse. The first time, this process will be done in block, that is, the IMS will send a list containing all the authorized users.

Whenever an IMS updates his users data (new users, deleted users…) he will be in charge of informing about these changes to the Clearinghouse through this service, sending the appropriate user list and indicating which the action is (New, Update or delete).

The Clearinghouse will use this Authorization Data to allow or deny itself a request of charging when the service provider that the customer belongs to doesn't want to be asked and he is not of type prepayment.

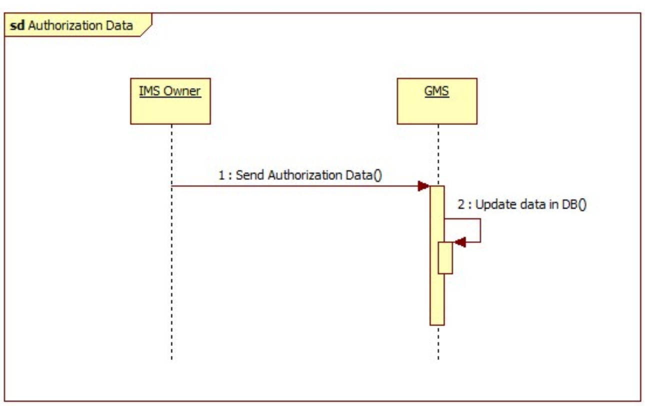

Figure 6 Authorization data exchange sequence diagram

C. Functionalities for Charging Point Management

This set of services covers the process of management of Charging Points: insert, update, delete and retrieve status information.

One of the services will allow each IMS to upload its own Charging Point information to the Clearinghouse.

Whenever an IMS updates his Charging Point data (new PR, deleted PRs…) he will be in charge of informing about these changes to the Clearinghouse, by sending the list of updated Charging Points.

Each time the Clearinghouse receives an update, it will send a notification to all the IMSs that have a roaming agreement with the IMS that has sent the message and the IMS will update the corresponding Charging Points.

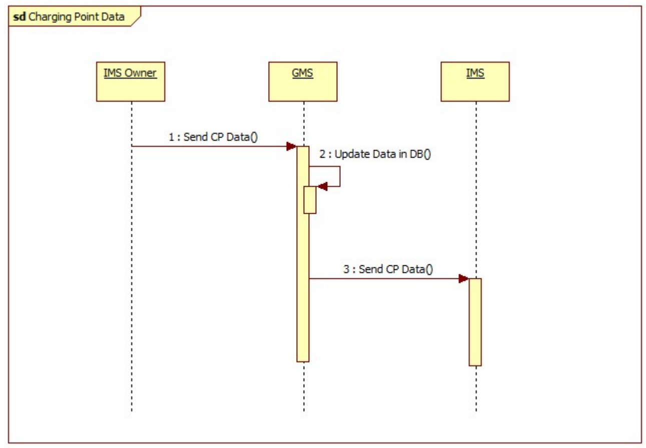

Figure 7 Charge point information exchange sequence diagram

Also, another service will allow each IMS to ask the Clearinghouse for the status of a Charging Point. It is called by the IMS who wants to know the status/information of one or a group of Charging Points.

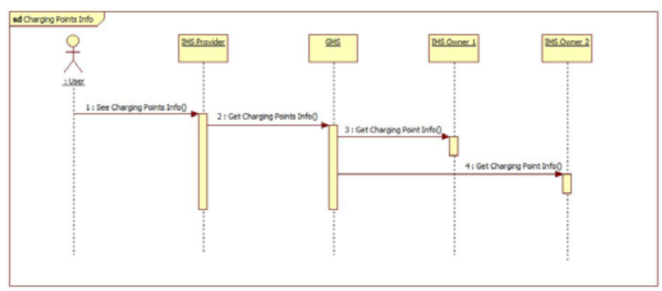

Figure 8 Charge point status sequence diagram

D. Functionalities for Reservation Process

This service covers the process of making a reservation for a Charging Point.

When a customer wants to reserve a Charging Point that doesn´t belong to his service provider, this service provider will ask the Clearinghouse to make this reservation. The Clearinghouse, in turn, will resend this request to the owner of the Charging Point.

If the customer wants to cancel a reservation, the service provider will inform the Clearinghouse, and the Clearinghouse will also inform the owner of the Charging Point.

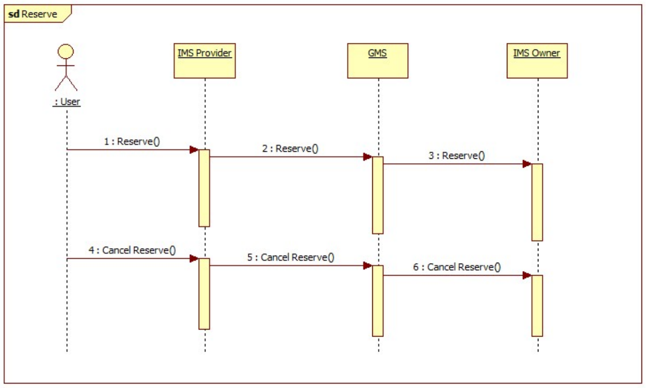

Figure 9

On the other hand, the owner of the Charging Point will inform the Clearinghouse when a reservation expires or when the customer has used it. In both cases, the Clearinghouse will inform the service provider.

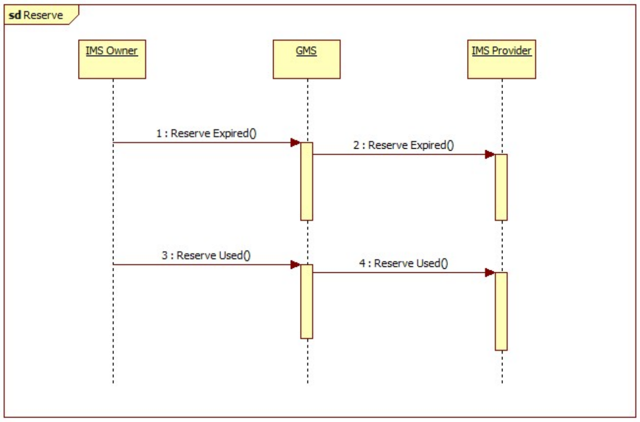

Figure 10

V. VALIDATION AND FURTHER STEPS

The clearinghouse has been successfully validated from the technical point of view and it is already deployed in the production environment.

Also an end user validation has been performed with positive results.

This validation has brought suggestions for some improvements.

The main one is that it would be useful to offer the users an establishment of international body for coordination of roaming platforms and verification of EVSEO/EMSP interfaces for operation in the global roaming scheme.

It is a very important issue because the Clearinghouse developed is not the only one in the market and it is expected that several roaming solutions coexist in the future.

So the European Commission insisted on in its “Deployment of Alternative Fuels Infrastructure” directive recently: “The operators of charging stations shall be allowed to provide electric vehicle recharging services to customers on a contractual basis, including in the name and on behalf of other service providers.”

Furthermore, the platform operatorse-clearing.net, GIREVE, MOBI.E, Enel and Hubject, has announce recently an initiative to launch a cooperation aimed at interconnecting five major eRoaming platforms in Europe. The so called Pan-European eRoaming initiative is open to other entities operating in the field of emobility who are interested in joining and it is a good opportunity for collaboration.

ISBN: 978-1-61804-321-4

Embedded mixed-integer predictive control of a water tank system

Jakub Novak and Petr Chalupa

***Abstract*—**Solution of the mixed-integer quadratic problem that arises from predictive control with a finite number of admissible input values has been restricted so far to powerful computational platforms. Given the growing computational power of embedded controllers, the use of mixed integer model predictive control strategies on this type of devices becomes more and more attractive In this paper embedded implementation of the solver based on a standard branch-and-bound method and interior point method for solution of the relaxed problem is considered. The target system is a microcontroller with low power and limited RAM memory. The simulation experiments with a MIMO water tank with binary, integer and continuous input signals is presented.

***Keywords*—**Embedded Systems, Predictive Control, Mixed-Integer Quadratic Programming, Branch-and-bound Method.

I. Introduction

The requirement for improved efficiency and safety induce the need for sophisticated control systems. Model predictive control (MPC) [1], [2] represents such control method which makes explicit use of a model of the process to obtain the control signal. The idea of Model Predictive Control is to determine an optimal control at the current time instant by solving an optimal control problem on a prediction horizon. The main reason for the wide-scale adoption of MPC is its ability to handle constraints on inputs and states that arise in most applications. Linear MPC has been applied to different industrial processes [1]. Process controls with a finite number of admissible values are common in a large number of relevant applications. For example, chemical plants are equipped with valves that can be either open or closed. A large potential for optimization is found as the number of potential modes of operation is hard to explore in an exhaustive way. The Mixed-Integer Quadratic Control or Hybrid optimal control as referred by several authors [3] addresses the optimal control problem of such systems.

The resulting mixed-integer quadratic problems (MIQP) are usually solved using the commercial solvers such as CPLEX or GUROBI that enables to deploy mixed-integer MPC on desktop platform. The necessity of these solvers limits the application to powerful computing platforms and slow dynamical systems.

Recently, efficient online solution methods for convex quadratic problem have been developed that can be implemented on the embedded hardware and are able to solve the problem at high sampling rate. An online MPC strategy with a good balance between computational speed and memory demand based that uses a fast gradient method was developed in [4]. An interior point solver was specifically designed for embedded applications in [5]. Many real-life problems can be represented as MLD (Mixed Logic Dynamical) systems [3] which are hybrid systems and whose MPC control requires solution of the MIQP problem [6]. Different methods for hybrid optimal control problem solution were evaluated in [7]. Currie, Prince-Pike and Wilson developed a MATLAB framework for generating fast model predictive controllers for embedded targets such as ARM processors and tested it on inverted pendulum in [8]. Bleris and Kothare present a real-time implementation of the MPC on a microcontroller for Glucose regulation in [9]. Implementation aspects of the MPC on Embedded System are also discussed in [10], [11] and [12]. The increase in computational power such as ARM Cortex processors and advances in optimization algorithms has opened a new trend which brings MPC capabilities also to complex and fast systems. With the development of cheap multi-core CPU in microcontrollers, the parallel computation might be the promising way for further decrease of computation time.

The aim of the paper is to illustrate the practical feasibility of mixed-integer MPC with constraints on a low cost embedded system where the problem is solved using branch-and-bound method and the relaxed quadratic programming problem is solved with interior point method. The paper is structured as follows: Section II briefly repeats the MIQP formulation and the branch-and-bound algorithm. The interior point method used for solution of the relaxed problem is described in Section III. The description of the example system is given in Section IV. Section V contains the results of the implementation of the solver on embedded system. Finally, the main conclusions are summarized in the last section.

The research was supported with financial support of research project NPU I No. MSMT-7778/2014 by the Ministry of Education of the Czech Republic and also by the European Regional Development Fund under the Project CEBIA-Tech No. CZ.1.05/2.1.00/03.0089.

Jakub Novak is with Faculty of Applied Informatics, Tomas Bata University in Zlin, nam. T.G. Masaryka 5555, 76001 Zlin, Czech Republic (email: jnovak@fai.utb.cz)

Petr Chalupa is with Faculty of Applied Informatics Tomas Bata University in Zlin, nam. T.G. Masaryka 5555, 76001 Zlin, Czech Republic (email: chalupa@fai.utb.cz).

II. BRANCH-AND-BOUND METHOD

In this section the description of the implemented branch-and-bound algorithm is given. Mixed-integer quadratic programming (MIQP) problems are optimization problems with a quadratic objective function, subject to linear equality and inequality constraints as presented below and where some variables are constrained to be integers. A common special case of MIQP is when the integer variables are constrained to binary values 0 or 1. The problem is non convex due to the fact that the optimized variables x_i belong to the binary set. The general formulation for a mixed-integer quadratic programming problem is the following,

$$\begin{aligned}
&\min 0.5\left[\boldsymbol{x}_c^T, \boldsymbol{x}_i^T\right] \boldsymbol{H} \begin{bmatrix} \boldsymbol{x}_c^T \\ \boldsymbol{x}_i^T \end{bmatrix} + f^T \begin{bmatrix} \boldsymbol{x}_c^T \\ \boldsymbol{x}_i^T \end{bmatrix} \\
&x_c \in R^{n_c}, x_i \in N^{n_i} : \boldsymbol{a}_j^T \begin{bmatrix} \boldsymbol{x}_c^T \\ \boldsymbol{x}_i^T \end{bmatrix} + b_j = 0, \quad j = 1, \dots, m_{ec} \\
&\qquad \boldsymbol{c}_j^T \begin{bmatrix} \boldsymbol{x}_c^T \\ \boldsymbol{x}_i^T \end{bmatrix} + d_j \geq 0, \quad j = 1, \dots, m_{ic}
\end{aligned} \tag{1}$$

where $\boldsymbol{H}$ is a positive definite n x n matrix ($n = n_i + n_c$), f is the n-dimensional vector. The n-dimensional vectors $\mathbf{a_j}$ and $\mathbf{c_j}$ and vectors $\boldsymbol{b}$ and $\boldsymbol{d}$ are used to set up the constraints. The numbers of equality and inequality constraints are specified with m_{ec} and m_{ic}, respectively. The equality and inequality constraints define a feasible region in which the solution to the problem must be located in order for the constraints to be satisfied. The only difference when compared to the convex QP is the presence of binary variables $\boldsymbol{x_i}$. Fortunately, if the binary variable is fixed or relaxed, a convex set is obtained and the problem can be solved using conventional methods for convex optimization. A constrained QP is usually solved either using an interior point method or an active set method.

Branch-and-bound has been the most used tool for solving large scale *NP*-hard combinatorial optimization problems since the branch-and-bound method is an order of magnitude faster than any of the other methods such as Generalized Benders Decomposition or Outer Approximation. The method is so fast due to the fact that that the QP subproblems are easy to solve. For MATLAB, free software like YALMIP [13] can be used. During the solution process, the status of the solution is described by a pool of yet unexplored subset of the solution space and the best solution found so far. The nodes in a dynamically generated search tree, which initially only contains the root, and each iteration of a classical branch-and-bound algorithm processes one such node represent unexplored subspaces. The iteration has two main components: selection of the node to process and branching strategy. The nodes created are then stored together with the bound of the currently processed node. The search stops when the pool of unexplored subset is empty and the optimal solution is then the one recorded as "current best".

There are two common node selection strategies for selection of the node to proceed in the next iteration. The first one is best-first-search, where the next node is always the one with the lowest dual bound. This method however requires a large amount of storage. The second class of node selection strategies depth-first-search where warm-starting can be successfully applied due to the similarity of the subproblems and also number of unexplored nodes is low, which significantly reduces the storage requirements. Due to the limited memory of the microcontroller the depth-first-search strategy is used in the example. Branching on a variable involves choosing the branching variable of the current optimal solution of the relaxed problem and then adding a constraint to it. The maximum fractional branching strategy which chooses the variable with the highest fractional part is used in the solver. The scheme of branch-and-bound method is depicted in Fig. 1.

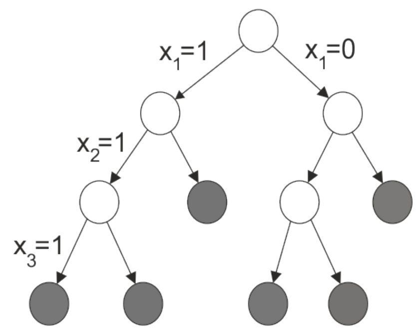

Fig. 1 branch-and-bound method

III. INTERIOR POINT METHOD

At each node the relaxed QP is solved solved either using an interior point method or an active set method. Interior-point methods solve problems iteratively where each iteration is computationally expensive but can make significant progress towards the solution. The solver uses the interior point method for solution of the relaxed problems:

$$\begin{aligned}
&\min 0.5\boldsymbol{x}^T \boldsymbol{H}\boldsymbol{x} + \boldsymbol{f}^T \boldsymbol{x} \\
&\quad x \in R^n : \boldsymbol{A}_c \boldsymbol{x} + \boldsymbol{b}_c = 0 \\
&\qquad\quad \boldsymbol{C}_c \boldsymbol{x} + \boldsymbol{d}_c \geq 0
\end{aligned} \tag{2}$$

where $\boldsymbol{A}$ is a m_{ec} x n matrix describing the equality constraints and C is an mic x n matrix describing the inequality constraints. $\boldsymbol{b}$ and $\boldsymbol{d}$ are m_{ec} x n and m_{ic} x n vectors respectively. The Lagrangian $\boldsymbol{L}$(x,y,z) with vectors $\boldsymbol{y}$ and $\boldsymbol{z}$ containing the Lagrange multipliers is defined as:

$$L(\boldsymbol{x},\boldsymbol{y},\boldsymbol{z}) = \frac{1}{2}\boldsymbol{x}^T \boldsymbol{H}\boldsymbol{x} + \boldsymbol{f}^T \boldsymbol{x} - \boldsymbol{y}^T(\boldsymbol{A}_c \boldsymbol{x} - \boldsymbol{b}_c) - \boldsymbol{z}^T(\boldsymbol{C}_c{}^T - \boldsymbol{d}_c) \tag{3}$$

ISBN: 978-1-61804-321-4

The following optimality conditions can be obtained with the introduction of the slack vector :

$$
\begin{aligned}
&\boldsymbol{H}x+\boldsymbol{f}-\boldsymbol{A}_c^{\,T}-\boldsymbol{C}_c\boldsymbol{z}=0\\
&\boldsymbol{A}_c\boldsymbol{x}-\boldsymbol{b}_c=0\\
&\boldsymbol{s}-\boldsymbol{C}_c\boldsymbol{x}+\boldsymbol{d}_c=0\\
&(\boldsymbol{z},\boldsymbol{s})\geq 0\\
&\mathrm{s}_i\, z_i=0
\end{aligned}
\tag{4}
$$

Defining the function ***F(***x,y,z,s) such that the roots of this function are solutions to the first four optimality conditions we obtain set of linear equation:

$$
\begin{bmatrix}
\boldsymbol{G} & -\boldsymbol{A}_c^{\,T} & -\boldsymbol{C}_c^{\,T} & 0\\
-\boldsymbol{A}_c & 0 & 0 & 0\\
-\boldsymbol{C}_c & 0 & 0 & \boldsymbol{I}\\
0 & 0 & \boldsymbol{S} & \boldsymbol{Z}
\end{bmatrix}
\begin{bmatrix}\Delta x\\ \Delta y\\ \Delta z\\ \Delta s\end{bmatrix}=
-\begin{bmatrix}
\boldsymbol{H}x+\boldsymbol{f}-\boldsymbol{A}_c^{\,T}\boldsymbol{y}-\boldsymbol{C}_c^{\,T}\boldsymbol{z}\\
\boldsymbol{A}_c\boldsymbol{x}-\boldsymbol{b}_c\\
\boldsymbol{s}-\boldsymbol{C}_c\boldsymbol{x}+\boldsymbol{d}_c\\
(\mathrm{s}*\mathrm{z})
\end{bmatrix}
\tag{5}
$$

where * is the element-wise multiplication of vectors. For solution of this set of equation predictor-corrector method proposed by Mehrotra is used. As a stopping criterion the following criterions are used:

$$
\begin{aligned}
&\left\|\boldsymbol{H}x+\boldsymbol{f}-\boldsymbol{A}_c^{\,T}\boldsymbol{y}-\boldsymbol{C}_c^{\,T}\boldsymbol{z}\right\|\leq\varepsilon\\
&\left\|\boldsymbol{A}_c\boldsymbol{x}-\boldsymbol{b}_c\right\|\leq\varepsilon\\
&\left\|\boldsymbol{s}-\boldsymbol{C}_c\boldsymbol{x}+\boldsymbol{d}_c\right\|\leq\varepsilon\\
&\left\|\mu\right\|\leq\varepsilon
\end{aligned}
\tag{6}
$$

and also maximum number of iterations k_{max} is specified. For the solution of the set of linear equations ***Ax=b*** from (5) the LDLT factorization is used.

$$
\boldsymbol{PAP}^T=\boldsymbol{LDL}^T \tag{7}
$$

where ***P*** is a permutation matrix, ***L*** is a unit lower triangular matrix and ***D*** is a block diagonal matrix with 1x1 and 2x2 blocks. Once a factorization has been computed, the solution to the linear system ***Ax = b*** can be computed at comparably low cost by solving a sequence of equations:

$$
\begin{aligned}
&\boldsymbol{Lu}=\boldsymbol{Pb}\\
&\boldsymbol{Dv}=\boldsymbol{u}\\
&\boldsymbol{L}^T\boldsymbol{w}=\boldsymbol{v}\\
&\boldsymbol{x}=\boldsymbol{P}^T\boldsymbol{w}
\end{aligned}
\tag{8}
$$

with intermediate vectors ***u,v,w***. The cost of the solve procedure (8) is most of the time negligible with respect to the cost of computing the factorization (7). The LDL factorization implemented in the LAPACK library [14] exploits the partial pivoting based on the Bunch-Kaufmann method [15].

IV. NUMERICAL EXAMPLE

The numerical example consists of the buffer and supply tanks. There are four control inputs: a two-stage pump, a continuous heater, and two on/off valves . The function of the plant is to receive liquid from an upstream process, and to deliver this liquid at some reference temperature to a downstream process.

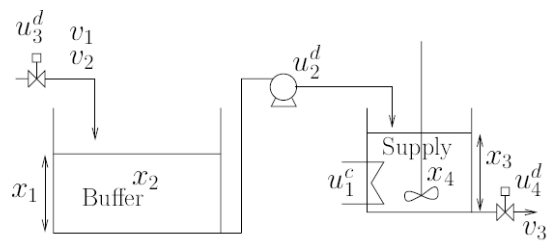

Fig. 2 two-tank system

The process dynamics is given by the following set of differential equations:

$$
\begin{aligned}
\dot{x}_1&=\frac{1}{A_b}\left(v_1u_3^d-\alpha u_2^d\right)\\
\dot{x}_2&=\frac{1}{A_bx_1}\left(-x_2v_1u_3^d+v_1v_2u_3^d\right)\\
\dot{x}_3&=\frac{1}{A_s}\left(\alpha u_2^d-v_3u_4^d\right)\\
\dot{x}_4&=\frac{1}{A_sx_3}\left(\left(x_2-x_4\right)\alpha u_2^d+\frac{u_1^c}{c_l\rho_l}\right)
\end{aligned}
\tag{9}
$$

where $x=\left[x_1\ x_2\ x_3\ x_4\right]^T$ is the state, $u=\left[u_1^d\ u_2^d\ u_3^d\ u_4^c\right]^T$ is the control input, and $v=\left[v_1\ v_2\ v_3\ \right]^T$ is the disturbance signal. The model parameters are given in Table I, the legend for the states, controls, and disturbances is given in Table II. The system was linearized at steady-state point $x^s=[7m,18\,^0C,1.5m,22\,^0C]^T$ for input signal $u^s=[280W,1,1,1]^T$. Maximal output of the heater is 560W.

Table I Model parameters

A_b	3.5 m^2	Buffer area
A_s	2 m^2	Supply area
c_l	4.2kJ/kgK	Specific liquid heat capacity
ρ_l	1000kg/m^3	Liquid density
α	1m^3/min	Pump capacity factor
Δ	0.25min	Sample period

Table II States, controls and disturbances

x_1,x_2	Buffer and supply levels
x_2,x_4	Buffer and supply temperatures
u_1^c	Heater
u_2^d	Pump
u_3^d, u_4^d	Inlet and outlet valves
v_1	Inflow
v_2	Temperature of inflow
v_3	Outflow

V. IMPLEMENTATION ON SELECTED HARDWARE PLATFORM

The proposed MIQP problem solver was implemented on The Stellaris® LM4F120 board which is a low-cost evaluation platform for 32-bit ARM® Cortex™-M4F-based microcontrollers from Texas Instruments (Fig 3).

The microcontroller runs at 80 MHz. The board has 32KB of SRAM memory, 256KB of flash memory and 2KB EEPROM. For implementation of the solver the requirements for memory and evaluation speed must be considered. The board has only 32KB of RAM however system parameters and constraints can be stored in flash memory as they are fixed and only read during the solution of the problem.

We have developed a simple implementation of branch-and-bound algorithm with interior point method for computation of the relaxed problem, written in C, using the LAPACK and BLAS libraries to carry out the numerical linear algebra computations such as matrix-vector multiplication, LDL^T decomposition and solution of system of algebraic equations. The solver is implemented using double precision floating-point arithmetic.

The mixed integer predictive control optimization problem is based on a time-invariant discrete process model and linear constraints:

$$\begin{aligned}
&\min_{\Delta u(k),\Delta u(k+1),\dots,\Delta u(k+N_c-1),} J(k) \\
&J(k) = \sum_{i=1}^{N_p} \left(\hat{y}(k+i) - y_r(k+1)\right)^T Q \left(y(k+i) - y_r(k+1)\right) + \\
&\qquad \sum_{i=1}^{N_c} \Delta u\left(k+i-1\right)^T R \Delta u\left(k+i-1\right) \\
&\textit{subject to}: \quad A_c \Delta u \le b_c
\end{aligned} \tag{10}$$

where $\hat{y}(k+i)$ is the ith step output prediction, $y_r(k+i)$ is the i-th step of the reference trajectory, $\boldsymbol{\Delta u(k)}$ is difference between $\boldsymbol{u(k)}$ and $\boldsymbol{u(k-1)}$, $\boldsymbol{R,Q}$ are positive definite matrices and N_p and N_c are the prediction and control horizons, respectively and $\boldsymbol{A_c}$ and $\boldsymbol{b_c}$ are the constraints matrix and vector that can be derived from process model and input and state constraints. Only the first element of the optimal predicted input sequence $\Delta \boldsymbol{u}(k)$ is applied to the plant:

$$u(k) = u(k-1) + \Delta u(k) \tag{11}$$

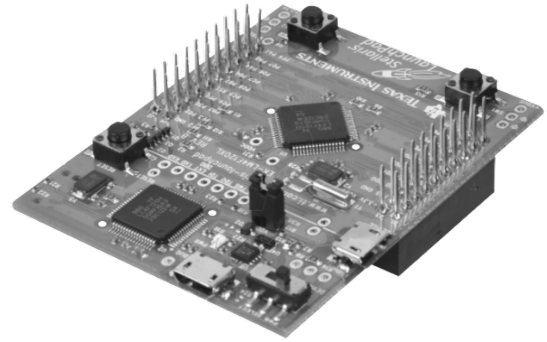

Fig. 3 Stellaris LM4F120 launchpad board

The normalized discrete linearized model of the plant is assumed in the form:

$$\begin{aligned}
\boldsymbol{x}(k+1) &= \boldsymbol{A}\boldsymbol{x}(k) + \boldsymbol{B}\boldsymbol{u}(k) \\
\boldsymbol{y}(k) &= \boldsymbol{C}\boldsymbol{x}(k)
\end{aligned} \tag{12}$$

where $\boldsymbol{u(k)}$ is the vector of manipulated variables or input variables; $\boldsymbol{y(k)}$ is the vector of the process outputs and $\boldsymbol{x(k)}$ is the state variable vector. The sampling time was set to 15s. Using the linear model the model predictive controller would exhibit steady – state offset in the presence of plant/model mismatch or unmeasured disturbance due to lack of integral action. In order to introduce integral behavior, a new state variable vector is chosen to be:

$$\boldsymbol{x} = \begin{bmatrix} \Delta\boldsymbol{x}(k) \\ \boldsymbol{y}(k) \end{bmatrix} \tag{13}$$

Combining (12) and (13) leads to the following state-space model:

$$\begin{aligned}
\begin{bmatrix} \Delta x(k+1) \\ y(k+1) \end{bmatrix} &= \begin{bmatrix} \boldsymbol{A} & 0 \\ \boldsymbol{CA} & I \end{bmatrix} \begin{bmatrix} \Delta x(k) \\ y(k) \end{bmatrix} + \begin{bmatrix} \boldsymbol{B} \\ \boldsymbol{CB} \end{bmatrix} \Delta u(k) \\
y(k) &= \begin{bmatrix} 0 & 1 \end{bmatrix} \begin{bmatrix} \Delta x(k) \\ y(k) \end{bmatrix}
\end{aligned} \tag{14}$$

The process state-space model can be rewritten as a prediction model for the current state vector $\boldsymbol{x}$ and control increment sequence $\Delta\boldsymbol{U} = \left[\Delta u(k), \Delta u(k+1), \dots, \Delta u(k+N_c-1)\right]^T$. For given horizons it can be formulated in terms of vectors as:

$$\boldsymbol{Y} = \boldsymbol{K}\boldsymbol{x} + \boldsymbol{L}\Delta\boldsymbol{U} \tag{15}$$

where $\boldsymbol{Y} = \left[\hat{y}(k+1), \hat{y}(k+2), \dots, \hat{y}(k+N_p)\right]^T$ and $\boldsymbol{K}$ and $\boldsymbol{L}$ are constant matrices derived from the process model.

ISBN: 978-1-61804-321-4

The Hessian matrix $\boldsymbol{H}$ and vector $\boldsymbol{f}$ from criterion (1) can then be formulated as:

$$\boldsymbol{H} = \boldsymbol{L}^T \boldsymbol{Q} \boldsymbol{L} + \boldsymbol{R},\ f = -\boldsymbol{R}(\boldsymbol{Y}_{\mathrm{r}} - \boldsymbol{K}\boldsymbol{x}(\mathrm{k}))^T \boldsymbol{L} \tag{16}$$

The control task is to keep the supply temperature at its nominal value while preventing overflow/emptying of the buffer and supply tank. Both the prediction and control horizons were set to 4 steps. The mathematical formulation of the predictive control for prediction and control horizon of 4 steps with constraints results corresponds to an MIQP with 4 continuous variables (Δu_1) and 8 binary variables ($\Delta u_3, \Delta u_4$) and 4 integer variables (Δu_2) and 48 inequality constraints. The weighting matrices $\boldsymbol{Q}$ and $\boldsymbol{R}$ were set identity matrices. Sixteen of the 48 inequality constraints are necessary to restrict the 8 binary values from 0 to 1. The execution times and number of relaxed QP solved at each sampling point is presented in Fig. 4. The closed-loop response of the MPC controller is presented in Fig. 5 and 6.

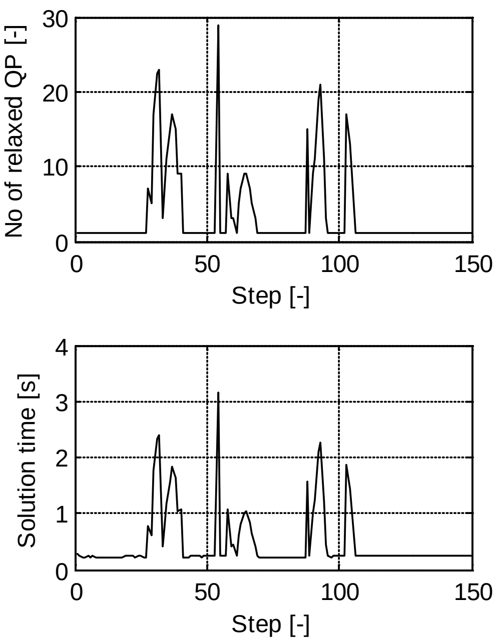

Fig. 5 number of solved relaxed quadratic problems and execution time

The matrices $H \in R^{nxn}$, $C_c \in R^{n_{ic}xn}$, $A_c \in R^n$ and vectors *f*, b_c, d_c for definition of constraints and cost function of the MIQP problem are stored in flash memory. The branch-and-bound method requires a pool for storing the nodes during the solution process. The memory requirements in bytes are given by two matrices for storage the additional constraints of the size $n_{pool} * n_i$, a double vector of the size n_{pool} to hold the bounds for each node in a pool and integer vector to store the priority of the nodes in the pool. Interior point method requires allocation of vectors $x, \Delta x, y, \Delta y, \mathrm{z}, \Delta z, s, \Delta s$, the matrix $\boldsymbol{A}$ and vector $\boldsymbol{b}$ of the system $\boldsymbol{Ax=b}$ in the memory. The matrix A is symmetric so only lower triangular part of the matrix A is stored. The number of elements of lower triangular matrix is given as:

$$\frac{1}{2}(\mathrm{n}+\mathrm{n}_{\mathrm{ic}}+\mathrm{n}_{ec})(\mathrm{n}+\mathrm{n}_{\mathrm{i}c}+\mathrm{n}_{ec}+1) \tag{17}$$

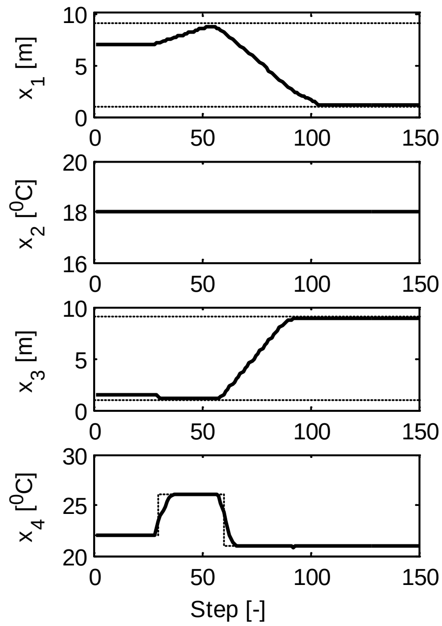

Fig. 5 closed-loop response of the two-tank system using mixed-integer predictive controller – system states (dotted line –system constraint and reference signal for x_4)

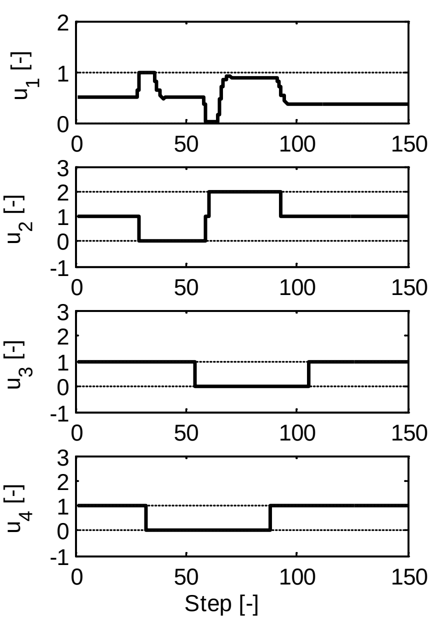

Fig. 6 closed-loop response of the two-tank system using mixed-integer predictive controller – system inputs (dotted line- input constraints)

VI. Conclusion

The results show that solution of the predictive control problem with 16 variables (4 continuous, 4 integer and 8 binary) and 48 constraints is manageable on the low power platform. Enough free time remains for the control loop including Kalman filter for state estimation and filtration. The simulation study showed that the memory as well as the computational demand of an MIQP solver implementation is decisive for real-time use on low-cost embedded systems. Future research will include more complex nonlinear systems and verification of the implementation of the embedded controller for real plants.

References

[1] S.J. Qin and B.J. Badgwell, "A survey of industrial model predictive control technology," *Control Engineering Practice*, vol. 11, pp. 733–764, 2003.

[2] J.M. Maciejowski, *Predictive Control with Constraints*, Prentice Hall, 2000.

[3] A. Bemporad and M. Morari, "Control of systems integrating logic dynamics and con-straints," *Automatica* , vol. 35, no. 3, pp. 407–427, 1999.

[4] Y. Wang and S. Boyd, "Fast model predictive control using online optimization," *IEEE Transactions on Control Systems Technology* vol. 18, pp. 267-278, 2010.

[5] A. Domahidi, E. Chu and S. Boyd, "ECOS: An SOCP solver for embedded systems," in *Proc. European Control Conference*, pp. 3071-3076, 2013.

[6] Y. Hammi, N. Zanzouri and M. Ksouri, "Modeling and Predictive Control of Tow Tank System by MLD Approach," in *Proc. 5th International Conference on Circuits, Systems, Control, Signals*, pp. 140-145, 2010.

[7] R.T. Meyer, M. Žefran and R. A. DeCarlo, "A comparison of the embedding method with multiparametric programming, mixed-integer programming, gradient-descent, and hybrid minimum principle-based methods, *IEEE Transactions on Control Systems Technology*, vol. 22 pp. 1784-1800, 2014.

[8] J. Currie, A. Prince-Pike and D.I. Wilson, "Auto-code generation for fast embedded model predictive controllers," in *Proc. International Conference on Mechatronics and Machine Vision in Practice* , pp. 122-128, 2012.

[9] L.G. Bleris and M. V. Kothare, "Implementation of Model Predictive Control for Glucose Regulation on a General Purpose Microprocessor," in *Proc. 44th IEEE Conference on Decision and Control*, Seville, pp. 5162-5168, 2005.

[10] P. Zometa, M. Kogel, T. Faulwasser and R. Findeisen, "Implementation aspects of model predictive control for embedded systems," in *Proc. the American Control Conference*, pp. 1205-1210, 2012.

[11] B. Huyck, H. J. Ferreau, M. Diehl, J. De Brabanter, J. F. M. Van Impe, B. De Moor and F. Logist, "Towards Online Model Predictive Control on a Programmable Logic Controller: Practical Considerations," *Mathematical Problems in Engineering* , vol. 2012, 2012.

[12] J. Novak, P. Chalupa, "Implementation Aspects of Embedded MPC with Fast Gradient Method," *International Journal of Circuits, Systems and Signal Processing*, vol. 8, 504-511, 2014.

[13] J. Lofberg, "YALMIP : a toolbox for modeling and optimization in MATLAB," in *Proc. IEEE International Symposium on Computer Aided Control Systems Design*, pp. 284-289, 2004.

[14] E. Anderson, Z. Bai, C. Bischof, S. Blackford, J. Demmel, J. Dongarra, J. Du Croz, A. Greenbaum, S. Hammarling, A. McKenney, D. Sorensen, *LAPACK Users' Guide*. Warrendale, PA: SIAM, 1999.

[15] J.R. Bunch and L. Kaufman, "Some stable methods for calculating inertia and solving symmetric linear systems," *Math. Comp.*, vol. 31, pp. 163–179, 1977.

ISBN: 978-1-61804-321-4

Robust control of twin rotor MIMO system

Petr Chalupa, Jakub Novák, Jan Přikryl

***Abstract*—**The paper is focused on modeling and robust control of the Twin Rotor MMO System – a real-time laboratory plant by Feedback Ltd. The plant resembles a helicopter. It consists of two propellers individually controlled by external controller. An initial nonlinear mathematical model is derived using first principles modeling and further improved to according to real-time measurements. Several linear black box models are identified by applying various input courses to the plant. This set of models is used for robust control design. Resulting robust controller is verified using both the nonlinear model and the real-time plant.

***Keywords*—**First principle modelling, Real-time control, Robust control

I. Introduction

MOST of current control algorithms are based on a model of a controlled plant [1]. It is obvious that some information about controlled plant is required to allow for design of a controller with satisfactory performance. A plant model can be also used to investigate properties and behavior of the modeled plant without a risk of damage or violating technological constraints of the real plant. The re two basic approaches of obtaining plant model: the black box approach and the first principles modeling (mathematical-physical analysis of the plant).

The black box approach to the modeling [2], [3] is based on analysis of input and output signals of the plant. The main advantage of the black box approach consists in the possibility of usage the same identification algorithm for wide set of various controlled plants [4], [5]. Contrary, the first principle modeling provides general models valid for whole range of plant inputs and states. A model is created by analyzing the modeled plant and combining physical laws [6]. But, there are usually many unknown constants and relations when performing analysis of a plant. Therefore first principle models are suitable for simple controlled plants with small number of parameters. First principle modeling can be also used for obtaining basic information about controlled plant (rage of gain, rank of suitable sample time, etc.). Some simplifications must be used to obtain reasonable results in more complicated cases. These simplifications must relate with the purpose of the model. The first principle modeling is also referred to as white box modeling.

The paper combines both methods. Basic relations between plant inputs and outputs are derived using first principles. The obtained model is further improved on the basis of measurements. This approach is known as grey box modeling [7]. The goal of the work was to obtain a mathematical model of the Twin Rotor MIMO System [8], design the model in MATLAB-Simulink environment and use this model for design of adaptive controller. The Twin Rotor MIMO System was developed by Feedback Instruments Ltd. and serves as a real-time model of nonlinear multidimensional system. A model, which represents the plant well, can considerably reduce testing time of different control approaches. Then only promising control strategies are applied to the real plant and verified.

The paper is focused on robust control design [9]. Robust control approach allows obtaining a stabilizing controller not only for a nominal controlled system but also for a wider set of controlled systems. The set can be defined in various ways. This paper deals with parametric uncertainty, namely interval uncertainty [10].

The paper is organized as follows. Section 2 presents the modelled system – Twin Rotor MIMO System. A derivation of the model is carried out in Section 3. Robust control design is presented in Section 4 and real-time experiments are described in Section 5.

II. Twin Rotor MIMO System

A photograph of the Twin Rotor MIMO System is presented in Fig. 1. The system is used to demonstrate the principles of a non-linear MIMO system, with significant cross-coupling. Its behavior resembles a helicopter but contrary to most flying helicopters the angle of attack of the rotors is fixed and the aerodynamic forces are controlled by varying the speeds of the motors. Significant cross-coupling is observed between the actions of the rotors, with each rotor influencing both angle positions [11].

There are two propellers driven by DC-motors at both ends of a beam, which is pivoting on its base. The joint allows the beam to rotate in such a way that its ends move on spherical surfaces. There is a counter-weight fixed to the beam and it

The work was performed with financial support of research project NPU I No. MSMT-7778/2014 by the Ministry of Education of the Czech Republic and also by the European Regional Development Fund under the Project CEBIA-Tech No. CZ.1.05/2.1.00/03.0089.

This work was supported by the European Regional Development Fund under the project CEBIA-Tech No. CZ.1.05/2.1.00/03.0089. This support is greatly acknowledged.

Petr Chalupa is with the Tomas Bata University in Zlin, Faculty of Applied Informatics, Regional Research Centre CEBIA-Tech, nam. T. G. Masaryka 5555, 760 01 Zlin, Czech Republic (phone: +420 57603 5316, e-mail: chalupa@fai.utb.cz).

Jakub Novák is with the Tomas Bata University in Zlin, Faculty of Applied Informatics, Regional Research Centre CEBIA-Tech (email: jnovak@fai.utb.cz).

Jan Přikryl studied master degree at the Tomas Bata University in Zlin, Faculty of Applied Informatics.

determines a stable equilibrium position. The controls of the system are the motors supply voltages. The measured signals are position of the beam in the space, i.e. two position angles [12].

Fig. 1. Twin Rotor MIMO System.

III. MODEL OF THE TWIN ROTOR MIMO SYSTEM

A nonlinear model of the plant is derived in this section. The model is based on first principle modeling [12], [13], and [14]. More details concerning modeling of the Twin Rotor MIMO System can be found in [15].

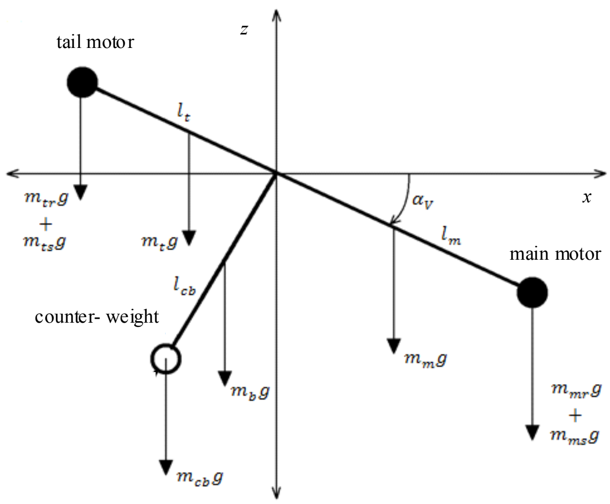

Fig. 2. Schematic front view of the Twin Rotor MIMO System with gravitation forces.

There are two outputs of the plant: position angle in the vertical plane – elevation (i.e. angle with respect to horizontal axis) and position in the horizontal plane – azimuth (i.e. angle with respect to vertical axis). First vertical plane will be considered, and then the horizontal angle will be focused on. A schematic front view of the free beam and connected parts of the Twin Rotor MIMO System is depicted in Fig. 2. The gravitation forces taking effect are presented as well.

Constant g represents gravitational acceleration, parameters l_t, l_m and l_{cb} stand for the length of the tail part of the beam, the length of the main part of the beam and the length of the counter-weight beam respectively. The mass of the tail motor with tail rotor, the mass of the tail shield and the mass of the tail part of the beam are represented by m_{tr}, m_{ts}, and m_t respectively. Constants m_b and m_{cb} represent the mass of the counter-weight beam and the mass of the counter-weight respectively. The mass of the main motor with tail rotor, the mass of the main shield and the mass of the main part of the beam are represented by m_{mr}, m_{ms}, and m_m respectively. Finally α_v stands for the pitch angle of the beam – elevation

A. *Initial model*

The derivation of moments in the vertical plane is based on Newton's second law of motion:

$$M_v = J_v \frac{d^2\alpha_v}{dt} \tag{1}$$

where M_v is a sum of components of moment of forces and J_v is a sum of moments of inertia relative to horizontal axis of individual parts of the plant:

$$M_v = \sum M_{vi} \tag{2}$$

$$J_v = \sum J_{vi} \tag{3}$$

The moments present in the horizontal plane can be derived in the similar way as the moments in the horizontal plane.

It is possible to derive state equations of the whole system:

$$\frac{dS_v}{dt} = \frac{g\left[\left(A-B\right)\cos\alpha_v - C\sin\alpha_v\right] + l_m F_v\left(\omega_m\right)}{J_v} - \frac{\frac{1}{2}\Omega_h^2\left(A+B+C\right)\sin 2\alpha_v + \Omega_v k_v}{J_v} \tag{4}$$

$$\frac{dS_h}{dt} = \frac{l_t F_h\left(\omega_t\right)\cos\alpha_v - \Omega_h k_h}{J_h} \tag{5}$$

$$\Omega_v = S_v + \frac{J_{tr}\omega_t}{J_v};\quad \Omega_h = S_h + \frac{J_{mr}\omega_m \sin\alpha_v}{J_v} \tag{6}$$

where A, B, and C are constants derived from the physical parameters of the plant; S_v and S_h are the angular momentum in vertical plane for the beam and the angular momentum in horizontal plane for the beam respectively. The moment of inertia in DC-motor – tail propeller subsystem and the moment of inertia in DC-motor – main propeller subsystem are represented by J_{tr} and J_{mr} respectively.

These equations describe dependence of output angles (elevation α_v and azimuth α_h) on rotations of the main and the tail motors – ω_m and ω_t respectively. The motors are controlled by control voltage according to the following combinations of linear dynamics and static non-linearity:

ISBN: 978-1-61804-321-4

$$\frac{du_{vv}}{dt} = \frac{1}{T_{mr}}\left(-u_{vv} + u_v\right), \quad (7)$$
$$\omega_m = P_v\left(u_{vv}\right)$$

$$\frac{du_{hh}}{dt} = \frac{1}{T_{tr}}\left(-u_{hh} + u_h\right), \quad (8)$$
$$\omega_t = P_h\left(u_{hh}\right)$$

where T_{mr} and T_{tr} are the time constant of the main motor – propeller system and the time constant of the tail motor – propeller system. Functions $P_v()$ and $P_h()$ describe the static nonlinearity of the main motor – propeller system and the static nonlinearity of the tail motor – propeller system. Inputs u_v and u_h represent the control voltage of the maim motor and the control voltage of the tail motor respectively.

B. *Enhanced model*

Documentation [12] provides parameters and relations of the Twin Rotor MIMO System which were presented in previous subsection. However real-time experiments showed that these parameters and equations should be refined or revised. This subsection is focused on modification of the initial model and parameters given in [12] in order to obtain better correspondence of the mathematical model and real time system.

1) Refinement of the dimensions

The dimensions of the modeled Twin Rotor MIMO System were measured to refine constants given in documentation [12]. Especially the length of the counter-weight beam is different from the value given in documentation.

2) Nonlinear static functions

The mode contains several nonlinear functions – e.g. equations (4), (5), (7) and (8). These functions have to be determined to design the final model. A phenomenological approach was used for their identification. A polynomial approximation was used without deep study of the physical fundamentals of the relation.

3) Cross coupling transfers

The cross coupling can be observed in the Twin Rotor MIMO System. The rotation of the tail motor slightly affects elevation angle while main motor strongly affects not only elevation but also azimuth. The influence of tail motor to elevation was modeled as linear function of tail rotor rotations.

The dependence of azimuth on rotations of the main motor is more complicated to model. An exponential function of the M_{v2} moment was used to cope with this problem. A Simulink scheme of this relation is presented in Fig. 3.

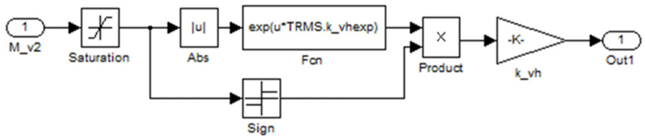

Fig. 3. Model of influence of main motor to the azimuth.

4) Cableways

A cableway between the fixed base of the Twin Rotor MIMO System and its beam plays a significant role especially in case of low rotation speed of the tail motor. Due to the cable way the system does not behave as an integrative but proportional behavior can be observed. The effect of the cableway is modelled as a nonlinear function of the azimuth.

IV. Design of Robust Controller

A design of robust controllers for the Twin Rotor MIMO System is based on parametric uncertainty approach. The parametric uncertainty can be used for both continuous-time and discrete systems [16].

The controlled plant was analyzed to obtain an interval uncertainty of the linear model of the system. For the control purposes, the Twin Rotor MIMO System was considered as two independent systems

- control voltage of the main rotor (input) – elevation (output)
- control voltage of the tail rotor (input) – azimuth (output)

The cross-couplings are considered as disturbances in this case.

Various step changes of the control input were applied to the plant, time responses of plant were measured and corresponding linear models were identified.

A. *Identification of main rotor – elevation subsystem*

Step changes of the control voltage of main rotor usually lead an oscillatory response of the elevation output. This system was modeled by a 3rd order linear system:

$$G_h\left(s\right) = \frac{b_{0h}}{a_{3h}s^3 + a_{2h}s^2 + a_{1h}s + 1} \quad (9)$$

Identification was performed in least squares sense using MATLAB function fminsearch. Results are summarized in Table I.

TABLE I. Intervals of the Main Rotor – Elevation Model

Parameter	Minimal value	Maximal value
b_{0h}	60	157
a_{3h}	0.23	1.30
a_{2h}	0.22	2.35
a_{1h}	0.81	2.74

Common notation for writing transfer functions of systems with interval uncertainties uses square brackets:

$$G_h\left(s\right) = \frac{\left[60; 157\right]}{\left[0.23; 1.30\right]s^3 + \left[0.22; 2.35\right]s^2 + \left[0.81; 2.74\right]s + 1} \quad (10)$$

Model behavior especially its stability is defined by position of transfer function poles – i.e. roots of the denominator. The interval model was obtained from 29 linear models which were identified from step responses. Poles of these 29 models are presented in Fig. 4. The poles are marked by asterisk and poles of each model are connected by a line.

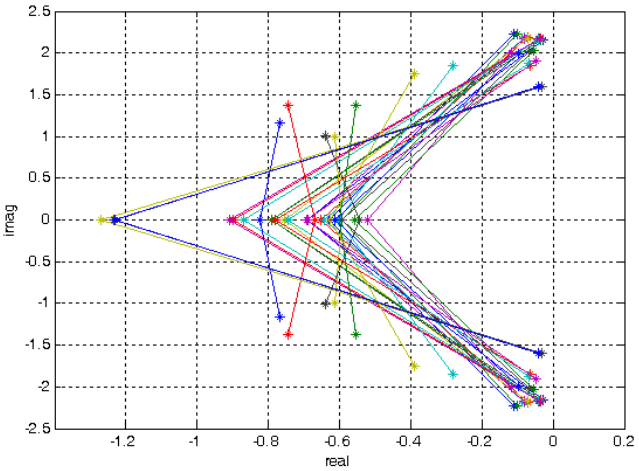

Fig. 4. Poles of the main rotor – elevation models

It can be seen that all models are stable (real parts are smaller than zero). Moreover all models are oscillatory because each model has a pair of complex conjugated poles.

Intervals of denominator of the interval model (10) form a box in the 3D space. Contrary to experiments not all transfer functions formed from the parameters inside this box are stable. The situation is presented in Fig. 5.

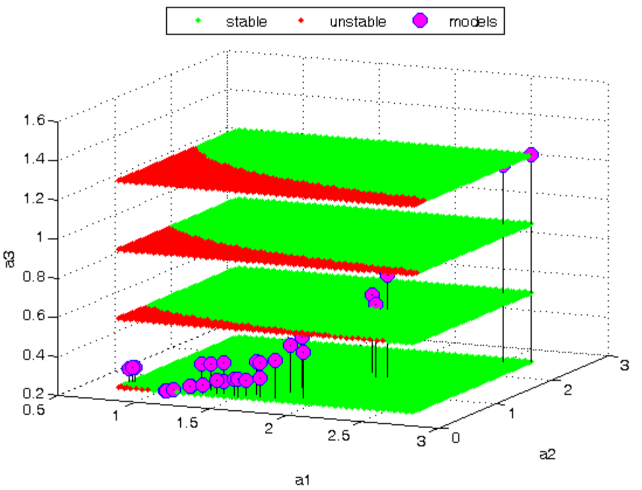

Fig. 5. Stability of interval model of the main rotor – elevation subsystem

Four crosscuts of the box are presented. The crosscuts are parallel to a_{1h} x a_{2h} plane. The upper and the lower crosscut correspond to the maximal and the minimal value of the a_{3h} parameter respectively. The other two crosscuts correspond to one third and two thirds between the minimum and maximum of a_{3h}. The red areas correspond to unstable systems while green areas correspond to stable systems. The magenta circles correspond to models identified from step responses.

B. Identification of tail rotor – azimuth subsystem

The tail rotor – azimuth subsystem was identified in the similar way as the main rotor – elevation subsystem. The main difference consists in fact that 2nd order models were used, because their accuracy was good enough.

$$G_v(s)=\frac{b_{0v}}{a_{2v}s^2+a_{vt}s+1} \tag{11}$$

The step responses where the plant reached a backstop were omitted from the identification. The positions of poles are presented in Fig. 6.

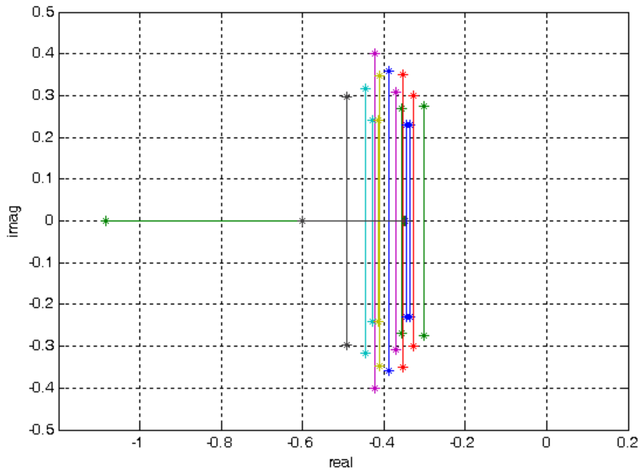

Fig. 6. Poles of the tail rotor – azimuth models

All the models presented in Fig. 6 are stable and most of them are oscillatory. Limits of the model parameters are summarized in Table II.

TABLE II. INTERVALS OF THE TAIL ROTOR – AZIMUTH MODEL

Parameter	Minimal value	Maximal value
b_{0v}	75	716
a_{2v}	2.63	6.04
a_{1v}	2.49	4.55

Resulting interval model can be written in the following form:

$$G_v(s)=\frac{[75;\,716]}{[2.63;\,6.04]s^2+[2.49;\,4.55]s+1} \tag{12}$$

Intervals of the denominator define a rectangle in a_{1v} x a_{2v} plane. As the denominator is a 2nd order degree polynomial and both a_{1v}, a_{2v} are always positive roots of denominator have always negative real part and therefore all the models are stable. Some of the models are oscillatory while the others are aperiodic. The situation is presented in Fig. 7. The magenta circles correspond to models identified from step responses.

ISBN: 978-1-61804-321-4

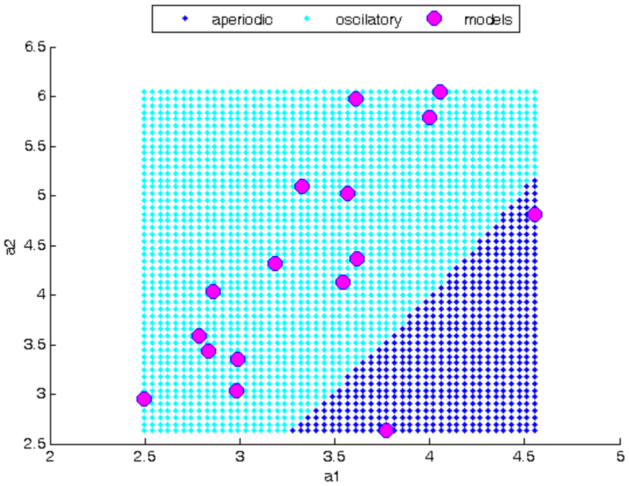

Fig. 7. Behavior of interval model of the tail rotor – azimuth subsystem

C. Design of robust 2DOF controller

Several controller types were tested and results of the 2DOF (Two Degree Of Freedom) controllers are presented in this paper. The scheme of the control loop with 2DOF controller is presented in Fig 8.

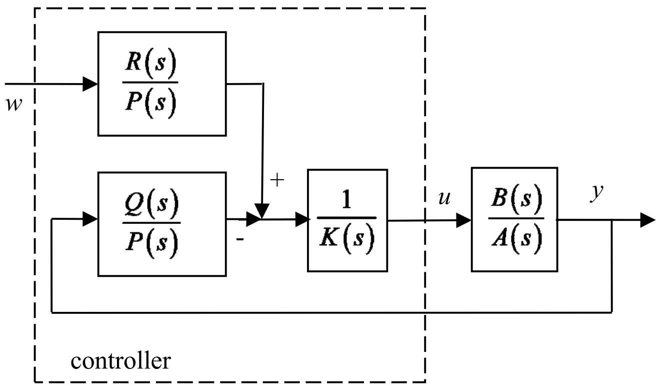

Fig. 8. 2DOF controller

Control signal is calculated according to the following equation:

$$U(s) = \frac{1}{K(s)}\left[\frac{R(s)}{P(s)}W(s) - \frac{Q(s)}{P(s)}Y(s)\right] = \\ = G_R(s)W(s) - G_Q(s)Y(s) \quad (13)$$

where $U(s)$, $W(s)$, and $Y(s)$ are Laplace transforms of $u(t)$, $w(t)$, and $y(t)$ signals respectively. Pole-placement method was used to calculate controllers' polynomials $R(s)$, $P(s)$, $Q(s)$ and $K(s)$. Detail can be found for example in [1].

Pole placement method is based on fixing poles of closed loop to the desired positions. For robust control of a system with interval uncertainties the controller is required to guarantee stability of closed loop for any combination of parameters from the given intervals. Unfortunately coefficients of the characteristic polynomial of the closed loop are not independent. Therefore Kharitonov polynomials cannot be used for stability testing [17].

Solving the robust closed loop stability is theoretically complicated task. Hence simplified approach was used:

1. Controller polynomials were calculated with respect to given position of poles and a nominal system.
2. Coefficient values equally spread through an interval were generated for each uncertainty interval.
3. Stability of the closed loop was tested for each combination of coefficient values.

Coefficients of the nominal system were defined as midpoints of the uncertainty intervals. Five coefficient values were generated for each interval. It leads to 5^4=625 combinations (systems) for the main rotor – elevation subsystem and 5^3=125 combinations (systems) for the tail rotor – azimuth subsystem.

Pole positions were defined in the simplest possible way. One multiple real pole was used. Hence the characteristic polynomial of the closed loop has the following form:

$$D(s) = (s+\alpha)^n \quad (14)$$

Whole task of computing the robust controller can be seen as an optimization problem with the goal of stabilizing all the generated systems and the pole position as a tuning parameter.

This approach does not guarantee stability of all possible coefficient combinations but its results in real-time environment were good no unstable behavior of the closed loop was observed.

V. Real-Time Experiments

This section presents several real-time experiments from a huge set of experiments performed. A sampling period of T_0 = 0.01s was used for sensors and actuators in all experiments.

Optimal value of pole position for elevation control was $\alpha_v = 1.7$ (i.e. multiple pole in position -1.7) and optimal value for azimuth control was $\alpha_h = 0.6$ (i.e. multiple pole in position -0.6). Elevation control and azimuth control were performed simultaneously to verify effect of cross-couplings. Courses of elevation control are presented in Fig. 9. Control of both real-time plant and nonlinear model derived in Section 3 are presented.

ISBN: 978-1-61804-321-4

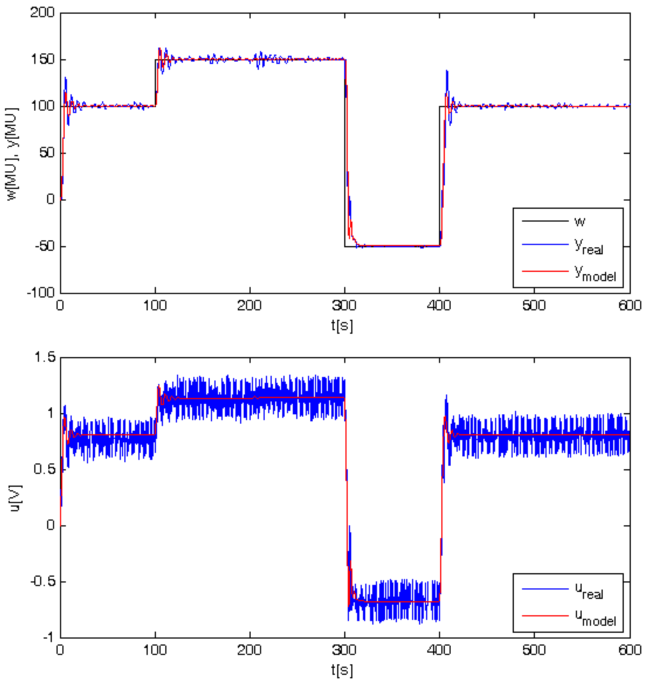

Fig. 9. Elevation control

Courses of azimuth control are presented in Fig. 10. Control of both real-time plant and nonlinear model derived in Section 3 are presented.

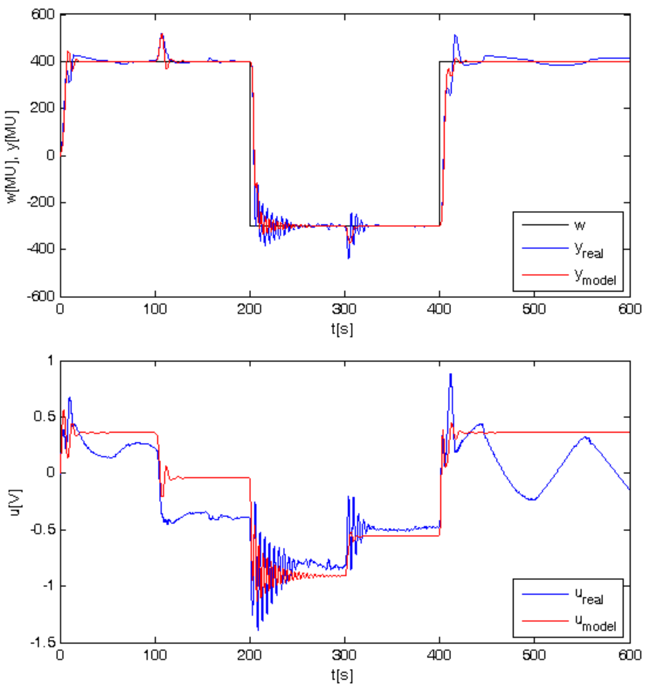

Fig. 10. Azimuth control

A satisfactory control behavior with a good reference tracking was observed. The greatest difference between nonlinear model and real-time plant was obtained for control signal of the tail rotor.

VI. Conclusion

A model of nonlinear real time system Twin Rotor MIMO System was derived using first principle modeling and then enhanced to correspond better with the real plant.

A simple robust control technique was presented and successfully verified in real-time conditions. Further improvement can be acquired by implementing better pole placement. Usage of several different poles would lead to even better control courses than the courses presented in the paper.

Further work will be focused on obtaining even better performance of a robust control and subsequent comparison of results of a robust control and an adaptive control. Moreover, the presented model will be used to design and verify model based predictive control of the Twin Rotor MIMO System.

References

[1] V. Bobál, J. Böhm, J. Fessl and J. Macháček. *Digital Self-tuning Controllers: Algorithms, Implementation and Applications*. London: Springer-Verlag, 2005.

[2] G. P. Liu, *Nonlinear identification and control – A neural network Approach.* London: Springer-Verlag, 2001.

[3] L. Ljung, *System identification: theory for the user*. Upper Saddle River, NJ: Prentice Hall PTR, 1999.

[4] J. Mikleš and M. Fikar. *Process modelling, identification, and control*. Berlin: Springer-Verlag, 2007.

[5] B. Codrons, *Process modelling for control: a unified framework using standard black-box techniques*. London: Springer-Verlag, 2005.

[6] D. M. Himmelblau and J. B. Riggs, *Basic principles and calculations in chemical engineering*. Upper Saddle River, N.J.: Prentice Hall, 2004.

[7] K.C. Tan and Y. Li, "Grey-box model identification via evolutionary computing", *Control Engineering Practice*, vol. 10, pp. 673–684, 2002.

[8] Feedback Instruments, *Twin Rotor MIMO System 33-007-PCI*, Crowborough, 2013.

[9] M. Morari and E. Zafiriou. *Robust process control*. Englewood Cliffs, N.J.: Prentice Hall, 1989.

[10] R. S. Sánchez-Peña and M. Sznaier. *Robust systems theory and applications*. New York: Wiley, 1998.

[11] *Twin Rotor MIMO*. Feedback [online]. Available: http://www.feedback-instruments.com/products/education/control_instrumentation/twin_rotor_mimo.

[12] Feedback, *Twin Rotor Mimo System – Advanced Teaching Manual 1 – 33-007-4M5*.

[13] D. Rotondo, F. Nejjari and V. Puig, "Quasi-LPV modeling, identification and control of a twin rotor MIMO system", *Control Engineering Practice*, vol. 21, pp. 829–846, 2013.

[14] A. Rahideha, M.H. Shaheed and H. J.C. Huijberts, "Dynamic modelling of a TRMS using analytical and empirical approaches", *Control Engineering Practice*, vol. 16, pp. 241–259, 2008.

[15] P. Chalupa, J. Přikryl and J. Novák "Modelling of Twin Rotor MIMO System", *Procedia Engineering*, vol. 100, pp. 249–258, 2015.

[16] R. Matušů "Robust Stability Analysis of Discrete-Time Systems with Parametric Uncertainty: A Graphical Approach", *International Journal of Mathematical Models and Methods In Applied Sciences*, vol. 8, pp. 95-102, 2014.

[17] R. Matušů and R. Prokop. "Control of Interval Systems Using 2DOF Configuration", *Procedia Engineering*, vol. 100, pp. 340 – 344, 2015.

ISBN: 978-1-61804-321-4

Inverse pendulum and its stabilization possibilities

Zdeněk Úředníček

***Abstract*—**Article deals with mathematical and double physical pendulum physical models and its stabilization in inverse instable position possibilities. Whereas classical stabilization by proximal joint horizontal movement of inverse mathematical pendulum is well known and in article is just why is possible, the case of stabilization by proximal joint vertical oscillation comings-out from chaos theory and is referred in article by physical models and their behavior.

***Keywords*—** Mathematical pendulum, double physical pendulum, inverse position stabilization, physical models.

I. Introduction

Is generally known that nonlinear dynamic systems may have, in contrast to linear systems, several balance states (singular points) and behavior in their neighborhoods is able to distinguish. In this contribution we will show what the nonlinear system singular point typical characteristics are and how we can affect them. Second part is then oriented on chaos and bifurcations principles theory results utilization for such way stabilization of inverted pendulum, which although its application is known from fourteenth century, only chaos theory clarified it.

II. Mathematical Pendulum Stabilization by Proximal Coupling Horizontal Movement

Fig.1 shows mathematical pendulum basic type ordering connected by proximal kinematic rotating pair to the material cart with one freedom degree in global axis x direction.

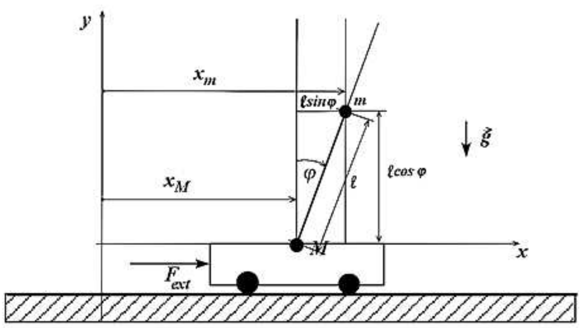

Fig.1 mathematic inverse pendulum ordering on material cart

Motional equations of this system are being:

Z. Úředníček (M’2012) is from Department of Automation and Control, Tomas Bata University in Zlin, Jižní Svahy, Nad Stráněmi 4511, 760 05, Zlin, Czech Republic. Email: urednicek@fai.utb.cz,
web: http://www.utb.cz/fai

$$\begin{aligned}(M+m)\cdot\ddot{x}_M + m\cdot\ell\cdot\cos\varphi\cdot\ddot{\varphi} &= F_{ext} + m\cdot\ell\cdot\sin\varphi\cdot\dot{\varphi}^2 \\ m\cdot\ell\cdot\cos\varphi\cdot\ddot{x}_M + m\cdot\ell^2\cdot\ddot{\varphi} &= m\cdot\ell\cdot g\cdot\sin\varphi\end{aligned} \quad (1)$$

For state vector

$$\underline{x}^T = [\dot{x}_M \quad \dot{\varphi} \quad x_M \quad \varphi]$$

the linearized system in the surrounding point of $\underline{x} = \underline{0}$ and for outgoing quantity $\boldsymbol{\varphi}$ is

$$\dot{\underline{x}} = \overbrace{\begin{bmatrix} 0 & 0 & 0 & -\frac{mg}{M} \\ 0 & 0 & 0 & \frac{M+m}{M\cdot\ell}g \\ 1 & 0 & 0 & 0 \\ 0 & 1 & 0 & 0 \end{bmatrix}}^{A} \cdot \begin{bmatrix} \dot{x}_M \\ \dot{\varphi} \\ x_M \\ \varphi \end{bmatrix} + \overbrace{\begin{bmatrix} \frac{1}{M} \\ -\frac{1}{M\cdot\ell} \\ 0 \\ 0 \end{bmatrix}}^{\underline{b}} \cdot F_{ext}(t); \quad (2)$$

$$\underline{y} = \overbrace{\begin{bmatrix} 0 & 0 & 0 & 1 \end{bmatrix}}^{\underline{c}^T} \cdot \begin{bmatrix} \dot{x}_M \\ \dot{\varphi} \\ x_M \\ \varphi \end{bmatrix}$$

As for controllability matrix $\mathbb{Q}$ is

$$\det\mathbb{Q} = -\frac{\omega_0^2}{M^4\cdot\ell^2} \neq 0$$

the system is for finite **M** controllable.
But as for observability matrix $\mathbb{N}$ is $\mathbf{det}\,\mathbb{N} = \mathbf{0}$, the system isn’t observable.
Matrix eigenvalues and eigenvectors of linearized system are

$$\lambda_1 = 0;\ \lambda_2 = 0;\ \lambda_3 = \sqrt{\frac{g\cdot(M+m)}{\ell\cdot M}};\ \lambda_4 = -\sqrt{\frac{g\cdot(M+m)}{\ell\cdot M}}$$

$$\underline{s}_{1,2} = \begin{bmatrix} 0 \\ 0 \\ 1 \\ 0 \end{bmatrix};\quad \underline{s}_3 = \begin{bmatrix} 1 \\ -\frac{M+m}{\ell\cdot m} \\ -\frac{1}{\sqrt{\frac{g\cdot(M+m)}{\ell\cdot M}}} \\ \frac{\sqrt{M(M+m)}}{m\cdot\sqrt{g\cdot\ell}} \end{bmatrix};\ \underline{s}_4 = \begin{bmatrix} 1 \\ -\frac{M+m}{\ell\cdot m} \\ \frac{1}{\sqrt{\frac{g\cdot(M+m)}{\ell\cdot M}}} \\ -\frac{\sqrt{M(M+m)}}{m\cdot\sqrt{g\cdot\ell}} \end{bmatrix} \quad (3)$$

Jordan’s canonical form of system is

$$\dot{x}_D(t)=\begin{bmatrix} -\sqrt{\frac{g(M+m)}{\ell\cdot M}} & 0 & 0 & 0 \\ 0 & \sqrt{\frac{g(M+m)}{\ell\cdot M}} & 0 & 0 \\ 0 & 0 & 0 & 1 \\ 0 & 0 & 0 & 0 \end{bmatrix}\cdot x_D(t)+\begin{bmatrix} \frac{m}{2M(M+m)} \\ \frac{m}{2M(M+m)} \\ -\frac{1}{(M+m)} \\ \frac{1}{(M+m)} \end{bmatrix}\cdot F_{ext}(t) \tag{4}$$

$$y=\begin{bmatrix} \frac{\sqrt{g\cdot M(M+m)}}{g\sqrt{\ell}\cdot m} & -\frac{\sqrt{g\cdot M(M+m)}}{g\sqrt{\ell}\cdot m} & 0 & 0 \end{bmatrix}\cdot x_D(t)$$

Corresponding block diagram is

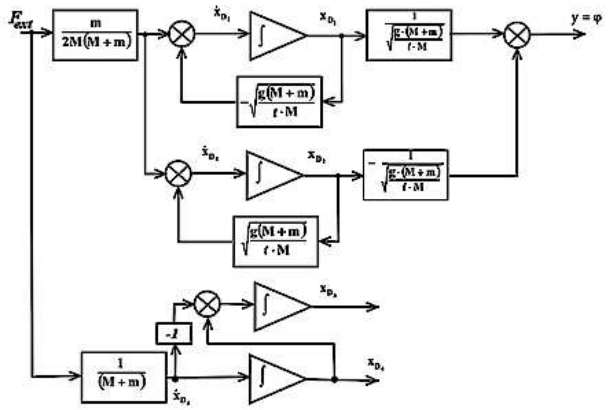

Fig.2 system diagram in Jordan's form

From diagram is see, why this system is controllable (all state quantities are influence able by input quantity $\mathbf{F_{ext}(t)}$). And also why isn't observable. Output, ergo φ, depends only on first two state quantities, so other two state quantities aren't „ seen“ in output.

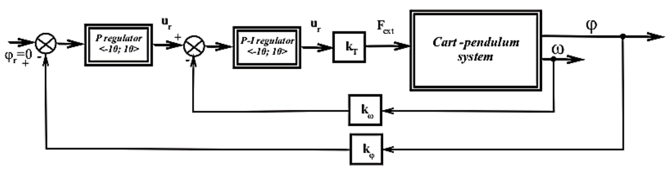

Fig.3 cascade controller diagram pendulum stabilization by force of cart movement

Fig. 3 shows diagram of hereof cart position control (mass M) and Fig. 4 shows its physical system multiport model including control law.

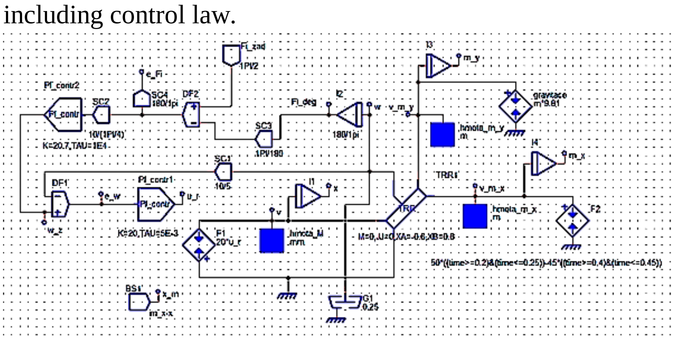

Fig.4 physical model of pendulum stabilization by means of cart movement set to the Dynast system

Fig.5 shows time dependencies of cart position, mathematical pendulum angle and its deviation from vertical position at response on outside perturbative force applied in axis **x** direction on mass **m**.

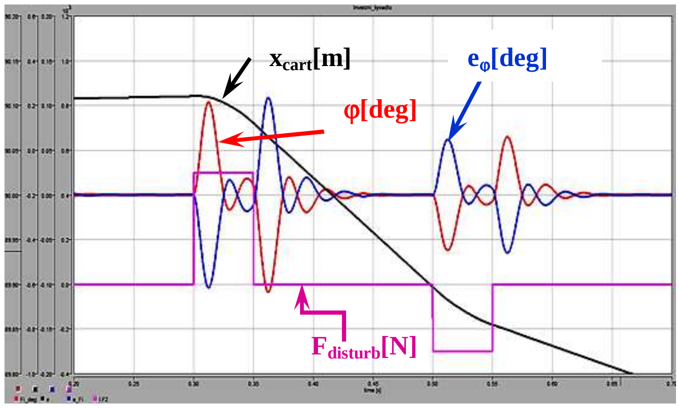

Fig.5 cart and pendulum behavior on outside perturbative force applied in direction **x** axis on mass **m**

III. Mathematical Pendulum Stabilization by Proximal Coupling Vertical Movement

Interesting and perhaps for many people surprising result will be further mentioned mathematical pendulum stabilization by proximal coupling vertical movement derived on chaos theory principle.

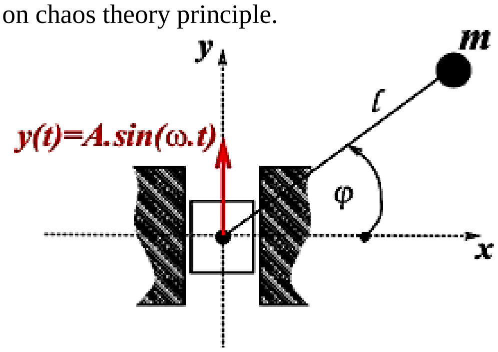

Fig.6 mathematical pendulum stabilization principle by proximal coupling vertical movement

System ordering is in Fig.6. Proximal joint of mathematical pendulum under consideration moves vertically harmoniously with certain amplitude and frequency.

Equation of motion describing existing motion is at proximal joint mentioned movement

$$m\cdot\ell^2\cdot\ddot{\varphi}=m\cdot\omega^2\cdot\ell\cdot A\cdot\sin(\omega\cdot t)\cdot\cos(\varphi)-m\cdot g\cdot\ell\cdot\cos(\varphi)\Rightarrow$$
$$\Rightarrow\ddot{\varphi}=\frac{\omega^2\cdot A}{\ell}\cdot\sin(\omega\cdot t)\cdot\cos(\varphi)-\frac{g}{\ell}\cdot\cos(\varphi)\Rightarrow \tag{5}$$
$$\Rightarrow\ddot{\varphi}=\left[\frac{\omega^2\cdot A}{\ell}\cdot\sin(\omega\cdot t)-\frac{g}{\ell}\right]\cdot\cos(\varphi)$$

So it's second - order nonlinear not-autonomous system with possible Ljapunov function

$$V(\varphi,\dot{\varphi})=\frac{1}{2}\dot{\varphi}^2(t)+\int_0^{\varphi}\left[\frac{g}{\ell}-\frac{\omega^2\cdot A}{\ell}\cdot\sin(\omega\cdot t)\right]\cdot\cos(\varphi)\cdot d\varphi=$$
$$=\frac{1}{2}\dot{\varphi}^2(t)+\left[\frac{g}{\ell}-\frac{\omega^2\cdot A}{\ell}\cdot\sin(\omega\cdot t)\right]\cdot\sin(\varphi) \tag{6}$$

ISBN: 978-1-61804-321-4

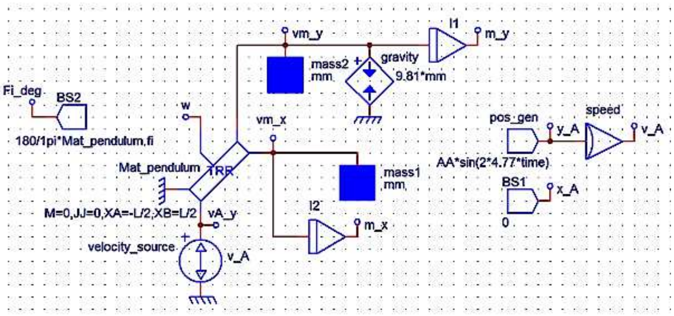

Fig.7 pendulum stabilization by means of proximal joint vertical movement physical model setting to the Dynast system

Fig.7 shows model setting to the physical simulation environment Dynast. Fig.8 shows mass at the end of immaterial arm behavior trajectory in 2D space at initial deviation about angle $\varphi(0) = -\pi/6$; $A = 0.42\mathrm{m}$; Proximal joint oscillation frequency in y axis direction is two time pendulum oscillation frequency.

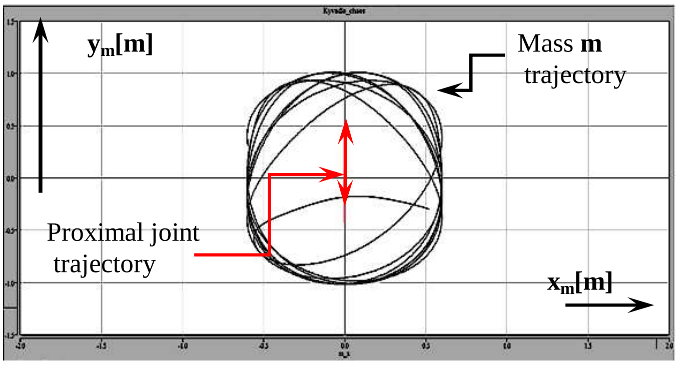

Fig.8 pendulum stabilization by means of proximal joint vertical movement physical model setting to the Dynast system

It's seen, that at sized oscillations amplitude A the pendulum begins be circulating around gripping axis.

At identical amplitude and specific frequency the arm oscillates around upper instable position according to Fig.9.

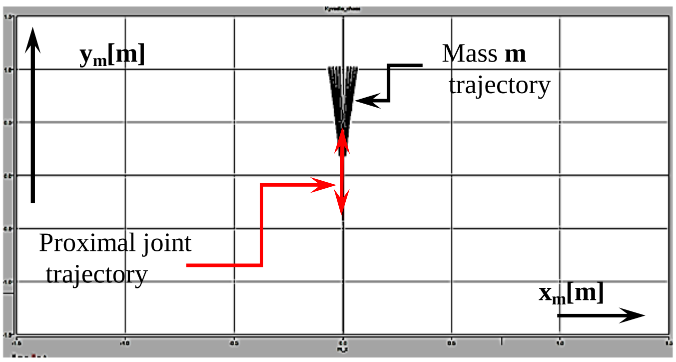

Fig.9 behavior trajectory of mass at the end of immaterial arm in 2D space at initial deviation about angle $\varphi(0) = \pi/2 - \pi/50$.

Detailed amplitude size and oscillation frequency reasoning and their computation already demonstrate Andrew Stephenson [1] in the year 1908.

IV. Double Physical Pendulum Stabilization by Proximal Coupling Vertical Movement

We introduce next possibility of two physical pendulums stabilization bonded by rotary kinematic pair partly with each other, partly to vertically moving proximal joint of the first of them- Fig . 10.

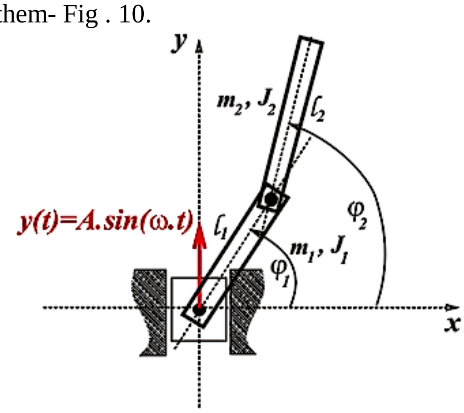

Fig.10 principle of double physical pendulums' stabilization by proximal coupling vertical movement

Already in the year 1738 Daniel Bernoulli shown, that telescopic pendulum (pendulum compound from **n** rigid articles) hung down is able to oscillate with any **n** natural frequencies, where with lowest frequency the pendulum articles swing more or less together, practically as if they form only one long pendulum and at highest frequency subsequently located pendulums oscillate in every instant in opposite directions.

On Fig.11 is setting of ordering from Fig. 10 to the Dynast simulation space.

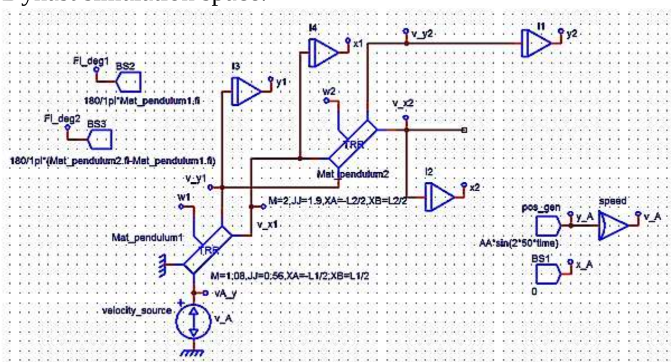

Fig.11 double physical pendulum stabilization by means of proximal joint vertical movement setting as physical model to the Dynast system

Fig.12 shows that both physical pendulums turn, at sufficient proximal join movement frequency, around 1^{st} and 2^{nd} joint against each other.

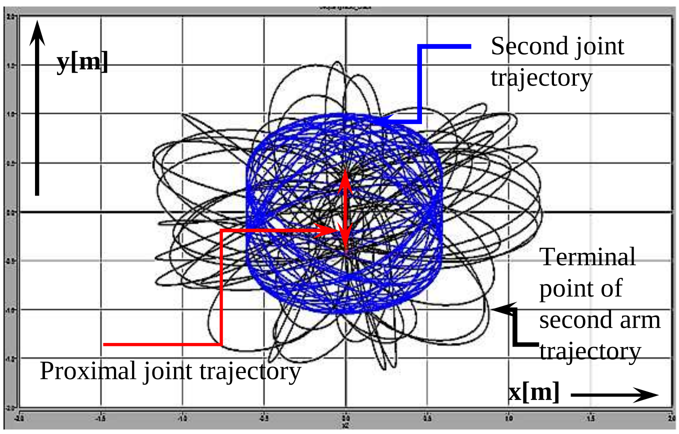

Fig.12 double physical pendulum behavior trajectory in 2D space at proximal joint high oscillation frequency

ISBN: 978-1-61804-321-4

At well select vertical oscillations' amplitude and frequency of the first joint it is possible to stabilize the both arms in inverted (upper) position -Fig. 13.

On Fig. 14 is practical experiment demonstration taken over from [8].

In fine we state, that mentioned problem is solvable also for continuously distributed mass. Mentioned problem is described in [6] and Fig.15 taken over [6] shows achieved experimental results.

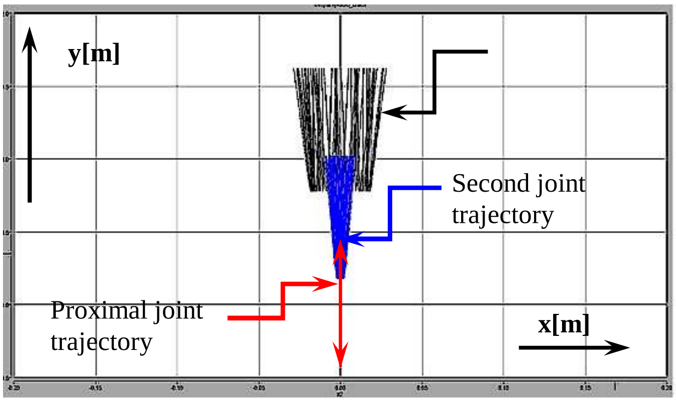

Fig.13 double physical pendulum behavior trajectory in 2D space at oscillation frequency and amplitude of proximal joint ensuring stabilization of both arms

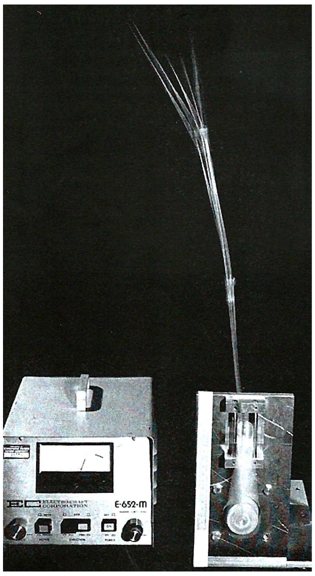

Fig.14 triple physical pendulum practical experiment at oscillation frequency and amplitude of proximal joint ensuring stabilization of arms

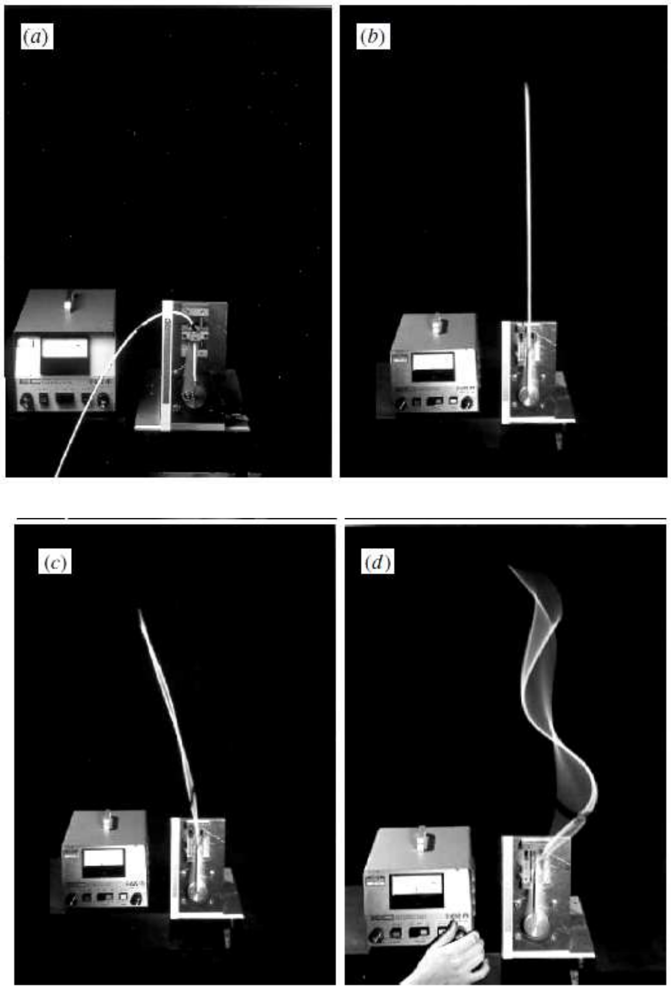

Fig.15 the experimental demonstration: (a) the sagging buckled wire; (b) the stabilized vertical wire; (c) leaning motion near the lower-frequency `falling-over' instability; and (d) motion near the higher-frequency dynamic instability.

Kindly note the [6] title: Indian trick with rope. Perhaps is concerned one of the most famous tricks in all of magic history: Rope ejected to the air doesn't fall down, but it will stay „stand still" in vertical position. The reference about this „trick" reaches until fourteenth century. And it is cross-eyed. Is it really cross - eyed?

V. Conclusion

Stated contribution shows mathematical and double physical inverse pendulum stabilization possibilities. In the first parts is described and simulated as physical model generally known inverse mathematical pendulum case stabilization by force of proximal joint horizontal movement, which is documented by cascade control of pendulum angular speed and position by means of cart with pendulum proximal joint.

In the second parts is stated mathematical, physical and double physical pendulum stabilization by vertical oscillations of proximal joint. Example is simulated by means of physical model in Dynast system and so forms suitable starting point to the next detailed analysis on chaos theory principle and its verification by simulation experiments.

ISBN: 978-1-61804-321-4

REFERENCES

[1] A. Stephenson, A, "On a new type of dynamical stability". *Mem. Proc. Manch. Lit. Phil. Soc*. 52 (8) 1908, 1-10.

[2] A. Stephenson, "On induced stability". *Phil. Mag. 15*, 1908, 233-236.

[3] D. J. Acheson, "A pendulum theorem". *Proc. R. Soc. Lond*. A443, 239-245.

[4] D. J. Acheson and T. Mullin, "Upside-down pendulums", Nature 366, 215-216 (18 November 1993).

[5] M. J., Clifford and S. R. Bishop, (2015, March 13). "Inverted oscilla-tions of a driven pendulum" [Online] Available: http://rspa.royalsocietypublishing.org/

[6] T. Mullin, A. Champneys, W.B. Fraser, J. Galan, and D.J. Acheson, (2015, March 13). „The `indian wire trick' via parametric excitation: a comparison between theory and experiment". [Online] Available: http://rspa.royalsocietypublishing.org/

[7] J-J.,E Slotine and W. Li, "Applied nonlinear control", 1991 by *Prentice-Hall, Inc*., A Division of Simon & Schuster, Englewood Cliffs, New Jersey 07632, ISBN 0-13-040890-5.

[8] D.J. Acheson, "1089 a další parádní čísla". *Dokořán, Praha 2006*, ISBN 80-7363-025-7. Original: D.J. Acheson, "1089 &all that: A journey into mathematics", *Oxford University Press* 2002.

[9] Sang-Yoon Kima, and Bambi Hub, (1998, Jun 6) "Bifurcations and Transitions to Chaos in An Inverted Pendulum", [Online] Available: http://arxiv.org/abs/chao-dyn/9802015

[10] Z. Úředníček, "Robotics" (in Czech), T. Bata unverzity in Zlin, Zlin 2012

[11] H.A. Darweesh, M. Roushdy , H. M. Ebied, and B.M. Elbagoury, "Design a cost effective non-holonomic vehicle for autonomous Driving applications". *Proceedings of the WSEAS International Conference Mathematical Applications in Science and Mechanics.* Dubrovnik, Croatia, June 25-27, 2013

[12] S. Hubalovsky, P. Kadlec, L. Mitrovic, and P. Hanzalova, "Computer simulation model of static mechanical properties of real technical device - elevator cab". *Proceedings of the 3rd International Conference on Mathematical Models for Engineering Science (MMES '12)*. Paris, France, December 2-4, 2012

Multilingual information retrieval: increasing the effectiveness of search by stemming

Said. Gadri, Abdelouahab. Moussaoui

Abstract— Stemming is a technique used to reduce inflected and derived words to their basic forms (stem or root). It is a very important step of pre-processing in text mining, and generally used in many areas of research such as: Natural language Processing NLP, Text Categorization TC, Text Summarizing TS, Information Retrieval IR, and other tasks in text mining. Stemming is useful in text categorization to reduce the size of terms vocabulary, and in information retrieval to improve the search effectiveness and then gives us relevant results.

In this paper, we propose a new multilingual stemmer based on the extraction of word root and in which we use the technique of n-grams. We validated our stemmer on three languages which are: Arabic, French and English.

Keywords— Root extraction; Stemming; Information retrieval; Bigrams technique; Text mining; Machine learning; Natural language processing.

I. Introduction

Text categorization process consists of assigning a set of texts to a set of predefined categories (classes/groups). For this purpose, we use many algorithms known in machine learning area such as: K-NN, SVM, RBF, NB, AdaBoost, ANN, Decision trees, etc. During the process of text categorization, the document must pass through a series of steps: removing punctuation and stop words which are considered irrelevant words, representing each document with a vector of terms, calculation of terms frequencies TF, and inverse document frequencies TF-IDF. One of the problems which we can meet is the big size of vectors used in the representation of documents, especially when we work on a big corpus of texts like “Reuters” which contains many thousands of documents with large sizes (dozens of pages). To solve such problem, several statistical methods are used to select some relevant terms in order to use them in the entry of learning algorithms. These methods allows us to reduce the dimension of the vector space representing the different documents in one hand, in the other hand, it permits to improve the quality of categorization process. Among these methods we can note: the mutual information MI, the information gain IG, and Khi2 law. Another method that seems very effective especially for Arabic text categorization is the selection of relevant terms by stemming.

Stemming is a technique in which we replace dozens of terms (words) which occur in different documents and semantically close by their basic forms (stems or roots) in order to reduce the dimension of terms vector and thus increase the quality of obtained categorization.

Several stemmers are developed for various languages as English, French, German and Arabic, but each one has its own advantages as well as limitations. Most of the stemming algorithms used in this field are language dependent [1]. So, it is important to develop a new stemmer which is language independent. In this way, we propose in our work a new multilingual stemmer based on the extraction of the word root, as well as the use of n-grams technique. The proposed stemmer was tested on three languages which are: Arabic, French, and English and gave promising results.

The paper is organized as follows: the first section presents some related works, so we review some papers that treat the problem of stemming and the used approaches. In the second section we introduce our new stemming algorithm. The third section presents the experiments that we have done to test our new stemmer and also presents the obtained results. In the last section we conclude our work by summarizing our realized work and giving some ideas to improve it in the future.

II. Related Work

Stemming algorithms can be classified in three groups: truncating methods, statistical methods, and mixed methods [2]. Each of these groups has a typical way of finding the stems of the word variants.

The first group is related to removing the affixes of a word. This was the first stemmer proposed by Lovins in 1968. It performs a lookup on a table of 294 endings, 29 conditions and 35 transformation rules [3]. The Lovins stemmer removes the longest suffix from a word. Once the ending is removed, the word is recoded using a different table that makes various adjustments to convert these stems into valid words. The advantages of this algorithm is it is very fast and can handle removal of double letters in words like ‘getting’ being transformed to ‘get’ and also handles many irregular plurals like – mouse and mice etc. Drawbacks of the Lovins approach are that it is time and data consuming. Furthermore, many suffixes are not available in the table of endings.

Porter stemming algorithm [4], [5] is until now one of the most popular stemming methods proposed in 1980. Many enhancements have been suggested on the basic algorithm. It is based on the idea that the suffixes in English are mostly made up of a combination of smaller and simpler suffixes. It has five steps, and within each step, many rules are applied until one of them passes the conditions. If a rule is accepted, the suffix is removed accordingly, and the next step is performed. The resultant stem at the end of the fifth step is returned. Porter designed a detailed framework of stemming

ISBN: 978-1-61804-321-4

which is known as ‘Snowball’ and that allow programmers to develop their own stemmers for different languages.

The Paice/Husk stemmer is an iterative algorithm with one table containing about 120 rules indexed by the last letter of a suffix [6]. On each iteration, it tries to find an applicable rule by the last character of the word. Each rule specifies either a deletion or replacement of an ending. If there is no such rule, it terminates. It also terminates if a word starts with a vowel and there are only two letters left or if a word starts with a consonant and there are only three characters left. Otherwise, the rule is applied and the process repeats. The advantage is its simple form, and every iteration taking care of both deletion and replacement as per the rule applied. The disadvantage is it is a very heavy algorithm and over stemming may occur.

Dawson Stemmer [7] This stemmer is an extension of the Lovins approach except that it covers a much more comprehensive list of about 1200 suffixes. Like Lovins it is too a single pass stemmer and hence is pretty fast. The suffixes are stored in the reversed order indexed by their length and last letter. In fact they are organized as a set of branched character trees for rapid access. The advantage is that it covers more suffixes than Lovins and is fast in execution. The disadvantage is it is very complex and lacks a standard reusable implementation.

The second group is called statistical methods, it contains stemmers which are based on statistical analysis and techniques. Most of the methods remove the affixes but after implementing some statistical procedure. In this group we can find the following stemmers:

N-Grams Stemmer [6], [8]: it is a language independent stemmer in which a string-similarity approach is used to convert word inflation to its stem. An n-gram is a set of n consecutive characters extracted from a word. The main idea behind this approach is that, similar words will have a high proportion of n-grams in common. For n equals to 2, the words extracted are called digrams. For example, the word ‘introductions’ results in the generation of the digrams: *i, in, nt, tr, ro, od, du, uc, ct, ti, io, on, ns, s* Where '*' denotes a padding space. Generally a value of 4 or 5 is selected for n. After that a document is analyzed for all the n-grams. This stemmer has an advantage that it is language independent and hence very useful in many applications. The disadvantage is it requires a significant amount of memory and storage for creating and storing the n-grams.

HMM Stemmer This stemmer was proposed by Melucci and Orio [9] and based on the concept of the Hidden Markov Model (HMMs) which are finite-state automata. At each transition, the new state emits a symbol with a given probability. This method does not need a prior linguistic knowledge of the dataset, and the probability of each path can be computed and the most probable path is found using the Viterbi coding in the automata graph.

The third group is called the mixed methods which contain:

The Inflectional and Derivational Methods: it involves both the inflectional and the derivational morphology analysis. The corpus should be very large to develop these types of stemmers and hence they are part of corpus base stemmers too. In case of inflectional, the word variants are related to the language specific syntactic variations like plural, gender, case, etc. Whereas, in derivational the word variants are related to the part-of-speech (POS) of a sentence where the word occurs.

Krovetz Stemmer (KSTEM): it was presented in 1993 by Robert Krovetz [10] and is a linguistic lexical validation stemmer. Since it is based on the inflectional property of words and the language syntax, it is very complicated in nature. It effectively removes inflectional suffixes in three steps. Since this stemmer does not find the stems for all word variants, it can be used as a pre-stemmer before applying a stemming algorithm. This would increase the speed and effectiveness of the main stemmer. This stemmer does not consistently produce a good recall and precision performance.

Xerox Inflectional and Derivational Analyzer The linguistics groups at Xerox have developed a lexical database for English and some other languages also which can analyze and generate inflectional and derivational morphology. The inflectional database reduces each surface word to the form which can be found in the dictionary, as follows [11]: nouns singular (e.g. children child), verbs infinitive (e.g. understood understand), etc. The derivational database reduces surface forms to stems which are related to the original in both form and semantics. The advantages of this stemmer are that it works well with a large document also and removes the prefixes also where ever applicable. All stems are valid words since a lexical database which provides a morphological analysis of any word in the lexicon is available for stemming. The disadvantage is that the output depends on the lexical database which may not be exhaustive. Since this method is based on a lexicon, it cannot correctly stem words which are not part of the lexicon. This stemmer has not been implemented successfully on many other languages.

Corpus Based Stemmer This method of stemming was proposed by Xu and Croft [8]. They have suggested an approach which tries to overcome some of the drawbacks of Porter stemmer. Corpus based stemming refers to automatic modification of conflation classes – words that have resulted in a common stem, to suit the characteristics of a given text corpus using statistical methods. The basic hypothesis is that word forms that should be conflated for a given corpus will co-occur in documents from that corpus. Using this concept some of the over stemming or under stemming drawbacks are resolved e.g. The way this stemmer works is to first use the Porter stemmer to identify the stems of conflated words and then the next step is to use the corpus statistics to redefine the conflation. The advantage of this method is it can potentially avoid making conflations that are not appropriate for a given corpus and the result is an actual word and not an incomplete stem. The disadvantage is that you need to develop the statistical measure for every corpus separately and the processing time increases as in the first step, and stemming algorithms are first used before using this method.

Context Sensitive Stemmer is done using statistical modeling on the query side. This method was proposed by Funchun Peng et. al [12]. Basically for the words of the input query, the morphological variants which would be useful for the search are predicted before the query is submitted to the search engine. This dramatically reduces the number of bad expansions, which in turn reduces the cost of additional computation and improves the precision at the same time. After the predicted word variants from the query have been derived, a context sensitive document matching is done for these variants. The advantage of this stemmer is it improves

ISBN: 978-1-61804-321-4

selective word expansion on the query side and conservative word occurrence matching on the document side. The disadvantage is the processing time and the complex nature of the stemmer. There can be errors in finding the noun phrases in the query and the proximity words.

Many Stemming algorithms have been developed for a wide range of languages including English [13], Latin [11], Swedish [14], German and Italian [15], French [16], Turkish [17], Chinese [18]. For Arabic Language, there are three different Stemming approaches: the root-based approach [19]-[24]; the light stemmer approach [25]-[29]; and the statistical stemmer approach (N-Grams) [30]-[32]. Yet no a complete stemmer for this language is available.

III. THE PROPOSED STEMMER

In our work, we proposed a new multilingual stemmer, in which we use also the n-grams technique to extract the root of a word belonging to one of the following languages: Arabic, French, and English. For this purpose, we proceed according to the following steps:

Step 1: we segment the word for which we want to find the root, and all the roots of the predefined list into bigrams (2-grams).

For example if we have the words: “يذهبون” in Arabic, “calculateur” in French, and “bellicism” in English, and the three lists of roots in the above languages as follows: (فتح ، خرج ، ذهب ، وهب), (assist, calcul, compt, conclu), (sciss, bell, dict, tele), we proceed the segmentation step as indicated in the following table:

TABLE I. AN EXAMPLE DESCRIBING THE SEGMENTATION STEP (STEP1)

Language	Word (W)/Bigrams	List of roots (Ri)/Bigrams
Arabic	يذهبون يذ ، ذه ، هب ، بو ، ون	R_1 = “فتح” ➔ (فت ، تح) R_2 = “خرج” ➔ (خر ، رج) R_3 = “ذهب” ➔ (ذه ، هب) R_4 = “وهب” ➔ (وه ، هب)
French	calculateur ca al lc cu ul la at te eu ur	R_1 = “assist” ➔ (as, ss, si, is, st) R_2 = “calcul” ➔ (ca, al, lc, cu, ul) R_3 = “compt” ➔ (co, om, mp, pt) R_4 = “conclu” ➔ (co, on, nc, cl, lu)
English	bellicism be el ll li ic ci is sm	R_1 = “sciss” ➔ (sc, ci, is, ss) R_2 = “bell” ➔ (be, el, ll) R_3 = “dict” ➔ (di, ic, ct) R_4 = “tele” ➔ (te, el, le)

Step 2: we calculate for each word the following parameters:

N_w : The number of bigrams in the word W

N_{R_i} : The number of bigrams in the root R_i

N_{wR_i} : The number of common bigrams between the word W and the root R_i

$N_{w\bar{R}_i}$: The number of bigrams belonging to the word W and do not belong to the root R_i ($N_{w\bar{R}_i} = N_w - N_{wR_i}$)

$N_{R_i\bar{W}}$: The number of bigrams belonging to the root R_i and do not belong to the word W ($N_{R_i\bar{W}} = N_{R_i} - N_{wR_i}$)

For the previous example we have:

TABLE II. CALCULATION OF WORD PARAMETERS (STEP 2)

Word (W)	N_w	Associated roots R_i	N_{R_i}	N_{wR_i}	$N_{w\bar{R}_i}$	$N_{R_i\bar{W}}$
يذهبون	05	R_1 = “فتح”, R_2 = “خرج” R_3 = “ذهب”, R_4 = “وهب”	2, 2 2, 2	0, 0 2, 1	5, 5 3, 4	2, 2 0, 1
calculateur	10	R_1 = “assist, R_2 = “calcul” R_3 =“compt”,R_4= conclu”	5, 5 4, 5	0, 5 0, 0	10, 5 10, 10	5, 0 4, 5
bellicism	08	R_1 = “sciss, R_2 = “bell” R_3 = “dict”, R_4 = “tele”	4, 3 3, 3	2, 3 1, 1	7, 6 8, 8	2, 0 2, 2

Step3: we take only the roots having at least one common bigram with the word W ($N_{wR_i} \geq 1$) as candidate roots among the list of all roots in order to reduce the calculation time. In our previous example, we have:

TABLE III. SELECTION OF CANDIDATE ROOTS (STEP 3)

Word (W)	N_w	Associated roots R_i	N_{R_i}	N_{wR_i}	$N_{w\bar{R}_i}$	$N_{R_i\bar{W}}$
يذهبون	05	R_3 = “ذهب”, R_4 = “وهب”	2, 2	2, 1	3, 4	0, 1
calculateur	10	R_2 = “calcul”	5	5	5	0
bellicism	08	R_1 = “sciss, R_2 = “bell” R_3 = “dict”, R_4 = “tele”	4, 3 3, 3	2, 3 1, 1	7, 6 8, 8	2, 0 2, 2

Step4: we calculate the distance $D(W, R_i)$ between the word W and each candidate root R_i according to the equation:

$$D(W, R_i) = (N_{w\bar{R}_i} + N_{R_i\bar{w}})/(N_w + N_{R_i}) \tag{1}$$

For the previous example we obtain:

TABLE IV. SELECTION OF CANDIDATE ROOTS (STEP 3)

Word(W)	N_w	Associated roots R_i	N_{R_i}	N_{wR_i}	$N_{w\bar{R}_i}$	$N_{R_i\bar{W}}$	Distance Value $D(W,R_i)$
يذهبون	05	R_3 = “ذهب”, R_4 = “وهب”	2, 2	2, 1	3, 4	0, 1	0.4285, 0.7142
calculateur	10	R_2 = “calcul”	5	5	5	0	0.3333
bellicism	08	R_1 = “sciss, R_2 = “bell” R_3 = “dict”, R_4 = “tele”	4, 3 3, 3	2, 3 1, 1	7, 6 8, 8	2, 0 2, 2	0.6923, 0.5

Step5: in the last step, we assign the root that has the lowest value of distance $D(W, Ri)$ among the candidate roots to the word W. it is the required root.

In our example, the roots of the given words are:

TABLE V. EXTRACTION OF THE WORD ROOT (STEP 5)

Word *(W)*	Extracted root *(R)*	Effective root
يذهبون	ذهب	ذهب
calculateur	calcul	calcul
bellicism	bell	bell

Finally, we note that our new algorithm has the following advantages:

1. It is language independent that means it is applicative for any language (a multilingual root based stemmer).
2. Does not require the removal of affixes, whose distinction from the native letters of the word is quite difficult.
3. Works for any word whatever the type of the root. (e.g., trilateral roots, quadrilateral, quinquelateral, and hexalateral roots in Arabic).
4. Valid for strong roots and vocalic roots, which pose generally problems in Arabic during their derivation, because the complete change of their forms.
5. Does not use any morphological rule nor grammatical patterns but only simple calculations of distances.
6. Very practical stemmer and easy to implement on machine.

IV. EXPERIMENTATION AND OBTAINED RESULTS

To validate our proposed stemmer, we have used for each language three corpus which can be classified according to their sizes into: small corpus, middle corpus, and large corpus. Each one is constituted of many files as indicated below:

1. The file of derived forms (gross words) which contains morphological forms of words derived from many roots.
2. The file of roots which contains many roots, we note that for Arabic language, these roots are trilateral, quadrilateral, quinquelateral, and hexalateral. We note also that many of them are vocalic roots which contain at least one vowel.
3. The file of golden roots which contain the correct roots of all words present in each corpus (the file in (1)), this golden list was prepared by an expert linguist and used as reference list, i.e., by comparison between the list of obtained roots (extracted by the system) and the reference list (established by the expert), we can calculate the roots extraction accuracy (success ratio).

TABLE VI. DATA SET USED IN EXPERIMENTATION

Corpus	Language	Size of the derived words file	Size of the roots file	Size of the golden roots file
Small corpus	Arabic	50	25	50
	French	44	36	44
	English	92	56	92
Middle corpus	Arabic	270	140	270
	French	180	220	180
	English	346	165	346
Large corpus	Arabic	1200	550	1200
	French	1000	585	1000
	English	1000	545	1000

TABLE VII. EXAMPLES OF MORPHOLOGICAL FORMS (GROSS WORDS)

Arabic		French		English	
مأخذ	أمرهم	apprentissage	commandement	bicycle	equilateral
مؤاخذة	يأتمرون	assemblage	communication	transactions	equidistant
مؤاخذون	باحث	assistance	communicant	scissors	extract
مؤاخذات	بحوث	assistante	comparaison	geography	extraordinary
مؤازرة	أبحاث	association	compréhension	geostrategy	extraterrestrial
مؤامرة	جموع	calculatrice	concepteur	hydraulic	intrapersonal

TABLE VIII. EXAMPLES OF ARABIC ROOTS (TRILATERAL, QUADRILATERAL, QUINQUELATERAL, HEXALATERAL)

Trilateral roots	Quadrilateral roots	Quinquelateral roots	Hexalateral roots
زرع	أكرم	انطلق	استعمل
صنع	أعان	انكسر	استحسن
جمع	حطّم	اقتصد	اخشوشن
أبى	علّم	اجتمع	اعشوشب
سعل	طمأن	تنازل	اقشعرّ
صدع	زلزل	تدحرج	اطمأنّ

TABLE IX. EXAMPLES OF FRENCH AND ENGLISH ROOTS.

French		English	
apprend	command	cycle	omni
assist	conclu	action	tele
associ	comprend	geo	equi
assur	confirm	aqua	therm
autoris	concev	graph	extra
calcul	connaît	hydra	bio
compt	construi	path	cardio
chang	invest	man	intra

TABLE X. EXAMPLES OF OBTAINED RESULTS WHEN SEGMENTING WORDS AND ROOTS INTO BI-GRAMS

Word(W)	N-grams	Nb.Ng (N_w)	Root	N-grams	Nb.Ng (N_{R_i})
يتعلّمون	يت تع عل لّ ّم مو ون	7	علّم	عل لّ ّم	3
اقتصاد	اق قت تص صا اد	5	اقتصد	اق قت تص صد	4
سنستدرجهم	سن نس ست تد در رج جه هم	8	درج	در رج	2
apprentissage	ap pp pr re en nt ti is ss sa ag ge	12	apprend	ap pp pr re en nd	6
calculatrice	ca al lc cu ul la at tr ri ic ce	11	calcul	ca al lc cu ul	5
connaissance	co on nn na ai is ss sa an nc ce	11	connaît	co on nn na aî ît	6
bicycle	bi ic cy yc cl le	6	cycle	cy yc cl le	4
transactions	tr ra an ns sa ac ct ti io on ns	9	action	ac ct ti io on	5
geopolitics	ge eo op po ol li it ti ic cs	10	geo	ge eo	2

TABLE XI. EXTRACTION OF SOME WORDS ROOTS USING THE NEW STEMMER.

Word (W)	Nearest Roots R_i	Nb.Common Bigrams (N_{wR_i})	Distance Values $D(W, R_i)$	Extracted Root	Correct Root
Arabic					
يتعلمون	كّلم ، علم ، علم ، علج	1 ، 1 ، 3 ، 2	0.77 , 0.77 , **0.4**, 0.6	علم	علم
سنستدرجهم	درج	2	**0.6**	درج	درج
French					
Apprentissage	Apprend, assembl, assist, associ, assur, autoris, comprend	4, 1, 2, 1, 2, 1, 2	**0.55**, 0.9, 0.78, 0.89, 0.77, 0.9, 0.78	apprend	apprend
connaissance	avanc, command, commenc, concev, conclu, connaît	3, 2, 3, 4, 3, 4	0.64, 0.78, 0.68, **0.57**, 0.66, 0.57	concev	connaît
English					
transactions	action, extra, intra, dict	5, 2, 2, 1	**0.28**, 0.69, , 0.69, 0.83	action	action
geopolitics	Action, geo, poly	1, 2, 2	0.86, **0.66**, 0.69	geo	geo

ISBN: 978-1-61804-321-4

TABLE XII. OBTAINED RESULTS WHEN EXTRACTING THE WORDS ROOTS

Corpus	Language	Nb.Roots	Nb.Words	Correct Results	Wrong Results	Succes_Rate (%)	Error_Rate (%)
Small	Arabic	25	50	47	03	94,00	06,00
	French	36	44	41	03	93,18	06,82
	English	56	92	85	07	92,39	07,61
Middle	Arabic	140	270	198	72	73,33	26,67
	French	220	180	152	28	84,44	15,56
	English	165	346	309	37	89,30	10,70
Large	Arabic	550	1200	812	388	67,66	32,34
	French	585	1000	762	238	76,20	23,80
	English	545	1000	865	135	86,50	13,50

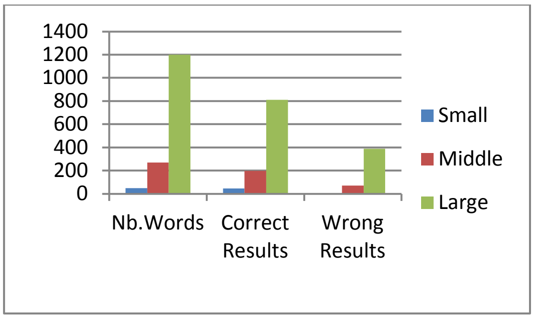

Fig. 1. Correct and wrong results in number of words (Arabic)

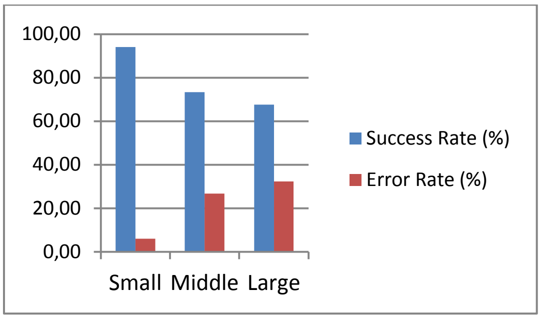

Fig. 2. Calculation of success rate and error rate (Arabic)

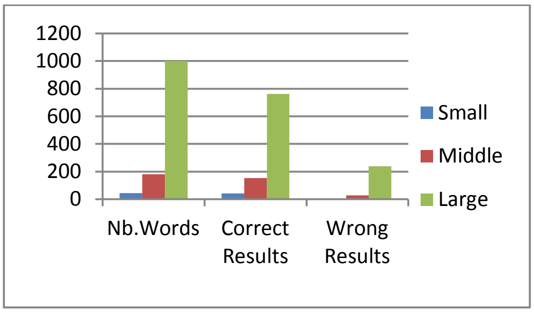

Fig. 3. Correct and wrong results in number of words (French)

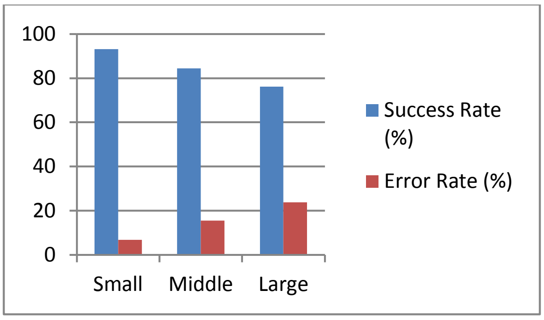

Fig. 4. Calculation of success rate and error rate (French)

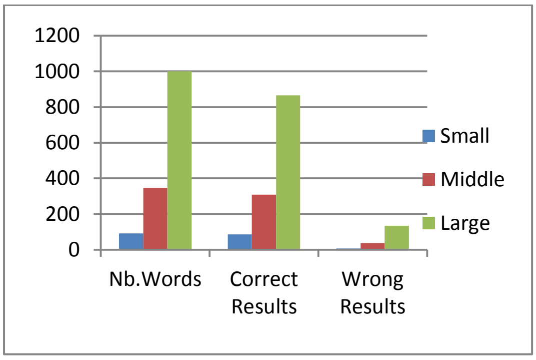

Fig. 5. Correct and wrong results in number of words (English)

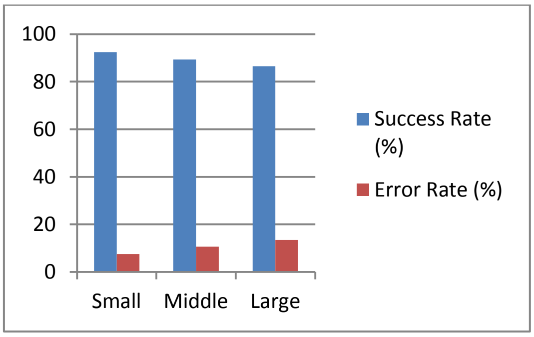

Fig. 6. Calculation of success rate and error rate (English)

V. DISCUSSION

Firstly, it is important to note that it was more beneficial to compare our multilingual stemmer with other existing ones, unfortunately this is not possible, because all existing stemmers are monolingual, i.e., for each language there is a collection of stemmers with varying performances. That leaving to say, that the main advantage of our proposed stemmer is that it's general and independent of any language (Multi-lingual).

ISBN: 978-1-61804-321-4

We can also see on table 8, that the quality of stemming decreases each time the words base increases, this due to the fact that the increase of the words base must be accompanied by the enrichment of the roots base also (the reference file of roots), if no, new words don't find their roots in the reference file.

Another thing very important and needs to be reported here, that is the rate of stemming for Arabic is still low compared to French and English ones, this is influenced by the used segmentation method based on bigrams. In this method, each bigram is formed of two letters which are mandatory successive (the letter and its successor). This doesn't pose any problem for French and English where the root of a word consists of a sequence of successive letters extracted from the word itself. E.g., for French we can find couples (word, root) as follows: (Assistant , assist), and similarly for English (transaction, trans). which is not always possible for Arabic in which the root may consist of a sequence of letters that can not necessarily be consecutive, or the number of common n-grams between the word and the candidate root decreases as well the calculated distance between them, and therefore there will be a divergence between the word and its candidate roots, for example:

reference file of roots), if no, new words don't find their roots in the reference file.

(كتاتيب, كتب)-(علماء, علم).

For this purpose, and to improve the rate stemming for Arabic, we propose another method to form bigrams of words and candidates roots by taking all possible combinations of letters not only the two successive letters:

(e.g., علماء ➔ عل، عم، عا، عء، لم، لا، لء، ما، مء، اء).

VI. Comparison with Other Stemmers

Stemmer	**Type/Used approach**	**Advantages**	**Disadvantages**
Lovins stemmer	Truncating method Affixes removal (Rule-based stemmer)	-Fast stemmer - Simple pass - Removal of double letters in words - Handles many irregular plural words	- Time consuming - Frequently fails to form words from stems - Depends on the used vocabulary
Porter stemmer	Truncating method Affixes removal (Rule-based stemmer)	-Produces best results of stemming - Less error rate - It's a light stemmer - The snowball stemmer framework is a language independent	- Generated stems arn't always the real words. -Works on several steps.. - Time consuming.
Paice/Husk stemmer	Truncating method Affixes removal (Rule-based stemmer)	- Simple stemmer - Each iteration takes care of deletion and replacement	- Heavy algorithm - Over stemming may occur
Dawson stemmer	Truncating method Affixes removal (Rule-based stemmer)	-Covers more suffixes (1200) -Fast in execution.	- Very complex - Lacks a standard implementation
Krovetz stemmer	Inflectional & derivational method	- It's a light stemmer. - Can be used as pre-stemmer for other stemmers.	-Not efficient for large documents -Enable to cope with words outside the lexicon -doesn't produce good results.
Youssef N et al stemmer (Arabic)	Statistical method (N-grams approach)	- Based on bigrams and string comparison - doesn't require morphological rules - Language independent	- Space consuming -Time consuming. -Based on a reference base of roots.
Our proposed stemmer	Statistical method (An improved n-grams approach)	- Multilingual stemmer. -Based on an improved n-grams approach and string comparison - doesn't require morphological rules - Language independent - For Arabic, it works for any word whatever the type of the root. (3, 4, 5, 6-lateral roots). - Valid for strong roots and vocalic roots, which pose problems in Arabic during their derivation, - Very practical and easy to implement on machine. - It can be applied as lemmatizor.	-Time consuming for big corpus. -Based on a reference base of roots.

ISBN: 978-1-61804-321-4

VII. Conclusion and Perspectives

In this paper we have studied the problem of stemming and its positive influence on text categorization, information retrieval, and other areas of natural language processing and text mining especially for the reduce of terms vocabulary (text categorization), and the increase of the effectiveness in search engines (information retrieval). We exposed the most known approaches and techniques in the field, notably: truncating methods, statistical methods, and mixed methods. For each one, we gave their advantages and their weaknesses.

In the light of the studied approaches, we proposed a new stemmer, which is multilingual and so it is language independent, based on the technique of n-grams and thus it belongs to the statistical approach, and does not require prior linguistic knowledge.

Our multilingual stemmer is able to find all the types of roots, especially for Arabic, which is a very rich language, having a difficult structure and a complex morphology. The obtained success rates of the root extraction for the previous three languages are very promising and can be improved in future works.

References

[1] M.Hadni, S.A.Ouatik and A.Lachkar.2013. Effective arabic stemmer based hybrid approach for arabic text categorization. International Journal of Data Mining & Knowledge Management Process (IJDKP) . 3, 4 (July 2013), DOI : 10.5121/ijdkp.2013.3401

[2] A. Jivani. 2011.A Comparative Study of Stemming Algorithms, Int. J. Comp. Tech. Appl IJCTA. 2, 6, 1930-1938, NOV-DEC 2011, ISSN:2229-6093

[3] J. B. Lovins. 1968. Development of a stemming algorithm, Mechan.Trans.& Comp.Ling.11, 1/2, 22-31, (1968).

[4] M.F. Porter.1980. An algorithm for suffix stripping. Program. 1980; 14, 130-137.

[5] M.F. Porter: Snowball. 2001. A language for stem.Algo.

[6] P.D.Chris.1990. Another stemmer. ACM SIGIR,24,3, 56-61

[7] J. Dawson. 1974. Suffix removal and word conflation. Bul.of.Assoc.for Liter&Ling.Comp. 2, 3, 33–47 (1974)

[8] Xu Jinxi and Croft Bruce W. 1998. Corpus-based stemming using co-occurrence of word variants. ACM Transactions on Information Systems. 16, 1, 61-81.

[9] Melucci Massimo and Orio Nicola. 2003. A novel method for stemmer generation based on hidden Markov models. In Proceedings of the twelfth international conference on Information and knowledge management, 131-138.

[10] Krovetz Robert. 1993. Viewing morphology as an inference process. In Proceedings of the 16th annual international ACM SIGIR conference on Research and development in information retrieval. 1993, 191-202.

[11] Hull D. A. and Grefenstette,. A detailed analysis of English Stemming Algorithms, XEROX Technical Report on http://www.xrce.xerox.

[12] Funchun Peng, Nawaaz Ahmed, Xin Li and Yumao Lu. 2007. Context sensitive stemming for web search. In Proceedings of the 30th annual international ACM SIGIR conference on Research and development in IR, 639-646.

[13] Greengrass, M., Robertson, A. M., Robyn, S., and Willett, P. 1996. In Processing morphological variants in searches of Latin text. Information research news. 6, 4, 2-5

[14] Carlberger, J., Dalianis, H., Hassel, M., and Knutsson, O. 2001.Improving precision in information retrieval for Swedish using stemming. In Proceedings of NODALIDA '01 - 13th Nordic conference on computational linguistics. Uppsala, Sweden.

[15] Monz, C. and de Rijke, M. 2001. morphological analysis in monolingual information retrieval for German and Italian. In Cross-language information retrieval and evaluation: in Proceedings of the CLEF 2001 workshop, C. Peters, Ed.: Springer Verlag, (2001).

[16] Moulinier, I., McCulloh, A., and Lund, E. West group at CLEF 2000: Non-English monolingual retrieval. In Crosslanguage information retrieval and evaluation: Proceedings of the CLEF 2000 workshop, C. Peters, Ed.: Springer Verlag, 176-187, (2001).

[17] Ekmekcioglu, F. C., Lynch, M. F., and Willett, P. 1996. Stemming and N-Gram matching for term conflation in Turkish texts. Information Research News, 7, 1, 2-6.

[18] A.-H.Tan and P.Yu. 2000. A Comparative Study on Chinese Text Categorization Methods, Workshop on Text&WebMining, Melbourne,pp.24-35, (2000).

[19] Khoja S. 1999. Stemming Arabic Text. Lancaster, U.K., Computing Department, Lancaster University. 1999.

[20] Al-Fedaghi S. and F. Al-Anzi. 1989. A new algorithm to generate Arabic root-pattern forms. In proceedings of the 11th national Computer Conference and Exhibition, 391-400.

[21] Larkey L. and M. E. Connell. 2001. Arabic information retrieval at UMass in TREC-10. In Proceedings of TREC 2001, Gaithersburg: NIST. (2001).

[22] Fatma Abu Hawas1 and Keith E. Emmert. 2014. Rule-based Approach for Arabic Root Extraction, New Rules to Directly Extract Roots of Arabic Words Journal of Computing and Information Technology - CIT 22, 1 (2014), 57–68, doi:10.2498/cit.1002174

[23] M.Momani. and J.Faraj, "A novel algorithm to extract tri-literal Arabic roots," in International Conference on Computer Systems and Applications.IEEE Xplore Press, 2009, pp. 309–315.

[24] M.Y.Al-Nashashibi, D.Neagu, and A.A.Yaghi, "An improved root Extraction technique for arabic words," in Proceeding of 2nd International Conference on Computer Technology and Development (ICCTD). IEEE Xplore Press, 2010, pp. 264–269.

[25] Al-omari, A., Abuata, B., Al-kabi, M. 2013. Building and Benchmarking New Heavy/Light Arabic Stemmer. The 4th International conference on Information and Communication systems (ICICS'13), (2013).

[26] Al-shalabi, R., Kanaan, G., Al-Serhan, H. 2003. New Approach for Extracting Arabic Roots. Proceedings of the International ArabConference on Information Technology (ACIT'2003), Alexandria, Egypt, 42–59. (2003).

[27] M.Y.Al-Nashashibi, D.Neagu, and A.Y.Ali, "Stemming techniques For arabic words: A comparative study," in 2nd International Conference on Computer Technology and development (lCCTD 2010), 2010.

[28] G.Kanaan, R.Al-Shalabi, and M.Al-Kabi, "New approach for Extracting quadrilateral arabic roots," Basic Science and Engineering, vol. 14, pp. 51–66, 2005.

[29] A.Mohamad, R.Al-Shalabi, G.Kanaan, and A.Al-Nobani, "Building An effective rule-based light stemmer for arabic language to improve search effectiveness," The International Arab Journal of Information Technology, vol. 9, 2010.

[30] S.H.Mustafa and Q.A.Al-Radaideh, "Using n-grams for arabic text searching," Journal of the American Society for Information Science and Technology, vol. 55, p. 10021007, 2004.

[31] Hmeidi, I.I., Al-Shalabi, R., Al-Taani, A.T., Najadat, H., and Al-Hazaimeh, S.A. 2010. A novel approach to the extraction of roots from Arabic words using bigrams. J. Am. Soc. Inform. Sci. Technol., 61, 583-591. DOI: 10.1002/asi.21247 .(2010)

[32] Yousef, N., Aymen, A.E., Ashraf, O., Hayel, K.. 2014. An Improved Arabic Word's Roots Extraction Method Using N-gram Technique, Journal of Computer science JSC. (2014) DOI:10.3844/jcssp.2014.716.719, Vol. 10, No. 4,

Modeling and simulation of collagen protein hydrolysis reactor

Hana Vašková, Karel Kolomazník and Radek Matušů

Abstract—Hydrolysis processes offer a reasonable and environment-friendly solution for the processing of certain part of wastes arising from the leather industry. Collagen protein contained in e.g. leather shavings can be further effectively utilized. This paper deals with the mathematical-physical model for alkaline hydrolysis of shavings. The description of the hydrolysis process is based on the linearized state model. The model is based on the mass balance of the input substances and the resulting hydrolysate protein, moreover on an enthalpy balance for the reaction mixture and saturated steam serving in reactor as the heat transfer medium. The simulations of the protein hydrolysis process model are performed in Matlab Simulink.

Keywords—Collagen protein, chromium, hydrolysis, leather waste processing, mathematical modeling.

I. Introduction

ENVIRONMENTAL protection is one of the global challenges attracting lot of attention in recent years. People realize the status quo is not sustainable and it is a necessary to change the approach to a wide range of activities. One of these activities is waste reduction and waste treatment. Ideal is using safe, environmentally and economically favourable ways. However, their implementation is not usually straightforward.

A significant share of waste arises from manufacturing sector. In this paper it is dealt with an area of leather industry. Leather products like footwear, clothing, handbags, wallets, fashion accessories, upholstery, etc. are among the objects of our everyday needs. Achieving the final products comprise a lot of waste arising from the raw material processing and creating specific items. Only in tanneries million tons of waste is generated annually.

The selected leather wastes, such as shavings, can be processed by hydrolytic reaction in alkaline or acidic medium. In these cases the protein is liquified and after further treatment can be applied in forms of gelatin or protein hydrolyzates in e.g. pharmaceutical, food industry or in agriculture.

The literature search shows the automatic control in leather/hide processing respectively leather waste processing is not very widespread. Rather the automated and robotic devices are implemented within the secondary manufacturing. These sectors include especially footwear industry, which process over the half of the produced leather, textile industry and extensive use is also for upholstery and automotive industry

The level of measurement and control systems applications is low apart from others due to the lack of quantitative models allowing the use of some modern control methods. However, in recent years, efforts are being made to implement the automation into the leather processing to increase productivity, precision of operations, time efficiency and last but not least to reduce physically demanding work, restrict acts of the health hazards of employees and contribute to the work environment improvement.

The problems of processing the leather industry wastes including proposals for technological devices equipped with automatic control are solved in last decades at our workplace, at the Faculty of Applied Informatics at Tomas Bata University in Zlín. [1, 2]

Closely related and lately discussed issue comprises also the hexavalent chromium problematics. Currently the chrome-tanning is the most common type of tanning worldwide. Complex salts of trivalent chromium are used in the tanning process and effectively influenced the desired functional properties of leather. The fibril-forming collagens are the major structural proteins of hides and skins. Trivalent chromium stabilizes a hide by crosslinking the collagen fibers and supply required qualities. However, CrIII contained in leather can be under various conditions in small amounts oxidized to another form – hexavalent chromium. Hexavalent chromium belongs among toxic elements and is classified as carcinogen in the contrast to the trivalent form, which is benign, safe and largely beneficial. [3, 4] Although knowledge of trivalent to hexavalent chromium conversion is well described in literature, the precise mechanism is complex and details are not clearly explained. [5]

This work is supported by the Ministry of Education, Youth and Sports of the Czech Republic, by European Regional Development Fund under the project CEBIA-Tech No. CZ.1.05/2.1.00/03.0089 and its continuing project, i.e. by Narodni program udrzitelnosti No. 1.05/2.1.00/03.0089

Hana Vaskova is with the Faculty of Applied Informatics, Tomas Bata University in Zlin, nám. T. G. Masaryka 5555, 760 01 Zlín, Czech Republic (e-mail: vaskova@fai.utb.cz).

Karel Kolomaznik is with the Faculty of Applied Informatics, Tomas Bata University in Zlin, nám. T. G. Masaryka 5555, 760 01 Zlín, Czech Republic (e-mail: kolomaznik@fai.utb.cz).

Radek Matušů is with the Faculty of Applied Informatics, Tomas Bata University in Zlin, nám. T. G. Masaryka 5555, 760 01 Zlín, Czech Republic (e-mail: rmatusu@fai.utb.cz).

II. Leather waste treatment

The complex processing of chromium-containing waste materials is based on the collagen protein hydrolysis. In simplified way this process can be divided into the following phases, as displayed in Fig. 1.

In the first stage the collagen protein is liquefied and separated from the chromium sludge. Chromium sludge can be subjected to revitalization for obtaining chromium in a form of salts for further leather tanning [6]. The part of resulting gelatinous protein, a high-quality gelatin, finds many applications e. g. in food industry, pharmacy or cosmetic and therefore can be used cost-effectively. The rest of gelatinous protein is used for the purpose of further processing. Enzyme activity leads in alkaline conditions to molar mass decrease of gelatinous hydrolyzate. Further splitting of protein chain can continue by the act of acid [7]. Then the hydrolyzate with lower molar mass is acquired and can find application as biostimulator in agriculture.

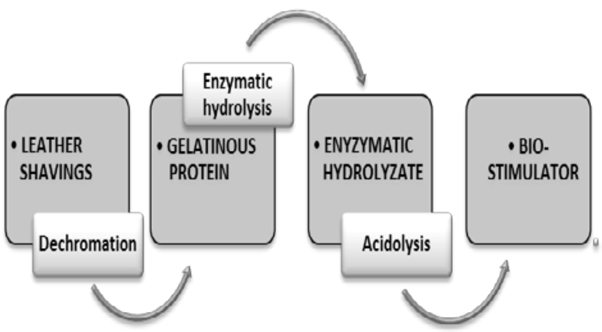

Fig. 1 structure of a dechromation process

III. Mathematical model

Linearized state mathematical model including input, output variables and inner-state variables is used for the process description.

A. State model of dynamic system

Diagram of system used is shown in Fig. 2. Continuous nonlinear system is described by equations:

$$\dot{X} = F(X,U) \tag{1}$$

$$Y = G(X,U) \tag{2}$$

Where $\mathbf{X} = (x_1, x_2, \ldots, x_n)$ is the state vector,
$\mathbf{U} = (u_1, u_2, \ldots, u_r)$ is the input vector,
$\mathbf{Y} = (y_1, y_2, \ldots, y_m)$ is the output vector,
$F = (f_1, f_2, \ldots, f_n)$ and $G = (g_1, g_2, \ldots, g_m)$ are vector functions and $\dot{\mathbf{X}} = \frac{\mathbf{d}X}{\mathbf{d}t}$.

B. Model linearization

Linearized model is obtained by introducing deviations of state and input variables from their stationary states and then linearized using Taylor series.

$$\mathbf{\Delta X} = \mathbf{X} - \mathbf{X^0} \tag{3}$$

$$\mathbf{\Delta U} = \mathbf{U} - \mathbf{U^0} \tag{4}$$

$\mathbf{X^0}$ and $\mathbf{U^0}$ are stationary states values, the time derivative of state variables gives zero.

$$\Delta \dot{X}^{\mathbf{0}} = \Delta\mathbf{F}(\mathbf{X^0}, \mathbf{U^0}) = 0 \tag{5}$$

Continuous linear system is described by the state equation and output status

$$\Delta \dot{\mathbf{X}} = \mathbf{A}\Delta\mathbf{X} + \mathbf{B}\Delta\mathbf{U} \tag{6}$$

$$\Delta\mathbf{Y} = \mathbf{C}\Delta\mathbf{X} + \mathbf{D}\Delta\mathbf{U} \tag{7}$$

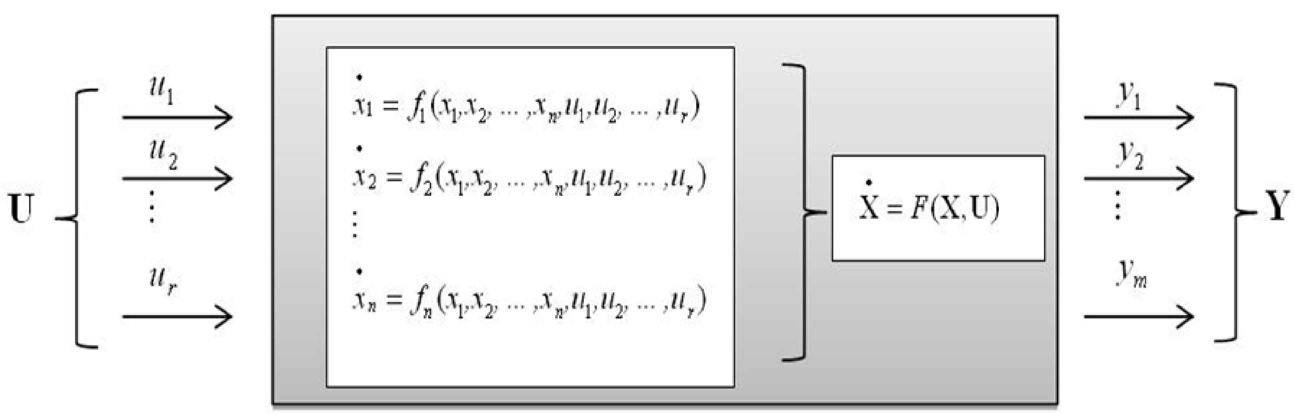

Fig. 2 mathematical model of the system

where A is state matrix, $\dim \mathbf{A} = n \times n$,
B is the input matrix, $\dim \mathbf{B} = n \times r$,
C is the output matrix, $\dim \mathbf{C} = m \times n$,
D is the zero matrix, $\dim \mathbf{D} = m \times r$.

The state matrix A is given, the other matrixes are determined in a similar way.

$$A = \begin{bmatrix} \frac{\partial f_1^0}{\partial x_1} & \frac{\partial f_1^0}{\partial x_2} & \cdots & \frac{\partial f_1^0}{\partial x_n} \\ \frac{\partial f_2^0}{\partial x_1} & \frac{\partial f_2^0}{\partial x_2} & \cdots & \frac{\partial f_2^0}{\partial x_n} \\ \vdots & \vdots & \vdots & \vdots \\ \frac{\partial f_n^0}{\partial x_1} & \cdots & \cdots & \frac{\partial f_n^0}{\partial x_n} \end{bmatrix} \tag{8}$$

This system as a real system fulfils the strong physical condition of the feasibility, i.e. the outputs are functions only of the state variables. This means that for

$$\Delta \mathbf{Y} = \Delta \mathbf{X} \tag{9}$$

the matrix **C** is the identity matrix and D is the zero matrix.

C. *Hydrolysis of the collagen protein*

Mathematical-physical model for shavings alkaline hydrolysis description is based on the mass balance of the input substance, the resulting hydrolyzate protein, enthalpy balance for the reaction mixture and the heat transfer medium, which is the saturated steam. The hydrolysis process takes place in a flow reactor with a stirrer ensuring the state variable independence on the position in the reactor. It is considered as system with lumped parameters. The mixing the heat transfer medium is also presumed. The mathematical model is given by the balance equations (10) – (14). The used symbols are specified in Table 1.

Mass balance for protein

$$\dot{m}_{RS}\, a_P = \dot{m}_{RS}\, a_B + k m_R a_B + m_R \frac{\mathbf{d}a_B}{\mathbf{d}t} \tag{10}$$

Mass balance for hydrolyzate

$$0 = \dot{m}_{RS}\, a_E - k m_R a_B + m_R \frac{\mathbf{d}a_E}{\mathbf{d}t} \tag{11}$$

Enthalpy balance for reaction mixture

$$\dot{m}_{RS}\, c_{RS} T_{RS} + KS(T - T_R) = \dot{m}_{RS}\, c_{RS} T_R + m_R c_{RS} \frac{\mathbf{d}T_R}{\mathbf{d}t} \tag{12}$$

Enthalpy balance for heat transfer fluid

$$\dot{m}_P\, H + \dot{m}_P\, c_P T_0 = \dot{m}_P\, c_P T + KS(T - T_R) + m_P c_P \frac{\mathbf{d}T}{\mathbf{d}t} \tag{13}$$

Table 1 used variables

Designation	Physical quantity	Unit
m_R	Mass of reaction mixture (RS)	kg
m_P	Mas of water	kg
$\dot{m}_{RS}$ (= $dmRS$)	Mass flow of reaction mixture	kg/s
$\dot{m}_P$ (= dmP)	Mass flow of heating stem, respectively water	kg/s
a_P	Initial mass fraction of protein in RS	1
a_B	Mass fraction of decomposed protein in the reactor	1
a_E	Mass fraction of undecomposed protein in the reactor	1
T_{RS}	Temperature of RS	K
T_R	Temperature of reaction	K
T_0	Temperature of stem, the output	K
T	Temperature of the reactor shell = temperature of water, the output	K
c_{RS}	Specific heat of RS	J/kgK
c_P	Specific heat of water	J/kgK
K	Heat transfer coefficient	W/m^2K
S	Area of reactor heated by steam	m^2
H	Specific latent heat of vaporization	J/kg

D. *Transfer matrix*

Taking the Laplace transform of (6) and (7) yields

$$s\Delta X(s) = A\Delta X(s) + B\Delta U(s) \tag{14}$$
$$\Delta Y(s) = C\Delta X(s) + D\Delta U(s) \tag{15}$$

and

$$\Delta X(s) = (sI - A)^{-1} B\Delta U(s) \tag{16}$$

After the substitution for $\Delta\mathbf{X}(s)$ in the output equation (15) together with (9) we get

$$G(s) = (sI - A)^{-1} B \tag{17}$$

Expression of matrices A and B is then based on the mathematic model (10) – (13). The transfer matrix is calculated from (17) and expressed using values of physical quantities for a real reactor.

IV. Simulation

Simulations based on the state description concerning matrixes A and B and the calculated transfer matrix G were performed in Matlab Simulink to obtain the progress of the state what in this case means also the output values. The diagram of the model simulation is displayed in Fig. 3.

First, simulations with the unit step function were performed

ISBN: 978-1-61804-321-4

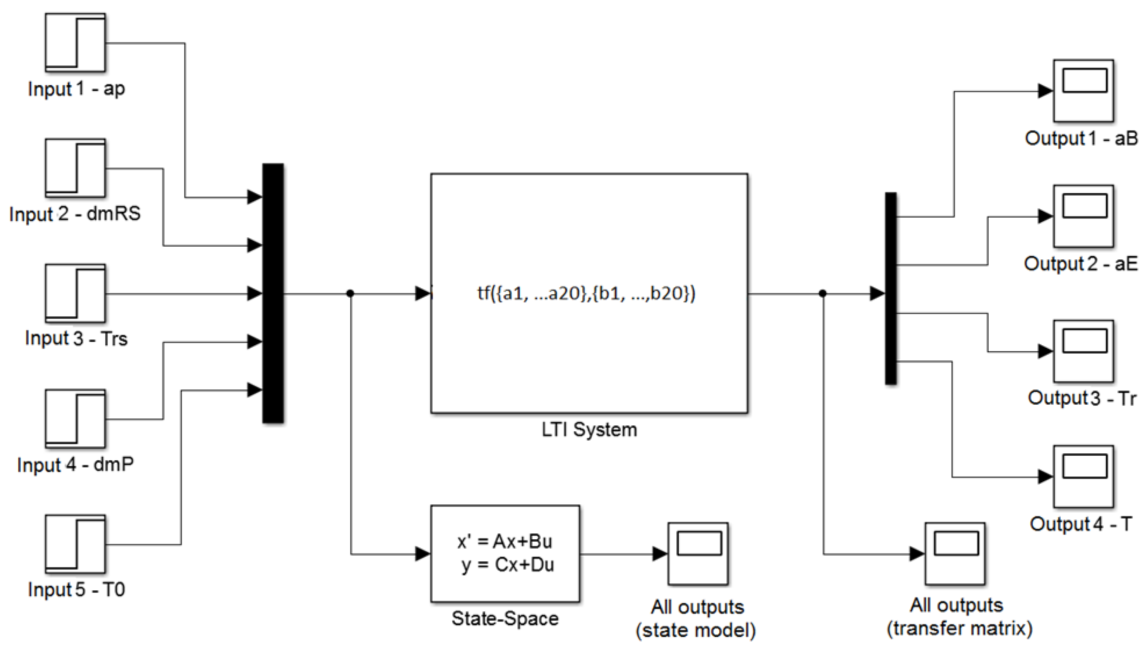

Fig. 3 diagram of the mathematical model simulation

on each input separately, and all combinations thereof. The reaction of the system was assessed on the basis of physical principles and knowledge from previous experiments. Time responses to a unit step function for all input variables are shown in Fig. 4.

The performed simulations and their physical consideration show that a_B and a_E are most affected by inputs $a_{P,}$ and *dmRS*. T_R is significantly affected by T_{RS} and *dmRS*. T_0 have influence especially on the temperature *T*. These reactions are confirmed also by other combinations.

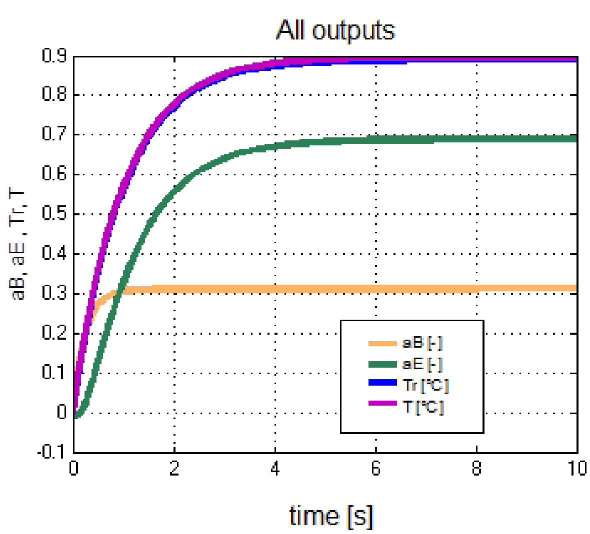

Fig. 4 step response for all output variables

V. Conclusion

Mathematical-physical model for the hydrolysis of collagen protein from tannery wastes is presented in the paper. This treatment offers safe, environmentally friendly and also economically effective method for reduction of waste gained from leather manufacturing sector. Simulations of the model can serve for further laboratory and pilot scale experiments contribute to automated control of the production process.

References

[1] Vašek, V., Dolinay, J., Dostálek, P., Janáčová, D., Kolomazník K. Microcontrollers in Tannery Waste Recycling Control. *In 1th Int. Leather Eng. Symp. "Leather Industry, Environment and Progressive Technologies"*. Izmir, Age University, 2009.

[2] Kolomazník, K., Vašek, V., Janáčová, D.: Control recycling technology of tannery chromium wastes. *In: Proceedings of the 13th WSEAS International Conference on Computers*. Rhodes, WSEAS Press, 2009, p. 550-554.

[3] Hang, X., Zhang, X., Wang, X., Jin, L., Yang, Z., Jiang, C., Chen, Q. Chronic occupational exposure to hexavalent chromium causes DNA damage in electroplating workers. *BMC Public Health*. Vol. 11, No. 1, 2011, p. 224-232

[4] Kolomazník, K., Adámek, M., Anděl, I., Uhlířová, M.: Leather waste - Potential threat to human health, and a new technology of its treatment. *Journal of Hazardous Materials*. Vol. 160, 2008, p. 514-520.

[5] Chaudhuri, D., Chakraborti, R. Further studies on the official methods of analysis for determination of hexavalent chromium level in leather. *J. Am. Leather Chem. Assoc.*, Vol.98, 2003, p.388 – 399

[6] Kolomaznik, K,. Mladek, M., Langmaier, F., Janacova, D., Taylor, M., M. *J. Am. Leather Chem. Assoc.*, Vol.94, 2000, p.55 – 63.

[7] Pecha, J., Fürst, T., Kolomaznik, K., Friebrova, V., Svoboda, P. Ameracian institute of engineers (AIChE) Journal. Vol. 58, No. 7, 2011, p. 2010-2012.

Simulation of PIR detector heating by interrupted radiation

Rudolf Drga, Dagmar Janáčová, and Hana Charvátová

Abstract— Work is focused on PIR detectors that operate in the infrared region and are used in the security industry. The paper explains the principle of PIR detector and how to measure their activity. It was created a workplace implemented interrupted source of thermal radiation. For a description of the behavior of the detector, was created a mathematical model and a simulation in COMSOL Multiphysics.

Keywords—PIR detector, pyroelement, radiation, mathematical model.

I. INTRODUCTION

THIS work deals with the testing of sensors of security systems in the field of infrared radiation and its use in the security industry. The work is focused mainly on the PIR detectors, which are used most widely in security technologies.

The output of work may also be used in courses technical means of security industry, electronic security systems, which are the subjects of teaching at the Department of Security Engineering, Faculty of Applied Informatics, of Tomas Bata University in Zlin.

The principle of the PIR detector is shown in Fig. 1. The detector consists of pyro element 1 which is receiving radiation from an intruder. This radiation passes through the filter 2, which suppresses radiation of wavelength less than 8 micron and greater than 12 micron and is therefore permeable for the 8 to 12 micron with a maximum of 10 micron wavelength, which corresponds to the temperature of the intruder, i.e. about 37 ° C. Infrared optics detector 3 performs the concentration of thermal radiation on pyro element while creating segments 4, wherein the detector "see" and "not see". If over these areas intruder moves tangentially 5, this leads to intermittent radiation after passing through the filter to generate pyro element charge whose magnitude is measured after signal processing 6 then sent as an alarm message on I&HAS security system.

For thermal balance PIR detector and pyro element was necessary to design a mathematical model described below and perform simulations of the thermal behavior of the sensors in the environment of COMSOL Multiphysics to verify the accuracy of the measurement pyro element time close to zero at low density thermal radiation.

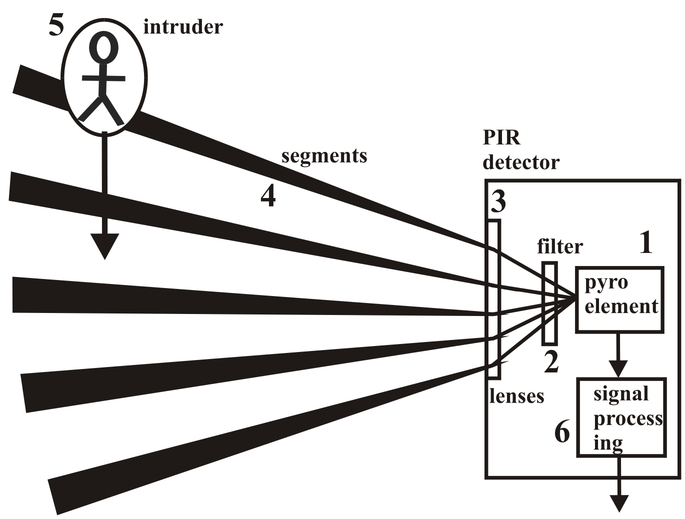

Fig. 1 principle of PIR detector

II. CALCULATION RATION SPEED OF THE CHOPPER

To calculate the rotational speed of the chopper on the simulated work measurement of PIR were used basic data from producer to define the minimum and maximum speed of movement of the intruder. The method of calculation corresponds to Fig. 2, which is drawn by the actual movement of an intruder and the position of the chopper, whose task is to simulate the movement of an intruder.

The work was performed with financial support of research project NPU I No. MSMT-7778/2014 by the Ministry of Education of the Czech Republic and also by the European Regional Development Fund under the Project CEBIA-Tech No. CZ.1.05/2.1.00/03.0089.

R. Drga, Tomas Bata University in Zlín, Faculty of Applied Informatics, Department of Security Engineering, nám. T. G. Masaryka 5555, 760 01 Zlín, Czech Republic (e-mail: rdrga@fai.utb.cz)

D. Janáčová, Tomas Bata University in Zlín, Faculty of Applied Informatics, Department of Automation and Control Engineering, nám. T. G. Masaryka 5555, 760 01 Zlín, Czech Republic (e-mail: janacova@fai.utb.cz)

H. Charvátová, Tomas Bata University in Zlín, Faculty of Applied Informatics, Department of Automation and Control Engineering, nám. T. G. Masaryka 5555, 760 01 Zlín, Czech Republic (e-mail: charvatova@fai.utb.cz)

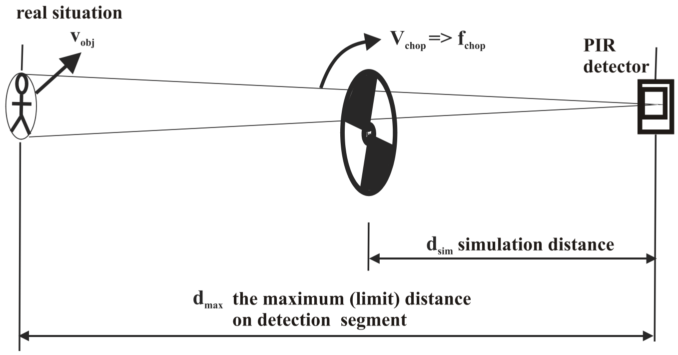

Fig. 2 the layout of actual movement of an intruder and simulation in the workplace PIR detectors

$$v_{chop} = \frac{v_{obj}}{d_{\max}} d_{sim} \qquad (1)$$

Where:

d_{max} – maximum range detector

$v_{obj\ min}$ – minimum speed of object

$v_{obj\ max}$ – maximum speed of object

d_{sim} – the distance from the radiation source to PIR detector

v_{chop} – speed of point chopper

where:

d_{max} = 10 m

$v_{obj\ min}$ = 0,2 m/sec

$v_{obj\ max}$ = 3 m/sec

d_{sim} = 1 m

Substituting the values $v_{obj\ min}$ a $v_{obj\ max}$ from the manufacturer gave the following values:

$v_{chop\ min}$ = 0,02 m/sec and $v_{chop\ max}$ = 0,333 m/sec

As shown in Fig. 3, a point located on the diameter D_{chop} = 180 mm executes circular path during one rotation:

$$s_{chop} = \pi D_{chop} = v_{chop}\,\tau_{rot} \Rightarrow \tau_{rot} = \frac{\pi D_{chop}}{v_{chop}} \qquad (2)$$

after substituting real values D_{chop} = 180 mm and counted v_{chop} get:

$\tau_{rev\ min}$ = 28.274 sec and $\tau_{rev\ max}$ = 0.169 sec

average period of rotation is then:

$\tau_{rev\ aver}$ = 14.221 sec

when choper is divided into 4 slices then average period of thermal pulses is:

$\tau_{imp\ aver}$ = 7.111 sec

in the experimental part of the work was used the basic value of $\tau_{rev\ aver}$ = 10 sec.

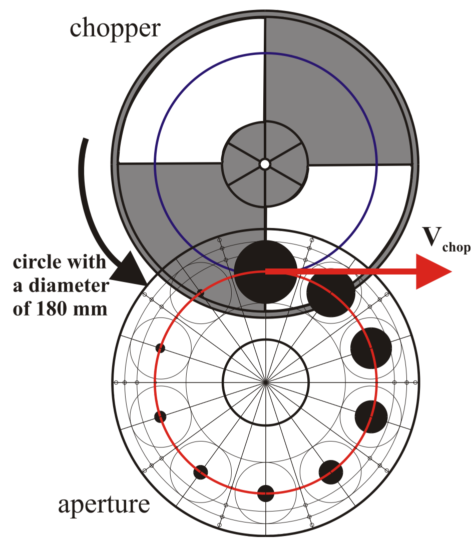

Fig. 3 chopper and aperture disc

For an explanation of thermal condition in pyro element was necessary to simulate the behavior of the sensor in COMSOL Multiphysics.

III. Mathematical Model of Heating Sensor by Radiation

Thermal radiation incident on the sensor is partially reflected and some is absorbed by the sensor, thereby to ensure that the temperature measured at the beginning of the measurement does not fully effective temperature.

For the quantitative description of the temperature distribution in the heated pyro element radiation we used the Stefan-Boltzmann law, according to which the density of heat flow between the source and the heated surface expressed as (3) [3]:

$$q(\tau) = \sigma C (T_2^4 - T_1^4) \qquad (3)$$

where:

q - heat flow density, [Wm^{-2}]

σ - Stefan-Boltzmann constant, $\sigma = 5.67.10^{-8} Wm^{-2}K^{-4}$

ISBN: 978-1-61804-321-4

C – constant which characteriyes emission surface and geometric properties, [1]
T_2 – source temperature, [K]
T_1 – temperature of heated surface, in this case the surface temperature, [K]

$$\frac{\partial T}{\partial \tau} = a\,\frac{\partial^2 T}{\partial x^2}\,,\ (\,0 \le x \le b,\, 0 < \tau\,) \tag{4}$$

$$\left(\frac{\partial T}{\partial x}\right)_{x=0} = 0 \tag{5}$$

$$\lambda\left(\frac{\partial T}{\partial x}\right)_{x=b} = q \tag{6}$$

$$T = T_p \quad \text{for} \quad \tau = 0 \tag{7}$$

where:
b - half the thickness of the sensor, [m]
x - direction coordinates, [m]
λ - the thermal conductivity of sensor material, [W.m^{-1}.K^{-1}]
T_P – initial temperature of the sensor surface, [K]
τ - time of heating, [s]

By Laplace transform of equation (3) with conditions (4) to (7) has been obtained analytical solution of non-stationary temperature field for symmetrically heated by radiation sensor of plate shape:

$$\frac{T-T_p}{T_c-T_p} = K_i\left[Fo + \frac{1}{2}\left(\frac{x}{b}\right)^2 - \frac{1}{6} - 2\sum_{n=1}^{\infty}\frac{\cos\left(\frac{x}{b}\,p_n\right)}{p_n^{\,2}\cos\ p_n}\,e^{(-Fop_n^{\,2})}\right] \tag{8}$$

where K_i is Kirpičev criterion (9)

$$K_i = \frac{q\,b}{\lambda(T_c - T_p)} \tag{9}$$

where T_c is medium temperature of radiation source.
Fourier criterion Fo represents the dimensionless heating time. Fo is calculated by the equation:

$$Fo = \frac{a\,\tau}{b^2} \tag{10}$$

where:
τ - duration of heating, [s]
a - thermal diffusivity of sensor, [m^2.s^{-1}]:

$$a = \frac{\lambda}{\rho\,c_p} \tag{11}$$

where:
λ - the thermal conductivity of sensor material, [W.m^{-1}.K^{-1}]
ρ - the density of the sensor material, [kg.m^{-3}]
c_p - the specific heat capacity of the sensor material, [J.kg^{-1}.K^{-1}].

Members p of the analytical solution of (8) are determined from equation (12):

$$p_n = n\ \pi \tag{12}$$

According to the form the solution (8) it is evident that with increasing time of heating, influence of the series members decrease, i.e. we can also expect Fourier criterion Fo_k for which influence of infinite series may be neglected and for $Fo > Fo_k$ the temperature at any point of the wall will be almost linear function of time and temperature profile across the plate (x-axis direction) will be parabolic.

IV. SIMULATION OF PYRO ELEMENT HEATING BY COMSOL MULTIPHYSICS

As shown on fig. 4. involving intermittent heating pyro element due to the rotation of the chopper.

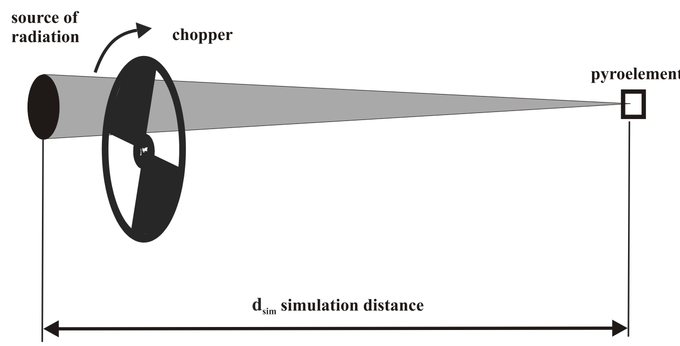

Fig. 4 interruption of heat flow chopper

We done simulations by Heat Transfer module of Comsol Multiphysics. Pyro element was represented by prism of the dimensions 1 x 2.3 x 5 mm with relative emissivity 0.8. On the prism impakts thermal radiation of 1 W/m^2 to precisely defined time, which is determined by the rotational speed of chopper. The following Fig. 5 shows the temperature distribution in the prism.

ISBN: 978-1-61804-321-4

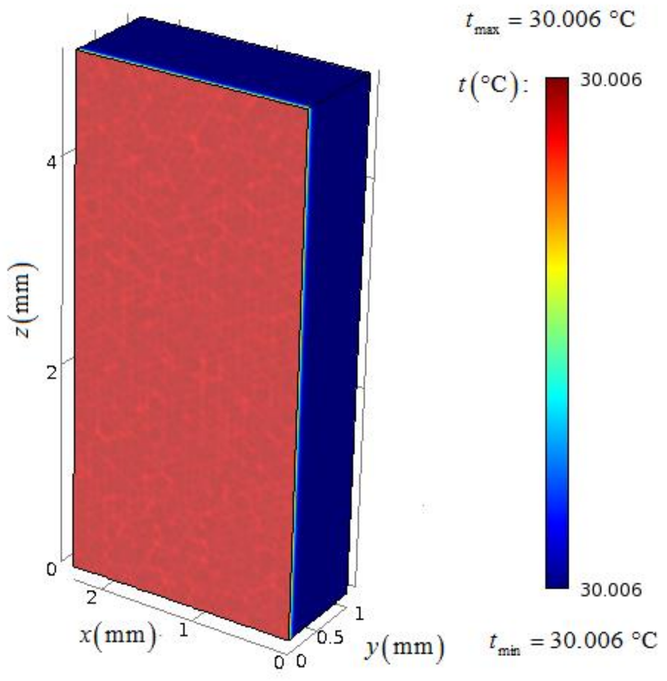

Fig. 5 the temperature distribution in the prism of pyro element

It is obvious that the surface temperature of pyro element is in given time almost the same as the temperature throughout its thickness, which has been confirmed experimentally.

The following figures show the temperature distribution in pyro element at different times.

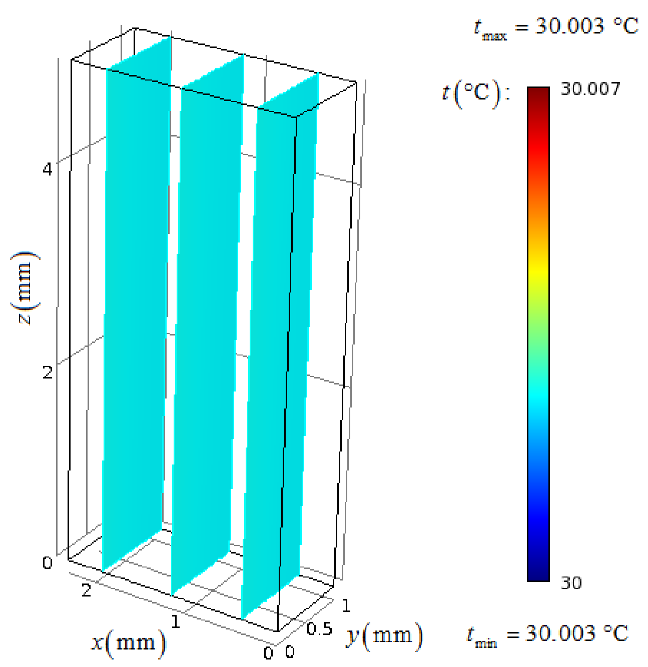

Fig. 6 pyro element temperature distribution in time of 7.5 sec with a 10 sec period

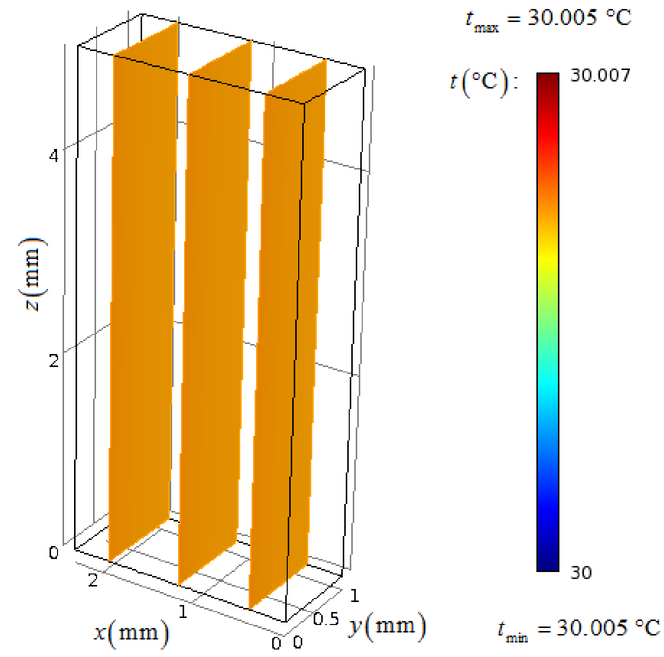

Fig. 7 pyro element temperature distribution in time of 17.5 sec with a 10 sec period

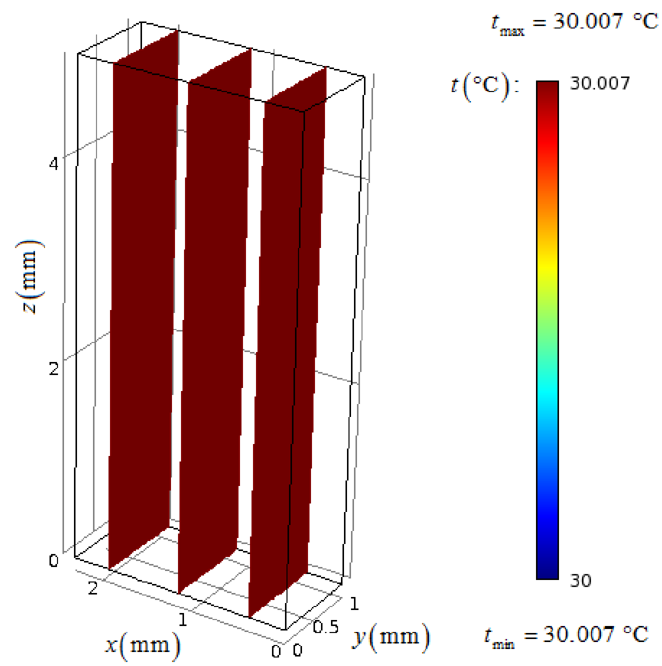

Fig. 8 pyro element temperature distribution in time of 27.5 sec with a 10 sec period

ISBN: 978-1-61804-321-4

Fig. 9 shows the long-term heating of the surface of the pyro element depending on time for an intermittent radiation chopper rotation period 10 sec.

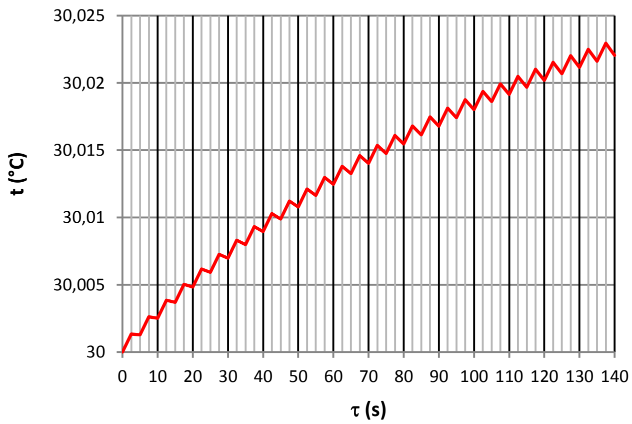

Fig. 9 long-term heating of the surface of the pyro element

The following chart shows the course of heating at different speed rotation chopper for periods of 5, 10, 15 sec.

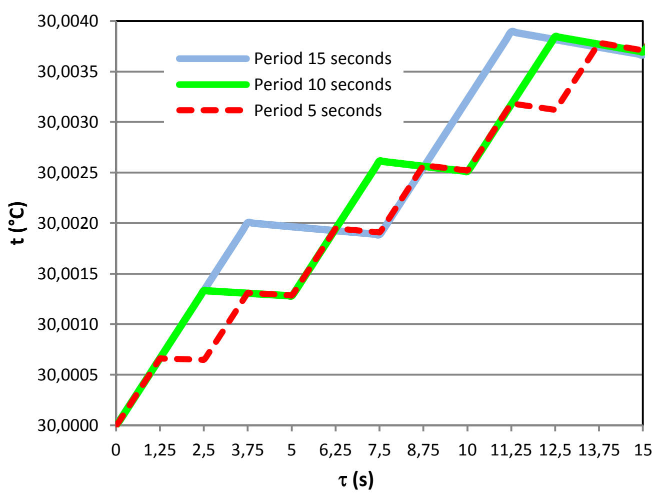

Fig. 10 heating of pyro element for different periods of rotation of the chopper

The initial temperature of pyro element 30 °C
Relative emissivity of the surface of a pyro electric element 0.8
Thermal conductivity of the pyro electric element $2.255.10^{-6}$ m^2/s
Incident density of radiant flux 1 Wm^{-2}
Coefficient at heat transfer and radiation $\alpha_s + \alpha_p = 30\ Wm^{-2}K^{-1}$

V. Conclusion

Simulation was performed of heating PIR detector by intermittent radiation.
The graph 10 shows the dependences of rotational frequency chopper on the course of the heating pyro element.
It was experimentally found that the pyro element upon rotation of the chopper with the period of 10 sec generates such a charge, which is sufficient for further processing, while for higher and lower speed of chopper generates charge that is not sufficient to activate the PIR detector to generate an alarm of I&HAS system.
This is due to the fact that pyro element is sensitive to a change in radiation and if the change is too fast, so the charge does not produced and when the change of radiation is too slow, so the charge is also not generated.
In the future, we can assume that will be created pyroeletric materials whose sensitivity will be higher [12] [13] and signal processing will be used new algorithms [14] [15], which allows to reliably detect the occurrence of an intruder in the protected area.

References

[1] J. D. Vincent, *Fundamentals of infrared detector operation and testing.* USA, Texas: WILEY, 1990.
[2] G. F. Knoll, *Radiation detection and measurement*. USA, Texas: WILEY, 2000.
[3] B. Saleh, *Fundamentals of photonics*. USA, Texas: WILEY, 2007.
[4] K. Kolomazník, *Teorie technologických procesů III*. (in Czech). Brno: University of Technology in Brno, 1978.
[5] A., R. Jha, . *Infrared technology*. USA – Texas: WILEY, 2006.
[6] C. Hotz, *Přenos tepla zářením* (in Czech), Prague: SNTL, 1979.
[7] K. Kolomazník, *Modelování zpracovatelských procesů*. (in Czech), Brno: University of Technology in Brno, 1990.
[8] K. Židek and J. Piteľ, "Smart 3D Pointing Device Based on MEMS Sensor and Bluetooth Low Energy," in *Proceedings of the 2013 IEEE Symposium on Computational Intelligence in Control and Automation (CICA)*, Singapore, April 16-19, 2013, pp. 165-168.
[9] R. Makovník and O. Líška, "Contribution to experimental identification and simulation problems of dynamic systems", *Ovidius University Annual Scientific Journal*. vol. 9, No. 1, 2007.
[10] M. Feriančik. O. Líška. M. More, "Navigation of industrial manipulator based on computer vision". *Transfer inovácií*. vol. 28. 2013. pp. 140-142.
[11] M. Fodor, O. Líška, "Design and realization sensorial system on detection obstacle". [CD-ROM]. in *8th International Symposium on Applied Machine Intelligence and Informatics*, Herľany, Slovakia, 2010.
[12] Liang, Z., Li, S., Liu, Z., Jiang, Y., Li, W., Wang, T., Wang, J. High responsivity of pyroelectric infrared detector based on ultrathin (10 μm) LiTaO3, *Journal of Materials Science: Materials in Electronics*, 26 (7), pp. 54005404, 2015.
[13] Oishi, K., Yonemaru, S., Akai, D., Ishida, M. SiO2/SiN multilayerstack infrared absorber integrated on Pb(Zr0.4,Ti0.6)O3 film pyroelectric sensors on γAl2O3/Si substrate, *Sensors and Materials*, 27 (2), pp. 217-227, 2015.
[14] Zhou, W., Xiong, J., Li, F., Jiang, N., Zhao, N. Fusion of multiple pyroelectric characteristics for human body identification, *Algorithms*, 7 (4), pp. 685702, 2014.
[15] Yun, J., Lee, S.S. Human movement detection and identification using pyroelectric infrared sensors, *Sensors* (Switzerland), 14 (5), pp. 8057-8081, (2014).

ISBN: 978-1-61804-321-4

Lithium-ion batteries used in electric vehicles

Michał Sierszyński, Michał Pikula, Paweł Fuć, Piotr Lijewski, Maciej Siedlecki, Marta Galant

Abstract— The development of civilization brings a continuous increase in energy demand. Fuel consumption increases, which causes an increase in environmental pollution with harmful exhaust gas components such as carbon monoxide (CO), carbon dioxide (CO_2), hydrocarbons (HC), nitrogen oxides (NO_x) and particulate matter (PM). The development of vehicle propulsion systems so focused on the search for alternative drivetrains, which include primarily hybrid and electric. Such drives are characterized by a favorable ecological and economical performances. The problem is the performance of used batteries, which differ significantly from the large-scale use of fossil fuels such as petrol and diesel.

The subject of this study concerns the analysis of the concept of the world's existing lithium-ion batteries used in electric vehicles. The study contains a presentation of innovative solutions that can improve the performance characteristics of alternative drives.

Keywords – battery, alternative vehicle drives, lithium-ion technology

I. Introduction

THE development of vehicle propulsion systems is focused on the use of alternative technologies, which include primarily hybrid and electric motors. Due to their environmental, functional and economical characteristics, exploitation of vehicles equipped with these kinds of drives is especially beneficial in urban conditions. In the cities, vehicles often start and stop moving. Often, these phases are separated by the vehicle being idle. Under these conditions, a classic vehicle drive the combustion engine is running in a large range of power, speed and efficiency. The overall energy efficiency of classical drive vehicles are also degraded by the irreversible conversion of kinetic energy into heat during frequent deceleration. Another aspect promoting the electrification of powertrains is regulations requiring the reduction of emission limits of harmful exhaust emission components. The main performance parameters of energy storages include: energy density, power density, storage efficiency, conversion efficiency, lifetime, overload resistance, reliability and no need for maintenance. Table 1 shows a comparison of these parameters for basic types of energy storages [1]. The kinetic energy storages stores energy in the mechanical form, typically using a rotating flywheel. The hydropneumatic equivalent of energy storage accumulates elastic energy in the form of elasticity of solid or gas, or in the form of potential energy of the load, using the phenomenon of increasing pressure of the medium.

Table 1 Basic properties of different types of energy storages [developed based on 5, 6]

Property	Energy storage type		
	kinetic	hydropneumatic	electro-chemical
Energy density [kJ/kg]	up to 10 (360)	up to 3,2	up to 400
Power density [W/kg]	unlimited	up to 300	up to 200
Storage efficiency:			
Short-term	(+)	(+)	(+ +)
Long-term	(– –)	(+)	(o)
Conversion efficiency	(+)	(–)	(–)
Lifetime	(+ +)	(+ +)	(– –)
Overload resistance	(+)	(+)	(– –)
Reliability	(+)	(+)	(–)
No need for maintenance	(+)	(+)	(– –)
Overall cost (+ = low)	(+)	(–)	(– –)
Legend: (+ +) – great, (+) – good, (o) – average, (–) – poor, (– –) – very poor			

Electrochemical batteries are characterized by the best indicators of power and energy density compared with other battery types and for this reason, despite the highest cost, gained the most popularity. In order for electric vehicles to achieve the range approaching that of the hydrocarbon fuel vehicles it is necessary to use large and heavy electrochemical batteries [1]. This results in a significant increase in vehicle weight affecting the amount of energy required to move, and thus also the cost of its operation. For several years the lithium-ion (Li-Ion) batteries are increasingly used, replacing the older technologies of nickel-metal hydride (NiMH) batteries.

Michal Sierszynski is with the Development Department, Solaris Bus & Coach, Obornicka 46, Bolechowo-Osiedle 62-005 Owinska, Poland (e-mail: michal.sierszynski@solarisbus.com).

Michal Pikula is with the Development Department, Solaris Bus & Coach, Obornicka 46, Bolechowo-Osiedle 62-005 Owinska, Poland (e-mail: michal.pikula@solarisbus.com).

Pawel Fuc is with the Faculty of Machines and Transport at Poznan University of Technology, Piotrowo 3 60-965 Poznan, Poland (e-mail: pawel.fuc@put.poznan.pl).

Piotr Lijewski is with the Faculty of Machines and Transport at Poznan University of Technology, Piotrowo 3 60-965 Poznan, Poland (e-mail: piotr.lijewski@put.poznan.pl).

Maciej Siedlecki is with the Faculty of Machines and Transport at Poznan University of Technology, Piotrowo 3 60-965 Poznan, Poland (e-mail: maciej.s.siedlecki@doctorate.put.poznan.pl).

Marta Galant is with the Faculty of Machines and Transport at Poznan University of Technology, Piotrowo 3 60-965 Poznan, Poland (e-mail: marta.m.galant@doctorate.put.poznan.pl).

II. LITHIUM-ION TECHNOLOGY

The ability to charge batteries makes them different from galvanic cells, where the principle is the same, but its function is fulfilled once. The chemical energy stored in the galvanic cell can only be used once. Electrodes originally used in batteries were made of basic nickel oxide (III) NiO(OH) (cathode) and metallic cadmium (anode). So they were called rechargeable nickel-cadmium batteries (NiCd). This solution was characterized by low density capacity values and above all, the occurrence of the memory effect, i.e. Recharging before the full cycle discharge is complete will decrease the capacity of the battery. The next generation of batteries used nickel in combination with metal and hydrogen (NiMH). The change had a positive effect on battery performance and reduced the memory effect. This technology was used in the first hybrid vehicles like the Toyota Prius in the years 1997-2010 [7]. Both solutions were characterized by a low voltage of a single cell of 1.2 V.

An opportunity to improve the battery performance was to use the lightest metal - lithium. The main advantage of this solution was the lack of the memory effect, and higher values of energy and power density than in previous solutions. Lithium-ion batteries are currently used in electric and hybrid vehicles. The charging and discharging is associated with the transfer of lithium ions through the electrolyte. During charging, they collect electrons from the negative electrode while simultaneously being fixed in its structure as neutral atoms. During discharge they pass the electron to the electrode and move into the electrolyte as lithium ions. A similar but reverse process occurs at the positive electrode. The first vehicle, which used this technology was the Mercedes S500 Hybrid unveiled in 2010. The main obstacle in the earlier introduction of this technology have been problems with the overheating of the batteries. The Mercedes-Benz S500 Hybrid uses an additional air flow for battery cooling [4].

The main trend in the development of electric drives is associated with the search for technology that would enable increased energy density per unit volume and mass of the battery. Theoretical calculations indicate that the battery energy capacity of a Li-Ion battery can be increased to 2 700 Wh/kg which is approximately 20 times higher than the currently used solutions. It is envisaged that this will be achieved by the use of fullerene nanotubes [8]. This publication provides an overview of modern lithium-ion batteries together with an indication of their main characteristics.

III. OVERVIEW OF THE LATEST SOLUTIONS FOR LITHIUM-ION BATTERIES

A. LTO batteries

In LTO batteries (Lithium-titanate) the anode is made of titanium oxide ($Li_4Ti_5O_{12}$). These batteries are increasingly used in the automotive industry. Due to their properties they are used in hybrid and electric vehicles. They can operate in temperatures as low as -46°C (charging and discharging) at which other batteries have very low capacity [10]. At -30°C the batteries have over 80% of their base capacity in the ambient temperature of 20°C [11]. The result is that they have proved themselves applicable in many climate zones, as well as in extreme temperatures (maximum operating temperature is approx. 70°C). The current parameters of batteries of this type are a capacitance of maximum 90 Wh/kg and 250 Wh/dm^3 [9]. In addition, this type of battery can be charged with high voltages.

Tests showed that after 7 000 cycles of full charging and discharging, the battery capacity has changed in relation to the original by less than 20%. The relationship between the number of cycles of discharge/charge and the battery capacity is shown in Figure 1.

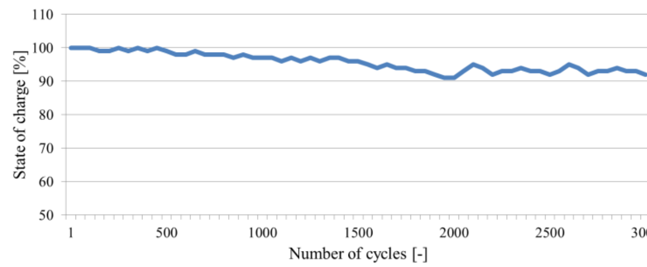

Fig. 1 The relation between the number of discharge/charge cycles and the LTO battery capacity [11]

Unused batteries self-discharge by a small amount. Due to its properties batteries can be used in applications in which the rapid charging is needed. For example: fast charging of 125kWh battery in the bus at the ends of lines with the power up to 450kW. The disadvantages of the LTO battery is the voltage produced by one cell, it is only approx. 2.4 V, but this value is still higher than for lead-acid batteries (2 V).

B. LFP batteries

LFP batteries (Lithium ferrophosphate) are characterized by the cathode being made of lithium compound, iron, phosphorus and oxygen ($LiFePO_4$). These batteries, like the LTO variety, are suitable for automotive applications. This type of a battery is characterized by high resistance to self-discharge when charging cycles are incomplete, which is desirable in hybrid vehicles. In the case of LFP battery voltage of a single cell is up to 3.2V, however, it should not be allowed to discharge below 2.5V, or the charging voltage to reach more than 4.2V, as this may damage the battery [12]. The batteries respectively recharged could gives over 2000 full cycles while retaining 80% of original capacity. The dependence of the capacity on the number of full discharge/charge cycles is shown in Figure 2.

ISBN: 978-1-61804-321-4

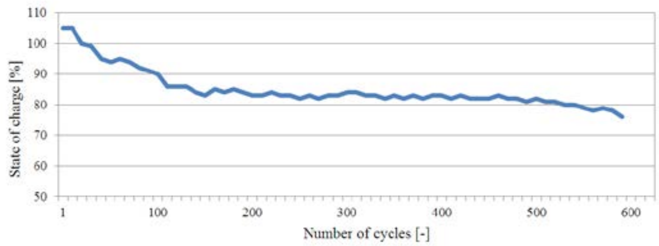

Fig. 2 The change of LFP battery capacity with the number of discharge/charge cycles [13]

The compound used for the cathode is environmentally safe and non-flammable. Operating temperature range is 0 to 60°C, and the energy density reaches over 120 Wh/kg, which is a high and desirable value. LFP batteries, due to higher specific energy than LTO batteries, are typically used in electric vehicles with extended range required on a single charge.

C. NMC batteries

NMC battery type (Lithium Nickel Manganese Cobalt Oxide) is characterized by the use of a $LiNiMnCoO_2$ compound with the cobalt content of 10-20% as a cathode. These batteries use nickel, which has been used on a large scale in NiMH and NiCd batteries, later replaced by lithium-ion batteries. Maximum voltage is 4.1V, and the minimum operating voltage is 2.7V [14]. Batteries of this type are characterized by high energy density reaching up to 250-270 Wh/kg, and in combination with SiC even more than 300 Wh/kg. At the same time the danger of overheating or damage compared to LTO and LFP solutions is higher. Operating temperature range is -20 to 55°C [14]. This value results from the instability of nickel at higher temperatures. Number of complete cycles of discharge/charge while maintaining 80% of the original capacity is 1 000, so less than the aforementioned solutions.

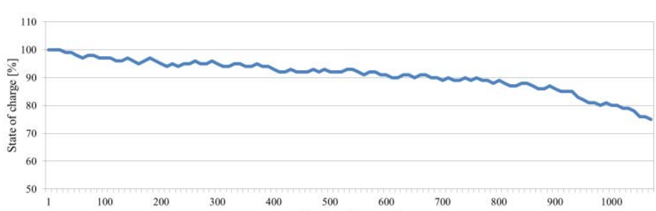

Fig. 3 The change of NMC battery capacity with the number of discharge/charge cycles [15]

This type of battery is not as popular as the LFP and LTO batteries for electric vehicles due to higher danger of overheating or damage compared to LTO and LFP solutions.

D. LMO batteries

LMO batteries (Lithium manganese spinel) are characterized by the use of manganese oxide in combination with lithium as the cathode ($LiMn_2O_4$). They have the possibility of storing large amounts of energy (up to 240 Wh/kg), while maintaining better safety in the case of overheating than NMC batteries [16]. This type of batteries are still in the testing phase, but they are considered a viable prospect for energy recovery systems in Formula One vehicles. LMO-type battery manufacturers do not publish data of the number of cycles of discharge/charge and how it affects the battery capacity. There is only the information that the batteries are characterized by a number of full cycles of discharging and recharging while maintaining 80% of the original capacity stated as 1 800 [16].

E. Lithium-ion KOKAM batteries

KOKAM batteries are batteries made with lithium-ion technology and patented by Dow Kokam. Their primary objective was to increase the operational parameters of lithium-ion technology, especially energy density. Dow Kokam received a grant for a new technology in 2009, and already in 2012 started mass production of a new battery. One of the objectives was to organically produce the batteries in a way that does not use fossil fuels, but rather energy from natural sources. The cathode is made of nickel, magnesium and cobalt. At the time of launching on the market KOKAM batteries were characterized by an energy density of 143 mAh/g (130 – 200 Wh/kg), and a large number of cycles of full discharge and charge while maintaining 80% of the initial capacity (2 500), as illustrated in Figure 4.

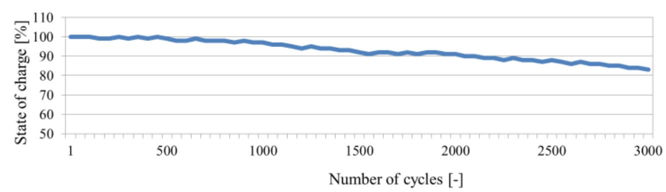

Fig. 4 The change of KOKAM battery capacity with the number of discharge/charge cycles [3]

In addition, KOKAM-type batteries have the ability to be charged with a higher current when compared to other battery solutions. All of these are the key parameters in terms of the use of batteries for automotive applications. In addition, they offer less heating during operation and greater safety for the environment in case of damage. Charging temperature ranges from 0 to 40°C, and discharging from -20 to 60°C. The batteries are characterized by low rate of self-discharging and no memory effect. Figure 5 shows the percentage of battery capacity KOKAM after 2 weeks.

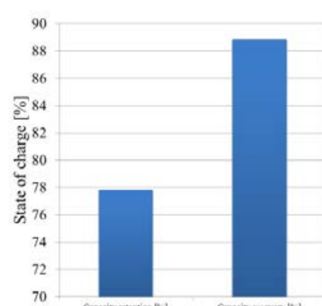

Fig. 5. Percentage of battery capacity of a KOKAM battery after 2 weeks [3]

F. A123 batteries

The overall performance and reliability of the battery depends largely on the chemical compounds used in the construction of a single cell. For example, lithium-ion technology is used both in electric vehicles, network storage systems and a variety of industrial applications. The company A123 Systems announced Nanophosphate® technology. This technology was developed by a team of professor Yet-Ming Chiang at the Massachusetts Institute of Technology. It utilises lithium-ion batteries constructed at the nanoscale level with specific structural and chemical properties, allowing for maximization of performance. Figure 6 shows schematically the structure of Nanophosphate®.

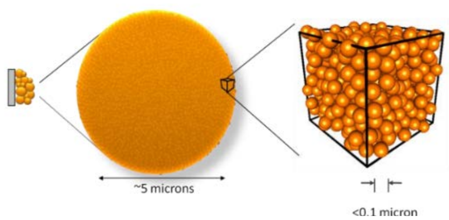

Fig. 6 Schematic visualisation of the Nanophosphate structure used in lithium-ion battery produced by A123 [2]

The main advantages of A123 batteries include: high energy value useful in a wide range of SOC (state of charge) and extended maintenance interval achieved through the use of specialized patented nanostructure. Single cell voltage is 3.3 V [17]. The batteries allow to have high power values per mass (2 400 W/kg), volume (500 W/dm3), and capacity (up to 300 Wh/dm3 and 165 Wh/kg) [17]. The value of the operating temperature range (from -30 to 55°C) and storage (-40 to 60°C) should also be noted. A123 batteries also feature a very low watt-hour cost.

A particularly important indicator when using this type of battery in vehicles is the unusual, when compared to other technological solutions used, independence of the battery power from the battery charge level. Typically, this involves a significant voltage drop along with the discharging of the battery, in this case the character of the curve is closer to flat (Fig. 7).

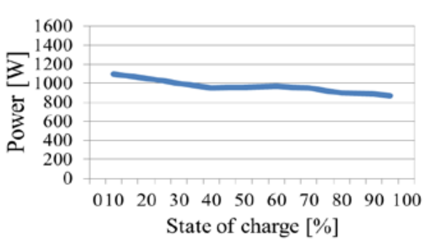

Fig. 7 The relation between battery power and the level of charge held [2]

A very important aspect of battery usage is safety. A123 batteries, although this is not currently required, have passed crash tests assessing their ability to maintain the required level of safety in the event of deformation. Such tests will be mandatory for batteries in vehicles only since 2016. This ensures their applicability in future vehicles. The last mentioned advantage applies to retention of the original capacity depending on the number of cycles (Figure 8).

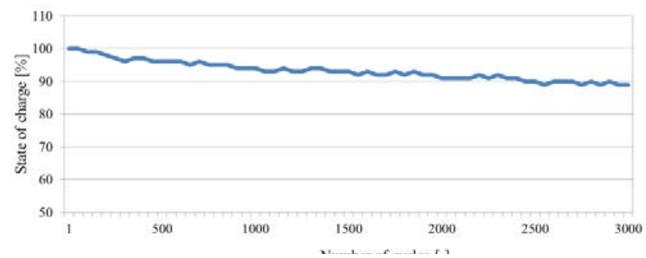

Fig. 8 The relation between the A123 battery capacity and the number of discharge/charge cycles [2]

A123 batteries continue to hold approx. 90% of the original capacity after 3 000 cycles. This distinguishes them from other solutions available on the market. Comparable battery solutions after the same number of cycles have only approx. 80% of their original capacity.

IV. Conclusion

The development of lithium-ion technology leads to the creation of newer and newer types of batteries. The main goal of battery designers is to achieve the greatest energy and power density. Currently, the achieved values are significantly lower than those available in hydrocarbon fuels that are used on a large scale. The review of the technologies used in batteries shows that there is no such solution, which would facilitate the best indicators in all relevant aspects of use; some form of a compromise has to be made. Batteries with high energy and power density typically have a limited number of charge cycles to a specified loss of capacity. The operating temperature range, which depends on local conditions in which the vehicle will be utilized, is also important.

Solaris Bus & Coach in their vehicles, which required the use of electrochemical batteries and fast charging decided to use the LTO technology. Such batteries are characterized by relatively small values of voltage across a single cell (2.4 V) and small energy density. However, they have the largest operating temperature range (-50°C to 70°C) and the largest number of full charge and discharge cycles to the agreed capacity loss value - reducing the initial capacity to 80% of the initial value.

These aspects are very important for the Solaris Bus & Coach company, which offers its products in many countries with different climate conditions. The operating conditions of urban buses, for example frequent starting and braking phases requiring the use of substantial torque, depending on the used battery charging method can significantly affect the deterioration of batteries, so it is important to keep it at the highest level. The maximum theoretical gravimetric (or volumetric) energy density for LTO batteries is quite small compared to competing solutions, but in the case of city buses the latter aspect is not as important. The batteries can be

ISBN: 978-1-61804-321-4

placed for example on the roof of the vehicle and by solutions in which they are often recharged (at the ends of the line), their capacity could be much smaller in comparison to the LFP batteries, which are used in buses with extended range on a single charge.

V. SUMMARY

The development of civilization brings with it a continuous increase in energy demand. Fuel consumption increases, which causes an increase in environmental pollution harmful exhaust gas components such as carbon monoxide (CO), carbon dioxide (CO_2), hydrocarbons (HC), nitrogen oxides (NO_x), and particulate matter (PM). The development of vehicle propulsion systems is therefore directed to the search for alternatives, which include primarily hybrid and electric drives. Such drives are characterized by favorable environmental and economic performance. The problem is caused by the properties of utilized batteries, which differ significantly from those of fossil fuels used on a large scale.

The subject of this study concerns the analysis of the existing concepts of lithium-ion batteries used in electric vehicles around the world. The development includes a presentation of innovative solutions that can improve the performance characteristics of alternative drives. In conclusion, the choice of LTO batteries as the main solution used by SBC has been justified.

REFERENCES

[1] L. Jaroszyński, Akumulatory litowe w pojazdach elektrycznych,“ Przegląd Elektrotechniczny 08/2011; 8:280-283.
[2] A123 Systems materials.
[3] KOKAM materials.
[4] Mercedes-Benz materials.
[5] J. Merkisz, P. Fuć, M. Bajerlein, P. Lijewski, Ł. Rymaniak, A. Ziółkowski, “The impact of application of photovoltaic cells for bus ecological properties”. Journal of KONBiN, 2012, no. 2 (22), p. 159-170.
[6] J. Merkisz, I. Pielecha, “Alternatywne napędy pojazdów, “ Wydawnictwo Politechniki Poznańskiej, Poznan 2006, p. 35-37.
[7] Page: http://www.toyota.pl/new-cars/prius/index.json, access:: 15.01.2015.
[8] Page: http://www.bosch-professional.com/, access: 1.03.2015.
[9] Page: http://samochodyelektryczne.org/, access: 15.04.2015.
[10] Page: http://www.batteryspace.com/Lithium-Titanate-Battery.asp, access: 1.02.2015.
[11] Page: http://www.ev-power.eu/LTO-Tech/, access: 12.05.2015.
[12] Page: http://www.batteryspace.com/lifepo4cellspacks.aspx, access: 17.02.2015.
[13] Page: http://www.homepower.com/lfp-precautions, access: 23.04.2015.
[14] Page: http://www.batteryspace.com/LiNiMnCo-Cells/Packs.aspx/, access: 17.05.2015.
[15] Page: http://batteryuniversity.com/learn/article/lithium_based_batteries, access: 24.05.2015
[16] Page: http://energy.gov/, access: 23.05.2015
[17] Page: http://www.greencarcongress.com/, access: 19.01.2015

Seamless multimodal journey planning merging private and public transport offers, the MyWay approach

Marco Boero, Marco Garré, Giovanni Casella, Michal Jakob, Stefano Persi

***Abstract*—**The European project MyWay will enhance journey planning and services for travelers facilitating personalized seamless integration of public and private transport modes into a single trip and making travelling around the city effortless, swift and pleasurable. Along with integrated booking information and real-time updates, all possible transport modes available will be presented to the user in an integrated fashion, thus encouraging the use of cleaner modes of transport.

***Keywords*—** multimodal journey planning, personalized mobility services, crowd sourcing, cloud services.

I. Introduction

FOURTEEN partners across seven EU countries shared the effort of designing and implementing the MyWay European Smart Mobility Resource Manager (MyWay).

MyWay aims to enable a better balance between public and transport modes, stimulate service cooperation and market development, enhance the personalization and user adaptation of mobility services and foster ICT transformative technologies in smart mobility.

ICT solution & service providers, research organizations, local authorities and stakeholders compose the Consortium, bringing the full range of knowledge necessary to achieve these objectives.

The project runs for 30 months until February 2016 with working prototypes validated in three different phases with real users across three 'Living Lab' Catalonia (Spain), Berlin (Germany) and Trikala (Greece). The evaluation will be performed by the end of 2015 through an iterative approach, which will increase in each phase the number of features available for the test users.

MyWay project is co-funded by the Seventh Framework Programme for Research and Development of the European Union.

Marco Boero is head of Research and Innovation at Softeco Sismat S.r.l., Genoa, Italy and coordinator of the project.

Marco Garré is a computer engineer and researcher at Softeco Sismat S.r.l., Genoa, Italy.

Giovanni Casella is a computer engineer and researcher at Softeco Sismat S.r.l., Genova, Italy.

Michal Jakob is deputy head of the Agent Technology Center at Ceske Vysoke Uceni Technicke v Praze, Prague, Czech Republic.

Stefano Persi is Co-founder and director at ENIDE, Barcelona, Spain.

II. Background

For many decades, mobility evolved around private car, causing many problems such as congestions, noise and pollution. Nowadays citizens can benefit from the presence of dense public transport and complementary transport modes, even non-motorized or zero-emission, from a variety of new sustainable and complementary mobility schemes, including just-in-time vehicle sharing, real-time carpooling, demand-responsive transport, Electric-Vehicles (EVs) sharing.

In addition, the amount of information available to travelers and related to their journey, also called context information, has greatly increased. Users can access real-time information about traffic conditions, weather forecasts, service disruptions or more in general context conditions that can potentially have an impact on their plan.

A complete integration of both mobility schemes and travel related information is, however, missing, making the car still the preferred alternative of many users.

In the MyWay Vision public and private transport mobility offers are holistically, seamlessly and efficiently combined, stimulating the market and service cooperation and finding the right compromise for each single traveler, offering a solution closest to each traveller's personal needs, preferences and real-time changing condition.

In these terms the frequent use of MyWay by the travelers will contribute to reducing congestionand GHG[1] emissions, thus improving air quality in European cities and encouraging the modal shift of European citizens.

The integration of all the mobility schemes and context information is addressed by the development of a technology platform, which integrates existing journey-planners through a meta-planner approach and provides pre-trip and on-trip advanced support services feeding mobile clients for the most used environments iOS and Android.

MyWay platform and mobile clients prototypes are tested in three different Living Labs: Catalonia/Barcelona (Spain), Berlin (Germany) and Trikala (Greece) (see Fig. 1 below). These three zones offers the possibility to test the MyWay prototype in different conditions in terms of size, mobility offers and habits, a perfect eco-system for the challenging objectives of the project.

[1] Green House Gas is a gas in an atmosphere that absorbs and emits radiation within the thermal infrared range causing the green house effect.

ISBN: 978-1-61804-321-4

Fig. 1 MyWay project Living Labs

III. The MyWay Technology Platform

The vision and concepts described in the previous section are addressed through the implementation and experimental validation of a technological platform whose high-level functional reference architecture is summarized in the following figure.

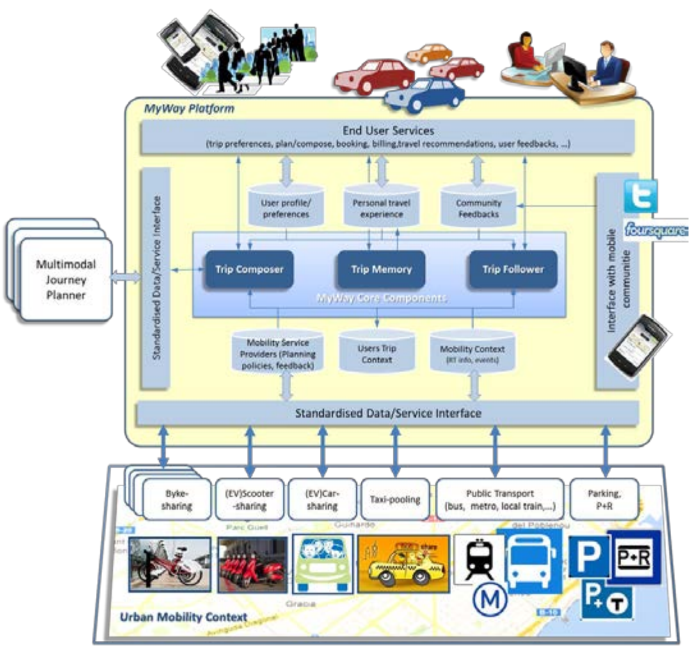

Fig. 2 MyWay High Level Functional Architecture

One of the objective of the designers of the MyWay architecture is to maximize the reuse of existing data and services. Nowadays, also thanks to the Open Data initiatives, the number of available datasets and service interfaces, both for data query or for journey calculation, has greatly increased.

Unfortunately, in most of the cases such data and services are offered using proprietary format or standards different from one provider to another. The MyWay platform feature an open interface, based on the multi-standard data and service model investigated in the eMOTION project [1] and validated in the European pilot projects In-Time [2] and Co-Cities[3].

The atomic data and services are consumed by the platform to enable the main innovations aspects of the MyWay platform. These innovations are linked with the three key MyWay core components: *TripComposer*, *TripMemory* and *TripFollower*, which are briefly presented in the following sections.

A. TripComposer Component

The *TripComposer* component implements all core logics required to combine travel options provided by existing journey planning services with public and private mobility solutions meeting user preferences and sustainability criteria. Giving the particular complexity of these concepts, the complete functionality is divided to several sub-components (*Preference Engine*, *Trip Meta-Planner* and *Mobility Resource Manager*) each responsible for providing an implementation of the specific single aspect.

The *Preference Engine* translates the initial human understandable high-level trip request made by the user into machine/low level trip planning query. The request is than elaborated by the *Meta-planner*, combining results from the existing journey planners (sub-planners), real-time information (context data from trusted sources and crowd source data) and negotiating the availability and the possibility to reserve a particular mobility resource through the *Mobility Resource Manager*. Each trip suggestion is finally composed, filtered if necessary, and sent back to the *Preference Engine* to score the individual trip suggestions against the profile and history of the user, enabling a highly personalized mobility experience to travelers.

B. TripMemory Component

The *TripMemory* component is responsible for storing the history of all trips and feedback, enabling the creation of a knowledge base crucial to offer and react fast to users' requests or to changing context conditions.

C. TripFollower Component

The *TripFollower* component offers on-trip monitoring facilities to the traveler, enabling situation-aware dynamic evaluation and re-planning capabilities to face any change in the user or transport context.

The modularity of the system, the loose coupling between components and the open design adopted in the early stage of the project, permit to offer a scalable system, supporting several deployment scenarios and ready to take advantage of the cloud environments available nowadays.

The services of the platform are exposed to the mobile clients, Android and iOS, developed within the project through an Open API. This Open API can be used in the future also by other B2C and B2B providers, enabling many different exploitation scenarios.

IV. An Example Use Case: Electrical Vehicle Sharing Service Integration

The core objective of integrating private and public mobility schemes is reinforced by the presence in the Consortium of local authorities and private mobility operators. For example in the Catalonia Living Lab the different transport modes are represented by the local government (Generalitat of Catalunia), the transport authority (Autoritat del Transport Metropolita) and by the local provider (Going Green) of a free-floating electric vehicle sharing service called Motit (see Fig. 3).

Fig. 3 A Motit Electrical Scooter

During the first months of the project, a total of sixteen scenarios have been elaborated in order to extract use-cases, functional and non-functional requirements used to guide the platform design, implementation and validation. Some of them are strictly related to the integration of mobility schemes. For example the Scenario S7, elaborated in Catalonia, states: "*Lluís often uses his own bike when travelling around Barcelona. Today he finds his bicycle has a puncture, but he is in a hurry to get to university. He uses MyWay to find out the state of shared bikes, and he can see there are many available bikes in slot near his house and it looks as if he will have no trouble returning the bike to a slot near his destination. He decides to go with the shared bike this morning, and fix his own later. At the end of the day, Lluís is tired but remembers that he still has to fix his puncture. He decides to find a faster way of getting home than using the shared bikes again. MyWay recommends electric scooter, which he has never used before. Lluís decides that it looks fun, and does not cost very much. He uses MyWay to book an electric scooter and arrives home with enough energy to fix his bike tire the same evening*".

In order to achieve the goal of integrating the services of this kind of mobility service, in the implementation phase the Consortium has conceived a model to describe it.

The main inputs considered in the TripComposer component were:

1. The operational area, in terms of bounding box, in which the service is available,
2. Within this area the description of sub-area characterized by their dimension and a probability of finding a vehicle in that sub-area with enough battery to serve the request.

This model has some consequences for the workflow of the operations/algorithm that is used to calculate trip suggestions to be proposed to the user:

1. after receiving the first request from the user the statistical data is used in order to propose or not the use of the mobility service to the user,
2. then if the user decide to take advantage of the suggestion, the booking process is started, assigning a specific resource (scooter) to the specific user.

This approach has two main advantages. First is a "disconnected" approach without the need to overload the external services while composing the trip. Secondly, permits to address the common use-case of "near-immediate" use of the booked resource. In this kind of service, a user can normally book a resource if it will use it immediately after the request, generally within the next 20-30 minutes [5]. The same concept is applicable to any other bookable resource, like for example a parking spot or a recharging station.

V. The MyWay Mobile Clients

The MyWay platform will be tested in the three Living Labs in three different test phases using the two mobile clients, for the two main platform Android and iOS, developed within the project.

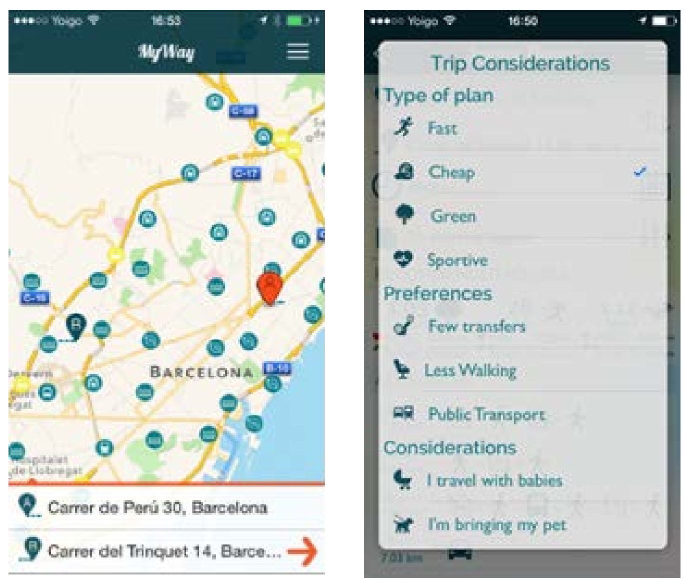

Fig. 4 Planning a trip

As briefly described in Section III, the mobile clients consume the RESTful services made available by the MyWay Platform through the Open API, and in particular to:

- User and Profile Management to permit the registration / login of the user and the modification of his/her profile.
- City Information which offer Location Based Services to get geo-localized information about the surroundings (e.g. Public Transport stop points, Parking, Point of interest)

- Trip planning services, using the profile and preferences of the user.
- Trip following capabilities, to follow the user in his/her trip and react in case of changing conditions.
- Feedbacks provision, to permit to users to express his/her judgement of the service/data or to report new context information (e.g. a traffic event near his/her position).

The application is designed around the trip planning functionality (see Fig. 4). All the other available function are related to this main service.

The user input his/her destination and origin, if different from the current position, and can sets some high-level preferences as the type of trip (Fast, Cheap, Green, Sportive) and some constraints (e.g. less walking, travelling with babies).

The request is sent to the MyWay platform, which in turn responds with some trip suggestions, giving also some more information about the estimated CO2 emission of the plan, the estimated KJ and where applicable also the estimated cost of the trip.

Fig. 5. Trip following active

After the selection of the trip, the user can opt-in to use the trip following functionality. Once activated the trip following screen is presented to the screen (see Fig. 5), showing to the user his/her current position. The application continuously feeds the MyWay Platform with the position/speed of the user, which is used together with the context information related to the specific trip (e.g. real time traffic conditions) to elaborate and propose to the user trip alternatives in case a better solution is found.

At the end of the trip, the arrival is automatically detected and the user is requested to express a feedback about the trip he/she just made (see Fig. 6).

This information is sent back to the MyWay platform and can be used by the system to improve the suggestion for the other users who are requesting a similar trip and also to improve future suggestion for the specific user taking into account his/her previous feedback.

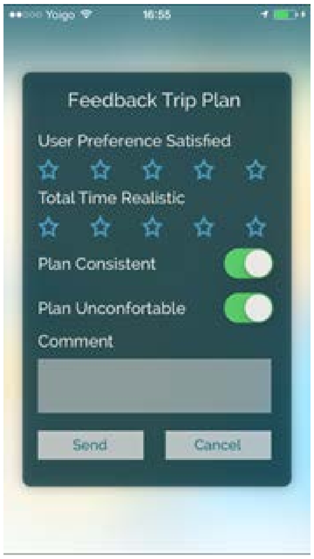

Fig. 6. Feedback about the trip plan

VI. Conclusion

This paper described the MyWay project that aims to create a European Smart Mobility Manager, co-funded under the European Seventh Framework Programme. The paper reports the technological solution developed underlining the innovative potential of integrating public and private mobility offerings through one of the use case, seamless integration and booking of free-floating Electric Vehicle sharing, being validated in the largest Living Lab of the project (Catalonia/Barcelona).

Further information can be obtained from the authors, the project website (http://www.myway-project.eu) or the the project coordinator Marco Boero, SOFTECO SISMAT Srl, Via de Marini, 1 – WTC Tower, 16149 Genoa. E-mail: marco.boero@softeco.it

References

[1] eMOTION FP6 project. http://www.emotion-project.eu
[2] In-Time ICT PSP project: http://www.emotion-project.eu
[3] Co-Cities ICT PSP project: http://www.co-cities.eu
[4] Motit service: http://www.motitworld.com
[5] Car2Go how does it works : https://www.car2go.com/en/austin/how-does-car2go-work/

Testing Different Charging Strategies and Energy Supply Modes for High Capacity Electric Buses in Live Operational Demonstrations

Umberto Guida, Pauline Bruge

The Zero Emission Urban Bus System [ZeEUS] project, co-funded by the European Commission's FP7 Programme and coordinated by UITP, aims to bring electrification to the heart of the urban bus network. Ten live urban demonstrations in nine European countries will test and validate a range of plug-in hybrid, full electric and battery trolley buses with fast and slow charging strategies with different energy supply modes. The results and experiences gathered will help support decision makers with guidelines and tools on 'if', 'how' and 'when' to introduce electric buses..

Keywords— **electric bus; fast/slow charging; charging infrastructure; energy supply modes; KPI**

I. INTRODUCTION

ZeEUS evaluates the economic, environmental, operational and societal feasibility of electric urban bus systems through live operational demonstrations across Europe using series and pre-series plug-in hybrid, full electric and battery electric trolley buses. The ten core demonstrations have varied geographic, climatic, environmental and operational conditions which enables the project to fully validate the performance of the buses and produce meaningful statistical evaluation through Key Performance Indicators [KPI]. ZeEUS is testing all of the available fast and slow charging strategies incl. overnight, terminal and opportunity charging with a range of energy supply modes: plug-in, inductive, conductive and overhead line. The paper will focus on seven out of the ten demonstrations, since three new cities have just joined the project and are currently preparing their entry in the evaluation process.

II. EVALUATING THE CORE DEMONSTRATIONS: KEY PERFORMANCE INDICATORS (KPIS)

One of the key objectives of the ZeEUS project is to provide decision makers with guidelines and tools to determine 'if', 'how' and 'when' to introduce electric bus systems in the core urban network. In the ten core demonstrations, buses are running in full revenue operation in a range of different geographical, climatic, environmental and operational conditions. Both low and high rate data collected across such different systems will produce statistically meaningful evidence.

The data will be collected from all demonstrations in the form of Key Performance Indicators and aggregately analysed. The methodology covered all aspects of the sustainability paradigm, along the Triple Bottom-Line (TBL) concept first articulated by Freer Spreckley in [1], and later more widely known in the form of "People, Profit, and Planet" by John Elkington [2], as the three pillars of sustainability.

Figure 1: the sustainability paradigm: the triple Bottom-Line of J. Elkington

Using this basis, the ZeEUS project identified the roots of the KPI tree for an electric bus system and each demo site selected their own KPIs from the pre-defined list. Indicators were to be selected in a way that they are usable for comparison in before-after analyses; therefore, they have to

[1]F. Spreckley, "Social Audit - A Management Tool for Co-operative Working", Beechwood College, UK, 1981, pp.47

[2]J.Elkington, "Cannibals with Forks: the Triple Bottom Line of 21st Century Business", Capstone Publishing, Oxford, UK..1st edition 1997, 2nd edition 1999, pp.424.

allow the measurement for different technological options, i.e., both the one currently in use and the demonstrated one, which will likely replace (or be an alternative to) the existing one. No single KPI was mandatory, but each demonstrator was able to choose the KPIs, depending on the characteristics of the implemented electric bus system (e.g., extension of the case, technologies applied, current operation, etc.). However, for the benefit of successful global and horizontal analysis between the demonstrators, as many common KPIs as possible was encouraged.

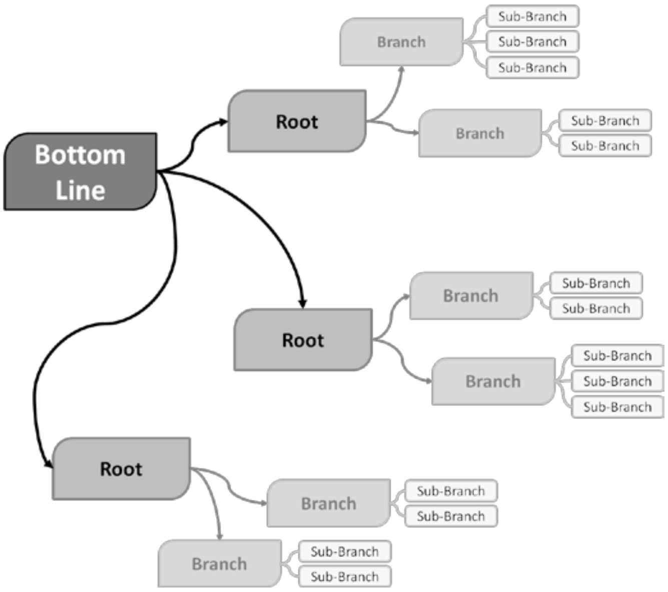

Figure 2: KPI Root Concept

When populating the KPI tree, the **independence** of each branch throughout the tree had to be guaranteed to prevent the overall analysis from being biased by the super-imposition of effects. Indicators needed to be independent from each other, i.e., not to bring the same information or represent partly or entirely the same performance. This means that the list of KPIs provided above could be grouped to meet this precondition.
The root was populated with further branches (in principle to be located under the current nodes), to cover the specific characteristics of the bus systems. When building the tree, one must also recognise that some parameters (to be measured) will reflect their behaviour in multiple indicators. As an example, one may consider passengers volume, which will be a component of the revenues, or energy efficiency, which will further influence costs, or the size of the investment, influencing even the leverage.
Eventually, the list of indicators had to be **exhaustive**, and had to prevent that other indicators, which cannot be reported or easily converted to the selected ones, are used in the performance analysis and evaluation of each demonstrator. Furthermore, the main criteria could be defined and allocated to separately assess all three essential areas of investments in an electric bus system, i.e.:

Infrastructure investments

- Vehicle investments
- Operation-based investments

The roots for the first bottom-line "**PEOPLE**" were chosen to entail the following roots: employment, quality of workplace and quality of (bus) service. These were the main categories that the joint evaluation team judged to be most relevant. Furthermore, each root was divided into two or more branches, as well as a number of subsequent sub-branches.

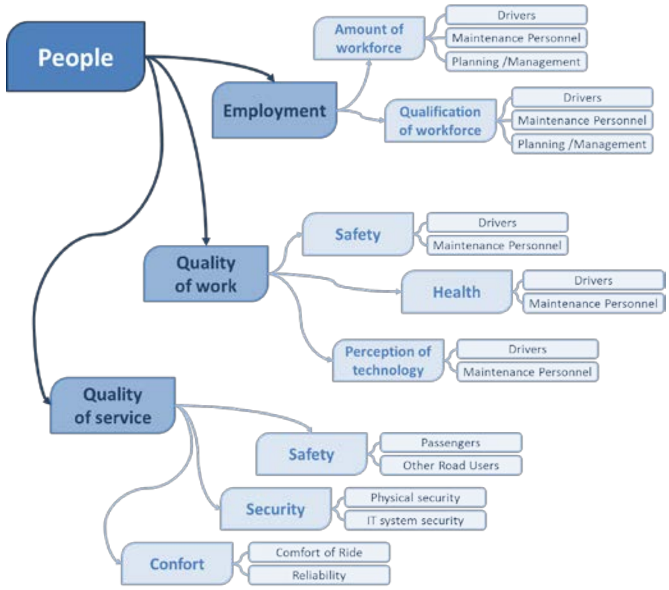

Figure 3: KPI Root 'People'

The second bottom-line "**PROFIT**" consists of investment costs (CAPEX) and operational costs (OPEX), but also from different types of revenue and items regarding financial sustainability.

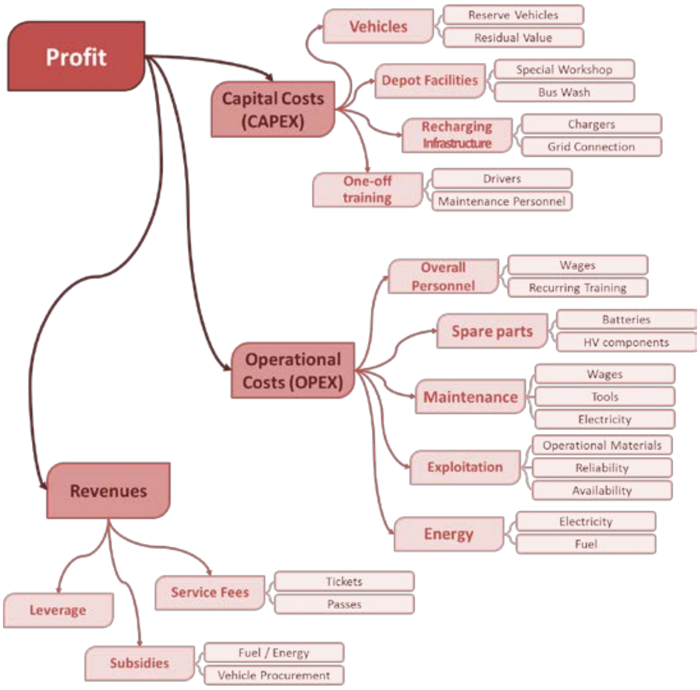

ISBN: 978-1-61804-321-4

Figure 4: KPI Root 'Profit'

Third bottom-line "**PLANET**" takes into account mainly the environmental consequences of building and operating electric buses and complete bus system. These consequences were determined to include various emissions, having an effect on global (GHG) or local level (NOx, PM, noise, EM). Production of hazardous waste is also an important issue, as the EV technology includes new materials of which some are potentially hazardous, if not properly treated. Furthermore, when the fleet goes all electric, many types of waste associated with ICE like used engine oils, will be wiped off totally.

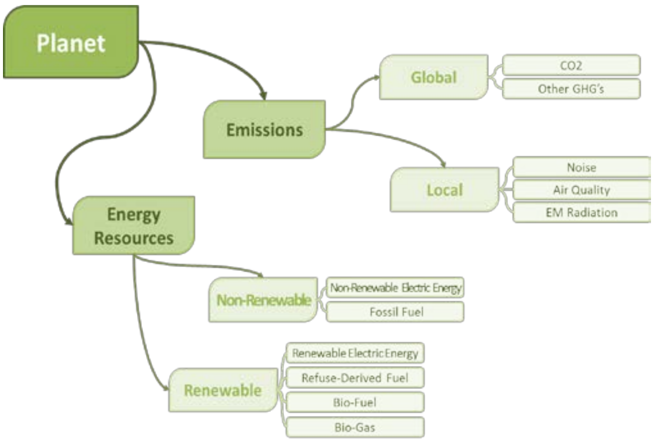

Figure5: KPI Root 'Planet'

III. Summary of Core Demo KPI Selection

As aforementioned, all of the core demonstrations were able to select which KPIs they wanted to use for the ZeEUS project. It was encouraged to select as many KPIs as possible from the maximum amount available so there are a broad number of KPIs that are selected by most or all demonstrations. The table below summarises the selection of the KPIs from the amount available by 7 out of the 10 demos:

	Root Root Segments			
	People (34)	**Profit** (42)	**Planet** (21)	**Total** (97)
Barcelona	31	38	19	88
Bonn	32	35	0	67
Cagliari	13	18	6	37
London	32	41	20	93
Muenster	31	41	20	92
Plzen	32	41	20	93
Stockholm	31	41	20	93

Table 1: Summary of the distribution of chosen KPI's in different ZeEUS demonstrations

As you can see from the table above all but two of the core demonstrations have selected most of the Key Performance Indicators that were available to them. Therefore, there will be many data sources that can be compared from one demo to another in varying operational conditions.

IV. Summary of Core Demo Charging Infrastructure Systems

The subsequent chapters of this abstract will provide detailed descriptions of the charging systems used in each core demonstration of the project but the Table 2 below summarises the main features of each:

Barcelona DC Slow charging overnight at the bus terminal.	**Bonn** DC Slow charging overnight at the bus terminal and AC fast charging at end stations via pantograph.
Cagliari Overhead contact line recharging (battery trolley bus) and slow DC charging at the depot.	**London** Wireless opportunity charging along the route.
Muenster Fast opportunity charging at end stations and bus depot via bus shelter to roof connection and stationary battery system	**Paris** Slow at depot (overnight) for entire day service (target) some fast recharging systems at terminals could be necessary
Plzen DC Slow charging overnight at the bus terminal and AC fast charging at end stations.	**Randstad** Various brands/types (procurement on-going), slow charging at depot (at terminal, could include battery swap), fast at terminals
Stockholm Fast opportunity charging via pantograph system at the roof of the bus. Additional slow charging at the bus depot	**Warsaw** slow at the depot (overnight); fast at terminals

Table 2: Summary of different charging technologies used in different ZeEUS demonstrations

V. Barcelona Demo

The electric bus used in the Barcelona demonstration is only charged overnight at the depot, and thus infrastructure at bus terminals is not necessary. The electric bus has to be charged in special places where the charging points and the cable from the charging station have to be supported from the specific technology. The charging station has to be installed to leave free space enough for worker, fulfilling the accident

ISBN: 978-1-61804-321-4

prevention rules. The charging station must be installed over 10 centimetres from the pavement to protect from the possible accidentally touching of the technicians and mechanics working around the bus. The charging schedule to charge more than 300 kWh will start when the bus arrives to the depot (after cleaning).

The electric vehicles will change somewhat the logistic protocol to repair the buses, because buses have to be charged during all of the night (4 hours minimum, depending on the energy consumed during the day). Therefore, Barcelona Demo has to plan the preventive and the corrective maintenance to take place during this charging process, and thus it is necessary to install the charging system near the place where the maintenance is made.

The charging station is based on a direct charging system using DC cable. Specifically, it is a Mode 4 charging system: EV indirect connection to the AC grid using an external DC charger. The plug type ensures that only a matching EV can be connected. Up to 400 A current is allowed.

The charger is composed of, amongst other things, the following elements:

- Power source. The power sources provide isolated current +16 VDC and +24 VDC.
- Forced ventilation. To cool the internals components.
- Line voltage transducer. To control the voltage of the inverter.
- Line current Transducer. To control the currents injected to the grid by the inverter.
- AC/D Varistors. Protection against voltage peaks.
- Transformer. To adjust the voltage between the output of the inverter and the grid.

Initially the charging system proposed for developing electric bus was electromagnetic induction. However, given the high cost of its associated infrastructure and its low deployment in real scenarios, it was decided to redirect development to a system of direct DC load. Moreover, there are many different charging options for electric vehicles based on conductive and inductive technology. However, most of these technologies are still currently under development. Conductive charging by charging cable was one of the first solutions developed by the industry and thus, constitutes nowadays the most mature technology for EV charging.

Table below lists the number of KPI’s eventually chosen by the Barcelona demo according to their operational conditions and research priorities:

	Root	**Proposed**	**Barcelona**
People	A.1 Employment	9	9
	A.2 Quality of Work	14	12
	A.3 Quality of Service	11	10
Profit	B.1 Capital Costs	17	16
	B.2 Operational Costs	16	16
	B.3 Revenues	5	4
	B.4 Financial Sustainability	4	2
Planet	C.1 Emissions	10	8
	C.2 Resources	11	11
Total		97	88

Table 3: Number of KPI’s chosen by the Barcelona demo.

VI. BONN DEMO

The charging of the buses will take place in the bus depot and the terminal stop Ramersdorf. Both charging opportunities will use DC charging. Whereas the charging in the bus depot Friesdorf will require a charging power of approx. 70kW, the charging power at the terminal stop Ramersdorf will be 200kW or more. The charging is to be realised using a pantograph mounted on the roof of the bus. The preferred technical solution is the Schunk smart charging system or a similar solution.

The pantograph system is to be used in both the bus depot and the terminal stop Ramersdorf. For the bus depot a system that is able to charge approx. two thirds of the whole bus fleet at once is planned. The charging stations in the bus depot will be connected to a special substation to be erected for charging battery buses as part of the wider transformation process. The substation as such will be connected to the 10KV grid that supplies the city of Bonn. In opposite to that the charging station at the terminal stop Ramersdorf, which will most likely have two charging opportunities, will be connected to an existing substation that already feeds the underground rail system. The charging approach consisting of both overnight charging in the bus depot and supplementary, opportunity charging at the terminal stop Ramersdorf has been chosen as the charging in the bus depot would not alone meet the energy demand of the buses because they have a daily mileage of up to more than 300 kilometres.

The table below lists the number of KPI’s eventually chosen by the Bonn demo according to their operational conditions and research priorities:

	Root	**Proposed**	**Bonn**
People	A.1 Employment	9	9
	A.2 Quality of Work	14	12
	A.3 Quality of Service	11	11
Profit	B.1 Capital Costs	17	17
	B.2 Operational Costs	16	14
	B.3 Revenues	5	4
	B.4 Financial Sustainability	4	-
Planet	C.1 Emissions	10	-
	C.2 Resources	11	-
Total		97	67

Table 4: Number of KPI’s chosen by the Bonn demo.

VII. CAGLIARI DEMO

The Cagliari demo tests and validates the use of trolleybuses as Zero Emission Vehicles [ZEV] off power grid conection using batteries instead of a diesel engine to produce the needed power. For this purpose a new line has been designed (Linea

ISBN: 978-1-61804-321-4

5-ZeEUS). During the service the trolleybus bus will operate off contact line for altogether 6 kilometers circa: 1.5 kilometer in the city center along the historical waterfront and a further 4.5 kilometers to reach the protected area of the Poetto Beach (a Natura 2000 site).

The batteries will be recharged during the operation in "normal condition" (directly from the overhead contact line) and in the new terminal (Ospedale Marino) where a new recharging station will be built. The charging power at the terminal stop will be 750 Vcc as for contact line. At the end of the services the trolleybus will reach the depot operating in autonomous way (off contact line) for 3 kilometer. In the depot the battery will also be recharged.

The table below lists the number of KPI's eventually chosen by the Cagliari demo according to their operational conditions and research priorities:

	Root	Proposed	Cagliari
People	A.1 Employment	9	7
	A.2 Quality of Work	14	2
	A.3 Quality of Service	11	4
Profit	B.1 Capital Costs	17	8
	B.2 Operational Costs	16	7
	B.3 Revenues	5	3
	B.4 Financial Sustainability	4	-
Planet	C.1 Emissions	10	6
	C.2 Resources	11	-
Total		97	37

Table 5: Number of KPI's chosen by the Cagliari demo.

VIII. London Demo

As part of the London demonstration, coordinated by Transport for London (TfL) with support from lead evaluation partners TRL and partners TTR, the use range-extended double decker electric buses will be demonstrated as part of an operation service.

It is intended that up to four range-extended electric buses will be introduced into the fleet for a provisionally selected route 69 in London. In order to maximise the electric-only range, these buses will be opportunistically charged throughout the day at the end-of-route terminals, using high-powered wireless charging. Like in Glasgow, wireless power transfer technology is selected due to practicality, safety and minimum additional infrastructure required compared with plug-in solutions. Similar charging infrastructure as in Glasgow will provide 100kW charging power, which will allow charging of the buses during short, end-of-route stops. However, in London the vehicles are expected to be in operation for at least 20 hours per day, covering a minimum average of 250km per day and completing large proportion of the route in an EV-only mode. The demonstration is expected to last for at least 24 months, at the end of which, the results shall aim to provide the necessary supporting information as to whether these type of electric buses should be rolled out across the wider bus fleet in London.

The table below lists the number of KPI's eventually chosen by the London demo according to their operational conditions and research priorities:

	Root	Proposed	London
People	A.1 Employment	9	9
	A.2 Quality of Work	14	12
	A.3 Quality of Service	11	11
Profit	B.1 Capital Costs	17	17
	B.2 Operational Costs	16	16
	B.3 Revenues	5	4
	B.4 Financial Sustainability	4	4
Planet	C.1 Emissions	10	9
	C.2 Resources	11	11
Total		97	93

Table 7: Number of KPI's chosen by the London demo.

IX. Münster Demo

The Münster demonstration is testing 5 full electric buses along the central bus line no. 14 that runs through the core city. Selected for its high visibility and popularity, it serves locations such as the central railway station, the zoo and the central cemetery and is used on average by more than 3000 passengers every day. Electrification of bus line no. 14 is part of an ongoing German R&D project, called "SEB", which lays the foundations for the complete bus route electrification.

For the latter, five electric buses are needed in order to keep up with the former timetable, originally designed for diesel buses. These electric buses are planned to fit fast charging requirements. Therefore the bus battery has to have the capability for high charge currents. Fast charging stations are situated on each end of the bus line and in the bus depot. These are part of the bus shelter design. The usual charging frequency on such a terminal stop is three times per hour and during the rush hour the charging time can be as short as 4 minutes. The coupling procedure is initiated wirelessly. The new developed pneumatic coupling mechanics have a certain tolerance range between bus and bus shelter, which simplifies the positioning process of the vehicle. Once the bus is connected to the station, the conductive charging and the CAN communication are initiated. The key feature of the demonstrated concept is a unique, fast charging power of up to 500 kW, which - if charging endures only 4 minutes - equals an energy throughput of 33 kWh.

ISBN: 978-1-61804-321-4

The demonstration activities in Münster further employ a stationary battery storage unit to study the related grid interaction. The impact on the grid is caused by the massive energy amount, drained by the bus in a short time. Different load conditions, on both supply and demand sides, are buffered by the stationary battery as fast charging plays a dominant role in this application.

The table below lists the number of KPI's eventually chosen by the Münster demo according to their operational conditions and research priorities:

	Root	Proposed	Münster
People	A.1 Employment	9	9
	A.2 Quality of Work	14	12
	A.3 Quality of Service	11	10
Profit	B.1 Capital Costs	17	17
	B.2 Operational Costs	16	16
	B.3 Revenues	5	4
	B.4 Financial Sustainability	4	4
Planet	C.1 Emissions	10	9
	C.2 Resources	11	11
Total		97	92

Table 8: Number of KPI's chosen by the Münster demo.

X. Plzen Demo

The objective of ZeEUS project is to test in real conditions the new line of electric buses which are currently under development in Skoda Electric a.s.. The city of Pilsen has a long historical record of using Skoda´s tramways and trolleybuses. Pilsner Urban Transport Authority ("PMDP") has the responsibility for the operation of city transport composing of trams, trolleybuses and buses. It mean that 2/3 of public transport is already provided by zero emission vehicles. Notwhitstanding, The switch from diesel buses to pure electric buses is still considered as a landmark in Plzen's and Skoda´s common history. To create the best background for the demonstration project, a handful of key-role players have set their intent to create a consortium to prepare all necessary steps. Besides the aforementioned, the local energy provider company Plzenska Teplarenska a.s. and the PMDP a.s. and West Bohemian University form the entire demo team.

Two vehicles operate in the ZeEUS project and are 12m long electric-only battery buses. The electricity is used for propulsion, air-conditioning and heating system. The recharging facility is based on DC current. The charging power is delivered via external charger. Thanks to this philosophy of recharging equipment it is possible to save weight of the vehicle and also share the recharging equipment with other vehicles in order to reduce the cost. For the cable charging, DC Combo 2 couplers are used. For fast charging, contacting via roof contacts is utilised.

The charging power DC is up to 600 kW. If maximal charging power is used, a fully discharged vehicle can be recharged within circa 5-8 minutes. When the vehicle is close to the charging station, a screen with the charging visualisation is displayed on the driver's dashboard. During the charging process the vehicle controls the process and the charging station acts in a subordinate manner. The vehicle permanently sends the requirements of charging power, with the charging station following these requirements. When the final state of batter charge is achieved, the charging process stops automatically, and the pantographic system disconnects from the vehicle. When the pantographic system is back in safe position, the driver is informed, movement of the vehicle is again allowed, and the vehicle leaves the area of the station. The charging station is connected to the 22 kV grid and is galvanically insulated and an insulation monitor device is used.

Table below lists the number of KPI's eventually chosen by the Plzen demo according to their operational conditions and research priorities:

	Root	Proposed	Plzen
People	A.1 Employment	9	9
	A.2 Quality of Work	14	12
	A.3 Quality of Service	11	11
Profit	B.1 Capital Costs	17	17
	B.2 Operational Costs	16	16
	B.3 Revenues	5	4
	B.4 Financial Sustainability	4	4
Planet	C.1 Emissions	10	9
	C.2 Resources	11	11
Total		97	93

Table 9: Number of KPI's chosen by the Plzen demo.

XI. Stockholm Demo

The fast charging equipment for the Stockholm-demonstration consists also of a pantograph solution on a separate charging pole for charging connection at the roof of the bus and the specific bus charger transformer & inverter equipment in a separate housing at both bus route end stations. The fast charging equipment will be connected to the local low voltage grid sub-station via a three phase 400 V_{AC} supply line. The charging station DC power supply to the buses is designed at 600 V DC and 150 kW. The chosen charging technology is due to commercial agreements between Volvo Buses and the charging technology supplier. The charging equipment at the end stations will be procured and installed by Vattenfall Services Nordic and AB Storstockholms Lokaltrafik (SL) will be responsible for the procurement and installation of the additional over-night slow charging equipment at the bus depot.

ISBN: 978-1-61804-321-4

The table below lists the number of KPI's eventually chosen by the Stockholm demo according to their operational conditions and research priorities:

	Root	Proposed	Stockholm
People	A.1 Employment	9	9
	A.2 Quality of Work	14	12
	A.3 Quality of Service	11	11
Profit	B.1 Capital Costs	17	17
	B.2 Operational Costs	16	16
	B.3 Revenues	5	4
	B.4 Financial Sustainability	4	4
Planet	C.1 Emissions	10	9
	C.2 Resources	11	11
Total		97	93

Table 10 Number of KPI's chosen by the Stockholm demo.

XII. CONCLUSION

As stated, the key objectives of the ZeEUS project is to provide decision makers with guidelines and tools to determine 'if', 'how' and 'when' to introduce electric bus systems in the core urban network. The ZeEUS project is not going to perform a benchmark between the different solutions tested due to two main reasons:

Firstly, direct experiences and analysis done in past project like the European Bus System of the Future (EBSF), shows that one single technology solution for urban electric bus systems suitable for every operational and environmental condition does not exist, due to the large difference in terms of geographical, climatic, environmental and operational conditions. EBSF showed that every technical solution has its optimal place for operation.

Secondly, the public transport authorities of each city will take the decision about the electric bus solution to be implemented based on the Total Costs of Ownership (TCO). Today a single accepted model of TCO adopted by each city does not exist. Similarly for cost-benefit analysis, each city has developed its "trusted" model. For this reason, the aim of ZeEUS is to provide a set of data-set (aggregated measures statistically meaningful, for example) that could be used by the different cities to validate their model.

ZeEUS is the first project of its kind to test and validate a wide range of electric bus technologies with different fast and slow charging strategies and energy supply modes. Not only will the buses run in full operational conditions, but they will run in varying geographical climatic and operational conditions across the different demonstration sites that will bring invaluable results and experiences. Such information will support ZeEUS' mission as the flagship electric bus project in Europe to bring electrification to the heart of the urban bus network.

XIII. ACKOWLEDGMENT

The ZeEUS partners, the Technical Management Team and the following people contributed to the ZeEUS paper. They are as follows:

A. Freixas Mercadé, IDIADA Automotive Technology SA

D. Naberezhnykh, TRL Limited

F. Marangon, D'appolonia SPA

L. Spante, Vattenfall Research and Development AB

M. Winter, RWTH Aachen, Institute for Power Electronics and Electrical Drives

P. Kuch, SKODA Electric AS

T. Knote, Fraunhofer

Model of washed out component concentration field in biopolymer studied particularly at the start of bath washing

Hana Charvátová, Dagmar Janáčová, Miloslav Fialka, Karel Kolomazník, Rudolf Drga, and Ondrej Líška

***Abstract*—**In the paper we deal with a computer simulation of removing bound component from biopolymer into the wash liquid during bath washing process. In this case, formulated mathematical model of transport of washed out component in the biopolymer is described by Fick's second law with the relevant initial and boundary conditions. Its analytical solution was derived in the form of series. For some calculations can series slowly converge in the short times of washing. This can occur, for example, by computer simulation of the bound component washing from biopolymer of large size or if the removed components are strongly bonded to the structure of the biopolymer, etc. To avoid this potential situation, we focused on study of influence of the time near to zero when difference between the modelled and the real course of washed out component concentration field in the biopolymer can occur.

In contribution we present the test to find a simple condition that defines a certain start time, by which the space-time washed out component concentration field course in a model will be corresponding to the studied real process.

***Keywords*—**Equation of diffusion, mathematical model, bath washing, washed out component, concentration field, start time of bath washing, coincidence criterion, system Maple.

The work was performed with financial support of research project NPU I No. MSMT-7778/2014 by the Ministry of Education of the Czech Republic and also by the European Regional Development Fund under the Project CEBIA-Tech No. CZ.1.05/2.1.00/03.0089.

H. Charvátová, Tomas Bata University in Zlín, Faculty of Applied Informatics, Regional Research Centre CEBIA-Tech, nám. T. G. Masaryka 5555, 760 01 Zlín, Czech Republic (e-mail: charvatova@fai.utb.cz)

D. Janáčová, Tomas Bata University in Zlín, Faculty of Applied Informatics, Department of Automation and Control Engineering, nám. T. G. Masaryka 5555, 760 01 Zlín, Czech Republic (e-mail: janacova@fai.utb.cz)

M. Fialka, Tomas Bata University in Zlín, Faculty of Applied Informatics, Department of Mathematics, nám. T. G. Masaryka 5555, 760 01 Zlín, Czech Republic (e-mail: fialka@fai.utb.cz)

K. Kolomazník, Tomas Bata University in Zlín, Faculty of Applied Informatics, Department of Automation and Control Engineering, nám. T. G. Masaryka 5555, 760 01 Zlín, Czech Republic (e-mail: kolomaznik@fai.utb.cz)

R. Drga, Tomas Bata University in Zlín, Faculty of Applied Informatics, Department of Security Engineering, nám. T. G. Masaryka 5555, 760 01 Zlín, Czech Republic (e-mail: rdrga@fai.utb.cz)

O. Líška, Technical University of Košice, Mechanical Engineering Faculty, Department of Automation, Control and Human Machine Interactions, Letná 9, 042 00 Košice, Slovak Republic (e-mail: ondrej.liska@tuke.sk)

I. Introduction

Bath washing belongs to technological operations, which are often used in processing of natural polymers, when it is necessary to remove undesired component from a biomaterial, such as e.g. particles of various impurities or other substances which would complicate further processing operations, the quality of the final products, etc.

To study of these processes, under which it is possible to design an optimal technological procedure of washing in order to reduce operating costs and environmental burdens, are used except for the experimental testing in laboratory and pilot plant conditions also assembled computer simulations of mathematical models describing the washing process for specific initial and boundary conditions [1], [2].

But most of diffusion processes such as washing is difficult to mathematically described, because it is influenced by a number of specific conditions. In many cases, analytical solution can not be found and the need to seek solutions to numerical calculations. However, if the analytical solution can be found, it is often preferable to numerical solutions because of its greater accuracy and versatility of use. The analytical solutions of model of washing processes that we study in our department are derived in the form of a series [4]. The accuracy of these solutions is always influenced by the accuracy of simplifying the conditions introduced during the formulation of the mathematical model, and by selecting the number of terms of the sequence in the actual solution. With the increasing number of members increases accuracy of the solution. By computer simulation of the bound component washing from a biopolymer of large size, by using a small volume of wash liquid to the volume of biomaterial or if the removed components are strongly bonded to the structure of the biopolymer, etc., can series slowly converge in the short times of washing, which causes difference between the modeled and the real course.

To avoid these potential differences, we performed a test to find a simple condition that certain defines a start time, by which the space-time washed out component concentration field course in a model will be studied when corresponding to the real process.

II. Equation of Diffusion and its Use at Bath Washing

We present the following model of bound component bath washing and their solutions in the contribution.

Consider a three-dimensional space region Ω of all points (x, y, z), in which diffuses a certain mass substance. In our case the substance is represented by washed out component. The situation is described by the sought function $c(x, y, z, \tau)$ which defines the concentration of washed out component which diffuses out from the biopolymer owing to the penetrating liquid from the surrounding bath into the biopolymer. Above mentioned concentration represents the mass of investigated substance in the unit of volume at the point (x, y, z) and the time τ.

The flux density of substance w depends in general case not only on the position and time but also on the unit normal vector $\boldsymbol{n} = (n_1, n_2, n_3)$ of the surface $\partial\Omega$ across that considered substance diffuses. It is well known that the flux density of substance w also depends on the vector function ∇c called gradient of the concentration $c(x, y, z, \tau)$,whereas the substance diffuses from the positions having a higher concentration to the positions having a lower concentration, i.e. always in the opposite direction of concentration gradient. By linearization of that dependence we obtain for the case of isotropic homogeneous immobile surrounding Fick's first law [5]:

$$w = -D\nabla c\left(x,y,z,\tau\right)\cdot \boldsymbol{n} = -D\ \frac{\partial c\left(x,y,z,\tau\right)}{\partial \boldsymbol{n}} = -D\ \left(n_1\frac{\partial c\left(x,y,z,\tau\right)}{\partial x} + n_2\frac{\partial c\left(x,y,z,\tau\right)}{\partial y} + n_3\frac{\partial c\left(x,y,z,\tau\right)}{\partial z}\right) \tag{1}$$

where D is the diffusion coefficient and $\partial c\left(x,y,z,\tau\right)/\partial \boldsymbol{n}$ is the directional derivative of $c(x, y, z, \tau)$ with respect to (otherwise in direction) $\boldsymbol{n}$. This derivative is also called the outward normal derivative of the function $c(x, y, z, \tau)$ on the boundary $\partial\Omega$ of region Ω. Hence it is possible to obtain (by integrating and then passing to a limit) diffusion equation - Fick's second law [5]:

$$\frac{\partial c\left(x,y,z,\tau\right)}{\partial \tau} - D\Delta c\left(x,y,z,\tau\right) = 0\,, \qquad (x,y,z)\in\Omega\ , \quad \tau > 0\,,\tag{2}$$

where

$$\Delta = \nabla^2 = \left(\frac{\partial}{\partial x},\frac{\partial}{\partial y},\frac{\partial}{\partial z}\right)^2 = \frac{\partial^2}{\partial x^2}+\frac{\partial^2}{\partial y^2}+\frac{\partial^2}{\partial z^2}\,. \tag{3}$$

Δ is Laplace operator. Such equation is said to be equation of evolution or evolutionary equation, i.e. the equation includes some partial derivatives with respect to time-variable τ, e.g. the first order derivative $\partial c\left(x,y,z,\tau\right)/\partial\tau$ of the sought function $c(x, y, z, \tau)$ with respect to time τ. We say that the equation describes behavior of studied system as time-dependent phenomenon, in other words, the behavior of evolution of process. Our equation is the partial differential equation of the second order of the parabolic type and describes the diffusion of mass particles in space.

But equation in itself is not sufficient for modelling of a specific physical problem. The partial differential equation that is assumed to describe some law governing the evolution of a certain system possesses many solutions in principle. Therefore it is necessary to add subsidiary boundary conditions to the equation and in case of the evolutionary equations also to add the initial conditions. It is worth noting that diffusion problems, which differ from each other only by their auxiliary conditions at the same diffusion equation, represent completely separate and often significantly different mathematical problems in general.

III. Basic Concepts and Notation for Mathematical Model of the Biopolymer Bath Washing Process

The model is destined for description and solution of washing out of undesirable bound component from biopolymer into the wash liquid during washing process.

In this process, the solid phase – the biopolymer is put into the wash liquid water. The washing water neither flows in nor flows out the bath. We consider, for simplification, the bound component content in biopolymer is lower than its solubility in the same volume of wash liquid at the given temperature and the influence of flanges on diffusion inside of the biopolymer sample is neglectable. Under these assumptions we can formulate one-dimensional space model of bath washing of biopolymer by diffusion model of transport of washed out bound component of the biopolymer by means of partial differential equation (4) of parabolic type with following initial boundary conditions. The conditions ensure existence and unicity of solution of the undermentioned problem.

The solution of model is given by the field of concentration $c(x,\tau)$ of washed out component on half-stripe domain $G = \left\{ \left(x,\tau\right) \in \mathbf{R}\times\mathbf{R}^{+} \ \middle|\ 0\le x\le b\ ,\ \tau>0 \right\}$.

We want to find the concentration $c(x,\tau)$ which satisfies the initial boundary problem.

Diffusion of washed out component from biopolymer in the direction of liquid bath represents equation (4) [6]:

$$D\frac{\partial^2 c\left(x,\tau\right)}{\partial x^2} = \frac{\partial c\left(x,\tau\right)}{\partial \tau} + \frac{\partial c_A\left(x,\tau\right)}{\partial \tau}\,, \quad 0\le x\le b\,, \quad \tau>0\,. \tag{4}$$

The expression of the right hand side last therm of equation (4) depends on desorption mechanism of washing out component from biopolymer. Suppose that diffusion is determining for change rate of concentration, it is possible to express the dependence of $c_A(x,\tau)$ (of bound component) on the free component $c(x,\tau)$ by relation of Langmuir’s sorption isotherm. Suppose that considered concentration $c(x,\tau)$ of washed out component is very low, we can define domain in which sorption isotherm comes into the linear form [6]:

$$c_A(x,\tau) = A \cdot c(x,\tau)\,. \tag{5}$$

Initial distribution of washed out component concentration in biopolymer shows condition (6):

$$c(x,0) = c_p\,. \tag{6}$$

We will also suppose that concentration field of washed out component in biopolymer is symmetric. Then it holds:

$$\frac{\partial c}{\partial x}(0,\tau) = 0\,. \tag{7}$$

Relation (8) holds under condition of a perfectly mixed wash liquid :

$$c(b,\tau) = \varepsilon \cdot c_0(\tau)\,. \tag{8}$$

Balance condition (10) denotes the equality of the diffusion flux at the boundary between the solid and wash liquid with the speed of accumulation of the diffusing element in the surrounding.

$$\frac{\partial c}{\partial x}(b,\tau) = -\frac{V_0}{D \cdot S} \cdot \frac{\mathrm{d}c_0(\tau)}{\mathrm{d}\tau}\,. \tag{9}$$

We will also suppose that the washed out component is not present in the wash liquid at the beginning of washing:

$$c_0(0) = 0\,. \tag{10}$$

For simplification of solution of equation (5) with additional conditions (6 – 10) were introduced dimensionless variables:

$$C(X,Fo) = \frac{c(x,\tau)}{c_p}\,,\ Fo = \frac{D \cdot \tau}{b^2 \cdot (1+A)}\,,\ X = \frac{x}{b}\,,\ Na = \frac{V_0}{V}\,.$$

(11 a, b, c, d)

The analytic solution was obtained by means of Laplace transformation Final solution given by dimensionless concentration field of washed out component in biopolymer $C(X,Fo)$ holds [6]:

$$C(X,Fo) = \frac{\varepsilon(1+A)}{\varepsilon(1+A)+Na} - $$
$$-2Na \cdot \sum_{n=1}^{\infty} \frac{\cos(q_n X)\exp(-q_n^2 Fo)}{\varepsilon(1+A)\cos(q_n) - \dfrac{\varepsilon(1+A)}{q_n}\sin(q_n) - Na\, q_n \sin(q_n)}$$

(12)

where q_n is the n-th positive root of transcendent equation (12):

$$-\frac{Na \cdot q}{\varepsilon(1+A)} = \tan(q)\,. \tag{13}$$

The symbols mean:

- A - sorption constant (from Langmuir sorption isotherm), [1];
- b - half thickness of solid phase (i.e. biopolymer) , [m];
- C - dimensionless volume concentration of washed out component in biopolymer, [1];
- c - concentration of washed out component in biopolymer, [kg·m^{-3}];
- c_p - initial concentration of washed out component in biopolymer, [kg·m^{-3}];
- c_A - concentration of bound component in biopolymer, [kg·m^{-3}];
- c_0 - concentration of washed out component in bath, [kg·m^{-3}];
- D - effective diffusion coefficient of washed out component from solid phase, [m^2·s^{-1}];
- Fo - Fourier number (dimensionless time), [1];
- Na - dimensionless volume of wash liquid , [1];
- q_n - n^{th} root of a certain transcendent equation, [1];
- n - number of terms of series in numerical model of washed out component concentration in biopolymer, [1];
- S - area of biopolymer, [m^2];
- τ - time, [s];
- V - volume of biopolymer, [m^3];
- V_0 - volume of wash liquid , [m^3];
- X - dimensionless space coordinate, [1];
- x - space coordinate, [m];
- ε - porosity (ratio of pores volume to biopolymer volume), [1];

IV. Some Important Results from Theory

Diffusion equation describes irreversible phenomena with infinite propagation velocity of concentration change of diffusing substance.

This is physically impossible. The paradox is caused by the fact that the phenomenological approach has been used rather than the qualitative theory upon deriving the equation of diffusion taking into account the energy of vibrating molecules.

ISBN: 978-1-61804-321-4

We encounter the so-called smoothing effect here, that is, the solution is infinitely differentiable in both space and time variables for all $\tau > 0$ even if there is a singularity, such as a jump discontinuity, in the initial function. The so-called characteristics of diffusion equation are represented by the lines $\tau = const$. It has been proved in mathematics that behavior of a function satisfying the diffusion equation (here it is the concentration field in biopolymer) may be significantly different from reality near the characteristic $\tau = 0$ in general.

Anyway, the equation of diffusion gives a good insight into the diffusion phenomenon and has proved relatively satisfactory in practice, although the classical diffusion equation provides just approximate description of diffusion.

V. Motivation to the Introduction of a Coincidence Criterion of the Evolutionary Model with Real Process

During the study of washing process we observed that the used model is characterized by a distinctive oscillating feature of concentration field $c(x,\tau)$ around the highest possible initial concentration c_p in dependence on the space variable x until a certain time, in other words, in dependence on distance from the centre of biopolymer. In reality, the concentration should monotonically decrease on a concave curve with increasing distance and in addition the oscillating values should not exceed c_p. Oscillatory feature appears at time $\tau \approx 0$ most often and from the mathematical point of view it is caused by the cosine term $\cos(q_n X)$ of series (12).

For the assessment of dimensionless Fo_{start} and real τ_{start} respectively initial time of compatibility, by which we consider the real process course to be coincident with a mathematical model, we formulated the following criterion.

VI. Criterion of Coincidence or a Good Accordance of Concentration Field Evolutionary Model in Biopolymer with Real Process of Bath Washing since the Certain Start Time

Let us substitute the theoretical model of the concentration field $C(X,Fo)$ given by the infinite functional series (12) by using the corresponding numerical approximation with the finite sum of n terms of this series and let us briefly call this approximation "concentration field model" in the following text.

Let us represent that model with some 3D graphics. Let further $n, Na, \varepsilon, A, b, D$ be the constants. Then we say that the displayed 3D model is coincident with the real washing process with used graphics only from an instant of the start time Fo_{start} of already running washing process when the corresponding 2D model of concentration field $C(X,Fo)$ at time Fo_{start}, that is the concentration

$$C(0 \le X \le 1, Fo = Fo_{\text{start}}) \tag{14}$$

represented by function of one independent variable X satisfies the following coincidence condition

$$C(0 \le X < 0.9, Fo = Fo_{\text{start}}) \le 1.000005$$

and

$$C(0.9 \le X < 1, Fo = Fo_{\text{start}}) \le 0.999999 \qquad \text{(15 a, b)}$$

The figures follow, which represent the dimensionless 2D and 3D concentration field courses at chosen value of the sorption constant *A.* Besides the constant Fo there is also the corresponding real time τ.

In the Fig. 1 is shown concentration field of washed out component in biomaterial at the bath washing as 3D plots. Near the dimensionless time $Fo = 0$ are evident oscillations of the concentration field. For the calculation, we used the following parameters: $A = 6$, $D = 2.10^{-9}$ m^2/s, $\varepsilon = 0.5$, $Na = 2$.

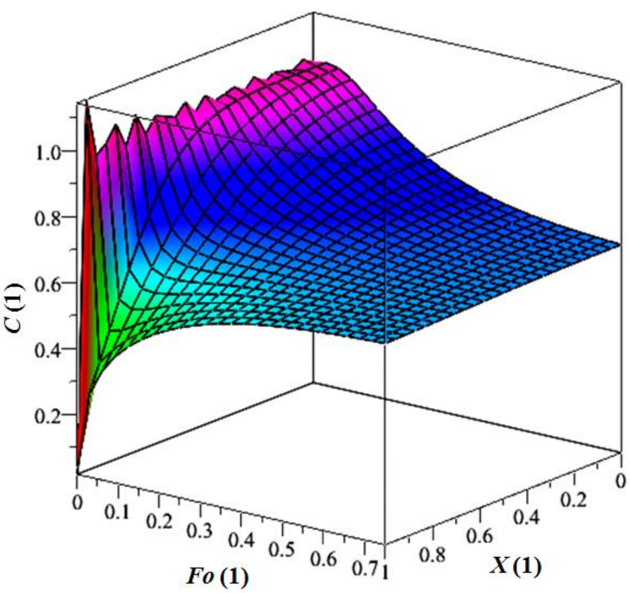

Fig. 1 concentration field of washed out component in biopolymer

Fig. 2 shows the concentration fields of washed out component in biomaterial at selected times of washing. In the left plots, the red curve shows the limit progress in dimensionless time $Fo = 0.00008$, which satisfies the condition (15). The right graph in Fig. 2 shows a detail of the concentration field in the limit dimensionless time.

As we mentioned, the time limit Fo_{start} or τ_{start} depends on the specific conditions of the washing process. An important factor in this regard is fixing power of washed out component in the structure of biopolymer, which is given by the value of sorption constant *A*. In our example, when the value of sorption constant $A = 6$, the limit time $\tau_{\text{start}} = 1$ s. With increasing values of the constants *A* time limit is increased. For example, for $A = 60$ is considered the conditions $\tau_{\text{start}} = 9$ s, for $A = 600$ is $\tau_{\text{start}} = 91$ s.

ISBN: 978-1-61804-321-4

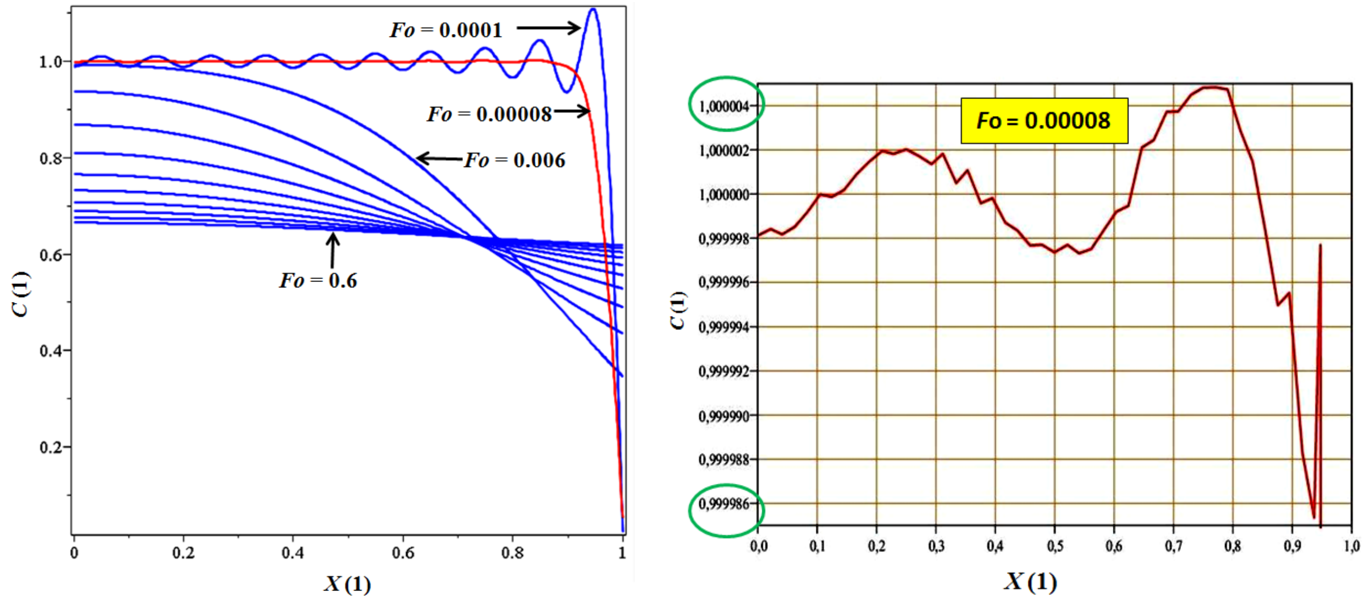

Fig. 2 concentration fields of washed-out component in biopolymer at selected times of washing. In the left plot, the red curve represents a curve in the limit dimensionless time, which satisfies the condition (15). The right plot shows a detail of the concentration field in the limit dimensionless time.

VII. Conclusion

In the contribution we presented the condition to find a certain practical criterion that defines a start time, by which the space-time concentration field course in an applied numerical solution model will be regarded as corresponding to the studied real process. We show that one possibility for the formulation of such a practical criterion is sufficient use 2D course of concentration field which depends at so called start time only on space distance from the centre of biopolymer and in which the concentrations otherwise still oscillate due to the cosine term in model, however their course already is not too in contradiction with the real process.

The time during which oscillations of function can occur depends on specific conditions of the washing process, mainly on the thickness of the biopolymer and diffusivity.

The problem with the oscillations of the function occurs for fast processes. The processes by which we deal with in our department are slow, thus oscillations can occur only at the beginning of the process.

References

[1] D. Janáčová, “Modeling of Extraction Processes“, (in Czech), Habilitation work, Tomas Bata University in Zlín, Zlín, 2003.

[2] D. Janáčová, et al., “Washing Processes Optimization”, in *Proceedings of International Union of Material Technologists and Chemists Societies*, London, 1997.

[3] K. Kolomazník, D. Bailey, and M. M. Taylor, “Deliming of un-bonded and bonded lime from white hide”, *Journal of American Leather Chemists Association*, vol. 102, 2007.

[4] D. Janáčová, H. Charvátová, K. Kolomazník, and V. Vašek, *Creating software applications for solving diffusion problems in the MAPLE interface*. (in Czech), Zlín: Tomas Bata University in Zlín, 2012.

[5] J. Crank, *The Mathematics of Diffusion*. Oxford: Clarendon Press, 1975.

[6] K. Kolomazník, et al., *Modeling of dynamical systems*. (in Czech), Brno: VUT Brno, 1988.

[7] H. Charvátová, “Modeling of Pelt Chemical Deliming”, (in Czech), Ph.D. dissertation, Tomas Bata University in Zlín, Zlín, 2007.

[8] D. Janáčová, H. Charvátová, K. Kolomazník, and V. Vašek, *Creating software applications for solving diffusion problems in the MAPLE interface*. (in Czech), Zlín: Tomas Bata University in Zlín, 2012.

[9] D. Janáčová, V. Vašek, and K. Kolomazník, “The cost function for extraction of bound component from material“, in *Latest Trends on Systems*, Volume II, Rhodes: Europment, 2014, pp. 395-398.

ISBN: 978-1-61804-321-4

Calculation of heat losses of the room with regard to variable outside air temperature

Hana Charvátová, and Martin Zálešák

Abstract**—**The paper deals with testing of thermal stability of a room. It describes the possibilities to determine the heat losses of the room with respect to a variable outside air temperature. For the theoretical calculation of heat losses was used running mean of outside air temperature. The calculated heat flux values were compared with the data obtained by computer simulation of the same process in the COMSOL Multiphysics software. The proposed procedure for determining the heat loss of the room will be used for testing of heat accumulation parameters of the building.

Keywords—Calculation of heat losses, computer simulation, temperature distribution in the room, running mean external temperature, daily mean temperature.

I. Introduction

REDUCING of energy consumption and the use of renewable energy in buildings are necessary to reduce energy dependence and greenhouse gas emissions. According to the Directive of the European Parliament and Council Directive 2010/31/EU on the energy performance of buildings should have all new buildings almost zero energy consumption since December 31, 2020. The new buildings occupied and owned by public authorities must comply with these requirements since December 31, 2018 [1].

To comply aim at 2018 and 2020 for the energy consumption of buildings, the Czech Republic have introduced arrangements under which must be from January 2013, anyone who wants to sell or rent their property, or who builds or makes greater structural adjustment Building energy performance certificate.

Part of each energy certificate (label) the property must be a graphical representation of energy performance, protocol and classification into one of the seven existing classes (A - G). Performance Class A is very efficient, and the demands of class G is extremely wasteful vice versa. The card has also assessed how much energy consumed comes under heating, lighting, water heating, ventilation and cooling [2], [3].

To comply aim at 2018 and 2020 for the energy consumption of buildings in the Czech Republic have introduced arrangements under which must be from January 2013, anyone who wants to sell or rent their property, or who builds or makes greater structural adjustment Building energy performance certificate.

Part of each energy certificate (label) the property must be a graphical representation of energy performance, protocol and classification into one of the seven existing classes (A - G). Performance Class A is very efficient, and the demands of class G is extremely wasteful vice versa. The card has also assessed how much energy consumed comes under heating, lighting, water heating, ventilation and cooling.

For lack of evidence can be individuals fined up to 100,000 Czech crowns (4,000 Euros), corporate entities to 200,000 Czech crowns (about 8,000 Euros), or up to 5 million Czech crowns (about 200,000 Euros) depending on the severity of the administrative offense and on the person who committed it [3], [4].

There are national and international standards and technical reports, stipulating the criteria for thermal comfort and indoor air quality (EN ISO 7730, CR 1752). These documents specify various types and categories of criteria that could affect energy demand. They contain thermal environment criteria for the heating season and cooling season. [5].

According to the Czech technical standard CSN 73 0540-2 [6], which deals with the thermal protection of buildings, the thermal stability of a room is defined for summer and winter seasons. It is required that the highest daily air temperature room will be not higher than 27°C to comply the conditions of thermal stability in the summer. For residential buildings, it is possible to accept exceeded the required value most about 2°C for continuous maximum duration of two hours during the day, if the investor agrees. A critical room is a room with the largest area of direct sunlight, doors, windows facing west, southwest, south, southeast and east. [5].

According to CSN 73 0540, the thermal stability in the winter is defined via the parameter resulting decrease in temperature $\Delta t_v(\tau)$ in a critical room [6]. In the critical rooms (with staying of people after an interruption of heating radiators, radiant panels and hot-air heating), the resulting temperature $\Delta t_v(\tau)$ can't decrease more than about 3 °C. The temperature can't decrease by more than 4 °C in a room with heating stove and underfloor heating. Critical room is a room with the highest overall heat transfer coefficient, respectively,

The work was performed with financial support of research project NPU I No. MSMT-7778/2014 by the Ministry of Education of the Czech Republic and also by the European Regional Development Fund under the Project CEBIA-Tech No. CZ.1.05/2.1.00/03.0089.

H. Charvátová, Tomas Bata University in Zlín, Faculty of Applied Informatics, Regional Research Centre CEBIA-Tech, nám. T. G. Masaryka 5555, 760 01 Zlín, Czech Republic (e-mail: charvatova@fai.utb.cz)

M. Zálešák, Tomas Bata University in Zlín, Faculty of Applied Informatics, Department of Automation and Control Engineering, nám. T. G. Masaryka 5555, 760 01 Zlín, Czech Republic (e-mail: zalesak@fai.utb.cz).

with the largest area of cooled constructions. Usually it is a corner of room under the roof [6].

In cases where the supply of heat to the room does not ensure steady-state indoor temperature, mathematical description required for calculation of the thermal parameters of thermal techniques is very complicated. The calculation procedure of some thermal parameters of thermal technology provides Czech technical standard CSN 06 022 [7]. The method of calculating the dynamic conditions specified in this standard has been derived on the basis of boundary conditions simplifying mathematical model of the dynamic course of room temperature and the heat output of the radiator [7].

Another way to carry out an assessment thermal parameters is the use of advanced software tools and simulate a simplified model of a real object, as we show in the this paper. In the following sections we compare results obtained by both these methods.

II. Description of Studied Problem

For calculating of heat losses of the room, we consider the case where the supply of thermal energy into the room causes non-stationary state of temperature of the air inside the room. In addition, the outside air temperature is changing.

Mathematical description, whereby it is possible to determine the temperature distribution in the room for a given heating and cooling time and also the consequent heat loss of the room, is very complicated. It depends on many conditions. To simplify the calculation, we consider only elements which significantly influence the heat flux between the room and its surroundings.

We assumed that the main heat losses occur by heat passage through the outside wall of the room because the inner walls are surrounded by heated rooms. Heat losses through the ceiling of the room are also small because it is thermally insulated from the surroundings. In the calculation we also consider ventilation.

III. Methods Used for the Heat Losses Calculation

As we describe in previous section, we used two methods to calculate the heat losses of the room. The first method consisted of experimentally determining of the temperature distribution in the tested room during the cyclical heating and cooling for 9 days. Based on the results of the measurements we performed theoretical calculation of heat flux through outside wall of the room in accordance with the Czech Technical Standards CSN EN 15251 and CSN 06220 [4], [7].

The second method consisted in a computer simulation of non-stationary heat transfer in the assembled simplified model of the tested room under the required initial and boundary conditions, which corresponds to the conditions of the experiment. For the simulations, we used the software COMSOL Multiphysics that performs numerical calculations by finite element method.

For the theoretical calculation of the heat flux through the wall of room according the CSN 06220 it holds (1) [2]:

$$\Phi = A \cdot U\left(\theta_i(t) - \theta_e(t)\right), \tag{1}$$

A - heat transfer surface, [m^2],
U - heat passage coefficient, [W.m^{-2}.K^{-1}],
θ_ι - temperature of air inside the room, [°C],
θ_e - temperature of air inside the room, [°C],
Φ - heat flux through the external wall, [W],
t – time, [s].

The heat passage coefficient (U) through the multilayer wall of the room can be computed according to equation (2) [4]:

$$U = \frac{1}{\frac{1}{h_i} + \frac{1}{h_e} + \sum_{j=1}^{n} \frac{\delta_j}{\lambda_j}}, \tag{2}$$

h_ι - heat transfer coefficient of the inner wall surface, [W.m^{-2}.K^{-1}],
h_ι - heat transfer coefficient of the outside wall surface, [W.m^{-2}.K^{-1}],
δ_j - thickness of the layer, [m],
λ_j - thermal conductivity of the layer, [W.m^{-1}.K^{-1}],
n – number of the layers, [-].

For a theoretical calculation, we determined the outside air temperature as daily mean air temperature calculated from measured values of the outside air temperature in a given timeframe.

To assess the energy performance of buildings is recommended according to Czech Technical Standard CSN EN 15251 to determine the temperature of the outside air as a running mean external temperature (3) [7]:

$$\theta_{rm} = (1-\alpha)\left\{\theta_{ed-1} + \alpha \cdot \theta_{ed-2} + \alpha^2 \cdot \theta_{ed-3} \ldots\right\}. \tag{3}$$

The equation (3) can be simplified as follows:

$$\theta_{rm} = (1-\alpha) \cdot \theta_{ed-1} + \alpha \cdot \theta_{rm-1}, \tag{4}$$

where

θ_{rm} - running mean external temperature for the evaluated day, [°C],
θ_{rm-1} - running mean external temperature for the previous day, [°C],
θ_{ed-1} - daily mean external temperature for the previous day, [°C],
θ_{ed-2} - daily mean external temperature two days before the evaluated day, [°C],
θ_{ed-3} - daily mean external temperature three days before the evaluated day, [°C],
α - coefficient from 0 to 1. Its recommended value is 0.8 [1].

ISBN: 978-1-61804-321-4

For numerical calculation of the non-stationary heat transfer COMSOL Multiphysics uses the balance equation (5) [10]:

$$\rho \cdot c_p \frac{\partial T}{\partial t} + \rho \cdot c_p \cdot u \cdot \nabla T = (\lambda \cdot \nabla T) + \Phi_S \,, \qquad (5)$$

where:

ρ - density, [kg.m^{-3}],
c_p - heat capacity at constant pressure, [J.kg^{-1}.K^{-1}],
λ- thermal conductivity, [W.m^{-1}.K^{-1}],
u - the fluid velocity, [m.s^{-1}],
Φ_S - the heat source (or sink), [W],
T – temperature, [K],
t – time, [s].

IV. Experimental Part

A. Description of a tested room

Geometry sketch of the tested room module is shown in Fig. 1. The used geometry is a simplification of reality. Therefore it contains only elements that significantly influence heat flux between the room and its surroundings. Sketch of placement of tested room inside a building is shown in Fig. 2. One of the walls and ceiling of the room are surrounded by the outside environment. Other walls and floor are surrounded by rooms and corridor inside the building. Physical properties of main geometrical elements of the tested room are given in Table 1.

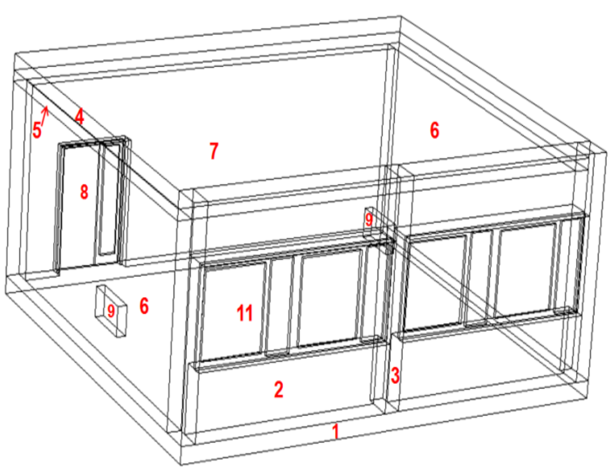

Fig. 1 Geometry sketch of the tested room model

1 – floor, 2 - wall under the windows (outside wall), 3 - reinforced concrete column, 4 - ceiling insulation, 5 – ceiling, 6 - inner sidewall, 7 - the inner rear wall, 8 – door, 9 - electrical heaters.

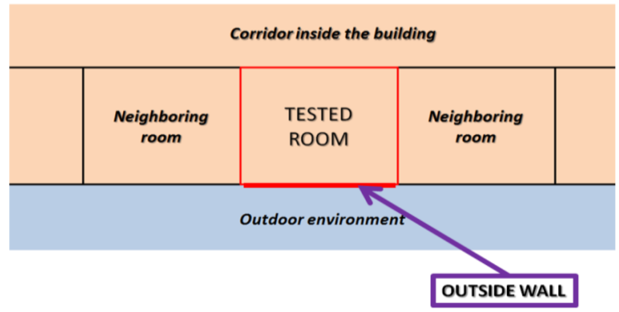

Fig.2 Geometry sketch of placement of tested room inside a building

Table 1 Physical properties of main geometrical elements of the tested room

Geometrical element	Thermal conductivity [W.m^{-1}.K^{-1}]	Density [kg.m^{-3}]	Specific thermal capacity [J.kg^{-1}.K^{-1}]
Inner walls	0.27	900	960
Door frames	58	7850	440
Door	0.11	800	1500
Floor, ceiling structure, reinforced concrete pillar	1.43	2300	1020
Ceiling insulation	0.039	30	1270
Wall under the windows	0.15	800	960
Window frame	0.18	400	2510
Window	0.76	2600	840
Construction above the windows	0.025	2300	1020

B. Conditions of testing

Testing of the heat losses in the room was carried under cyclic heating and cooling 9 days. The room was heated by two heaters with the input power of about 3 kW and 2 kW (see Fig. 4, Fig. 5).

For a theoretical calculation, we determined the outside air temperature as daily mean air temperature calculated from measured values of the outside air temperature in a given timeframe. Measured outside air temperature we took from meteorological data available on the server of Tomas Bata University in Zlín [9]. The used data are shown in Fig. 3. Table 2 gives the calculated values of the daily mean temperatures.

Assumed heat transfer coefficient between the walls of the room and the air inside the building was 8 W.m^{-2}.K^{-1}. Assumed heat transfer coefficient between the walls of the room and outside air was 23 W.m^{-2}.K^{-1}. The air temperature of neighboring rooms was throughout the experiment between 18°C and 20°C.

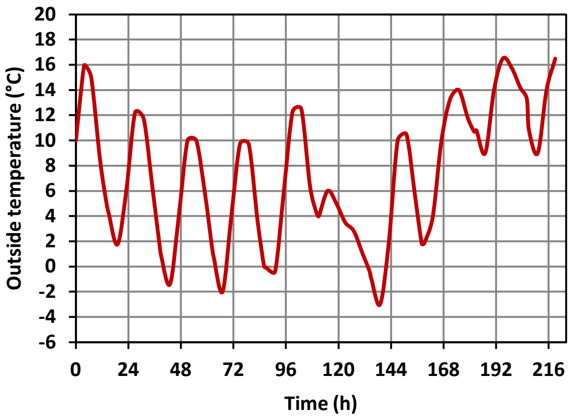

Fig. 3 Measured outside air temperature [9]

Table 2 Computed daily mean external temperature

Day	Daily mean external temperature (°C)	Day	Daily mean external temperature (°C)
1	9.05	**6**	0.71
2	5.07	**7**	6.21
3	4.31	**8**	11.94
4	4.08	**9**	13.37
5	7.19		

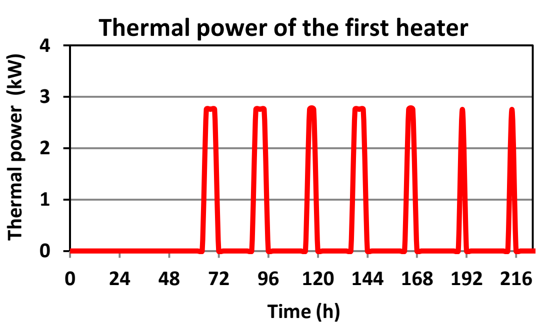

Fig. 4 Thermal power of the first heater during testing

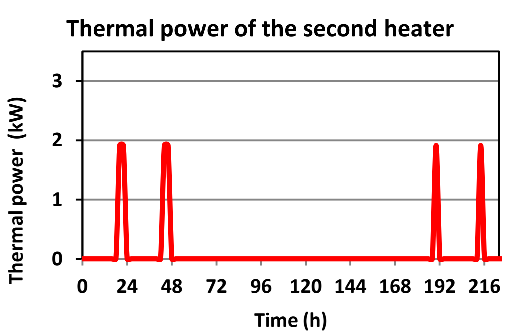

Fig. 5 Thermal power of the second heater during testing

C. Results of testing

In the Fig. 6 is compared experimentally determined temperature of the air inside the room with the room air temperature determined by simulations in model of the tested room with COMSOL Multiphysics. The most significant difference between the measured and simulated values occurred during the first day of the testing, when the maximum deviation between measured and simulated values of temperature was about 1.4 °C. In other days of testing the average deviation was about 0.7 °C.

The differences may be due to a simplified model used for computer simulation compared to the real conditions of measurement.

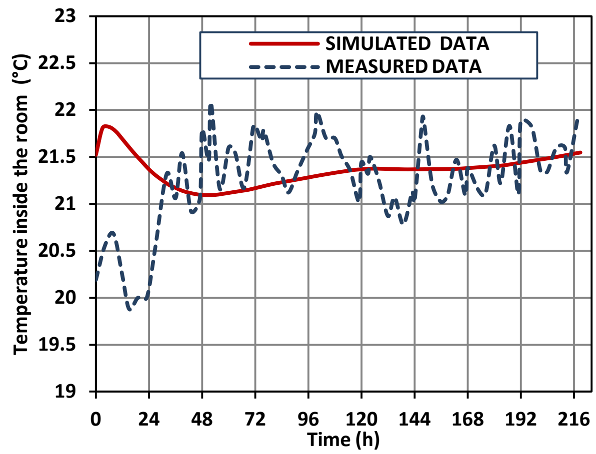

Fig. 6 Comparing of the measured temperature course inside the room with temperature course obtained by computer simulation

In the Fig. 7 is compared the heat flux through the outside wall obtained by theoretical calculation and computer simulation. The differences between theoretically calculated values and heat flux values obtained by computer simulation are mainly caused by the fact that while the computer simulations were used current measurement values of outside air temperature, the average daily temperature of the outside air was used for theoretical calculating of the heat flux. The results are also influenced by simplifying of the model used for computer simulation in comparison with the real conditions in which the experiment was carried out.

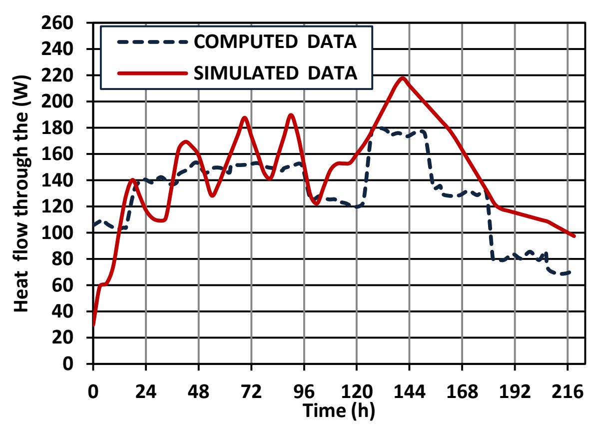

Fig. 7 Comparing of theoretically calculated and simulated heat flux through the outside wall of the room

Determination of heat losses through the external wall after 8 days of cyclic heating and cooling of the room we made also by comparing simulation results with theoretical calculations for moving mean outdoor air temperature. The moving mean outdoor air temperature we calculated according to equation (3). Depending on the choice of the coefficient α for calculation of moving mean outdoor air temperature according to (8), the heat losses were in the range from 81.95 to 184.5 W (see Table 3). The heat losses determined by computer simulation were 115 W, which corresponds with theoretically calculated heat losses for coefficient α = 0.55.

Table 3 Theoretically calculated running mean external temperature and heat losses through the external wall after 8 days of cyclic heating and cooling of the room

Coefficient α (1)	Running mean external temperature after eight days of cyclic heating and cooling of the room (°C)	Heat losses through the external wall (W)
0	11.94	81.95
0.1	11.32	86.62
0.2	10.62	92.65
0.3	9.88	99.08
0.4	9.11	105.72
0.5	8.33	112.45
0.6	7.53	119.37
0.7	6.65	127.04
0.8	5.47	137.19
0.9	3.56	153.72
1	0	184.5

V. Conclusion

We performed two methods for calculation of the heat losses of the room. The first method was a theoretical calculation of heat flux through the outside wall in accordance with the recommendations described in the Czech Technical Standards CSN EN 15251 and CSN 06220.

The second method was computer simulation of non-stationary heat transfer in the simplified model of the tested room for the required initial and boundary conditions.

Comparison of the results showed that the theoretical calculation of heat losses through the outside wall influenced by errors caused by using the average daily temperature and by selecting values between 0 – 1 as coefficient α for calculating of a running mean external temperature.

For testing room we established value of the coefficient α = 0.55, for which the heat losses determined by computer simulation were in accordance with the theoretically calculated heat losses.

References

[1] *Directive of the European Parliament and Council Directive 2010/31/EU on the energy performance of buildings (recast).* (2010). (in Czech). [Online]. Available: http://www.tzb-info.cz/pravni-predpisy/smernice-evropskeho-parlamentu-a-rady-2010-31-eu-o-energeticke-narocnosti-budov-prepracovani

[2] *Energy labeling of buildings: Every twentieth was okay*. (in Czech). [Online]. Available: http://zpravy.aktualne.cz/ekonomika/energeticke-stitky-budov-kazdy-dvacaty-nebyl-v-poradku/r~3b52dd6eb2b011e4bdad0025900fea04/

[3] *The energy label of the building (house, apartment, real estate).* (in Czech). [Online]. Available: http://www.nemovitosti-katastr-nahlizeni.cz/energeticky-stitek/

[4] *CSN EN 15251: Indoor environmental input parameters for design and assesment of energy performance of buildings – addressing indoor air quality, thermal environment, lighting and acoustics*. (in Czech). Prague: Office for Standards, Metrology and Testing, 2011.

[5] L. Šteffek and M. Ostrý. *Influence of insolation factors on the thermal stability of the room and its determination.* (2013). (in Czech). [Online]. Available: http://stavba.tzb-info.cz/prostup-tepla-stavebni-konstrukci/10294-vliv-cinitele-osluneni-na-tepelnou-stabilitu-mistnosti-a-jeho-urceni

[6] *CSN 73 0540-2: Thermal protection of buildings - Part 2.* Prague: Office for Standards, Metrology and Testing, 2011.

[7] *CSN 06 022: Heating systems in buildings – Dynamic behaviour.* (in Czech). Prague: Czech Standards Institute, 2006.

[8] H. S. Carslav and J. C. Jaeger. *Conduction of Heat in Solids*. Oxford: Clarendon Press. 2008.

[9] V. Gerlich. "Verification of possibility of using COMSOL Multiphysics as simulation tool for heat transfer calculation in systems with accumulation." (in Czech). Ph.D. dissertation. Tomas Bata University in Zlín . 2012.

[10] *Introduction to Heat Transfer Module* (2013). [Online]. Comsol. Available: http://www.comsol.com/model/download/173021/IntroductionToHeatTransferModule.pdf

[11] *Meteo* (2015). [Online]. Available: http://meteo.utb.cz/MeteoData.aspx

[12] D. Janacova. V. Vasek. P. Mokrejs. J. Krenek. and R. Drga. "Temperature Fields Solving in Two-Layer Plate with COMSOL Multiphysics Software." in *The 22nd International DAAAM Symposium*. Vienna. Austria. 2011.

[13] M. Feriančik. O. Líška. M. More. "Navigation of industrial manipulator based on computer vision". *Transfer inovácií*. vol. 28. 2013. pp. 140-142.

[14] D. Janáčová, V. Vašek, P. Mokrejš and K. Kolomazník. "Mathematic model of asymmetric heat field in a plane plate. " in *Proceedings of the 21st International DAAAM Symposium "Intelligent Manufacturing & Automation: Focus on Interdisciplinary Solutions"*. Vienna. Austria. 2010.

[15] J. Mižáková, J. Piteľ and S. Hrehová. "Some Simulation Results of Heat Transfer through the Wall Model." *International Journal of Mathematical Models and Methods in Applied Sciences*. Vol. 8. 2014. pp. 1-8.

Creating a 3D model of area using ultrasonic sensors to control the movement of wheeled robot

Miroslav Popelka, Jan Struska and Martin Struska

***Abstract*— In this paper, ultrasonic signal processing method have been described. Analytical method has been used to obtain sufficient obstacle resolution and its representation in useful form. Results from this method will be served to steer wheeled robotic platform, which will be used for fire detection and extinguishing system in different type of environment. Typical type of environment, where wheeled robot will perform any action, will be warehouse with racks and boxes. Achieved results of this method has been displayed into 3d model.

***Keywords*— Signal processing, Time of flight, Ultrasonic sensors wheeled robot platform

I. Introduction

Ultrasonic localization of obstacles has been studied in recent years by many researchers. This studies has been mainly focused on improvement of achieved result due to two dimensional arrays with dozen of ultrasonic sensors for example. In these studies authors used various methods for accomplishing desired results. Most of them used methods like beamforming and its variation. This approach give sufficient results, nevertheless it makes high demands on hardware and software. Especially processing data from all sensors in array take significant amount of time.

In this paper it will be shown two representation of data in order to locate obstacle position and their proportion in 3D. This goal was achieved by mathematical method. Method is bases on analytical knowledge to manage the goal has been described and applied on this specific problem to detect obstacle. Method is very spread in different research array, however in this field is very rarely use.

Data was obtained from created ultrasonic measured board with four pair of ultrasonic sensors. At first raw data was processed in microcomputer on ultrasonic measured board and after that was send via selected UART interface into personal computer. In PC was data processed and displayed into appropriate form with Matlab software. Measurement has not been performed in any special acoustic laboratory, but in ordinary environments, where will be robot operate in real situation.

In comparison with others methods for obstacle recognition ultrasonic detection is commonly used in various industry sectors. Main advantages of ultrasonic detection are its low cost and ability to operate in various environments with reduced visibility, where camera systems are not very effective.

II. Measurement system

A. Ultrasonic measurement board

Raw data were obtained from ultrasonic measurement board and evaluated by analytical and least square method. Proportion of ultrasonic measurement board is 15x 15 (cm). This distance between has been chosen to simulate humans hearing system

Ultrasonic measurement board contains four transceiver 400ST160 and four receiver 400ST/R160. Moreover on this measurement board are placed: 32 bit microcomputer STM32F407VG core ARM Cortex-M4F and 192 kB RAM. Microcomputer has sixteens 12 bit ad converter and four DA converters. Power supply is done by switching power supply, which supply microcomputer itself (3,3V) and also operational amplifiers TLC274AC (±18V)

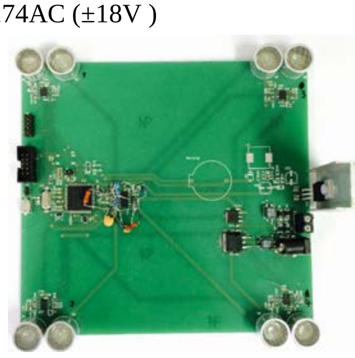

Fig. 1 ultrasonic measurement board

This work was supported by Internal Grant Agency of Tomas Bata University under the project IGA/FAI/2015/028, No. IGA/FAI/2015/027 and No. IGA/FAI/2015/031.

Miroslav Popelka is with Department of Automation and Control Engineering, Faculty of Applied Informatics, Tomas Bata University in Zlín, Czech Republic (corresponding author, e-mail: popelka@fai.utb.cz).

Jan Struška is with Department of Automation and Control Engineering, Faculty of Applied Informatics, Tomas Bata University in Zlín, Czech Republic (corresponding author, e-mail: jstruska@fai.utb.cz).

Martin Struška is with Department of Automation and Control Engineering, Faculty of Applied Informatics, Tomas Bata University in Zlín, Czech Republic (corresponding author, e-mail: mstruska@fai.utb.cz).

Operational amplifiers are inverting amplifiers and their gain is given by connected resistors.

Circuit on following picture Fig.2. shows input inverting amplifiers, which amplifies received ultrasonic signal. These circuit has been used for all four ultrasonic receivers.

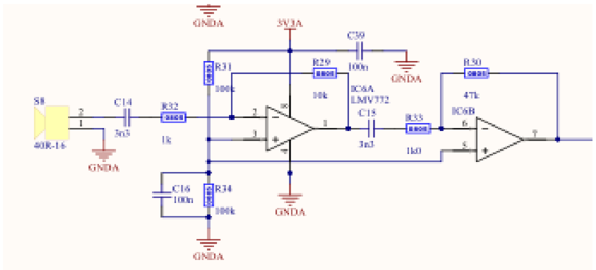

Fig. 2 electrical circuit of input inverting amplifiers

Following circuit on figure Fig3 has been used for transfer of generated ultrasonic signal. This circuit was also used for all four ultrasonic transmitters.

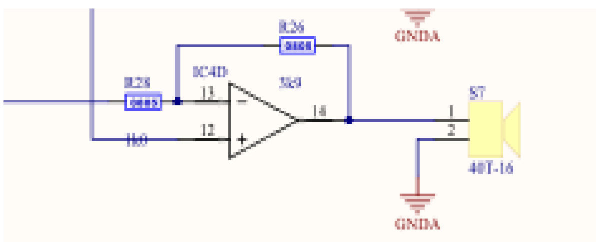

Fig. 3 electrical circuit of output inverting amplifiers

B. Processing of raw data

Created program which was implemented into microcomputer generates ultrasonic signal with 1/40 000 second width see on Fig. 4.This signal is amplified and sent into one of ultrasonic transceivers. After transfer of ultrasonic signal, data are read from coupled receiver and send via serial link to the pc. This method is repeat for all four pairs of sensors.

For this approach, it was used DMA controller, which is included in above mentioned microcomputer. The DMA controller uses its own bus connecting memory and chosen output. From the foregoing is clear that data transfer between AD converter and memory does not use computing power of CPU. Data flow is controlled by DMA controller by itself.

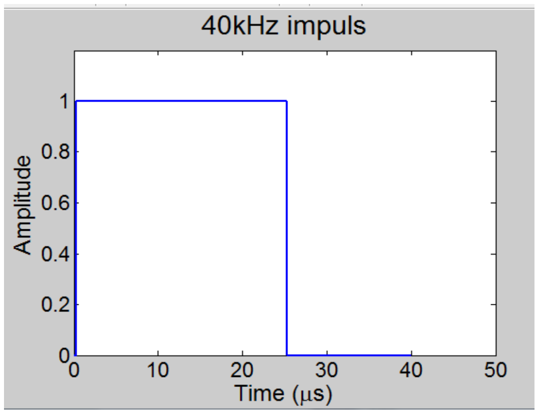

Fig. 4 generated square impulse

When data are saved into memory of microcomputer, after that are processed. Data, which were collected from one of four receivers, are mapped into appropriate form as can be seen on Fig. 6. Original raw data from one receiver are shown on Fig. 5

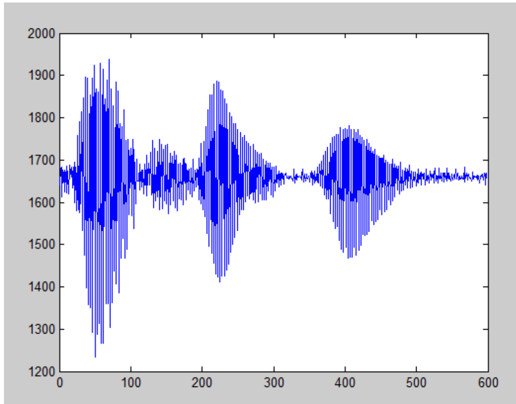

Fig. 5 measured data from one ultrasonic sensor

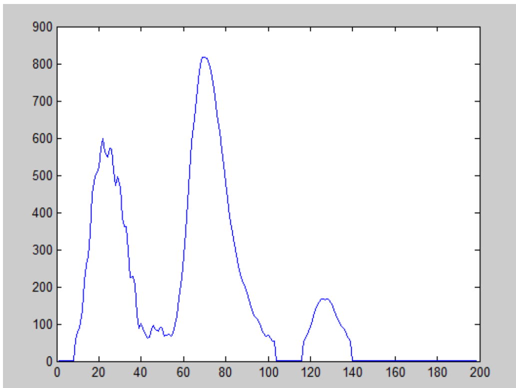

Fig. 6 modified data from one sensor

From previous Fig.6 can be deduced performed changes. First change was to define mean value and move all values in such way, that obteined mean value will be in origin of coordinate system. Last change was to average three consecutive values into one.

III. Processing Algorithms

Algorithms created in this paper are based on intersection of the spheres. The sphere is used because that ultrasonic signal is spreading in air in spherical surfaces. This means that if we use measured data we can create 200 spheres with radius, which matches distance of ultrasonic signal reflection from obstacle. Therefore the radius is calculated from distance and ultrasonic wave speed in air (about 350 m/s).

Further, it is important to process another included information in obtained data see in Fig5 and 6. Amplitude in every time, in given distance, represent size of reflected energy from distant obstacle. This reflected energy can be marked as significant value, which will be identifying value in following process. Every point of sphere have this value and its value determine if this point is interesting for us or not.

IV. Analytical Method

On base of dimension of square ultrasonic measurement board with a side equal 15 cm was established four centers: S1= [0,0,0], S2= [15,0,0], S3= [0,15,0], S4= [15,15,0]. In these centers were progressively generated points for all 200 spheres with radius from 0,875 to 175 cm see Fig 4

.

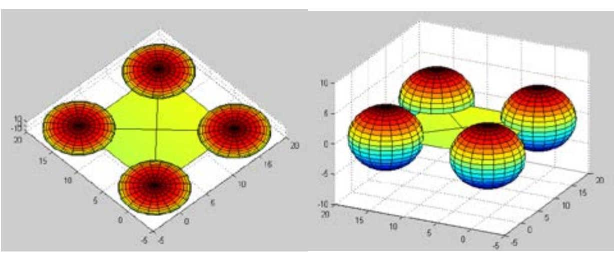

Fig. 7 placement of spheres centers

Radius values are calculated from received data by following formula

$$r = (1\,\text{až}\,200\,/40\,000) * 350\,00 \text{ [cm]} \tag{1}$$

, where values 1 to 200 can be seem on Fig.3, 40 000 is used for conversion into seconds and 35 000 is speed of ultrasonic signal in air.

The algorithm, which generate all point of intersection of spheres is: In first step is chosen one sensor and after that intersection of all neighboring spheres are calculated.

From analytical geometry the sphere equation is:

$$(x - x_0)^2 + (y - y_0)^2 + (z - z_0)^2 = r^2 \tag{2}$$

Intersection of sphere S1 and S3 is given as follows:

$$2 \cdot S3_y y - S3_y{}^2 - r_1{}^2 + r_3{}^2 = 0 \tag{3}$$

Calculation of intersection of S1 and S2 will be defined same way. Obtained plane equation are used for calculation of final intersect see Fig. 8.

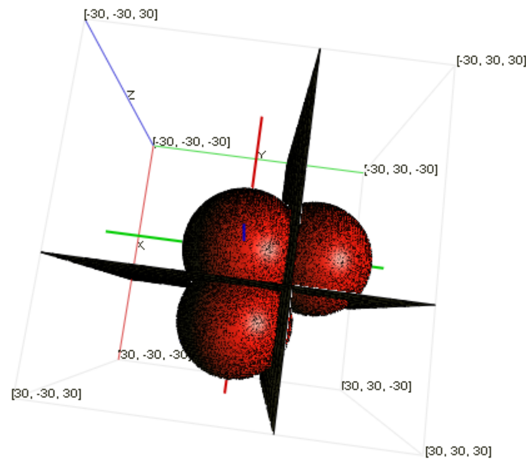

Fig. 8 intersection of three generated spheres

The transversal line of above mentioned planes and original sphere with center S can be calculated from distance of plane and center S1[0,0,0] of sphere and direction vector:

Distance of a first plane

$$2S2_x x - S2_x{}^2 - r_1{}^2 + r_2{}^2 = 0 \tag{4}$$

and center S1 [0,0,0]

$$v_x = \frac{\left|2 \cdot 2_x \cdot x - S2_x{}^2 - r_1{}^2 + r_2{}^2\right|}{\sqrt{(2 \cdot S2_x)^2}} \tag{5}$$

And distance of second plane and center S1.

$$v_y = \frac{\left|2 \cdot S2_y \cdot y - S2_y{}^2 - r_1{}^2 + r_3{}^2\right|}{\sqrt{(2 \cdot S2_y)^2}} \tag{6}$$

Direction vector was defined as $\vec{u}$ = (v_x,v_y,1-2t) and after introduced into the formula of sphere with center S1 coordinates of intersect points will be :

$$\begin{aligned} P1 &= [v_x, v_y, 1 - 2 \cdot t_1] \\ P2 &= [v_x, v_y, 1 - 2 \cdot t_2] \end{aligned} \tag{7}$$

Refine of obtained results can be done by including measured data from fourth sensor.

V. Measurement

These generated points will be assign calculated values of energy, which have been collected from receivers, in given distance from every sensor. Values of energy in every distance

ISBN: 978-1-61804-321-4

from each sensor are multiplied. This value determines which point can be displayed

A. *Algorithm for displaying data into 3d model*

Chosen algorithm, which display significant point into 3d model, searches maximal value of energy from measured data on one sensor. This maximal energy says where ultrasonic reflected from object and its energy lost was minimal.

In this phase, it is selected set of generated points. All points are saved in three dimensional array, where first dimension determines radius of sphere S1, second dimension radius of sphere S2 and last one radius third sphere.

From foregoing is clear that now is only necessary to find combination of radius of sphere S1, where is energy equal to the found energy maximum. For example selected set of points can include ten triads, in which first value will be distance given by maximal energy form first sensor. Another two values will be pointer at energy in measurement data on sensor S2 and S3. The values of energy are multiplied and compared with others nines calculated energies. Maximum of this multiplied energy values will be corner point, which is displayed on Fig. 9.

This method is repeated for every sensor and results are corners points of sensed obstacle. See Fig. 9

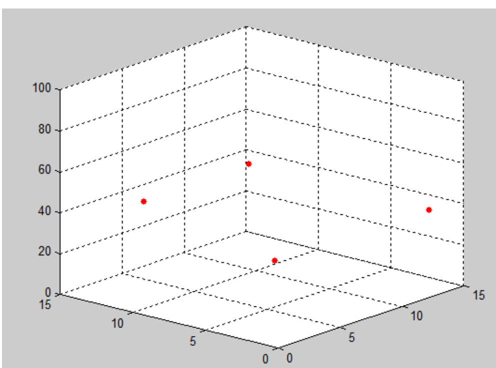

Fig. 9 four corner points of scanned board

The described algorithm is suitable for simple and regular shapes, because only significant values are selected and used in following processing.

VI. Discussion

In this paper has been presented method for obstacle detection based on mathematical knowledge in analytical geometry Method has been chosen due to ability to interpret obtained results. Method is mainly used in triangulation method for obtaining target position in GSM networks [4].

Obtained results from presented algorithm was displayed in 3d graph by software MATLAB. This 3d model can be improved by adding another significant points, however overall image of scanned area will not be clear as is now.

VII. Conclusion

Main aim of this work was to create 3d model of scanned area for steering wheeled robotic platform. This aim was achieved by 3d model algorithm and results obtained was displayed in 3d model by MATLAB software. Next step in my actual research is to use this created model to steer real robotic platform and perform basic avoiding actions.

Acknowledgment

We thank Zdeněk Úředniček, Tomas Bata University in Zlin, for his support and helpful advice. Thanks go to Libor Smýkal for his cooperation in data collection without which the present study could not have been completed.

References

[1] B. D. Steinberg, "Digital beamforming in ultrasound." *Ultrasonics, Ferroelectrics, and Frequency Control, IEEE Transactions,* vol. 39, no. 6, pp. 716-721, November 1992.

[2] N. Wagner, Y.C. Eldar, Z. Friedman, "Compressed beamforming in ultrasound imaging." *Signal Processing, IEEE Transactions,* vol. 60 no. 9, pp. 4643-4657, 1992

[3] H. Poor, *An Introduction to Signal Detection and Estimation*. New York: Springer-Verlag, 1985, ch. 4.

[4] C. C. Nilsen, and I. Hafizovic. "Beamspace adaptive beamforming for ultrasound imaging." *Ultrasonics, Ferroelectrics, and Frequency Control, IEEE Transactions*, vol 56, no. 10, pp. 2187-2197, 2009

[5] G. R. Lockwood, J. R. Talman, and S. S. Brunke. "Real-time 3-D ultrasound imaging using sparse synthetic aperture beamforming." *Ultrasonics, Ferroelectrics, and Frequency Control, IEEE Transactions*, vol. 45, no.4, pp. 980-988, 1998.

[6] L. J. Morales-Mendoza, and et al. "Enhancing Images using the Forward-Backward UFIR Algorithm" in *Latest Trends on Systems. International Conf. on systems, vol 1, pp. 273-277.*

[7] K. Židek, A. Hošovský, and J. Dubják. "New Approach to Thresholding and Contour Detection for Object Surface Inspection in Machine Vision." in *Latest Trends on Systems. International Conf. on systems, vol 1, pp. 306-309.*

[8] Y. Maeda, M. Sugimoto, H. Hashizume, "A robust doppler ultrasonic 3D imaging system with MEMS microphone array and configurable processor." *Ultrasonics Symposium (IUS)*, pp. 1968-1971, 2011

[9] Z. H. Liu, C. Lu, "Ultrasonic Phased Array 3D Imaging for the Steel Butt Weld Defects", Applied Mechanics and Materials, Vols. 727-728, pp. 799-803, Jan. 2015.

CICT holographic information geometry

Rodolfo A. Fiorini

Abstract*—** Recently, as essence of information geometry, Barbaresco has synthetized the analogies between both Koszul and Souriau characteristic function models, and reduced their definitions to the exclusive Cartan Inner Product. Interpreting Legendre transform as Fourier transform in (Min,+) algebra, he concludes with a definition of entropy given by a relation mixing Fourier/Laplace transforms. The computational methods currently used in classic and quantum geometric science of information (GSI) are based on the discretization of differential equations. The purpose of this paper is to arrive to the proposal of a stronger computational point of view. *CICT* new awareness of a rational hyperbolic geometry framework of coded heterogeneous hyperbolic structures, underlying the familiar ***Q Euclidean surface representation system, can open the way to holographic information geometry (HIG). This formulation has the great merit of maintaining close contact between the mathematical description and the physical phenomenon described, showing how to obtain a purely algebraic formulation of information and physical laws relating directly elementary information generators to experimental measurements.

***Keywords*—** biomedical engineering, CICT, geometric science of information, holographic information geometry.

I. Introduction

RECENTLY, Barbaresco has synthetized the analogies between both Koszul and Souriau characteristic function models, and reduced their definitions to the exclusive Cartan Inner Product, starting from generalization of Characteristic Functions (CF) concept by Jean-Louis Koszul in Mathematics and by Jean-Marie Souriau in Statistical Physics [2]. As essence of Information Geometry (IG), in [2] Barbaresco develops Koszul-Vinberg Characteristic Function (KVCF) as a transverse concept in Thermodynamics, in Statistical Physics and in Probability. From general KVCF definition, he introduces Koszul Entropy as the Legendre transform of minus the logarithm of KVCF, and compares both functions by analogy with the Dual Massieu-Duhem potentials in thermodynamics. Definition of entropy has been widely debated and a systemic entropy conundrum solution proposal, by algorithmic information point of view, has appeared recently [3]. The concept of CF was developed by Gibbs and Duhem in thermodynamics with the concept of potentials, and introduced by Poincaré in probability, based on François Massieu 1869 idea to derive some mechanical and thermal properties of physical systems from CFs. This approach found applications in many scientific and engineering disciplines (as an early example see [10]). Based on the cornerstone concept of the Koszul-Vinberg Characteristic Function, Koszul Entropy is defined as the Legendre transform of the Koszul characteristic function. Then, this definition of Entropy is extended by interpretating Legendre transform as Fourier transform in (Min,+) algebra, and concluding with a definition of Entropy given by a relation mixing Fourier/Laplace transforms [2]. Eventually, Koszul Entropy has a Shannon Entropy structure [16]. On the other hand, theoretical physicist Licata et al. have presented a Fisher-Bohm information geometric point of view for quantum information [13]. Given the relation between the number of the system microstates *W*, function of the macrostates and given the entropies *S* as Cartesian coordinates, the reference can be changed and from Euclidean coordinates of the entropies, in which the observers are independent, one can move to a non Euclidean space of the parameters (averages, variances, …). In this background it is possible to compute covariant derivatives in the parameter space and we can obtain by entropy the Bohm quantum potential and the quantum effects [13]. The approach suggested in this background leads to the idea that, in the extreme condition of Fisher information (FI), Bohms quantum potential emerges as an information channel determined by informational lines associated with the vector of the superposed Boltzmann entropies. In a relativistic curved space-time, the informational lines associated with the quantum entropy appear as real intermediaries between gravitational and quantum effects of matter, determining a high coupling between the effects of gravity on geometry and the quantum effects on the geometry of space-time [13]. In IG, the Fisher-information matrix is used to calculate the covariance matrices associated with maximum-likelihood estimator (MLE). MLE gives a unified approach to estimation, which is well-defined in the case of the normal distribution and many other problems. In this paper, our goal is to show that Computational Information Conservation Teory (*CICT*) new awareness [8],[9] of a rational HG (hyperbolic geometry) framework of coded heterogeneous hyperbolic structures [4], underlying the familiar *Q* Euclidean surface representation system can open the way to holographic information geometry (HIG) [4]-[6],[7],[9].

II. The Root of the Problem

Sometimes, IG tensorial formulation may become cumbersome and computational difficulties do occur: in such

Rodolfo A. Fiorini is with the Department of Electronics, Information and Bioengineering (DEIB), Politecnico di Milano University, Milano, 32 Piazza Leonardo da Vinci, MI 20133, ITALY (phone: +39 022399 3350; fax: +39 022399 3360; e-mail: rodolfo.fiorini@polimi.it).

ISBN: 978-1-61804-321-4

problems MLEs are unsuitable or do not exist. Computational information geometry (CIG) uses a top-down (TD) point-of-view (POV). All approaches using TD POV allow for starting from an exact solution panorama of global analytic solution families, which always offers a shallow downscaling local solution computational precision compromise to real specific needs (overall system information from global to local POV is not conserved [4]). Usually it is necessary further analysis and validation to get localized computational solution of any practical value. To develop resilient and antifragile application, we need stronger biological and physical system computational correlates; we need asymptotic exact global solution panoramas combined to deep local solution computational coherent precision for information conservation and vice-versa. Two sorts of functions are to be distinguished. First, functions in which the independent variable x may take every possible value in a given interval; that is, the variable is thought continuous. These functions belong to the domain of Sublime Calculus or Infinitesimal Calculus (IC). Secondly, functions in which the independent variable x takes only given values; then the variable is thought to be discontinuous or discrete. In the same way, we talk of continuous probability distribution and discrete probability distribution. To discrete variable the classic methods of IC are NOT applicable. To deal with discrete variables, we need the Finite Differences Calculus (FDC). FDC deals especially with discrete functions, but it may be applied to continuous function too and to continuum problems, with no loss of generality. It can deal with both discreteness and continuum problem categories conveniently. Unfortunately, classic FDC approach is unable to conserve overall system information. In fact, traditional FDC is unable to capture and to manage not only the full information content of a single Real Number in $\boldsymbol{R}$, but even Rational Number $\boldsymbol{Q}$ is managed by information dissipation on digital machine (e.g. finite precision, truncating, rounding, etc.) To grasp stronger physical and biological system correlates, scientists need two intelligently articulated hands: both stochastic and combinatorial approaches synergically articulated by natural coupling. The former, applied under the "continuum hypothesis" assumption, has reached highly sophistication level, and worldwide audience. Many "Science 1.0" scientists up to scientific journals assume it is the ultimate language of science. The latter, less developed under the "discreteness hypothesis" assumption in specific scientific disciplines, has been considered in peculiar areas only. It has been further slowly developed by a few specialists and less understood by a wider audience. In the past, he above two large mathematical research areas have followed completely separate development paths with no articulated synergic coupling. A few attempts to arrive to a continuum-discrete unified mathematical approach have been proposed, all of them with big operational compromises, and we can go back at least to the introduction of the Riemann-Stieltjes integral, published in 1894 by Dutch mathematician Thomas Joannes Stieltjes (1856-1894) [15], which unifies sums and integrals. If we want to achieve overall system information conservation, we have to look for convenient arbitrary multi-scaling bottom-up (BU) POV (from discreteness to continuum view ≡ BU POV) to start from first, and NOT the other way around! Then, a TD POV can be applied for overall final model validation and endorsement. Current human made application and system can be quite fragile to unexpected perturbation because Statistics can fool you, unfortunately. Deep epistemic limitations reside in some parts of the areas covered in risk analysis and decision making applied to real problems [17]. Furthermore, Stochastic vs. Combinatorially Optimized Noise generation ambiguity emphasises the information double-bind (IDB) problem in current most advanced instrumentation systems, just at the inner core of human knowledge extraction by experimentation in Science [4]. The basic principles, to synergically articulate *CICT* by natural coupling to GSI and IG, by BU POV, have been developing at Politecnico di Milano University, since the 1990s. In 2013, the basic principles of *CICT*, from discrete system parameter and generator, appeared in literature [8],[9]. *CICT* defines arbitrary-scaling discrete Riemannian manifold uniquely, under HG metric, so that, for arbitrary finite point precision W going to infinity (exact solution theoretically), it is isomorphic (even better, homeomorphic) to traditional SGI and IG Riemannian manifold [5].

III. CICT Fundamental Relationship

CICT founding principles are the same on which Riemannian manifold theories are founded; principles of relativity and covariance, of optimization (least action and geodesic principles), applied to scale and accuracy relativity transformations of the reference system in HG. Increasing the subspace representation accuracy, the total number of allowed convergent paths, as monotonic power series, for instance (as allowed subspace paths), increases accordingly till maximum machine word length and beyond, like discrete quantum paths denser and denser to one another, towards a never ending "blending quantum continuum," originating "quantum mixtures" by a TD perspective. The finer geometry of subspace itself becomes scale dependent. While differentiable trajectories found in standard mathematical physics are automatically scale invariant, it is the main insight of the *CICT* theory that also certain non-differentiable paths (resultant paths, emerging from lower scales combined quantum trajectories, which explicitly depend on the scale and accuracy of the observer) can be scale invariant as underlined in [1],[14]. The first *CICT* fundamental general relationship that ties together numeric body information of divergent and convergent monotonic power series in any base (in this case decimal, with no loss of generality), with D ending by digit 9, is given by the following *CICT* LTR (left-to-right) and RTL (right-to-left) *CICT* fundamental correspondence equation [8]:

$$\frac{1}{D} = \sum_{k=0}^{\infty} \frac{1}{10^W} \left(\frac{\overline{D}}{10^W} \right)^k \Rightarrow \ldots \Leftarrow \; Div\left(\frac{1}{D} \right) = \sum_{k=0}^{\infty} (D+1)^k \quad (01)$$

where $\overline{D}$ is the additive 10^W complement of D, i.e. $\overline{D}$ = (10^W – D), W is the word representation precision length of the denominator D and "*Div*" means "Divergence of". Furthermore, When $\overline{D}$ > D the formal power series on the left of (01) can be rescaled mod D, to give multiple convergence paths to 1/D, but with different "convergence speeds." The total number of allowed convergent paths, as monotonic power series, is given by the corresponding Q_L value, at the considered accuracy level L. So, increasing the level of representation accuracy, the total number of allowed convergent paths to 1/D, as monotonic power series (as allowed conservative paths), increases accordingly and can be counted exactly, and so on, till maximum machine word length and beyond, like discrete quantum paths denser and denser to one another, towards a never ending "blending quantum continuum," by a TD perspective. By using this approach, it is possible to generate LTR and RTL remainder sequences that show same quotient body information (multi-scale periodic) and specific quotient head and tail information to compute deterministic boundary values, to sustain body periodicity with no information dissipation (full information conservation and reversibility) [8]. Further generalizations of (01) related to D ending by digit 1, 3 and 7 are straightforward. In fact, we can re-write (01) as:

$$\frac{1}{D} = \sum_{k=0}^{\infty} \frac{1}{10^W} \left(\frac{\overline{D}}{10^W} \right)^k \Rightarrow \ldots \Leftarrow \; Div\left(\frac{1}{D} \right) = \sum_{k=0}^{\infty} G^k \quad (02)$$

where G is a specific RTL generator. Then, it is immediate to verify that for G = (9D + 1), G = (3D + 1) and G = (7D + 1):

$$Div\left(\frac{1}{D} \right) = \sum_{k=0}^{\infty} G^k \quad (03)$$

will match RTL exactly the sequences LTR generated by:

$$\frac{1}{D} = \sum_{k=0}^{\infty} \frac{1}{10^W} \left(\frac{\overline{D}}{10^W} \right)^k \quad (04)$$

with a number word D of length W, right ending by digit 1, 3 and 7 respectively. Rational representations are able to capture two different types of information at the same time, modulus (usual quotient information) and associated outer or extrinsic period information, which inner or intrinsic generator phase (generator intrinsic period) can be computed from. So, rational information can be better thought to be isomorphic to vector information rather than to usual scalar one, at least. Furthermore, our knowledge of *RFD* Q_L and corresponding *RFD* R_L can allow reversing numeric power convergent sequence to its corresponding numeric power divergent sequence uniquely [8]. Reversing a convergence to a divergence and vice-versa is the basic property to reach information conservation, i.e. information reversibility, as from (01). In present paper, *CICT* results are presented in term of classical power series to show the close relationships to classical and modern control theory approaches for causal continuous-time and discrete-time linear systems. Usually, the continuous Laplace transform is in Cartesian coordinates where the x-axis is the real axis [11] and the discrete z-transform is in circular coordinates, where the rho-axis is mapping the real axis [12]. By using *CICT* approach, it is possible to generate LTR and RTL remainder sequences that show same quotient body information (arbitrary-scale periodic) and specific quotient head and tail information to compute deterministic boundary values, to sustain body periodicity with no information dissipation (full information conservation and reversibility) [8].

IV. Computational Example

In different scientific and technical fields different conventions are often used for defining DFT (discrete Fourier transform) and IDFT (inverse DFT), but all of them differ in the multiplicative constant used to relate direct-inverse transformation, usually. For instance, in signal processing application IDFT is multiplied by 1/n where n is the total number of samples in the sequence, while its corresponding DFT is multiplied by 1.0. In data analysis application the reverse is true, i.e. the DFT is multiplied by 1/n and its corresponding IDFT by 1.0. In any case the zero frequency term appears at first position (LTR) in the resulting sequence. In the case of finite fields, the DFT over any ring is commonly called Number-Theoretic Transform (NTT) and data analysis multiplicative constant rule is applied. In that case the direct transformation is called DNTT and the inverse one, INTT, for short, respectively. The associated quotient and remainder information for SN (solid number, see [8]) can always be regenerated anew by remainder information only, but not vice-versa (see [8]). Elementary arithmetic long division remainder sequence is a combinatorially optimized sequence of phased elementary generators, indistinguishable from traditional random noise sources [4],[9]. A common operation in analyzing various kinds of data is to find the DNTT (or spectrum) of a list of values. The idea is typically to pick out components of the data with particular frequencies or ranges of frequencies. From Fiorini and Laguteta [8] we recall the following:

"…the remainder R_L is the fixed multiplicative ratio of a power series, the computation of 3^n (mod 7) for n = 1, 2, 3, … till its exponential closure, gives the 'Fundamental Cyclic Remainder Sequence' (*FCRS*):

$$R_1 = 3;\ R_2 = 2;\ R_3 = 6;\ R_4 = 4;\ R_5 = 5;\ R_6 = 1 \quad (05)$$

from which the 'Fundamental Cyclic Quotient Sequence' (*FCQS*) can be readily regenerated by 7 * R_L (mod 10):

$$Q_1 = 1;\ Q_2 = 4;\ Q_3 = 2;\ Q_4 = 8;\ Q_5 = 5;\ Q_6 = 7." \quad (06)$$

The way to compute the right result for SN = 7 by DNTT is to format input information according to the following "original" six digit sequence:

$$7, 0, 0, 0, 0, 0. \qquad (07)$$

Then the output result is the following six complex number "spectrum" sequence:

$$1.16667 + 0.0\,I,\ 1.16667 + 0.0\,I,\ 1.16667 + 0.0\,I,\\ 1.16667 + 0.0\,I,\ 1.16667 + 0.0\,I,\ 1.16667 + 0.0\,I, \qquad (08)$$

where $I = \sqrt{-1}$, is the usual imaginary unit. As expected, in this case, all the imaginary components are zero and we get a sequence of real values only, each of them equal to 1/6 by 7.0 or 7/6. By applying INTT to sequence (08), the original sequence in (07) is recovered. Now, we apply INTT to the following input sequence:

$$3, 2, 6, 4, 5, 1 \qquad (09)$$

which is the *FCRS* of SN = 7 from (05), pretending to be the SN spectrum sequence. The output result is the following six complex number sequence:

$$(21.0 + 0.0\,I),\ (–5.0 – 1.73205\,I),\ (0.0 + 0.0\,I),\\ (7.0 + 0.0\,I),\ (0.0 + 0.0\,I);\ (–5.0 + 1.73205\,I). \qquad (10)$$

As you can see the first term of sequence (10) is $F_{INTT} = 21.0 = 3 * 7$, and the sum of all the imaginary components is zero. Easily, it can be shown that any SN number can be always recovered from the INTT of its associated *FCRS* by the following simple equation [4]:

$$SN = (2 * F_{INTT})/T_p; \qquad (11)$$

where T_p is the digit string length of SN *FCRS*. Now, by using a little signal processing knowledge, let us left juxtapose one zero to the beginning of sequence (09) to obtain the following seven digit input sequence:

$$0, 3, 2, 6, 4, 5, 1 \qquad (12)$$

and applying INTT to it. The result is the following seven complex number sequence:

$$(21.0 + 0.0\,I),\ (–8.07338 + 0.493353\,I),\\ (–0.961968 – 1.68784\,I),\ (–1.46466 – 5.16312\,I),\\ (–1.46466 + 5.16312\,I),\ (–0.961968 + 1.68784\,I),\\ (–8.07338 – 0.493353\,I). \qquad (13)$$

Again, $F_{INTT} = 21.0 = 3 * 7$, and the sum of all the imaginary components is zero. But this time, quite different from previous computation, even the sum of all the real components of output sequence is zero! So, this time, the sum of all the real and imaginary components is zero respectively, and that is a general result for arbitrary SN *FCRS*. The interested reader to dig deeper is referred to [4]. *CICT* LTR and RTL correspondence (01) allows to focus our attention on combinatorically optimized number pattern generated by LTR or RTL phased generators and by convergent or divergent power series with no further arbitrary constraints on elementary generator and relation. In other words, elementary arithmetic long division quotient sequences directly encode HG projective relativistic geometric structures, emerging out of a subspace of modular geometric power sequences, offering many competitive LTR and RTL computational advantages over classic Euclidean approach only. Traditional Number Theory, modern Numeric Analysis and current computational algorithms, like classic FDC or CIG, are based on usual numeric string monodirectional interpretation (LTR) only for ***Q*** Arithmetic numeric group generator with no related remainder knowledge. In this way, information entropy generation cannot be avoided in current computational application (extrinsic world representation POV) [8]. On the contrary, according to *CICT*, it is quite simple to compute corresponding RTL elementary phased generator to achieve information reversibility and conservation, by using basic considerations only (intrinsic world representation POV) [8]. Thanks to the above properties, traditional long division algorithm can be related to modular group theory in a natural way, becoming free from trial and error like in Finite Segment *p*-adic representation systems, but with no associated usual coding burden [8]. The rich operative scenario offered by combinatorial modular group theory is full of articulated solutions to information processing problems. *CICT* is a natural framework for arbitrary multi-scale modeling and simulation in the current landscape of modern Geometric Science of Information (GSI) [2].

V. Conclusion

Considering information not only on the statistical manifold of model states but but also on the combinatorial manifold of low-level discrete, phased generators and empirical measures of noise sources, related to experimental high-level overall perturbation, *CICT* achieves to bringing classical and quantum information theory together in a single framework. Traditional elementary arithmetic long division remainder sequences can be interpreted as combinatorially optimized exponential cyclic sequences (OECS) for HG structures, as points on a discrete Riemannian manifold, under HG metric, indistinguishable from traditional random noise sources by classical Shannon entropy, and current most advanced instrumentation [7]. *CICT* new awareness of the rational hyperbolic geometry framework of encoded heterogeneous hyperbolic structures, underlying the familiar rational ***Q*** Euclidean surface representation system can open the way to holographic information geometry (HIG). This formulation has the great merit of maintaining close contact between the mathematical description and the physical phenomenon described, showing how to obtain a purely algebraic (if desired) formulation of information and physical laws relating directly elementary information phased generators to experimental measurements.

REFERENCES

[1] C. Auffray, L. Nottale, "Scale relativity theory and integrative systems biology: 1. Founding principles and scale laws," *Progr. Biophys. Mol. Bio.*, vol.97, no.1, pp.79-114, May 2008.

[2] F. Barbaresco, "Information Geometry and Souriau Geometric Temperature/Capacity of Lie Group Thermodynamics," *Entropy*, vol.16, pp.4521-4565, 2014.

[3] R.A. Fiorini, "The Entropy Conundrum: A Solution Proposal," *First International Electronic Conference on Entropy and Its Applications*, Sciforum Electronic Conference Series, vol.1, 2014, available: http://sciforum.net/conference/ecea-1/paper/2649.

[4] R.A. Fiorini, "How Random is Your Tomographic Noise? A Number Theoretic Transform (NTT) Approach," *Fundamenta Infomaticae*, vol.135, no.1-2, pp.135-170, 2014.

[5] R.A. Fiorini, "Computational Information Conservation Theory: An Introduction," in *2014 Proceedings of the 8th International Conference on Applied Mathematics, Simulation, Modelling (ASM '14)*, N.E. Mastorakis, M. Demiralp, N. Mukhopadhyay, F. Mainardi, eds., Mathematics and Computers in Science and Engineering Series, No.34. NAUN Conferences, WSEAS Press, November 22-24, 2014, Florence, Italy, pp.385-394.

[6] R.A. Fiorini, "Stronger Physical and Biological Measurement Strategy for Biomedical and Wellbeing Application by CICT," in *2014 Proceedings of the 3rd International Conference on Health Science and Biomedical Systems (HSBS '14)*, N.E. Mastorakis, Atsushi Fukasawa, eds., Series: Recent Advances in Biology and Biomedicine Series No.6. NAUN Conferences, WSEAS Press, November 22-24, 2014, Florence, Italy, pp.36-45.

[7] R.A. Fiorini, "Computerized Tomography Noise Reduction by CICT Optimized Exponential Cyclic Sequences (OECS) Co-domain," *Fundamenta Informaticae*, 2015, in press.

[8] R.A. Fiorini, G. Laguteta, "Discrete Tomography Data Footprint Reduction by Information Conservation," *Fundamenta Informaticae*, vol.125, no.(3-4), pp.261-272, 2013.

[9] R.A. Fiorini, A. Condorelli, G. Laguteta, "Discrete Tomography Data Footprint Reduction via Natural Compression," *Fundamenta Informaticae*, vol.125, no.(3-4), 273-284, 2013.

[10] R.A. Fiorini, E.H. Gassenfeit, J.D. Powell, "A/F Estimation from Internal Combustion Engine Cylinder Pressure Using Fast Fourier Transform Descriptors," in: *1988 Proceedings of the American Control Conference.* Atlanta, GE: ACC Press, 1988, pp.124-132.

[11] G.F. Franklin, J.D. Powell, A. Emami-Naeini, *Feedback Control of Dynamical Systems.* Upper saddle river, NJ: Pearson Higher Education, Inc., 2010.

[12] G.F. Franklin, J.D. Powell, M. Workman, *Digital Control of Dynamic Systems*. Half Moon Bay, CA: Ellis-Kagle Press, 1998.

[13] I. Licata, A. Fiscaletti, "A Fisher-Bohm Geometry for Quantum Information," *E.J.T.P.*, vol.11, no.31, pp.1-18, 2014.

[14] L. Nottale, C. Auffray, "Scale relativity theory and integrative systems biology: 2. Macroscopic quantum-type mechanics," *Progr. Biophys. Mol. Bio.*, vol.97, no.1, pp.115-157, May 2008.

[15] H. Pollard, "The Stieltjes Integral and Its Generalizations," *The Quarterly J. of Pure and applied Math.*, vol.19, pp.45-56, 1920.

[16] C.E. Shannon, "A Mathematical Theory of Communication," *Bell System Tech. J.*, vol.27, pp.379-423, 1948.

[17] N. N. Taleb, *Silent Risk.* Preliminary Book Draft, January, 2015.

Effective safety and security modeling in Healthcare by GSI & CICT coupled support

R. A. Fiorini, G. F. Santacroce

***Abstract*—** In the last decade, molecular principles and pathogenetic factors involved in the development of many diseases have been successfully discovered. Early biological concepts based on reductionistic systemic and cybernetic approaches have been revisited and overshadowed by recent molecular and pathogenetic findings for healthcare safety management. Mid-20th century biological concepts based on systematic and classic cybernetic thoughts fell into oblivion. Unfortunately, current system still can be quite fragile to unespected event, and unpredictable changes can be very disorienting at enterprise level. The needs to answer tighter regulatory processes (safety, security, environmental control, health impacts, etc.) and to assess resilient and antifragile performances for complex systems have led to the emergence of a new industrial simulation challenge to take uncertainties into account when dealing with complex numerical simulation frameworks. Current uncertainty quantification (UQ) approaches aim to include uncertainty in mathematical models and quantify its effect on output of interest used in decision making. Nevertheless, to grasp a more reliable representation of reality and to get more resilient and antifragile techniques, researchers and scientists need two intelligently articulated hands: both stochastic and combinatorial approaches synergically articulated by natural coupling. CICT & GSI coupled support can offer an effective and convenient framework to develop more competitive and reliable complex system modeling. This paper is a relevant contribute to show how CICT & GSI can offer stronger and more effective system modeling solutions in Healthcare.

***Keywords*—** biomedical engineering, CICT, healthcare, uncertainty quantification.

I. Introduction

In the last decade, molecular principles and pathogenetic factors involved in the development of many diseases have been successfully discovered. Early biological concepts based on reductionist inference systemic and classic cybernetic approaches have been largely revisited and overshadowed by more recent molecular and pathogenetic findings for healthcare security and safety management, creating a brand new cultural approach. As a result, mid-20th century biological concepts based on classic systematic and cybernetic thoughts fell into oblivion and new cultural readings updated old ones, in specific knowledge areas. Unfortunately new cultural reference and knowledge, like any other physical property, require time to diffuse and percolate through multi-articulated scientific and social systems. Today, competitive applications development is ranging from "Internet of Medical Devices" (IoMD), telemedicine and telecare apps, anticipatory learning system (ALS), health information management system, etc., up to health governance policy system for advanced Health Organization (HO). Most current applications are designed to function in an ideal network environment, by an ideal user, etc., but that's never the case in the real world. Quite often, applications have to face unexpected perturbation, from network behavior and configuration to user problematic interface, etc., and to address the errors that inevitably surface, if they are programmed for. Unfortunately, current system still can be quite fragile to unespected event, and unpredictable changes can be very disorienting at enterprise level. As a matter of fact, Statistics can fool you, unfortunately [1]. These major changes, usually discontinuities referred to as fractures in the environment rather than trends, will largely determine the long-term future of organization. To develop resilient and antifragile application, we need stronger biological and physical system correlates. The needs to reliably answer tighter regulatory processes (safety, security, environmental control, health impacts, etc.) and to assess resilient and antifragile performances for complex systems have led to the emergence of a new industrial simulation challenge to take uncertainties into account when dealing with complex numerical simulation frameworks. Current uncertainty quantification (UQ) approaches aim to include uncertainty in mathematical models and quantify its effect on output of interest used in decision making. To face the challenge of complex system modeling (hierarchical heterogeneous multi-scale system modeling), we need to be able to control system quantification uncertainty from macroscale, through mesoscale, till nanoscale and beyond. We need more robust, resilient and antifragile application to be ready for next generation systems [2],[3]. They are mandatory to develop antifragile self-organizing and self-regulating system further. While the amount of data doubles every 1.2 years, the processing power doubles every 1.8 years. Unfortunately, the complexity of networked systems is growing even faster. Paradoxically, as economic diversification and cultural evolution progress, a big government approach would increasingly fail to lead to good decisions [4]. The logical

Rodolfo A. Fiorini is with the Department of Electronics, Information and Bioengineering (DEIB), Politecnico di Milano University, Milano, 32 Piazza Leonardo da Vinci, MI 20133, ITALY (phone: +39 022399 3350; fax: +39 022399 3360; e-mail: rodolfo.fiorini@polimi.it).

Giulia F. Santacroce is with BV-Tech (S.p.A), Piazza Armando Diaz, 6, 20123, Milano, Italy.

ISBN: 978-1-61804-321-4

answer is to use distributed self-control (i.e. bottom-up (BU) self-regulating systems). Cybernetics (i.e. advanced control theory) and complexity theory tell us that it is actually feasible to create resilient social and economic order by means of self-organization, self-regulation, and self-governance [5],[6]. If we want to to achieve self-organization, self-regulation in a competitive arbitrary-scalable system reference framework, we need application resilience and antifragility at system level first. In fact, attempts to optimize multi-scale systems in a top-down (TD) way will be less and less effective, and cannot be done in real time. That is the main reason why, over the last few years, integration of stochastic methods into a multi-scale framework (from macro-scale to nano-scale) or development of multi-scale models in a stochastic setting for epistemic uncertainty quantification (UQ) is becoming an emerging research frontier for systems modeling, innovation and competitive development in Science and Technology. Current UQ approach aims to include uncertainty in mathematical models and quantify its effect on output of interest used in decision making. Traditional human approach to experience is based on risk analysis and decision making in a natural uncertain environment by incomplete knowledge. In the past three centuries, stochastic and applied probabilistic theory became the core of classic scientific knowledge and engineering applications at system macroscale level. It was applied to all branches of human knowledge under the "continuum hypotesis" assumption, reaching highly sophistication development, and a worldwide audience. Even today, many "Science 1.0" researchers and scientists up to scientific journals assume it is the ultimate language of science and it is the traditional instrument of risk-taking. Unfortunately, deep epistemic limitations reside in some parts of the areas covered in risk analysis and decision making applied to real problems [1],[7]. From this POV, current most advanced "embedded intelligent system" is a "deficient system," a fragile system, because its algorithms are based on statistical intelligence or knowledge only, and are lacking a fundamental system component (see Section III, Method). Unfortunately, the "probabilistic veil" can be very opaque computationally in arbitrary multi-scale modeling, and misplaced precision leads to information dissipation and confusion [8]. The problems are exactly what we are now seeing. Statisticians just do not yet have all the fixes and are looking for better ways of thinking about data, like Extreme Value Statistics (EVS) or Extreme Value Theory (EVT) [9]. EVT concerns the study of the statistics of the maximum or the minimum of a set of random variables and has applications in climate, finance, sports, all the way to physics of disordered systems where one is interested in the statistics of the ground state energy. While the EVS of "uncorrelated" variables are well understood, little is known for correlated or strongly correlated random variables. Only recently this subject has gained much importance both in statistical physics and in probability theory as extreme events are ubiquitous in Nature. They may be rare events but when they occur, they may have devastating consequences and hence are rather important from practical points of view. To name a few, different forms of natural calamities such as earthquakes, tsunamis, extreme floods, large wildfire, the hottest and the coldest days, stock market risks or large insurance losses in finance, new records in major sports events like Olympics are the typical examples of extreme events. But, it is easy to see that any traditional stochastic data analysis method will eventually hit a wall [7], and some common sense will be needed to get the process moving again. In fact, if the various methods come up with different answers, that is a suggestion to be more creative and try to find out why, which should lead to a better understanding of the underlying reality. Paradoxically if you do not know the generating process for the folded information, you cannot tell the difference between an information rich message and a random jumble of letters. This is the information double-bind (IDB) problem in contemporary classic information and algorithmic theory [8], just at the inner core of human knowledge extraction by experimentation in current Science [8]. To develop resilient and antifragile application, we need stronger biological and physical system correlates; in other words, we need asymptoctic exact global solution panoramas combined to deep local solution computational precision with information conservation and vice-versa. The present paper can give a relevant contribute to that perspective and to achieve practical operative results quite quickly.

II. The Root of the Problem

An organism and all the biologically relevant processes that it experiences must have an extremely "many-atomic" structure and must be safeguarded against haphazard, "single-atomic" events attaining too great importance. In fact, we are thaught that all atoms perform all the time a completely disorderly heat motion, which, so to speak, opposes itself to their orderly behaviour and does not allow the events that happen between a small number of atoms to enrol themselves according to any recognizable laws. Only in the co-operation of an enormously large number of atoms do statistical laws begin to operate and to represent the behaviour of these assemblies with an accuracy increasing as the number of atoms involved increases. It is in that way that the events acquire truly orderly features at macroscale level. All the physical and chemical laws that are known to play an important part in the life of organisms can be represented by this statistical kind. Any other kind of lawfulness and orderliness that one might think of is being perpetually disturbed and made inoperative by the unceasing heat motion of the atoms. Every particular physiological process that we observe, either within the cell or in its interaction with the cell environment, appears, or appeared a hunred years ago, to involve such enormous numbers of single atoms and single atomic processes that all the relevant laws of physics and physical chemistry would be safeguarded even under the very exacting demands of statistical physics in respect of large numbers; this demand

ISBN: 978-1-61804-321-4

illustrated just by the well-known √n rule. That, the "naive physicist" tells us, is essential, so that the organism may, so to speak, have sufficiently accurate physical laws on which to draw for setting up its marvellously regular and well-ordered working. This is the main reason why statistical and applied probabilistic theory became the core of classic scientific knowledge and engineering applications at system macroscale level. It was applied to all branches of human knowledge under the "continuum hypotesis" assumption, reachig highly sophistication development, and a worldwide audience. Many "Science 1.0" researchers and scientists up to scientific journals assume it is the ultimate language of science and it is the traditional instrument of risk-taking. How do these conclusions, reached, biologically speaking, a priori (that is, from the purely physical point of view), fit in with actual biological facts? Today, we know that this question is generated by an ill-posed problem and trying to find a sound answer to it requires enlarging our worldview first of all. In fact, incredibly small groups of atoms, much too small to display exact statistical laws, do play a dominating role in the very orderly and lawful events within a living organism. They have control of the observable large-scale characteristics of its functioning, and in all this very sharp and very strict biological laws are displayed. The great revelation of quantum theory (QT), discovered by Max Planck in 1900, is that features of a discreteness were discovered in the Book of Nature at system microscale (nanoscale) level, in context in which anything other than continuity seemed to be absurd according to the views held until then at macroscale level. On the side of QT it took more than a quarter of a century till in 1926-7 the QT of the chemical bond was outlined in its general principles by W. Heitler and F. London. The Heitler-London theory involved the most subtle and intricate conceptions of the development of QT at that time, called "quantum mechanics" (QM) or "wave mechanics" (WM). In the 1920s the problem of creating a QM theory of the electromagnetic field originated early quantum field theory. In particular de Broglie in 1924 introduced the idea of a wave description of elementary systems. In 1925, Werner Heisenberg, Max Born, and Pascual Jordan constructed such a theory by expressing the field's internal degrees of freedom as an infinite set of harmonic oscillators and by employing the canonical quantization procedure to those oscillators. The first reasonably theory of early quantum electrodynamics, which included both the electromagnetic field and electrically charged matter (specifically electrons) as quantum mechanical objects, was created by Paul Dirac in 1927 [10]. Pascual Jordan and Wolfgang Pauli showed in 1928 that quantum fields could be made to behave in the way predicted by special relativity during coordinate transformations (they showed that the field commutators were Lorentz invariant). The early development of the field involved Dirac, Fock, Pauli, Heisenberg and Bogolyubov. This phase of development culminated with the construction of the theory of quantum electrodynamics (QED) in the 1950s [11]. Parallel developments in the understanding of phase transitions in condensed matter physics led to the study of the renormalization group. This in turn led to the grand synthesis of theoretical physics, which unified theories of particle and condensed matter physics through quantum field theory (QFT). This involved the work of Michael Fisher and Leo Kadanoff in the 1970s, which led to the seminal reformulation of QFT by Kenneth G. Wilson in 1975 [12]. QFT has emerged from a major paradigm shift with respect to Classical Physics which still provides the framework of the vision of nature of most scientists. This change of paradigm has not yet been completely grasped by contemporary Science so that not all the implications of this change have been realized hitherto, even less their related applications. So, the discreteness approach, developed under the "discreteness hypotesis" assumption, in specific scientific disciplines, has been considered in peculiar application areas only. It has been further slowly developed by a few specialists and less understood by a wider audience. It is the fresh QFT approach (Science 2.0). Unfortunately, the above two large scientific research areas (continuum based and discreteness based) have followed separate mathematical development paths with no articulated synergic coupling. That is the main reason why QFT is still mostly overlooked by traditional scientific and engineering researchers for system multi-scale modeling, from system nanoscale to macroscale.

III. Method

To find competitive solutions, we need an extended, wider panorama, by using new eyes. While the advantage of differentiating between natural (aleatoric) and epistemic uncertainty in analysis is clear, the necessity of distinguishing between them is not, by an operative point of view.

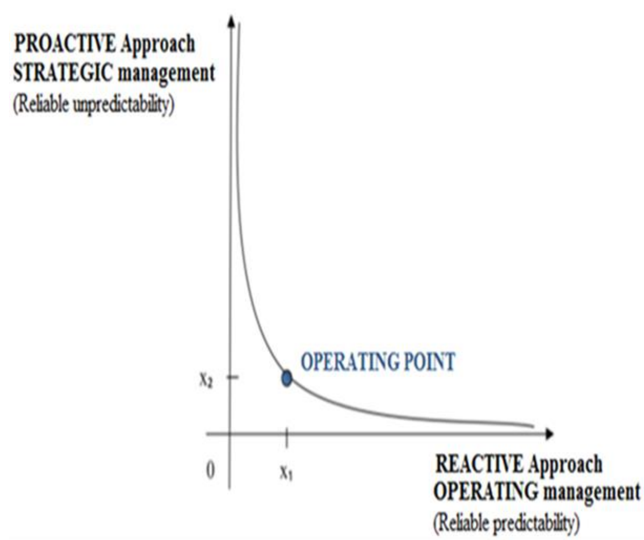

Fig. 1. Operating Point can emerge as a new Trans-disciplinary Reality Level, based on Two Complementary Irreducible Subsystems (see text).

As a matter of fact, epistemic and aleatory uncertainties are fixed neither in space nor in time. What is aleatory uncertainty in one model can be epistemic uncertainty in another model, at least in part. And what appears to be aleatory uncertainty at the present time may be cast, at least in part, into epistemic uncertainty at a later date [13]. It is much better to consider ontological uncertainty [14] as an emergent phenomenon out of a complex system [15] (Fig. 1). Then, our ontological perspective can be thought only as an emergent, natural operating point out of, at least, a dichotomy of two coupled irreducible complementary ideal asymptotic concepts:

A) reliable predictability,
B) reliable unpredictability,

both interacting with their common environment, which they are immersed within. To grasp a more reliable representation of reality and to get stronger biological and physical system measurement and correlates, researchers and scientists need two intelligently articulated hands, both stochastic and combinatorial approaches synergically articulated by natural coupling. In the past, many attempts to arrive to a system continuum-discrete unified mathematical approach have been proposed, all of them with big operational compromises. All these attempts used a TD point-of-view (POV). From a computational perspective,all approaches that use a TD POV allow for starting from an exact global solution panorama of analytic solution families, to arrive to a shallow local solution computational precision to real specific needs. In other words, overall system information from global to local POV is not conserved, as misplaced precision leads to information dissipation [8]. On the contrary, to develop resilient and antifragile system [15], we need asymptotic exact global solution panoramas combined to deep local solution computational precision with information conservation [16].

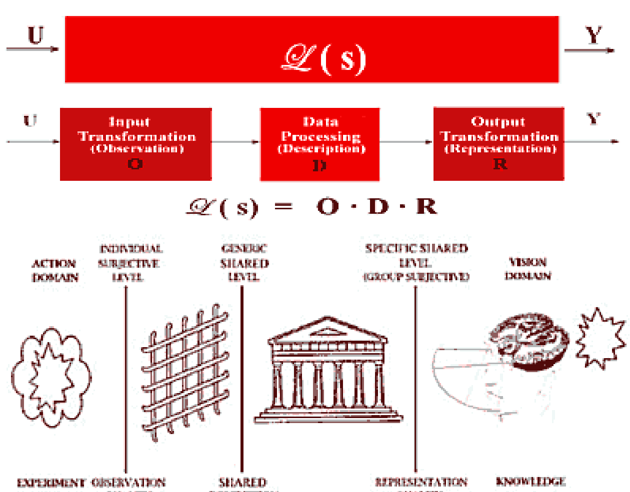

Fig. 2. Top Diagram: Traditional Single Domain Channel (SDC) Transfer Function. Middle Diagram: Decomposition of SDC Transfer Function into more structured ODR Functional Sub-domain Transfer Function (Observation, Description and Representation Functional Blocks). Bottom Diagram: ODR Information Channel Co-domain Diagram for System Information Conservation [17].

The first attempt to identify basic principles to get this goal, and related stronger physical and biological measurement and correlates from experiment, has been developing at Politecnico di Milano University since the 1990s. In the past five decades, trend in Systems Theory, in specialized research area, has shifted from classic single domain information channel transfer function approach (Fig.2 Top Diagram) into the more structured ODR Functional Sub-domain Transfer Function Approach (Observation, Description and Representation, Fig.2 Middle Diagram) [17]. Shortly, the ODR approach allows for fitting theoretical system design consideration to practical implementation needs much better (according to information "Input, Processing, Output" paradigm, respectively) than classic single domain channel approach. Thanks to the ODR approach, a deeper awareness about information acquisition and generation limitations by classical experimental observation process has been grown. In fact, Computational Information Conservation Theory (CICT) showed that classic Shannon entropy is completely unable to reliably discriminate so called computational "random noise" (RN) from any combinatorially optimized encoded message by OECS, called "deterministic noise", DN for short in [8]. According to [15], to cope with ontological uncertainty effectively at system level, we can use two asymptotic coupled complementary irreducible information management subsystems, based on the following ideal dichotomy "Information Reliable Predictability" and "Information Reliable Unpredictability." In this way, to behave realistically, overall system can guarantee both "Logical Closure" (LC) and "Logical Aperture" (LA), both fed by "Environmental Noise." So, a reliable operating point can always emerge as a new trans-disciplinary reality level, out of the interaction of two asymptotic coupled complementary irreducible information management subsystems [15]. As a simple example, the former subsystem is ODR Representation function *f*, and the latter one has to be an ODR *f* extension (ODR Co-domain function *g*) able to capture as much as possible useful information from the open interaction of the two related entities and their environment.

A. *Reliable Predictability Information Subsystem (LC)*

The amount of information an individual can acquire in an instant or in a lifetime is finite, and minuscule compared with what the milieu presents; many questions are too complex to describe, let alone solve, in a practicable length of time. The same is true for all other cascading functional blocks in the ODR transmission channel from source to destination, if careful information conservation countermeasure is not provided at each step. In the Observation phase, interaction between an "Experimental Field" with an "Action Domain" is established and discrete data are captured. Observation is properly described as a fact-finding rather than a fact-collecting procedure, because the idea of finding includes both selection by controlled perturbation and efficient structured collection. The quality of Observation does then depend on the degree of completeness by which experimental unfolded information is allowed to be efficiently captured from our experimental field into our subjective structured Action Domain and properly formatted, according to observation experience and shared rules (System Input Transformation), to

ISBN: 978-1-61804-321-4

be passed to next processing block. Then the second step, Description, can formalize folded subjective observation into an unfolded systemic minimal insured accuracy Representation framework, shared by the majority of interacting entities which use the same formal language to communicate (System State), to be passed to the last step. Finally, the quality of the Representation stage does depend on the degree of completeness by which unfolded information is allowed to be focused and presented to specific shared human knowledge to be validated and endorsed, according to convenient Representation support quality for cultural analytics and information/perceptual aesthetics (System Output Transformation) [18].

B. Reliable Unpredictability Information Subsystem (LA)

ODR Functional Sub-domain Transfer Function block diagram (Fig.2, Top Diagram) must be extended by a matching complementary "ODR Information Channel Co-domain Diagram" to get reliable overall information conservation dynamic functional closure (arbitrary-scale closure). Traditionally, the horizons of accumulating ignorance are expanding faster than any person can keep up with. The proliferation of new sciences extends our powers of sense and thought, but their rigorous techniques and technical language hamper communication; the common field of knowledge becomes a diminishing fraction of the total store. By biomedical cybernetics point of view, to get closer to real computational information conservation, ODR Functional Sub-domain Transfer Function block diagram (Fig.2, Middle Diagram) must be matched by a corresponding irreducible complementary "ODR Information Channel Co-domain Diagram" (for short, Co-ODR) to get reliable strategic overall information dynamic functional closure (Fig.2, Bottom Diagram). As a matter of fact, by iterating full process over repeated controlled "Observations" thanks to Co-ODR support (Fig.2, Bottom Diagram), it is possible to improve the accuracy level of any associated "Description," validated by a related endorsed "Representation," and therefore to better the overall system knowledge under test; human beings call this process "learning by experience." Co-ODR knowledge allows to build the scenario planning for future unknown *f* values and to choose the best match, even under severe perturbation. The future plays an active way in how we think and act in the present. The traditional understanding, that past events are the primary drivers that influence how we understand the present, is undermined. Both the past and the future are forces that simultaneously and actively influence the present. By interpreting the present as the time where the forces of the past and future meet, our understanding of the present changes from a "thin" (the present as a boundary without any extension between past and future) to a "thick present" (the present as the collection of contemporaneous events) [19]. Moreover, by giving the future scientific legitimacy, a novel vision of science arises where a fully scientific (i.e., not allusive, metaphorical or mystical) treatment of "final" causation (≡ anticipation) is included and not rejected as is the case in the traditional scientific paradigm. The notion of anticipation is coming to the foreground as an emerging field of study [19]. This approach can offer highly computational competitive and convenient solutions with respect to traditional "Science 1.0" methods (a few orders of magnitude, theoretically [20],[21]). Furthermore, due to its intrinsic self-scaling properties, this system approach can be applied at any system scale: from single quantum system application development to full system governance strategic assessment policies and beyond [20]. This approach allows you even to develop more antifragile anticipatory learning system (ALS), for more reliable, safe and secure medical application and system (cybersafety) [15].

IV. RESULTS

The first attempt to identify basic principles, to synergically articulate CICT by natural coupling to the Geometric Science of Information (GSI) and Information Geometry (IG), for scientific research and technology application, has been developing at Politecnico di Milano University since the 1990s. In 2013, the basic principles on CICT, from discrete system parameter and generator, appeared in literature and a brief introduction to CICT appeared in 2014 [22]. CICT defines an arbitrary-scaling discrete Riemannian manifold uniquely, under HG metric, that, for arbitrary finite point accuracy *W* going to infinity (exact solution theoretically), under the criterion of scale relativity invariance, is isomorphic (even better homeomorphic) to classic SGI and IG Riemannian manifold (exact solution theoretically) [22]. Traditional Number Theory and modern Numeric Analysis use LTR (left-to-right) mono-directional interpretation for $\boldsymbol{Q}$ Arithmetic single numeric group generator, so information entropy generation cannot be avoided in contemporary computational algorithm and application. On the contrary, according to CICT, it is quite simple to show information conservation and RTL (right-to-left) generator reversibility, by using basic considerations only. The first CICT fundamental general relationship that ties together numeric body information of divergent and convergent monotonic power series in any base (in this case decimal, with no loss of generality), with *D* ending by digit 9, is given by the following CICT LTR-RTL fundamental correspondence equation [20] :

$$\frac{1}{D} = \sum_{k=0}^{\infty} \frac{1}{10^W} \left(\frac{\overline{D}}{10^W} \right)^k \Rightarrow \ldots \Leftarrow \; Div\left(\frac{1}{D}\right) = \sum_{k=0}^{\infty} \left(D+1\right)^k \qquad (01)$$

where $\overline{D}$ is the additive 10^W complement of *D*, i.e. $\overline{D}$ = (10^W - *D*), *W* is the word representation precision length of the denominator *D* and "*Div*" means "Divergence of". When $\overline{D}$ > *D* the formal power series on the left of (01) can be rescaled mod *D*, to give multiple convergence paths to 1/*D*, but with different "convergence speeds." The total number of allowed convergent paths, as monotonic power series, is given by the corresponding Q_L value, at the considered accuracy level *L* [20]. So, increasing the level of representation accuracy, the total number of allowed convergent paths to 1/*D*, as monotonic power series (as allowed conservative paths), increases accordingly and can be counted exactly, and so on, till maximum machine word length and beyond, like discrete quantum paths denser and denser to one another, towards a never ending "blending quantum continuum," by a TD perspective [20]. Further generalizations related to D ending by digit 1, 3 and 7 are straightforward [23]. Here, we like to show an example for f starting with Natural numbers and their geometric powers, to compute their coherent functional closures, by using decimal system operative representation (r = 10), with no loss of generality. Usual knowledge on significant figures of a number teaches that any 0 digit that comes before the first nonzero digit (leading zeros) can be omitted in a number string in positional notation representation system [24]. When leading zeros occupy the most significant digits of an integer, they could be left blank or omitted for the same numeric value [24]. Therefore, the usual decimal notation of integers does not use leading zeros except for the zero itself, which would be denoted as an empty string otherwise [24]. However, in decimal fractions between 0 and 1, the leading zeros digits between the decimal point and the first nonzero digit are necessary for conveying the magnitude of a number and cannot be omitted [24]. If we like to look for an approach achieving computational information conservation (computation conservation reversibility), CICT tells us to compute a convenient co-domain as a coherent functional closure to our traditional computational domain [8]. Here, to get a coherent functional closure the rule is quite simple. One digit word number to the second power gives two digit number word, to the third power gives a three digit number word, to the fourth power gives four digit number word, and so on. This time leading zeroes do count, so you have to fill in all word digits. As an example, we start with Natural number D = 3, and W = 1, where W is the word representation precision length of number D and k the power exponent, k = 1, 2, 3, …. We have:

$$
\begin{array}{lll}
3^1=3 & 10^1-3^1=\overline{D}\cdot(1)_1 & =\ 7 \\
3^2=09 & 10^2-3^2=\overline{D}\cdot(13)_2 & =\ 91 \\
3^3=027 & 10^3-3^3=\overline{D}\cdot(139)_3 & =973 \\
\bullet\bullet\bullet & \bullet\bullet\bullet & \\
3^k & 10^k-3^k=\overline{D}\cdot\begin{pmatrix}3^0\cdot 10^{k-1}+3^1\cdot 10^{k-2}+ \\ \ldots+3^{k-2}\cdot 10^1+3^{k-1}\cdot 10^0\end{pmatrix}_k & .
\end{array}
\tag{02}
$$

On the left column we have the powers of 3 and on the right part their corresponding coherent functional closures. Now, it is simple to see that for k going to infinity the asymptotic expression in round bracket $(:\,:\,:)_k \equiv$ PC in (02) becomes an infinite polynomial and therefore an uncomputable expression. Nevertheless it has quite a definite and unique evolutive structure, easily to compute exactly to any arbitrary precision by CICT [23]. Starting from (02), we can write [23]:

$$D_r^k + \overline{D}_r \cdot \left(\sum_{m=0}^{k-1} D_r^m \cdot r^{W(k-m-1)}\right)_k - r^{W\cdot k} = 0 \quad , \tag{03}$$

where $\overline{D}_r$ is the additive r^W complement of D_r, i.e. $\overline{D}_r = (r^W - D_r)$. Equation (03) is the CICT fundamental relationship for LTR sequences, that relates their evolutive polynomially ordered representation structure to their power information counterpart exactly, for any base r and for any Natural number D. In previous paper, we already saw that CICT can supply us with co-domain Optimized Exponential Cyclic numeric Sequences (OECS) perfectly tuned to their low-level multiplicative noise source generators, related to experimental high-level overall perturbation [23]. Now, by (03), polynomial co-domain information functional closure can be used to evaluate any computed result at arbitrary scale, and to compensate conveniently, to achieve multi-scale computational information conservation by LTR sequences.

V. Conclusion

CICT general relationships to compute information coherent functional closure for any computational system from low-level multiplicative noise source generators, related to experimental high-level overall perturbation were presented and discussed. CICT brings classical and quantum information theory together in a single framework, by considering information not only on the statistical manifold of model states but also on the combinatorial manifold of low-level discrete phased generators and empirical measures of noise sources, related to experimental high-level overall perturbation. Traditional elementary arithmetic long division remainder sequences can be interpreted as combinatorially optimized exponential cyclic sequences (OECS) for hyperbolic structures, as points on a discrete Riemannian manifold, under HG metric, indistinguishable from traditional random noise sources by classical Shannon entropy, and current most advanced instrumentation approach [8]. CICT defines an arbitrary-scaling discrete Riemannian manifold uniquely, under HG metric, that, for arbitrary finite point accuracy W going to infinity (exact solution theoretically), is isomorphic (even better homeomorphic) to traditional information geometry Riemannian manifold [22]. In other words, HG can describe a projective relativistic geometry directly hardwired into elementary arithmetic long division remainder sequences, offering many competitive computational advantages over traditional Euclidean approach. It turns out that, while free generator exponentially growing sequences (OECS) can be divergent or convergent, their coherent functional closures can be defined in terms of complete homogeneous polynomial structures. In previous paper, we already saw that CICT can supply us with OECS co-domain perfectly tuned to low-level multiplicative noise source generators [8]. Associated OECS co-domain polynomial information structure can be used to evaluate any computed result, and to compensate for achieving computational information conservation for any computational system in any polynomial base. To grasp a more reliable representation of reality and to get more resilient and antifragile techniques, researchers and scientists need two intelligently articulated hands, both stochastic and combinatorial approaches synergically articulated by natural coupling. CICT and GSI coupled support can offer an effective and convenient framework to develop more competitive complex system modeling. Due to its intrinsic self-scaling properties, this system approach can be applied at any system scale, from single quantum system application development to full system governance strategic assessment policy system development and beyond. This approach allows you even to develop more antifragile anticipatory learning system (ALS), for more reliable, safe and secure medical application and system (cybersafety). Specifically, advanced HO, high reliability organization (HRO), mission critical project (MCP) system, very low technological risk (VLTR) and crisis management (CM) system will be highly benefitted mostly by these new techniques. This paper is a relevant contribute to show how CICT and GSI coupled support can offer stronger and more effective system modeling solutions in Healthcare.

REFERENCES

[1] N.N. Taleb, *Fooled by Randomness*. New York: Random House, 2nd Ed., 2005.

[2] R.A. Fiorini, G.F. Santacroce, "Economic Competitivity in Healthcare Safety Management by Biomedical Cybernetics ALS," in *Proc. International Symposium, The Economic Crisis: Time For A Paradigm Shift -Towards a Systems Approach*. Valencia, Spain: Universitat de València, January 24-25, 2013.

[3] R.A. Fiorini, G.F. Santacroce, "Systems Science and Biomedical Cybernetics for Healthcare Safety Management," in *Proc. International Symposium, The Economic Crisis: Time For A Paradigm Shift - Towards a Systems Approach*. Valencia: Universitat de València, January 24-25, 2013.

[4] D. Helbing, "The World After Big Data: What the Digital Revolution Means for Us," FuturICT, Tuesday, 20 May 2014. Available: http://futurict.blogspot.it/2014/05/the-world-after-big-data-what-digital.html.

[5] E. Ostrom, *Governing the Commons: The Evolution of Institutions for Collective Action*. Cambridge: Cambridge University Press, 1990.

[6] E. Ostrom, "Beyond Markets and States: Polycentric Governance of Complex Economic Systems," *American Economic Review*, vol. 100, no. 3, pp.641–72, 2010. Available at http://bnp.binghamton.edu/wp-content/uploads/2011/06/Ostrom-2010-Polycentric-Governance.pdf.

[7] N.N. Taleb, *Silent Risk.* Preliminary Book Draft, January, 2015.

[8] R.A. Fiorini, "How Random is Your Tomographic Noise? A Number Theoretic Transform (NTT) Approach," *Fundamenta Infomaticae*, vol.135, no.1-2, pp.135-170, 2014.

[9] S.N. Majumdar, A. Pal, Extreme value statistics of correlated random variables, workshop on Advances in Nonequilibrium Systems, Galileo Galilei Institute, Florence, Italy, August, 2014.

[10] P.A.M. Dirac, "The Quantum Theory of the Emission and Absorption of Radiation," *Proceedings of the Royal Society of London A*, vol.114, no.767, pp.243–265, 1927.

[11] R. P. Feynman, "Mathematical Formulation of the Quantum Theory of Electromagnetic Interaction," *Physical Review*, vol.80, no.3, pp. 440–457, 1950.

[12] K. Wilson, "The renormalization group: Critical phenomena and the Kondo problem," *Reviews of Modern Physics*, vol.7, no.4, pp.773, 1975.

[13] T.C. Hanks, C.A. Cornell, "Probabilistic Seismic Hazard Analysis: A Beginner's Guide," in *Proceedings of the Fifth Symposium on Current Issues Related to Nuclear Power Plant Structures, Equipment and Piping*. Raleigh, N.C.: North Carolina State University, 1994, pp.I/1-1 to I/1-17.

[14] D.A. Lane, R.R. Maxfield, "Ontological Uncertainty and Innovation," *J. Evol. Econ.*, no.15, Springer-Verlag, pp.3-50, 2005.

[15] R.A. Fiorini, G.F. Santacroce, "Application Resilience and Antifragility from the Internet of Medical Devices to Healthcare Governance Systems," in *European Journal for Biomedical Informatics Special Issue on Apps for Medicine, Health and Home Care - Elements of Safety and Effectiveness,* F. Pinciroli, A. Moen, Eds. EJBI, vol.11, no.3, en28-en36, 2015.

[16] R.A. Fiorini, "More effective biomedical experimentation data by CICT advanced ontological uncertainty management techniques," *Int. J. of Biol and Biomed Eng*, vol.9, pp.29-41, 2015.

[17] R.A. Fiorini, *Strumentazione Biomedica: Sistemi di Supporto Attivo*. Milano: CUSL, Collana Scientifica, Italy, 1994.

[18] L. Manovich, *Software Takes Command*. New York: Bloomsbury Academic, 2013.

[19] R. Rosen, *Anticipatory Systems*. Oxford: Pergamon Press, 1985.

[20] R.A. Fiorini, G. Laguteta, "Discrete Tomography Data Footprint Reduction by Information Conservation," vol.125, no.3-4, pp.261-272, 2013.

[21] R.A. Fiorini, "Anticipatory Smart Sensing System Interface by CICT," in *Proceedings of the 15th International Conference on Automation & Information (ICAI '14)*, Geneva, Switzerland, December 29-31, 2014, Recent Advances in Electrical Engineering and Electronic Devices, Recent Advances in Electrical Engineering Series n.43, Nikos E. Mastorakis, Demetrios Kazakos, Eds. WSEAS Press, 2014, pp.98-107.

[22] R.A. Fiorini, "Computational Information Conservation Theory: An Introduction," in *Recent Advances in Applied mathematics, Modelling and Simulation, Mathematical and Computers in Science and Engineering Series n.34*, Nikos E. Mastorakis, Metin Demiralp, Nitis Mukhopadhyay, Francesco Mainardi, (eds.). WSEAS Press, 2014, pp.385-394.

[23] R.A. Fiorini, "Computerized Tomography Noise Reduction by CICT Optimized Exponential Cyclic Sequences (OECS) Co-domain," *Fundamenta Informaticae*, 2015, in press.

[24] R.A. Fiorini, "Stronger Quantum Decoherence Incomputability Modeling by CICT," in *2014 Proceedings of the 3rd International Conference on Applied and Computational Mathematics (ICACM '14)*, Geneva, Switzerland, December 29-31, 2014, Mathematics and Computers in Science and Engineering Series n.39, Nikos E. Mastorakis, Gen Qi Xu, Eds. WSEAS Press, 2014, pp.78-86.

CICT phased generator for arbitrary multi-scale quantification uncertainty effective modeling

R. A. Fiorini, G. Laguteta

***Abstract*—** The needs to assess resilient and antifragile performances for complex systems and to answer tighter regulatory processes (security, safety, environmental control, and health impacts, etc.) have led to the emergence of a new industrial simulation challenge to take uncertainties into account when dealing with complex numerical simulation frameworks. Current uncertainty quantification (UQ) approaches aim to include uncertainty in mathematical models and quantify its effect on output of interest used in decision making. For observing and determining single molecule transport characteristics or for detecting a minute change in resistance or capacitance at biostrucuture nanoscale, we need stronger research modeling and computational tools. To get stronger solution to advanced problems, like resonant nanoparticle, nanophotonic, optifluidics structure modeling, etc., we have to look for convenient arbitrary multi-scaling (AMS) BU (bottom-up) point-of-view (POV) (from discrete to continuum view ≡ BU POV) to start from first, and NOT the other way around! We present a simple example on multiscale quantification uncertainty modeling by unfolding the full information content hardwired into Rational OpeRational (OR) representation (nano-microscale discrete representation) and relating it to a continuum framework (meso-macroscale) with no information dissipation. This paper is a relevant contribute to show how *CICT* and GSI can offer stronger and more effective AMS quantification uncertainty solution to complex system modeling.

***Keywords*—** biomedical engineering, CICT, complex system, GSI.

I. Introduction

To face the challenge of complex system modeling (hierarchical heterogeneous component multi-scale system modeling), we need to be able to control system quantification uncertainty from macroscale, through mesoscale, till nanoscale and beyond. We need more robust, resilient and antifragile application to be ready for next generation systems [1],[2]. Attempts to optimize multi-scale systems in a top-down (TD) way will be less and less effective, and cannot be done in real time. That is the main reason why, over the last few years, integration of stochastic methods into a multi-scale framework (from macro-scale to nano-scale) or development of multi-scale models in a stochastic setting for epistemic uncertainty quantification (UQ) is becoming an emerging research frontier for systems modeling, innovation and competitive development in Science and Technology. Current UQ approaches aim to include uncertainty in mathematical models and quantify its effect on output of interest used in decision making. Traditional human approach to experience is based on risk analysis and decision making in a natural uncertain environment by incomplete knowledge. In the past three centuries, statistical and applied probabilistic theory became the core of classic scientific knowledge and engineering applications at system macroscale level. It was applied to all branches of human knowledge under the "continuum hypotesis" assumption, reaching highly sophistication development, and a worldwide audience. Even today, many "Science 1.0" researchers and scientists up to scientific journals assume it is the ultimate language of science and it is the traditional instrument of risk-taking. Unfortunately, Deep epistemic limitations reside in some parts of the areas covered in risk analysis and decision making applied to real problems [3],[4]. From this POV, current most advanced "embedded intelligent system" is a "deficient system," a fragile system, because its algorithms are based on statistical intelligence or knowledge only, and are lacking a fundamental system component (see section III, Multi-Scale Quantification Uncertainty). Today, we know that incredibly small groups of atoms, much too small to display exact statistical laws, do play a dominating role in the very orderly and lawful events within a living organism. They have control of the observable large-scale characteristics of its functioning; and in all this very sharp and very strict biological laws are displayed. The great revelation of quantum theory (QT), discovered by Max Planck in 1900, is that features of a discreteness were discovered in the Book of Nature at system microscale (nanoscale) level, in context in which anything other than continuity seemed to be absurd, according to the views held until then at macroscale level. It took more than a quarter of a century till in 1926-7 the QT of the chemical bond was outlined in its general principles by W. Heitler and F. London. The Heitler-London theory involved the most subtle and intricate conceptions of the development of QT at that time, called "quantum mechanics"

Rodolfo A. Fiorini is with the Department of Electronics, Information and Bioengineering (DEIB), Politecnico di Milano University, Milano, 32 Piazza Leonardo da Vinci, 20133 Milano, ITALY (phone: +39 022399 3350; fax: +39 022399 3360; e-mail: rodolfo.fiorini@polimi.it).

Giuseppe Laguteta is with HITACHI DATA SYSTEMS ITALIA Srl, Via del Bosco Rinnovato 8, edificio U4, 20090 Assago (MI), ITALY (e-mail: giuseppe.laguteta@hds.com).

(QM) or "wave mechanics" (WM). In the 1920s the problem of creating a QM theory of the electromagnetic field originated early quantum field theory (QFT). In particular de Broglie in 1924 introduced the idea of a wave description of elementary systems. QFT has emerged from a major ontological paradigm shift with respect to Classical Physics which still provides the framework of the vision of nature of most scientists. This change of paradigm has not yet been completely grasped by contemporary science so that not all the implications of this change have been realized hitherto, even less their related applications. So, the discreteness approach, developed under the "discreteness hypotesis" assumption, in specific scientific disciplines, has been considered in peculiar application areas only. It has been further slowly developed by a few specialists and less understood by a wider audience. Unfortunately, the above two large scientific research areas (continuum based and discreteness based) have followed separate mathematical development paths with no articulated synergic coupling. That is the main reason why QFT is still mostly overlooked by traditional scientific and engineering researchers for system multiscale modeling, from system nano-microscale to macroscale. Unfortunately, the "probabilistic veil" can be very opaque computationally, in a continuum-discrete arbitrary multi-scale environment, and misplaced precision leads to information dissipation and confusion. As a matter of fact, Stochastic vs. Combinatorically Optimized Noise ambiguity emphasises the current information double-bind (IDB) problem, in current most advanced research laboratory and instrumentation system, just at the inner core of human knowledge extraction by experimentation in current Science [5].

II. THE IDB PROBLEM IN SCIENCE

Traditional scientific knowledge teaches that the only way to generate truly random numbers is through a random physical process, such as tossing dice or measuring intervals between radioactive decays. On the contrary, all computer programs can compute "random" numbers from defined calculations. Since the sequence of numbers is reproducible, mathematicians say that the numbers are "pseudo-random." Stochastic computer simulation uses extensively random number generation and the quality of these generators can play a crucial role on final simulation results. A full discussion of computer generate randomness quality is beyond the scope of this paper and for further reading, the interested reader is referred to [6]. Shannon's entropy (usually denoted by *H(x)* is used as a fast stochastic measure of probabilistic information uncertainty in every information processing system. *H(x)* is the average unpredictability in a random variable, which is equivalent to its information content. The concept was introduced by Claude E. Shannon in his seminal 1948 paper "A Mathematical Theory of Communication" [7]. The interested reader in digging deeper details into mathematical theory of entropy and information theory, inference, and learning algorithms, is referred to [8] and [9] respectively. As an example, let us use a 256-shades grey image. Let us think of an image as a square matrix of N^2 cells (pixels).

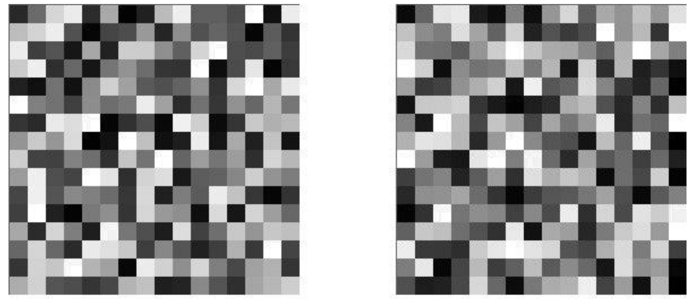

A B

Fig. 1 A) Magnification of a 16x16 pixel instance for an image by a stochastic pseudo-random noise (white noise) generator (256 shades of grey); B) Magnification of a 16x16 pixel instance for an image by CICT combinatorially optimized (deterministic) generator (256 shades of grey).

In this case, to maximise Shannon's entropy, each cell must have one shade of grey, out of $M = 256$ possible ones (M values), different from all the other ones in the matrix. Our image can be thought as a system of linear equations that can be an underor overdetermined system. In the case of an underdetermined system there are more M values(shades of grey) than available equations N^2 (available cells). Hence an image with $N^2 < M$ pixels is unable to exploit the full dynamic range of a 256-shades of grey ideal random noise source generator. On the other hand, an image with $N^2 > M$ pixels is an overdetermined system and, inevitably, at least two pixels will have the same value (shade of grey). Then, if we like to maximize $H(x)$, it is sufficient to have $N = 16$ and to use a 16 by 16 pixel image to be sure to visualize an instance image out of all the 256^{256} (a transcomputational number [10]) possible gray variation combinations generated by an ideal random noise source, as depicted in Fig.1A (an ideal random source always produces an apparently uniform grey image). In this case we used, for simplicity, a computer generated pseudo-random source from open source software. Then, Shannon's entropy for pseudo-random grey image (Fig.1A) is $H_1(x)$ = 0:893995, in single precision, $H_2(x)$ = 0:893995239236685, in double precision and $H_3(x)$=0:8939952392366848774964724918765288132199273 122746343439319551627 with 64-digit precision arithmetic. As you can see, $H_1(x)$ is far away from theoretical value $H(x)$ = 1:0. By using this approach, you can even define a "stochastic quality descriptor" for noise source in a quite simple way. According to *CICT* point of view [11], it is possible to generate a corresponding visibly similar image to previous one (Fig.1A), by using the so called Solid Number (SN) approach in [11],[12]. In this case, combinatorial optimization is easily achieved by finding the best SN p (i.e. SN p = 257, a Fermat prime) which allows to minimize our desired constraint within a specified interval, to be sure to visualize an instance image out of all the combinatorially optimized ($2 \times 2^2 \times 2^8$) = 2048

ISBN: 978-1-61804-321-4

grey images offered by this specific SN. Shannon's entropy computation for combinatorially optimized grey image (Fig.1B) is then $H_1(x)$ = 1:000000, in single precision, $H_2(x)$ = 1:000000000000000, in double precision and $H_3(x)$=1:000000000000000000000000000000000000000000000000000000000 with 64-digit precision arithmetic. So, to an observer who is not familiar with the encoding scheme used, a combinatorially optimized message of this type (Fig.1B) would be entirely indistinguishable from a corresponding instance generated by a "pseudo-random noise" source (Fig.1A), or even from a random physical process. Now, one might be tempted to say that perhaps one could tell the two apart by spotting patterns within particular frequency bands of the message, or by performing some other decomposition of the overall signal. This possibility is however ruled out by the maximization of the Shannon's information entropy: any regularities that would allow one to draw such a distinction are necessarily the result of less-than-optimal encoding. In 2004, Newman, Lachmann and Moore (NLM), have extended the pioneering 1940s research of Shannon to electromagnetic transmission. Specifically, they show that if electromagnetic radiation is used as a transmission medium, the most information-efficient format for a given message is indistinguishable from blackbody radiation [13]. Since many natural processes maximize the Gibbs-Boltzmann entropy, they should give rise to spectra indistinguishable from optimally efficient transmissions. By our image example, we have found analogous result to NLM [13]. So, paradoxically if you don't know the code used for the message you can't tell the difference between an information-rich message and a random jumble of letters. This is the information double-bind (IDB) problem in contemporary classic information theory. Scientific community laid itself in this IDB situation. Even the most sophisticated, current instrumentation system is completely unable to reliably discriminate so called "random noise" (RN) from any combinatorially optimized encoded message, which we can then now call "deterministic noise," DN for short. It is a problem to solve clearly and reliably, before taking any quantum leap to more competitive and convenient, at first sight, post-human cybernetic approaches in Science and technology. As a matter of fact, to grasp a more reliable representation of reality, researchers and scientists need two intelligently articulated hands; both stochastic and combinatorial approach synergically articulated by natural coupling [11]; let's say we need a fresh "Science 2.0" approach.

III. Multi-Scale Quantification Uncertainty

As an example with important implications, let us consider classical relativistic electrodynamics applied to biological system modeling (e.g. fullwave electromagnetic modeling of brain waves). It is well known that both the time domain and frequency domain based numerical computational electromagnetic methods (i.e. Method of Moments (MoM), the Finite Element Method (FEM), etc.) for solving the Maxwell's equations suffer from the so-called "low-frequency-breakdown" problem [14]. They can only go down to a few hundred MHz in frequency, below which the result they yield becomes very inaccurate relatively quickly. It is not uncommon, therefore, to resort to quasi-static solvers once the frequency of interest falls below a certain frequency (say a few MHz), and to ignore the contribution of the displacement currents, and, hence, the coupling between the electric and magnetic fields. Unfortunately, however, this approximation is not valid for most of the materials inside the head, since the $\sigma/(\omega\varepsilon)$ ratio ($\sigma \equiv$ medium conductivity, $\omega \equiv$ (angular) frequency, $\varepsilon \equiv$ medium permittivity ratio) of these materials is typically close to 1 [14],[15]. In fact, the quasi-static potential differs from the full-wave potential by nearly 30 % to 50 % [16], supporting the argument that a fullwave solution should be derived even at low frequencies for the head-modeling problem, since the quasi-static approach is not sufficiently accurate for the problem at hand. All the above, taking into account that neural activity inside the brain results in low frequency waves known as brain waves at system macroscale level. These brain waves can be further classified into delta (0.1 to 3 Hz), theta (4 to 7 Hz), alpha (8 to 12 Hz), beta (12 to 30 Hz) and gamma (30 to 100 Hz) waves based on the rate of neural activity inside the brain. The successes of neuroscience in the study of the structural and biochemical properties of neurons, glia cells, and all the biological units and cellular structures in the brain have not yet filled the gap between the behavior understood at cellular level (microscale) and the macroscopic dynamics involved in the traffic between the brain and the world around it. There is an essential problem in the study of brain function (mesoscale dynamics) that even today, after so many years since Karl Lashley posed his dilemma, still waits for a solution. As recalled many times in the literature, in the mid 1940s he wrote [17]:

" .... Here is the dilemma. Nerve impulses are transmitted ...from cell to cell through definite intercellular connections. Yet, all behavior seems to be determined by masses of excitation...within general fields of activity, without regard to particular nerve cells... What sort of nervous organization might be capable of responding to a pattern of excitation without limited specialized path of conduction? The problem is almost universal in the activity of the nervous system."

In quantum physics, the space-time distribution of matter and energy has a coarse-grained structure which allows its representation as an ensemble of quanta (particle representation). The local phase invariance is shown to hold if a field exists which is connected to the space-time derivatives of the phase. If we take into consideration a generic electromagnetic field F, described by Riemann-Silberstein vector [18], and we follow the line of thought reported in spacetime algebra (STA) [19]-[21], we can build an effective model quite easily. STA is built up from combinations of one time-like basis vector γ_0 and three orthogonal space-like

ISBN: 978-1-61804-321-4

vectors $\{\gamma_1, \gamma_2, \gamma_3\}$ [19]. F is defined as a complexified 3-dimensional vector field. The value of F at an event is a bivector according to Geometric Calculus (GC) [21]. The field bivector F is the same for all observers; there is no question about how it transforms under a change of reference system. However, it is easily related to a description of electric and magnetic fields in a given inertial system. For the purpose of mapping the brain, we are interested in estimating the fields at different points inside the head in the frequency range of 0.1–100 Hz when either one or many sources are located inside the head. In the case of a system made up of electrically charged components (nuclei and electrons of atoms), as, for instance, a biological system, this is just the electromagnetic (e.m.) potential $\boldsymbol{A}\mu$, where μ is the index denoting the usual four space-time coordinates $\gamma_0 = ct$, $\gamma_1, \gamma_2, \gamma_3$. The electric and magnetic fields are suitable combinations of the space-time derivatives of $\boldsymbol{A}\mu$. In order to get the local phase invariance, we should assume that the system Lagrangian is invariant with respect to specific changes of the field $\boldsymbol{A}\mu$. Thus a specific principle of invariance, named "gauge invariance," emerges; hence the name "gauge field" denotes $\boldsymbol{A}\mu$. Actually it is well known that the Maxwell equations just obey the "gauge invariance," which in quantum physics becomes the natural partner of the "phase invariance" to produce our world. Quantum fluctuations give rise to e.m. potentials which spread the phase fluctuations beyond the system at the phase velocity. This gives an intrinsic nonlocalizability to the system and prevents a direct observation of quantum fluctuations. Through the e.m. potential, the system gets a chance to communicate with other systems. Notice that all e.m. interactions occur in a two-level way; the potential keeps the interacting particles phase-correlated whereas the combination of its space-time derivatives, named e.m. field, accounts for the forces involved. The lower level, the potential, becomes physically observable only when the phase of the system assumes a precise value. The structure of electrodynamics makes possible the presence of a potential also when both electric and magnetic fields are absent, whereas on the contrary fields are always accompanied by potentials. The above solution, which stems from the mathematical formalism of QFT [22], opens the possibility of tuning the fluctuations of a plurality of systems, producing therefore their cooperative behavior. However, some conditions must be met in order to implement such a possibility. Let us, first of all, realize that in quantum physics the existence of gauge fields, such as the e.m. potential, dictated by the physical requirement that the quantum fluctuations of atoms should not be observable directly, prevents the possibility of having isolated bodies. For this reason, the description of a physical system is given in terms of a matter field, which is the space-time distribution of atoms/molecules, coupled to the gauge field with the possible supplement of other fields describing the nonelectromagnetic interactions, such as the chemical forces. According to the principle of complementarity, there is also another representation where the phase assumes a precise value; this representation, which focuses on the wave-like features of the system, cannot be assumed simultaneously with the particle representation. The relation between these two representations is expressed by the uncertainty relation, similar to the Heisenberg relation between position and momentum:

$$\Delta N \, \Delta \Phi \geq ½ \; , \qquad (01)$$

connecting the uncertainty of the number of quanta (particle structure of the system) ΔN and the uncertainty of the phase (which describes the rhythm of fluctuation of the system) $\Delta\Phi$. Consequently, the two representations we have introduced above correspond to the two extreme cases:

(A) If $\Delta N = 0$, the number of quanta is well defined, so that we obtain an atomistic description of the system, but lose the information on its capability to fluctuate, since $\Delta\Phi$ becomes infinite. This choice corresponds to the usual, classic description of objects in terms of the component atoms/molecules.

(B) If $\Delta\Phi = 0$, the phase is well defined, so that we obtain a description of the movement of the system, but lose the information on its particle-like features which become undefined since ΔN becomes infinite. Such a system having a well-defined phase is termed "coherent" in the physical jargon.

In the phase representation, the deepest quantum features appear since the system becomes able to oscillate with a well-defined phase only when the number of its components becomes undefined, so that it is an open system able to couple its own fluctuations to the fluctuations of the surroundings. In other words, such a coherent system, like a biological one, is able to "feel" the environment which is immersed within, through the e.m. potential created by its phase dynamics. In conclusion, a coherent system involves two kinds of interaction:

(1) an interaction similar to that considered by Classical Physics, where objects interact by exchanging energy. These exchanges are connected with the appearance of forces. Since energy cannot travel faster than light, this interaction obeys the "principle of causality;"

(2) an interaction where a common phase arises among different objects because of their coupling to the quantum fluctuations and hence to an e.m. potential. In this case there is no propagation of matter and/or energy taking place, and the components of the system "talk" to each other through the "modulations of the phase field" travelling at the phase velocity, which has no upper limit and can be larger than c, the speed of light.

IV. CICT Phased Generators

CICT defines an arbitrary-scaling discrete Riemannian manifold uniquely, under HG metric, that, for arbitrary finite point accuracy *W* going to infinity (exact solution theoretically), under the criterion of scale relativity invariance, is isomorphic (even better homeomorphic) to the classic Geometric Science of Information (GSI) and Information Geometry (IG) Riemannian manifold (exact solution theoretically) [23]. Traditional Number Theory and modern Numeric Analysis use LTR (left-to-right) mono-directional interpretation for ***Q*** Arithmetic single numeric group generator, so information entropy generation cannot be avoided in contemporary computational algorithm and application. On the contrary, according to *CICT*, it is quite simple to show information conservation and RTL (right-to-left) generator reversibility, by using basic considerations only. If we want to achieve overall system information representation conservation and to get stronger modeling solution to advanced problems, like resonant nanoparticle, nanophotonic, optifluidics structure modeling, etc., we have to look for convenient arbitrary scaling BU (bottom-up) pointof-view (POV) (from discrete to continuum view ≡ BU POV) to start from first, and NOT the other way around! Traditional digital computational resources are unable to capture and to manage not only the full information content of a single Real Number in ***R***, but even Rational Number ***Q*** is managed by information dissipation (e.g. finite precision machine, truncating, rounding, etc.) *CICT* is a natural framework for arbitrary multi-scale computer science and systems biology computational modeling in the current landscape of modern QFT [5],[23]. According to fresh *CICT* result, scientific community has acquired new awareness about traditional rational number system ***Q*** numeric properties, quite recently [11]. Thanks to this line of generative thinking, it is possible to realize that traditional rational number system can be even regarded as a highly sophisticated open logic, powerful and flexible LTR and RTL formal language of languages, with self-defining consistent words and rules, starting from elementary generators and relations [11]. Further, *CICT* ODR (Observation, Description, Representation) approach [5] can take advantage immediately from those properties to develop system computational functional closures to achieve information conservation countermeasure at each operative stage automatically. Then, all computational information usually lost by classic information approach, based on the traditional noise-affected data stochastic model only, can be captured and fully recovered to arbitrary precision by a corresponding complementary co-domain, step-by-step. Theoretically, co-domain information can be used to correct any computed result, achieving computational information conservation (virtually noise-free data), according to *CICT* Infocentric World-view [24]. In this way, overall system resilience and antifragility can be developed quite easily [4]. *CICT* new awareness of discrete HG (hyperbolic geometry) subspaces (reciprocal space) of coded heterogeneous hyperbolic structures [5], underlying the familiar ***Q*** Euclidean (direct space) surface representation can open the way to arbitrary multi-scale information conservation by the *CICT* phased generator (PG) approach [5],[23]. First, let us introduce a LTR symbolic compression operator SCO ≡ <M | DS>, where DS is a finite digit string of length *W* and M is the number of times DS is repeated to get the final unfolded digit string in full (e.g. <4 | 1> ≡ 1111 or <2 | 123> ≡ 123123). Usual symbolic string operations can be applied to SCO. Then, we can write usual rational number OpeRational Representation (OR) [11] corresponding to their Symbolic Representation (SR) as:

$$
\begin{aligned}
Q1 &= \frac{1}{D1} = \frac{1}{9} = 0.11111111111\ldots \\
Q2 &= \frac{1}{D2} = \frac{1}{99} = 0.010101010101010101010101\ldots \\
Q3 &= \frac{1}{D3} = \frac{1}{999} = 0.001001001001001001001001001001001\ldots \\
&\ldots\ldots
\end{aligned}
\tag{02}
$$

in a more compact *RFD* (Representation Fundamental Domain, [11]) Q_W format as:

$$
\begin{aligned}
Q1 &= \frac{1}{D1} = \frac{1}{9} \equiv 0.<\infty \mathrm{I}1> = 0.<\infty \mathrm{I}(0\mathrm{I}0 >< 1\mathrm{I}1>)> \\
Q2 &= \frac{1}{D2} = \frac{1}{99} \equiv 0.<\infty \mathrm{I}01> = 0.<\infty \mathrm{I}(1\mathrm{I}0 >< 1\mathrm{I}1>)> \\
Q3 &= \frac{1}{D3} = \frac{1}{999} \equiv 0.<\infty \mathrm{I}001> = 0.<\infty \mathrm{I}(2\mathrm{I}0 >< 1\mathrm{I}1>)> \\
&\ldots\ldots \\
Qn &= \frac{1}{Dn} = \frac{1}{< n\mathrm{I}9} \equiv 0.<\infty \mathrm{I}(n\mathrm{I}0 >< 1\mathrm{I}1>)> \\
&\ldots\ldots
\end{aligned}
\tag{03}
$$

In the same way, we can write:

$$
\begin{aligned}
P1 &= \frac{1}{DD1} = \frac{1}{1} = 0.99999999999\ldots \\
P2 &= \frac{1}{DD2} = \frac{1}{11} = 0.09\,0909090909090909\ldots \\
P3 &= \frac{1}{DD3} = \frac{1}{111} = 0.009\,009\,009\,009\,009\,009\,009\ldots \\
&\ldots\ldots
\end{aligned}
\tag{04}
$$

in a more compact *RFD* Q_W format as:

$$
\begin{aligned}
P1 &= \frac{1}{DD1} = \frac{1}{1} \equiv 0.<\infty \mathrm{I}9> = 0.<\infty \mathrm{I}(0\mathrm{I}0 >< 1\mathrm{I}9>)> \\
P2 &= \frac{1}{DD2} = \frac{1}{11} \equiv 0.<\infty \mathrm{I}09> = 0.<\infty \mathrm{I}(1\mathrm{I}0 >< 1\mathrm{I}9>)> \\
P3 &= \frac{1}{DD3} = \frac{1}{111} \equiv 0.<\infty \mathrm{I}009> = 0.<\infty \mathrm{I}(2\mathrm{I}0 >< 1\mathrm{I}9>)> \\
&\ldots\ldots \\
Pn &= \frac{1}{DDn} = \frac{1}{< n\mathrm{I}1>} \equiv 0.<\infty \mathrm{I}(n\mathrm{I}0 >< 1\mathrm{I}9>)> \\
&\ldots\ldots
\end{aligned}
\tag{05}
$$

ISBN: 978-1-61804-321-4

Now, we can realize that P_1 *RFD* is related by Q_1 *RFD*, P_2 *RFD* is related by Q_2 *RFD*, P_3 *RFD* is related by Q_1 *RFD*, … and vice-versa by periodic scale relativity (precision length) W = 1, 2, 3, …, respectively. So, to conserve the full information content of rational correspondence between Q_1 and P_1, Q_2 and P_2, Q_3 and P_3, …, we realize that we have to take into account not only the usual Q_1 and P_1, etc., modulus information, but even their related periodic precision length information W = 1, 2, 3, …, respectively (external or extrinsic phase representation). Furthermore we see that:

$$
\begin{aligned}
&O1 = \frac{1}{DDD1} = \frac{1}{9} \equiv 0.<\infty \mathrm{I} 1> = 0.<\infty \mathrm{I}(<1\mathrm{I}1>)> \\
&O2 = \frac{1}{DDD2} = \frac{1}{09} \equiv 0.<\infty \mathrm{I} 11> = 0.<\infty \mathrm{I}(<2\mathrm{I}1>)> \\
&O3 = \frac{1}{DDD3} = \frac{1}{009} \equiv 0.<\infty \mathrm{I} 111> = 0.<\infty \mathrm{I}(<3\mathrm{I}1>)> \\
&\quad .... \\
&On = \frac{1}{DDDn} = \frac{1}{<(<n\mathrm{I}0><1\mathrm{I}9>)>} \equiv 0.<\infty \mathrm{I}(<n\mathrm{I}1>)> \\
&\quad ....
\end{aligned}
\tag{06}
$$

The coherent representations DDD_1, DDD_2, DDD_3, etc. emerge out of a LTR infinity of symbolic structured infinite length sequences as in (06). So, DDD_n in (06) is the coherent relation representation of traditional scalar modulus D_1 in (02) as denominator at precision W, while scalar modulus D_n in (02) has to be interpreted as the decoherenced relation representation of DDD_n denominators in (06). In general, for any Natural number D in $\boldsymbol{N}$ we can write:

$$
\begin{aligned}
&\frac{1}{<n\mathrm{I}RFD(D)>} \equiv \\
&\equiv <(<k+W(n-1)\mathrm{I}0><1\mathrm{I}D>)>.<(<k+W(n-1)\mathrm{I}0><1\mathrm{I}D>)>
\end{aligned}
\tag{07}
$$

where *RFD* is *CICT D* "Representation Fundamental Domain" at precision W and k is the number of leading zeros in *RFD* (if any) at precision W. Now, for n→∞, we get:

$$
\begin{aligned}
&\frac{1}{<n\mathrm{I}RFD(D)>} \equiv \\
&\equiv <(<k+W(n-1)\mathrm{I}0><1\mathrm{I}D>)>.<(<k+W(n-1)\mathrm{I}0><1\mathrm{I}D>)> = \\
&= \bar{0}D.\bar{0}
\end{aligned}
\tag{08}
$$

By this point of view, Natural numbers $\boldsymbol{N}$ emerge from (08) as a conceptual abstraction, just from the rightmost approximated part of those structured sequences when n → ∞, for n in $\boldsymbol{N}$, with truncated decimal part (represented by zero on any finite computational machine). In this way we lose the basic relationship with its fundamental string generators (i.e. information dissipation and information system decoherence) completely. Leading zeros in positional notation representation system for *CICT* $\boldsymbol{Q}$ Arithmetic do count effectively, and can model the system quantum-classical transition quite effectively [25]. If we do not take into account leading zeros information, we lose the correct rational *RFD* correspondence information (coherence), which an inner or intrinsic phase for each RTL string generator can be computed from (i.e. from their optimized exponential cyclic sequences (OECS) of R_W [11]). The *CICT* fundamental relationship that ties together numeric body information of RTL divergent monotonic power series in any base (in this case decimal, with no loss of generality) with D ending by digit 9 is given by the following equation:

$$
\frac{1}{D} = \frac{1}{\sum_{k=0}^{\infty} (D+1)^k} \quad . \tag{09}
$$

Further generalizations of (09) related to D ending by digit 1, 3 and 7 are straightforward [24]. Rational representations are able to capture two different types of information at the same time, modulus (usual quotient information) and associated outer or extrinsic phase (period) information, which inner generator phase (generator intrinsic period) can be computed from. So, rational information can be better thought to be isomorphic to vector information rather than to usual scalar one, at least. According to our SCO approach, previously presented, the correct coherent relation representation of traditional scalar modulus D = 7 as denominator of an Egyptian fraction, is given by:

$$
\begin{aligned}
&CQ1 = \frac{1}{CD1} \equiv \frac{1}{<\infty \mathrm{I}(<\infty \mathrm{I}0><1\mathrm{I}7>)>} \equiv \\
&\equiv 0.<\infty \mathrm{I}RFD(7)> \equiv 0.<\infty \mathrm{I}142857>
\end{aligned}
\tag{10}
$$

To conserve the full information content of rational correspondence at higher level, we realize that we have to take into account not only the usual modulus information, but even the related periodic precision length information W = 6 (numeric period or external phase representation) in this case (i.e. CD_1 = 000007 as base *RFD*). We can use Euler's formula to establish the usual fundamental relationship between trigonometric functions and the complex exponential function:

$$
e^{ix} = \cos x + i \sin x \ , \tag{11}
$$

where e is the base of the natural logarithm and i = √-1. The final result is:

$$
CQQ1 = \frac{1}{CDD1} = \frac{1}{7} e^{i\frac{\pi}{3}} = \frac{1}{7}\left(\cos\left(\frac{2\pi}{6}\right) + i \sin\left(\frac{2\pi}{6}\right)\right) \tag{12}
$$

and

$$
CDD1 = \frac{1}{CQQ1} = 7 e^{-i\frac{\pi}{3}} = 7\left(\cos\left(-\frac{\pi}{3}\right) + i \sin\left(-\frac{\pi}{3}\right)\right) = 7\left(\frac{1}{2} - i\frac{\sqrt{3}}{2}\right) \tag{13}
$$

CICT shows that any natural number n in $\boldsymbol{N}$ has an associated specific, non-arbitrary phase relationship (OECS Optimized

Exponential Cyclic Sequence coherence information [25]) that we have to take into account to full conserve its information content by computation in Euclidean space [5]. The interested reader will have already guessed the relationship of our result to de Moivre number or root of unity (i.e. any complex number that gives 1.0 when raised to some integer power of *n*). In this way, we can exploit much better Rational numbers ***Q*** full information content to get stronger solutions to current arbitrary multi-scale system modeling problems [11].

V. Conclusion

The process of the emergence of coherent structures out of a crowd of independent component particles has been investigated in the last decades and is presently quite well understood [22],[26]-[28]. According to QFT, the gauge invariance in quantum physics becomes the natural partner of the phase invariance to produce our world. Quantum fluctuations give rise to e.m.potentials which spread the phase fluctuations beyond the system at the phase velocity. This gives an intrinsic nonlocalizability to the system and prevents a direct observation of quantum fluctuations. Through the e.m. potential, the system gets a chance to communicate with other systems and subsystems. The presence of this field has received experimental corroboration by the discovery of the so-called "Lamb shift," named after the Nobel prize winner Lamb [29]. He discovered as far back as in 1947 that the energy level of the electron orbiting around the proton in the hydrogen atom is slightly shifted (about one part per million) with respect to the value estimated when assuming that no e.m. field is present. Further corroboration for the existence of vacuum fluctuations is provided by the Casimir effect [30]. Therefore a weak e.m. field is always present, just the one arising from the vacuum quantum fluctuations. Eventualy, we have seen that the correct modeling of a coherent system must involve two kinds of interaction:

(1) an interaction similar to that considered by Classical Physics, where objects interact by exchanging energy. These exchanges are connected with the appearance of forces measured by their magnitude (modulus) only, in an assumed continuum manifold that may be approached and studied by traditional statistical and probabilistic tools offered by the large arena of the Geometric Science of Information (GSI). Since energy cannot travel faster than light, this interaction obeys the principle of causality (Science 1.0 paradigm). The missing part of this worldview is usually called "system noise," "background radiation," etc. on cosmic scale by human beings;

(2) an interaction where a common phase arises among different objects because of their coupling to the quantum fluctuations and hence to an e.m. potential. In this case there is no propagation of matter and/or energy taking place, and the components of the system "talk" to each other through the modulations of the phase field travelling at the phase velocity, which has no upper limit and can be larger than *c*, the speed of light (Science 2.0 approach). *CICT* new awareness of discrete HG (hyperbolic geometry) subspaces (reciprocal space) of coded heterogeneous hyperbolic structures [5], underlying the familiar ***Q*** Euclidean (direct space) surface representation, shows that any natural number *n* in ***N*** has associated a specific, non-arbitrary phase relationship that we have to take into account to full conserve overall system information content by computation in Euclidean space. This awareness opens the way to arbitrary multi-scale information conservation by the *CICT* phased generator (PG) approach [11],[23].

We have shown a simple example of arbitrary multi-scale quantification uncertainty modeling by unfolding the full information content hardwired into Rational OR representation (nano-microscale discrete representation) and relating it to an assumed continuum framework (meso-macroscale) with no information dissipation. *CICT* PG approach can offer an effective and convenient "Science 2.0" universal framework, by considering information not only on the statistical manifold of model states but also on the combinatorial manifold of low-level discrete, phased generators and empirical measures of noise sources, related to experimental high-level overall perturbation. This paper is a relevant contribute towards arbitrary multi-scale computer science and systems biology modeling, to show how the *CICT* approach can offer an effective and convenient "Science 2.0" universal framework to develop innovative application and beyond, towards a more sustainable economy and wellbeing, in a global competition scenario

References

[1] R.A. Fiorini, G.F. Santacroce, "Economic Competitivity in Healthcare Safety Management by Biomedical Cybernetics ALS," in *Proc. International Symposium, The Economic Crisis: Time For A Paradigm Shift -Towards a Systems Approach.* Valencia, Spain: Universitat de València, January 24-25, 2013.

[2] R.A. Fiorini, G.F. Santacroce, "Systems Science and Biomedical Cybernetics for Healthcare Safety Management," in *Proc. International Symposium, The Economic Crisis: Time For A Paradigm Shift - Towards a Systems Approach.* Valencia, Spain: Universitat de València, January 24-25, 2013.

[3] N.N. Taleb, *Fooled by Randomness*. New York: Random House, 2nd Ed., 2005.

[4] N.N. Taleb, *Silent Risk.* Preliminary Book Draft, January, 2015.

[5] R.A. Fiorini, "How Random is Your Tomographic Noise? A Number Theoretic Transform (NTT) Approach," *Fundamenta Infomaticae*, vol.135, no.1-2, pp.135-170, 2014.

[6] K. Svozil, "The quantum coin toss-Testing microphysical undecidability," *Physics Letters A*, vol.143, pp.433–437, 1990.

[7] C.E. Shannon, "A Mathematical Theory of Communication," *Bell System Technical Journal*, vol.27, no.3, pp.379–423, July/October 1948.

[8] N. Martin, J. England, *Mathematical Theory of Entropy*. Cambridge, MA: Cambridge University Press, 2011.

[9] D. MacKay, *Information Theory, Inference, and Learning Algorithms*. Cambridge, MA: Cambridge University Press, 2003.

[10] H. Bremermann, "Quantum noise and information," in *5th Berkeley Symposium on Mathematical Statistics and Probability*. Berkeley, CA: Univ. of California Press, 1965.

[11] R.A. Fiorini, G. Laguteta, "Discrete Tomography Data Footprint Reduction by Information Conservation," *Fundamenta Informaticae*, vol.125, no.3-4, pp.261–272, 2013.

[12] R.A. Fiorini, A. Condorelli, G. Laguteta, "Discrete Tomography Data Footprint Reduction via Natural Compression," *Fundamenta Informaticae*, vol.125, no.3-4, pp.273–284, 2013.

[13] M. Lachmann, M. Newman, C. Moore, "The physical limits of communication or Why any sufficiently advanced technology is

indistinguishable from noise?," *Amer. J. of Physics*, vol.72 no.10, pp.1290–1293, 2004.

[14] S. Jain, R. Mittra, J. Wiart, "Full Wave Modeling of Brain Waves as Electromagnetic Waves," *Progress In Electromagnetics Research*, vol.151, pp.95–107, 2015.

[15] C. Peratta, A. Peratta, "Dielectric properties of biological tissues," *Topics in Engineering, Modelling the Human Body Exposure to ELF Electric Fields*, vol.47, pp.21–40, 2010.

[16] C. A. Bossetti, M. J. Birdno, W. M. Grill, "Analysis of the quasi-static approximation for calculating potentials generated by neural stimulation," *Journal of Neural Engineering*, vol.5, no.1, pp.44–53, 2008.

[17] K. Lashley, *The Mechanism of Vision*. Provincetown, MA: Journal Press, 1948, pp. 302–306.

[18] A. Aste, "Complex representation theory of the electromagnetic field," *Journal of Geometry and Symmetry in Physics*, vol.28, pp.47–58, 2012.

[19] D. Hestenes, *Spacetime Algebra*. New York: Gordon and Breach, 1966.

[20] D. Hestenes, "Proper Dynamics of a Rigid Point Particle," *J. of Math Physics*, vol.15, pp.1778–1786, 1974.

[21] D. Hestenes, G. Sobczyk, *Clifford Algebra to Geometric Calculus, a Unified Language for Mathematics and Physics*. Dordrecht/Boston, MA: G. Reidel Publ. Co., 1984, paperback, 1985. Third printing, 1992.

[22] M. Bischof, "Skalarwellen und Quantenfelder als mögliche Grundlage biologischer Information," *Erfahrungsheilkunde*, vol.47, no.5, pp.295–300, 1998.

[23] R.A. Fiorini, "Computational Information Conservation Theory: An Introduction," in *2014 Proceedings of the 8th International Conference on Applied Mathematics, Simulation, Modelling (ASM '14)*, Mathematics and Computers in Science and Engineering Series, No.34, N.E. Mastorakis, M. Demiralp, N. Mukhopadhyay, F. Mainardi, Eds. NAUN Conferences, WSEAS Press, 2014, pp.385-394.

[24] R.A. Fiorini, "Computerized Tomography Noise Reduction by CICT Optimized Exponential Cyclic Sequences (OECS) Co-domain," *Fundamenta Informaticae*, 2015, in press.

[25] R.A. Fiorini, "The Entropy Conundrum: A Solution Proposal," in *First International Electronic Conference on Entropy and Its Applications*, Sciforum Electronic Conference Series, a011; doi:10.3390/ecea-1-a011, 2014. Available: http://sciforum.net/conference/ecea-1/paper/2649.

[26] M. Bischof, "Holism and field theories in biology—nonmolecular approaches and their relevance to biophysics," in *Biophotons*, J. J. Chang, J. Fisch, and F. A. Popp, Eds. Dordrecht, The Netherlands: Kluwer Academic, 1998, pp. 375–394.

[27] M. Bischof, E. Del Giudice, "Communication and the Emergence of Collective Behavior in Living Organisms: A Quantum Approach," *Molecular Biology International*, 2013, Article ID 987549, 19 pages, DOI:http://dx.doi.org/10.1155/2013/987549.

[28] E.M. Trukhan, V.N. Anosov, "Vector potential as a channel of informational effect on living objects," *Biofizika*, vol.52, no.2, pp.376–381, 2007.

[29] W.E. Lamb, R.C. Retherford, "Fine structure of the hydrogen atom by a microwave method," *Physical Review*, vol.72, no.3, pp.241–243, 1947.

[30] U. Mohideen, A. Roy, "Precision measurement of the Casimir force from 0.1 to 0.9 µm," *Physical Review Letters*, vol.81, no.21, pp.4549–4552, 1998.

ISBN: 978-1-61804-321-4

Station network triangulation positioning system

Marios Sfendourakis[1] , Nilavalan Rajagopal[1] , and Emmanuel Antonidakis[2]

1 Brunel University, School of Engineering and Design

2 TEI of Crete, School of Applied Science, Dep. of Electronic Engineering

***Abstract*—**This paper examines the triangulation problem approached from the perspective of a network of fixed stations/sensor. An initial state A of n sensors (SRs) and m transmitters (TRs).might change from its initial state to a new state B and m +1 transmitters The fixed stations /sensors should recognize the new state B and find the new transmitters that entered in the area by finding with triangulation procedures the positions of the new transmitters. Cases of misinterpretation of data and accuracy problems when more than three lines intersect are explored. It is also shown that when there is a high number of transmitters and a lot of readings the data analysis procedure becomes more complex.

***Keywords*—** Triangulation, Fixed Stations Network, Intersection lines, Triangulation Polygons, Pseudo-Triangulation, Transmitters Positioning.

1 .INTRODUCTION

Triangulation problem is still under examination and a lot of research is still ongoing as triangulation is used in many applications like GPS positioning, Areas of Mobile phone technology, Robotics position finding etc. Yet the ability to detect the existence of a possible intersection between pairs of objects can be important in a variety of problem domains such as geographic information systems, CAD/CAM geometric modelling, networking and wireless computing.[1]

In many cases we have a number of transmitters and a number of sensors which have to acquire and interpret data. But relative positioning of the transmitters is strongly related with a right triangulation procedure in order to have correct data analysis and extract right information. Intersection detection is complex problem and algorithms are used to speed up the process are still being explored for various applications, [2].

The software which has been designed allows the user to enter an amount of sensors and a set of data for each sensor. Those data are the bearings that each sensor detects a transmitter in the area. In addition an extra parameter of accuracy is entered which is common for all sensors, meaning that this accuracy is fixed with the assumption that it is the maximum error of detection for the Fixed Sensors Network.

2 .TRIANGULATION PROBLEM

The triangulation problem is not new in the computing technology as it is used in many applications. Relative bearings between sensors will intersect at certain points. A Network of SRs and TRs is depicted in Fig 1

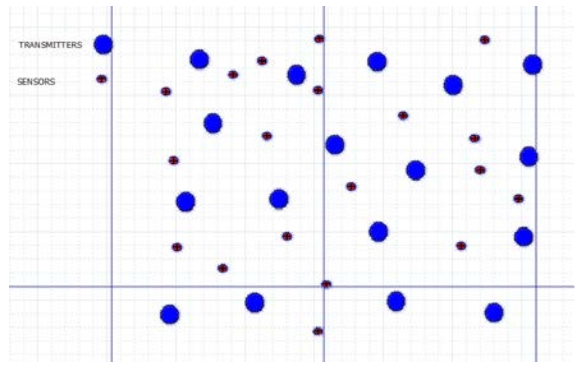

Fig 1

where this status is before the application of the triangulation procedure. By depicting the relative set of bearings for each sensor we see a complex web like the one that appears in Fig 2.

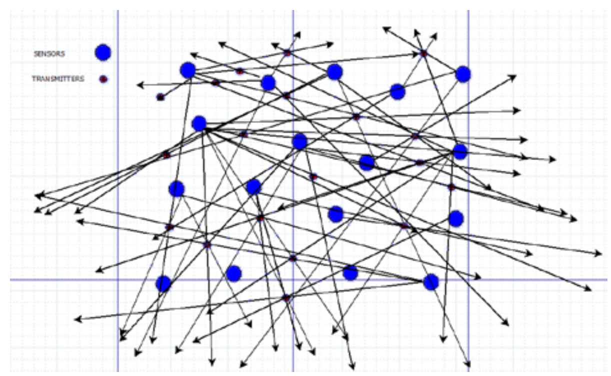

Fig 2

SRs detect the bearing of a transmitter with certain accuracy. Assume that there is an amount of accuracy in the bearings, usually of a few degrees. Then, the bearings are not considered as lines but as sectors of a circle, usually a few degrees wide. With this assumption that there will be a plus-minus amount of accuracy in the bearings, Fig. 3. At long distances the segments of intersection have large areas of uncertainty since the sector opens up, see Fig 4. After applying the triangulation procedure there will be many correct triangulations (TNs) and many pseudo triangulations (PTNs). This assumption is applied in the software which is designed.

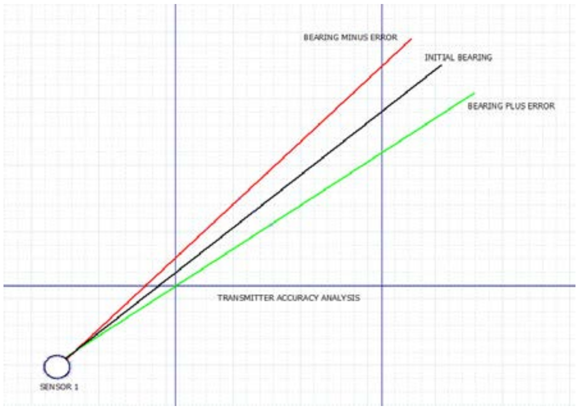

Fig 3

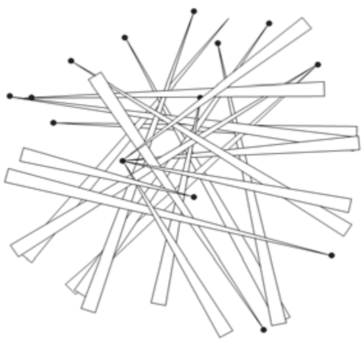

Fig 4

which doesn't allow to exact correct data. In addition minimum errors at long distances can create areas of uncertainty like in Fig 5 where we can't have accurate results of positioning.

2.1 Intersection Area

Intersection areas of three SRs is depicted in Fig.5

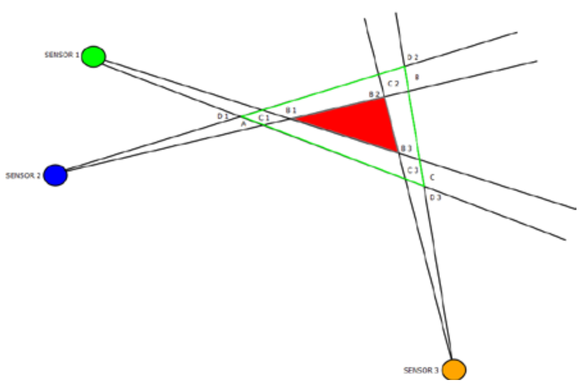

Fig 5

2.2 Triangulation rejection Code

For the rejection of a triangulation we use the following hypothesis which uses Polygons centroids in combination with triangles centroids.

Hypothesis

-C 1 C 2 C3 are the Centroids of the three Polygons A,B,C respectively Fig.5
-Triangle C1 C2 C3 Centroid Point is D
B1 B2 B3 are the closest points of polygons C1 C2 C3 to the point D and they form the triangle B1 B2 B3.

Triangle B1 B2 B3 Centroid is E
Condition 1
POLYGONS A, B, C - ''HAVE NOT COMMON POINTS''
Condition 2
D AND E - ''ARE BOTH INSIDE '' Triangle B1 B2 B3
Condition 3
D AND E ARE NOT COMMON POINTS OF POLYGONS A, B AND C

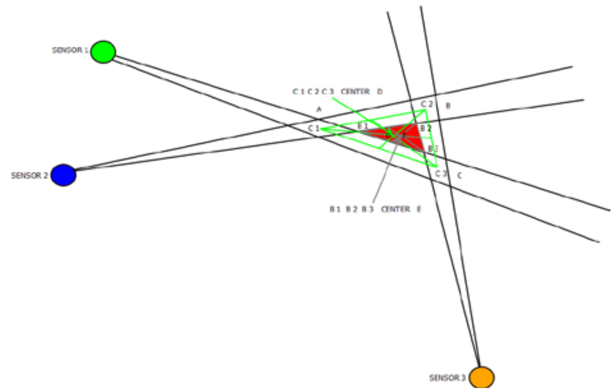

Fig 6

We define the triangle D1 D2 D3 Fig.7 which is formed by the following rule:
-D 1 is the maximum diagonal distance point in Polygon A and point B 1
-D 2 is the maximum diagonal distance point in Polygon B and point B 2
-D 3 is the maximum diagonal distance point in Polygon C and point B 3
We divide the area of the two triangles, Formula 1.

$$\frac{\textbf{Triangle B 1 B 2 B 3}}{\textbf{Triangle D 1 D 2 D 3}} = \boldsymbol{\lambda}$$

Formula 1

-If $\mathbf{0} < \boldsymbol{\lambda} < 1$ and λ close to 1, then the triangle B1 B2 B3 lies within the triangle D1 D2 D3 and we don't have triangulation Fig.5
-If **λ is close to 0** The triangle B1 B2 B3 lies within the triangle D1 D2 D3 and the Centroid point E lies within the common area of triangulation and we have a triangulation Fig. We also see that the area of triangle B1 B2 B3 is much lower than the area of the triangle D 1 D 2 D 3.

Condition three should also be true or D will be very close to E.

ISBN: 978-1-61804-321-4

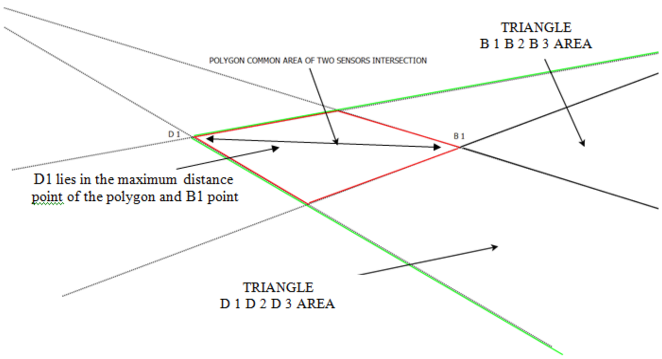

Fig 7

2.3 Real triangulation

In this case all three polygons intersect and they have common area which is shown in following Fig.8.This case is considered as a real triangulation. The smaller the triangle area Fig 8 (a), red triangle, the triangulation is weaker. The bigger the triangle area Fig 8 (b), green triangle, the triangulation is stronger.

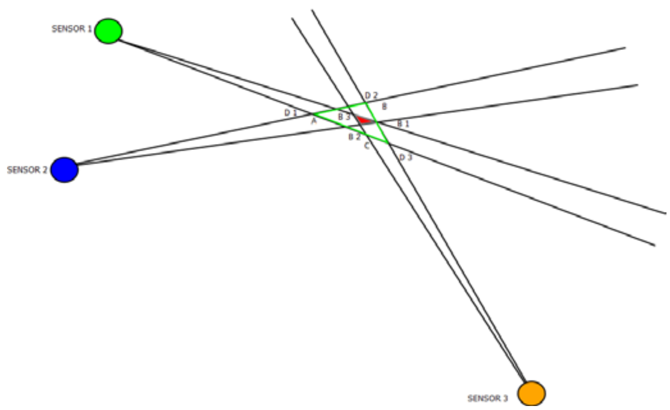

(a)

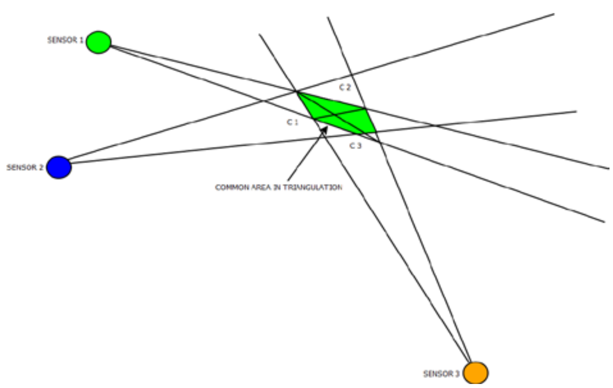

(b)
Fig 8

3 . Software Architecture

The Software starts with the acquirement and storage of the data in a set of arrays. This is achieved by prompting the user to enter the number of sensors and their coordinates and then the data for each transmitter that has been detected in the area. The language used is JAVA and the arrays are two dimensional and dynamic. By that way the user can create a Network of the scale that he wants. At this point for each Sensor the maximum number of allowed bearings detected is defined by the programmer. This parameter can change if more data are required for analysis. Details concerning the software code are beyond the scope of this paper. Software architecture is shown in fig.9

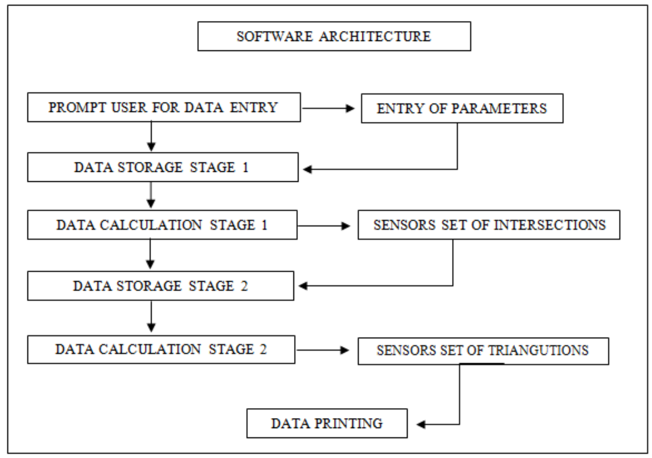

Fig. 9

3.1 Software functions

The Software uses Veness [3] formulas in order to calculate relative bearing and distance between SRs and TRs. Coordinates of intersection points are calculated as pairs between SRs and then the software search for triangulations were three, or more than three lines converge from different SRs.

3.3 JavaScript Code for calculations

Veness [3] provides code for implementation and calculations between geographical points. During this research the following code has been used:

- Intersection of two paths given start points and bearings
- Bearing between two points when their coordinates are known.

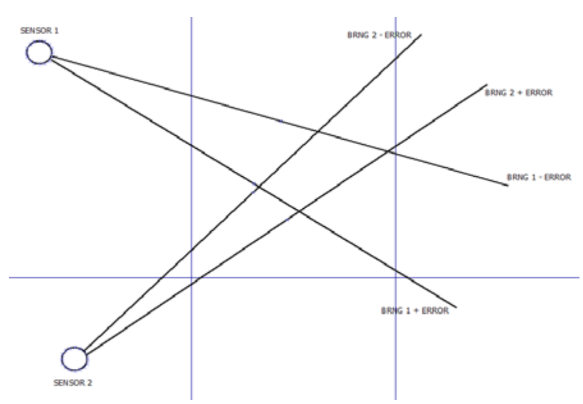

ISBN: 978-1-61804-321-4

Fig. 10

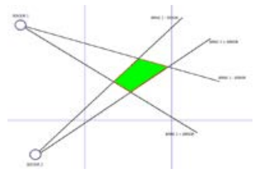

(a)

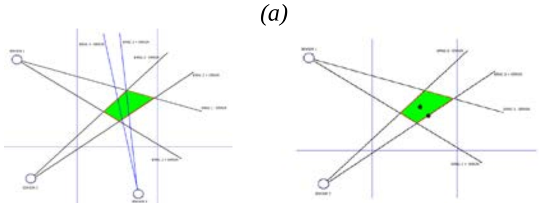

(b) *(c)*

Fig. 11

3.3 Intersection between Sensors Routine

The routine which used is the following:

if (CheckBrng1 == θ13 - x || CheckBrng1 == θ13 + x
||
(θ13 - x < CheckBrng1) && (CheckBrng1 < θ13 + x)

&&
(CheckBrng2 == θ23 - x || CheckBrng2 == θ23 + x ||
(θ23 - x < CheckBrng2) && CheckBrng2 < θ23 + x))

where CheckBrng1 and CheckBrng2 are the bearings θ13 , θ23 from Sensor 1 Coordinates ,Point 1 and Sensor 2 Coordinates Point 2 related with the intersection point Point 3 as it is depicted in Fig 10, Fig 11 (a),(b),(c). Point 3 is defined as an intersection between a bearing of SR1 or a bearing from SR2 and a bearing from another SR's set. That point is on the boundaries defined by the green colored polygon Fig 11.That polygon is the common area of intersection between the two SRs.

4. Pseudo-Triangulation Cases

Triangulations are shown with a circle with a cross inside. The colorless ones are considered pseudo-triangulations.

4.1 Pseudo-triangulation case 1

A set of sensors are used for each triangulation. A sensor located on the direction between another sensor in the set and the intersection point must be excluded from the set. The following figure shows that SR4 should be excluded from the triangulation of TR2 since SR2 is included. Also SR 4 should be excluded from the triangulation of TR1 since SR7 is included, see Fig 12.

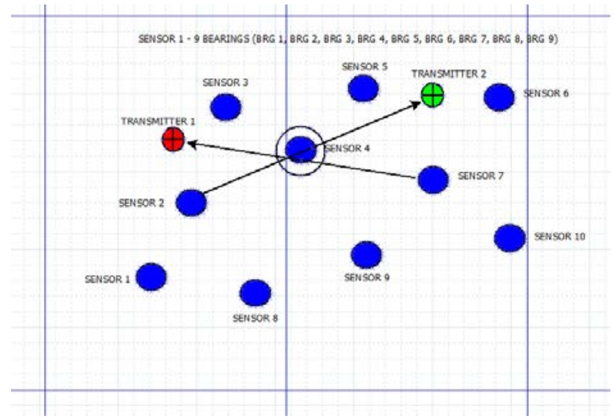

Fig.12

4.2 Pseudo-triangulation case 2

There is false transmitter detection due to the extending of intersection lines. Not all crossings of 3 lines are considered triangulation points, Fig 13

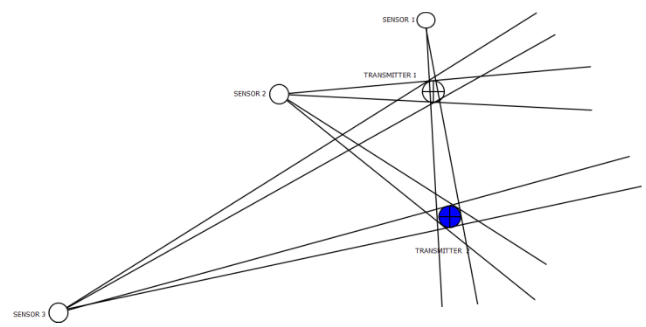

Fig.13

4.3 Pseudo-triangulation case 3

When two TRs fall into the intersection polygon of two SRs then it cannot be differentiated that there are two TRs. Only when there are different sensors near the two TRs then they may be able to be differentiated, Fig 14 (a), (b).

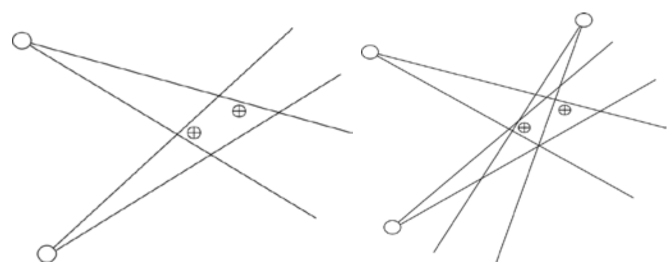

(a) *(b)*

Fig. 14

4.4 Pseudo-triangulation case 4

There are more complicated cases where a mixture of the above and more may happen as the scale of the NFSs increases Fig 15.

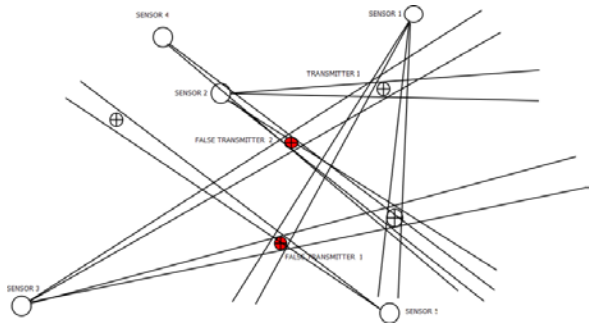

Fig. 15

4.4 Pseudo-triangulation case 5

In the following Fig 16 SR 1 and SR 2 detect on TR at the same bearing. Other TRs should reveal that at that bearing there are more than one TRs on the same line.

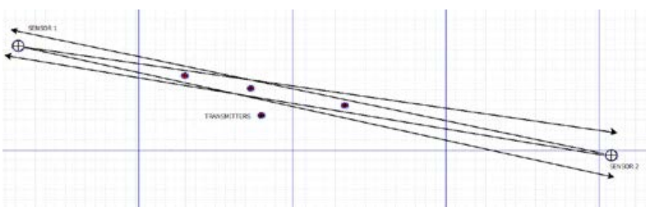

Fig. 16

4.5 Ways to tackle the Pseudo-triangulation cases

As it was obvious in all the pre-mentioned cases of PT the software should tackle with them with a combination of ways in order to minimize false triangulations and PTRs. Ways to tackle these cases are under testing and already are showing positive results.

4.5.1 Partioning of the search area

Fig. 17

4.5.2 Rejection of Sector to Sector bearings

By adequate software programming in order to avoid sector to sector bearings the results are more promising while false triangulations of SR to SR are rejected Fig 18. In other words the SRs search for bearings which are out from other SRs region.

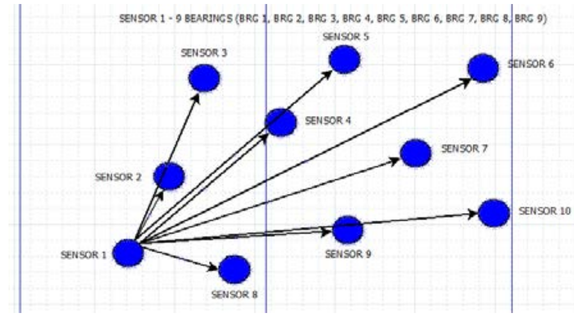

Fig. 18

5. Conclusion

As a conclusion we can mention that a triangulation problem is becoming high complicated when we have a large number of sensors and transmitters. The software of the FSN which will have to deal with the triangulation problem should be designed to deal with cases of inaccuracies and false detections. It needs to be tested and configured in order to avoid triangulation cases that are problematic and lead the user to misinterpretation of readings. This research shows that there are relative sensors bearings and data readings that have to be checked in a case by case basis.

Future work might involve the inclusion of more parameters of the sensors like power and antenna size which will lead to new sets of data and additional software architecture in order to acquire correct interpretation of acquired data and avoid cases of false triangulations.

References

[1] Chaman L Sabharwal, Jennifer L Leopold, Douglas McGeehan "Triangle-Triangle Intersection Determination and Classification to Support Qualitative Spatial Reasoning" *Research Journal on Computer Science and Computer Engineering with Applications* Issue 48 (July–December 2013), pp. 13–22, 2013

[2] N. Eloe, J. Leopold, C. Sabharwal, and Z. Yin,"Efficient Computation of Boundary Intersection and Error Tolerance in VRCC-3D+ ", *Proceedings of the 18h International Conference on Distributed Multimedia Systems (DMS'12)*, Miami, FL, Aug. 9- 11, 2012, pp. 67 – 70, 2012.

[3] Veness, Chris.2007a. "Calculate distance, bearing and more between two latitude/longitude points".
Available at http://www.movable-type.co.uk/scripts/latlong.html

Cooperative Highway Traffic Safety Management Systems

Sadko Mandzuka, Boris Huzjan, Goran Kos

***Abstract*—** Road safety represents the interaction between a man, a road and a vehicle. By affecting on each factor, safety status on the roads can be improved. The research problem in this paper is the elaboration of the real-time cooperative approach to highway traffic safety management. The objective of this study was to analytically determine the process of accident occurrence on the motorways, by analyzing the factors of impact of man, vehicle and the road. Based on the risk analysis, a cooperative model to reduce the crash potential on motorways was made.

***Keywords*—**Intelligent Transport Systems, Cooperative Systems, Road Traffic Safety, Control System.

I. Introduction

Through the analysis of relevant factors a model of accident occurrence on the motorways was designed and verified. Based on the created algorithm and using the cooperative ITS system, efficient management of traffic flow aimed at reducing the crash potential is enabled. Certain principles have been established by mutual evaluation and ranking of the relevant parameters at accident occurrence on the motorways as well as by bringing this data to correlation with the basic parameters of traffic flow, [1]. Real-time model of traffic management using the input on the characteristic of traffic flow (speed, sequence, density, homogeneity etc.) and input data on external factors in traffic flow (input data) allows the calculation of the level of crash potential.

The model is based on the management of traffic flows on motorways in order to reduce the crash potential. Traffic flow management is carried out by cooperative ITS devices – Road cooperative unit and Vehicle cooperative unit. Also, same information is passed to road variable message signs (VMS) and light text signs. Vehicle cooperative unit will be used to automatic (or assisted) change the maximum allowed speed, and light text signs will give drivers various text alerts. This traffic safety management system is used to achieve traffic flow with the minimum crash potential.

The possibilities of use of modern ITS in traffic safety improvements can be divided into following, [2, wiley]:

a) Systems related to infrastructure (roads, bridges, tunnels…)
b) Systems related to vehicles
c) Systems based on cooperation

A particularly potent approach was recognized in the possibility of application of cooperative systems in traffic. Cooperation can be viewed as a basic form of organization, in a broad sense, and as a problem of communication of a moving entity (vehicle) with road infrastructure and/or other moving entities, in a narrow sense. In the broad sense Ramage defined the cooperative system as a combination of technologies, people and organizations which enables communication and coordination required for achieving a common goal of a certain group which performs various activities, for the benefit of all participants [3]. In the narrow sense of the cooperation definition, the following communications were recognized: V2V – vehicle to vehicle (link 1), V2I – vehicle to infrastructure (link 2), V2P – vehicle to pedestrian (link 3), I2P – infrastructure to pedestrian (link 4), see Fig. 1. Dedicated short-range communications (DSRC) is one of basic vehicular communications technology used for these applications.

The main characteristics of a cooperative approach are:

1. Consider the driver, vehicle, infrastructure and other road users as a unique system.
2. Consider operational and management needs of the entire system.
3. Integrated approach to safety of traffic and all participants.
4. Apply technology in a coherent manner in order to support overall integration of system parts.

Currently we recognize the following systems onto which the cooperative approach can be successfully applied: navigation systems and travel information systems, warning systems, various road traffic safety systems, emergency services' vehicle management, priority management in urban public transport, intelligent systems for speed management, support systems for endangered transport users and others.

The research reported in this paper is supported by the FP7 - Collaborative Project: Intelligent Cooperative Sensing for Improved traffic efficiency - ICSI (FP7-317671) and by the EU COST action TU1102.

Sadko Mandzuka is with the Faculty of Transport and Traffic Sciences, University of Zagreb, HR-10.000 Zagreb, Vukeliceva 4, CROATIA (corresponding author to e-mail: sadko.mandzuka@fpz.hr).

Boris Huzjan is with the Rijeka – Zagreb Motorway, HR-10.000 Zagreb, Širolina 4, CROATIA (e-mail: boris.huzjan@arz.hr).

Goran Kos is with the Institut for Tourism, HR-10.000 Zagreb, Vrhovec 5, CROATIA (e-mail: goran.kos@iztzg.hr).

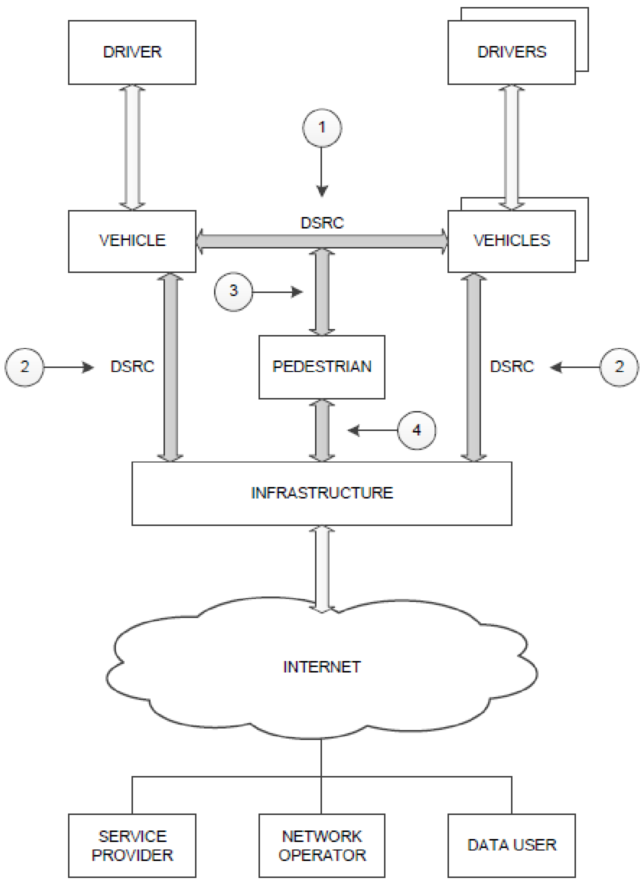

Fig 1 Basic topology of cooperative system in traffic and transportation

II. MODEL OF HIGHWAY TRAFFIC SAFETY

For the development of the model a test section of the motorway between Zagreb and Rijeka with two carriageways with two lanes each, and one emergency lane on each carriageway was chosen. The motorway passes the lowland zone, hilly and mountainous terrain. A detailed analysis of statistical data on traffic accidents was made for the test section, and the field research of traffic flow characteristics was carried out, [1].

The analysis of statistical data on traffic accidents on the test section found that most of the accidents happen in normal traffic conditions, i.e. 70 per cent of accidents happen at maximum legally permissible speed limit (130 km/h on the lowland part, or 110 km/h on the hilly part), and 73 per cent of accidents happen at a flow rate of up to 30 per cent of total capacity of the section.

Model of increasing traffic safety on the motorways and ITS systems will have an influence on the reduction of the number of accidents caused under normal traffic conditions. The model is based on measuring values of traffic flow parameters in real-time and external factor which affect the traffic flow and based on this a message or speed limit will be shown to drivers with the aid of which the minimum crash potential will be achieved.

Crash potential is defined through a relative danger degree of accident occurrence. Danger degree was brought into correlation with the existing statistic data on accidents on the test section and traffic flow data measured during research.

The analysis of previous research concluded that the development of the new real-time model of traffic flow management aimed to prevent the occurrence of accidents will be based on the model presented in [4] which was further modified in 2004 in line with the new research [5]. The new model will be made for four-lane motorways. Model calibration is based on the analysis of traffic flows recorded on the test section and the analysis of statistical data on accidents.

The basic linear logarithmic model of crash was developed by Lee et al. is as follows:

$$\begin{aligned} \ln(F) = \Theta + \lambda_{CVS(i)} + \lambda_{Q(j)} + \lambda_{COVV(k)} + \ldots \\ \ldots + \lambda_{R(l)} + \lambda_{P(m)} + \beta \ln(EXP) \end{aligned} \tag{1}$$

where:
F - expected number of accidents in the observed period,
Θ - constant,
$\lambda_{CVS(i)}$ - coefficient of variation of speed (CVS),
$\lambda_{Q(j)}$ - difference of average speed between the beginning and end of observed section (km/h),
$\lambda_{COVV(k)}$ - influence of traffic lane change (Covariance of Volume difference between the upstream and downstream of a specific location),
$\lambda_{R(l)}$ - effect of road geometry (control factor),
$\lambda_{P(m)}$ - effect of peak/off-peak traffic load (control factor),
β - parameter for exposure,
EXP - exposure to accident occurrence based on vehicle/kilometer.

According to equation (1) it can be seen that authors have chosen three main factors which have shown to be the most important for the prediction of crash potential: current difference between the speed of individual vehicles at a fixed location as a proof of speed stability between the vehicles, speed change along the observed section (small changes indicate constant speed and low acceleration, while large changes indicate sudden acceleration or speed reduction which points to crash potential) and frequency of traffic lane change.

Since there are significant differences between the conditions in which the model was developed (1) and the traffic flow conditions on the four-lane motorways which prevail in the Republic of Croatia the factors to be taken into account for the analysis of crash potential on such motorways were determined.

The main significant factor is the difference (deviation) of vehicle speed in traffic flow on the fixed location. Speed deviation at fixed location points to speed stability of the vehicle in the traffic flow. The factor is obtained through the ratio of standard deviation and average speed for each traffic lane and marked as coefficient of variation of speed (CVS), [1]. The calculation for identification of the speed change on the fixed location (CVS) is shown in the equation:

ISBN: 978-1-61804-321-4

$$CVS = \frac{1}{n}\sum_{i=1}^{n}\frac{(\sigma_s)_i}{\bar{v}_i} \qquad (2)$$

where:

CVS - Coefficient of Variation of Speed,

$(\sigma s)i$ - standard deviation of speed on traffic lane i during the period Δt (km/h),

$\bar{v}_i$ - average speed on traffic lane i during period Δt (km/h),

n - total number of traffic lanes.

By analyzing the expression (2) we can conclude that, if there are smaller changes in speed (standard deviations) the traffic flow is balanced. If there is a significant increase in speed change, certain number of drivers will have to change the speed more frequently, which leads to instability in traffic flow, or increase in crash potential.

Large deviation of speed is very unfavorable for traffic safety as proved by many studies. The first study on the subject was conducted in 1964, [6]. The research determined the relationship between vehicle speed in traffic accidents and the average speed of traffic flow (Fig. 2).

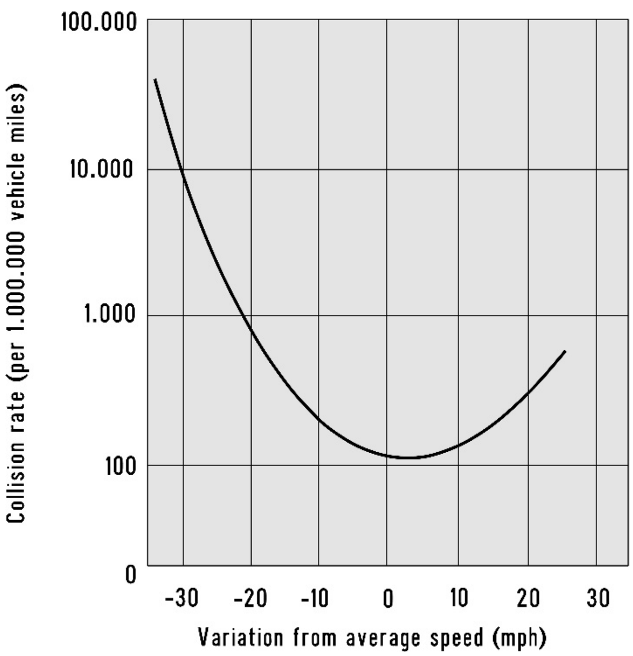

Fig. 2 Solomon curve (Source: [6])

It is possible to conclude from the curve that the most accidents happen at speeds that are different from average and that the larger number of accidents is represented at lower speeds than average.

In this study the speed deviation is observed on the entire test section, or one motorway direction was considered to be one traffic lane. Thus the amount of the CVS factor is:

$$CVS = \frac{\sigma_s}{\bar{s}_i} \qquad (3)$$

The specified value will be considered average value of the CVS factor. If the specified value using light text signs or variable message signs decreases, the crash potential will also reduce.

Another factor shows the change in average traffic flow speed between two points on the observed section of the motorway. Value of speed change on the observed section gives an insight into the change of the average speed of traffic flow between two points on the basis of which a conclusion can be made on traffic flow behavior on the observed section. If there is a minor change in average speed on the observed section this means that the vehicle speed is almost constant, or that there is no considerable acceleration or deceleration. In case that the value of factor of average speed variation on the observed section assumes a considerable change, it can be concluded that there have been considerable changes in speed of individual vehicles which means that for some reason there was a significant acceleration or deceleration. The calculation to determine speed changes in the observed section according to [7] is:

$$Q = \overline{v_1} - \overline{v_2} = $$
$$= \frac{t_p}{\Delta t}\sum_{t=t^*-\Delta t}^{t^*}\left(\frac{1}{n_1}\sum_{i=1}^{n_1} v_{1i}(t)\right) - \frac{t_p}{\Delta t}\sum_{t=t^*-\Delta t}^{t^*}\left(\frac{1}{n_2}\sum_{i=1}^{n_2} v_{2i}(t)\right) \qquad (4)$$

where:

Q - average speed difference between beginning and end of observed section (km/h),

$\overline{v_1}, \overline{v_2}$ - average speeds during period Δt on end points of observed section (km/h),

t_p - duration of time interval of observed speed (seconds),

Δt - observation time (seconds),

t^* - time of traffic accident occurrence,

$v_{1i}(t)$ - speed on traffic lane i in time t at the end of the section (km/h),

$v_{2i}(t)$ - speed on traffic lane i in time t at the beginning of the section (km/h),

n_1, n_2 - number of traffic lanes on end points of observed section.

According to the model [5] the frequency of lane change was taken into account as a very important factor. The factor was calculated based on the average covariance difference of load of an individual lane on the observed motorway section. The Covariance is the value that indicates how much two variables vary together, as opposed to the variance, which describes the changes in the value of a single variable. The coefficient of lane change frequency shown by equation (1) (COVV) is not relevant for the some types of motorways, since the overtaking lane is used for overtaking and not for driving. For this reason, the volume change in each lane used in [7] was not an appropriate way to determine the frequency of lane change (in this case overtaking frequency).

The impact of weather conditions is an important factor in traffic safety on the motorways. According to research of the dependency of the number accidents and weather conditions and the state of the carriageway at the time of the accident (dry, wet, covered in snow), data was received that 71 per cent of accidents happen in the conditions of dry pavement, or in favorable meteorological conditions.

III. ARCHITECTURE OF TRAFFIC COOPERATIVE INTELLIGENT TRANSPORT SYSTEM

The concept of approach presented in this paper is based on ITS architecture developed by the FP7 - Collaborative Project: Intelligent Cooperative Sensing for Improved traffic efficiency – ICSI. The goal of the project is to define a new architecture to enable cooperative sensing in intelligent transportation systems and to develop a reference end-to-end implementation. The project results will enable advanced traffic and travel management strategies, based on reliable and real-time input data. The effectiveness of such new strategies, together with the proposed system, will be assessed in two field trials.

ICSI is a pervasive system based on WSN and vehicular networks. This implies that it should be able to collect and process a large amount of sensed data in a scalable and reliable way. For this reason the ICSI system is composed by heterogeneous components, [8], see Fig. 3:

- Control Centers

Control centers are able to collect, store and process big amount of data coming from the other components of the system. They can also act on the transport system to keep it efficient and to ensure safety.

- Road-Side Units (RSUs)

RSUs are positioned along the road for collecting measurements through sensors (e.g. flow sensors, park sensors, etc.), actuating feedbacks (e.g. variable message signs, EV charging spots, etc.) and can act as a gateway toward the Internet to realize gateway-to-gateway communication. They can be wired or wirelessly interconnected forming wireless sensors networks and vehicular networks.

- On-Board Units (OBUs)

The OBU resides into the car and can be equipped with sensors and wireless networking equipment for V2X communications within the vehicular network. OBUs can optionally have Internet connectivity through cellular networks.

- User devices

User equipment like tablets, smartphones, etc., consists of portable devices used by pedestrians or drivers which are involved in collecting of news, travel information and other kinds of information. Sensed data will be processed in a cooperative manner performing content aggregation and integration since the earliest stages, e.g. information about traffic flows can be collected by a visual WSNs based on low-cost camera sensors and stored locally sending to the control center only statistical data for long-term evaluation.

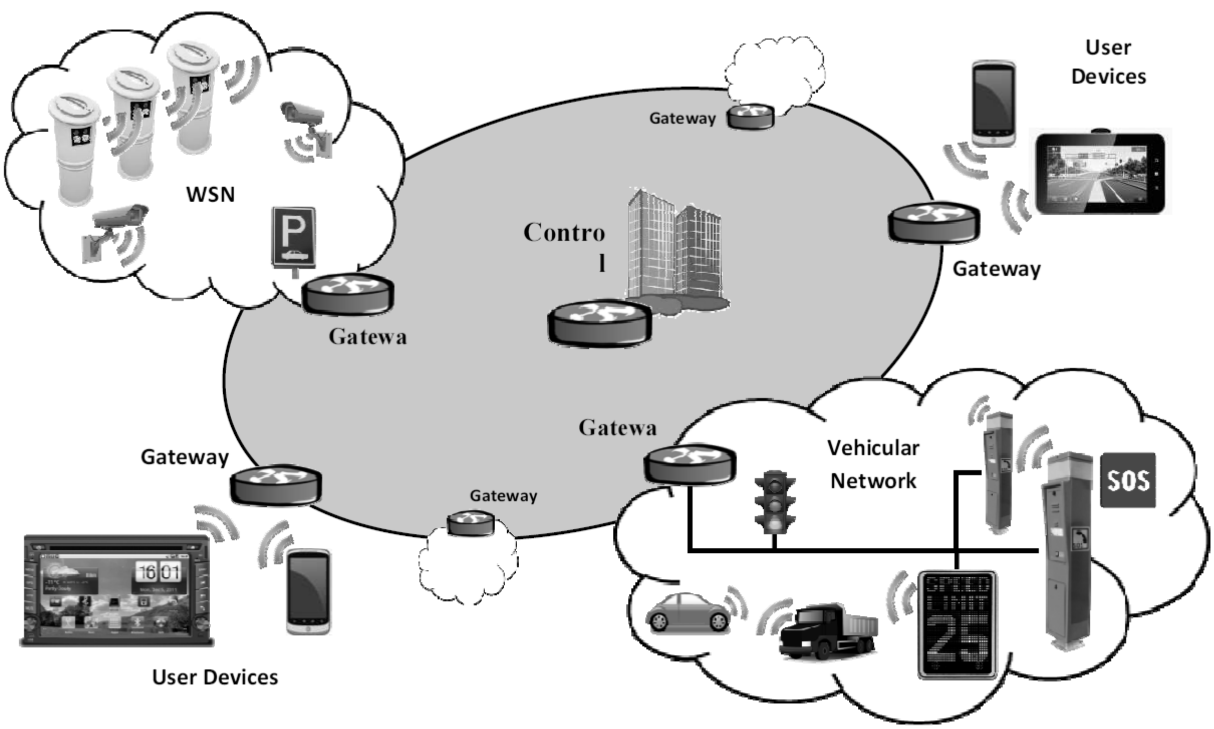

Fig. 3 ICSI System architecture

In order to do that ICSI defines two key concepts:

- Gateway (GW).

A gateway refers to a physical entity consisting in an RSU or a control center and able to join areas.

- Areas.

An area is composed by:

- o a set of gateways (at least one),
- o communications among these gateways (when multiple gateways are present),
- o a criteria to define the area perimeter (e.g. based on

the density of population, traffic, ICT elements, etc.).

An overview of the main characteristics of control algorithm used in this ICSI environment is exposed in next sections.

IV. CONTROL ALGORITHM

Application of the model in real time is possible for traffic safety management on four-lane motorways. By measuring basic parameters of traffic flow and entering them into model it is possible to determine the value of the factor of danger. If high value of danger factor is determined, the system of variable message signs for speed restrictions will affect the traffic flow to reduce the value of the parameter that increases the factor of crash potential. Based on input data, the value of the factor for crash potential will be calculated. The theoretical value of factors can be from 0 to 1, and the value of the factor will be divided into three categories: low, acceptable and high, Fig 4.

The mathematical model can be converted into an algorithm for traffic security management on the motorways by changing the value of the speed limit. Based on the input data on the traffic flow characteristics, weather conditions and daylight the algorithm calculates the crash potential.

When risk factor exceeds the area of high value, the algorithm will first activate the message with the warning “Caution! Drive within the speed limit!”. It is assumed that the above message can affect traffic flow directly (automatic mode) or in a way to encourage drivers to drive within the speed limit (assisted mode). In this way deviation of speed will be reduced together with the average speed and the amount of overtaking. By changing these three parameters the crash potential will also be reduced.

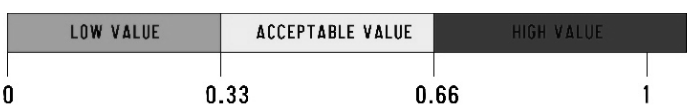

Fig 4 Range of danger factors (n)

If the value of the danger factor in this situation falls within the scope of acceptable values, the textual message will remain active. If the danger factor remains in the high area, command in automatic mode (or message in assisted mode) for speed restriction to 100km/h will be activated. This will further reduce the average speed, deviation and share of overtaking. If the factor value in that situation falls within the scope of acceptable, the restriction will remain active. If the danger factor still remains in the high area, the speed restriction will be reduced to a lower value, to 80 km/h.

When the parameters of traffic flow and other parameters begin to normalize and the value of danger factors falls into the area of "low value", the algorithm will gradually increase the value of the speed restriction and deactivate the text message in order not to unnecessarily slow down traffic or to provide redundant information to drivers.

The algorithm developed as a part of this research is interacting with the existing algorithms and scenarios for managing light variable speed limit signs on the basis of meteorological conditions and the conditions of ensuring maximum throughput.

The developed model and algorithm of real-time management of traffic safety can be displayed schematically (Fig. 5). The developed algorithm for traffic safety management integrated with the existing algorithms for the management of traffic flows on the test section is shown in Fig. 6.

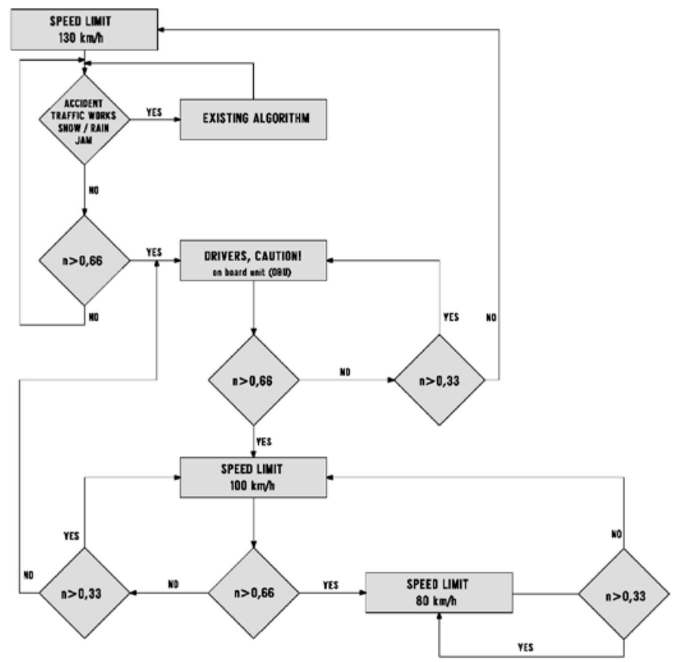

Fig. 5 Flowchart of the control algorithm

V. CONCLUSION

Road traffic safety is a constant subject of study for the purpose of reducing traffic accidents (and the implications they bring) and increasing the basic capacity of the infrastructure. In the Republic of Croatia and its wider European setting, road infrastructure is mainly of characteristic profile with a high level of serviceability. This is a four-lane profile with separated carriageways with one driving, overtaking, and emergency lane. That is why the research was conducted for such motorways.

Research conducted within this paper brings the relation of traffic accidents to correlation with basic parameters of traffic flow measured in the zone and the moment of accident occurrence. Model of real-time traffic safety management was made on the motorways with the purpose of reducing the crash potential factor. Model development is based on the final calibration of Lee’s model. The model defines the total crash potential according to current parameters of traffic flow as a function of risk due to speed variation on the fixed location

between the two points, on grounds of overtaking, traffic volume and traffic flow at night.
The model distinguishes between the three risk levels (low, acceptable and high value) and based on that an algorithm is defined which allows traffic harmonization by regulating speed limits on motorways. This new model can be integrated as an upgrade of existing algorithms and scenarios which are used to manage variable message signs.

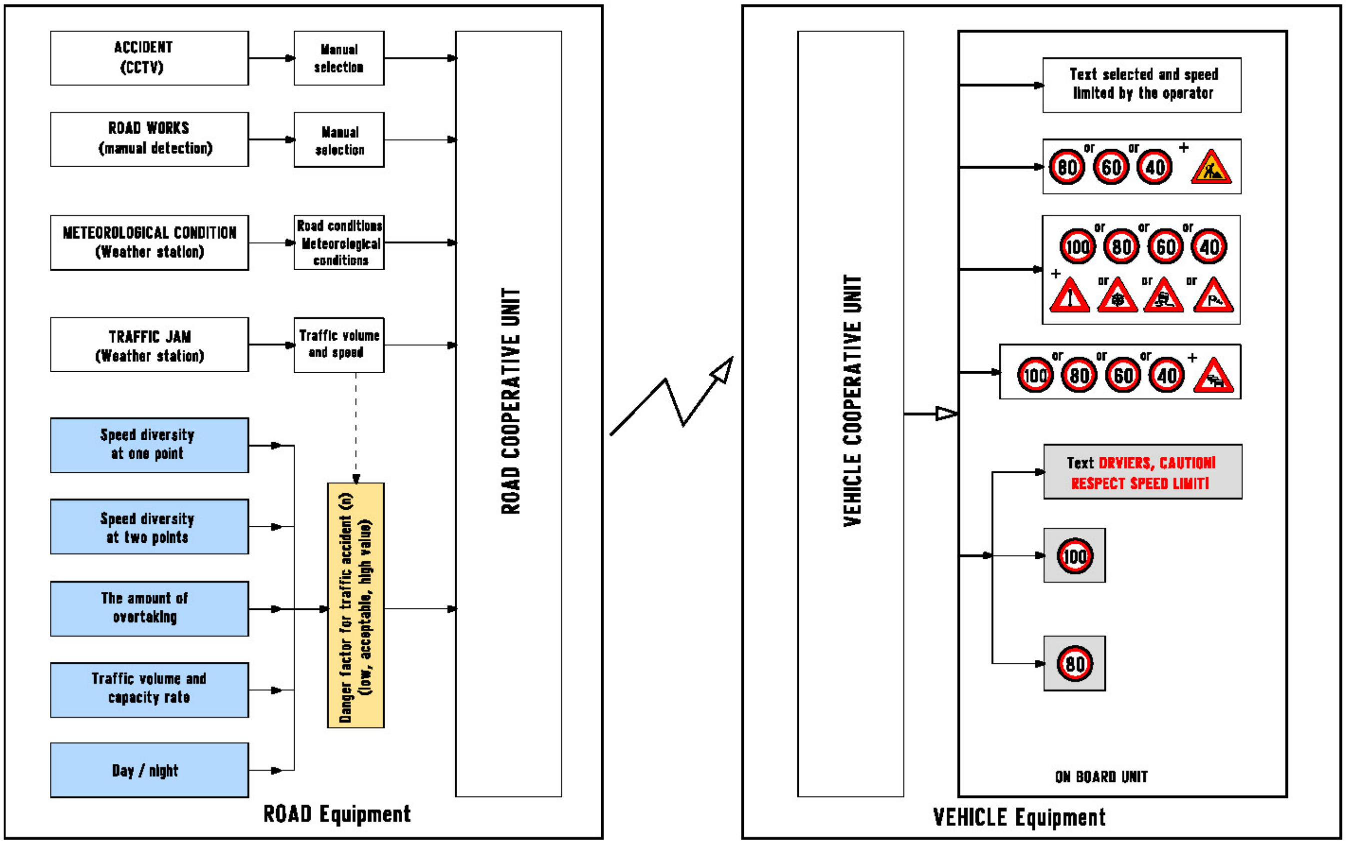

Fig. 6 Algorithm for cooperative safety management, integrated with existing algorithms for traffic management

ACKNOWLEDGMENT

The research reported in this chapter is supported by the FP7 - Collaborative Project: Intelligent Cooperative Sensing for Improved traffic efficiency - ICSI (FP7-317671) and by the EU COST action TU1102.

REFERENCES

[1] B. Huzjan, S. Mandžuka, G. Kos, “Model of real-time traffic safety management on four-line motorways”, Technical Gazette., submitted for publication.
[2] S. Mandžuka, E. Ivanjko, M. Vujić, P. Škorput, M. Gregurić, “The Use of Cooperative ITS” in Urban Traffic Management in In*telligent Transp. Systems: Technologies and Applications*, Wiley, ISBN: 978-1-118-89478-1.
[3] Ramage, M., Evaluation of learning, evaluation as learning, SIGOIS Bulletin, 1996.
[4] C. Lee, F. Saccomanno, B. Hellinga, “Analysis of Crash Precursors on Instrumented Freeways”, Transportation Research Record 1748, TRB, National Research Council, Washington, D.C., 2002, pp. 1-8.
[5] C. Lee, B. Hellinga, F. Saccomanno, “Assessing Safety Benefits of Variable Speed Limits”, Transportation Research Record No. 1897, 2004, pp. 183-190.
[6] D. Solomon, D “Accidents on main rural motorways related to speed, driver, and vehicle”, Technical report, U.S. Department of Commerce/Bureau of Public Roads, 1964, reprinted 1974.
[7] C. Lee, B. Hellinga, F. Saccomanno, “Real-Time Crash Prediction Model for Application to Crash Prevention in Freeway Traffic” Transportation Research Record No. 1840, 2003, pp. 67- 77.
[8] ICSI project, Deliverable D1.3.2 - SYSTEM ARCHITECTURE, 2014.
[9]

Impact factors for success of implementation and use of Business Intelligence in the Slovak enterprises

Peter Mesároš, Štefan Čarnický, Martina Habiňaková, Tomáš Mandičák

Abstract — Business Intelligence (BI) is an important tool to support decision-making in enterprises. Several studies have demonstrated the positive impact of BI to decision-making. The first step is to put in place the company. The implementation process is influenced by several factors. This contribution discusses the issue of factors affecting to successful implementation. The paper describes the key factors for successful implementation and use of business intelligence based on multiple studies. The main objective of the paper is to verify the effects and dependence of selected factors and proposes a model of key factors for successful implementation of BI. Success factors and the proposed model are studied in Slovak enterprises.

Keywords — Business Intelligence, success factors, implementation of BI.

I. INTRODUCTION

THE application of Business Intelligence (BI) systems in business practice is associated not only with more advantages and benefits, but on the other hand, it also brings certain barriers, problems and risks. During the design process, implementation and use of BI solutions, businesses can run into many problems and complications that will need to be resolved. Not only technology plays a key role, but above factors, such as people, processes, management style and culture of the organization, are also important. These factors often represent a big problem and can disrupt or prevent attempts and efforts of implementing effective BI solutions in organizations.

Every BI project should provide clearly identified effects. Achieving these final effects (expected benefits related to the use of BI), and thus the overall level of success of BI projects into practice, identify success factors. What is the success factor and what is the point? For a more precise definition of content essence of success factors we can use the work of Pour [1,2,3] and the success factor define as follows:

Success factor represents the knowledge and application of best approaches and experiences in managing BI that will lead to achieving the objectives of BI, as well as to achieving the desired economic and non-economic effects. Similarly, Novotný et al. [4] define the essence of the concept of success factor, where by success factor they mean the set of properties or parameters of the solutions, or application of the best approaches and experiences that will lead to achieving defined objectives.

Success factors identified by several authors as Novotný − Pour − Slánský, Atre, Eckerson, Loshin, Howson, Hwang, Turban, Panta, Škanta, Adelman − Schrader and more [4,5,6,7,8,9,10,11,12,13]. Based on the above-mentioned sources it was created baseline model of factors affecting successful implementation and use of BI. The starting point in identifying the key success factors for BI was a study of numerous contributions, publications, independent studies and surveys, as well as our knowledge and experience in this field. In addition, we have consulted and discussed this topic with several experts in the theory and practice of business, who are dealing with this issue. In particular, we have examined common characteristics of organizations that succeed in implementing and using BI, implying the difference between success and failure. We have identified and confirmed some of the most common BI key success factors, which are necessary for successful implementation and use of BI. Based on the results of the examination we have identified seven key success factors of implementation and use of BI in enterprises (Figure 1).

Proper implementation and effective use of BI in the managing companies determines the number of success factors of differing importance and intensity of action. The most significant of these factors are referred to as critical or key success factors of BI. Knowledge targeted monitoring and management of key success factors of BI accelerate the process of implementation of these systems [14]. BI also enables more efficient use of them in support of decision-making processes in the company, which ultimately facilitate

The paper presents partial results of the research project VEGA No. 1/0562/14 „The impact of Business Intelligence tools on corporate performance“.

Peter Mesároš, Technical University of Košice, Faculty of Civil Engineering, Vysokoškolská 4, 042 00 Košice, Slovakia (peter.mesaros@tuke.sk, phone: +421556024378, fax:+421556233219)

Štefan Čarnický, University of Economics in Bratislava, Faculty of Business Economy with seat in Košice, Tajovského 13, 041 30 Košice, Slovakia (stefan.carnicky@euke.sk)

Martina Habiňaková, University of Prešov, Faculty of management, Konštantínova 16, 080 01 Prešov, Slovakia (martina.habinakova@gmail.com)

Tomáš Mandičák, Technical University of Košice, Faculty of Civil Engineering, Vysokoškolská 4, 042 00 Košice, Slovakia (tomas.mandicak@tuke.sk)

the achievement of the expected final effect − benefits.

Fig. 1 Key success factors for the implementation and use of BI in corporate governance [4,5,6,7,8,9,10,11,12,13]

II. Problem statement

The complexity of the current business environment creates opportunities and threats on which companies have to react quickly and flexibly. To improve the response capabilities of enterprises, they use various computer-controlled systems designed to support management decision-making. Most commonly used information systems are not able to properly evaluate a large amount of business data stored in various databases across the enterprise. If they want to operate sophisticated businesses and make the right strategic decisions, corporate managers need relevant and consolidated information on the current situation in the company and current events in the market to enable them to decide competently and on time. A good solution to the problem is technology called Business Intelligence (BI). Properly implemented and utilized BI solution is a source of significant effects − benefits especially help increase overall business performance. It is also a source of competitive advantage for enterprises. Many empirical studies and practical results but suggest that businesses are faced with several problems in implementing BI. It can be concluded that to ensure the overall success of the implementation and use of BI in managing companies is therefore necessary to recognize, understand and then manage key success factors of BI.

Based on defined research problem: analysis of relationships and connections between defined success factors of BI and overall success in the deployment and use of BI in the management of enterprises in Slovakia.

The problem can also be formulated in the form of central examination questions:

What kind of relationships and connections exist between the defined factors of success and the overall success of BI deployment and use of BI in the management of enterprises in Slovakia?

Baseline model (Figure 1) contains seven key success factors of BI, which were defined in particular in the light of experience and the results of foreign experience.

III. Methodology

Based on the model of key success factors of BI that have been defined, the dependent variable and seven independent variables. The dependent variable is the overall success of the implementation and use of Business Intelligence in managing companies in Slovakia, which means the correct implementation and effective use of these systems in supporting decision-making processes in the enterprise. This will achieve the desired effects.

Independent variables are the success factors of BI which can be classified into two main groups:

- personnel and organizational: strong sponsor, close cooperation, enterprise-wide solution scope, right team of qualified and experienced Business Intelligence workers and open corporate culture
- technological factors: the quality of the source data, flexible architecture and BI tools

We assume the existence of a positive relationship respectively connection between the independent and dependent variable. Hypotheses (H1 − H7) are defined as follows:

H1: The active involvement of a strong sponsor to the Business Intelligence project is positively related to the overall success of the introduction and use of Business Intelligence in managing companies in Slovakia.

H2: The quality of the source data in the information systems of company positively related to the overall success of the introduction and use of Business Intelligence in managing companies in Slovakia.

H3: Properly chosen, flexible architecture and Business Intelligence tools are positively related to overall success of the introduction and use of Business Intelligence in managing companies in Slovakia.

H4: Implementation and use of Business Intelligence across the enterprise positively related to the overall success of the introduction and use of Business Intelligence in managing companies in Slovakia.

H5: Creating the right team of qualified and experienced Business Intelligence workers is related to positive overall success of the implementation and use of Business Intelligence in managing companies in Slovakia.

H6: Ensuring close cooperation between the sponsor of the Business Intelligence project, technologists and ordinary business users of Business Intelligence positively related to the overall success of Business Intelligence in managing companies in Slovakia.

H7: Open corporate culture promoting decision-making based on facts and concrete positive results of analyzes is positively related to the overall success of the implementation and use of Business Intelligence in managing companies in Slovakia.

Through statistical testing of hypotheses H1−H7, expected significant positive correlation between each of the proposed seven success factors and the overall BI success has been gradually established respectively unconfirmed.

Confirmed (unconfirmed) hypotheses happened feedback to the original model of success factors of BI deployment and use − test results of statistical hypotheses verification allowed modification (extension) of the baseline model.

A. The research sample

Available set of business subjects that meet the above selection criteria was created through direct addressing software companies − providers of BI solutions in the domestic market. Based on this group of companies it was subsequently randomized defined research sample. Choice of subjects in the survey sample was not limited by other criteria such as industry or occupation of the enterprise, region or company size etc. It can be concluded that the fundamental requirement of ensuring representativeness of the survey sample was complied with.

On cooperation in the implementation of research, we asked several software and consulting companies in the domestic market offer software products and extensive services in the field of latest information technology − including technical consultation, analysis, development, training and certification and so on. We contacted companies that have knowledge and experience in providing BI technologies and support their implementation and process management in Slovakia. The leading providers group of BI solutions include, for example, SAP, IBM - Cognos, Oracle, Microsoft, SAS, NESS, Asseco and many other companies.

Main characteristics of research subjects in terms of the size of the company we can see down. In the survey, the questionnaire was completed by 11 small businesses, what is 20.4% of the survey sample, 12 medium-sized companies, what constitutes 22.2% of the survey sample and 31 large enterprises, representing 57.4% of the sample.

The distribution of samples of research in the performed economic activities to the classification used SKNACE is given in Table 1.

Table 1 Research sample structure – industry areas

Sectors of corporate activities (the subject of economic activity)	**Absolute frequency *n***	**The relative frequency%**
Industrial production	18	33,3 %
Electricity, gas, steam and air conditioning supply	2	3,7 %
Civil engineering	1	1,9 %
Wholesale and retail trade	4	7,4 %
Transport and storage	2	3,7 %
Accommodation and food services	4	7,4 %
Information and communication services	8	14,8%
Financial and insurance activities	5	9,3 %
Real estate activities	1	1,9 %
Public administration and defense	1	1,9 %
Education	1	1,9 %
Health care and social assistance	2	3,7 %
Other activities	1	1,9 %
Information not provided	4	7,4 %
Together	*54*	*100 %*

B. Methods for data obtaining and gathering

The questionnaire survey featured data collection using the online questionnaire. Link to the online questionnaire was together with an explanatory covering letter sent to respondents in electronic form. The questionnaire titled "Success Factors deployment and use of Business Intelligence in the management of Slovak enterprises" was created as a system of targeted questions designed for managers, professional IT workers and ordinary (non-technological) business users of BI solutions in selected companies in Slovakia.

The dependent variable and independent variables were interval only. In the case of a dependent variable (i.e. the total percentage deployment and use of BI), was used a continuous scale with the assessment failed (1) - rather unsuccessful (2) - relatively successful (3) - very successful (4) the introduction and use of BI solutions in the management of the business.

The answer key in the case of independent variables consisted of an interval of five-point Likert-type scale in the range "to any fundamental" importance of the factor for the overall success of BI project, namely no (1) - rather weak (2) - average (3) - quite strong (4) - substantial (5) above.

C. Methods for solving the problem

Due to the nature of the problem and the main objective of the paper they were selected appropriate statistical methods that can detect and analyze relationships between variables of interest − correlation and regression analysis. The objective of correlation and regression analysis is a description of the statistical properties of the relationship between two variables.

Within inductive statistics were performed statistical hypothesis tests (tests of statistical significance). Statistical hypothesis testing is a process of verifying the correctness or incorrectness hypothesis using the results obtained at random. When testing the statistical hypothesis of the research have been observed following, generally known steps (www.rimarcik.com).

1. Formulation of the null hypothesis (H0), which expresses

the independence of variables, i.e. absence of a relationship between variables.

2. The formulation of the alternative hypothesis (HA), which shows statistical dependence variables, namely the existence of a statistically significant relationship between variables.

3. Determining the level of significance (α).

The significance level α is the probability of error of the first kind, which we do, if we reject the null hypothesis (H0) that actually pays. Was determined significance level $\alpha = 0.05$ (5%).

4. Calculation of test statistics and probability.

The test statistic was calculated from the sample, which has provided the veracity of the null hypothesis (H0) the probability distribution. P-value is the lowest level of significance, leading to the rejection of the null hypothesis (H0) - the lower, the more we are convinced that the null hypothesis (H0) is not true and should be rejected.

5. The decision - rejected or not to reject the hypothesis.

It formulated a conclusion statistical test. If $p < \alpha$, i.e. if $p < 0,05$ null hypothesis (H0) was against the relevant alternative hypothesis (HA) rejected, which means between variables exists relationship, if $p \geq \alpha$, that is, if $p \geq 0,05$ zero hypothesis (H0) has been rejected. We did not have sufficient evidence to have argued that there is a relationship between variables. There have been used three degrees values of significance p:

*** $p < 0.001$ - very highly statistically significant relationship

** $p < 0.01$ - statistically highly significant relationship

* $p < 0.05$ - significant relationship

IV. Results of research

Correlation analysis was carried out in the form of correlation matrix, prepared for all variables of the parent model. To express the degree of correlation dependence between variables in the correlation matrix was used so-called The Pearson correlation coefficient pairwise. The correlation matrix contains 28 possible correlation relationships of the 28 correlation coefficients for all pairs of variables of interest.

Using a two-sided t - test within T - distribution of the test statistic tests were performed statistical significance correlation coefficients. The results are presented in Table 2. Table contains a correlation matrix with the calculated value of the correlation coefficient r of the pairs of variables significance pa information on the number of values n, of which the calculation carried out.

As we expected, all seven independent variables correlated with the dependent variable (TPD) positive, with the highest degree of correlation with the dependent variable, depending achieve independent variable (atomizing) with a value of $p < 0.001$, which represents a highly statistically highly significant relationship. Statistically highly significant correlation variable (TPD) was observed by the variables (StSp), (QSD), (RTW) a (OCC).

Table 2 The results of tests of statistical significance correlation coefficients of variables starting model

The variable	1.	2.	3.	4.	5.	6.	7.	8.
1. TPD	1							
2. StSp	**0,415**	1						
3. QSD	**0,389**	0,393	1					
4. FlexArch	**0,174**	0,386	0,297	1				
5. EWSS	**0,463**	0,305	0,475	0,188	1			
6. RTW	**0,378**	0,493	0,394	0,295	0,456	1		
7. CCop	**0,151**	0,561	0,398	0,334	0,253	0,406	1	
8. OCC	**0,388**	0,604	0,493	0,287	0,417	0,532	0,340	1

***p<0,001, **p<0,01, *p<0,05; n = 54

(Source: the output of SPSS Statistics)

(TPD) − total percentage deployment and use of BI in the management of companies in Slovakia

(StSp) − existence and active involvement of a strong sponsor to BI project

(QSD) − the quality of the source data

(FlexArch) − flexible architecture and BI tools

(EWSS) − enterprise-wide solution scope

(RTW) − right team of qualified and experienced Business Intelligence workers

(CCop) − close cooperation,

(OCC) − open corporate culture

The hypotheses were verified on the basis of the results of tests of statistical significance correlation coefficients presented in Table 2. In a key objective of the research was certified seven hypotheses (H1 − H7):

ISBN: 978-1-61804-321-4

***H1:** The active involvement of a strong sponsor to the Business Intelligence project positively related to the overall success of the introduction and use of Business Intelligence in managing companies in Slovakia.*

The hypothesis H1 assumes that active involvement of powerful sponsor increases the success rate of introduction and use of BI in corporate governance.

The results of correlation analysis have confirmed the hypothesis H1. For variable (StSp) was calculated correlation coefficient r = + 0.415. Using the statistical significance test of the correlation coefficient using two-sided t - test, we have demonstrated a highly statistically significant relationship with the corresponding value of p = 0.002, where we note that p <α, that is, p <0.05.

***H2:** The quality of the source data in the information systems of company positively related to the overall success of the introduction and use of Business Intelligence in managing companies in Slovakia.*

This hypothesis suggests that if the corporate data stored in various source systems have achieved the required level of quality, then increases the success rate of introduction and use of BI in corporate governance.

The results of correlation analysis have confirmed the hypothesis H2. For variable (QSD) was calculated correlation coefficient r = + 0.389. Test the statistical significance of the correlation coefficient using two-sided t - test, we have demonstrated a highly statistically significant relationship with the corresponding value of p = 0.004, where it can be concluded that p <α, that is, p <0.05.

***H4:** Implementation and use of Business Intelligence across the enterprise positively related to the overall success of the introduction and use of Business Intelligence in managing companies in Slovakia.*

Expressly provides that the more functional areas, departments or sections of enterprise BI solution covers, the higher the success rate of its use.

Based on the results of correlation analysis, H4 hypothesis was confirmed. For variable (atomizing) was calculated by the highest correlation coefficient r = + 0.463. Test the statistical significance of the correlation coefficient using two-sided t - test we have demonstrated statistically highly significant relationship demonstrated the value of p = 0.000, where we note that p <α, that is, p <0.05.

Enterprise-wide BI projects scope, that use BI to the enterprise level as a whole, which implies the involvement of all functional areas, respectively departments of the company to the BI project, is statistically significantly related to the overall success of the introduction and use of BI in corporate governance.

***H5:** Creating the right team qualified and experienced Business Intelligence workers is related to positive overall success of the implementation and use of Business Intelligence in managing companies in Slovakia.*

This hypothesis suggests that if the BI team consisting of skilled workers with past experience of implementation and use of BI solutions was created, then the success rate of introduction and use of these solutions in the enterprise increases.

Based on the results of correlation analysis H5 hypothesis was confirmed. For variable (RTW) was calculated correlation coefficient r = + 0.378. Using two-sided t - test, we have demonstrated a highly statistically significant relationship with the value of p = 0.005, where it can be concluded that p <α, that is, p <0.05.

***H7:** Open corporate culture to change, promoting decision-making based on facts and concrete positive results of analyzes related to the overall success of the implementation and use of Business Intelligence in managing companies in Slovakia.*

The hypothesis H7 assumes that when a corporate culture is able to adapt to changes in management style of organizations, then the success rate of introduction and use of BI in company increases.

The results of correlation analysis H7 hypothesis were confirmed. For variable (horseshoes) was calculated correlation coefficient r = + 0.388. Using the two-sided t - test, we have demonstrated a highly statistically significant relationship with the corresponding value of p = 0.004, where we note that p <α, that is, p <0.05.

The results of correlation analysis did not confirm the hypothesis H3 and H6.

***H3:** Properly chosen, flexible architecture and business intelligence is related to positive overall success of the introduction and use of Business Intelligence in managing companies in Slovakia.*

***H6:** Ensuring close cooperation between the sponsor of the Business Intelligence project, technologists and ordinary business users Business Intelligence positively related to the overall success of Business Intelligence in managing companies in Slovakia.*

The calculated correlation coefficients of variables (FlexArch) and (CCop), although at a positive value (0 <r<1), which given the independent variables and the dependent variable indicating the existence of the association of a positive trend, the dependence of the correlation is not statistically significant. Test the statistical significance of the correlation coefficients using the t - test demonstrated in both cases statistically significant relationship with the value of p> α, where α = 0.05.

In accordance with the defined main goals of the work were subsequently calculated and verified in terms of statistical significance also tested the correlation coefficients that characterize the strength of correlation between the dependent variable (TPD) and other defined variables.

V. Discussion and Conclusion

The sample consists of 54 business entities of different sizes with a diverse nature in Slovakia pursuit of economic activities in which BI solutions are currently implemented and used in support of decision-making processes.

Based on the results of the correlation analysis, tests of statistical significance correlation coefficients were confirmed hypotheses **H1, H2, H4, H5** and **H7**, which consistently demonstrated a statistically significant relationship with the dependent variable - i.e. total success of implementation and use of BI. As a part of the testing of hypotheses **H3** and **H6** positive correlation with the dependent variable was not confirmed at the statistically significant level.

The starting model considered key success factors of BI has been modified by the new BI success factors that have been in business practice identified and validated by relevant analyzes as key factors, i.e. factors of particular importance for the proper implementation and effective use of BI solutions.

Results of the research are directed to the formulation of one of the conclusions, and that enterprises of different sizes operating in different sectors today through successful implementation and use of technology and BI tools achieve significant positive effects − benefits.

Upon confirmation of hypotheses and interdependence of the extension of the original model as follows:

Fig. 2 The newly established model of key success factors of Business Intelligence (Source: own processing)

REFERENCES

[1] J. Pour, Faktory úspěšnosti Business Intelligence − užití a řešení. *Systémová Integrace*. ISSN 1210-9479, 2005, no. 1, pp. 377 - 388.

[2] J. Pour, Co lze očekávat od Business Intelligence? *Systémová integrace*. ISSN 1336-5916, 2006, no.1, pp. 47 - 58.

[3] J. Pour, and D. Slánský, Efekty a rizika Business Intelligence. *Systémová integrace*. ISSN 1210-9479, 2004, vol. 11, no. 2, pp. 24-33.

[4] O. Novotný, and J. Pour and D. Slánský, *Business Intelligence − jak využít bohatství ve vašich datech*. Praha: Grada Publishing, 2005. ISBN 80-247-1094-3.

[5] S. Atre, *The Top 10 Critical Challenges for Business Intelligence Success*. [online]. 2003. Available on internet: <http://www.computerworld.com/computerworld/records/images/pdf/BusIntellWPonline.pdf>

[6] W. Eckerson, *Smart Companies in the 21st Century: The Secrets of Creating Successful Business Intelligence Solutions.* [online]. 2003. Available on internet: <http://cstl-hcb.semo.edu/eom/mi430/protected/assignments/smartcompanies.pdf>

[7] D. Loshin, *Business Intelligence − The Savvy Manager's Guide*. San Francisco: Morgan Kaufmann Publishers, 2003. ISBN 978-1-55860-916-7.

[8] C. Howson, *Successful Business Intelligence: Secrets to Making BI the Killer App*. New York: McGraw-Hill Companies, 2008. ISBN 978-0-07-149851-7.

[9] X. Hwang, *Success Factors for Business Intelligence: Perceptions of Business Professionals.* [online]. 2008. Available on internet: <http://www.myacme.org/ACMEProceedings09/p44.pdf>

[10] E. Turban, et al., *Business Intelligence − A Managerial Approach*. New Jersey: Prentice Hall, 2008. ISBN 978-0-13-610066-9.

[11] P. Panta, *Business Intelligence − How to Build Successful Business Intelligence Strategy.* [online]. 2009. Available on internet: <http://www.deloitte.com/assets/Dcom-SouthAfrica/Local%20Assets/Documents/Business%20intelligence%20that%20aligns%20with%20enterprise%20goals.pdf>

[12] J. Škanta, Kritické faktory úspěšnosti Business Intelligence. In *IT Systems*. ISSN 1212-4567, 2010, vol. 11, č. 6, s. 30-31.

[13] S. Adelman, and D. Schrader, *Practical Tips to Overcome Barriers to Pervasive BI.* [online]. 2012. Available on internet: <http://mlmsim.com/whitepapers/practical-tips-to-overcome-barriers-to-pervasive-bi-by-sid-adelman-and-dave-schrader/>

[14] B. Kršák, Review of usability of selected geodetic methods from the view of their economic efficiency in spatial data collection process, *13th International Multidisciplinary Scientific Geoconference, SGEM* 2013 Location: Albena, BULGARIA, vol. 2, pp. 89-396.

Business Intelligence as an effective tool for management and increase overall corporate performance in Slovak companies

Štefan Čarnický, Peter Mesároš, Martina Habiňaková, Tomáš Mandičák, Daniela Káposztásová

Abstract — Currently, top management must make decisions quickly and well. The relevant information is support for decision making. Work with information is difficult. The information must be timely, realistic and attainable at the moment of decision. Time digital economy brings wealth of information. Top management must be provided by the significant and important information for the right decisions. Currently, it is therefore necessary to find systematic solutions that will assist in decision-making. In recent years come to the fore Business Intelligence (BI) tools. Business Intelligence is an effective and supportive tool for decision making. It is a tool that can be implemented into any business. Improve the overall corporate performance of the company and improve its competitiveness are the main reason for implementation of decision support solutions. Paper discusses the issue of use Business Intelligence tools in the Slovak companies. The main objective of this paper is to analyze the impact of the implementation of Business Intelligence to overall business performance and competitiveness. This paper describes the situation abroad from available studies. On this basis, a similar study was conducted in Slovak companies.

Keywords — Business Intelligence, overall corporate performance, competiveness, Slovak companies.

I. Introduction

THE current business environment is complex. The complexity of the organization's environment creates opportunities and threats. Companies must respond to these threats quickly and flexibly. Controlled systems for decision support improve response capability organizations. Most commonly used information systems (IS) are not able to properly and quickly assess large amounts of data stored in various databases across the enterprise (for example, payroll information, financial data, data relating to customers, suppliers etc). That is the reason why cannot fully meet the current information needs of managers (corporate decision-makers). They often fail in order to share information with each other, get information late, inaccurate or even wrong. For this reason, they are often not able to make use of strategically relevant information and receive correct and timely decision. The solution to this problem is a technology called Business Intelligence.

Technologies and systems designed to improve business operations and business decisions gradually, under different names, introduce a use for over 30 years. To meet the current needs of organizations they are continually being developed, using new ways and supplemented by innovative and modern software tools and methods. The idea of BI is thus not so brand new, although this designation was first used in 1989 by an analyst at Gartner Group, Howard J. Dresner.

II. Business Intelligence and overall corporate performance abroad

Business Intelligence is a set of technologies and processes that allow people at all levels of the organization access to data and analysis, in order to drive business, increase corporate efficiency, reveal opportunities and operate efficiently [1]. Successful use of BI allows getting multiple benefits. According to Gartner Group survey which has been conducted several years ago, BI systems have been implemented in almost 80% corporations in the U.S. and in about 50% of companies in Europe. This relatively high percentage of extending BI is primarily due to the benefits or effects for the success and performance of business enterprises [2]. In this section, we will try to point out some of these benefits, whether quantitative or qualitative, which are not so obvious at first glance.

Implementation and use of BI solutions brings to the firm a number of benefits – there are positive economic and non-economic benefits or effects that businesses should gain if they successfully manage the BI implementation of solutions. Some benefits are quantitatively and objectively measurable, but many are qualitative and cannot be expressed by exact numbers [3]. It is important to monitor overall corporate performance. BI is a crucial element of Business Performance

The paper presents partial results of the research project VEGA No. 1/0562/14 „The impact of Business Intelligence tools on corporate performance“.

Štefan Čarnický, University of Economics in Bratislava, Faculty of Business Economics with seat in Košice, Tajovského 13, 041 30 Kosice, Slovak Republic (phone: +421557223232; fax: +421556230620; e-mail: stefan.carnicky@euke.sk)

Martina Habiňaková, University of Presov, Faculty of management, Konštantínova 16, 080 01 Prešov, Slovakia (martina.habinakova@gmail.com)

Peter Mesároš, Technical University of Kosice, Faculty of Civil Engineering, Vysokoškolská 4, 042 00 Kosice, Slovakia (peter.mesaros@tuke.sk)

Tomáš Mandičák, Technical University of Kosice, Faculty of Civil Engineering, Vysokoškolská 4, 042 00 Kosice, Slovakia (tomas.mandicak@tuke.sk)

Daniela Káposztásová, Technical University of Kosice, Faculty of Civil Engineering, Vysokoškolská 4, 042 00 Kosice, Slovakia daniela.kaposztasova@tuke.sk)

Management. If BI is an effective tool, the question is as follows: Has BI a positive effect on overall corporate performance? Or how does the business performance management system look like? Is there any correlation with the use of BI?

According to Turban, the Business Performance Management (BPM) is an integrated set of processes, metrics, methods and applications designed to control financial and operational performance of the company. BPM helps to change the strategy and objectives of the plan, monitor corporate performance in relation to this plan, analyzing the differences between planned and achieved results and, depending on the results of these analyses, assesses and adjusts the objectives and activities of the organization [4]. BPM is based on the methodology of Balanced Scorecard, which by linking the objectives set and the results actually recorded a framework for the definition, implementation and management of corporate strategy. BPM forms a closed loop that links strategy to execution to optimize the overall performance of the organization (Figure 1).

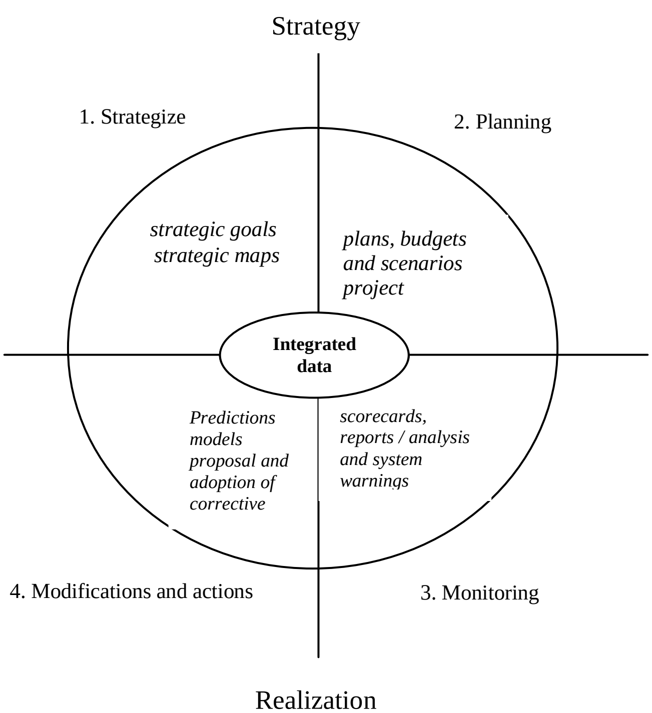

Fig. 1 Business Performance Management Process [4]

To link actions and activities of the organization with its strategy, objectives, plans and analysis systems can be very difficult for the organization. BPM Standards Group is a group of leading organizations in the successful implementation and use of corporate performance management systems. That group together was created by companies like Hyperion, IBM, SAP, and TDWI and others. The group defines BPM as a framework for scheduling, organizing, automating and analyzing business processes, indicators, processes and systems in order to manage organizational performance.

Eckerson argues that BPM combines the strategy of the organization to its implementation that improves [5]:

- **communication** - BPM provides an effective mechanism for senior management to interpret and clarify strategies and expectations of managers and employees at all levels of the organization, through the planning model and performance metrics linked to business objectives,
- **cooperation** - BPM supports two-way exchange of information and intentions horizontal direction - between departments or groups at one level of the organization, and vertical - between all levels within the organization,
- **control** - BPM continually provides up to date information about the market situation and the state of operational processes, thus enabling employees to continually adjust plans in a timely manner to correct or improve operational activities,
- **coordination** - BPM improves coordination between business resp. business units of the company.

To monitor business performance and set objectives, it is necessary to define key performance indicators (KPI). This is the most important performance indicators that reflect the organization's strategic objectives and measure performance achieved in relation to these objectives. Methods for identifying and selecting suitable KPIs are examined in studies of Eckerson [5].

Howson [1] considers the increase of overall corporate performance as the most significant effect resulting from the use of BI. The extent, to which BI contributes to enhance the performance of the organization, would be, according her opinion, a priority measure of the success of these solutions in practice. This argument relies on the results of research conducted in 2006 on a sample of 513 companies. Based on the responses of participating respondents, she could graphically illustrate the extent, to which BI was affecting the performance of surveyed companies. On Figure 2, the y-axis shows the number of respondents expressed in %, x-axis degree of influence to change the BI performance as perceived by addressed participants. In addition to increasing business performance author presents other major benefits that emerged from the survey (Figure 3).

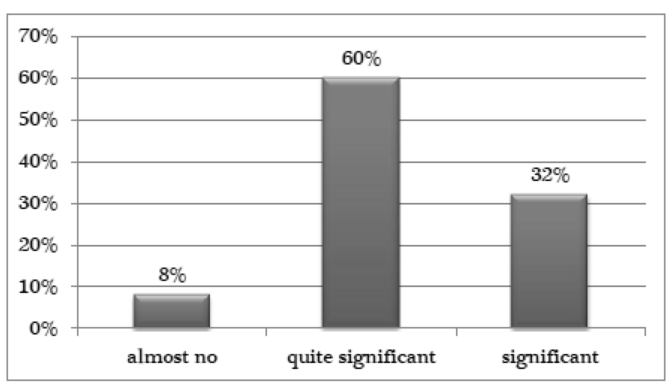

Fig. 2 Impact of BI to change the overall performance of the organization [1]

Specifically, it is relating to the following benefits associated with application of BI:

- cost savings,
- increase in the number of active users,
- Return on Investment (ROI),
- simplified user perception,
- support of key shareholders,
- better access to data,
- enhancement of business performance.

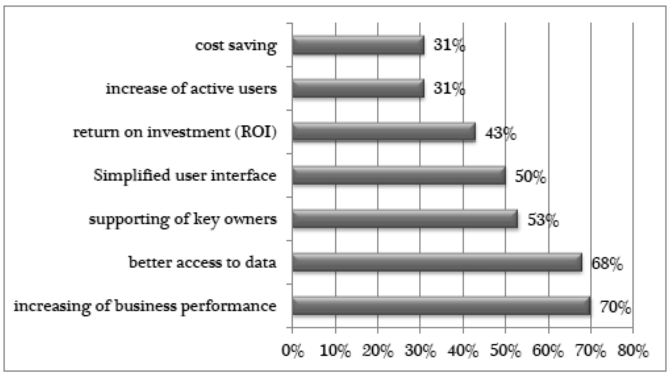

Fig. 3 The benefits associated with application of BI
Source: Howson (2007).

Turban et al. [4] perceive the ability of BI systems as their most significant effect for the company to be able in the case of need to provide accurate information rapidly, including looking at the overall performance of the company and its individual components in real time. Such information is, according to them the need for all kinds of decisions for strategic planning and even the survival of the company.

III. Methodology

The obtained data were processed primarily analyzed using Microsoft Office Excel 2007 using a statistical system IBM SPSS Statistics. Effective layout of the data obtained in order to gain concise and transparent information about the statistical series is an essential condition for further analysis. When processing the data obtained in this study, graphical presentation of data sets - frequency charts, graphical tools (especially columns and pie charts) was used.

A. Methods for data obtaining and gathering

The questionnaire survey featured data collection using the online questionnaire. Link to the online questionnaire was together with an explanatory covering letter sent to respondents in electronic form. The questionnaire titled was created as a system of targeted questions designed for managers, professional IT workers and ordinary (non-technological) business users of BI solutions in selected companies in Slovakia. In order to verify the questionnaire, mainly to test the formulation of clarity of individual items, it was a sample of 20 business projects, realized within pre-research.

B. The research sample

Available set of business subjects that meet the selection criteria was created through direct addressing by software companies - providers of BI solutions in Slovakia. Based on this group of companies, it was subsequently randomized defined research sample. Choice of subjects in the survey sample was not limited by other criteria such as industry or occupation of the enterprise, region or company size etc. It can be concluded that the fundamental requirement of ensuring representativeness, the survey sample was complied with.

On cooperation in the implementation of research, we asked several software and consulting companies in Slovakia, that offer software products and extensive services in the field of latest information technology - including technical consultation, analysis, development, training and certification and so on. We contacted companies that have knowledge and experience in providing BI technologies and support their implementation and process management in Slovakia. The leading providers group of BI solutions include, for example, SAP, IBM - Cognos, Oracle, Microsoft, SAS, NESS, Asseco and many other companies.

Main characteristics of research subjects in terms of the size of the company we can see down. Participated in the survey and a questionnaire completed by 11 small businesses, what constitutes 20.4% of the survey sample, 12 medium-sized companies, what constitutes 22.2% of the survey sample and 31 large enterprises, representing 57.4% of the sample (Figure 4).

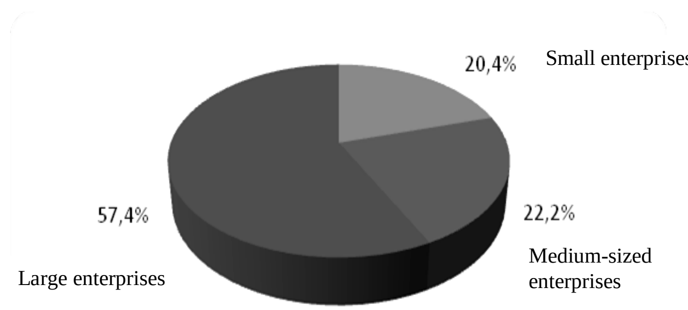

Fig. 4 Characteristics of the survey sample by size of enterprise

The distribution of samples of research in the performed economic activities to the classification used SK NACE is given in Table 1.

Table 1 Research sample structure – industry areas

Sectors of corporate activities (the subject of economic activity)	**Absolute frequency *n***	**The relative frequency%**
Industrial production	18	33,3 %
Electricity, gas, steam and air conditioning supply	2	3,7 %
Civil engineering	1	1,9 %
Wholesale and retail trade	4	7,4 %

ISBN: 978-1-61804-321-4

Transport and storage	2	3,7 %
Accommodation and food services	4	7,4 %
Information and communication services	8	14,8%
Financial and insurance activities	5	9,3 %
Real estate activities	1	1,9 %
Public administration and defense	1	1,9 %
Education	1	1,9 %
Health care and social assistance	2	3,7 %
Other activities	1	1,9 %
Information not provided	4	7,4 %
Together	*54*	*100 %*

IV. Results and discussion

The sample consists of 54 business entities of different sizes with a diverse nature in Slovakia, with economic activities in which BI solutions are currently implemented and used in support of decision making processes.

The rate of overall success of the introduction and use of BI in the management of surveyed enterprises is presented on Figure 5. Up to 66.7% of companies said their BI solution as relatively successful, 22.2% of enterprises considered it to be very successful and in 11.1% cases the solution assessed as rather unsuccessful. The overall success of BI projects is considered individually in companies. The expected achievement of the business from the implementation and use of BI solutions depends on company´s aims and values (the specific final effects - benefits).

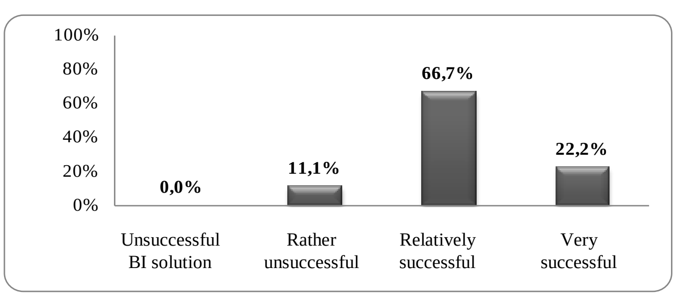

Fig. 5 Percentage deployment and use of Business Intelligence in companies in Slovakia

Results of the research are directed to the formulation of one of the conclusions, that enterprises of different sizes operating in different sectors today through successful implementation and use of technology and BI tools achieve significant positive effects - benefits.

The most significant benefits associated with the use of BI are usually considered increasing the overall performance and competitiveness of businesses. For this reason, it was subsequently examined the extent to which the BI contributes to increasing overall corporate performance (Figure 6) or competitiveness (Figure 7) enterprises in Slovakia.

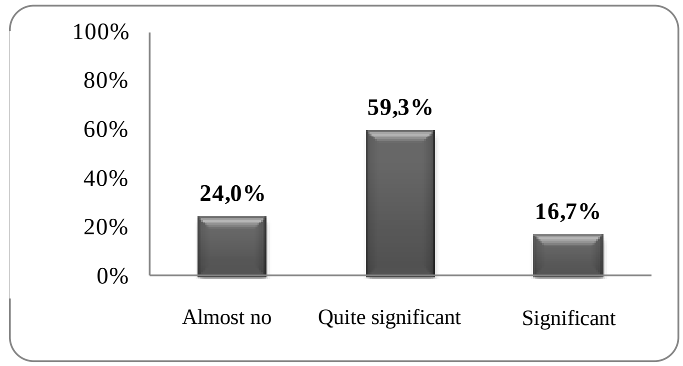

Fig. 6 Business Intelligence impact on the overall performance of companies in Slovakia

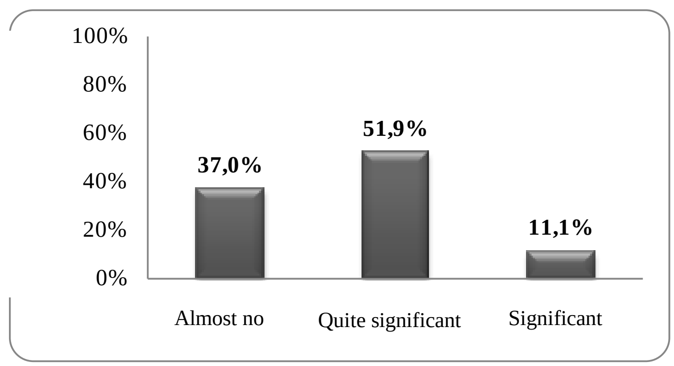

Fig. 7 Business Intelligence impact on the competitiveness of companies in Slovakia

The research results confirm that the effect of the use of BI in changing the overall corporate performance and competitiveness of businesses is really important.

Properly implemented and effectively used enterprise BI solution brings indisputable advantages. This statement can be justified by the other major findings and results of the research. Some of the benefits of BI are quantitatively and objectively measurable, but others are qualitative. They are often intangible and very difficult to measure, or to achieve them there in the long term, it is therefore quite difficult to express them in the form of specific numbers - for example, traditional BI evaluate the success of the project based on the value of the indicator ROI - return on investment in BI technology.

Realized survey further revealed the fact to which it should be noted, despite the declared and undeniable benefits associated with BI - many businesses during the life of BI projects encounter certain challenges that are an obstacle to the successful use of such solutions - achieved real benefits often do not correspond to their businesses and the objectives set for BI.

When compared to foreign studies and the situation in the Slovak companies are as follows. Most companies confirmed an increase in overall corporate performance following the implementation of BI. It is a roughly equal number of enterprises in relative terms. Companies abroad, however, indicate a greater extent and significant contribution of BI to overall business performance. Conversely, Slovak enterprises at a rate of 24% reported that the implementation of BI has little impact on the overall business performance.

V. CONCLUSION

Given the wide possibilities of using Business Intelligence solutions in the area of analytical and planning activities of enterprises and given the significant positive effects associated with their use (quantitative and qualitative benefits), maybe in the next years continue to expect increasing range of implementation and use of BI solutions in corporate governance in Slovakia.

International experience and the results of its own survey shows that businesses of all sizes operating in different sectors are able through proper implementation and use BI to achieve significant positive effects - benefits. If the BI solution implemented correctly and effectively used, then the company is able not only to make better use of market opportunities, but also in time to identify potential operational problems, making it competitive strength and its effective functioning. In particular, the impact of the use of BI to improve the overall performance and competitiveness of businesses, the study demonstrated as significant. Despite the undeniable benefits associated with BI, it is necessary to point out the other reality resulting from the recent survey - many businesses during the project meets certain challenges that are an obstacle to the successful use of BI solutions.

For the most significant recent trends in application possibilities of technology and Business Intelligence can be considered:

- Consolidation of the market for BI tools, maturity and stability instruments.
- Measurement and management support corporate performance through the integration of BI and Business Performance Management tools.

Monitoring and management of organizational performance through tools BPM is one of the leading trends in the field of BI. BPM process is usually based on the methodology of Balanced Scorecard, which enables organizations to track the performance of a number of mutually integrated aspects. Use BI has great potential. Even on the basis of the study it is obvious that BI has a positive effect on business performance and competitiveness.

REFERENCES

[1] C. Howson, C. *Successful Business Intelligence: Secrets to Making BI the Killer App*. New York : McGraw-Hill Companies, 2008. ISBN 978-0-07-149851-7

[2] Š. Čarnický and P. Mesároš. *Informačné systémy podnikov*. Bratislava: Ekonóm, 2009, 265. p. ISBN 978-80-225-2676-0

[3] Š. Čarnický, et al. *Business Intelligence: Theory and practice*. Rzeszow − Košice: Publishing House of Rzeszow University, 2011. ISBN 978-83-7338-692-1

[4] E. Turban, et al. *Business Intelligence - A Managerial Approach*. New Jersey : Prentice Hall, 2008. ISBN 978-0-13-610066-9

[5] W. ECKERSON, *Seven Strategies for Creating High-Performance Business Intelligence Teams.* TDWI, What Works in Enterprise Business Intelligence Volume 30. [online]. 2010. Available on internet: <http://tdwi.org/whitepapers/2010/10/what-works-volume 30.aspx?tc=page0>

BTS infrastructure impact analysis and design of an advanced BTS filtering for UKF-based positioning algorithm

Jon Goya, Leticia Zamora-Cadenas, Saioa Arrizabalaga, Gorka de Miguel, Iñigo Adin and Jaizki Mendizabal

***Abstract*—This article focuses on the impact of the BTS infrastructure and a possible alternative to improve the Unscented Kalman Filter (UKF) positioning algorithm. This enhancement applies the key idea of the satellite positioning. The analysis of the dilution of prediction (DOP) is realized to obtained the most suitable combination and improving the performance of the positioning algorithm. The BTS infrastructure analysis is based on the performance that several mobile operator give based on the results obtained with the UKF algorithm. First, the influence of the BTS distribution and number of neighbor BTS is discussed. Second, the improvement of the performance based on the DOP is developed. Results for the three mobile operator are compared for each of the defined test scenarios. It is proved that the infrastructure of the BTS has a direct influence in the positioning algorithm. Furthermore, the application of a observable pre-filtering method provides and enhancement in the positioning results.**

***Index Terms*—Positioning, Dilution of Precision, DOP, BTS, 3G, Kalman Filter, UKF.**

I. Introduction

THERE has been increased interest in developing location services for wireless communications systems over the last several years. Both network-based positioning methods (where the measurements are taken at cellular base stations) and handset-based positioning methods (where measurements are taken at the handset) have been developed. Hybrid methods are also defined, where measurements can be taken at the handset, and the location calculation can be done at the base stations. No matter where the position is calculated, it is mainly obtained based on the analysis of specific physical characteristics of radio signal such as Received Signal Strength (RSS), Time of Flight (ToF) - which includes Time of Arrival (ToA) and Time Difference of Arrival (TDoA) - or Angle of Arrival (AoA). All methods of distance measurement and location and derived from the measurements described above, alone or in combination [1].

First and second generation cellular networks were not conceived with location applications in mind. Third generation cellular networks have protocol and organizational provisions for network-based location services [2], [3].

J. Goya, L. Zamora-Cadenas, S. Arrizabalaga, G. de Miguel, I. Adin and J. Mendizabal at CEIT and Tecnun (University of Navarra) in Manuel de Lardizábal 15, 20018 San Sebastián, Spain.Tel.: (+34) 943 212800 Fax: (+34) 943 213076.

jgoya@ceit.es, lzamora@ceit.es, sarrizabalaga@ceit.es, gdemiguel@ceit.es, iadin@ceit.es and jmendizabal@ceit.es

New approaches for positioning algorithms that include more advance techniques such as Kalman filters have also been researched in literature [4], [5]. 3G-based positioning has been included for several applications: person and asset tracking, location-based advertising, location services for vehicles and traffic [1], [6], and recently for the first time also in railway in the EATS project [7]. In the latter, the Advanced Train Location Simulator (ATLAS) for developing, testing and validating on-board railway location systems has been implemented [8]. This platform allows to compare not only different positioning algorithms but also different environment and infrastructure configurations. This is of high interest as the accuracy of the location estimation depends also on the dispersion of the reference stations (known as Base Transceiver Stations (BTS) in 3G) in relation to the target. When the reference stations are grouped together, the times of arrival or time differences of arrival will not differ enough to give accurate solutions in solving the simultaneous equations. This is the case when, for example, satellites used for a GPS measurement are all in the same portion of the sky. The best arrangement of fixed stations relative to the target is when the circles, in the case of TOA, or hyperbolas in TDOA, cross at or close to right angles at the target [1].

It is the aim of this paper to analyze the effect of the dispersion of 3G reference stations in a real scenario, by comparing different 3G operators infrastructures (Orange, Movistar and Vodafone) and the performance of the positioning in urban, suburban and rural environments. Moreover, a new approach based on Dilution of Precision concept currently used in GPS, is proposed to intelligently select the most appropriate BTSs to get better performance.

The rest of this article is organized as follows. Section 2 describes the selected scenarios for the analysis of the impact of the BTS infrastructure. Section 3 presents and discuss the results obtained from the analysis based on the scenarios defined in the previous section. Section 4 describes the Dilution of Precision concept and its use for BTS filtering criterion. Section 5 describes the implementation of the filtering method inside the Unscented Kalman Filter (UKF) positioning algorithm and the performance results obtained. Finally, some conclusion are drawn in the Section 6.

ISBN: 978-1-61804-321-4

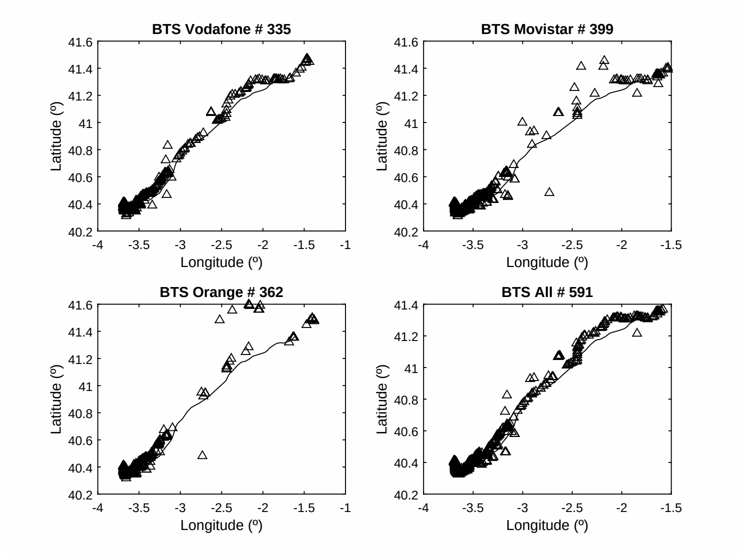

Fig. 1. BTS distribution for Vodafone, Movistar, Orange and All mobile operators

II. Analysis Setup

This section describes the analysis setup that is been conf gured in order to test the impact of the different 3G real BTS infrastructure in the positioning algorithm. ATLAS platform [8] provides high conf gurability and automated tools to make this research possible. Route characterization, measurements for the algorithms, the algorithm themselves and the performance analysis of the results are integrated in the same tool.

First of all, the route and infrastructure needs to be def ned: a real trajectory has been modeled from Madrid to Calatayud as a sequence of WGS84 coordinates, where the information about the environment (e.g. urban, suburban, rural) is added. Related to the BTS infrastructure, three different mobile operators are going to be analyzed. In the trajectory def ned, the closest 16 BTSs for each trajectory point have been included in the BTS infrastructure conf guration f les, for each of the three operators. For each 3G BTS, its WGS84 coordinates, a unique cell identif er and the operator code are specif ed. In Figure 1 the location of the BTSs can be seen for each of the mobile operators along the Madrid-Calatayud trajectory which starts in 40.4060644 N,-3.6900831 E, and f nishes in 41.3619562 N ,-1.6122613 E coordinates.

Second, the measurement generation in the platform needs to be conf gured. In this case, the RTT (Round Trip Time) observable has been selected for the 3G technology, because it does not include any codif cation error. For each point where the position is going to be calculated, the RTT measurements are generated for the hearable BTSs for the selected mobile operator.

Eq. 1 def nes the RTT value for one of the track points.

$$RTT = \frac{2 \cdot \sqrt{(x-x_o)^2 + (y-y_o)^2 + (z-z_o)^2}}{c} + \upsilon_{RTT} \tag{1}$$

where x is the BTS position and x_o is the target position.

$$\upsilon_{RTT} \sim \mathcal{N}\left(0, \sigma_{RTT}\right) \tag{2}$$

The characterization and error parameters are different for each environment; in fact, the error characterization is based on the ITU-Advanced Model Channel [9].

To make a deeper analysis of the impact of the number of measurements available, three different sets of observables are generated (for each operator): observables up to a maximum of 16, for a maximum of 4 observables (as it is the minimum amount necessary to position by triangulation [10]) and for a maximum of 8 observables as an intermediate case. The selection of the BTS for which the observable is generated relies on the received signal strength (RSS).

Third, the positioning algorithm is def ned. In this case, a positioning algorithm that includes an Unscented Kalman Filter (UKF) [11] based on RTT observable has been included. By default it uses all the observables it hears, no matter how many there are.

Finally, the performance analysis is done by the platform, based on the following statistical parameters for the horizontal error.

a) Mean Distance Error: The mean distance error of the estimated positions is given by Eq. 3. It represents the arithmetic mean of the distance error for every member of the population, in this case, the estimated positions:

$$\widehat{\mu}_x = \frac{1}{N_{\mathrm{MC}}} \sum_{n=1}^{N_{\mathrm{MC}}} \hat{x} \tag{3}$$

where $\hat{x}$ def nes the horizontal error.

b) Standard Deviation: The standard deviation of the distance error of the estimated positions is given by Eq. 4:

$$\widehat{\sigma}_x = \sqrt{\frac{1}{N_{\mathrm{MC}}} \sum_{n=1}^{N_{\mathrm{MC}}} \left(\hat{x} - \widehat{\mu}_x\right)} \tag{4}$$

where N_{MC} is the number of iterations.

c) Root Mean Square position error: The root mean square error (RMSE) accuracy is a measure of the square root of the deviation of the estimated position about the true position, so it combines both the variance and the bias. For a two dimensional space, the RMSE is given by Eq. 5

$$\mathrm{RMSE} = \sqrt{E\left[(\hat{x}-x)^2 + (\hat{y}-y)^2\right]} \tag{5}$$

where E is the expectation operator.

d) Cumulative Distribution Function: The Cumulative Distribution Function (CDF) of the positioning shows the probability of a having a distance error in positioning of less than a certain value (see Eq. 6):

$$\mathrm{P}\left(\mathrm{x}\right) = \int_0^{\mathrm{x}} p\left(x\right) dx \tag{6}$$

where $p(x)$ is the density function of the distance position error, and x the selected value of the distance error.

The most basic performance analysis conf guration permits the selection of the output f les to be analyzed. In this case, the

ISBN: 978-1-61804-321-4

outputs of the two location approaches used in the receiver of the head coach are selected.

The analysis will provide results for each operator (Orange, Movistar, Vodafone and All), the number of maximum hearable observables for the positioning algorithm (16, 8 and 4) and each environment (Urban, Suburban, Rural) which give in total 36 different scenarios, which are going to be analyzed in detail in the following section.

III. Characterization of the BTS infrastructure impact

All the study case is based on the ATLAS [8] simulation platform developed for the EATS project [7].

The number of BTS used in each of the environments is an important factor to take into account an to mention in each of the result. As observed in Fig 1 the lack of BTS in the last part of the track is an issue for the position algorithm performance. The reduced number of BTS or the lack of them produce a negative effect on the performance.

Table I shows all the statistical parameters that have been used in the comparison such as Mean Error, Standard Deviation, RMSE and CDF.

In Fig. 2, Fig. 3 and Fig. 4 the mean error values for each of the conf gurations are shown. In the set of Fig. 2, Fig. 3 and Fig. 4 the performance obtained with the use of the different operator and a limitation of used BTS. The black dot that appears on the f gures is the average number of observables that is using in each concrete scenario.

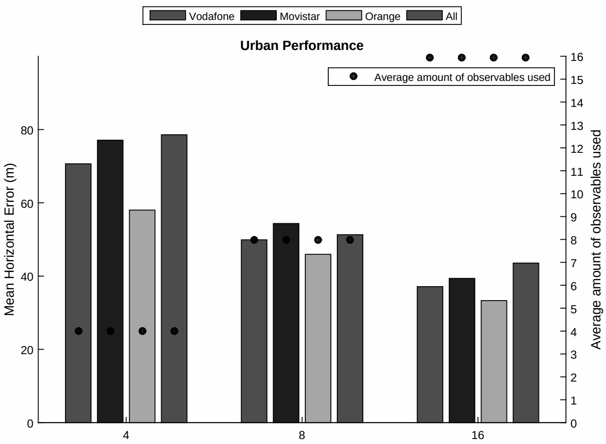

Fig. 2. Urban performance analysis

Figures present the mean horizontal error for the different scenarios. The different scenarios where the generated input are limited by a maximum number are marked in the x-axis. The different bar color in each of the x-axis points are linked to a different operator, that means that a different infrastructure is used for the calculation. The y-axis on the left is the mean horizontal error obtained after the simulation of each of the cases. Opposite to the y-axis is def ned the scale for the average number of observables used by the positioning algorithm that is marked as a f lled dot for each of the color bars. Finally, this representation is realized for the def ned environments (Urban, Suburban and Rural).

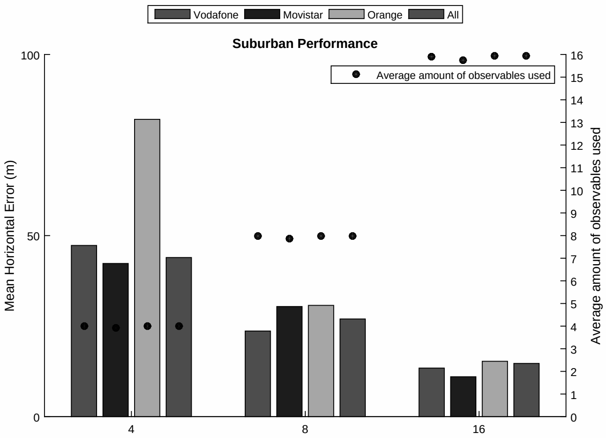

Fig. 3. Suburban performance analysis

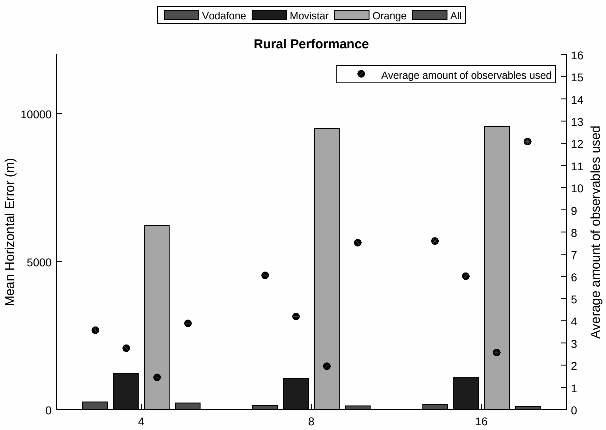

Fig. 4. Rural performance analysis

The obtained results have been analyzed and the following conclusions are drawn.

- In the Urban and Suburban environments the maximum amount of generated observables is the same as the average number of observables used. This makes both environments to behave similarly. In the case of the Rural environment, the lack of BTSs produces a lower number of observables compared with the established maximum limit. This effect is clearly seen on the irregular average observables used and a poorer performance in the Rural environment, as it can be seen in Fig. 4.
- The mean horizontal error in the Urban and the Suburban environments is lower as the maximum number of generated observables increases (see Table I).
- Suburban mean horizontal error is lower that the Urban one. This effect is also observed in the ITU-Advance Channel Model [9] where the error is bigger in Urban environment due to the multi-path effects.
- The lack of BTSs along the track increases the mean horizontal error. It can be seen in the Rural environment and with the Orange mobile operator. Orange mobile operator has the lowest number of BTSs which are poorly distributed along the track (see Fig. 1).
- All the results are different even if the average number of

TABLE I
STATISTICAL PERFORMANCE ANALYSIS FOR DIFFERENT MOBILE OPERATORS AND ENVIRONMENTS

	Orange			Movistar			Vodafone			All		
	4	8	16	4	8	16	4	8	16	4	8	16
Mean Urban	58.02	45.94	33.32	77.10	54.36	39.38	70.65	49.90	37.13	78.59	51.29	43.56
STD Urban	101.56	102.18	85.21	106.71	89.88	82.89	105.01	90.21	80.49	119.23	92.12	80.83
RMSE Urban	116.95	112.01	91.48	131.63	105.02	91.75	126.55	103.08	88.63	142.78	105.42	285.50
CDF 95 Urban	281.13	229.66	74.45	341.90	154.13	138.33	239.42	193.94	168.60	367.92	225.96	128.44
Mean Suburban	82.10	30.73	15.29	42.30	30.41	11.02	47.28	23.65	13.41	43.95	26.98	14.70
STD Suburban	60.53	28.11	17.58	40.89	54.01	11.49	37.58	22.21	14.20	34.32	37.38	13.13
RMSE Suburban	102.00	41.64	23.29	58.83	61.98	15.92	60.40	32.44	19.53	55.76	46.10	19.71
CDF 95 Suburban	192.77	82.03	40.18	115.64	150.11	31.24	128.42	72.51	40.16	108.87	85.60	36.68
Mean Rural	6224.94	9502.31	9567.20	1220.84	1057.16	1074.80	254.79	139.96	165.70	219.72	121.32	102.35
STD Rural	7066.81	12107.81	12046.52	1601.29	1424.24	1417.65	373.78	260.63	343.17	295.11	265.61	266.53
RMSE Rural	9417.41	15391.13	15383.24	2013.57	1773.69	1779.00	452.36	295.82	381.08	367.92	292.00	285.50
CDF 95 Rural	21785.53	38697.70	38487.10	5158.67	4620.12	4653.85	922.04	484.82	648.61	725.91	445.16	538.22

used observables is the same. Infrastructure geometry is the cause of this performance differentiation (see Table I focusing on Movistar and Vodafone)

In order to analyze the geometry of the infrastructure other metrics are needed. The most common metric to analyze the geometrical distribution of a certain set of sensors, satellites or information sources when are used for positioning is the Dilution of Precision (DOP). This metric is also used in GPS to select the best satellite constellation in order to improve the positioning performance.

IV. DILUTION OF PRECISION (DOP)

The Dilution of Precision (DOP) is an extended parameter used in the GPS position algorithms [12]. The evaluation of the best combination of satellites is assessed combining their information to obtain the most accurate position, because the geometrical disposition of the information sources has direct effect on the position uncertainty.

Fig. 5 shows two different scenarios. In (a), the position uncertainty is small (low dilution of precision). In (b), transmitter 2 is moved closer to transmitter 1, and, although the measurement uncertainty is the same, the position uncertainty is considerably larger (high dilution of precision) [13].

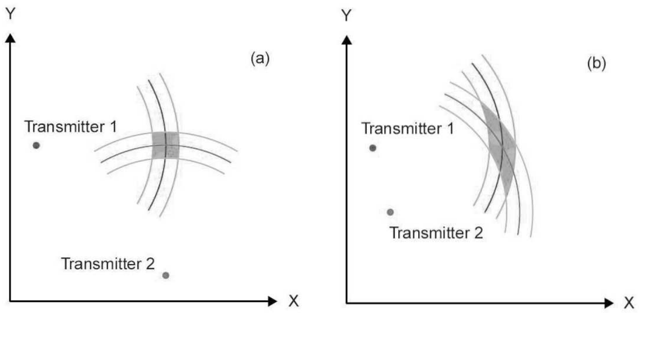

Fig. 5. Dilution of Precision [13]

First of all, pseudo-range equations need to be linearized in a certain point and then the correction obtained. In this case the RTT observable information is simple to transform and obtain the pseudo-range value (ρ).

$$\rho = \frac{RTT}{2} \cdot c \tag{7}$$

where c is the speed of light ($3 \cdot 10^8 m/s$).

Eq. 8 is the resultant problem to solve based on simple linear equations.

$$\Delta P_c = A \cdot \Delta X \tag{8}$$

Where ΔP_c is the difference between the transformed observables to pseudo-ranges and the modeled pseudo-ranges. this modeled pseudo-ranges is the estimated values that should be observed in the c point. A matrix is the partial derivative matrix of the pseudo-ranges with respect to the unknowns [13].

$$A = P_F(x, y, z) = \begin{bmatrix} \frac{\partial y_1}{\partial x} & \frac{\partial y_1}{\partial y} & \frac{\partial y_1}{\partial z} \\ \frac{\partial y_2}{\partial x} & \frac{\partial y_2}{\partial y} & \frac{\partial y_2}{\partial z} \\ \frac{\partial y_3}{\partial x} & \frac{\partial y_3}{\partial y} & \frac{\partial y_3}{\partial z} \\ \frac{\partial y_4}{\partial x} & \frac{\partial y_4}{\partial y} & \frac{\partial y_4}{\partial z} \end{bmatrix} \tag{9}$$

The calculation of the accuracy is determined by the law of propagation of error. As the result the covariance matrix C gives the standard deviation of the error, allowing to calculate the DOP or other evaluation term to f lter the observable selection.

$$C_{\Delta X} = (A^T \cdot A)^{-1} = \begin{bmatrix} \sigma_{11} & \sigma_{12} & \sigma_{13} \\ \sigma_{21} & \sigma_{22} & \sigma_{23} \\ \sigma_{31} & \sigma_{32} & \sigma_{33} \end{bmatrix} \tag{10}$$

Eq. 11 def ne the DOP for the 3-D case. The DOP values is based on the geometrical distribution of information sources [12]. It can be used a measure of metric (MOM) to f lter the used observables by the positioning algorithm, as GPS systems do with the selected satellites for the position calculation.

$$DOP = sqrt(\sigma_{11}^2 + \sigma_{22}^2 + \sigma_{33}^2) \tag{11}$$

This method is implemented to improve the positioning a gorithm adding an advanced observable f ltering. This methc is described in the following Section V.

V. Advanced BTS Filtering in the Unscented Kalman Filter positioning algorithm

Based on the DOP concept previously explained, an a vanced BTS f ltering approach has been introduced in tl Unscented Kalman Filter positioning algorithm, as shown the block diagram depicted in Fig. 6.

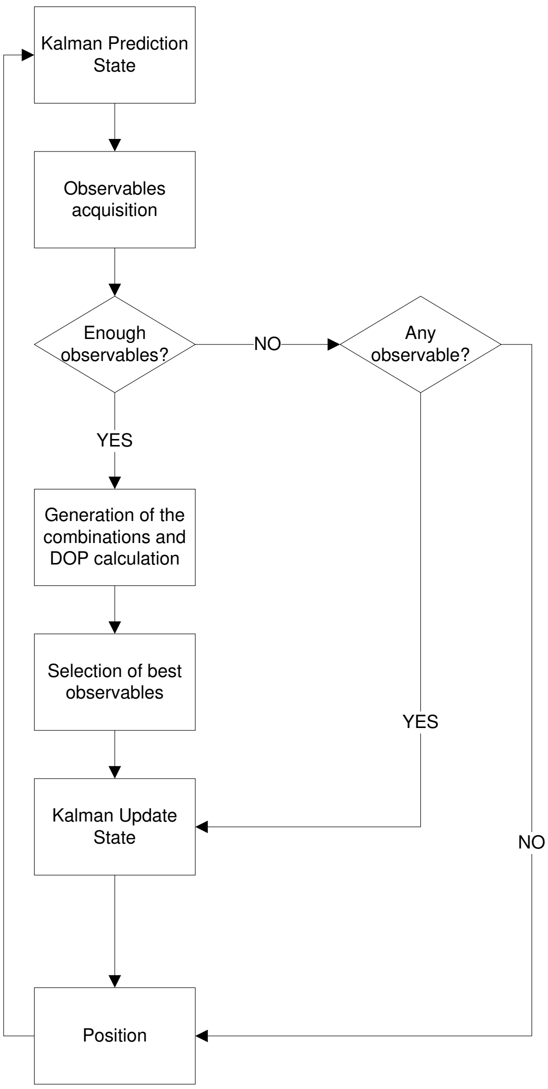

Fig. 6. Advanced UKF BTS Filtering

Kalman Filter is based on two steps. The f rst step is the prediction state, where the system position is modif ed based on a mathematical model. The second step is the update state, where the position is updated with the observables that the system accepts as an input. At this stage the advanced BTS f ltering takes part and performs the DOP calculation for all the possible combinations in case the minimum number of observables is reached. Once all the calculation is performed,

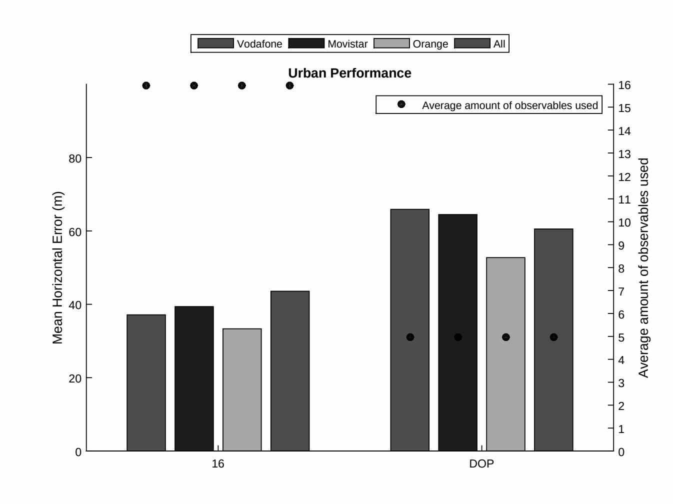

Fig. 7. Urban performance comparison

the selection of the f nal observables is done based on the DOP metric. These f ltered observables are the ones that are going to be used as input for the kalman update state, producing in the end the f nal position.

The combinations should be generated following the next list of rules:

- The order is not important.
- BTSs are not repeated.
- Reference BTS is always used.
- Items are taken in smaller sets than the total of BTS.

The smaller sets minimum number of items it has to be def ned depending on the calculation of the DOP. For example, in case x, y, z have to be calculated the minimum number of items should be at least 3.

The number of possible combinations is calculated with a simple combination formula (see Eq. 12).

$$C_m^n = \frac{m!}{n!(m-n)!} \tag{12}$$

where n is the number of selected items out of m that is the total number of items that can be selected.

Table II presents the number of combination for all the cases starting from the minimum number of BTS observables where the position of a target can be resolved in x, y and z components. The maximum values are limited by the number of neighbor BTSs that can be observed.

From the realized simulations with the obtained results, (see Table III and Fig. [7 8 9]), the following conclusions can be pointed out.

- In all the environments the average amount of observables used is reduced.
- In Urban and Suburban environments the advanced selection of the used observables have reduced the mean horizontal error for all the mobile operators.
- In Rural environment the performance is similar in both cases as mainly results come from the existing observables, which are the same as the selected ones by the advanced f ltering technique (see Table III in the Rural environment Vodafone and All operators).

ISBN: 978-1-61804-321-4

TABLE II
NUMBER OF COMBINATIONS

C_m^n	C_{16}^3	C_{16}^4	C_{16}^5	C_{16}^6	C_{16}^7	C_{16}^8	C_{16}^9	C_{16}^{10}	C_{16}^{11}	C_{16}^{12}	C_{16}^{13}	C_{16}^{14}	C_{16}^{15}	C_{16}^{16}
Combinations	560	1820	4368	8008	11440	12870	11440	8008	4368	1820	560	120	16	1

TABLE III
COMPARISON BETWEEN NON-FILTERED AND FILTERED OBSERVABLES TECHNIQUE IN THE UKF POSITIONING ALGORITHM

	Orange		Movistar		Vodafone		All	
	16	DOP	16	DOP	16	DOP	16	DOP
Mean Urban	33.32	28.57	39.38	34.45	37.13	32.74	43.56	34.64
STD Urban	85.21	87.33	82.89	92.55	80.49	85.25	80.83	92.76
RMSE Urban	91.48	91.74	91.75	98.60	88.63	91.18	91.81	98.86
CDF 95 Urban	74.45	82.58	138.33	126.04	168.60	180.69	128.44	116.71
Mean Suburban	15.29	10.54	11.02	9.42	13.41	8.55	14.70	7.89
STD Suburban	17.58	13.87	11.49	13.65	14.20	10.81	13.13	10.66
RMSE Suburban	23.29	17.41	15.92	16.58	19.53	13.78	19.71	13.25
CDF 95 Suburban	40.18	31.87	31.24	28.78	40.16	29.86	36.68	24.58
Mean Rural	9567.20	10344.47	1074.80	1058.82	165.70	169.99	102.35	107.08
STD Rural	12046.52	19726.50	1417.65	1592.85	343.17	355.93	266.53	268.87
RMSE Rural	15383.24	22270.76	1779.00	1912.40	381.08	394.38	285.50	289.36
CDF 95 Rural	38487.10	64618.21	4653.85	5066.34	648.61	663.00	538.22	540.83

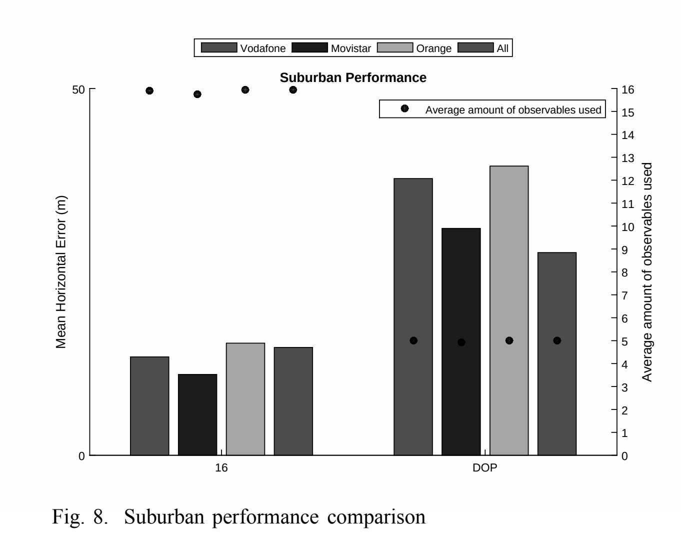

Fig. 8. Suburban performance comparison

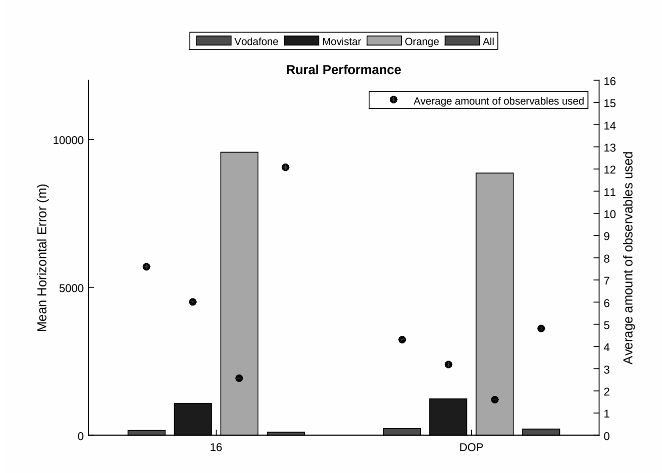

Fig. 9. Rural performance comparison

VI. CONCLUSION

The impact of the infrastructure and the geometry of the BTSs in the positioning algorithms has been demonstrated in the paper. The advanced f ltering technique is better as the number of neighbor BTSs increases. This is reasonable because it gives to the f ltering method more combinations to f nd out the most suitable. In case of the unfavorable environment, the f ltering algorithm performs similar to the non-f ltering algorithm. Summarizing, the f ltering method can be a valid approach to improve the positioning algorithm performance.

ACKNOWLEDGMENT

The research leading to these results has received funding from the European Communitys Framework Program FP7/EATS project under the grant agreement no.314219 and H2020/ERSAT-EAV project under grant agreement, no. 640747.

This work has been possible thanks to the support of the computing infrastructure of the i2BASQUE academic network. 5

REFERENCES

[1] A. Bensky, *Wireless positioning technologies and applications*, 2008. [Online]. Available: https://fama.us.es/record=b2065701 S5*spi

[2] Y. Zhao, "Standardization of mobile phone positioning for 3G systems," *IEEE Communications Magazine*, vol. 40, no. July, pp. 108–116, 2002.

[3] F. Gustafsson and F. Gunnarsson, "Mobile positioning using wireless networks: Possibilities and fundamental limitations based on available wireless network measurements," *IEEE Signal Processing Magazine*, vol. 22, no. 4, pp. 41–53, 2005.

[4] C. Liu, P. Shui, and S. Li, "Unscented extended kalman f lter for target tracking," *Systems Engineering and Electronics, Journal of*, vol. 22, no. 2, pp. 188–192, April 2011.

[5] Y. Hao, Z. Xiong, F. Sun, and X. Wang, "Comparison of Unscented Kalman Filters," *2007 International Conference on Mechatronics and Automation*, pp. 895–899, 2007. [Online]. Available: http://ieeexplore.ieee.org/lpdocs/epic03/wrapper.htm?arnumber=4303664

[6] S. Tao, S. Rodriguez, and A. Rusu, "UMTS mobile positioning simulator for vehicle location," in *Wireless, Mobile and Multimedia Networks (ICWMNN 2010), IET 3rd Int. Conf. on*, 2010, pp. 344–347.

[7] S. Arrizabalaga, J. Mendizabal, S. Pinte, J. Sánchez, J. Gonzalez, J. Bauer, M. Themistokleous, and D. Lowe, "Development of an Advanced Testing System and Smart Train Positioning System for ETCS applications," *TRA2014*, 2014.
[8] J. Goya, L. Zamora-Cadenas, S. Arrizabalaga, A. Brazález, J. Meléndez, and J. Mendizabal, "Advanced Train Location Simulator (ATLAS) for developing, testing and validating on-board railway location systems," *European Transport Research Review*, vol. 7, no. 3, p. 24, 2015. [Online]. Available: http://link.springer.com/10.1007/s12544-015-0173-5
[9] Report ITU-R M.2135-1, "Guidelines for evaluation of radio interface technologies for IMTadvanced," *Evaluation*, vol. 93, 2009. [Online]. Available: http://www.ncbi.nlm.nih.gov/pubmed/19923880
[10] G. Blewitt, "Basics of the GPS Technique : Observation Equations," *Time*, pp. 1–46, 1997.
[11] S. Julier and J. Uhlmann, "Unscented Filtering and Nonlinear Estimation," *Proceedings of the IEEE*, vol. 92, no. 3, pp. 401–422, Mar. 2004. [Online]. Available: http://ieeexplore.ieee.org/lpdocs/epic03/wrapper.htm?arnumber=1271397
[12] C. Yang, T. Nguyen, and E. Blasch, "Mobile positioning via fusion of mixed signals of opportunity," *IEEE Aerospace and Electronic Systems Magazine*, vol. 29, no. 4, pp. 34–46, 2014.
[13] R. B. Langley, "Dilution of Precision," *GPS World*, vol. 10, no. May, pp. 52–59, 1999.

Jon Goya was born in San Sebastián, Spain, in 1987. He received the M.Sc. degree in Telecommunication Engineering from TECNUN (School of Engineering of San Sebastián), Spain, in 2011. He joined the CEIT-IK4 Research Centre in San Sebasti´n in 2011, and he is currently a Researcher with the Electronic and Communication Department of CEIT. His professional research activity lies in the f eld of communication protocols, software development, positioning, Embedded Systems and Information Technology.

Leticia Zamora-Cadenas has been a research staff member at the Electronic and Communications department of CEIT-IK4 since 2008. She has also been a teaching assistant from 2010 and a lecturer from 2014 at TECNUN, the technological campus of the University of Navarra in San Sebastián, Spain. She received her B.Sc. and M.Sc. in Telecommunications Engineering from the University of Valladolid in 2005 and 2008, respectively, and her Ph.D. in Electrical and Electronics Engineering from University of Navarra in and 2014. Her research interests include localization systems for both indoor and outdoor environments, positioning algorithms and Bayesian f ltering, data fusion and signal processing for telecommunication systems. She has been involved in international and national projects related to UWB, CSS, UMTS, GSM-R and AAL technologies.

Saioa Arrizabalaga is a lecturer at TECNUN (University of Navarra), and a researcher at CEIT-IK4. She received her M.Sc. degree in Telecommunication Engineering from the Faculty of Engineering in Bilbao (University of the Basque Country) in 2003, and her Ph.D. degree in Engineering from TECNUN in 2009. Her professional research activity lies in the f eld of Embedded Systems and Information Technologies: communication protocols, QoS, Cloud-computing, Positioning. She has been involved (or is currently involved) in the participation in 12 research projects, direction of 5 doctoral theses, 15 scientif c and technical publications in national and international journals and conferences and is the author of the book "Multi-Service QoS Architecture for a Multi-Dwelling Gateway".

Gorka de Miguel was born in San Sebastián, Spain in 1991. He received the M.Sc. degree in Telecommunications Engineering from TECNUN (School of Engineering of San Sebastián), Spain, in 2015. He joined the CEIT-IK4 Research Centre in San Sebastián in 2015, and he is currently a Researcher Assistant with the Electronics and Communications Department. His research activity lies in the f eld of positioning and software development.

Iñigo Adin is a researcher at CEIT-IK4 since 2003 and associated professor at the University of Navarra since 2005. He received his M.Sc. Degree in Electronics Engineering in 2003 and his Ph.D. in 2007 from the University of Navarra. He carried out his masters thesis in the Fraunhofer Institut of Erlangen. From 2003 to 2007 he worked towards his PhD focused on CMOS RF front-ends for multi- standard wireless applications in the 5GHz U-NII band. Among other projects in the f eld of RFICs and ESD protection, he has been involved in design and verif cation of a safety critical receiver for an ERTMS BTM for high speed trains. His research interest include safety critical designs, with special interest in electromagnetic compatibility and transport interoperability. He is author, or co-author, of one patent, 2 technical book, an invited chapter and 19 articles in journals and international conferences. He was the coordinator of the FP7 European Project TREND (www.trend-eu.org) : Test of Rolling stock ElectromagNetic compatibility for cross-Domain interoperability contract number 285259.

Jaizki Mendizabal was born in Zarautz, Spain. He received his M.Sc. and Ph.D. degrees in Electrical Engineering from TECNUN (University of Navarra, San Sebastián, Spain) in 2000 and 2006 respectively. He joined Fraunhofer Institut fr Integrierte Schaltungen, Erlangen (Germany) and SANYO Electric Ltd, in Gifu (Japan) as RF-IC designer. Nowadays, he is at CEIT-IK4, in San Sebastián (Spain) where his research interests include communications and signalling systems for the railway industry. He is lecturing "Communications Electronics" and "Communications via Radio" at TECNUN (University of Navarra).

Usability of cost-effective WLAN-based indoor location system for 2.4 and 5 GHz bands

Adam Zając, Łukasz Chruszczyk, Damian Grzechca

Abstract— This paper presents comparison of personal indoor location system using 2.4 and 5 GHz bands. There are compared statistical metrics, such as mean error and variation. The location system uses widely available WLAN components. Method of location is based in Received Signal Strength Indication (RSSI) returned by most of RF ICs (including WLAN). The main focus is research of how much accuracy (and usefulness) can be expected from used standard WLAN hardware. Static and dynamic scenarios have been tested.

Keywords— indoor location, personal location, wireless LAN, RSSI measurement.

I. Introduction

NAVIGATION is one of the most important technical issue of all times- starting with first lighthouse in 400BC, towards improving maritime navigation systems in Middle Ages ending with GPS in the 1970s. The last mentioned system is constantly developing and it is used by many different applications, working in different environments.

most popular currently available and used global satellite navigation systems are GPS, Glonass, Galileo and Beidou. These systems are free and accurate. Progress in electronics made them affordable and truly portable: small, light and less power-hungry devices. Unfortunately, this progress is not enough yet to overcome main limitations of currently available receivers: noise figure. Thus, all nowadays satellite navigation can be used only in outdoor environment. On the other hand, there are still missing effective alternatives for indoor use. Although there has been proposed a variety of location methods, based on various physical phenomena (e.g. video, ultrasound, MEMS dynamics, UWB pulses), none of them is dominating. The main reasons are: cost of infrastructure, cost of data processing, low accuracy. Therefore it is currently impossible to use signals from satellites in order to set an indoor localization system which would work in environments such as mines, metro stations or airports.

The infrastructure used in prototype indoor systems is existing WLAN infrastructure – since it is a cost effective approach and because using 802.11 signals does not interfere the normal work of the hardware. There are many ways of gathering data from Wi-Fi access points (APs). Mentioned approaches are based on analysis of the following signal parameters [1]:

- Time of Arrival (TOA),
- Time Difference of Arrival (TDOA),
- Angle of Arrival (AOA),
- Received Signal Strength Indication (RSS).

Data gathered using one these methods can be applied in selected algorithms to:

- compute distance between user and network access points of known coordinates,
- compare gathered data with previously prepared map of signal parameters for the location, where system is running (*fingerprinting*).

System which is a subject of this paper uses RSSI values to compute distances between user and corresponding Wi-Fi access points. It must be noted that RSSI is not a Received Signal Power Indication (RSPI) – a true received signal power measurement. Such systems are much more expensive and impractical in scope of consumer electronics. The RSSI is assumed to be time-invariable function of a RSPI, defined (with some accuracy) by manufacturer of a RF IC. It is further altered by receiving path (antenna, PCB transmission line, impedance mismatch etc.). However, it is assumed that the total relation between RSSI and a received signal is similar and constant for all used devices.

Main difficulties, that have influence on system accuracy are:

- reflection, diffraction and dissipation of electromagnetic waves,
- presence of interfering signals in the environment.

Solving those problems, for example with complex algorithms, will certainly improve the system accuracy.

One of main objectives of this paper is to compare the system accuracy in two available 802.11 frequency bands: 2.4 GHz and 5 GHz. Comparison is based on system tests in two environments: indoor and outdoor.

The tests included both static (motionless user) and

This work was supported by the Ministry of Science and Higher Education funding for statutory activities of young researchers (decision no. 8686/E-367/M/2015 of 12 March 2015).

Adam Zając is during MSc study at Faculty of Automatic Control, Electronics and Computer Science of the Silesian University of Technology, Gliwice, Poland (e-mail: adam.zajac@ymail.com).

Łukasz Chruszczyk is with the Faculty of Automatic Control, Electronics and Computer Science, Silesian University of Technology, Gliwice, Poland (e-mail: lch@polsl.pl).

Damian E. Grzechca is with the Automatic Control, Electronics and Computer Science, Silesian University of Technology, Gliwice, Poland (e-mail: Damian.Grzechca@polsl.pl).

ISBN: 978-1-61804-321-4

dynamic scenarios (user in motion). In both cases, APs of known position (infrastructure) are transmitters and send their *beacons*. Client performs self-location using RSSI of received signals. Such approach enables non-colliding cooperation of WLAN network and location system. Additionally, no software and hardware modification of the infrastructure is required.

II. Mathematical models

A. Theory of Electromagnetic Wave Propagation

First problem concerned the way of modeling electromagnetic wave dissipation with the distance. In an ideal situation, assuming the wave is propagating in free space, to compute received power P_R could be used *Friis equation* [2, 3]. However for practical reasons, other approach is used, as suggested in [4].

B. RSSI Log Model

$$RSSI\ [dBm] = RSSI(d_0) - 10n_p log_{10}\left(\frac{d}{d_0}\right) \tag{1}$$

where:

- d_0 – reference distance of 1 m,
- $RSSI(d_0)$ – RSSI indication at reference distance [dBm]
- n_p – attenuation factor

The log model has been used for 2.4 GHz frequency band. Other models can be found in [1, 5-7].

After experiments with the system, other equation has been proposed for the 5 GHz frequency band:

$$RSSI\ [dBm] = RSSI(d_0) - 10n_p log_{10}\left(\frac{d}{d_0}\right) - \delta^2 \tag{2}$$

where:

- δ^2 – variances of previously gathered RSSI in 5 GHz band,

and other symbols have the same meaning as in (1). This original modification, based on [4-7], significantly improved location accuracy. Details are presented in corresponding sections of this paper.

It appears that the motionless user can achieve the biggest advantage. It can be used in order to compute starting position in a well-developed system, i.e. system using fingerprinting. Unfortunately, this approach has not been useful for 2.4 GHz frequency band, because of <u>very high dynamics of the read RSSI values</u>. One of the reasons could be interfering signals in commonly used 2.4 GHz band.

Another way to improve accuracy has been increasing the attenuation factor n_p, if the computed distance has been to long regarding to known geometry of the room. This has been used for both bands.

C. Trilateration

After computing the distance *d* between the receiver and all *n* access points, with known coordinates x_i and y_i, the next step is to compute the position of the receiver. Starting point to compute it is (1):

$$\begin{cases} d_1 = \sqrt{(x-x_1)^2 + (y-y_1)^2} \\ d_2 = \sqrt{(x-x_2)^2 + (y-y_2)^2} \\ \dots \\ d_i = \sqrt{(x-x_i)^2 + (y-y_i)^2} \\ \dots \\ d_n = \sqrt{(x-x_n)^2 + (y-y_n)^2} \end{cases} \tag{3}$$

Then, after simple mathematical operations:

$$2x(x_n - x_i) + 2y(y_n - y_i) = d_i^2 - d_n^2 - x_i^2 - y_i^2 + x_n^2 + y_n^2 \tag{4}$$

Because this is a linear equation, it is possible to use its matrix form:

$$Ax_{user} = B \tag{5}$$

where:

$$A = \begin{bmatrix} 2(x_n - x_1) & 2(y_n - y_1) \\ 2(x_n - x_2) & 2(y_n - y_2) \\ \dots & \dots \\ 2(x_n - x_{n-1}) & 2(y_n - y_{n-1}) \end{bmatrix} \tag{6}$$

and:

$$B = \begin{bmatrix} d_1^2 - d_n^2 - x_1^2 - y_1^2 + x_n^2 + y_n^2 \\ d_2^2 - d_n^2 - x_2^2 - y_2^2 + x_n^2 + y_n^2 \\ \dots \\ d_{n-1}^2 - d_n^2 - x_{n-1}^2 - y_{n-1}^2 + x_n^2 + y_n^2 \end{bmatrix} \tag{7}$$

$$x_{user} = \begin{bmatrix} x \\ y \end{bmatrix} \tag{8}$$

III. Localisation system setup

Main criteria for choosing WLAN infrastructure is its low cost. The chosen hardware is commonly used TL-WDR3500 produced by TP-Link, because even though the hardware price is low, it supports both 2.4 GHz and 5 GHz frequency bands independently.

System used 7 routers as access points and 1 router as users' receiver. The receiver used *iwlist*, that is part of *wireless tools* library for Linux, to gather RSSI values.

It was therefore important for client hardware to allow installing GNU/Linux distribution for WLAN devices: OpenWRT.

The research aimed at proving that the usage of WLAN infrastructure (working as a part of location system) would not interfere with normal operation of used devices. The abovementioned TP-Link routers fulfilled the above criteria.

IV. Static Test

Tests with motionless user were taken in both outdoor and indoor environments and in two previously mentioned frequency bands.

The tests' purpose was to check the accuracy of the system, thus the computed position was subtracted by actual position in order to get an absolute error.

Probability density estimation was conducted on the values of absolute errors which were obtained by 50 measurements taken in each point.

Most important properties such as minimal, maximal and mean value are gathered in tables. Highlighted values differ noticeably. In order to increase readability of the figures, the error value is divided into error value along X axis and error value along Y axis.

A. *Outdoor Environment: introduction*

Access points in the outdoor space had a clean line of sight communication, but the area was surrounded by small amount of trees. It was located between faculty building and a car park. The APs have been places 130 cm above the ground level. The outdoor environment map is shown in the fig. 1.

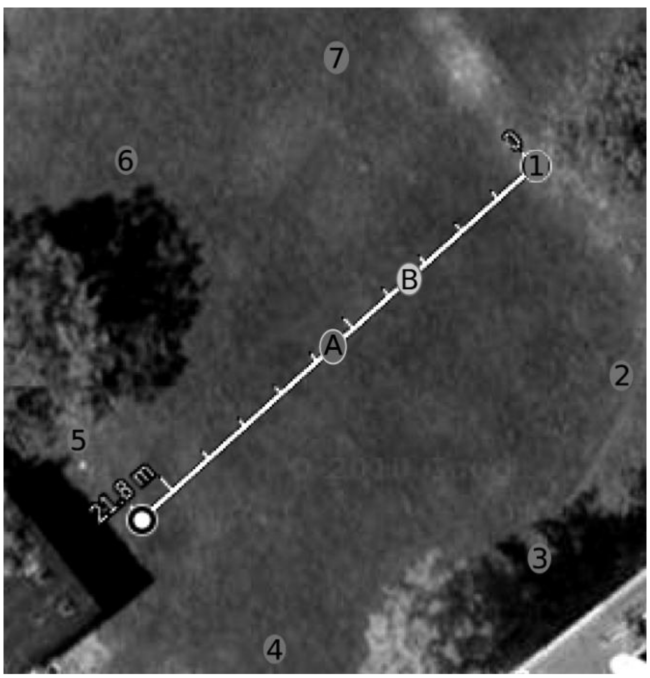

Fig. 1. Outdoor area map.

Raw positions of access points are shown in table 1.

Table 1. AP positions.

AP	1	2	3	4	5	6	7
X[m]	0	2.75	8.9	21	21.8	14.7	4
Y[m]	13.5	3.75	0	4	16	23	22.2

Two different points, A and B, have been selected for static tests, with positions in the tab. 2.

Table 2. Positions of the selected test points.

Reference position	A	B
X[m]	11.1	12.4
Y[m]	7.35	12.4

B. *Outdoor Environment: analysis*

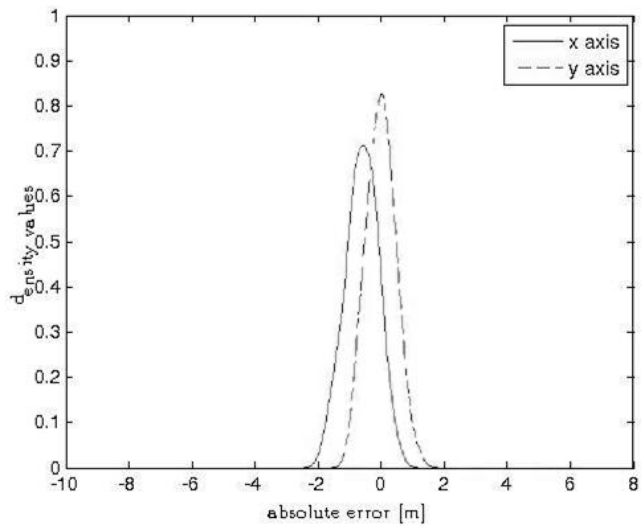

Fig. 2. Test results at point A (2.4 GHz frequency band).

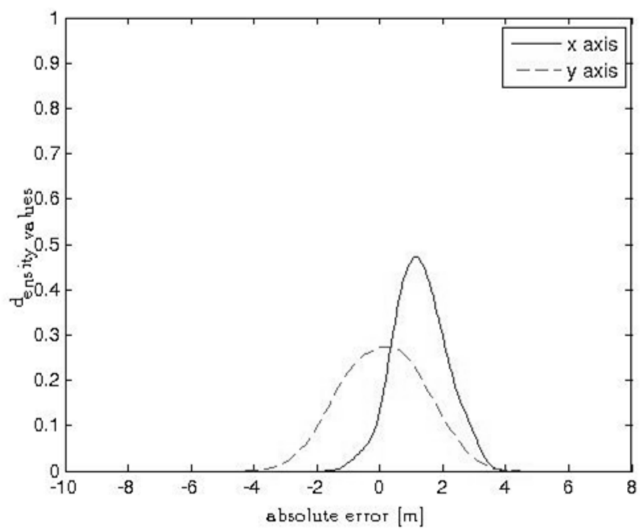

Fig. 3. Test results at point A (5 GHz frequency band).

Table 3. Comparison at point A.

Error Value [m]	Frequency band [GHz]			
	2.4		5	
	x	y	x	y
Min.	0	0	0	0
Max.	-2.2	1.6	3.8	4.2
Mean	0.5	0	1	0.3

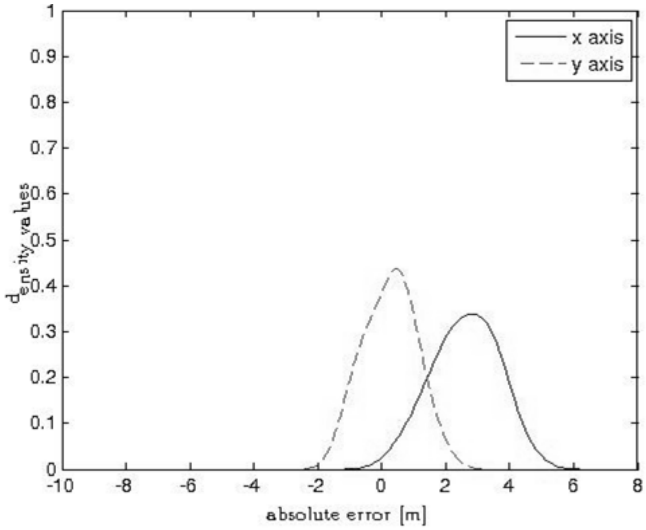

Fig. 4. Test results at point B (2.4 GHz frequency band).

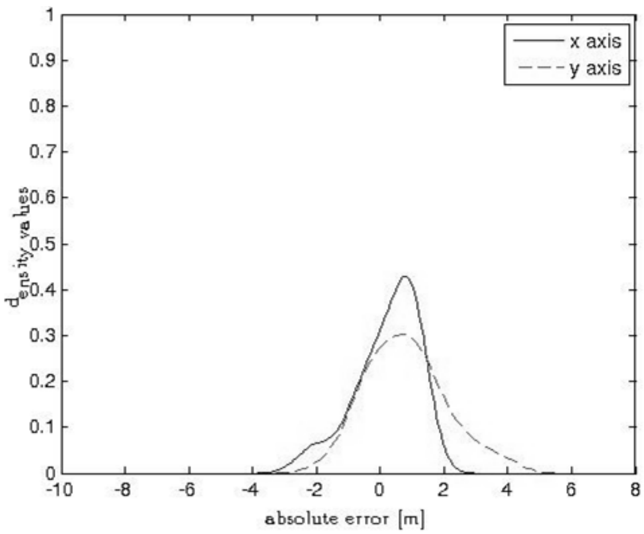

Fig. 5. Test results at point B (5 GHz frequency band).

Table 4. Comparison at point B.

Error Value [m]:	Frequency band [GHz]			
	2.4		5	
	x	y	x	y
Min.	0	0	0	0
Max.	5.6	1.6	-3.5	5
Mean	**3**	0	**0.8**	0.9

C. *Indoor Environment: introduction*

A laboratory room elongated shape (15 m *x* 4.8 m) inside the faculty building served as the indoor location area. Access points had no clean line of sight and large amount of obstacles in the area were significant difficulties for the system. However, it was possible to obtain useful location data. The indoor environment is shown in the fig. 6.

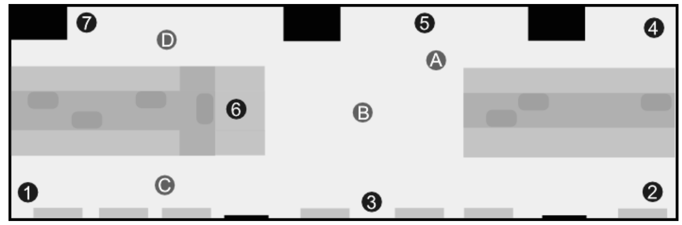

Fig. 6. Indoor environment map.

D. *Indoor Environment: analysis*

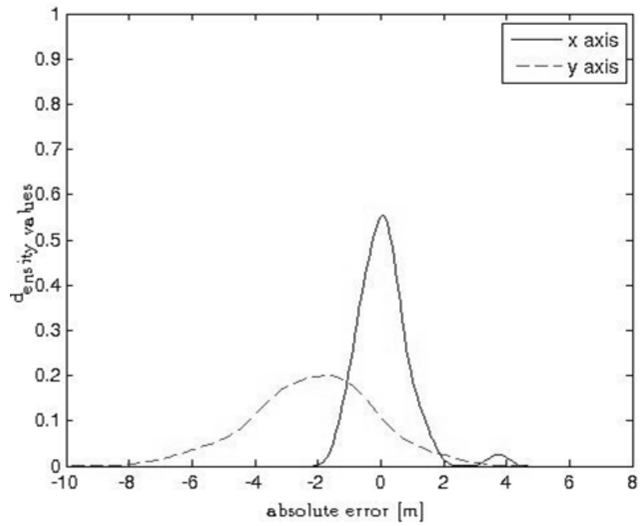

Fig. 7. Test results at point A (2.4 GHz frequency band).

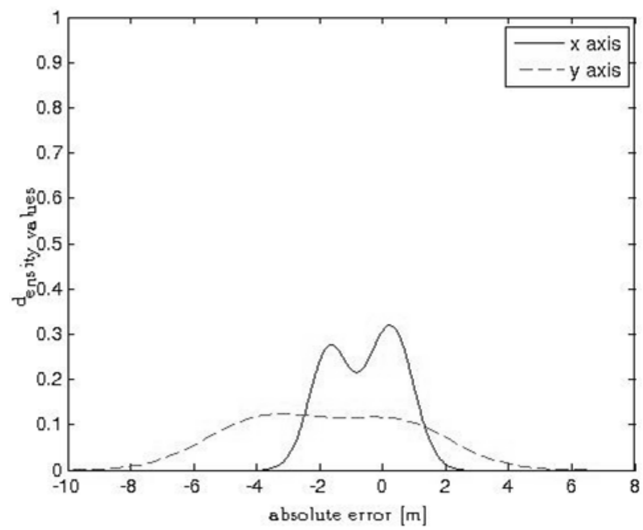

Fig. 8. Test results at point A (5 GHz frequency band).

Table 5. Comparison at point A.

Error Value [m]:	Frequency band [GHz]			
	2.4		5	
	x	y	x	y
Min.	0	0	0	0
Max.	4	-8	-3.5	-8
Mean	0	-2	-1	0.9

ISBN: 978-1-61804-321-4

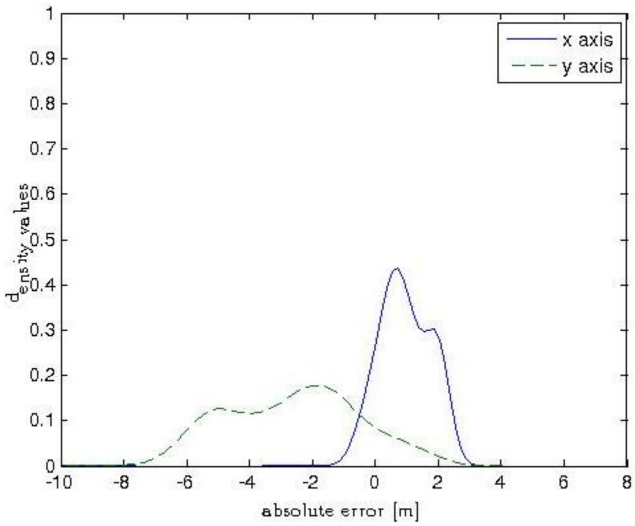

Fig. 9. Test results at point B (2.4 GHz frequency band).

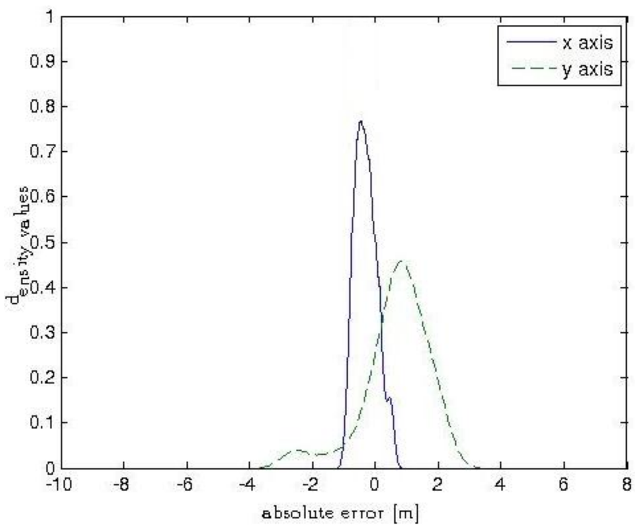

Fig. 10. Test results at point B (5 GHz frequency band).

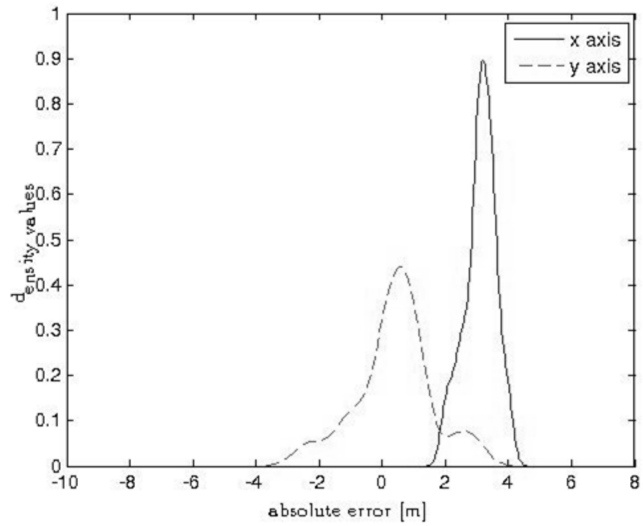

Fig. 11. Test results at point C (2.4 GHz frequency band).

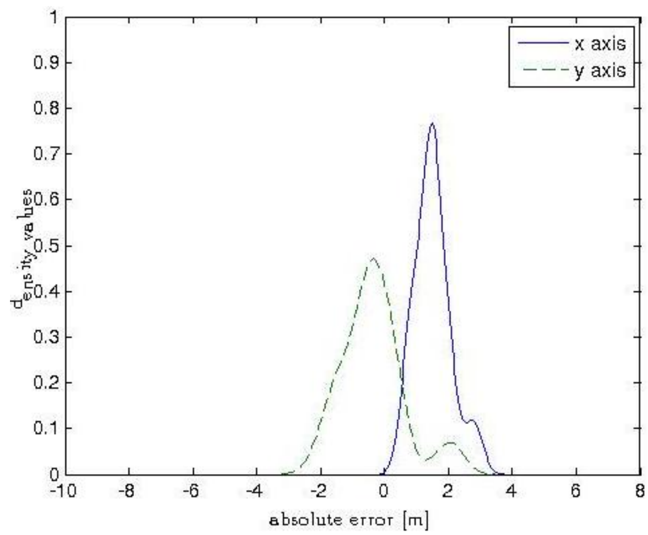

Fig. 12. Test results at point C (5 GHz frequency band).

Table 6. Comparison at point B.

Error Value [m]:	Frequency band [GHz]			
	2.4		5	
	x	y	x	y
Min.	0	0	0	0
Max.	**3**	**-7**	**-1.2**	**3.7**
Mean	1	**-3**	-0.8	**1**

Table 7. Comparison at point C.

Error Value [m]:	Frequency band [GHz]			
	2.4		5	
	x	y	x	y
Min.	1.8	0	0	0
Max.	4.3	4	3.8	3.8
Mean	**3.7**	0.5	**1.5**	0.4

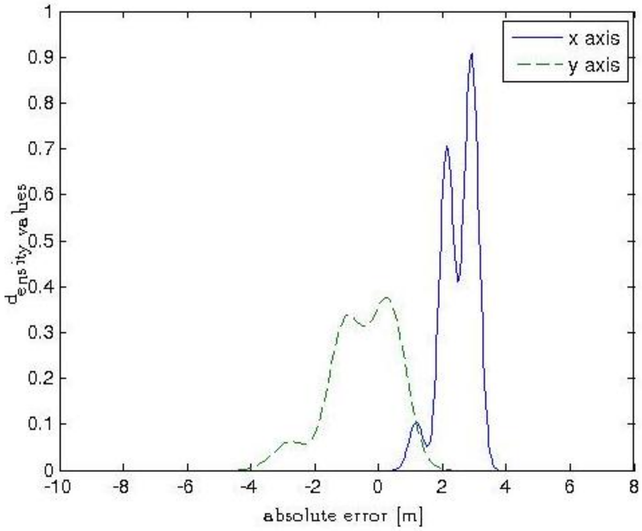

Fig. 13. Test results at point D (2.4 GHz frequency band).

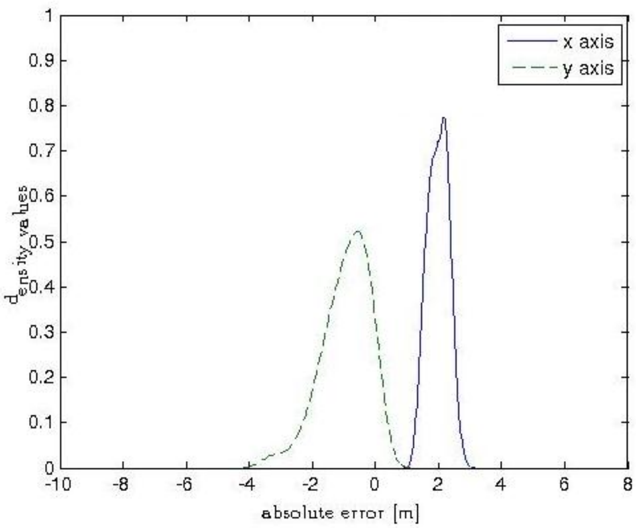

Fig. 14. Test results at point D (5 GHz frequency band).

Table 8. Comparison at point D.

Error Value [m]:	Frequency band [GHz]			
	2.4		5	
	x	y	x	y
Min.	0.3	0	1	0
Max.	4	-4	3	-4
Mean	0.2	2.3	2	1

E. Indoor Environment: human interaction analysis

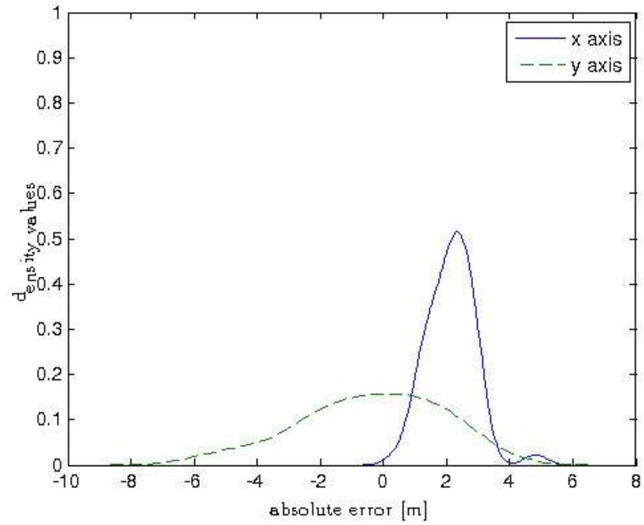

Fig. 15. Human standing near the receiver at point B (2.4 GHz).

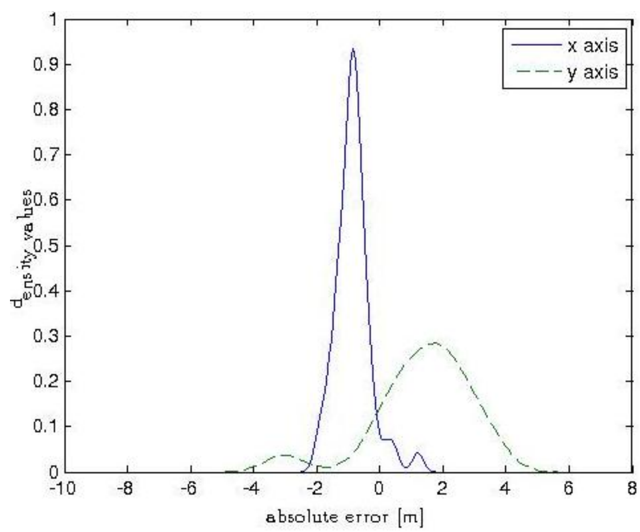

Fig. 16. Human standing near the receiver at point B (5 GHz).

Table 8. Comparison at point B with human standing nearby.

Error Value [m]:	Frequency band [GHz]			
	2.4		5	
	x	y	x	y
Min.	0	0	0	0
Max.	**6**	**-8**	**-2.3**	**5**
Mean	2.3	0	1	1.8

The plots representing test results with human interaction are wider and shorter, which means system less frequently pointed at mean value.

An outcome of this test is that 5 GHz band works better as a medium allowing more accurate localization in this project. It had less serious minimal, maximal and mean errors.

V. Dynamic Test

Tests with user in motion were taken in both outdoor and indoor environments and in two previously mentioned frequency bands. The tests' purpose was to check the path tracking ability of the system.

Plots present test environment, computed points and *zones of correctness*. Whole area was divided to three zones, which means points in that zone are:

- correctly computed,
- threshold values,
- incorrectly computed.

A. Outdoor Environment

Test was run the same environment which was introduced in chapter IV. User moved between two points:

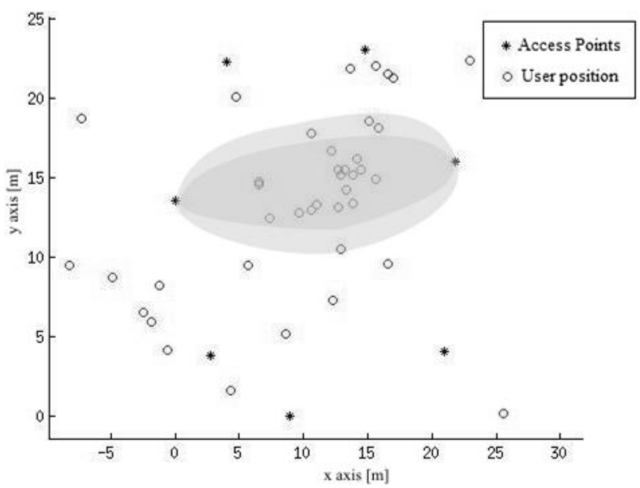

Fig. 17. Test results in 2.4 GHz frequency band.

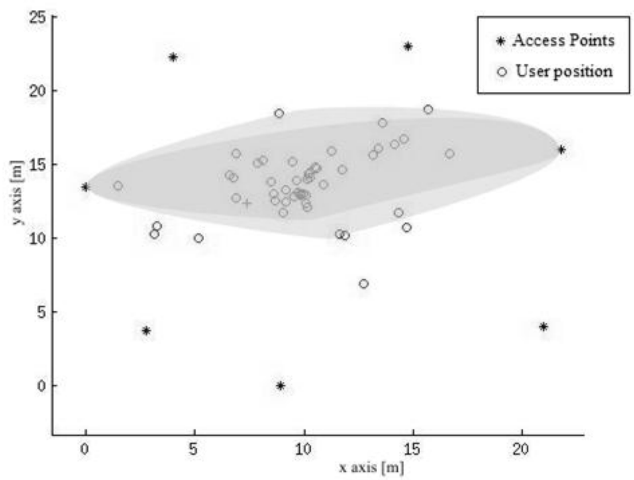

Fig. 18. Test results in 5 GHz frequency band.

Table 9. Comparison of 2.4 GHz and 5 GHz in path tracking ability.

Frequency band	Correct	Threshold	Incorrect
2.4GHz	17	4	29
5GHz	40	5	5

B. Indoor Environment

Test was run with the same conditions as in outdoor environment. The indoor environment was the laboratory introduced in chapter IV.

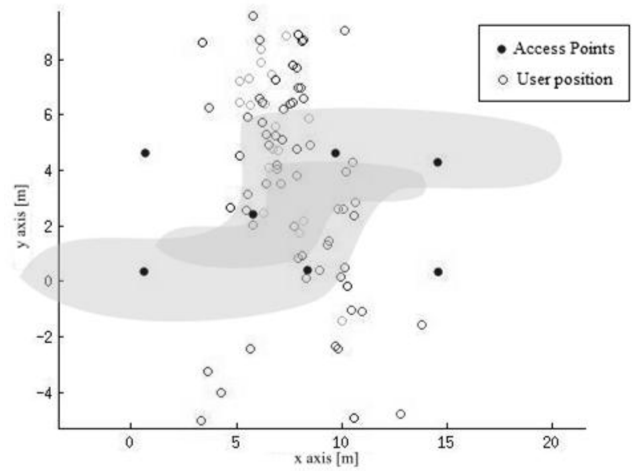

Fig. 19. Test results in 2.4 GHz frequency band.

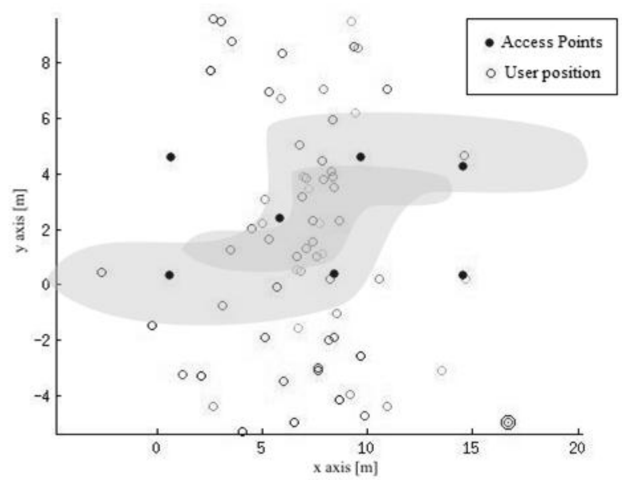

Fig. 20. Test results in 5 GHz frequency band.

Table 10. Comparison of 2.4 GHz and 5 GHz in path tracking ability.

Frequency band	Correct	Threshold	Incorrect
2.4GHz	15	25	60
5GHz	20	13	37

Results of this test show that 5 GHz frequency band has an advantage over 2.4 GHz frequency band - more points were added to first (correct) zone in both indoor and outdoor environment.

ISBN: 978-1-61804-321-4

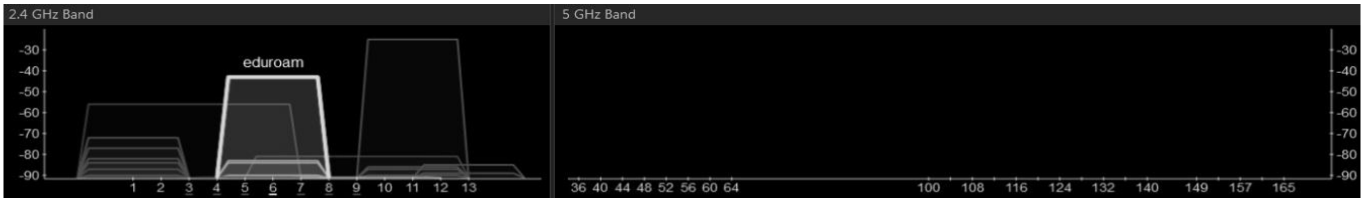

Fig. 21. Interfering signals in indoor environment.

Fig. 22. Interfering signals in outdoor environment.

VI. Conclusions

The tests in outdoor environment showed that the problems with the system are not only connected with signal reflection (from obstacles, walls) that is transmitted by access points.

The problem is also connected with other signals in the frequency band, because the 2.4 GHz band is a more crowded frequency band it may be worse for localization purposes. Fig. 21 and 22 shows how the other signal interfere on signals used in localization system:

The dynamics of the change of power level and imperfect mathematical models are the major problem.

The indoor environment tests showed that using the equations obtained only from the power received will not allow for very exact localization system.

A method based on RSSI measurements can support the adjustment of the data gathered on previously prepared map of signal parameters for the location where the system is running. This method together with fingerprinting method might improve the results. Another way to improve the system is using complex algorithms for minimizing the mean error.

References

[1] Zhonghua Li, Zijing Zhou, Chunhui He and Xiao Huang "Advances in RFID-ILA: The Past, Present and Future of RFID-based Indoor Location Algorithms", 24th Chinese Control and Decision Conference (CCDC), Taiyuan, 2012, pp. 3830 – 3835

[2] Bernard Sklar, "Digital Communications: Fundamentals & Applications", Second Edition, 2005, ISBN0-13-084788-7

[3] H.T.Friis,Proc. IRE, vol. 34, 1946, pp. 254

[4] Chang-Beom Lim, Sung-Hun Kang, Hyun-Hun Cho, Sin-Woo Park, Joon-Goo Park, "An Enhanced Indoor Localization Algorithm Based on IEEE 802.11 WLAN Using RSSI and Multiple Parameters", Fifth International Conference on Systems and Networks Communications, Nice, 2010, pp. 238 – 242

[5] Ndeye Amy Dieng, Maurice Charbit, Claude Chaudet, Laurent Toutain, Tayeb Ben Meriem, "A Multi-Path Data Exclusion Model for RSSI-based Indoor Localization", 15th International Symposium on Wireless Personal Multimedia Communications (WPMC), Taipei, 2012, pp.336 – 340

[6] Long Cheng, Cheng-Dong Wu ,Yun-Zhou Zhang, "Indoor Robot Localization Based on Wireless Sensor Networks", IEEE Transactions on Consumer Electronics, 2011, pp. 1099 – 1104.

[7] Raida Al Alawi, "RSSI Based Location Estimation in Wireless Sensors Networks", 17th IEEE International Conference on Networks (ICON2011), Singapore, 2011, s.118 – 122

[8] Chia-Yen Shih, Pedro Jose Marron, "COLA: Complexity-Reduced Trilateration Approach for 3D Localization in Wireless Sensor Networks", Fourth International Conference on Sensor Technologies and Applications, Venice, 2010, pp. 24 – 32.

Adam Zając received BSc from Institute of Electronics, Silesian University of Technology, Gliwice, Poland in 2015. Currently, he is during master's studies continuing his Bachelor's Thesis. His main area of interest is positioning of indoor and outdoor objects, signal processing and Internet of Things. He is gaining work experience in Polish IT Company ComArch.

Lukas Chruszczyk (M'15) received MSc and PhD from the Institute of Electronics, Silesian University of Technology, Gliwice, Poland in 2004 and 2009, respectively. His main areas of interest and research are evolutionary optimization methods and fault diagnosis of analog and mixed-signal electronic circuits. He gained industrial experience in FIAT R&D Centre, Turin, Italy (2006-2007). His current research also concerns Power-Line Communication (PLC) and indoor-location techniques and applications.

Damian E. Grzechca (M'05-SM'11) received MSc, PhD and DSc. from the Institute of Electronics, Silesian University of Technology, Gliwice, Poland in 1998, 2003 and 2013, respectively. His current research concerns data fusion and artificial intelligence methods for localization and positioning of indoor and outdoor objects, fault detection and localization in analog and mixed-signal electronic circuits. He cooperates with industry in the field of test solutions (Delphi Corp.), functional safety (Bombardier Corp.), and security systems (Katowice airport). He has been a visiting researcher at the Bournemouth University, UK and at TIMA laboratory in Grenoble, France.

Comparison of two different approaches to a construction of 24 / 12 V voltage converter

Martin Pospisilik, Milan Adamek, and Rui Miguel Soares Silva

Abstract**—** For a longer time, the voltage converters have been one of common devices to be found inside several electronic appliances. To simplify their design, the manufacturers of electronic devices created a countless number of custom integrated circuits, using different approaches and philosophies. Currently, the market of electronic components provides a great variety of different drivers that can simply be used as step-up, step-down and/or voltage inverting converters, depending on several changes in the topology of the circuit on the basis of the device manufacturer's proposal. Paradoxically, this can complicate the designer's work as he is forced to find the cheapest solution for his project, but the different drivers, delivering similar parameters according to their datasheets, can behave in different way, especially when integrated as a part of a more complex system. Therefore this paper was created, trying to provide the insight into this problem by means of comparison of two quite common constructions of 24 to 12 V step down converters. One of them is based on the well-known, cheap and frequently used low-cost driver MC 34063, while the second one is based on the more expensive driver AP 1501 that should provide better performance. Within the paper, not only the static parameters are compared, but also the data obtained by measurement of the electromagnetic interference of the constructed circuits measured in the EMC laboratory are provided as well.

Keywords**—** Electromagnetic interference, Fixed frequency controller, Step-down converter, Self-oscillating converter

I. Introduction

ACCORDING to the width of the current offer of the market of electronic components, it can be confusing to choose the proper driver for a construction of a low-cost step-down voltage converter. There are various chips with different internal organization that were designed on the basis of different approaches. This paper brings a comparison of real results obtained with two different constructions of low-cost and low-power step-down converters. The main difference between the two constructions lies in the fact that one of the converters is operated at a constant frequency, that is given by its internal oscillator, and its regulation is provided right by means of a pulse-width modulation, while the second converter oscillates at random frequency that is given by its output load and input voltage and its regulation is provided by interrupting of its operation when the output voltage is exceeded. Surprisingly, from the view of the user, the performance of both circuits is similar in terms of their voltage stability, output power, power efficiency etc. and even more surprisingly, from the point of view of the standard EN 61000-6-3 the converter driven by the internal oscillator provides higher interference than the randomly oscillating one, despite the fact, that the power density of his interference is much lower. All these phenomena are described within the framework of this paper.

This work was supported in part by the European Regional Development Fund under the project CEBIA-Tech No. CZ.1.05/2.1.00/03.0089 and by OPVK project CZ.1.07/2.3.00/30.0035.

Martin Pospisilik is with Faculty of applied informatics, Tomas Bata University in Zlin, Nad Stranemi 4511, 76005 Zlin, Czech Republic (corresponding author, phone: +420 606 417 702; e-mail: pospisilik@fai.utb.cz)

Milan Adamek is with Faculty of applied informatics, Tomas Bata University in Zlin, Nad Stranemi 4511, 76005 Zlin, Czech Republic (corresponding author, phone: +420 606 417 702; e-mail: adamek@fai.utb.cz)

Rui Miguel Soares Silva is with Polytechnic Institute of Beja, Campus do Instituto Politécnico de Beja Rua Pedro Soares, 7800-295 Beja, Portugal (e-mail: ruisilva@acm.org)

II. Description of the Tested Converters

Both converters, the performance of whose is compared within this paper, were constructed according to the following requirements:

- input voltage: 20 to 28 V,
- output voltage: 12 V,
- power efficiency: higher than 80 %,
- output power: at least 20 W.

The description of their philosophy, construction and operation is described in the text below.

A. Randomly Oscillating Converter with MC 34063

This converter is based on the well-known low-cost driver MC 34063 [4], the internal construction of which is based on a modified traditional 555 timer. The circuit diagram of this converter is depicted in Fig. 1. The input voltage is connected to the clamps X1 while the output voltage is connected to the clamps X2.

Because the peak switching current of the internal switch of the driver is limited to 1.5 A, external switching transistor Q2 is employed, being driven by an inverter based on the transistor Q1. The circuit operates as follows:

1. When the power is delivered to the circuit, the switching transistor Q2 is opened and the current through the inductor L1 rises in time. The rate of the rise is given by the inductance of the inductor.
2. Once the current flowing through the inductor L1 reaches the limit set by the value of the resistor R1 (the voltage drop at the resistor exceeded 0.3 V), the switching

ISBN: 978-1-61804-321-4

transistor is closed. Now the current flowing through L1 continues to flow through the load and the diode D1. However, as the energy delivery is stopped, the current decreases in time.

3. The circuit waits for a period given by the capacitor C2. Once the off time expires, the transistor Q2 is opened again and new cycle of the circuit begins.
4. Provided the output voltage exceeded the limit given by the internal reference V_SEN (connected via a voltage divider based on the resistors R6 and R7 to the output of the converter), the transistor Q2 is switched off before the input current reaches the limit set by R1.

From the above described principle of operation of the circuit the following conclusions can be made:

1. The operating frequency of the circuit varies in time according to the output current and input voltage of the circuit.
2. The regulation is provided by means of the pulse width modulation. The time of the "off" state is fixed, being given by the capacitor C2, while the time of the "on" state is variable.
3. The spectrum of the interferences generated by this circuit should theoretically be continuous, whilst the distribution of energy within this spectrum is unpredictable.

The price of the circuit can be very low, because no specialized components are used. Therefore it is expected to provide rather poor performance.

More detailed description of this circuit can be found in [6].

B. Advanced Converter with Fixed Operating Frequency Based on AP1501A

This converter was built on the basis of a custom integrated circuit AP1501A with respect to the manufacturer's notes provided within the datasheet of the circuit [5].mThe circuit diagram of this converter is depicted in Fig. 2.

The circuit is supplied from the output of the backup unit by means of X1 clamps. Its operation can be externally hibernated by LVTTL voltage connected to SL1 connector.

The detailed description of AP1501A-12 can be found in [6]. The switching transistor is integrated on the chip. The manufacturer claims that the operating frequency of this integrated circuit is 150 ±25 kHz and the minimum achievable output current is 2 A. The inductance of L1 inductor is calculated in that way so the circuit operated in a continuous mode with a minimum output current of 0.1 A and maximum input voltage of 28 V. With a series resistance of 0.1 Ω maximum, the expected power dissipation is lower than 0.4 W. The saturation voltage of the switching transistor is approximately 1.7 V, so a power dissipation of approximately 3.5 W can be expected at the output current of 2 A. The expected total efficiency is 80 % at the output current of 2 A.

The circuit is equipped with the output current monitor based on the operating amplifier IC1. The values of the devices are calculated so the conversion ratio was approximately 2.2 V/A and the cut-off frequency was as low as 100 Hz (only DC component is measured). For the purposes of measurements described in this paper, the current sensing circuit is unnecessary as well as the possibility to hibernate the converter by means of connecting TTL voltage to the input HIBERNATE.

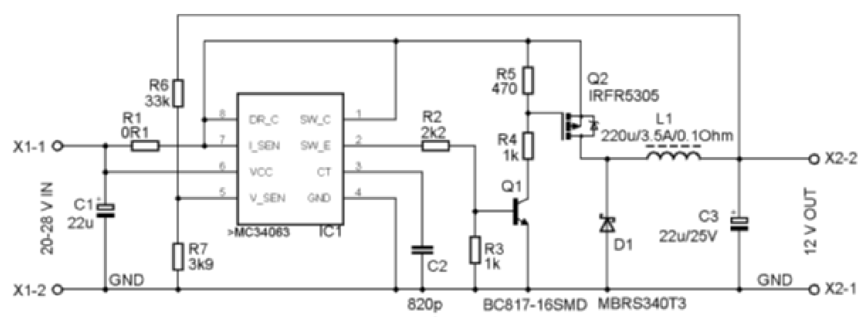

Fig. 1 circuit diagram of a voltage converter based on MC 34063

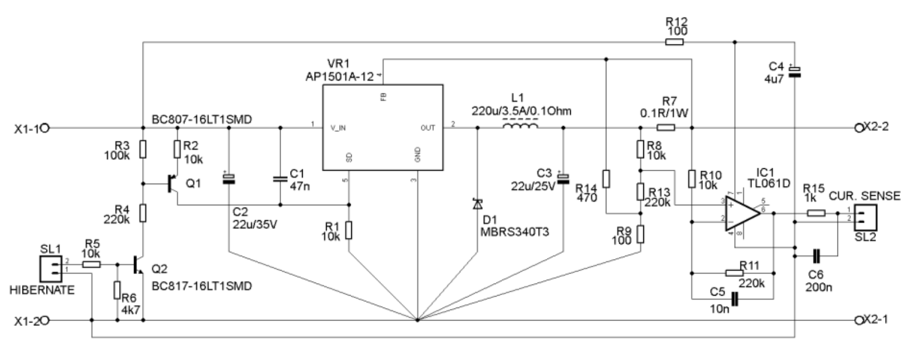

Fig. 2 circuit diagram of a voltage converter based on MC 34063

ISBN: 978-1-61804-321-4

As described in the text above, this circuit runs at a fixed frequency, using a pulse width modulation to regulate its output power according to the output load and the input voltage. In comparison with the randomly oscillating converter it was supposed to achieve better performance.

For the purposes of testing the current sensing resistor R7 was replaced by a wire in order to discard the current sensing circuit and to make the circuit comparable to that one based on MC 34063A.

III. Measurements and Results

Both circuits were constructed as functional samples and tested for achieving of the required parameters. Consequently a set of tests were made in order to gain data on the basis of which the two different converters could have been compared one with the other. For the purposes of testing of the electromagnetic compatibility of the created samples, the standard EN 61000-6-3 has been chosen, since the target use of the circuits was not specified. The tests were as follows:

- output voltage stability versus input voltage,
- output voltage stability versus output load,
- power efficiency at different output loads and input voltages,
- maximum output power according to the cooling capability of the components,
- electromagnetic interference without a cover according to EN 61000-6-3,
- interference currents on the input cables measured by a current clamp according to EN 61000-6-3.

Whereas the DC parameters were measured as “static” ones without any transients, the measurements related to the electromagnetic compatibility were made in the frequency ranges covering the requirement of EN 61 000-6-3.

A. Measurement Configurations

The DC parameters were measured with the aid of linear stabilized laboratory power source and the programmable electronic load Array 3721A that was operated in a constant current mode. The output voltage and current was measured directly by the electronic load while the input current was measured by a laboratory multimeter GW Instek GDM-8245.

The intensity of electromagnetic interference was measured by means of a bilogarithmical antenna Teseq Bilog CBL 6112 inside a semi anechoic chamber Frankonina SAC 3 plus according to the requirements of the standard EN 61 000-6-3. As the receiver Rohde&Schwarz ESU 8 receiver and spectral analyser was used. During the measurement, both converters were loaded by the electronic load Array 3721A that sunk a current of 1 A. The potential interferences caused by the electronic load were excluded by additional measurement during which the converters were bypassed. The data obtained by the receiver were processed by means of EMC 32 software.

The interfering currents on the cables between the linear power source and the converters were measured separately on both wires by means of a current clamp FCC F-52 connected to the receiver Rohde & Schwarz ESU 8. The data obtained by the receiver were processed by means of EMC 32 software and afterwards in MS Excel. During the measurement the converters were also loaded with the electronic load Array 3721A in order to achieve the required load current.

B. Obtained Results

Under the conditions described in the subchapter above, a large set of results was obtained. Because the space of this paper is limited, only the most interesting results are displayed in the text below.

1) Maximum achievable output power

The maximum achievable output power was in both cases limited by the heat produced by the components on the printed circuit boards after a continuous current load lasting approximately 5 minutes. This also corresponds with the efficiency of the converters that became poor at high loads. Generally, it can be said that the converters were operated in safe area until their power efficiency dropped below 70 %. The maximum achievable output power and the total power dissipation of the components mounted on the printed circuit boards of the functional samples of the converters are enlisted in the table below.

Table I Maximum achievable output power and total power dissipation of the converters

Converter	**Input voltage [V]**	**Output power [W]**	**Power dissipation [W]**
AP 1501	22	27.8	11.65
	26	33.3	12.21
MC 34063	22	20.14	8.46
	26	20.53	6.25

Based on the results enlisted in Table I, the load current was limited to 2 A in case of MC 34063 (randomly oscillating) and to 3 A in case of AP 1501 (fixed frequency). It is obvious, that the converter with MC 34063 achieved lower maximum output power. Partially this was caused by the fact, that the most dissipating component is the transistor Q2 (see Fig. 2) the case of which is less efficient in cooling as the case of AP1501A that was the most dissipating device of the other converter. More information on this topic is provided in discussion further in the text.

2) Power Efficiency

The power efficiency was calculated from the measured input power and the measured output power achieved by the converters. A comparison of power efficiency achieved by both converters at the nominal input voltage of 24 V is depicted in Fig. 3.

Dependences of the power efficiencies of the converters on the output loads and input voltages are depicted in Fig. 4 for MC 34063 and Fig. 5 for AP 1501A.

As can be seen in Fig. 3 to Fig. 5, the converter based on MC 34063A reaches a slightly worse efficiency and operates without excessive power dissipation with the output power up to 15 W. With higher output load its efficiency drops steeply.

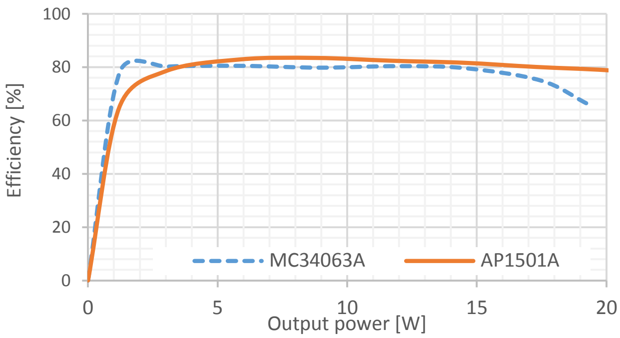

Fig. 3 comparison of power efficiency of the converters depending on their output power

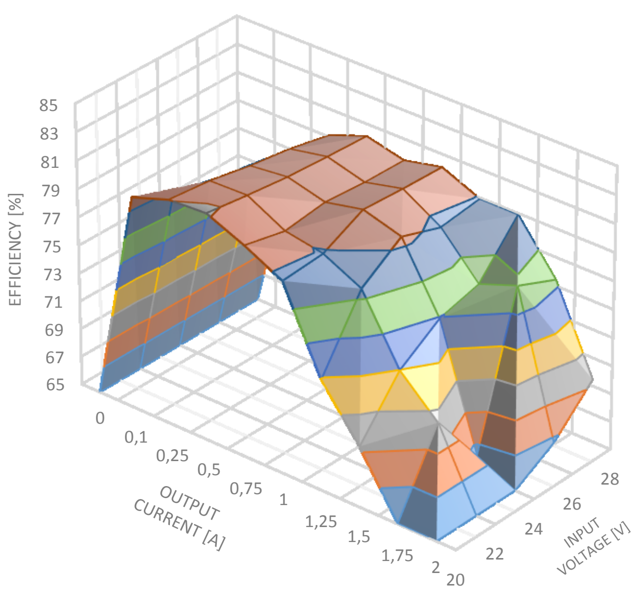

Fig. 4 dependence of power efficiency of the converter based on MC 34063 on the input voltage and the output current

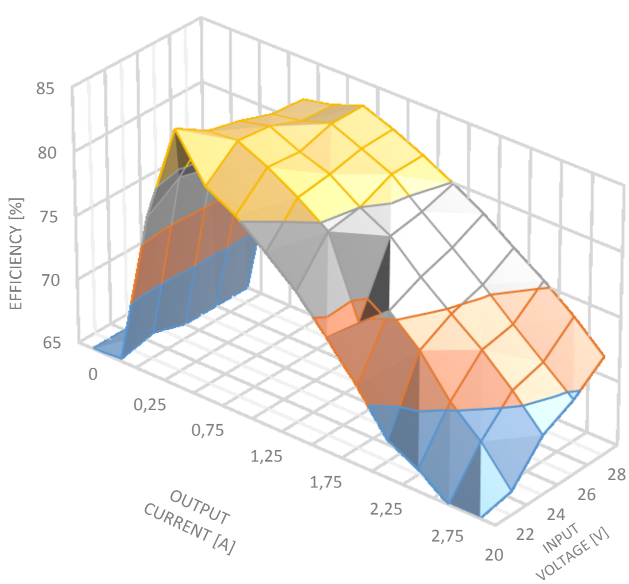

Fig. 5 dependence of power efficiency of the converter based on AP 1501A on the input voltage and the output current

On the other hand, the voltage converter based on AP 1501A reaches worse efficiency at low output powers. Its decreasing efficiency with the increasing output power is partly caused by the power sensing circuit that is connected at the output of the converter.

3) Output voltage stability

The output power stability of the converters depends on many factors as input voltage, output current, temperature, aging of devices etc. For the purposes of this test only the dependence on the input voltage and on the output current was observed.

A direct comparison of the two converters is provided in Fig. 6 and Fig. 7. Fig. 6 shows the dependence of the output voltage of both converters on their input voltage when a constant current load of 1 A is ensured. Fig. 7 shows the dependence of the output voltages of both converters when the output current is changed while the put voltage is stabilized at the nominal value of 24 V. Complex view of this parameter is provided in Fig. 8 and Fig. 9. Whereas the Fig. 8 shows the dependence of the output voltage of the converter based on MC 3406A on both, the input voltage and the output current, the Fig. 9 shows the same dependence for the converter based on AP 1501A. It is worth recommending that the output current sensing circuit that has been integrated on the converter (see Fig. 2) was bypassed by replacing the resistor R7 by a wire so no voltage drop caused by this circuit should be observed at the output of the converter.

The results show that the voltage stability of the converter based on AP 1501A is better, but both converters provide a similar performance with the load up to approximately 1.6 A (this corresponds to the output power of approximately 19 W).

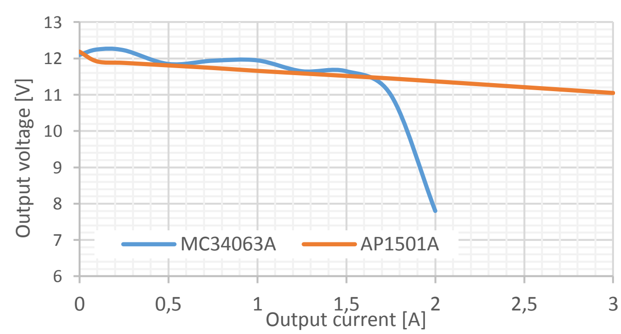

Fig. 6 output voltage dependence of both converters on the input voltage at the constant load current of 1 A

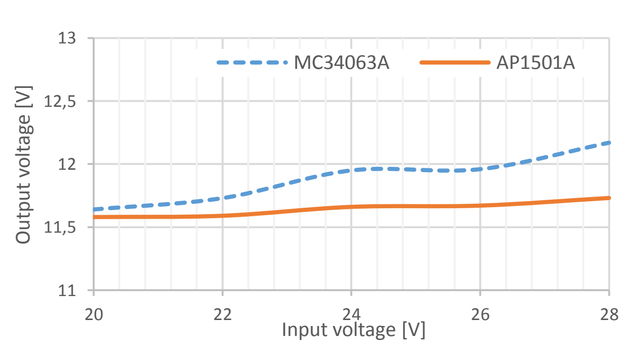

Fig. 7 output voltage dependence of both converters on the output current at the constant input voltage of 24 V

ISBN: 978-1-61804-321-4

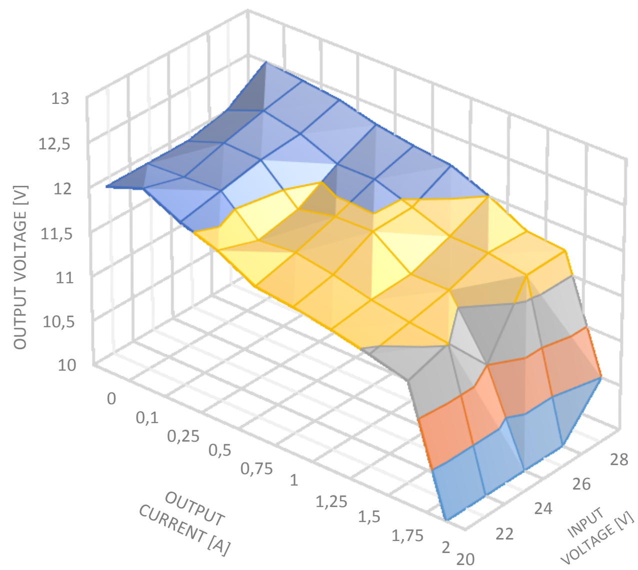

Fig. 8 output voltage dependence on the input voltage and load current – converter based on MC 34063

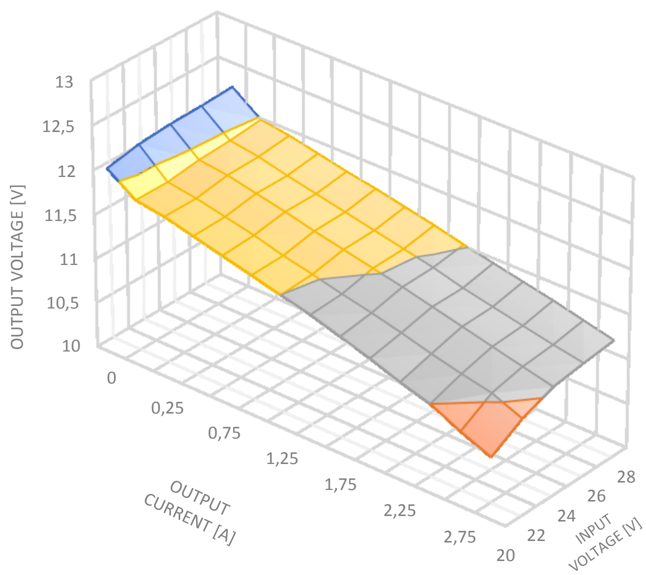

Fig. 9 output voltage dependence on the input voltage and load current – converter based on AP 1501A

4) *Electromagnetic Interferences*

The electromagnetic interferences were measured according to the requirements of the standard EN 61000-6-3. This standard requires measurement at frequencies exceeding 30 MHz. The measurement was processed in the base band from 30 MHz to 1 GHz and both converters, although not mounted in a shielding, passed the test without any problem. This is caused mainly by the fact that the converters are operated at low frequencies where radiation by means of electromagnetic field is not probable. More interesting are inductive and capacitive couplings to other circuits operating in the near field of the converters and the interference currents spread by means of the input and output cables of the converters.

5) *Interferences on the Input Wires*

According to the principle of their operation, the voltage converters create interfering current ripples at their input and output cables. Because the gained data are too complex, only the measurements on the active power supply wires are described here.

On the figures below the dependences of the measured ripple current spectrums on the output currents of the converters are depicted. Both converters were supplied with a constant input voltage of the nominal value 24 V. As described in the text above, the ripple currents were measured by a current clamp and are reported in dBμA. Maximum values (MaxPeak detector) were indicated.

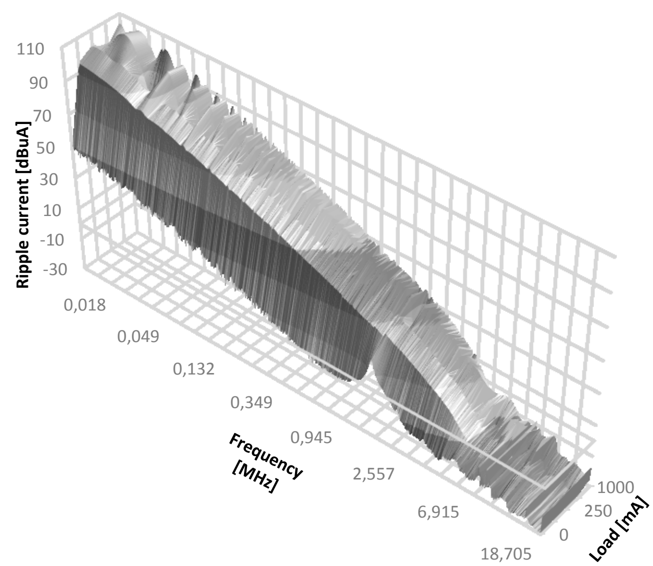

Fig. 10 ripple current spectrum on the input of the converter based on MC34063A (input voltage 24 V)

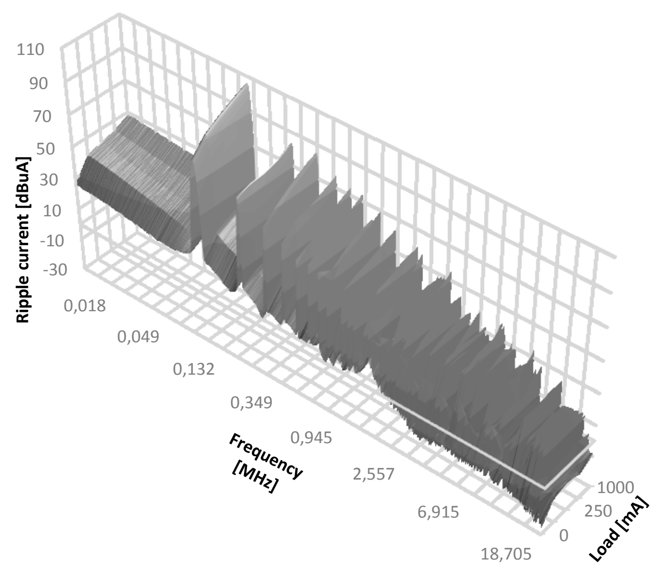

Fig. 11 ripple current spectrum on the input of the converter based on AP 1501A (input voltage 24 V)

ISBN: 978-1-61804-321-4

Based on the results depicted in Fig. 10 and Fig. 11, although the driver based on MC 34063A generates "more rich" spectrum, the maximum measured values generated by both converters are comparable. On the other hand, differences in spectral amplitude densities can be observed, as depicted in Fig. 12 and Fig. 13.

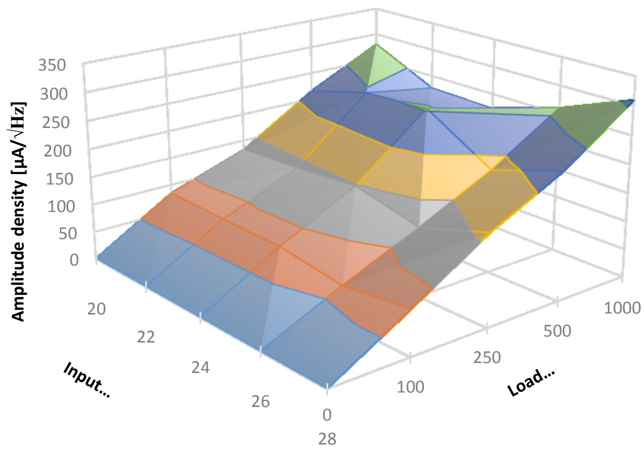

Fig. 12 spectral amplitude density of ripple currents generated by the converter based on MC 34063A

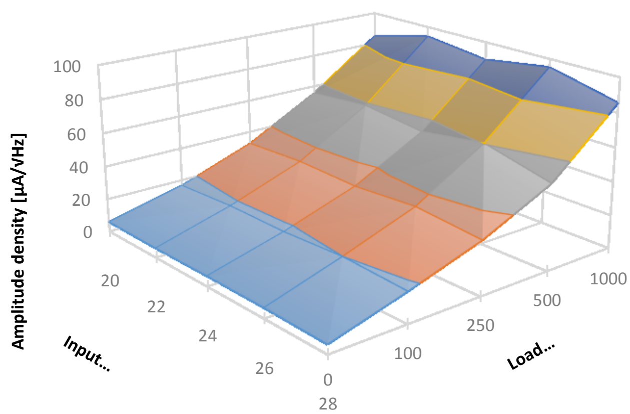

Fig. 13 spectral amplitude density of ripple currents generated by the converter based on AP 1501A

IV. Results Discussion

According to the expectations, the voltage converter based on AP 1501A has shown better performance, but there is a question whether the improvement, compared to the converter based on MC 34063, is worth the increased costs of the design of the circuit.

Concerning the electromagnetic compatibility, both converters require efficient input filters as their input interference currents greatly exceed the requirements given by the standard EN 61000-6-3. From this point of view there is no difference between them as the peak levels of the interfering currents were comparable.

Concerning the voltage stability, the output voltage of the converter based on MC 34063 was more dependent on the input voltage (scatters by 4.5 % within the range of the input voltages), but on the other hand, when the output load was changed, the performance of both circuits was comparable up to the output power of 20 W. Then, in case of MC 34063 the current limitation occurred, while the converter based on AP 1501A operated without current limiting, being secured only by the internal overheat and short-circuit protection. In this case, the performance of the circuit based on MC 34063 could be improved by improved construction of the switching transistor's driver.

V. Conclusion

This paper provides a comparison of two step-down voltage converters, both decreasing the voltage from 24 V to 12 V, but each built according to a different philosophy. One of them is a very cheap one, self-oscillating, with operating frequency dependent on its load and other factors, while the second one is based on a specialized driver that incorporates an internal oscillator as well as the switching transistor and other necessary circuits.

Unfortunately, the set of results obtained by the measurements greatly exceeds the framework of one paper, so only the most interesting results are described. Nevertheless, these results include interesting findings about voltage converters operating at low powers. The most interesting is probably the fact, that although the simple and cheap self-oscillating converter produces great interference currents on its power supply wires (the maximum spectral amplitude density was approximately 310 $\mu A/\sqrt{Hz}$ versus 85.55 $\mu A/\sqrt{Hz}$), from the point of view defined by the standard EN 61000-6-3 they both produce excessive peaks that must be eliminated by means of input filters. The measured peak values are comparable for both converters (approximately 105 dBµA for AP 1501A and 110 dBµA for MC 34063).

Further research will be focused on increasing the performance of the driver based on MC 34063 concerning the deficiencies in the power switching. Based on the results obtained by the tests described within the paper, there is a chance to tune the cheap self-oscillating converter in order to achieve performance comparable to the more complex drivers.

However, it is expectable, that the fixed-frequency converters will still be preferred in the future as the disturbing ripple voltages can be eliminated by high-order passive filters, including band-stops tuned to their operating frequency.

References

[1] J. Svacina, *Electromagnetic Compatibility [Elektromagneticka kompatibilita]*, Brno: VUT Brno, 2002.

[2] C. R. Paul, *Introduction to Electromagnetic Compatibility*, New York: John Wiley, 1992.

[3] P. A. Chatterton, M. A. Houlden, *EMC – Electromagnetic Theory to Practical Design*, New York: John Wiley, 1991.

[4] ON Semiconductor. (2010, August). MC34063 Datasheet. [online]. Available: http://www.onsemi.com/pub_link/Collateral/MC34063A-D.PDF

[5] Diodes Incorporated. (2009, January). AP1501 Datasheet. [online]. Available: http://www.diodes.com/datasheets/AP1501.pdf

[6] M. Pospisilik., T. Dulik, "Backup power source for Ethernet devices using Power over Ethernet technology", *International Journal of Circuits, Systems and Signal Processing*, Volume 8, 2014, pp 518 – 528

[7] M. Mann, B. Gutheil, J. Zastrau, P. Weiss, "Electromagnetic field measurements – Means of verification", In *Proc. of the 5th WSEAS/IASME Int. Conf. on Electric Power Systems, High Voltages, Electric Machines*, Tenerife, Spain, December 16-18, 2005, pp 591-595

ISBN: 978-1-61804-321-4

Maple algorithm for evaluation of damping quality of anechoic and semi anechoic chambers

Martin Pospisilik, Rui Miguel Soares Silva, and Milan Adamek

***Abstract*—** With the increasing interaction of various electronic devices, the issues of their electromagnetic compatibility is gaining greater precedence. The measurement of the phenomena associated with these issues are, for practical reasons, processed with the help of anechoic and semianechoic chambers. As there is a need of proper electromagnetic shielding of these chambers, their walls are made of conductive materials. Undesirable reflections occurring inside them are a natural consequence that must be eliminated by suitable absorbers. Naturally, the reflections cannot be eliminated absolutely in any case, but the aim of the constructers of such chambers is always to minimize them as well as possible. As the constructions of the chambers differ, each of them shows different resonant frequencies and standing waves displacement, although it complies with the standards for electromagnetic compatibility measurement. This phenomenon increases in its importance when the chamber is intended to be used for scientific purposes. In some cases, the knowledge of its behavior is crucial for various experiments. In this sense, the anechoic or semi anechoic chamber can be understood as a cavity resonator equipped with massive damping. The authors of this paper developed an algorithm that, based on the frequency responses of the chamber measured at different places inside its space, evaluate the quality of the damping in the form of the detection of the resonant peaks that occur inside the chamber. These peaks can be described with the following parameters: frequency, quality factor, and space coordinates. The description of this approach and the example of application of this algorithm are the subjects of this paper.

***Keywords*—** Anechoic chamber, Cavity resonator, Electromagnetic compatibility, Reflections damping

I. Introduction

WITH the increasing demand for testing various electrical devices for their electromagnetic compatibility, the importance of semi anechoic chambers is currently increasing. The semi anechoic chambers are constructed in that way so they simulated measurements in open space area, with no reflections from lateral directions and from above, but with defined reflections from the ground. Therefore the semi anechoic chambers are equipped with absorbers displaced around their walls and ceilings while their floor is made of conductive material (metal) and being uncovered by any material that would affect the natural reflections. These chambers are suitable for both main groups of electromagnetic compatibility radiation measurements – the electromagnetic susceptibility (EMS), consisting of exposure of the tested devices to the electromagnetic field radiated by the antenna, and also the electromagnetic interference (EMI), consisting of measurement of the electromagnetic field that is being emitted by the tested device. [3]

When the antenna measurements are operated on for other scientific reasons, the floor of the semi anechoic chamber can also be covered by the absorbers. In this case the absorbers are installed at are reflecting surfaces inside the chamber and the chamber is called fully anechoic. [3]

However, in both cases, there is a demand for effective shielding of the room inside the chamber from outer electromagnetic fields (GSM phones, radios, TV channels etc.) that would spoil the results of the measurement. Therefore the outer surfaces of the chambers are made of conductive materials (metal) and because of that they are highly reflective – not only for outer electromagnetic waves, but also for the inner ones. In this case the performance of the absorbers is crucial, although ideal absorbers with 100% effect at all frequencies cannot be constructed. When aiming to eliminate the occurrence of high amplitude standing waves at isolated places within the chamber, the shape of the chamber can also be irregular, pointing the respective reflections to various directions. This approach was also applied to the chamber that was analyzed within the research described in this paper. The description of the chamber is provided in the text below.

Because at Tomas Bata University in Zlin a semi anechoic chamber is used, its behavior was studied by mapping the electric field distribution within its space, especially at the frequencies that are expected to be close to the dominant modes of the chamber. The results of rough mapping of the spectrum inside the chamber are described in the framework of this paper as well as the algorithm that was used to detect the resonant peaks in the frequency response of the chamber at different points. The goal of this research is to find a simple method of evaluation of the behavior of the absorbers inside the chamber on the basis of the Q-factors calculated for the resonance peaks

This work was supported in part by the European Regional Development Fund under the project CEBIA-Tech No. CZ.1.05/2.1.00/03.0089 and by OPVK project CZ.1.07/2.3.00/30.0035.

Martin Pospisilik is with Faculty of applied informatics, Tomas Bata University in Zlin, Nad Stranemi 4511, 76005 Zlin, Czech Republic (corresponding author, phone: +420 606 417 702; e-mail: pospisilik@fai.utb.cz)

Tomas Riha is a student of Faculty of applied informatics, Tomas Bata University in Zlin, Nad Stranemi 4511, 76005 Zlin, Czech Republic

Milan Adamek is with Faculty of applied informatics, Tomas Bata University in Zlin, Nad Stranemi 4511, 76005 Zlin, Czech Republic (corresponding author, phone: +420 606 417 702; e-mail: adamek@fai.utb.cz)

Rui Miguel Soares Silva is with Polytechnic Institute of Beja, Campus do Instituto Politécnico de Beja Rua Pedro Soares, 7800-295 Beja, Portugal (e-mail: ruisilva@acm.org)

that occurred at different places of the chamber. With the algorithm described in this paper, once any changes in the configuration of the chamber are applied, the measurement can be processed once again and from the measured results the changes of the chamber's behavior can quickly be visualized.

II. Problem Formulation

The goal of the research was to propose an algorithm that would analyze the big amount of frequency responses measured inside the anechoic or semi anechoic chamber at different places and provided information on the quality of damping of the inner reflections. Evaluation based on calculated Q-factor was chosen. In the text below, the problem of reflections as well as the reasons for choosing this method is described.

A. *Default space configuration for EMC measurements*

As stated in the text above, the simplest configuration for Electromagnetic interference measurements according to the CISPR 16-1 standard is an Open Area Test Site the configuration of which is depicted in Fig. 1.

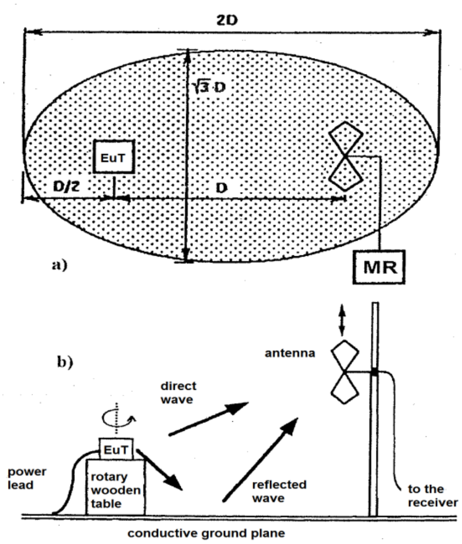

Fig. 1 generic open area test site configuration [3]

With the accordance to the standards, the distance measurement D is usually 3, 10, 30 or 100 m. The accuracy of the measurement increases proportionally to the distance, but with the increase of the distance, the level of disruptive ambient fields would become critical. Sufficient attenuation of the reflected waves is reached when highly reflective surfaces are kept behind the area of the ellipse depicted in Fig. 1. To ensure the reproducibility of measurements, additional specifications of the shape of the grounded metal flooring at the site are prescribed by relevant standards [3]. Then the height of the measurement antenna is adjusted in several steps and the Equipment under Test (EuT) is rotated as well in order to find the worst case of interference.

B. *Application of semi anechoic chambers*

In order to achieve relevant results, the level of ambient disruptive fields should be at least 20 dB lower than the level of the field radiated by the EuT [3]. Currently, this condition is not easy to be achieved as there are many sources of electromagnetic fields almost at all places inhabitated by people. Therefore, electromagnetically shielded chambers are used to process the measurement in practice. Unfortunately, the shielded chamber acts as a cavity resonator. Its resonant frequencies can be calculated according to the following equation:

$$f_{ijk} = \frac{c}{2\pi\sqrt{\mu_r \varepsilon_r}} \sqrt{\left(\frac{i\pi}{L}\right)^2 + \left(\frac{j\pi}{H}\right)^2 + \left(\frac{k\pi}{W}\right)^2} \tag{1}$$

Where:
c – field propagation velocity [m/s],
μ_r – relative permeability [-],
ε_r – relative permittivity [-],
i, j, k – wave indexes (case i = j = k = 0 is forbidden),
L – box length [m],
H – box height [m],
W – box width [m].

As a result of this, a great variety of resonant frequencies inside the chamber occurs. A typical frequency response of an undamped chamber is depicted in Fig. 2.

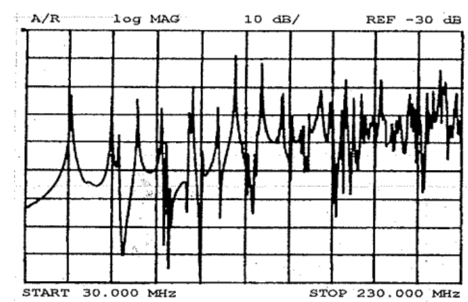

Fig. 2 typical frequency response of undamped semi anechoic chamber [3]

The number of modes occurring within the chamber can be high, but usually the most significant are those of low i, j, k numbers. Several visualizations of energy displacement for various modes are provided in the figures below. It was obtained by simulation applet [11]. The detailed description on the modes can also be found in [1].

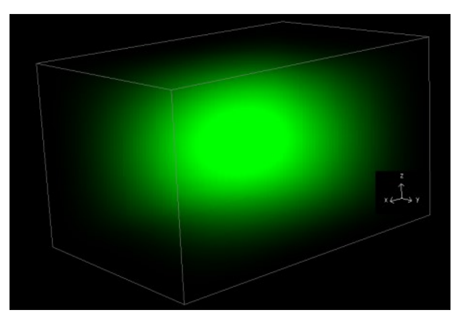

Fig. 3 energy displacement visualisation for mode TE_{101}

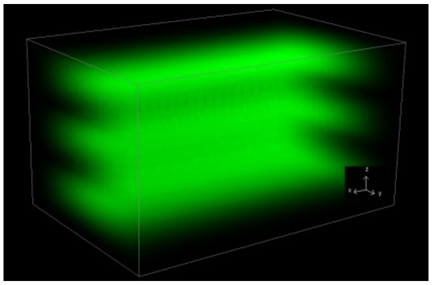

Fig. 4 energy displacement visualization for mode TE_{013}

As stated above, the damping is ensured by absorbers that are displaced around the reflective surfaces inside the chamber. In most cases a combination of two types of absorbers is used:

- Flat ferrite absorbers that can be tuned to desired frequency and damping factor by their thickness and perforation,
- Pyramidal absorbers the performance of which is more wideband, but they are space demanding and in a compromise design not effective at lower frequencies.

More detailed information on the behavior of the absorbers can be found for example in [2]. Generally it can be stated that the performance of the absorbers is dependent on the frequency of the damped waves and poor at low frequencies where the dominant resonances in the chamber are likely to occur. This was also confirmed by measurement and analysis that is provided in [10].

C. *Experiment to be evaluated by the algorithm*

The experiment to be evaluated by the algorithm is described in [10] in details as well as the obtained results. It consisted in measurement of frequency responses of the chamber in 15 different points. Semi anechoic chamber Frankonia SAC-3 Plus was employed in it, being declared by its manufacturer as a suitable unit for emission measurements according to EN 55022 / CISPR 22 class B and immunity tests according to IEC/EN 61000-3-4. The construction of the chamber is specific for its cylindrically shaped ceiling. The manufacturer claims that the dome shaped roof as well as its optimized absorber layout, with ferrite and partial hybrid absorber lining, minimizes the reflections in between 26 MHz and 18 GHz [4]. The frequency range of the experiment was from 10 to 80 MHz with the aim to drive the dominant mode of electrical field in this spectrum. Generic configuration of the chamber is depicted in Fig. 6.

According to the documentation, the internal dimensions of the chamber are listed in Table I. The height of the chamber varies according to position, as the ceiling is of cylindrical shape. The maximum height is in the longitudinal plane of the centre of the chamber, the minimum height is near the longer walls of the chamber. As the chamber is equipped with cone absorbers, the internal area is effectively restricted to approximately 8,120 x 5,150 mm.

The configuration of the points of measurement is depicted in Fig. 10. Transmitting antenna (ANT) was an omnidirectional monopole fed with the power of 0 dBm. At the positions (A) to (O) the mutual distances of which was 1,300 mm, Rohde & Schwarz omnidirectional spherical field probe HZ-11 was placed in order to measure the frequency response of the chamber to the transmitted electrical field. The field probe was always placed at a height of 1,500 mm.

Table I. Dimensions of the chamber

Length	9,680 mm
Width	6,530 mm
Height	9,500 mm (maximum)
	6,000 mm (minimum)

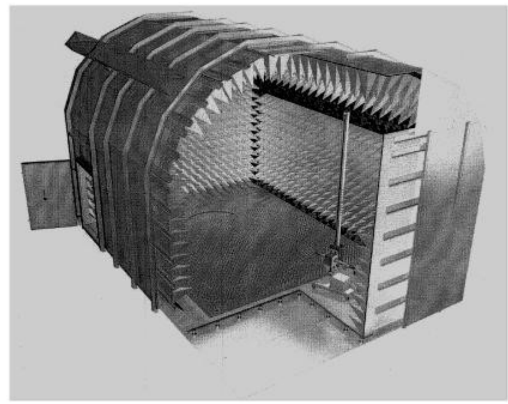

Fig. 5 semi anechoic chamber Frankonia SAC 3 – plus [4]

As a result, 15 frequency responses in the range from 10 to 80 MHz were obtained. The dominant mode as well as several higher modes was observed in them, in compliance with the expectations gained from calculations that were based on the dimensions of the chamber. The chamber acted mainly as a cuboidal resonator. The comparison of the measured and calculated dominant frequencies is provided in the Table II. The diagrams are displaced according to the points of measurement as depicted in Fig. 6.

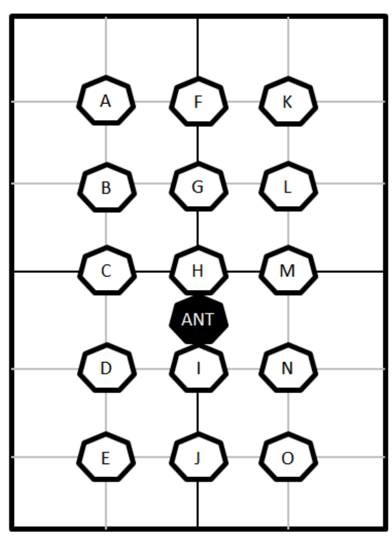

Fig. 6 displacement of the measurement points in the chamber

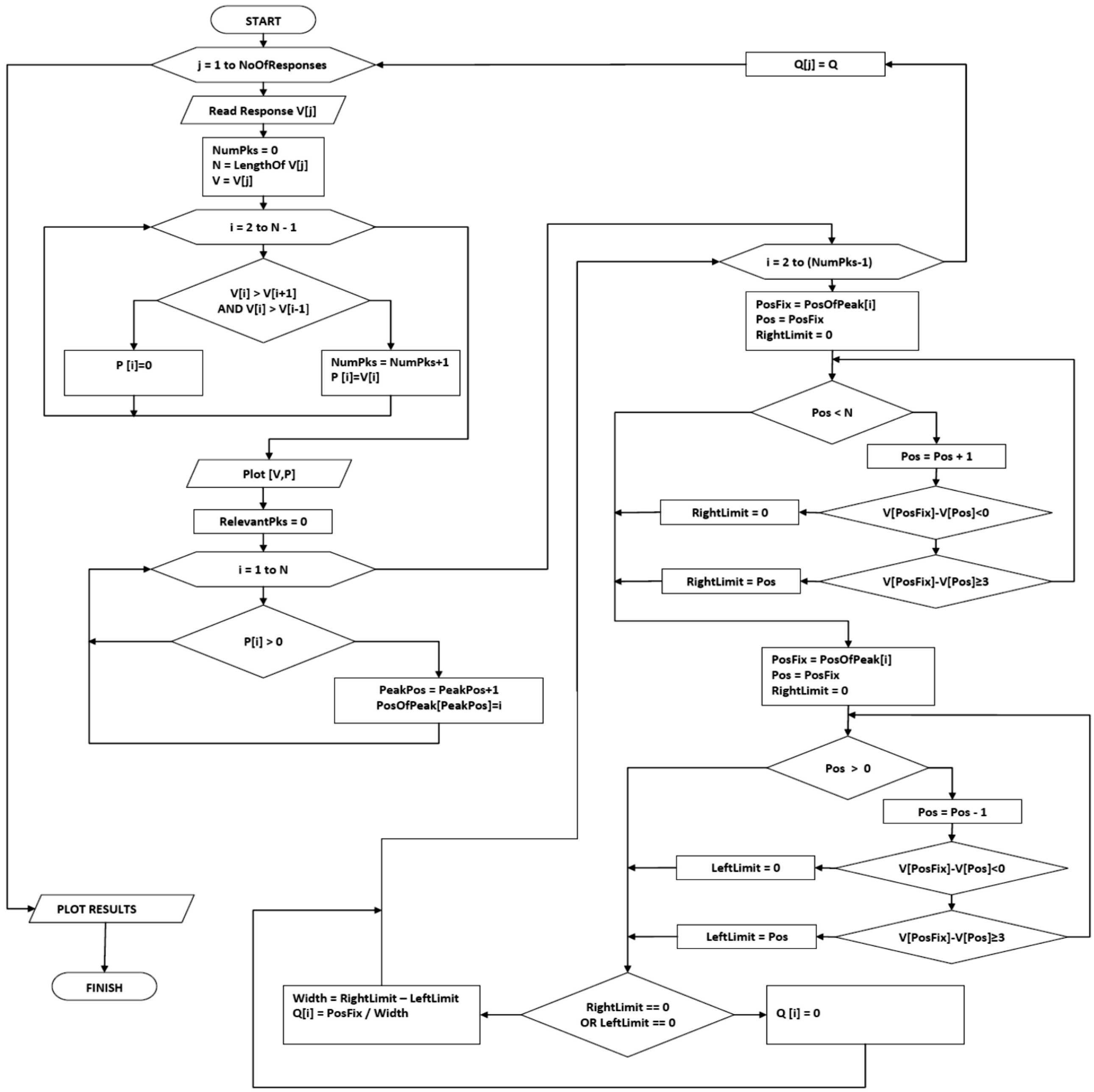

Fig. 7 Maple algorithm flowchart

D. *Demands on the algorithm*

As obvious from the data obtained in the experiment (see [10] and/or Table II), there is a numerous set of results to be analyzed. For each of the response, 625 points at the frequency axis are recorded, corresponding to the resolution of approximately 112.179 kHz. These data were obtained by the controlling software of the laboratory devices and exported into an Excel table.

The main demand is to isolate the main peaks occurring in the diagrams of the responses and to evaluate these peaks by a simple set of values.

Table II. Comparison of dominant frequencies identified by the measurement and expected on the basis of calculations

Point of measurement	**Frequency [MHz]**	**Closest mode**	**Deviation from the calculated frequency [MHz]**
A	36.81	TE111	- 0.34
B	36.81	TE111	- 0.34
C	37.15	TE111	+ 0.02
D	28.17	TE101	+ 0.47
E	25.71	TE101	- 1.99
F	35.58	TE111	- 1.55

G	27.95	TE101	+ 0.25
H	27.61	TE101	- 0.09
I	41.41	TE102	+ 2.70
J	50.83	TE201	+ 2.63
K	38.72	TE102	+ 0.01
L	36.03	TE111	- 1.10
M	35.46	TE111	- 1.67
N	38.27	TE102	- 0.44
O	24.25	TE101	- 3.45

III. Description of the Algorithm

As stated above, the algorithm should identify and isolate peaks in the frequency response and calculate Q-factor for them. Once a reduced set of data is obtained, it can also be visualized. By plotting the data into one diagram, also the position of the peaks on the frequency axis of the responses measured at various points can be compared.

A. Implementation

First of all, the data from the Excel table are loaded in a form of an array. The dimension of the array is 15 x 625, as there are 625 measured points at 15 different palaces. Because the frequency range is known (10 to 80 MHz), the frequency for each point can be calculated as follows:

$$f_i = f_{min} + \left((i-1)\frac{f_{max} - f_{min}}{N-1}\right) \tag{3}$$

Where:

f_i - frequency corresponding to the i-th measured point [Hz],
f_{min} – frequency at which the measurement started [Hz],
f_{max} – frequency at which the measurement finished [Hz],
i – position of the point of the measurement,
N – total number of the points of the measurement.

For the purposes of the research described in [10], the parameters are as follows: $f_{min} = 1\cdot10^6$ Hz, $f_{max} = 8\cdot10^6$ Hz, N = 625. The calculated relevant frequencies are loaded into a separated vector.

Then the whole rest of the algorithm is included in a cycle running from 1 to 15, because each frequency response is

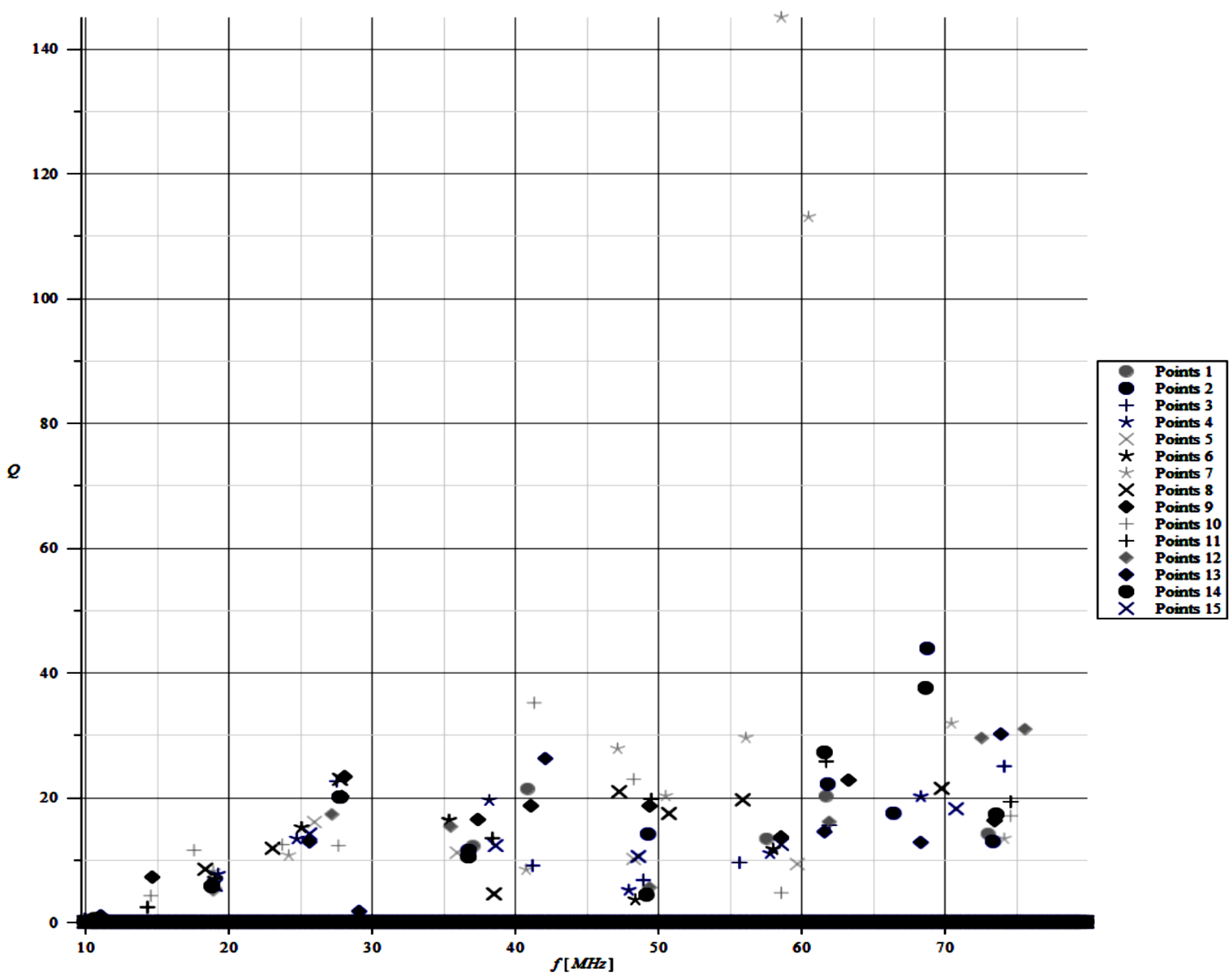

Fig. 8 cumulative diagram for all resonances discovered in the chamber within the experiment [10] processed separately.

In each of the run of the cycle, the following steps are processed. Firstly, all peaks are identified. Every value that is higher than its predecessor as well as its successor is recognized as a peak. To store these peaks, a new vector P (1..625) is created and the value of the peak is stored in it at the position corresponding to its frequency. For the frequencies at which no peak was detected, the value P[i] is set to 0. The total number of detected peaks is then stored in a variable NumPks.

Secondly, from the set of the local maxima only the relevant (substantial) peaks must be isolated. Only those peaks are marked as relevant, that comply with the following criteria:

- On both sides (left, right) of the peak a point can be find, the level of which is at least 3 dB lower (3dB criteria). The positions of such points are stored to variables LeftLimit and Right Limit.
- Concurrently, no point between LeftLimit and RightLimit is of a higher level than the examined peak.

Once the position of the peak is known as well as the position of the closest points to the peak that comply to the 3dB criteria, the Q-factor for this peak can be calculated, using a modification of formula (2):

$$Q_i = \frac{i_{Pk}}{i_{RightLimit} - i_{LeftLimit}} \tag{4}$$

Where:
Q_i – Q-factor calculated for the i-th frequency point,
i_{pk} – position of the identified peak,
$i_{RightLimit}$ – positon of the first point to the right from i_{pk} that comply with the 3dB criteria.
$I_{LeftLimit}$ – positon of the first point to the left from i_{pk} that comply with the 3dB criteria.

As a result of the computation, a new array of Q-factors is obtained, containing zeros at the positions, where no relevant peaks were detected, and values of calculated Q_i at the positions where the peak detection was successful. Finally, this array can be visualised according to the current needs.

The algorithm flowchart is depicted in Fig. 7.

B. Application

The algorithm was applied to the data obtained by experiment described in [10]. Because the space of this paper is limited, only the final, cumulative diagram, is depicted in Fig. 8. This diagram shows maxima detections and Q factor calculations for all 15 frequency responses obtained within the experiment [10]. From their position, that can be extracted from the set of results, in the [x,y] space it can be observed how the resonant frequencies differ in space and how good is their damping.

IV. Conclusion

This paper describes one of possible methods of evaluation of the quality of internal damping of semi anechoic and anechoic chambers. This method is based on automated search for resonant peaks obtained from frequency responses measured at different positions within the space of the chamber and calculation of equivalent Q factor for a resonant circuit that would show the same response.

Whereas with the cavity resonators the higher Q-factor is, the better is the resonator, within the semi anechoic and anechoic chambers the situation is reversed. While precise cavity resonators reach Q-factors higher than 10,000 [13], with the semi anechoic or anechoic chamber, it is important to reach as low values as possible.

From Fig. 8 it is obvious that the Q-factor of most of the resonances is kept below 25. Isolated clusters of points can be observed in the proximity of calculated frequencies (see Table 2 or [10]). Only in two causes high Q-factor values were detected (Q = 144.2 at 58.6 MHz and Q = 112.6 at 60.7 MHz). These values are ambiguous.

It is also interesting that the values of Q-factor tend to increase in accordance with the frequency. This effect was not expected, as the absorbers are generally supposed to perform better at higher frequencies.

References

[1] S. Radu. (N/A). *Engineering Aspect of Electromagnetic Shielding,* Sun Microsystems. [online]. Available: http://ieee.rackoneup.net/rrvs/09/Engineering%20Aspects%20of%20Electromagnetic%20Shielding.pdf.

[2] Compliance Engineering. (2015). *Flat Ferrite RF Absorber: SFA version* [online]. Available: http://www.ferret.com.au/c/compliance-engineering/sfa-version-flat-ferrite-tile-rf-absorbers-from-compliance-engineering-n892923.

[3] J. Svačina, *Electromagnetic compatibility: Principles and notes [Elektromagnetická kompatibilita: Principy a poznámky],* 1st edition. Brno: Vysoké učení technické, 2001. ISBN 80-214-1873-7.

[4] Frankonia, (2012). *Anechoic Chambers / RF-Shielded Rooms*. [online]. Available: http://www.frankoniagroup.com/cms/fileadmin/shared/downloads/rooms%26chambers/Anechoic_Chambers.pdf.

[5] Rohde&Schwarz. (1999). *Probe Set HZ-11 for E and H near-field Measurements*. [online]. Available: http://cdn.rohde-schwarz.com/pws/dl_downloads/dl_common_library/dl_brochures_and_datasheets/pdf_1/Hz-11_en.pdf.

[6] Z. Trnka, *Theory of Electrical Engineering [Teoretická elektrotechnika]*, Bratislava: SNTL Alfa, 1972.

[7] Radio-Electronics (2015). *Quality Factor*. [online]. Available: http://www.radio-electronics.com/info/formulae/q-quality-factor/basics-tutorial.php.

[8] T.I Maris et al., "Electromagnetic field identification using artificial neural networks", In *Proceedings of the 8th WSEAS International Conference on Neural Networks*, Vancouver, British Columbia, Canada, June 19-21, 2007.

[9] M. Mann, B. Gutheil, J. Zastrau, P. Weiss, "Electromagnetic field measurements – Means of verification", In *Proc. of the 5th WSEAS/IASME Int. Conf. on Electric Power Systems, High Voltages, Electric Machines*, Tenerife, Spain, December 16-18, 2005.

[10] M. Pospisilik, J. Soldan, "Electromagnetic field distribution within a semi anechoic chamber", In *Proceedings of the 18th International conference on systems*, Santorini island, Greece, July 17-21, 2014, ISBN 978-1-61804-244-6.

[11] (N/A).(2014). [online]. Available: http://www.falstad.com/embox/.

[12] D. Pozar, *Microwave engineering*. 2nd edition. New York: John Wiley, 1998.

[13] COMSOL. (2014). *Computing Q-Factors and Resonant Frequencies of Cavity Resonators,* [online]. Available: http://www.comsol.com/model/download/156535/models.rf.cavity_resonators.pdf.

Station for measurement of a shielding effectiveness of materials and its controlling

Martin Pospisilik, Milan Adamek, and Rui Miguel Soares Silva

***Abstract*—**The paper describes a measurement station for measurement of a shielding effectiveness of composite materials according to the standards MIL-STD 285 and IEEE Std. 299-2006 as well as its controlling algorithm created in Agilent VEE environment. This kind of measurement is demanded by aircraft industry that develops new, lightweight materials for construction of aircrafts with reduced weight and dimensions and increased number of electronic devices. Besides the fact, that it is necessary to ensure mutual electromagnetic compatibility of the equipment mounted on the aircraft's board, all the devices must also sustain interferences caused by High Intensity Radiated Field (HIRF). This is important all the more, as in the past, there were several aircraft crashes recorded as a result of interference of their equipment with terrestrial transmitters. The hereby described station enables comparative measurements, based on comparing of two measurement results, one obtained without the shielding material and the second one obtained with the shielding material the shielding effectiveness of which is to be measured. The results can also be compared with a reference sample of the shielding material – a brushed steel plate. The hereby described controlling software enables synchronizing of the measuring instruments employed at the measurement station as well as their automatic setting and direct evaluation of the obtained results.

***Keywords*—** Shielding Effectiveness, Composite Materials, Electromagnetic Compatibility

I. Introduction

SHIELDING effectiveness is a parameter of a material, that describes how the material eliminates the power of electromagnetic field radiated by a source that is placed behind this material. Its basic definition is as follows:

$$SE = 10 \cdot log\frac{P_1}{P_2}\ [dB] \tag{1}$$

This work was supported in part by the European Regional Development Fund under the project CEBIA-Tech No. CZ.1.05/2.1.00/03.0089 and by OPVK project CZ.1.07/2.3.00/30.0035.

Martin Pospisilik is with Faculty of applied informatics, Tomas Bata University in Zlin, Nad Stranemi 4511, 76005 Zlin, Czech Republic (corresponding author, phone: +420 606 417 702; e-mail: pospisilik@fai.utb.cz)

Tomas Riha is a student of Faculty of applied informatics, Tomas Bata University in Zlin, Nad Stranemi 4511, 76005 Zlin, Czech Republic

Milan Adamek is with Faculty of applied informatics, Tomas Bata University in Zlin, Nad Stranemi 4511, 76005 Zlin, Czech Republic (corresponding author, phone: +420 606 417 702; e-mail: adamek@fai.utb.cz)

Rui Miguel Soares Silva is with Polytechnic Institute of Beja, Campus do Instituto Politécnico de Beja Rua Pedro Soares, 7800-295 Beja, Portugal (e-mail: ruisilva@acm.org)

Where:
P_1 – Power generated by the source of the interference [W],
P_2 – Power being spread behind the shielding material [W].

A. Shielding mechanisms

In fact, there are three different mechanisms that contribute to the ability of the material to shield the electromagnetic field. A short description of all of them is provided below in this text. Generally, these contributions can be described as follows:

$$SE_{dB} = R_{dB} + A_{dB} + M_{dB} \tag{2}$$

Where:
R – Attenuation on the interface with different impedances,
A – Attenuation caused by the absorption of the materiel (heat loss),
M – Attenuation caused by multiplicated reflections.

1) Attenuation on the interface with different impedances

The attenuation R_{dB} describes how much energy is reflected back from the shielding material. In case the shielding material creates a partition M between two different environments A and B, the attenuation caused by the reflection can be described as follows:

$$R = 20 \cdot log\left|\frac{Z_A + Z_M}{2 \cdot Z_M} \cdot \frac{Z_M + Z_B}{2 \cdot Z_B}\right|\ [dB] \tag{3}$$

Where:
Z_A – impedance of the environment A [Ω],
Z_B – impedance of the environment B [Ω],
Z_M – impedance of the shielding material M [Ω].

2) Attenuation by the absorption

The attenuation due to absorption of the energy by the material can be described on the basis of the calculation of the intrusion depth δ:

$$A = 20 \cdot log\left|e^{\frac{t}{\delta}}\right|\ [dB] \tag{4}$$

$$\delta = \sqrt{\frac{2}{\omega\mu\sigma}} \tag{5}$$

Where:
t – material thickness [m],
δ – intrusion depth [m],
σ – material conductivity $[S \cdot m^{-1}]$,
μ - material permeability $[H \cdot m^{-1}]$,
ω – wave frequency $[rad \cdot s^{-1}]$.

3) Attenuation by multiple reflexes

The principle of attenuation caused by multiple reflexes is depicted in Fig. 1. It does not apply if (t >> δ), but if (t << δ), its value can be negative, decreasing the total shielding effect of the material. According to [5] it can be described by the following equation:

$$M = 20 \cdot log \left| 1 - \left(\frac{Z_O + Z_M}{Z_O + Z_M} \right)^2 \cdot e^{-\frac{2t}{\delta}} \cdot e^{-j\frac{2t}{\delta}} \right| \; [dB] \qquad (6)$$

Where:
Z_0 – impedance of the surroundings of the material [Ω],
Z_M – impedance of the material [Ω],
t – material thickness [m],
δ – intrusion depth [m].

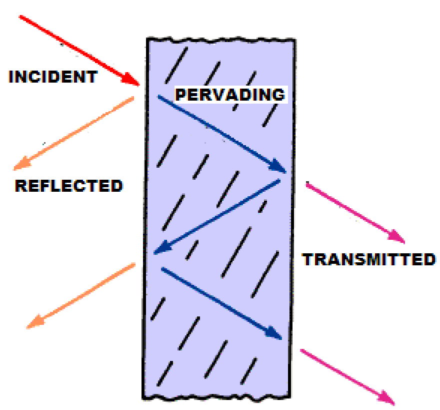

Fig. 1 principle of attenuation caused by means of multiple reflections. Incident, reflected, pervading and transmitted waves are shown. [5]

B. Importance of the research

With the increase of the number of electronic devices in all sectors, the problem of their mutual electromagnetic compatibility is gaining greater precedence, all the more so when it comes to critical systems, such as aircraft electronics.

Not only in the past, the aircraft industry has been one of the driving forces in the area of electromagnetic compatibility. The constructers had to face many problems raising at the field of mutual electromagnetic compatibility of devices that had to be in a concurrent operation. For example, as described in [1], in 1984 the NATO airplane "Tornado" crashed in Germany after its circuits interfered with a powerful transmitter in Holkirchen.

In the framework of the latest trends in the production of small aircrafts, the demand on their electronic equipment is increased, whilst there is a legitimate pressure on decreasing of their weight. The constructers endeavor to use composite materials, creating a pressure on their intensive advancements and one of the observed parameters of such materials is right their shielding effectiveness.

C. Measurement of the shielding effectiveness

Usually, for the purposes of the aircraft industry, the measurements are processed according to the standards MIL-STD 285 and IEEE Std. 299-2006 that prescribe the framework of the approach to the measurement. The configuration of the measurement station is as depicted in Fig. 2. There is a well shielded box with such dimensions that ensure that its dominant resonant frequency lies below its operating frequency range. Inside this box a receiving antenna is placed, while outside the box, there is a transmitting antenna. In one of the sides of the box, there is a window with defined dimensions, in which the measure material is mounted. By means of a comparative method, the frequency response of the environment between the antennas is measured with and without the measured sample and then the shielding effectiveness of the measured sample is evaluated.

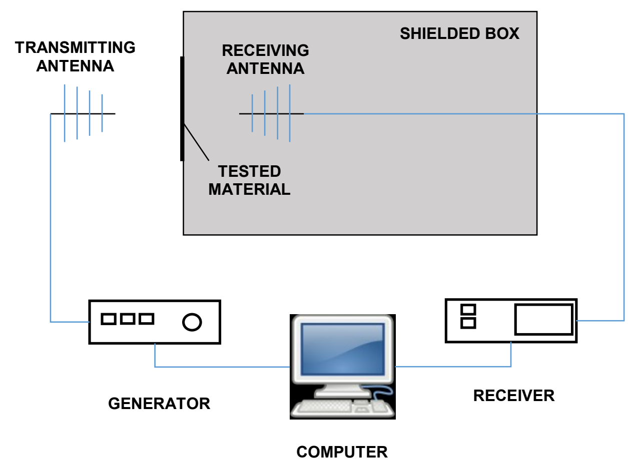

Fig. 2 schematic diagram of a measurement station for measuring of the shielding efficiency of material samples

II. Description of the Measuring Station

The measuring station consists of a steel box in which an antenna, electromagnetic power absorbers and a window for clamping of the measurement sample are incorporated, one external antenna on a tripod, a set of instruments and a computer on which the controlling software is run. The description of these items is provided below in this chapter.

A. Shielded steel box

The construction of the shielded steel box can be observed in Fig. 2. The standards define only dimensions of the window for clamping of the measured material and the method of its mounting. As it is expected to process the measurements on the frequencies around 1 GHz and above, the dimensions of the box were chosen in that way so its dominant resonant mode was safely below the lowest operating frequency of the measurement site. According to [4], the resonant modes of a closed box can be calculated as follows:

$$f_{ijk} = \frac{1}{2\sqrt{\mu\varepsilon}}\sqrt{\left(\frac{i}{a}\right)^2 + \left(\frac{j}{b}\right)^2 + \left(\frac{k}{c}\right)^2}\ [Hz] \tag{7}$$

Where:
μ - material permeability $[\mathrm{H \cdot m^{-1}}]$,
ε – material permitivity $[\mathrm{F \cdot m^{-1}}]$,
i, j, k – mode indexes,
a, b, c – dimensions of the box [m].

When the length of the box is 2 m and other dimensions are chosen proportionally, the dominant resonant frequency according to the equation (7) is approximately 170 MHz. The higher resonant phenomena are suppressed by the internal absorbers. On one of its sides, the box is equipped with a strongbox type door in order to enable manipulation with the sensors mounted inside the box. The door employs Cu-Be shielding seal. At the back side of the box, a penetration panel is mounted, incorporating the following equipment:

- Grounding screw,
- 16 A single phase power mains filter with high attenuation,
- N-type connectors for connecting of coaxial cables,
- circular waveguide.

The measured materials are attached by means of a flat frame that is mounted to the body of the box by 20 clamping screws. This facilitates the manipulation with the material samples and enables uniform pressing force around the perimeter of the samples.

Fig. 3 construction of the shielded steel box

B. Antennas

For the basic measurement, two equal horn antennas are used, as depicted in Fig. 4. SAS 571 or HF 906 horns are utilized. Both antennas must be in the same height, placed at a distance of 0.3 m from the measured sample.

The external antenna is mounted on a tripod, while the internal antenna is mounted on a non-conductive support.

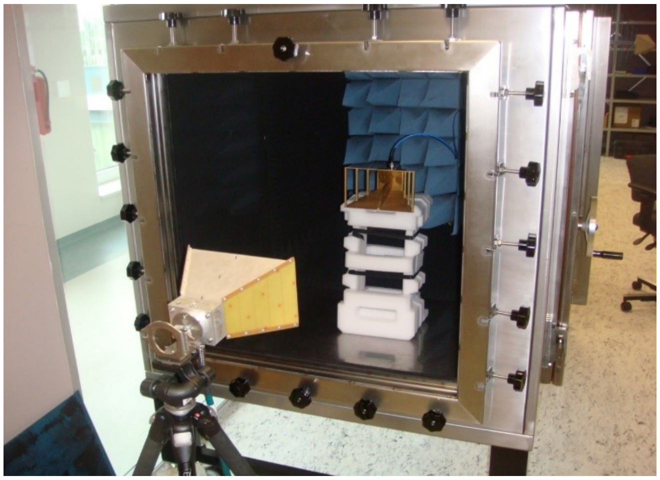

Fig. 4 antennas for shielding effectiveness measurements

C. Measuring instruments

For the purposes of the basic measurement, remotely controlled generator Rohde & Schwarz SMR-20 and spectrum analyser Rohde & Schwarz FSP-40 are used. The settling time of the instruments for measurement at a constant frequency and a constant transmitted power is approximately 0.25 s.

III. Controlling Software

The controlling software is run on a computer that controls both, the signal generator, and the receiver / spectrum analyser. The software has been created in Agilent Vee environment and employs the interconnection between the devices established on the basis of the GPIB bus.

A. Requirements on the software

Basically, the following requirements were applied when the controlling software was developed:

- Direct export to MS Excel file according to the path defined by the user,
- shortening the measurement time as much as possible,
- setting of the number of the measurement points by the user,
- automatic setting of the transmitting power,
- automatic calibration and shielding effectiveness evaluation.

B. User's view

From the user's perspective, the steps performed during the measurement are as described by the diagram depicted in Fig. 5. Once the measuring station is prepared, the user checks the distance between the antennas and specifies the initial parameters in the control panel of the controlling software. These parameters are as follows:

- Frequency range (from – to),
- number of measurement points,
- path to the file the results should be exported to.

The selection of the generator's power and the receiver's attenuator are done automatically by the software, as well as the proper timing of the actions.

ISBN: 978-1-61804-321-4

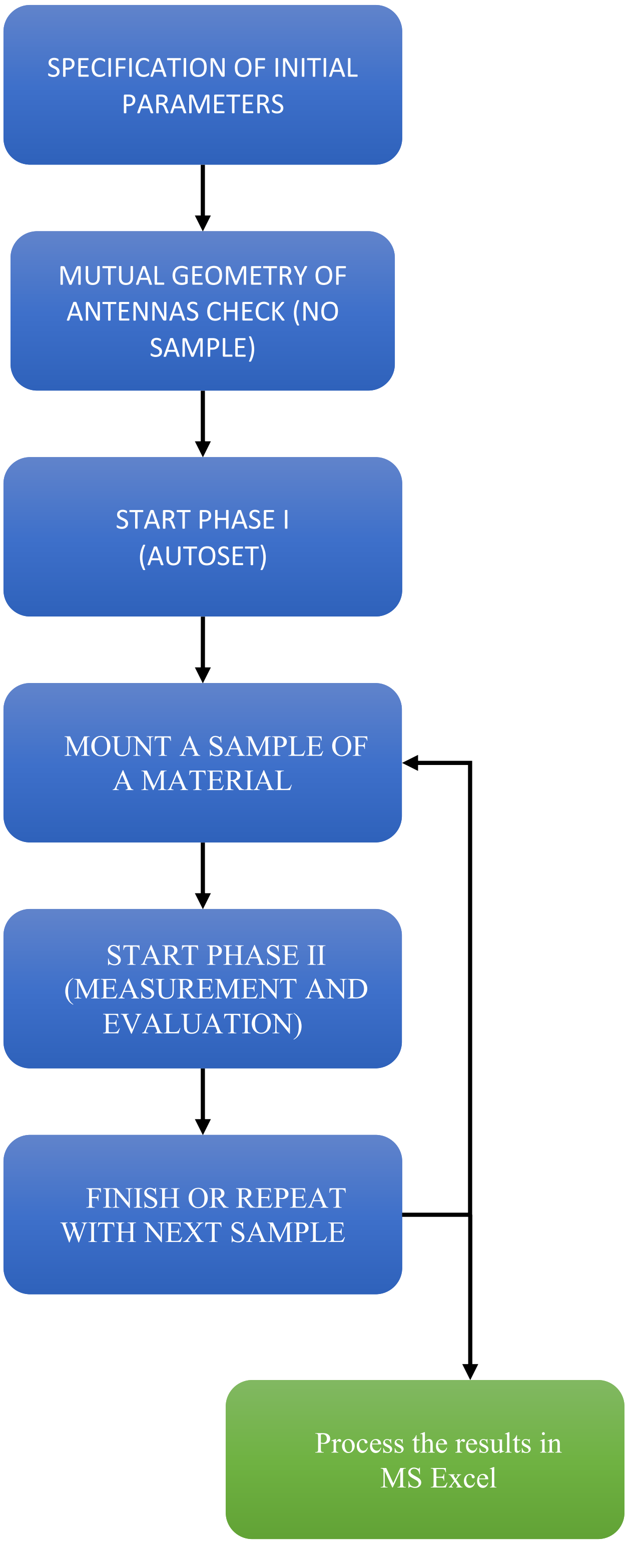

Fig. 5 steps performed during the measurement from the user's view

C. *Description of the algorithm*

Once the measurement is initiated, the software runs through the following steps:

- Initializing of the connected devices,
- Autoset and storage of the reference curve,
- Measurement of the shielding effectiveness of the sample. This step can be repeated arbitrarily, employing the results of the previous steps.

Description of the above mentioned steps is provided in the subchapters below.

1) *Initializing of the connected devices*

Only those devices that are described in this paper are permitted to be controlled by means of the hereby described software. Due to the nature of the measurement, which is processed gradually on separated discrete frequencies, the setting of the instruments are as described in Table I.

Table I. Initial parameters set at the instruments

Spectrum analyzer FSP-40	
Bandwidth	1 kHz
Frequency span	1 MHz
Continuous mode	OFF
Marker 1	ON Reads the value at the specified frequency.
Attenuator	70 dB (initial value)
Generator SMF100A	
Mode	Sinus
Output power	-30 dBm (initial value)
Output state	ON

2) *Autoset and storage of the reference curve*

The reference curve refers to the frequency response of the path between the antennas when no sample to be measured is applied. Before this curve is measured, automatic setting of the transmitting power and the receiver's attenuator must be done, in order the measurement was not affected by noise of overloading of the receiver's input. The same automatic setting of these parameters must also be done when each of the material samples are measured.

The automatic setting is provided in the following steps:

1. According to the Table I, the output power of the generator is set to -30 dBm and the attenuator of the receiver is set to 70 dB.
2. The software choses one frequency in the middle between the minimum and maximum limit and the measurement of the received electrical field at this frequency is being processed while the setting of the receiver's attenuation is gradually decreased.
3. When the receiver indicates overload of its input, the setting of the attenuator is increased by 10 dB. When no overload is indicated even when the attenuator is set to 0 dB, the output power of the generator is gradually increased.
4. The frequency response of the path between the generator and the receiver is measured at each fourth point of the measurement. The evaluation is processed in the same way as in steps 2 and 3.

ISBN: 978-1-61804-321-4

5. Now the frequency response is measured at all points and the final check for overload is made in the same way as in steps 2 and 3.
6. Once the attenuator and the transmitting power are set to the proper levels, the reference curve can be measured. The measurement is repeated ten times and the average is the calculated and stored. If there is any overload detected by the receiver during each of the measurements, the setting of the attenuator is either increased, or, when the attenuator is at 60 dB, the output power of the generator is decreased and a new set of 10 measurements is obtained afterwards.
7. The xls file is created. In the column A the frequencies at which the measurement was taken are enlisted while in the column B the values referring to the reference curve are stored.

3) Measurement of the material sample

This measurement can be repeated as many times as needed. Every time, the same reference curve is applied. Once the Autoset finished, the software performs the following steps:

1. The user is prompted to mount the sample of the material into the window of the measurement box. The antennas as well as other components may not be moved. By clicking OK he starts the Phase II as depicted in Fig. 5.
2. Before the measurement is processed, it is necessary to find new suitable combination of the generator's output power and the receiver's attenuator. The output power of the generator is increased by 30 dBm, but not higher than to +15 dBm in order to avoid the overexcitation of the generator. The receiver's attenuator is set to maximum.
3. The generator produces sinusoidal signal at the frequency that lies between the maximum and the minimum and the setting of the attenuator is gradually decreased until the overload is indicated. Then the setting of the attenuator is increased by 10 dB.
4. The frequency response of the path between the generator and the receiver is measured at each fourth point of the measurement. The evaluation is processed in the same way as in the Autoset described in the previous subchapter.
5. Once the suitable setting of parameters is achieved, the measurement of the shielding efficiency is processed. The frequency response is measured ten times and the average is calculated. If the overload is indicated anytime, the setting of the attenuator is increased and the whole measurement is repeated.
6. The difference between the measured curve and the reference curve is computed and stored in the xls file.
7. The user can now finish the measurement or change the sample to be measured and repeat the hereby described steps.

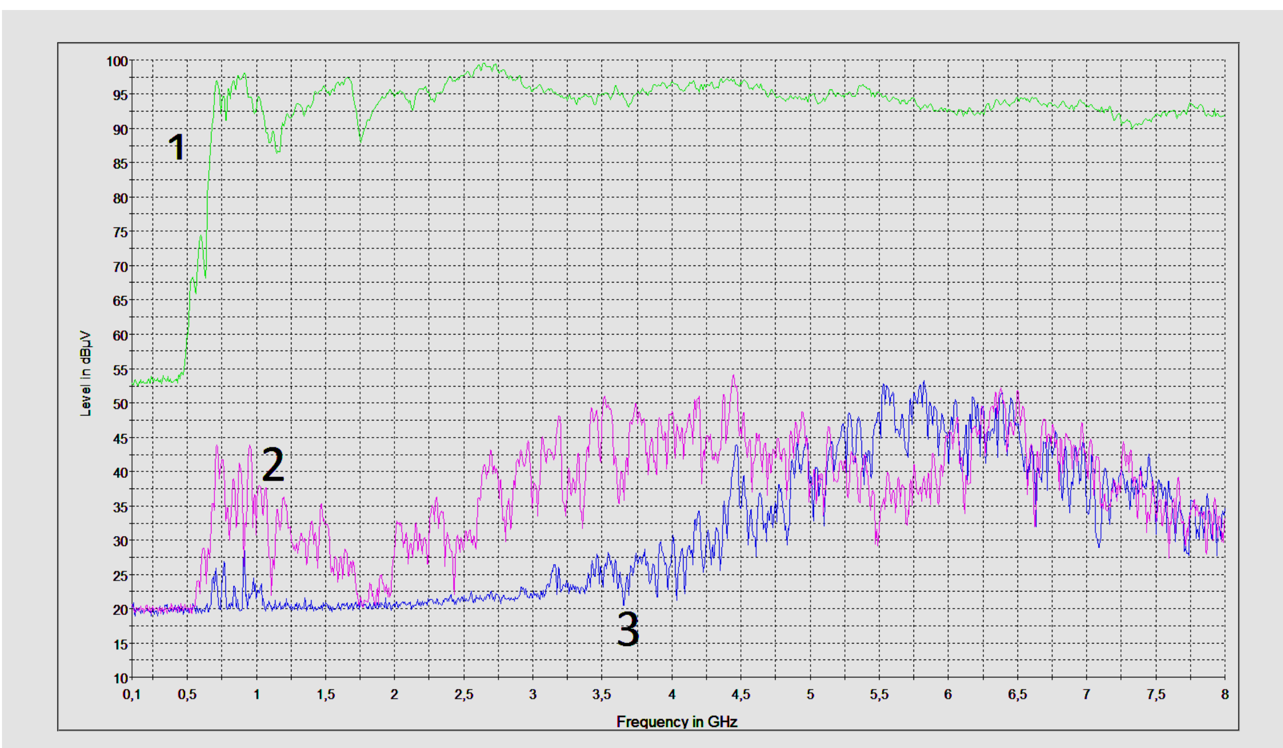

Fig. 6 example of measurement taken by the measurement station (see description in text)

IV. Achieved Results

In the time of creation of this paper, the hereby described algorithm has been a subject to finish the final tests and the measurement station has been operated by means of the previous version that did not included the automatic setting of the attenuator and the transmitting power. However, the performance of the measurement station was successfully verified by measurements at different material samples.

The example of the measured results is provided in Fig. 6. There are three curves in the diagram, numbered by numbers 1 to 3. Their meaning is explained in Table II.

Table II. Description of spectra depicted in Fig. 6

Spectrum No.	Description
1	Reference frequency response. No material was inserted between the measurement antennas.
2	Frequency response measured when a sample of composite material was attached in the window of the measurement box.
3	Frequency response measured when a steel plate was attached in the window of the measurement box.

V. Conclusions

The paper describes construction and controlling of a measurement station for measuring of the shielding effectiveness of composite materials. These measurements are requested by minor aircraft producers for the purposes of their material innovations. Special attention is paid to the design of the controlling software that enables automation of the steps of the measurement and rapidly shortens time that is needed to obtain valid results, compared to convenient method of manual measurement.

Both, the hardware and the software of the measurement station are still undergoing improvements the purpose of whose is to improve the performance of the station.

As this topic is currently solved by many research teams across the world, the concerned readers can find relevant information in many publications, like [7], [8] or [9].

References

[1] C. R. Paul, *Introduction to Electromagnetic Compatibility*. New York: John Wiley, 1992.

[2] P. A. Chatterton, M. A. Houlden, *EMC – Electromagnetic Theory to Practical Design*. New York: John Wiley, 1991.

[3] J. A. Cartrysse, “Measuring method for the characterization of shielding gaskets”, In *8th International Conference on Electromagnetic Compatibility*, pp 251 – 253, Heriot-Watt University, Edinburgh, UK, September 1992.

[4] IEEE Standard Method for Measuring the Effectiveness of Electromagnetic Shielding Enclosures, IEEE Std 299 – 2006.

[5] J. Svacina, *Electromagnetic Compatibility [Elektromagneticka kompatibilita]*, Brno: Brno University of Technology, 2002.

[6] Z. Trnka, *Theory of Electrical Engineering [Teoretická elektrotechnika]*, Bratislava: SNTL Alfa, 1972.

[7] M. H. Vogel, *Impact of lightning and high-intensity radiated fields on cables in aircraft*, IEEE Electromagetic Compatibility Magazine, Volume 3, Issue 2, ISSN: 2162-2264

[8] A. Schroder et. al, *Analysis of High Intensity Radiated Field Coupling into Aircraft Using the Method of Moments*, IEEE Transactions on Electromagnetic Compatibility, Volume 56, Issue 1, ISSN: 0018-9375.

[9] R. Wang, W. S. Gray, O. R. González, J. R. Cháves-Fuentes, *Tracking Performance of Distributed Recoverable Flight Control Systems Subject to High Intensity Radiated Fields*, IEEE Transactions on Aerospace and electronic Systems, Vol. 2013, Issue 1, DOI: 10.1109/TAES.2013.6404118

Indoor positioning based on the radio signal strength indicator with the use of iBeacon technology

Damian. Grzechca, Piotr Pelczar, Łukasz Chruszczyk

***Abstract*—**The paper presents an indoor positioning of a mobile device on the basis of the iBeacon technology. The end-user positioning is important from at least two points of view: in a museum like building it allows localization and waypath creation. Second, the customer behavior in the market may improve different action (discounts) addressed to a particular group of people. The authors evaluate the indoor positioning trilateration algorithms for three most visible iBeacons and for all of them. For exemplary hall, the radio signal strength indicator (RSSI) map (radiomap) has been created and the logarithmic propagation model has been designed. The logarithmic model estimated distance with average error 1.75m and after trilateration the positions with average error 2.45m has been achieved.

A statistical analysis for acquiring data leads to final conclusions which enhance knowledge about positioning based on the iBeacon technology

***Keywords*—**Bluetooth indoor positioning, iBeacon, radiomap, trilateration.

I. Introduction

Many indoor positioning techniques have been proposed for mobile devices [1]. Some of them are based on custom hardware utilizing Bluetooth Classic, especially in scanning phase to obtain RSSI or Link Quality [2, 3]. Unfortunately, Bluetooth Classic scanning phase is energy-consuming, because obtaining Link Quality metrics requires devices connection. The Bluetooth 4.0 (known also as Low Energy or BLE) released in 2011 and now it is widely supported by smartphones vendors. This has opened a new opportunity to discover devices and obtain RSSI in the lower energy cost way. BLE beacon devices broadcasts short packets in specific interval, which gives new possibility to use beacon standard in wide range people population holding these devices in pockets.

In 2013 Apple released iBeacon standard as proximity location method, which utilizes Bluetooth 4.0 GATT profile and standardized frame data contents [4]. Then, many vendors have started producing low-cost hardware broadcasting beacon frames, which can be discovered by mobile devices and take some action. This standard is natively supported on Apple iOS mobile devices, but it is easy to implement in every platform which has access to Bluetooth Host Controller Interface (HCI), such as on devices running on Android or Windows Phone.

Power based positioning techniques rely on the signal attenuation property of the radio wave propagation to estimate distance from wave emitter [5]. There are two common approaches to determine object's position. One is creating radiomap of room in offline (static) phase, means there are many RSSI once-collected samples in many points stored in the database and in the online phase, when object is collecting samples of RSSI to determine its position, some nearest-neighbor algorithms determining object's position comparing to samples from the database. Another one employs surveying RSSI's to build path-loss signal model that estimates the distance from emitter based on signal-strength. By knowing three or more distances the trilatrate algorithms can be applied in order to obtain the final position of an object.

In this paper, the Logarithmic Distance Path-Loss estimation model has been tuned by the simplex algorithm to determine distance based on RSSI. Additionally, radiomaps have been created for all accessible beacons in a number of points in the room. Created model have been used to determine distances from beaons in each radiomap point and trilateration algorithms have been used to compute final posision. Estimated distances and positions have been compared to radiomap data in order to designate errors and measure the effectiveness of the proposed approach.

II. Building a Path-loss model

There are several path-loss models available to determine distance from wave emitter by measuring signal strength [6, 7]. First, log-distance path loss model has been investigated:

$$RSSI = RSSI_0 - 10\gamma\log_{10}\frac{d}{d_0} + X_\sigma \qquad (1)$$

where: d is the distance from wave emitter, $RSSI$ indicates the received power [dBm] (signal strength), $RSSI_0$ is power measured in the distance d_0, X_σ is the Gaussian random noise variables with mean value of zero and mean variance of σ. The coefficient γ represents the path-loss exponent defining the rate at which the power falls. In free space it is equal 2, but in real

This work was supported by the Ministry of Science and Higher Education funding for statutory activities.

Damian Grzechca and Ł. Chruszczyk are with the Silesian University of Technology, Faculty of Automatic Control, Electronics and Computer Science, Gliwice, Poland (+48322372717; e-mail: dgrzechca@ polsl.pl).

Piotr Pelczar is a PhD Student at the Silesian University of Technology, Faculty of Automatic Control, Electronics and Computer Science (e-mail: me@athlan.pl).

environment it depends on many elements such as surrounding objects, wave reflections, scattering, diffraction and signal multipath [5, 6]. The factory has been designated in the optimization process by fitting gathered RSSI samples to the model (1). The process gives results from 1 to 1.4 for coefficient γ.

The equation (1) can be rearranged and the distance d as a function of $RSSI$:

$$d = 10^{\left[\frac{RSSI_0 - RSSI + X_\sigma}{10\gamma} + \log_{10}(d_0)\right]} \tag{2}$$

What is important, estimated d value should be greater than d_0, because formula bases on path loss and $RSSI_0$ - $RSSI$ should be greater than 0. There is no sense to make distance estimation for $d < d_0$ in context of path-loss, because in this case power will increase.

III. Data Acquisition and Analysis

A. Path-loss model creation

In order to create a relatively high precision path loss model, data acquisition and fundamental statistics analysis should be applied.

Fig. 1 Data acquisition points (red) from beacon (blue point).

For a single position in the room a set of 100 RSSI readings per a beacon (anchor) has been collected. The distance between following points has been set to 1m which gives 21 points in straight line.

The human body wave power absorbiton has also been taken into account – RSSI readings have been collected for line-of-sight (LOS) facing towards the beacon and non-LOS directed back to the beacon. The measurements have been collected on a 5m wide hallway (presented in the fig. 1) with walls made of two materials: from one side glass (windows) and another side reinforced concrete. All data (RSSI) in the position has been aggregated into single RSSI value by computing median. The RSSI values and its standard deviation over distance has been presented in fig. 2a, 2b.

The relationship between distance from the beacon and RSSI for both LOS and non-LOS has been calculated with Pearson correlation coefficient (3) which gives 90.1%.

$$r_{XY} = \frac{\mathrm{cov}(XY)}{\sigma_X \sigma_Y} = \frac{\sum_{i=1}^{n}(x_i - \bar{x})(y_i - \bar{y})}{\sqrt{\sum_{i=1}^{n}(x_i - \bar{x})^2}\sqrt{\sum_{i=1}^{n}(y_i - \bar{y})^2}} \tag{3}$$

So, the distance have almost the same impact on the signal strength. Moreover, there is no correlation between standard deviation and distance, even after reducing input samples by filtering 20% extreme values with respect to median (fig. 2b). The signal quality indicator can not rely on this metric.

In equation (1) X_σ is denoted as the Gaussian random noise variables with zero mean and mean variance of σ. The RSSI samples distribution has been investigated in distance 1m (fig. 3a), 3m (fig. 3b), 5m, 7m, 10m, 15m and 20m. The Chi-square statistical test with 5% significance level and Shapiro-Wilk with 5% significance level has been run to ensure, that the RSSI samples has Gaussian distribution. Tests have rejected this hypothesis in several cases, so empirically measured X_σ is a noise with Gaussian distribution (fig. 3b). In this case, it has been decided to tune γ path-loss exponent factor and X_σ noise in the model optimization process.

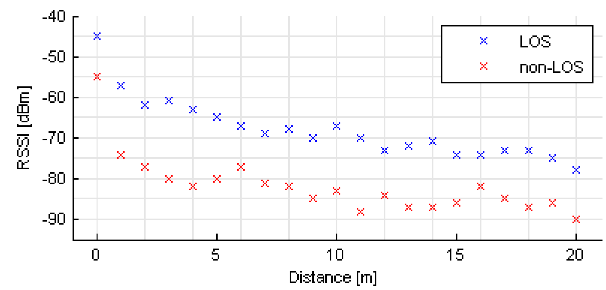

Fig. 2a Median of measured RSSI (LOS and non-LOS)

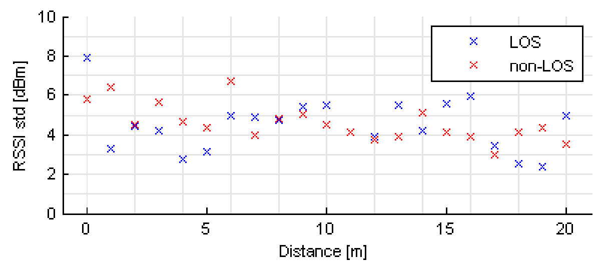

Fig. 2b Standard deviation of measured RSSI (LOS and non-LOS)

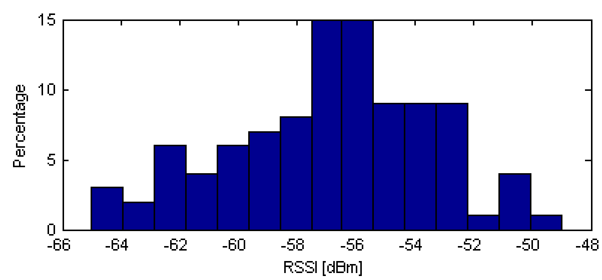

Fig. 3a RSSI distribution on distance 1m

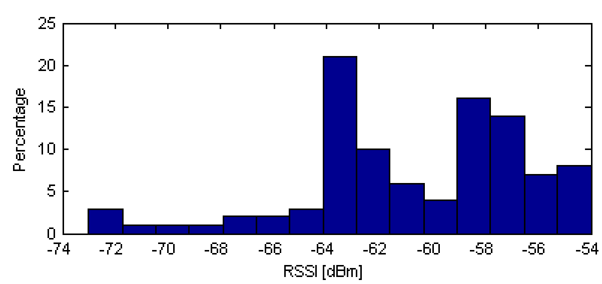

Fig. 3b RSSI distribution on distance 3m

According to Apple documentation for iBeacon standard the reference $RSSI_0$ value for 1m distance must be acquired at first. Fortunately, the acquired samples have Gaussian distribution in this distance what is important for formula

ISBN: 978-1-61804-321-4

model (1) and X_σ value.

Another important doubts flow from a source of measurements, i.e. HCI (Host Controller Interface). The question is whether the HCI is a source with a memory or it produces random values independent from history. In other words, a source stability and the unexpected randomless have been investigated. To detect if RSSI samples are time-dependent, the series test has been made for window size $w = 5$ and $w = 7$, which contains sequenced n samples. The test has been performed for the whole dataset (100 samples) in one choosen point where $RSSI_0$ reference value is obtained on d_0 equals to 1 m. We performed n-w tests on samples $x_1, x_2, \ldots x_{n-w}$. All performed tests have rejected hypothesis, that samples are time-independent and random. Obtained RSSI samples over time has been presented in fig. 4.

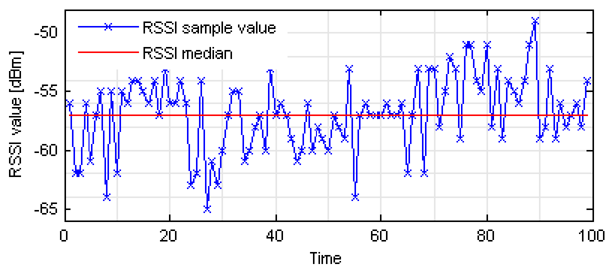

Fig. 4 RSSI samples vs. time on distance 1m

B. *The radiomap creation*

The trilateration algorithms (V.A. and V.B.) position estimation and validation of the tuned model of the radiomap have been created for the exemplary room. 100 RSSI samples from 5 different beacons in each radiomap point have been acquired. The radiomap has been placed on the 8m × 6m mesh with a gap of 1m (fig. 5).

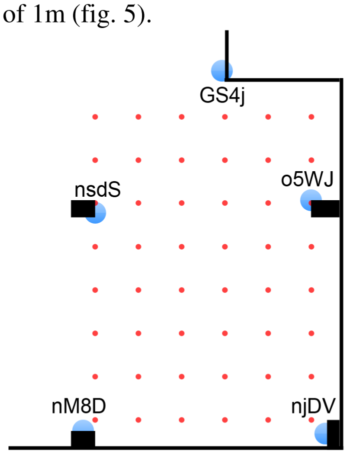

Fig. 5 Data acquisition points (red) from beacons (blue points).

A basic statistic like median for all accessible devices (anchors) in each point have been calculated. A beacon (an anchor) has been mounted under the ceiling (on the top part of wall to minimize furniture signal absorption) at the height 2m from the floor, but measurements have been collected at the height of 1m, because it seems to be natural smarphone position while using by human. Exemplary radiomap for one beacon device has been presented in fig 6.

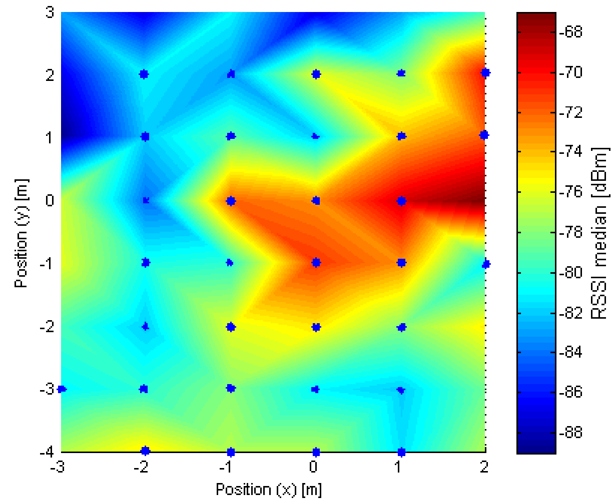

Fig. 6. Radiomap (RSSI mean value) for one beacon device placed in point P(2,0)

IV. Tuning Path-loss model

Formula (1) path-loss model has been tuned by using data collected in section III.A. Matlab environment has been used for fitting data with model (1). The Nelder-Mead simplex direct search, iterative method (known also as downhill simplex method) against quality function based on MSE of model has been used as an unconstrained nonlinear optimization method. The algorithm returns γ = -1.33379 for $RSSI_0$ equals to -56.8687 dBm (the model has been compared with the acquired data and result has been presented in fig 7a). The equation (1) can be transformed to (2) and the distance based on RSSI can be estimated what is presented in fig. 7b.

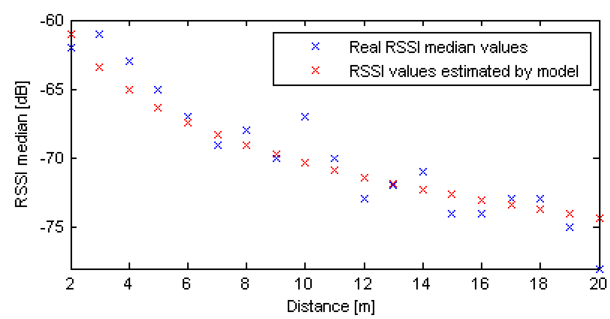

Fig. 7a Tuned path-loss model

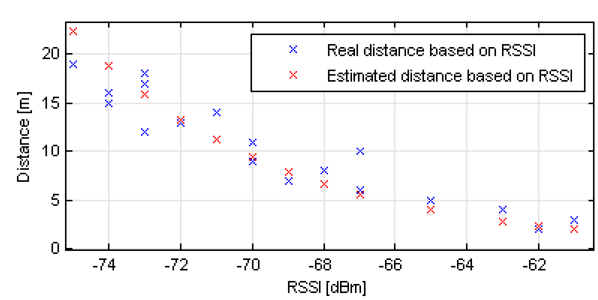

Fig. 7b Distance estimated by tuned model compared to real distance

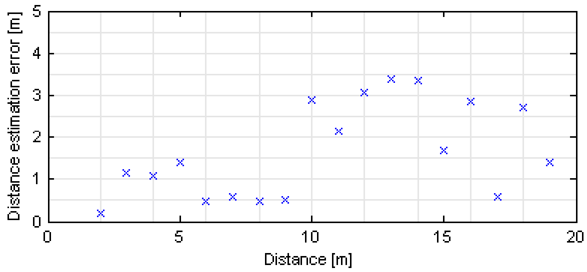

Fig. 7c Error of Distance estimation by tuned model over the distance

Fig. 7c presents the error between obtained model and mean measured distance. Its effectiveness and accessibility is true for the first 9 meters, but it is enough because it will be the most common distance from the beacon in small areas. In [5] the two-function path loss model has been proposed in which distance is estimated by different coefficients for near and far distances. In addition, only the nearest 3 beacons can be used to trilateration to reduce long distances from far beacons.

Another important data processing has been applied, i.e. a filter for input data. The survey should indicate if the processing is required and what kind of processing is preferred. Model (1) for distance estimation has been used based on the obtained data. The following methods of filtering data (all collected samples) in order to obtain a single *RSSI* reference value in a specific point have been applied:

- The average value of all samples acquired at a specific point over distance up to 20m (step 1m);
- The median value of all samples acquired at a specific point over distance up to 20m (step 1m);
- The average value after applying moving average filter with window size 6;
- The average value after deleting 50% samples of the input data at a specific point. The subset contains acquired RSSI with the smallest error with respect to the **average** of all data. (in short: Avg. of 50% near Avg.);
- The average value after deleting 50% samples of the input data at a specific point. The subset contains acquired RSSI with the smallest error with respect to the **median** of all data. (in short: Avg. of 50% near Median);

The aforementioned techniques allow for obtaining a single RSSI value (reference value) at a specific distance from the beacon. The results of distance estimation using filtering data are shown in figures 8a and 8b and also in Table 1.

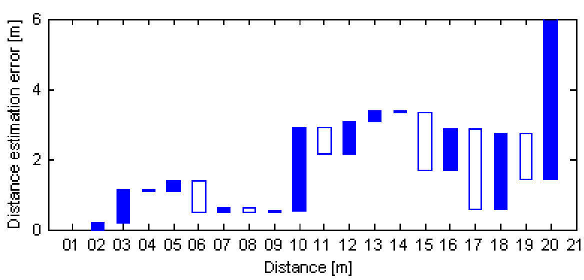

Fig. 8a. Error of Distance estimation by tuned model over the distance (Average method)

The candles plots represent the variation of errors changes over the distance. The Average value from the subset of 50% values that are near average value results in less standard deviation and less error dynamics. For both examples, the model is accurate enough in the range 0-9 m, while over 10 m dynamics of estimation error increases.

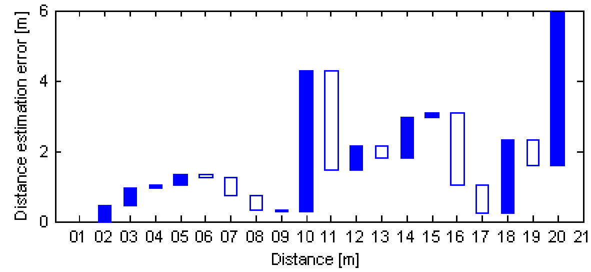

Fig. 8b. Error of Distance estimation by tuned model over the distance (Avg of 50% hist. values near Avg).

TABLE 1. PATH-LOSS MODEL DISTANCES ESTIMATION ERROR FOR PROPOSED DATA PROCESSING METHODS..

Method of transformation input data	$RSSI_0$ [dBm]	γ_{opt}	Avg. dist. estim. Error [m]
Median	-57	-1.41279	2.6533
Average	-56.87	-1.33379	2.4914
Moving average (window size 6)	-56.83	-1.41455	2.4696
Avg. of 50% near Avg.	-56.79	-1.33330	2.2703
Avg. of 50% near Median	-56.79	-1.41982	2.6799

As expected, rejecting 50% values from histogram that are not near average reduces standard deviation and final distance estimation error. In case of median value results are not better because of sorting phase while significant values can be shifted from the center.

V. TRILATERATION ALGORITHMS

There are two trilateration algorithms investigated for an unbounded n number of beacons at positions (x_i, y_i) and distances d_i.

A. *Algorithm 1*

Denote matrix $B_{n\times 2}$ as reference points and distances vector $R_{n\times 1}$:

$$B = \begin{bmatrix} x_1 & y_1 \\ x_2 & y_2 \\ \vdots & \vdots \\ x_n & y_n \end{bmatrix} \quad R = \begin{bmatrix} d_1 \\ d_2 \\ \vdots \\ d_n \end{bmatrix}$$

One primary reference point is selected $P_r(x_r, y_r)$ at the distance d_r, e. g. $B_1(x_1, y_1)$, and matrix $D_{(n-1)\times 2}$ for $I = 1 .. n$ and $I \neq r$ is filled as follows:

$$D = \begin{bmatrix} \vdots & \vdots \\ 2\cdot(x_r - x_i) & 2\cdot(y_r - y_i) \\ \vdots & \vdots \end{bmatrix}$$

Vector $B_{(n-1)\times 1}$ for $I = 1 .. n$ and $I \neq r$ is defined as follows:

ISBN: 978-1-61804-321-4

$$B = \begin{bmatrix} \vdots \\ x_r^2 - x_i^2 + y_r^2 - y_i^2 - d_r^2 + d_i^2 \\ \vdots \end{bmatrix}$$

Matrix $Q_{1 \times 2}$ indicates the final position of object relative to reference points and distances, by resolving equation:

$$Q = (D^T \cdot D) D^T \cdot B$$

B. Algorithm 2

Pick one primary reference point $P_r(x_r, y_r)$ at the distance d_r, e. g. $B_1(x_1, y_1)$, and matrix $H_{(n-1) \times 2}$ for $I = 1 .. n$ and $I \neq r$ is filled as follows:

$$H = \begin{bmatrix} \vdots & \vdots \\ x_i - x_r & y_i - y_r \\ \vdots & \vdots \end{bmatrix}$$

Vector $b_{(n-1) \times 1}$ for $I = 1 .. n$ and $I \neq r$ is defined as:

$$b = \begin{bmatrix} \vdots \\ \frac{1}{2}((x_i - x_r)^2 + (y_i - y_r)^2 - d_i + d_r) \\ \vdots \end{bmatrix}$$

Next, the equation is resolved:

$$H \cdot x = b$$

The final position is defined as matrix Q

$$Q = \begin{bmatrix} x_r \\ y_r \end{bmatrix}$$

After computing:

$$Q = x^T + [x_r \quad y_r]$$

VI. Experimental Results

The tuned model has been applied to surveyed roadmap to compare estimated distances and positions after trilatration. The reference value $RSSI_0$ has been obtained at d_0=1,532m distance. For each radiomap point the *RSSI* aggregate based on 100 samples has been calculated by using different methods of filtering and aggregating to single value presented in section IV.

Moreover, for all above aggregating methods the tuned model has been recalculated using the same method to obtain new γ_{opt} value. The average distance estimation error has been calculated as an absolute value of difference from model estimation and real distance, which is presented in the Table 2. The error has also been presented as heatmap in the fig 9.

Analyzing tab. 1 it can be said that for every case rebuilding model with the same method of filtering input data implicate lower distance estimation error: about 0.04m which is only ~2%. It is doubtful if model calibration for specific metric is needed. The results of estimating distance for radiomap (Table 2) are better than distance estimation presented for tuned model (Table 1) because almost all distances in radiomap are in the range 0-9 m, where estimation error is about 1 m for tuned model (fig. 7c).

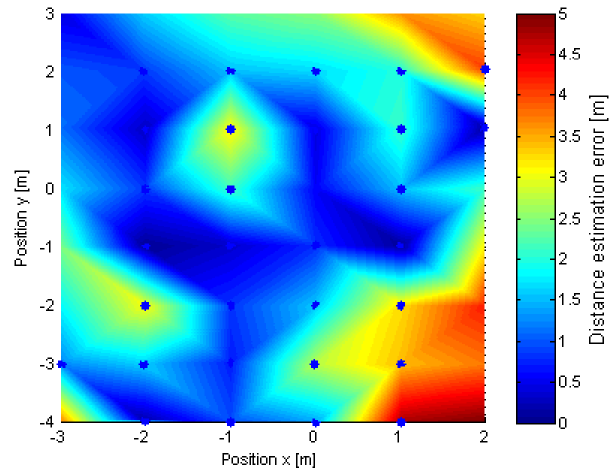

Fig. 9. Distance estimation error for one beacon device placed in point P(2,0)

TABLE 2. PATH-LOSS MODEL DISTANCES AND POSITIONS ESTIMATION ERROR – RESULTS.

Processing method	$RSSI_0$ [dBm]	γ_{opt}	Avg. distance estim. error [m]
Median	-81.00	-1.33379	2.20171
Average	-81.45	-1.33379 -1.41279♦	2.10073 2.06802♦
Moving average (window size 6)	-81.28	-1.33379 -1.41455♦	2.11107 2.06361♦
Avg of 50% near Avg	-80.90	-1.33379 -1.41982♦	2.23454 2.23513♦
Avg of 50% near Median	-81.56	-1.33379 -1.33330♦	2.15095 2.09592♦

The symbol ♦ denotes that model has been rebuilt with the data filtered the same method.

Estimated distances have been utilized as input parameters for trilateration algorithms to compute the final position. The average error of all points in a whole radiomap has been measured by comparing the estimated position and real radiomap position. Results have been presented in Table 3.

TABLE 3. PATH-LOSS MODEL DISTANCES AND POSITIONS ESTIMATION ERROR – RESULTS.

Method of transformation input data	$RSSI_0$ [dBm]	γ_{opt}	Avg. position error after trilateration [m]	
			Alg 1	Alg 2
Median	-81.00	-1.33379 n/a	2.90381	2.81877
Average	-81.45	-1.33379 -1.41279♦	2.76580 2.73706♦	2.44952 2.44984♦
Moving average (window size 6)	-81.28	-1.33379 -1.41455♦	2.78216 2.74580♦	2.45469 2.44152♦
Avg of 50% near Avg.	-80.90	-1.33379 -1.41982♦	2.93677 2.89945♦	2.58144 2.58771♦
Avg of 50% near Median	-81.56	-1.33379 -1.33330♦	3.02006 3.02047♦	2.65461 2.65490♦

The symbol ♦ denotes that model has been rebuilt with the data filtered the same method.

Second algorithm achieved better results. In each case the effectiveness of estimating position is strictly related with the

ISBN: 978-1-61804-321-4

quality of input data. Average-based methods given better results. It has been proven, the filtering methods give better results than calculating median, while the second approach to compute metric is less time and memory consuming. In addition, the error of distance estimation using average of 50% near average value which reduces the standard deviation of estimated distance significantly (Table 1 and Table 2) have no positive effect on trilateration algorithms results.

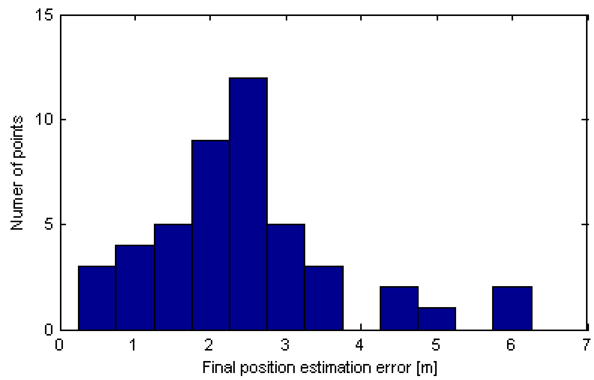

Fig. 10. Final position estimation error for whole radiomap.

Most of final position estimation errors after trilateration using second algorithm are less than 2.5m (60.87%), what is presented in fig. 10.

VII. Conclusion

Bluetooth Low Energy and iBeacon standard opened a new way to build low power based positioning techniques. Obtained RSSI can be used for estimation device positioning. Distance estimation model gives more information than standard API's defined in iBeacon standard, which returns only proximity range name if the object is immediate, near or far away (without estimating distance as a value). BLE is widely supported on devices so it can be utilized to customer's waypath or shop indoor segments tracking.

This paper reveals several facts about RSSI values from beacons. The proposed path-loss distance model is a good solution to determine device distance from the beacon in a range 1 – 9 m, because 1 m error is acceptable. The standard deviation of surveyed samples does not depend on distance from the beacon. Research proved that the wave multipath, interferation, diffraction has an impact on RSSI distribution, especially the human body absorbs the signal strength what should be included while determining position. Samples are not Gaussian distribution in all surveyed points.

In positioning context, the better results can be achieved by correlating RSSI's with accelerometer, gyroscope and other sensors. Another solution is to use more sophisticated metrics than Euclidean such us: excluding zones where object can not move, restricting situations when objects moved back while accelerometer measurements does not notice this fact.

When the data are analyzed massively (big-data context), the fuzzy set logic can be used on the edges of the areas which is being analyzed for determining it's traffic of popularity. On the edges of the area, the membership function can determine the certainty factor or quality of measurement in the final summary report.

References

[1] Hui Liu, Houshang Darabi, Pat Banerjee, and Jing Liu, "Survey of Wireless Indoor Positioning Techniques and Systems", IEEE Transactions on Systems, man and cybernetics - part C: Applications And Reviews, Vol. 37, No. 6, November 2007

[2] A. K. M. Mahtab Hossain and Wee-Seng Soh, "A comprehensive study of Bluetooth signal parameters for localization" on *The 18th Annual IEEE International Symposium* on PIRMC'07.

[3] Ambili Thottam Parameswaran, Mohammad Iftekhar Husain, Shambhu Upadhyaya, "Is RSSI a Reliable Parameter in Sensor LocalizationAlgorithms – An Experimental Study", Department of Computer Science and Engineering State University of New York at Buffalo, USA

[4] Matthew S. Gast, "Building Applications with iBeacon", O'Reilly Media, Inc., 2014, pages 13-18.

[5] Atreyi Bose and Chuan Heng Foh, "A Practical Path Loss Model For Indoor WiFi Positioning Enhancement", School of Computer Engineering, Nanyang Technological University, Singapore

[6] V.S. Abhayawardhana, I.J. Wassell, D.Crosby, M.P. Sellars, M.G.Brown "Comparison of Empirical Propagation Path Loss Models for Fixed Wireless Access Systems"

[7] Andreas F. Molisch, "Wireless Communications, Second Edition", John Wiley & Sons, Ltd, 2011, Appendix 7A – 7G

[8] Apple Inc., "Getting Started with iBeacon", Version 1.0, June 2, 2014 [Online]. Available: https://developer.apple.com/ibeacon/Getting-Started-with-iBeacon.pdf

Demonstration of gear ratios using mathematical software and the System SMPSL

Radek Nemec, Andrea Berkova, Stepan Hubalovsky
Faculty of Education, Department of Informatics, University of Hradec Kralove, Hradec Kralove, CZECH REPUBLIC
radek.nemec@uhk.cz, andrea.berkova@uhk.cz, stepan.hubalovsky@uhk.cz
http://www.uhk.cz

Abstract**—**This article describes development of Set for measuring the transfer gears. The display element is used SMPSL System. Set mechanism of transfer gears clearly defines the ratio between rounds. Set is constructed of three motors, one of which is driving and the other two driven. Driven engines therefore represent a speed sensor. System SMPSL is a measurement system using a computer in the school laboratory, which will be very cheap to assemble the hardware and software available for free. SMPSL system displays the speed of the driven wheels. For further idea of pupils there are used animations of gears in a dynamic interactive geometry GeoGebra.

Keywords**—** developing, DAQ, measurement system, computer aided experiment, measurement, datacollection, DIG GeoGebra

I. Introduction

THE goal of developing measurement transfer kits for gears demonstration of speed gears using the system SMPSL is the real speed of the display to the number of gears. This is due To produce an assembly for measuring the transfer gears and the possibility of measurement system for the measurement using a computer. SMPSL system [1], [2]. The system using constant during the measurement on the graph shows the progress [3]. Subsequently, work of gears is demonstrated to students through animations.

II. System SMPSL

System SMPSL was created by eProDas platform, Developed in the University of Ljubljana, Slovenia. [4] An important feature of the system is the ability to produce it yourself as much due to the very low price, thanks to freely available libraries and documentation. [5]

The hardware part of the system is connected via USB. The hardware part contains 4 analog inputs, 4 digital outputs and 1 analog output. See figure 1.

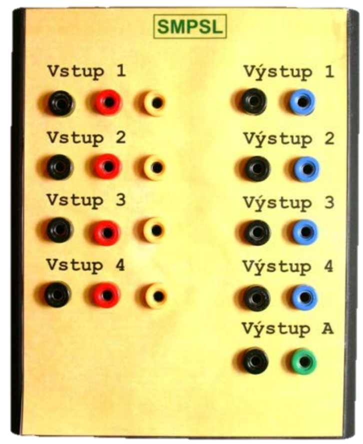

Fig. 1 - System SMPSL – hardware part

The software part allows the connection of hardware to your computer. The software is a user interface for measurement using a computer with which users control their own measurements, setup, operation and management of the system itself. See figure 2a, 2b.

Fig. 2a - System SMPSL – software part

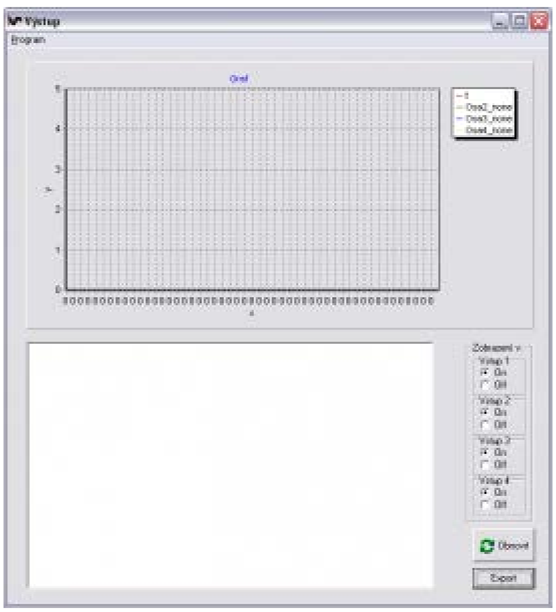

Fig. 2b - System SMPSL – software part

III. Set for measuring the transfer gears

Set for measuring the transfer gears to be composed of three motors and base of the company Merkur [6]. One is used as the source. Source engine is intended as a drive. It is powered by an external power supply. Another two electric motors are used as driven. It therefore outputs.

Set transfer mechanism gears serve to demonstrate the relationship between the individual wheels. This can be expressed using the variable named gear ratio i:

$$i = \frac{n_2}{n_1} = \frac{d_1}{d_2} = \frac{z_1}{z_2}$$

wherein n1 is the frequency of rotation of the drive wheel, n2 is the frequency of rotation of the driven wheel, d1 is the radius of the drive wheel radius d2 is driven gear z1 is the number of teeth of the driving wheel, z2 are numbers of teeth of the driven wheel.

The set uses gears with a given number of teeth. The drive wheel 34 is fitted with teeth. Driven wheels are fitted with castors on the number 34 and 83 teeth. On the basis of the relationship can be calculated ratio. SMPSL system displays the resulting stress on the driven wheels. Number of teeth of the drive wheel 34 is z1, the number of teeth of the driven gear in the first case z2 = 34. The ratio is 1: 1st In the second case the number of teeth of driven gear 83. Output Z2 = ratio 1: 1 (34:34) is 4.14 V. The output transfer 34:83 1.67 V. If the number of teeth substituted into relationship, so when released 34:83 ratio of teeth 1,7. As can be seen from the results, as well as constructed by measuring the ratio corresponds. [7] The real measurement shows theoretically calculated values. which is the main purpose of measurement using a computer. [8] the set for measuring transfer gears shown in Figures 3, 4 and 5.

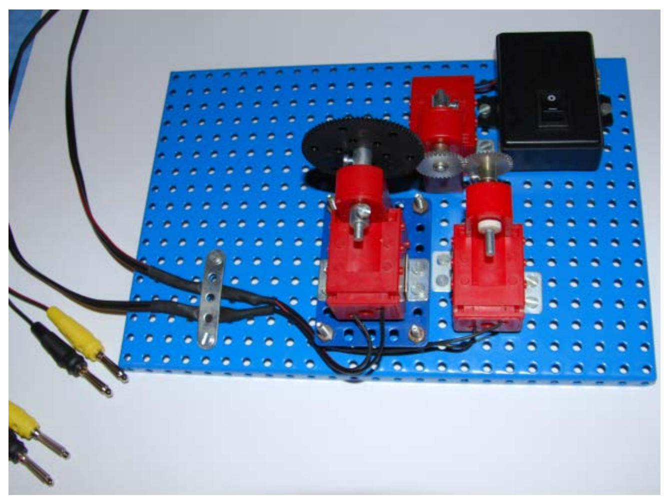

Fig. 3a - Set for measuring the transfer gears

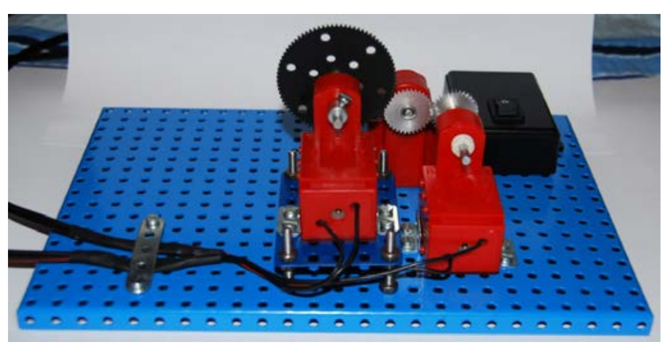

Fig. 3b - Set for measuring the transfer gears

ISBN: 978-1-61804-321-4

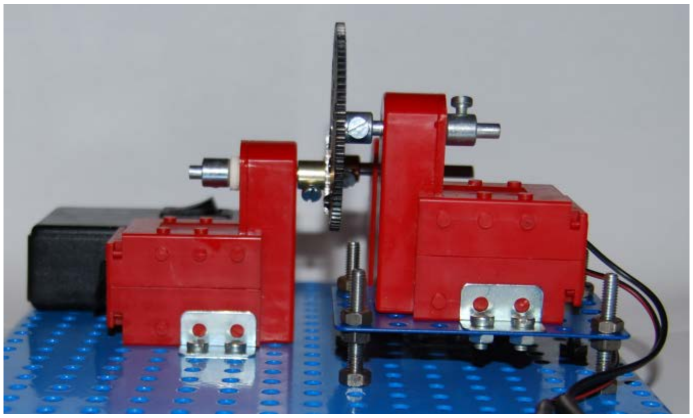

Fig. 3c - Set for measuring the transfer gears

IV. LABORATORY WORK

This laboratory work can be processed into prepared laboratory protocols. Pupils on the theory and leadership teacher creates predictions (hypotheses), is written and devise a procedure for their verification. An example can be seen in the following figure 6 and [9].

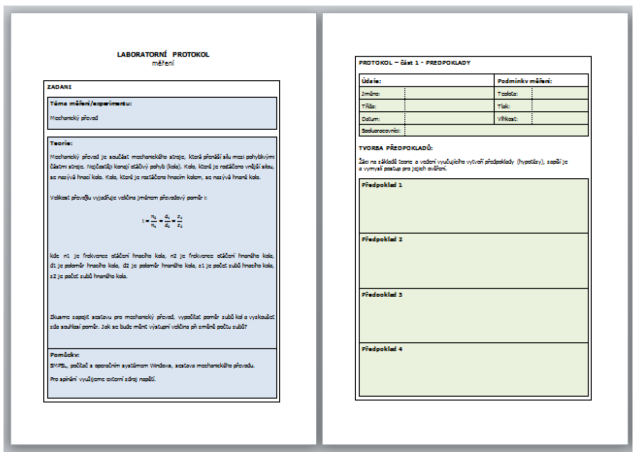

Fig. 4a - Laboratory protocol

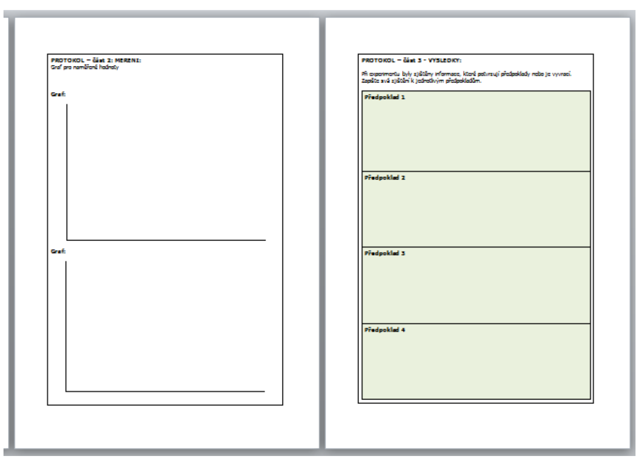

Fig. 4b - Laboratory protocol

V. DEMONSTRATIONS USING GEOGEBRA

In lessons of computer technology, pupils learn how to work with a dynamic interactive geometry system GeoGebra [10]. Following the laboratory work animations of gears are shown (Fig. 5) to students in computer technology lesson. The students have to then create their own similar (but simplified schematic only) animations to represent work of gears. in this work, therefore, there is a connection of school subjects. In this subject, therefore, there is a connection objects.

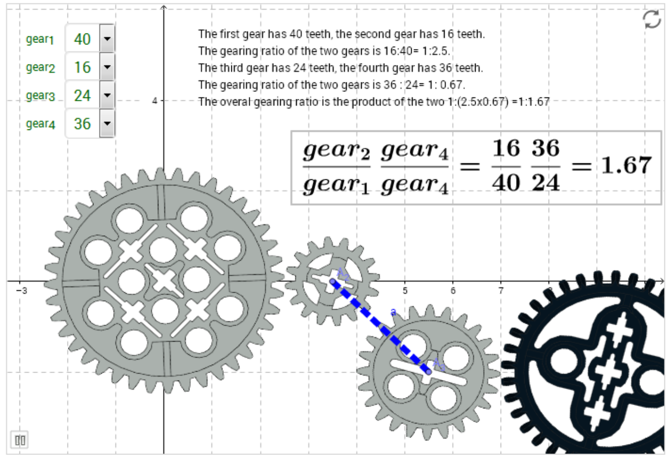

Fig. 5 - Gears in GeoGebra (taken from the materials available in [10])

VI. CONCLUSION

Set for measuring the transfer gears for demonstration of speed gears using the system SMPSL used to help demonstrate display wheel speed to ratio gears and thus confirm the theoretically calculated values and reality. The actual measurement and animations are for pupils more demonstrative than purely calculated value.

ACKNOWLEDGMENT

This research work has been supported by specific research project of University of Hradec Kralove, Faculty of Education in 2014 (No. 2146) and in 2015 (2142)

REFERENCES

[1] NĚMEC R., TŘÍSKA J., ŠEDIVÝ J. System SMPSL. In: The 4th NAUN International Conference on CIRCUITS, SYSTEMS, CONTROL, SIGNALS (CSCS '13). Valencia, 2013, ISBN: 978-960-474-318-6. P. 43-47.

[2] NĚMEC Radek., TŘÍSKA Jan., ŠEDIVÝ Josef. System for measurement using a computer in the school laboratory. In: International Journal of Education and Information Technologies, Volume 8, 2014, s 37-47, ISSN: 2074-1316

[3] NĚMEC, R., TŘÍSKA, J.. Natural experiments using ICT. In: Circuits, systems, control, signals (CSCS 2013) : proceedings of the 4th international conference. Athens: World scientific and engineering academy and society, 2013, s. 48-52. ISBN 978-960-474-318-6.

[4] COMLAB - Computerised Laboratory in Science and Technology Teaching: Home [online]. 2008 [cit. 2013-10-10]. Dostupné z WWW: <http://e-prolab.com/en/>.

[5] Data Acquisition system, Users' guide and programming manual [online]. 2007 [cit. 2013-10-20]. Dostupné z WWW: <http://lie.fe.uni-lj.si/eProDas/eProDas_Version_1_0.pdf>.

[6] Merkur [online]. 2014 [cit. 2014-12-30]. Dostupné z: http://www.merkurtoys.cz/

[7] ŠPILKA, R., MANĚNOVÁ, M. Screencasts as Web-Based Learning Method for Math Students on Upper Primary School. 2013. In. Recent Advances in Information Science: Proceedings of the 4th European Conference of Computer Science (ECCS´13). France: Paris 2013. ISBN 978-960-474-344-5. ISSN 1790-5109. pgs. 246-250

[8] HUBALOVSKA, M., HUBALOVSKY, Š. Implementation of the Systems Approach in Mathematical Modeling, Dynamic Simulation and Visualization Using MS Excel Spreadsheet. International Journal of Mathematics and Computers in Simulation. 2013, vol. 7, no. 2, pp. 267-276. ISSN 1998-0159.

[9] NĚMEC, Radek. Systém pro měření pomocí počítače ve školní laboratoři [online]. 2014 [cit. 2014-12-30]. Dostupné z: http://smpsl.radeknemec.cz/wp-content/uploads/21-Mechanick%C3%BD-p%C5%99evod.docx

[10] GEOGEBRA. [online]. [cit. 2015-07-02]. Dostupné z: http://tube.geogebra.org/

The research results of pedagogical experiment using measurement systems using computers in the Czech Republic

Radek Nemec, Andrea Berkova, Stepan Hubalovsky
Faculty of Education, Department of Informatics, University of Hradec Kralove, Hradec Kralove, CZECH REPUBLIC
radek.nemec@uhk.cz, andrea.berkova@uhk.cz, stepan.hubalovsky@uhk.cz
http://www.uhk.cz

Abstract—This article describes the results of research focused on the impact of the use of measurement systems using computers in school science laboratories to acquire more knowledge than when teaching without measurement system using a computer. The results showed a positive effect of the use of such systems at a significance level of 0.05.

Keywords—developing, DAQ, measurement system, computer aided experiment, measurement, datacollection.

I. Introduction

THE research was conducted at the secondary school in the Czech Republic. The system SMPSL [1], [2], [3] for measuring using a computer was used in experimental group to support teaching of physics. Lessons of physics were managed in the traditional way in the control group (with the support of only the blackboard, textbooks, etc.). The didactic test in CAA (Computer-aid assessment) Maple TA [4] focused on the topic of temperature [5], [6] was statistically processed at a significance level of 0.05 (95%) in MS Excel and NCSS. The results were evaluated using the following methods: Two-sample F-test for the conformity of variances. Then there was applied to two-sample t-test to test the hypothesis of equality of means of control and experimental group.

II. Used instruments

System SMPSL was designed as a cheap and flexible interface for recording the values of transmitting using via USB interface (Fig. 1 and 2). System SMPSL is based on eProDas platform, resulting in the University of Ljubljana, Slovenia. eProDas is very affordable system, easily attachable to a computer, offering many possibilities of measuring and processing of data. It is suitable for science experiments. eProDas is seen as a platform for providing data acquisition and signal generation for performing different experiments in the natural sciences such as physics, chemistry, biology, medicine, mathematics and engineering. SMPSL system consists of hardware delivery and control software available for free. Instructions for the preparation of the hardware and instructions for downloading software controls are on the website of this system: http://smpsl.radeknemec.cz.

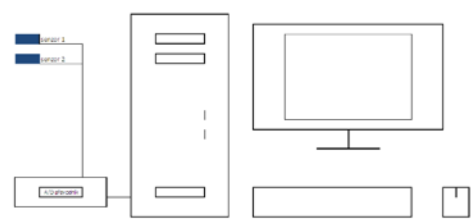

Fig. 1 – System for measuring using a computer

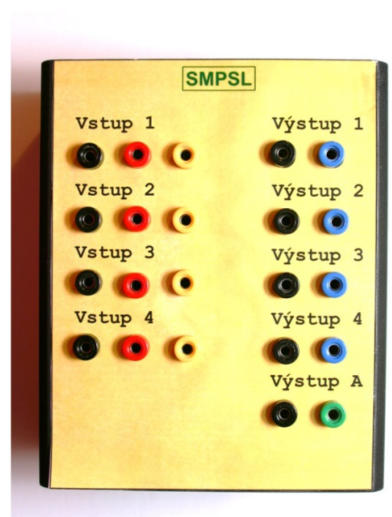

Fig. 2 – System SMPSL

As already mentioned, for examining differences in pupils' knowledge was created objectively scored didactic test, which were used as pre and posttests. For the creation of didactic test the CAA system Maple TA was used. Maple T.A (Web-based Testing and Assessment for Math Courses) is an educational system distributed by Maplesoft to support training mathematics and science subjects [7]. Maple T.A provides students rich interactive environment using CAS (Computer Algebra System) Maple. Inside tests there were included

ISBN: 978-1-61804-321-4

questions of various types. Maple TA program allows creation of a whole range of different types of questions (Fig. 3).

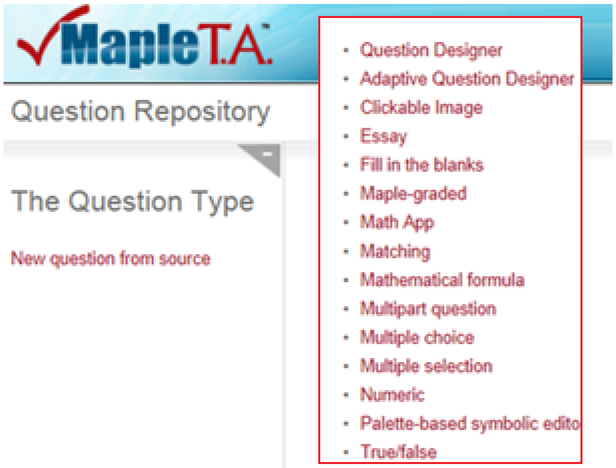

Fig. 3 The Question types in Maple TA

To maintain objectivity mainly closed questions (eg. multiple choice) exceptionally open questions with brief answers were selected.

III. Pretest

Before the execution of research there has been pretest to determine comparable knowledge of control and experimental groups [8].

The results are summarized in the following tables:

	Control gr.	*Exp. gr.*
Expected value	3,636364	3,52381
Variance	3,385281	2,361905
Observation	22	21
Difference	21	20
F	1,433284	
P(F<=f) (1)	0,212466	
F crit (1)	2,112399	

Fig. 4 F-test of pretest

Hypothesis of identical variances was not rejected because the test criterion F was smaller than F crit (Fig. 4). It was further applied to the two-sided T-test to determine whether pupils from both the control and experimental groups have comparable knowledge before the experiment. The reader can get acquainted with the results in Figure 5.

	Control gr.	*Exp. gr.*
Expected value	3,636364	3,52381
Variance	3,385281	2,361905
Observation	22	21
The common variance	2,886073	
Hyp. median difference values	0	
Difference	41	
t Stat	0,217167	
P(T<=t) (1)	0,414578	
t crit (1)	1,682878	
P(T<=t) (2)	0,829155	
t crit (2)	2,019541	

Fig. 5 T-test of pretest

The test criterion t is less than t crit and therefore the hypothesis of identical means is not rejected. I tis assumed that pupils from both the control and experimental groups have comparable knowledge before teaching itself.

IV. Posttest

The experiments use of research focused on the impact of the use of measurement systems using computers in school science laboratories to acquire more knowledge than when teaching without measurement system using a computer are as follows. Is it measuring of temperature - measurement of melting ice (fig. 6), measurement of deflection of roller (fig. 7 and 8), light metering (fig. 9), measurement of charging and discharging of capatitor (fig. 10).

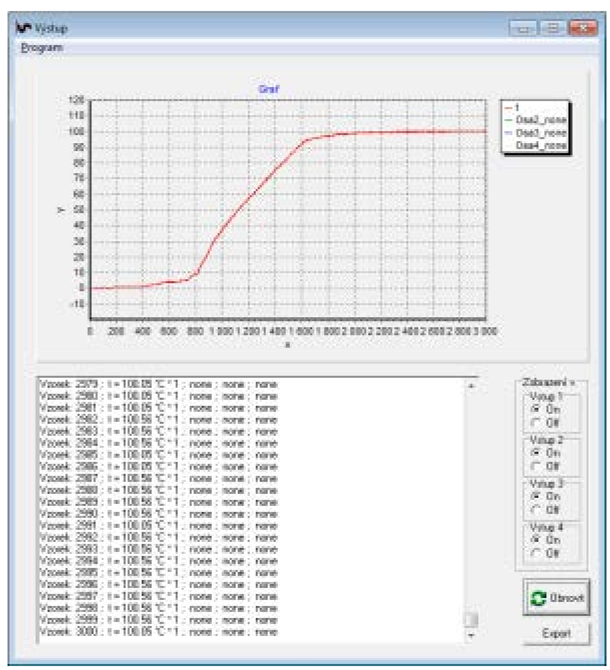

Fig. 6 - Measurement of melting ice

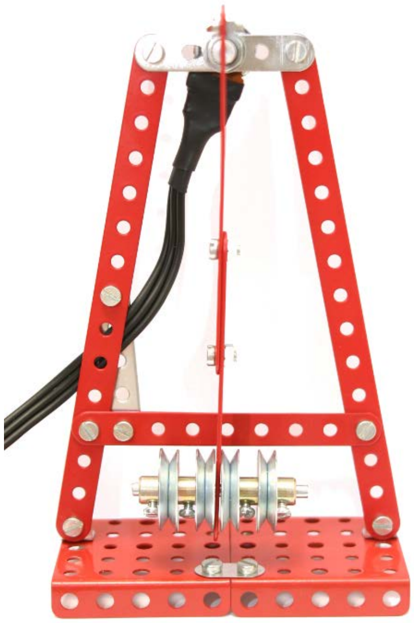

Fig. 7 - Measurement of deflection of roller

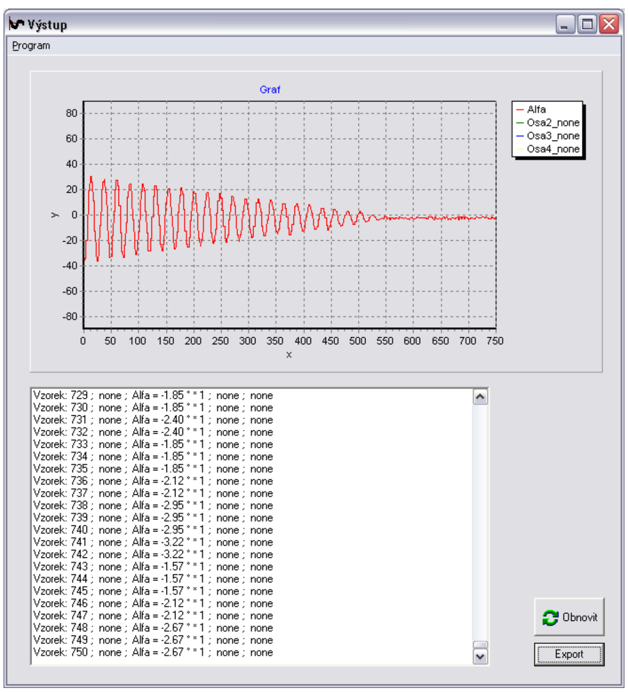

Fig. 8 - Measurement of deflection of roller

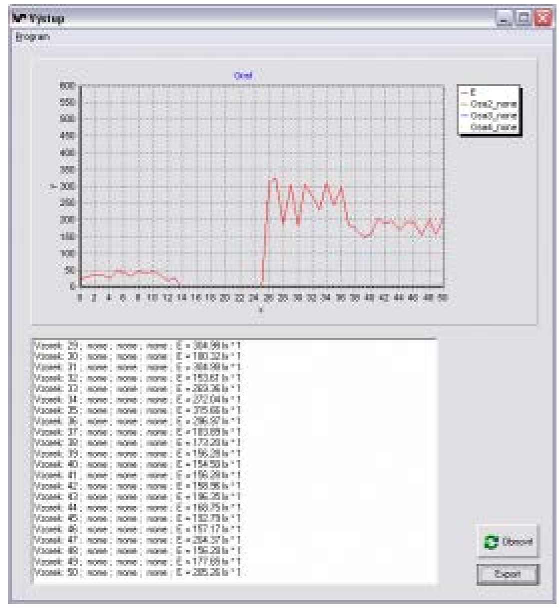

Fig. 9 - Light metering

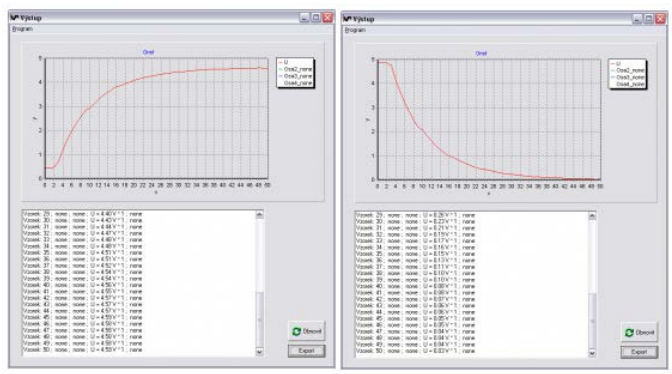

Fig. 10 - Measurement of charging and discharging of capatitor

For the implementation of these attempts and experiments were developed on the site of a series of typical tasks and video clips. Examples of types of tasks are shown in the following figure 11.

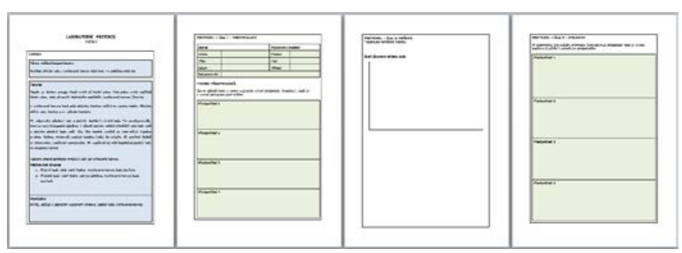

Fig. 11 – Examples of types of tasks

Therefore, it was subsequently conducted an experiment - teaching control and experimental groups ended with posttest (pretest identical).

ISBN: 978-1-61804-321-4

Posttest results are as follows:

	Control gr.	*Exp. gr.*
Expected value	4,909090909	8,952381
Variance	4,467532468	2,447619
Observation	22	21
Difference	21	20
F	1,825256456	
P(F<=f) (1)	0,091975987	
F crit (1)	2,112398899	

Fig. 12 F-test of posttest

The hypothesis of identical variance whereas the F test criterion is smaller than F crit is not rejected (Fig 12). Therefore, T-test can be used again (Fig 13).

	Control gr.	*Exp. gr.*
Expected value	4,909090909	8,952381
Variance	4,467532468	2,447619
Observation	22	21
The common variance	3,482208848	
Hyp. median difference values	0	
Difference	41	
t Stat	-7,102222093	
P(T<=t) (1)	5,91293E-09	
t crit (1)	1,682878002	
P(T<=t) (2)	1,18259E-08	
t crit (2)	2,01954097	

Fig. 13 T-test of posttest

Based on these results it is suggested that students in the experimental group showed acquisition of more knowledge than when teaching without measurement system using a computer. This can be seen in the box plot (Fig. 14). [9]

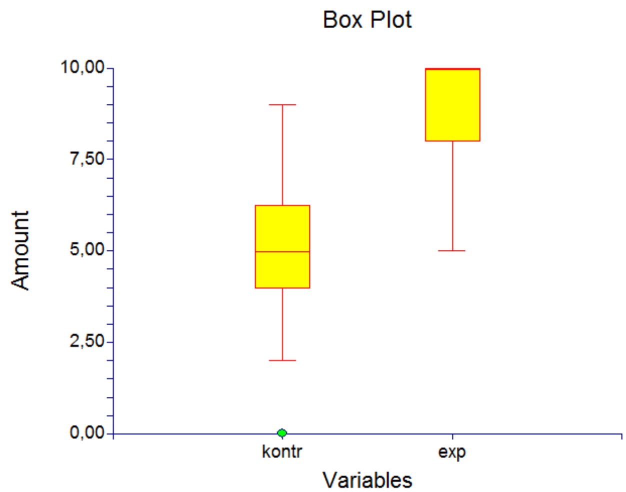

Fig. 14 Box plot of posttest

V. Conclusion

Use of systems for measurement using a computer, as indicated by the research found a positive effect on the acquisition of more knowledge in the field of temperature in the Czech secondary school. The results of the acquisition of knowledge, as shown by the Box plot, are considerably higher.

Two months after the experiment there will be performed new measurement (retest) and it will be determined whether the use of measurement systems using computers has a positive effect on the acquisition of knowledge among pupils.

Acknowledgment

This research work has been supported by specific research project of University of Hradec Kralove, Faculty of Education in 2014 (No. 2146) and in 2015 (2142)

References

[1] NĚMEC R., TŘÍSKA J., ŠEDIVÝ J. System SMPSL. In: The 4th NAUN International Conference on CIRCUITS, SYSTEMS, CONTROL, SIGNALS (CSCS '13). Valencia, 2013, ISBN: 978-960-474-318-6. P. 43-47.

[2] HUBALOVSKY, S., Modeling and simulation of real experimental device - seven storey rectification column. In: WSEAS International Conference on System Theory and Scientific Computation (ISTASC'11), Florence, WSEAS Press, 2011, p. 63 -68, ISBN 978-1-61804-027-5.

[3] HUBALOVSKY, S., HANZALOVA, P., Modeling, simulation and visualization of automatic cryptoanalysis of the short monoalphabetical substituted cipher text. In: International Journal of Mathematics and Computers in Simulation. Issue 2, Vol. 7, 2013, p. 134–143. ISSN 1998-0159.

[4] BERKOVA, A, Approaches to learning and studying in mathematical analysis classes. In 8th International Technology, Education and Development Conference, Valencia, Spain. 2014. ISSN: 2340-1079. Publisher: IATED.

[5] NĚMEC R., HUBÁLOVSKÝ Š.. The use systems for measurement using a computer in the school laboratory to explanation for temperatures during the water heating, In: 18th International Conference on Circuits, Systems, Communications and Computers (CSCC '14),

Advances in Educational Technologies. Athens: World scientific and engineering academy and society, 2014, s. 103-107. ISBN: 978-1-61804-238-5

[6] NĚMEC, R., TŘÍSKA, J.. Natural experiments using ICT. In: Circuits, systems, control, signals (CSCS 2013) : proceedings of the 4th international conference. Athens: World scientific and engineering academy and society, 2013, s. 48-52. ISBN 978-960-474-318-6.

[7] *Maple T.A. - Web-based Testing and Assessment for Math Courses* - Maplesoft. [online]. [cit. 2015-05-26]. Available: http://www.maplesoft.com/products/mapleta.

[8] NĚMEC Radek., TŘÍSKA Jan., ŠEDIVÝ Josef. System for measurement using a computer in the school laboratory. In: International Journal of Education and Information Technologies, Volume 8, 2014, s 37-47, ISSN: 2074-1316

[9] ŠPILKA, R., MANĚNOVÁ, M. Screencasts as Web-Based Learning Method for Math Students on Upper Primary School. 2013. In. Recent Advances in Information Science: Proceedings of the 4th European Conference of Computer Science (ECCS´13). France: Paris 2013. ISBN 978-960-474-344-5. ISSN 1790-5109. pgs. 246-250

The new method of investigation of the problem of synchronization electrical machine with power network.

D. SKUBOV, K. KHODZHAEV
Department mechanics and processes of control
St.-Petersburg Polytechnic University, IPME RAS
195251, Russia, St.-Petersburg, Polytechnicheskay str. 29
RUSSIA
skubov.dsk@yandex.ru

Abstract: - Connecting a generator to the network, either in a normal regime or under a significant load change, is possible with greater (than commonly accepted now) initial differences between the rotor speed and the frequency of the stator current, OR, possible with small frequency differences and any misalignment angle between the magnetic axis of spinning rotor and the rotary electro-magnetic field of the stator.

Key-Words: - synchronous electric machines, powerful network, transient processes, Routh's structure of asymptotically simplified equations

1. Introduction

In modern turbine-generators, the control system which maintains voltage at the output is based on feedback control (or, direct control based on the given voltage). The modern high power machines use the rotary field, with another low-power excitation generator mounted on the same shaft as the main generator. The embodiment often includes a high-frequency electromechanical excitation generator based on non-contact inductor generators, as well as thyristor brushless excitation systems with a rotating transformer, et al. This control system can be simplified or enhanced based on this study.

The study investigated the regimes of direct synchronization of a turbine-generator unit with the power network. "Direct" here implies that a voltage at the stator windings is set (predetermined) in the form of harmonic functions of a given amplitude and frequency (50 or 60 Hz), the voltage at the windings is ~ 10 kV and current ~ 20 kA, and therefore, the power is in the range 100-300 MW. It is assumed that the output voltage of the generator is set (predetermined), although the practice its modification is possible.

The problem of direct synchronization (without control) is modeled as a transition process when the generator is connected to the network under the given initial conditions, which include: the misalignment angle between the magnetic axis of spinning rotor and of the electro-magnetic field of the stator, which rotate with frequency of 50/60 Hz (the last rotate due to distribution of the stator three-phase winding), and the initial difference in the rotational speeds of the rotor and the stator field (slip).

The basics of the mathematical model of synchronous machine are well known (see, for example [4], [5], [7], [8]) and the transient processes are under consideration we can make the main following assumptions:

a) Only the first harmonic with the spatial period equal to the double pole division is taken into account when the spatial distribution of the fields of self-induction of windings of the rotor and stator is considered;

b) A real damper winding (for explicit-pole machines) or the rotor body acting as a damper winding (for implicit-pole machines) is replaced by two equivalent damper contours located in longitudinal (contour t) and transversal (contour k) axes of the machine. Longitudinal axis of the rotor d passes through the mid-pint of the rotor pole and has the direction coinciding with the direction of the magnetic field of the excitation winding. The direction of the current in the longitudinal damper contour is positive if the direction of magnetic flux due to this current is coincident with the positive direction of axis d. The transverse axis of rotor q is located between the neighbouring magnetic poles of rotor and forms the angle of 90 electric degree to axis d. The positive direction of axis q is that for which this axis is behind axis d. The positive direction of current in contour k coincides with that in contour t;

c) The phase windings of the stator (anchor) are spools distributed over the stator circumferences and connected to each other by means of the star-connection or delta connection. The magnetic axes of the three-phase system of spools a, b, c are shifted to each other on 120 electric degree. Without loss of generality, in what follows we consider the model of implicit-pole synchronous machine with a three-phase stator winding. The location of the contours of the idealized model of synchronous machine is shown in Fig.1

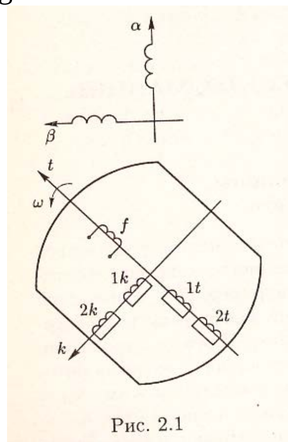

Fig.1

2. Problem formulation

The problem of reducing equations of the synchronous machine in the case of powerful network is considered in most books on transient processes in synchronous machines (see [5], [8]]). The full description of this model used Park-Gorev transformation [1] you can find, for example in [5]. These equations have Lagrange-Maxwell form for electromechanical systems in quasi stationary electromagnetic field

$$
\begin{aligned}
&\frac{d}{dt}\left[Li_a + M\cos\frac{2\pi}{3}(i_a+i_b) + (M_f i_f + M_t i_t)\cos\vartheta - M_k i_k \sin\vartheta\right] + R_a i_a + R_0 i_0 = U\cos\Omega_0 t, \quad (a,b,c)\\
&\frac{d}{dt}\left\{M_f\left[i_a\cos\vartheta + i_b\cos\left(\vartheta-\frac{2\pi}{3}\right) + i_c\cos\left(\vartheta+\frac{2\pi}{3}\right)\right] + L_f i_f + M_{ft} i_t\right\} + R_f i_f = 0,\\
&\frac{d}{dt}\left\{M_t\left[i_a\cos\vartheta + i_b\cos\left(\vartheta-\frac{2\pi}{3}\right) i_c\cos\left(\vartheta+\frac{2\pi}{3}\right)\right] + L_t i_t + M_{ft} i_f\right\} + R_t i_t = 0,\\
&\frac{d}{dt}\left\{-M_k\left[i_a\sin\vartheta + i_b\sin\left(\vartheta-\frac{2\pi}{3}\right) + i_c\sin\left(\vartheta+\frac{2\pi}{3}\right)\right] + L_k i_k\right\} + R_k i_k = 0,\\
&J\frac{d^2\vartheta}{dt^2} = -\left\{(M_f i_f + M_t i_t)\left[i_a\sin\vartheta + i_b\sin\left(\vartheta-\frac{2\pi}{3}\right) + i_c\sin\left(\vartheta+\frac{2\pi}{3}\right)\right] + M_k i_k\left[i_a\cos\vartheta + i_b\cos\left(\vartheta-\frac{2\pi}{3}\right) + i_c\cos\left(\vartheta+\frac{2\pi}{3}\right)\right]\right\} + M_m,\\
&\frac{d\vartheta}{dt} = \Omega \qquad (1)
\end{aligned}
$$

It is also possible to pass on to the introduced system of relative units from any known system of relative units, say from the system x_{ad} or from the system of equal magnetomotive forces (mmf) [5]. After what we introduce non-dimensional currents and flux linkages in axes d. The final expressions for the flux linkages in the introduced system of relative units are as follows

$$
\begin{aligned}
\Psi_d &= (1+\sigma_d)i_d + i_f + i_t,\\
\Psi_f &= i_d + (1+\varepsilon_r\sigma_f)i_f + i_t,\\
\Psi_t &= i_d + i_f + (1+\varepsilon_r\sigma_t)i_t, \qquad (2)\\
\Psi_q &= (1+\sigma_q)i_q + i_k,\\
\Psi_k &= i_q + i_k,
\end{aligned}
$$

where

$$
1+\sigma_d = \frac{L_d}{L_{ad}},\ 1+\sigma_q = \frac{L_q}{L_{aq}},\ 1+\varepsilon_r\sigma_f = \frac{L_q}{L_{af}},\quad 1+\varepsilon_r\sigma_t = \frac{L_t}{L_{at}},
$$

$$
L_{ad} = \frac{3}{2}\frac{M_f M_t}{M_{ft}},\ L_{af} = \frac{M_f M_{ft}}{M_t},\quad L_{at} = \frac{M_t M_{ft}}{M_f}
$$

more detail about introducing non-dimensional variables you can see in [8]. It's important that small parameters $\varepsilon_r\sigma_f$ and $\varepsilon_r\sigma_t$ characterize the dissipation between contours t and f. Subtracting expression for Ψ_t from expression for Ψ_f in equation (2) we obtain

$$
\varepsilon_r\Psi_r = \Psi_f - \Psi_t = \varepsilon_r(\sigma_f i_f - \sigma_t i_t),
$$

where the quantity Ψ_r is proportional to the flux linkage of the dissipation between the excitation winding and the damper contour in longitudinal axis. Parameter ε_r is small because this dissipation is small as compared with the main flux. However parameter ε_r is not small for hydrogenerators and some types of turbogenerators, in this case the asymptotic transformation of equations of synchronous machine is carried out in [12].

When modelling the initial non-linear system (using Park-Gorev equations), three important small parameters are introduced: it is assumed that the network period (0.02 sec) is more small with respect to the decay time (0.4-0.5 sec) of the transient processes in the damper circuits (such as the rotor body wholly as a steel cask), and the ratio of the network period to the mechanical time constant, which determined as ratio of amplitude kinetic energy of rotation and machine power. These expressions the next:

$$
\varepsilon = \frac{1}{\omega_* T_k},\ \varepsilon_f\nu_f = \frac{R_a T_k}{L_{ad}},\ \varepsilon_f e_f = \frac{E_f T_k}{L_{af}\, i_{d*}},
$$

ISBN: 978-1-61804-321-4

$\varepsilon_\omega = \frac{3}{2}\frac{L_{ad}\, i_{d*}^2 T_k}{J\omega_*}$,

where $T_k = \frac{L_k}{R_k}$ denotes the time constant of the damper contour in axis k. The main small parameter $\varepsilon = 1/\omega_* T_k$, where ω_* denotes the synchronous frequency, is given by ratio of the period of network voltage to the time constant of damper contour. This parameter is small for all synchronous machines (for turbogenerators its characteristic value is 0.02).

3. Problem Solution

Before we proceed to derivation of the asymptotically simplified equations for synchronous machine let us explain a necessity of using axes $\alpha, \beta, 0$ for separation of slow processes in the stator circuits. As follows from equations for the stator circuits in axes d, q, in the transient regime variables Ψ_d, Ψ_q have a fast oscillating component. In the case of the small sliding these equations are quasi-linear, therefore transient to the axes α, β (Fig.1) is somehow equivalent to the Van-der-Pol replacement in the theory of nonlinear oscillations.

After that the asymptotic averaging method for analysis of transient process at connecting a generator to the network is used. The asymptotically simplified equations of the transient processes can be written down in the form

$$\begin{aligned}
&\dot{\Psi}_f + \frac{r_f}{l}\left(\Psi_f - \gamma cos\delta\right) = e_f,\\
&\dot{\Psi}_k + \frac{r_k}{l}\left(\Psi_k - \gamma sin\delta\right) = 0, \qquad (3)\\
&\kappa\ddot{\delta} + \frac{\gamma}{l}\left(\Psi_f sin\delta + \Psi_k cos\delta\right) = m.
\end{aligned}$$

The new variable $\delta = \vartheta - \vartheta_0$ is an angle of rotor rotation “relative to the network”, where $\vartheta_0 = \omega_* t$ and $s = \dot{\delta}$ is a sliding. Additionally, another dimensionless “slow” time $\tau = \sqrt{\varepsilon\varepsilon_\omega/\sigma_d}\,\omega_* t$ is introduced. Variable δ formally is fast (the rate of change is of the order of unity), but we consider only the motions under which sliding is small and δ changes slowly. This corresponds to analysis of particular solutions of the system with two fast phases in the case of principle resonance. Here dimensionless parameters have expressions

$$r_f = \sqrt{\frac{\varepsilon\sigma_d}{\varepsilon_\omega}}\frac{\varepsilon_f \nu_f \nu_t}{\left(\nu_f + \nu_t\right)}, r_k = \sqrt{\frac{\varepsilon\sigma_d}{\varepsilon_\omega}}\nu_k \kappa = \frac{1}{\sigma_d},$$

$$l = \frac{\sigma_d}{1+\sigma_d}, \gamma = \frac{u}{\sigma_d}, \nu_n = \frac{R_a T_k}{L_{at}}, \nu_t = \frac{R_t T_k}{L_{at}}.$$

Equations (3) have a structure of Routh’s equations in which Ψ_f and Ψ_k are the quasi-cyclic generalized momenta and δ is the positional generalized coordinate. This allows one to make use Lagrange equations which are more comfortable in this case. Let us introduce the currents (generalized velocities)

$$I_f = \frac{1}{l}\left(\Psi_f - \gamma cos\delta - \frac{l e_f}{r_f}\right), I_k = \frac{1}{l}\left(\Psi_k + \gamma sin\delta\right)$$

We obtain the equations

$$\begin{aligned}
&l\dot{I}_f - \gamma\dot{\delta} sin\delta + r_f I_f = 0,\\
&l\dot{I}_k - \gamma\dot{\delta} cos\delta + r_k I_k = 0, \qquad (4)\\
&\kappa\ddot{\delta} + \gamma\left(I_f sin\delta + I_k cos\delta\right) + \frac{\gamma e_f}{r_f} sin\delta = m.
\end{aligned}$$

It is remarkable that the averaged equations has a more smaller dimension and preserve the Lagrangian structure (they described a pendulum with a damping conducting circuit, rotating together with the pendulum in a constant magnetic field, Fig. 1[1])

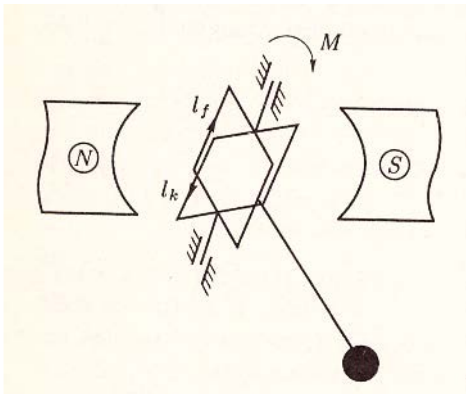

Fig.2

These equations (4) describe both swinging of the rotor of synchronous machine and the motions of pendulum with the magneto-electric extinguishers [13] subjected to gravity and external moment m with the only difference that for the pendulum the factor γe_f must be replaced by another dimensionless parameter. In this case the extinguishers have a single contour with currents I_f and I_k and these contours’ planes being mutually perpendicular and the coefficient of mutual induction between the contours being equal to zero. The contours are placed in the homogeneous magnetic field and exhibit angular vibra-

[1] Non-Linear Electromechanics” by D. Skubov, K. Khodzhaev, Springer, 2008

ISBN: 978-1-61804-321-4

tions or revolve when the pendulum vibrates and rotates, see Fig.2.
In the case in which the inductance l is negligible in eq. (4) and the resistances are equal to $r_f = r_k = r$, this system reduces to the well-known Tricomi equation [2], [7], [11]

$$\ddot{\delta} + \beta\dot{\delta} + sin\delta = \tilde{m}, \qquad (5)$$

where the differentiation is performed with respect to dimensionless time $\tau = \Omega t$ and $\Omega^2 = \frac{\gamma e_f}{r\kappa}, \beta = = \frac{\gamma^2}{r\Omega}, \tilde{m} = \frac{m}{\kappa\Omega^2}$. If $\tilde{m} < 1$, eq.(4) has two equilibrium position $\delta_* = arcsin\frac{m}{\gamma e_f}$ and $\pi - \delta_*$ for the zero currents I_k, I_f and sliding $\dot{\delta} = 0$. For the pendulum without extinguishers the first equilibrium is stable and the second one is unstable. The extinguishers strengthen stability, i.e. a stable equilibrium becomes asymptotically stable whereas an unstable equilibrium remains unstable. If we are changing initial value of sliding so for stationary solution of system (4) we can obtain as stable equilibrium position or rotatory motions of the pendulum which correspond periodic motion in $\dot{\delta}$ with a constant mean value after the sliding period $\dot{\delta} > 0$ (for $m > 0$) what for synchronous machine is equivalent to asynchronous motion. Our task consists in finding as themselves rotations so relation of parameters determining the type of transient process. Moreover the considerable interest has a solution of the problem of investigation the transient processes at switching of load of synchronous electric motor namely the possible level of jump of load. Rotatory motions of the equivalent pendulum are analysed with the help of method of harmonic balance. Used the replacement

$$\begin{aligned} x_1 &= I_f sin\delta + I_k cos\delta, \\ x_2 &= I_f cos\delta - I_k sin\delta \end{aligned}$$

and introducing the independent variable δ instead t in eq. (4) yields

$$\begin{aligned} &\omega x_1' - \omega x_2 - \gamma\omega + r x_1 = 0, \\ &\omega x_2' + \omega x_1 + r x_2 = 0, \\ &\omega\omega' + \gamma x_1 + e_f sin\delta + \beta\omega = m \end{aligned} \qquad (6)$$

Approximate rotatory solutions of eq. (6) is sought in the form

$$\begin{aligned} \omega &= \omega_0 + \omega_s sin\delta + \omega_c cos\delta, \\ x_1 &= x_{10} + x_{1s} sin\delta + x_{1c} cos\delta, \\ x_2 &= x_{20} + x_{2s} cos\delta - x_{2c} sin\delta \end{aligned} \qquad (7)$$

After substitution (7) into (6) we obtain cubic equation for constant component of ω

$$\beta\omega_0^3 - m\omega_0^2 + (r^2\beta + \gamma^2 r)\omega_0 - mr^2 = 0 \quad (8)$$

and the constant components of fluxes

$$x_{10} = \frac{\gamma r\omega_0}{\omega_0^2 + r^2}, \quad x_{20} = -\frac{\gamma\omega_0^2}{\omega_0^2 + r^2} \qquad (9)$$

The Descartes rule gives that equation (8) has three real positive roots. For parameters, corresponding turbogenerator TVV-200 MWT the graph of eq. (8) is shown on Fig.3

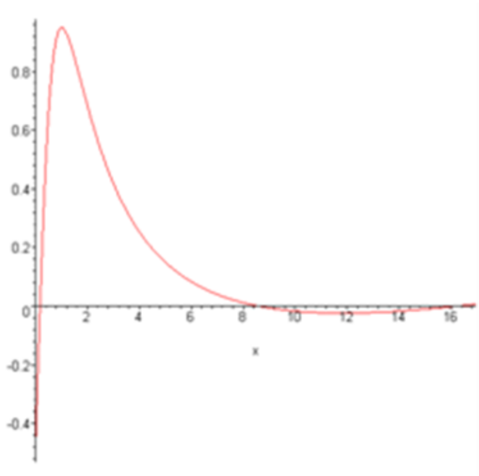

Fig.3

Two last roots completely coincide with results of calculation of Cauchy problem for system (6) and middle mode is unstable and mode with greater root is stable. The question founding the attractive field of the mode with first lesser value of ω_0 is more difficult and now have not solution.
The graphs of transient processes at different initial values of sliding $s(0)$ are shown on Fig.4. The initial fluxes are determined from condition of switching of machine with power network at initial misalignment angle between the magnetic axis of spinning rotor and of the electromagnetic field of the stator, which in our case equal $\delta_0 = \pi/3$. At these Fig.4 next designations are input $x4(t) = \dot{\delta}$ and $x1(t) = x_1$, $x2(t) = x_2$.

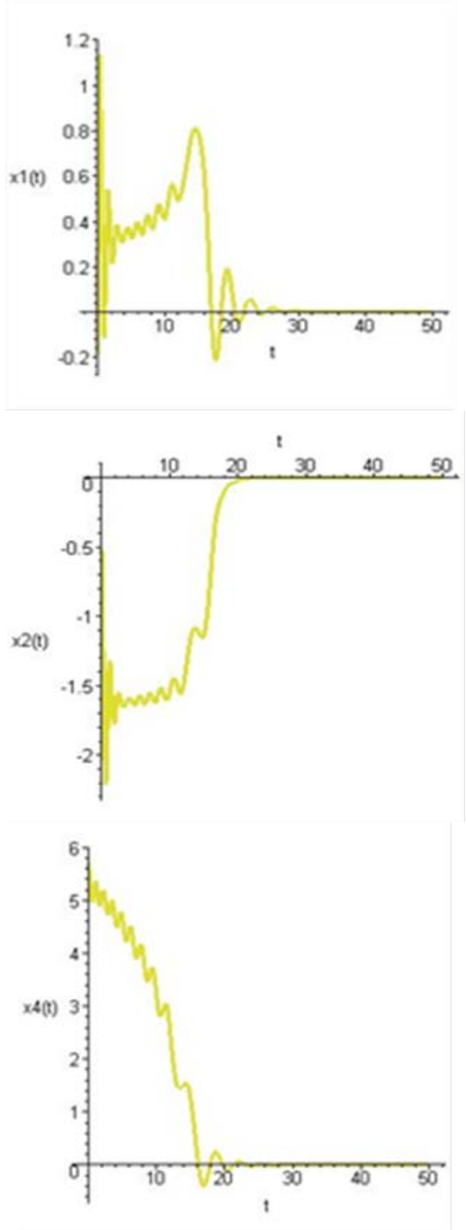

Fig.4

At these graphs we can see the some processes of synchronization with network at substantial values of initial sliding, which can achieved $S(0) = 2 \div 3$ Hz (the last graph at Fig.4) Undoubtedly, that so large values of initial sliding gives us the possibility the more simple method to connection of synchronous electric machine in power network.

4. Conclusion

The mathematical model realized by numerical-analytic method used for simplifying the equations of the transient processes at connecting a generator to power network gives the possibility more reliable (rough) method of its synchronization with power network.

References:

[1] Park R.H. Two reaction theory of synchronous machines. AIEE Trans., 1933, Pt.2, pp. 352-355

[2] Stoker J.J. Nonlinear vibrations. Interscience, N.Y., 1950

[3] Halanay A. Stability problems for synchronous machines. VII International Konferenz uber nichtlineare Schwingungen. Berlin, 1977, №5, S. 407-421

[4] Othman H.A., Lesieutre B.C., Sauer P.W. Averaging Theory in Reduced-Order Synchronous Machine Modelling. In: Proc. of 19th Annual North American Symposium, NAPS 87, Edmonton, N.Y., 1987

[5] Vazhnov A.I., Transient processes in the alternate current machines (in Russian), Leningrad, Energy, 1980

[6] Gelig A.H., Leonov G.A., Yakubovich V.A. Stability of nonlinear systems with non-unique position of equilibrium (in Russian). Leningrad, Nauka, 1977

[7] Leonov G.A., Smirnova V.B. Mathematical problems of phase synchronizations theory, St. Petersburg: Nauka, 2000

[8] Skubov D. Yu., Khodzhaev K.Sh. Non-Linear Electromachanics, Springer-Verlag Berlin, p.397, 2008

[9] Yanko-Trinitskiy A.A. New method of analysis of work of synchronous motor under sharply changing loads (in Russia), Leningrad, Gosenergoizdat, 1958

[10] Volosov V.M., Morgunov B.I. Method of averaging in theory of nonlinear systems (in Russian). Moscow, Pubishers of Moscow State University, 1971

[11] Skubov D. Yu. Bifurcation of the motions of loading electrically damping pendulum (synchronization of the electrical machine with network). Moscow, Proc. UBS, №42, p.75-99, 2014

[12] Vlasov E.N., Sablin A.D., Khodzhaev K.Sh. Equation of slow transient processes of synchronous machine. Electricity, 1980, №9, pp.41-44

[13] Skubov D.Yu., Khodzhaev K.Sh. System with electro-magnetic vibration exinguishers, Transaction of the RAS, MTT (Mechanics and Solids), 1996, №2, pp. 64-74

Authors Index

ISBN: 978-1-61804-321-4

ISBN: 978-1-61804-321-4